Erol Tutumluer
Xiaobin Chen
Yuanjie Xiao *Editors*

Advances in Environmental Vibration and Transportation Geodynamics

Proceedings of ISEV 2018

Springer

Lecture Notes in Civil Engineering

Volume 66

Lecture Notes in Civil Engineering (LNCE) publishes the latest developments in Civil Engineering—quickly, informally and in top quality. Though original research reported in proceedings and post-proceedings represents the core of LNCE, edited volumes of exceptionally high quality and interest may also be considered for publication. Volumes published in LNCE embrace all aspects and subfields of, as well as new challenges in, Civil Engineering. Topics in the series include:

- Construction and Structural Mechanics
- Building Materials
- Concrete, Steel and Timber Structures
- Geotechnical Engineering
- Earthquake Engineering
- Coastal Engineering
- Ocean and Offshore Engineering; Ships and Floating Structures
- Hydraulics, Hydrology and Water Resources Engineering
- Environmental Engineering and Sustainability
- Structural Health and Monitoring
- Surveying and Geographical Information Systems
- Indoor Environments
- Transportation and Traffic
- Risk Analysis
- Safety and Security

To submit a proposal or request further information, please contact the appropriate Springer Editor:

– Mr. Pierpaolo Riva at pierpaolo.riva@springer.com (Europe and Americas);
– Ms. Swati Meherishi at swati.meherishi@springer.com (Asia—except China—and Australia/NZ);
– Ms. Li Shen at li.shen@springer.com (China).

Indexed by Scopus and Compendex

More information about this series at http://www.springer.com/series/15087

Erol Tutumluer · Xiaobin Chen ·
Yuanjie Xiao
Editors

Advances in Environmental Vibration and Transportation Geodynamics

Proceedings of ISEV 2018

 Springer

Editors
Erol Tutumluer
Department of Civil and Environmental
Engineering
University of Illinois at Urbana-Champaign
Urbana, IL, USA

Xiaobin Chen
School of Civil Engineering
Central South University
Changsha, Hunan, China

Yuanjie Xiao
School of Civil Engineering
Central South University
Changsha, Hunan, China

Organization

Proceedings of the 8th International Symposium on Environmental Vibration and Transportation Geodynamics (ISEV 2018)
October 26–28, 2018, Changsha, China

Edited by

Erol Tutumluer, Xiaobin Chen, and Yuanjie Xiao

Organized by

Central South University, Changsha, China

Under the auspices of

The International Society for Soil Mechanics and Geotechnical Engineering (ISSMGE) Technical Committee (TC) 202 on Transportation Geotechnics

Scientific Committee

Honorary Chairmen

Hirokazu Takemiya, Okayama University, Japan
Yunmin Chen, Zhejiang University, China
Guangyun Gao, Tongji University, China
Huawu He, Chinese Academy of Engineering, China
Hongqi Tian, Central South University, China
Yeongbin Yang, Chongqing University, China
Wanming Zhai, Southwest Jiaotong University, China

ISEV 2018 Chairmen

Erol Tutumluer, University of Illinois at Urbana-Champaign, USA
Zhiwu Yu, Central South University, China

Members

Imad L. Al-Qadi, University of Illinois at Urbana-Champaign, USA
Lutz Auersch, Federal Institute for Materials Research and Testing, Germany
Dimitri E. Beskos, University of Patras, Greece
Degou Cai, Chinese Academy of Railway Sciences, China
Yuanqiang Cai, Zhejiang University, China
Jinchun Chai, Saga University, Japan
Renpeng Chen, Hunan University, China
Xiangsheng Chen, Shenzhen University, China
Xiaobin Chen, Central South University, China
António Gomes Correia, University of Minho, Portugal
Pedro Alves Costa, University of Porto, Portugal
Yujun Cui, Ecole des Ponts ParisTech, France
Geert Degrande, University of Leuven, Belgium
Qingsong Feng, East China Jiaotong University, China
Liang Gao, Beijing Jiaotong University, China
Guangyun Gao, Tongji University, China
Francisco Grajales, Technological University of Panama, Panama
Jie Han, University of Kansas, USA
Toshiki Hamamoto, University of Toyama, Japan
Hong Hao, Curtin University of Cambridge, UK
Kimitoshi Hayano, Yokohama National University
Xia He, Beijing Jiaotong University, China
Carlton Ho, University of Massachusetts, Amherst, USA
XiangChen Hou, Harbin Institute of Technology, China
Hesong Hu, Guangzhou Institute of Building Sciences, China
Baoshan Huang, University of Tennessee, USA
Linchong Huang, Sun Yat-sen University, China
Maosong Huang, Tongji University, China
Hai Huang, Pennsylvania State University, USA
Hugh Hunt, University of Cambridge, UK
Buddhima Indraratna, University of Wollongong, Australia
Tatsuya Ishikawa, Hokkaido University, Japan
Jianqun Jiang, Zhejiang University, China
Guojing Jing, Beijing Jia Tong University, China
Peerapong Jitsangiam, Chiang Mai University, Thailand

Yuanjie Xiao, Central South University, China
Weiping Xie, Wuhan University of Technology, China
Bin Xu, Nanchang Institute of Nottingham, UK
Youlin Xu, The Hong Kong Polytechnic University, HK
Jun Yang, The University of Hong Kong, HK
Yangping Yao, Beihang University, China
Jongdar Yau, Tamkang University, Taipei
Zhanping You, Michigan Technological University, USA
Jian-Hua Yin, The Hong Kong Polytechnic University, China
Hai-sui Yu, The University of Nottingham, UK
Zhiwu Yu, Central South University, China
Ma Zhanguo, Chinese Academy of Railway Sciences, China
Feng Zhang, Nagoya Institute of Technology, Japan
Nan Zhang, Beijing Jiaotong University, China
Xiong Zhang, Missouri University of Science and Technology, USA
Junhui Zhang, Changsha University of Science and Technology, China
Jianlong Zheng, Changsha University of Science and Technology, China
Shunhua Zhou, Tongji University, China
Yan Zhuang, Southeast University, China
Franz Ziegler, Vienna University of Technology, Austria

Organizing Committee

Chairmen

Chunyang Chen, Central South University, China
Youjun Xie, Central South University, China
Yan Yang, Central South University, China

Vice Chairmen

Shifan Qiao, Central South University, China
Xiaobin Chen, Central South University, China
Jinfeng Zou, Central South University, China
Zhihui Zhu, Central South University, China
Chunyan Zhao, Central South University, China

Secretary General

Yuanjie Xiao, Central South University, China

Members

Xuecheng Bian, Zhejiang University, China
Degou Cai, Chinese Academy of Railway Sciences, China
Yonggui Chen, Tongji University, China
Xiaobin Chen, Central South University, China
Hancheng Dan, Central South University, China
Yingfei Du, Central South University, China
Liang Gao, Beijing Jiaotong University, China
Zheng Han, Central South University, China
Zhongming He, Changsha University of Science and Technology, China
Hesong Hu, Guangzhou Institute of Building Sciences, China
Guoqing Jing, Beijing Jiaotong University, China
Liangxin Jin, Central South University, China
Wuming Leng, Central South University, China
Dongping Li, Central South University, China
Yuliang Lin, Central South University, China
Weizheng Liu, Central South University, China
Rusong Nie, Central South University, China
Jiandong Niu, Central South University, China
Xiaolin Song, Southwest Jiaotong University, China
Jidong Teng, Central South University, China
Peng Tu, Central South University, China
Pengcheng Wang, Chinese Academy of Railway Sciences, China
Weidong Wang, Central South University, China
Qiyun Wang, Fuzhou Institute of Technology, China
Shuying Wang, Central South University, China
Xinghua Wang, Central South University, China
Xuan Wang, Central South University, China
Limin Wei, Central South University, China
Yin Wen, Central South University, China
Junhua Xiao, Tongji University, China
Hong Xiao, Beijing Jiaotong University, China
Fang Xu, Central South University, China
Linrong Xu, Central South University, China
Changbin Yan, Zhengzhou University, China
Qi Yang, Central South University, China
Weichao Yang, Central South University, China

Sheng Zhang, Central South University, China
Xuemin Zhang, Central South University, China
Jiasheng Zhang, Central South University, China
Chunyan Zhao, Central South University, China
Lianheng Zhao, Central South University, China
Jinfeng Zou, Central South University, China

Preface

This symposium is the eighth symposium in the series initiated by late Professor H. Takemiya of Okayama University, Japan, and Academician Yunmin Chen of Zhejiang University, China, and was held in Zhejiang University, Hangzhou, China, in 2003. The subsequent six symposia were successfully convened in Okayama University, Japan (2005); National Taiwan University, Taipei (2007); Beijing Jiaotong University, China (2009); Southwest Jiaotong University, China (2011); Tongji University, China (2013); and Zhejiang University, China (2016), respectively. With the increasing impact over academia and industry, the symposia have attracted much attention from government officials, scientific and research communities, and engineering professionals. Geotechnical challenges associated with dynamic loads on railroad track and road pavements often require scientific and technological breakthroughs for design innovations. To effectively reflect such frontiers, this symposium has been renamed as International Symposium on Environmental Vibration and Transportation Geodynamics since 2016 and was held under the auspices of the International Society for Soil Mechanics and Geotechnical Engineering (ISSMGE) TC202 Transportation Geotechnics Committee.

The scope of the 8th International Symposium on Environmental Vibration and Transportation Geodynamics 2018 (ISEV 2018) continued to cover environmental vibrations induced by industrial, civilian, and transportation activities, problems associated with dynamic vehicular loading on road foundations, and sustainability challenges of transportation infrastructures and the built environment. The ISEV 2018 was organized and successfully held by Central South University in Changsha, China, on October 26–28, 2018, and attended by 499 registered delegates from 14 countries. The ISEV 2018 consisted of a workshop dedicated to the 2nd meeting of Young Transportation Geotechnics Engineers (YTGE) and plenary and breakout sessions as well as a technical exhibition for the dissemination of research findings and engineering best practices. Thirteen keynote speakers (in last name alphabetical order: Xuecheng Bian, Yujun Cui, Antonio Gomes Correia, Carlton Ho, Dingqing Li, Andrei Metrikine, William Powrie, Fumio Tatsuoka, Peter Woodward, Academician Yeong-bin Yang, Jian-Hua Yin, Academician Wanming Zhai, and Academician Jianlong Zheng) delivered speeches on topics

covering laboratory behavior of soils, pavements, railroads, bridges, field settlements, compaction, stabilization, and offshore structures. In addition, there were 29 invited presentations, 16 parallel sessions, and 55 paper presentations. The ISEV 2018 event served as a significant platform for academic exploration, experience exchange, and thought inspiration among the practitioners engaged in management, design and construction of large-scale civil and transportation infrastructure, researchers, academics, and students.

This proceedings book includes 70 paper contributions selected from 83 accepted papers submitted to the ISEV 2018 in the areas of high-speed railway geodynamics, heavy haul railway geodynamics, environmental vibration and noise control, soil dynamics and soil-structure dynamic interaction, subway/metro vibration and geodynamics, transportation geodynamics, and structural dynamics. At least two, but often three reviewers, including members of the scientific committee, subjected all submitted contributions to an exhaustive refereed peer-review procedure. Based on the reviewers' recommendations, those contributions which best suited the conference goals and objectives were chosen for inclusion in the proceedings.

We would like to thank the ISEV 2018 scientific committee members and individual reviewers for their dedication and contributions of their time and efforts to ensure the high technical quality of the accepted papers. In addition, sincere thanks are extended to all speakers for sharing their work, experience, and insight at the conference and to all authors for ensuring that final manuscripts were in accordance with English language standards and publication format requirements. Finally, we would like to gratefully acknowledge the Conference Honorary Chairmen, Chair and Co-chair of the ISEV 2018, Chair and Co-chair of the 2nd YTGE group, and organizing committee members for their help, suggestions, and contributions to the management of the symposium event.

Urbana, IL, USA   Erol Tutumluer
July 2019   Xiaobin Chen
                                                                      Yuanjie Xiao

Contents

Structural Dynamics

About the Editors

Erol Tutumluer is a Professor in the Department of Civil and Environmental Engineering, University of Illinois at Urbana-Champaign, USA. He specializes in transportation geotechnics, and has been active in transportation engineering and transportation geotechnics research, education, and practice for more than 23 years. Prof Tutumluer is a Paul F. Kent Endowed Faculty Scholar, and is a member of many professional societies. He chairs ISSMGE technical Committee 202 on Transportation Geotechnics. Prof Tutumluer has authored more than 300 peer-reviewed publications, including 150 journal papers and over 220 conference papers.

Xiaobin Chen is a Professor in the Department of Geotechnical Engineering, Central South University, China. He is a committee member of ISSMGE-TC202 Transportation Geotechnics, Committee Member of TRB (Transportation Research Board) AFP70 Mineral Aggregates, as well as Committee Member of WTC(World Transportation Conference). His research interests include Transportation Geotechnics (coarse-grained engineered materials), Engineering geological disaster, Railway embankment, Foundation protection technologies of the existing railway infrastructure, and Grouting technologies. He has authored more than 92 peer-reviewed journal papers, including 30 peer-reviewed international journal papers.

Yuanjie Xiao is an Associate Professor in Central South University's School of Civil Engineering (China). His research interests include geomechanics, soil dynamics for railway, highway, and airfield infrastructure, testing and modeling of pavement and railroad track geo-materials. He is a member of multiple professional societies, including ASCE, ISSMGE, AREMA, etc, ad serves as a reviewer for many reputed journals. He has authored more than 35 research research papers and holds 1 patent.

Environmental Vibration and Noise Control

In Situ Test and Analysis on Ground Vibration and Noise Induced by Tram Passing Small-Radius Curve Track

Deyun Ding and **Haiyuan Fang**

Abstract In order to explore the characteristics of ground vibration and noise due to tram operation, a small-radius curve section of a trial operation tram line in a city is selected as the test object, as well as a straight-line section. During the in situ test, the same tram is used to run repeatedly at different speeds, and the measured data of ground vibration and noises inside and outside the tram are obtained. The test results show that: (1) The ground vibration acceleration in the small-radius curve section is mainly concentrated between 80 and 400 Hz, and the noise is mainly between 1000 and 8000 Hz, which are both greater than those in the straight-line section. The noise inside the tram is slightly greater than that outside in the frequency band below 630 Hz in the small-radius curve section; but they exchange when it above 630 Hz. In the straight section, the noises inside and outside the tram are basically same. (2) With the increase of the train speed, there is no significant difference in ground vibration below 100 Hz, but above 100 Hz, the maximum vibration difference is between 5 and 8 dB. The maximum increase of noises inside and outside the tram is, respectively, about 6 and 2 dB(A). (3) The ground vibration acceleration level outside the curve is larger than that inside, and the maximum difference is about 15 dB, meanwhile, the noise inside the small-radius curve is greater than that outside, and the maximum difference is about 6 dB(A).

Keywords Tram · Vibration and noise · Small-radius curve track · In situ test

1 Introduction

With the speedy development of urban rail transit in China, tramway as a medium and low volume rail transit has entered a large-scale, high speed and supernormal development period [1, 2]. By the end of December 2017, 20 tramway lines in 14

D. Ding (✉) · H. Fang

Beijing Jiuzhouyigui Shock and Vibration Isolation Technology Co., Ltd., Beijing 100070, China

e-mail: dyding2301@163.com

cities or regions have been operated, and the operation mileage is up to 236.14 km. Moreover, more than 39 tramway lines with a total mileage of 620.55 km have been under construction in 22 cities or regions. In addition, according to incomplete statistics, there are more than 565 planning tramway lines in over 100 cities or regions, with a total mileage of 10,378 km.

With the improvement of people's requirement for environmental quality, the vibration and noise induced by tramway operation have attracted increasing attention in recent years [3, 4]. The tramways are built on the arterial roads in cities, which influences on the residents life in the adjacent buildings. So that influence of tramway operation cannot be ignored, especially in the small-radius curve section.

In China, the characteristics of ground vibration and noise caused by tramway passing through small radius section are poorly studied [5, 6]. Based on the in situ test, the characteristics of ground vibration and noise induced by tram operation are revealed in this paper.

2 Project Outline

A selected tram line has a length of 19.592 km and includes a total of 25 stations, and its engineering investment has reached up to 3.11 billion RMB.

The small radius of the main line is equal to 50 m. The type of the track is monolithic bed with no-sleepers, and the thickness of the track bed is 290 mm. The type of rail is 60R2 groove rail, and the elastic material packages are installed at both sides of the rail Web. The CM-A ordinary fasteners are used in the track.

The tram as shown in Fig. 1 is a kind of 100% low floor vehicle, including five modules with three bogies. The full length of the tram is 34.8 m long, and has an

Fig. 1 Trial operation of a selected tram line

axle weight of 11 tons. During the trial operation, strong vibration and noise radiation have appeared in the small-radius curve section.

3 In Situ Tests

3.1 Trial Sections

Based on the condition of the trial tram line, a typical small radius section (R = 50 m) and a typical straight-line section are adopted, as shown in Fig. 2, to test the ground vibration and the background noise and noises outside and inside the tram. Test range is within 10 m from the rail of the track.

In order to ensure the accuracy of the test data, the same tram is used to run repeatedly on the same test track. At different speeds of 8 and 13 km/h, the tram has been carried out five reciprocating tests on above-mentioned sections.

3.2 Experimental Setup

On small radius section, the accelerometers as shown in Fig. 3a were mounted in the middle of the small-radius curve, and four measurement points were numbered by VCI-1, VCI-2, VCO-1 and VCO-2, which were, respectively, placed at the distances of 1.3, 8, 1.3 and 6 m from the left and right rails, as shown in Fig. 2. On straight-line section, four measurement points were assigned by VLI-1, VLI-2, VLO-1 and VLO-2, and they were also placed at the distances of 1.3, 8, 1.3 and 6 m from the left and right rails, as shown in Fig. 2.
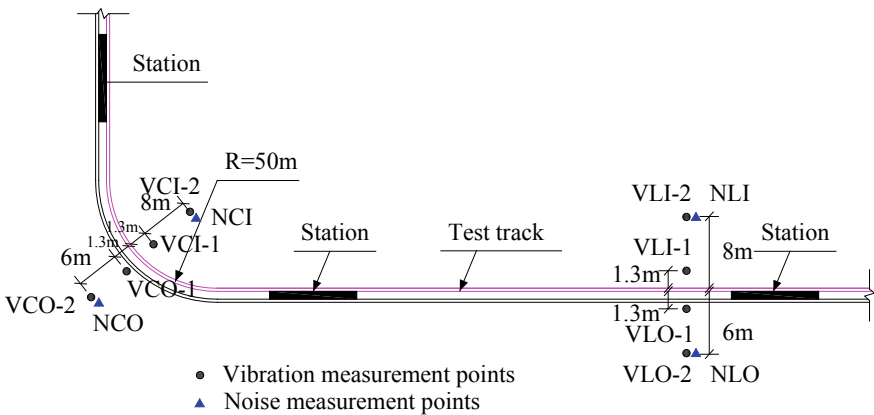
Fig. 2 Trial sections and measurement points
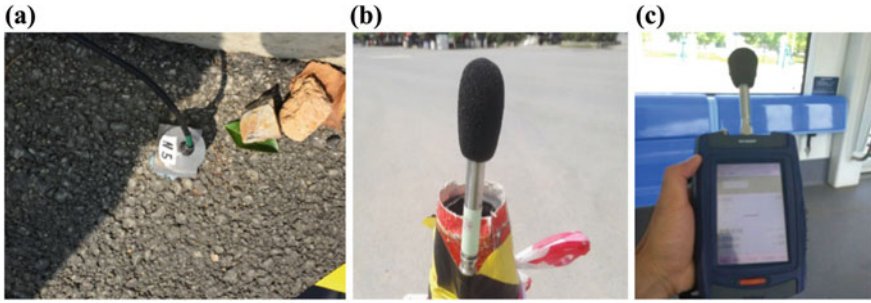
Fig. 3 Experimental set up: accelerometer (**a**), sound pressure sensor (**b**) and hand-held noise collector (**c**)

On small radius section, the sound pressure sensors were arranged in the middle of the small-radius curve, and two measurement points were numbered by NCI and NCO, which were, respectively, placed at the distances of 8 and 6 m from the left and right rails, as shown in Fig. 2. On straight-line section, two measurement points were assigned by NLI and NLO, and they were also placed at the distances of 8 and 6 m from the left and right rails, as shown in Fig. 2. The height of all sound pressure sensors as shown in Fig. 3b was 0.8 m from the ground.

A hand-held noise collector as shown in Fig. 3c was used to test the noises inside the tram. It was located in the middle of the tram, and with a height of 1.2 m from the tram ground.

3.3   Test Equipment

The ground vibration signals and noise signals outside the tram were recorded using Dynamic Data Acquisition and Analysis System made by China Orient Institute of Noise & Vibration. A high-performance hand-held noise collector was used to record the noise signals inside the tram. Some main test equipments are listed in Table 1.

4   Analysis of Test Data

4.1   Vibration Acceleration Level

The vibration acceleration level (VAL, dB) is expressed by:

Table 1 Test equipment

Name	Model type	Manufacturer
Dynamic data acquisition and analysis system	INV3020C	China Orient Institute of Noise & Vibration
Accelerometer	9828	China Orient Institute of Noise & Vibration
Accelerometer	LC0130	QUATRONIX Electronics Co., Ltd.
A high-performance hand-held noise collector	INV3080P	China Orient Institute of Noise & Vibration
Sound pressure sensor	INV9206	China Orient Institute of Noise & Vibration
Sound pressure sensor	46AE	G.R.A.S
Sound calibrator	46AB	G.R.A.S

$$\mathrm{VAL} = 20\lg\left(\frac{a}{a_0}\right) \qquad (1)$$

where a is the root mean square (RMS) of vibration acceleration, and $a_0 = 10^{-6}$ m/s^2 is the reference vibration acceleration.

Figures 4 and 5 show the relationship between ground vibration acceleration level and one-third octave center frequency in the small radius section and in the straight-line section. It can be obvious that the ground vibration acceleration in the small-radius curve section is mainly concentrated between 80 and 400 Hz. With the increase of the train speed, there is no significant difference in ground vibration below 100 Hz, but above 100 Hz, the maximum vibration difference is between 5 and 8 dB. The ground vibration acceleration level outside the curve is larger than that inside, and the maximum difference is about 15 dB.

4.2 A Sound Pressure Level

Figure 6 illustrates the one-third octave band spectrum of noises in the small radius section, considering the *A* weight calculation. It can be seen that main energy of the noise is mainly concentrated between 1000 and 8000 Hz. The noise inside the tram is slightly greater than that outside in the frequency band below 630 Hz, but they exchange when it above 630 Hz.

There are two peak points in the 1000 and 4000 Hz, respectively, and the peak value at the 4000 Hz is more prominent, which has the obvious characteristic of roaring noise. The main reason is that when the tram passes through the small-radius curve section, the frictions between the inner and outer wheels of the bogie and rails are completely inconsistent.
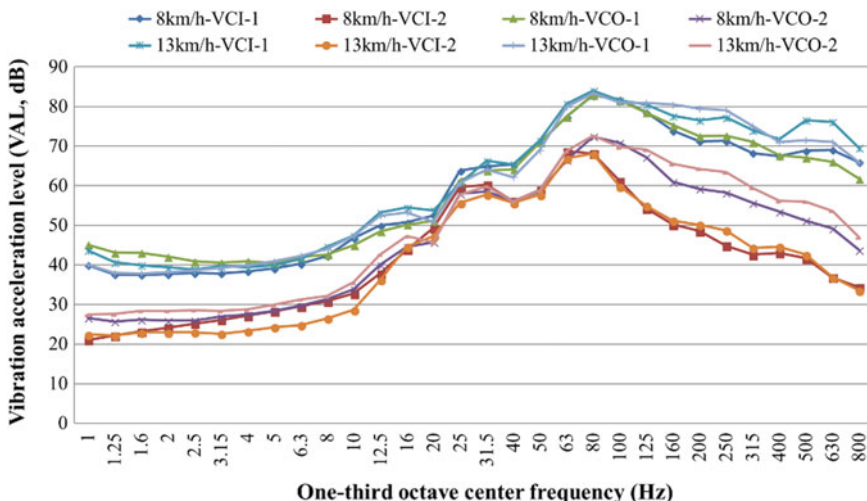
Fig. 4 Ground vibration acceleration level versus one-third octave center frequency in the small radius section
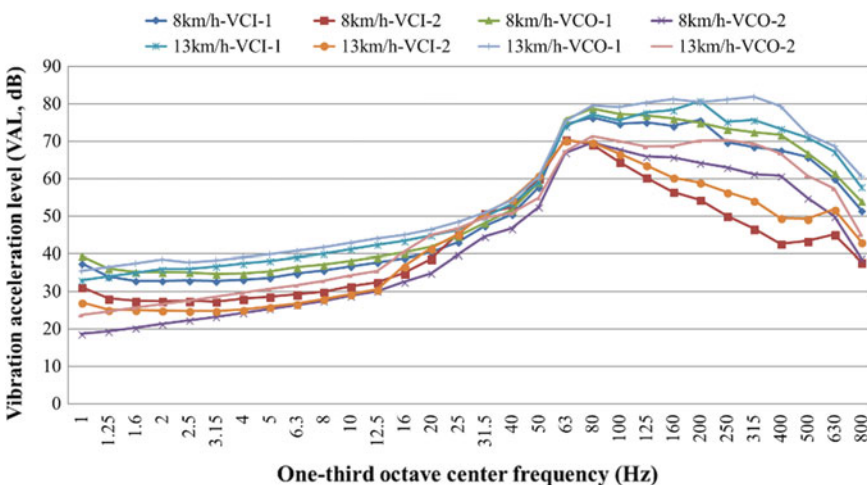
Fig. 5 Ground vibration acceleration level versus one-third octave center frequency in the straight-line section

Figure 7 shows the one-third octave band spectrum of noises in the straight-line section, considering the *A* weight calculation. In the straight-line section, the noises inside and outside the tram are basically same. Main energy of the noise is mainly concentrated between 160 and 2000 Hz.
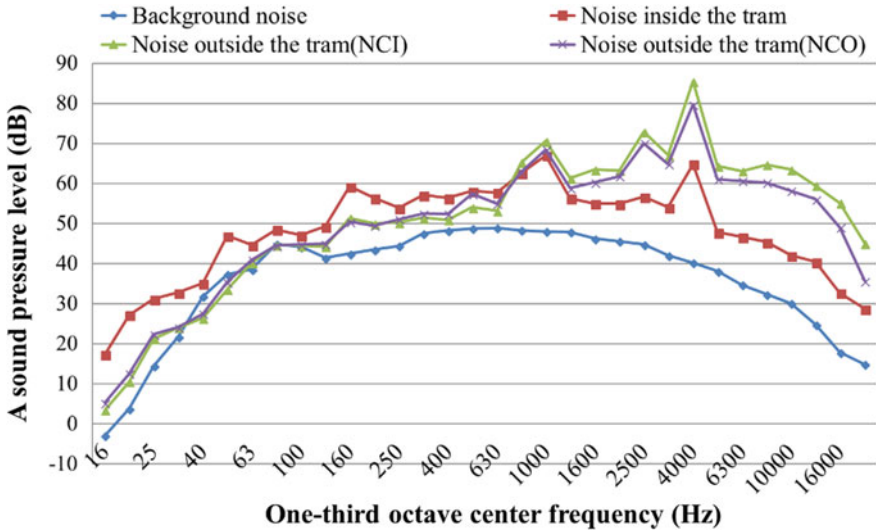
Fig. 6 One-third octave band spectrum of noises in the small radius section, considering the *A* weight calculation
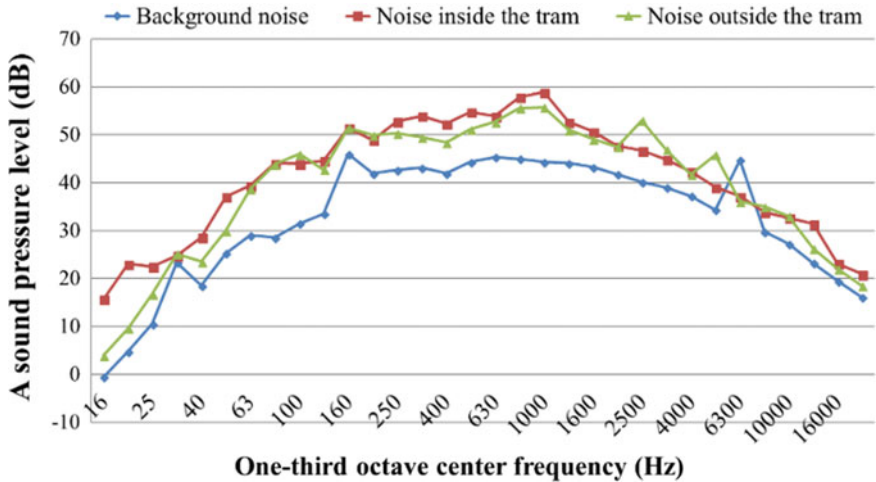
Fig. 7 One-third octave band spectrum of noises in the straight-line section, considering the *A* weight calculation

4.3 Equivalent Sound Pressure Level

Equivalent sound pressure level is defined by average energy of *A* sound pressure level at a specified time, and it is represented by L_{Aeq} and can be obtained by:

$$L_{Aeq} = 10\lg\left(\frac{1}{T}\int_0^T 10^{0.1L_A}\mathrm{d}t\right) \tag{2}$$

where L_A is instantaneous sound pressure level at t time, and T is the prescribed measurement time.

Table 2 summarizes the L_{Aeq} inside and outside the tram and L_{Aeq} of background noise. In general, the noise in small radius section is greater than that in the straight-line section. With the increase of the tram speed, the maximum increase of noises inside and outside the tram is, respectively, about 6 and 2 dB(A). The noise inside the small-radius curve is greater than that outside, and the maximum difference is about 6 dB(A).

4.4 Beyond Limit Analysis

Table 3 listed the measured value and limit value of noise at a speed of 13 km/h. It can be seen that with reference to GB 14892-2006, the limit value of noise inside the tram is 75 dB(A) [7], and there is no exceeding standard in the small radius curve section. Meanwhile, referring to the standard VDV154-2011, the maximum of noise exceeding standard inside the tram is 4.35 dB [8]. With reference to GB/T 7928-2003, the limit value of noise outside the tram is 80 dB [9], and the maximum of noise exceeding standard outside the tram is 9 dB in the small-radius curve section. Meanwhile, referring to the standard VDV154-2011, the maximum of noise exceeding standard outside the tram is 14 dB. In the straight-line section, measured values of noise are less than the limit values, in other words, they satisfy noise control requirement.

Table 2 L_{Aeq} statistics

Type	Tram speed (km/h)	NCI [dB(A)]	NCO [dB(A)]	NLI [dB(A)]	NLO [dB(A)]
Noise outside the tram	8	83.16	78.70	62.54	64.65
	13	89.00	83.84	65.68	66.65
Noise inside the tram	8	70.35		63.40	
	13	72.35		64.50	
Background noise	–	56.35		57.04	

Table 3 Comparison of measured and limit values of noise at a speed of 13 km/h

Type	Description	Noise in curve section [dB(A)]	Noise in line section [dB(A)]
Noise inside the tram	Measured value	72.35	64.65
	Limit value 75 dB(A) (GB 14892-2006)	√	√
	Limit value 68 dB(A) (VDV 154-2011)	× (4.35)	√
Noise outside the tram	Measured value	89.00	66.65
	Limit value 80 dB(A) (GB/T 7928-2003)	× (9)	√
	Limit value 75 dB(A) (VDV 154-2011)	× (14)	√

5   Conclusions

This paper summarizes important observations of ground vibration and noise measurements performed in a trial tram line with the small radius section. The following conclusions can be drawn from the present analysis.

(1) The ground vibration acceleration in the small-radius curve section is mainly concentrated between 80 and 400 Hz, and the noise is mainly between 1000 and 8000 Hz, which are both greater than those in the straight-line section. The noise inside the tram is slightly greater than that outside in the frequency band below 630 Hz in the small-radius curve section, but they exchange when it above 630 Hz. In the straight section, the noises inside and outside the tram are basically same.

(2) With the increase of the train speed, there is no significant difference in ground vibration below 100 Hz, but above 100 Hz, the maximum vibration difference is between 5 and 8 dB. The maximum increase of noises inside and outside the tram are, respectively, about 6 and 2 dB(A).

(3) The ground vibration acceleration level outside the curve is larger than that inside, and the maximum difference is about 15 dB, meanwhile, the noise inside the small-radius curve is greater than that outside, and the maximum difference is about 6 dB(A).

(4) With reference to GB 14892-2006, the limit value of noise inside the tram is 75 dB(A), and there is no exceeding standard in the small-radius curve section. Meanwhile, referring to the standard VDV154-2011, the maximum of noise exceeding standard inside the tram is 4.35 dB(A).

(5) With reference to GB/T 7928-2003, the limit value of noise outside the tram is 80 dB(A), and the maximum of noise exceeding standard outside the tram is 9 dB(A) in the small-radius curve section. Meanwhile, referring to the standard VDV154-2011, the maximum of noise exceeding standard outside the tram is 14 dB(A).

The experimental results could be regarded as a reference for developing methods to control ground vibration and noise and for adopting countermeasures.

References

1. China Association of Metros (2018) 2017 annual statistics and analysis report of urban rail transit in China. China Association of Metros News, 17
2. Modern Tram Branch of China Association of Metros (2017) Blue book of China tram
3. Esveld C (2001) Modern railway track, 2nd edn. MRT-Productions, the Netherlands
4. Ding D-Y, Liu W-N, Li K-F, Sun X-J, Liu W-F (2011) Low frequency vibration tests on a floating slab track in an underground laboratory. J Zhejiang Univ Sci A (Appl Phys Eng) 12 (5):345–359
5. Ding D, Gupta S, Liu W, Lombaert G, Degrande G (2010) Prediction of vibrations induced by trains on line 8 of Beijing metro. J Zhejiang Univ Sci A (Appl Phys Eng) 11(4):280–293
6. Jiang X (2017) Characteristics and optimization of the vibration and noise reduction of an embedded track structure for tram. Southwest Jiaotong University
7. GB 14892-2006 (2006) Noise limit and measurement for train of urban rail transit
8. VDV 154-2011 (2011) Noise from mass transit rail vehicles acc. to BOStrab
9. GB/T 7928-2003 (2003) General technical specification for metro vehicles

Research on the Influences of the Geometric Parameters of the Vibration Isolation Effect of Miniature Concrete Vibration-Isolated Piles for Rail Transit

Jing-lei Liu[ID], **Ao-yun Wang**[ID], **Chuan-qing Yu**[ID], **Qian Zhao**[ID] and **Jian Zhang**[ID]

Abstract To study the vibration isolation effect of miniature concrete vibration-isolated piles for rail transit on shallow surfaces, the evaluation parameters were set, and a model was tested to analyze different geometric parameters of vibration-isolated piles. The results show the following. When the ratio of the pile length to the wavelength is between 1.024 and 1.125, an increase in the pile length has less effect on the vibration isolation effect. When the ratio of the pile spacing to the wavelength is between 0.013 and 0.080, the vibration effect can be maintained at a good level. When the ratio of the spacing to the wavelength is greater than 0.080, the vibration isolation effect gradually decreases with an increase in the pile spacing. When the ratio of the pile section width to the wavelength is greater than 0.058, an increase in the pile section width gradually weakens the effect of the vibration isolation. Finally, when the ratio of the vibration-isolated pile section width to the pile length and the ratio between the pile spacing and the pile length are both small, vibration-isolated piles can obtain a good vibration isolation effect. Using elongated and densely arranged single-row piles can provide a good vibration isolation effect. If the location of a vibration-isolated pile is not close to the source of vibration, the pile can obtain a better vibration isolation effect. When the ratio of the vibration source distance to the pile length is in the range of 0.9–1.2, setting vibration-isolated piles at a certain distance from the vibration source can achieve a better vibration isolation effect.

J. Liu (✉) · A. Wang · C. Yu · Q. Zhao · J. Zhang
Hebei Key Laboratory of Diagnosis, Reconstruction and Anti-disaster of Civil Engineering, Zhangjiakou 075000, Hebei, China
e-mail: kingbest_1118@163.com

J. Liu · A. Wang · C. Yu · Q. Zhao · J. Zhang
School of Civil Engineering, Hebei University of Architecture, Zhangjiakou 075000, Hebei, China

1 Introduction

1.1 A Subsection Sample

As society has progressed, rail transit has greatly developed as a more rapid mode of transportation. However, when a train passes through a building or a factory, the continuous vibration adversely affects the health of humans, the building stability, and the normal use and maintenance of precision instruments [1–4]. Many scholars have conducted various degrees of research on the effect and mechanism of the isolation of various isolation measures. Kumar et al. [5] found that the propagation mode of vibration waves in soil is based on two forms of waves, i.e., physical waves and surface waves, at the same time and that 70% of the energy is carried by surface waves. In an investigation presented by Murillo et al. [6], surface waves were the primary cause of vibration in railway operation; blocking the propagation path of surface waves in the soil can effectively reduce the impact of vibration on the surrounding environment. Wang et al. [7–10] used model tests and field tests to study the vibration characteristics of the crushed rock embankment during train operation. Hou et al. [11] used ANSYS to establish a model of an empty trench and analyzed the isolated vibration effect of empty trenches. The study found that the depth of the trenches had the greatest impact on the vibration isolation effect and that a high-frequency vibration has a better vibration isolation effect for open trenches. Zhang et al. [12] proposed a numerical method that can determine the vibration law of the soil behind open trenches in high-speed railways. The analysis of the open trench depth has a significant effect on the vibration isolation effect. Woods et al. [13] proposed using open trenches as barriers to isolate vibrations. The wavelength was studied as a parameter, and the relationship between the trench depth and the wavelength of the vibration wave on the mechanism was analyzed. Liu et al. [14, 15] used an indirect boundary integration equation method to simulate vibration isolation from several rows of elastic piles; the study found that the multiple rows of piles should be adopted for low-frequency waves, but more than three rows of piles will not significantly improve the vibration isolation effect for high-frequency waves.

However, in the above study on the isolation of vibrations, the vibration isolation effect of open trenches or row piles was regarded as a single-factor analysis. Most studies focus on a comparison of the vibration isolation effects and an analysis of the influencing factors and lack multivariate analysis of the isolation mechanisms for the vibration isolation effects.

A single-row vibration-isolated pile is used as a vibration isolation barrier in this test. The pile section size, pile length, pile spacing, and other factors are taken into account, and the test result adopts the reduction ratio of the amplitude (Ar) [13] to indicate the vibration isolation effect of the miniature concrete vibration-isolated piles.

2 Field Site and Instrumentation of the Test Layout

2.1 Field Site

Considering that the nature of sand is relatively stable in this test and the test variables are easy to control, the planar dimensions of the sand foundation form a rectangle with a size of 3 m × 2 m × 1.5 m. The planar particle size of sand is less than 5.0 mm, and the moisture content of the sand is controlled from 9 to 10%. With sand layer backfilling and then consolidation, the density of the sand is controlled from 9 to 10%.

2.2 Equipment Instrumentation

The main equipment is composed of a set of control systems named WS-Z30, which consists of a data acquisition controller, a power amplifier, an electric charge amplifier, a signal generator, an accelerometer amplifier, a signal amplifier, an electromagnetic exciter, a computer, and a few accelerometers (the sensitivity is 4 pc/ms^{-2}, the frequency response is $0.2 \sim 8000$ Hz, the measurement range is 50 m/s^2, and the quality is 28.5 g). The field site and the equipment used in the experiment are shown in Figs. 1 and 2.

The pile is poured using a strength grade of C30; in this test, the pile section is designed as a square with section widths of 5, 10, and 15 cm corresponding to the
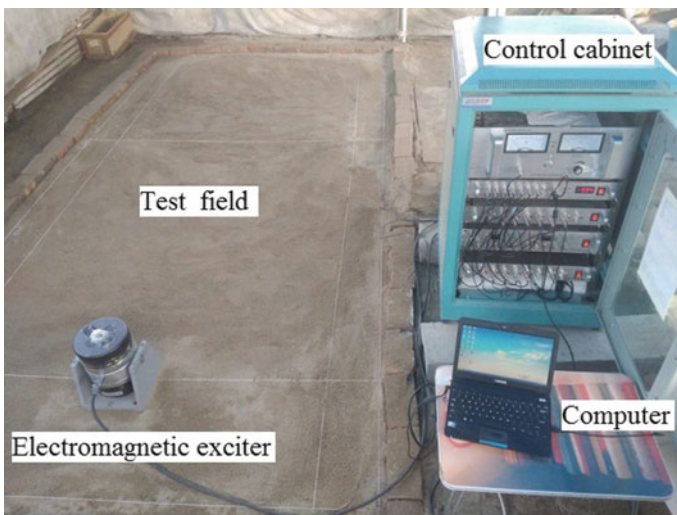
Fig. 1 Miniature concrete vibration-isolated pile and accelerometer arrangement
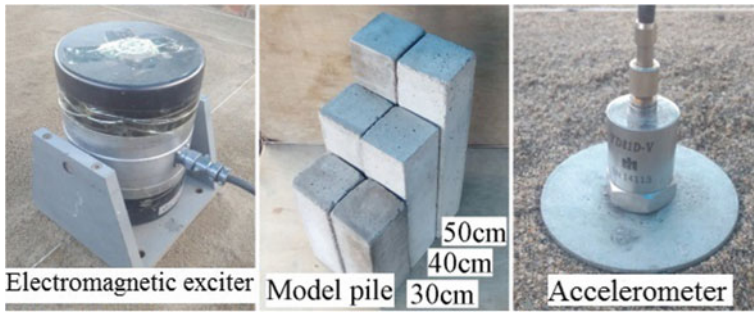
Fig. 2 Details of the test equipment

length of each section size of 30, 40, and 50 cm, respectively. There are a total of four accelerometers, and the details of the test site are shown in Fig. 3.

The excitation frequency of the exciter ranges from 10 to 150 Hz, the sampling frequency was set to 5000 times per second in the test, and the sampling time was 5 s. The charge amplifier values must be consistent in the test. The wave velocity of the excitation wave in the sand was tested in advance, and then the effect of the wavelength on the vibration isolation effect of single-row pile was analyzed.

Fig. 3 Vibration-isolated pile and acceleration sensor arrangement
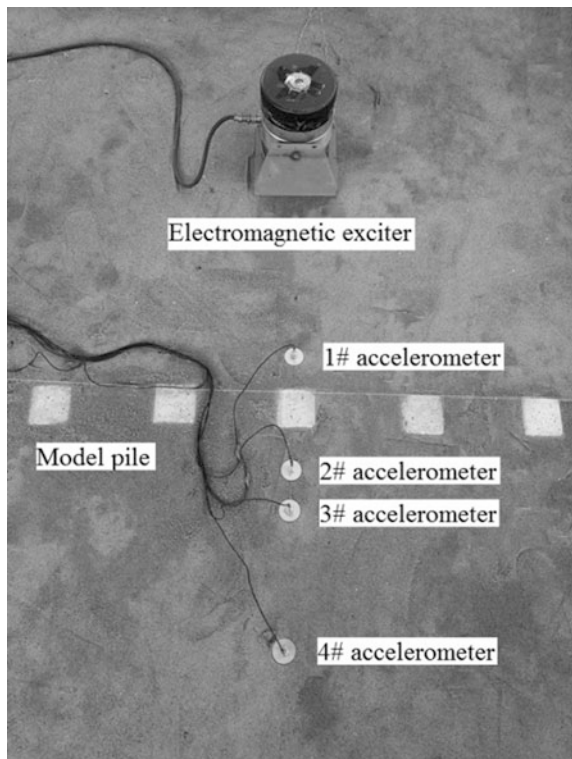
3 Determination of the Wave Velocity of a Soil Layer

3.1 Test Planning

This paper proposes a test method (spectral analysis of surface waves, SASW) [16, 17] to determine the wave velocity. The equipment layout that is involved is shown in Fig. 4.

Under the effect of the pulse load of the exciter, signal 1 and signal 2 were collected by the #1 accelerometer and the #2 accelerometer, respectively, and then a spectrum diagraph was obtained. Then, SASW is used to obtain the coherence function and the reciprocal power spectra of the two signals; if the coherence function value at a certain frequency exceeds the threshold value of 0.85 [16], these two signals have a significant correlation. Then, the reciprocal power spectra are used to determine the corresponding phase difference φ. Finally, the wave velocity definition is shown in Eq. (1).

$$V_R = 360 \cdot f \cdot x / \varphi \tag{1}$$

Fig. 4 Layout diagram of the test equipment
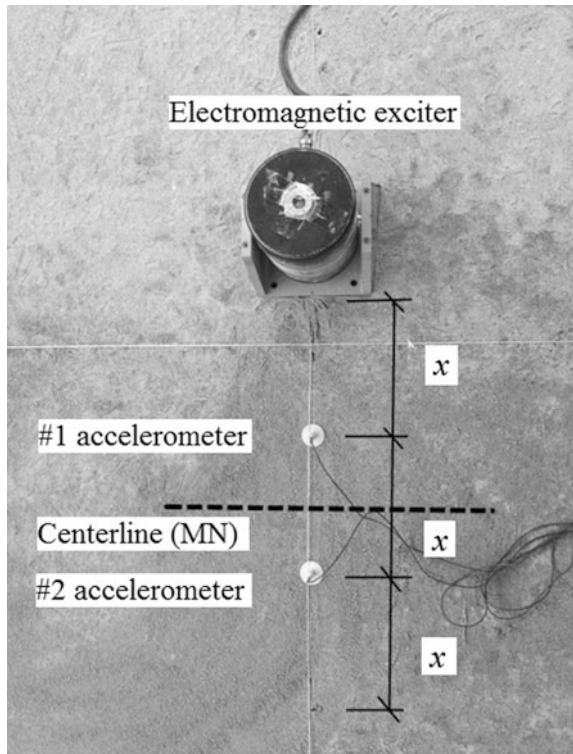
where V_R denotes the wave velocity, f denotes the excitation frequency, x denotes the distance between the #1 accelerometer and the #2 accelerometer, and φ denotes the phase difference.

The corresponding wavelength is defined as Eq. (2).

$$L_R = 360 \cdot x/\varphi \tag{2}$$

In the test, the consideration of the frequency of the source and the pile spacing mostly depends on the depth of the soil being tested [17]. Therefore, when measuring the shallow wave velocity (V_R), the vibration source is dominated by high frequencies, and the test signal is excited 4 times. The spacing (x) is in turn taken from Table 1. The forward test direction is defined as being from the #1 accelerometer to the #2 accelerometer. After the forward test is finished, the position of the accelerometer is not changed, the exciter is moved symmetrically to the other side of the centerline (MN), and then the above operation is repeated in the backward. The testing conditions are shown in Table 1.

3.2 Data Processing

Taking testing condition 5 from Table 1 as an example, the exciter is arranged on the right side of the centerline (MN). The coherence function to analyze the measured signals, i.e., signal 1 and signal 2, and the coherent coefficient corresponding to the excitation frequency of 150 Hz from the derived frequency-domain files are screened. The coherence function is shown in Fig. 5.

The value of 0.956 marked in Fig. 5 represents the coherence coefficient value of the corresponding signal when the excitation wave propagates from the #1 accelerometer to the #2 accelerometer under testing condition 5. The requirement that the coherence coefficient value is greater than 0.85 is satisfied [16]; then, the phase difference φ was found using the method of the cross-power spectrum. The cross-power spectrum is shown in Fig. 6.

Table 1 Testing conditions of the wave velocity test

Testing conditions	Frequency f (Hz)	Spacing x (cm)	Test direction
1	140	30	Forward
2	140	30	Forward
3	140	40	Forward
4	140	40	Forward
5	150	30	Backward
6	150	30	Backward
7	150	40	Backward
8	150	40	Backward
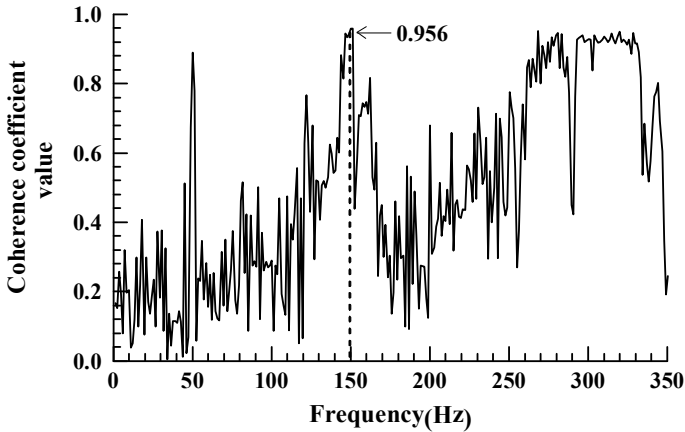
Fig. 5 Coherent function of testing condition 5
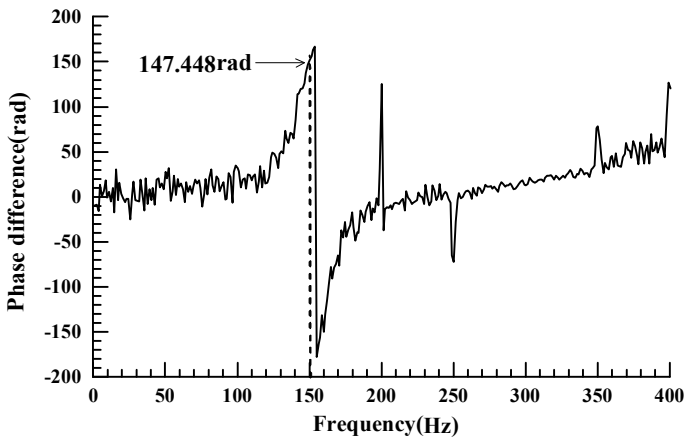
Fig. 6 Reciprocal power spectrum of testing condition 5

The value of 146.457 rad marked in Fig. 6 represents the phase difference (φ) value of the corresponding signal when the excitation wave propagates from the #1 accelerometer to the #2 accelerometer under testing condition 5.

Using the same method for the remaining conditions in Table 1, the arithmetic mean of the test results is taken in both directions as the measured wave velocities on the surface of the soil. The wave velocities are shown in Table 2.

After averaging the wave velocities (V_R) that were measured at each operating condition, the arithmetic mean was 109.989 m/s.

Table 2 Results of the wave velocity test

Testing conditions	Coherence value	Phase difference φ (rad)	Wave velocity V_R (m/s)	Arithmetic mean (m/s)
1	0.956	147.448	109.870	109.989
2	0.988	146.669	110.453	
3	0.976	147.748	109.646	
4	0.964	145.993	110.964	
5	0.975	247.443	109.116	
6	0.972	245.716	109.883	
7	0.968	248.187	108.789	
8	0.976	242.83	110.189	

4   Size Optimization of a Single Factor

4.1   Single-Factor Data Processing

The reduction ratio of the amplitude (Ar) is adopted to indicate the vibration isolation effect of a single-row vibration-isolated pile. A smaller Ar indicates that the vibration isolation effect of single-row piles is better [13].

The Ar is defined as in Eq. (3).

$$Ar = a_1/a_o \tag{3}$$

where a_1 denotes the vertical vibration acceleration of the ground after setting a single-row vibration-isolated pile and a_o denotes the vertical vibration acceleration of the free field that is excited in the same position.

The influences on the vibration isolation effect of the length of the pile (L), the size of the pile section ($B \times B$), the pile spacing (s), the distance from the vibration source (r), and the wavelength (L_R) are investigated. The following parameters are introduced to evaluate the effects of vibration isolation and are used as a measure of the vibration isolation effect of the vibration-isolated piles.

(1) **Depth parameter D**

The ratio D between the length (L) of the pile and the wavelength (L_R) represents the effect of different lengths of the piles on the vibration isolation effect of the vibration-isolated piles. The formula is shown in Eq. (4).

$$D = L/L_R \tag{4}$$

(2) **Width parameter W**

The ratio W between the width (B) of the pile and the wavelength (L_R) represents the influence of the different widths of the piles on the vibration isolation effect of the vibration-isolated piles. The formula is shown in Eq. (5).

$$W = B/L_R \tag{5}$$

(3) **Pile spacing parameter S**

The ratio S between the pile spacing (s) and the wavelength (L_R) indicates the influence of the density of the pile arrangement on the isolation effect of the vibration-isolated piles. The formula is shown in Eq. (6).

$$S = s/L_R \tag{6}$$

(4) **Vibration source distance parameter K**

The ratio K between the distance from the vibration source (r) and the wavelength (L_R) indicates the influence of the distance from the vibration-isolated pile to the vibration source on the vibration-isolated effect of the piles. The formula is shown in Eq. (7).

$$K = r/L_R \tag{7}$$

4.2   Influence of the Depth Parameter on the Vibration Isolation Effect of Piles

The length of the pile is the main factor that influences the vibration isolation effect [18]. First, the distance from the vibration source (r), the width of the pile section (B), and the pile spacing (s) were controlled. The effects of the pile length (L) on the vibration isolation of the pile were studied separately; the test arrangement is shown in Table 3.

The excitation frequency of the exciter ranges from 10 to 150 Hz; 10 Hz is used as the step length for gradual excitations. After the discrete data are removed, the remaining data are fitted using MATLAB. Under certain conditions, the regression

Table 3 Test arrangement of the parameter D

Testing conditions	Distance from the vibration source r (cm)	Section width of piles φ (cm)	Pile spacing s (cm)
1	60	15	10
2	50	10	10
3	35	5	10

Table 4 Correlation analysis for D and Ar

Category	Testing condition 1	Testing condition 2	Testing condition 3
Regression equation	$Ar = 0.069D^{-1.334}$	$Ar = 0.068D^{-1.413}$	$Ar = 0.065D^{-1.406}$
Degree of freedom (f)	40	42	39
Significance level (α)	0.05	0.05	0.05
Correlation coefficient (R)	0.9672	0.9465	0.9266
Critical value ($R_{\alpha,f}$)	0.3044	0.2973	0.3081
F	4.9531	4.3524	4.5426
F_α	4.0800	4.0720	4.0980

equations of the depth parameter (D) and the Ar are shown in Table 4. Significance tests on the regression equation were calculated to verify the correlations between the variables. The correlation coefficient R and the F value were derived using MATLAB. The correlation coefficient R and the F value are used to judge the statistical significance of the regression equation; if the correlation coefficient R is greater than the critical value $R_{\alpha,f}$ and closer to 1 and if the F value is greater than the critical value F_α, the regression equation is more obvious and the fitting is better. The $R_{\alpha,f}$ and F_α values of each testing condition are identified by using the tables of correlation coefficient critical values [19] and the F distribution table [19], as shown in Table 4.

Under testing conditions 1, 2, and 3, the correlation coefficient R is greater than the critical value of $R_{\alpha,f}$, and the value of F is greater than the value of F_α from Table 4. The results show that the regression equation is significant in each testing condition; thus, the regression equation is meaningful and can be accepted.

The fitting graph of the regression equation for various testing conditions is shown in Fig. 7.

Figure 7 shows D rapidly increasing from approximately 0.18 to 0.8 and the value of Ar decreasing rapidly. When D increasing to approximately 0.8, the change in Ar tends to flatten gradually, and when D is in the approximate range of 1.042–1.125, the slope of the fitting curve is approximately $Ar' \approx 0$. When the length of the pile (L) increases, the change in Ar tends to be stable. When the length of the pile (L) continues to increase, the influence of the vibration isolation effect will be weakened. Under the conditions of controlling other influencing factors, $D = 1.042$ can be used as the limiting range of the length of the effective pile body.

4.3 Influence of the Pile Spacing Parameter on the Vibration Isolation Effect of Piles

The distance between the nearest edges of adjacent piles obviously influences the vibration isolation effect of the vibration-isolated pile. According to the
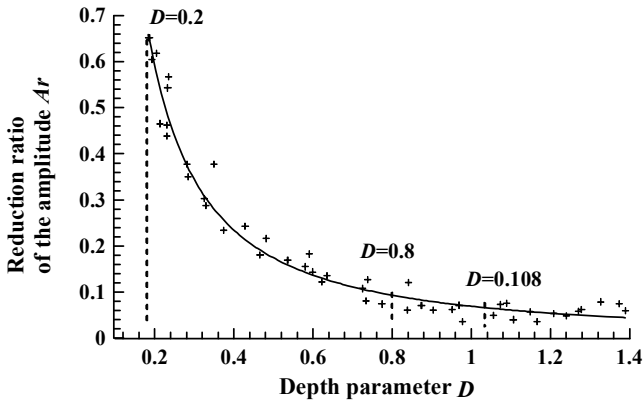
(a) Fitting curve of D and Ar under testing condition 1
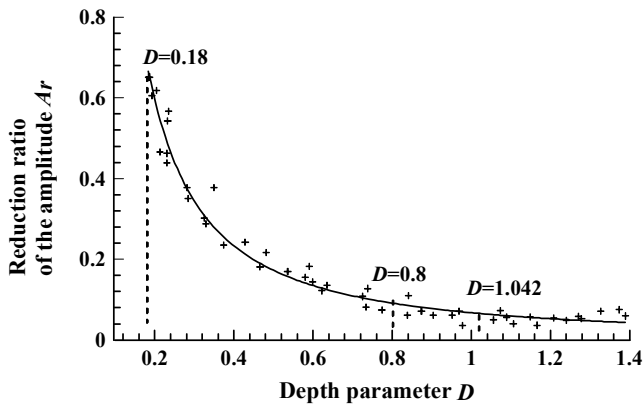
(b) Fitting curve of D and Ar under working condition 2
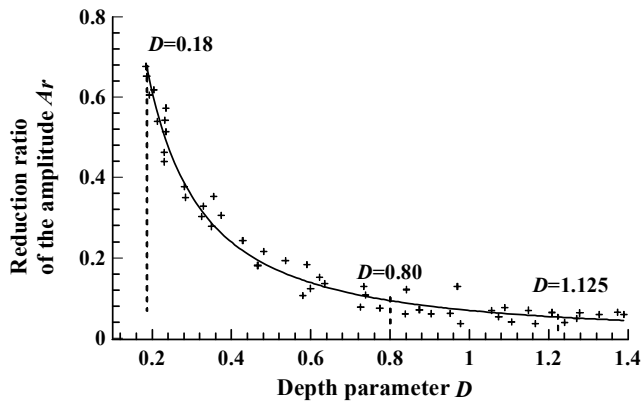
(c) Fitting curve of D and Ar under testing condition 3.

Fig. 7 Fitting curve of D and Ar

Table 5 Test arrangement of the parameter S

Testing conditions	Distance from the vibration source r (cm)	Section width of piles B (cm)	Pile of the length L (cm)
1	60	15	50
2	50	10	50
3	35	5	50

Table 6 Correlation analysis of S and Ar

Category	Testing condition 1	Testing condition 2	Testing condition 3
Regression equation	$Ar = 0.119 - 1.071S + 9.029S^2$	$Ar = 0.118 - 1.257S + 8.906S^2$	$Ar = 0.093 - 0.936S + 9.015S^2$
Degree of freedom (f)	38	41	40
Significance level (α)	0.05	0.05	0.05
Correlation coefficient (R)	0.9412	0.9532	0.9715
Critical value ($R_{\alpha,f}$)	0.3120	0.3008	0.3044
F	4.5143	4.6462	4.6523
F_α	4.098	4.076	4.080

optimization method of controlling other variables, the pile spacing parameter S is processed. The specific testing conditions are shown in Table 5.

The excitation method of the parameter S is the same as the parameter D in the test arrangement. Additionally, the discrete data are removed, and then the remaining data are fitted. Under certain conditions, the regression equations of the parameter S and the Ar are shown in Table 6. Statistical significance of the test is shown in Table 6.

Table 6 shows that the correlation coefficient R is greater than the critical value of $R_{\alpha,f}$ and that the F values are greater than the value of F_α. These results show that the regression equation is significant in each testing condition; thus, the regression equation is meaningful and can be accepted.

The fitting graphs of the regression equations for the various testing conditions are shown in Fig. 8.

Figure 8 shows that when S is increasing from approximately 0.013 to 0.0804, the value of Ar changes slowly and sustains a lower level, demonstrating that a single-row pile can obtain a better vibration isolation effect. After S increases to approximately 0.0804, the change in Ar tends to grow rapidly, and then the vibration isolation effect decreases gradually. Under the conditions of controlling other influencing factors, the pile spacing (s) can be maintained at a lower level ($S = 0.013$), while the better vibration isolation effect can be obtained.
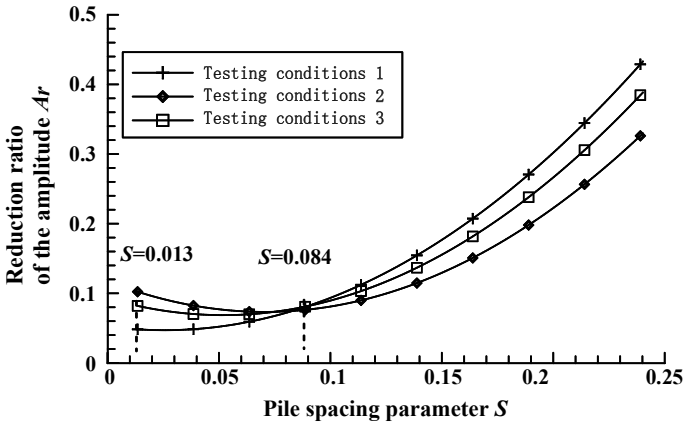
Fig. 8 Fitting curve of S and Ar

4.4 Influence of the Width Parameter on the Vibration Isolation Effect of Piles

The influence of the width parameter (W) on the vibration isolation of vibration-isolated piles is studied; the test arrangement is shown in Table 7.

The excitation method of the parameter W is the same as the parameter D in the test arrangement. Additionally, the discrete data are removed, and then the remaining data are fitted. Under certain conditions, the regression equations of the parameter W and the Ar are shown in Table 8. The statistical significance of the test is shown in Table 8.

Table 8 shows that the correlation coefficient R is greater than the critical value of $R_{\alpha,f}$ and that the F values are greater than the value of F_{α}. The results show that the regression equation is significant in each testing condition; thus, the regression equation is meaningful and can be accepted.

The fitting graphs of the regression equations for the various testing conditions are shown in Fig. 9.

Figure 9 shows that when W is increasing from approximately 0.004 to 0.058, the value of Ar increases rapidly. Additionally, the vibration isolation effect is weakened rapidly. W increases to approximately 0.058, and with an increase in W, the change in

Table 7 Test arrangement of the parameter W

Testing conditions	Distance from the vibration source r (cm)	Pile length L (cm)	Pile spacing s (cm)
1	60	50	10
2	50	40	10
3	35	30	10

Table 8 Correlation analysis of W and Ar

Category	Testing condition 1	Testing condition 2	Testing condition 3
Regression equation	$Ar = 0.689\ W^{0.106}$	$Ar = 0.694\ W^{0.1562}$	$Ar = 0.632\ W^{0.166}$
Degree of freedom (f)	37	40	41
Significance level (α)	0.05	0.05	0.05
Correlation coefficient (R)	0.9345	0.9563	0.9641
Critical value ($R_{\alpha,f}$)	0.3160	0.3044	0.3008
F	4.2351	4.5474	4.3542
F_α	4.107	4.08	4.076
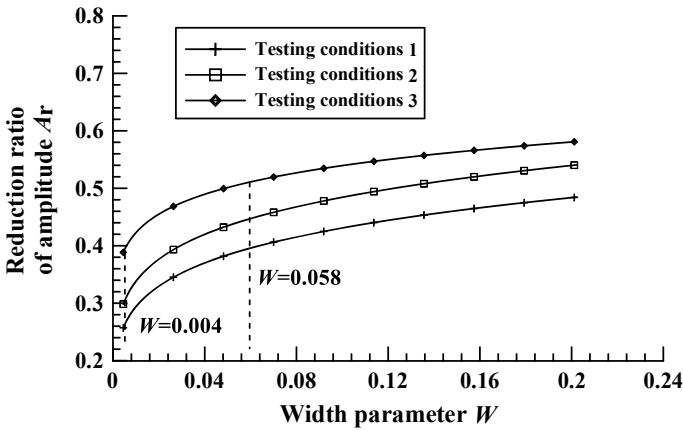
Fig. 9 Fitting curve of W and Ar

Ar tends to gradually shallow. In other words, with an increase in the width of a square pile, the change in the vibration isolation effect is not significant. This is similar to the conclusion of Hou En-ping's [18] study that a single-row vibration-isolated pile section size change has no significant influence on the vibration isolation effect. When the vibration-isolated pile is practically engineered, choosing a reasonable section size of vibration-isolated pile is of guiding significance.

4.5 Influence of the Vibration Source Distance Parameter on the Vibration Isolation Effect of Piles

When a vibration wave is transmitted over a distance and the energy of the wave is consumed continuously, it is advantageous to improve the vibration isolation effect

Table 9 Test arrangement of the parameter K

Testing conditions	Section width of piles B (cm)	Pile length L (cm)	Pile spacing s (cm)
1	15	50	10
2	10	40	10
3	5	30	10

Table 10 Correlation analysis of K and Ar

Category	Testing condition 1	Testing condition 2	Testing condition 3
Regression equation	$Ar = 0.409 - 0.742K + 1.221K^2$	$Ar = 0.375 - 0.992K + 1.463K^2$	$Ar = 0.449 - 0.720K + 1.213K^2$
Degree of freedom (f)	40	41	39
Significance level (α)	0.05	0.05	0.05
Correlation coefficient (R)	0.9561	0.9436	0.9674
Critical value ($R_{\alpha,f}$)	0.3044	0.3008	0.3081
F	4.1124	4.3513	4.8521
F_α	4.08	4.076	4.08

by arranging the positions of the vibration-isolated piles rationally. The specific testing conditions are shown in Table 9.

The excitation method of the parameter K is the same as the parameter D in the test arrangement. Additionally, the discrete data are removed, and then the remaining data are fitted. Under certain conditions, the regression equations of K and Ar are shown in Table 10. The statistical significance of the test is shown in Table 10.

Table 10 shows that the correlation coefficient R is greater than the critical value of $R_{\alpha,f}$ and that the F values are greater than the value of F_α. The results show that the regression equation is significant in each testing condition; thus, the regression equation is meaningful and can be accepted. The fitting graphs of the regression equations for the various testing conditions are shown in Fig. 10.

Figure 10 shows that when K rapidly increases from approximately 0.031 to 0.291, the value of Ar shows a decreasing phenomenon, and when K increases in the approximate range from 0.291 to 0.357, regions of minima occur, and the vibration isolation effect is relatively excellent. When K increases to approximately 0.357, the change in Ar tends to increase gradually. Under the conditions of controlling other influencing factors, K values between 0.291 and 0.357 can be used as a reference index for determining the reasonable positions of vibration-isolated pile.
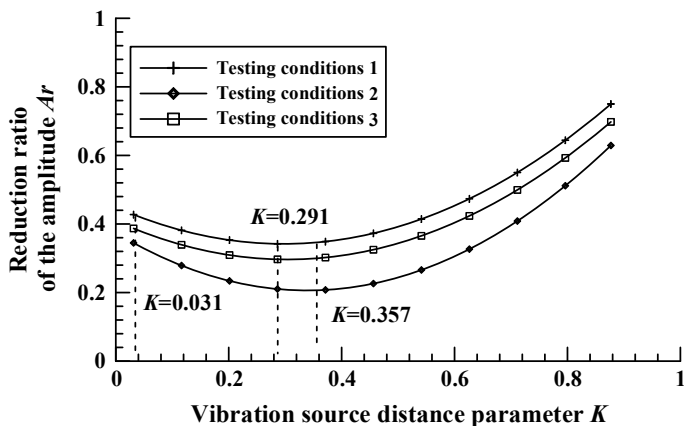
Fig. 10 Fitting curve of K and Ar

5 Size Optimization of Two Factors

5.1 Two-Factor Data Processing

In single-factor analysis, the influences of the pile length (L), the pile cross-sectional size ($B \times B$), the pile spacing (s), and the vibration source distance (r) on the vibration isolation effect of the single-row pile are analyzed individually. The influence of the pile length (L) on the vibration isolation effect is the most obvious.

Therefore, the parameters of the two-factor analysis are introduced into the length of the pile using the single-factor analysis results of the reasonable pile length (L) range and are then used to define the reasonable range of the section width (B), the pile spacing (s), and the vibration source distance (r).

The setting parameters are as follows:

(1) **Slenderness ratio δ**

The ratio δ between the section width (B) and the length of the pile (L) represents the degree of elongation of the pile. The formula is shown in Eq. (8).

$$\delta = B/L \tag{8}$$

(2) **Relative spacing of piles β**

The ratio β between the pile spacing (s) and the length of the pile (L) represents the single-row piles' layout density. The formula is shown in Eq. (9).

$$\beta = s/L \tag{9}$$

(3) **Relative vibration source distance γ**

The ratio γ between the distance from the vibration source (r) and the length of the pile (L) represents the position of a single-row pile relative to the vibration source. The formula is shown in Eq. (10).

$$\gamma = r/L \tag{10}$$

5.2 Influence of the Slenderness Ratio δ on the Vibration Isolation Effect of the Piles

The vibration isolation effect of the pile width and the length of the pile were studied by preparing a test group and a control group, respectively. The test results of the experimental group were validated by the test results of the control groups. The specific testing conditions are shown in Table 11.

In the test and control groups, the section width of the pile was 5, 10, or 15 cm corresponding to a length of each section size of 30, 40, and 50 cm, respectively; the ratio δ has nine kinds of values. Vibration frequencies of 10, 50, and 100 Hz were selected, and then the vibration frequencies were tested. The vibration isolation effect of each testing condition was compared. The results of the test are shown in Figs. 11 and 12.

Figure 11 shows that the corresponding graphs of the two groups show a similar trend. When δ is between 0.1 and 0.2, corresponding value of Ar changes gently. When δ is greater than 0.2, the value of Ar increases rapidly with the δ. For each high, medium, and low frequency, the rule is consistent insomuch that the value of Ar increases with δ, showing a smooth change in a certain interval and then an increasing phenomenon.

Figure 12 shows that the change laws of the corresponding figures in the test and control groups are consistent with those of the two groups.

Using both Figs. 11 and 12 and further analyzing the test results, it is found that when the size of the pile has a smaller δ for a vibration-isolated piles, it can obtain a

Table 11 Test arrangement of the parameter δ

| Testing conditions | Test group | | Testing conditions | Control group | |
	Pile spacing s (cm)	Distance from the vibration source r (cm)		Pile spacing s (cm)	Distance from the vibration source r (cm)
1	10	50	3	15	50
2	10	60	4	15	60
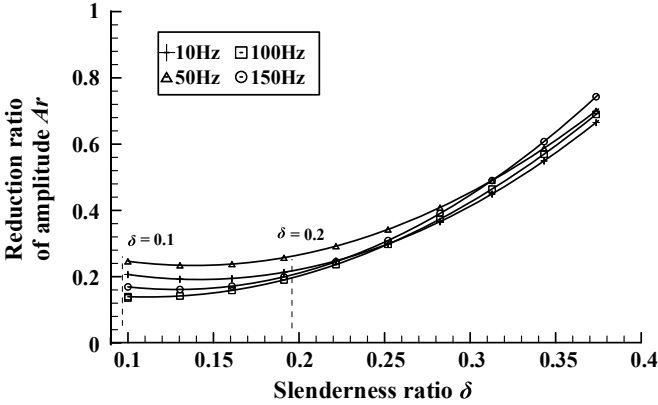
(a) Changing relation between *Ar* and *δ* for testing condition 1
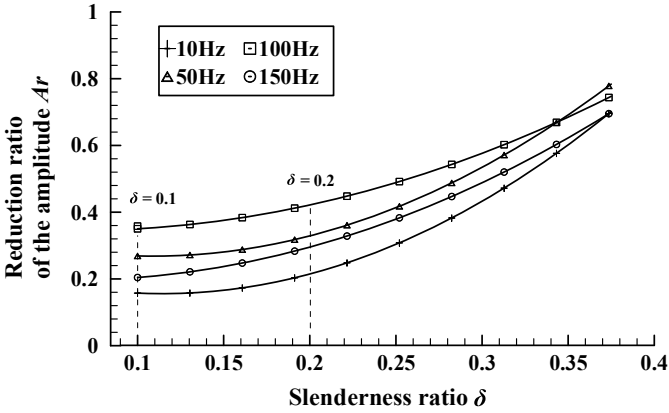
(b) Changing relation between *Ar* and *δ* for testing condition 2

Fig. 11 Changing relation between *Ar* and *δ* in the experimental group

better vibration isolation effect; when the size of the vibration-isolated pile is less than *δ*, the vibration isolation effect of a vibration-isolated pile is weakened. The vibration isolation effect of the vibration-isolated pile is maintained at a good level when *δ* is kept between 0.1 and 0.2.

5.3 Influence of the Relative Spacing of the Piles *β* on the Vibration Isolation Effect of the Piles

The relative spacing of the pile (*β*) reflects the influence of the density of the vibration-isolated piles on the vibration isolation effect. To study the relationship
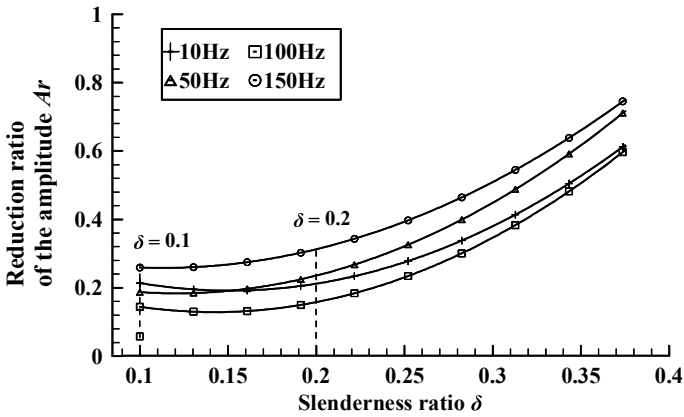
(a) Changing relation between *Ar* and *δ* for testing condition 3
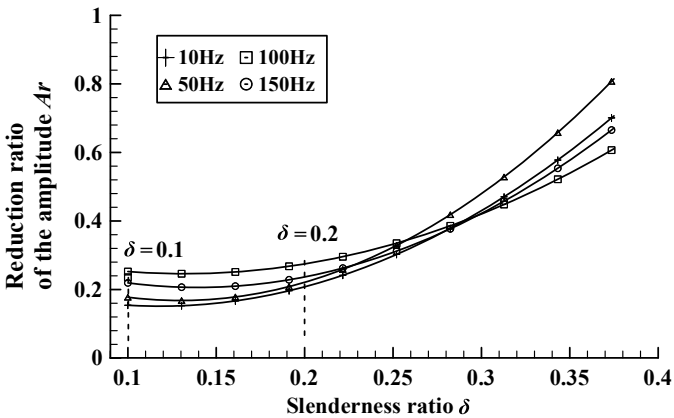
(b) Changing relation between *Ar* and *δ* for testing condition 4

Fig. 12 Changing relation between *Ar* and *δ* in the control group

between *β* and *Ar*, the test group and control group were prepared; the test arrangement is shown in Table 12.

The specifications of the vibration-isolated pile and the excitation frequencies used in the test are the same as the arrangement of the *δ* test, and the test results are shown in Figs. 13 and 14.

Figure 13 shows that the corresponding figures of the two group testing conditions show a similar trend in the two group testing conditions for the test group. For each of the high, medium, and low excitation frequencies in the figure, the value of *Ar* increases rapidly with an increase in *β*.

Figure 14 shows that the change laws of the corresponding figures in the test and control groups are consistent with those of the two groups.

Table 12 Test arrangement of the parameter β

Testing conditions	Test group		Testing conditions	Control group	
	Section width B (cm)	Distance from the vibration source r (cm)		Section width B (cm)	Distance from the vibration source r (cm)
1	10	50	3	15	50
2	10	60	4	15	60

(a) Changing relation between Ar and β for testing condition 1

(b) Changing relation between Ar and β for testing condition 2

Fig. 13 Changing relation between Ar and β for the experimental group
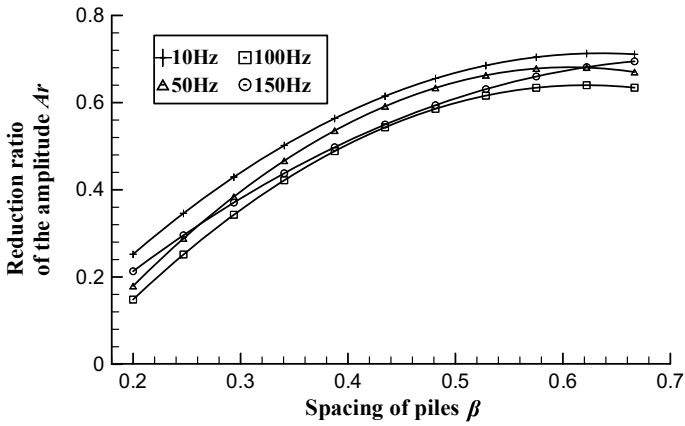
(a) Changing relation between *Ar* and *β* for testing condition 3
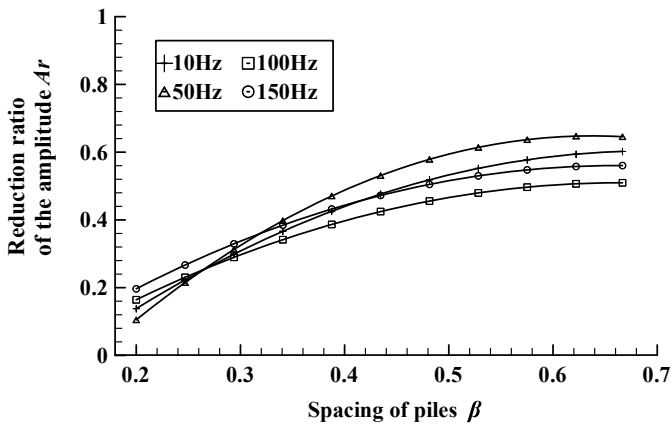
(b) Changing relation between *Ar* and *β* for testing condition 4

Fig. 14 Changing relation between *Ar* and *β* for the control group

Using both Figs. 13 and 14, it is found that when *β* is small, the single-row pile has a better isolation effect when adopting a long pile and a dense arrangement; when *β* is large, the isolation effect of the vibration-isolated pile will weaken when a sparse arrangement of short piles is used.

Table 13 Test arrangement of the parameter γ

Testing conditions	Test group		Testing conditions	Control group	
	Section width B (cm)	Pile spacing s (cm)		Section width B (cm)	Pile spacing s (cm)
1	10	10	3	15	10
2	10	15	4	15	15

5.4   Influence of the Relative Vibration Source Distance γ on the Vibration Isolation Effect of the Piles

The relative vibration source (γ) reflects the influence of the arranged positions of vibration-isolated piles on the vibration isolation effect. The test group and control group were prepared to study the relationship between γ and Ar; the test arrangement is shown in Table 13.

The specifications of the vibration-isolated pile and the excitation frequencies used in the test are the same as those in the arrangement of the δ test; the test results are shown in Figs. 15 and 16.

Figure 15 shows that the corresponding figures of two group testing conditions show similar trends in the two group testing conditions for the test group. For each of the high, medium, and low excitation frequencies in the figure, γ rapidly grows from approximately 0.7 to 0.9, and the value of Ar decreases gradually with an increase in γ. When γ increases from approximately 0.9 to 1.2, regional minima are presented, and when γ increases to approximately 1.2, with an increase in γ, the change in Ar tends to increase gradually.

Figure 16 shows that the change laws of the corresponding figures in the test and control groups are consistent with those of the two groups.

Using both Figs. 15 and 16, it is found that if the position of the vibration-isolated pile is not closer to the vibration sources, a better vibration isolation effect can be obtained by a vibration-isolated pile. However, when the layout of the vibration-isolated pile satisfies the requirement that the γ reaches the range of 0.9–1.2, it can obtain a better vibration isolation effect.
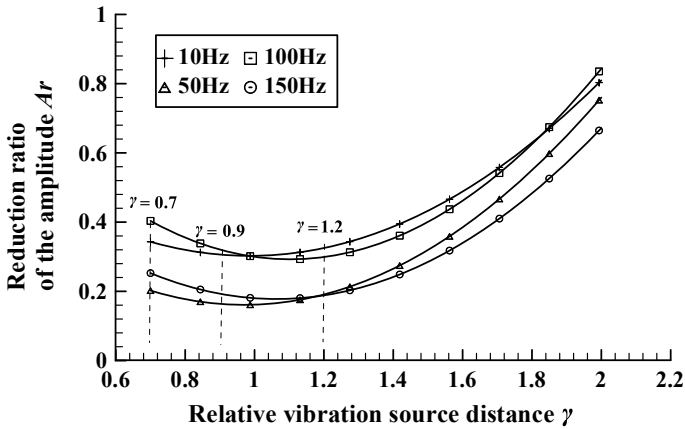
(a) Changing relation between Ar and γ for testing condition 1
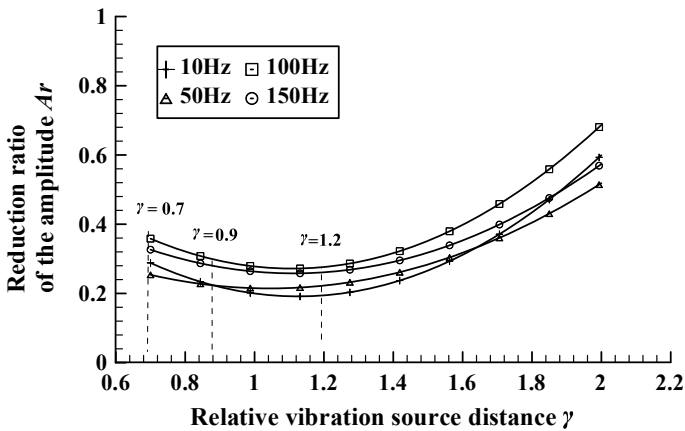
(b) Changing relation between Ar and γ for testing condition 2

Fig. 15 Changing relation between Ar and γ for the experimental group

6 Conclusions

To study each of the factors that affect the vibration isolation effect of a concrete vibration-isolated pile, single-factor analysis and two-factor analysis methods are applied on model tests while considering the length of the pile and the pile cross section; the following conclusions are obtained:

(1) When D increases to approximately 1.042–1.125, the change in Ar tends to become stable with an increase in the length of the pile (L). When the length of the pile (L) continues to increase, the enhancement of the vibration isolation
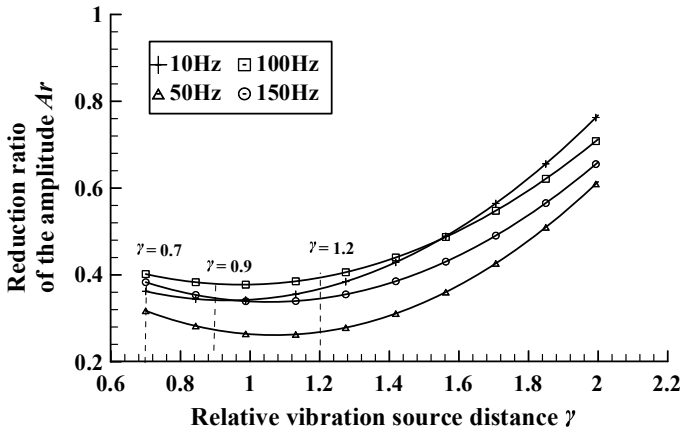
(a) Changing relation between Ar and γ for testing condition 3
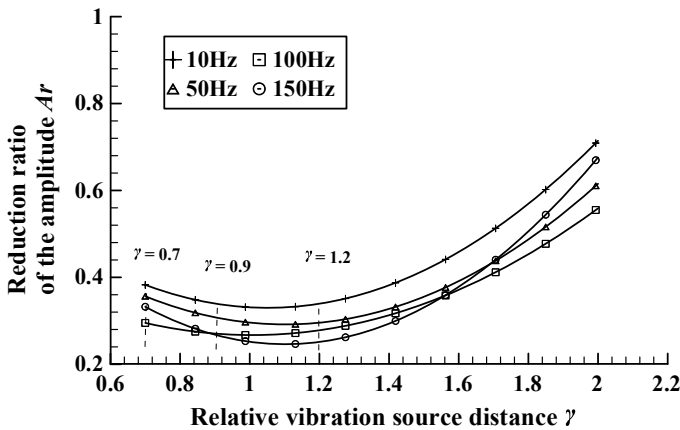
(b) Changing relation between Ar and γ for testing condition 4

Fig. 16 Changing relation between Ar and γ for the control group

effect will be nonsignificant. When the depth parameter ($D = 1.042$) can be used as the limit range of the length of the effective pile body, a better vibration isolation effect can be obtained.

(2) When the width of a vibration-isolated pile increases, the change in the vibration isolation effect is not significant; when the vibration-isolated pile is furnished and the pile spacing (s) is bigger, the vibration isolation effect will weaken.

(3) When the position of a vibration-isolated pile is not closer to the vibration source, a better vibration isolation effect can be obtained by a vibration-isolated pile. When K is between 0.291 and 0.357, it can be used as a reference index for determining reasonable positions of vibration-isolated piles.

(4) The vibration-isolated pile length (*L*) has the most obvious influence on the vibration isolation effect when increasing the length of the vibration-isolated pile, and *Ar* can reach levels below 0.1.

(5) When the slenderness ratio (*δ*) is between 0.1 and 0.2, a vibration-isolated pile can obtain a better vibration isolation effect, and the minimum value of *Ar* can reach 0.2. If the relative pile spacing (*β*) is larger, the vibration isolation effect of a vibration-isolated pile is worse.

(6) If the location of a vibration-isolated pile is not close to the source of vibration, the vibration-isolated pile can obtain a better vibration isolation effect, and if the relative vibration source distance (*γ*) is between 0.9 and 1.2, the value of *Ar* can reach 0.3 ∼ 0.4.

References

1. Ma M, Liu WN, Wang WB et al (2016) Evaluation of train-induced environmental vibrations considering the factor of exposure time. J Vib Shock 35(11):207–211
2. Hong JQ, Liu WQ, Wang SG (2008) Vibration analysis of base-isolated building near urban rail transit. J Vib Shock 27(11):37–50
3. Ma LH (2014) Research on vibration of Shanghai-Nanjing intercity high-speed railway and its environment impact. Beijing Jiaotong University, Beijing
4. Ma LH, Liang QH, Gu AJ et al (2015) Research on impact of Shanghai-Nanjing intercity high-speed railway induced vibration on ambient environment and foundation settlement of adjacent Beijing-Shanghai railway. J China Railw Soc 37(2):98–105
5. Kumar P, Sand HK, Chakraborty SK (2014) Isolation of plane shear wave using water saturated trench barrier. Soil Dyn Earthq Eng 59:42–50
6. Murillo C, Thorel L, Caicedo B (2009) Ground vibration solation with geofoam barriers centrifuge modeling. Geotext Geomembr 27(6):423–434
7. Wang QY, Zhang JS, Meng F et al (2013) Simulation of train vibration load on the subgrade testing model of high-speed railway. J Vib Shock 32(6):43–46
8. Zhan YX, Jiang GL (2010) Study of dynamic characteristics of soil subgrade bed for ballastless track. Rock Soil Mech 31(2):392–396
9. Gao GY, Li ZY, Feng SJ et al (2007) Experimental results and numerical predictions of ground vibration induced by high-speed train running on Qin-Shen railway. Rock Soil Mech 28(9):11817–11822
10. Qu CZ, Wang YH, Wei LM et al (2012) In-situ test and analysis of vibration of subgrade for Wuhan-Guangzhou high-speed railway. Rock Soil Mech 33(5):1451–1456
11. Hou DJ, Lei XY, Luo XW (2006) The numerical analysis of railway vibration by trenches. J Railw Sci Eng 3(2):48–52
12. Zhang LG, Liu JL, Song XG et al (2017) The numerical analysis of effect and influencing factor of vibration by open trench on high-speed railway. J Railw Sci Eng 14(7):1356–1359
13. Woods RD, Barnett NE, Sangesser R (1974) Holography, a new tool for soil dynamics. J Geotech Eng Div ASCE 100(11):1234–1247

14. Liu ZX, Wang SJ (2016) Isolation effect of discontinuous pile-group barriers on plane P and SV waves: simulation based on 2D broadband indirect boundary integration equation method. Rock Soil Mech 37(4):1195–1207
15. Li ZY, Gao GY, Qiu C et al (2006) Analysis of multi-row of piles as barriers for isolating vibration in far field. Chin J Rock Mech Eng 24(21):3990–3995
16. Wu SM, Zeng GX, Chen YM et al (1988) Measurement of wave velocity of soil deposits by spectral analysis of surface waves. Earthq Eng Eng Vib 8(4):28–31
17. Chen YM, Wu SM, Zeng GX (1992) Spectral analysis of surface waves and its application. China J Geotech Eng 14(3):61–64
18. Hou EP, Liu JL, Zhang RH et al (2017) Model test study on vibration isolation effect of concrete rows piles for railway subgrade. Railw Eng (3):141–145
19. He W, Xue WD, Tang B (2015) Optimization test design method and data analysis, 1st edn. Chemical Industry Press, Beijing

Vibration Isolation Mechanism of Row Piles Under Single-Point Excitation

Jing-lei Liu , Rui-heng Zhang , Xiao-yu Zhao and Huan Liu

Abstract To study the vibration isolation mechanism of row piles exposed to vibrations generated at a single point, a finite element model of a foundation using infinite element boundaries is established based on the theory of an elastic half-space body. The model included a single-point vibration source in the free field and piles arranged in a row, and corresponding contour maps of the amplitude dissipation ratio (*Ar*) were drawn. The results show that the vibration waves radiate out from the excitation point and that their acceleration amplitude decays continuously. The overall vibration isolation progressively improves as the number of piles and the row depth increase. However, the degree of improvement in the isolation effect decreases with increasing depth. If the spacing between row piles is too large, the vibration isolation effect of the row piles will be unsatisfactory. However, reducing the row spacing does not necessarily improve the vibration isolation effect of row piles. Compared with a hollow pile, a solid pile has a better vibration isolation effect, but the difference is not significant. Additionally, the vibration isolation effect of a circular pile is worse than that of a square pile. As the distance between the vibration source and the row piles decreases, the isolation effect becomes more pronounced, but the difference is not pronounced. Furthermore, the isolation effect of row piles is better for low-frequency vibrations than for intermediate- and high-frequency vibrations.

Keywords Vibration isolation · Row piles · Mechanism analysis · Infinite boundary · Finite element analysis

J. Liu (✉) · R. Zhang · X. Zhao · H. Liu
School of Civil Engineering, Hebei University of Architecture,
Zhangjiakou 075000, Hebei, China
e-mail: kingbest_1118@163.com

1   Foreword

With the rapid development of modern industry and accelerating urbanization, contamination from various types of environmental vibrations has received widespread public attention [1–3]. International organizations have listed vibration pollution as one of the seven major environmental hazards in the world [4].

Currently, vibration pollution control is one of the most important topics being investigated by scholars in China and abroad [5, 6]. Yang et al. [7] suggested that installing vibration isolation barriers in foundation soil can effectively control environmental vibration pollution. Woods [8] studied a discontinuous insulation barrier and proposed that the pile diameter of a single-row pile isolation barrier should be greater than one-sixth the wavelength of the barrier. Andersen and Nielsen [9] studied empty and filled trenches and found that empty trenches are more effective isolation barriers. Furthermore, a combined barrier involving both empty trenches and row piles is more effective than using a single isolation barrier alone. Aviles and Sanchez-Sesma [10, 11] studied the scattering effect of single-row piles on an SH wave and showed that the vibration isolation effect of a rigid pile is better than that of a flexible pile. Hayakawa [12] studied the mechanism and propagation laws of vibration waves and proposed a prediction method for environmental vibration levels. Xu et al. [13] and Xia et al. [14] studied the effects on the vibration isolation of various forms of barriers with respect to SV waves and proposed that the vibration isolation effect of discontinuous hollow pipe pile barriers increases with decreasing pile spacing, providing a basis for practical applications. Shi and Gao [15] used a semi-analytic boundary element method to study the vibration isolation of far-field single-row piles in saturated soils. These researchers concluded that increasing the pile length, pile diameter and pile shear modulus effectively improves the vibration isolation effect of row piles. Ba et al. [16] considered the influence of the track and layered foundations and studied the vibration isolation effect of empty trenches on a foundation using the 2.5-dimensional indirect boundary element method. They concluded that different foundation models, the depth of the empty trenches and the distance between the empty trenches and the foundation impact the vibration isolation effect. Chen and Huang [17] studied the vibration isolation effect of filled trenches for traffic vibrations in viaducts and concluded that ring-shaped filled trenches can achieve a good vibration isolation effect. Feng et al. [18] and Zhang et al. [19] used model tests to analyze the vibration isolation effects of typical vibration isolation barriers, such as empty trenches, filled trenches and row piles, and these researchers obtained results that are beneficial to engineering practice.

These results demonstrate that various types of vibration isolation barriers can help mitigate vibration pollution, and we describe studies on the effects of vibration isolation factors associated with vibration isolation barriers. Most of these studies examined points or lines behind the isolation barrier, but few studies have examined

the sources of vibrations and planes within a certain range around the barrier. Therefore, to objectively describe the vibration isolation effect of a row pile system in a plane within a certain range subjected to single-point vibration, we compare the vertical acceleration at the ground surface at points where no vibration isolation measures are available to that at points where row pile vibration isolation is available to determine the surface amplitude dissipation ratio (Ar). Additionally, this work creates a corresponding Ar contour map, determines the effect of different factors on the vibration isolation effect over a certain range and acts as a reference for research on vibration and vibration isolation.

2 Vibration Isolation Principle

When operating a train, track irregularities, orbital seams, and wheel and track interactions generate a reciprocating load at a certain speed, which is transmitted to and propagates through the surrounding soil, vibrating the soil. This process is the main cause of vibrations in rail transit systems. Because of its small dynamic strain, this vibration appears as an elastic wave in the soil. Therefore, for rail transit vibrations, the soil can be analyzed as an elastic half-space body. Jiang et al. [20] numerically calculated the integral expression of the half-space body response and obtained the response and surface displacement of all points inside the elastic half-space body. A vibration wave propagates in the soil in the form of a body wave and a surface wave. The vibration wave propagates along the surface of the soil, mainly in the form of a surface wave, and the main component of the surface wave is a Rayleigh wave. Rayleigh waves are surface waves that propagate at a one-time wavelength depth. The decay rate of the wave is slow, causing the ground to vibrate violently. Because of the large difference in the impedance ratio between a vibration isolation barrier and the soil, vibration isolation measures placed in the transmission path of a vibration wave can block the vibration wave. A vibration wave advances in a uniform medium without changing direction. When the vibration wave encounters an obstacle, it is decomposed into a reflected wave, a diffracted wave and a transmitted wave. This effect is the basic mechanism responsible for the shielding effect of a barrier.

3 Verifying the Validity of Finite Element Analysis

To verify the effectiveness of finite element analysis for vibration-related fields, model tests were conducted, and finite element models of the same size as the model tests were established. The results were compared to ensure that the results of the finite element analysis are consistent with the actual results.

3.1   Model Test Overview

The model test used an outdoor square sand pit with a length × width × height of 3.0 × 2.0 × 1.5 m filled with 98% sand with a grain size distribution ranging from 1.75 to 0.075 mm. The soil moisture content was maintained at 9–10%. The soil mass was layered and compacted. The soil density was 1700–1800 kg/m^3. The test adopted a WS-Z30 shaking table control system. The equipment mainly included a data acquisition controller, a power amplifier, a charge amplifier, an exciter, a signal generator, an accelerometer amplifier and an acceleration sensor.

The row piles were fabricated from C30 concrete with a square cross section, with cross-sectional dimensions of 10.0 × 10.0 cm and a height of 40 cm. The first pile was positioned at the geometric center of the row pile test site, and the other piles were arranged at 15 cm intervals in the transverse direction. The exciter used in the experiment was positioned 90 cm in front of the central pile. The test used four accelerometers on the soil surface along the longitudinal axis to collect vertical acceleration data from the soil itself. Sensor #1 was placed 10 cm in front of the row piles, and sensors #2–4 were placed 10 cm, 20 cm and 50 cm behind the row piles, respectively. The pile and sensor layout are shown in Fig. 1. For the experiment, a sine wave with an excitation frequency of 10 Hz was selected, and a sampling frequency of 5000 times/s was used with a sampling time of 10 s. During this period, the charge amplifier values needed to be consistent.

3.2   Finite Element Model Overview

3.2.1   Model Size and Boundary Settings

In this paper, a three-dimensional model is used for calculation, and a finite element model of the same size as the model test is established. To prevent the model from acting as a fixed boundary and causing vibration wave reflection, an infinite element is used as the perimeter and the bottom boundary. Therefore, the CIN3D8 infinite element is used for the surrounding and bottom elements of the model, while the other parts use the finite element C3D8R three-dimensional stress element. The finite element model is shown in Fig. 2.

3.2.2   Model Material Parameters and Load Selection

The model soil and pile material parameters are shown in Table 1. The three-dimensional stress element uses sand properties, and the surrounding and bottom infinite elements use soil properties to simulate the actual situation of the test site more accurately.

The test uses an excitation frequency of 10 Hz. The vibration load includes a static load and a dynamic load, as shown in Eq. (1):

Fig. 1 Layout of concrete pile and sensor
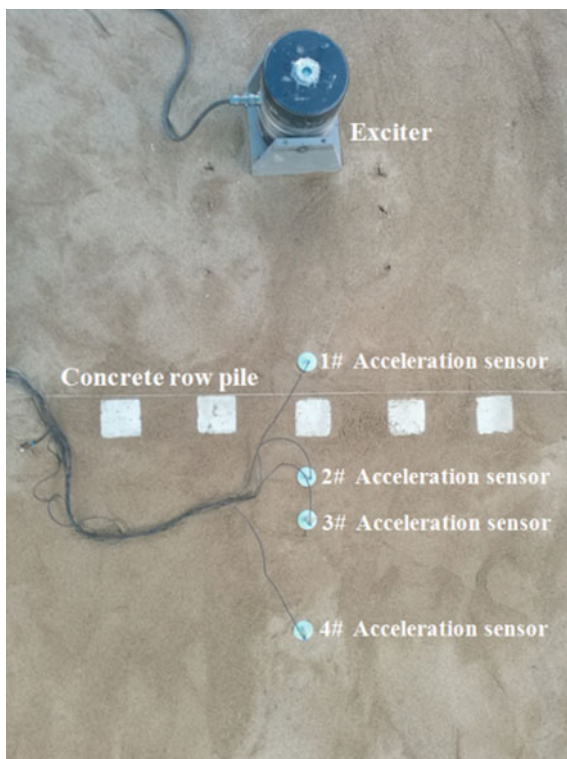
Fig. 2 FE model corresponding to the size of the experiment
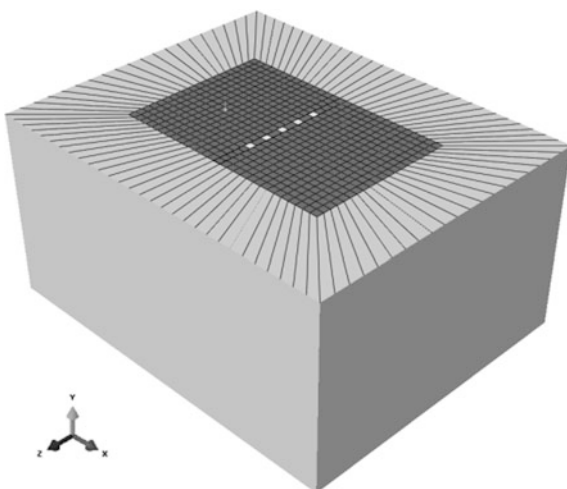
Table 1 Material parameters

Type	Density (kg m^{-3})	Elastic modulus (Pa)	Poisson's ratio	α	β
Sand	1750	2.00E+07	0.3	0.406	0.072
Soil	1900	2.00E+07	0.3	0.406	0.072
Pile	2200	2.20E+10	0.2	0.112	0.020

$$F(t) = P_0 + P_1 \sin(\omega_1 t) \tag{1}$$

where P_0 (kN) is the exciter's weight, P_1 (kN) is the dynamic load peak, and ω_1 is the vibration circle frequency.

According to the experimental data, the excitation function is shown in Eq. (2).

$$F(t) = 0.25 + 0.08 \sin 62.8t \tag{2}$$

3.3 Comparison of Results

3.3.1 Data Processing Method

The row pile vibration isolation effect is expressed using Ar. The expression is shown in Eq. (3), and the smaller the value of Ar is, the better the vibration isolation effect [17].

$$Ar = \frac{a_1}{a_0} \tag{3}$$

In the above equation, a_1 is the acceleration value with vibration isolation measures, and a_0 is the acceleration value without vibration isolation measures.

3.3.2 Comparison of the Model Test and FE Calculation Results

To verify the reliability of the finite element analysis calculation, a model of the same size as the finite element model was used for comparison with the finite element model. In the calculation of the model test and the finite element model, two isolation schemes, i.e., no vibration isolation measures and row pile vibration isolation (section size: 5.0 cm; depth: 40.0 cm; pile spacing: 15.0 cm), were used. A vibration force at a frequency of 10 Hz was used, and the test results are expressed as vertical acceleration.

Figure 3 and Table 2 show the soil acceleration values and amplitude dissipation ratio for the model test and the finite element analysis for two conditions. In the model test and the finite element analysis, the vertical acceleration at a distance of

Fig. 3 Changes in acceleration as a function of distance

(a) Model test

(b) Finite element analysis
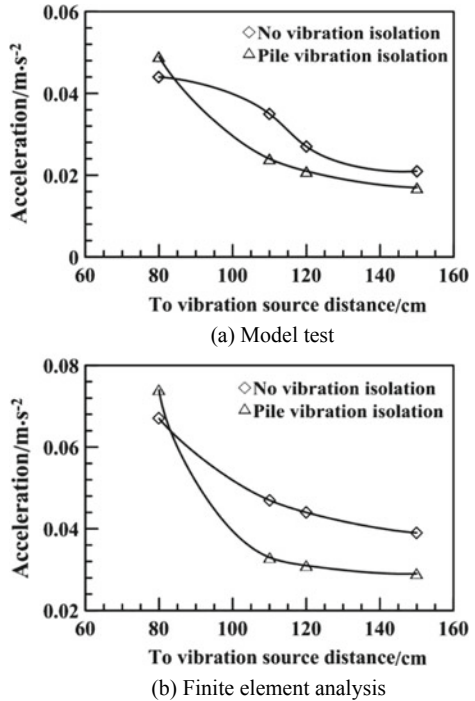
Table 2 Comparison of the acceleration for the two conditions

Vibration source distance (cm)	Model test			Finite element analysis		
	Acceleration (m s^{-2})		Amplitude dissipation ratio (Ar) (%)	Acceleration (m s^{-2})		Amplitude dissipation ratio (Ar) (%)
	No vibration isolation measures	Row pile vibration isolation		No vibration isolation measures	Row pile vibration isolation	
80	0.067	0.074	110.45	0.044	0.049	111.36
110	0.047	0.033	70.21	0.035	0.024	68.57
120	0.044	0.031	70.45	0.027	0.021	77.78
150	0.039	0.029	74.36	0.021	0.017	80.95

80 cm from the vibration source increased after the isolation barrier was set; the amplitude dissipation ratios were 111.36 and 110.45%, respectively. This effect is observed because a reflected wave is generated at the front of the piles in the isolation barrier, which increases the vertical acceleration. In the model test and finite element analysis, the amplitude dissipation ratios of the measurement points behind the isolation barrier were 70.21–74.36 and 68.57–80.95%, respectively. Thus, the accelerations were lower by 19.05–31.43 and 25.64–29.79%,

respectively. There is a better vibration isolation effect within a certain range of the row pile. The model test is consistent with finite element analysis in terms of regularity. In summary, finite element analysis reflects the effectiveness of the vibration isolation barrier and verifies its feasibility for predicting vibration isolation effects.

4 Establishing the Finite Element Model and Design Scheme

4.1 Establishing the Finite Element Model

4.1.1 Model Size and Boundary Settings

This study uses ABAQUS software to create a three-dimensional model for the calculations. The model surface layout is shown in Fig. 4.

The model is based on the theory of an elastic half-space body. To prevent the model from requiring a fixed boundary and causing the reflection of any vibration waves, an infinite boundary is used as the surrounding and bottom boundaries. The length, width and height of the model are 50 m, 50 m and 30 m, respectively. A CIN3D8 infinite element with a thickness of 10 m is used for the surrounding and bottom units; other parts use a C3D8R three-dimensional stress unit with dimensions of $30 \times 30 \times 20$ m. To prevent the infinite boundary from affecting the surroundings, 5 m finite element units are left as transitional areas. The constant value line drawing area is centered at 20×20 m. The finite element calculation model is shown in Fig. 5.

Fig. 4 Model surface layout
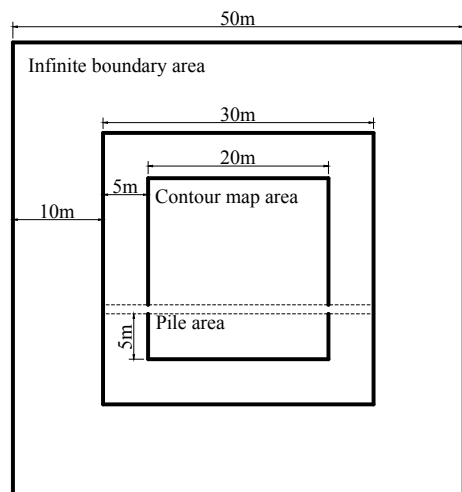
Fig. 5 Finite element calculation model
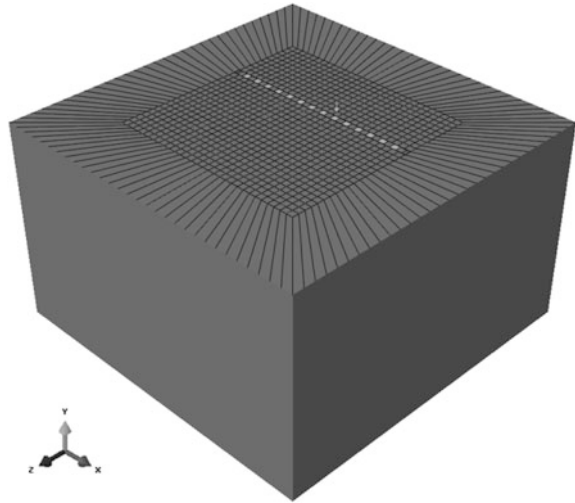
4.1.2 Model Material Parameters

The model was calculated using elastic materials. The model material parameters are shown in Table 3.

Because the vibration waves are attenuated in the soil and piles, it is necessary to provide damping to the soil and piles. The model uses Rayleigh damping in ABAQUS to define the damping of soil and piles. For the soil, the mass damping coefficient α is 0.406, and the stiffness damping coefficient β is 0.072. For the pile–soil system, the mass damping coefficient α is 0.112, and the stiffness damping coefficient β is 0.020.

4.1.3 Vibration Load Setting

Single-point vibration excitation is used to generate the vibration. The vibration uses a simple harmonic wave. A vibration force function is used to simulate the vibration load, which includes a static load simulation of the total vibration source weight and a dynamic load to simulate a source vibration. The expression is shown in Eq. (4):

$$F(t) = P_0 + P_1 \sin(\omega_1 t) \tag{4}$$

Table 3 Model material parameters

Type	Density (kg m^{-3})	Elastic modulus (Pa)	Poisson's ratio
Soil	1900	2.00E+07	0.300
Pile	2500	2.20E+10	0.200

Table 4 Vibration wave amplitude in different frequency bands

Frequency	Amplitude α_1 (mm)
Low frequency	3.5
Intermediate frequency	0.4
High frequency	0.08

where P_0 (kN) is the total weight of the vibration source and P_1 (kN) is the vibration load peak corresponding to the vibration source circular frequency ω_1.

The total weight of the vibration source is $P_0 = 100$ kN, and the expression of the peak vibration load P_1 is shown in Eq. (5):

$$P_1 = M_0\alpha_1\omega_1 \tag{5}$$

where α_1 (mm) is the amplitude corresponding to the vibration source circular frequency ω_1 and M_0 (kg) is the mass of the vibration source.

The mass of the vibration source is $M_0 = 750$ kg, and the vibration wave amplitude α_1 in different frequency ranges is shown in Table 4. The expression of the circular frequency ω_1 is shown in Eq. (6):

$$\omega_1 = 2\pi f \tag{6}$$

where f (Hz) is the vibration wave frequency.

The low, intermediate and high frequencies are represented by 10 Hz, 50 Hz and 120 Hz, respectively. The low-, intermediate- and high-frequency vibration functions are given by Eqs. (7), (8) and (9), respectively:

$$F(t) = 100 + 10.35\sin(62.8t) \tag{7}$$

$$F(t) = 100 + 29.58\sin(314.0t) \tag{8}$$

$$F(t) = 100 + 34.07\sin(753.6t) \tag{9}$$

4.2 Schematic Design

This study changes the number of piles, pile depth, pile spacing, pile shape, vibration source to row pile distance and source vibration frequency. The influence of different factors on the vibration isolation of row piles is studied by generating an *Ar* contour map. The smaller the *Ar* value behind the row piles is, the better the vibration isolation effect. The specific scheme is shown in Table 5.

Experiment nos. 0–1 to 0–5 are isolation tests without vibration. Because the row piles are noncontiguous vibration isolation barriers, the relative locations of the vibration source and the row piles are divided into two situations: the vibration source directly opposite the pile center and the vibration source directly between two piles. A schematic diagram is shown in Fig. 6.

Table 5 Test plan table

Test number	Number of piles	Pile depth (m)	Pile spacing (m)	Pile shape	Vibration source to row pile distance (m)	Source vibration frequency (Hz)	Vibration source location
0–1	0	–	–	–	1	10	–
0–2	0	–	–	–	3	10	–
0–3	0	–	–	–	5	10	–
0–4	0	–	–	–	3	50	–
0–5	0	–	–	–	3	120	–
1	1	10	1.0	Solid square	3	10	Pile center
2	2	10	1.0	Solid square	3	10	Between two piles
3	3	10	1.0	Solid square	3	10	Pile center
4	4	10	1.0	Solid square	3	10	Between two piles
5	14	10	1.0	Solid square	3	10	Between two piles
6	15	10	1.0	Solid square	3	10	Pile center
7	14	5	1.0	Solid square	3	10	Between two piles
8	15	5	1.0	Solid square	3	10	Pile center
9	14	15	1.0	Solid square	3	10	Between two piles
10	15	15	1.0	Solid square	3	10	Pile center
11	14	10	0.5	Solid square	3	10	Between two piles
12	15	10	0.5	Solid square	3	10	Pile center
13	14	10	1.5	Solid square	3	10	Between two piles
14	15	10	1.5	Solid square	3	10	Pile center
15	14	10	1.0	Hollow square	3	10	Between two piles
16	15	10	1.0	Hollow square	3	10	Pile center
17	14	10	1.0	Solid circle	3	10	Between two piles
18	15	10	1.0	Solid circle	3	10	Pile center

Table 5 (continued)

Test number	Number of piles	Pile depth (m)	Pile spacing (m)	Pile shape	Vibration source to row pile distance (m)	Source vibration frequency (Hz)	Vibration source location
20	15	10	1.0	Solid square	1	10	Pile center
21	14	10	1.0	Solid square	5	10	Between two piles
22	15	10	1.0	Solid square	5	10	Pile center
23	14	10	1.0	Solid square	3	50	Between two piles
24	15	10	1.0	Solid square	3	50	Pile center
25	14	10	1.0	Solid square	3	120	Between two piles
26	15	10	1.0	Solid square	3	120	Pile center

Fig. 6 Relative locations of the vibration source and the row piles

(a) Vibration source directly opposite the pile center

(b) Vibration source directly between two piles
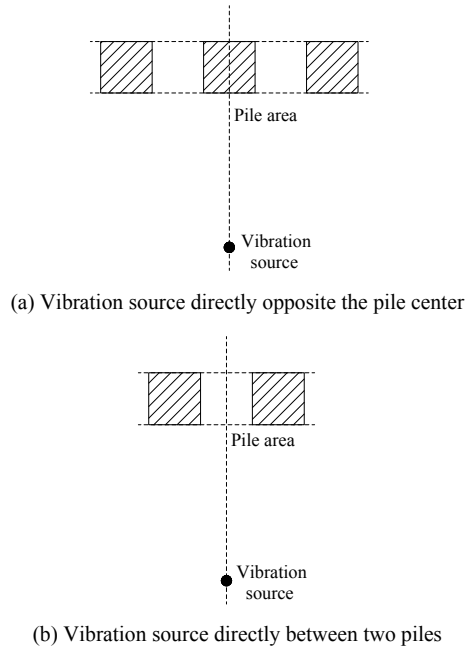
5　Analysis of the Results

5.1　*Analysis of the Acceleration Characteristics of Row Pile Vibration Isolation*

To study and analyze the characteristics of the vibration propagation from vibration excitation at a single point and the principle of the vibration isolation of row piles, contour maps of acceleration were drawn for situations with and without row pile vibration isolation. No vibration isolation was used in test no. 0–2, and row pile vibration isolation was used in test no. 6. The data acquisition interval is 1 m, and a total of 441 measurement point data were collected. The acceleration contours from test no. 0–2 are shown in Fig. 7. The acceleration contours for test no. 6 are shown in Fig. 8.

As shown in Fig. 7, in the absence of vibration isolation, the vibration wave is centered on the excitation point and spreads outward. The acceleration is constantly attenuated as the distance increases. During the initial period, the acceleration decay rate is fast but gradually decreases as the distance increases. Finally, the acceleration gradually levels off and slowly approaches zero.

As shown in Fig. 8, the acceleration diffuses to the periphery behind the row pile vibration isolation. Acceleration near the excitation point is greater than that in the isolation case without vibration, and the rate of acceleration decay increases. At the same time, the acceleration in the area far from the excitation point is considerably less than that in the isolation case without vibration.

To further analyze the acceleration attenuation characteristics of row pile vibration isolation, the profile line L1 passing through the excitation point and parallel to the *y*-axis was used as the reference line to create an acceleration profile. The results are shown in Figs. 9 and 10.

As shown in Fig. 9, the vibration point is located at 2 m, and the acceleration is 2.553 m/s^2. As the distance from the excitation point increases, the acceleration and the acceleration attenuation rate decrease. The acceleration decreases most rapidly at distances from 2 to 3 m, and the acceleration is 0.774 m/s^2 at 3 m. The acceleration decreased by 1.279 m/s^2 compared to that of the excitation point, corresponding to approximately 62.30% of the acceleration at the excitation point. From 3 to 6 m, the rate of acceleration decay gradually decreases, with the acceleration at 6 m being 0.162 m/s^2, corresponding to 29.84% of the acceleration at the excitation point. From 6 to 20 m, the acceleration decays slowly and gently, and the acceleration is reduced to 7.72% of that at the excitation point.

As shown in Fig. 10, the excitation point is located at 2 m, and the row piles are arranged in the range from 5 to 6 m. Compared with the isolation case without vibration, the case with row piles features greater acceleration near the excitation point because the row piles reflect the vibration wave; however, the acceleration attenuation is more rapid. The acceleration at the excitation point is 2.278 m/s^2, which is 10.96% higher than that without vibration isolation. From 2 to 6 m, the
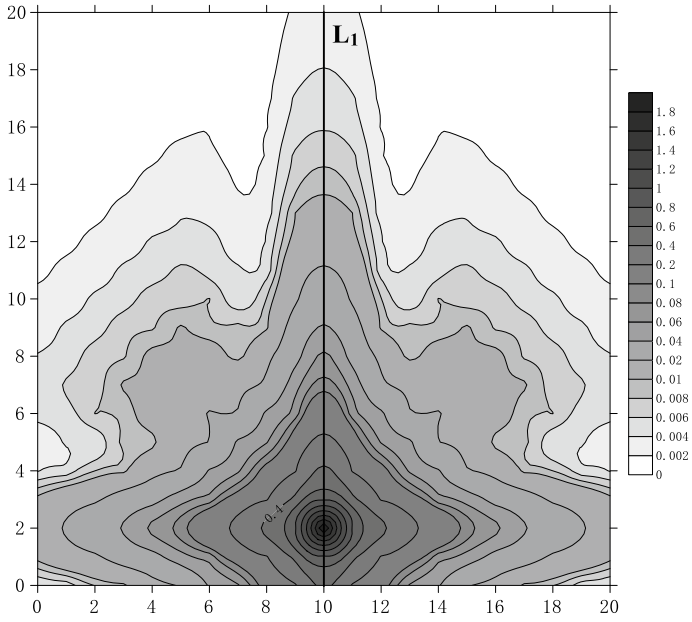
Fig. 7 Acceleration contour map for test no. 0–2
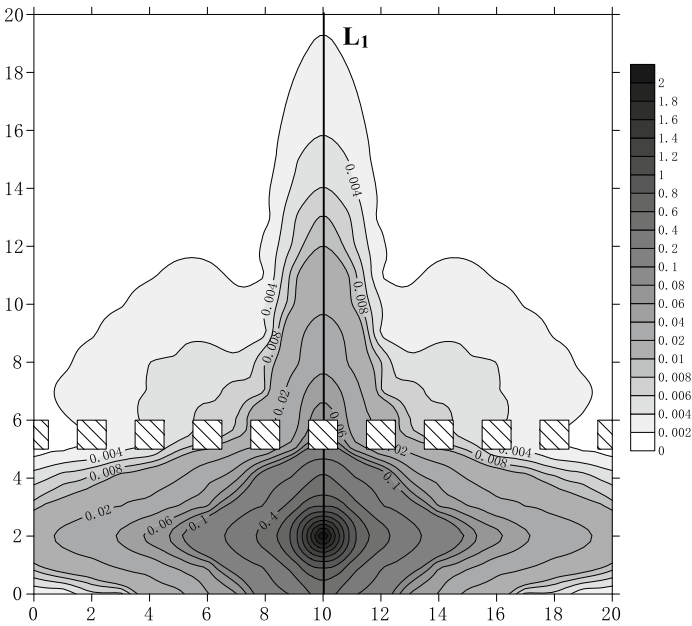
Fig. 8 Acceleration contour map for test no. 6

Fig. 9 Acceleration profile
for line L1 in test no. 0–2
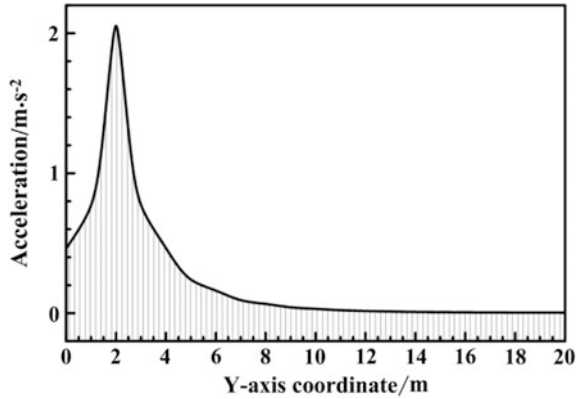
Fig. 10 Acceleration profile
for line L1 in test no. 6
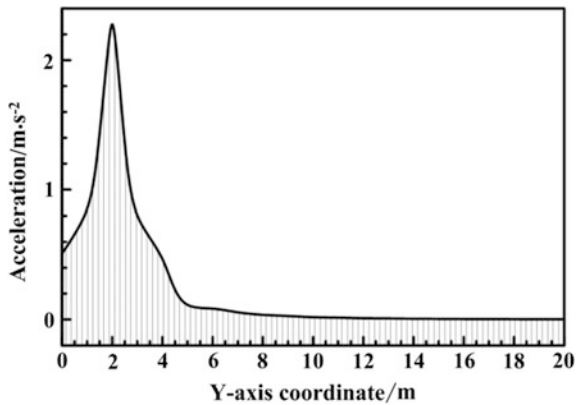
acceleration decays rapidly, with an acceleration at 6 m of 0.084 m/s^2, corresponding to 96.30% of that at the excitation point. The acceleration is 47.78% lower than that at the same position in the isolation case without vibration, meaning that the row piles had an obvious vibration isolation effect. From 5 to 20 m, the acceleration slowly declines with a gentle trend, and the acceleration reaches 3.62% of that at the excitation point.

To further study the acceleration change induced by the row piles, acceleration results at each point in test no. 6 are divided by those at each point in test no. 0–1 to obtain the Ar value at each point and to draw an Ar contour map. The results are shown in Fig. 11.

Figure 11 shows that, in front of the row piles and especially in the area near the middle line, the Ar in most areas is greater than 1.0 because the vibration wave reflects off the row piles. Behind the row piles, the Ar values are between 0.3 and 0.7, which represents a good vibration isolation effect. In particular, in the area far from the midline, Ar is 0.3–0.4, and the vibration isolation effect is good. Ar near
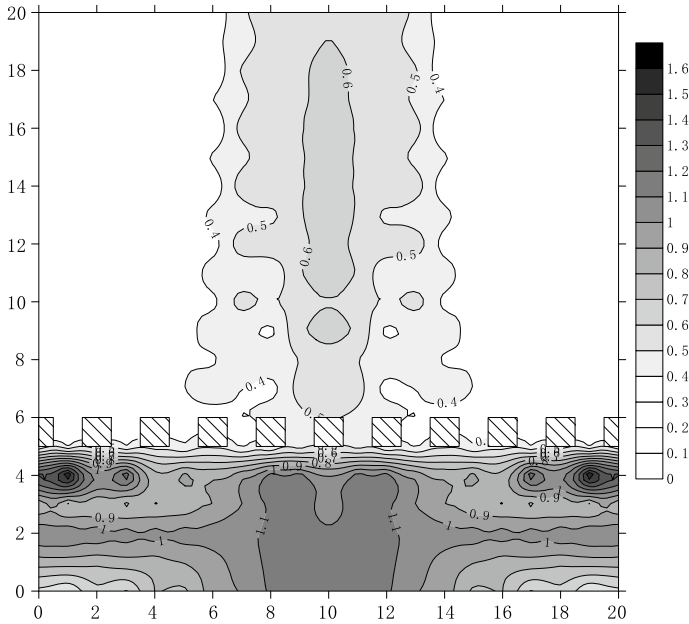
Fig. 11 Comparison of acceleration between test no. 6 and test no. 0–1

the midline area is 0.4–0.7. This finding reveals that areas closer to the midline exhibit larger Ar values. The convergence of diffracted waves causes large Ar values from 0.6 to 0.7.

5.2 Influence of the Row Pile Parameters on the Vibration Isolation Effect

5.2.1 Number of Row Piles

Next, we examined the effect of the numbers of row piles on the vibration isolation effect. Using a single pile (test no. 1), two piles (test no. 2), three piles (test no. 3), four piles (test no. 4), a row of piles (test no. 5 and no. 6) and a test without isolation (test no. 0–2), Ar contour maps were created and analyzed. The results are shown in Figs. 12, 13, 14, 15, 16 and 17. The squares filled with cross-hatching show the arrangement of the row piles.

From Figs. 12, 13, 14, 15, 16 and 17, we see that the vibration isolation effect becomes more obvious as the number of row piles increases. For vibration isolation using a single pile, the vibration isolation effect is good on both sides of the pile and in the rear area. Ar is essentially less than 0.6, and part of the area behind the single pile reaches values less than 0.5. In the vibration isolation case using two piles, the
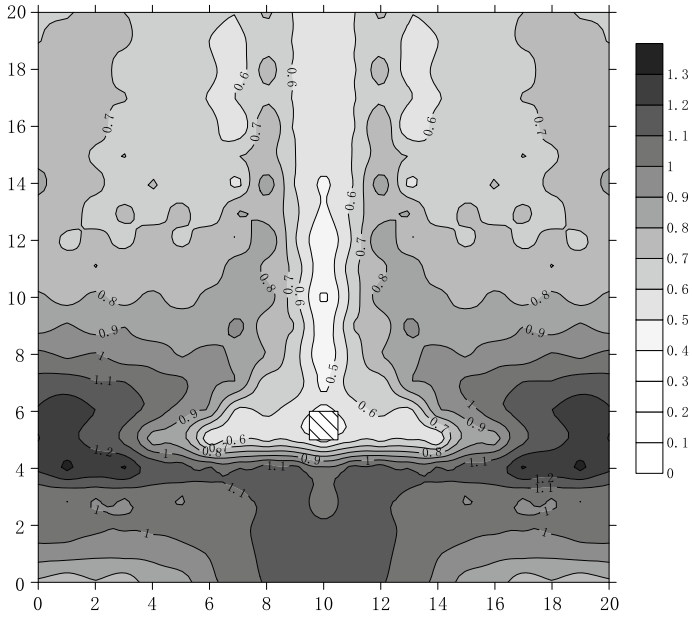
Fig. 12 Test no. 1 *Ar* contour map
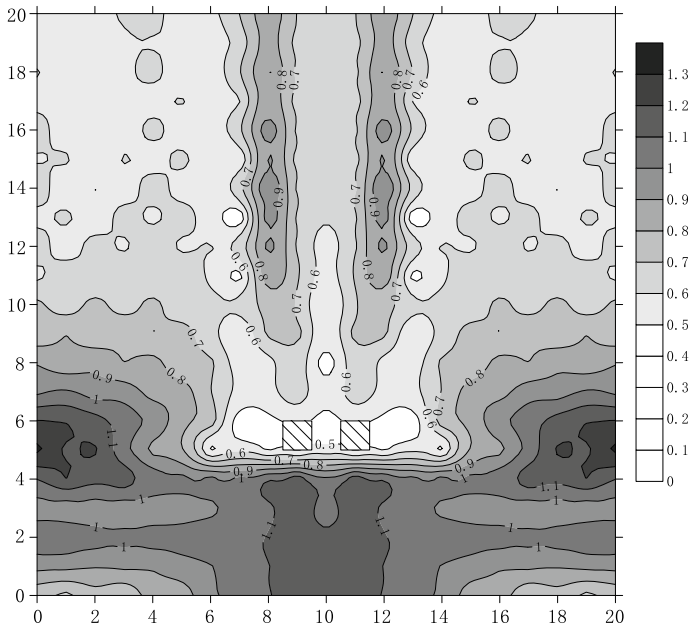
Fig. 13 Test no. 2 *Ar* contour map
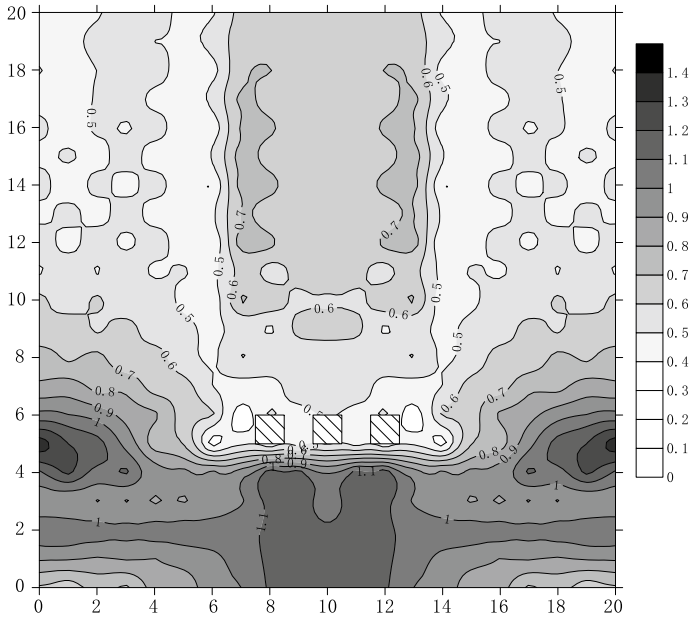
Fig. 14 Test no. 3 *Ar* contour map
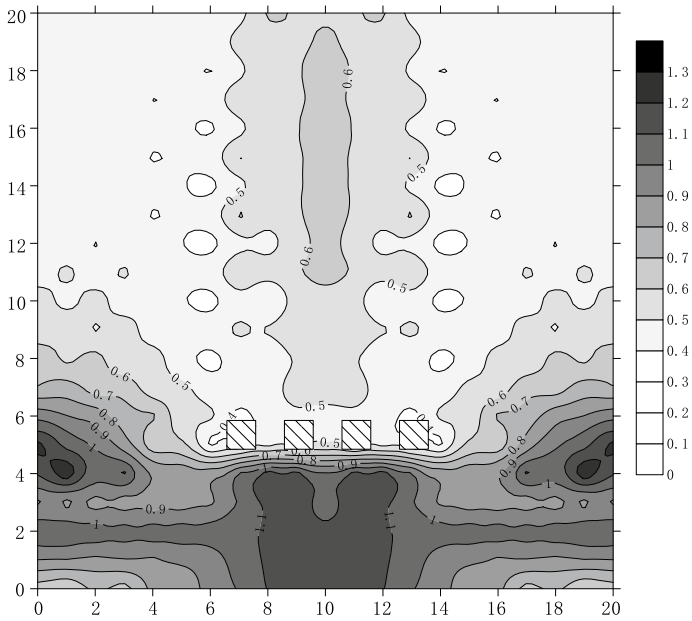
Fig. 15 Test no. 4 *Ar* contour map
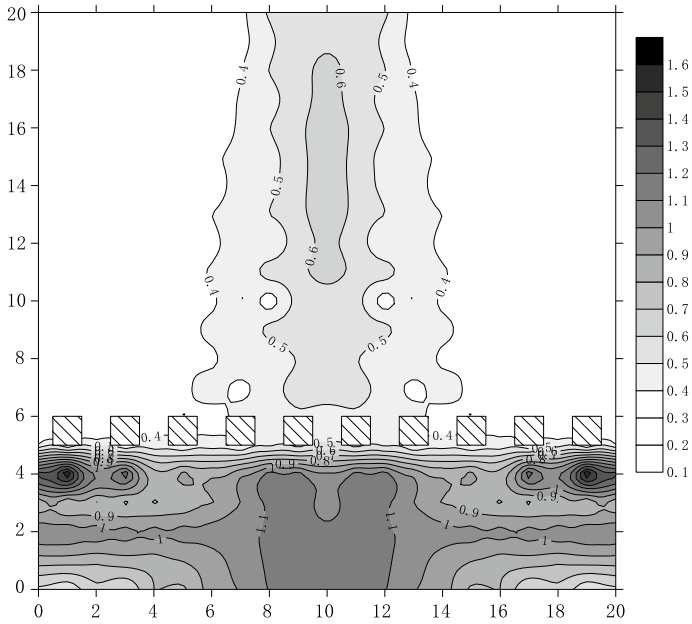
Fig. 16 Test no. 5 *Ar* contour map
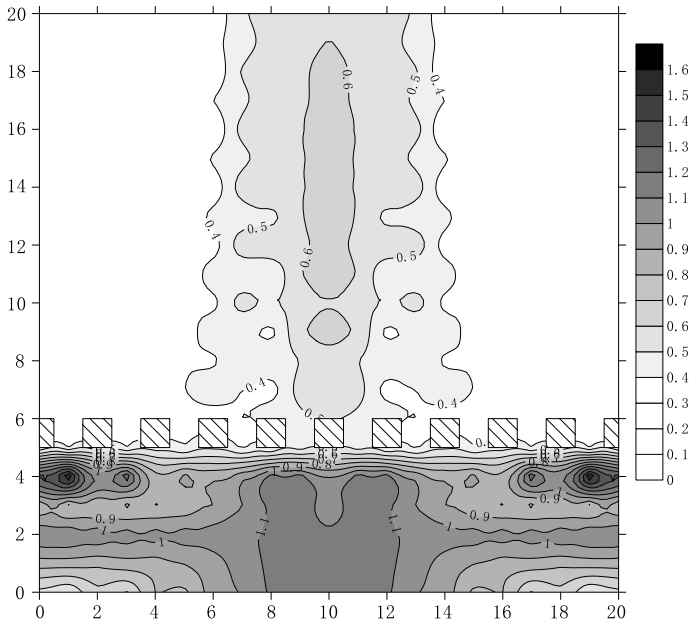
Fig. 17 Test no. 6 *Ar* contour map

areas between and on both sides of the two piles experience the best vibration isolation effect, and the middle-rear area of the two piles also sees positive effects. However, poor isolation is observed immediately behind the two piles. For the vibration isolation case using three piles, there is a poor vibration isolation effect in the rear area but a good vibration isolation effect on both rear sides. In the vibration isolation case using four piles, the vibration isolation effect is similar to but slightly worse than that for a row of piles. The vibration isolation effect is good on both sides of the isolation piles, but the isolation effect on the rear side of the isolation piles is poor. For the vibration isolation case using a row of piles, the overall vibration isolation effect is the same regardless of whether the vibration source is directly opposite the pile center or the vibration source is directly between the two piles. Behind the row of piles, the vibration isolation effect on both sides is better than that in the middle area. In addition, the vibration isolation effect when the vibration source is directly between the two piles is slightly better than that when the vibration source is directly opposite the pile center.

5.2.2 Pile Depth

Next, we studied the effect of different pile depths on the vibration isolation effect. Depths of 5 m (tests no. 7 and no. 8), 10 m (tests no. 5 and no. 6), 15 m (tests no. 9 and no. 10) and a test without isolation (test no. 0–2) were used to draw Ar contour maps, which were then analyzed. The results are shown in Figs. 16, 17, 18, 19, 20 and 21.

From Figs. 16, 17, 18, 19, 20 and 21, we see that the trend for the vibration isolation effect is generally the same, and a vibration superposition enhancement region appears in the front of the row piles. The overall vibration isolation effect in the rear of the row piles is good, and the vibration isolation effect on both sides of the row piles was better than that in the middle area. This pattern is observed because of vibration wave convergence in the middle. In addition, the vibration isolation effect when the vibration source is directly between the two piles is slightly better than that when the vibration source is directly opposite the pile center.

Figures 18 and 19 show Ar contour maps constructed at a 5 m depth. Compared with the case with a 10 m row depth, the case with a 5 m row depth features areas with worse vibration isolation effects on both sides and in the middle. In general, the vibration isolation effect at a row depth of 5 m is worse than that at a depth of 10 m.

Figures 20 and 21 show Ar contour maps constructed at a 15 m depth. The area with poor vibration isolation in this case is smaller than that in the case with a 10 m depth. In general, the vibration isolation effect for a row depth of 15 m is better than that for a row depth of 10 m, but the difference is not large.

In summary, the vibration isolation effect increases as the depth of the row piles increases, but the ability to increase the vibration isolation effect decreases as the depth of the row piles increases.
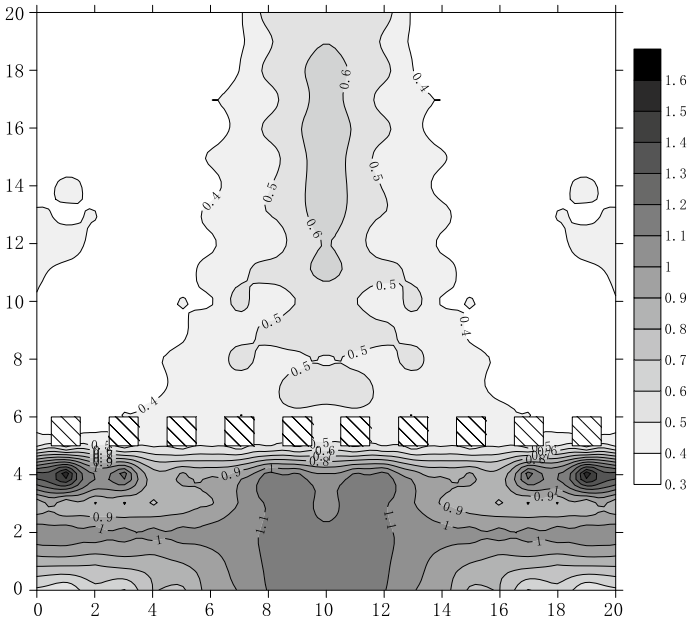
Fig. 18 Test no. 7 *Ar* contour map
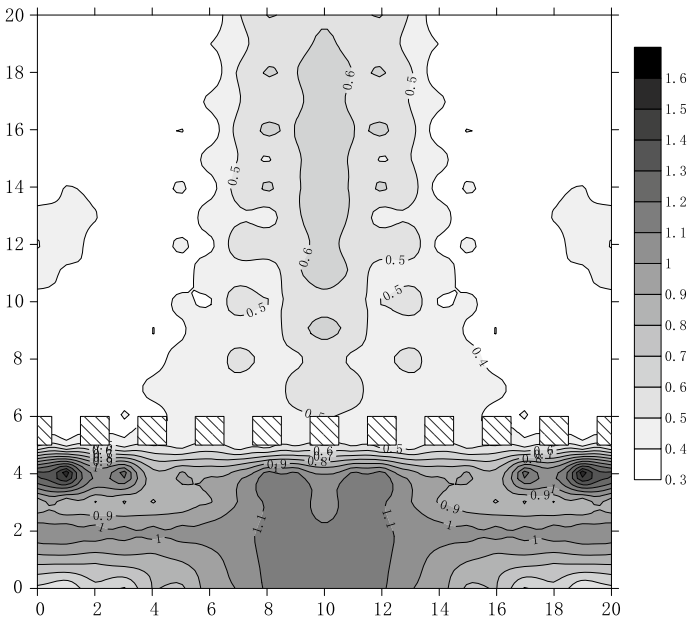
Fig. 19 Test no. 8 *Ar* contour map
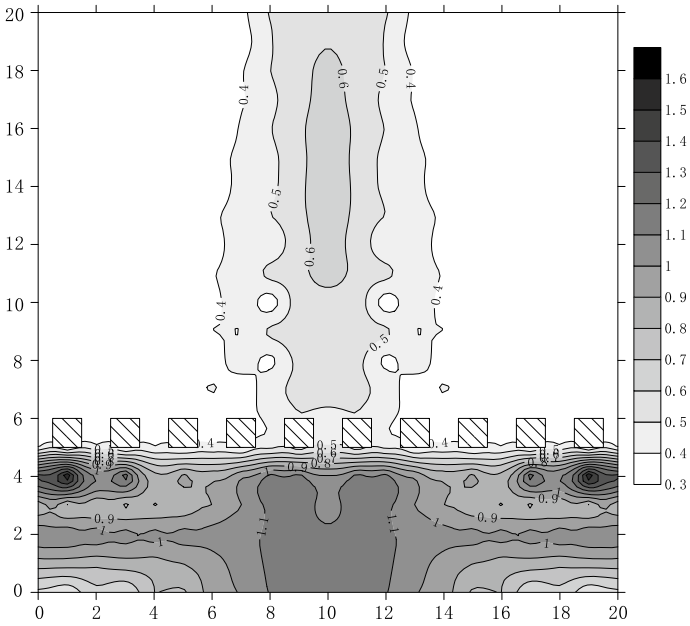
Fig. 20 Test no. 9 *Ar* contour map
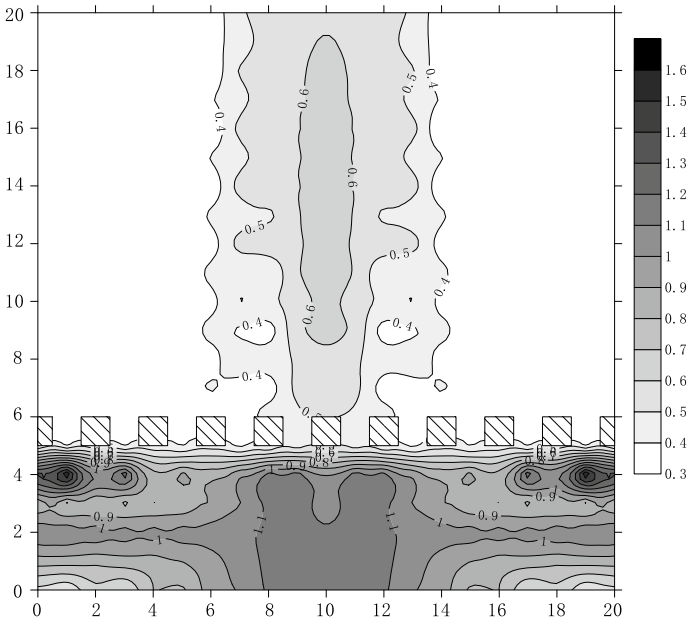
Fig. 21 Test no. 10 *Ar* contour map

5.2.3 Pile Spacing

Next, we investigated the effect of pile spacing on the vibration isolation effect using a spacing of 0.5 m (tests no. 11 and no. 12), a spacing of 1 m (tests no. 5 and no. 6), a spacing of 1.5 m (tests no. 13 and no. 14) and a test without isolation to construct and analyze *Ar* contour maps. The results are shown in Figs. 16, 17, 22, 23, 24 and 25.

From Figs. 16, 17, 22, 23, 24 and 25, we see that the vibration isolation effect changes greatly with the pile spacing and that the vibration wave superposition area appears in front of the row piles. When the pile spacing is 0.5 or 1.0 m, the isolation effect of the row piles is generally good. However, when the pile spacing is 1.5 m, there is a large area with poor isolation behind the row piles.

Figures 22 and 23 show *Ar* contour maps for a pile spacing of 0.5 m. Compared with a pile spacing of 1.0 m, the pile spacing of 0.5 has a larger area with an *Ar* of 0.6 and a smaller area with an *Ar* of 0.4. However, this pile spacing also has a larger area with an *Ar* between 0.5 and 0.6. When the vibration source is between two piles, there are several small areas with *Ar* values greater than 0.8 and an area with *Ar* values of less than 0.4 alternating with *Ar* values from 0.4 to 0.5. When the vibration source is directly opposite the pile center, only three small areas at the midline feature *Ar* values greater than 0.6; however, the area with *Ar* values of 0.4–0.5 is considerably larger.
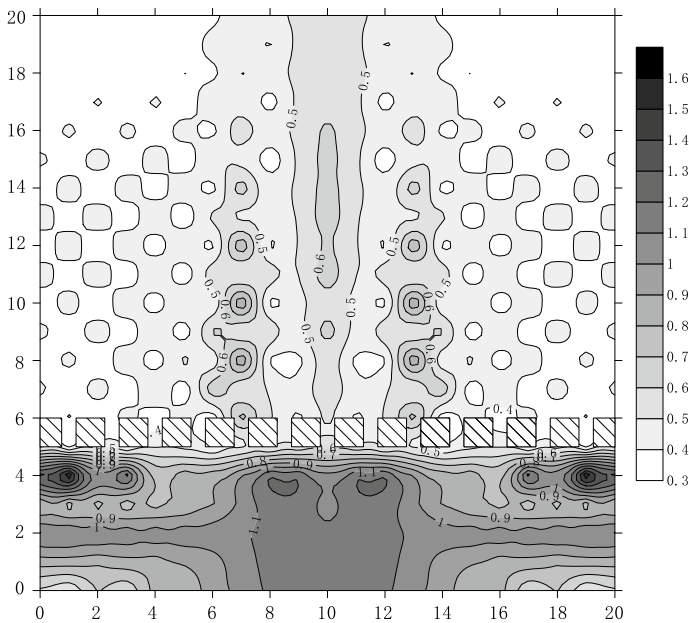
Fig. 22 Test no. 11 *Ar* contour map
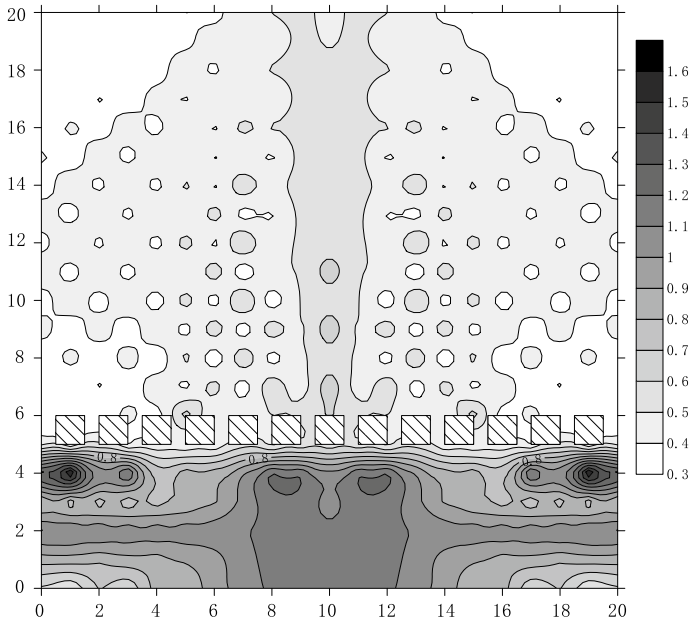
Fig. 23 Test no. 12 *Ar* contour map
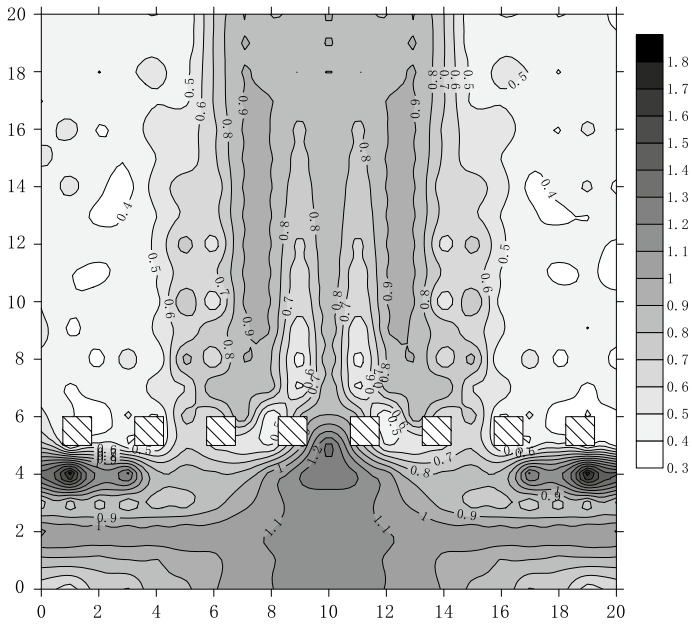
Fig. 24 Test no. 13 *Ar* contour map
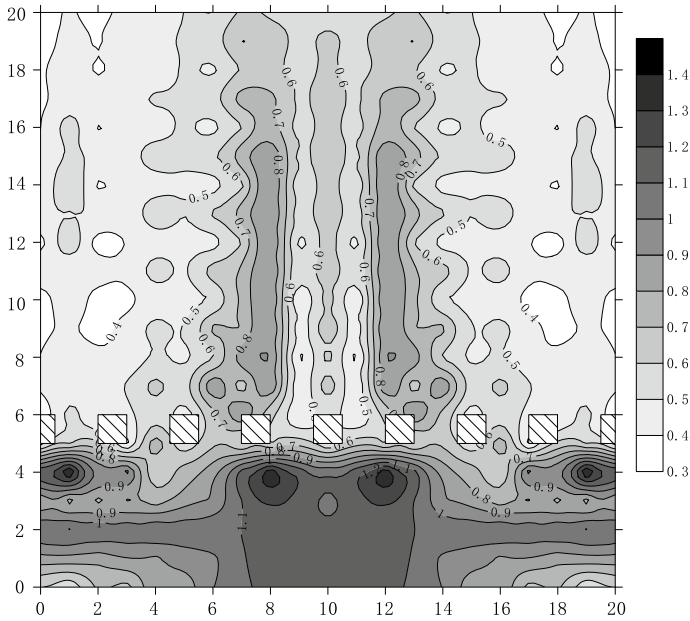
Fig. 25 Test no. 14 *Ar* contour map

Figures 24 and 25 show *Ar* contour maps for a pile spacing of 1.5 m. Compared with a pile spacing of 1.0 m, the pile spacing of 1.5 m is associated with few areas that have an *Ar* value less than 0.4, and an area where *Ar* is greater than 0.8 is present in the middle. When the vibration source is between two piles, the area with poor vibration isolation expands to the rear in an inverted triangle shape. Large areas with poor vibration isolation exhibit *Ar* values greater than 0.9. The overall vibration isolation effect is poor. When the vibration source is directly opposite the pile center, the overall trend is similar to that when the vibration source is between two piles. However, when the vibration source is directly opposite the pile center, the overall *Ar* value is lower by 0.1–0.2, and the vibration isolation effect is slightly better than that when the vibration source is between two piles but is still poor compared to that with a pile spacing of 1.0 m.

In summary, changing the pile spacing greatly impacts the vibration isolation effect of row piles. Excessive pile spacing will cause an unsatisfactory vibration isolation effect but reducing the pile spacing may not improve the vibration isolation effect.

5.2.4 Pile Shape

To examine the effect of pile shape on the vibration isolation effect, we tested hollow square piles (tests no. 15 and no. 16), solid square piles (tests no. 5 and no.

6), solid circular piles (tests no. 17 and no. 18) and a test without isolation (test no. 0–2) to construct and analyze *Ar* contour maps. The results are shown in Figs. 16, 17, 26, 27, 28 and 29.

From Figs. 16, 17, 26, 27, 28 and 29, we see that the overall trend for the vibration isolation effect of hollow square piles is similar to that of solid square piles. In contrast, the overall trend of vibration isolation for solid circular piles is different from that of square solid piles. Square row piles (both solid and hollow) have a better vibration isolation effect than circular piles of the same diameter.

Figures 26 and 27 show *Ar* contour maps for hollow square piles. Compared with the case with solid square piles, the case with hollow square piles has vibrations that are superimposed at the rear of the row piles and offset to both sides when the vibration source is directly between two piles; the area corresponding to *Ar* 0.4–0.7 is greater, and a number of small and discontinuous areas with *Ar* 0.7–0.8 are present. Overall, the vibration isolation effect of the hollow square piles is slightly worse than that of the solid square piles. When the vibration source is directly opposite the pile center, the vibration superposition area at the rear of the row piles shifts backward, but the area is approximately the same. The area corresponding to *Ar* 0.5–0.6 shifts backward and decreases slightly. However, the area corresponding to *Ar* 0.4–0.5 decreases in the rear and increases in the front, resulting in an overall increase in area. Overall, the vibration isolation effect is slightly worse for the hollow square piles than for the solid square piles.
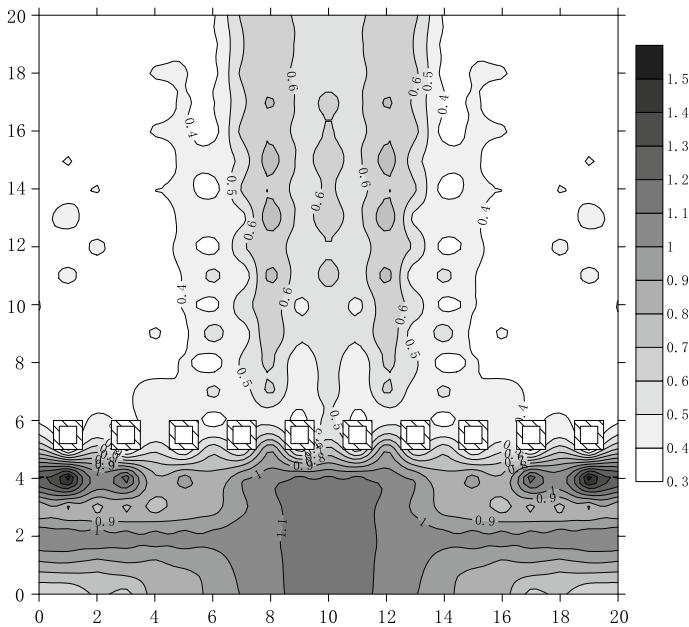
Fig. 26 Test no. 15 *Ar* contour map
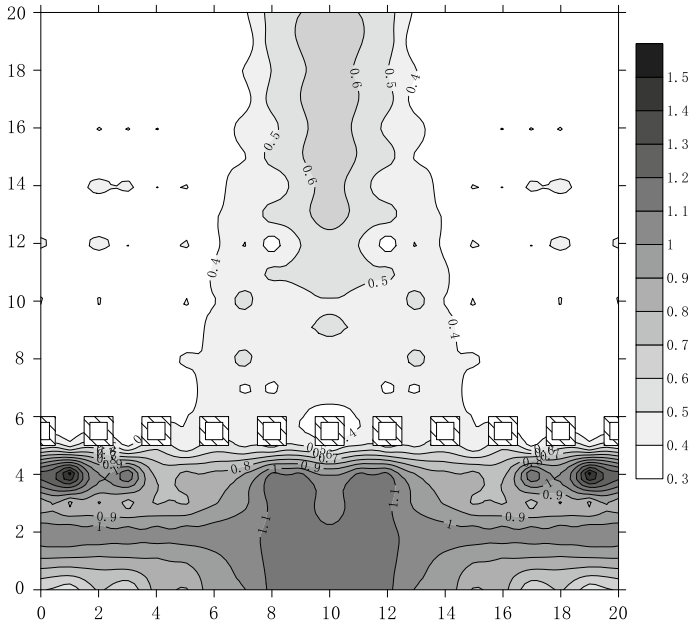
Fig. 27 Test no. 16 *Ar* contour map
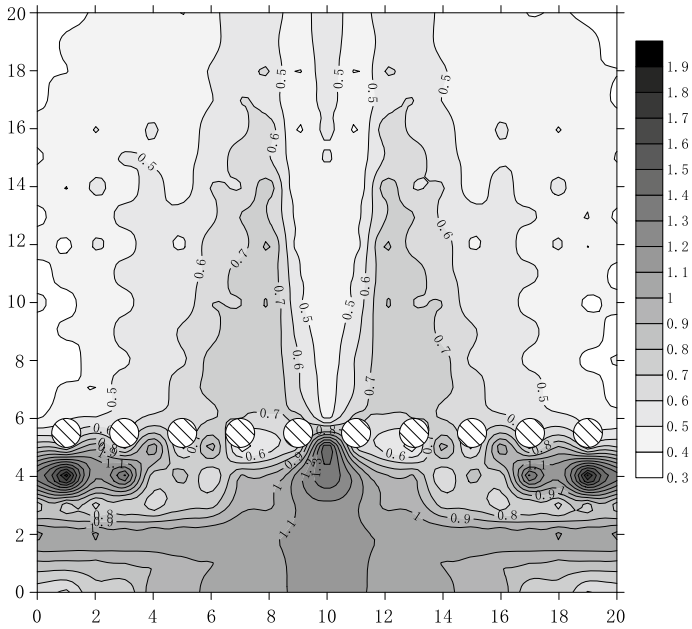
Fig. 28 Test no. 17 *Ar* contour map
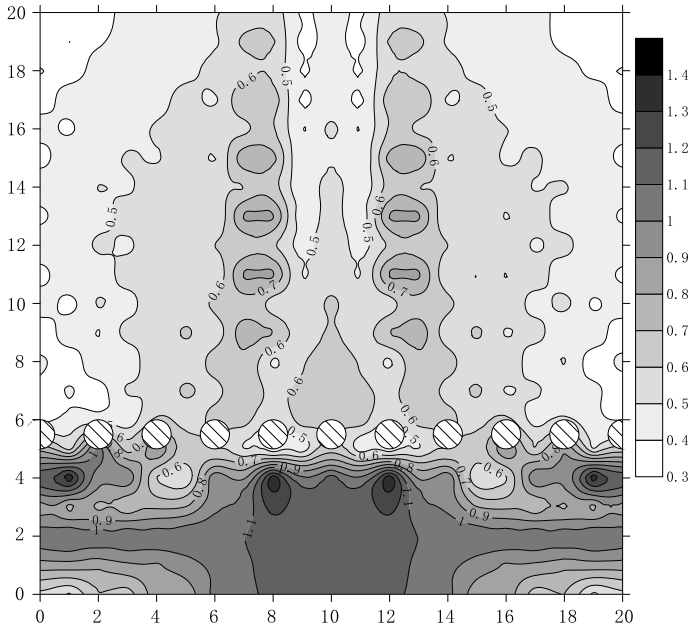
Fig. 29 Test no. 18 *Ar* contour map

Figures 28 and 29 show the *Ar* contour maps for solid circular piles. When the vibration source is directly between the two piles, the vibration superposition area appears on both sides and in the middle of the front part of the row pile. An area of *Ar* 0.5–0.6 appears in the middle of the area behind the row piles, an area of *Ar* 0.7–0.8 appears on both sides of the row piles, and the *Ar* gradually decreases on both sides. When the vibration source is directly opposite the pile center, *Ar* values of 0.6 or greater appear on both sides of the area behind the row pile, and the *Ar* values gradually decrease as the vibration propagates.

In summary, hollow piles have a better vibration isolation effect than solid piles, but vibration isolation effects are not significantly different. However, circular piles of the same diameter are less effective than square piles.

5.2.5 Vibration Source Location

Next, we studied the effect of vibration source location on the vibration isolation effect using distances between the vibration source and the row piles of 1 m (tests no. 19 and no. 20), 1 m (test no. 5 and no. 6), 1 m (test no. 21 and no. 22) and tests without isolation (tests no. 0–1, no. 0–2 and no. 0–3) to construct and analyze *Ar* contour maps. The results are shown in Figs. 16, 17, 30, 31, 32 and 33.

From Figs. 16, 17, 30, 31, 32 and 33, we see that the vibration isolation effects are similar. An area of superimposed vibration behind the row piles appears in the
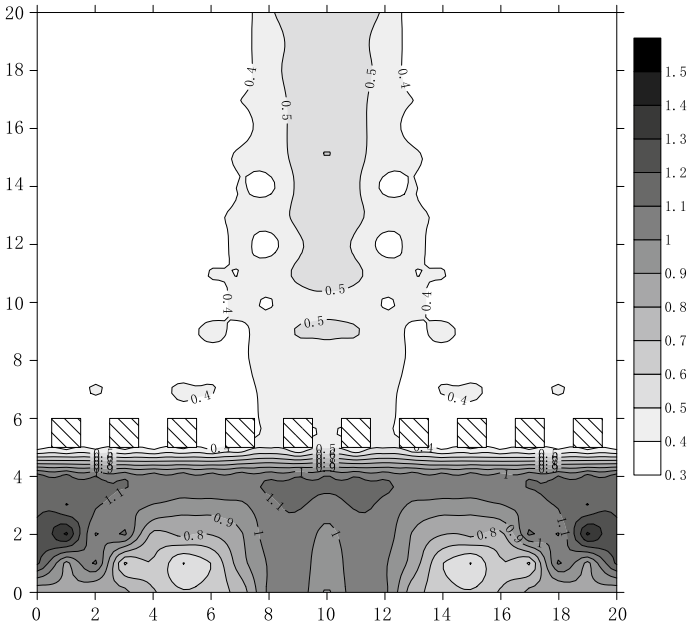
Fig. 30 Test no. 19 *Ar* contour map
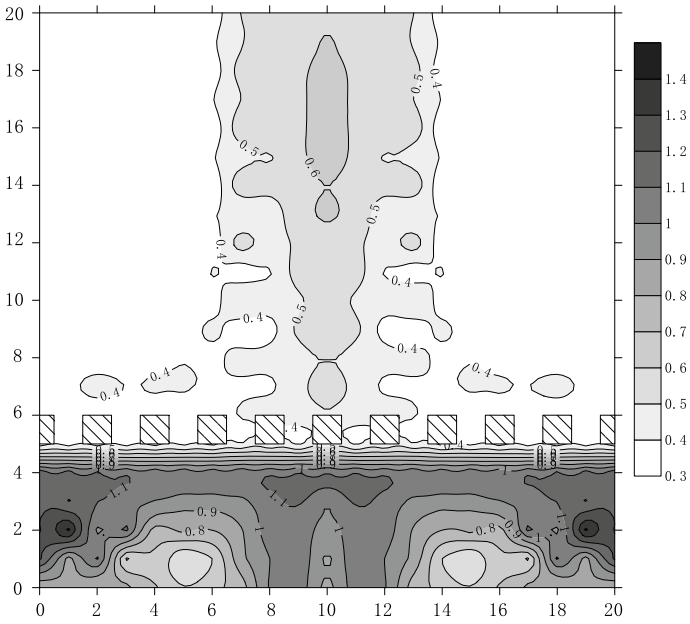
Fig. 31 Test no. 20 *Ar* contour map
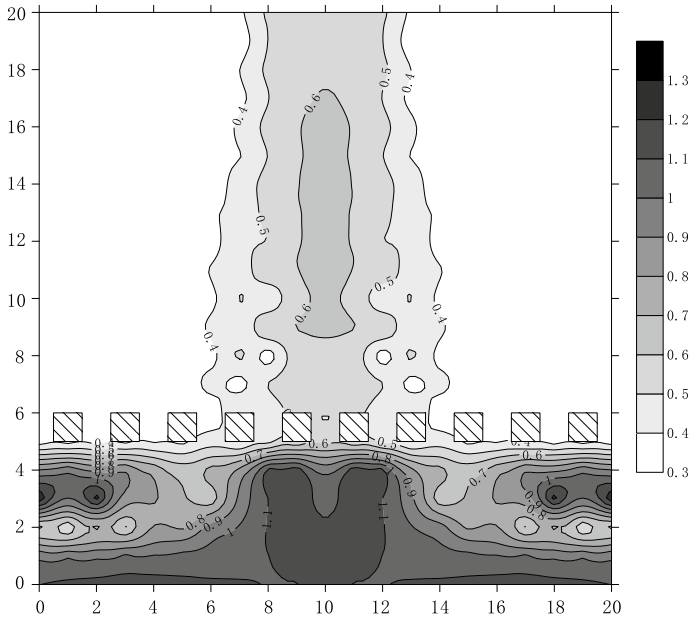
Fig. 32 Test no. 21 *Ar* contour map
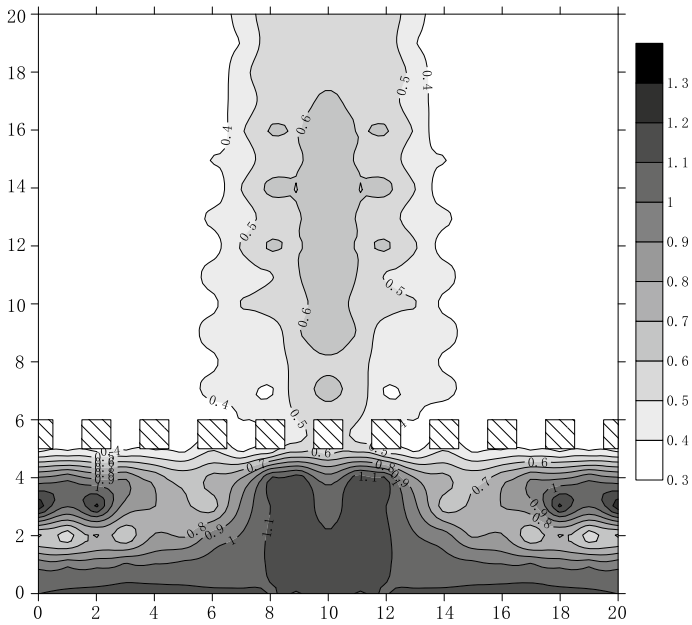
Fig. 33 Test no. 22 *Ar* contour map

middle in all cases. The vibration isolation effect at both sides is more pronounced than that in the middle area.

Figures 30 and 31 show Ar contour maps for a vibration source distance from the row piles of 1 m. Compared with a vibration source distance from the row pile of 3 m, a vibration source distance from the row piles of 1 m is associated with a vibration wave superposition area in front of the row piles that has shifted backward and Ar values in the middle area that have decreased to slightly above 1.1. The area where Ar is greater than 0.4 in the rear of the row piles is reduced. In general, the vibration isolation effect of a vibration source distance of 1 m is better than that of a vibration source distance of 3 m, but the difference is not significant.

Figures 32 and 33 show Ar contour maps for a vibration source distance from the row piles of 5 m. Compared with a vibration source at a 3 m distance from the row pile, a vibration source distance from the row piles of 5 m is associated with a vibration wave superposition area in front of the row piles that has shifted backward and Ar values in the middle area that have increased to slightly above 1.0. Behind the row piles, the area where Ar is greater than 0.4 is approximately the same, but the area where Ar is greater than 0.6 is larger. In general, the vibration isolation effect for a vibration source distance of 5 m is worse than for a vibration source distance of 3 m, but the difference is not significant.

In summary, the vibration isolation effect improves as the distance from the source to the row piles decreases, but the differences are not significant.

5.2.6 Vibration Source Frequency

Finally, we examined the effect of vibration source frequency on the vibration isolation effect using a low-frequency vibration (10 Hz, tests no. 5 and no. 6), an intermediate-frequency vibration (50 Hz, tests no. 23 and no. 24), a high-frequency vibration (120 Hz, tests no. 25 and no. 26) and tests without isolation (tests no. 0–2, no. 0–4 and no. 0–5) to construct and analyze Ar contour maps. The results are shown in Figs. 16, 17, 34, 35, 36 and 37.

From Figs. 16, 17, 34, 35, 36 and 37, we see that the vibration isolation effects tend to be similar for intermediate- and high-frequency vibrations but are significantly different for low-frequency vibrations. For intermediate- and high-frequency vibrations, the vibration isolation effect behind the row piles is not ideal.

Figures 34 and 35 show Ar contour maps for a vibration source frequency of 50 Hz. The area where the Ar is greater than 1.0 is large behind the row piles; there are even small areas where the Ar value is greater than 1.5. As the distance from the row piles increases, Ar gradually decreases, and the area where Ar is less than 0.2 appears far from the row piles.

Figures 36 and 37 show Ar contour maps for a vibration source frequency of 120 Hz. The Ar pattern behind the row piles for the high-frequency vibration is similar to that for the intermediate-frequency vibration. However, the rate of decrease in Ar is greater for high-frequency vibration than for intermediate-frequency vibration. Overall, the vibration isolation effect of the row
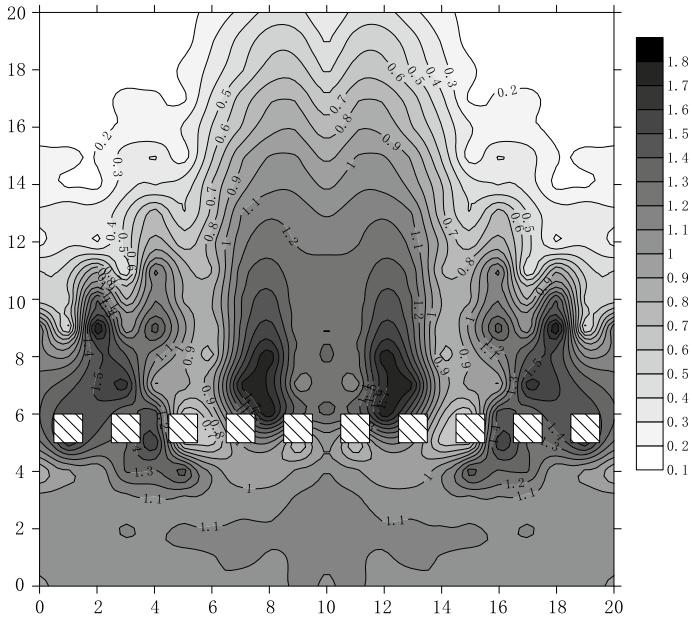
Fig. 34 Test no. 23 *Ar* contour map
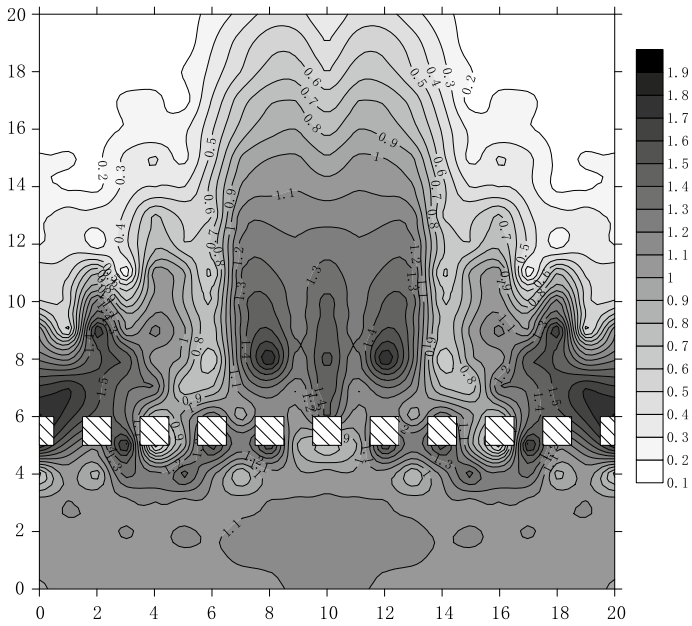
Fig. 35 Test no. 24 *Ar* contour map
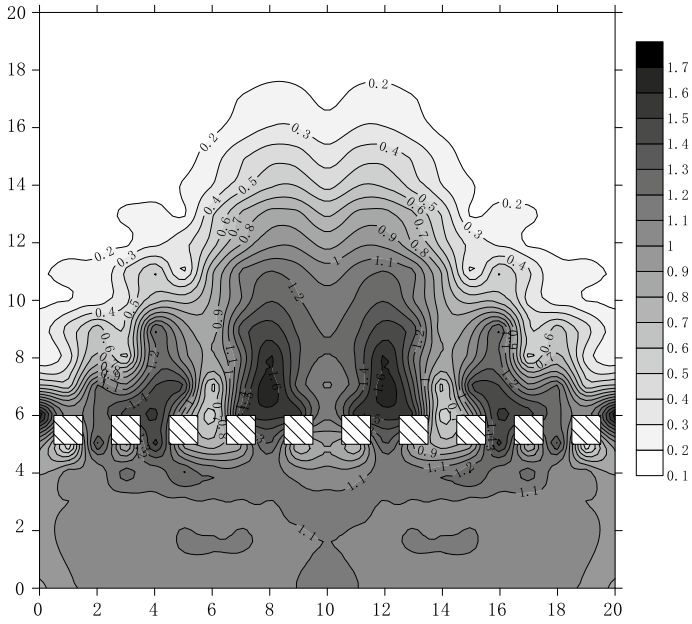
Fig. 36 Test no. 25 *Ar* contour map
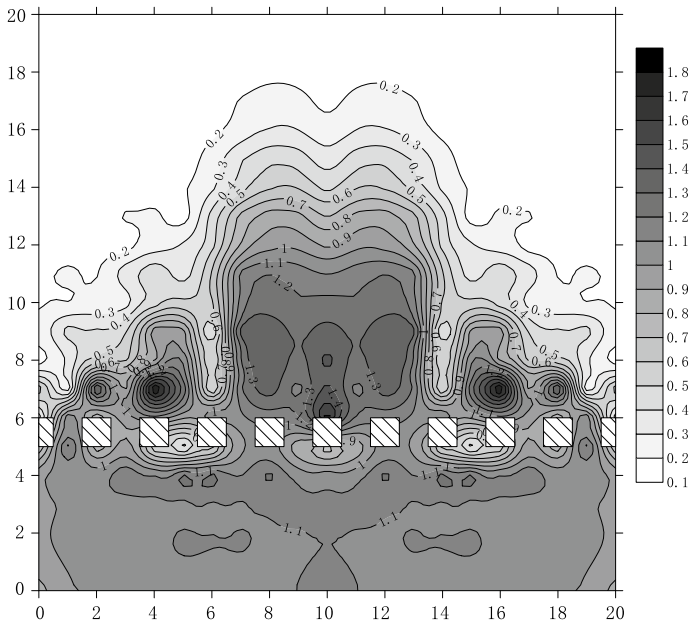
Fig. 37 Test no. 26 *Ar* contour map

piles for a high-frequency vibration is slightly better than that for an intermediate-frequency vibration.

In summary, row piles are not ideal for vibration isolation of high- and intermediate-frequency vibrations but exhibit good vibration isolation effects for low-frequency vibrations.

6 Analysis of the Results

In this work, a finite element model of a foundation with an infinite element boundary was established based on the theory of an elastic half-space body. The model included a single-point vibration source in the free field and piles arranged in a row. The results were used to construct contour maps of the amplitude dissipation ratio (Ar) with respect to cases without vibration isolation. The conclusions from this work are as follows:

(1) A finite element model using infinite element boundaries can effectively reflect the actual effects of vibration isolation measures.
(2) Radial vibration waves propagate from the excitation point, and their acceleration amplitudes continuously decay until they eventually stabilize. The row pile vibration isolation increases the acceleration in front of the row piles and reduces the acceleration behind the row piles.
(3) The vibration isolation effect increases with the number of vibration isolation piles. The vibration isolation effect increases as the depth of the row piles increases but only up to a point. Excessive pile spacing produces an unsatisfactory vibration isolation effect, but reducing the pile spacing may not improve the vibration isolation effect. Hollow piles have a better vibration isolation effect than solid piles but not significantly. Circular piles with the same diameter as square piles are more effective. The vibration isolation effect increases as the distance between the source and the row piles decreases, but the increase is not significant. Row piles are not ideal for vibration isolation of high- and intermediate-frequency vibrations but do produce a good vibration isolation effect for low-frequency vibrations.

References

1. Ahmad S, Al-Hussaini TM, Fishman KL (1996) Investigation on active isolation of machine foundations by open trenches. J Geotech Eng 122:454–461
2. Gao GY, Feng SJ, Li W (2007) 2-D analysis of vibration isolation by wave impeding block in layered ground. J Vib Eng 20(2):174–179
3. Gao GY, Wang F, Chen GQ (2014) Active vibration isolation of the saturated ground with wave impedance block inside and under the load of the travelling train. J Vib Eng 27(3):433–440

4. Yang XJ (1992) Soil dynamics in industrial environment vibration. Chin J Geotech Eng 14 (2):82–88
5. Deng YH, Xia TD, Chen JY (2007) Analysis of efficiency of vibration isolating groove subjected to vehicle load. Rock Soil Mech 5:883–887, 894
6. Xiao SW, Lei CS, Guo C (2011) Numerical analysis of vibration reduction of open trench for high-speed railway. J Railw Eng Soc 8:23–29
7. Yang XJ, Xu J, Zhang CH (2013) Soil–foundation vibration and vibration isolation, 1st edn. China Architecture & Building Press, Beijing
8. Woods RD (1968) Screening of surface waves in soil. J Solids Mech Found Div 94 (SM4):951–979
9. Andersen L, Nielsen SRK (2005) Reduction of ground vibration by means of barriers or soil improvement along a railway track. Soil Dyn Earthq Eng 25(7):701–716
10. Aviles J, Sanchez-Sesma FJ (1983) Piles as barriers for elastic waves. J Geotech Eng 109 (9):1133–1146
11. Aviles J, Sanchez-Sesma FJ (1988) Foundation isolation from vibration using piles as barrier. J Eng Mech 114(11):1854–1870
12. Hayakawa K (1992) Reduction effects of ballast mats and EPS blocks on ground vibration caused by train and its evaluation. Inter-Noise 4:233–240
13. Xu P, Zhou XM, Xia TD (2007) Discontinuous barrier used a row of elastic piles for incident elastic waves. J Vib Eng 20(4):388–395
14. Xia TD, Sun MM, Chen C (2011) An improved method for multiple scattering and isolation of horizontal shear wave using double row of elastic discontinuous barrier. Rock Soil Mech 32(8):2402–2408
15. Shi G, Gao GY (2010) Three-dimensional analysis of a row of piles as passive barriers in saturated soil. J Vib Eng 23(05):546–553
16. Ba ZN, Wang JY, Liang JW (2016) Reduction of train-induced vibrations by using a trench in a layered foundation. J Vib Eng 5:860–873
17. Chen F, Huang MS (2008) Isolation analysis of an annular in-filled trench against the environmental vibrations from a highway viaduct. J Vib Eng 21(3):241–247
18. Feng GS, Liu JL, Zhang RH (2017) Experimental research for influence of filling properties on vibration isolation effect of sand-filled trench. Railw Eng 57(02):151–155
19. Zhang LG, Liu JL, Hou EP (2017) Model test research on vibration isolation effects of filling barriers for railway subgrade. Railw Eng 04:146–150
20. Jiang JQ, Zhou HF, Zhang TQ (2004) Steady-state response of an elastic half-space under a moving point load. Chin J Geotech Eng 26(4):440–444

Ground Vibration Induced by Moving Train Loads on Unsaturated Ground Using 2.5D FEM

G. Y. Gao, S. F. Yao and Qingsheng Chen

Abstract Vibration of an unsaturated ground subjected to moving train loads is investigated using a two-and-a-half-dimensional finite element method (2.5D FEM). The track system is simplified as an Euler beam resting on the unsaturated porous medium, the governing equations are transformed to the frequency–wavenumber domain, and the results in time-space domain are obtained through the fast Fourier transform (FFT). Train speed and degree of saturation are mainly analyzed as important factor influencing ground vibration and excess pore water pressure. The results indicate that, at the track center, the vibration displacement amplitude increases significantly when the ground changes from near saturated ($S_r = 99\%$) to fully saturated state. Also, the acceleration amplitude of unsaturated ground is larger and it decreases more rapidly with time than its counterparts for the scenarios of the saturated ground subjected to the train loading at the same speed. The development of excess pore water pressure of the unsaturated ground at the track center prevails in the shallow depth ($0 \sim 4.5$ m), and the peak value appears at about 1.8 m beneath ground surface. The pore water pressure decreases as the degree of saturation decreases.

G. Y. Gao (✉) · S. F. Yao
Department of Geotechnical Engineering, Tongji University, Shanghai 200092, China
e-mail: gaoguangyun@263.net

S. F. Yao
e-mail: ifengfire@163.com

G. Y. Gao · S. F. Yao
Key Laboratory of Geotechnical and Underground Engineering of Ministry of Education, Tongji University, Shanghai 200092, China

Q. Chen
School of Civil Engineering and Architecture, East China Jiaotong University, Nanchang 330013, China
e-mail: chqsh2006@163.com

Q. Chen
Department of Civil and Environmental Engineering, National University of Singapore, Singapore 117576, Singapore

1 Introduction

In recent years, high-speed railway has developed rapidly as a convenient way of transportation in China. However, at the same time, the train-caused ground vibration has increasingly affected people's life, work and the normal use of precision instruments [1]. It is of great significance to evaluate the train-caused ground vibration in the design and construction process of high-speed railway.

The track-subsoil reaction under moving loads was widely investigated over the past five decades. The subsoil was firstly simplified as a single-phase elastic medium, and a series of achievements were obtained [2–4]. Yang and Hung [5], and Takemiya and Bian [6] studied the dynamic response of elastic and layered subsoil under moving load using the 2.5D finite element method, and they pointed out that the 2.5D FEM has great advantages for the fast calculation and high precision in solving the dynamic problems under moving loads. The finite element discretization is only required in a profile perpendicular to the track direction in the 2.5D FEM formulations, which can significantly reduce the computation cost without losing accuracy at the same time.

To consider the pore water effects in the subsoil subjected to moving loads, Burke and Kingsbury [7] presented an analytical solution for a saturated porous medium based on the Biot theory [8]. Jin et al. [9] studied the stress and excess pore pressure of saturated porous half-space subjected to moving loads analytically and numerically. Lefeuve-Mesgouez and Mesgouez [10] theoretically investigated the displacements of the solid and fluid phases of the porous viscoelastic half-space caused by a vertical moving load, in which the ground is modeled as totally or partially saturated using the complete Biot theory. Gao et al. [11–13] investigated the dynamic responses of homogeneous or transversely isotropic and layered saturated ground under moving loads using the 2.5D FEM.

In the above studies, the subsoil was usually regarded as single-phase or water-saturated media. However, due to large amounts of evaporation and transpiration, the subsoil in arid and semiarid areas is usually in the unsaturated state [14]. The water saturation has an obvious influence on the dynamic characteristics of the unsaturated soil [15, 16]. In contrast to the scenario of saturated soil, even a small change of water saturation can greatly affect the displacement of soil skeleton and the pore water. Therefore, it is of great significance to take account of the effects of the pore gas in seeking more accurate estimation of ground vibration caused by high-speed trains.

To investigate the unsaturated ground vibration caused by high-speed train loads, the 2.5D FEM formulations are presented herewith. The track system is simplified as an Euler beam resting on the unsaturated porous medium. The governing equations of unsaturated soil and beam are transformed to the frequency–wavenumber domain, and the 2.5D FEM formulations are then derived. The results

in time-space domain are obtained through the fast Fourier transform (FFT). Numerical calculations are presented to show the influences of the degree of saturation and the train speeds on the ground vibration and excess pore water pressure induced by the moving loads.

2 2.5D FEM Formulations for Unsaturated Ground Vibration

2.1 2.5D FEM of Unsaturated Soil

The following assumptions are made for the unsaturated soil: (1) the mechanical and permeability properties are uniform; (2) the liquid and gas in the solid skeleton obey the generalized Darcy's law; (3) the soil particle density is related to the fluid pressure and volume deformation, while the water and gas densities are functions of their pressures. The Fourier transform with respect to t and x is defined as

$$\tilde{\tilde{u}}(\varepsilon_x, y, z, \omega) = \int\limits_{-\infty}^{+\infty} \int\limits_{-\infty}^{+\infty} u(x, y, z, t) e^{i\varepsilon_x x} e^{-i\omega t} dx dt \tag{1}$$

Considering the influence of water pressure and volume deformation on the density of solid medium, the mass conservation of solid skeleton can be expressed as [17]:

$$\frac{\partial n}{\partial t} = \frac{\alpha - n}{K_g} \frac{\partial (S_r p^w + (1 - S_r) p^a)}{\partial t} + (\alpha - n)\nabla \cdot \dot{u} \tag{2}$$

where n is the porosity; u is the soil displacement; "·" represents the first derivative of time; and ∇ is Laplace operator. K_g is compression modulus of soil particle, $\alpha = 1 - K_{sk}/K_g$ is Biot coefficient, K_{sk} is the compression modulus of soil skeleton, $p_c = S_r p^w + (1 - S_r) p^a$ is the fluid pressure of unsaturated soil, p^w and p^a are the pressure of pore water and gas, respectively, $S_r = S_r(s)$ is the degree of saturation, and $s = p^a - p^w$ is the matric suction.

The mass conservation of pore water and pore gas can be expressed as [17]:

$$S_r \rho_w \frac{\partial n}{\partial t} + nS_r \frac{\partial \rho_w}{\partial t} + n\rho_w \frac{\partial S_r}{\partial t} + \rho_w nS_r \nabla \cdot \dot{u}^w = 0 \tag{3}$$

$$(1 - S_r)\rho_a \frac{\partial n}{\partial t} + n(1 - S_r)\frac{\partial \rho_a}{\partial t} - n\rho_a \frac{\partial S_r}{\partial t} + n(1 - S_r)\rho_a \nabla \cdot \dot{u}^a = 0 \tag{4}$$

where ρ_w is the water density; ρ_a is the gas density; u^w is the water displacement; and u^a is the displacement of air. By considering the relationship between fluid density and fluid pressure [17], the following two formulas can be obtained:

$$A_{11}\dot{p}^w + A_{12}\dot{p}^a + A_{13}\nabla\dot{u} + A_{14}\nabla\dot{u}^w = 0 \tag{5}$$

$$A_{21}\dot{p}^w + A_{22}\dot{p}^a + A_{23}\nabla\dot{u} + A_{24}\nabla\dot{u}^a = 0 \tag{6}$$

where the coefficients are:

$$A_{11} = \frac{(\alpha - n)S_r^2}{K_g} + \frac{nS_r}{K_w} - A_{ss}\left(n - \frac{(\alpha - n)S_r s}{K_g}\right);$$
$$A_{12} = \frac{(\alpha - n)S_r(1 - S_r)}{K_g} + A_{ss}\left(n - \frac{(\alpha - n)S_r s}{K_g}\right);$$

$$A_{13} = S_r(\alpha - n);$$
$$A_{14} = nS_r; A_{21} = \frac{(\alpha - n)S_r(1 - S_r)}{K_g} + A_{ss}\left(n + \frac{(\alpha - n)(1 - S_r)s}{K_g}\right);$$

$$A_{22} = \frac{(\alpha - n)(1 - S_r)^2}{K_g} + \frac{n(1 - S_r)}{p^a} - A_{ss}\left(n + \frac{(\alpha - n)(1 - S_r)s}{K_g}\right);$$
$$A_{23} = (1 - S_r)(\alpha - n); A_{24} = n(1 - S_r);$$

in which $A_{ss} = \partial S_r/\partial s$ is the partial derivative of saturation with respect to the matric suction; and K_w is the bulk modulus of water.

By applying the Fourier transform to the seepage equations of pore water and pore gas [17], the average displacement of fluid in frequency domain can be obtained as follows:

$$\tilde{u}_i^w = (F_w\tilde{u}_i - \tilde{p}_i^w)/(F_w - \rho_w\omega^2) \tag{7}$$

$$\tilde{u}_i^a = (F_a\tilde{u}_i - \tilde{p}_i^a)/(F_a - \rho_a\omega^2) \tag{8}$$

where "$\cdot\cdot$" denotes the second order derivative with time, "$\sim$" represents the solution in frequency domain; $F_a = n(1 - S_r)\rho_a g\omega i/k_a$, $F_w = nS_r\rho_w g\omega i/k_w$, and ω is the circular frequency. With Eqs. (7) and (8) and by applying the Fourier transform to Eqs. (5) and (6), the mass conservation equations of pore water and pore gas in frequency domain are obtained as follows:

$$\left(A_{13} + \frac{A_{14}F_w}{F_w - \rho_w\omega^2}\right)\tilde{u}_{i,i} - \frac{A_{14}}{F_w - \rho_w\omega^2}\tilde{p}_{ii}^w + A_{11}\tilde{p}^w + A_{12}\tilde{p}^a = 0 \tag{9}$$

$$\left(A_{23} + \frac{A_{24}F_a}{F_a - \rho_a\omega^2}\right)\tilde{u}_{i,i} - \frac{A_{24}}{F_a - \rho_a\omega^2}\tilde{p}_{ii}^a + A_{21}\tilde{p}^w + A_{22}\tilde{p}^a = 0 \tag{10}$$

The momentum conservation equation of unsaturated medium can be expressed as follows [17]:

$$\mu u_{i,jj} + (\lambda + \mu)u_{i,ji} - S_r p_i^w - (1 - S_r)p_i^a = \bar{\rho}_s \ddot{u}_i + \bar{\rho}_w \ddot{u}_i^w + \bar{\rho}_a \ddot{u}_i^a \quad (11)$$

where σ_{ij} and F_i are the stress and body force of the soil; $\bar{\rho}_s = (1 - n)\rho_s$, $\bar{\rho}_w = nS_r\rho_w$, $\bar{\rho}_a = n(1 - S_r)\rho_a$ are the relative density of solid, water and gas, respectively; ε_{ij} is the strain of the soil; δ_{ij} is Kronecker symbol; λ and μ are the Lame constants of soil, and the complex form of Lame constants $\bar{\lambda} = (1 + 2i\eta_s)\lambda$, $\bar{\mu} = (1 + 2i\eta_s)\mu$ are used to replace the λ and μ in Eq. (11) to reflect damping effects of the soil, where η_s is the damping coefficient.

By applying the Fourier transform to Eq. (11), and using Eqs. (7) and (8), one can finally obtain the dynamic equations of unsaturated soil in the frequency domain:

$$\bar{\mu}\tilde{u}_{i,jj} + (\bar{\lambda} + \bar{\mu})\tilde{u}_{i,ji} - S_r\tilde{p}_i^w - (1 - S_r)\tilde{p}_i^a + \omega^2\left[(1 - n)\rho_s + \frac{nS_r\rho_w F_w}{F_w - \rho_w\omega^2} + \frac{n(1 - S_r)\rho_a F_a}{F_a - \rho_a\omega^2}\right]\tilde{u}_i$$
$$- \frac{\omega^2 nS_r\rho_w}{F_w - \rho_w\omega^2}\tilde{p}_i^w - \frac{\omega^2 n(1 - S_r)\rho_a}{F_a - \rho_a\omega^2}\tilde{p}_i^a = 0$$

$$(12)$$

For drainage boundary of porous media, the boundary conditions stress, pore pressure and flux for partial differential Eqs. (9), (10) and (12) can be expressed, respectively, as $\sigma_{ij}^s n_j = f_i$, $p = p'$, $-k_d p_j' n_j = \rho_f g v_n = q$, where u'_i is the boundary displacement; n_j is the direction vector; f_i is the stress at the boundary; p' is the pore pressure at the boundary; v_n and q are the velocity and flux at the boundary, respectively; ρ_f is the flux density; k_d is the permeability coefficient; and g is the gravity acceleration.

From Eq. (12) and the boundary conditions of stress, by introducing the virtual displacement δu_i^* and effective stress in frequency domain $\tilde{\sigma}_{ij,j}'$, the governing equations of unsaturated media as follows can be obtained based on the virtual work principle, parts integration property and Gauss formula:

$$\int \left[\delta\varepsilon_i^*\tilde{\sigma}_{ij}' - \delta u_i^*\omega^2\left[(1 - n)\rho_s + \frac{nS_r\rho_w F_w}{F_w - \rho_w\omega^2} + \frac{n(1 - S_r)\rho_a F_a}{F_a - \rho_a\omega^2}\right]\tilde{u}_i\right]dV$$
$$+ \int \left(\delta u_i^*\frac{\omega^2 nS_r\rho_w}{F_w - \rho_w\omega^2}\tilde{p}_i^w - \delta\varepsilon_i^*\delta_{ij}S_r\tilde{p}_i^w\right)dV \quad (13)$$
$$+ \int \left(\delta u_i^*\frac{\omega^2 n(1 - S_r)\rho_a}{F_a - \rho_a\omega^2}\tilde{p}_i^a - \delta\varepsilon_i^*\delta_{ij}(1 - S_r)\tilde{p}_i^a\right)dV = \int \delta u_i^* f_i dS$$

The 4-node isoparametric element is used for discretization, and the corresponding 2.5D governing equation in matrix form can be obtained as follows using the conventional FEM and wavenumber transform in track direction:

$$(\mathbf{K}'_{\mathbf{up}} - \mathbf{M}_{\mathbf{up}})\tilde{\tilde{\mathbf{u}}} + (\mathbf{Q}'_{\mathbf{up}} - \mathbf{Q}_{\mathbf{up}})\tilde{\tilde{\mathbf{p}}}^{\mathbf{w}} + (\mathbf{G}'_{\mathbf{up}} - \mathbf{G}_{\mathbf{up}})\tilde{\tilde{\mathbf{p}}}^{\mathbf{g}} = \tilde{\tilde{\mathbf{f}}}^{\mathbf{s}}_{\mathbf{up}} \tag{14}$$

where "-" represents the parameters in wavenumber domain, $\mathbf{K}_{\mathbf{up}}$, $\mathbf{M}_{\mathbf{up}}$, $\mathbf{Q}_{\mathbf{up}}$, $\mathbf{G}_{\mathbf{up}}$, $\mathbf{f}^{\mathbf{s}}_{\mathbf{up}}$ are stiffness matrix, mass matrix, liquid contribution matrix, gas contribution matrix and equivalent nodal force matrix, and their detailed expressions are:

$$\mathbf{K}'_{\mathbf{up}} = \sum_e \iint (\mathbf{B}^*\mathbf{N})^{\mathrm{T}}\mathbf{D}(\mathbf{BN})|\mathbf{J}|\mathrm{d}\eta\mathrm{d}\xi; \tilde{\tilde{\mathbf{f}}}^{\mathbf{s}}_{\mathbf{up}} = \sum_e \iint \mathbf{N}^{\mathrm{T}}\tilde{\tilde{\mathbf{f}}}|\mathbf{J}|\mathrm{d}\eta\mathrm{d}\xi;$$

$$\mathbf{M}_{\mathbf{up}} = \omega^2 \left[(1-n)\rho_s + nS_r\rho_w \frac{F_w}{F_w - \rho_w\omega^2} + n(1-S_r)\rho_w \frac{F_a}{F_a - \rho_a\omega^2} \right]$$
$$\times \sum_e \iint \mathbf{N}\mathbf{N}^{\mathrm{T}}|\mathbf{J}|\mathrm{d}\eta\mathrm{d}\xi;$$

$$\mathbf{Q}_{\mathbf{up}} = \alpha S_r \sum_e \iint (\mathbf{B}^*\mathbf{N})^{\mathrm{T}} m\overline{\mathbf{N}}|\mathbf{J}|\mathrm{d}\eta\mathrm{d}\xi; \mathbf{Q}'_{\mathbf{up}} = \frac{\omega^2 nS_r\rho_w}{F_w - \rho_w\omega^2} \sum_e \iint \mathbf{N}^{\mathrm{T}}\overline{\mathbf{B}\mathbf{N}}|\mathbf{J}|\mathrm{d}\eta\mathrm{d}\xi;$$

$$\mathbf{G}_{\mathbf{up}} = \alpha(1-S_r) \sum_e \iint (\mathbf{B}^*\mathbf{N})^{\mathrm{T}} m\overline{\mathbf{N}}|\mathbf{J}|\mathrm{d}\eta\mathrm{d}\xi;$$

$$\mathbf{G}'_{\mathbf{up}} = \frac{\omega^2 n(1-S_r)\rho_a}{F_a - \rho_a\omega^2} \sum_e \iint \mathbf{N}^{\mathrm{T}}\overline{\mathbf{B}\mathbf{N}}|\mathbf{J}|\mathrm{d}\eta\mathrm{d}\xi.$$

where "$*$" represents the conjugate matrix; $\mathbf{N}$ and $\overline{\mathbf{N}}$ are shape functions in time and frequency domain, its component in time domain $N_i(\eta, \xi) = 0.25(1 + \eta_i\eta)(1 + \xi_i\xi)$, where η, ξ are local coordinates and η_i, ξ_i are local coordinates of node. $\mathbf{J}$ is Jacobi matrix; $\mathbf{D}$ is stress matrix; and $\mathbf{B}$ is partial derivative matrix. By applying Galerkin method to Eqs. (9) and (10) and using the boundary conditions of flux and pore pressure, the 2.5D FEM formula in matrix form of unsaturated media can be obtained as follows:

$$(\mathbf{H}_{\mathbf{md}})\tilde{\tilde{\mathbf{u}}} + (\mathbf{Q}_{\mathbf{md}} + \mathbf{Q}'_{\mathbf{md}})\tilde{\tilde{\mathbf{p}}}^{\mathbf{w}} + (\mathbf{G}'_{\mathbf{md}})\tilde{\tilde{\mathbf{p}}}^{\mathbf{g}} = \tilde{\tilde{\mathbf{f}}}^{\mathbf{w}} \tag{15}$$

$$(\mathbf{H}_{\mathbf{dw}})\tilde{\tilde{\mathbf{u}}} + (\mathbf{Q}'_{\mathbf{dw}})\tilde{\tilde{\mathbf{p}}}^{\mathbf{w}} + (\mathbf{G}_{\mathbf{dw}} + \mathbf{G}'_{\mathbf{dw}})\tilde{\tilde{\mathbf{p}}}^{\mathbf{g}} = \tilde{\tilde{\mathbf{f}}}^{\mathbf{g}} \tag{16}$$

where

$$\mathbf{H}_{\mathbf{md}} = \left(A_{13} + \frac{A_{14}F_w}{F_w - \rho_w\omega^2} \right) \sum_e \iint \overline{\mathbf{N}}^{\mathrm{T}} m^{\mathrm{T}}\mathbf{B}\mathbf{N}|\mathbf{J}|\mathrm{d}\eta\mathrm{d}\xi;$$

$$\mathbf{H}_{\mathbf{dw}} = \left(A_{23} + \frac{A_{24}F_a}{F_a - \rho_a\omega^2_g} \right) \sum_e \iint \overline{\mathbf{N}}^{\mathrm{T}} m^{\mathrm{T}}\mathbf{B}\mathbf{N}|\mathbf{J}|\mathrm{d}\eta\mathrm{d}\xi;$$

$$\mathbf{Q_{md}} = \frac{A_{14}}{F_w - \rho_w \omega^2} \sum_e \iint (\mathbf{B_s^* \overline{N}})^\mathbf{T} (\mathbf{B_s \overline{N}}) |\mathbf{J}| \mathrm{d}\eta \mathrm{d}\xi;$$

$$\mathbf{G_{dw}} = \frac{A_{24}}{F_a - \rho_a \omega^2} \sum_e \iint (\mathbf{B_s^* \overline{N}})^\mathbf{T} (\mathbf{B_s \overline{N}}) |\mathbf{J}| \mathrm{d}\eta \mathrm{d}\xi;$$

$$\mathbf{Q'_{md}} = A_{11} \sum_e \iint \mathbf{\overline{N}^T \overline{N}} |\mathbf{J}| \mathrm{d}\eta \mathrm{d}\xi; \mathbf{Q'_{dw}} = A_{21} \sum_e \iint \mathbf{\overline{N}^T \overline{N}} |\mathbf{J}| \mathrm{d}\eta \mathrm{d}\xi;$$

$$\mathbf{G'_{md}} = A_{12} \sum_e \iint \mathbf{\overline{N}^T \overline{N}} |\mathbf{J}| \mathrm{d}\eta \mathrm{d}\xi;$$

$$\mathbf{G'_{dw}} = A_{22} \sum_e \iint \mathbf{\overline{N}^T \overline{N}} |\mathbf{J}| \mathrm{d}\eta \mathrm{d}\xi; \tilde{\mathbf{\bar{f}}}^w_{up} = - \sum_e \iint \frac{F_w \rho_w g \tilde{\mathbf{v}}_n}{k_w} |\mathbf{J}| \mathrm{d}\eta \mathrm{d}\xi;$$

$$\tilde{\mathbf{\bar{f}}}^g_{up} = - \sum_e \iint \frac{F_g \rho_g g \tilde{\mathbf{v}}_n}{k_g} |\mathbf{J}| \mathrm{d}\eta \mathrm{d}\xi.$$

Assembling Eqs. (14), (15) and (16) together, the final governing equations in 2.5D FEM formula of unsaturated media can be obtained as follows:

$$\mathbf{KU} = \mathbf{R} \tag{17}$$

where

$$\mathbf{K} = \begin{bmatrix} \mathbf{K'_{up}} - \mathbf{M_{up}} & \mathbf{Q'_{up}} - \mathbf{Q_{up}} & \mathbf{G'_{up}} - \mathbf{G_{up}} \\ \mathbf{H_{md}} & \mathbf{Q_{md}} + \mathbf{Q'_{md}} & \mathbf{G'_{md}} \\ \mathbf{H_{dw}} & \mathbf{Q'_{dw}} & \mathbf{G'_{dw}} + \mathbf{G_{dw}} \end{bmatrix}, \mathbf{U} = \begin{bmatrix} \tilde{\tilde{\mathbf{u}}} \\ \tilde{\tilde{\mathbf{p}}}^w \\ \tilde{\tilde{\mathbf{p}}}^g \end{bmatrix}, \mathbf{R} = \begin{bmatrix} \tilde{\tilde{\mathbf{f}}}^s_{up} \\ \tilde{\tilde{\mathbf{f}}}^w \\ \tilde{\tilde{\mathbf{f}}}^g \end{bmatrix}.$$

2.2 Euler Beam Model of Track System

In this paper, the Euler beam model is used to simulate the track system (including the rails and the embankment). The dynamic equation of the track system in frequency–wavenumber domain can be expressed as [13]:

$$(EI\xi_x^4 - m\omega^4)u_r^{xt} = f_{IT}^{xt}(\xi_x, \omega) + p_0^{xt}(\xi_x, \omega) \tag{18}$$

where u_r^{xt} is the displacement of track in frequency–wavenumber domain, and ξ_x is the wavenumber variable, EI is the bending stiffness of the track, m is the comprehensive quality of the track and sleepers, $f_{IT}(x,t)$ is the contact reaction force of the ground, $p_0^{xt}(\xi_x, \omega)$ is the dynamic load on the track in frequency–wavenumber domain, where p_0 is the vehicle load.

2.3　Model Verification and Calculation Parameters

Equations (17) and (18) are governing equations of the track–ground system in frequency–wavenumber domain. The solution in the frequency–wavenumber domain can be obtained, and results in the time-space domain can be obtained through the FFT. Figure 1 shows the 2.5D FEM of track–ground model and the viscoelastic boundary. The viscoelastic dynamically wave absorbing boundary for 2.5D FEM is deduced in detail in [12]. The ground layers distribution and soil parameters of the Sweden X2000 train site [6] are adopted to verify the proposed model. The train load model and its parameters in the frequency–wavenumber domain are also in accordance with [6]. The track parameters are shown in Table 1 [6]. When the degree of saturation $S_r = 0$, it is degraded to the calculation model of elastic soil. It can be seen from Fig. 2 that the predicted data are in good agreement with the measured ones [6], which illustrate the accuracy of the proposed model.

For the following dynamic analysis, the V-G model [17] $S_e = [1 + (\alpha_1 s)^k]^{-m}$ is used to describe the relationship between the water saturation and the pore suction and the Mualem model [17] is adopted to describe the permeability coefficients of fluid: $k_w = \rho_w g \kappa / \eta_w \cdot \sqrt{S_r} \{1 - [1 - (S_e)^{\frac{1}{m}}]^m\}^2$ $k_g = \rho_g g \kappa / \eta_g \sqrt{1 - S_r} [1 - (S_e)^{\frac{1}{m}}]^{2m}$, where $\alpha_1 = 1 \times 10^{-5}$, $k = 4$, $m = 1 - 1/k = 0.75$ are fitting parameters; $S_e = (S_r - S_{w0})/(1 - S_{w0})$ is the effective saturation, where $S_{w0} = 0.05$ is the
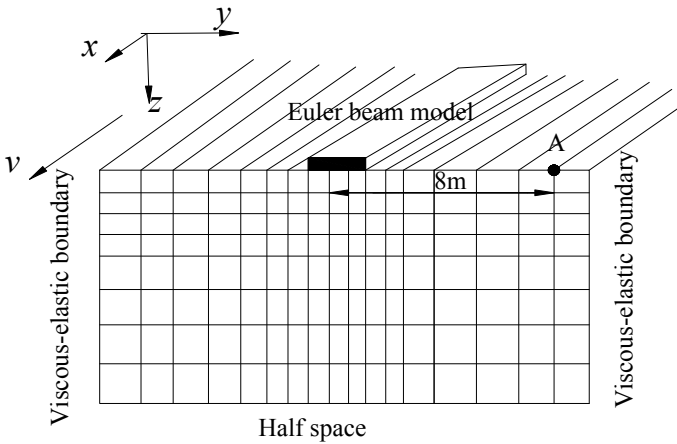
Fig. 1 2.5D FEM of track–ground model and the viscoelastic boundary

Table 1 Parameters of track structure of X2000 [6]

Parameters	Value
Track width $2B$ (m)	3
Density M (t m^{-1})	10.8
Bending stiffness EI (MN m^2)	200
Damping coefficient	0.10
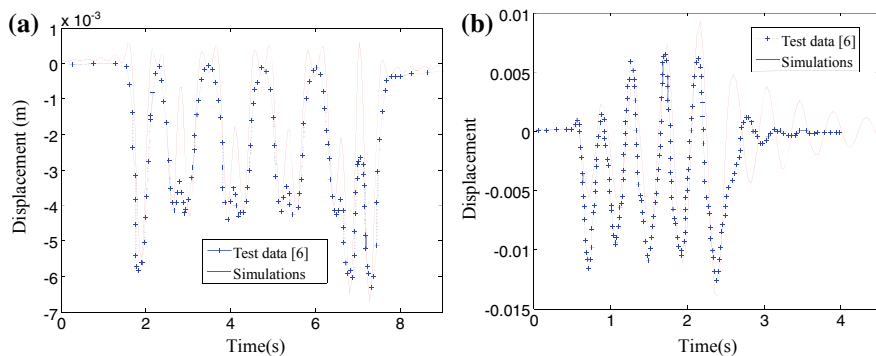
Fig. 2 Time history curve of ground vertical displacement at the track center for both test data and simulations with different train speeds: **a** 70 km/h; **b** 200 km/h

irreducible saturation of water; $\eta_w = 1.0$ mPa · s, $\eta_g = 0.015$ mPa · s are viscosity coefficients of pore water and gas; $\kappa = 1.0$ μm^2 is the intrinsic permeability of soil. The bulk modulus of pore water $K_w = 2.1 \times 10^9$ N/m^2. The physical parameters of pore fluid are assumed to be constants in the numerical calculation. The ground surface is set as the drainage and exhaust boundary, while the bottom and infinite side of the subgrade are set up as non-drainage and non-exhaust boundaries. The atmospheric pressure is taken as the reference air pressure. Since the high-speed train lines in China are mostly distributed in the southeast coastal area, the high water saturation condition (100, 99 and 90%) for the subsoil is considered in this paper.

3 Ground Vibration at Different Train Speeds

3.1 Analysis of Ground Vibration at the Track Center

Figure 3 is the time history curves of ground vertical displacement (Fig. 3a) and acceleration (Fig. 3b) at the track center at different degrees of saturation (100, 99 and 90%) and train speeds (200 and 350 km/h). From Fig. 3a, at low speed (200 km/h), the saturated ground displacement amplitude is substantially larger than that of unsaturated ground. When the degree of saturation decreases from 100% (fully saturated) to 99% (nearly saturated), the displacement amplitude significantly decreases although the reduction in the degree of saturation is very small. However, when the degree of saturation reduces from 99 to 90%, the decrease in displacement amplitude is not evident, although the gas content change is larger than that from 100 to 99%. That is to say, a very small amount of gas entrance into the saturated soil at low speed can cause a sharp decrease in the displacement amplitude, or, the displacement amplitude increases significantly when the subsoil state varies from the nearly saturated to the fully saturated state. The fully saturated

state is the most unfavorable state for the ground vibration at low speed. This is possibly caused by the completely phase change of the soil (from three phase of nearly saturated to two phase of fully saturated), which brings a completely change in soil dynamic characteristics. The resonance of saturated ground occurs when the train speed is close to the shear wave velocity of saturated soil (about 220 km/h), while for unsaturated ground the vibration displacement at the track center is smaller due to the pore gas. The water saturation reduction has a limited influence on the displacement amplitude at high speed (350 km/h), and the unsaturated ground has almost equivalent displacement amplitude of saturated ground. It is also seen from Fig. 3a that for a given speed, the unsaturated ground vibration displacement attenuates rapidly with time compared to the saturated ground, and the difference is due to the existence of pore gas. The duration time of the ground displacement vibration decreases as the speed increases.

From Fig. 3b, it can be observed that, at a given speed, the acceleration amplitude of the ground at the degree of saturation with 90% has slight difference from that at the degree of saturation with 99%, while both of which are greater than
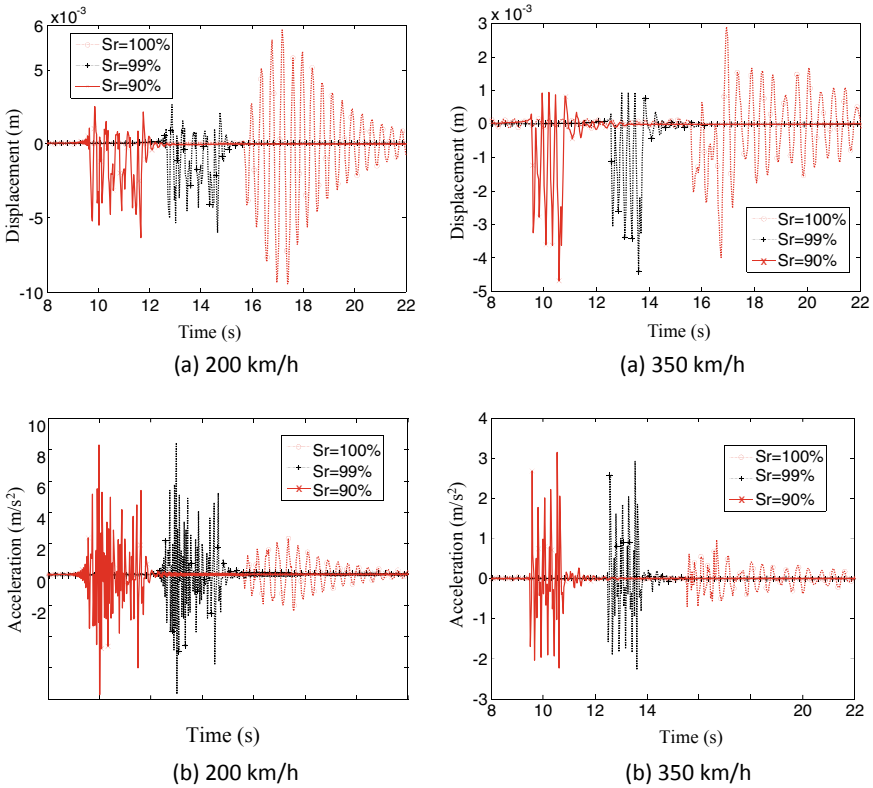
Fig. 3 Time history curves of ground vertical displacement and acceleration at the track center at different degrees of saturation and train speeds: **a** displacement; **b** acceleration

that of the saturated ground. This is possibly due to that, the pore gas in unsaturated ground may enhance the wave scattering and reflection during its propagation, thereby increasing the unsaturated ground acceleration. In addition, it is found that, for a given speed, the vibration acceleration attenuates more slowly with time in saturated ground compared with the unsaturated ground. Also, the duration time of the vibration acceleration and displacement of the unsaturated ground becomes increasingly short as the speed increases.

By comparing Fig. 3a with Fig. 3b, it can be found that, at low speed (200 km/h), the acceleration amplitude on unsaturated ground is larger than that on the saturated ground. In contrast, the displacement amplitude on unsaturated ground is smaller than its counterpart on the saturated ground. As the train speed increases to be 350 km/h, the acceleration amplitude on the unsaturated ground is still larger than that on the saturated ground, while the displacement amplitude on unsaturated ground tends to be equal to its counterpart on the saturated ground.

Figure 4 is the vertical amplitude of displacement and acceleration of the ground at different degrees of saturation at the track center corresponding to different train speeds. From Fig. 4a, it can be found that, at the track center, when the speed is below 270 km/h, the displacement amplitude of saturated ground is larger than its counterpart of the unsaturated ground. When the train speed is beyond 270 km/h, the displacement amplitude of unsaturated ground tends to be slightly larger than that of the saturated ground. For saturated ground, the ground displacement amplitude significantly decreases as the train speed increases from 200 to 300 km/h, and then slightly increases as the train speed exceeds 300 km/h. In contrast, for the unsaturated ground, the displacement amplitude decreases as the train speed increases from 200 to 250 km/h; however, the displacement amplitude of unsaturated ground remains almost constant as train speed exceeds 250 km/h. Therefore, in the ground at high degree of saturation (90–100%), the train speed is recommended to maintain between 250 and 350 km/h (better at 300 km/h) for controlling
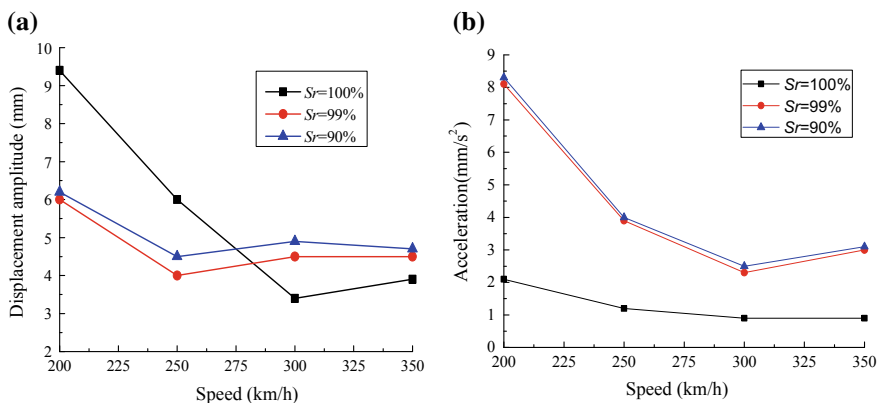
Fig. 4 Ground vertical amplitude of displacement and acceleration at different degrees of saturation at the track center corresponding to different train speeds

the ground vibration displacement amplitude at the track center. It is also observed that, at a given speed, the displacement amplitude of unsaturated ground differs slightly corresponding to the scenarios for different degrees of saturation, i.e., the influence of degree of saturation on the unsaturated ground displacement amplitude is insignificant.

Figure 4b indicates that, for a given speed, slight difference exists between the acceleration amplitudes of the unsaturated ground at $S_r = 90$ and 99%, however, both of which are larger than the counterparts of the saturated ground. For example, the acceleration amplitude of the unsaturated ground subjected to moving load at the speed of 200 km/h is about 4 times of its counterpart for the scenario of the saturated ground. As the speed increases from 200 to 300 km/h, the acceleration amplitudes of both unsaturated ground and saturated ground decrease; however, the decreasing rate of acceleration amplitude of unsaturated ground is much higher than that of the saturated ground. It is also observed that, the acceleration amplitude of the unsaturated ground subjected to moving load with the speed of 300 km/h is about 2 times of the counterparts of saturated ground. As the train speed exceeds 300 km/h, the acceleration amplitude keeps almost constant for the saturated ground, but increases slightly for the unsaturated ground. In the region with high degree of saturation (90–100%), the train speed is recommended to maintain at about 300 km/h, in order to reduce the ground acceleration amplitude at the track center.

3.2 Analysis of Ground Vibration at 8 m Away from the Track Center

Figure 5 presents the time history curve of vertical acceleration of ground surface at 8 m away from track center corresponding to different degrees of saturation and train speeds. The acceleration amplitude of unsaturated ground is obviously greater than its counterpart of the saturated ground for a given speed. The acceleration amplitude increases significantly when the degree of saturation decreases from 100% (fully saturated) to 99% (nearly saturated); however, when the degree of saturation reduces from 99 to 90%, the decrease of the acceleration amplitude is not evident, although the gas content change is larger than that from 100 to 99%. This is possibly due to that, when entering a small amount of gas, the saturated soil has a thorough phase change (from two phase of fully saturated to three phase of nearly saturated), which brings a substantial change of its dynamic characteristics. The pore gas in unsaturated ground enhanced the wave scattering and reflection during its propagation, which amplifies the unsaturated ground acceleration in the far distance from the track center. From the time history curves, it is also seen that, as the train speed increases, the vibration duration time of the unsaturated ground decreases, while the counterpart of the saturated ground increases correspondingly. The shear wave propagating through the saturated pore water may enhance
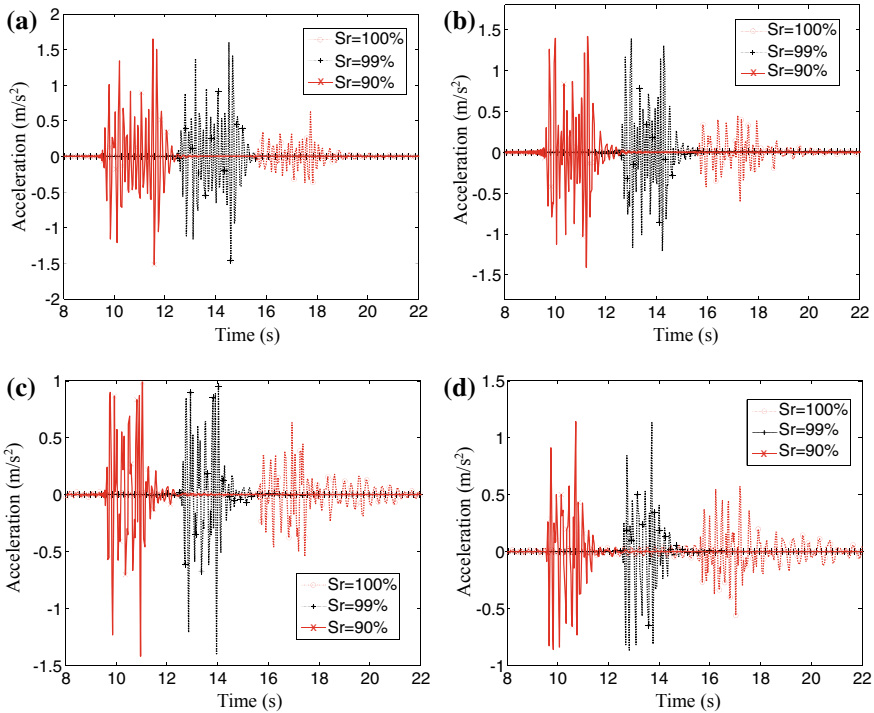
Fig. 5 Time history curve of vertical acceleration of ground surface at 8 m away from track center at different train speeds and degrees of saturation

vibration acceleration and makes it dissipate slowly. It can also be seen from Fig. 5 that, at 300–350 km/h, the vibration acceleration of saturated ground diminishes more slowly with time than that of the unsaturated.

Figure 6 shows the vertical acceleration amplitude of ground with various degrees of saturation at 8 m away the track center corresponding to different train speeds. It can be seen clearly that, the acceleration amplitudes of unsaturated ground at $S_r = 90$ and 99% are almost equal, but both of which are greater than its counterpart of the saturated ground under the moving load at the same speed. This may be due to that, the pore gas in the unsaturated ground enhanced the wave scattering and reflection during its propagation, which amplifies the ground acceleration 8 m away the track center. The acceleration amplitude of unsaturated ground decreases with the increase in the train speed, while the acceleration amplitude of saturated ground decreases slightly at first following by a slight increase when the train speed is beyond 300 km//h.

Fig. 6 Vertical acceleration amplitude of ground with various degrees of saturation at 8 m away the track center corresponding to different train speeds

4 Excess Pore Water Pressures Under the Track at Different Train Speeds

Figure 7 shows the variation of excess pore water pressure with depth under track center at different train speeds and degrees of saturation. It can be found that the development of excess pore water pressure prevails in the unsaturated subgrade at shallow depth (within 3.5 m), but decreases sharply at 3.5–4.5 m. The peak value of the excess pore water pressure appears at about 1.8 m beneath the ground surface, and it is significantly influenced by the degree of saturation of the ground. For example, at a given train speed, the amplitude of excess pore water pressure in the ground at degree of saturation with 99% is about 3 times greater than its counterparts in the ground at degree of saturation with 90%. At degree of saturation

Fig. 7 Excess pore water pressure distribution with depth under the track center at different train speeds and degrees of saturation

with 99%, the excess pore pressure amplitude in the ground decreases slightly as the train speed increases. Beyond 4.5 m depth, the excess pore water pressure amplitude in the ground at degree of saturation with 99% is also larger than that of the ground at the degree of saturation 90%. For instance, the excess pore pressure in the ground at degree of saturation with 99% is about 0.6 kPa, and 0.2 kPa at the depth of 6 m and 10 m, respectively. In contrast, as the degree of saturation decreases to be 90%, the excess pore pressure in the ground is about 0.1 and 0.02 kPa, respectively (about 17 and 10% of that at saturation 99%). The peak value of the excess pore water pressure in the ground at degree of saturation with 90% is about 1 kPa; hence, the excess pore water pressure in the ground with low degree of saturation (<90%) induced by the high-speed train can be neglected.

5   Conclusion

This paper presents 2.5D FEM formulations for analyzing the unsaturated ground vibration induced by high-speed trains. Effects of the degree of saturation and the train speed are investigated, and the following conclusions can be drawn:

(1) At the track center: the displacement amplitude increases significantly when the ground transforms from the nearly saturated to the fully saturated state. The fully saturated state is the most unfavorable state for the ground displacement vibration at low speed. For a given speed, the displacement amplitude of unsaturated ground decreases more rapidly with time than its counterpart at saturated ground. At low speed, the acceleration amplitude of unsaturated ground is greater than that of the saturated ground, while the displacement amplitude of unsaturated ground is smaller than that of the saturated ground. In contrast, as the train speed reaches 350 km/h, the acceleration amplitude of unsaturated ground is still larger than that of the saturated ground, while the displacement amplitude of unsaturated ground tends to be equal to that of the saturated ground.

(2) At the track center, when the speed is below 270 km/h, the displacement amplitude of saturated ground is larger than its counterpart of the unsaturated ground. For a given speed, the acceleration amplitude of the unsaturated is significantly larger than the counterpart of the saturated ground. For the unsaturated ground at high saturation (90–100%), the train speed is recommended to maintain between 250 and 350 km/h (better at 300 km/h) in order to reduce the ground vibration displacement amplitude and acceleration amplitude at the track center.

(3) The development of excess pore water pressure of unsaturated subgrade prevails in the shallow depth (within 4.5 m) and decreases sharply at about 3.5–4.5 m beneath the ground surface. The peak value of the excess pore water pressure appears at about 1.8 m and decreases obviously as the saturation decreases. The excess pore water pressure in unsaturated ground with low saturation (<90%) induced by the high-speed train can be neglected.

References

1. Xia H (2010) Traffic environment vibration engineering. Science Press, China
2. Coel J, Huth J (1958) Stresses produced in a half space by moving loads. J Appl Mech 25:433–436
3. Eason G (1965) The stresses produced in a semi-infinite solid by a moving surface force. Int J Eng Sci 2:581–609
4. Xia H, Cao YM, Roeck GD (2010) Theoretical modeling and characteristic analysis of moving-train induced ground vibrations. J Sound Vib 329(7):819–832
5. Yang YB, Hung HH (2001) A 2.5D finite/infinite element approach for modeling visco-elastic bodies subjected to moving loads. Int J Numer Meth Eng 51:1317–1336
6. Takemiya H, Bian XC (2005) Substructure simulation of inhomogeneous track and layered ground dynamic interaction under train passage. J Eng Mech 131(7):699–711
7. Burke M, Kingsbury HB (1984) Response of poroelastic layers to moving loads. Int J Solids Struct 20:499–511
8. Biot MA (1956) Theory of propagation of elastic waves in a fluid-saturated porous solid. 1. Low-frequency range. J Acoust Soc Am 28(2):168–178
9. Jin B, Yue ZQ, Tham LZ (2004) Stresses and excess pore pressure induced in saturated poroelastic half space by moving line load. Soil Dyn Earthq Eng 24:25–33
10. Lefeuve-Mesgouez G, Mesgouez A (2008) Ground vibration due to a high-speed moving harmonic rectangular load on a poroviscoelastic half-space. Int J Solids Struct 45(11–12):3353–3374
11. Gao GY, Chen GQ, Li J (2014) Numerical analysis of dynamic characteristic of transversely isotropic saturated soil foundation subjected to high-speed train load. Chin J Rock Mech Eng 33(1):189–198 (In Chinese)
12. Gao GY, He JF, Yang CB (2011) Ground vibration induced by trains moving on saturated ground using 2.5D FEM. Chin J Geotech Eng 33(2):234–241 (In Chinese)
13. Gao GY, Chen QS, He JF (2012) Investigation of ground vibration due to trains moving on saturated multi-layered ground by 2.5D finite element method. Soil Dyn Earthq Eng 40(3):87–98
14. Fredlund DG, Rahardjo H (1997) Soil mechanics for unsaturated soils. Architecture and Building Press, China
15. Yang J (2002) Saturation effects of soils on ground motion at free surface due to incident SV waves. J Eng Mech 128(12):1295–1303
16. Jafarzadeh F, Sadeghi H (2012) Experimental study on dynamic properties of sand with emphasis on the degree of saturation. Soil Dyn Earthq Eng 32(1):26–41
17. Xu MJ, Wei DM (2011) 3D non-axisymmetrical dynamic response of unsaturated soils. Eng Mech 28(3):78–85 (In Chinese)

Strategy for Constructing Environment Vibration Control System for High-Speed Railway

Zhenxing He, Guangtian Shi, Xiaoan Zhang, Nengneng Bao, Shuzhen Wang and Jiangang Xu

Abstract With the acceleration of urbanization and the rapid development of rail transit, more and more high-speed railways are built and connected with urban rail transit of the big cities. It is the trend to deduce the train-induced environmental vibration of the high-speed railway by using vibration damping tracks, but it is still in the exploration stage for using damping tracks in the high-speed railway. After more than 10 years of rapid development, urban rail transit has established an environment vibration control system. Because of the great difference between the high-speed railway and the urban rail traffic which exist in the speed of train and the maintenance standard, the problems of whether the vibration damping measures widely used in the urban rail transit are applicable, how to determine the key dynamic parameters of the vibration damping tracks, could not be avoided in design, construction, and operation of the high-speed railway vibration damping track. This study investigated the construction of environmental vibration control system for high-speed railway based on the experience of environmental vibration control of urban rail transit.

Keywords High-speed railway · Environmental vibration · Control system · Dynamics · Long-term service

1 Introduction

Reducing train-induced environment vibration is an important measure to reflect the friendly environmental characteristics of rail transit. With more and more attention been paid to environmental protection and "green development," the vibration reduction track has been widely adopted in urban rail transit. At present, the cases of high-speed railway entering densely populated urban areas and connecting with

Z. He (✉) · G. Shi · X. Zhang · N. Bao · S. Wang · J. Xu
School of Mechanical Engineering, Institute of Vibration and Noise Control,
Lanzhou Jiaotong University, Lanzhou, China
e-mail: 383645442@qq.com

urban rail transit network are increasing. In order to reduce the vibration and noise, using the vibration reduction track has been the trend of high-speed railway development [1–3].

After more than 10 years of engineering practice and theoretical investigation, the environmental vibration control system of urban rail transit was established. The empirical formula method is used to predict the vibration superscalar of the vibration-sensitive point [4–6]. Various types of vibration damping tracks are adopted, and the vibration damping layers or components are usually arranged at three positions (the rail fastener, the sleeper, and the track bed) of the track system [7–9]. According to the damping effect, the vibration damping track is divided into three levels. Based on the results of the environmental vibration evaluation and the usage of the damping track in the entire network, the type selection design of the vibration damping track for a certain line is carried out [10]. The actual effect of the vibration damping track is usually tested and evaluated before the line is officially put into operation [7].

When the vibration damping track is used for the high-speed railway with heavier axle load and higher speed grade, how to draw on the experience of urban rail transit and establish the environmental vibration control system suitable for high-speed railway has become an unavoidable engineering problem for the design, construction, and maintenance of high-speed railway.

2 Characteristics of Rail Transit Environmental Vibration Control

Environmental vibration control of rail transit is a systematic project, which includes three aspects. The first is to determine the sensitive point of vibration and predict the vibration's superscalar; the second is to choose the appropriate track vibration damping measures according to the vibration's superscalar, and the third is to maintain the safety, stability of train running, and vibration damping performance of track in a long term. According to Table 1, the above three aspects of jobs worked throughout the whole process of the design, construction, and operation of rail transit. A reasonable control system is needed to efficiently support the environmental vibration control of high-speed railway.

The design and construction stages of rail transit generally continue for four to six years, and the process needs the participation of many units such as management, design, construction, and manufacturing. Correspondingly, the participation of each unit in every period is different. The determination of the vibration-sensitive point and the prediction of the vibration superscalar are completed by the environmental impact assessment (EIA) specialty in the stage of the feasibility study of the rail transit project, and the cost of vibration damping measures is taken into the track construction cost. The EIA report must be submitted to the competent department of environmental protection for approval after being reviewed by

Table 1 Time sequence and implementation units of environmental vibration control

Design and construction units	Design unit							Construction unit		Manufacturing unit	
	EIA major	Driving major	Line major	Track major	Civil engineering major	Stray current protection	Relevant interfaces	Track laying	Civil construction	Core components manufacturing	Auxiliary components manufacturing
Engineering feasibility study	★	◆	◆	◆							
Preliminary design		◆	◆	★	◆	◆	◆				
Construction drawing design				★	◆	◆	◆	★	◆	★	★
Construction				◆				◆			
Operation				◆				◆		◆	◆

★ High degree of participation; ◆ Low degree of participation

experts. The EIA reports, appraisal opinions, and approval documents formed as the basis of the subsequent design phase.

In the preliminary design stage, the major track carries out the type selection design of vibration damping track and the second interface design according to the above research results. The possibility of line adjustment in the initial design stage can lead to the vibration superscalar changes of the environmental vibration-sensitive points. Generally, the track major is in charge of predicting the vibration superscalar according to the principles and prediction methods provided by the EIA report. In order to ensure that different specialties have the same prediction results for environmental vibration in different construction periods of rail transit, the prediction method must be unified, the evaluation scale must be clear, and the influence of the subjective factors must be eliminated as much as possible.

3   Research Status of Environmental Vibration Control of High-Speed Railway

Recently, the research on the environmental vibration control of high-speed railway is mainly focused on the law of vibration propagation, and the engineering application research vibration damping track is still in the exploratory stage.

3.1   Vibration Propagation Characteristics of High-Speed Railway

The theoretical research methods of environmental vibration propagation characteristics of high-speed railway can be divided into time-domain method and frequency-domain method [11–16]. The representation of time-domain method is a numerical simulation method based on the theory of vehicle-track coupling dynamics [13]. This method has developed rapidly in recent years, its main characteristics are: Through model expansion, the track foundation and the structures around the line can be considered together [16]. In the study of the influence of vibration on and structures, the dynamic influence factors of the main components of vehicles and all kinds of track structures can be taken into consideration by the dynamic interaction model of wheel and rail.

In China, a large number of field measurement studies have been carried out on the environmental vibration of high-speed railway. China Railway Corporation has issued guiding opinions on the value and governance principles of noise and vibration sources for environmental impact assessment of railway construction projects (revised 2010) basing on the field test results of Beijing–Tianjin, Shijiazhuang–Taiyuan, Wuhan–Guangzhou, Zhengzhou–Xian, and other high-speed railways. This document provides a prediction formula for environmental vibration similar to urban rail transit.

$$VL_z = \frac{1}{n} \sum_{i=1}^{n} \left(VL_{z0,i} + C_i \right)$$

$VL_{z0,i}$ is vibration source intensity, C_i is the vibration correction term, including velocity correction, axle load correction, line type correction, classification of the track, geological correction, distance adjustment, and building modification.

Unlike urban rail transit, the distance between vibration source reference point and the center line of the track is 30 m, and the vibration source intensity grade is decided by different speed levels and line conditions. According to the construction and operation experience of urban rail transit and high-speed railway, the above prediction formula is simple and easy to use by engineers. It can meet the needs of environmental vibration prediction of high-speed railway.

3.2 Engineering Application of Vibration Reduction Track in High-Speed Railway

The vibration damping track used in high-speed railway is mainly used to reduce the dynamic influence on the track foundation. To prevent the underwater tunnel soft soil liquefaction risk, The Guangzhou–Shenzhen–Hong Kong high-speed railway has adopted vibration-reducing slab track in the Lion Ocean large section tunnel. In order to adapt to the stiffness difference between the subgrade and the bridge foundation, the elastic mattress is used at the bottom of the track at the second double line of Lanzhou to Xinjiang.

In recent years, some application research of vibration reduction track has been carried out in national railways with higher speed. For example, the Chengguan express railway line has tried to lay an elastic mattress in the speed range below 80 km/h. "Engineering research of unballasted track vibration and noise-reducing engineering in environmentally sensitive areas" is being studied as one of the fifteen engineering test projects of Chengdu–Lanzhou railway. The Guangzhou–Foshan Loop and the Guangzhou–Zhuhai line underpass the Foshan Museum, and relevant departments have carried out special research on environmental vibration problems.

It can be seen that the prediction mode of environmental vibration of high-speed railway has been formed, but the research on vibration damping track is not sufficient, and the relationship between the vibration prediction and the application of vibration reduction track has not been established. After the vibration damping track is adopted, the influence on the running stability of train and maintenance of track during the long-term operation is not clear. There is an urgent need to carry out research on the formation of a high-speed railway environmental vibration control system.

4 The Key Technical Issues of High-Speed Railway Environmental Vibration Control

The construction of a high-speed railway environmental vibration control system may reference urban rail transit experience. Based on the mature experience of vibration damping track in urban rail transit, and combining the operation speed, vehicle characteristics and track foundation structures of the high-speed railway, the key dynamic parameters of vibration damping track should be studied, grade vibration damping strategy is established, and the principle of classifying vibration damping track is determined.

4.1 The Availability of the Existing Typical Vibration Reduction Tracks

In view of the fact that the vibration damping track has been widely used in urban rail transit, the usability of the existing typical vibration damping track in high-speed railway should first be studied theoretically to provide theoretical support for the engineering test study.

The typical vibration reduction measures which are representative and have good comprehensive performance in urban rail transit are selected as the research object among the fastener vibration reduction measures, sleeper vibration reduction measures and track bed vibration reduction measures. The study should be carried out by combining theory with engineering test, and the theoretical study should precede the engineering test study. The dynamic calculation model established by theoretical analysis should be able to reflect the dynamic interaction between the vehicle and the track system and the characteristics of vibration propagating through the track to the periphery of the line. The vehicle dynamic response, track dynamic response, and vibration damping effect corresponding to typical vibration damping track and the common track should be comprehensively compared and analyzed. The influence of the existing vibration damping track on the dynamic response of the vehicle and track system when it is used in high-speed railway should be studied clearly. The quantitative evaluation results of the availability of the existing typical vibration damping track could be given.

4.2 Value Range of Key Dynamic Parameters of Vibration Damping Tracks

Since the vibration source intensity of environmental vibration prediction formula of the high-speed railway is based on different speed grade and line condition, the value of the key dynamic parameters of the vibration damping track should also be

studied according to different speed grade and line condition, so that a corresponding relationship is established between the reasonable range of key dynamic parameters of the vibration damping track and the prediction results of environmental vibration.

According to the application and research experience of urban rail transit, the following key parameters should be studied in depth. For fastener vibration reduction measures, the key dynamic parameters are node stiffness and damping. For sleeper vibration reduction measures, the key dynamic parameters are sleeper mass, the stiffness, and damping of the sleeper support pad. For track bed vibration reduction measures, the key dynamic parameters are the mass of track bed, the stiffness, and the damping under the track bed. Figure 1 shows the influences of the dynamic parameters of the vibration track in urban rail transit.

The mass unit of the sleeper damping track is the sleeper mass. As for the track bed damping measures, the mass units are track bed. The influence trend of the mass units on the vibration damping effect and stability of train-track system should be studied, and the reasonable value range is determined according to the
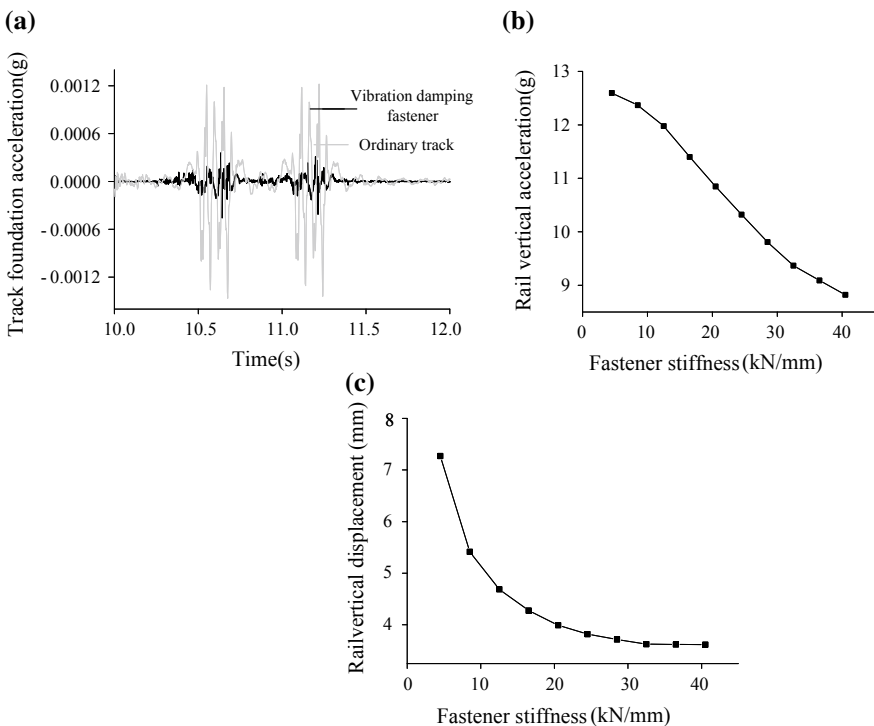
Fig. 1 Influence of the key dynamic parameters of the vibration damping track: **a** comparison of acceleration; **b** rail acceleration trend; and **c** rail displacement trend

characteristics of different rail foundations. Similarly, the reasonable value ranges of stiffness and damping of the vibration damping tracks could be determined according to different train speeds.

4.3 Graded Vibration Damping and Performance Classify

Urban rail transit generally divides the vibration damping track into three grades according to the vibration damping capacity. Usually, damping requirements below 5 dB are called mid-level, damping requirements within the scope of 5–10 dB are called high level, damping requirements more than 10 dB is called special level; mid-level measures mainly refer to the vibration damping fasteners. The high-grade measures mainly include elastic sleepers. The track bed vibration damping measures such as steel spring floating slabs are generally are the representative of special level. Whether the classification principle of vibration damping measures established by urban rail transit is applicable to high-speed railway needs further study. The main factors to be considered in the study include the type of vibration damping track, train running speed, required vibration damping capacity, and the maintenance mechanism of high-speed railway.

Therefore, we can draw from the experience of urban rail transit on the basis of the research on the availability of vibration damping track and the key dynamic parameters of the track, then putting forward the classification strategy of high-speed railway vibration reduction track and defining the principle of reasonable vibration damping level classification and the specific vibration damping track measures at all levels. The above is the foundation of establishing environment vibration control system for high-speed railway.

4.4 Research Strategy of High-Speed Railway Environment Vibration Control System

The research on the availability of the typical vibration damping track in high-speed railway and the key dynamic parameters of the vibration damping track is the basis of formulating the classification principle of the classified vibration damping strategy. In order to ensure the reliability and usability of the above research results, the two key scientific problems must be solved.

The first is to comprehensively consider the dynamic response evaluation index of the vehicle system, track system, and the vibration damping effect and to carry out the multi-index comprehensive evaluation. The theoretical model needed to be established for the calculation of dynamic evaluation index is huge and has many factors to consider. Different indexes in the dynamic response evaluation system have different sensitivities to various kinds of excitations. The trend of growth and

decline of some indicators is even diametrically opposite, as shown in Fig. 2. On the same issue, using different evaluation indicators may lead to diametrically opposite conclusions. Therefore, a reasonable multi-index evaluation method should be selected for comprehensive evaluation [17].

The second is the close connection between theoretical calculation and engineering application. It means a unified model and evaluation scale are adopted to systematically study the availability and key dynamic parameters of the typical vibration absorption track. It means a unified model and evaluation scale are adopted to systematically study the availability and key dynamic parameters of the vibration damping track. At present, there is a lack of a unified evaluation scale in the study of the value range of key dynamic parameters of high-speed railway vibration damping tracks and the analysis of stiffness transition between different track structures. It is difficult to obtain measured data to compare the response of deterministic irregularity excitation. However, the corresponding evaluation scale can be obtained through dynamic calculation according to the rules and standards for deterministic irregularity excitation. That is to say, parameter analysis and comprehensive evaluation are carried out under the principle of dynamic response equivalence. Based on the above analysis, a theoretical research mode of an environmental vibration control system for the high-speed railway is put forward in this paper, as shown in Fig. 2.
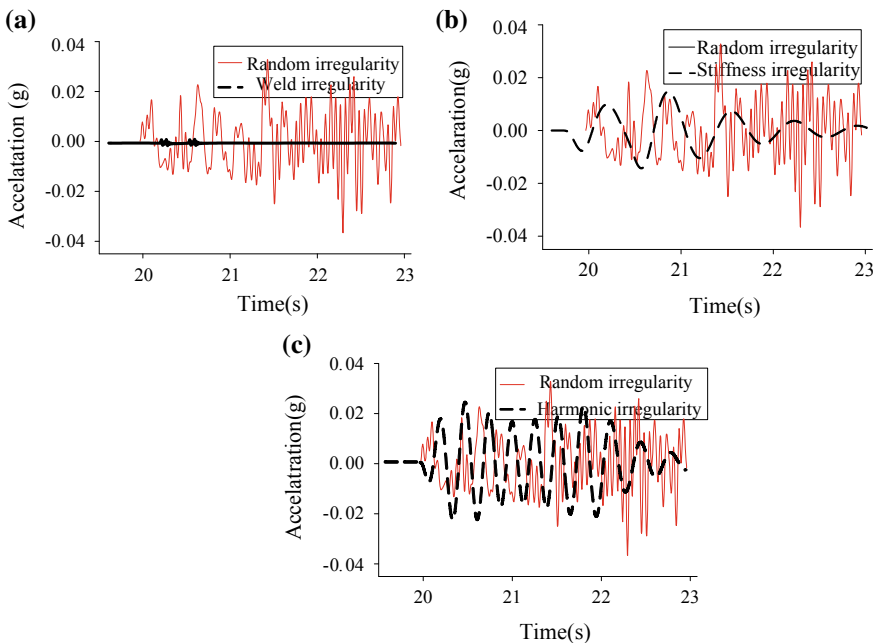
Fig. 2 Vehicle dynamic response corresponding to track irregularities: **a** corresponds to weld irregularity; **b** corresponds to stiffness irregularity; and **c** corresponds to harmonic irregularity

Firstly, the mature and reliable theory is adopted to establish a complete theoretical calculation model for the interaction of vehicles, tracks, and foundations. The model is used to calculate the evaluation parameters, including the running quality of the vehicle system, the interaction between train and track, the stability of the track system, vibration propagation, and damping effect. The calculated evaluation parameters can be compared with the commercial software and the measured data of urban rail transit and high-speed railway to ensure the reliability of the calculation results.

The interaction between vehicle and track is caused by the irregularities between wheels and rails. Although the dynamic response of the vehicle and track system caused by the single deterministic irregularity is difficult to be obtained through the field measurement, it can be accurately calculated by the dynamic model. In the design, acceptance and operation specifications and standards of urban rail transit and high-speed railway, there are clear limits for certain geometric irregularities such as weld irregularities and harmonic irregularities. Therefore, the irregularities between wheels and rails used in the dynamic calculation model can be determined depending on the engineering specifications.

In order to construct a multi-index comprehensive evaluation method, using the above dynamic calculation model, the evaluation scale and evaluation object is determined by calculation. The multi-index comprehensive evaluation method based on gray theory can give a quantitative evaluation of the availability of existing typical vibration damping tracks in high-speed railways. It is also possible to determine the reasonable range of key dynamic parameters of high-speed railway vibration damping track. Then, combined with the experience of an urban railway and the test results of high-speed railway, the classified vibration damping strategy of the high-speed railway can be determined (Fig. 3).

The above research method is characterized in that the evaluation index calculation and evaluation process are based on the same model and the same evaluation scale, which can eliminate process errors.

The wheel–rail irregularity originates from the engineering standards. The theoretical model is verified by engineering measured data. The formulation of the grading vibration damping strategy takes into account the experience of the urban railway and the test results of high-speed railway vibration damping track. Through the above steps, the theoretical research process and engineering practice are closely combined to ensure the reliability and usability of the research conclusions.

5   The Property Maintenance of the Vibration Damping Track

Under the long-term loading, the components of the vibration damping track will gradually age, and the damping capacity will recede. The daily inspection of the railway maintenance department can hardly find the performance change of the
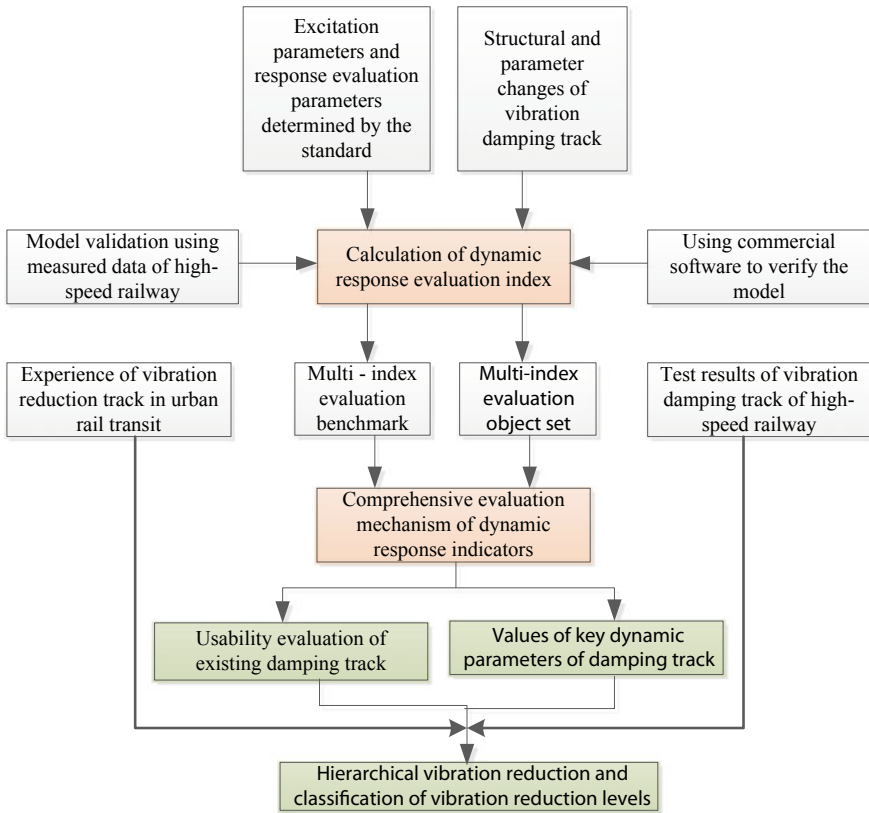
Fig. 3 Research model of key issues in high-speed railway environment vibration control system

vibration damping track. When the vibration reduction capability reduced to a certain degree, the vibration of the sensitive points will exceed the standard and cause the complaint event. In recent years, there are more and more complaints caused by environmental vibration around urban rail transit.

The railway maintenance department will investigate the performance attenuation of the vibration damping track after receiving the complaint report. It is usually to replace vibration absorber parts or upgrade vibration damping measures to solve the problem of excessive vibration at sensitive points. The above method of resolving vibration complaints is a passive process, as shown in Fig. 4. Although the complaint of over vibration can be solved, the vibration may have caused
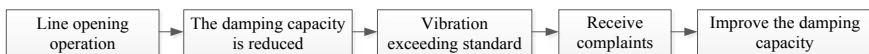
Fig. 4 Passive upgrade process of vibration damping track

damage or loss to vibration-sensitive points and it affects the reputation of rail transit. Therefore, the damping effect of vibration mitigation measures should have a certain amount of redundancy when selecting the type of vibration damping track. Generally, it can be considered about 3 dB in urban rail transit.

For the large-scale applications of vibration damping track in urban rail transit, the dynamic problems have also aroused widespread concern. Abnormal wave grinding, poor train running comfort and increased noise are common in vibration damping track areas. Compared with the urban rail transit, the trains in high-speed railway have larger axle loads and higher speed. Thus, in order to avoid the above problems of vibration damping track in long-term service, the experience of urban rail transit should be used for reference to research the environment vibration control system in high-speed railway. Of course, the high-speed railway engineering test results of the vibration reduction track are also of the important reference value.

6 Conclusion

For the environment vibration control, the characteristics are summarized in rail traffic and the research status is presented in high-speed railway. Thus, the key points and research models of establishing environment vibration control system in high-speed railway is put forward.

The environment vibration control of high-speed railway is a systematic project. Based on a large number of on-site tester search, simple and feasible prediction formulas have been established. However, the application of vibration damping tracks in high-speed railway is still in an exploratory stage. The establishment of environment vibration control system needs to be studied. In the vibration control system of high-speed railway, the key issues are that the study of the availability of existing typical vibration damping track seeks the reasonable value range of key important dynamical parameters of the damping track and formulates the strategies and the classification principle of graded vibration reduction.

The research method of the environmental vibration control system in high-speed railway is constructed in this paper. The dynamic response of train and track systems, the dynamic response of foundations, and structures can be considered comprehensively. The multi-index comprehensive evaluation method should be considered in future dynamic response research. The quantitative analysis of the availability and key dynamics parameters of the typical vibration reduction track can be carried out based on a unified model and evaluation scale.

References

1. The National Development and Reform Commission of the People's Republic of China (2018) Guidance on promoting rational development and construction of surrounding areas in high-speed railway station. 2018-514
2. Zhai W, Zhao C (2016) Frontiers and challenges of sciences and technologies in modern railway engineering. J Southwest Jiaotong Univ 51(2):209–226
3. Gu Xiaoan (2017) Analysis and research of the railway environmental vibration influence conditions and its control techniques. Railw Energy Sav Environ Prot Occup Saf Health 7(5):222–228
4. Ministry of Ecological Environment of the People's Republic of China (1988) GB10070-88 standard of vibration in urban area environment. China Standard Press, China, Beijing
5. Ministry of Ecological Environment of the People's Republic of China (1989) GB10071-88 measurement method of environmental vibration in urban areas. China Standard Press, Beijing
6. Ministry of Ecological Environment of the People's Republic of China (2008) HJ453-08 technical guidelines for environmental impact assessment—urban rail transit. China Standard Press, China, Beijing
7. Zhang J, Duan Y, Qu L, Wang A (2016) Stiffness range selecting of railway fastener under medium speed. Dev Appl Mater 31(4):12–17
8. He Z, Yang X (2016) Dynamic response analysis of asymmetric coupled vehicle-track system generated by voided elastic two-block sleeper. Shock Vib 2016
9. Jiang Q, Wang Y, Wei G et al (2017) Optimum analysis of vibration reduction performance for floating slab track based on shear hinge. China Railw Sci 38(4):15–22
10. Ministry of Housing and Urban-Rural Development of the People's Republic of China (2013) GB 50157-13 code for subway design. China Building Industry Press, China, Beijing
11. Bian X, Jiang H, Chang C et al (2015) Track and ground vibrations generated by high-speed train running on ballastless railway with excitation of vertical track irregularities. Soil Dyn Earthq Eng 76:29–43
12. Sheng X, Zhong T, Li Y (2017) Vibration and sound radiation of slab high-speed railway tracks subject to a moving harmonic load. J Sound Vib 395:160–186
13. Zhai W (2007) Vehicle-track coupling dynamics, 3rd edn. Science Press, Beijing
14. He Z (2008) Research of environment vibration generated by unballasted slab track. Southwest Jiaotong University
15. El Kacimi A, Woodward PK, Laghrouche O (2013) Time domain 3D finite element modelling of train-induced vibration at high speed. Comput Struct 118:66–73
16. Kouroussis G, Van Parys L, Conti C (2014) Using 3-dimensional finite element analysis in time domain to model railway-induced ground vibrations. Adv Eng Softw 70:63–76
17. He Z (2017) Research on the evaluation method of structural difference irregularity of vibration damping track. J Railw Eng Soc 34(2):53–58

Numerical Analysis of Train-Induced Vibrations Effect on Existing Masonry Building

Qian Xia, Wen-Jun Qu, Yi-Qing Li, Jin Zhao and Meng-Yun Gan

Abstract Based on the masonry structures in Shanghai adjacent to the subway, this paper sets up a detailed numerical model. Measured vibration acceleration serves as the input excitation, and the parameters of the model were calibrated by the measured vibration response. Through numerical analysis, it is studied that metro train-induced vibrations and their influences on existing masonry building from two aspects—one is the vibration level changing with the story height, and the other is the vibration level changing at all the rooms on one floor—the different slab properties, different room size, and other factors affected vibration response distribution. In the precast slab room, the vertical vibration arrangement is greater than that in the cast in situ floor slab room. Vertical vibration at the ash between the precast slabs had a certain amplification effect; the room depth parameters had a small effect on the vibration intensity. The width of the room has a significant effect on the vertical vibration.

Keywords Subway-induced vibration · Masonry building · Numerical analysis · Vibration distribution characteristics · Slab properties

Q. Xia (✉)
School of Civil Engineering and Architecture, Xi'an University of Technology, Xi'an 710048, China
e-mail: ice69pipiniu@163.com

W.-J. Qu
College of Civil Engineering, Tongji University, Shanghai 200092, China
e-mail: quwenjun.tj@tongji.edu.cn

Y.-Q. Li · J. Zhao
Shaanxi Jianda Weigu Quality Testing Technology Co. Ltd, Xi'an 710055, China
e-mail: liyiqing1984@163.com

J. Zhao
e-mail: zhaojin13335@163.com

M.-Y. Gan
School of Civil Engineering, Tianjin University, Tianjin 300350, China
e-mail: gmy_why@163.com

1 Instructions

The urban transportation route selected for this study is based on its forecast on the volume of travelers; the route does not avoid densely populated areas, the safety of sensitive, and demand for special functions that are affected by long-term vibration. In recent years, studies both local and international on free-field ground motion regularity caused by the subway have been unrestricted. Research on special sensitive construction affected by the vibration was mainly focused on the forecasting methods and the evaluation of the case [1]. Subjects of the studies include bank buildings [2, 3], scientific research institutes [4, 5], places of historic interest [6, 7], and museums [1]. The varied materials and the construction form of these buildings introduce difficulties to the study of the vibration distribution.

Masonry structure, compared with the different construction forms of tall steel structures, such as steel and concrete composite structure, has a single architectural form. Its structure is usually the same as the surrounding buildings in the area, with the same materials, number of layers, scale, and shape. As such, the study of its corresponding vibration distribution is convenient. In this paper, the background of the old city in Shanghai is presented, in which its existing masonry buildings are influenced by the subway. By integrating two residential projects in Shanghai, this paper will discuss the field testing of the three directions of vibration on one vertical and two horizontal directions, i.e., the X-, Y-axes of the masonry buildings resulting from the subway movement. A numerical model for the two residential buildings is also presented showing the collection of real information of the two buildings. Thereafter, an analysis and comparison of the results from two different methods which are field-measured data and numerical analysis model vibration data will be discussed. Beyond presenting the principles of the vibration system of the masonry structure, this paper will also provide valid data to guide future research.

This paper combines the numerical simulation and testing method to study the existing masonry structure in a vibration environment caused by the urban rail movement. This will address the environmental vibration problems in this aspect.

2 Experimental Introduction

The test site is located by the subway line of a station in Shanghai. The test field includes two ordinary brick residential buildings close to metro line one (Fig. 1).

The test residential buildings were built in the 1960s. The two buildings are a five-story brick and concrete, rectangular structure. Building 1 has an east–west length at 28.8 m, with its north–south dimensions approximately 12.1 m wide, with a construction area of approximately 1742 m^2; Building 2 has an east-west length of 22.5 m, with a north–south width of approximately 12 m. The first and second buildings' distances from the centerline of the orbit are 22 m and 10 m, respectively. The structures are horizontal load-bearing wall systems with no basements. And the floor spacing 2.8 m on each floor is a precast slab.
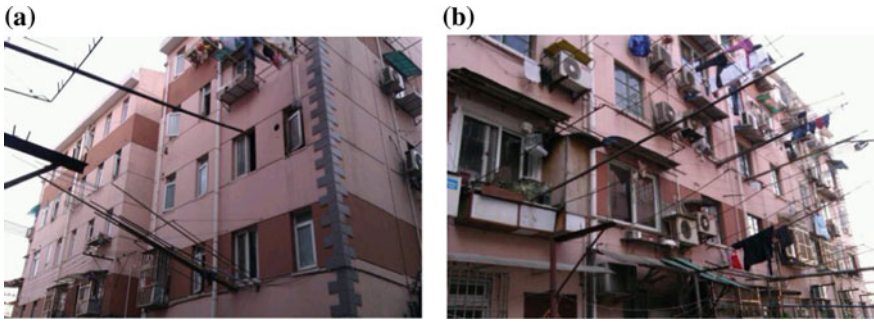
Fig. 1 Test building photographs: **a** north elevation, **b** south elevation

The sensor arrangement of the building is shown in Fig. 2. The B-D axis of Building 1 and Building 2 is a stairwell with a span of 1.35 m. The two spans of B-D and D-E in Building 1 and Building 2 are both indoor rooms. The span of the slab is 4.8 m and 5.2 m, respectively. In order to compare the vibrations in the three directions of the slab, sensors are installed in the stairwells on the first, third, and fifth floors of Building 1 and Building 2 and the indoor floor on the second and fourth floors. In order to compare the vibration of the floor slab, a second placement scheme was made for Building 2, and a sensor was placed on each floor of the stairwell to test the vertical direction (Z-direction) and horizontal direction (X-direction along the longitudinal direction of the building and Y-direction along the lateral direction of the building). Because of the limited number of sensors, the vertical and horizontal vibrations of buildings are tested in groups.
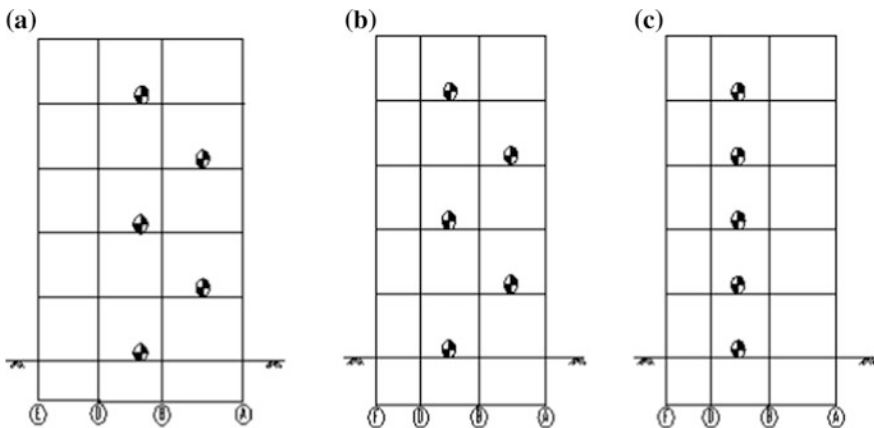
Fig. 2 Layout of measuring points on buildings: **a** in Building 1, **b** plan 1 for Building 2, **c** plan 2 for Building 2

3   Numerical Analysis of Masonry Building

Several factors such as vibration source, propagation path, and building structure influence the metro-induced vibration of the buildings. All subsystems considered during numerical modeling can cause complications and result in inaccurate predictions. The three-dimensional finite element model of the masonry structure is set up in this paper, using the measurements of the part of the room to adjust model parameters, and the adjusted model is applied to the analysis of the vibration distribution of each room in the entire building.

3.1   The Research Object and Size of the Model

The simulation study is based on Building 2 as the research object; the building's distance from the centerline of the orbit is 10 m. The model in this article is set up based on the actual situation of the masonry structure. In order to simulate the vibration of real masonry structure as far as possible, the numerical model is established by ANSYS finite element software according to the actual situation of masonry structure including staircase (Fig. 3).

3.2   Unit Type and Component Section

The floor and wall of the building are simulated by SHELL181, and the beam and column are made of BEAM188. The thickness of the brick wall is 240 mm; the single-layer SHELL element is used to give masonry material property. The thickness of prestressed hollow slabs is 100 mm, and that of some cast-in-place slabs is 100 mm, to give concrete properties. It is worth knowing that, because of the plastering gap connection between the precast slabs, the strength of the plastering gap is much lower than that of the precast slab; it can be neglected, that is, when the model is established, the plastering gap edge of the precast slab connection is
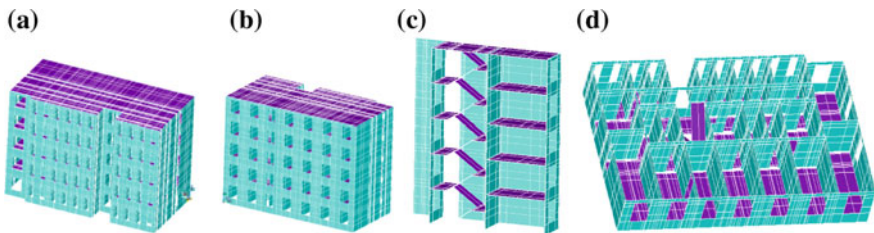
Fig. 3   Sketch map of the finite element model: **a** north elevation, **b** south elevation, **c** profile map of the staircase, **d** plane graph

considered by the free side. However, because of the huge memory occupied by the building 3D numerical model and the limited computing ability of the computer, it is not possible to make the simulation of the plastering gap between the various precast slabs. Therefore, the author only makes the plastering gap treatment on the wall edge position of the precast slab layout direction, that is, the precast slab boundary is made into a free edge. The sections of beams and columns are user-defined, and longitudinal steel bars are arranged at four corners. As shown in Figs. 4 and 5, the section of the ring beam is 240×240, the section of the staircase beam is 240×300, and the section of the column is 240×240. With the same reinforcement at the bottom and top of the section of the ring beam and the structural column, the longitudinal reinforcement area is $A_s = 24 \times 24 \times 2 = 1152 \, \text{mm}^2$. The ratio of reinforcement at the bottom and top of the section is 2.0%.

Fig. 4 Section of a ring beam
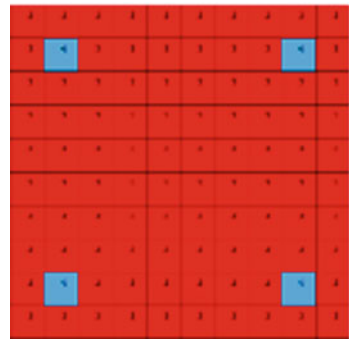
Fig. 5 Section of a structural column
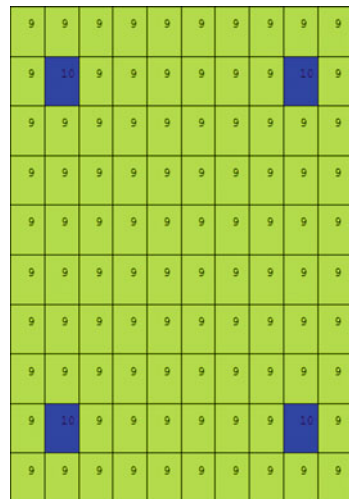
3.3 Material Properties and the Selection of the Model Size

The material data collected on the spot are limited, so it is only for reference. In the program, the strength grade of sintered ordinary brick is MU10, mortar strength grade is M2.5, and the design value of compressive strength of sintered ordinary brick masonry is 1.30 MPa. It is considered that the quality control grade of masonry construction can reach the B level specified in <Code for acceptance of construction quality of masonry engineering> (GB 50203-2002) [8] and take the partial coefficient of material properties γ_f = 1.6.

$$f_k = \gamma_f \times f = 1.6 \times 1.30 = 2.08\,\text{MPa} \tag{1}$$

According to <Unified standard for reliability design of building structures> GB 50068 [9], the relationship between the standard value of masonry strength and the average value is

$$f_k = f_m(1 - 1.645\delta_f). \tag{2}$$

In the formula: f_k—standard value of masonry strength;

δ_f—the coefficient of variation of masonry strength, that is determined by statistics of test results.

According to the description of provisions of <Code for design of masonry structures> (GB 50003-2001), the coefficient of variation in the formula of the average strength of sintered ordinary brick masonry is δ_f = 0.205. The masonry structure studied in this paper was constructed between 1985 and 1994 and, therefore, takes a low coefficient of variation δ_f = 0.1. So the average value of masonry strength is:

$$f_m = \frac{f_k}{(1 - 1.645\delta_f)} = \frac{2.08}{(1 - 1.645 \times 0.1)}\,\text{MPa} \approx 2.5\,\text{MPa} \tag{3}$$

The strength grade of concrete is C20, the design value of the compressive strength f_c is 9.6 MPa, the average value of the compressive strength of the masonry f_m is 2.5 MPa, the strength classes of steel bar are HRB335, and the design value of the yield strength f_y is 300 MPa. The material properties are shown in Table 1.

Table 1 Material properties

Properties	Initial elastic modulus (MPa)	Poisson ratio	Density (kg/m^3)	Damping ratio	Intensity (MPa)
Concrete	0.912×10^4	0.2	2500	0.1	9.6
Masonry	0.1553×10^4	0.16	1800	0.07	2.5
Steel bar	2.1×10^5	0.3	7850	–	300

The mathematical expression of stress–strain relation of concrete under axial compression proposed by <Code for design of concrete structures> (GB 50010) [10] is as follows:

$$\left.\begin{array}{ll} \sigma_c = f_c\left[1 - \left(1 - \frac{\varepsilon_c}{\varepsilon_0}\right)^n\right] & \varepsilon_c \le \varepsilon_0 \\ \sigma_c = f_c & \varepsilon_0 < \varepsilon_c \le \varepsilon_{cu} \end{array}\right\} \tag{4}$$

$$n = 2 - \frac{1}{60}(f_{cu} - 50) \tag{5}$$

$$\begin{aligned} \varepsilon_0 &= 0.002 + 0.5(f_{cu} - 50) \times 10^{-5} \\ \varepsilon_u &= 0.0033 - (f_{cu} - 50) \times 10^{-5}. \end{aligned} \tag{6}$$

The stress–strain relationship of masonry materials under compression is shown in Fig. 6.

The vibration of the subway studied in this paper belongs to elastic deformation, so the stress–strain curves of masonry at $f_m = 2.5$ MPa are shown in Fig. 7.

In order to simulate the subway environment vibration performance of the real structure, and based on the past studies [11], the present study has chosen the concrete damping ratio at 10% and the masonry material damping ratio at 7%.

In analyzing the unit division of the structure, considering the small speed of the bending wave, and following 1/8 of the fluctuation refining standard, the unit division of the beam, the column, and the slab, the maximum size of the unit is mainly affected by the beam height and the slab thickness. The largest unit size is 0.5 m when the vibration frequency is 80 Hz. The accuracy of the calculation is ensured following the size of this division.
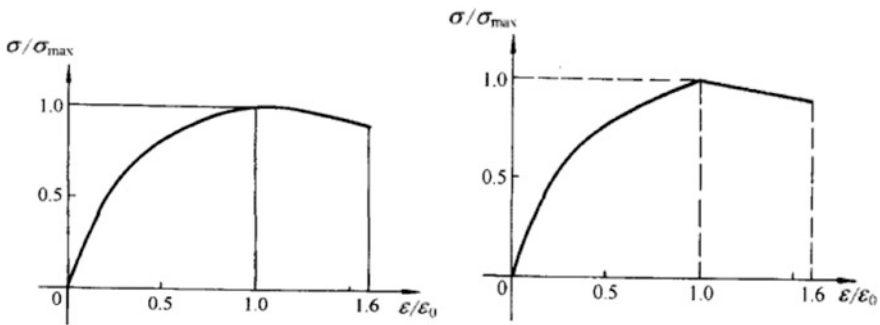
Fig. 6 Compressive stress–strain curve of masonry

Fig. 7 Compressive stress–strain curve of masonry used in this paper (using elastic section)
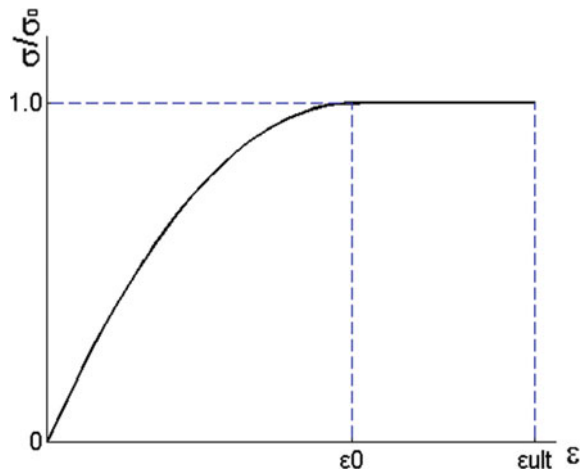
3.4 Incentive Load Input

In order to analyze the vibration response discipline, the interaction between the soil and the structure is disregarded, and the relative motion method is used. Past studies [12] recommend that under the vibration environment, the building's vibration may be calculated regardless of the interaction between the soil and the structure. The building's bottom input data consider the measured acceleration time history in the wall–floor junction and input the data based on the consistent incentive method (Fig. 8). Studies [13, 14] also recommend the safety of this method. Using Rayleigh damping, with the building fundamental frequency and 80 Hz, the system damping ratio is 0.05, thus obtaining the Rayleigh damping coefficient. The Newmark direct integral method is adopted from dynamic analysis, and the time step is 0.005 s.

It can be observed from Fig. 8 that the duration of the influence of the subway train on the vibration of the building is about 10 s. In the frequency spectrum, the vibration has a peak value in both 0–20 and 40–70 Hz, and the peak value of 40–70 Hz is larger.

4 Model Checking

4.1 Vertical Vibration Level Analysis Comparison

The vertical acceleration at indoor rooms on floors 2, 4 and in the staircase on floors 3, 5 is used to check the model. Details for each room are shown in Fig. 9.
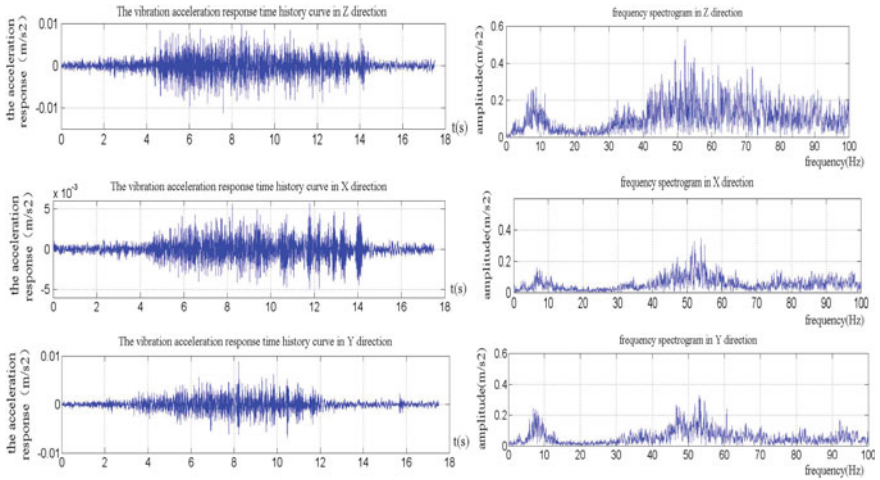
Fig. 8 Time history and Fourier spectrum of input accelerations

toilet3 W3	toilet1 W1	toilet4 W4		toilet5 W5	toilet6 W6	toilet2 W2	toilet7 W7	toilet9 W9	indoor room9 SN9
indoor room8 SN8	staircase It								
	kitchen1 C1	kitchen3 C3		indoor room10 SN10	kitchen2 C2	kitchen4 C4	kitchen5 C5		
indoor room1 SN1	indoor room2 SN2	indoor room3 SN3	indoor room4 SN4	indoor room5 SN5		indoor room6 SN6	indoor room7 SN7		

Fig. 9 Interior room details

Figure 10 shows the change curve with the changing stories of the calculated and the measured values of Z vibration level. The changes in rules and values are consistent, and the maximum deviation is 1.4 dB (Table 2).

Fig. 10 Comparison of calculated and measured vertical vibration level
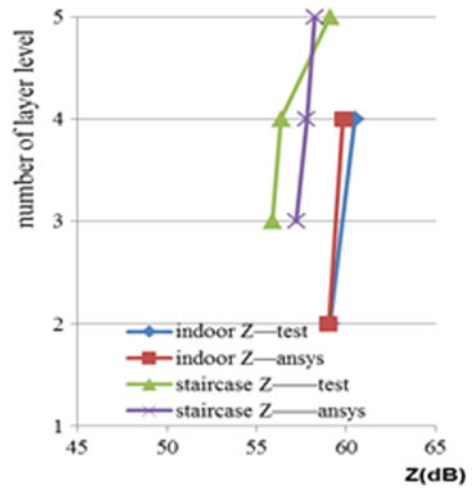
Table 2 Calculation error of vertical vibration level

Maximum deviation	Indoor room	Staircase
2nd floor	−0.1	–
3rd floor	–	1.3
4th floor	−0.7	1.4
5th floor	–	−0.8

Negative values represent the model vibration results less than the test vibration results

4.2   Vibration Acceleration Level Comparison

As a further contrast of vibration response in different positions on one floor in the one-third octave band domain, only vertical acceleration level of the fourth floor is shown because of the limited length (Fig. 11). The visible contrast corresponds with the calculated value in each center frequency.
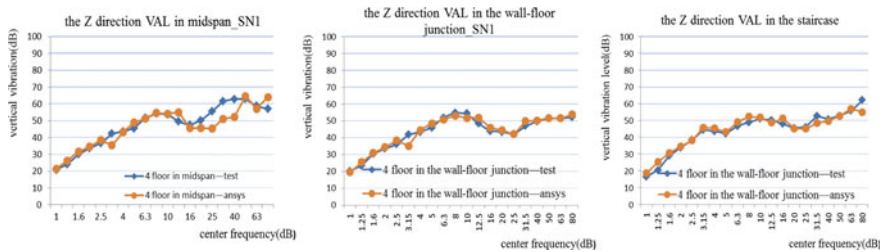
Fig. 11 Comparison of calculated and measured acceleration level in a vertical direction

5 Analysis of Vibration Response Regularity

In order to compensate for the limitations of the test, the model was checked and the vibration response regularity was further analyzed in different rooms.

5.1 Changes in Vibration Along Floor Heights

Comparison of Vibration Between the Mid-span and the Wall–Floor Junction
Contrasting the vertical vibration between the mid-span and the wall–floor junction, with the subway passing the structure, the rooms SN2, C1, C2, W1, and W2 were taken as examples. Figure 12 lists only the vibration of the two floors (the second and fifth floors) because of limited length. The results show that when the subway passed, the vertical vibration at larger mid-spans was 1–3 dB higher than that at the junction. The vertical vibration in smaller rooms such as the kitchen or restroom was 0.3–2 dB higher than that in the wall–floor junction. The vibration response in all rooms indicates that the vibration level on the fifth floor is higher than that on the second floor at the mid-span and the wall–floor junction.

Comparison of Vibrations Between the Precast Slab Room and the Cast In Situ Floor Slab Room This study aims to examine the existing masonry structure of environmental vibration and floor characteristics. The two kinds of slab features are the precast slab and the cast in situ floor slab. In the actual structure, the majority of older buildings use precast slab, and only certain portions of the building use the cast in situ slab, following the building function. This situation is a common practice. The two buildings in the experiment belong to this type. A numerical model was set up close to the actual situation, as well as the establishment of the precast slab and cast in situ floor slab. These are essential for the analysis of the floor characteristics.

In the test building, with the need for function, the bathroom floor uses the cast in situ floor slab and the rest of the room use cheap precast slab. In order to avoid other factors on the characteristics of the floor in the research on the effects of

Fig. 12 Vibration response comparison on the 2nd and 5th floor at mid-span and the wall–floor junction
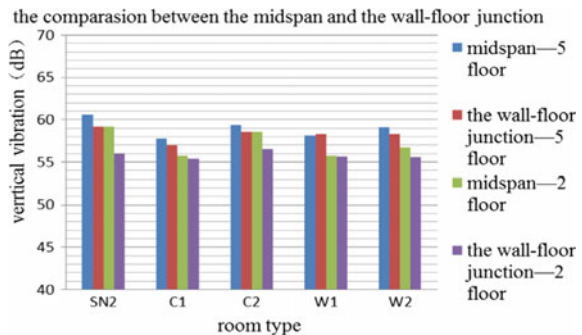
vibration, almost the same kitchen of other parameters was chosen, compared with the vibration of the position corresponding to the toilet. Figure 13 shows the comparison of the C1 and W1, and C2 and W2; it can be seen, in every floor, vertical vibration level: Vibration strength of C1 and W1 generally is consistent, and vertical vibration of C2 is higher than the vibration of the W2 about 3–3.5 dB. Overall, the cheap precast slab has a certain extent amplification effect of vertical vibration, while the cast in situ floor slab has a relative attenuation effect of vertical vibration; the reason should be its material properties.

Precast slab ash seam position (arrow position) vibration intensity compared with no mortar joint processing of the precast slab vibration intensity is high about 2–3 dB; it is visible of the vibration strength amplification between the precast slabs of ash seam, and the magnifying effect cannot be ignored. From the point of view about the simplified model, mortar joint treatment only sets up at the corner of the wall along the precast slab layout direction. The actual situation, that is, the mortar joint is built between each precast slab, further infers that vertical vibration strength of the precast slab room is greater than that in the cast in situ floor slab room (Fig. 14) [15, 16].
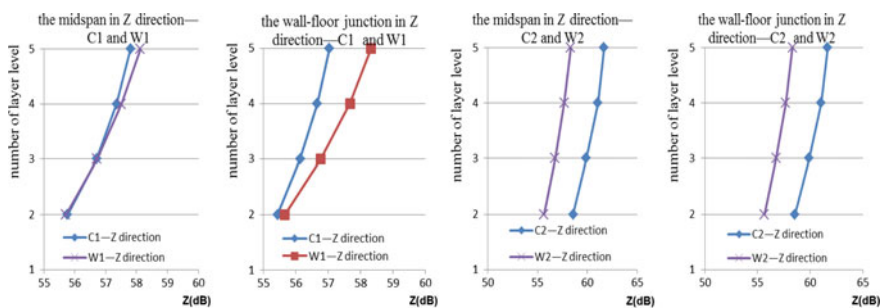
Fig. 13 Comparison of vibration level in the vertical directions at mid-span and the wall–floor junction with the story height between the kitchen room and washroom
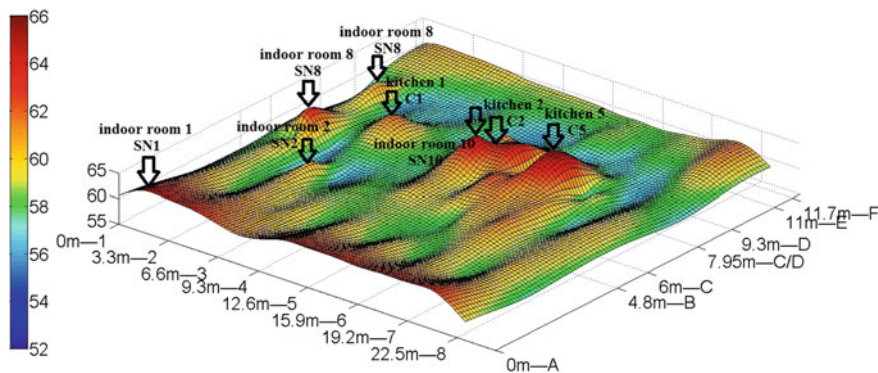
Fig. 14 Three-dimensional images of vertical vibration at all rooms on one floor

**Impact of Width and Depth of the Room and the Wall Constraint Condition
on Vibration** In order to study the parameter about the depth of the room influence
on the vibration, this paper chose the SN1 and SN2 in which the depth of the room
is different, while the other parameters are almost the same and compare the
vibration of these two rooms. The width of the two rooms is all 3.3 m, and the
depth of the two rooms is 6 m and 4.8 m, respectively (Fig. 15). In addition to the
same vibration strength in the Y-direction on 3 and 4 floors, the vibration strength in
three directions on each floor is that in SN2 it is greater than that in SN1. The
maximum deviation is only 0.2 dB; the depth of the room influence on the vibration
strength is small and negligible.

In order to study the influence of room width on vibration, C1 and C5 were
selected. The room widths are different, whereas the other parameters and the
constraint condition are almost the same. Thus, the vibration of C1 and C5 is
compared. The rooms both have depths of 3.15 m, and the widths of C1 and C5 are
1.65 m and 3.3 m, respectively. The results are shown in Fig. 16. The comparison
of vibration level in the three directions obtained from the two rooms indicates that
the horizontal vibration intensity is almost the same, and the vertical vibration in C5
is greater than that in C1. The maximum deviation is only 3.6 dB on the top of the
floor; the width of the room has no significant effect on horizontal vibration and
greatly affects vertical vibration. The large width of the room corresponds to great
vibration intensity.
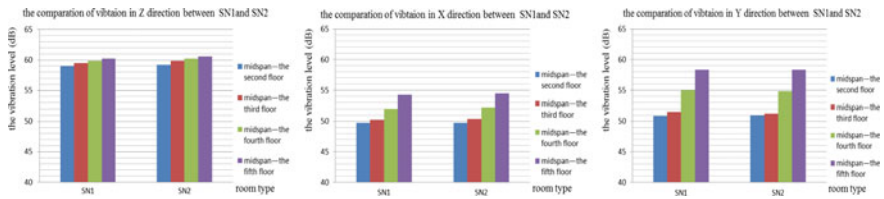
Fig. 15 Comparison of vibration level in the three directions in the mid-span floor along the floor
height between the SN1 and SN2
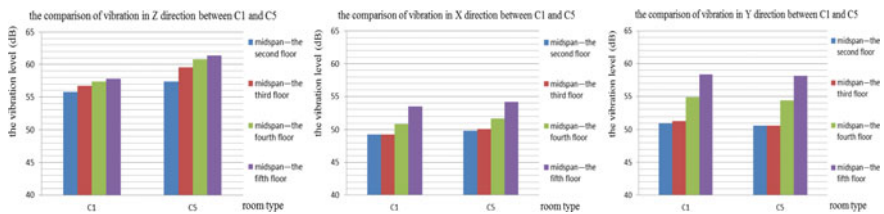
Fig. 16 Comparison of vibration level in the three directions in the mid-span of the floor with
story height between Kitchen 1 and Kitchen 5
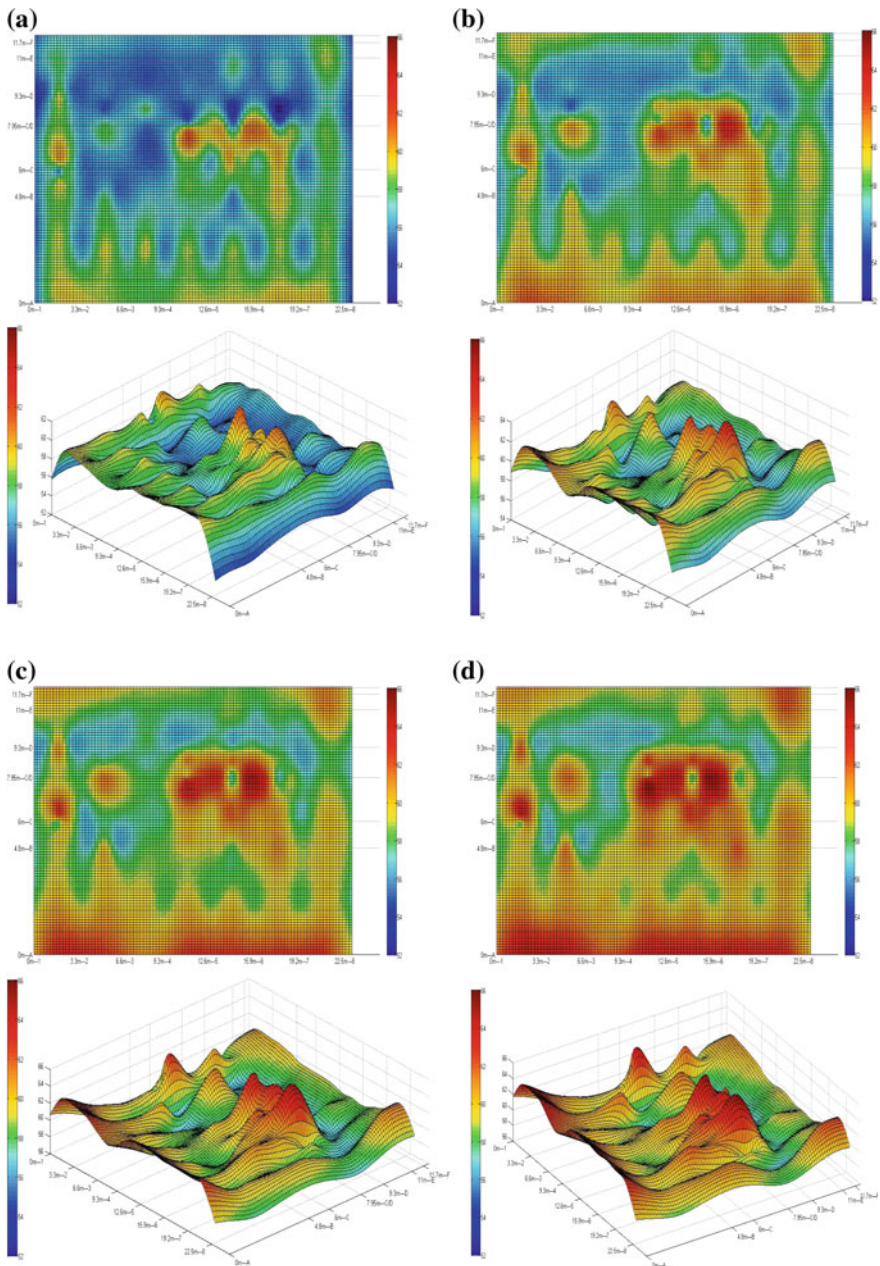
Fig. 17 Three-dimensional images of vertical vibration at all rooms on each floor: **a** the second floor, **b** the third floor, **c** the fourth floor, **d** the fifth floor

5.2 Distribution Regularity of Vibration Response on the Same Floor

The analysis of the existing structure is limited to the vibration in several rooms. The detailed description of the vibration situation in each room was not described. The 3D cloud image displays the vibration situation in each room, and Fig. 17 indicates the vibration strength distribution in each room on every floor when the subway passes by the building, which can provide a basis for macro-comparison.

Figure 17 shows the three-dimensional cloud result based on the numerical analysis in Sect. 5.1. In addition, it shows that vibration intensity has relationships with certain parameters, such as room depth and room width, slab properties, and floor location. The three-dimensional images facilitate visual qualitative analysis of the train-induced vibration and provide a strong basis for the environmental assessment of the existing structures and their subsequent isolation analysis [15].

6 Conclusion

1. When the subway passes, the vertical vibration level in the center of the large span indoor floor slab is 1–3 dB larger than that in the wall–floor junction, and the vertical vibration level in the center of the small span floor slab is 0.3–2 dB larger than that in the wall–floor junction.
2. The cheap precast slab has a greater amplification effect of vertical vibration than that of the cast in situ floor slab. The vibration intensity in precast slab ash seam position compared with that of the precast slab without mortar joint processing is higher by approximately 2–3 dB, and the vibration strength amplification between the precast ash seam slab is visible.
3. (a) The influence of room depth on vibration strength is small and negligible; (b) the influence of room width on vertical vibration is high. Greater room width results in higher vibration intensity.
4. Vibration intensity has relationships with certain parameters, such as room depth and room width, slab properties, and floor location.

References

1. Zhang N, Xia H, Yang WG et al (2011) Prediction and control of building vibration under metro excitations. In: Proceedings of the 8th international conference on structural dynamics (EURODYN 2011), Leuven, Belgium, pp 705–711
2. Banlendra T, Chua H, Lo KW et al (1989) Steady-state vibration of subway-soil-building system. J Eng Mech 115(1):145–162
3. Chua KH, Lo KW et al (1995) Building response due to subway train traffic. J Geotech Eng 121(11):747–754
4. Gupta S, Liu WF, Degrande G et al (2008) Prediction of vibrations induced by underground railway traffic in Beijing. J Sound Vib 310(3):608–630
5. Ding DY, Gupta S, Liu WN et al (2010) Prediction of vibrations induced by trains on line 8 of Beijing metro. J Zhejiang Univ Sci A 11(4):208–293
6. Erkal A, Laefer D, Fanning P, Durukal E, Hancilar U, Kaya Y (2010) Investigation of the rail-induced vibrations on a masonry historical building. In: 7th international conference on structural analysis of historic constructions: strengthening and retrofitting
7. Breccolotti M, Materazzi AL, Salciarini D et al (2011) Vibrations induced by the new underground railway line in Palermo, Italy—experimental measurements and FE modeling. In: Proceedings of the 8th international conference on structural dynamics (EURODYN 2011), Leuven, Belgium, pp 719–726
8. Development Planning Committee of Shaanxi Province (2002) Code for acceptance of constructional quality of masonry engineering (GB 50203-2002). China Architecture & Building Press, Beijing
9. Ministry of Construction of the People's Republic of China (2001) Unified standard for reliability design of building structures (GB 50068-2001). China Architecture & Building Press, Beijing
10. Ministry of Construction of the People's Republic of China (2002) Code for design of concrete structures (GB 50010-2002). China Architecture & Building Press, Beijing
11. Chopra AK (2005) Dynamics of structures: theory and applications earthquake engineering (trans: Xie L). Higher Education Press, Beijing
12. Wang TY (2007) Metro train-induced vibrations and study on the isolation method of buildings. College of Civil Engineering, Tongji University
13. Hanazato T, Ugai K, Mori M et al (1991) Three-dimensional analysis of traffic-induced ground vibrations. J Geotech Eng 117(8):1133–1151
14. Chua KH, Lo KW, Balendra T (1995) Building response due to subway train traffic. J Geotech Eng 121(11):747–754
15. Xia Q, Qu WJ (2017) Experimental and numerical studies of metro train-induced vibrations on adjacent masonry buildings. Int J Struct Stab Dyn 16(10):1550067–1550094
16. Xia Q, Qu WJ (2014) Numerical analysis on metro train-induced vibrations and their influences and affecting factors on existing masonry building. J Vib Shock 33(6):189–200

Determination of Environmental Vibration Source Based on Natural Frequency of Different Bearing Slabs

Qian Xia, Wen-jun Qu, Yi-qing Li and Ya-ni Sun

Abstract   Based on the residential buildings adjacent to the metro line in Shanghai, the self-vibration frequency of cast-in-place and prefabricated boards was calculated with the energy method and a numerical model was validated with the finite element method. Results show that the self-vibration frequency of different support slabs calculated by theoretical calculation is approximately similar to that by the numerical simulation, which proves the correctness of the results obtained from the theoretical formula. And according to the analysis results of the self-vibration frequency of different supports, whether the floor vibration caused by people's discomfort really originates from the urban traffic vibration is verified. Calculation and the verification method of the self-vibration frequency of different supports can provide the basis for the vibration control and vibration isolation of the floor.

Keywords Energy method · Self-vibration frequency · Numerical simulation · Theoretical calculation

Q. Xia (✉)
School of Civil Engineering and Architecture, Xi'an University of Technology,
Xi'an 710048, China
e-mail: ice69pipiniu@163.com

W. Qu
Department of Structural Engineering, Tongji University, Shanghai 200092, China
e-mail: quwenjun.tj@tongji.edu.cn

Y. Li
Institute of Architecture Design, Xi'an University of Architecture and Technology,
Xi'an 710055, China
e-mail: liyiqing1984@163.com

Y. Sun
College of Architecture and Civil Engineering, Xi'an University of Science
and Technology, Xi'an 710054, China
e-mail: sunyn1995@126.com

1 Instructions

The vibration of the architectural floor slab is not a new issue, as Tredgold had already written the literature which is "Griders Always Should be made as deep as They Can, to Avoid the Inconvenience of Not Being Able to Move on the Floor without Shaking Everything in the Room [1]." Soon after, the vibration of the floor slab has attracted the attention of many experts and scholars, and an abundance of research achievements came out directly to vibration problems which are caused by some other movements rather than subway or trains. However, when analyzing the vibration distribution in the room caused by urban transportation, it is impossible to determine which floor slabs' vibration is caused by urban transportation and which is caused by non-urban transportation factors (such as equipment vibration, rhythmic movements and construction works around the buildings). Only by accurately calculating the natural frequency of the floor, when the value is within the frequency range of the floor vibration excited by a certain vibration source, it can be proved that the vibration is caused by the vibration source. This analytical method is still not talked about among the researches by other teams; this paper will focus on the research of accurate calculation of the natural vibration frequency of the slab and verify whether the floor vibration caused by people's discomfort really originates from the urban traffic vibration so as to provide the basis for the vibration control and vibration isolation of the floor. Usually, the vibration caused by subway and ground vehicles is called urban complex traffic; hereafter, the author will use the short name urban traffic.

This paper mainly studies the vertical vibration of the floor system; corresponding natural frequency is the vertical natural frequency; for layout rule, mass distribution and simple boundary conditions of the floor system, the first mode vibration plays a controlling role; and in the following description, the natural frequency refers to the first natural frequency of the vertical vibration of the floor system.

2 Theoretical Calculation

2.1 Basic Assumption and Vibration Differential Equation

A plate has a thickness far less than the other two sizes of the elastic plank, and the material is assumed to be isotropic. The plank vibration theory is based on three assumptions:

(1) Plank bending deformation in the middle surface line is still in the middle surface line. This is the straight-line assumption with the transverse shear deformation ignored.

(2) The deflection of the plank is much smaller than the thickness of the plank, the middle surface of the plate does not deform when the plate is bent, and the middle surface is the neutral surface.

(3) The lateral positive stress of the plate can be ignored.

On this basis, if the deflection of the plate is not calculated from the plane position, and from the equilibrium position, the differential analysis of the plate parallelepiped, the equilibrium condition, the deformation coordination conditions, the physical equation of the bending equilibrium equation and then the analysis of the total dynamic balance of the plate in the vibration process, the free vibration differential equation can be obtained:

$$\frac{\partial^4 W}{\partial x^4} + 2\frac{\partial^4 W}{\partial x^2 \partial y^2} + \frac{\partial^4 W}{\partial y^4} + \frac{\overline{m}}{D}\frac{\partial^2 W}{\partial t^2} = 0 \tag{1}$$

where W is the deflection function of the board; $\bar{m} = \rho h$, in which ρ is the board density and h is the plate thickness; $D = Eh^3/12(1 - v^2)$ is the flexural rigidity of the board, in which E and v are the elastic modulus and Poisson ratio, respectively; and t is the time variable. The form of the solution to differential Eq. (1) is the deflection of each point on the thin plate.

$W = \sum_{m=1}^{\infty}(A_m \cos \omega_m t + B_m \sin \omega_m t)F_m(x, y)$ is expressed as the superposition of the deflection of numerous modes, and the deflection of each mode is represented by the shape function $F_m(x, y)$. In order to obtain the shape function F_m under the various modes and the corresponding circular frequency ω_m, let the solution of the equation be as follows:

$W = F(x, y)(A \cos \omega t + B \sin \omega t)$, substitute for (1)
$$\frac{\partial^4 F}{\partial x^4} + 2\frac{\partial^4 F}{\partial x^2 \partial y^2} + \frac{\partial^4 F}{\partial y^4} - \alpha^4 F = 0 \tag{2}$$

where $\alpha^4 = \omega^2 \rho h/D$. For example, $x = 0$, and the corresponding boundary conditions are:

Fixed edge: fixed edge displacement and corner for 0, $F = \frac{\partial F}{\partial x} = 0$.

Simply supported edge: simply supported edge displacement and moment for 0, $F = \frac{\partial^2 F}{\partial x^2} = 0$.

Free edge: free edge moment and shear force for 0, $\left(\frac{\partial^2 F}{\partial x^2} + v\frac{\partial^2 F}{\partial y^2}\right)_{x=0} = 0$, $\left[\frac{\partial^3 F}{\partial x^3} + (2 - v)\frac{\partial^3 F}{\partial x \partial y^2}\right]_{x=0} = 0$.

2.2 Energy Method

The energy method is an approximate method by D. C. L. Rayleigh to calculate the minimum natural frequency of a thin plate. Its basic principle is as follows: When a plate vibrates freely with a circular frequency ω and its shape function $F(x, y)$, its instantaneous deflection can be expressed as

$$W(x, y, t) = (A \cos \omega t + B \sin \omega t)F(x, y) \tag{3}$$

The natural vibration frequency is mainly studied here, assuming the external load and free vibration of the thin plate. When the plate passes through the balanced position, there are $W = 0$, $\sin \omega t = 0$, $\cos \omega t = \pm 1$; at this time, the speed is up to the maximum $\pm \omega F$, deformation potential energy of the plate is 0, and the kinetic energy reaches maximum, that is,

$$T_{max} = \frac{1}{2} \iint \overline{m} \omega^2 F^2 \mathrm{d}x \mathrm{d}y \tag{4}$$

When the vibration plate is in the equilibrium position farthest, there are $W = \pm F$, $\sin \omega t = \pm 1$, $\cos \omega t = 0$; at this point, the kinetic energy of the plate is 0 and the deformation potential energy of the plate is the largest, that is,

$$U_{max} = \frac{D}{2} \iint \left\{ (\nabla^2 W)^2 - 2(1 - v)\left[\frac{\partial^2 W}{\partial x^2} \frac{\partial^2 W}{\partial y^2} - \left(\frac{\partial^2 W}{\partial x \partial y} \right)^2 \right] \right\} \mathrm{d}x \mathrm{d}y \tag{5}$$

According to Green's theorem, we can deduce:

$$\iint \left[\frac{\partial^2 W}{\partial x^2} \frac{\partial^2 W}{\partial y^2} - \left(\frac{\partial^2 W}{\partial x \partial y} \right)^2 \right] \mathrm{d}x \mathrm{d}y = \int \left[\frac{\partial W}{\partial x} \frac{\partial^2 W}{\partial x \partial y} \mathrm{d}x + \frac{\partial W}{\partial x} \frac{\partial^2 W}{\partial y^2} \mathrm{d}y \right] \tag{6}$$

For a rectangular thin plate with no free edges, only with simply supported edges and fixed edges, on the boundary where X is a constant, there are $\mathrm{d}x = 0, \frac{\partial^2 W}{\partial y^2} = 0$, $\mathrm{d}y = 0, \frac{\partial W}{\partial x} = 0$, and then, Formula (5) can be simplified as:

$$U_{max} = \frac{D}{2} \iint (\nabla^2 W)^2 \mathrm{d}x \mathrm{d}y \tag{7}$$

According to the law of conservation of energy, the maximum kinetic energy is equal to the maximum potential energy, that is,

$$U_{max} = T_{max} \tag{8}$$

Using this equation, the self-vibration frequency can be obtained.

2.3 Deduction of Calculation Formula for Natural Vibration Frequency of Rectangular Thin Plate

The minimum natural vibration frequency in engineering was calculated by the energy method [2, 3]. Generally speaking, the mode shape function (displacement function) only needs to satisfy the displacement boundary conditions, not necessary to satisfy the internal force boundary condition, because internal force boundary conditions are equilibrium conditions, and in the energy method, the equilibrium condition has been replaced by energy relation. Of course, if you can, meanwhile, meet some or all of the internal force boundary conditions, getting the lowest natural vibration frequency can have better accuracy. If the mode shape curve is accurate, the corresponding vibration frequency is also accurate. If the mode shape curve is an approximation, the corresponding frequency is also approximate.

Assume the mode shape function to derive the formulas for calculating the natural frequencies of the four-side supported rectangular plates with six different boundary conditions. Six different forms of the border are shown in Fig. 1a–f.

1. Simply supported rectangular plate with four sides

Simply supported plate with four sides is shown in Fig. 1a; taking the mode-type function as double trigonometric series proposed by C. L. Navier: $F = \sum_{m=1}^{\infty} \sum_{n=1}^{\infty} C_{mn} \sin \frac{m\pi x}{a} \sin \frac{n\pi x}{b}$, which meets the displacement boundary conditions, substitution of (4) and (5) yields:
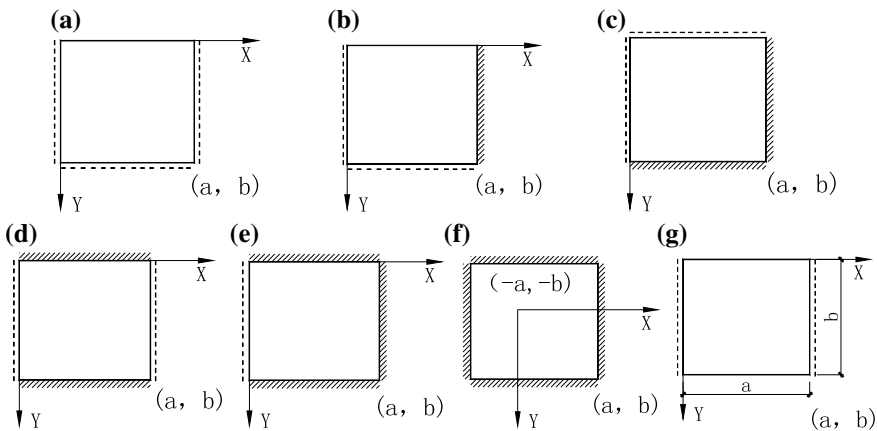
Fig. 1 Supporting plates under different conditions: **a** four-side simple branch, **b** three-side simple branch, one-side fixed support, **c** adjacent edge simply supported, adjacent edge solid support, **d** one-side simple support, one-side fixed support, **e** three-side solid support, one-side simple support, **f** four-side solid support, **g** one-side simple support, one-side free

$$T_{\max} = \frac{\omega^2 \overline{m} ab}{8} \sum_{m=1}^{\infty} \sum_{n=1}^{\infty} C_{mn}^2, \quad U_{\max} = \frac{\pi^4 abD}{8} \sum_{m=1}^{\infty} \sum_{n=1}^{\infty} C_{mn}^2 \left(\frac{m^2}{a^2} + \frac{n^2}{b^2} \right)^2$$

When $m = n = 1$, the minimum frequency can be obtained from Formula (8)

$$\omega_1 = \pi^2 \left(\frac{1}{a^2} + \frac{1}{b^2} \right) \sqrt{\frac{D}{\overline{m}}} \tag{9}$$

The vibration mode function of a simply supported plate with four sides is accurate, which not only satisfies the displacement boundary conditions but also meets the internal force boundary conditions. The calculated vibration frequency is also the exact solution.

2. Three-side simple branch, one-side fixed support

The plate with three-side simple branch, one-side fixed support is shown in Fig. 1b, and the mode function $F = (2x^4 - 3ax^3 + a^3x) \sin \frac{\pi y}{b}$ can satisfy $x = a$ one-side fixed support, $x = 0, y = 0, y = b$ three-side simple branch condition. The following equation can be obtained from (4), (5) and (8):

$$T_{\max} = \frac{19\omega^2 \overline{m}}{4 \times 630} a^9 b, \quad U_{\max} = \frac{Da^5 b}{4} \left(\frac{36}{5} + \frac{19\pi^4 a^4}{630 b^4} + \frac{24\pi^2 a^2}{35 b^2} \right)$$

$$\omega_1 = \frac{1}{a^2} \sqrt{\frac{126}{19} \left(36 + \frac{24\pi^2 a^2}{7 b^2} + \frac{19\pi^4 a^4}{126 b^4} \right)} \sqrt{\frac{D}{\overline{m}}} \tag{10}$$

3. Adjacent edge simply supported, adjacent edge solid support

As shown in Fig. 1c, the mode function $F = C_1(2x^4 - 3ax^3 + a^3x)(2y^4 - 3by^3 + b^3y)$ can satisfy $x = 0, y = 0$ adjacent edge simply supported, $x = a, y = b$ adjacent edge solid support boundary condition. The following equation can be obtained from (4), (5) and (8):

$$T_{\max} = \frac{19\omega^2 \overline{m}}{2 \times 630^2} a^9 b^9, \quad U_{\max} = \frac{Da^5 b^5}{2} \left(\frac{36 \times 19}{5 \times 630} a^4 + \frac{36 \times 19}{5 \times 630} b^4 + \frac{2 \times 12^2}{35^2} a^2 b^2 \right)$$

$$\omega_1 = \frac{6}{a^2} \sqrt{\frac{126}{19} \left(1 + \frac{144a^2}{133b^2} + \frac{a^4}{b^4} \right)} \sqrt{\frac{D}{\overline{m}}} \tag{11}$$

4. One-side simple support, one-side fixed support

As shown in Fig. 1d, the mode function $F = \sin\frac{\pi x}{a}\left(1 - \cos\frac{2\pi y}{b}\right)$ can satisfy $x = 0, x = a$ simple support, $y = 0, y = b$ fixed support boundary conditions. The following equation can be obtained from (4), (5) and (8):

$$T_{max} = \frac{3\omega^2\overline{m}}{2\times 4}ab, \ \ U_{max} = \frac{Dab}{2}\left(\frac{3\pi^4}{4a^4} + \frac{4\pi^4}{b^4} + \frac{2\pi^4}{a^2b^2}\right)$$

$$\omega_1 = \frac{\pi^2}{a^2}\sqrt{1 + \frac{8a^2}{3b^2} + \frac{16a^4}{3b^4}}\sqrt{\frac{D}{m}} \tag{12}$$

5. Three-side solid support, one-side simple support

As shown in Fig. 1e, the mode function $F = (2x^4 - 3ax^3 + a^3x)\left(1 - \cos\frac{2\pi y}{b}\right)$ can satisfy $x = 0$ one-side edge fixation, $x = a, y = 0, y = b$ three-side simple branch boundary condition. The following equation can be obtained from (4), (5) and (8):

$$T_{max} = \frac{3\times 19\omega^2\overline{m}}{4\times 630}a^9b, \ U_{max} = \frac{Da^5b}{2}\left(\frac{36\times 3}{5\times 2} + \frac{16\times 19\pi^4a^4}{2\times 630b^4} + \frac{2\times 24\pi^2a^2}{35b^2}\right)$$

$$\omega_1 = \frac{1}{a^2}\sqrt{\frac{420}{19}\left(\frac{54}{5} + \frac{48\pi^2a^2}{35b^2} + \frac{152\pi^4a^4}{630b^4}\right)}\sqrt{\frac{D}{m}} \tag{13}$$

6. Four-side solid support

As shown in Fig. 1f, the side lengths of the rectangular plate are 2a and 2b, and the vibration coefficient $F = C_1(x^2 - a^2)^2(y^2 - b^2)^2$ can satisfy the boundary conditions. The following equation can be obtained from (4), (5) and (8):

$$T_{max} = \frac{2^{15}\omega^2\overline{m}}{81\times 25\times 49}a^9b^9, U_{max} = \frac{2^{14}Da^5b^5}{9\times 25\times 7}\left(a^4 + b^4 + \frac{4}{7}a^2b^2\right)$$

$$\omega_1 = \frac{1}{a^2}\sqrt{\frac{63}{2}\left(1 + \frac{4a^2}{7b^2} + \frac{a^4}{b^4}\right)}\sqrt{\frac{D}{m}} \tag{14}$$

Based on the above analysis, the formulas of the natural frequency of rectangular plates with different boundary conditions are obtained.

Rectangular sheets have no free edge, so we do not have a pair of edge simple support, a pair of free boundary conditions for analysis. The following is the derivation of the natural frequency of the boundary condition as shown in Fig. 1g.

The differential equation of the transverse free vibration of plate is Formula (2), and the classical expression of the mode function is given as follows:

$$F = (A_m sh\alpha_1 y + B_m ch\alpha_1 y + C_m \sin \alpha_2 y + D_m \cos \alpha_2 y) \sin \alpha x \qquad (15)$$

In the formula, $\alpha = m\pi/a$, $\alpha_1 = \sqrt{\gamma^2 + \alpha^2}$ and $\alpha_2 = \sqrt{\gamma^2 - \alpha^2}$. Formula (15) satisfies vibration differential equation and $x = 0, x = a$ boundary conditions. According to the boundary conditions $y = 0, y = b$, four homogeneous linear equations with A_m, B_m, C_m and D_m as unknown quantities which are not all zero are obtained, and the frequency equation is obtained [3]

$$2\alpha_1\alpha_2\left[\gamma^4 - (\mu - 1)^2\alpha^4\right]^2 (ch\alpha_1 b \cos \alpha_2 b - 1)$$
$$+ \left\{\alpha_\alpha^2\left[\gamma^2 + (1 - \mu)\alpha^2\right]^4 - \alpha_1^2\left[\gamma^2 + (\mu - \mu1)\alpha^2\right]^4\right\}sh\alpha_1 b \sin \alpha_2 b = 0 \qquad (16)$$

Corresponding to a certain value of m, the corresponding natural frequency $\omega_{m1}, \omega_{m2}, \omega_{m3}\ldots$ can be obtained by Eq. (16), where $m = 1$ is the fundamental frequency. The mode function shown in Formula (15) must satisfy $m < \gamma a/\pi$, that is, $\omega > \frac{m^2\pi^2}{a^2}\sqrt{\frac{D}{m}}$. So the traditional view is that the minimum natural frequency of the plate is equal to the natural frequency of a simply supported beam, which is

$$\omega_1 = \frac{m^2\pi^2}{a^2}\sqrt{\frac{D}{m}} \qquad (17)$$

In summary, the formulas of the natural frequency of the plate with seven boundary conditions are deduced and summarized.

2.4 Calculation Natural Frequency of Rectangular Thin Plate

The research object is building No. 2 which is field measured and numerically simulated by the author of this paper in the literature [4–7], as shown in Fig. 2, and each room name and plane layout are shown in Fig. 3. The floor of the residential building has mainly two kinds of precast panels and cast-in-place board, respectively, as the boundary conditions for a pair of free, one-side simple support and four-side solid support. In order to obtain the natural experiment frequency of the concrete floor, the following typical buildings are selected for calculation, and the material is concrete $E = 0.912 \times 10^4$ MPa, $v = 0.2$, $\rho = 2500$ kg/m^3.

1. Prefabricated room

Three prefabricated board rooms, which are indoor 1 (SN1), indoor 2 (SN2) and kitchen room five (C5), with room sizes of 3.3 m × 6 m, 3.3 m × 4.8 m and 3.3 m × 3.15 m, respectively, are selected. A thick prefabrication plate of the lap is a pair of edge simply supported by a pair of free support. Analyzed by
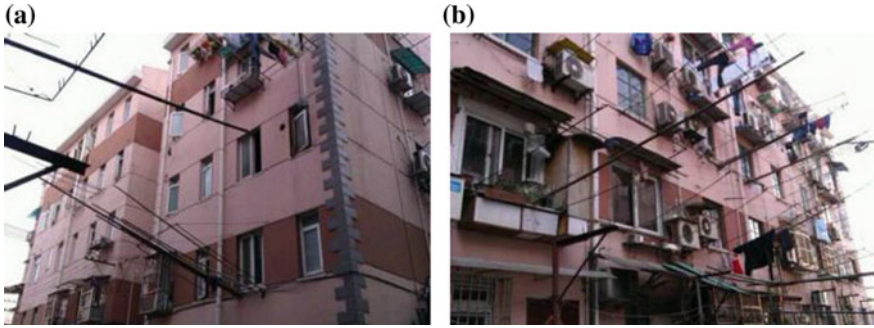
Fig. 2 Test building photographs: **a** north facade photograph, **b** south facade photograph
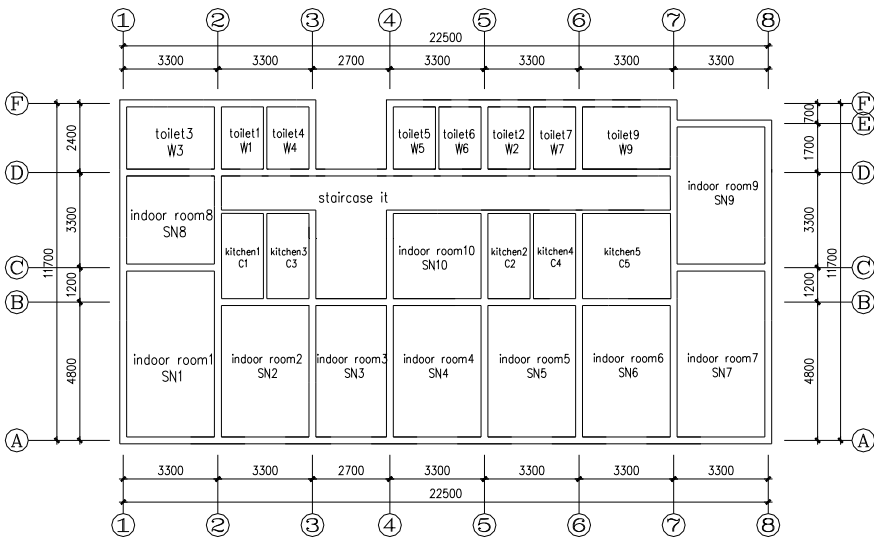
Fig. 3 Name and location of each room

Formula (17), the natural frequency is only related to the span of the board, so the three rooms have the same natural frequency.

Bending stiffness of plates: $D = \frac{Eh^3}{12(1-v^2)} = \frac{0.912 \times 10^4 \times 10^6 \times 0.1^3}{12(1-0.2^2)} = 791,666.67$;

Quality of the prefabricated panel unit area (thickness of 100): $\overline{m} = 164.2\,\text{kg/m}^2$;

Prefabricated panel frequency: $\omega_1 = \frac{\pi^2}{a^2} \sqrt{\frac{D}{\overline{m}}} = \frac{\pi^2}{3.3^2} \sqrt{\frac{7}{9}1,666.67164.2} = 62.9$;

Prefabricated natural frequency: $f = \frac{\omega}{2\pi} = \frac{62.9}{2\pi} = 10.01\,\text{Hz}$.

2. Casting board room

Select bathroom 9 (W9), whose size is $2a \times 2b = 3.3$ m $\times$ 2.4 m. The supporting condition is four sides of solid support, according to Eq. (14) calculation.

Bending stiffness of plates: $D = \frac{Eh^3}{12(1-v^2)} = \frac{0.912 \times 10^4 \times 10^6 \times 0.1^3}{12(1-0.2^2)} = 791,666.67;$

Unit area quality of cast-in-place slab (thickness of 100): $\overline{m} = \rho h = 2500 \times 0.1 = 250 \, \text{kg/m}^2;$

Circle frequency of cast-in-place slab:

$$
\begin{aligned}
\omega_1 &= \frac{1}{a^2} \sqrt{\frac{63}{2} \left(1 + \frac{4a^2}{7b^2} + \frac{a^4}{b^4}\right)} \sqrt{\frac{D}{m}} \\
&= \frac{1}{(3.3/2)^2} \sqrt{\frac{63}{2} \left(1 + \frac{4}{7}\left(\frac{3.3/2}{2.4/2}\right)^2 + \left(\frac{3.3/2}{2.4/2}\right)^4\right)} \sqrt{\frac{7}{9} 1,666.67250}; \\
&= 275.85 \, \text{Hz}
\end{aligned}
$$

Natural vibration frequency of cast-in-place slab: $f = \frac{\omega}{2\pi} = \frac{275.85}{2\pi} = 43.9 \, \text{Hz}.$

3 Floor Numerical Model Analysis

The finite element model of the prefabricated floor is shown in Fig. 4a. A single prefabricated plate is selected for the numerical model plate, and the dimensions are referenced in the literature [8], for 3.3 m $\times$ 0.5 m, plate thickness 0.1 m, choose plate hole 5, aperture 0.08 m, concrete material $E = 0.912 \times 10^4$ MPa, $v = 0.2$, $\rho = 2500 \, \text{kg/m}^3$. The material properties are listed in Table 1. Plate unit chooses beam unit. The mesh size is 0.2. The long span boundary of plate is processed by simply supported edges, and the vertical long span boundary is treated by free edges. The modal analysis was performed to extract the first-order natural frequency by 9.85 Hz. Compared with the natural frequency of the prefabricated slab calculated by energy method 10.01 Hz above, the calculated values of the two methods are basically the same.

(a)   **(b)**
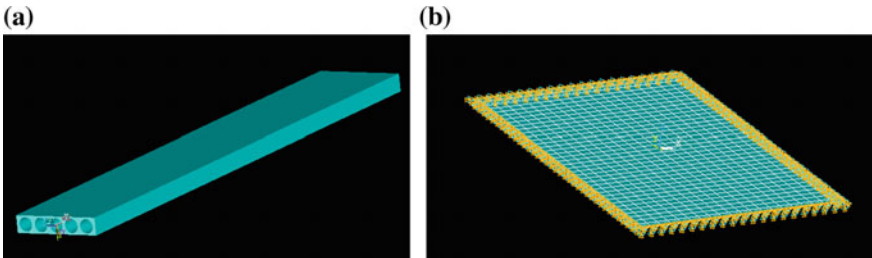
Fig. 4 Numerical model of plate: **a** model of prefabricated plate, **b** model of cast-in-place

Table 1 Material properties

Material	Initial elastic mode (MPa)	Poisson's ratio	Density (kg/m³)	Damping ratio	Strength (MPa)
Concrete	0.912×10^4	0.2	2500	0.1	9.6
Reinforcement	2.1×10^5	0.3	7850	–	300

The finite element model of cast-in-place is shown in Fig. 4b. The size is 3.3 m × 2.4 m, material parameters are the same as above, the board unit adopted SHELL181, and four sides consolidated. The modal analysis was performed to extract the first-order natural frequency of 43.244 Hz. Compared with the natural frequency of cast-in-place calculated by energy method 43.9 Hz above, the calculated values of the two methods are basically the same.

For further inference, in the test room of the experimental residential building, the natural vibration frequency of the prefabricated board is about 10 Hz and that of the cast-in-place is about 43 Hz.

4 Vibration Analysis of Floor Caused by Subway

Vibration in the building is mainly caused by construction near building construction, urban traffic and earthquakes. The vibration frequency of road surface caused by subway is concentrated between 40 and 90 Hz, in which 60–80 Hz corresponds to the largest vibration level, while the vibration frequency transmitted to the building is mainly low within 20 Hz [9, 10]; the vibration frequency of road surface caused by ground vehicles is concentrated between 10 and 20 Hz [11]; the vibration frequency of ground caused by the train is 10–100 Hz [12]; the vibration frequency of ground caused by elevated road is 5–45 Hz [13]; the main frequency of earthquakes is generally below 5 Hz, the vibration frequency of ground caused by blasting is generally 15–45 Hz, but duration of its main oscillation is much shorter than earthquake, generally not more than 0.5 s [14]; the vibration frequency of static pressure pile construction mainly is 4–7 Hz [15]; the frequency of foundation vibration caused by hammer and vibration piling is mostly 10–30 Hz, and the impact of foundation vibration caused by construction on the adjacent building has been rather slight at 2–3 m near the source of vibration [16]. It can be seen that the main frequency bands of ground vibration caused by different excitations are different, and some differences are larger.

The Fourier spectrum of typical rooms with prefabricated slabs and cast-in situ slabs in the No. 2 building under the excitation of subway and ground vehicles is analyzed by field measurement and numerical simulation by author of this paper in reference [5–7]. As the limit of length, only the numerical simulation results of C5 and W9 are listed, as shown in Fig. 5. An analysis under the incentive of urban traffic vibration frequency band of the same room position in each floor shows that:
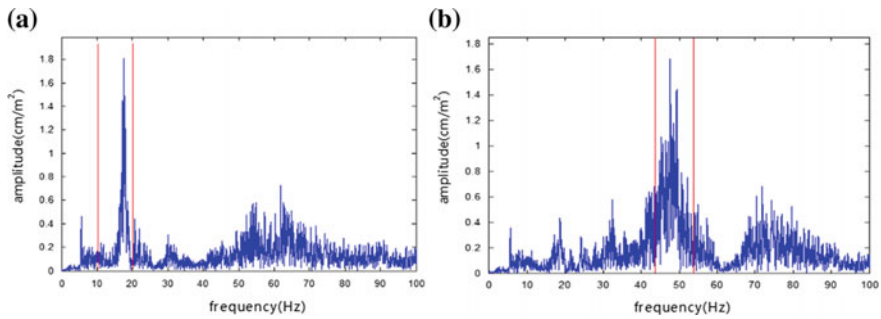
Fig. 5 Fourier spectrum of the top floor of the concrete slab: **a** prefabricated panel (C5) top mid-span Fourier spectrum, **b** cast-in-place plate (W9) top mid-span Fourier spectrum

vibration of the inner floor of the C5 in the kitchen room is mainly in the range of the 10–20 Hz frequency band; bathroom W9 floor vibration occurs mainly in the 45–55 Hz band range.

In Sect. 2.4 analysis, the theoretical calculation values of the natural frequencies of prefabricated and cast-in situ panels are 10.01 and 43.9 Hz, respectively. Analysis shows that the natural frequency of prefabricated panels belongs to urban traffic caused by prefabricated room floor vibration which occurs within the band frequency range; and the natural frequency of the cast-in-place board is close to the cast-in-place floor vibration frequency range, which shows that the resonance of the prefabricated floor can be caused by urban traffic incentives, vibration of cast-in-place floor slab cannot cause resonance effect, but it also has a small vibration effect on its vibration. Therefore, the amplitude of the prefabricated board which is easy to resonate under the urban traffic excitation is obviously higher than the amplitude of the cast-in-place plate. Plate properties affect the conclusion "vertical vibration strength of the room with prefabricated plate should be greater than that of the current casting room," and this phenomenon is consistent with the literature [5–7].

5   Conclusion

1. The self-vibration frequency formula of concrete floor slab under seven boundary conditions is calculated by energy method, and then, the self-vibration frequency of concrete floor slab in a typical building is obtained. The self-vibration frequency in the room with prefabricated slabs is about 10.01 Hz. The natural vibration frequency in the room with cast-in-place slabs is 43.9 Hz. Compared with the numerical model with the same parameters, the results are similar to each other, which verify the correctness of the natural vibration frequency obtained by the energy method.

2. The calculated value of the natural vibration frequency of the prefabricated slab is within the range of the vibration frequency of the slab caused by urban traffic. It can be judged that the vibration of the slab is caused by the excitation of urban traffic. Therefore, the vibration control measures of the floor slab are mainly considered to increase the natural vibration frequency of a floor slab or to avoid resonance by changing the natural vibration frequency of the whole structure. The calculated value of natural vibration frequency of cast-in-place slab is close to the range of floor vibration frequency caused by urban traffic, although it cannot cause resonance phenomenon but can slightly increase the vibration intensity of the floor slab.

3. The calculation method of the natural vibration frequency can provide the basis for calculating the natural vibration frequency of the floor slab for different buildings and verify whether the vibration of the floor slab in the building is caused by the urban traffic excitation. For the vibration of the floor slab caused by urban traffic, it can easily cause resonance when the natural vibration frequency of the floor slab is close to the frequency transmitted to the building by traffic excitation. So in order to reduce the vibration intensity of the floor slab on the existing building under the traffic excitation, it is necessary to avoid resonance by increasing the natural vibration frequency of the floor slab or changing the natural vibration frequency of the whole structure, which provides a theoretical basis for the vibration isolation measures of the existing structure.

Statement

The residential buildings in the paper are measured with the permission of the owners.

The residential buildings were accessed for the present study. In articles [4–7], the author of this paper measured and simulated the residential building.

References

1. Tredgold, Hassan OAB (1824) Train-induced ground borne vibration and noise in buildings. Multi-Science Publishing Co. Ltd., UK
2. Chang W (2012) Calculation of the natural vibration frequency of rectangular thin plates with four edges supported. Shanxi Archit 38(5):63–65
3. Xu Q, Zhang F, Ji H (2000) Discussion about the solution of the free vibration frequency of rectangular plate with two opposite ends simply supported and two opposite ends free. J Zhengzhou Univ Technol 21(4):1–3
4. Xia Q, Qu W (2016) Experimental and numerical studies of metro train-induced vibrations on adjacent masonry buildings. Int J Struct Stab Dyn 16(10):1550067-1–1550067-27
5. Xia Q, Qu W, Shang X (2013) Test for effects of metro train-induced vibration on existing masonry buildings. J Vib Shock 32(12):11–16

6. Xia Q, Qu W (2014) Numerical analysis on metro train-induced vibrations and their influences and affecting factors on existing masonry building. J Vib Shock 33(6):189–194
7. Xia Q (2014) Study on subway-induced existing building vibration and isolation method. Tongji University, Shanghai
8. Office of Central South Area Building Standards Design Team (2003) Office of the building standard design co-operation group in the south China area. 03ZG401. Prestressed concrete hollow slab
9. Lou M, Jia X, Yu J (2009) Field measurement and analysis of ground vibration induced by subway trains. J Disaster Prev Mitig Eng 29(3):282–288
10. Yan W, Zhang Y, Ren M et al (2006) In situ experiment and analysis of environmental vibration induced by urban subway transit. J Beijing Univ Technol 32(2):149–154
11. Zong G, Zhang Y, Li G et al (2017) Measurement and research on metro vibration attenuation law predicted by road traffic. Chin J Undergr Space Eng 13(1):229–235
12. Xia H (2010) Traffic induced environmental vibrations and controls. Science Press, Beijing
13. Chang L, Ren M, Yan W et al (2008) In situ experiment and of vibration induced by urban road and elevated road transit. J Beijing Univ Technol 34(10):1053–1058
14. Shen L, Wang X, Yu Y et al (2002) Monitoring and analysis of impact vibration cause by tippling of a chimney with height of 100 meters. Eng Blast 8(4):16–19
15. Yao D, Zhang Y, Ye Y et al (2013) Impact of jacked pile construction vibration on environment and its control measures. Chin J Undergr Space Eng 9(S1):1739–1743
16. Wabg B, Tang H (2005) To analyse the cause made by a base constructing the vibration. Chin Overseas Archit 2:100–101

Experimental Study on Environmental Vibration Induced by Streetcar

Tian Zhang, Fei Du and Gang Yang

Abstract The environmental vibration tests by streetcar were carried out on a certain section along Line 202 in Dalian City, and the ground acceleration time history curve was obtained. Time-domain and frequency-domain analysis methods were used for processing the acceleration data, then draw the 1/3 octave spectrum of the vibration acceleration and obtain the vibration level of the environmental vibration so as to assess the environmental vibration effect and study the propagation law of the vibration response induced by the tram car. The measured result shows that the main frequency band of the environmental vibration by the tram car is 30–70 Hz; the maximum vibration level at different measuring points is 75–93 dB, and in winter the effective value of vibration acceleration is greater than the value in summer. This is because the low temperature increases the strength and stiffness of the subgrade, which leads to an increase in the effective value of the acceleration in the longitudinal direction. In addition, the vibration response is reduced with the increase in distance from the vibration source. The maximum vibration level at 10 m from the central line of the downlink track is about 93 dB when the speed of the vehicle is 40 km/h, about 77 dB at 30 m, so it can meet the vibration standard of urban environment.

Keywords Streetcar · In situ test · Environmental vibration response · Spectrum analysis · Vibration level

With the rapid development of urbanization in China, urban population is growing rapidly, so the demand for urban public transportation is also increasing. To a large extent, rail transit can share the urban traveling pressure because of its huge passenger volume. Compared with other public transports, rail transit has many advantages: it is convenient, efficient, low energy consumption, low pollution and can promote the development of social and economic development along the line. At the same time, rail transit will also bring some negative effects. The environ-

T. Zhang (✉) · F. Du · G. Yang
College of Transportation Engineering, Dalian Maritime University, Dalian 116026, China
e-mail: saghb@126.com

135

mental vibration and noise generated by train operations will have a significant impact on the health of citizens, the use of precision instruments in universities, hospitals and research institutes, and the life of old buildings near the line [1–6]. In situ test, as one of the most important methods for studying environmental vibration, has important theoretical and social significance. The measurement results can reflect the vibration response of the train as a vibration source intuitively and can be used to verify the correctness of the theoretical analysis model, confirm the rationality of the numerical simulation model and provide data for evaluating the environmental vibration caused by the rail transit system [7]. The accumulation of a large amount of measured data can lay the foundation for the study of the propagation law and mechanism of environmental vibration.

Common rail transit system includes subway, light rail, tram car and so on. As a public transport system with a large passenger volume, the subway has the characteristics with closed lines and dedicated signals. Lines generally consist of underground tunnels, closed-surface lines, elevated bridges and underground or elevated stations. However, the construction cost of subways exceeds RMB 1 billion/km, which has deterred the subway construction in many cities. At the same time, the maintenance and repair costs of subways have remained high, which has become a heavy burden on subway operators. Even in cities with large passenger traffic, such as Beijing, the subway is hard to make profit. Of course, as a public transport means, the ticket price of the subway cannot be too high. The cost of the new streetcar system is much lower (about 200–300 million/km), and the economy is good, but the passenger traffic is lower than the subway and higher than the bus; the one-way capacity is about 15,000 person/h. So the streetcar is very suitable public transportation means for small- and medium-sized cities. The line is generally in the form of all terrain or ground + elevated [8].

From the above perspectives, it is very necessary to research the environmental vibration caused by streetcar. Therefore, the environmental vibration tests were carried out on a certain section along Line 202 in Dalian and the ground acceleration time history curve was obtained. Time-domain and frequency-domain analysis methods were used for processing the acceleration data so as to assess the environmental vibration effect and study the propagation law of the vibration response induced by the tram car.

1 Test Equipment and Test Site Layout

Line 202 in Dalian streetcar is divided into Uplink (Xiaopingdao Front Station–Xinggong Street Station) and Downlink (Xinggong Street Station–Xiaopingdao Front Station), passing through Dalian Maritime University, the Second Hospital of Dalian Medical University, Dalian Institute of Chemical Physics and so on. The train lines are close to these venues, and the resulting vibrations are bound to affect them. Tram forms are shown in Fig. 1. In order to study the vibration characteristics induced by the streetcar, and to minimize the influence of other forms of

Fig. 1 Line 202 streetcar in Dalian

transportation, a site near Star Sea Square is selected for in situ test place. The site is wide and close to the side of the tram line, far from the urban major road. From the test results, the vibration caused by road traffic does not interfere the result.

In the in situ tests, there are some experiment instruments, including the piezoelectric acceleration sensor with sampling frequency 0.2–2.5 kHz, four-channel intelligent data acquisition instrument and analysis system with sampling frequency of 10.24 kHz, and the hand-held speedometer. In order to research the environmental vibration response and propagation law caused by trams, four measuring points were set at the distances of 10, 15, 20 and 30 m from the centerline of the track to lay out vibration acceleration sensors. Data collection will be performed when the tram is coming, and a hand-held speedometer will be used to record the speed and save the measured data. The measuring point position is shown in Fig. 2.

Fig. 2 Layout plan of measuring points
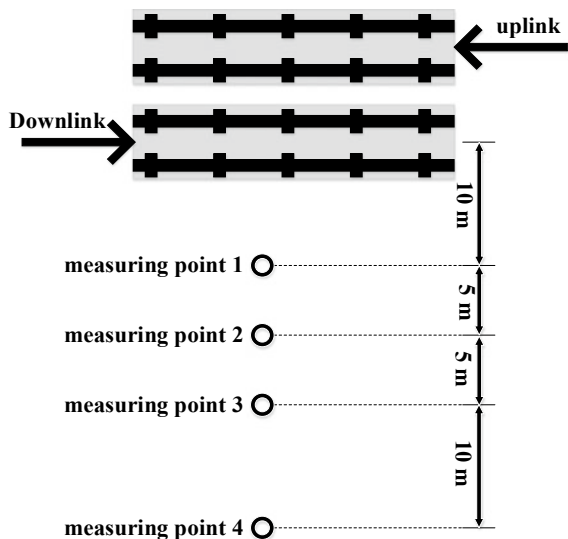
2   Data Analysis and Processing Methods

The ground vibration response is evaluated by the vibration acceleration in this test. Therefore, this article mainly discusses the Z vibration level [9] and 1/3 octave frequency vibration acceleration and variation law caused by the tram. In the "*Urban Area Environmental Vibration Standard*" (GB 10070-1988), when evaluating the magnitude of two different frequency vibrations, vibration acceleration levels are commonly used, which do not take into account the weighting correction of different frequencies. So-called vibration acceleration level, that is, the average energy of the vibration is represented by the effective value of the acceleration [10, 11]. The effective value a_e of the acceleration is defined as the square root of the average value of the square of instantaneous acceleration value a with respect to time T

$$a_e = \sqrt{\frac{1}{T} \int_0^T a^2 \mathrm{d}t} \tag{1}$$

The above formula can be applied for the known acceleration function. For the discrete data in experiment test, Eq. (1) can be transformed into:

$$a_e = \sqrt{\frac{1}{n} \sum_{i=1}^{n} a_i^2} \tag{2}$$

where n is the sample number, and a_i is the value of acceleration. The vibration acceleration level can be defined as follows:

$$\mathrm{VAL} = 20 \cdot \lg \frac{a_e}{a_0} \tag{3}$$

where a_0 is the reference value of the acceleration vibration level, $a_0 = 1 \times 10^{-6}$ m/s^2.

Research indicates that the vertical vibration response is a major factor affecting the daily lives of residents. According to the provisions of "*Urban Area Environmental Vibration Standard*" and ISO 2631, the vibration acceleration level obtained by modifying the whole body vibration with different frequency weighting factors is called vibration level. The indicator of environmental vibration caused by urban rail transit is the vertical Z vibration level. The vibration level is calculated by 1/3 frequency octave method, that is, the index evaluating the environmental vibration is obtained by correcting the acceleration effective value according to the following formula:

$$\mathrm{VL} = 10 \cdot \lg \left[\sum_{i=1}^{20} 10^{(\mathrm{VAL}_i + \mathrm{cf})/10} \right] \tag{4}$$

Table 1 Correction value of 1/3 octave center frequency

Octave center frequency f (Hz)	1	2	4	8	16	31.5	63	80
Vertical correction cf	−6	−3	0	0	−6	−12	−18	−20

In the above formula, VAL_i is the vibration acceleration level of the center frequency f; cf is the correction value shown in Table 1.

3 Analysis of Experimental Results

During in situ test, eight tests were performed on the uplink and downlink vehicles of Line 202 in Dalian, and six groups of data were selected for comparative analysis. The collected vibration acceleration signals are analyzed in time domain and frequency domain. In order to compare and analyze the effects of different soil properties in different seasons on the environmental vibration response caused by trams, the in situ tests were conducted on the same place in the summer and winter.

3.1 Time-Domain Analysis

The in situ tests were carried out to obtain the ground vibration response; in order to avoid the impact of other ground traffic, the acceleration response is collected in every test when the tram goes alone. After several tests in the field, it was found that the vibration acceleration responses are approximately equal at the same distance from the vibration source when the uplink vehicle and the downlink vehicle pass at the same speed. Therefore, only the vibration response by the downlink vehicle is used as the analysis research.

In order to ensure the authenticity and accuracy of the data, the acquisition time for every test is more than 15 s, and the acceleration curve can show the vibration response by passing trains well. For the downlink direction, the measured data for the measuring point 1, 2, 3 and 4 are shown in Fig. 3 during the summer and winter at a tram speed of 40 km/h.

From Fig. 3, we can find acceleration peaks of ground vibration at the four measuring points when the tram passes. The distance from the center of the track increases, the peak value of the generated vibration acceleration decreases. The closer the distance from the track center is, the faster the vibration acceleration decays. Comparing the time histories of vibration accelerations in summer and winter, it was found that the measured results are similar at the same speed of the streetcar and measuring points.
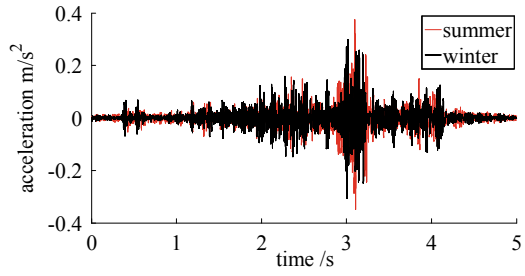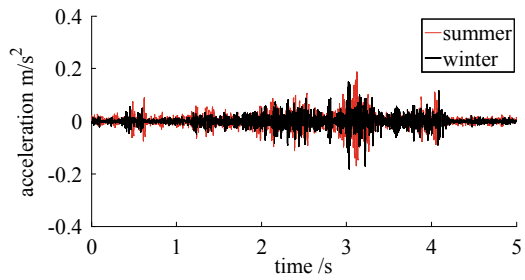
(a) Measuring point 1
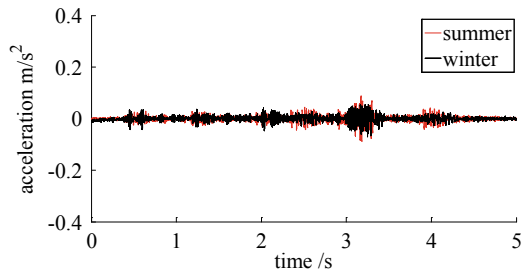
(b) Measuring point 2
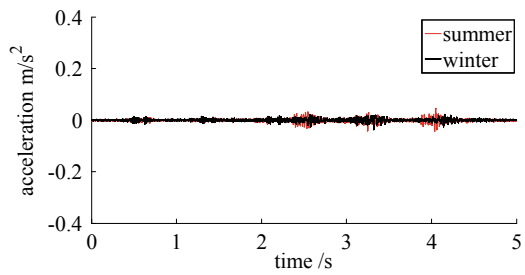
(c) Measuring point 3

(d) Measuring point 4

3.2 Frequency-Domain Analysis

In order to study the characteristics of environmental vibration induced by trams in the frequency domain, the vibration acceleration time histories in field measurement were analyzed in frequency domain, and the vibration acceleration spectrum was obtained.

For the downlink vehicle at a speed of 40 km/h, the measured results in the summer and winter are transformed to frequency domain, as shown in Fig. 4.

It can be seen from the vibration acceleration spectrum of each measuring point that the main frequency band of the environmental vibration response is between 30 and 70 Hz, and the acceleration peaks at different measuring points all are in the same frequency range.

The distribution of the vibration acceleration at the same speed in summer and winter is similar, and the peak value is almost the same. From Figs. 3 and 4 in the time domain or frequency domain, it can be found that seasonal changes do not have much influence on the environmental vibration response, but the frequency distribution has some different at the high-frequency section, such as 55–75 Hz.

3.3 1/3 Octave Analysis

The measured vibration acceleration is analyzed by 1/3 octave spectrum, and the vibration acceleration level is finally obtained to evaluate the standard of the environmental vibration. The 1/3 octave spectrum of vibration acceleration for different measuring points is compared at the different streetcar speed for the results in summer, as shown in Fig. 5, where the abscissa is the center frequency of octave, and the ordinate is the division frequency vibration acceleration level VAL (dB).

It can be seen from Fig. 5 that the vibration level of these four measuring points caused by passing streetcar are in the range of 70 dB to 90 dB when the speed are 35–40 km/h. At the same time, Fig. 5 shows the maximum vibration level at different driving speed and measuring points, and dispalys the change law of vibration level. It can be found that the vibration level changes are the same with the time-domain analysis. For the same measuring point, the higher the streetcar operating speed is, the higher the vibration level is. For the same speed, the farther the distance from the measurement point to the centerline of the track is, the smaller the vibration level is and the change is nonlinear.

3.4 Effective Value of Vibration Acceleration

According to Eq. (4), the effective value of vibration acceleration at different measuring points for downlink tram at different speeds was analyzed. There are

Fig. 4 Spectrum of measured
vibration acceleration
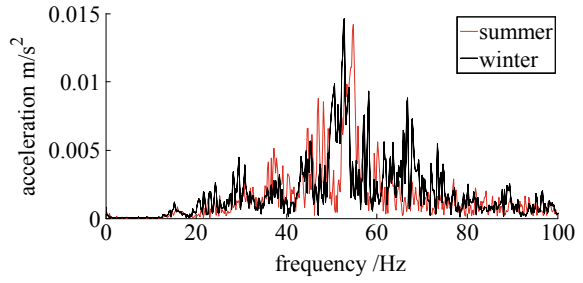
(a) Measuring point 1
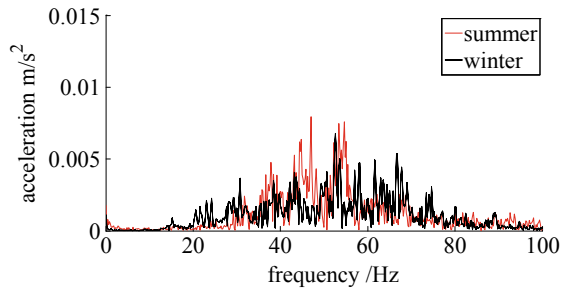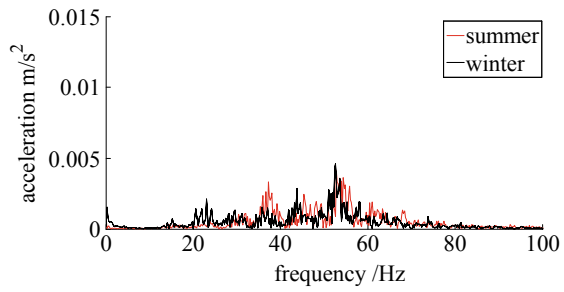
(b) Measuring point 2
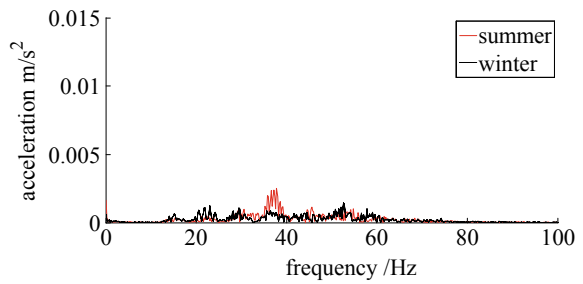
(c) Measuring point 3

(d) Measuring point 4

Fig. 5 Division frequency Z vibration level curve of measuring points
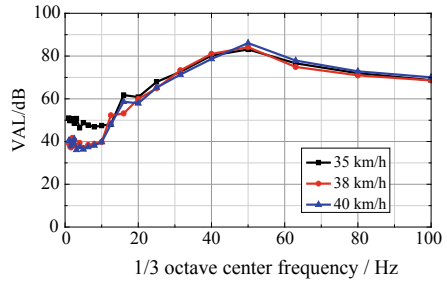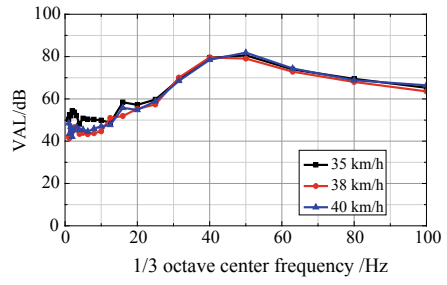
(a) Measuring point 1
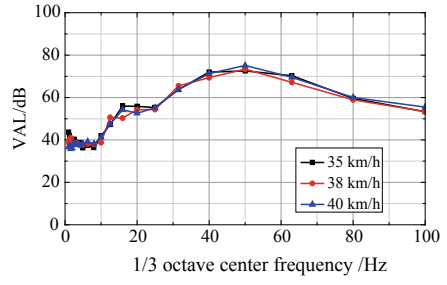
(b) Measuring point 2
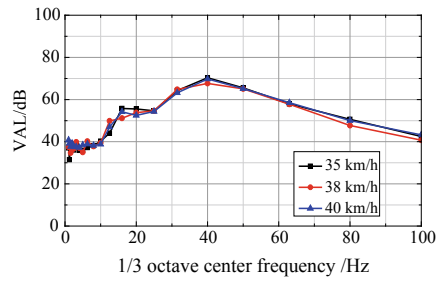
(c) Measuring point 3

(d) Measuring point 4

three cases for different tram speeds, that is, the speed of the tram 35, 38 and 40 km/h, and the effective value of vibration acceleration for the results in summer is shown in Fig. 6.

According to the variation curve of the effective value of acceleration at different speeds, the faster the train speed is, the greater the ground vibration is. And the farther the distance from the center of the track is, the smaller the vibration is, but the vibration attenuates and changes nonlinearly, and the attenuation gradually becomes slower.

The measured data are processed at the speed of 40 km/h in summer and winter, and the changing curve of the vibration acceleration is shown in Fig. 7. The effective value of the ground vibration acceleration in winter is greater than that in summer near the track, but the result is opposite at greater distance.

Fig. 6 Effective value of ground vibration acceleration at the different tram speeds
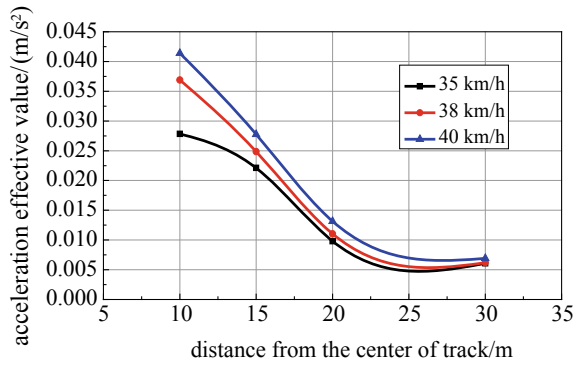
Fig. 7 Effective value curve of acceleration in different seasons
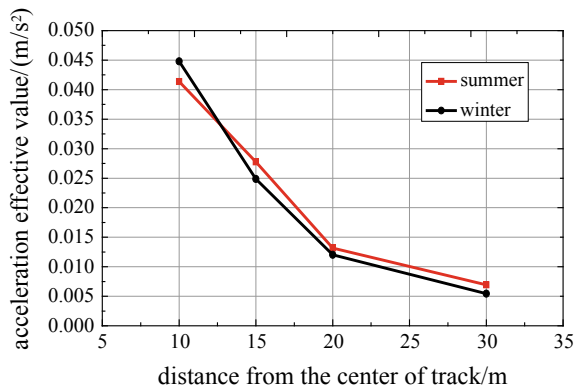
4 Evaluation of Environmental Vibration Caused by Tram

The "*Urban Area Environmental Vibration Standard*" (GB 10070-1988) formulated by China is an environmental vibration evaluation standard, which relates to the peak of vibration level. It evaluates the vibration level of the surrounding ground and building vibration in different areas. The vibration level in different regions should not exceed the values listed in Table 2 [12].

The division frequency Z vibration level is calculated, and the vertical total vibration level of each measuring point under different driving speeds is obtained. Then the environmental vibration which is induced by Line 202 Tram in Dalian is evaluated according to the criteria in Table 2. As shown in Fig. 8, it is the total vibration level curve summarized by the division frequency vibration level.

In Table 2, the ground vibration level outside the 30 m on both sides of the railway line shall not be more than 80 dB. According to the arrangement of on-site measurement points, the distance is 30 m from the measuring point 4 to the center line of the track. From Fig. 8, when the tram passes, at measuring point 4 the maximum value of total vibration level is 76.72 dB and the minimum value is 75.65 dB, not more than 80 dB. This shows that the vibration level is regulated in accordance with the urban environmental vibration standard.

Table 2 Standard of vibration in urban area environment

Area of application	Day	Night
Special residential area	65	65
Residential, cultural, educational area	70	67
Mixed area, commercial district	75	72
Industrial district	75	72
Both sides of main road lines	75	72
Both sides of main railway lines	80	80

Fig. 8 Vibration level curve of measuring points
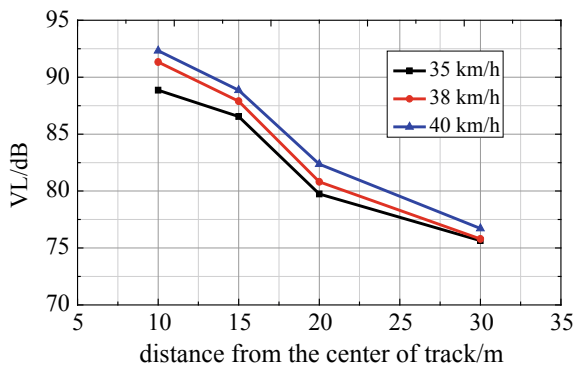
Fig. 9 Vibration level curve
in different seasons
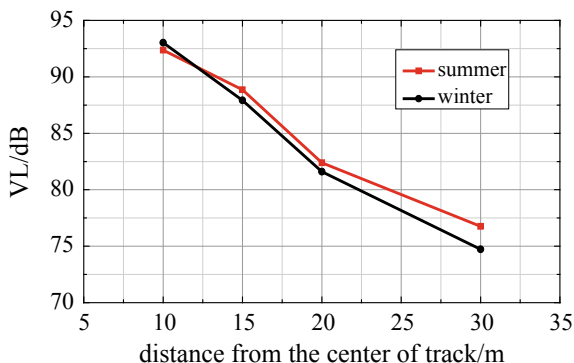
The measured data are processed at the speed of 40 km/h in summer and winter, and the changing curve of the total vibration level is shown in Fig. 9. Similar to the effective value of vibration acceleration, in the winter the total vibration level of the ground vibration near the track is greater than the value in the summer, but the result is opposite at greater distance. This phenomenon is due to the effect of the ambient temperature change, and the temperature is too low to increase stiffness of the subgrade, which leads to an increase in the effective value of the vertical acceleration.

5   Conclusions

Taking Line 202 in Dalian as the research object, the environmental vibration response caused by trams was studied by means of the in site measurement of the ground vibration acceleration, and the measured results were analyzed in the time-frequency domain. The following conclusions were obtained:

(1) The main frequency band of the environmental vibration by the tram car is 30–70 Hz; the total vibration level is about 75–93 dB.
(2) The vibration acceleration response caused by a tram increases with the tram speed and decreases with the distance from the track centerline, but the vibration attenuates and changes nonlinearly, and the attenuation rate gradually decreases. The change law of the vibration level is similar to the vibration acceleration.
(3) The environmental vibration caused by trams is affected by seasonal changes. In the winter, the temperature is too low and the roadbed stiffness is increased. As a result, the effective acceleration value and total vibration level is different between summer and winter.
(4) The total vibration level of environmental vibration caused by trams is less than 80 dB away from 30 m which is the distance from the measuring point 4 to the track centerline, meeting the vibration standard of urban environment.

References

1. Zhu ZH, Yu ZW, Zhu YL et al (2013) Analysis on environment and building vibration induced by passing trains on bridge structures. J China Railw Soc 35(4):102–109
2. Li K, Liu W, Jia Y (2011) Tests and analysis of traffic-induced vibration effects on surrounding historic buildings. J Beijing Jiaotong Univ 35(1):79–83
3. Liu WF, Liu WN, Gupta S et al (2010) Prediction of vibrations in the tunnel and free field due to passage of metro trains. Eng Mech 27(1):250–256
4. Verbraken H, Lombaert G, Degrande G (2011) Verification of an empirical prediction method for railway induced vibration by means of numerical simulation. J Sound Vib 330(8): 1692–1703
5. Geng W, Liu D, Cai Y et al (2014) Prediction of the influence of the proposed Beijing metro line 16 on a precise instrument of Peking University. Earthq Eng Eng Dyn 34(6):19–25
6. Vouiatzis K (2012) Protection of the cultural heritage from underground metro vibration and ground-borne noise in Athens Centre: the case of the Kerameikos Archaeological Museum and Gazi Cultural Centre. Int Acoust Vib 17(2):59–72
7. Wei H, Lei X, Lv S (2008) The field testing and prediction analysis for environmental vibration induced by railroad trains. Environ Pollut Control 30(9):17–22
8. Wang HQ (2004) Study on the theory and method of urban rail transit network planning. Southwest Jiaotong University
9. Tian M, Xiong CM, Yuan FQ et al (2013) Study on train caused ground-borne vibration. Noise Vib Control 33(1):143–147
10. Yang Y, Liu WN, Wang WB (2014) Experiments on environmental vibration propagation characteristics induced by metro traffic. J China Railw Soc 36(4):99–104
11. Ditzel A, Herman GC (2004) The influence of a rail embankment on the vibrations generated by moving trains. J Sound Vib 271:937–957
12. Chen JG, Xia H, Chen SL et al (2010) Investigation on running-train-induced ground vibrations near railway. Eng Mech 27(1):98–103

Study on the Train-Induced Vibration Transmission Within the Over-Track Building

Lihui Xu , Xiaojing Sun and Rongning Cao

Abstract The integrated complexes, known as the over-track building and metro depot complexes, have been widely developed in recent years in China. The construction of the over-track buildings has great merits of reductions in occupying urban land, conveniences in commuting to work, and comprehensive exploitation of the upper spaces. Such complexes have some negative effects that the train operation into and out of the depots can induce structural vibrations causing discomfort on occupants inside the buildings. To characterize the vibration transmissions between the floors, the three-dimensional dynamic finite element model of soil-platform-building has been established. The coupled train–track model was studied and applied as well in this paper. Diverse analyses of vibration responses have been conducted including vibration acceleration levels and vibration acceleration spectra in frequency domain and in 1/3 octave frequency. It found that vibration transmission law across floors in the horizontal orientation inside the over-track building absolutely differs from that in the vertical orientation. Train-induced vibrations inside the over-track building are mainly distributed in high frequency within 30–80 Hz, which have potential to make impacts on the occupants. Dynamic responses have revealed the key insights into the vibration transmissions in different orientations inside the over-track buildings.

Keywords Metro depot · Over-track building · Vibration · Numerical simulation · Vibration acceleration level · Frequency domain · 1/3 octave spectrum

L. Xu · X. Sun (✉) · R. Cao
Beijing Jiaotong University, Beijing 100044, China
e-mail: xjsun1@bjtu.edu.cn

L. Xu
e-mail: 17121129@bjtu.edu.cn

149

1   Introduction

Urban rail transit has great advantages in reducing the highway traffic in metropolitan city. For urban rail transit, subways have been widely developed due to its characteristics of efficient operation and less occupation of the ground areas. By the end of December 2017, in-service subway lines have spread over 34 cities with a total of 3884 km in mainland China [1]. The train depots are the subway or railway facilities for the regular maintenance, examination, and storage for the trains and usually occupy the large ground areas [2]. Traditional metro depots with low density of buildings hold larger ground spaces which make significant influences on the space and the environment, and it's not conducive to efficient utilization of the urban land and space due to the low density of the buildings [3]. Comprehensive utilization of the spaces above the depots can not only improve the utilization efficiency of the urban land, but also have great economic advantages. So, many cities in mainland China like Beijing and Wuhan have begun developing the over-track building complexes, which are built with a new structural system with large platforms, for residents and workers above the metro depot. The platforms above the metro depot are used for entertaining and parking, supported by the columns which are set in between train tracks.

However, the subway operation into and out of depots can generate excessive vibrations due to interaction between rails and wheels, which propagate from the tracks directly into the over-track buildings through ballast, columns, and platforms, radiating noises within the buildings that adversely affect the living qualities and even the health of the building occupants. It is essential to predict the train-induced vibration level prior to construction within the over-track buildings and take appropriate measures to mitigate the vibration for human comfort.

Massive researches have been conducted to characterize the vibration at the sources, in the propagation paths, and in the receivers inside the buildings induced by subway trains and operation lines. The vibration characteristics at the sources and in the propagation paths induced by railways have been summarized in detail [4–8]. Anderson [9] conducted measurements to collect the vibration data from two buildings caused by the railway operation and got that the perceptible vibrations, which are mainly between 5 and 50 Hz, can transmit into the building through the ground. Xia et al. [10] took in situ experiment to examine the vibration levels induced by running trains near Shenyang–Harbin railway line within two buildings and found the acceleration levels in the buildings exceeded the allowance by the Chinese Code. Sanayei et al. [11, 12] performed measurements of train-induced and subway-induced vibrations in different areas in Boston. It provided the basis that the vibration levels in sensitive locations inside the buildings induced by train operations should be estimated precisely. Numerous prediction modeling methods have been developed to predict the subway-induced vibration from the underground lines [13–16].

The vibration transmission in metro depots entirely differs from that around the operation line and subways, for the trains work on the ground right under the platform and the over-track buildings which is not the case with the operation lines and

subways. Some studies have been conducted on the transmission characteristics and levels of the vibration on the grounds, platforms, and over-track buildings in the metro depots. Field measurements were conducted to study the law of the vibration attenuation in the ground, platforms, and the over-track buildings subject to the vibration input in throat area [17], in testing line area [18], and in both throat and testing line areas [2, 3]. The measured maximum vertical vibration levels were lower than the limitation by Chinese standard [19] according to these researches. Numerical models were established to analyze the vibration response of the over-track buildings [20–22]. Vibration data of the sources were measured in the time domain on site and applied into the established numerical model. The results from the numerical model were well consistent with the measured vibration in the over-track buildings in both time and frequency domain, and the models were used to predict the vibration levels prior to the construction of the over-track buildings. He et al. [23] studied the impact of the train speed on the vibration within the over-track buildings and concluded that limiting the train speed into and out of the metro depot is an efficient way to attenuate the vibration within the over-track buildings.

This passage is to study the characteristics of the vibration transmission inside the over-track building above the main body in a typical metro depot under the influence of subway operation. A three-dimensional dynamic finite element model of soil-platform-building was built according to a metro depot to characterize the vibration transmission, and the train-induced vibrations were compared with the limitation by Chinese standard. It is efficient and reliable to apply this model to predict the vibration levels in the over-track building before constructing.

2 Description of Metro Depot and Over-Track Building

The metro depot related to this study is situated in Beijing, China. Its total occupying land use is approximately 314,200 m², including 266,000 m² for the functions of metro depot and 48,200 m² for the exploitation, which makes the metro depot the biggest one in China. Two avenues are situated at the north and west of the metro depot, respectively, as shown in Fig. 1. The soil layers consist of artificial accumulation layer, recent sedimentary layer, new Quaternary alluvium, and late Quaternary Pleistocene flood alluvium below the ground in this area. There is a main body, a throat area, and so on in the metro depot, and the tracks in the main body are straight. The area above the metro depot preserved for the construction of the over-track buildings with 12 floors is about 150,000 m², which will serve for the occupants and workers.

All the buildings are constructed using reinforced concrete columns with large open spans from the ground to the platform, whose height is 16.3 m to guarantee enough space for the trains. The columns supporting the platform have the sectional dimensions of 1.2 m by 1.2 m and are located on a grid of 6.0 m × 6.0 m, which is the same case with the columns supporting the over-track buildings according to the plan. The support structures for over-track building from the first floor to the top consist of frame structures with 12 floors with the height of 5.6 m in the first floor
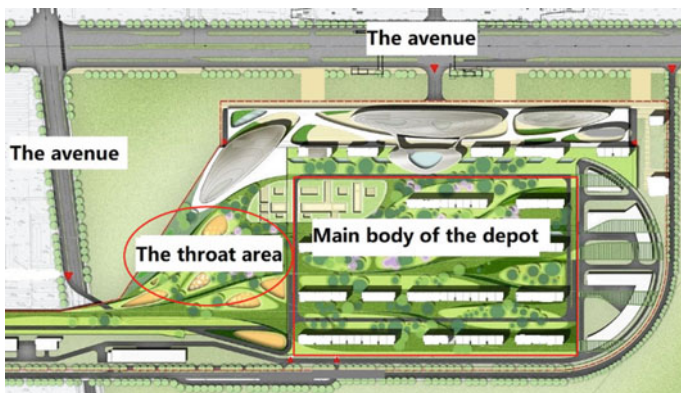
Fig. 1 Areas distribution in Beijing metro depot

Fig. 2 A sketch map of the metro depot in vertical direction
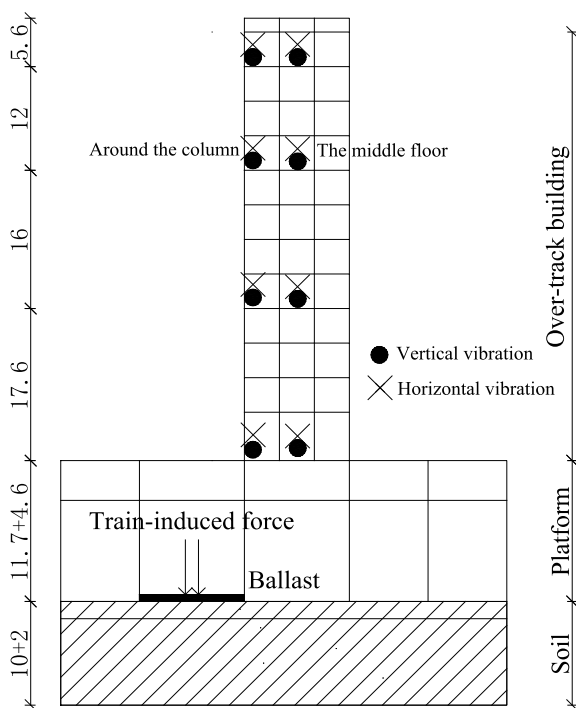
and the height of 4 m in standard floors, and load-bearing walls with the thick of 0.2 m, as shown in Fig. 2. The beams inside over-track building have the sectional size of 0.4 m × 0.6 m.

This study focused on vibration transmissions within an over-track building with 12 floors above the main body of the depot induced by the train operation into and out of the metro depot.

3 Establishment of the Finite Element Model

3.1 The Finite Element Model

As described above, the studied metro depot captures a large land use area. The vibration induced by the subway operation attenuates quickly with the propagation of the vibration wave, which makes it unnecessary to take all areas of metro depot into account in the study. A part of metro depot is applied in this model that must take a reasonable size for the reasons that a model which is too large can increase the computational cost and which is too small can affect the accuracy and reliability of the results [24]. The lengths of this model which are parallel to the track lines are 96 m and the widths which are perpendicular to the track lines are 51 m to make sure it is accurate and reliable to predict the vibrations. The height of the platform is 16.3 m to provide enough space for the trains.

The structure modeling and dynamic analysis are accomplished in the finite element software, ANSYS, which is widely used for modeling and analysis in statics and dynamics. The finite element model is shown in Fig. 3, and Fig. 2 shows the positions of train-induced forces which is a function of time acting at the point where fasteners and sleepers contact with each other. The points where the vertical and horizontal vibration data is gathered inside the over-track buildings, including the points on the floors around the column and the points in the middle of floors, are also illustrated in Fig. 2. In this model, all the beams and columns with different sectional size are simulated by the beam elements, BEAM4, which do not allow for shear deformations of the units. All the floors and walls are modeled using the surface elements, PLANE42, and soil and ballasts are regarded as the physical

Fig. 3 Finite element model of metro depot
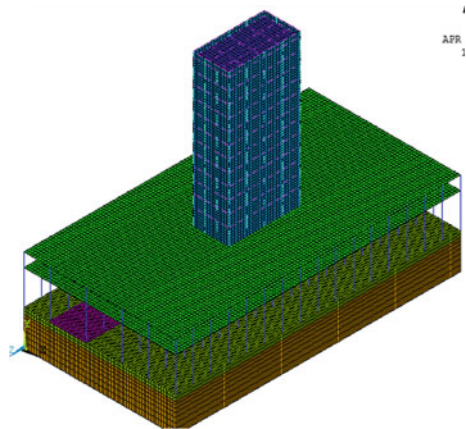
elements, SOLID45. The elements should be divided into small elements with the right sizes, which should be small enough to accurately determine the full wave-form when vibration waves are propagating in the units and big enough to reduce the calculation time [24]. For the purpose of impeding wave reflection in the cut-off boundaries which are employed to take constraints to models from the infinite stratum into consideration, the viscoelastic boundaries are applied with the advantages of good behaviors in numerical stability and accuracy and its conve-nience of application in the finite element models [25].

Impacts of ballast, formation, building foundations, frame structures, and wall panels on the wave propagation in the depot are taken into account, and the effects of decorative components such as wall materials are ignored in this three-dimensional finite element dynamic model.

3.2 Damping

Damping is a so complicated mechanism of energy dissipation that many damping models have been put forward to make it easy to consider it in the researches and the Rayleigh damping model with a linear combination of stiffness and mass matrix is widely used. In order to determine the damping coefficients, the modal analysis is required to obtain the natural frequency of the building, and the first five levels of modal frequencies obtained from the modal analysis of the soil-platform-structure model are 1.00, 1.36, 2.40, 3.47, and 5.48 Hz, respectively. The mass damping coefficient and stiffness damping coefficient are acquired by taking the first two natural frequencies and damping ratios into Eq. (1).

$$
\begin{cases}
\alpha = \dfrac{4\pi f_i f_j \left(\varepsilon_j f_i - \varepsilon_i f_j\right)}{f_i^2 - f_j^2} \\
\beta = \dfrac{\left(\varepsilon_i f_i - \varepsilon_j f_j\right)}{\pi\left(f_i^2 - f_j^2\right)}
\end{cases}
\tag{1}
$$

where α and β are mass and stiffness damping coefficient, f_i, f_j, ε_i, ε_j are the ith and jth natural frequencies and damping ratios, which are 1.0 Hz, 1.36 Hz, 0.03, and 0.03 when i equals to 1 and j equals to 2, respectively. The value of α and β on the basis of Eq. (1) are 0.217 and 4.04×10^{-3}.

4 Vibration Sources

Simulation of train-induced excitation at the sources is one of the key processes in this study on the train-induced vibration transmission within the over-track build-ing, because whether the input excitation is well consistent with the measured

excitation directly make impacts on correctness of the results. The method to calculate the excitation in frequency domain with coupled train–track dynamic model presented by Ma [26, 27], which has been confirmed by a number of field measurements, is studied and applied in this work.

4.1 The Coupled Train–Track Model

In the coupled train–track system, the trains which can move forward at the speed of v on the rails consist of several individual vehicles, and each vehicle is made up of three parts including a body, two bogies, and four wheelsets that each part connects to the others with parallel springs and dampers, as shown in Figs. 4 and 5. There are 10 degrees of freedom for a single vehicle, including ups and downs of the body, two bogies, and four wheelsets, as well as rotations about the axial direction of the body and two bogies. The suspended mass and the interactions between wheels and rails are also taken into account in this model. The interactions across the interfaces between rails and sleepers are nonlinear that are represented by a series of springs and dampers, which is the same case with sleepers and ballasts, as well as ballasts and foundations.

In vehicle model, there are 10 degrees of freedom for a certain vehicle, and the equation of motion in different degree of freedom should be formed to obtain the dynamic response. The equation of motion is shown as Eq. (2), on the basis of D'Alembert principle.
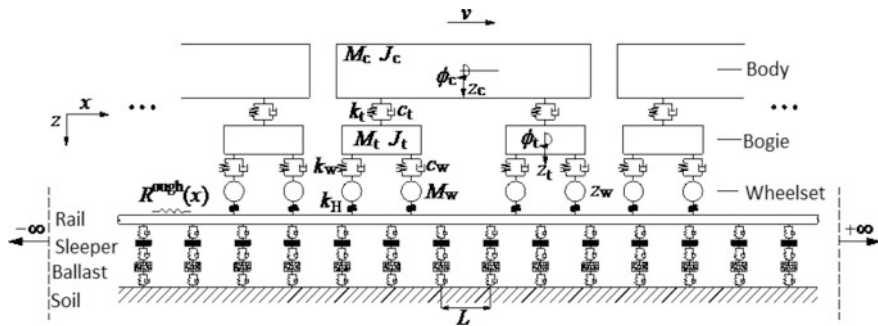
Fig. 4 Coupled train–track model
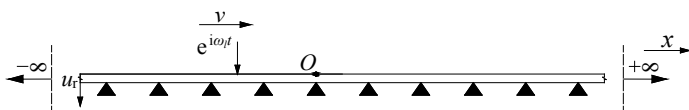
Fig. 5 Basic cell in global coordinate system

$$\mathbf{M}_m\ddot{\mathbf{A}}_m(t) + \mathbf{C}_m\dot{\mathbf{A}}_m(t) + \mathbf{K}_m\mathbf{A}_m(t) = \mathbf{Q}_m(t) \tag{2}$$

where $\ddot{\mathbf{A}}_m(t), \dot{\mathbf{A}}_m(t), \mathbf{A}_m(t)$ are the acceleration, velocity, and displacement vector of the certain vehicle, $\mathbf{Q}_m(t)$ are the excitation vector and $\mathbf{M}_m$, $\mathbf{C}_m$, and $\mathbf{K}_m$ are the mass, damping, and stiffness matrix.

Rails in this model are simplified as the Euler–Bernoulli beams ignoring the shear deformations across the transverse sections, which are infinite in the space and periodically supported by the vertical springs and dampers. The dynamic displacement of the infinite beam can be written as Eq. (3).

$$E_r^* I_r \frac{\partial^4 u_r}{\partial x^4} + m\frac{\partial^2 u_r}{\partial t^2} = e^{i\omega_l t}\delta(x - x_0^F - vt) - \sum_{n=-\infty}^{n=+\infty} f_n(t)\delta(x - x_n) \tag{3}$$

where u_r represents the vertical displacement, $E_r^* = E_r(1 + i\eta_r)$ are the elastic modulus which allows for the real elastic modulus E_r and the damping loss factor η_r. I_r and m are the sectional moment of inertia and mass per unit length, respectively. x_0^F is the location of the load at the initial time, and $x_n = nL$ is the location of the nth fastener where L represents the spacing between the adjacent fasteners. $f_n(t)$ is the support force from the nth fastener.

Solution of dynamic responses of the infinite beams can be carried out in a basic cell with the length of L, and the operations are conducted in global coordinate system in frequency domain, as shown in Fig. 5 and expressed as Eq. (4).

$$E_r^* I_r \frac{\partial^4 u_r}{\partial x^4} + m\frac{\partial^2 u_r}{\partial t^2} = e^{i\omega_l t}\delta(x - x_0^F - vt) \tag{4}$$

Fourier transformation is used to transform Eq. (4) from the time domain to the frequency domain, expressed as Eq. (5)

$$E_r^* I_r \frac{d^4 \hat{u}_r}{dx^4} - \omega^2 m\hat{u}_r = \frac{1}{v}e^{i\frac{\omega_l-\omega}{v}\left(x-x_0^F\right)} \tag{5}$$

where the $\hat{u}_r$ is the vertical displacement of the basic cell in frequency domain.

The displacements of a fixed point in the basic cell due to the unit harmonic moving load acting at the beams can be calculated using the method proposed by Ma [26, 27], and displacements of the points in other ranges are derived from solutions of the basic cell, which must comply with the periodic-infinite structure theory, expressed as Eq. (6).

$$\hat{u}_r(\widehat{x}, \omega, \omega_l) = e^{i(\omega_l-\omega)n_L L/v} \cdot \hat{u}_r(x, \omega, \omega_l) \tag{6}$$

where $\widehat{x}$ and x obey the relation of $\widehat{x} = x + n_L L$, L represents the length of basic cells, n_L refers to the number of the basic cells between the point at $\widehat{x}$ and x, and $\hat{u}_r(x, \omega, \omega_l)$ is the displacement of the basic cell in frequency domain.

Continuous discrete displacements of points in whole beams induced by the unit harmonic moving load $F(t) = e^{i\omega_l t}$ at the speed of v are obtained through making the angular frequency ω continuous discrete values at the focused range in frequency domain. Then, applying the inverse discrete Fourier transformation, the displacements in frequency domain can be transformed to the displacements in time domain.

Train's passage would generate dozens of moving loads with certain magnitude, and all of them make contribution to the total displacements of the targeted point that are the linear superposition of influence under the individual one. The actual forces interacting across interfaces between rails and foundation are products of the actual displacements and composite stiffness allowing for the stiffness between the rails and sleepers, sleepers and ballasts, as well as the ballasts and foundation.

4.2 Excitation Due to Moving Trains

This work is based on operation of the Type-B train at the speed of 25 km/h which is integrated by six single vehicles. The vehicle parameters and track parameters are listed in Tables 1 and 2. The simulated excitation is illustrated as Fig. 6. The maximum of interacting forces between the rails and foundation induced by train operations are approximately 6×10^4 N, and the forces are mainly in low frequency within 10 Hz. The force magnitude in high frequency is low.

Table 1 Vehicle parameters

Parameter's name		Values
Body parameters	Vertical stiffness	480 kN/m
	Vertical damping	60 kN s/m
	Mass of an individual vehicle	43 t
Bogies parameters	Vertical stiffness	1650 kN/m
	Vertical damping	15 kN s/m
	Mass of a single bogies	3.418 t
Wheelsets parameters	Mass of an single wheel	1.61 t
	Radius of the wheels	0.84 m
	Spacing between wheels in one bogie	2.2 m

Table 2 Track parameters

Parameter's name		Values
Steel rail parameter	Mass per unit length	$m = 121.28\,\text{kg/m}$
	Elastic modulus	$E_r = 2.059 \times 10^{11}\,\text{N/m}^2$
	Moment of the inertia across the section	$I_r = 6.434 \times 10^{-5}\,\text{m}^4$
	Damping loss factor	$\eta_r = 0.01$
Fastener parameter	Stiffness	$k_r = 1.2 \times 10^8\,\text{N/m}$
	Damping	$c_r = 6 \times 10^4\,\text{N s/m}$
	Spacing between adjacent fasteners	$L = 0.6\,\text{m}$
Ballast parameter	Density	$\rho_b = 1.8 \times 10^3\,\text{kg/m}^3$
	Elastic modulus	$E_b = 1.1 \times 10^8\,\text{N/m}^2$
	Damping	$c_b = 5.88 \times 10^4\,\text{N s/m}$

(a) Force in time domain   (b) Force in frequency domain
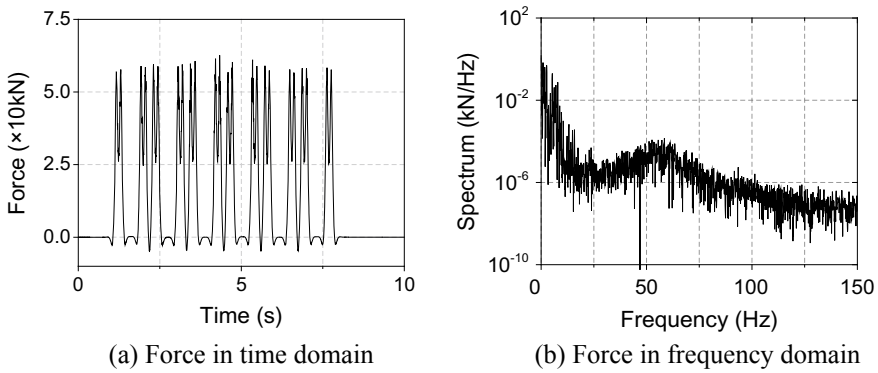
Fig. 6 Train-induced interacting force between rails and foundation

5 Train-Induced Vibrations Inside the Over-Track Building

In order to characterize the vibration transmissions inside the over-track building subjected to the train operation, points for gathering vertical and horizontal vibration data are appointed to be located at each floor around the column and in the middle of each floor, as illustrated in Fig. 2. The analyses of vibration responses are conducted in three aspects including vibration acceleration levels, vibration acceleration spectra in frequency domain, and in 1/3 octave frequency. According to ISO 2631-1 [28], the main frequencies of vibration impacts on humans are within 1–80 Hz. As a result, frequencies in this study range from 1 to 100 Hz.

5.1 Vibration Acceleration Level

The vibration acceleration levels are used for evaluating impacts of vibrations inside buildings, which are induced by the vibration sources within the buildings, such as elevators, motors, and so on, formulated by GB/T 50355-2005 [29]. The method of calculating the vibration acceleration level has been made by it, expressed as Eq. (7).

$$L_a = 20 \lg \frac{a_{rms}}{a_0} \tag{7}$$

where a_0 is the reference acceleration with the value of 1×10^{-6} m/s^2, a_{rms} is the root mean square of acceleration value (m/s^2), and L_a represents the vibration acceleration level (dB).

Figure 7 shows vertical vibration acceleration levels around the column and in the middle of the floor inside the building. The vertical vibration acceleration levels are attenuated between the first to the ninth floor around the column and the first to tenth floor in the middle of floors and amplified greatly at the top floor, with the minimum of approximately 46.2 and 52.6 dB, respectively. What is more, the vertical vibration acceleration level around the column is less than that in the middle of the floor by 1.8–6.9 dB in the same floor. Vertical constraint from the column makes the floor vibration weaker around the column, and vibration waves from various propagation paths strengthen each other in amplitude in the middle of floors, which may contribute to that phenomenon.

The horizontal vibration acceleration levels around the column and in the middle of the floor inside the building are shown in Fig. 8. The horizontal vibration acceleration levels around the column and in the middle of the floor in the same height are comparably close, with little differences in magnitude. The horizontal vibration levels show the tendency of slight amplification on the whole, with no

Fig. 7 Vertical acceleration level inside the building
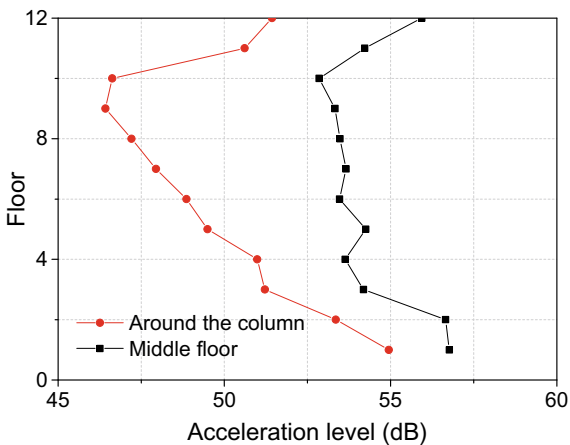
Fig. 8 Horizontal acceleration level inside the building
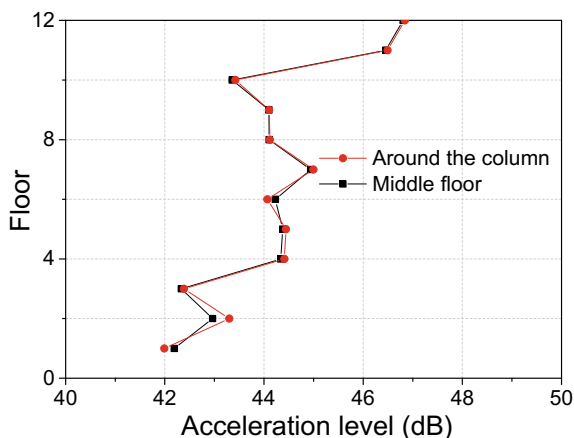
attenuation, with the increase in height, which can be explained by the cause that the floors are more weakly restrained in the horizontal direction in higher floors.

Comparing Figs. 7 and 8, it is evident that the vibration acceleration levels in vertical orientation are greater than those in horizontal orientation by 7.8–14.6 dB in the same floor. This is because the moving loads induced by the train operation in the straight track are mainly vertical and stiffness in vertical direction are smaller than that in horizontal direction in the middle of the floor that vibrations are amplified with the stiffness degradation.

5.2 Spectrum in Frequency Domain

Figures 9, 10, and 11 typically show a portion of vibration acceleration spectra in frequency domain both around the column and in the middle of the floors. In both vertical and horizontal directions, the train-induced vibrations inside the building are mainly distributed in high frequency within 30–80 Hz, which could make impacts on the occupants, and the dominant frequency decreases with the rise in height. As shown in Figs. 9 and 10, the dominant frequencies of vertical vibrations in the middle of the floors are basically consistent with these on the same floor around the column, which range from 50 to 70 Hz. Moreover, the dominant frequencies of the floor vibrations in horizontal direction, varying between 30 and 55 Hz, are lower in comparison with these in vertical direction by about 15 Hz, as shown in Fig. 11. Also, the maximums of the horizontal vibration amplitudes are obviously below these in vertical direction.

There exist the regularities that the vibrations inside the over-track building are enhanced at certain frequencies, which are near 23, 35, 75 Hz. That is because the train-induced vibrations within the building have triggered the certain bending mode of the floor slabs, whose frequencies are exactly corresponding to these where

(a) First floor

(b) Fifth floor

(c) Ninth floor

(d) Twelfth floor
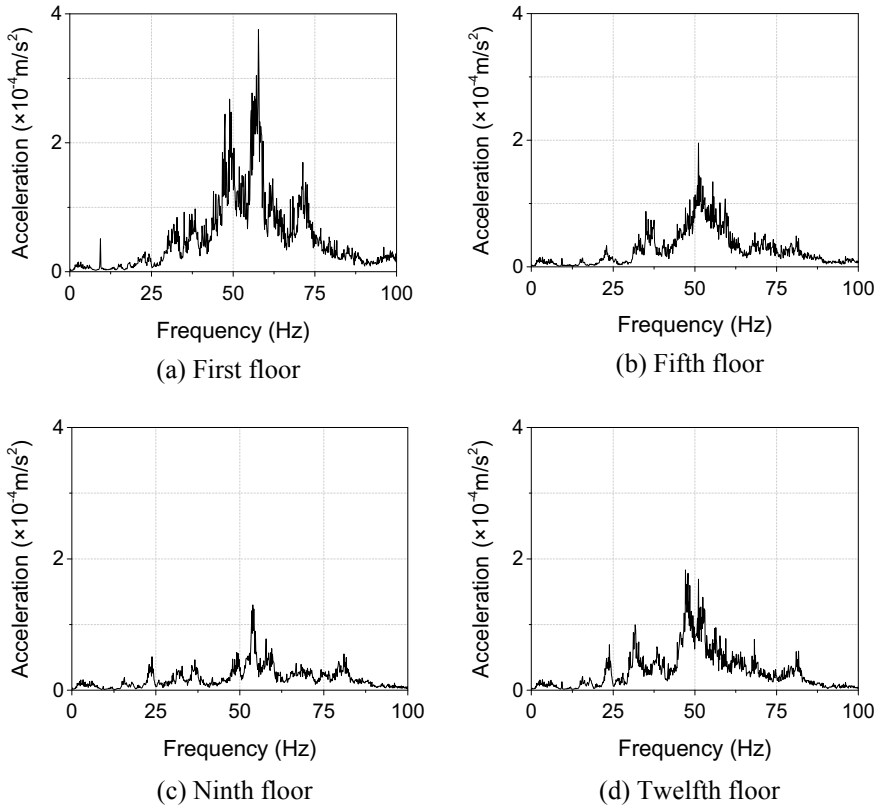
Fig. 9 Train-induced vertical vibrations in the middle of the floors

the vibrations are largely amplified. Additionally, it is quite clear from the graphic area enclosed by the curves of the vibration acceleration spectra and the transverse axis that the horizontal vibration energy, which is mostly distributed at some specific frequencies, is more concentrated than the vertical vibrations in frequency domain.

5.3 1/3 Octave Spectrum

The vertical vibration acceleration spectra in 1/3 octave frequency on the floors around the column and in the middle of the floors are shown in Figs. 12 and 13. It can be obviously found that when the central frequency is below 10 Hz, the vertical acceleration levels of each floor are approximately equivalent, with the differences below 5 dB. The vertical vibrations attenuate slowly in the low frequency during the transmission between floors. When beyond 16 Hz, the acceleration levels

(a) First floor

(b) Fifth floor

(c) Ninth floor

(d) Twelfth floor
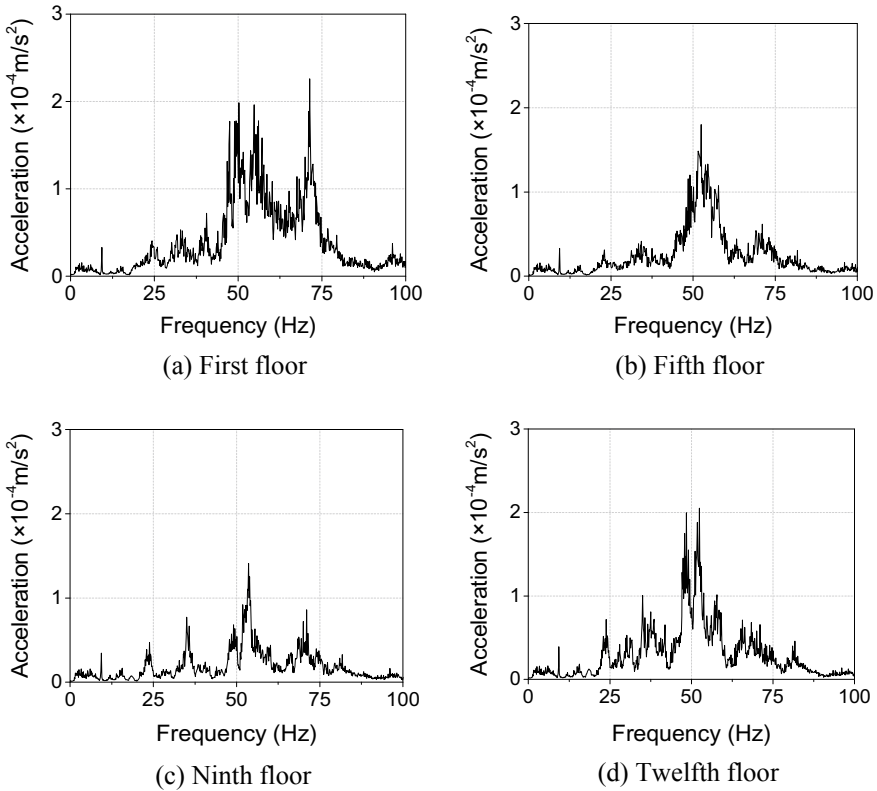
Fig. 10 Train-induced vertical vibrations around the column

change quickly with the rise in height. It also can be noticed that the vertical acceleration level reaches a peak value at 16 Hz and the maximum at 63 Hz. Then above 63 Hz, the acceleration levels fall off rapidly. Comparing to allowance by the standard of limit and measurement method of vibration in the room of residential buildings [29], the vertical acceleration levels inside the over-track building are far below the limitation.

Figure 14 shows the 1/3 octave spectra of the horizontal vibration acceleration levels in the middle of the floors. The horizontal vibration levels increase monotonously and greatly with the rise in height, in which the vibration level in the first floor is lower than that in the top floor by about 20 dB, when the central frequency is smaller than 6.3 Hz. Inversely, when above that, the vibration levels change slowly and the differences are not that great between different floors. Meanwhile, the horizontal vibration levels are of little changes in the low frequency, and these are in sharp variations when the central frequency goes beyond 6.3 Hz. And the acceleration levels in horizontal direction reach the maximum at the 31.5 Hz.

(a) First floor

(b) Fifth floor

(c) Ninth floor

(d) Twelfth floor
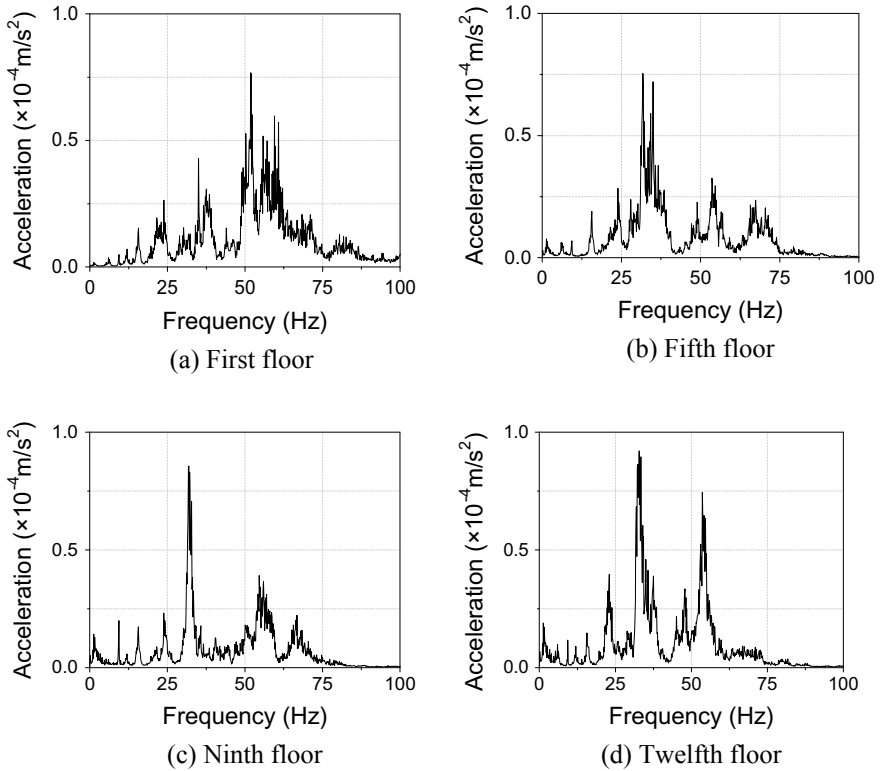
Fig. 11 Train-induced horizontal vibrations in the middle of the floors

Fig. 12 1/3 octave spectra of the vertical vibrations in the middle of the floors
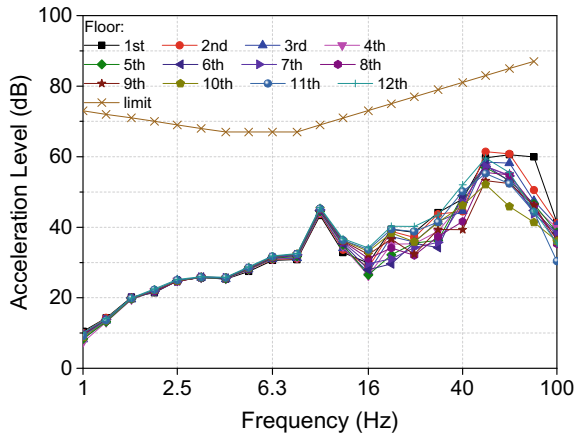
Fig. 13 1/3 octave spectra of the vertical vibrations around the column
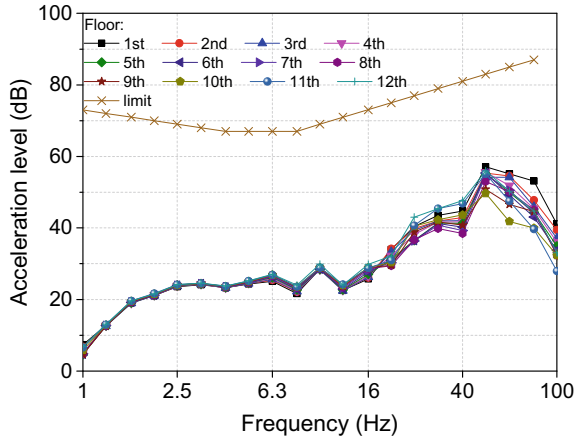
Fig. 14 1/3 octave spectra of the horizontal vibrations in the middle of the floors
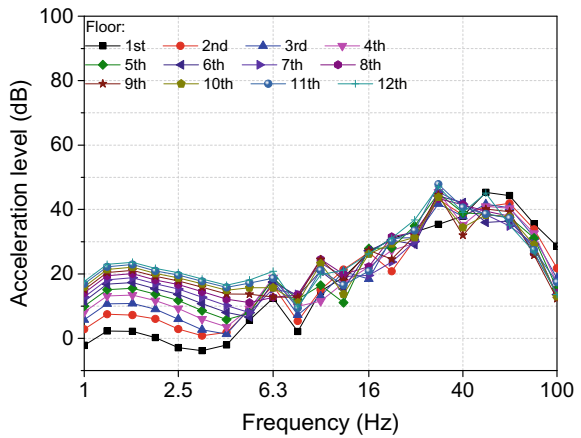
It can be inferred from the analyses above that the vibration transmission law across the floors in the horizontal orientation inside the over-track building absolutely differs from that in the vertical orientation. What is more, there are some diversities between the distribution of the horizontal vibration 1/3 octave spectra in the first floor of the building and that in standard floor in high frequency, whose heights are 5.6 and 4 m, respectively. This is because the horizontal constraints to the first floor are imposed by the platform, which could make it vibrate in a different way.

6 Conclusion

Three-dimensional dynamic finite element model of soil-platform-building was established to characterize the vibration transmissions inside the over-track building induced by the train operations into and out of the metro depot. The coupled train–track model was studied and applied as well. These findings have revealed the key insights into the vibration transmissions inside the over-track buildings, including:

1. Vibration waves from various propagation paths strengthen each other in amplitude in the middle of floors, which results in amplifying the vertical vibrations by more than 1.8 dB in comparison with the vertical vibration levels around the columns inside the building. The horizontal vibration levels are comparable in the same floor.
2. The weaker constraints to the higher floors in horizontal direction make main contributions to the vibration enhancement that makes horizontal vibration levels with the tendency of amplification on the whole with the rise in height. The vertical vibrations are attenuated by the floors and amplified at the top floor.
3. Train-induced vibrations inside the over-track building are mainly distributed in high frequency within 30–80 Hz, which have potential to make impacts on the occupants, and the dominant frequency decreases with the rise in height in both vertical and horizontal direction.
4. In the 1/3 octave frequency, the vertical vibration acceleration levels in high frequencies change more obviously with the increasing floor, and the horizontal vibration acceleration levels in low frequencies change more obviously with the increasing floor.

References

1. Urban Rail Transit Association (2017) Annual statistics and analysis report of urban rail transit of 2017—the 2nd version. http://www.camet.org.cn. Accessed 2018/04/08
2. Zou C, Wang YM, Wang P et al (2015) Measurement of ground and nearby building vibration and noise induced by trains in a metro depot. Sci Total Environ 536:761–773
3. Zou C, Wang YM, Moore JA et al (2017) Train-induced field vibration measurements of ground and over-track buildings. Sci Total Environ 575:1339–1351
4. Connolly DP, Kouroussis G, Laghrouche O, Ho CL, Forde MC (2015) Benchmarking railway vibrations-track, vehicle, ground and building effects. Constr Build Mater 92:64–81
5. Kouroussis G, Connolly DP, Verlinden O (2014) Railway-induced ground vibrations–a review of vehicle effects. Int J Rail Transp 2(2):69–110
6. Hung H, Yang Y (2000) A review of researches on ground-borne vibrations with emphasis on those induced by trains. Proc Nat Sci Counc Part A Phys Sci Eng 25(1):1–16
7. Newland DE, Hunt HEM (1991) Isolation of buildings from ground vibration: a review of recent progress. Proc Inst Mech Eng Part C Mech Eng Sci 205(1):39–52
8. Avillez J, Frost M, Cawser S, Skinner C, El-Hamalawi A, Shields P (2012) Procedures for estimating environmental impact from railway induced vibration: a review. In: ASME 2012

noise control and acoustics division conference at InterNoise 2012, Aug 2012. American Society of Mechanical Engineers, pp 381–392

9. Anderson DC (1994) Engineering prediction of railway vibration transmitted in buildings. Environ Eng 7(1):14–19
10. Xia H, Zhang N, Cao YM (2005) Experimental study of train-induced vibrations of environments and buildings. J Sound Vib 280(3–5):1017–1029
11. Sanayei M, Maurya P, Moore JA (2013) Measurement of building foundation and ground-borne vibrations due to surface trains and subways. Eng Struct 53:102–111
12. Sanayei M, Moore JA, Brett CR (2014) Measurement and prediction of train-induced vibrations in a full-scale building. Eng Struct 77:119–128
13. Gupta S, Hussein MFM, Degrande G, Hunt HEM, Clouteau D (2007) A comparison of two numerical models for the prediction of vibrations from underground railway traffic. Soil Dyn Earthq Eng 27(7):608–624
14. Hussein MFM, Hunt HEM (2009) A numerical model for calculating vibration due to a harmonic moving load on a floating-slab track with discontinuous slabs in an underground railway tunnel. J Sound Vib 321(1–2):363–374
15. Thornely-Taylor RM (2004) The prediction of vibration, ground-borne and structure-radiated noise from railways using finite difference method—part 1—theory. Proc Inst Acoust 26(Pt 2):69–79
16. Jones S (2010) Ground vibration from underground railways: how simplifying assumptions limit prediction accuracy. Ph.D. thesis, University of Cambridge, Cambridge
17. Zou C, Wang YM, Wang ZH et al (2015) Field measurement and analysis of ground vibration in the throat area of metro depot. J Vib Shock 34(16):200–206
18. Lin CJ, Qi YK, Xing Y et al (2015) Propagation law of vibration from test line in metro depot. Urban Rapid Rail Transit 28(05):77–81
19. Ministry of Environment Protection of the People's Republic of China (1988) GB 10070-88: standard of vibration in urban area environment
20. Li XL (2003) Study on influence of vibration induced by subway train on ground and ground structures. Ph.D. thesis, Beijing University of Technology, Beijing
21. Wu YB, Zhang B, Liu YH et al (2015) Law of vibrations influence of subway on metro depot superstructure. J China Railw Soc 37(08):98–103
22. Xie WP, Chen YM, Yao CQ (2016) Vibration analysis of train depot over-track buildings induced by train load. J Vib Shock 35(08):110–115
23. He L, Song RX, Wu YB et al (2015) Analysis on actual measurement of train speed influence on the vibration of over-track buildings of metro depot. Build Struct 45(19):96–99
24. Liu WN, Ma M et al (2014) Prediction, evaluation and control of the environmental vibration induced by subway trains. Science Press, Beijing
25. Gu Y, Liu JB, Du YX (2007) 3D consistent viscous-spring artificial boundary and viscous-spring boundary element. Eng Mech 24(12):31–37
26. Ma LX (2015) Study on the model of coupled vehicle and track and the analysis model for tunnel-ground vibration response based on the periodic-infinite structure theory. Ph.D. thesis, Beijing Jiaotong University, Beijing
27. Ma LX, Liu WN, Li KF (2014) Fast numerical algorithm of floating slab track vibration response under moving loads in the frequency domain. J China Railw Soc 36(02):86–94
28. International Organization for Standardization (1997) ISO 2631-1: mechanical vibration and shock—evaluation of human exposure to whole-body vibration—part 1: general requirements
29. Ministry of Construction of the People's Republic of China (2005) GB/T 50355-2005: standard of limit and measurement method of vibration in the room of residential buildings

Soil Dynamics and Soil Structure Dynamic Interaction

Limit Analysis of Slope Stability During Pile Driving Considering Energy Dissipation Due to Deformation of Inner Friction

Ying Liu, Zhihao Mo, Qing Sheng Chen and Henglin Xiao

Abstract In most existing limit analysis studies of slope stability, it was often assumed that the logarithmic spiral landslide body is a rigid body, and the energy dissipation in the process of landslide occurs only on the sliding surface. Although the calculation of energy dissipation could be significantly simplified by employing this assumption, the energy dissipation due to internal friction could not be taken into account in the slope stability analysis, thereby often leading to inaccuracy in the evaluation of slope safety factor. In this paper, a multi-block partitioning method is adopted to quantify the internal dissipation during the pile driving process. By employing the limit analysis method, the safety factor incorporating the effects of energy dissipation due to internal friction for evaluating the slope stability subjected to pile driving is calculated. Comparison studies of the results with and without consideration of internal-friction-induced energy dissipation are presented and discussed. The results show that the slope safety factor with consideration of the energy dissipation due to inner friction-induced deformation is greater than its counterpart neglecting such effects. The energy dissipation significantly contributes to improving the anti-slide capacity of slope, which should be taken into account in the slope stability analysis in practice.

Y. Liu
College of Civil Engineering and Architecture, Nanchang Institute Technology,
Nanchang 330099, China
e-mail: 28152680@qq.com

Z. Mo
School of Environment and Architecture, University of Shanghai for Science
and Technology, 200093 Shanghai, China
e-mail: zhihaomo1@163.com

Q. S. Chen (✉)
Department of Civil and Environmental Engineering,
National University of Singapore, Singapore 117576, Singapore
e-mail: ceecq@nus.edu.sg

H. Xiao
Technology Research Center of Ecological Road Engineering,
Hubei University of Technology, 430068 Wuhan, China
e-mail: xiao-henglin@163.com

Keywords Slope stability · Pile driving · Multi-block partitioning method · Energy dissipation · Upper bound limit analysis

1 Introduction

Slope stability analysis is one of the classic problems of soil mechanics and also an important subject in geotechnical field. Slope instability disasters caused by natural landslides [1], debris flow [2] and human activities [3] often lead to huge losses of life, property and economy.

Over the past decades, various studies have been carried out to investigate the effect of pile driving on slope stability. Yuan [4] employed the theory of column hole expansion to investigate the soil stress and excess pore water pressure under piling and proposed the expressions for calculating the safety factor with the theory of arc sliding theory. Xu [5, 6] used simplified Bishop method to establish the limit state equation and studied the slope stability by regarding the excess pore water pressure as the main influencing factor. On the basis of the upper bound limit analysis, Sun [7] studied a series of problems such as the slope stability in two-dimensional and three-dimensional cases.

Among existing methods, limit analysis method (LAM) [8–10] is one of the most commonly used approaches for assessing the stability of slopes due to its simplicity and efficiency. In LAM, the sliding surface with highest potential to failure is investigated by converting the effect of pile driving force into the form of external force work and the anti-slide effect of the pile into the form of internal energy dissipation, respectively. In the majority of existing LAM studies for slope stability, it was assumed that the logarithmic spiral landslide body is a rigid body, and the energy dissipation in the process of landslide occurs only on the sliding surface. Although the calculation of energy dissipation is simplified by employing this assumption, the energy dissipation due to internal friction could not be taken into account, thereby leading to inaccuracy in the evaluation of slope safety factor.

To address the above issues, a multi-block partitioning method is adopted to quantify the internal dissipation during the pile driving process. The safety factor of slope during pile driving with consideration of the effects of internal friction on energy dissipation is calculated. Thereafter, comparison studies of the results with and without consideration of internal-friction-induced energy dissipation are presented and discussed.

2 Energy Dissipation Due to Deformation of Inner Friction

It is assumed that the upper bound limit analysis here satisfies the associated flow rule, where the straight sliding surface and the rational logarithmic spiral sliding surface are employed in the slope stability analysis. For the case of a straight sliding surface, the landslide velocity is assumed to be uniform, and the internal surface does not produce relative friction. For the case of a logarithmic spiral sliding surface, as the diameter of the logarithmic spiral line increases and the curvature decreases, the rotation would not be a standard circular motion. To accommodate the decreasing curvature, the landslide body would be deformed, which would result in extra energy dissipation. From this point of view, it is not accurate to treat the logarithmic spiral landslide body as a rigid.

2.1 A Quantitative Method for Energy Consumption of Friction Deformation

In order to quantify the energy dissipation rate in the adaptive process, a multi-block partitioning method [11] is adopted. The whole logarithmic spiral landslide body can be decomposed into multiple blocks. When the number of partitions is large enough (10 is used in current study), the friction deformation energy consumption of each block would be negligible. As a result, the respective blocks can be treated as rigid bodies, and the friction energy consumption occurs only on the contact surfaces of the respective rigid blocks, as shown in Fig. 1. In addition, since the polar angle of each block is small when the number of partitions is large enough (10 is used in
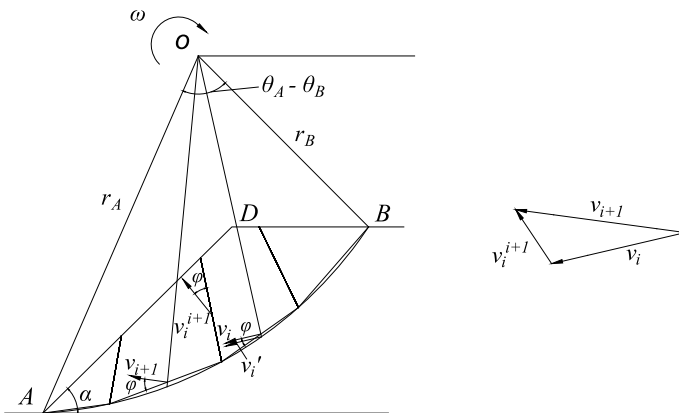
Fig. 1 Principle of multi-block partitioning method

current study), the arc is very close to the corresponding secant line. As shown in Fig. 1, the above-described multi-block partitioning method is equivalent to converting the logarithmic spiral sliding surface into a multi-segment polyline sliding surface and generating a block contact surface at the inflection point.

2.2 The Realization of Multi-block Partitioning Method

For the relative velocity v_i^{i+1} on each contact surface as shown in Fig. 1, a closed vector triangle should be constituted in order to meet the velocity compatible condition. To facilitate the calculation of the vector angle, the azimuth of the vector is defined as the angle counterclockwise from the x-axis positive direction to the vector's direction as shown in Fig. 2. According to the geometric relationship, the relationship between the azimuth of the velocity vector η_i and its corresponding polar angle θ_i is:

$$\eta_i = \pi - \theta_i + \pi/2 = 3\pi/2 - \theta_i \tag{1}$$

Each block velocity $\mathbf{v_i}$ is obtained by evenly distributing the landslide polar angle range θ_B to θ_A. Then, the velocities of adjacent two blocks combined with the closed vector relationship would give all information of vector $\mathbf{v}_i^{i+1}$.

In the present work, the polar diameter of each velocity point r_i is obtained by bisecting the polar angle range θ_i to θ_{i+1} and then multiplied by the angular velocity ω to get the block velocity v_i. According to the geometric relationship in Fig. 2, the following expressions are obtained:

$$v_i^{i+1} = \sqrt{v_i^2 + v_{i+1}^2 - 2v_i v_{i+1} \cos(\eta_i - \eta_{i+1})} \tag{2}$$

Fig. 2 Vector relationship of compatible velocity field
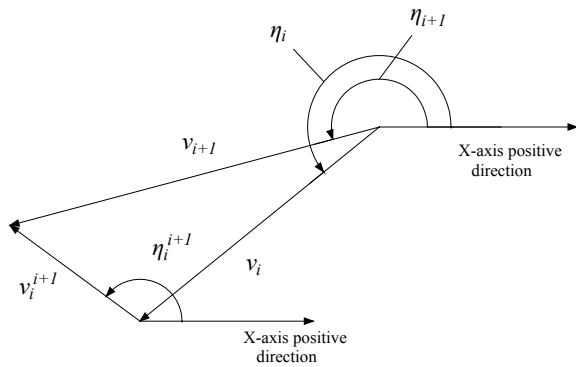
$$\frac{v_i}{\sin(\eta_{i+1} - \eta_i^{i+1})} = \frac{v_i^{i+1}}{\sin(\eta_i - \eta_{i+1})} \tag{3}$$

For the sake of convenience, this paper assumes that the straight line of the block contact surface also passes through the pole of the logarithmic helix. Since the position of the block contact surface is determined, the length d_i of each block contact surface can be obtained according to the geometric relationship. If the polar angle of the landslide is divided into n parts, n block contact surfaces would be formed between the adjacent velocity v_i. Thus, the energy dissipation due to inner friction is the sum of energy consumption among the contact surfaces:

$$P_c' = c \cos \varphi \sum_{i=1}^{n} v_i^{i+1} d_i \tag{4}$$

In the present work, the calculated safety factor tends to converge when the number of block contact surfaces is greater than 9. In following calculation, the number of block contact surfaces is 10.

3 Stability Analysis of Slopes During Pile Driving Considering Energy Dissipation Due to Deformation of Inner Friction

3.1 Rotational Failure Mechanism

As illustrated in Fig. 3, the sliding surface is a logarithmic spiral sliding surface that could be described as $r(\theta) = r_0 \exp[(\theta - \theta_B) \tan \varphi]$. H and α represent the slope height and the slope angle, respectively. S represents the distance between the pile
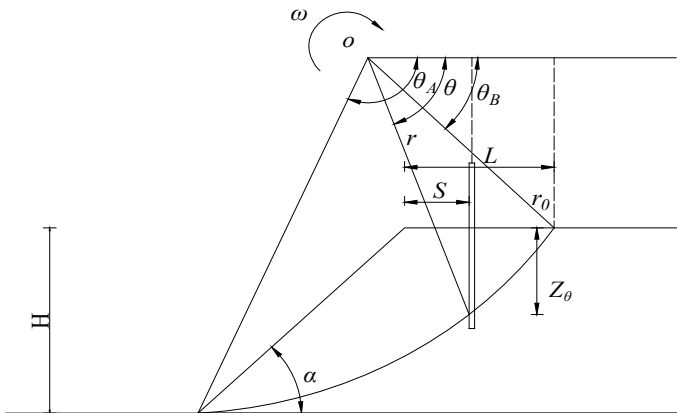
Fig. 3 Geometry of the pile driving force working

position and the slope shoulder. Z_θ represents the depth of the pile in the soil. ω represents angular velocity.

3.2 The Safety Factor

In this paper, the safety factor f_s is used to quantify the slope stability. f_s is defined as the ratio of the actual soil strength parameter to the minimum soil strength parameter required to maintain slope stability. The expression is:

$$f_s = \frac{c}{c_m} = \frac{\tan \varphi}{\tan \varphi_m} \tag{5}$$

where c_m and φ_m are the reduced parameters, respectively.

3.3 Internal Power and External Power

According to the principle of upper bound limit analysis method, the external work rate is equal to the energy dissipation rate of the slope when the slope is in the limit state.

$$P_w + P_T = P_c + P_c' \tag{6}$$

For the slope subjected to pile driving, the external work rate includes landslide weight rate P_w and the pile driving force rate P_T, while the energy dissipation rate includes the sliding surface dissipation rate P_c and the internal friction deformation energy consumption P_c'. The expressions for P_w and P_c presented by Chen [8] were adopted herewith. The calculation method of internal friction energy dissipation is described in Sect. 2.

The pile resistance R is calculated as follows [12]:

$$R = R_s + R_p = (0.5 + \frac{z}{100})P_s d + 2(0.025p_S + 25)\frac{z}{S_t} \tag{7}$$

where R_s is pile tip resistance, $R_p = \left(0.5 + \frac{z}{100}\right)P_s d$. R_p is pile side resistance $R_s = 2(0.025p_S + 25)\frac{z}{S_t}$. S_t and P_s represents the sensitivity of soil and penetration resistance, respectively.

The impact coefficient of pile area used as the reduction parameter is expressed as follows:

$$\eta = \frac{\pi d}{4t} \tag{8}$$

The equivalent pile tip resistance and equivalent pile side resistance, respectively, are expressed as:

$$R_p^{'} = \eta R_p \tag{9}$$

$$R_s^{'} = \eta R_s \tag{10}$$

Before the pile passes through the sliding surface, the expression of the pile driving force power P_T is:

$$P_T = \Omega \eta R(z) r \cos \theta \tag{12}$$

After the pile passes through the sliding surface, only the pile side resistance within the failure surface depth works. The pile driving force power is then expressed as:

$$P_T^{'} = \Omega R_s^{'}(z_\theta) r \cos \theta \tag{13}$$

4 Stability Variation During Pile Driving

To investigate the performance of the proposed approach, case study with the model illustrated in Fig. 3 is carried out, where the parameters for the pile and soil properties are presented in Table 1.

Following the procedure as described in Sects. 2 and 3, the safety factor for the slope subjected to pile driving is calculated. The change of f_s with pile driving process is shown in Fig. 4.

In Fig. 4, curve A is the safety factor curve considering inner energy consumption and its mean curve C has a value of 1.54, while curve B is the safety factor curve without accounting for the effect of inner energy consumption and its mean curve D has a value of 1.38. It can be observed that the safety factor is

Table 1 Model parameters of soil and pile

Unit weight (γ)	Cohesion (c)	Internal friction angle (φ)	Sensitivity of soil (S_t)	Penetration resistance (P_s)
19 kN/m³	32 kPa	24°	2.0	1.2 Mpa
Slope height (H)	Pile diameter (d)	slope angle (α)	Pile spacing (t)	Shear strength of pile (c')
20 m	0.4 m	45°	2 m	4Mpa
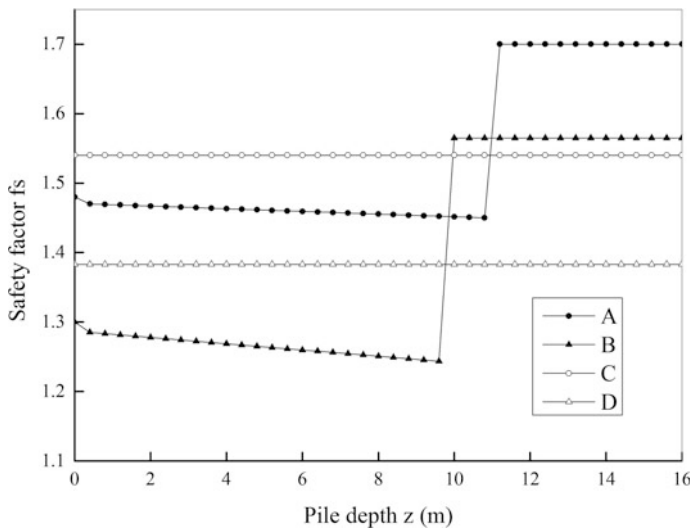
Fig. 4 Change of the safety factor of slope stability during pile driving

reduced suddenly when the pile body is jacked into the soil. Before the pile passes through the sliding surface, the safety factor decreases as the depth of pile jacked in the soil increases. After the pile passes through the sliding surface, the safety factor tends to rise dramatically, thereafter remaining stable subsequently at a relatively high level. It is worth noting that when considering the internal friction energy dissipation, the sliding surface depth at the pile sinking position is greater than that when the internal friction energy dissipation is not considered. After the pile passes through the sliding surface, the safety factor will increase rapidly due to the lack of work of pile tip resistance, leading the safety factor for curve A to be smaller than the safety factor for curve B when the pile depth is between 10 and 11 m.

In most existing limit analysis, the logarithmic spiral landslide body is often regarded as a rigid body, which ignores the inner friction deformation energy dissipation due to adaptive deformation during the land-sliding process. However, it can be observed in Fig. 4 that the energy dissipation due to the friction-induced deformation plays a significant role in the safety factor for the slope subjected to pile driving, which should be taken into account in the slope stability analysis.

5   Conclusions

Based on the upper bound limit analysis method, the slope stability during pile driving process is analyzed with consideration of effects of the internal friction deformation energy consumption taken into account. The safety factor is adopted to characterize the slope stability herewith. The results show that:

(1) The multi-block partitioning method is capable of quantifying the energy dissipation due to frictional deformation in the logarithmic spiral landslide.
(2) The energy dissipation due to the friction-induced deformation plays a significant role in the safety factor for the slope subjected to pile driving, which should be taken into account in the slope stability analysis.
(3) The results show that the slope safety factor with consideration of the energy dissipation due to inner friction-induced deformation is greater than its counterpart neglecting such effects. The energy dissipation contributes to improving the anti-slide capacity of slope.

References

1. Evans NC (1997) The natural terrain landslide study. Slope Eng Hong Kong
2. Zhao WJ, Yin ZQ, Xu Q, Qin XG (2016) Formation mechanisms and geomorphic evolution of the Erlian mudflow fans, eastern guide basin of the upper reaches of yellow river. Acta Geol Sin (Engl Ed)
3. Yang KJ (2004) Practical pile foundation engineering. China Communications Press, Beijing (in Chinese)
4. Yuan HP (2006) Study on the stability of wharf slope under pile driving conditions. HoHai University, Nanjing (in Chinese)
5. Xu Y, Sun ZH (2009) Reliability analysis on stability of wharf slopes during pile driving. Port Waterw Eng. (in Chinese)
6. Xu Y, Li TC, Mo JB (2010) Influence of excess pore water pressure induced by pile driving on stability of warf slopes. Rock Soil Mech. (in Chinese)
7. Sun ZB (2013) Upper bound analysis of slope stability and approaches to parameter back analysis. Central South University, Changsha (in Chinese)
8. Chen WF (1975) Limit analysis and soil plasticity. Elsevier
9. Li XP, He SM, Wang CH (2006) Stability analysis of slopes reinforced with piles using limit analysis method. Adv Earth Struct Res Pract
10. Ausilio E, Conte E, Dente G (2001) Stability analysis of slope reinforced with piles. Comput Geotech Elsevier
11. Xia YY, Chen CS (2017) Limit analysis of reinforced slopes with prestressed anchor cables considering energy dissipation due to deformation of inner friction. Chin J Geotech Eng. (in Chinese)
12. Fan XY (2007) Study of sinking-resistance and compaction effect of static-press pile. Tongji University, Shanghai (in Chinese)

Influencing Factors and Significant Analysis of Mechanical Properties of Silty Clay Subgrade in Seasonal Frozen Area

Hong-huan Cui, **Chen Xing**, **Wei-xing Cheng**, **Xin Yang** **and Wen-tao Wang**

Abstract To explore the influence of different factors on the mechanical properties of highway subgrade soil, taking the soil specimen of the highway roadbed in Zhangjiakou as a research object, the factors of freezing and thawing times, water content, compaction degree, and freezing negative temperature are investigated. Using an orthogonal test design, freeze–thaw, temperature monitoring, and static triaxial tests are conducted. Significance analysis of the orthogonal test results is applied to determine the effect of the interaction between the factors, both individually and in combination, on the static strength, internal friction angle, and cohesion of the soil. Test results show that (1) after freeze–thaw cycles, the factors that significant influence the soil strength, cohesion, and internal friction angle are water content, compaction degree, freeze–thaw cycles, and freezing negative temperature; (2) these factors affect the freezing and thawing rate of soil samples, which affects the change of soil mechanical properties; (3) for increasing freezing and thawing times, the soil strength decreases continuously, and the intensity decay trend is slow after the fifth freeze–thaw cycle.

Keywords Freeze–thaw cycles · Freeze–thaw rate · Interaction · Orthogonal test · Significance analysis

H. Cui (✉) · C. Xing · W. Cheng · X. Yang · W. Wang
Reconstruction and Anti-Disaster of Civil Engineering,
Hebei Key Laboratory for Diagnosis,
075000 Hebei Zhangjiakou, China
e-mail: Cuihonghuan729@163.com

H. Cui · C. Xing · W. Cheng · X. Yang · W. Wang
School of Civil Engineering, Hebei University of Architecture,
075000 Hebei Zhangjiakou, China

1   Introduction

In China, permafrost and seasonally frozen areas distribute widely; the frozen areas distribute mainly in the northern region of China [1]. With the demands of economic construction, national defense construction, resource development, and improvement of the living standards of rural residents, the frequency of production and living activities in these areas has been increasing. From previous engineering accidents, it has been found that only an in-depth understanding of the nature of the frozen area can reduce the economic losses caused by accidents.

After many years of exploration, experts and scholars at home and abroad have conducted a lot of research on the changes of soil static and dynamic strength, elastic modulus, soil quality, and compressive modulus after freezing and thawing cycles. Simonsen finds that the elastic modulus of soil is reduced after freeze–thaw cycles [2]. Based on freeze–thaw experiments on Jinzhou silty clay, Zhang Wenjiao concludes that the volume of Jinzhou silty clay increases after the freeze–thaw cycle, the cohesion decreases, and the internal friction angle first increases and then decreases [3]. Through a triaxial test of Qinghai–Tibet clay, Wang Dayan finds that the elastic modulus of Qinghai–Tibet clay first decreases and then increases after freeze–thaw cycles [4]. The strength of the sample decreases at first but increases after the tenth cycle, and the cohesion decreases gradually, while the angle of internal friction fluctuates between 15° and 30°. Through a triaxial test of saturating clay, Yu Linlin finds that the cohesion decreases after freezing and thawing and that the internal friction angle increases; the cohesion and internal friction angle gradually stabilize after 5–7 freeze–thaw cycles [5]. The lower the freezing temperature, the smaller the effect on both cohesion and internal friction angle. Wang Weina et al. use a load-bearing plate method to measure the rebound modulus of a roadbed and conclude that the rebound modulus of the subgrade soil decreases with an increase in freezing and thawing times and is basically stable after six freeze–thaw cycles [6]. Through a freeze–thaw cycle test on sandy clay and light sub-clay open systems, Yang Chengsong et al. find that during repeat freeze–thaw cycles, the soil dryness tends to a certain value [7]. Tan Yunzhi et al. study the effect of the freeze–thaw cycle on the strength of modified silt and conclude that the strength of modified silt decreases with increase in the number of freeze–thaw cycles; they observe stabilization after six freeze–thaw cycles [8]. Through the uniaxial compression tests conducted for silty clay freeze–thaw cycle of the Qinghai–Tibet Railway, Zhang Ying et al. find that the soil achieves dynamic stability after 30 freeze–thaw cycles [9]. Through a freeze–thaw cycle test for silty clay and loess, Qi Ji Lin et al. find that soil dry weight affects soil cohesion and early consolidation pressure, and that soil cohesion and early consolidation pressure of soil samples decreases after freeze–thaw cycles [10, 11]. Based on silty clay in the area of Tianjin and loess in the Lanzhou area, freeze–thaw cycles are simulated after remodeling and over consolidation, and it is concluded that the cohesion is decreased and the internal friction angle is increased. After freeze–thaw cycles, Ono et al. conducted a non-drainage shear test on normal consolidated remolded clay,

loose silty soil, low-density clay, and remolded clay and finds that shear strength increases [12–14]. Wang Xiaobin et al. conduct consolidated drainage shear tests on undisturbed soil and remolded clay, respectively, after a freeze–thaw cycle and demonstrated that the cohesive force decreases and the internal friction angle increases after freezing and thawing, and that freezing and thawing temperatures have little effect on soil strength [15]. Li Shunqun et al. study the influencing factors of the mechanical properties of frozen soils, with the main aim of investigating the interaction between factors and the significance of the various factors [16]. Their results show that temperature has the greatest influence on the mechanical properties of frozen soil, and that water content, salt content, and strain rate have different degrees of influence; moreover, an interaction effect between different influencing factors is found. Chang Dan et al. conducted a conventional triaxial shear test on the siltation of Qinghai–Tibet silt to study the effects of the freeze–thaw cycle on stress–strain curve, static strength, elastic modulus, and static strength [17]; finally, the significance of the effects of freeze–thaw cycles, freezing negative temperature, confining pressure, and factors on the mechanical effects of silt soil is determined.

In previous studies, the main focus is usually on damage strength, static strength parameters, elastic modulus, water migration, and stress–strain curves. In recent years, Li Shunqun and Chang Dan conducted a significance analysis of existing research results. In previous studies, the influencing factors investigated include confining pressure, freezing negative temperature, freezing and thawing times, water content, strain rate, and salt content; most of these studies used three factors in their significant analyses. In this study, the effects of freezing and thawing cycles on the static properties of silty clay are investigated. In the case of interaction, the influence of different factors is determined using an orthogonal test, and the factors influencing soil strength as well as the significant interaction factors are determined.

2 Test Content and Method

Following the *Test Methods for Soils Highway Engineering*, the basic soil parameters are determined experimentally; the maximum dry density is 1.98 g/cm³, and the optimum water content is 11.3%. According to the method specifications, a number of soil samples are prepared, with a height of 80 mm and a diameter of 39.1 mm. After each sample is prepared, it is frozen in a low-temperature box, at a temperature of between −10 and −5 °C, before melting at a melting temperature of 20 °C, with freezing and melting times of 12 h. To investigate the effects of freezing negative temperature, freeze–thaw cycles, water content, compaction degree, and confining pressure on the mechanical properties of soil, the specific test scheme shown in Table 1 is followed.

To investigate the effect of freezing negative temperature, freeze–thaw cycles, water content, compaction degree, and confining pressure on the mechanical properties of soil during freezing and thawing, an orthogonal experiment is carried

Table 1 Table of the freezing–thawing test

Test number	Compaction degree (%)	Water content (%)	Freezing negative temperature (°C)	Thawing temperature (°C)	Freeze–thaw cycles (n)
1	94	11	−5	20	0, 1, 5, 11
2	97				
3	94	13			
4	97				
5	94	11	−10	20	
6	97				
7	94	13			
8	97				

out to explore the interaction between the factors. Considering the interaction, using an L16 (4×2^{12}) orthogonal table, a table is designed as shown in Table 2. Table 3 is an orthogonal experimental design scheme of L16 (4×2^{12}). A denotes the number of freeze–thaw cycles, which is 0, 1, 5, or 11. B represents the degree of compaction, which is 97 or 94%. C represents the water content, which is 11 or 13%. D represents the freezing negative temperature, which is −10 or −5 °C.

3 Significance Analysis Principle

Factors affecting the mechanical properties of silty clay usually include water content, compaction degree, freezing negative temperature, and freeze–thaw cycles. In this study, these four aspects are subjected to significance analysis. Significance analysis is actually an analysis of variance; a single-factor test analyzes the changes in only one factor, while a multi-factor test analyzes the changes in a number of factors. The multi-factor analysis can be divided into repeated tests and multi-factor no-repeat tests. There are four factors in this analysis; multiple factors without repeated tests and the interaction between factors are considered.

Considering the interaction between the factors, the theoretical analysis of the four factors is as follows. First, the factors are numbered A, B, C, and D, where factor 1 has a levels, as A_1, A_2, …, A_a, factor 2 has b levels, as B_1, B_2, …, B_b, factor 3 has c levels, as C_1, C_2, …, C_c, and factor 4 has d levels for D_1, D_2, …, D_d. A test is conducted at each combination level (A_i, B_j, C_k, D_l); test results are labeled X_{ijkl}.

The calculation process is as follows:

The total sum of squares is:

$$S_T = \sum_{i=1}^{a} \sum_{j=1}^{b} \sum_{k=1}^{c} \sum_{l=1}^{d} X_{ijkl}^2 - \frac{T_{ijkl}^2}{abcd}$$

Table 2 Top-of-form design for considering the interactions between the four factors

Factor number	Test number												
	1	2	3	4	5	6	7	8	9	10	11	12	13
4	A	B	$(A \times B)_1$	$(A \times B)_2$	$(A \times B)_3$	C	$(A \times C)_1$	$(A \times C)_2$	$(A \times C)_3$	$B \times C$	D	–	–
	A	B	$C \times D$	–	–	C	$B \times D$	–	–	$(A \times D)_1$	D	$(A \times D)_3$	$(A \times D)_2$

Table 3 Orthogonal experiment design scheme A of L16 (4×2^{12})

Test number	A	B	(A × B)1	(A × B)2	(A × B)3	C	(A × C)1	(A × C)2	(A × C)3	B × C	D	空	空
	1	2	3	4	5	6	7	8	9	10	11	12	13
1	1(0)	1(94)	1	1	1	1(11)	1	1	1	1	1(−10)	1	1
2	1	1	1	1	1	2(13)	2	2	2	2	2(−5)	2	2
3	1	2(97)	2	2	2	1	1	1	1	2	2	2	2
4	1	2	2	2	2	2	2	2	2	1	1	1	1
5	2(1)	1	1	2	2	1	1	1	2	1	1	2	2
6	2	1	1	2	2	2	2	2	1	2	2	1	1
7	2	2	2	1	1	1	1	1	2	2	2	1	1
8	2	2	2	1	1	2	2	2	1	1	1	2	2
9	3(5)	1	2	1	2	1	1	1	2	1	2	1	2
10	3	1	2	1	2	2	2	2	1	2	1	2	1
11	3	2	1	2	1	1	1	1	2	2	1	2	1
12	3	2	1	2	1	2	2	2	1	1	2	1	2
13	4(11)	1	2	2	1	1	1	2	1	1	2	2	1
14	4	1	2	2	1	2	2	1	2	2	1	1	2
15	4	2	1	1	2	1	1	2	1	2	1	1	2
16	4	2	1	1	2	2	2	1	2	1	2	2	1

The variance squared sum of factor A is

$$S_A = \frac{1}{bcd} \sum_{i=1}^{a} T_1^2 - \frac{T_{ijkl}^2}{abcd}$$

The variance squared sum of factor B is

$$S_B = \frac{1}{acd} \sum_{j=1}^{b} T_2^2 - \frac{T_{ijkl}^2}{abcd}$$

The variance squared sum of factor C is

$$S_C = \frac{1}{abd} \sum_{k=1}^{c} T_3^2 - \frac{T_{ijkl}^2}{abcd}$$

The variance squared sum of factor D is

$$S_D = \frac{1}{abc} \sum_{l=1}^{d} T_4^2 - \frac{T_{ijkl}^2}{abcd}$$

where

$$T_{ijkl} = \sum_{i=1}^{a} \sum_{j=1}^{b} \sum_{k=1}^{c} \sum_{l=1}^{d} X_{ijkl}$$

$$T_1 = \sum_{j=1}^{b} \sum_{k=1}^{c} \sum_{l=1}^{d} X_{ijkl}$$

$$T_2 = \sum_{j=1}^{a} \sum_{k=1}^{c} \sum_{l=1}^{d} X_{ijkl}$$

$$T_3 = \sum_{i=1}^{a} \sum_{j=1}^{b} \sum_{l=1}^{d} X_{ijkl}$$

$$T_4 = \sum_{i=1}^{a} \sum_{j=1}^{b} \sum_{k=1}^{c} X_{ijkl}$$

Considering the interaction of the four factors, according to the different permutations and combinations, the interaction can be divided into six cases for $A \times B$, $A \times C$, $A \times D$, $B \times C$, $B \times D$, and $C \times D$, and the calculation process is as follows (each case follows the example given).

Table 4 Critical values $F_\alpha(f_1, f_\alpha)$ for F test

Significance level α	$F_\alpha(f_1, f_2)$		
	$f_1 = 1$ $f_2 = 2$	$f_1 = 1,$ $f_2 = 5$	$f_1 = 1,$ $f_2 = 8$
	$f_1 = 3,$ $f_2 = 2$	$f_1 = 3,$ $f_2 = 5$	$f_1 = 3,$ $f_2 = 8$
0.100	8.53/9.16	4.06/3.62	3.46/2.92
0.050	18.51/19.16	6.61/5.41	5.32/4.07
0.010	98.5/99.17	16.26/12.06	11.26/7.59
0.005	198.5/199.2	22.78/16.53	14.69/9.60
0.001	998.5/999.2	47.18/33.20	25.42/18.49

Considering the interaction, the sum of the squares of factors A and B is

$$S_{A \times B} = \frac{1}{cd} \sum_{i=1}^{a} \sum_{j=1}^{b} \left(\sum_{k=1}^{c} \sum_{l=1}^{d} X_{ijkl} \right)^2 - S_A - S_B + \frac{T_{ijkl}^2}{abcd}$$

The variance estimates for the various combinations of factors, and the different combinations of factors are calculated as (using the sum of the squares of factors A and B as an example):

$$F_A = (S_A/f_A)/(S_E/f_E)$$

$$F_{A \times B} = (S_{A \times B}/f_{A \times B})/(S_E/f_E)$$

where f_A, $f_{A \times B}$, and f_E are, respectively, the degrees of freedom of factor A, factor $A \times B$, and the error.

At different levels of significance, α, when $F_A \geq F_\alpha(f_1, f_\alpha)$ (using the F distribution table shown in Table 4), indicating that the impact of factor A on the test is significant, and vice versa; the other factor is not significant; the same reasoning can be applied to other factors to determine the significance of the different characteristics. According to the test, the hypothesis value can be divided into six significance levels: $\alpha < 0.001$, defined as level 1; $0.001 \leq \alpha < 0.005$, defined as level 2; $0.005 \leq \alpha < 0.01$, defined as level 3; $0.01 \leq \alpha < 0.05$, defined as level 4; $0.05 \leq \alpha < 0.1$, defined as level 5; and $\alpha \geq 0.1$, defined as level 6.

4   Analysis of Test Results

The silty clay samples, with the different values of water content, compaction degree, freezing negative temperature, and freezing and thawing times, are shown in Table 1, as well as a control sample, and are subjected to freeze–thaw tests. After the end of the test, according to the methods described in *Highway Geotechnical*

Test Procedures, a static triaxial test is conducted. The test strain rate is set to 0.8 mm/min, and the peak strain is 15%, which is the specimen failure strain. The test results are shown in Table 5.

4.1 Analysis of Static Intensity of Soil

After the orthogonal analysis, the values of soil strength, internal friction angle, and soil cohesion under different working conditions are collated in an orthogonal table. The static soil strength is analyzed statistically for variations in freezing and thawing times, moisture content, compaction degree, and freezing negative temperature. The results are shown in Tables 6 and 7.

Through the analysis of Tables 6 and 7, it can be found that the effect of each factor on the static strength of the soil is $B > C > B \times C > A > A \times D > A \times C > B \times D > D > A \times B > C \times D$, for a confining pressure of 20 kPa, considering the interaction between the factors, that is, compaction degree > water content > interaction of water content and compaction degree > freezing and thawing times > freezing negative temperature > interactions between water content and freezing negative temperature > interaction between freezing and thawing times and water content > interaction between compaction degree and freezing negative temperature effect.

Table 5 Orthogonal experimental results of the triaxial test

Test number	Static strength ($\sigma_3 = 20$ kPa)	Static strength ($\sigma_3 = 100$ kPa)	Static strength ($\sigma_3 = 180$ kPa)	Cohesion (kPa)	Internal friction angle (°)
1	436.4	604.7	774.8	111.55	30.93
2	472.0	619.6	746.7	134.97	27.49
3	703.4	872.4	1027.2	192.04	30.19
4	385.4	535.6	668.6	106.95	27.99
5	391.0	569.9	741.7	97.83	31.52
6	393.1	548.2	691.1	106.4	28.82
7	625.2	806.3	952.2	167.01	30.36
8	331.8	482.4	621.3	89.38	28.35
9	512.6	718.0	929.4	120.75	33.76
10	305.1	469.8	616.5	79.35	29.54
11	333.8	530.1	690.5	84.05	31.76
12	359.1	517.3	672.8	93.22	29.67
13	501.0	698.0	901.0	120.01	33.85
14	300.8	462.1	611.8	77.49	29.52
15	324.4	522.6	683.7	81.26	31.88
16	350.4	515.9	666.4	91.56	29.80

Table 6 Significance test A of soil strength considering interactions

Source of variation	SS	Df	MS	F	Significance level
A	40836.29	3	13612.1	398.24	2
B	63491.4	1	63491.4	1857.53	1
AB	837.16	3	279.05	8.16	6
C	77715.5	1	77715.5	2273.67	1
AC	2898.62	3	966.21	28.27	4
BC	21017.75	1	21017.75	614.90	2
D	565.25	1	565.250	16.54	4
e	68.36	2	34.18	–	–
Total variation	207498.7	13	–	–	–

Table 7 Significance test B of soil strength considering interactions

Source of variation	SS	Df	MS	F	Significance level
A	40836.29	3	13612.1	60.94	1
B	63491.4	1	63491.4	284.23	1
CD	70.98	3	23.66	0.11	6
C	77715.5	1	77715.5	347.91	1
BD	2618.88	3	872.96	3.91	5
AD	21086.11	3	7028.70	31.47	2
D	565.25	1	565.25	2.53	6
e	1045.92	2	522.96	–	–
Total variation	208547.2	17	–	–	–

When the confining pressure is 20 kPa, the factors influencing soil strength are the interaction of water content, compaction degree, freezing and thawing times, moisture content and compaction degree, and the interaction between freezing temperature and freezing and thawing times. The effect of the combination of water content, the degree of compaction, freezing temperature, and the number of freeze–thaw cycles on the soil strength is calculated, as shown in Tables 8 and 9.

According to Tables 8 and 9, for B_1C_1, A_1D_1, the static strength of the soil has a maximum; here, the combination is no freeze–thaw times, a water content of 10%, a compaction degree of 97%, and freezing temperature of −10 °C. For B_2C_2 and A_4D_1, the static strength of the soil has a minimum value. Here, the combination is 11 freeze–thaw cycles, a water content of 12%, a compaction degree of 94%, and a

Table 8 Tie-in effect calculation of $B \times C$

$B \times C$	B_1	B_2
C_1	588.8	390.325
C_2	376.925	323.425

Table 9 Tie-in effect calculation of $A \times D$

$A \times D$	A_1	A_2	A_3	A_4
D_1	544.4	466.95	410.4	402.7
D_2	454.2	388.4	350.3	341.6

freezing negative temperature of −5 °C. The maximum value represents the static strength of the soil without freeze–thaw cycles, and the minimum represents the largest combination of all the factors.

Similarly, according to the data given in Table 5, it can be calculated that when the confining pressure is 100 kPa, the influence of the static strength on the soil is: $B > C > B \times C > A > A \times D > A \times C > D > A \times B > B \times D > C \times D$. When the confining pressure is 180 kPa, the influence of the static strength on the soil is: $B > C > B \times C > A > A \times D > A \times B > A \times C > B \times D > D > C \times D$.

As can be seen from Table 4, when the critical value is less than F0.010, the value for F0.005 is significantly smaller than that for F0.010, so it can be assumed that the critical value is less than F0.01 when the impact is not significant. After analyzing the influence of the static strength values on the three kinds of confining pressure, the factors influencing the strength value are determined to be the interaction between water content and compaction degree and numbers of freeze–thaw cycles.

4.2 Effect of Freezing and Thawing Rate on Soil Strength

Considering such factors as water content, compaction degree, environmental temperature, and freezing and thawing times, the silty clay samples are subjected to freeze–thaw experiments. The internal temperature of the specimen is measured under different working conditions: freezing time, freezing temperature, cold duration, and time to reach the ambient temperature, that is, the negative temperature stability. The results are shown in Table 10.

After the orthogonal test is completed, the data for the different working conditions is combined into the orthogonal table. The freezing and melting rates of the soil samples are analyzed for variations in freezing and thawing times, moisture content, compaction degree, and freezing temperature. The results are as follows:

(1) During the freezing process, the degree of influence on the freezing rate is in the order of environmental temperature > compaction degree > water content > interaction between compaction degree and water content.

(2) During the freezing process, the degree of influence on the degree of freezing temperature is (from large to small) in the order of environmental temperature > compaction degree > water content > interaction between the degree of compaction and water content.

Table 10 Orthogonal experimental results of temperature test

Test number	Freeze 0 °C (min)	Supercooled start (min)	Supercooled temperature (°C)	Duration (min)	Negative temperature stability (min)
1	63	126	−3.7	24	314
2	40	60	−3.7	7	286
3	58	74	−3.7	16	412
4	78	152	−3.7	38	490
5	69	126	−3.7	37	404
6	43	58	−3.7	9	289
7	67	78	−3.7	20	372
8	71	151	−3.7	44	521
9	46	78	−3.7	6	305
10	72	133	−3.7	29	421
11	82	153	−3.7	28	505
12	56	71	−3.7	17	430
13	44	62	−3.7	8	261
14	68	122	−3.7	35	383
15	81	157	−3.7	33	470
16	47	73	−3.7	23	391

(3) The freezing temperature is unchanged under different working conditions, indicating that the freeze–thaw cycles only changes the mechanical properties of the soil without changing the physical properties of the soil [18, 19].

In the analysis of the influence of freeze–thaw cycle on soil strength, the results obtained for the combination of freezing rate and soil strength show that the factors influencing the strength of the soil are compaction degree, water content, compaction degree, and water content interaction. Therefore, it is considered that different factors affect the freezing and thawing rate of soil, which affect the strength of soil.

5 Conclusion

Experiments show that soil strength, cohesion, and internal friction angle decrease with increasing numbers of freeze–thaw cycles. After a slow decline, the soil properties stabilize after the fifth freeze–thaw cycle. The orthogonal test and significance analysis demonstrate that the factors that influence the strength of the soil are compaction degree, water content, interaction between compaction degree and water content, and the number of freeze–thaw cycles.

During the experiments, the internal temperature of the specimen is monitored periodically. The results show that such factors as compaction degree, water content,

and freezing temperature change the freezing rate of the specimen, and the freezing and thawing rate affect soil strength. The effect of freezing and thawing factors on soil strength is explained by the change of freezing rate.

References

1. Xu XZ, Wang JC, Zhang LX (2001) Frozen soil physics. Science Press, Beijing, p 11
2. Simonsen E, Janoo VC, Isacsson U (2002) Resilient properties of unbound road materials during seasonal frost condition. J Cold RegNs Eng 16(1):28–50
3. Zhang WJ, Wang ZQ, Song BY (2014) Effect of freeze-thaw cycling on the engineering properties of silty clay. Railw Constr 7(36):121–123
4. Wang DA, Chang XX, Sun ZZ, Feng WJ, Zhang JW (2005) Physico-mechanical properties changes of qinghai-tibet clay due to cyclic freezing and thawing. Chin J Rock Mechan Eng 24(23):4313–4319
5. Yu LL, Xu XZ, Qin MG, Li PF, Yan ZL (2010) Influnce of freeze-thaw on shear strength properties of saturated silty clay. Rock Soil Mech 31(8):2448–2452
6. Wang WN, Zhi XY, Mao XS, Hou ZJ, Lei MX (2010) Experimental study of resilience modulus of subgrade soil under circles of freezing and thawing. J Glaciol Geocryol 32(5):954–959
7. Yang CS, He P, Cheng GD, Zhu YL, Zhao SP (2008) Testing study on influence of freezing and thawing on dry density and water contest of soil. Chin J Rock Mech Eng 22(Z2):2695–2699
8. Tan YZ, Wu P, Fu W, Wan Z, Zhang H, Zhang ZH (2013) Strengh and micromechanism of improved silt under freeze-thaw cycle effect. Rock Soil Mech 34(10):2827–2834
9. Zhang Y, Bing H, Yang CS (2015) Influences of freeze-thaw cycles on mechanical properties of silty clay based on sem and mip test. Chin J Rock Mechan Eng 34(Z1):3597–3603
10. Qi JL, Ma W, Song CX (2008) Influence of ferrze-thaw on engineering properties of a silty soil. Cold Reg Sci Technol 53(3):397–404
11. Qi JL, Ma W (2006) Influence of freezing-thawing on strength of over consolidated soils. Chin J Geotech Eng 28(12):2082–2086
12. Ono T, Mitachi T (1997) Computer controlled triaxial freeze-thaw-shear apparatus. In: Proceeding 8th International Symposium on Ground Freezing. A A Balkema, Rotterdam, pp 335–339
13. Alkire BD, Morrison JM (1983) Change in soil structure due to freeze-thaw and repeated loading. Transp Res Rec 918:15–21
14. Ogata N, Kataoka T, Komiya A (1985) Effect of freezing-thawing on the mechanical properties of soil. Proceeding 4th international symposium on ground freezing. A A Balkema, Rotterdam, pp 201–207
15. Wang XB, Yang P, Wang HB, Dai HM (2009) Experimental study on effects of freezing and thawing on mechanical properties of clay. Chin J Geotech Eng 31(11):1768–1772
16. Li SQ, Gao LX, Chai SX (2012) Significance and interaction of factors on mechanical properties of frozen soil. Rock Soil Mech 33(4):1173–1177

17. Chang D, Liu JK, Li X, Yu QM (2014) Experiment study of effects of freezing-thawing cycles on mechanical properties of qinghai-tibet silty sand. Chin J Rock Mechan Eng 33(7): 1496–1502
18. Zhou JZ, Tan L, Wei CF, Wei HZ (2015) Experimental research on freezing temperature and super-cooling temperature of soil. Rock Soil Mech 36(3):777–785
19. Ma W, Wang DY (2014) Frozen soil mechanics. Science Press, Beijing, p 7

Study on a Method of Horizontal Bearing Capacity of Anti-slide Pile Based on "C" Method

Liqun Zhang and Jingyu Hu

Abstract The foundation coefficient method is generally safe because of its clear concept and simple method. Therefore, it is more common at home and abroad to use this method to calculate the horizontal bearing capacity of anti-slide piles. This paper focuses on the surface weathered foundation and uses the ground coefficient method "c" method as the background. By changing the "c" method, a new algorithm for the horizontal bearing capacity of anti-slide piles is deduced, and an engineering example is analyzed. Using MATLAB to analyze and calculate, through comparison of different calculation methods, it was finally verified that the calculation method of the horizontal bearing capacity of the anti-slide pile is closer to the actual test data than the classical method, which provides a feasible method for the calculation of the horizontal bearing capacity of the anti-slide pile in the future.

Keywords Lateral bearing capacity · Anti-slide pile · MATLAB

1 Introduction

In recent years, with the continuous development of science, large-scale engineering and railway bridges span increasing, the load acting on the pile foundation is more and more big. It is far from satisfying the needs of today's development to adopt the pile with low cross section and side bearing capacity. Through decades of development, the analysis of pile under lateral load, at present, the foundation coefficient method is mostly adopted. The foundation coefficient method considers that the size of soil resistance of pile side is not only related to the type of soil but also related to the lateral displacement caused by lateral force or torque. For soil resistance of pile side, at present, people use Winkler's elastic foundation beam

L. Zhang · J. Hu (✉)
HeBei University of Architecture, 075000 Zhangjiakou, China
e-mail: 296728518@qq.com

theory [1]. For pile side soil resistance of the foundation coefficient, Chinese scholars Zhang Youling assume that depth of pile lateral soil foundation coefficient is a constant, but it turns out that only preconsolidation clay can approximate this assumption; Some Soviet scholars believed that the foundation coefficient increased along the depth. There are also domestic scholars who believe that it is along parabolic growth [2]. It is proved that different methods have their own applicability and deficiency, and the research on theory is still being explored.

Anti-slide pile is a kind of pile which is subjected to transverse load, it is widely used in practice, in the calculation of the foundation resistance, the variation of the foundation coefficient along the depth varies, and the ground foundation coefficient can be divided into "k" method, "m" method, and "c" method; When the local base coefficient is a convex parabola, the proportional coefficient of the ground coefficient with depth changes is denoted by c, which is called "c" method [3].

For traditional "k" method, "m" method and "c" method are both steep and sometimes not suitable for the actual situation [4]; the method of this paper is based on the derivation of traditional "c" method, and the foundation coefficient is smoother than the traditional "c" method, which is more applicable to the actual situation.

2   New Method for Horizontal Bearing Capacity of Piles

Assume that the unit width of the pile wall is used as the elastic foundation beam placed vertically. The active earth pressure on the outside acts as the horizontal load applied to the pile. Vertical elastic piles are subjected to lateral loads at the ground (horizontal force H_0 and bending moment M_0), selecting coordinate origin and the direction of the coordinate axis, take the microsegment d_x on the pile, and through analysis, guided differential equations:

$$\mathrm{EI}\frac{\mathrm{d}^4y}{\mathrm{d}x^4} + b_0 p(x, y) = 0$$
$$p(x, y) = ax^{0.25}y \tag{1}$$

In the formula,

$p(x, y)$ The resistance of pile side soil on unit area;
y horizontal displacement;
x depth below the ground;
b_0 The calculated width of the pile;

b_0 is calculated width of the pile, If the round pile diameter d or rectangular pile width b is equal to or greater than 1 m:

$$\text{Rectangular pile:} \, b_0 = b + 1$$

$$\text{Round pile:} \, b_0 = 0.9(d + 1)$$

If the round pile diameter d or rectangular pile width b is less than 1 m:

$$\text{Rectangular pile:} \, b_0 = 1.5b + 0.5$$

$$\text{Round pile:} \, b_0 = 0.9(1.5d + 0.5)$$

For the "k" method, the "m" method, the "c" method, and the methods in this paper, the law of the depth coefficient at depth x with depth can be represented by such a formula: $C_x = mx^n$, the law of the change of the ground coefficient with depth for various methods [5] is shown in (Fig. 1).

Let the solution of the differential equation be:

$$y = f(x) \tag{2}$$

Expand the above formula into a McLaughlin series:

$$
\begin{aligned}
y = f(x) = f(0) &+ \frac{f'(0)}{1!}x + \frac{f''(0)}{2!}x^2 + \frac{f'''(x)}{3!}x^3 \\
&+ \frac{f^{(4)}(x)}{4!}x^4 + \cdots + \frac{f^{(r)}(0)}{r!}x^r + \cdots
\end{aligned}
\tag{3}
$$

| n=0 | n=1 | n=1/2 | n=1/4 |
| k method | m method | c method | The method of this article |

X
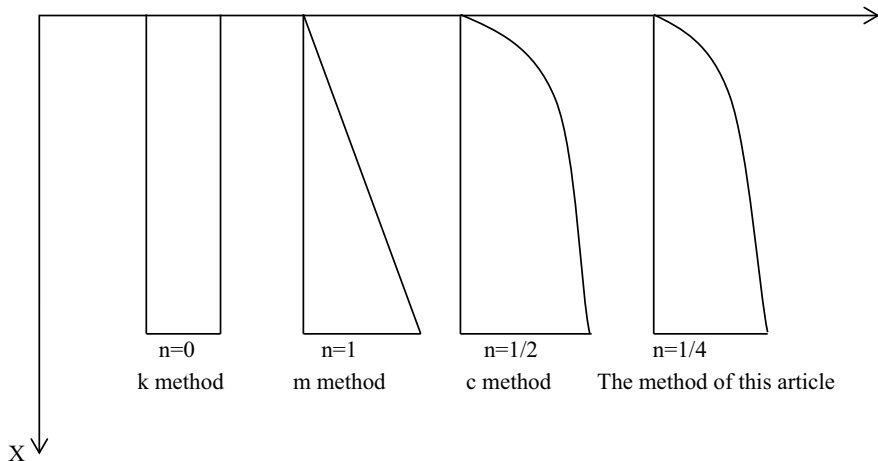
Fig. 1 Comparison of ground coefficient of various methods

Known from the material mechanics:

$$f'(x) = \frac{dy}{dx} = \varphi_x$$
$$f''(x) = \frac{d^2y}{dx^2} = \frac{M_x}{EI}$$
$$f'''(x) = \frac{d^3y}{dx^3} = \frac{Q_x}{EI}$$
$$f^{(4)}(x) = \frac{d^4y}{dx^4} = \frac{q_x}{EI}$$

(4)

So,

$$f'(0) = \frac{dy}{dx}\bigg|_{x=0} = \varphi_0 \quad f''(0) = \frac{d^2y}{dx^2}\bigg|_{x=0} = \frac{M_0}{EI}$$
$$f'''(0) = \frac{d^3y}{dx^3}\bigg|_{x=0} = \frac{Q_0}{EI} \quad f^{(4)}(0) = \frac{d^4y}{dx^4}\bigg|_{x=0} = \frac{q_0}{EI}$$

(5)

Substituting the Formulas (5) into (3), the displacement y, shear force Q, the direction of the foundation reaction force is positive with the positive direction of the y-axis; when the right side of the pile is pulled, M is positive, otherwise is negative; counterclockwise φ_0 is negative, and clockwise is positive. Get the solution at depth x and further derivation:

Lateral displacement:

$$y = y_0 A_1 + \frac{\varphi_0}{\alpha} B_1 + \frac{M_0}{\alpha^2 EI} C_1 + \frac{Q_0}{\alpha^3 EI} D_1$$

(6)

Pile side stress:

$$\sigma_z = mxy$$
$$= mx\left(y_0 A_1 + \frac{\varphi_0}{\alpha} B_1 + \frac{M_0}{\alpha^2 EI} C_1 + \frac{Q_0}{\alpha^3 EI} D_1\right)$$

(7)

Corner:

$$\varphi = \alpha y_0 A_2 + \varphi_0 B_2 + \frac{M_0}{\alpha EI} C_2 + \frac{Q_0}{\alpha^2 EI} D_2$$

(8)

Bending moment:

$$M = \alpha^2 EI\left(y_0 A_3 + \frac{\varphi_0}{\alpha} B_3 + \frac{M_0}{\alpha^2 EI} C_3 + \frac{Q_0}{\alpha^3 EI} D_3\right)$$

(9)

Among them $\alpha = \sqrt[4.25]{\frac{ab_0}{EI}}$, y_0, φ_0, M_0, Q_0 are the displacements, corners, bending moments, and shear forces, respectively, at the pile surface, coefficient $A_1, B_1 \ldots C_4, D_4$ is a function about αx, through the lookup table can be determined; with these parameters, some characteristics of the pile can be found [6].

Among them,

$$A_1 = 1 - \frac{0.25!}{4.25!}(\alpha x)^{4.25} + \frac{4.5!0.25!}{8.5!4.25!}(\alpha x)^{8.5} - \frac{8.75!4.5!0.25!}{12.75!8.5!4.25!}(\alpha x)^{12.75} \ldots$$

$$B_1 = \alpha x - \frac{1.25!}{5.25!}(\alpha x)^{5.25} + \frac{5.5!1.25!}{9.5!5.25!}(\alpha x)^{9.5} - \frac{9.75!5.5!1.25!}{13.75!9.5!5.25!}(\alpha x)^{13.75} \ldots$$

$$C_1 = \frac{1}{2}\left[(\alpha x)^2 - \frac{2.25!}{6.25!}(\alpha x)^{6.25} + \frac{6.5!2.25!}{10.5!6.25!}(\alpha x)^{10.5} - \frac{10.75!6.5!2.25!}{14.75!10.5!6.25!}(\alpha x)^{14.75} \ldots\right]$$

$$D_1 = \frac{1}{6}\left[(\alpha x)^3 - \frac{3.25!}{7.25!}(\alpha x)^{7.25} + \frac{7.5!3.25!}{11.5!7.25!}(\alpha x)^{11.5} - \frac{11.75!7.5!3.25!}{15.75!11.5!7.25!}(\alpha x)^{15.75} \ldots\right]$$

$$(10)$$

As for A_2, B_2, C_2, and D_2, respectively, the above A_1, B_1, C_1, and D_1 are derived from x and divided by. The same arguments for A_3, B_3 to C_4, and D_4 are also the same reason for derivation.

3   Case Analysis

For a strong weathered foundation in the north, due to engineering needs, anti-sliding piles shall be installed, in which the total length of the pile is 26 m, the suspended ground is 10 m, the length of the pile body embedded in the soil is 16 m, and the width of the positive section of the anti-slide pile is 1 m. The height of the pile section is 2 m. The parameters of the soil and cantilever piles are shown in Table 1. According to the test pile data, the surface displacement is 10 mm when the pile top acts at 40kN.

Table 1 Basic parameters

Model material	Density/ kg m^{-3}	Elastic modulus/MPa	Cohesion/ KPa	Internal friction angle/(°)	Poisson's ratio
Anti-slide pile	2500	11,000	—	—	0.25
Soil	1800	21	25	25	0.3

3.1 Determination of Foundation Coefficient

For the ground coefficient mentioned in this article's method $\alpha = \sqrt[4.25]{\frac{ab_0}{EI}}$, according to the test pile data, the load at the surface displacement of 10 mm is 40 kN; when the load is 40 kN, the ground coefficient is continuously assumed, according to Formula (6) and formulas for solving y_0 and φ_0; until the calculated $y_0 = 10$ mm, the foundation coefficient at this time is required foundation coefficient [6].

According to the above ideas, the MATLAB program was written; when other initial values are determined, different values α are input, different values y_0 are output correspondingly, and continuous attempts are made. The results are shown in Table 2.

Table 2 shows, when α is gradually increased, the value of y_0 is gradually decreasing; when the value α is 0.14, the value y_0 is connected to 10 mm, and it is consistent with the assumption of the assumed foundation coefficient; in this numerical simulation, the foundation coefficient is determined to be 0.14.

3.2 Pile Displacement Results

For the pile bottom displacement, the load is 40 kN, the pile bottom displacement is determined according to Formula (6), and the solution of other parameters is determined according to the programmed MATLAB program, as shown in Table 3.

The displacement of pile is calculated according to the Formula (6) and MATLAB, and then, the displacement value of pile under 40 kN load is calculated, see Table 4.

According to the table data, the calculated theoretical values are plotted. The results are shown in Fig. 2.

Table 2 Determination of value α

α	αh	y_0 (mm)
0.10	1.6	37.5
0.11	1.76	25.4
0.12	1.92	17.9
0.13	2.08	13.1
0.14	2.24	9.9

Table 3 The value of each parameter of pile bottom displacement

A_1	B_1	C_1	D_1	A_2	B_2	C_2	D_2	A_3	B_3
0.218	1.821	2.339	1.816	−1.464	0.023	1.768	2.325	−2.047	−1.827

C_3	D_3	A_4	B_4	C_4	D_4	Q_0	M_0	y_0	y
−0.099	1.729	−1.800	−2.551	−2.053	−0.190	4×10^4	4×10^5	9.9	−4.8

Table 4 Displacement values for different pile lengths

Pile length (m)	0	1	2	3	4	5	6	7	8
Displacement (mm)	9.9	8.6	7.4	6.3	5.2	4.1	3.2	2.3	1.4
Pile length (m)	9	10	11	12	13	14	15	16	
Displacement (mm)	0.55	−0.24	−1.0	−1.8	−2.5	−3.2	−3.9	−4.8	

Fig. 2 Pile displacement figure
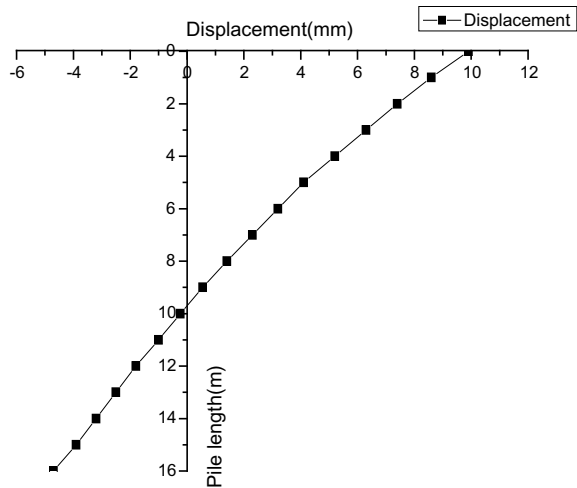
3.3 Comparison of Different Methods of Bending Moment Diagram

For the method in this paper, the pile bending moment is calculated when the load is 40 kN, the above foundation coefficient is substituted into (9), and the theoretical value is calculated according to the MATLAB procedure, as shown in Table 5.

Through the above table, the theoretical value of the bending moment of the pile when the load is 40 KN is made, and then, it is compared with the "m" method, the "c" method, measured bending moments, and methods in this article [7, 8] Fig. 3 shows.

4 Numerical Simulation

4.1 Model Establishment

The numerical simulation is based on the anti-slide pile test. Through the study of the local elastic foundation beam, the numerical simulation is used to establish the

Table 5 The bending moment of different pile lengths

Pile length (m)	0	1	2	3	4	5	6	7	8
Bending moment (kN m)	400	434.21	453.86	458.35	448.62	426.24	393.14	351.46	303.43
Pile length (m)	9	10	11	12	13	14	15	16	
Bending moment (kN m)	251.37	197.65	144.68	94.90	50.78	14.88	−10.23	−21.87	

Fig. 3 Comparison of bending moment diagrams of various methods
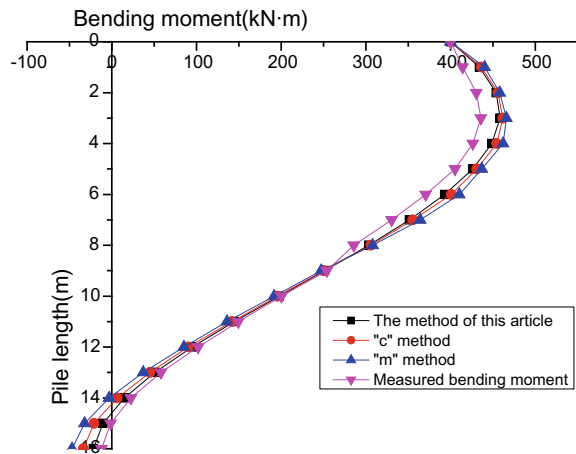
finite difference numerical model of the anti-slide pile and carry out numerical simulation. This time value model consists of soil and anti-slide piles. The value of the boundary range has a great influence on the numerical simulation results. Therefore, the large range of the model before and after the anti-slide pile is taken to reduce the influence of the boundary effect on the calculation results.

There are two calculation methods for the establishment of the anti-slide pile solid model: one is to use a large finite element software that is convenient for solid modeling to build a solid model and then import it into FLAC3D; the other is to use the Fish language in FLAC3D software to program the model. Enter the anti-slide pile information to form a solid model. This article uses the second method. Therefore, the model established by FLAC3D is shown in Fig. 4.

Fig. 4 Building a model
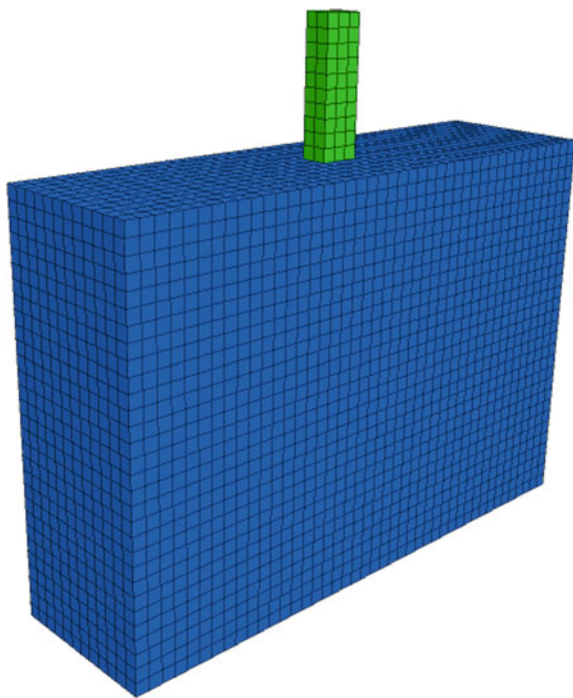
4.2   Model Parameter Selection and Boundary Conditions

In the design process, two different calculation models are adopted for the soil and anti-slide piles. The Mohr–Coulomb model is adopted for the soil, and the anti-slide pile takes into account the characteristics of the pile itself, so the full elastic model is adopted. Different parameters are used according to different calculation models; among them, BULK (elastic modulus), COHESION (cohesion), FRICTION (internal friction angle) of the input material in the Mohr–Coulomb model; and required in the full elastic model Enter the material's BULK (bulk modulus) and so on.

After determining the parameters, it is also necessary to determine the contact mechanics parameters of the anti-slide pile body and the soil. Generally speaking, there are two types of such parameters: one is the tangential parameters of the pile body, and the other is the normal parameters of the pile body; these parameters are generally obtained through experiments in practice; however, they cannot be obtained or obtained in the field. In case of difficulty, it can also be obtained according to certain rules. It is assumed that the damage between the piles occurs inside the soil, and the parameters of the pile body and the parameters of the pile-soil contact can be set sufficiently large; this makes the result more accurate.

This simulation uses a symmetrical boundary. The model mainly receives the lateral load of the pile top and the effect of gravity. The lateral load of the pile top is the surface load acting on the cantilever pile.

4.3 Model Results Analysis

When the pile top adopts different lateral loads, the variation law of the bending moment and lateral displacement of the pile body is monitored by FLAC3D software. In this simulation, the lateral loads of the pile top were taken in seven different cases of 40, 50, 60, 70, 80, 90, and 100 kN, and the seven cases were numerically simulated and studied.

Figure 5 shows the relationship between the bending moment of the pile body when the pile top is used with different loads. It can be seen from the figure that the bending moment of the pile body generally shows a trend of changing first and then becoming smaller, wherein the maximum bending moment is obtained at about 4 m below the ground; As a whole, the larger the load, the greater the bending moment of the body also shows an increasing trend

Figures 6 and 7 show the comparison of theoretical values and numerical simulations of pile bottom and pile surface displacement when different pile loads are used. It can be seen from the figure that with the increase of pile top load, pile bottom, pile surface, and pile top, the lateral displacement has increased, and the displacement also shows an increasing trend as the load increases.
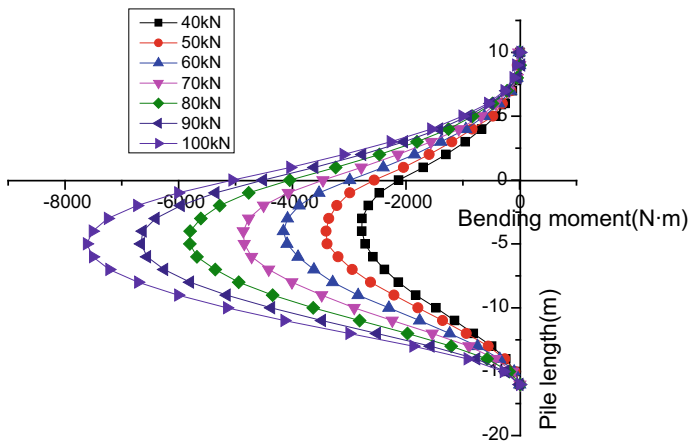
Fig. 5 Moment diagrams under different loads

Fig. 6 Comparison of theoretical and numerical simulation values of pile bottom displacement under different loads
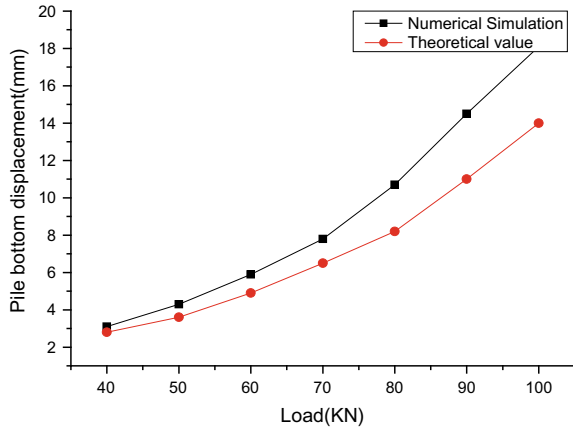
Fig. 7 Comparison of theoretical and numerical simulation values of pile surface displacement under different loads
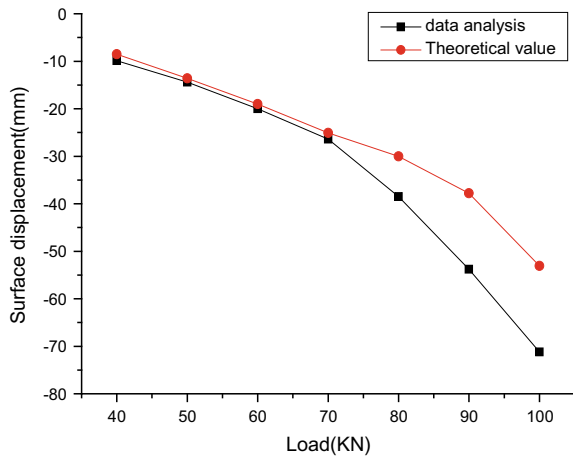
5   Conclusions

In this paper, by introducing the basic theory of elastic foundation beam, a method of lateral bearing capacity of pile is deduced. In the case analysis, the examples are calculated and analyzed by MATLAB programming. Through this study, the following conclusions have been drawn:

(1) It can be seen from the displacement diagram of the pile body that when the top of the anti-sliding pile is loaded, the displacement of the pile body is gradually reduced below the ground; finally, at the bottom of the pile, the displacement and the displacement at the ground are reversed.

(2) It can be seen from the results of numerical simulation that when the top of the anti-slide pile is subjected to different loads, the bending moment of the whole pile body tends to increase first and then decrease, and the maximum bending is obtained approximately 4–5 m below the ground. Moment; as the pile top load increases, the bending moment also tends to increase.

(3) It can be seen from the bending moment diagram that when the load is applied to the top of the anti-sliding pile, the bending moment of the whole pile generally shows a trend of increasing first and then decreasing, and the maximum bending moment is approximately 2–3 m below the surface.

(4) By comparing the bending moment diagrams of different methods, we can see that the measured bending moment is smaller than method of this article, "c" method and "m" method in the range of approximately 9 m below the ground, but more than nine meters is bigger than the other three; for the methods of this paper, the "c method" and the "m" method, the method of this paper should be closer to the measured bending moment.

(5) Through the above research, the method deduced in this paper is closer to the actual situation than the "c" method and the "m" method for the weathered foundation. For the weathered foundation, the method proposed in this paper has a certain reference.

References

1. Long Y (1981) Calculation of elastic foundation beams. People's Education Press, Beijing
2. Jilin Institute of Transportation Sciences (1979) Highway bridge bored Pile calculation manual. People's Communications Press
3. Chen L (2002) Analysis of lateral bearing capacity of elastic long Piles. Dalian University of Technology
4. Railway Third Survey and Design Institute (2005) Railway bridge culvert foundation and basic design specification. China Railway Publishing House
5. Bai X (2016) A modified analysis method for beam foundations on elastic foundation and finite element method analysis for layered soil. Hunan University
6. Hu R (1987) Analysis and design of bridge pile foundations. China Railway Publishing House
7. Song C, Xiong H (2007) Application of beam method with elastic foundation in the design of pile-anchor retaining structure. Railw Constr
8. Xuexiang Y, Yu Z (2010) Comparative analysis of the calculation of internal forces of retaining piles by beam method on elastic foundation and classical earth pressure method. Engineering

Numerical Investigation on Screening Surface Waves Using a Buried Trench with Plate

Jian-ping Li, Xiao-lei Zhang, Dong-mei Zhang and Shi-jin Feng

Abstract This article is aimed at studying the effectiveness of a buried trench with a plate in screening the ground vibrations. Influence of various geometrical parameters normalized by Rayleigh wavelength is investigated to identify key parameters of the buried trench. Three types of the buried barriers depending on the relative position between plate and trench are considered herein: (a) trench with source-oriented plate, (b) T-shape trench and (c) trench with receiver-oriented plate. Screening effectiveness of these cases is compared to that of the buried trench without a plate. Parameters study shows that adding a plate to buried trench has a considerable beneficial effect on screening vibrations, and some design considerations of the buried trench with the plate are made for enhancing the screening efficiency.

Keywords Vibration isolation · Buried trench · Wave barrier · Finite element

1 Introduction

Ground vibrations are generated by a variety of sources like industrial machinery, traffic and construction activities. Excessive vibrations may cause annoyance to residents, malfunction of sensitive equipment and even damage to structures.

J. Li · X. Zhang (✉) · D. Zhang · S. Feng
Department of Geotechnical Engineering, Tongji University, 200092 Shanghai, China
e-mail: xiaolei_zhang@tongji.edu.cn

J. Li
e-mail: 1610149@tongji.edu.cn

D. Zhang
e-mail: dmzhang@tongji.edu.cn

S. Feng
e-mail: fsjgly@tongji.edu.cn

X. Zhang · D. Zhang · S. Feng
Key Laboratory of Geotechnical and Underground Engineering of Ministry of Education,
200092 Shanghai, China

The most effective and direct measure to reduce vibration is setting an intervention at the source [1]. Taking measures in structures disturbed by vibration is another choice [2]. Placing a wave barrier in the ground between the vibration source and receiver is also a good alternative for vibration control.

Woods [3] conducted a series of field tests on vibration isolation of open trench and stated that the ratio of barrier depth to Rayleigh wavelength is the most relevant geometric parameter. However, a deep open trench in engineering practice is difficult to meet the requirements of stability in a long-term isolation process [4, 5], and therefore soft or stiff materials are filled into the trenches [6–9]. In general, the open trench is more effective than in-filled trench on screening surface waves as the fact is that the incident waves would transmit through the filled materials in addition to scattering (mode transform) and diffraction underneath the trench [6, 10].

The previous works primarily focused on unburied open or in-filled trenches except for Castanheira-Pinto [11], who numerically studied the screening efficiency of buried periodic inclusions, a discontinuous barrier. This paper aims to investigate numerically the potential use of buried trench in screening surface waves. Three cases depending on the relative position between plate and trench are considered and compared to the trench without a plate. A 2D finite element (FE) model is firstly created and verified by the previous literature. Then, a parametric study of the geometric effect on the screening effectiveness of buried trench is committed to investigating the influence of the plate. Finally, the extra contribution of the plate on screening effect is intuitively exhibited and some proposals are tabled to design a similarly buried trench with a plate.

2   Problem Definition and Modeling

2.1   Three Cases of Buried Trenches with Plate

Three cases depending on the relative position between the plate and buried trench are considered as shown in Fig. 1b–d: trench with a source-oriented plate (Case 2), T-shape trench (Case 3) and trench with a receiver-oriented plate (Case 4). For comparison, the buried trench without a plate is termed as Case 1 (Fig. 1a).

2.2   Degree of Isolation

The screening effectiveness of a barrier could be assessed in terms of amplitude reduction factor A_R defined as the ratio of maximum surface displacement amplitudes between with and without barrier [5].

The amplitude reduction factors over the range measurement s beyond the barrier were not uniform, so the average amplitude reduction factor $\overline{A}_R$ was used instead:
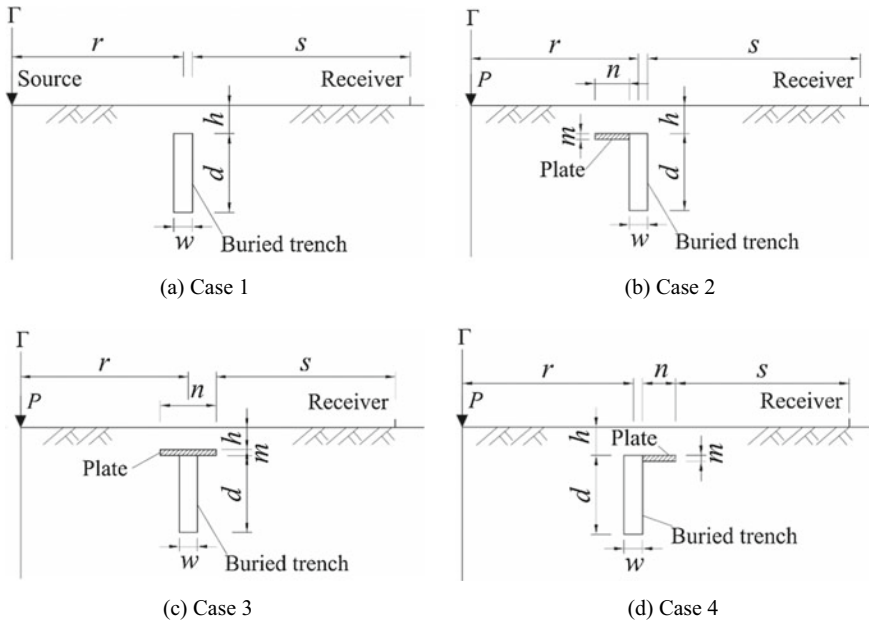
Fig. 1 Four schematics of different buried trenches: **a** buried trench without plate (Case 1); **b** trench with a source-oriented plate (Case 2); **c** T-shape trench (Case 3); and **d** trench with a receiver-oriented plate (case 4)

$$\overline{A}_R = \frac{1}{s} \int A_R(x) dx \tag{1}$$

Obviously, smaller values of A_R and $\overline{A}_R$ imply a better screening effect.

2.3 Finite Element Model and Validation

A 2D model is sufficient to predict the vibration isolation effect of the screen [12, 13] and takes advantage of much lower computing cost than a three-dimensional model; therefore, a 2D model (Fig. 2) with the dimension of length 60 m and depth 40 m is constructed in COMSOL Multiphysics for the current study. The foundation and screen are modeled as linear elastic, homogeneous and isotropic. Perfectly matched layer boundaries are applied to simulate the half-space. The elastic modulus E, Poisson's ratio v, density ρ and damping ratio ξ of the half-space are characterized as 46 MN/m^2, 0.25, 1890 kg/m^3 and 0.05, respectively. The plate is made of concrete, and the corresponding E, v, ρ, ξ are 25,500 MN/m^2, 0.2, 2500 kg/m^3 and 0.30, respectively.

Fig. 2 Typical model of problem
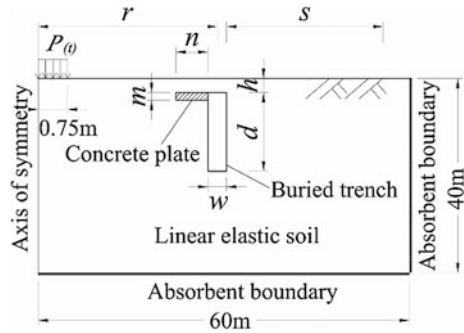
A unit harmonic load of magnitude $P = 1$ kN and frequency $f = 30$ Hz is applied at the footing with a width of 0.75 m (Fig. 2). The Rayleigh wavelength (L_R) is then calculated as 3.0 m. Therefore, the element size ξ is set as 0.3 m to meet the relationship of $\xi = L_R/k$, where k is a coefficient ranging from 4 to 10 [14]. The footing's mass is neglected as it plays an unimportant role in the screening effectiveness of barriers [15].

An isolation case of an open trench (depth $d = 1.0 \, L_R$ and width $w = 0.1 \, L_R$) in an elastic half-space located at a distance $r = 5 \, L_R$ from a rigid footing subjected to a vertical harmonic load was taken to validate the model. The values of A_R with respect to normalized distance from the source are shown in Fig. 3. As can be seen, the present results agree well with the previous work [6], demonstrating the correctness and feasibility of the proposed model.

3 Parametric Study of Buried Trenches with Plates

With reference to buried barriers shown in Fig. 1, the following dimensionless parameters are adopted: $R = r/L_R$, $D = d/L_R$, $W = w/L_R$, $H = h/L_R$, $S = s/L_R$, $N = n/L_R$ and $M = m/L_R$ and unless otherwise stated, $R = 5.0$, $D = 1.0$, $W = 0.1$, $H = 0.2$, $M = 0.2$ and $N = 1.0$. Moreover, the extent of reduction zone s beyond the

Fig. 3 Comparative study for vibration isolation by open trench
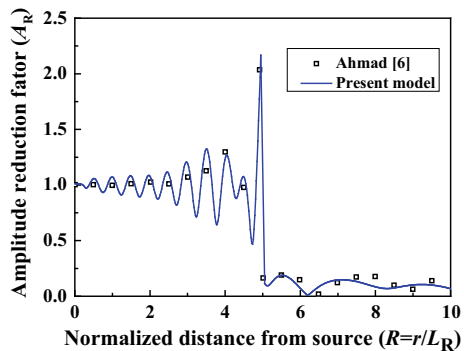
barrier is adopted as $S = 5.0$ as the previous work [6], which has illustrated that a zone of $5L_R$ would be long enough to represent the average amplitude reduction factors. The trench width is assumed to be a constant value $W = 0.1$ as it does not have much influence on the efficiency of isolation [3, 6].

3.1 Effect of Buried Trench Location

Obviously, the average amplitude reduction factor $\overline{A}_R$ of Cases 2 and 4 is much less than that of Case 1, which means that the source- and receiver-oriented plate has a positive influence on the buried barrier system. However, the plate of T-shape trench (Case 3) is not always beneficial to the screening efficiency (adverse influence is exerted when R is even times Rayleigh wavelength) as the plate would transmit the wave energy to the rear of the barrier (adverse effect) in addition to cutting down the diffraction phenomenon (positive effect). Moreover, the $\overline{A}_R$ values of the four cases show somewhat oscillation with normalized distance R (Fig. 4). This is because the intricate screening phenomena occur when the incident wave propagates to the buried trench, including wave reflection, scattering and diffraction [6]. The $\overline{A}_R$ value corresponding to $r = 5L_R$ can be used as a representative estimate of $\overline{A}_R$ for barrier locations at $r > 5L_R$ to some extent; therefore r is set as $5L_R$ in the following.

3.2 Effect of the Plate Location

The relationships between $\overline{A}_R$ and normalized trench depth D for Cases 1, 2 and 4 are generally similar; meanwhile, Cases 2 and 4 have better screening effectiveness than Case 1, i.e., a decrease of more than 0.15 (0.20) for Case 2 (Case 4) in $\overline{A}_R$,

Fig. 4 Effect of distance between buried barrier and source
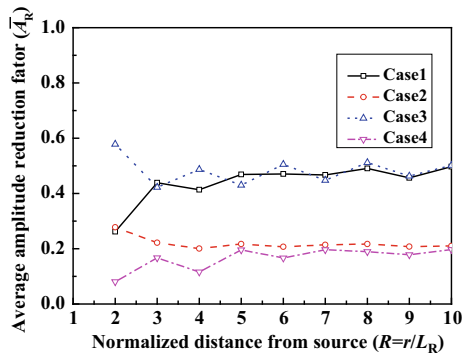
indicating the advantage of embedded plate (Fig. 5). For the reason that the plates have diminished diffraction phenomenon. The plate of T-shape trench (i.e. Case 3) is beneficial for deeper buried depth ($H > 0.2$), while it exerts an adverse influence on screening effect for shallower buried depth, e.g., $H \leq 0.2$. That is probably because the plate above the trench may help waves transmit to the rear of the barrier. Moreover, receiver-oriented plate (Case 4) seems to be more effective than the other two cases with plates.

3.3 Effect of Plate Thickness and Width in Case 4

For Case 4, the values of $\overline{A}_R$ consistently decrease with increasing normalized plate width N indicating an improved screening effect for $M = 0.1$. However, for $M \geq 0.2$, $\overline{A}_R$ first decreases until $N > 1.2$ and then almost keeps stable, which means that a wider plate than $N = 1.2$ hardly increases the screening effectiveness (Fig. 6). This is mainly because the receiver-oriented plate can cut down diffracted
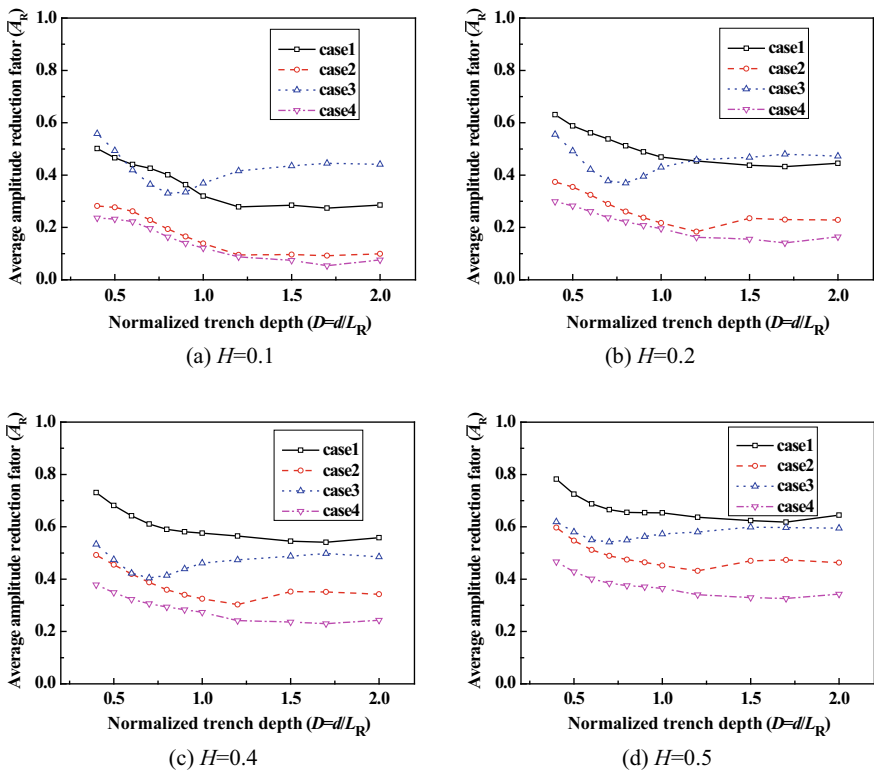
Fig. 5 Effect of the plate location

waves (positive effect), but can also guide waves to get through the trench (adverse effect). Therefore, a plate with $1.2L_R$ would be enough to reduce the transmitted waves by diffraction. Moreover, increasing the thickness of the plate is always beneficial to screening efficiency. Only a slight decrease of $\overline{A}_R$ at $N = 1.2$ when increasing the normalized plate thickness for $M > 0.2$. In light of this, $M = 0.2$ and $N = 1.2$ can be regarded as a better choice.

3.4 The Benefits of a Plate in a Buried Trench System

To intuitively illustrate the extra contribution of the receiver-oriented plate in Case 4 on screening effect, the ratio of the average amplitude reduction values between Case 4 and Case 1 ($\Delta \overline{A}_R = \overline{A}_R^{\text{Case 4}} - \overline{A}_R^{\text{Case 1}}$) was calculated (Fig. 7). Their average values are also depicted with a solid line. As can be seen, the plates achieve optimal performance when H is around 0.3. Such a phenomenon can be explained by the positive and adverse influences of the receiver-oriented plate on screening waves as described in Sect. 3.3. For shallower buried trenches, the transmitted wave energy by diffraction is small and even some surface waves are guided through the barrier,

Fig. 6 Effect of plate thickness and width in Case 4
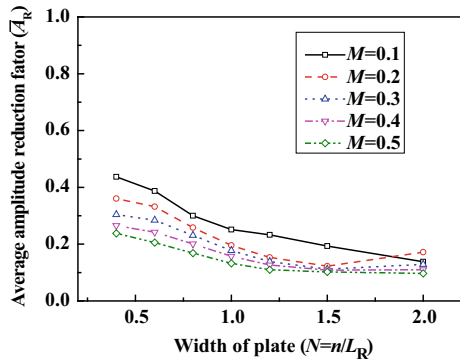
Fig. 7 Ratio of $\overline{A}_R$ between Case 4 and Case 1
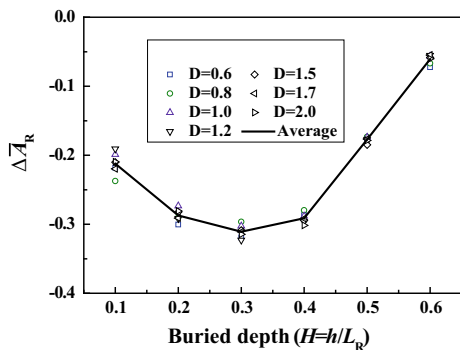
which results in a limited positive effect of the plate. With increasing buried depth, the proportion of diffracted wave to transmitted waves is increasing, which results in the growth of screening efficiency of the plate. For deeper buried trenches, most of the waves would pass through the zone overlying the barrier directly and thereby smaller extra contribution was provided by the plate.

4   Conclusions

A 2D finite element study is performed to investigate the screening effectiveness of buried trench with a plate (three cases depending on the relationship between plate and trench) in a linear elastic, homogeneous and isotropic half-space. The extra contribution of the plate on the screening effect is compared to that of the buried trench without a plate. The principal conclusions and design considerations about buried trench with the plate are as follows:

(1) A source-oriented plate (Case 2) or a receiver-oriented plate (Case 4) is always beneficial to screening effect of the buried trench, a decrease of more than 0.15 (0.20) for Case 2 (Case 4) in $\overline{A}_R$ ($M = 0.2$ and $N = 1.0$) compared with the barrier without a plate. The plate of T-shape trench (Case 3) has a positive influence on screening effect only when R is odd times Rayleigh wavelength for deeper buried depth ($H > 0.2$).

(2) Case 4, with receiver-oriented plate, is the first alternative for buried trench as it seems to be more effective than the other two cases.

(3) The geometric dimensions of $M = 0.2$ and $N = 1.2$ for a buried trench with a receiver-oriented plate can be regarded as a better choice.

(4) The receiver-oriented plate would achieve optimal performance when the buried depth is around 0.3 L_R.

References

1. Nam BH, Kim J, An J et al (2013) A review on the effects of earthborne vibrations and the mitigation measures. Int J Railw 6(3):95–106
2. Newland DE, Hunt HEM (1991) Isolation of buildings from ground vibration: a review of recent progress. ARCHIVE Proc Inst Mech Eng Part C J Mech Eng Sci 205(13):39–52
3. Woods RD (1968) Screening of surface waves in soils. Placement and improvement of soil to support structures. ASCE 1968:407–435
4. Garinei A, Risitano G, Scappaticci L (2014) Experimental evaluation of the efficiency of trenches for the mitigation of train-induced vibrations. Transp Res Part D Transp Environ 32(1):303–315
5. Tsai PH, Chang TS (2009) Effects of open trench siding on vibration-screening effectiveness using the two-dimensional boundary element method. Soil Dyn Earthq Eng 29(5):865–873
6. Ahmad S, Al-Hussaini TM (1991) Simplified design for vibration screening by open and in-filled trenches. J Geotech Eng 117(1):67–88

7. Massarsch KR (2005) Vibration isolation using gas-filled cushions. In: Proceedings of the geo-frontiers 2005 congress, American Society of Civil Engineers, Austin, Texas
8. Murillo C, Thorel L, Caicedo B (2009) Ground vibration isolation with geofoam barriers: centrifuge modeling. Geotext Geomembr 27(6):423–434
9. Çelebi E, Fırat S, Beyhan G et al (2009) Field experiments on wave propagation and vibration isolation by using wave barriers. Soil Dyn Earthq Eng 29(5):824–833
10. Hung HH, Yang YB, Chang DW (2004) Wave Barriers for Reduction of Train-Induced Vibrations in Soils. J Geotech Geoenvironmental Eng 130(12):1283–1291
11. Castanheira-Pinto A, Alves-Costa P, Godinho L et al (2018) On the application of continuous buried periodic inclusions on the filtering of traffic vibrations: a numerical study. Soil Dyn Earthq Eng 113:391–405
12. Andersen L, Jones CJC (2006) Coupled boundary and finite element analysis of vibration from railway tunnels—a comparison of two-and three-dimensional models. J Sound Vib 293(3–5):611–625
13. Bo Q, Ali L, Irini DM (2014) Numerical study of wave barrier and its optimization design. Finite Elem Anal Des 84:1–13
14. Mino GD, Giunta M, Liberto CMD (2010) Assessing the open trenches in screening railway ground-borne vibrations by means of artificial neural network. Adv Acoust Vib 2009(1687–6261)
15. Beskos DE, Dasgupta B, Vardoulakis IG (1986) Vibration isolation using open or filled trenches. Comput Mech 1(1):43–63

Influence of Fibre-Reinforced Load Transfer Platform Supported Embankment on Floating Columns Improved Soft Soils

Cong Chi Dang and Liet Chi Dang

Abstract Fibre reinforcement has been proved to be effective in improving geotechnical characteristics of both untreated and cemented soils, such as shear and compressive strength, bearing capacity, ductility and load-settlement behaviour. The application of fibre-reinforced soils could be beneficial to construction of embankments over soft soils because it can maintain its proper strength and bearing capacity when suffering from large total and differential settlements. In this study, fibre-reinforced cemented soil foundation is proposed to be used as a fibre-reinforced load transfer platform (FRLTP) combined with columns supported (CS) embankment constructed on multilayers of soft soils. To investigate the effect of addition of FRLTP into the CS embankment system, a numerical investigation based on the finite element analysis (FEA) using PLAXIS 2D was conducted. Moreover, a parametric analysis was carried out to evaluate the influence of the FRLTP thickness on the performance of the CS embankment when considering the vertical and differential settlements during the embankment construction and post-construction stages. The predicted results indicate that the vertical settlement and the lateral deformation considerably reduce with the insertion of FRLTP into the CS embankment system. Meanwhile, the outcomes of the parametric study reveal that the FRLTP thickness has a significant influence on the enhancement in the time-dependent differential settlement. Although the vertical settlement significantly decreases with increasing the FRLTP thickness, the post-construction vertical settlement was predicted to be most likely independent of the FRLTP thickness. The findings of this study could enable geotechnical engineers and designers to design a time-dependent performance-based FRLTP for a CS embankment over soft soils and aim to enhance the related design codes.

C. C. Dang
Faculty of Civil Engineering, Ho Chi Minh City University of Technology,
VNU-HCM, 268 Ly Thuong Kiet Street, District 10, Ho Chi Minh City, Viet Nam
e-mail: 1870139@hcmut.edu.vn

L. C. Dang (✉)
School of Civil and Environmental Engineering, University
of Technology Sydney, Sydney, NSW 2007, Australia
e-mail: dangchiliet@gmail.com

Keywords Fibre-reinforced materials · Columns · Embankments · Soft soils · Ground improvement · FRLTP · Sustainable civil infrastructure

1 Introduction

Fibre reinforcement has been proved to be effective in improving geotechnical characteristics of both untreated and cemented soils, such as shear and compressive strength, bearing capacity, ductility and load-settlement behaviour. The application of fibre-reinforced soils could be beneficial to construction of embankments over soft soils because it can maintain its proper strength and bearing capacity when suffering from larger total and differential settlements. In recent years, a number of researchers [1–5] conducted physical and numerical investigations on the potential use of lime/cement-treated soils [1, 3] or industrial waste materials, recycled fibre-reinforced cemented soils [2] to be adopted as an alternative load transfer platform (LTP) positioned on top of columns/piles supported embankments. It can be noted the applications of ground improvement technique using industrial waste materials such as fly ash [6, 7], bagasse ash [8–10] and recycled fibre-reinforced cemented soils [11–14] in construction of embankment foundation could be considered as an eco-friendly, low-cost and green solution for sustainable civil infrastructure development. This is because it enables to mitigate the harmful effects of waste materials on the environment.

Okyay and Dias [1] investigated the mechanical characteristics of lime/cement-stabilised soils used as an LTP using numerical analysis of a unit cell model. Anggraini et al. [2] studied the performance of a platform made of lime-fibre-reinforced soil and rigid piles supported embankment over soft soil by both physical and numerical modelling using a two-dimensional (2D) axisymmetric unit cell model. However, as a 2D unit cell model scaled down was adopted in their study, the influences of the lime-fibre reinforced LTP and the group effect of rigid pile interactions on the lateral deformation, the soil arching effect and the variations of excess pore water pressure were critically important but not taken into account in the physical and numerical modelling.

Jamsawang et al. [15] analysed the influence of deep cement mixing (DCM) columns and cement-stabilised soil mat supported embankment system on the lateral movement of precast reinforced concrete (PFRC) wall induced by an adjacent deep excavation based on three-dimensional numerical simulations. The results of the numerical analysis indicated that a stabilised mat with a thickness of 0.5 m had a considerable influence on the lateral movement of the PFRC wall, because it tied DCM columns together and behaved as a stiffer unit in resisting lateral earth pressure and displacement. Nguyen et al. [3] conducted 2D numerical investigations on the failure pattern of column-supported embankment with cement-stabilised slab (LTP) by taking the effect of the cement-stabilised slab on the failure pattern of DCM columns into account. The results of FEA revealed that the stabilised LTP thickness and compressive strength exhibited notable influences

on the embankment horizontal displacement. Nguyen et al. [3] reported that the influences of the stabilised LTP on the yield stress of columns subjected to the embankment loading were greater for the higher LTP thickness regardless of the compressive strength. Dang et al. [4] conducted a 2D numerical assessment of fibre inclusion in LTP as a likely replacement of geosynthetics reinforced traditional angular LTP and piles to support high embankments founded on soft clay. By comparing the predicted result of numerical simulations with both the measured and predicted results, available in the literature, they concluded that the combined use of FRLTP and piles supported embankments experienced similar engineering characteristics when compared to the geosynthetics reinforced traditional angular LTP to support embankments with piles. Numerical studies performed by Dang et al. [16, 17] using a full geometry embankment model emphasised the effects of the mechanical properties of FRLTP on the overall behaviour of a CS embankment. The results of their numerical analysis showed that the FRLTP shear strength properties tend to be the most influential factors and need to be considered in the design stages of a target CS-FRLTP-embankment system. However, none of these investigations fully focused on investigating the influence of the FRLTP thickness on the deformation behaviour of a CS embankment during construction and post-construction periods.

In this paper, a 2D numerical simulation of floating DCM columns supported embankment without or with FRLTP, using a full geometry embankment model, was proposed and conducted to model mechanical behaviour of embankments over multilayers of soft soils during construction and post-construction periods. A parametric study on the influences of the FRLTP thickness was also performed to provide a comprehensive understanding of the deformation behaviour of the floating columns supported embankment with a varied FRLTP thickness. Some key parameters to design a CS embankment consisting of the vertical and differential settlements are evaluated and compared to comprehend the influences of adding FRTLP with a varied thickness on the time-dependent behaviour of embankments over multilayered soft soils. The FEA findings will enable geotechnical engineers and designers to select an appropriate FRLTP thickness based on the time-dependent performance for a CS embankment reinforced with an FRLTP as well as aim to enhance the associated design standards and guidelines.

2 Description of Case Study

In this numerical analysis, a 6 m high embankment reinforced with FRLTP and DCM columns in soft clay layers is considered [16]. The embankment geometry is shown in Fig. 1, representing only the right half of the domain of the embankment since the embankment is symmetrical along its centreline. The embankment is 20.8 m wide and 6 m high with a 1V:1.8H side slope. It is made of good quality soil with cohesion of 20 kPa, a friction angle of 35° and an average unit weight of 19 kN/m³. The embankment is constructed on a 1 m thick fill material as a surface
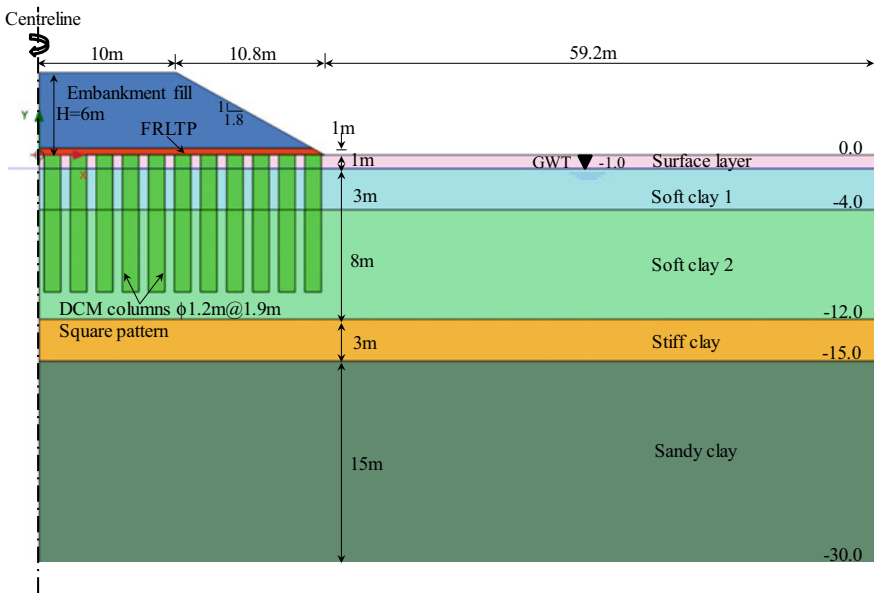
Fig. 1 Schematic representation of a highway embankment supported by FRLTP and DCM columns in soft soils (not to scale)

layer overlaying an 11 m thick deposit of soft clay. This deposit of soft clay overlies a 3 m thick stiff clay stratum followed by a 15 m thick sand layer. The ground-water table is located at a depth of 1 m below the ground surface. Details of these soil layers are summarised in Tables 1 and 2. A fibre-lime-soil layer [2, 4, 16] is used in this numerical study and serves as an FRLTP of 1 m that is placed on the top of DCM columns. The DCM columns with 1.2 m diameter and 10 m length are introduced to improve soft soils. The columns are arranged in a square grid pattern with a centre-to-centre distance of 1.9 m. Furthermore, the construction sequence of the embankment is assumed to be in 0.5–1 m lifts at an average filling rate of 0.06 m/day [17, 18] to a total height of 6 m including the FRLTP with a height of 1 m. Following the completion of embankment construction, the investigated embankment is left for two years to simulate the consolidation progress.

3 Numerical Modelling

3.1 Finite Element Models and Parameters

A 2D plane strain FEA model incorporated in finite element software PLAXIS 2D (2017) and the equivalent 2D numerical analysis method proposed by previous researchers [1, 4, 19, 20] were adopted to model overall behaviour of

Table 1 Material properties of subgrade soil layers used in modified Cam-clay model

Parameters	Surface layer	Soft clay 1	Soft clay 2	Stiff clay
Depth (m)	0–1	1–4	4–12	12–15
Material model	MCC[a]	MCC	MCC	MCC
Unit weight, γ (kN/m^3)	16	13.4	14.3	18
Poisson's ratio, v	0.15	0.15	0.15	0.15
Compression index, λ	0.25	0.87	0.43	0.12
Swelling index, κ	0.025	0.087	0.043	0.012
Over consolidation ratio, OCR	1.5	2.5	1.2	1.0
Slope of the critical state line, M	1.2	1.2	1.2	1.4
Initial void ratio, e_0	1.5	3.1	2.49	0.8
Vertical permeability coefficient, k_v (m/day)	6×10^{-4}	4.4×10^{-4}	4.6×10^{-4}	2.5×10^{-3}
Horizontal permeability coefficient, k_h (m/day)	9.1×10^{-4}	6.6×10^{-4}	6.9×10^{-4}	2.5×10^{-3}
Material behaviour	Undrained	Undrained	Undrained	Undrained

[a]*MCC* modified Cam-clay

Table 2 Material properties of the embankment, FRLTP, DCM columns and sandy clay strata adopted in Mohr-Coulomb model

Parameters	Sandy clay	FRLTP	Embankment fill	Column
Depth (m)	15–30	–	–	–
Material model	MC[b]	MC	MC	MC
Unit weight γ (kN/m^3)	19	12.5	19	15
Young's modulus, E (MPa)	20	125.8	1	100
Poisson's ratio, v	0.10	0.32	0.40	0.15
Effective cohesion, c' (kPa)	20	75	20	$c_u = 500$
Effective friction angle, φ' (°)	35	42	35	–
Initial void ratio, e_0	0.7	–	–	–
Vertical permeability coefficient, k_v (m/day)	2.5×10^{-2}	–	–	4.6×10^{-4}
Horizontal permeability coefficient, k_h (m/day)	2.5×10^{-2}	–	–	4.6×10^{-4}
Material behaviour	Drained	Undrained	Drained	Undrained

[b]*MC* Mohr-Coulomb model, c_u undrained cohesion

FRLTP-supported highway embankment with DCM columns. The equivalent 2D FEA model was selected because of less analysis time consuming, while generating results with reasonable accuracy. The DCM columns were modelled by continuous plane strain walls of 0.6 m thickness for the entire columns length of 10 m to maintain the same area of replacement ratio of columns to surrounding soil, taking

into account the equivalent normal stiffness (EA) as implemented by many researchers [21–23] for numerical simulations of column-supported embankments. Meanwhile, the centre-to-centre spacing between two adjacent walls in this numerical simulation was remained the same as the 1.9 m centre-to-centre spacing between two adjacent DCM columns.

In this modelling, the DCM columns, FRLTP, embankment fill and sandy clay were modelled as a linear elastic-perfectly plastic material using the Mohr-Coulomb (MC) model [24, 25]. Meanwhile, the surface, soft soil and stiff clay layers were represented by modified Cam-clay (MCC) model. The required parameters for the MC and MCC material models are presented in Tables 1 and 2. It is assumed that the values of horizontal permeability (k_h) are about 1.5 times the corresponding values of vertical permeability (k_v) of the subgrade soils, whereas the horizontal and vertical permeability of DCM columns and sandy clay are equal. Due to an increase in embankment load during construction in stages, the hydraulic permeability was changed owing to the relationship between the void ratio change and the corresponding embankment load. Hence, the permeable change index $C_k = 0.5e_0$ was adopted in this investigation.

For this 2D simulation, a half-fine mesh was used because of geometrical symmetry of the embankment system as presented in Fig. 2. The foundation soil was taken to 30 m depth from the ground surface to sandy clay stratum. Meanwhile, the horizontal length of the FEA model was made to be 80 m, which was almost three times the half-width of the embankment base in order to eliminate the boundary influence. A detailed description of the vertical and horizontal boundary conditions can be found in the numerical modelling by Dang et al. [16]. It should be noted that as the results presented in this paper are part of an ongoing research project of modelling behaviour of FRLTP and columns supported embankments over soft soils, the proposed FEA model for a CS embankment was properly validated. The predicted results showed a good agreement with the field measurement data reported in the literature. Hence, the proposed FEA model is suitable for modelling behaviour of CS embankments built on multilayers of soft soils. Further evaluation of the proposed model validation could be found in the previous investigation by Dang et al. [16].

4 Analysis Results and Discussion

4.1 Influence of FRLTP Addition on the Maximum Settlement and the Lateral Displacement

Figure 3 displays the influence of FRLTP addition on the behaviour of columns supported embankment by comparing the maximum vertical settlement at the embankment base centre. As illustrated in Fig. 3, when the embankment load increased, the addition of FRLTP with a height of 1 m combined with CS embankment was generally found to result in a noticeable reduction of the maximum vertical
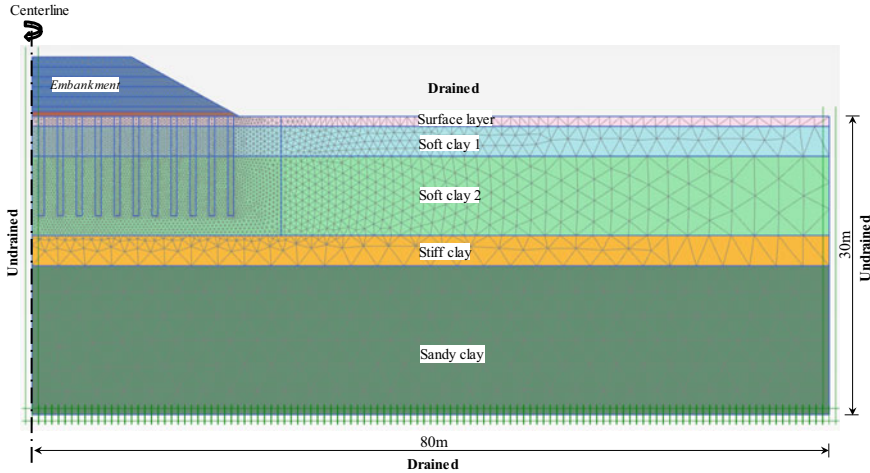
Fig. 2 Mesh and boundary conditions for a 2D FEM analysis of embankment

settlement as compared to embankment without FRLTP. Inspection of Fig. 3 also notes that a nonlinear increase in the maximum vertical settlement of the ground surface was observed for both the embankment without or with FRLTP as the embankment load increased. However, the maximum vertical settlement was calculated to be larger for the embankment without FRLTP as compared to the embankment reinforced with an FRLTP with a height of $H = 1$ m. Moreover, the maximum settlement difference from embankment without FRLTP to embankment with FRLTP was found to steadily increase when the load associated with the embankment fill increased, as shown in Fig. 3. For example, about 30% difference in the maximum settlement between the embankment without FRLTP and with FRLTP were calculated at the completion of the embankment construction as evident in Fig. 3. In other words, by comparing with the embankment without FRLTP, the introduction of an FRLTP with a thickness of 1 m into the DCM columns supported embankment system corresponded to a considerable reduction of approximately 30% of the maximum vertical settlement during the embankment construction stage. The improvement in the maximum vertical settlement corroborates the effectiveness of adding FRLTP into the CS embankment system. According to Dang et al. [22], the maximum vertical settlement was greatly improved with an FRLTP inclusion because of the enhanced stiffness and the arching effect of the entire embankment system contributed from the FRLTP insertion. This phenomenon could enable more of the embankment load to be transferred from soft foundation soil to DCM columns and consequently reduce the vertical ground surface settlement.

Figure 4 presents the changes of lateral displacement at the column head under the embankment toe with an increase in the embankment load from 10 kPa to around 120 kPa. By examining Fig. 4, it is noteworthy to state that a nonlinear relationship between the lateral displacement and the embankment load was visibly observed to

Fig. 3 Influence of adding
FRLTP on the maximum
settlement at the ground
surface under the
embankment base centre
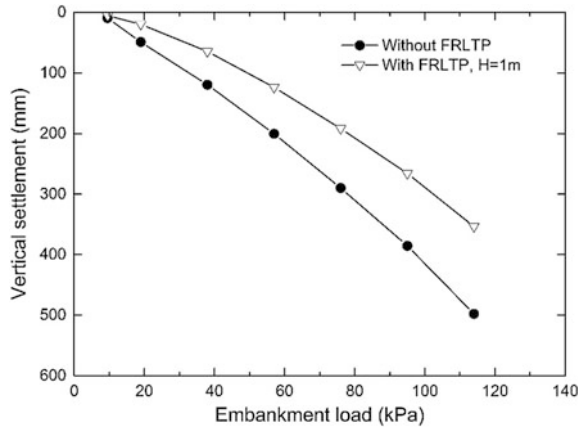
be a predominant mechanism for the CS embankment with or without FRLTP
($H = 1$ m). Moreover, as Fig. 4 indicates, the addition of FRLTP into the CS
embankment was found to have a significant influence on the changes of the lateral
displacement. For example, by comparing with the embankment without FRLTP,
the embankment with an FRLTP thickness of $H = 1$ m was calculated to reduce
approximately 90% of the lateral displacement at the embankment construction end.
Therefore, this finding reveals that the introduction of the FRLTP and DCM columns
supported embankment can be very effective in controlling the embankment lateral
displacement and hence, increase the stability of the entire embankment system
placed on top of multilayers of soft soils. The improvement in the lateral displace-
ment observed for the embankment with FRLTP could have resulted from the
insertion of fibre-reinforced cemented soil to be used as FRLTP. Referring to
Jamsawang et al. [15], the insertion of a stabilised soil mat (e.g. FRTLP) links DCM
columns together from the top part and tends to act as a stiffer unit resulting in the
better resistance to the lateral earth pressure and displacement.

Fig. 4 Influence of adding
FRLTP on the lateral
displacement at the
embankment toe
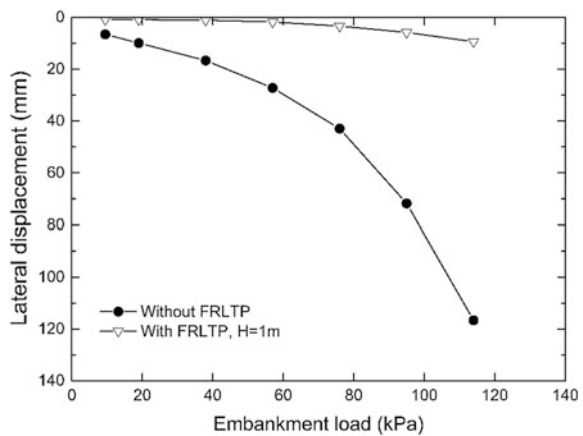
4.2 Influence of FRLTP Thickness (H) on the Vertical Settlement

Figure 5 illustrates the results of the parametric study on the influences of various FRLTP thickness (height) on the vertical settlement of the floating DCM columns supported embankment at the construction end and the two years post-construction. It can be noted that the FRLTP thickness was varied from $H = 0$ m representing the embankment without FRLTP to $H = 3$ m showing the embankment reinforced with an FRLPT thickness of 3 m. Figure 5 shows that the vertical settlement at the base of the embankment centre was significantly influenced by the FRLTP thickness. However, the FRLTP thickness was found to have an insignificant effect on the changes of the vertical settlement from the construction end to the two years post-construction cases. To be more specific, as presented in Fig. 5, the vertical settlements at the construction end were observed to gradually reduce by approximately 40% when the FRLTP thickness increased from 0 to 3 m. Inspection of Fig. 5 also notes that when the FRLTP thickness increased, a similar pattern of the vertical settlement reduction was found in both the cases of the construction end and the two years post-construction. This pattern implies that effect of the FRLTP thickness on the long-term vertical settlement was negligible. Nonetheless, the higher settlement was observed in Fig. 5 for the case of the two years post-construction. The consolidation of the underlying unimproved soil layers could be mainly responsible for the increased post-construction settlement of the examined embankment. It is of interest to note that as the greater reduction of the vertical settlement was predicted for the thicker FRLTP, this finding corroborates that the thickness of the FRLTP plays a key role in controlling the vertical settlement of the CS embankment reinforced with an FRLTP. It can also be noted that the thicker FRLTP assists in alleviating the possibility of the FRLTP punching failure induced by penetration of column heads.

4.3 Influence of FRLTP Thickness (H) on the Differential Settlement

Figure 6 shows the variation of the construction end and two years post-construction differential settlements at the embankment base centre in conjunction with an increase in the FRLTP thickness in a typical range of 0-3 m. It can be noted that in this numerical simulation, the differential settlement is defined as the maximum difference in the vertical settlement between the column top and ground surface in the middle of two adjacent columns. As expected, the differential settlement was found to significantly decrease as the thickness of FRLTP increased. For example, when increasing the FRLTP thickness ranging from 0 to 1 m, a significant reduction of approximately 100% of the differential settlement (almost zero differential settlement) was observed for both the construction end and the
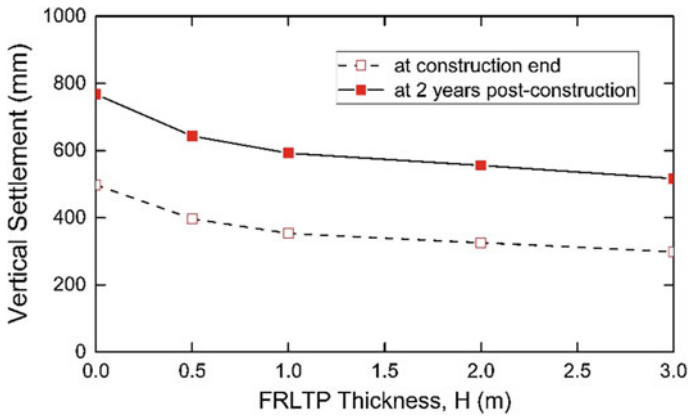
Fig. 5 Variations of vertical settlement for different FRLTP thickness at the construction end and two years post-construction
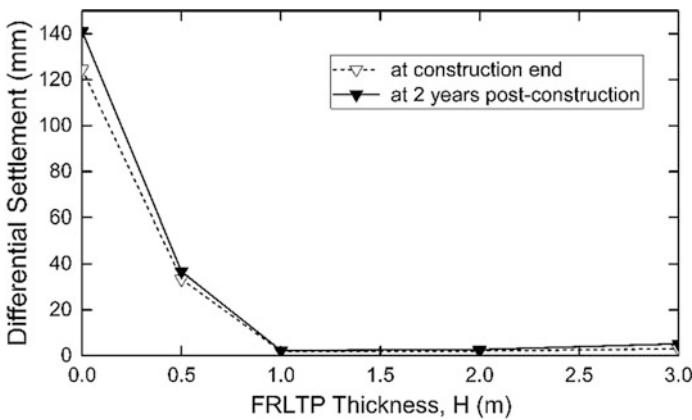
Fig. 6 Variations of differential settlement for various FRLTP thickness at the construction end and two years post-construction

two years post-construction cases. Further increase in the height of FRLTP was noted to cause the differential settlement to remain zero. Moreover, as Fig. 6 indicates, the difference in the embankment differential settlement from the case of construction completion to the post-construction case was predicted to be considerable when the embankment was not reinforced with an FRLTP ($H = 0$ m). Subsequently, the difference in the time-dependent differential settlements became negligible and converted to almost the same value as the FRLTP thickness increased further to $H = 3$ m. Therefore, it is possible to conclude that the FRLTP thickness was found to have a substantial influence on the time-dependent

differential settlement of the investigated embankment. The application of FRLTP with a height of $H = 1$ m could control the insignificant (almost zero) differential settlement occurring at the ground surface under the embankment base.

5 Conclusions

An equivalent 2D finite element model of a full geometry embankment was developed to examine the time-dependent behaviour of floating columns supported embankment without or with FRLTP. The effect of the FRLTP thickness on the embankment performance during the construction and post-construction periods was numerically investigated by a parametric study. The main findings of this study can be summarised as follows:

- The application of the FRLTP with a height of 1 m combined with DCM columns supported embankment reduced a great amount of approximately 30% of the maximum vertical settlement, 90% of the lateral displacement and 100% of the differential settlement during the construction stage when comparing with the CS embankment without FRLTP.
- The FRLTP thickness was found to have significant influences on the time-dependent differential settlements of the investigated embankment. Whereas its influence on the post-construction vertical settlement was predicted to be negligible.
- The findings of this simulation indicate that the thickness of the FRLTP plays a vital role in improving the vertical and differential settlements of the CS embankment by effectively enhancing the vertical and horizontal stiffness on the entire embankment system as well as the load transfer mechanism between DCM columns and surrounding soft soils.
- Finally, it is important to note that this numerical study has provided a deeper insight into making use of agricultural waste materials (e.g. jute fibre, bagasse fibre [12–14, 26–28], coir fibre) as reinforcing components of fill materials for sustainable civil infrastructure construction development.

References

1. Okyay US, Dias D (2010) Use of lime and cement treated soils as pile supported load transfer platform. Eng Geol 114(1–2):34–44
2. Anggraini V, Asadi A, Huat BBK, Nahazanan H (2015) Performance of chemically treated natural fibres and lime in soft soil for the utilisation as pile-supported earth platform. Int J Geosyn Ground Eng 1(3):1–14
3. Nguyen BTT, Takeyama T, Kitazume M (2016) Numerical analyses on the failure of deep mixing columns reinforced by a shallow mixing layer. JGSSP 2(63):2144–2148

4. Dang LC, Dang CC, Fatahi B, Khabbaz H (2016) Numerical assessment of fibre inclusion in a load transfer platform for pile-supported embankments over soft soil. In: Geo-China 2016: Material, Design, Construction, Maintenance, and Testing of Pavement, GSP 266, ASCE, pp 148–155

5. Ishikura R, Yasufuku N, Brown MJ (2016) An estimation method for predicting final consolidation settlement of ground improved by floating soil cement columns. Soils Found 56 (2):213–227

6. Fatahi B, Khabbaz H (2013) Influence of fly ash and quicklime addition on behaviour of municipal solid wastes. J Soils Sediments 13(7):1201–1212

7. Fatahi B, Khabbaz H (2015) Influence of chemical stabilisation on permeability of municipal solid wastes. Geotech Geol Eng 33(3):455–466

8. Dang LC, Hasan H, Fatahi B, Jones R, Khabbaz H (2016) Enhancing the engineering properties of expansive soil using bagasse ash and hydrated lime. Int J GEOMATE 11 (25):2447–2454

9. Dang LC, Khabbaz H (2018) Assessment of the geotechnical and microstructural characteristics of lime stabilised expansive soil with bagasse ash. In: 71st Canadian geotechnical conference and the 13th Joint CGS/IAH-CNC groundwater conference (GeoEdmonton 2018). Canadian Geotechnical Society, Alberta, Canada

10. Dang LC, Hasan H, Fatahi B, Khabbaz H (2015) Influence of bagasse ash and hydrated lime on strength and mechanical behaviour of stabilised expansive soil. In: 68th Canadian geotechnical conference and the 7th Canadian permafrost conference (GEOQuébec 2015). Canadian Geotechnical Society, Québec City, Canada

11. Dang LC (2019) Enhancing the engineering properties of expansive soil using bagasse ash, bagasse fibre and hydrated lime. University of Technology Sydney, NSW, Australia

12. Dang LC, Khabbaz H, Fatahi B (2017) An experimental study on engineering behaviour of lime and bagasse fibre reinforced expansive soils. In: 19th international conference on soil mechanics and geotechnical engineering. ISSMGE, Seoul, Republic of Korea, pp 2497–2500

13. Dang LC, Fatahi B, Khabbaz H (2016) Behaviour of expansive soils stabilized with hydrated lime and bagasse fibres. Procedia Engineering 143:658–665

14. Dang LC, Khabbaz H, Fatahi B (2017) Evaluation of swelling behaviour and soil water characteristic curve of bagasse fibre and lime stabilised expansive soil. In: PanAm Unsaturated Soils 2017, GSP 303, ASCE, Texas, USA, pp 58–70

15. Jamsawang P, Voottipruex P, Jongpradist P, Bergado DT (2015) Parameters affecting the lateral movements of compound deep cement mixing walls by numerical simulations and parametric analyses. Acta Geotech 10(6):797–812

16. Dang LC, Dang CC, Khabbaz H (2019) Modelling of columns and fibre-reinforced load-transfer platform-supported embankments. Ground Improv 0(0):1–19

17. Dang LC, Dang CC, Khabbaz H (2018) A parametric study of deep mixing columns and fibre reinforced load transfer platform supported embankments. In: Khabbaz H, Youn H, Bouassida M (eds) New prospects in geotechnical engineering aspects of civil infrastructures. Springer, Cham, Switzerland. pp 179–194

18. Dang LC, Dang CC, Khabbaz H (2017) Behaviour of columns and fibre reinforced load transfer platform supported embankments built on soft soil. In: 15th international conference of the international association for computer methods and advances in geomechanics. Wuhan, China

19. Tan S, Tjahyono S, Oo K (2008) Simplified plane-strain modeling of stone-column reinforced ground. J Geotech Geoenviron Eng 134(2):185–194

20. Dang CC, Dang LC (2020) Evaluation of the at-rest lateral earth pressure coefficient of fibre reinforced load transfer platform and columns supported embankments. In CIGOS 2019: Innovation for Sustainable Infrastructure, Lecture Notes in Civil Engineering, Volume 54, 2020, Springer, Singapore. pp 647–652

21. Yapage N, Liyanapathirana D, Poulos H, Kelly R, Leo C (2015) Numerical modeling of geotextile-reinforced embankments over deep cement mixed columns incorporating strain-softening behavior of columns. Int J Geomech 15(2):04014047

22. Dang LC, Dang CC, Khabbaz H (2018) Numerical analysis on the performance of fibre reinforced load transfer platform and deep mixing columns supported embankments. In: Bouassida M, Meguid MA (eds) Ground improvement and earth structures. Springer, Cham, Switzerland, pp 157–169
23. Dang CC, Dang LC (2020) Numerical investigation on the stability of soil-cement columns reinforced riverbank. In: Correia AG, et al. (eds) Information Technology in Geo-Engineering, Springer Series in Geomechanics and Geoengineering. Springer, Cham, Switzerland, pp 879–888
24. Huang J, Han J (2010) Two-dimensional parametric study of geosynthetic-reinforced column-supported embankments by coupled hydraulic and mechanical modeling. Comput Geotech 37(5):638–648
25. Liu KW, Rowe RK (2015) Numerical modelling of prefabricated vertical drains and surcharge on reinforced floating column-supported embankment behaviour. Geotext Geomembr 43(6):493–505
26. Dang LC, Khabbaz H (2018) Enhancing the strength characteristics of expansive soil using bagasse fibre. In: Wu W, Yu HS (eds) Proceedings of China-Europe conference on geotechnical engineering, springer series in geomechanics and geoengineering. Springer, Cham, Switzerland, pp 792–796
27. Dang LC, Khabbaz H (2019) Experimental investigation on the compaction and compressible properties of expansive soil reinforced with bagasse fibre and lime. In: McCartney JS, Hoyos LR (eds) Recent advancements on expansive soils. Springer, Cham, Switzerland, pp 64–78
28. Dang LC, Khabbaz H (2018) Shear strength behaviour of bagasse fibre reinforced expansive soil. In: IACGE 2018: Geotechnical and Seismic Research and Practices for Sustainability, GSP 304, ASCE: Chongqing, China, pp 393–402

Stability Analysis of Fractured Rock Slopes with Vertical Cracks Subjected to the Hydraulic Effect Based on the Hoek–Brown Failure Criterion

Xiao-qing Pi, Lian-heng Zhao, Xiao Cheng and Han-hua Tan

Abstract In this paper, the stability of fractured rock slopes subjected to the hydraulic effect is studied using the upper bound limit analysis. The Hoek–Brown failure criterion and the strength reduction technique are introduced to obtain the expression of the safety factor of slopes considering hydraulic effect. Based on the nonlinear sequential quadratic programming, the safety factor (Fs) and critical failure surface for fractured rock slopes are investigated with different groundwater levels and crack depths. Besides, the detailed parametric analyses of Hoek–Brown failure criterion (i.e., Geological Strength Index (GSI), the disturbance coefficient (D) and the material constant (m_i) obtained by compression tests) on fractured rock slopes are carried out. The results show that with an increase in the groundwater level and crack depth, the Fs of the fractured rock slope gradually decreases. The nonlinear strength parameters also have significant effect on the slope stability: As GSI increases, the values of Fs increase significantly; with an increase in D, the Fs gradually decreases; and with an increase in m_i, the Fs gradually decreases when the groundwater level is low but gradually increases when the groundwater level is high.

Keywords Fractured rock slope · Vertical crack · Pore water pressure · Upper bound limit analysis · Strength reduction technique · Hoek–Brown failure criterion

X. Pi · L. Zhao · X. Cheng (✉)
School of Civil Engineering, Central South University, 410075 Changsha, Hunan, China
e-mail: chengxiao@csu.edu.cn

L. Zhao (✉)
Key Laboratory of Heavy-Haul Railway Engineering Structure,
Ministry of Education, Central South University, 410075 Changsha, Hunan, China
e-mail: zlh8076@163.com

H. Tan
Guizhou Provincial Institute of Planning, Prospecting and Designing of Communications
Infrastructures, 550001 Guiyang, China

1 Introduction

In practical engineering, cracked slopes are a common occurrence [1]. The existence of cracks can reduce the stability of a slope because the cracks in slopes provide seepage paths for water to flow into the inside of slopes. Then, the rising groundwater level causes an increase in the pore water pressure and the water pressure in the cracks, which may lead to the failure of the slope [2, 3]. Therefore, it is important to study the effects of groundwater levels on the stability of cracked slopes.

Many studies considered the effects of groundwater level fluctuations on slope stability. Viratjandr and Michalowski [4] investigated the stability of slopes near a river by using linear and logarithmic spiral failure surfaces based on the upper bound limit analysis (UBLA) method and provided a series of calculation charts. Michalowski [5, 6] approximated the pore water pressure on the failure surface by introducing a coefficient of pore water. The pore water pressure was considered as the external force when calculating the energy dissipation. Wang et al. [7, 8], Kim et al. [9] and Yin et al. [10] explored the effects of the pore water pressure on the slope stability based on the upper and lower bound finite element limit analysis theorem. However, the condition of cracks in the slope is always ignored.

Michalowski [1] considered cracks as the part of failure mechanism by calculating the energy dissipation during crack formation. The influence of cracks on slope stability was analyzed using the UBLA method. Utili [11] investigated the effect of water pressure in cracks on the stability of the slope using the UBLA method, assuming that the water in the cracks would not penetrate into the soil mass under the cracks. Then, Utili [12] and Michalowski [13] discussed the method used to assess the stability of cracked slopes, considering both the crack depth and position described by Michalowski [14]. Deng and Li [2] investigated the stability of slopes with tensioned cracks under seepage conditions based on the limit equilibrium theory. The sliding surface in the analysis was assumed to be a linear, circular and arbitrary curve. Utili [15] and Zhao et al. [16] examined the stability of homogeneous slopes with cracks subjected to seismic loading by using the UBLA technique and the pseudo-static method. The charts were obtained for cracks of a known depth but unknown location, cracks of a known location but unspecified depth and cracks of an unspecified depth and location.

Regardless of whether the effect of slope surface cracks is considered, the above studies are based on the assumption that the rock and soil materials are subject to the linear Mohr–Column (M-C) strength criterion. This assumption is not consistent with practical engineering, where the material of the rock and soil mass is generally subject to nonlinear strength characteristics [17–23]. For rock materials, the Hoek–Brown (H-B) failure criteria [17–19] reflect the rock mass of the inherent characteristic and nonlinear characteristic as well as the rock strength, structural plane group numbers and effects of the stress state of the rock mass strength. Therefore, a stability analysis based on the H-B failure criterion is more suitable for practical engineering. Benz et al. [24] presented a numerical simulation on rock and soil

slope stability based on the H-B failure criterion but did not consider the influence of the groundwater level or the crack. Hammah et al. [25] and Zheng et al. [26] considered the stability of the rock and soil slopes based on the H-B failure criterion. Li et al. [27, 28] investigated the static and dynamic stability of the rock slopes using the upper and lower bound finite element limit analysis method with the H-B failure criterion and compared the results with the limit equilibrium method results. Saada et al. [29] studied the effects of osmotic stress on water-saturated rock slopes based on the modified H-B failure criterion but did not consider the effects of the water level fluctuation or the crack. Yang et al. [30] introduced the H-B failure criterion of the shear strength parameters based on the external tangent method introduced by Collins et al. [31] and Drescher and Christopoulos [32] and determined the effect of the pore water pressure on the stability of the rock mass slopes, but still did not consider the influence of the surface cracks.

Based on the above analysis, this paper primarily aims to extend the previous works of Michalowski [1, 13, 14], Utili [11, 12] and Zhao et al. [16] by following the M-C criterion to the H-B criterion and to extend the works of Yang et al. [30] and Saada et al. [29] to consider the fractured rock slope with vertical cracks. The influences of the hydraulic effect on the stability of fractured rock slopes with vertical cracks based on the H-B failure criterion were performed. The safety factor function was established to consider the effect of pore water pressure on the fractured rock slope with vertical cracks by using the UBLA method and the H-B failure criterion combined with the strength reduction technology and adopting the logarithmic spiral failure mechanism. The influences of the groundwater level, the crack depth and the H-B failure criterion parameters on the Fs of the fractured rock slopes were investigated. The variation in the associated critical failure surface with the groundwater level and the crack depth was also studied, and the validity of this method was verified through comparative analyses.

2 The H-B Strength Criterion

2.1 The Generalized H-B Failure Criterion

Hoek et al. [33] proposed the latest version of expressions of the generalized H-B (GHB) strength criterion, as follows:

$$\sigma_1 = \sigma_3 + \sigma_c (m\sigma_3/\sigma_c + s)^n \tag{1}$$

$$m = m_i \exp[(\text{GSI} - 100)/(28 - 14D)] \tag{2}$$

$$s = \exp[(\text{GSI} - 100)/(9 - 3D)] \tag{3}$$

$$n = 1/2 + 1/6 \cdot (e^{-\text{GSI}/15} - e^{-20/3}) \tag{4}$$

where σ_1 and σ_3 are the maximum and minimum principal stress of the rock; σ_c is the uniaxial compressive strength of the rock mass; D is the rock mass disturbance factor; and the two dimensionless coefficients m and s are related to the lithology and rock integrity, respectively.

2.2 The UBLA Method Based on the H-B Failure Criterion

The idea of the external tangent of Drescher and Christopoulos [32] and Collins et al. [31] is shown in Fig. 1, where the H-B failure curve is in $\sigma - \tau$ space which is an approximation to that defined in principal stress space [18].

The tangent line is through a single point on the H-B failure curve, and its intercept on the τ-axis is the c value, with the arctangent value of its slope being the φ value. The tangent method is used to establish the relationship between c and φ rather than to determine the strength index of rock mass. Because the c and φ values are related to the normal stress σ_n of the sliding surface, they vary according to with different σ_n values in different positions of the foundation. Accordingly, the c and φ are instantaneous values and not constants, named c_t and φ_t. The shear failure envelope can be determined by the following two formulae [31, 32]:

$$\frac{\tau}{\sigma_c} = \frac{\cos \varphi_t}{2} \left[\frac{mn(1 - \sin \varphi_t)}{2 \sin \varphi_t} \right]^{\frac{n}{1-n}} \tag{5}$$

$$\frac{\sigma_n}{\sigma_c} = \left(\frac{1}{m} + \frac{\sin \varphi_t}{mn} \right) \left[\frac{mn(1 - \sin \varphi_t)}{2 \sin \varphi_t} \right]^{\frac{1}{1-n}} + \frac{s}{m} \tag{6}$$

where τ and σ_n are the shear stress and tangential stress of the H-B envelope line and φ_t is the angle between the tangent line at a point and the horizontal line. The relationship between the c_t and the φ_t can be expressed as

Fig. 1 Diagram of the H-B failure criterion
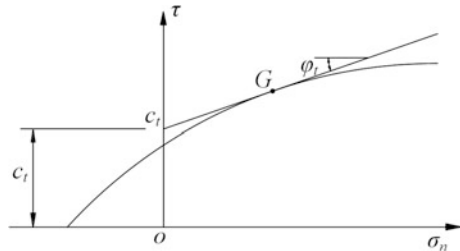
$$\tau = c_t + \sigma_n \tan \phi_t \tag{7}$$

Further, the relationship between c_t and φ_t can be written in the following form:

$$\frac{c_t}{\sigma_c} = \frac{\cos \varphi_t}{2} \left[\frac{mn(1 - \sin \varphi_t)}{2 \sin \varphi_t} \right]^{\frac{n}{1-n}} - \frac{\tan \varphi_t}{m} \left(1 + \frac{\sin \varphi_t}{n} \right) \left[\frac{mn(1 - \sin \varphi_t)}{2 \sin \varphi_t} \right]^{\frac{1}{1-n}} + \frac{s}{m} \tan \varphi_t \tag{8}$$

where the nonlinear shear strength index φ_t is unknown in the calculation of the upper bounds, which can reflect the instantaneous change in the tangent, and the c_t to be obtained by Eq. (8) is unknown. Their final values are optimized by the principle of minimum energy consumption.

2.3 The Strength Reduction Technique Based on the H-B Failure Criterion

Based on the tangent equation of the H-B failure criterion, using the shear strength reduction technique, strength indexes through the reduction are expressed as

$$\begin{cases} c_f = c_t/F_s \\ \varphi_f = \arctan(\tan \varphi_t/F_s) \end{cases} \tag{9}$$

where the nonlinear shear strength parameter φ_t is an unknown parameter in the upper limit calculation and c_t is obtained by Eq. (8).

3 Stability Analysis of the Fractured Rock Slopes with Vertical Cracks Subjected to the Hydraulic Effect Based on the H-B Failure Criterion

Generally, the stability analysis method for analyzing the effects of the pore water pressure on rock slopes can be divided into the following two categories: (1) reasonably simplifying the seepage flowing net and the saturation line to calculate the pore water pressure [2, 7, 8] and (2) considering the pore pressure to be the component of the overburden pressure such that the pore water pressure coefficient can be introduced [4–6, 11, 14]. Viratjandr and Michalowski [4] discussed four types of water drawdown situations (sudden, gradual, slow and steady drop) and gave the formula of work rate of the pore water pressure of the slope near rivers as follows:

$$W_u = \gamma_w r_0^3 \omega f_5 \tag{10}$$

where γ_w is the bulk density of water, r_0 is the polar diameter of the starting point of the logarithmic spiral failure line, ω is the angular acceleration of the sliding mass around the center of rotation, and f_5 is a function related to work rate done by the groundwater.

This paper adopted the pore water pressure calculation method of Viratjandr and Michalowski [4] to simplify the actual hydraulic gradient distribution by assuming the vertical potential line. The assumption ensured conservative calculation results and safer designs.

3.1 Failure Mechanisms of Fractured Rock Slopes with Vertical Cracks

For the sake of simplification of calculation, cracks were assumed vertical at the top of slopes (EF in Fig. 2), following the assumption by Utili [11] and we analyzed the failure mechanisms with the logarithmic spiral line beneath the toe of slopes, as shown in Fig. 2, including the two cases of water-filled cracks (Fig. 2a) and dry cracks (Fig. 2b).

The various symbols used in Fig. 2 are as follows: W, the gravity of the sliding mass; F_w, the concentrated force of water in the cracks; F_p, the pore water pressure; z_1, z_2 and z_3, the vertical distances between the slope water level and the sliding surface in the three regions; H, the slope height; β, the slope angle; δ, the crack depth; δ_w, the water level in the crack; h, the vertical distance from the groundwater level to the slope toe; l, the horizontal distance from the crack to the point E of the slope edge; L_1, the horizontal distance from point E to point F; L_2, the horizontal distance from the crack to point F; θ_0, θ_h and β', angle parameters of the failure

(a) $0 \le H - h \le \delta$ (b) $H - h > \delta$
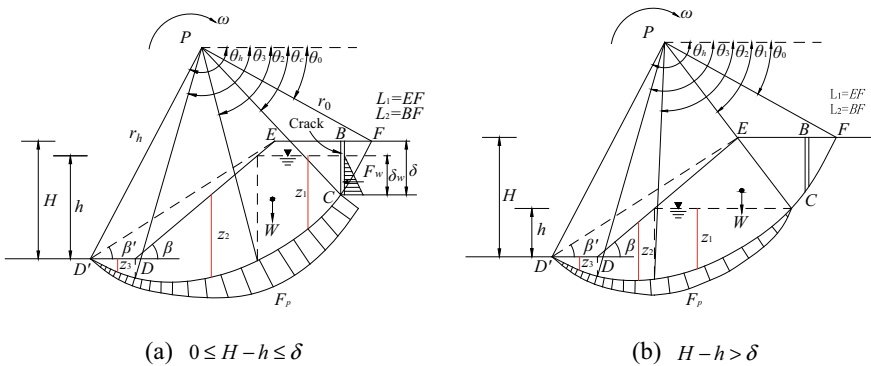
Fig. 2 Failure mechanisms

mechanism; θ_1–θ_3, angle parameters of the groundwater levels; θ_c, the angle related to the cracks; ω, the angular acceleration of the sliding mass around the center of rotation; r_0 and r_h, the polar diameters of the logarithmic spiral line; and P, the center of rotation.

The geometric relationship of the failure mode is as follows:

$$\frac{L_1}{r_0} = \frac{\sin(\theta_h - \theta_0)}{\sin \theta_h} - \left\{ e^{(\theta_h - \theta_0)\tan \varphi} \sin \theta_h - \sin \theta_0 \right\} \frac{\sin(\theta_h + \beta')}{\sin \beta' \sin \theta_h} \qquad (11)$$

$$\frac{L_2}{r_0} = \frac{\sin(\theta_c - \theta_0)}{\sin \theta_c} - \frac{\cos \theta_c}{\sin \theta_c} \left\{ e^{(\theta_c - \theta_0)\tan \varphi} \sin \theta_c - \sin \theta_0 \right\} \qquad (12)$$

Due to the assumption of the failure mechanisms through the bottom of the cracks, the crack depth δ and location l are not independent of each other. When the crack depth is known, θ_c can be determined by the unknown θ_0, β' and θ_h, as can l.

$$\begin{cases} e^{\tan \varphi_t \cdot \theta_c} \sin \theta_c = e^{\tan \varphi_t \cdot \theta_0} \sin \theta_0 \left(1 - \frac{\delta}{H}\right) + \frac{\delta}{H} e^{\tan \varphi_t \cdot \theta_h} \sin \theta_h \\ l/H = \left\{ \begin{array}{l} \frac{\sin(\theta_h - \theta_0)}{\sin \theta_h} - \left[e^{(\theta_h - \theta_0)\tan \varphi_t} \sin \theta_h - \sin \theta_0 \right] \\ \cdot \frac{\sin(\theta_h + \beta')}{\sin \beta' \sin \theta_h} - \left[\cos \theta_0 - e^{(\theta_c - \theta_0)\tan \varphi_t} \cos \theta_c \right] \end{array} \right\} / \frac{H}{r_0} \end{cases} \qquad (13)$$

3.2 Work Rate of the External Force

The work rate of the external force includes the work rate of gravity W_r, the work rate of the water pressure in the crack W_w and the work rate of the pore water pressure W_u.

Work rate of gravity. The work rate of gravity is calculated by the work rate of the soil weight in the area of PFD′ minus those in PEFPED′, EDD′ and BCF. The last is equal to the work rate of soil weight in the area of PFC minus those in PFB and PBC.

$$W_r = \omega \gamma r_0^3 (f_1 - f_2 - f_3 - f_4 - p_1 + p_2 + p_3) \qquad (14)$$

where f_1–f_4 and p_1–p_3 are functions related to α, θ_0, θ_c, θ_h, β, β' and φ_t, whose specific expressions are presented in Appendix.

Work rate of the pore water pressure. The work rate of the pore water pressure is calculated using the integral method. The groundwater level determines the work rate of the water pressure in the crack and the integral range of the work rate of the pore water pressure. Both of these work rates are discussed in the two cases of $0 \leq H - h \leq \delta$ and $H - h > \delta$, which are divided by the groundwater level in the bottom of the crack.

The expressions of z_1, z_2 and z_3 (Fig. 2) are easily obtained from the geometric relation and are as follows:

$$\begin{cases} \frac{z_1}{r_0} = e^{(\theta-\theta_0)tan\varphi_t} \sin\theta - e^{(\theta_1-\theta_0)tan\varphi_t} \sin\theta_1 \\ \frac{z_2}{r_0} = e^{(\theta-\theta_0)\tan\varphi_t} \sin\theta - e^{(\theta_h-\theta_0)\tan\varphi_t} \sin\theta_h \\ \qquad + \left(e^{(\theta-\theta_0)\tan\varphi_t} \cos\theta - e^{(\theta_3-\theta_0)\tan\varphi_t} \cos\theta_3\right)\tan\beta \\ \frac{z_3}{r_0} = e^{(\theta-\theta_0)\tan\varphi_t} \sin\theta - e^{(\theta_h-\theta_0)\tan\varphi_t} \sin\theta_h \end{cases} \tag{15}$$

The angle parameters θ_1, θ_2 and θ_3 are expressed as

$$\begin{cases} \sin\theta_1 e^{(\theta_1-\theta_0)\tan\varphi_t} = \sin\theta_0 + (H-h)/r_0 \\ \cos\theta_2 e^{(\theta_2-\theta_0)\tan\varphi_t} = \cos\theta_0 - L_1/r_0 - (H-h)/r_0 \cot\beta \\ \cos\theta_3 e^{(\theta_3-\theta_0)\tan\varphi_t} = \cos\theta_0 - L_1/r_0 - H/r_0 \cot\beta \end{cases} \tag{16}$$

1. $0 \leq H - h \leq \delta$

When $0 \leq H - h \leq \delta$, the groundwater level is higher than the bottom of the crack, the work rate of the water pressure in the crack should be considered, and the integral starting point of the work rate of the pore water pressure is the angle θ_c, as shown in Fig. 2a.

(1) Work rate of water pressure in the crack

Considering the water pressure in the crack as a concentrated force, the expression by its work rate is as follows:

$$W_w = \gamma_w \omega r_0^3 f_w \tag{17}$$

where

$$f_w = \frac{1}{2}\left(\frac{\delta+h-H}{r_0}\right)^2 \cdot \left(e^{(\theta_c-\theta_0)\tan\varphi} \sin\theta_c - \frac{1}{3}\frac{\delta+h-H}{r_0}\right) \tag{18}$$

When the crack is full of water, θ_1 is equal to θ_0 in Eq. (16), and h is equal to H in Eq. (18).

(2) Work rate of the pore water pressure

The method of Viratjandr and Michalowski [4] for calculating the work rate of the pore water pressure was adopted, as follows:

$$W_u = \gamma_\omega \cdot r_0^3 \cdot \omega \cdot \tan\varphi \cdot \left(f^1 + f^2 + f^3\right) \tag{19}$$

The work rate of the pore water pressure can be obtained by the integral method; namely, f^1, f^2 and f^3 in Eq. (19) can be expressed by other parameters, as follows:

$$f^1 = \int_{\theta_c}^{\theta_2} \frac{z_1}{r_0} e^{2(\theta-\theta_0)\tan\varphi_t} d\theta \tag{20}$$

$$f^2 = \int_{\theta_2}^{\theta_3} \frac{z_2}{r_0} e^{2(\theta-\theta_0)\tan\varphi_t} d\theta \tag{21}$$

$$f^3 = \int_{\theta_3}^{\theta_h} \frac{z_3}{r_0} e^{2(\theta-\theta_0)\tan\varphi_t} d\theta \tag{22}$$

Specific calculation results of f^1–$f3$ are presented in Appendix:

2. $H - h > \delta$

When the groundwater level is lower than the bottom of the crack, the work rate of the water pressure in the crack W_w is zero, and the integral starting point of the work rate of the pore water pressure is the angle θ_1, as shown in Fig. 2b. The calculation formula of the pore water pressure is nearly the same for Eq. (19), only with the f^1 changing into f^{1*}, expressed as

$$f^{1*} = \int_{\theta_1}^{\theta_2} \frac{z_1}{r_0} e^{2(\theta-\theta_0)\tan\varphi_t} d\theta \tag{23}$$

The specific calculation result of f^{1*} is presented in Appendix:

3.3 Inner Energy Dissipation Rate

For the energy analysis method, the internal energy dissipation rate only contains the energy dissipation rate of the soil mass at the intersection CD'. Further, D' coincides with the D when the failure surface is through the toe of the slope. The internal energy dissipation rate is

$$W_d = c_t \omega r_0^2 \frac{e^{2\tan\varphi_t(\theta_h-\theta_0)} - e^{2\tan\varphi_t(\theta_c-\theta_0)}}{2\tan\varphi_t} \tag{24}$$

3.4 Safety Factor

According to the principle of virtual work, the objective function can be obtained by equating the inner energy dissipation rate with the work rate of the external force:

$$W_w + W_u + W_r = W_d \tag{25}$$

Based on the H-B failure criterion, using the shear strength reduction technique, the strength indexes through the reduction are expressed as Eq. (10). Then, the Fs of the slope can be obtained:

$$F_S = \frac{c_f}{\gamma H} \frac{e^{2 \tan \varphi_f (\theta_h - \theta_0)} - e^{2 \tan \varphi_f (\theta_c - \theta_0)}}{2 \cdot \tan \varphi_f \left\{ f_1 - f_2 - f_3 - f_4 - p_1 + p_2 + p_3 + \frac{\gamma_w}{\gamma} \cdot \tan \varphi_f \cdot (f^1 + f^2 + f^3) + \frac{\gamma_w}{\gamma} \cdot f_w \right\}} \frac{H}{r_0}$$

(26)

where the internal friction angle φ_t and the cohesion c_t in the f_1–f_4, p_1–p_3, f^1–f^3 and f_w are replaced by φ_f and c_f.

The Fs is considered as the objective function, and its minimum value is optimized by the sequential quadratic programming method to obtain the failure mechanism and crack location.

4 Verification Calculation and Analysis

4.1 Comparisons of the Homogeneous Slopes Based on the H-B Failure Criterion

Three available cases (Benz et al. [24], Hammah et al. [25] and Zheng et al. [26]) of homogeneous slopes without cracks are used to verify the reliability of the H-B failure criterion for the stability analysis method of the rock slopes. The detailed parameters used in these cases are presented in Table 1. The comparisons of the present results with the available results from the three works noted above are shown in Table 2.

The comparison shows that when this paper adopts the tangential method to introduce the shear strength parameters of the H-B failure criterion, the errors between this method and the existing various calculation methods are small, with the maximum error being less than 6%. When using the EMC failure criterion, the errors between this method and the existing various calculation methods are also small, with the maximum error being less than 8%. Thus, the comparison calculation verifies the applicability of the calculation method in this paper.

In addition, the upper and lower bound finite element method of Li et al. [27, 28] is used to verify the reliability of the present method. In theory, when the basic parameters of the rock slopes are fixed and the stability evaluation index reaches the mean critical stability coefficient (N) of the upper and lower bounds defined by Li et al. [27, 28], the Fs of rock slopes should be 1.0. Based on the same parameters of the generalized H-B failure criterion, the calculated results of five examples are compared, as shown in Table 3.

Table 1 Detail parameters of available cases

Cases	β (°)	H (m)	γ (kN/m³)	σ_c (Mpa)	GSI	D	m_i	m	s	n	c (kPa)	φ (°)
Benz et al. [24]	35.5	10	25	30	5	0	2	–	–	–	20	20.89
Hammah et al. [25]	45	10	25	30	5	0	2	0.619	2.5×10^{-5}	0.619	20	20.89
Zheng et al. [26]	25	300	25	–	–	–	–	0.422	2.404×10^{-4}	0.5	317	22

Note c and φ are the material strength parameters used in the calculation of the equivalent M-C criterion (EMC)

Table 2 Comparisons of the Fs between the present results and the common approach solutions based on the H-B failure criterion

Cases	Available results				This paper	
	Bishop	FEM		Spencer	UBLA	
	EMC	EMC	GHB	EMC	EMC	GHB
Benz et al. [24]	1.37	1.37	1.51	–	1.374	1.424
Hammah et al. [25]	1.153	1.15	1.15	1.152	1.159	1.18
Zheng et al. [26]	–	1.1	1.06	1.08	0.999	1.001

Note the FEM is the finite element method

Table 3 Comparisons between the Fs of the present results and solutions by the upper and lower bound finite element method for the limit analysis based on the H-B failure criterion

β	GSI	m_i	$\sigma_c/\gamma H$	Li et al. [27, 28] (LBFEM)	Li et al. [27, 28] (SLIDE)	Present study	Maximum error (%)
75	70	35	0.717	1.0	1.016	1.032	3.2
60	70	35	0.200	1.0	1.005	1.038	3.8
45	70	15	0.176	1.0	1.012	1.046	4.6
30	70	15	0.075	1.0	1.023	1.060	6.0
15	70	15	0.026	1.0	1.010	1.060	6.0

The comparison shows that under all circumstances, the Fs values obtained in this paper were slightly larger than the lower limit of the finite element calculation results, and the maximum absolute error is no more than 6.0%. The statement of Li et al. [27, 28], "Mean results of the upper and lower bound finite element limit analysis method can bound the true stability coefficient (N) within $\pm$ 9% of the upper and lower solution," which means the upper solutions of Li et al. [27, 28] are no more than 9% larger than the lower solutions, shows that the method presented in this paper has the equivalent precision, thus proving that this method is effective.

4.2 Comparisons of Homogeneous Slopes Full of Water Based on the H-B Failure Criterion

Considering the effect of pore water pressure, the present results are compared with those of Saada et al. [29] under the condition of non-fractured rock slopes to further verify the reliability of this method. The parameters used in Saada et al. [29] were: $\beta = 60°$, $\gamma = 20$ kN/m³, $\sigma_c = 10$ Mpa, GSI= 30, $D = 0.0$, $m_i = 17$, $H = 6$–20 m, and the pore water pressure coefficient r_p values were 0.1 and 0.2, respectively. The present method uses γ_w/γ to express r_p in the non-fractured rock slopes full of water, adopting the definition of the safety factor (Γ) in Saada et al. [29] (that is, the ratio between the maximum resistance and the external force). The present results are compared with those of Saada et al. [29], as shown in Fig. 3. The results show that
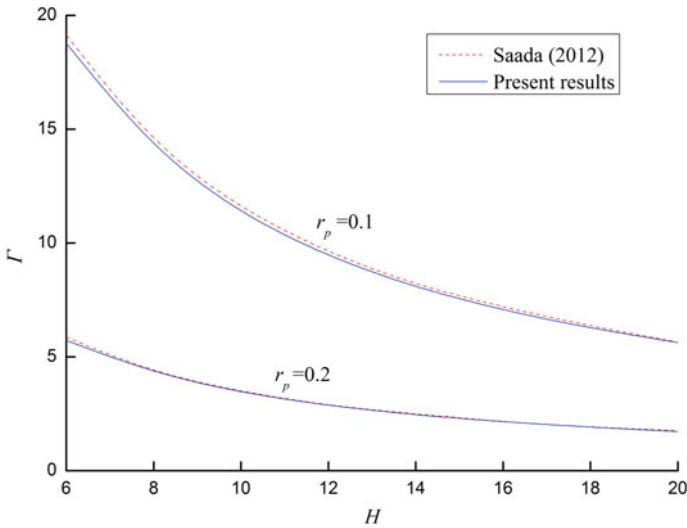
Fig. 3 Comparisons of the safety factor (Γ) of the slopes subjected to the hydraulic effect based on the H-B failure criterion

in the two cases, the results of this paper are slightly smaller than those calculated by Saada et al. [29], which indicates the results calculated using this method are closer to the real upper bound results.

5 Parametric Analysis

In this section, the influences of different parameters on the Fs and the potential slip surface of the fractured slopes subject to the hydraulic effect under the H-B failure criterion are analyzed.

5.1 Influence of the Groundwater Level and H-B Failure Criterion Parameters on the Fs

Considering the influence of the groundwater level and the H-B failure criterion parameters on the slope stability, Figs. 4, 5 and 6 present the changes in the Fs for various case parameters, as shown in Table 4.

Figures 4, 5 and 6 illustrate that the Fs of the slope decreases with the underground water level and the value of D increasing or the GSI decreasing. For these cases as shown in Fig. 5, when the m_i increases, the Fs decreases at a growing rate when the groundwater level is high ($h > 0.4H$) and increases at a reducing rate

(a) δ/H=0.1   (b) δ/H=0.3
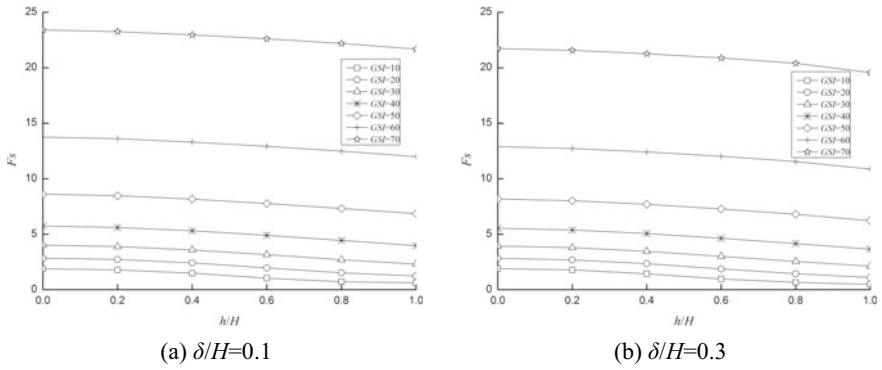
Fig. 4 Influence of the groundwater level and GSI on the Fs

(a) δ/H=0.1   (b) δ/H=0.3
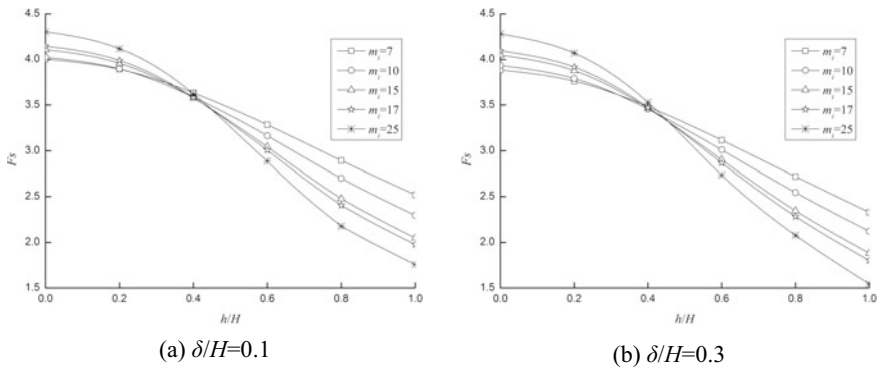
Fig. 5 Influence of the groundwater level and m_i on the Fs

(a) δ/H=0.1   (b) δ/H=0.3
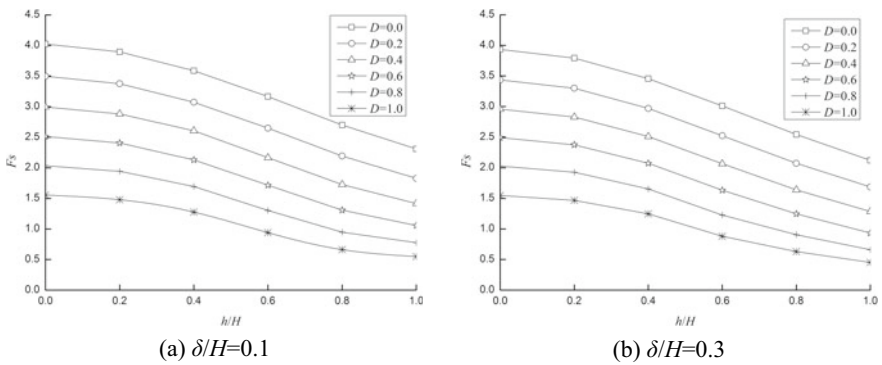
Fig. 6 Influence of the groundwater level and D on the Fs

Table 4 Calculation parameters

Serial number of figure	α (°)	β (°)	H (m)	γ (kN/m³)	γ_w (kN/m³)	σ_c (Mpa)	GSI	m_i	D	h/H	δ/H
Figure 4a	0	60	10	26	10	40	10–70	10	0	0–1	0.1
Figure 4b	0	60	10	26	10	40	10–70	10	0	0–1	0.3
Figure 5a	0	60	10	26	10	40	30	7–25	0	0–1	0.1
Figure 5b	0	60	10	26	10	40	30	7–25	0	0–1	0.3
Figure 6a	0	60	10	26	10	40	30	10	0–1	0–1	0.1
Figure 6b	0	60	10	26	10	40	30	10	0–1	0–1	0.3

when the groundwater level is low ($h < 0.4H$). The effect of the groundwater level is not discernible, especially with the high GSI. Moreover, when the GSI increases, the Fs exhibits a significant upward trend. It is found that the changes in the Fs level off when both the D value and the groundwater level are high.

5.2 Influence of the Crack Depth and H-B Failure Criterion Parameters on the Fs

Considering the influence of the crack depth and H-B failure criterion parameters on the slope stability, Figs. 7, 8 and 9 present the changes in the Fs for various case parameters, as shown in Table 5.

Figures 7, 8 and 9 illustrate that the Fs of the slope decreases with the crack depth and the D increasing or the GSI decreasing. The effect of the crack depth is less significant than that of the other parameters. For the cases as shown in Fig. 8, when
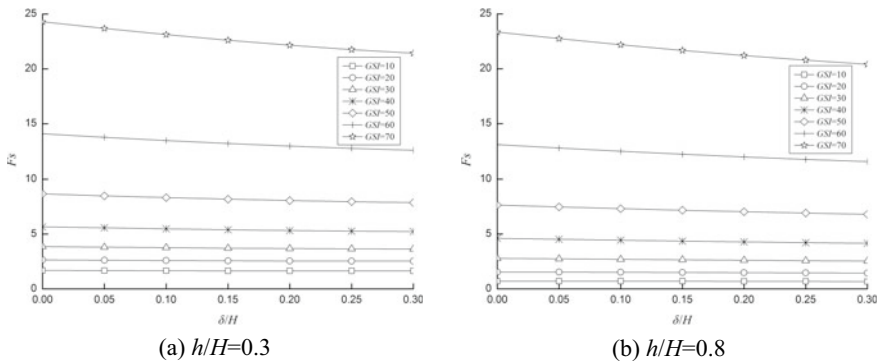
(a) h/H=0.3   (b) h/H=0.8

Fig. 7 Influence of the crack depth and GSI on the Fs
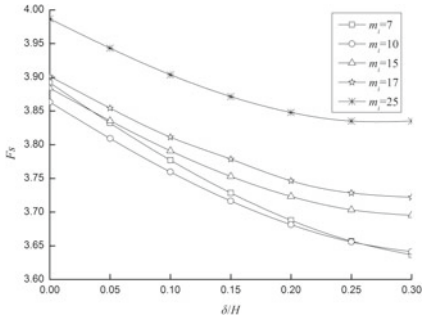
(a) h/H=0.3
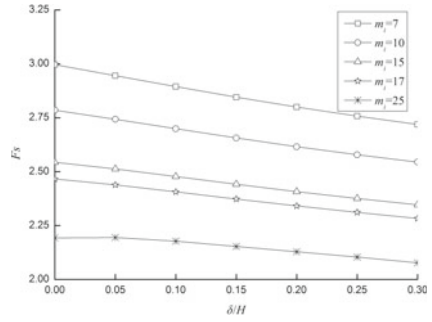
(b)`h/H=0.8

Fig. 8 Influence of the crack depth and m_i on the Fs
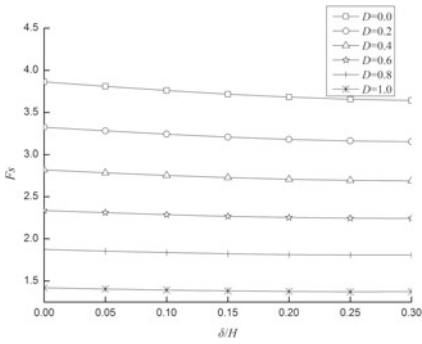
(a) h/H=0.3
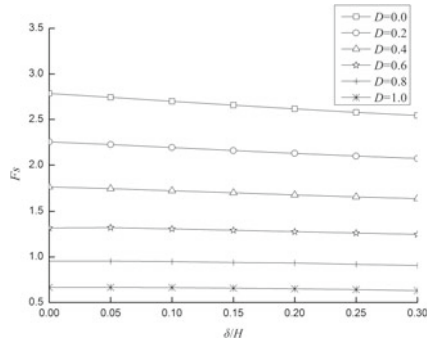
(b) h/H=0.8

Fig. 9 Influence of the crack depth and D on the Fs

Table 5 Calculation parameters

Serial number of figure	α (°)	β (°)	H (m)	γ (kN/m³)	γ_w (kN/m³)	σ_c (Mpa)	GSI	m_i	D	h/H	δ/H
Figure 7a	0	60	10	26	10	40	10–70	10	0	0.3	0.0–0.3
Figure 7b	0	60	10	26	10	40	10–70	10	0	0.8	0.0–0.3
Figure 8a	0	60	10	26	10	40	30	7–25	0	0.3	0.0–0.3
Figure 8b	0	60	10	26	10	40	30	7–25	0	0.8	0.0–0.3
Figure 9a	0	60	10	26	10	40	30	10	0–1	0.3	0.0–0.3
Figure 9b	0	60	10	26	10	40	30	10	0–1	0.8	0.0–0.3

the m_i increases, the Fs decreases when the groundwater level $h = 0.8H$ (>0.4H) and generally increases when the groundwater level $h = 0.3H$ (<0.4H), which is consistent with the analysis presented above.

5.3 Influences of the Groundwater Level and Crack Depth on the Slope Critical Failure Surface

The influences of the groundwater level and crack depth on the critical failure surface of the slope are studied in this section.

For the cases of Fig. 4a, b, with a fixed GSI = 30 in Table 4, the influences of the groundwater level on the critical failure surface of the slope and the corresponding failure mechanisms are studied, as shown in Fig. 10. With the increase in the groundwater level, the critical crack gradually expands to the edge of the slope but moves away from the edge of the slope when the groundwater level is elevated to the crack position. Even with this observation, the general trend of the failure domain is gradually reduced.

For the cases of Fig. 7a, b, with a fixed GSI = 30 in Table 5, the influences of the crack depth on the critical failure surface of the slope and the corresponding failure mechanisms are studied, as shown in Fig. 11. With the increase in the slope crack depth, the critical crack edge gradually moves toward the edge of the slope, which means that the failure surface gradually moves closer to the slope surface and

(a) $\delta/H = 0.1$ (b) $\delta/H = 0.3$
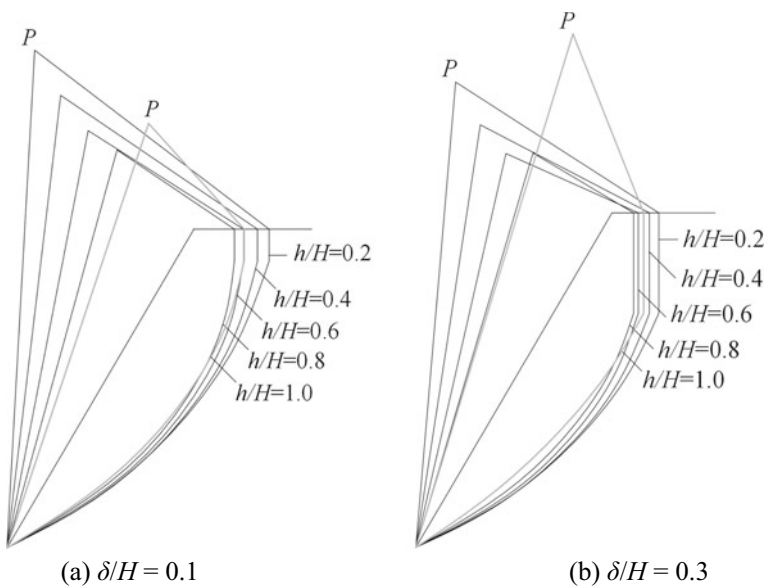
Fig. 10 Influence of the groundwater level on the slope critical failure surface

(a) h/H=0.3   (b) h/H=0.8
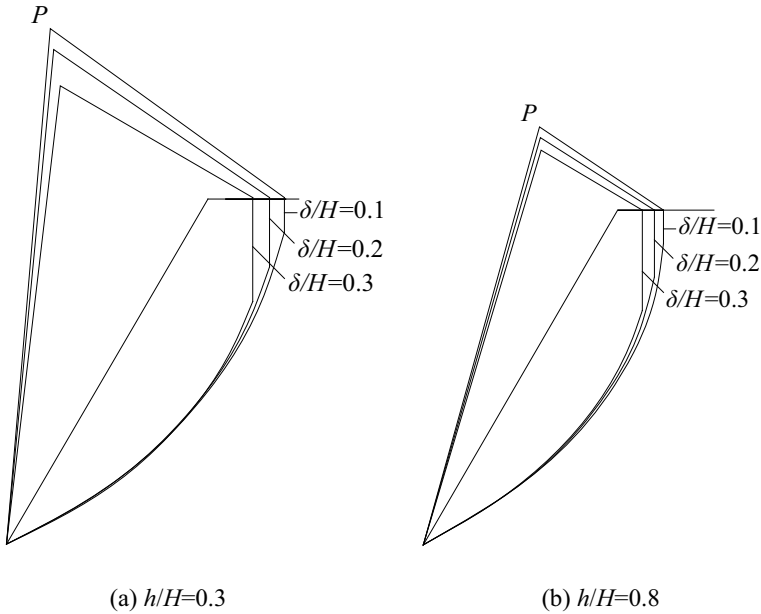
Fig. 11 Influence of crack depth on the slope critical failure surface

the damage area gradually decreases. Moreover, when the crack extends to the groundwater level and the crack is filled with water, the effect of crack depth becomes less significant.

6 Discussion

The H-B failure criterion assumes that the rock mass is isotropic, and as an analysis object, the slope rock mass must be isotropic as well. The rock mass can be divided into three groups according to the condition and the number of group of the structural surface. Group 1 is intact rock, Group 2 is rock containing a small amount (one or two sets of different directions) of joint surfaces, and Group 3 is rock containing a large amount (four groups and above) of joint surfaces. According to the scope of application of the Hoek–Brown failure criterion, when the rock mass is intact rock with no structural surface, jointed or fractured rock mass with four (or more) joint surfaces which are on the equivalence scale, in equal space and at the same level of strength, or weak rock with low strength, the rock mass could be regarded as an isotropic and homogeneous rock mass meeting the hypothesis of homogenization and equivalent continuum, which can be directly applied to the H-B failure criterion.

This paper carried out the upper bound limit analysis based on the assumption of plastic mechanics of rock and soil. As for complete rock mass with no structural surface, if considering the existence of fracture characteristics in the rock mass, it is necessary to determine whether the intact rock mass belongs to the plastic mode and to analyze the fracture development and its corresponding characteristics of energy consumption. The process is so complicated that the method in this paper is not applicable to the stability analysis of intact rock mass.

It has been shown that the H-B failure criterion could be directly applied to the jointed and fractured rock mass with four (or more) joint surfaces which are on the equivalence scale, in equal space and at the same level of strength and weak rock with low strength. Considering the fact that the multiple or multiple directional structure surfaces in the rock mass may have a direct effect on the distribution of fractures, this paper only studies the fractured slopes due to the characteristics of the distribution of slope cracks. In the meantime, this paper assumes that the cracks are developed vertically with known depth; thus, the analysis of the influence of crack depth and hydraulic conditions is simplified. The specific conditions such as crack inclination or the unknown crack depth are worthy of further studies.

7 Conclusions

(1) The safety factor formula of the fractured rock slope with vertical cracks under the effect of pore water pressure was obtained based on the H-B failure criterion. The influences of the groundwater level, crack depth and H-B failure criterion parameters on the Fs of the fractured rock slopes were investigated.

(2) When the groundwater level and crack depth increased, the Fs of the fractured rock slope gradually decreased. When the GSI increased, the Fs of the fractured rock slope significantly increased. When the D increased, the Fs of the fractured rock slope gradually decreased. When the m_i increased, the Fs gradually decreased when the groundwater level was low but gradually increased when the water level was higher.

(3) When the groundwater level and crack depth increased, the critical crack gradually moved to the edge of the fractured rock slope but moved away when the groundwater level rose to the crack position. Even with this observation, the general trend of the failure domain is gradually reduced.

Appendix

$$f_1 = \left[e^{3(\theta_h - \theta_0)\tan\varphi_t} (3\tan\varphi_t \cos\theta_h + \sin\theta_h) \right.$$
$$\left. - 3\tan\varphi_t \cos\theta_0 - \sin\theta_0 \right] / 3\left(1 + 9\tan^2\varphi_t\right) \tag{27}$$

$$f_2 = \frac{1}{6}\sin\theta_0 \frac{L_1}{r_0}\left(2\cos\theta_0 - \frac{L_1}{r_0}\right) \tag{28}$$

$$f_3 = \frac{1}{6}e^{(\theta_h - \theta_0)\tan\varphi_t}\left[\sin(\theta_h - \theta_0) - \frac{L_1}{r_0}\sin\theta_h\right]\left(\cos\theta_0 - \frac{L_1}{r_0} + e^{(\theta_h - \theta_0)\tan\varphi_t}\cos\theta_h\right) \tag{29}$$

$$f_4 = \frac{1}{2}\left(\frac{H}{r_0}\right)^2(\cot\beta' - \cot\beta)\left[\cos\theta_0 - \frac{L_1}{r_0} - \frac{1}{3}\frac{H}{r_0}(\cot\beta' + \cot\beta)\right] \tag{30}$$

$$p_1 = \left[e^{3\tan\varphi_t(\theta_c - \theta_0)}(3\tan\varphi_t\cos\theta_c + \sin\theta_c) - 3\tan\varphi_t\cos\theta_0 - \sin\theta_0\right]/3\left(1 + 9\tan^2\varphi_t\right) \tag{31}$$

$$p_2 = \frac{1}{6}\sin\theta_0\frac{L_2}{r_0}\left(2\cos\theta_0 - \frac{L_2}{r_0}\right) \tag{32}$$

$$p_3 = \frac{1}{3}e^{2\tan\varphi_t(\theta_c - \theta_0)}(\cos\theta_c)^2\left\{e^{\tan\varphi_t(\theta_c - \theta_0)}\sin\theta_c - \sin\theta_0\right\} \tag{33}$$

$$f^1 = \left[e^{3\tan\varphi_t(\theta_2 - \theta_0)}(3\tan\varphi_t\sin\theta_2 - \cos\theta_2) + e^{3\tan\varphi_t(\theta_c - \theta_0)}\right.$$
$$\left. (\cos\theta_c - 3\tan\varphi_t\sin\theta_c)\right]/\left(1 + 9\tan^2\varphi_t\right)$$
$$- \frac{\sin\theta_1}{2\tan\varphi_t}\left(e^{(2\theta_2 - 3\theta_0 + \theta_1)\tan\varphi_t} - e^{(2\theta_c - 3\theta_0 + \theta_1)\tan\varphi_t}\right) \tag{34}$$

$$f^2 = [(3\tan\varphi_t\sin\theta_3 - \cos\theta_3)e^{3(\theta_3 - \theta_0)\tan\varphi_t}$$
$$+ e^{3(\theta_2 - \theta_0)\tan\varphi_t}(\cos\theta_2 - 3\tan\varphi_t\sin\theta_2)]/\left(1 + 9\tan^2\varphi_t\right)$$
$$- \frac{\sin\theta_h}{2\tan\varphi_t}\left[e^{(2\theta_3 + \theta_h - 3\theta_0)\tan\varphi_t} - e^{(2\theta_2 + \theta_h - 3\theta_0)\tan\varphi_t}\right]$$
$$+ \tan\beta[(3\tan\varphi_t\cos\theta_3 + \sin\theta_3)e^{3(\theta_3 - \theta_0)\tan\varphi_t}$$
$$- e^{3(\theta_2 - \theta_0)\tan\varphi_t}(\sin\theta_2 + 3\tan\varphi_t\cos\theta_2)]/\left(1 + 9\tan^2\varphi_t\right)$$
$$- \frac{\cos\theta_3\tan\beta}{2\tan\varphi_t}\left[e^{3(\theta_3 - \theta_0)\tan\varphi_t} - e^{(2\theta_2 + \theta_3 - 3\theta_0)\tan\varphi_t}\right] \tag{35}$$

$$f^3 = [(3 \tan \varphi_t \sin \theta_h - \cos \theta_h)e^{3(\theta_h - \theta_0)\tan \varphi_t}$$
$$+ e^{3(\theta_3 - \theta_0)\tan \varphi_t}(\cos \theta_3 - 3 \tan \varphi_t \sin \theta_3)]/(1 + 9 \tan^2 \varphi_t) \tag{36}$$
$$- \frac{\sin \theta_h}{2 \tan \varphi_t}\left[e^{3(\theta_h - \theta_0)\tan \varphi_t} - e^{(2\theta_3 + \theta_h - 3\theta_0)\tan \varphi_t}\right]$$

$$f^{1*} = \frac{[(3 \tan \varphi_t \sin \theta_2 - \cos \theta_2)e^{3(\theta_2 - \theta_0)\tan \varphi_t} + e^{3(\theta_1 - \theta_0)\tan \varphi_t}(\cos \theta_1 - 3 \tan \varphi_t \sin \theta_1)]}{1 + 9 \tan^2 \varphi_t}$$
$$- \frac{\sin \theta_1 \left[e^{(2\theta_2 - 3\theta_0 + \theta_1)\tan \varphi_t} - e^{3(\theta_1 - \theta_0)\tan \varphi_t}\right]}{2 \tan \varphi_t}$$
$$\tag{37}$$

References

1. Michalowski RL (2012) Cracks in slopes: limit analysis approach to stability assessment. In: Geo-Congr ASCE, pp 442–50
2. Deng DP, Li L (2013) Stability analysis of slope with tensile crack under condition of seepage. J CentL South Univ (Sci Technol) 44(1):294–302
3. Zhao LH, Zou S, Deng DP, Han Z, Zhao B (2018) Development mechanism for the landslide at Xinlu Village, Chongqing, China. Landslides 15(10):2075–2081
4. Viratjandr C, Michalowski RL (2006) Limit analysis of submerged slopes subjected to water drawdown. Can Geotech J 43(8):802–814
5. Michalowski RL (1995) Slope stability analysis: a kinematical approach. Geotechnique 128 (4):283–293
6. Michalowski RL (2002) Stability charts for uniform slopes. J Geotech Geoenviron Eng 123 (6):351–355
7. Wang JX, Li Z, Chen W (2005) Lower bound analysis of soil slope stability using finite elements subjected to pore water pressure. Rock Soil Mech 26(8):1258–1262
8. Wang JX, Li Z (2007) Upper bound analysis of stability of soil slope subjected to pore water pressure using finite elements. Rock Soil Mech 28(2):213–218
9. Kim JM, Salgado R, Yu HS (1999) Limit analysis of soil slope subjected to pore-water pressures. J Geotech Geoenviron Eng ASCE 125(1):49–58
10. Yin JH, Chen J, Li CF (2003) A rigid finite element method for upper bound limit analysis of soil slopes subjected to pore water pressure. Chin J Geotech Eng 25(3):273–277
11. Utili S (2013) Investigation by limit analysis on the stability of slopes with cracks. Geotechnique 63(2):1–15
12. Utili S (2014) Discussion of "Stability assessment of slopes with cracks using limit analysis". Can Geotech J 51(7):822–825
13. Michalowski RL (2014) Reply to the discussion by Utili on "Stability assessment of slopes with cracks using limit analysis". Can Geotech J 51(7):826–827
14. Michalowski RL (2013) Stability assessment of slopes with cracks using limit analysis. Can Geotech J 50(10):1011–1021
15. Utili S, Abd AH (2016) On the stability of fissured slopes subject to seismic action. Int J Numer Anal Methods Geomech 40(5):785–806
16. Zhao LH, Cheng X, Zhang YB, Li L, Li DJ (2016) Stability analysis of seismic slopes with cracks. Comput Geotech 77:77–90

17. Hoek E, Brown ET (1980) Empirical strength criterion for rock masses. J Geotech Eng Div 106(15715):1013–1035
18. Hoek E, Brown ET (1997) Practical estimates of rock mass strength. Int J Rock Mech Min Sci 34(8):1165–1186
19. Zhu HH, Zhang Q, Zhang LY (2013) Review of research progresses and applications of Hoek-Brown strength criterion. Chin J Rock Mechan Eng 10:1945–1963
20. Zhao LH, Yang F, Zhang YB et al (2015) Effects of shear strength reduction strategies on safety factor of homogeneous slope based on a general nonlinear failure criterion. Comput Geotech 63:215–228
21. Zhao LH, Cheng X, Li L, Chen JQ, Zhang YB (2017) Seismic displacement along a log-spiral failure surface with crack using rock Hoek-Brown failure criterion. Soil Dyn Earthq Eng 99 (12):74–85
22. Zhao LH, Cheng X, Li DJ, Zhang YB (2019) Influence of non-dimensional strength parameters on the seismic stability of cracked slopes. J Mt Sci 16(1):153–167
23. Zhao LH, Yang XP, Huang F, Tang YG, Hu SH (2018) Variational analysis of the ultimate pullout capacity of shallow circular anchor plates in rock foundations based on the Hoek-Brown failure criterion. Int J Rock Mech Min Sci 106:190–197
24. Benz T, Schwab R, Kauther RA et al (2008) A Hoek-Brown criterion with intrinsic material strength factorization. Int J Rock Mech Min Sci 45(2):210–222
25. Hammah RE, Yacoub TE, Corkum BC, Curran JH (2005) The shear strength reduction method for the generalized Hoek-Brown criterion. Alaska Rocks. In: The 40th US symposium on rock mechanics (USRMS): rock mechanics for energy, mineral and infrastructure development in the northern regions. ARMA, Alaska, pp 1–6
26. Zheng H, Sun GH, Liu DF (2009) A practical procedure for searching critical slip surfaces of slopes based on the strength reduction technique. Comput Geotech 36(1–2):1–5
27. Li AJ, Merifield RS, Lyamin AV (2008) Stability charts for rock slopes based on the Hoek-Brown failure criterion. Int J Rock Mech Min Sci 45(5):689–700
28. Li AJ, Lyamin AV, Merifield RS (2009) Seismic rock slope stability charts based on limit analysis methods. Comput Geotech 36(1–2):135–148
29. Saada Z, Maghous S, Garnier D (2012) Stability analysis of rock slopes subjected to seepage forces using the modified Hoek-Brown criterion. Int J Rock Mech Min Sci 55(55):45–54
30. Yang XL, Li L, Yin JH (2004) Stability analysis of rock slopes with a modified Hoek-Brown failure criterion. Int J Numer Anal Methods Geomech 28(2):181–190
31. Collins IF, Gunn CIM, Pender MJ et al (1986) Slope stability analyses for materials with a non-linear failure envelope. Int J Numer Anal Methods Geomech 12(5):533–550
32. Drescher A, Christopoulos C (1988) Limit analysis slope stability with nonlinear yield condition. Int J Numer Anal Methods Geomech 12(3):341–345
33. Hoek E, Carranze-Torres C, Corkum B (2000) Hoek–Brown failure criterion-2002 edition. In: Proceedings of the North American Rock mechanics society meeting, pp 267–273

Permanent Deformation Behavior of Coarse-Grained Residual Subsoil Under Large Amplitude Loading Cycles

Xiao-bin Chen, Liguo Chen and Jiasheng Zhang

Abstract Traffic-load-induced deformations in a subgrade occur due to long-term loading and unloading cycles. Residual soils with coarse-grained gradation have been extensively used as subgrade soil in the mountainous region of China. It is of practical value to study the permanent deformation behavior of coarse-grained residual soils subjected to different cyclic stress ratios (CSRs) under their optimal moisture content conditions. This paper presents an experimental investigation of the effect of the CSR on the accumulative deformation behavior of a residual soil as well as field tests on the traffic-load-influenced depths in a case subgrade. A series of large-scale monotonic triaxial (TX) tests and large-scale cyclic TX tests, wherein 50,000 loading cycles were applied, were conducted under optimal moisture content conditions. An increasing CSR increases the breakage of the coarse-grained particles. The values of the particle breakage under monotonic loading conditions are compared to corresponding values under cyclic loading conditions using the Hardin relative breakage index. For the cyclic TX tests, the long-term cyclic loading produces a >1.5-times greater Hardin breakage index compared to the values obtained from monotonic TX tests. The obtained experimental results show that an increasing CSR increases the cumulative strain but, in contrast, decreases the resilient modulus. The CSR primarily shapes the strain–stress curves obtained from the cyclic TX tests. Based on the laboratory results, a cumulative strain prediction

X. Chen (✉)
School of Civil Engineering, Key Laboratory of Heavy-Haul
Railway Engineering Structures, Central South University, 22 South Shaoshan Road,
410075 Changsha, Hunan, China
e-mail: chen_xiaobin@csu.edu.cn

L. Chen
School of Civil Engineering, Central South University, 22 South Shaoshan Road,
410075 Changsha, Hunan, China
e-mail: anselchen1119@gmail.com

J. Zhang
School of Civil Engineering, National Engineering Laboratory for High-Speed
Railway Construction, Central South University, 22 South Shaoshan Road,
410075 Changsha, Hunan, China
e-mail: jszhang_csu@vip.163.com

formula, as well as a formula for the prediction of the steady resilient modulus, was established. The field tests were also involved in the case study on accumulative deformation prediction. Consequently, the traffic-load-influenced depths were identified, and an empirical method for predicting traffic-load-induced deformation was established for this residual soil subgrade. The magnitude of the CSR, the number of traffic-loading cycles, and the in situ confining pressure are considered in the empirical method. Good agreement between the predicted deformation and the measured deformation indicates the feasibility of this method. The intensity of dynamic stresses on the subgrade surface and the attenuation law of the dynamic stresses along with the subgrade depth were also discussed. The findings are expected to improve our understanding of the permanent deformation behavior of coarse-grained residual soil under optimal moisture content conditions when subjected to long-term traffic loading.

1 Introduction

Residual soil is widely distributed, especially in the mountainous regions of the Hunan Province of China [1, 2]. Blight and Leong [3] noted that residual soil is a soil-like material, derived from the weathering and decomposition of rock fragments that have not been transported from its original location. Therefore, the properties of residual soil depend on the properties of the parent rock and the weathering conditions. The tested local residual soil derives from local red mudstone and has been extensively used as the subsoils of expressways under optimal moisture content conditions. The local red mudstone belongs to soft rock, which commonly has uniaxial compressive strengths of less than 15 MPa and a density of less than 2.65 g/cm^3. When naturally weathered, this mudstone breaks into blocky flakes and eventually into residual coarse-grained soil, which is often used as fills when constructing embankments in mountainous regions in China. As expected, the subgrade of an expressway subjected to traffic-loading cycles results in unwanted deformation. Due to its coarse-grained gradation and the insufficient studies on this local residual subsoil, the long-term deformation of red mudstone residual subsoil remains unknown. It is therefore of great practical relevance to investigate the cyclic deformation behavior of the local residual subsoil under optimal moisture content conditions.

The literature includes numerous studies on soils subjected to cyclic loading, including [4–16] small-scale cyclic triaxial (TX) tests have become a common testing setup for investigating the cyclic behaviors of fine-grained soils under saturated conditions [17–20]. Several permanent strain prediction methods have been proposed for fine-grained subsoil. For instance, Li and Selig [21] improved the documented methods in the literature for predicting the cumulative deformation of

fine-grained subgrade soil under cyclic loads. Chai and Miura [5] developed an empirical equation for the permanent strain evaluation of sensitive clay subsoil; they found that the traffic-load-influenced depth was approximately 6 m. Hatanaka et al. [22] presented the results of a series of laboratory tests on in situ sandy soils to investigate the accumulative deformation. Cui et al. [6] analyzed the critical cyclic stress ratio (CSR) for alluvial silt subsoil based on in situ tests to simulate the permanent deformation of traffic-load-induced depths. Guo et al. [23] studied the long-term deformation behavior of saturated soft clays using a type of undrained cyclic loading test, and an empirical formula for permanent strain as a function of the number of cycles, cyclic stress amplitude and confining pressure were established. Wichtmann and Triantafyllidis [24] focused on the accumulative deformation due to the stress relaxation of average effective stresses when cyclic loading was applied under undrained TX conditions. Empirical methods used to determine long-term cyclic load-induced deformation have been established using the cumulative shear strain of fine-grained soils in their saturated conditions.

Due to the different gradation forms of fine-grained soils, the properties of coarse-grained soils have become an interest of researchers. Studies have been conducted on the properties of coarse-grained soils using large-scale laboratory tests and full-scale field tests [25–32]. Pitman et al. [29] investigated the effect of the coarse grain content on soil porosity. Vallejo and Mawby [31] studied the shear strength at different coarse grain contents using large-scale TX tests. Lade et al. [28] investigated the effect of the coarse grain content on the collapsibility of a granular mixture. Elias and Titi [33] investigated the correlations between the resilient modulus and the basic properties of various Wisconsin coarse-grained subgrade soils using repeated load TX testing. Dash and Sitharam [26] investigated the stress–strain relationships of coarse-grained soil, the critical state characteristics of which were the focus of Bandini and Pham [25]. Trani and Indraratna [34] estimated the limitation of the Kozeny–Carman formula by computing the parameters of hydraulic conductivity for fully saturated granular materials. Zhao and Zhang [32] conducted drained and undrained TX tests on several widely graded soils with different coarse contents at low confining stresses. They found that the soil microstructure changes from a fine-controlled structure to a coarse-controlled structure beyond a critical coarse content of $\sim 70\%$. Ban and Park [35] conducted repeated-load resilient modulus-deformation tests on coarse-grained subgrade soils mixed with various stabilizers to investigate the strength and deformation characteristics of modified soil mixtures. The large-scale cyclic setups were also used to investigate and model coarse-grained granular materials and residual soils [36–38]. The loading-induced deformation of coarse-grained subsoil has been highlighted by several laboratory studies and numerical simulations [39–41]. Karg and Haegeman [42] presented an experimental investigation of strain accumulation in granular soils due to dynamic loading during long-term cyclic loading, therein illustrating the parameters that influence strain accumulation. Craciun and Lo [43] presented a

cyclic TX testing system and associated experimental techniques that overcome the challenges of testing unbound granular base materials as unsaturated soils. Considering the stress state, the void ratio, and the dynamic loading amplitude, Karg et al. [44] proposed a cumulative deformation model for granular non-cohesive soils at small strain levels. Trinh et al. [13] studied the mechanical behavior of fouled ballasts in the laboratory using a large-scale TX cell. Each specimen was reconstituted to a dry density of 2.01 kg/m^3 at three water contents (4, 6, and 12%) corresponding to saturation degrees of 32, 48, and 100%, respectively. The authors set up a constitutive model for permanent deformation that accounts for the stress level, the number of cycles, and the soil water content. The deformation behavior of coarse-grained materials depends on their grading, and the deformation of coarse-grained granular materials is the result of densification/dilation, distortion, and attrition [45]. A number of deformation prediction methods have been proposed for coarse-grained soil and granular materials, namely empirical equation methods, numerical methods, and equivalent static loading methods. Most empirical equations have been derived based on an empirical relation between permanent deformations (or strains) and the number of load cycles at a particular stress state (i.e., [46–49]. Among them, the power equation proposed by Monismith et al. [50] and the model developed by Li and Selig [21] have been widely used for cohesive soil under repeated loading. Most empirical functions are limited in terms of predicting cumulative deformation under a given confining pressure because the model parameters ignore the influence of the confining pressure on the cumulative strain. The confining pressure strongly influences the permanent deformation of specimens in TX tests. Moreover, most of the tested coarse-grained materials are in saturated conditions. A challenge could be encountered when the documented methods are used to predict the permanent deformation of residual subsoil under optimal moisture content conditions.

Although few empirical methods and numerical methods have been proposed to predict the permanent deformation behavior of fine-grained soils, an ideal standard for extended usage has yet to be developed due to the variations in soil properties (i.e., the gradation and the moisture content). Most such soils are saturated clay, silty sands, or silty clay. Commonly, the numbers of loading cycles in the TX are very limited, i.e., the limited number of cycles was no more than 1000. A large number of loading cycles are particularly important for the deformation behavior of subsoils on site. Wichtmann and Triantafyllidis [24] found that a high cyclic loading (large number of cycles, i.e., $N \geq 1000$) may lead to strain accumulation or stress relaxation in the soil even though the strain amplitude is small. Local red mudstone residual soil has been extensively used as subsoils under optimal moisture content conditions, and its gradation is far different from that of fine-grained subsoils. However, studies on the deformation behavior of residual subsoils subjected to long-term cyclic loading have not been sufficiently documented. The use of these documented methods to predict the permanent deformation of residual subsoil under optimal moisture content conditions is not acceptable. It has been documented that the cyclic cumulative deformation behaviors of subsoils in the TX tests are influenced by the CSR, confining pressure, loading frequency, number of loading cycles, loading history, drainage conditions

[23]. Among them, the CSR, number of loading cycles, and confining pressure are typically dominant. It is of practical value to evaluate the influences of the CSR and the confining pressure on the particle breakage, resilient modulus and cumulative deformation of the tested residual soils when each specimen is subjected to 50,000 loading cycles. To address this insufficiency, this paper first presents an experimental investigation of the effects of the CSR on the deformation behavior of local coarse-grained residual subsoil. To further understand the deformation behavior of this subsoil, monotonic and long-term cyclic TX tests were conducted using large-scale specimens (300 mm in diameter and 600 mm in height). The usage of large-scale specimens attempts to reduce the discrete behavior caused by the use of large particles [51]. Each specimen is tested under optimal moisture content conditions. In the following section, the materials and test method are detailed, followed by the results and analysis. The cyclic permanent strain of the tested soils was compared under different CSRs. The values of particle breakage under the monotonic loading condition are compared to corresponding values for the cyclic loading condition calculated using the Hardin relative breakage index. Furthermore, this paper presents the results of a field test to determine the significant traffic-load-influenced depth for subgrade filled with coarse-grained residual soils. An empirical method for predicting traffic-load-induced deformation is established for a subgrade constructed with residual soil, and the predicted deformation of the case subgrade is compared to the deformation predicted by other methods. The findings are expected to improve our understanding of the permanent deformation behavior of coarse-grained residual soil under optimal moisture content conditions when the soil is subjected to long-term traffic loading.

2 Materials and Testing Methods

2.1 Testing Materials

The tested soils were taken from the top layer of a subgrade constructed with coarse-grained residual soil, as observed in Fig. 1a. The residual soil is light red and is produced from the weathering and decomposition of red mudstone (parent rock). The parent rock is very soft and has a uniaxial compressive strength of 6.2 MPa under dry conditions and a uniaxial compressive strength of 3.6 MPa under saturated conditions. Its main chemical compounds are S_iO_2, Al_2O_3, and Fe_2O_3. The grain size distribution (GSD) of the residual soil is plotted in Fig. 1b, and the soil's basic physical parameters are summarized in Table 1. The median grain size diameter (d_{50}) is 6.33 mm, and the uniformity coefficient (Cu) is 33, indicating well-graded subsoil. This soil can be classified as GP-GC according to the Unified Soil Classification. The void ratio is 0.56, corresponding to a relative density of 74%. The optimal moisture content and maximum dry density were obtained using the standard Proctor compaction test (ASTM, D1557).
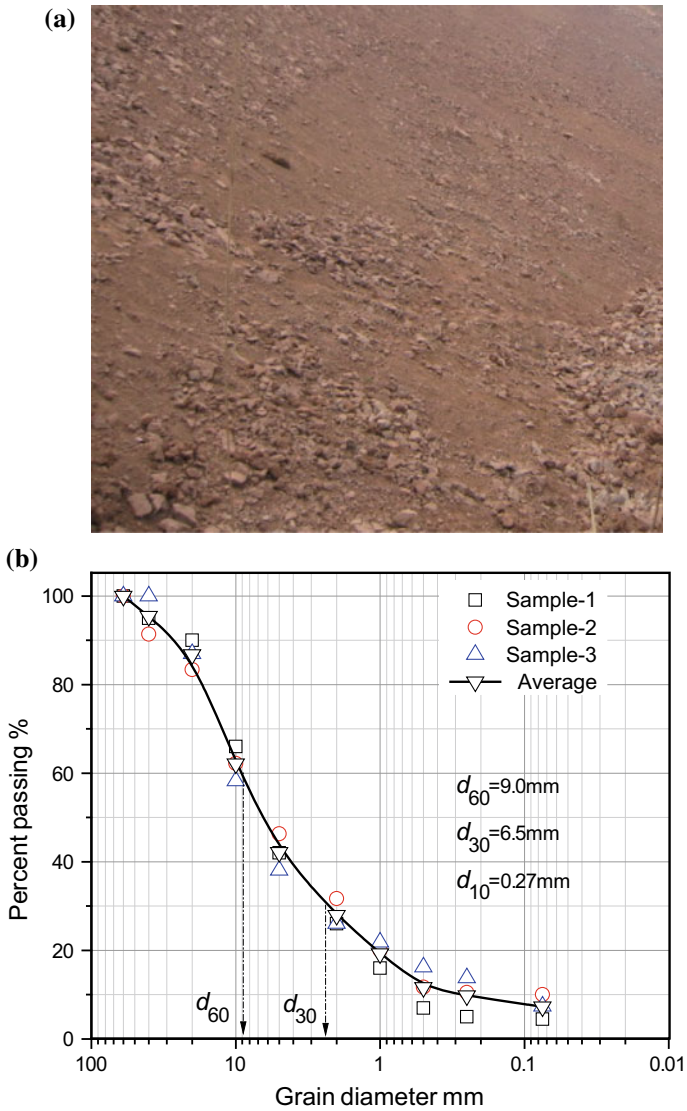
Fig. 1 Red residual soil and GSD: **a** Red residual soil, **b** GSD

Table 1 Basic physical parameters of tested soil

Bulk density (g/cm^3)	Moisture content (%)	Max dry density (g/cm^3)	Optimum moisture content (%)	Liquid limit (Fines) (%)	Plastic limit (Fines) (%)
1.99	7.1	1.94	8.9	27.0	18.5

2.2 Testing Apparatus

The utilized apparatus is a large-scale TX testing setup (shown in Fig. 2a), with a high control and measuring precision. The setup is an electromechanical monotonic and cyclic loading TX testing setup, and the stress controlling unit supplies the cyclic loading under different frequencies. The apparatus complies with the standard procedures of ASTM D7181-11 [52], ASTM D5311-92 [53], and ASTM D3999-91 [54]. The basic parameters of the apparatus are detailed in Table 2.
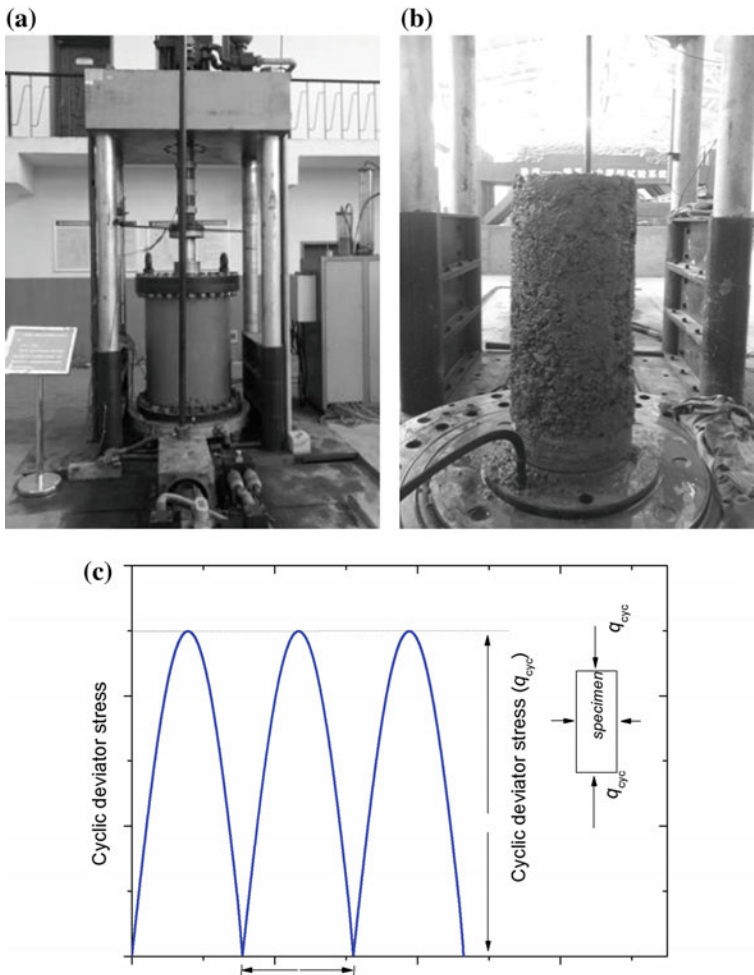
Fig. 2 Testing apparatus and cyclic loading wave, **a** testing apparatus, **b** large scale specimen, **c** cyclic loading wave

Table 2 Parameters of large-scale TX testing apparatus

Parameters	Value
Axial force/kN	0–150
Axial force accuracy/%	<0.05% of full scale
Axial displacement range/mm	120
Axial displacement accuracy	0.1 mm(i.e., <0.01% strain)
Confining pressure range/MPa	0–1.0
Confining pressure accuracy	<0.05% of full scale
Drained volumetric accuracy	0.5 mm^3 (i.e., <0.01% volumetric strain)
Frequency of cyclic loading/Hz	0–15
Dimension of specimen	300 mm × 600 mm

2.3 Testing Methodology

Each specimen is 300 mm in diameter and 600 mm in height (i.e., an aspect ratio of 2.0), as shown in Fig. 2b. This satisfies the widely accepted suggestion proposed by Varadarajan et al. [51], who suggested that the grain's diameter should not be greater than 1/6–1/10 of the specimen diameter. The relative compaction degree of each specimen is set as 96% to satisfy the in situ compaction degree requirements. During specimen compaction, the residual soil was poured into a cylindrical steel mold in five layers. The residual soil was then compacted layer by layer to achieve the target density. Each layer was compacted to a target dry density, namely 1.86 g/cm^3, to obtain a relative compaction degree of 96%. All the specimens were compacted and tested under optimum moisture content conditions. Then, each specimen was isotropically consolidated under a given confining pressure. Finally, a strain-controlled monotonic load or a principal stress-controlled cyclic load was applied to the specimen under undrained conditions. Because each specimen retains the optimal moisture content before and after the test, there are no saturation and drainage procedures performed during the TX testing. The testing method applied during the monotonic TX test was generally consistent with ASTM D7181-11, and the procedures applied during the cyclic loading tests were generally consistent with ASTM D5311-92 [53]. In the monotonic TX test, the rate of shear displacement was 0.1 mm/min. Table 3 summarizes the monotonic TX testing programs.

In the cyclic TX tests, the stresses were controlled by the different CSRs, which are defined in Eq. (1).

$$CSR = q_{cyc}/q_f \tag{1}$$

where q_{cyc} is the cyclic deviator stress and q_f is the undrained peak shear strength of the monotonic TX test. A semi-sinusoidal wave type with a constant frequency of 5 Hz was applied to each partially saturated specimen, as shown in Fig. 2c. The 50,000 long-term cycles were applied to each specimen unless its strain exceeded 5% (the monotonic loading failure state). Seven CSRs were applied under 50, 100, and

Table 3 Undrained monotonic TX tests and peak shear strength q_f

Specimens	Confining pressure (kPa)	Static failure deviator stress $(\sigma_1 - \sigma_3)_f$ (kPa)	Relative compaction degree (%)
T_1	25	175.6	96
T_2	50	333.4	96
T_3	100	496.6	96
T_4	200	695.0	96

Table 4 Cyclic loading TX testing programs

Specimens	Confining pressure (kPa)	Cyclic stress ratio (CRS)	Loading cycles (n)	Drainage conditions
C_{1-7}	50	0.1, 0.2, 0.3, 0.4, 0.5, 0.6, 0.8	$\leq 50,000$	Undrained
C_{8-14}	100	0.1, 0.2, 0.3, 0.4, 0.5, 0.6, 0.8	$\leq 50,000$	Undrained
C_{15-21}	200	0.1, 0.2, 0.3, 0.4, 0.5, 0.6, 0.8	$\leq 50,000$	Undrained

200 kPa confining pressures. The testing programs for the long-term cyclic loading TX tests are summarized in Table 4.

In addition, both pre- and post-testing sieve analyses were performed for each specimen in the TX tests. To evaluate the particle breakage due to the compaction of a specimen, three specimens were sieved prior to the TX tests. An average particle breakage index (PBI) was obtained, and the results showed that the average particle breakage due to compaction was 1.9%. This value was subsequently subtracted from the breakage index for the specimens produced by the long-term cyclic loading TX tests.

3 Results and Discussion

3.1 Testing Results

Figure 3a presents the monotonic TX results in the form of deviator stress and axial strain. Figure 3b presents the monotonic TX results in the form of deviator stress and the mean effective stress. All the stresses are effective stresses because no pore water pressure was produced during the testing. Figure 3a shows that the stress–strain curves exhibit a similarity under different confining pressures. Generally, the deviatoric stress increases to a peak at an axial strain of 3–5%, followed by a slow decline to a steady value. The experimental results indicate that the specimen fails when the axial strain exceeds 5%. The increasing confining pressure increases the

peak deviatoric stress as well as the residual deviatoric stress in the steady state. This peak deviatoric stress is called the undrained peak shear strength of the monotonic TX test: q_f. The peak shear strength of each specimen is summarized in Table 4. Figure 3b plots the linear Mohr–Coulomb envelope of the mean effective stress versus the deviator stress coordinate system. When the confining pressure is relatively low, a nonlinearity is observed in the Mohr–Coulomb envelope for the coarse-grained soil. For example, the peak deviator stress does not sit on the linear Mohr–Coulomb envelope when the confining pressure is 25 kPa. This is consistent with the finding of Trani and Indraratna [34], who believed that the shearing dilation of coarse-grained granular soil accounts for the nonlinearity of the Mohr–Coulomb envelope. Using the linear envelop, the cohesion force of the tested residual soil is identified as 86 kPa, and the friction angle is found to be 24°.

A total of 21 specimens were successfully tested under cyclic loading in undrained conditions. The similarity of the changing pattern between the accumulative strain and the resilient modulus was observed during testing. Figure 4a presents a typical axial stress-loading cycle curve for specimen C_{12}. The initial confining pressure is 100 kPa, and the CRS is 0.5 (the cyclic deviator stress = 156 kPa). Figure 4a shows that the permanent axial strain dramatically increases as the number of loading cycle increases to 3000 cycles, and then, the axial strain continues to slowly increase with a decreasing accumulation rate. The cumulative axial strain increases from 0% to 0.85% in the first 3000 loading cycles, followed by a marginal increase of 0.35% within the next 47,000 loading cycles. The cumulative strain produced in a single loading cycle decreases with increasing number of loading cycles. This illustrates that the inclination of the stress–strain hysteretic loops decreases with increasing number of loading cycles. Figure 4b draws typical variations in the resilient modulus with increasing loading cycles. The resilient modulus, M_R, is defined as follows in this study:

$$M_R = \frac{q_{cyc}}{\varepsilon_{a,r}} \qquad (2)$$

where q_{cyc} is the cyclic deviator stress and $\varepsilon_{a,r}$ is the resilient portion of the axial strain. Figure 4b shows that the resilient modulus decreases with increasing number of loading cycles. The resilient modulus decreases dramatically in the first few thousand loading cycles, followed by a slow decline to a steady state beyond 30,000 cycles.

3.2 Particle Breakage Index

During cyclic TX testing, the similarity of the changing pattern of the grain size distribution curve is observed under different confining pressures. Typical pre- and post-cyclic loading test grain size distribution curves are shown in Fig. 5a under a confining pressure of 50 kPa. The post-test grain distribution curve is similar to the
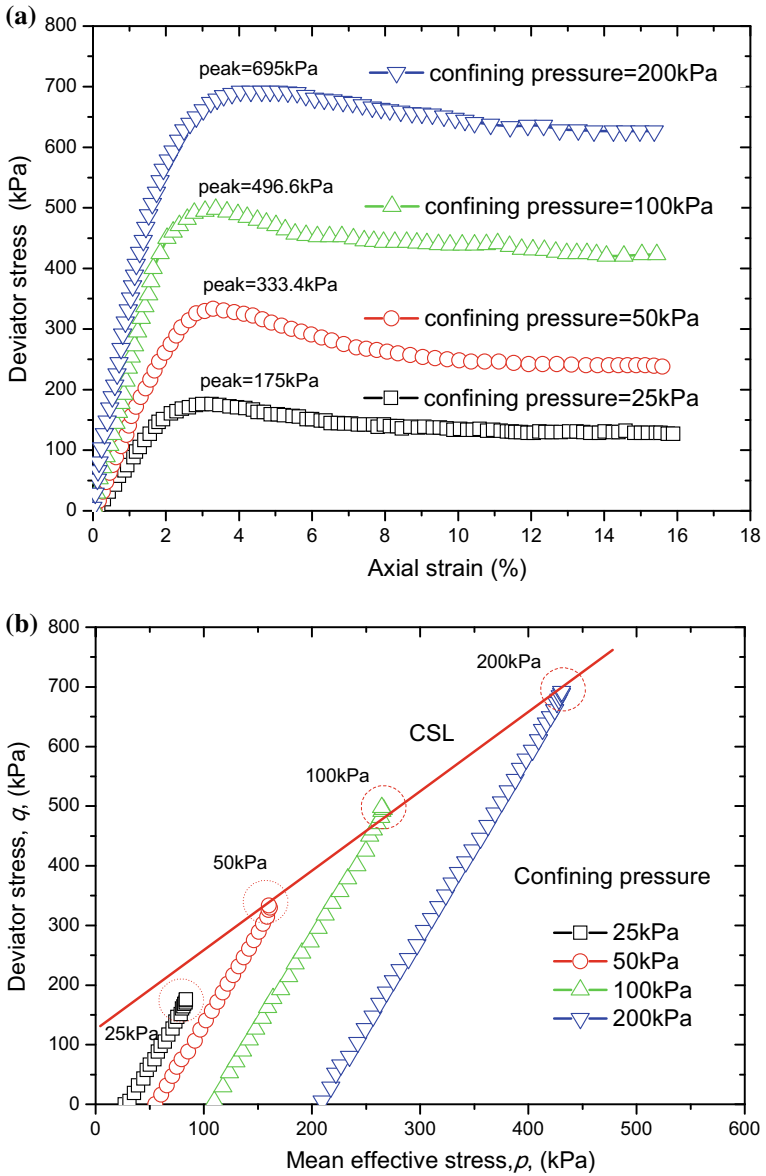
Fig. 3 Results of monotonic tests: **a** Deviator stress versus axial strain, **b** deviator stress versus mean stress
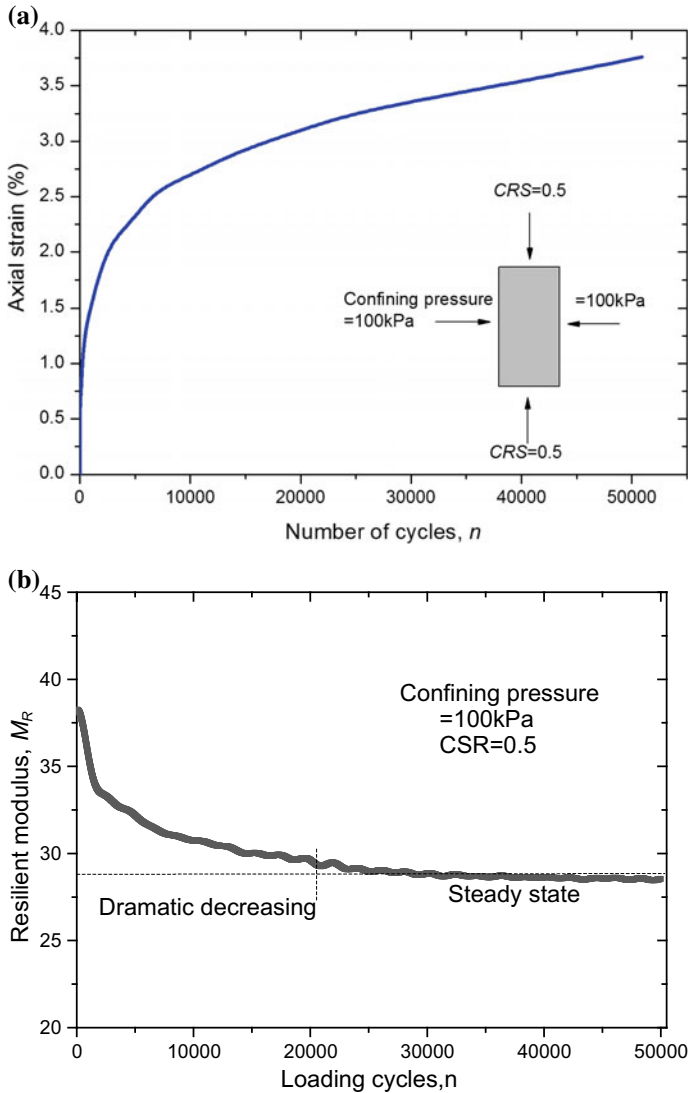
Fig. 4 Typical results of specimen C_{12}, **a** Permanent axial strain, **b** variation of resilient modulus

pre-test curve at lower CSRs, whereas it deviates from the pre-test curve at higher CSRs. The initial medium grain size, d_{50}, of the tested specimen is 6.3 mm. After cyclic testing, d_{50} of the specimen is 5.1, 4.6, 4.2, 3.6, 3.1, 2.6, and 1.9 mm for CSRs of 0.1, 0.2, 0.3, 0.4, 0.5, 0.6, and 0.8, respectively. The increase in CSR decreases the medium grain size of the residual soil, indicating that greater particle breakage occurs at higher CSRs. The degree of particle breakage can be defined by the difference between the pre- and post-test grain distribution curves. Several
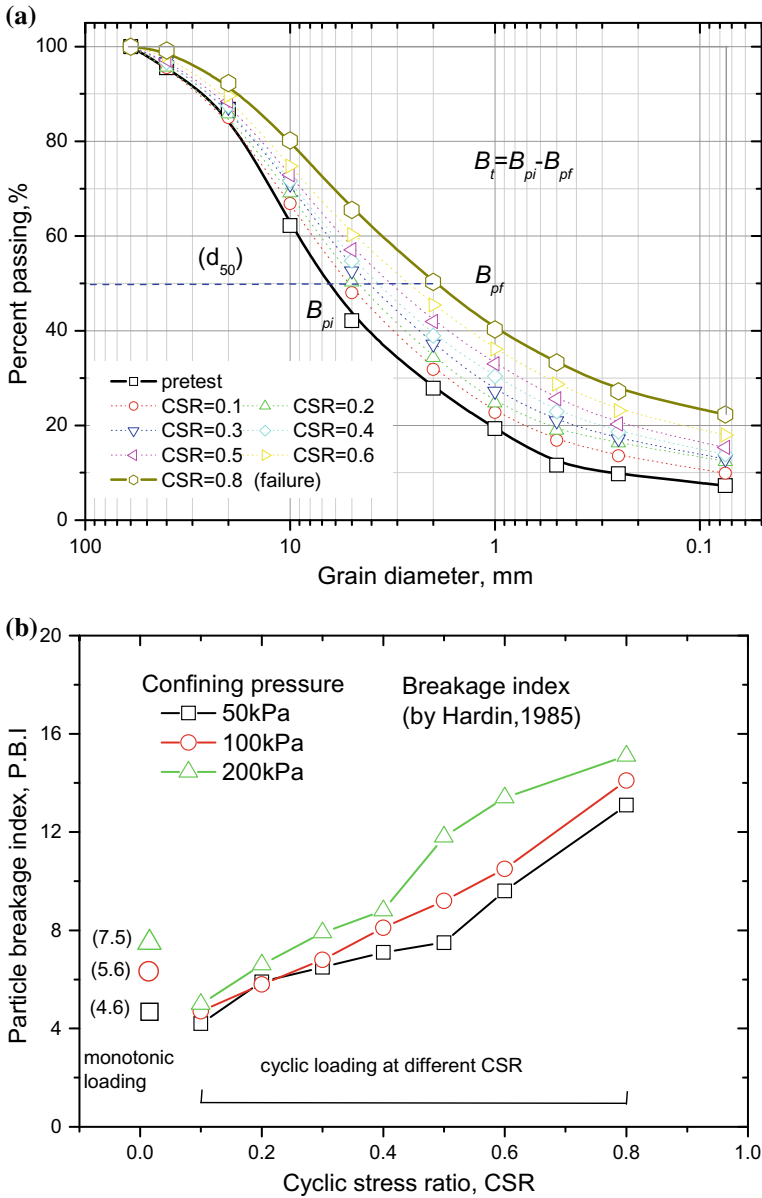
Fig. 5 Particle breakage in cyclic loading TX test: **a** Typical grain size distribution, **b** PBI versus confining pressure

methods are used to quantify particle breakage (e.g., [55–58]. Of these, the relative PBI technique developed by Hardin [55] is widely accepted as being able to adequately integrate particle breakage over a wide size fraction:

$$B_{\mathrm{r}} = \frac{\left(B_{\mathrm{pi}} - B_{\mathrm{pf}}\right)}{B_{\mathrm{pi}}} \tag{3}$$

where B_{r} is the relative breakage index; B_{p} is the breakage potential, which is defined as the area formed by three lines, namely the grain size distribution curve, a horizontal line passing 100% finer, and a vertical line passing #200 sieve (i.e., the shaded area in Fig. 5a; B_{pi} is the pre-test breakage potential; B_{pf} is the post-test breakage potential; and the value of $B_{\mathrm{pi}} - B_{\mathrm{pf}}$ represents the total breakage. Figure 5b presents the change in the breakage index as a function of CSR under different confining pressures. The figure indicates that an increase in CSR results in an increase in PBI, accompanied by a larger accumulative axial strain. Figure 5b also indicates that at lower CSR (CSR = 0.1 and 0.2), corresponding to low cumulative strain levels, the PBI is relatively low; in contrast, at higher CSR (CSR = 0.6 and 0.8), the PBI is relatively high. The maximum PBI under a 200 kPa confining pressure is 5.0, 6.6, 7.9, 8.8, 11.8, 13.4, and 15.1% for CSRs of 0.1, 0.2, 0.3, 0.4, 0.5, 0.6, and 0.8, respectively. Under higher CSRs, a greater cyclic deviator stress is applied to the specimen. Consequently, a greater effective cyclic stress is produced on the coarse grains in the tested soil matrix, resulting in a high concentration of contact stresses at particle contacts. As a result, the particles are likely to be crushed or broken, as evidenced by the increase in the PBI.

Figure 5b presents the PBI versus confining pressure for both the monotonic TX tests and the cyclic TX tests. The PBI in the monotonic TX test is 4.6, 5.6, and 7.5 under 50, 100, and 200 kPa confining pressures, respectively. Generally, the increasing confining pressure results in an increasing PBI. Figure 5b shows that the PBI resulting from cyclic loading is greater than the PBI produced by monotonic loading when the CSR is larger than 0.3. For the cyclic TX tests, the long-term cyclic load results in $a > 1.5$-times greater Hardin breakage index compared to the values obtained from the monotonic TX test. This demonstrates that the cyclic loading results in a greater deviation of the GSD from the pre-test conditions compared to the monotonic TX test. Because of the long-term cyclic loading, the concentration of stresses has sufficient time to progressively crush particles, which accounts for why particle breakage occurs even under low pressures. This means that the coarse grains in the residual soil are more easily crumbled when they are subjected to dynamic loading. Compared to the influence of the CRS, the influence of the confining pressure on the PBI is marginal.

3.3 Resilient Modulus Prediction

The resilient modulus, M_R, is a key parameter for the analysis and design of a subgrade subjected to traffic loads. Figure 6a presents a typical resilient modulus, M_R, varying with the number of loading cycles under different CSRs when the confining pressure is 50 kPa. Generally, the resilient modulus decreases with increasing number of cycles for all CSRs. Figure 6a shows that the resilient modulus is a function of the loading cycles, n. When n is smaller than 100, the resilient modulus remains stable. When n falls in the range of 100–20,000, the resilient modulus decreases with increasing number of loading cycles, including a dramatic decreasing phase within the first several thousands of cycles. When n is greater than 20,000, the resilient modulus remains steady again. After 50,000 loading cycles, the steady resilient modulus represents the minimum resilient modulus of the tested soil subjected to long-term cyclic loading. The decreasing resilient modulus is likely due to the coarse-grained particle breakage, which in turn results in the rearrangement of the soil fabric. Figure 6a also shows that the effect of the CSR on the resilient modulus is apparent. The resilient modulus decreases with increasing CSR although under different rates of decrease. When the CSR exceeds 0.4, the decreasing rate of the resilient modulus is smaller than the decreasing rate of the resilient modulus under CSRs of 0.1, 0.2, and 0.3. As an illustration, when the number of loading cycles is 10, the resilient modulus is 55.6, 47.3, 45.5, 43.9, and 38.6 MPa, corresponding to CSRs of 0.1, 0.2, 0.3, 0.4, and 0.5; when the number of loading cycles is 50,000, the resilient modulus is 42.42, 35.88, 34.51, 29.856, and 28.55 MPa, corresponding to CSRs of 0.1, 0.2, 0.3, 0.4, and 0.5.

Figure 6b plots the resilient modulus as a function of the confining pressure when the CSR is 0.5. It is found that the resilient modulus is a function of the confining pressure. Figure 6b shows that, when the confining pressure is 50 kPa, the resilient modulus starts to decrease at the first few hundreds of cycles with a smaller decreasing rate and is followed by a further smaller decreasing rate. When the confining pressure is 200 kPa, a dramatic decreasing of the resilient modulus occurs at the first few thousands of cycles, which is followed by a greater decreasing rate. This also occurs when the confining pressure is 100 kPa. When the CSR obtains a certain value, the resilient modulus increases with increasing confining pressure due to the better confinement applied to the specimens. This is consistent with the results of [1, 48, 59, 60]. Lekarp et al. [48] found that the resilient modulus of granular materials increases with increasing confining pressure and/or bulk stress and increases slightly with the deviator stress. The deformation behavior is characterized as stress hardening. Palmeira et al. [61] analyzed the results of large-scale cyclic and monotonic loading tests of unreinforced and geosynthetic-reinforced unpaved roads. They found that a better confinement leads to an increasing resilient modulus and decreasing axial cumulative strain of the tested soil in the cyclic TX test.
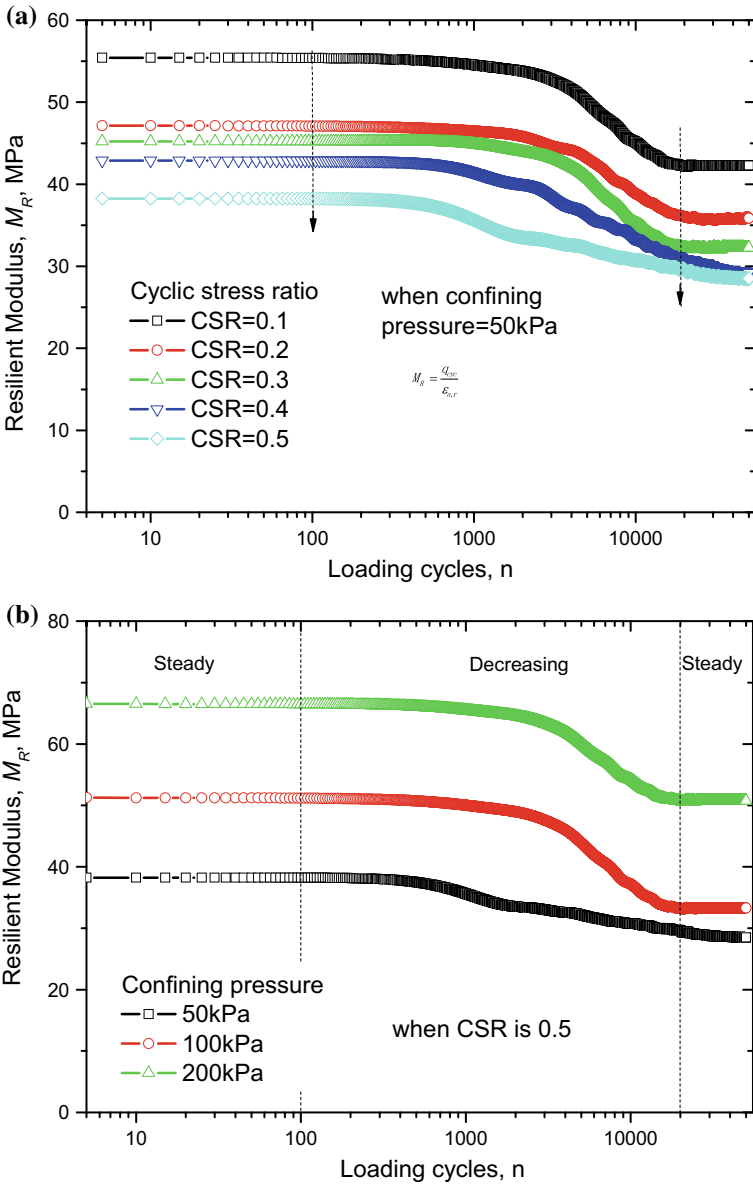
Fig. 6 Resilient modulus varying with the loading cycles: **a** Under different CSR, **b** under different confining pressure

The resilient modulus nonlinearly decreases with increasing CSR. The experimental finding is consistent with those results obtained by several authors, including Chen et al. [62], Xiao and Tutumluer [63], Guo et al. [23], and Frost et al. [64]. Among them, Chen et al. [62] found that the resilient modulus of lignosulfonate-treated sandy silt decreased with increasing CSR and increasing number of cycles. Xiao and Tutumluer [63] observed that the resilient moduli of unbound aggregate materials increase with increasing stress states (stress hardening), especially under confining pressure/bulk stress. Guo et al. [23] found that the normalized steady resilient modulus of saturated soft clay decreases with increasing CSR until reaching a constant value. The same results were also observed by Frost et al. [64] based on cyclic TX tests on clay and silty clay after 1000 loading cycles. Because the resilient modulus is remarkably influenced by the confining pressure, the steady resilient modulus is normalized as

$$M_R' = M_R / (\sqrt{\sigma_3 / p_a}) \tag{4}$$

where σ_3 is the confining pressure and p_a is atmospheric pressure, i.e., 101.3 kPa. Figure 7 presents the normalized steady resilient modulus under different CSRs. Figure 7 shows that the normalized resilient modulus falls on a single nonlinear curve irrespective of confining pressure. An empirical formula is proposed for the nonlinearity between the normalized steady resilient modulus and the CSR:

$$M_R' = k_1 (1 + CSR)^{k_2} \tag{5}$$
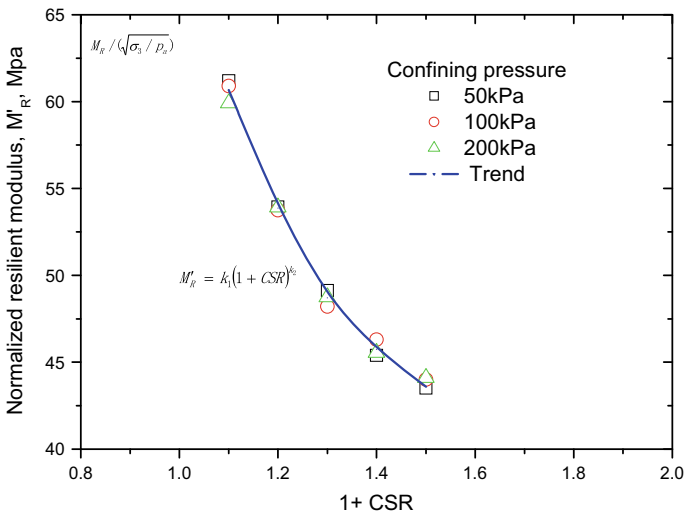
Fig. 7 Normalized steady resilient modulus versus (1 + CSR)

Combining Eqs. (2), (4), (5) can be rewritten as

$$M_R = k_1 \sqrt{\frac{\sigma_3}{p_a}} \left(1 + \frac{q_{cyc}}{q_f} \right)^{k_2} \tag{6}$$

where k_1 and k_2 are parameters that can be identified using multiple regression analyses. Based on the experimental results, with a regression coefficient of 0.96, k_1 is found to be 67, and k_2 is found to be -1.2. The proposed formula is specific to the tested coarse-grained residual soil or soils with similar gradation because the properties of a soil dominantly depend on its gradation.

3.4 Deformation Behaviors

3.4.1 Influence of CSR

Figure 8 presents the variation in cumulative axle strain with CSR under different confining pressures. The VSR varies in the range of 0.1–0.8, and the maximum number of loading cycles is 50,000. Figure 8 shows that the increasing CRS increases the axial strain and that the CSR shapes the curves showing the relationship between the cumulative strain and the number of loading cycles. Using an example of a 50 kPa confining pressure, the final axial strain is 0.42, 0.80, 1.20, 1.98, and 3.50% after 50,000 cycles, corresponding to CSRs of 0.1, 0.2, 0.3, 0.4, and 0.5. A rapid deformation is produced after the first few thousands of cycles under a lower CSR, and the later load cycling accumulates substantially less permanent strain after each set of 1000 cycles. The specimen remained stable when it was subjected to a lower CSR, namely CSR < 0.5. When the CSR is lower than 0.5, the cumulative strain rapidly increases during the initial phase (first few thousands of cycles), followed by an increasing phase with a lower strain cumulative rate. A substantially rapidly increase in cumulative axial strain occurs at the first few hundred of loading cycles under a higher CSR. When the CSR is greater than 0.6, the cumulative strain dramatically increases and exceeds the failure cumulative strain (5%, the monotonic loading failure state) after several thousands of cycles. For example, the cumulative axial strain reaches 5% after 2750 loading cycles when the sample is subjected to a CSR of 0.8 under a 50 kPa confining pressure. A critical CSR is identified from the curves in Fig. 8. The critical CSRs of the tested specimens fall in the small range of 0.5–0.6. Three stages of cumulative strain are observed when the CSR is greater than the critical CSR, namely the primary (stable) stage, the secondary (transitional) stage, and the tertiary (failure) stage, as observed in Fig. 8b. When the CSR is lower than 0.4, the deformation behavior of the specimen exhibits the primary (stable) stage; when the CSR falls in 0.5–0.6, the deformation behavior of the specimen exhibits the primary stage and the secondary stage; and when the CSR is greater than 0.6, the deformation

Fig. 8 Relationship between permanent strain and loading cycles, **a** $\sigma_3 = 50$ kPa, **b** $\sigma_3 = 100$ kPa, **c** $\sigma_3 = 200$ kPa
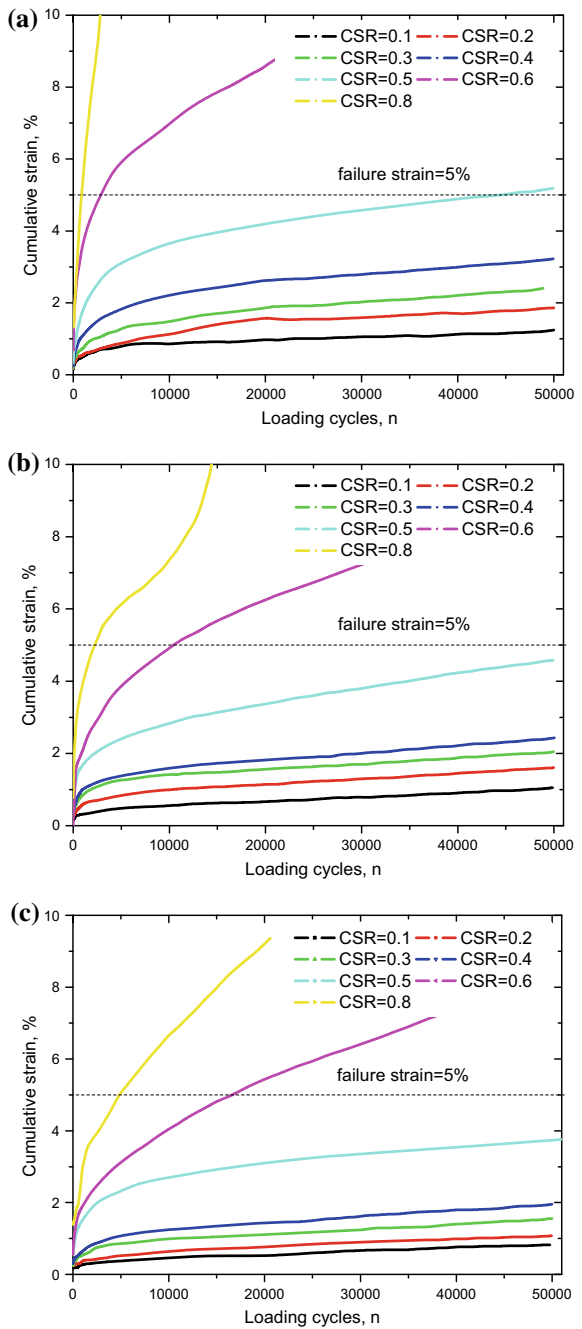
behavior of the specimen exhibits the primary stage, the secondary stage, and the tertiary stage. The primary stage is characterized by a decreasing rate of cumulative axial strain and a relatively small permanent strain magnitude, which most likely results from the abrasion of the coarse-grained particles. Under a lower CSR, the PBI is relatively low, as observed in Fig. 5b. In the secondary stage, cumulative axial strain linearly accumulates at a constant rate likely due to the rearrangement of the coarse-grained particles in the soil fabric. In the tertiary stage, the cumulative axial strain accumulates at an increasing rate, and failure occurs in the first few thousands of loading cycles. The tertiary stage is accompanied by a higher PBI, as evidenced by Fig. 5b. The traffic loading produces a dynamic soil stress in the subgrade and consequently produces cumulative deformation in the form of long-term settlement. The critical CSR is expected to be used to control the long-term settlement of a subgrade in an acceptable stage. When the magnitude of the dynamic stress in the subgrade is smaller than the CSR of the subsoil, the traffic-load-induced settlement remains in a stable and acceptable stage. When the magnitude of the dynamic stress in the subgrade exceeds the critical stress ratio of the subsoil, the traffic-load-induced settlement is found in an unstable and unacceptable stage.

3.4.2 Influence of Confining Pressure

Figure 9a presents a comparison of the cumulative strain with three different confining pressures: 50, 100, and 200 kPa. All three specimens were tested under a CSR of 0.4. The comparison illustrates that the increase in confining pressure leads to an increasing cumulative strain at a given CSR. For instance, the final axial strain is 5.2, 4.6 and 3.7% under confining pressures of 50, 100, and 200 kPa. It is observed that a larger cumulative strain is produced under lower confining pressure due to the weak confinement applied to the tested soil. When the applied confining pressure is lower, namely 50 kPa, the confinement of the specimen is relatively weak. Hence, the cumulative strain produced by cyclic loading is relatively high. When the confining pressure is higher, namely 200 kPa, the confinement of a similar specimen is relatively strong, and the cumulative strain of the specimen is relatively low.

Figure 9b presents a comparison of the number of cycles at failure under different confining pressures. Figure 9b shows that an increasing CSR decreases the number of cycles at failure and that an increase in confining pressure results in a rapid increase in the number of loading cycles at failure. When the CSR is 0.6, the numbers of loading cycles at failure are 2884, 10,543, and 16,672, corresponding to 50, 100, and 200 kPa confining pressures; when the CSR is 0.8, the numbers of loading cycles at failure are 1059, 2305, and 5058.
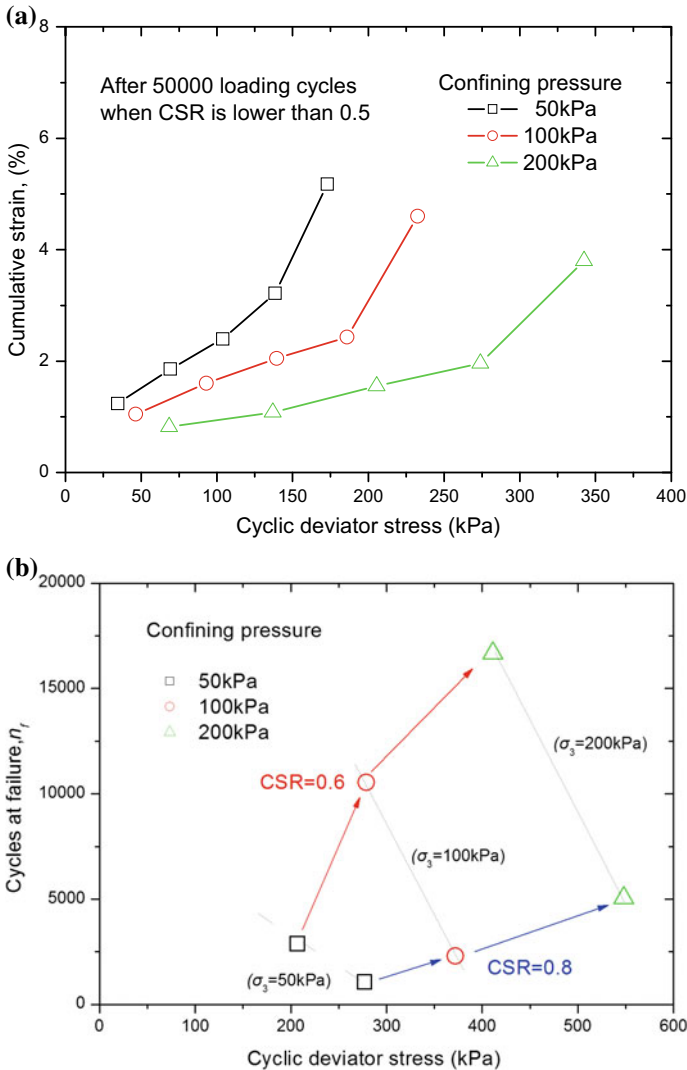
Fig. 9 Cycles at failure under different confining pressure, **a** permanent strain after 50,000 cycles, **b** cycles at failure

3.4.3 Modeling of Cumulative Strain

The cumulative deformation depends not only on the soil properties as a function of void ratio, moisture content, and gradation but also on the cyclic preloading history. It is of practical significance to be able to predict the permanent deformation of subsoil produced by traffic loading. Based on repeated loading tests, various models have been documented for the cumulative deformation prediction of fine saturated

soil or granular soil, including Barksdale [46], Monismith et al. [50], Li and Selig [21], and Lekarp et al. [48]. Among them, power law functions and logarithmic functions are the most widely used, i.e., the power equation proposed by Monismith et al. [50] and Li and Selig [21].

$$\varepsilon_{\mathrm{p}} = a \left(\frac{\sigma_{\mathrm{d}}}{\sigma_{\mathrm{sf}}} \right)^{m} N^{b} \tag{7}$$

$$\Delta s = \int_{0}^{h} \varepsilon_{\mathrm{p}} \mathrm{d}t \tag{8}$$

where ε_{p} is the cumulative strain; N is the number of repeated cycles; σ_{d} is the dynamic soil deviator stress caused by traffic loading; σ_{sf} is the static deviator stress at failure; a, b, and m are parameters that are dependent on the subsoil; Δs is the deformation caused by traffic loading at an influenced depth; and h is the traffic-load-influenced depth. The majority of those empirical functions are limited in terms of characterizing the cumulative deformation behavior under a given confining pressure because the model parameters ignore the influence of the confining pressure on the cumulative strain. To address this limitation, a specific model needs to be setup for the tested subsoil. In this paper, the accumulative strain is normalized as

$$\varepsilon_{\mathrm{p}}' = \varepsilon_{\mathrm{p}} \cdot \sqrt{4 \frac{\sigma_{3}}{p_{\mathrm{a}}}} \tag{9}$$

where σ_{3} is the confining pressure, ε_{p} is the cumulative axial strain, $\varepsilon_{\mathrm{p}}'$ is the normalized strain, and p_{a} is atmospheric pressure, namely 101.3 kPa. Figure 10a plots the normalized strain, $\varepsilon_{\mathrm{p}}'$, versus the number of loading cycles when the CSR is less than 0.6 (primary and secondary strain phases only). Figure 10a shows that the normalized strain linearly increases logarithmically with the number of loading cycles. The linearity between $\log \varepsilon_{\mathrm{p}}'$ and $\log n$ (denoted by the dashed line in Fig. 10a) is observed irrespective of the CSR. A linear formula is setup to fit the linearity as in Eq. [45].

$$\log \varepsilon_{\mathrm{p}}' = a + b \log n \tag{10}$$

where a and b are parameters that are identified using multiple regression analyses of the cyclic load TX test data. The good agreement between the measured data and the predicted data is observed with a correlation coefficient of 0.94. Figure 10b shows the parameters versus the CSR. It is apparent that the parameter a increases linearly with increasing CSR, as does the parameter b. Hence, the parameters a and b are rewritten as linear functions as follows:
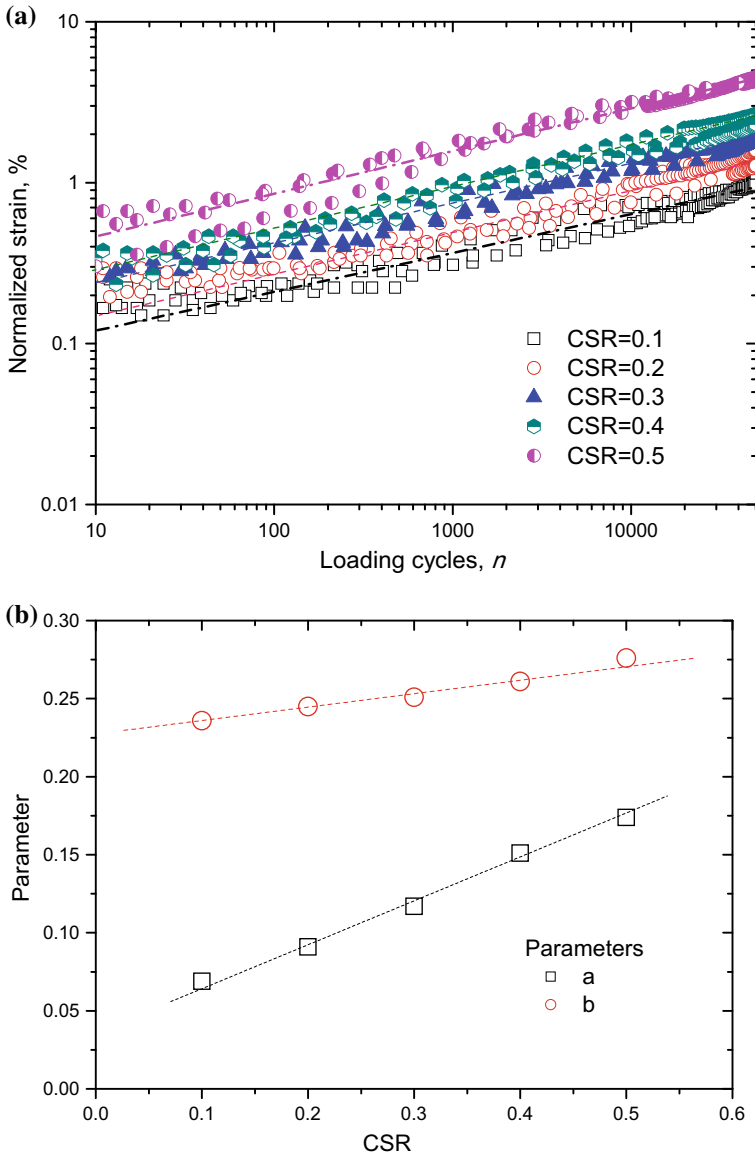
Fig. 10 Normalized axial strain under different CSRs. **a** Normalized strain versus loading cycles, **b** parameters versus CSRs

$$a = c + d \cdot \text{CSR} \tag{11}$$

$$b = e + f \cdot \text{CSR} \tag{12}$$

Using multiple regression analyses, c is found to be 0.035, d is found to be 0.29, e is found to be 0.23, and f is found to be 0.07. Consequently, Eq. (9) is rewritten as

$$\varepsilon_\text{p} = \left(0.035 + 0.29 \frac{q_\text{cyc}}{q_\text{f}} \right) \cdot \left(\frac{\sigma_3}{p_\text{a}} \right)^{-1/4} \cdot n^{\left(0.23 + 0.07 \frac{q_\text{cyc}}{q_\text{f}} \right)} \tag{12}$$

The proposed formulation of the cumulative strain is specific to soils with a similar gradation under similar loading conditions because the regression parameters obtained from the fitting cyclic TX tests vary with the soil gradation, soil properties, loading conditions, and moisture content.

4 Case Study of Deformation Prediction

4.1 Field-Testing Programs

A highway subgrade is selected as the case study for the deformation prediction, and the subsoil is the tested residual soil. The field tests were used to investigate the dynamic soil attenuation of the subgrade. The highway (the Changzhang highway) was constructed in 2007 and has a total length of 159.35 km. This four-lane highway has a designed speed of 120 km/h. The expected service life of the pavement is 20 years, yielding a total of 1.2×10^7 cycles of equivalent standard traffic loading (Ministry of transportation of the People's Republic of China, Specifications of cement pavement design for highway, 2002 JTG D40-2002 and Specifications for design of highway asphalt pavement, JTG D5010-2006). This indicates that the annual average number of loading cycles is 600,000. Each traffic load is a standard axle load of 100 kN.

The height of the subgrade is 18 m. The composite pavement has five structural layers: The surface pavement is a 150-mm-thick standard hot mix asphalt (HMA); the upper-base course is a 160-mm-thick concrete base blended with 5% cement (by weight); the middle-base course is a 160-mm-thick granular soil base blended with 4% cement (by weight); the subbase is a layer of 180-mm-thick aggregates blended with 4% cement (by weight); and the underlying subsoil is red mudstone residual soil. The basic mechanical parameters of the pavement are listed in Table 5. A total of 14 dynamic soil stress gauges (PS_{1-14}) and 2 settlement meters (S_{1-2}) were installed in the case subgrade. Figure 11a shows the positions of each soil stress gauge and deflection meter. Each of the dynamic soil stress gauges was calibrated using the tested residual subsoil. The peak dynamic stresses produced by loading using a testing truck were obtained by a data acquisition system before the highway

Table 5 Basic mechanical parameters of composite pavement

Pavement layers	Friction angle (°)	Cohesion force (kPa)	Bulk density (g/cm^3)	Compressive strength (MPa)	Poisson's ratio	Young's modulus (MPa)
HMA surface	na	na	2.5	na	0.35	1400
Upper-base	60	350	2.4	5.0	0.25	1200
Middle-base	40	250	2.4	5.0	0.25	800
Subbase	40	250	2.2	4.5	0.25	800

was opened to traffic. Subsequently, the profiles of the truck-induced dynamic stresses were built up as the stress attenuation law along the depth of the case subgrade. Then, the traffic-load-influenced depth was determined using the dynamic soil attenuation law for the case subgrade. The testing truck was a freight truck, which repeatedly drove over the dynamic soil stress gauges, as observed in Fig. 11b. The maximum axle load was 66, 105, and 157 kN, and the testing speed was 60, 80, and 100 km/h. The long-term traffic-induced deformations of this case subgrade were measured by settlement meters (S_{1-2}) after the highway was opened to traffic.

4.2 Traffic-Influenced Depth

Figure 12 presents the obtained peak dynamic soil stresses along the depth of the subgrade under different axle loads. Each dynamic soil stress is the average of two peak dynamic soil stresses at the same depth. Figure 12 shows that the increasing axle load results in increasing dynamic soil stresses; however, the rate of increase decreases with depth. For example, at the subgrade surface, the range of the peak dynamic stress falls in the range of 20–25 kPa when the axle load is 66 kN; the peak dynamic stress falls in the range of 28–37 kPa when the axle load is 105 kN; and the peak dynamic stress falls in the range of 38–45 kPa when the axle load is 157 kN. At a depth of −3.0 m, the peak dynamic soil stresses remain at 4.6, 5.3, and 6.4 kPa for axel loads of 66, 107, and 157 kN. The experimental data show that the dynamic stress attenuation dramatically decreases along the depth in the subgrade. Comparing the peak dynamic stresses, it is observed that the influence of the truck speed on the dynamic soil stress is minimal. This agrees with the laboratory results of Indraratna et al. [65] on unbounded aggregate subsoil. They found that the effect of the loading frequency on the dynamic response is marginal when the dynamic loading frequency is less than 40 Hz.

To better understand the attenuation of dynamic soil stresses along the depth, the peak dynamic soil stress is normalized by the peak dynamic stress at the subgrade surface. Figure 13 plots the normalized peak dynamic stress along the depth when the speed is 100 km/h. Figure 13 shows that the normalized dynamic stress rapidly

Fig. 11 Instruction of
dynamic soil pressure,
a instrumentation of sensors,
b testing truck
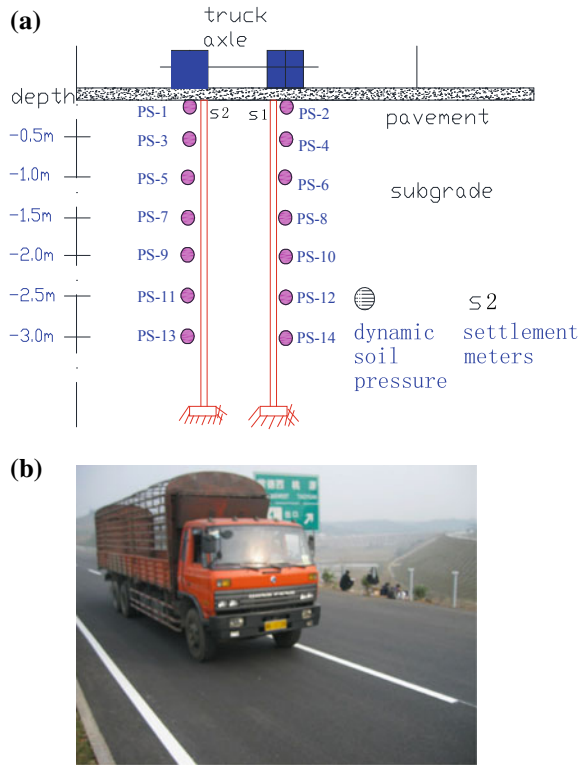
decreases when the depth is less than 1.5 m, followed by a slow decreasing for
depths from −1.5 to −3.0 m. The normalized dynamic stress decreases from 1.0 to
0.3 when the depth increases from 0 to 1.5 m. The normalized dynamic stress
decrease from 0.3 to 0.1 when the depth increases from 1.5 to 3.0 m. Huang et al.
[66] found that the traffic-load-induced deformation is marginal when the dynamic
stress is smaller than 10% of the weight stress. In this paper, the
traffic-load-influenced depth of the tested subgrade is determined when the nor-
malized dynamic stress is greater than 10%. Based on the field test results, Table 6
summarizes the traffic-load-influenced depth of the tested subgrade subjected to
different axle loads. Table 6 shows that the increasing of the traffic axle load
slightly increases the traffic-influenced depth; however, the influence of the speed
remains limited. The significant traffic-load-influenced depths in this case subgrade
are determined to be 2.7, 2.8, and 3.0 m when the axle loads are 66, 105, and
157 kN, respectively. The traffic-induced deformation prediction is limited to the
traffic-load-influenced depth in the case study.

Fig. 12 Variation of peak dynamic pressure, **a** axle load = 66 kN, **b** axle load = 105 kN, **c** axle load = 157 kN
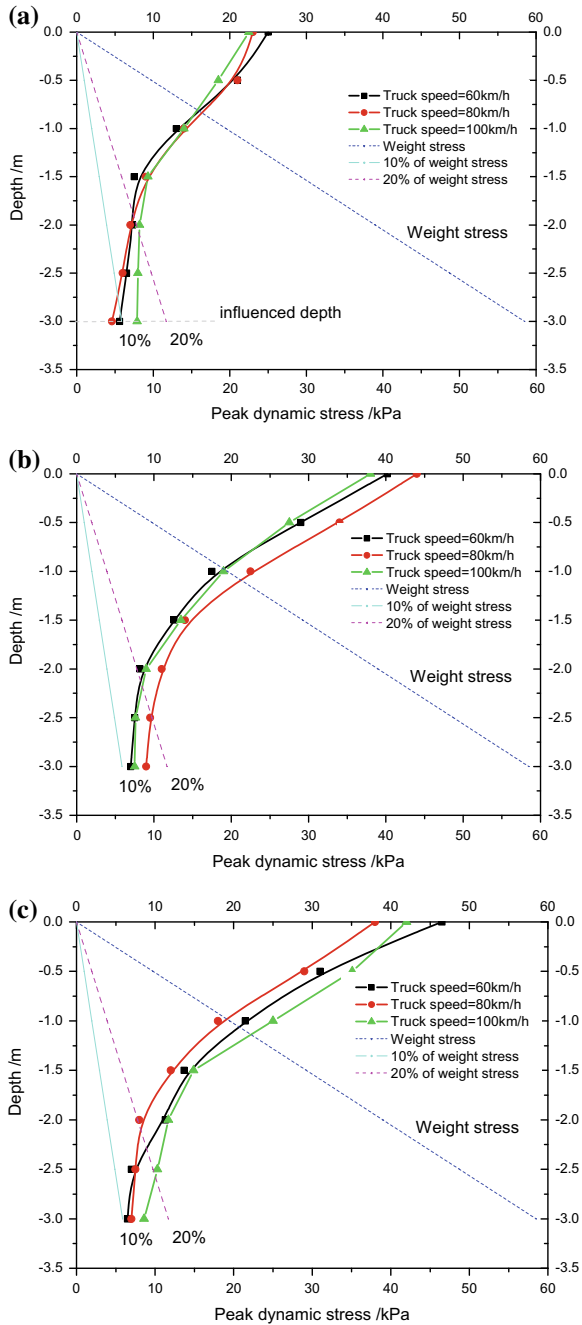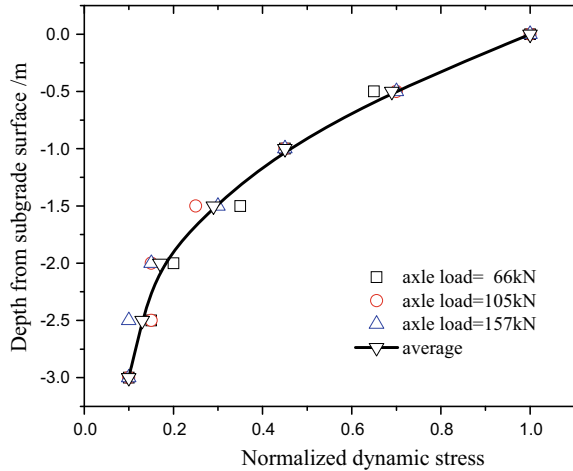
Table 6 Traffic-load-influenced depth in tested subgrade

Speed (km/h)	Traffic-load-influenced depth (m)		
	Axle load = 66 kN	Axle load = 105 kN	Axle load = 157 kN
60	2.65	2.78	2.93
80	2.66	2.83	2.95
100	2.69	2.82	3.00

4.3 Deformation Prediction

Equation (12) is used to predict the deformation as a function of the traffic-load-induced depth as follows:

$$S_d = \int_0^{h_d} \left[(0.035 + 0.29 \cdot \text{CSR}) \cdot \left(\frac{\sigma_3}{p_a} \right)^{-1/4} \cdot n^{(0.23 + 0.07 \cdot \text{CSR})} \right] dz \qquad (13)$$

where S_d is the accumulative deformation; h_d is the traffic-load-induced depth of the subgrade, observed in Table 6; n is the total accumulation of traffic cycles, which is set as 600,000 cycles per year; σ_3 is the soil pressure, which is calculated using the theory of soil pressure at rest; and CSR is the ratio between the measured peak dynamic soil stress and the critical shear strength calculated using Mohr–Coulomb theory.

Figure 14 presents the predicted accumulative deformation five years after the highway was opened to traffic. The predicted deformations were compared with the measured settlement. The measured settlement during the construction period is ascribed to the weight of the subsoil and pavement, and the measured settlement

remains steady before the highway was opened to traffic. During the construction period, the total subgrade settlement was 103 mm. Figure 14 shows that three deformation stages were found in the measured settlement deformation history. After the highway was opened to traffic, the measured settlement quickly increases during the first several hundreds of days, followed by accumulation with a constant rate in the first thousand days. Beyond the first thousand days, the settlement remains nearly steady. Compared with the predicted settlement under different axle loads, only two deformation stages were found to be exhibited by the predicted traffic-load-induced settlements. Figure 14 shows that the predicted deformation dramatically increases during the first hundred days, followed by a slightly increasing deformation at a constant rate. As expected, the increasing axle load increases the predicted settlement because of the increasing CSR. The traffic-load-induced deformations are 62, 73, and 87 mm for axle loads of 66, 105, and 157 kN after 5 years of being open to traffic. A good agreement is generally observed between the predicted deformation and the measured deformation. The detailed comparison shows that the predicted settlement under 66 kN axle load is slightly lower than the measured value, and the predicted settlement under the 157 kN axle load is slightly higher than the measured value. In the first year, a better agreement is observed between the measured settlement and the predicted settlement under the 157 kN axle load. Later, a better agreement is observed between the measured settlement and the predicted settlement under the 105 kN axle load. This indicates the feasibility of the proposed method for traffic-induced deformation prediction when applied to coarse-grained residual subsoil. It must be emphasized that the proposed method is based on a case subgrade where the stress state was below the critical state and where the subsoil has a similar gradation as the tested soil.
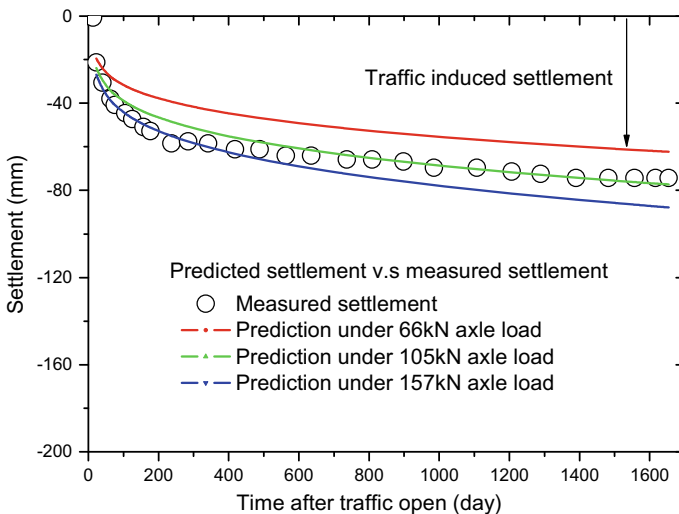
Fig. 14 Predicted deformation versus measured deformation

5   Conclusions

An experimental investigation of the deformation behavior of coarse-grained residual soil under optimal moisture content conditions is presented in this paper. The laboratory tests consisted of large-scale monotonic TX tests of four specimens and long-term cyclic TX tests of 21 specimens subjected to 50,000 loading cycles. A series of field tests were also used to determine the traffic-load-influenced depth in the case study. Considering the CSRs and confining pressures, the effects of particle breakage on the deformation behavior of residual soil were analyzed. The resilient modulus and cumulative strain of the tested samples were also evaluated under different CSRs and confining pressures. Based on these tests, the following conclusions specific to the tested residual soil (i.e., similar gradation as the tested residual soil) can be drawn:

(1) An increasing CSR increases the cumulative strain while, in contrasting, decreasing the resilient modulus. Considering the cyclic stress amplitude and confining pressure, an empirical formula for the steady resilient modulus was established. The predicted steady modulus using this formula is in good agreement with the testing results. Additionally, a prediction formula for the cumulative strain independence of the cyclic stress amplitude, number of loading cycles, and confining pressure was established. The agreement between the predicted strain and the tested strain indicates the feasibility of this prediction formula for cumulative strain prediction.

(2) The obtained results suggest that increasing the CSR and number of load cycles beneficially influences particle breakage as well as increases the confining pressure. The PBI under cyclic loading is generally 1.5-times greater than the PBI under monotonic loading. The higher CSR results in three cumulative strain stages accompanied by an increasing PBI, i.e., the primary stage, the secondary stage, and the tertiary stage.

(3) The field tests provide the intensity of dynamic stresses on the subgrade surface and the attenuation law of the dynamic stresses along the subgrade depth. The influence of the truck speed on the traffic-load-influenced depth is minimal. An increasing axle load results in increasing dynamic soil stresses and traffic-load-influenced depth in the subgrade. The traffic-load-influenced depth varies with increasing axle load. In the case study, the traffic-load-influenced depths were 2.7, 2.8, and 3.0 m corresponding to axle loads of 66, 105, and 157 kN.

(4) An empirical method for predicting traffic-load-induced deformation is established for subgrades constructed with residual soil. The method considers the magnitude of the CSR, the number of traffic-load applications, and the confining pressure on site. The method is used to predict the permanent traffic-load-induced deformation of a case subgrade after being opened to traffic.

References

1. Chen X, Zhang J, Li Z (2014) Shear behaviour of a geogrid-reinforced coarse-grained soil based on large-scale triaxial tests. Geotext Geomembr 42(4):312–328
2. Liu DW, Xiong CR (2003) Experimental study on properties of red sandstone for road applications. CentL South Highw Eng 28(4):27–32
3. Blight GE, Leong EC (2012) Mechanics of residual soils. CRC Press
4. Cetin KO, Bilge HT (2012) Cyclic large strain and induced pore pressure models for saturated clean sands. J Geotech Geoenvironmental Eng 138(3):309–323
5. Chai JC, Miura N (2002) Traffic-load-induced permanent deformation of road on soft subsoil. J Geotech Geoenvironmental Eng 128(11):907–916
6. Cui X, Zhang N, Gao Z (2014) In situ tests simulating traffic-load-induced settlement of alluvial silt subsoil. Soil Dyn Earthq Eng 58(03):10–20
7. Fernando Emmanuel (2003) Analysis procedure for load-zoning pavements. Transp Res Rec 1860:117–125
8. Hsu CC, Vucetic M (2006) Threshold shear strain for cyclic pore-water pressure in cohesive soils. J Geotech Geoenvironmental Eng 132(10):1325–1335
9. Hu AF, Zhang XD, Jia YS (2014) Research on the permanent settlement of saturated soft subsoil. Adv Soil Dyn Found Eng (ASCE):168–77
10. Hu YY (2010) Long-term settlement of soft subsoil clay under rectangular or semi-sinusoidal repeated loading of low amplitude. Can Geotech J 47:1259–1270
11. Kohgo Y (2010) A cyclic plasticity model for unsaturated geo-materials: unsaturated soils. In: Theoretical and numerical advances in unsaturated soil mechanics, pp 647–653
12. Tang L, Chen H, Zhang S, Zhang J (2015) Determination of traffic-load-influenced depths in clayey subsoil based on the shakedown concept. Soil Dyn Earthq Eng 77(10):182–191
13. Trinh VN, Tang AM, Cui YJ, Dupla JC, Canou J, Calon N, Lambert L, Robinet A, Schoen O (2012) Mechanical characterisation of the fouled ballast in ancient railway track substructure by large-scale triaxial tests. Soils Found 52(3):511–523
14. Tsukamoto Y, Ishihara K, Nakazawa H, Kamada K, Huang YN (2002) Resistance of partly saturated sand to liquefaction with reference to longitudinal and shear wave velocities. Soils Found 42(6):93–104
15. Tsukamoto Y, Ishihara K, Umeda K, Enomoto T (2006) Cyclic resistance of clean sand improved by silicate-based permeation grouting. Soils Found 46(2):233–245
16. Xenaki VC, Athanasopoulos GA (2008) Dynamic properties and liquefaction resistance of two soil materials in an earth fill dam—laboratory test results. Soil Dyn Earthq Eng 28 (8):605–620
17. Biglari M, Jafari MK, Shafiee A, Mancuso C, d'Onofrio A (2011) Shear modulus and damping ratio of unsaturated kaolin measured by new suction-controlled cyclic triaxial device. Geotech Test J 34(5):525–536
18. Cai YQ, Gu CA, Wang J, Juang CH, Xu CJ, Hu XQ (2013) One-way cyclic triaxial behavior of saturated clay: comparison between constant and variable confining pressure. J Geotech Geoenvironmental Eng 139(5):797–809
19. Hsiao DH, Phan VTA, Hsieh YT, Kuo HY (2015) Engineering behavior and correlated parameters from obtained results of sand-silt mixtures. Soil Dyn Earthq Eng 77:137–151
20. Tsukamoto Y, Kawabe S, Matsumoto J, Hagiwara S (2014) Cyclic resistance of two unsaturated silty sands against soil liquefaction. Soils Found 54(6):1094–1103

21. Li D, Selig ET (1996) Cumulative plastic deformation for fine-grained subgrade soils. J Geotech Eng 122(12):1006–1013
22. Hatanaka M, Abe A, Masuda T (2006) Effect of degree of saturation on the liquefaction strength of in-situ sandy soils. In: Proceedings of recent development of geotechnical and geo-environmental engineering in Asia, pp 59–62
23. Guo L, Wang J, Cai Y, Liu H, Gao Y, Sun H (2013) Undrained deformation behavior of saturated soft clay under long-term cyclic loading. Soil Dyn Earthq Eng 50:28–37
24. Wichtmann T, Triantafyllidis T (2015) Stress attractors predicted by a high-cycle accumulation model confirmed by undrained cyclic triaxial tests. Soil Dyn Earthq Eng 69:125–137
25. Bandini P, Pham HV (2011) Bearing capacity of embedded strip footings in two-layered clay soils. Geo-Front ASCE 2011:332–341
26. Dash HK, Sitharam TG (2009) Undrained montonic response of the sand-silt mixtures: effect of nonplastic fines. Geotech Geol Eng 27:501–517
27. Indraratna B, Hussaini SKK, Vinod JS (2013) The lateral displacement response of geogrid-reinforced ballast under cyclic loading. Geotext Geomembr 39:20–29
28. Lade PV, Liggio CD, Yamamuro JA (1998) Effects of nonplastic fines on minimum and maximum void ratios of sand. Geotech Test J 21:336–347
29. Pitman TD, Robertson PK, Sego DC (1994) Influence of fines on the collapse of loose sands. Can Geotech J 31:728–739
30. Saxena KR, Anjaiah B, Indian Geotechnical Society Hyderabad Chapter, Institution of Engineers (India), A.P. State Centre (1981) Geomech 81. In: Symposium on engineering behaviour of coarse grained soils, boulders & rocks, 21–23 Dec 1981, Hyderabad, A.P., India, Meerut, Sarita Prakashan
31. Vallejo LE, Mawby R (2000) Porosity influence on the shear strength of granular material-claymixtures. Eng Geol 58:125–136
32. Zhao HF, Zhang LM (2013) Behaviour of coarse widely graded soils under low confining pressures. J Geotech Geoenviron Eng 139:35–48
33. Elias MB, Titi HH (2006) Evaluation of resilient modulus model parameters for mechanistic-empirical pavement design. Geol Prop Earth Mater 2006(1967):89–100
34. Trani LDO, Indraratna B (2010) The use of particle size distribution by surface area method in predicting the saturated hydraulic conductivity of graded granular soils. Geotechnique 60 (12):957–962
35. Ban H, Park SW (2014) Characteristics of modified soil-aggregate system and their application in pavements. KSCE J Civil Eng 18(6):1672–1678
36. Ishikawa T, Zhang Y, Tokoro T, Miura S (2014) Medium-size triaxial apparatus for unsaturated granular subbase course materials. Soils Found 54(1):67–80
37. Lenarta S, Koseki J, Miyashita Y, Sato T (2014) Large-scale triaxial tests of dense gravel material at low confining pressures. Soils Found 54(1):45–55
38. Nair AM, Latha GM (2012) Taming of large diameter triaxial setup. Geomech Eng 4(4): 251–262
39. Indraratna B, Khabbaz H, Salim W, Christie D (2006) Geotechnical properties of ballast and the role of geosynthetics in rail track stabilization. J Ground Improv 10(3):91–102
40. Mishra D, Qian Y, Kazmee H, Tutumluer E (2014) Investigation of geogridreinforced railroad ballast behavior using large-scale triaxial testing and discrete element modeling. Transp Res Rec J Transp Res Board (2462):98–108. (Transportation Research Board of the National Academies, Washington)
41. Tutumluer E, Huang H, Hashash YMA, Ghaboussi J (2006) Aggregate shape effects on ballast tamping and railroad track lateral stability. In: Proceedings of the AREMA annual conference, Louisville, Kentucky, USA, Sep 17–20
42. Karg C, Haegeman W (2009) Elasto-plastic long-term behavior of granular soils: Experimental investigation. Soil Dyn Earthq Eng 29(1):155–172
43. Craciun O, Lo SCR (2010) Matric suction measurement in stress path cyclic triaxial testing of unbound granular base materials. Geotech Test J 33(1):33–44

44. Karg C, Francois S, Haegeman W, Degrande G (2010) Elasto-plastic long-term behavior of granular soils: modelling and experimental validation. Soil Dyn Earthq Eng 30(8):635–646
45. Casini F, Viggiani GMB, Springman SM (2013) Breakage of an artificial crushable material under loading. Granular Matter 15(5):661–673
46. Barksdale RD (1972) Laboratory evaluation of rutting in base course materials. In: Proceedings of the 3rd international conference on asphalt pavements, University of Michigan, Ann Arbor 161–174
47. Brown SF, Chan F (1996) Reduced rutting in unbound granular pavement layers through improved grading design. In: Proceedings of the institution of civil engineers, Transport, vol 117, pp 40–49
48. Lekarp F, Isacsson U, Dawson A (2000) State of the art II: permanent strain response of unbound aggregates. ASCE J Transp Eng 126(1):76–83
49. Thom NH, Brown SF (1988) The effect of grading and density on the mechanical properties of a crushed dolomitic limestone. In: Proceedings of the 14th ARRB conference, part 7, pp 94–100
50. Monismith CL, Ogawa N, Freeme CR (1975) Permanent deformation characteristics of subgrade soils due to repeated loading. Transp Res Rec 537; Transportation Research Board, National Research Council, Washington, pp 1–17
51. Varadarajan A, Sharma KG, Venkatachalam K, Gupta AK (2003) Testing and modeling two rockfill materials. J Geotech Geoenvironmental Eng 129(3):206–218
52. ASTM D7181-11 (2011) Method for consolidated drained triaxial compression test for soils
53. ASTM D5311-92 (1996) Standard test method for load controlled cyclic triaxial strength of soil
54. ASTM D3999-91 (2003) Standard test methods for the determination of the modulus and damping properties of soils using the cyclic triaxial apparatus
55. Hardin BO (1985) Crushing of soil particles. J Geotech Engrg 111:1177–1192
56. Leslie DD (1963) Large-scale triaxial tests on gravelly soils. In: Proceedings of the 2nd Panamerican conference on soil mechanics and foundation engineering, Brazil, vol 1, pp 181–202
57. Leslie DD (1975) Shear strength of rockfill. Phys Prop Eng; Study no 526, South Pacific Division, Corps of Engineers Laboratory, Sausalito, Calif., Oct 1975, p 124
58. Marsal RJ (1965) Discussion of Shear strength. In: Proceedings of the 6th international conference on soil mechanics and foundation engineering, Montreal, vol 3, pp 310–316
59. Palmeira EM (2009) Soil-geosynthetic interaction: modelling and analysis. Geotext Geomembr 27:368–390
60. Tutumluer E, Huang H, Bian X (2012) Geogrid-aggregate interlock mechanism investigated through aggregate imaging-based discrete element modeling Approach. Int J Geomech 12 (4):391–398
61. Palmeira EM (2009) Soil–geosynthetic interaction: modelling and analysis. Geotext Geomembr 27(5):368–390
62. Chen C, Indraratna B, McDowell G, Rujikiatkamjorn C (2015) Discrete element modelling of lateral displacement of a granular assembly under cyclic loading. Comput Geotech 69: 474–484
63. Xiao Y, Tutumluer E (2014) Performance-based evaluation of unbound aggregates affecting mechanistic response and performance of flexible pavements. Dissertation, University of Illinois at Urbana-Champaign, 2014, Urbana, Illinois
64. Frost MW, Fleming PR, Rogers CDF (2004) Cyclic triaxial tests on clay subgrades for analytical pavement design. J Transp Eng-ASCE 130(3):378–386
65. Indraratna B, Thakur PK, Vinod JS (2010) Experimental and numerical study of railway ballast behavior under cyclic loading. Int J Geomech 10(4):136–144
66. Huang Q, Ling J (2011) Methodology study on defining subgrade's working area. J Tongji Univ (Nat Sci) 39(4):551–555

Utility Trench Backfill Compaction Using Vibratory Plate Compactor Versus Excavator-Mounted Hydraulic Plate Compactor

Chaoyi Wang, Tong Qiu, Ming Xiao and Jintai Wang

Abstract Excavator-mounted hydraulic plate compactors have been widely used in utility trench backfill compaction due to their efficiency. However, there are industry concerns on the possibility of pipe damage due to the combination of static downward earth pressure exerted by the excavator arm and dynamic earth pressure induced by the excavator-mounted hydraulic plate compactor. This paper presents the results of a field study that aims to compare the performances of utility trench compaction using a conventional walk-behind vibratory plate compactor with a lift thickness of 200 mm (8 in.) and an excavator-mounted hydraulic plate compactor with a lift thickness of 200 mm (8 in.), 300 mm (12 in.), 450 mm (18 in.), and 600 mm (24 in.). A flexible PVC pipe was used. The field test results indicate that the excavator-mounted hydraulic plate compactor delivered comparable compacted dry mass densities with a lift thickness of 200 and 300 mm as the walk-behind vibratory plate compactor did with a lift thickness of 200 mm; however, the excavator-mounted hydraulic plate compactor was not able to consistently achieve adequate compacted dry mass densities with a lift thickness of 450 and 600 mm. The excavator-mounted hydraulic plate compactor induced larger dynamic vertical earth pressures than did the walk-behind vibratory plate compactor.

Keywords Compaction · Trench backfill · Vibratory plate compactor

C. Wang
Department of Energy and Mineral Engineering, The Pennsylvania State University, University Park, PA 16802, USA
e-mail: cuw179@psu.edu

T. Qiu (✉) · M. Xiao · J. Wang
Department of Civil and Environmental Engineering, The Pennsylvania State University, University Park, PA 16802, USA
e-mail: tqiu@engr.psu.edu

285

1 Introduction

Utility pipes are typically installed through open-cut trenching and are backfilled with granular materials that need to be adequately compacted to provide proper ground support and minimize settlement of the trenching zone. Significant variations in pipe behavior can be caused by installation practices [1, 2], and trench backfilling and compaction-induced stresses may cause damage to the pipes. Hansen et al. [3] found that the generation of premature cracks found on small diameter (less than 36 in. or 90 cm) concrete pipes is linked to backfilling and compaction methods. American Concrete Pipe Association [4] considered the effects of heavy machinery on the integrity of buried concrete pipes in their installation manual and provided standards to avoid load concentrations during compaction. For example, it is recommended that care be taken to avoid damaging the pipe when impact or vibratory equipment is used for compaction, particularly for installations with less than 0.6 m (2 feet) of earthfill over the pipe.

Various researchers have investigated the pipe performance during installation and trench compaction (e.g., [5–7]). Different compaction equipment may impart different compaction energies to the backfill material and hence impact the pipe performance. For example, rammer compactors are found to produce greater backfill density than do the vibratory plate compactors with the same number of coverages and produce higher residual lateral soil stresses that contribute to better overall pipe performance during backfilling [1]. Conventional compaction equipment used in pipe installation includes the wacker packer, trench roller, vibratory roller compactor, and excavator compaction wheel [8]. The hydraulically operated vibratory plate compactor has greatly increased the efficiency of backfill compaction because it can be attached to the arms of an excavator (e.g., backhoe) and used for compacting backfill materials without requiring a worker operating a compactor in the trench. Hence, excavator-mounted hydraulic plate compactors have been widely used in trench backfill compaction recently. However, there are industry concerns on the possibility of pipe damage due to the combination of static downward earth pressure exerted by the excavator arm and dynamic earth pressure induced by the excavator-mounted hydraulic plate compactor [3]. Kararam [8] conducted a field investigation on a reinforced concrete pipeline using an excavator-mounted hydraulic plate compactor. It was found that the pipeline system was damaged by the heavy impulse load from the excavator-mounted hydraulic plate compactor; however, the damage occurred only when the first 150-mm (6-in.) layer of backfill material was being compacted above the pipe crown. Data on the performance of pipes backfilled with excavator-mounted hydraulic plate compactors are remarkably scarce in the literature; hence, additional research is needed to address the industry concern.

Currently, a maximum lift thickness of 200 mm (8 in.) for utility trench backfill compaction is specified by many Department of Transportations (DOTs) (e.g., [9] when a traditional vibratory compaction equipment is used. Given the high capacity of excavator-mounted hydraulic plate compactors in compacting granular materials

through a combination of static and dynamic forces, there is a growing industry demand in having the maximum lift thickness increased for excavator-mounted hydraulic plate compactors; however, there is a lack of field test data to support this demand. This paper presents the results of a field study that aims to compare the performances of utility trench compaction using a conventional walk-behind vibratory plate compactor with a lift thickness of 200 mm (8 in.) and an excavator-mounted hydraulic plate compactor with a lift thickness of 200 mm (8 in.), 300 mm (12 in.), 450 mm (18 in.), and 600 mm (24 in.). The performance data included compacted dry mass density of backfill material, compaction-induced earth pressure in backfill material, and compaction-induced strains in pipe. A 150-mm-diameter (6 in.) 6.1-m-long SDR-35 PVC sewer pipe (flexible pipe) was used. In the following sections, details of the testing program are first presented, followed by the results and discussions of the field tests. Conclusions are reached on the performance of the excavator-mounted hydraulic plate compactor in comparison with the vibratory plate compactor.

2 Field Testing Program

2.1 Trench Geometry, Backfill Materials, and Compaction Equipment

Figure 1 shows the trench geometry. Different terminologies have been used to describe different zones in a utility trench; the terminology used by the Florida Department of Transportation is generally followed in this paper [10]. The trench consisted of a bedding layer beneath the pipe, a cover zone that extends from the bottom of the pipe to 0.3 m (12 in.) above the top of the pipe, and a top zone above the cover zone. The 2B bedding material is consistent with the American Association of State Highway and Transportation Officials (AASHTO M145) specifications [11]. Figure 2 shows the gradation of the backfill soil used in this study, which can be classified as a well-graded gravel with sand (GW) based on the Unified Soil Classification System. The backfill soil has a maximum dry density of 2.17 g/cm3 (135.2 pcf), which is named as the standard proctor density (SPD) in Fig. 1 and an optimum moisture content of 7.7% as evaluated by the standard proctor test (ASTM D698).

The walk-behind vibratory plate compactor used in this study is a BOMAG BPR65/70D model, which has a basic operating weight of 570 kg (1257 lbs) and operates under 67 Hz with a centrifugal force of 69,000 N (15,525 lbs). The compaction plate has a dimension of 0.55 m by 0.98 m (22 in. by 39 in.). The excavator-mounted hydraulic plate compactor used in this study is an Allied HoPac 1000B model, which has an impulse force of 35,586 N (8000 lbs) and operates under 33 Hz (2000 cycles per minute). The compaction base plate has a dimension of 0.61 m by 0.71 m (24 in by 28 in.).
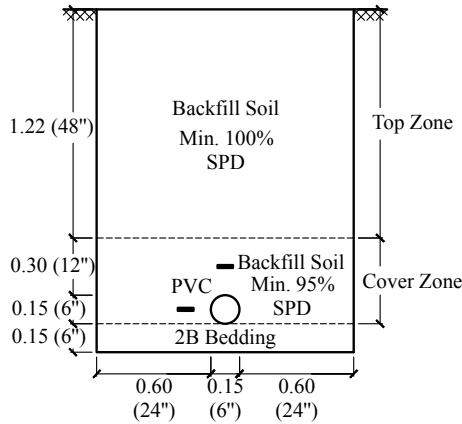
Fig. 1 Trench geometries and backfill materials
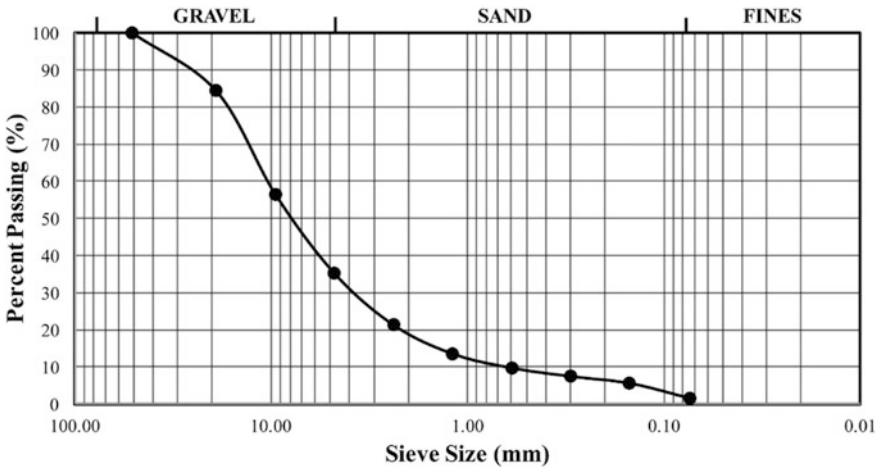
Fig. 2 Grain size distribution of backfill soil

2.2 Instrumentation

Dynamic pressure cells and strain gages were installed to monitor compaction-induced earth pressures in backfill and strains in the pipe, respectively. The dynamic pressure cells (Model 3510 from Geokon) are semiconductor pressure transducers that are capable of measuring dynamic pressures up to 400 kPa with an accuracy of 0.4 kPa. The pressure cells were calibrated by the manufacturer and verified by the project team using deadweights. Along the pipe, a total of six dynamic pressure cells were embedded on three equally spaced sections in the
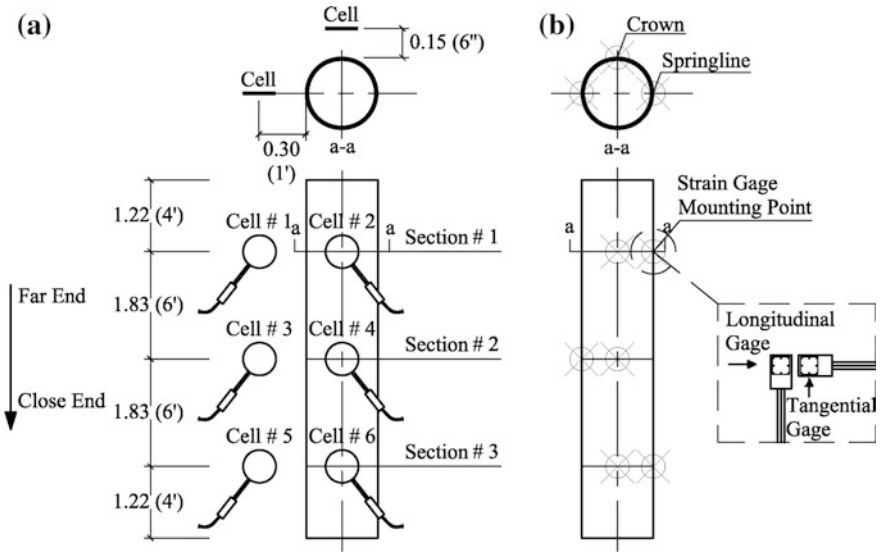
Fig. 3 Instrumentation layout: **a** pressure cells; **b** strain gages

backfill soil, and their layout is shown in Fig. 3a. To avoid rough contact between pressure cells and angular gravel-sized particles in the backfill material and for more reliable earth pressure measurement, a thin layer (about 25 mm) of the finer fraction of excavated soil was used as a seating material (i.e., cushion) between the pressure cells and backfill material. For each section of the pipe, two pairs of perpendicularly aligned strain gages were mounted on the crown and springline of the pipe to measure longitudinal and tangential (hoop) strains developed along the pipe during compaction. The layout of strain gages is shown in Fig. 3b.

2.3 Test Procedure

A total of five tests were conducted in this study. Table 1 presents a summary of these tests. SC-1 was conducted using a walk-behind vibratory plate compactor with a lift thickness of 200 mm (8 in.); HP-1, HP-2, HP-3, and HP-4 were conducted using an excavator-mounted hydraulic plate compactor with lift thicknesses of 600 mm (24 in.), 450 mm (18 in.), 300 mm (12 in.), and 200 mm (8 in.), respectively. For each test, backfill compaction in the top zone commenced after pipe was placed in trench, and cover zone was constructed according to Fig. 1. For Test SC-1, a lift thickness of 200 mm (8 in.) was used. For Tests HB-1 to HB-4, a lift thickness of 600 mm (24 in.) was first used for Test HB-1, and after backfill compaction was completed, the compacted backfill was excavated out of the top zone. A lift thickness of 450 mm (18 in.), 300 mm (12 in.), and 200 mm (8 in.) was

Table 1 Summary of field tests

Pipe type	Walk-behind vibratory plate compactor	Lift thickness	Excavator-mounted hydraulic plate compactor	Lift thickness
150 mm	SC-1	200 mm (8 in.)	HB-1	600 mm (24 in.)
(6 in.)			HB-2	450 mm (18 in.)
PVC pipe			HB-3	300 mm (12 in.)
Figure 1			HB-4	200 mm (8 in.)

subsequently used for Tests HB-2, HB-3, and HB-4, respectively, following similar procedure. The operators of the walk-behind vibratory plate compactor and excavator-mounted hydraulic plate compactor were different, but each had more than ten years of experience performing backfill compaction using their respective equipment. The operators were instructed to perform the backfill compaction based on their experience by continuously working back and forth in the trench, and no specific criterion on the number of passes was established. During backfill compaction in the top zone for each test, compaction-induced earth pressures in backfill and strains in pipe were continuously monitored.

3 Results and Discussions

3.1 Compacted Dry Mass Density

A nuclear density gage was used to measure the compacted dry mass density of backfill soil in general accordance with ASTM D 6938-08 and manufacturer's recommendations. The measurements were taken on the top of compacted surface at approximately 1.2 m from each end of the pipe after each lift was compacted. For the 200-mm-thick and 300-mm-thick lifts, a nuclear-gage penetration depth (i.e., length of penetration rod) of 200 and 300 mm was used, respectively; for the 450- and 600-mm-thick lifts, a penetration depth of 300 mm was used. For the 450-mm-thick lift, additional measurements were taken at 150 mm below the compacted surface by scraping off the compacted soil and creating a flat area that extended at least 300 mm in all directions. For the 600-mm-thick lift, additional measurements were similarly taken at 300 mm below the compacted surface.

The ratios of measured dry mass densities to the maximum dry density are shown in Fig. 4. The box plot is used to demonstrate the variations of the measured values, including the median, first quartile, and third quartile values. The box corresponds to the likely range of variation (i.e., between first and third quartiles). The lines extending from the bottom and top of each box mark the minimum and
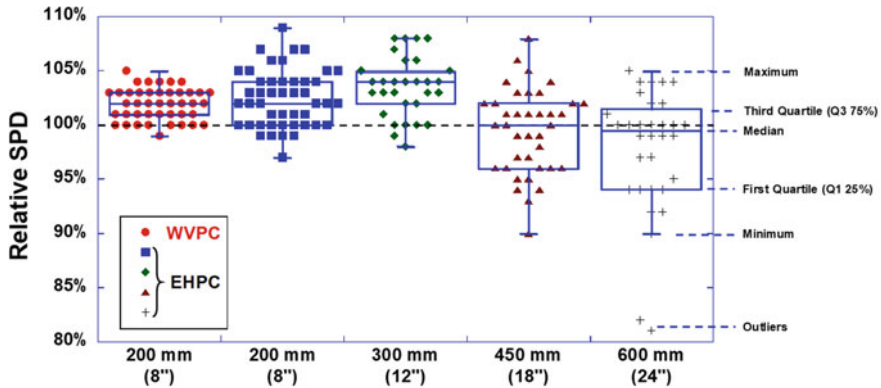
Fig. 4 Box plot of nuclear density gage results (WVPC: walk-behind vibratory plate compactor; EHPC: excavator-mounted hydraulic plate compactor)

maximum values, respectively, within a statistically acceptable range. Any value outside of this range, called an outlier, is displayed as an individual point. Figure 4 shows that the walk-behind vibratory plate compactor was able to generally achieve above 100% of SPD with a lift thickness of 200 mm. For the excavator-mounted hydraulic plate compactor, a compaction of above 100% of SPD was also generally achieved with lift thicknesses of 200 and 300 mm but was not consistently achieved with a lift thickness of 450 or 600 mm. The excavator-mounted hydraulic plate compactor, with the lift thickness of 200 or 300 mm, resulted in generally higher dry mass densities than the walk-behind vibratory plate compactor did with a lift thickness of 200 mm.

3.2 Compaction-Induced Earth Pressure

Figure 5 shows the recorded compaction-induced vertical pressure versus time from Cell #3 in Tests SC-1 and HB-4. Both tests were for the PVC pipe and a lift thickness of 200 mm. Figure 6 indicates that the excavator-mounted hydraulic plate compactor took half of the time on average to complete a trench compaction than the walk-behind vibratory plate compactor did. Figure 5 also shows that the recorded vertical pressure has two components: (1) a static component that increases with backfill thickness and (2) a dynamic component that fluctuates rapidly during compaction. The static vertical pressure is due to a combination of the self-weight of compacted fill on top of the pressure cell and the residual compaction-induced stress locked in from particle rearrangement. For example, the recorded initial pressure of approximately 25 kPa in Test SC-1 as shown in Fig. 5 is a combination of the overburden pressure and compaction-induced stress due to compaction in the cover zone. The recorded initial pressure (approximately 36 kPa)

Fig. 5 Comparison of
vertical earth pressure
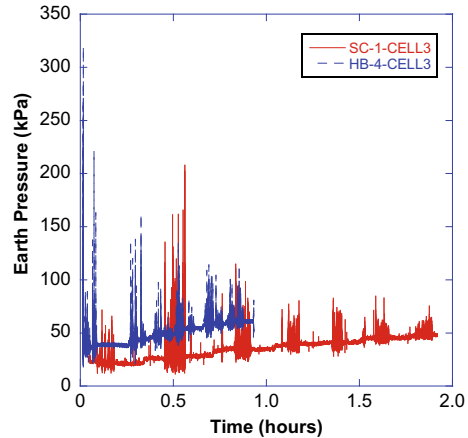
was higher in Test HB-4, which was due to the additional compaction-induced
stresses locked in from Tests HB-1 to HB-3 in the top zone. The dynamic vertical
pressure is due to the vibration of the compactors. For a given test, the recorded
dynamic vertical pressures are generally much larger than the static counterparts.
For example, the peak dynamic and static vertical pressures recorded for Test SC-1
were approximately 210 kPa and 50 kPa, respectively. Figure 5 also shows that the
excavator-mounted hydraulic plate compactor induced higher static and dynamic
vertical pressures than the walk-behind vibratory plate compactor did, which is due
to the higher compaction energy delivered by the excavator-mounted hydraulic
plate compactor. Similar results are observed from other pressure cells and hence
not presented herein.

3.3   Compaction-Induced Pipe Deformation

As the backfill soils are compacted, different sections of a pipe may undergo
compression or tension. Figure 6 shows the measured longitudinal strain versus
time of the pie in Test SC-1. At Sect. 1, the measured longitudinal strains were
mostly negative indicating that this section was under compression during com-
paction, whereas the positive longitudinal strains at Sect. 3 suggest that this section
was under tension. The spikes in the measured strains correspond to the compactor
being directly above or near the strain gages. Figure 6 shows that most of the strains
in the pipe were developed early in the compaction process, beyond which the pipe
was locked in preventing additional straining during subsequent compaction.
Different cross sections of a pipe may also undergo vertical compression or hori-
zontal compression depending on the relative magnitude of the vertical and hori-
zontal pressures acting on the cross section, which are illustrated in Fig. 7. Vertical
compression of a section results in compression at the crown and tension on the
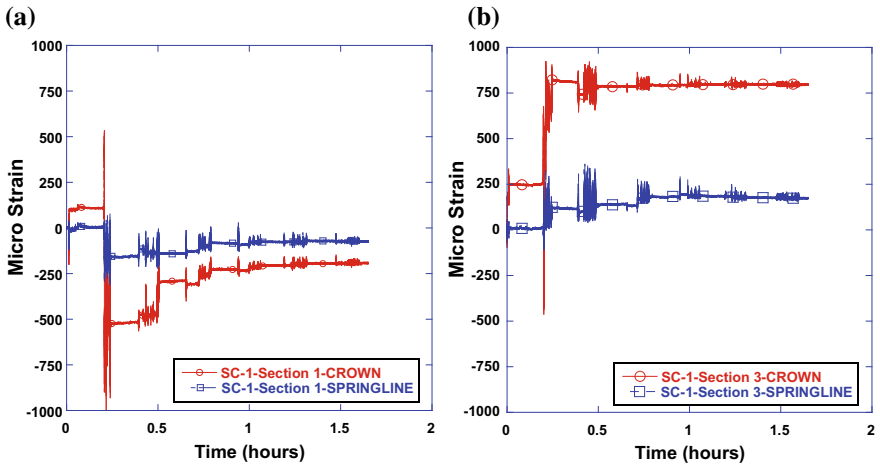
Fig. 6 Longitudinal strain measurements from Test SC-1: **a** Sect. 1; **b** Sect. 3
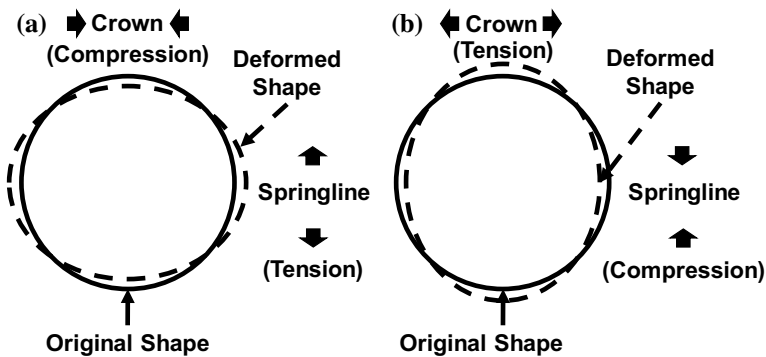
Fig. 7 Mode of deformation of a pipe cross section: **a** vertical compression; **b** horizontal compression

springline; horizontal compression results in the opposite. The deformation mode of a cross section may evolve during compaction. Figure 8 shows that the deformation mode of Sect. 3 in Test HB-4 evolved from horizontal compression to vertical compression during compaction, which is likely due to the movement of compactor relative to the pipe. The combination of downward force exerted by the excavator arm and compaction-induced stress is likely to result in vertical compression of the pipe when the compactor is compacting directly on top of the pipe but horizontal compression when the compactor is compacting on either side of the pipe. The maximum longitudinal and tangential strains are generally smaller than 3000 microstrains (0.3%) in the tests conducted. Typical plastic pipes have a yield strain

Fig. 8 Evolution of deformation mode for Sect. 3 during Test HB-4
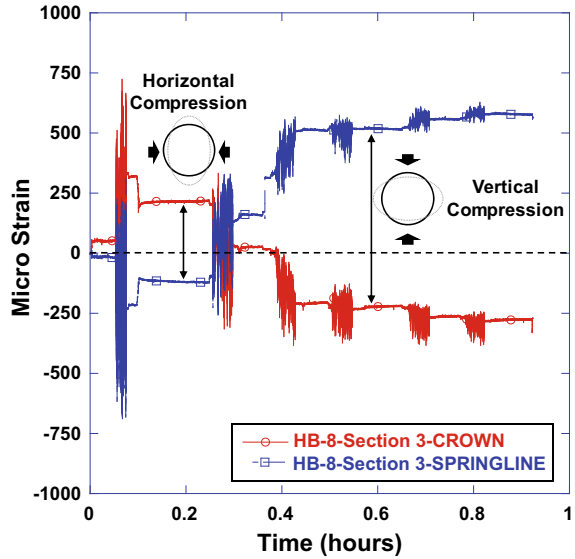
of 0.5% [12, 13]. Therefore, compaction-conducted strains in this study are unlikely to result in pipe damage, which is confirmed by visual inspections of the pipe excavated out of the trenches after tests.

4 Conclusions

This paper presents a field investigation that aims to compare the performances of utility trench compaction using a conventional walk-behind vibratory plate compactor and an excavator-mounted hydraulic plate compactor. Utility trench backfill compaction tests were conducted on a PVC pipe for each compactor. Performance data including compacted dry mass density of backfill material, compaction-induced earth pressure in backfill material, and compaction-induced strains in pipe are compared. Based on the test results, the following conclusions are reached:

1. The excavator-mounted hydraulic plate compactor took half of the time on average to complete a trench compaction than the walk-behind vibratory plate compactor did.
2. The excavator-mounted hydraulic plate compactor resulted in compacted dry mass densities, on average, greater than 100% SPD with backfill lift thicknesses of 200 and 300 mm, delivering a comparable compaction quality as the walk-behind vibratory plate compactor with a lift thickness of 200 mm. However, the excavator-mounted hydraulic plate compactor was not able to consistently achieve over 100% SPD with a lift thickness of 450 or 600 mm.

3. The excavator-mounted hydraulic plate compactor did not induce pipe damage in this study as the maximum strains in the pipe were smaller than 0.3%.

This study provided pertinent information and reference on the application of excavator-mounted hydraulic plate compactors to utility trench backfill compaction; however, the conclusions are based on the in situ and experimental conditions (e.g., backfill material, compaction equipment, trench geometries, and pipe) specific to this study. More field studies are needed to draw more general conclusions for a wide range of conditions including different models of excavator-mounted hydraulic plate compactors, pipe diameters and materials, and backfill materials.

References

1. Webb MC, McGrath TJ, Selig ET (1996) Field tests of buried pipe installation procedures. Transp Res Rec 1541:97–106
2. Zoladz GV, McGrath TJ, Selig ET (1996) Laboratory tests of buried pipe installation procedures. Transp Res Rec 1541:86–96
3. Hansen B, Lee D, Demartini C (1997) The cracking of stormwater pipes and the significance of construction loads. Research and Development Section, Brisbane City Council, Queensland, 8
4. American Concrete Pipe Association (ACPA) (2007) Concrete pipe installation manual. Irving, TX
5. McGrath TJ, Selig ET, Webb MC (1999) Instrument for monitoring buried pipe behavior during backfilling. ASTM Spec Tech Publ 1358:101–118
6. McGrath TJ, Selig ET, Webb MC (2000) Field tests of concrete pipe performance during backfilling. ASTM Spec Tech Publ 1368:73–88
7. Parmelee RA (1973) Investigation of soil-structure interaction of buried concrete pipe. Highw Res Board 443:32–39
8. Kararam A (2009) Nonlinear finite element dynamic analysis of the effect of compaction on underground conduits, Ph.D. Dissertation, The University of Texas, Arlington
9. Pennsylvania Department of Transportation (PennDOT) (2016) Specifications, Publication 408
10. Florida Department of Transportation (FDOT) (2017) Standard specifications for road and bridge construction, January, pp 1219
11. American Association of State Highway and Transportation Officials (AASHTO) (2005) Standard specifications for classification of soils and soil-aggregate mixtures for highway construction purposes. AASHTO M145, Washington
12. Moser AP (1981) Strain as a design basis for PVC pipe? In: Proceedings of the international conference on underground plastic pipe, ASCE, New York, pp 89–102
13. Molin J (1985) Long-term deflection of plastic sewer pipe. In: Proceedings of the international conference on advances in underground pipeline engineering, ASCE, New York, pp 263–277

Dynamic Behaviors of Overconsolidated Remolded Red Clay Under Cyclic Compressive Stress Paths

Guoyue Yang, Keyu Li, Yunlong Xu and Liangji Li

Abstract This paper presents a series of cyclically loading dynamic triaxial tests for remolded red clay with different overconsolidation ratios, confining pressures and dynamic stress amplitudes having been carried out using the GDS vibratory triaxial apparatus. Main target is the filling of red clay in the high-filling subgrade of CNPC Yunnan Petrochemical Railway special line. Results showed that the critical dynamic stress of overconsolidated remolded red clay increases linearly with the increase in overconsolidation ratio and confining pressure under the cyclic pure pressure dynamics, and an empirical formula for the critical dynamic stress of the region is obtained by regression analysis. Influence of overconsolidation ratio, confining pressure and vibration times on the development of cumulative dynamic strain was analyzed. Moreover, the dynamic strength of overconsolidated remolded red clay is proportional to the overconsolidation ratio and confining pressure. Number of cyclical vibrations has little effect on the dynamic internal friction angle of overconsolidated red clay but has a greater impact on the dynamic cohesion. These test results can provide certain practical value for the overconsolidation of red clay as a subgrade filling project in the area.

Keywords Overconsolidated · Remolded red clay · Dynamic triaxial test · Accumulative dynamic strain · Dynamic strength

G. Yang (✉) · K. Li · Y. Xu · L. Li
Hunan Key Laboratory of Geomechanics and Engineering Safety, Xiangtan University, Xiangtan 411105, China
e-mail: ygycsu@126.com

G. Yang · K. Li · Y. Xu · L. Li
College of Civil Engineering and Mechanics, Xiangtan University, Xiangtan 411105, China

1   Introduction

CNPC Yunnan Petrochemical Railway special line factory is located in Anning, Yunnan province. The relative height difference of the original ground of the factory is about 14 m. An artificial filling has been selected for the filling, in consideration of economy and environmental protection. The maximum fill height is 18 m, and it belongs to the deep artificial filling subgrade. The fillers are mainly based on red clay widely distributed locally. Red clay is a special soil with high natural moisture content, high plasticity, high void ratio, low density, poor compaction and other undesirable physical properties. Therefore, we carried out dynamic compaction when subgrade is being filled on the top floor. And on this basis, a preloading treatment was performed to overcome the poor engineering properties of the original red clay. The factory railway was designed as a ballastless monolithic track bed structure. The post-construction settlement of ballastless track subgrade should not be greater than 15 mm according to article 6.4.2 of the "High-Speed Rail Design Code" (TB10621-2014) [1]. And the dynamic characteristics of rock and soil are the key to engineering stability for transportation engineering. In addition, the research results of red clay are not very versatile because the physical and mechanical properties of red clay in different regions are quite different [2]. Therefore, the research on the dynamic characteristics of red clay is of great significance to the engineering construction in this area.

The domestic and foreign scholars have carried out a series of researches on the dynamic characteristics of red clay at present. Liu xiaohong et al. [3] studied the change law of dynamic strain of original structure red clay with vibration under cyclic loading. The critical dynamic stress of red clay under different water-bearing ratio, consolidation ratio and confining pressure was obtained. And the influence of various factors on the critical dynamic stress of red clay and the replacement thickness of the base bed of the subgrade were analyzed; Li Jian et al. [4] mainly study the influence of stress history on remolding red clay viscoelastic modulus and dynamic strength, and the corresponding influence law is obtained; Mu Kun et al. [5] studied the dynamic characteristics of original structure red clay in the Guangxi region, and the influence of natural moisture content, confining pressure, consolidation stress ratio, etc. on dynamic elastic modulus and damping ratio of red clay focus was analyzed; Li Zhiyong et al. [6] estimated the dynamic modulus of red clay in southern Hunan through dynamic triaxial tests; Fall et al. [7] analyzed the development law of accumulated plastic strains by conducting cyclic loading tests on red clay in western Senegal. Many of the research results on red clay are mostly against the original red clay. And the two-way load with both "pull" and "pressure" is used to simulate the seismic load in the cyclic loading process, while the real traffic load has only compressive stress. It will disturb the soil sample and form a certain overconsolidation after the deep artificial fill foundation is subjected to dynamic compaction and surcharge preloading in the actual project.

The red clay of the subgrade filler of CNPC Yunnan Petrochemical Railway special line is studied in this paper. A series of pure-pressure triaxial tests

simulating real traffic loads using GDS vibration triaxial apparatus was in progress. The dynamic characteristics of the overconsolidated remolded red clay were detailed studied. And the effects of confining pressure, dynamic stress ratio and other factors on the cumulative strain and dynamic strength of the overconsolidated remolded red clay are also considered.

2 Dynamic Triaxial Test

2.1 Test Soil Samples and Preparation

The test soil sample was taken from the railway loading and unloading yard of CNPC Yunnan Petrochemical Railway special line factory in Anning, Yunnan province. It is yellow-brown red clay. The basic physics and mechanics test is carried out with reference to the relevant specifications of the "Standard for Geotechnical Test Methods." Its natural moisture content is 29.47%, the maximum dry density of compacted red clay is 1.67 g/cm^3 as determined by standard compaction tests, and the optimum moisture content is 20.77%. Other physical and mechanical indexes of soil samples are shown in Table 1.

The sample adopts remodeling soil sample. The compaction degree of high-speed railway subgrade filler is greater than or equal to 92% according to article 6.4.1 of the "High-Speed Rail Design Code" (TB10621-2014) [1]. And the control dry density of the soil sample is 1.55 g/cm^3, which means that the degree of compaction is 93%. The quality of dry soil was evenly divided into five times to weigh and then making it compaction in split chase mold. Shaving at each junction to ensure good contact between layers made the sample 39.1 mm diameter and 80 mm height. Finally, the sample is evacuated to saturation by suction saturation method.

2.2 Test Parameter Selection

The test instrument is GDS dynamic cycle triaxial tester with a maximum vibration frequency of 5 Hz. The test adopts stress control loading method. The overconsolidation ratio (OCR) is 1, 2 and 4, respectively, to analyze the dynamic strength characteristics of overconsolidated remolded red clay formed by dynamic compaction and heap preloading combined with the actual load preloading height of the project in this experiment.

Table 1 Indexes of the physical property of red clay in Anning

Plastic limit (%)	Liquid limit (%)	Specific gravity	Porosity ratio	Liquid limit index (%)	Classification by plastic limit diagram
29.65	51.23	2.62	0.84	21.58	CH

Table 2 Parameter for the dynamic triaxial test

Test number	Overconsolidation ratio	Confining pressure σ_3 (kPa)	Frequency (Hz)	Critical cycling stress ratio
D1	1	50	5	0.2–0.6
D2	1	100	5	0.2–0.6
D3	1	200	5	0.2–0.6
D4	2	50	5	0.2–0.6
D5	2	100	5	0.2–0.6
D6	2	200	5	0.2–0.6
D7	4	50	5	0.2–0.6
D8	4	100	5	0.2–0.6
D9	4	200	5	0.2–0.6

The confining pressure is different due to the different in situ sampling depth of soil. Confirming the corresponding effective confining pressure according to the effective unit weight of soil and sampling depth, the effective confining pressure is calculated as

$$\sigma_3 = d \cdot \gamma' \tag{1}$$

where d = the soil depth; $\gamma' = g \cdot \rho'$ is the effective severity of soil; g = the acceleration of gravity; and ρ' = the effective density of soil based on isotropic hypothesis. The soil extraction depth is 6–15 m. Therefore, 50, 100 and 200 kPa were selected as the consolidation confining pressure.

The sinusoidal load can be approximated to simulate the vibration effect of traffic load on subgrade soil according to a lot of research [8]. The train operation mainly produces low-frequency effect on the subgrade, and the frequency of the most impact on the subgrade is the vibrational frequency when vehicle passing. It is related to train length l, driving speed v, etc. [9], namely the frequency = v/l. Take the G70 tank truck currently used in China as an example, whose length is 11.992 m. The test frequency is set to 5 Hz to simulate the load frequency applied to the subgrade by heavy-duty trains with a speed of 60 km/h comprehensive consideration of equipment conditions.

Changing the dynamic stress ratio CSR (CSR = $\sigma_d/2\sigma_3$, where σ_d = the dynamic stress), the dynamic stress ratio of this test is selected in the range of 0.2–0.6 according to the sample deformation CSR (Table 2).

2.3　Test Loading Step

(1) Making the sample back pressure saturation, the sample is considered to be fully saturated when the B value is greater than 0.97 in the B test.

(2) Performing isotropic consolidation under set confining pressure for normally consolidated soil. In order to obtain an overconsolidated sample, the sample is consolidated at a large effective confining pressure (σ_{3max}) first. And after the consolidation is stabilized, the effective confining pressure is unloaded to the set target confining pressure σ_3 to continue isotropic consolidation. The corresponding overconsolidation ratio (OCR = σ_{3max}/σ_3) is obtained after the water absorption of the sample is stabilized.

(3) Applying the static axial stress σ_1 ($\sigma_1 = \sigma_3 + \sigma_d$) to ensure the tensile stress is not produced when the dynamic load is applied. Followed by the application of dynamic stress σ_d for cyclic loading test. Actual subgrade fillers between fully drained and fully undrained conditions are more likely to destroy the subgrade without drainage. The dynamic loading process is carried out under undrained conditions for engineering safety reasons.

3 The Results and Analyses of the Test

3.1 Critical Dynamic Stress

Figure 1 shows the cumulative axial strain curves of different overconsolidated remolded red clays. It can be seen from the results of the curve change that the curve can be roughly divided into two types: one is a stable type, which is characterized by the cumulative axial strain rate which gradually decreases with the increase in the number of vibrations. The sample becomes dense and can resist the effect of external load after loading for a certain number of times. The sample only produces elastic strain, and the accumulated axial strain tends to be stable at this time; the other is a destructive type, which is characterized by a nonlinear increase in cumulative axial strain with an increasing number of vibrations. The structure of the sample is destroyed and the accumulated axial strain rapidly increases until the sample damaged when a certain number of vibrations is reached.

The accumulated axial strain follows vibration development trends consistent with previous research results [10]. The research of literature [11, 12] shows there is a critical state between the stable and destructive curves if the dynamic stress is refined, and the corresponding dynamic stress is called the critical dynamic stress.

The critical dynamic stress is a fixed value under certain conditions in theory. It is difficult to accurately determine the critical dynamic stress of soil samples through laboratory tests due to the experimental error and the uncertainty of soil samples. The maximum dynamic stress of a stable curve is taken as the minimum value of critical dynamic stress while the minimum dynamic stress of destructive curve is taken as the maximum value of critical dynamic stress in combination with actual engineering [13]. It is known from the test results that under the confining pressure of 50 kPa, the critical dynamic stress range of remolded red clay is 25–30 kPa when OCR = 1. The critical value for OCR = 2 is 30–35 kPa, and the critical dynamic stress for OCR = 4 is 45–50 kPa. The above method can be used to determine the critical dynamic stress range of overconsolidated remolded red clay under different confining pressures in the test scheme, as shown in Table 3.
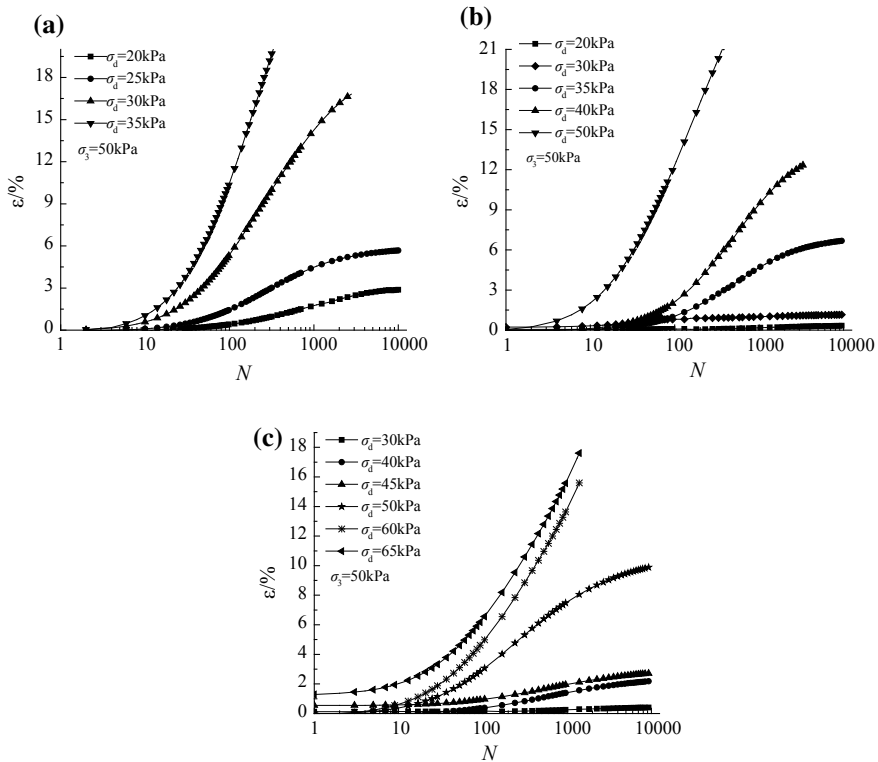
Fig. 1 Accumulated axial strain-cyclic number curves of remolded red clay with different values of OCR. **a** OCR = 1, **b** OCR = 2 and **c** OCR = 4

The average value of the critical dynamic stress range under the corresponding conditions is the critical dynamic stress corresponding to the remolded red clay combined with Table 3; it is plotted in Fig. 2. It can be seen from Fig. 2 that the critical dynamic stress of remolded red clay increases approximately linearly with the increase in overconsolidation ratio and confining pressure, and the greater the overconsolidation ratio, the greater the incremental gradient. It is more complicated for the design and construction unit due to a large amount of test work for determining the critical dynamic stress. The critical dynamic stress obtained by the experiment is applied to the SPSS software through multiple linear regression in order to facilitate the engineering application and summarizing the formula for estimating the critical dynamic stress of remodeled red clay in this area considering the overconsolidation ratio and confining pressure:

$$\sigma_{dcr} = 19.286\,OCR + 0.257\,\sigma_3 - 20.833. \tag{2}$$

Table 3 Values of critical dynamic stress of overconsolidated remolded red clay

Overconsolidation ratio	Confining pressure σ_3 (kPa)	Critical dynamic stress range (kPa)
	50	25–30
1	100	30–35
	200	40–45
	50	30–35
2	100	35–40
	200	45–50
	50	45–50
4	100	80–90
	200	130–140

(a)   **(b)**

Fig. 2 Influence of different factors on critical dynamic stress. **a** Different confining pressure. **b** Different overconsolidation ratios

3.2 The Development Law of Cumulative Strain

As can be seen from Fig. 3 that the cumulative axial strain of remolded red clay increases with the increase in vibration times. It can be seen from Fig. 3a that the accumulative axial strain increases when the rate of soil decreases accordingly with the increase in overconsolidation ratio under the same dynamic stress in combination with Fig. 1. For soil samples with overconsolidation ratios of 2 and 4, the corresponding cumulative axial strains are 1.15% and 0.25%, respectively, while the cumulative axial strain of normally consolidated soil reaches 14.25% when the cyclic dynamic stress $\sigma_d = 30$ kPa. This shows that the ooverconsolidated remolded red clay can effectively reduce soil deformation [14].

The relation curves of the cumulative strain and dynamic stress of the remolded red clay were drawn by the overconsolidation ratio of 4 and under each confining pressure at the time of vibration N = 1000 in Fig. 3b. As can be seen from figure,
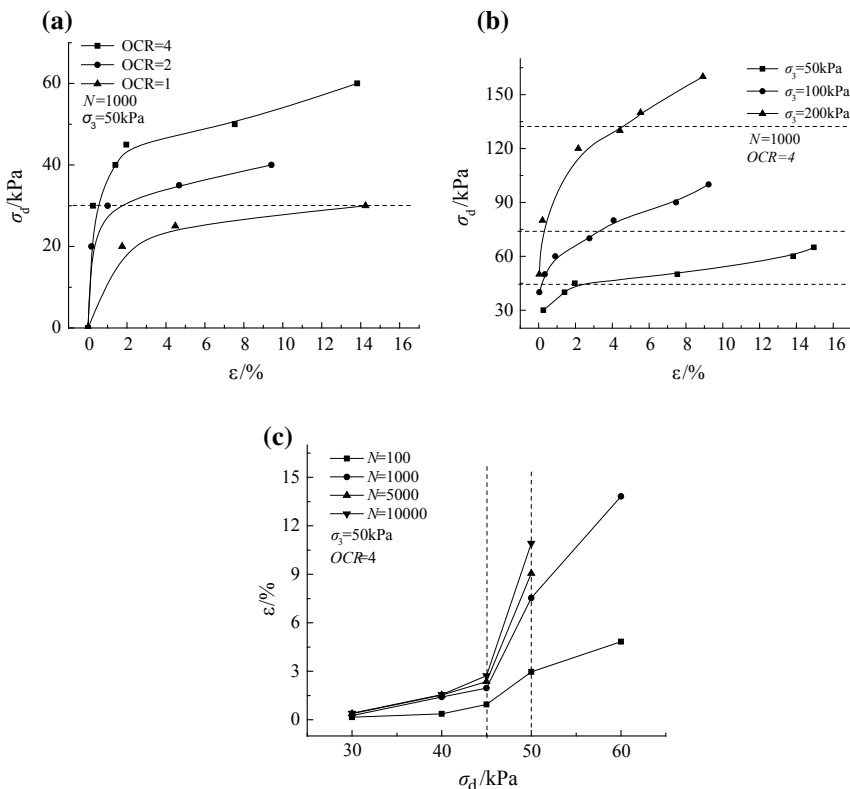
Fig. 3 Effect of different factors on the cumulative strain curve of overconsolidated remolded red clay. **a** Effects of overconsolidation ratio on the accumulated strain of remolded red clay. **b** Influence of confining pressure on the cumulative strain of overconsolidated remolded red clay. **c** Effect of vibration times on the cumulative strain of overconsolidated remolded red clay

the cumulative strain decreases as the confining pressure increases under the same dynamic stress conditions; the accumulative strain curve shows an obvious inflection point with the increase in dynamic stress. The curve is nonlinear before the inflection point, and the change trend is small. The curve is linear after the inflection point, and the change trend is large, which means the sample is destroyed at this point. It is shown that confining pressure can improve the deformation resistance of overconsolidated remolded red clay.

It can be seen from Fig. 3c that the cumulative axial strain of the overconsolidated remolded red clay is very small, and it is basically in the elastic strain stage when the dynamic stress is small; the accumulative strain of the remolded red clay whose overconsolidation ratio is 4 will reach the stable condition after the cyclical loading about 1000 times when the dynamic stress is less than a certain value. The same rule is found when the overconsolidation ratio is 2 according to Fig. 1; and the cumulative axial strain does not converge when the dynamic stress is greater than 45 kPa.

3.3 Dynamic Strength Characteristics

3.3.1 Dynamic Strength Curve

Dynamic strength refers to the dynamic stress value of a soil sample when it reaches damage under the action of a dynamic load [15]. Therefore, the determination of dynamic strength is related to the selected damage criteria. The standard for the destruction of soil has not yet reached a unified conclusion at present. Li Jian [4] found that taking 5–10% as a criterion for determining the dynamic strength of remodeling red clay is more reasonable. That is, why the cumulative axial strain of 5% has been selected as the damage criterion.

The relationship between soil sample strength τ_d and vibration times from the dynamic triaxial test is shown in Fig. 4. As can be seen from figure that the dynamic strength of red clay decreases with the increase in vibration times. It can be seen from Fig. 4a that the dynamic strength of red clay increases with the increase in overconsolidation ratio when the vibrations are the same. This is because the greater the overconsolidation ratio, the greater the pre-consolidation pressure on the soil sample. The plastic deformation part cannot be recovered, and the porosity decreases, i.e., the macroscopic manifestation is the increase in the strength after the soil sample undergoes unloading and rebound to the average consolidation stress; It can be obtained from Fig. 4b that the dynamic strength increases with the confining pressure increase under the same vibration. This is because when the confining pressure increases, then the lateral restraint effect of the soil increases, the internal particles become more tightly seized, and the slip between particles is difficult, thus the soil dynamic strength increases.
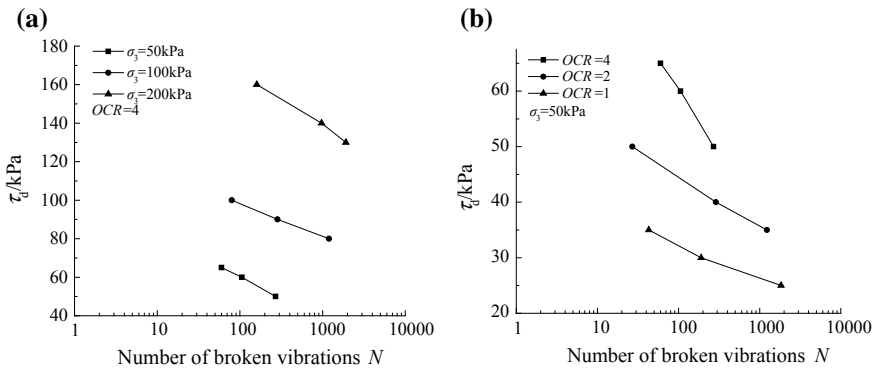
Fig. 4 Dynamic strength curve of overconsolidated remolded red clay under different factors. **a** Red clay dynamic strength curves with different overconsolidation ratios. **b** Dynamic curves of overconsolidated red clay under different confining pressures

Table 4 Fitting parameters of dynamic strength curve

OCR	Confining pressure (kPa)	a	b	R2
1	50	−6.04	44.46	0.97142
1	100	−8.9	61.76	0.94708
1	200	−18.31	97.08	0.96738
2	50	−9.11	62.87	0.99471
2	100	−12.13	81.72	0.90627
2	200	−14.3	105.13	0.96244
4	50	−23.13	106.40	0.99489
4	100	−17.01	132.16	0.99758
4	200	−27.35	220.60	0.99085

Using Formula (3) to fit the test data to obtain the cyclic load required under different conditions of overconsolidated remolded red clay under each vibration, the fitting results are shown in Table 4.

$$\tau d = a \lg N + b \tag{3}$$

where τ_d = the dynamic strength; N = damage vibration; a, b = the fitting parameters.

It can be seen from Table 4 that the correlation coefficient of the dynamic strength curve is greater than 0.90. This suggests that the vibration times are obviously related to dynamic strength. The parameter decreases as the overconsolidation ratio increases, i.e., the curve becomes steeper and steeper; the parameter b increases with the increase in the overconsolidation ratio and confining pressure, i.e., the dynamic strength increases with increasing b-value.

3.3.2 Dynamic Strength Parameters

The damaged dynamic stress is obtained corresponding to the remolded red clay when the overconsolidation ratio is 1, 2 and 4 when the confining pressure was 50, 100 and 200 kPa and the vibration is 10, 50, 100, 200, 500 and 1000 according to Formula (3). To find the corresponding dynamic strength index φ_d, c_d on the basis of the method used in calculating the dynamic strength index in literature [15], specifically as shown in Fig. 5.

It can be seen from Fig. 5 that both the dynamic internal friction angle φ_d and the dynamic cohesive force c_d decrease linearly with the increase in the damage time $\lg Nf$. Figure 5a reveals that the dynamic internal friction angle of remolded red clay increases with the increase in overconsolidation ratio, and the curve φd-$\lg Nf$ gradually flattens out with the increase in overconsolidation ratio; Fig. 5b shows that the dynamic cohesion of remolded red clay is reduced slightly under cyclic loading, basically remains unchanged when the overconsolidation ratio is 1. And the curve c_d-$\lg Nf$ is steeper when the overconsolidation ratio is greater than 1
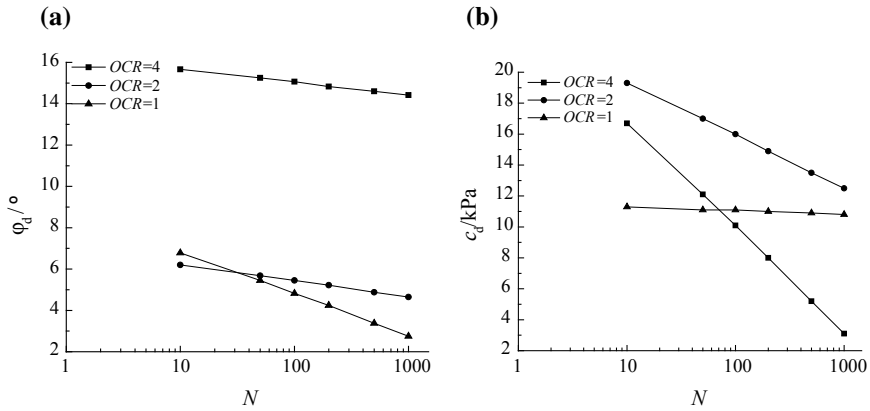
Fig. 5 Vibration of dynamic strength parameter with cyclic failure number. **a** The relation curve between the internal friction angle and the destructive vibration. **b** The relation curve of dynamic cohesion and destructive vibration

(OCR = 2, OCR = 4). This indicates that the number of cyclic vibrations has a greater influence on the cohesion of overconsolidated red clay, and the steeper the curve the more the overconsolidation ratio increases. It can also be obtained that the effect of vibration times on the dynamic internal friction angle of overconsolidated remolded red clay is small, and the effect on dynamic cohesion is greater under the action of pore-pressure cyclic loading by comparing Fig. 5a, b. This is because the internal friction angle mainly depends on the soil particle size distribution, mineral composition, water content, density, formation history and other factors [16]. However, the overconsolidated red clay subjected to higher consolidation pressure in advance, and the void ratio of the sample decreases while the density increases. Thus, the cyclical vibration has little effect on the above factors and the internal friction angle φ_d changes less in the undrained dynamic triaxial test; The cohesion force is closely related to the binding force between the particles. The interparticle bond strength decreases when the vibration times increase; that means the cohesive force decreases.

4 Conclusion

This paper focuses on the dynamic triaxial test of overconsolidated remolded red clay due to the phenomenon of overconsolidation formed by preloading of the high-filled subgrade of CNPC Yunnan Petrochemical Railway special line. The influence of overconsolidation ratio, confining pressure and dynamic stress on its dynamic characteristics was selectively analyzed. The conclusion of the experiment

can provide some reference value for the engineering and the design of dynamic parameters of overconsolidated remolded red clay in this area.

- The trend of cumulative axial deformation curves of overconsolidated remolded red clay is similar to the previous studies which are presented as both destructive and stable types.
- The critical dynamic stress of overconsolidated remolded red clay is proportional to the overconsolidation ratio and confining pressure according to the test results, and the linear relationship is satisfied; The empirical formula for estimating the critical dynamic stress suitable for the region has been summed, which has a certain practical value for the project in the region.
- The influence of overconsolidation ratio, confining pressure and cyclic loading times on the cumulative axial strain was analyzed. The overconsolidation ratio, the confining pressure and the cumulative strain increase are inversely proportional while it is directly proportion to the number of cyclic loading.
- The dynamic strength of overconsolidated remolded red clay increases with the increase in overconsolidation ratio and confining pressure. The dynamic internal friction angle of remolded red clay increases with the increase in overconsolidation ratio under pure pressure cyclic loading. Moreover, the larger the overconsolidation ratio, the less obvious the effect of the vibration; the effect of vibration times on the dynamic cohesive force of overconsolidated remolded red clay is greater, and it has less effect on the normal consolidation remolded red clay. The number of vibrations has little effect on the dynamic internal friction angle of the overconsolidation red clay, but it has a greater influence on the dynamic cohesion, both of which show a linear downward trend.

References

1. National Railway Administration of the People's Republic of China (2014) (TB10621-2014) Design specification standards for high-speed rail. China Railway Press, Beijing
2. Lin GY, Liu XH (2010) Red clay subgrade settlement control and dynamic stability analysis of ballastless track of high speed railway. China Railway Press, Beijing
3. Liu X, Yang G, Fang W (2011) Critical dynamic stress of red clay and replacement thickness of ballastless track cutting bed of high-speed railways. Chin J Geotech Eng 33(3):348–353
4. Jian J, Chen S, Jiang L, et al (2014) Experimental study on influence of stress history on dynamic properties of remolded red clay. Chin J Geotech Eng 36(09): 1657–1665
5. Mu K, Guo AG, Bai W et al (2015) Experimental study on dynamic properties of red clay in Guangxi under cyclic loading. China Earthq Eng J 37(02):487–493
6. Zhi-yong L, Cheng D, Jing-rong Z et al (2015) Research on experiment and prediction model of dynamic resilient modulus of laterite soil in Southern Hunan. Rock Soil Mech 36 (07):1840–1846
7. Fall M, Tisot JP, Cisse IK (1997) Undrained behaviour of compacted gravel lateritic soil from Western Senegal under Monotonic and cyclic triaxial loading. Eng Geol 47(1–2):71–87
8. Gong Q-M, Zhou S-H, Wang B-L (2004) Variation of pore pressure and liquefaction of soil in metro. Chin J Geotech Eng 26(2): 290–292

9. Xie Y, Pu-qiang YAN, Zhang D et al (1998) Measurement and analysis of bridge vibration when train passes by at a quasi-high-speed. J Vib Shock 17(1):53–58
10. Wu-ming LENG, Wen-jie LIU, Wen-quan ZHOU (2015) Testing research on critical cyclical stress of coarse-grained soil filling in heavy haul railway subgrade. J Vib Shock 34(16):25–30
11. Zhang JH, Yin Z, Zheng JL (2014) Research on critical stress level of shakedown of red clay in southern hot and humid areas. J Centl South Univ (Sci Technol) 45(04): 1288–1292
12. Zhang Y, Kong LW, Guo AG et al (2009) Cumulative plastic strain of saturated soft clay under cyclic loading. Rock Soil Mech 30(06): 1542–1548
13. Kong XH, Jiang GL, Zou ZY et al (2013) Dynamic characteristics and pavement performance of red mudstone subjected to cyclic loading. Chin J Rock Mech Eng 32(09):1813–1819
14. Sun L, Wang J, Sun HL et al (2015) Influence of cyclic confining pressure on cumulative deformation behavior of over consolidated clay. Chin J Rock Mechan Eng 34(03):594–600
15. Wu SM (2000) Soil dynamics. China architecture & Building Press, Beijing
16. Jing MENG, Yan-bin GAO, Ju-yun YUAN (2008) Study on the effective angle of internal friction of remolded clay in Shanghai. J Eng Geol S1:677–680

Study on the Stress Deformation Behaviour of Half-Cover Excavation

Xiu-zhu Yang, Yu-qing Zhang, Jin-shan Lei, Lai-yun Jiang, Ji-dong Dai and Jian-liang Wu

Abstract With the rapid development of urban rail transit in China, an increasing number of subway stations are being built in the centres of densely populated and congested cities. In such scenarios, the foundation pit constructed by one half-cover excavation can play a balanced role in the construction of the metro station. This study investigates a half-cover excavation of a subway station structure, considers the excavation sub-step, compares it with open-cut excavation, and analyses the force and deformation of the support structure. It also provides some references for practical construction and information monitoring.

Keywords Subway station · Half-cover excavation · Deep foundation pit · Numerical simulation

1 Introduction

Cities have built railway systems in order to alleviate traffic congestion on the ground. However, in the process of metro construction, cities with heavy traffic have experienced an increase in the number of traffic-related issues, especially in the construction of the station at the road intersection. Easing the traffic is an issue that has to be considered in the selection of construction methods. Construction using the open-cut method is convenient, but this can occupy pavement space for a long time, which can result in a considerable burden on urban traffic. The concealed excavation method can solve the above problems but involves a long construction period, high cost and increased difficulties in the work. The semi-cover excavation method can effectively alleviate heavy traffic in the city centre, but its support

X. Yang · Y. Zhang (✉) · J. Lei
School of Civil Engineering, Central South University, Changsha 410075, China
e-mail: iamzyq@foxmail.com

L. Jiang · J. Dai · J. Wu
Railway 5 Bureau Group Mechanization Engineering Co., Ltd., Hengyang 421000, China

structure is complicated, and its deformation law needs to be studied. Guoyong [1] compared the construction schemes of stations and calculated the force of the half-cover excavation structure under usual working conditions [1]. Zhang et al. [2] used an incremental method to analyse the deformation characteristics of the road surface and wall top of a half-cover excavation station [2]. Ren et al. [3] used FLAC3D software to study the deformation rules of columns in the foundation pit of a half-cover excavation station [3]. Because the unbalanced deformation of the foundation pit structure in the half-cover excavation method is one of the hidden dangers to the overall stability of foundation pits, it is necessary to study the similarities and differences between the forces and deformation rules of support structures at different sides under the conditions of a half-cover excavation method and open-cut excavation method [4]. Therefore, this study focuses on the construction of a half-cover excavation foundation pit of the pile support structure, which is used to analyse the force and deformation laws of the structure during the excavation step.

2 Overview of the Project

The railway station of Xi'an Metro line 5 is located at a busy downtown intersection, arranged along the east-west road, with a large vehicle flux on the ground. The station is a two-storey island type underground station, with the main foundation pit being 253.1 m long, with a standard section width of 21.2 m and depth of 18.1–19.28 m. The construction of the station adopts the method of half-width cover excavation. The paving system adopts the army girder, cover plate and asphalt pavement to form a temporary pavement system. The retaining structures of the foundation pit adopt the bored grouting piles. Furthermore, concrete support and two steel supports are erected in the foundation pit (see Fig. 1).

Fig. 1 Section of the supporting foundation pit
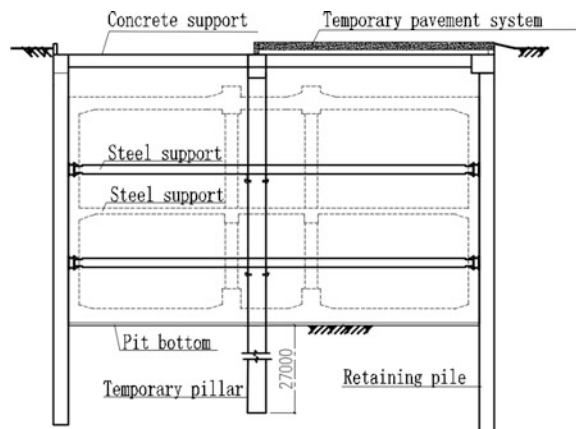
The terrain of the station is relatively flat in general, and the ground buildings around the station are dense. The stratigraphic conditions in the excavation range of the foundation pit are mainly the new loess existed in the Late Pleistocene of Quaternary and the silty clay existed in the Middle Pleistocene of Quaternary. Some saturated medium sand is contained in the clay layer, but is generally not a layer and is produced in the lens body. The underground water depth of the site is 9.3–11.0 m, and the water level elevation is 394.61–398.28 m. The comprehensive permeability coefficient is 12 m/d. According to the physical and mechanical properties of the soil in the excavation area provided by the geological exploration report, soil parameters are shown in Table 1.

The construction and excavation conditions of the station are as follows: ① The retaining pile, temporary pillar and temporary paving are constructed; ② the entire foundation is excavated to −2 m, within the first concrete support (1 m); ③ excavation of the middle part is to −5.5 m, the width of the soil platform is 2 m at both sides, with a gradient ratio of 1:1, and then, digging takes place on both sides; ④ excavation of the middle part is to −9 m, the width of the soil platform is 2 m at both sides, with a gradient ratio of 1:1. After the earth platform is excavated, the second steel bracing (−8 m) is constructed; ⑤ excavation of the middle part is to −12 m, the width of the soil platform is 2 m at both sides, with a gradient ratio of 1:1, and then, digging takes place on both sides; ⑥ excavation of the middle part is to −15 m, the width of the soil platform is 2 m at both sides, with a gradient ratio of

Table 1 Physical and mechanical parameters of each layer in the model

No.	Soil type	Thickness (m)	Weight (kN/m³)	Saturated unit weight (kN/m³)	Cohesion (kPa)	Internal friction angle (°)	Modulus E_0 (MPa)	Poisson ratio v
1	1–2 filling	2	17.5	18.5	15	10.0	4.5	0.35
2	3–1–1 loess	5	16.4	18.5	32	23.5	14	0.25
3	3–1–2 loess	2	18.0	19.0	30	22.5	12	0.30
4	3–2 paleosol	3	19.2	19.6	35	26.0	11	0.30
5	3–4 silty clay	23	19.7	20.1	36	26.5	15	0.29
6	3–7 medium sand	3	20.0	23.0	0	32.0	18	0.27
7	4–4 silty clay	19	19.6	19.9	42	23.0	20	0.30
8	4–7 medium sand	3	21.0	24.0	0	34.0	25	0.26

1:1. After the earth platform is excavated, the third steel bracing (−14 m) is con-
structed; ⑦ excavation of the middle part is to −18.4 m (bottom of the pit), the
width of the soil platform is 2 m at both sides, with a gradient ratio of 1:1, and then,
digging takes place on both sides.

3 The Process of Modelling

3.1 The Simulation Model

In this study, the formation size of a 150 m × 60 m rectangle was adopted, and the
medium sand layer was considered a continuous distribution (see Fig. 2). An
excavation section of rectangular shape was selected, with a width of 21.2 m and
excavation depth of 18.4 m. The Φ1000@1500 bored piles retain the structure, the
length of the pile on the right side of the section is 24.9 m, and the other side's
length is 25.4 m. The depth of the intermediate temporary pillar is 45.4, 11.55 m
from the right side and 9.65 m from the left side. Three supports are adopted. The
first support is a concrete support, with an elevation of -1 m. The second and third
supports are steel with elevations of −8 m and −14 m, respectively. The sectional
dimensions and materials of the model structure are shown in Table 2.

In the model, the stratum adopts a 2d plane strain element, the supporting
structure adopts a 1d beam element for simulation, and the overloading of the
ground on both sides of the foundation pit takes 20 kN/m. The temporary pavement
system adopts a zero-gravity plane strain unit, only considering its rigidity, and its
load according to the bridge design code uses the lane load, equivalent to a uni-
formly distributed load of 26 kN/m and a concentrated load of 225 kN/m.

The modified Mohr–Coulomb model was adopted as the constitutive model for
the soil unit of the formation, and the elastic model was adopted for the supporting
structure. The surface is taken as a free boundary, and the left and right boundaries
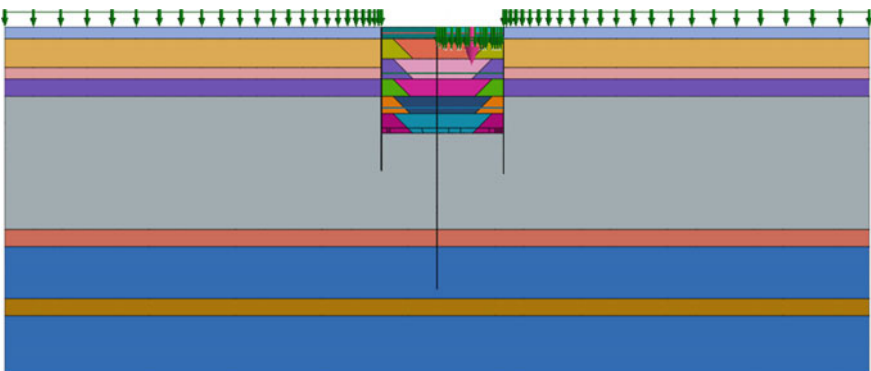
Fig. 2 Calculation model

Table 2 The size parameters of structures adopted in the model

No.	Grid name	Grid type	Section size	Materials	Level distance
1	Retaining piles	1D-beam	d = 1	C35	1.5 m
2	Concrete support	1D-beam	0.8 * 0.8	C35	7.5 m
3	Steel support	1D-beam	D = 0.609, t = 0.016	Steel	3.5 m
4	Temporary pillar	1D-beam	D = 1.2	C35	7.5 m

of the model ($x = -75$ m and $x = 75$ m) constrain its lateral displacement, while the lower boundary of the model ($y = -60$ m) constrains its lateral and vertical displacement.

3.2 Simulation of Construction Conditions

The model shall clear all displacements after creating an initial stress field, and it should take into consideration the construction sub-steps of excavating the middle groove of the foundation pit, simulate according to the setup of the aforesaid construction conditions, and perform partition block treatment according to the excavation stage and sequence (see Fig. 3).

In this study, the open excavation method, the half-cover excavation method and the half-cover excavation method (without consideration of sub-steps) are adopted for analysis of three working conditions. Among them, the half-cover excavation method (without consideration of sub-steps) does not take into account a situation where soil is retained in the middle drawing groove, and earthwork in each stage was excavated and formed once. See Table 3 for details of excavation zones for three types of conditions.

Fig. 3 Working conditions of excavation
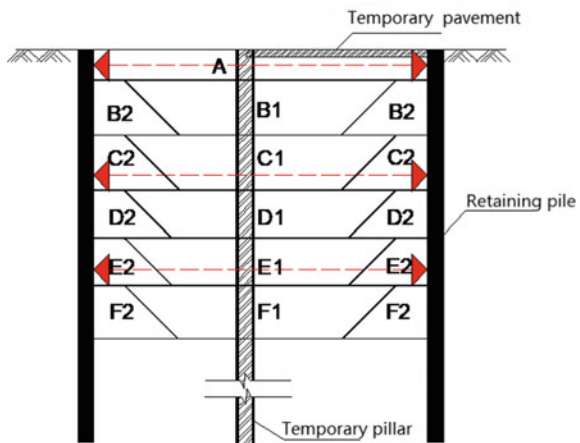
Table 3 Detailed list of excavation zones at each stage

Sub-step (open-cut, half-cover)	Condition	Stage1 dig	Stage 2		Stage 3		Stage 4		Stage 5		Stage 6	
			cut	dig	cut	dig	cut	dig	cut	dig	cut	dig
	Excavation zone	A	B1	B2	C1	C2	D1	D2	E1	E2	F1	F2
No sub-step (half-cover)	condition	Stage 1 dig	Stage 2 dig		Stage 3 dig		Stage 4 dig		Stage 5 dig		Stage 6 dig	
	Excavation zone	A	B1, B2		C1, C2		D1, D2		E1, E2		F1, F2	

4 Calculations and Analysis

4.1 Analysis of Lateral Deformation of Retaining Pile Wall

In this example, that right half of the foundation pit is covered with a temporary cover system, so the comparison analysis of the results of the finite element calculation is conducted on the left and right sides [5]. From the point of view of whether the half foundation pit is covered with temporary paving, the right side of the model refers to the half retaining pile on the side of the foundation pit covered with temporary paving, and the left side refers to the retaining pile without temporary covering on the other side of the foundation pit [6].

According to the working procedure of excavation conditions, the maximum lateral displacement of the pile body becomes larger with the increasing depth of excavation in the three groups of analysed cases [7–10]. It can be seen from Figs. 4 and 5 that the lateral displacement of the retaining pile in the foundation pit constructed by the open-cut excavation method is basically symmetrical on the left and right because there is no temporary overlaying on either side of the foundation pit. At the same time, the mass of the half-width paving itself and the road load acting on it also have a significant influence on the foundation pit surrounding structure; a large lateral displacement occurs, especially where the pile top position is close to the paving. The model analysis results show that the maximum lateral displacement of piles with the open-cut excavation method is 8.71 mm on the left and 8.83 mm on the right. The maximum lateral displacement of the pile body using the half-cover excavation method is 9.71 mm on the left and 8.92 mm on the right. The maximum lateral displacement of the pile shaft in half-cover (without sub-steps) is 8.52 mm on the left side and 7.85 mm on the right side. In each of the three sets of analyses, the right half of the model is slightly larger than the left half of the base, so the lateral displacement of the right side is more than the lateral displacement of the left side. Meanwhile, in the case of semi-cover excavation, because of the temporary cover and pavement load on the right side, the lateral displacement of the pile body on both sides is also influenced. The result shows that the lateral displacement of the left pile body is larger than the lateral displacement of the right pile shaft.
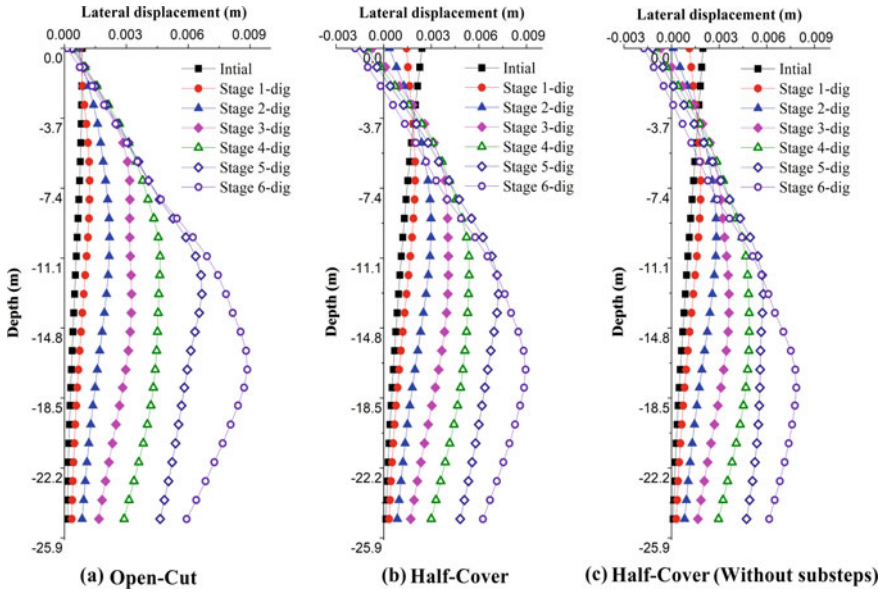
Fig. 4 Lateral displacement of the left cast-in-pile
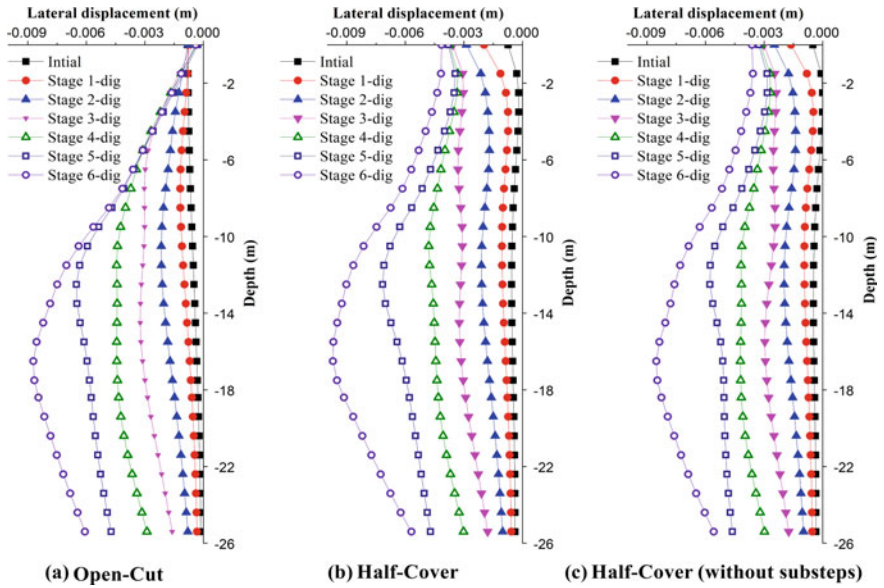
Fig. 5 Lateral displacement of the right cast-in-pile
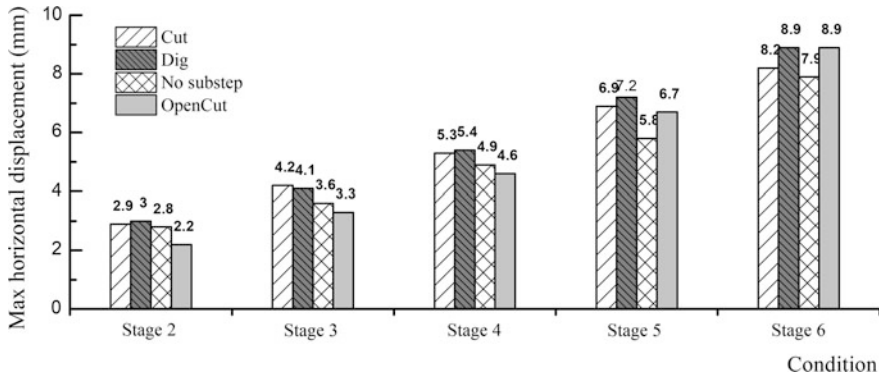
Fig. 6 Bar chart of the maximum lateral displacement of the pile

The deformation of the wall is closely related to the construction process of the foundation pit and the surrounding environment. When the construction process is slow and fails to erect the steel supports in time, the deformation of the piles will increase, which will appear as a space-time effect. The above effect can be seen from the comparison of pile body lateral displacement in the case of half cap excavation (whether or not sub-steps are accounted for). Since the excavating procedure is divided into the cutting and excavating of the two sides of the earth platform, when excavating the middle groove, the support is not installed, so the pile deformation is more serious than in the half-cover excavation method without the consideration of sub-steps (Fig. 6).

4.2 Analysis of the Bending Moment of the Pile

Retaining pile body bending moments can be calculated by the pile body stress field, and the relationship between the deformation and the retaining pile itself is also very close. Figure 7 shows the comparison of the bending moment between the retaining pile under the excavation method and the pile on the right side of the foundation pit (including the covered side) under half-cover excavation. The pile bending moment value of the foundation pit excavation to the pit bottom stage in three working conditions is compared (see Fig. 8).

As seen in Figs. 7 and 8, the maximum bending moment of the retaining pile in the foundation pit is basically consistent with the maximum lateral displacement of the pile body in the process of excavation, and both reach the maximum at the bottom of the excavation part. The maximum negative bending moment of the open-cut excavated pile is about 340 kN·m, and the maximum positive bending moment is about 280 kN·m. The maximum negative bending moment of the half-cover excavation pile body with consideration of sub-steps is about 350 kN·m, and the maximum positive bending moment is about 300 kN·m. For the pile body
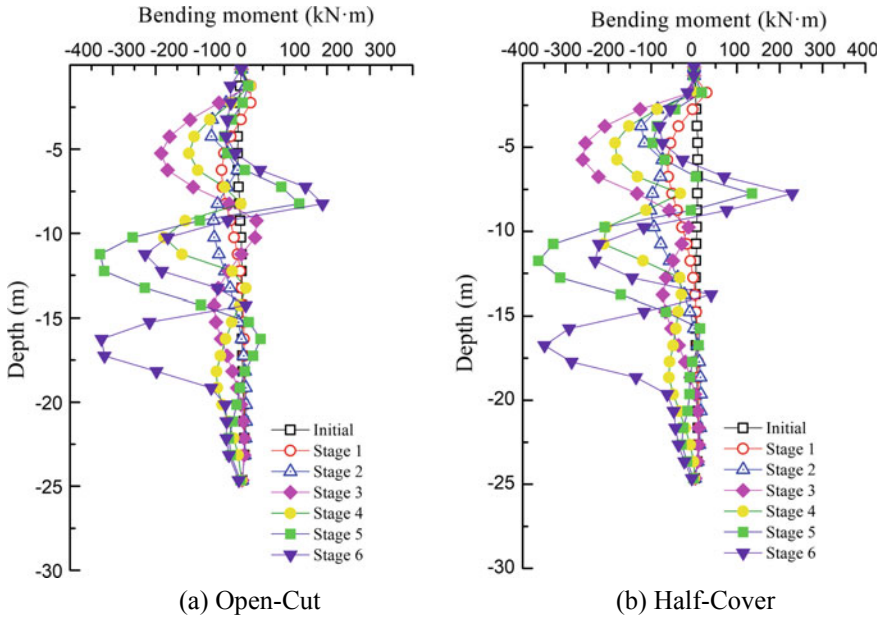
Fig. 7 Bending moment of the right retaining pile in different excavation stages

(a) Open-Cut

(b) Half-Cover

(a) Left side (unpaved)

(b) Right side (with cover)
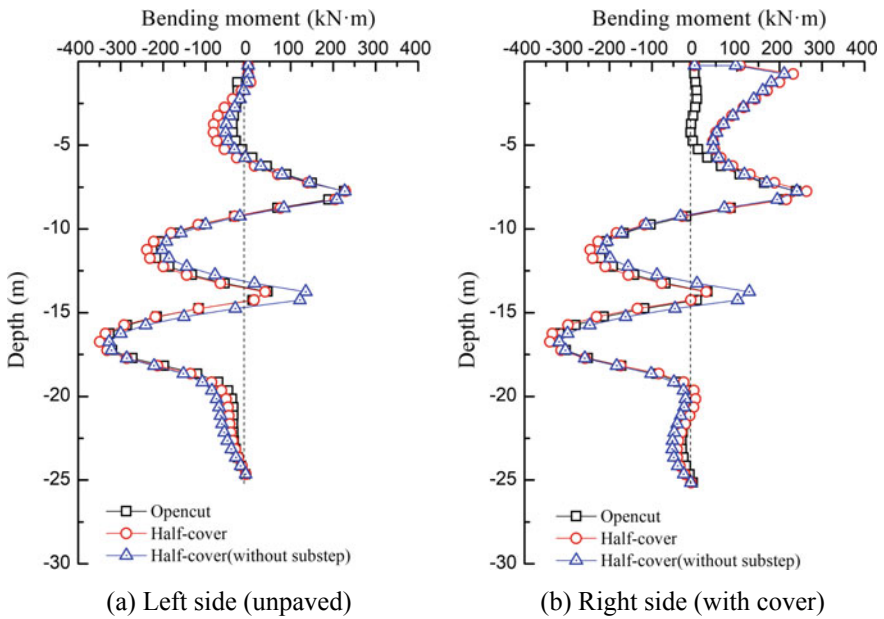
Fig. 8 Comparison of the bending moment of the retaining pile (last stage)

with the half-cover excavating method, irrespective of sub-steps, its maximum negative bending moment is about 330 kN·m and its maximum positive bending moment is about 280 kN·m.

At the same time, because of the existence of the temporary cover system, the foundation pit with half-cover excavation has a large stiffness and heavy load, which has a significant impact on the bending moment of the pile roof of the side of the cover. The analysis result shows that the tendency of the pile bending moment in the three sets of analyses is similar to that of the following parts. It can be considered that the temporary spreading cover has a certain range of influence depth on the bending moment of the surrounding pile, which is roughly the depth of the second support installation node.

4.3 Analysis of Support Axial Force

The internal force of the tensile support structure is affected by pile deformation and erection of the steel support. When the pile deformation is large, the stress of reinforcement is also large. Erection of steel support can improve the reinforcement stress of the envelope. The tensile and compressive stresses on both sides of the wall also indirectly coincide with the deformation curves of the wall.

The change in the supporting axial force is closely related to the lateral displacement of the wall. When the lateral deformation of the wall increases, the axial force of steel support clearly changes. At the same time, during the foundation pit construction, the axial force of the steel support fluctuates greatly due to the installation and removal of the steel support under earthwork excavation and the influence of weather and temperature. However, the general trend of the axial force change of upper concrete support is to increase gradually and then decrease gradually. The axial force of the first concrete support decreases when the steel support of the lower layer is installed. In the open excavation method, the axial force of the first concrete support, that is, the axial tension of the first concrete support, is positive. It also proves the necessity and importance of using a reinforced concrete structure for the first support. Because the steel support itself has poor tensile performance, tension can easily remove its exposure causing structural failure; both the compressive and flexural reinforced concrete's structural members must have enough safety reserve, which is more applicable to the first line of support.

In this study, the axial force is treated as positive pressure and negative tension. As shown in Fig. 9, in the open-cut excavation method of the model, the concrete support by the maximum tension is about 200 kN, occurring in the second stage after the groove cutting excavation, and the maximum pressure is about 350 kN, taking place in the third stage after installation of the second support. Using the half-cover excavation model, the maximum pressure on the concrete support is
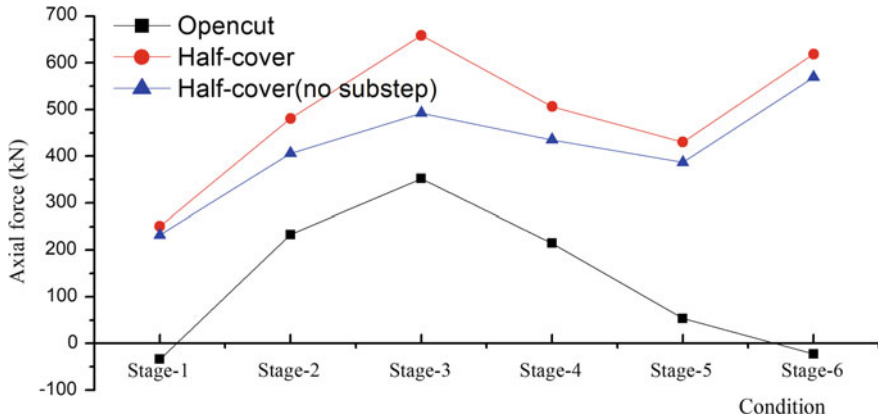
Fig. 9 Axial force of concrete support
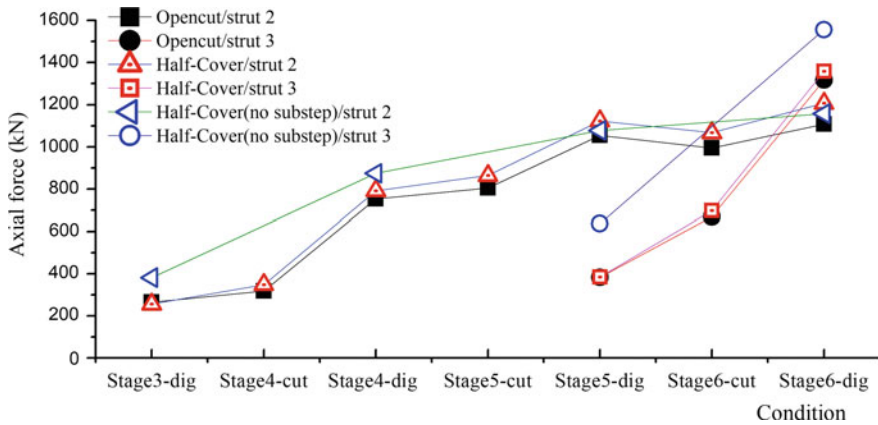
Fig. 10 Axial force of steel support

about 660 kN, also after the installation of the second support. However, the axial force of excavation in the late stage of both models changes. On the one hand, when the open-cut model digs at the bottom of the pit, the axial force of the first line of support changes from pressure to tension. On the other hand, the first support of the half-cover excavation method increases the pressure when the excavation is close to the bottom of the pit. It can be seen from Fig. 10, that, with the three groups of analysis, the axial force variation trend of steel support is similar for each, and it increases with the excavation.

5   Conclusion

This numerical simulation mainly analyses the influence of the temporary cover system on the stress field and displacement field of the supporting structure for the half-cover excavation of the foundation pit pile support structure. Specific conclusions and suggestions are as follows:

(1) In the excavation method, the size of the divided span of the foundation pit has a certain influence on the lateral displacement imbalance of the pile body. In the cover excavation foundation pit, the lateral displacement of the pile body on the opposite side will be greater because one side is covered with half paving. Therefore, in practical engineering, the deformation perturbation rule of the foundation pit excavation method type to the surrounding structure and surrounding environment should be taken into account, and measures, such as increasing the monitoring frequency and installing an inclined brace, should be taken into account for areas and stages with relatively high risk.

(2) The influence of the temporary pavement on the bending moment of the pile has a certain range, which is roughly above the second installation node depth. It is necessary to deepen the design of the temporary retaining pile to ensure enough safety reserves and prevent the pit from capsizing.

(3) The supporting axial force of the same foundation pit in the case of half-cover excavation will be greater than that of open-cover excavation, which may be caused by the influence of the rigidity of the temporary paving system and the road load of the temporary pavement. A more detailed model will be adopted in the future, and research will be carried out based on the results and analysis of the actual monitoring data.

(4) The model hypothesis does not take into account the precipitation conditions, surrounding buildings and other environmental conditions, which may also have a certain influence on the results. This will be tested further in the next study.

References

1. Guoyong RUAN (2011) Case study on design of semi cover and cut construction of metro station. Tunn Constr 31(6):693–700
2. Zhang X, Liu X (2015) The application and effect analysis of semi-covered excavation method in metro excavation. J Water Resour Arch Eng 13(2):207–211

3. Ren J, Ma J, Bai J et al (2017) Research on the deformation laws of center pillar of metro station excavated by semi-covered method. J Railw Eng Soc 34(9):103–108
4. Xu P, Han Y, Duan H et al (2015) Environmental Effects induced by deep subway foundation pit excavation in yellow river alluvial landforms. Geotech Geol Eng 33(6):1587–1594
5. Liyanapathirana DS, Nishanthan R (2016) Influence of deep excavation induced ground movements on adjacent piles. Tunnling Undergr Space Technol Inc Trenchless Technol Res 52:168–181
6. Wu J (2013) Study on pile-strut bracing structure of excavation with different excavation depth. J Railw Eng Soc 30(10):26–30
7. Yu J, Gong X (2002) Research on deformation of foundation-pit engineering. China Civ Eng J 35(4):86–90
8. Gao W, Dou YM, Zhou XL et al (2006) Studies on displacements and earth pressures of pit-retaining structure during excavation by steps. Chin J Geotech Eng 28(b11):1455–1459
9. Shakeel M, Ng C W (2017) Settlement and load transfer mechanism of a pile group adjacent to a deep excavation in soft clay. Comput Geotech
10. Xiao HB, Wang YH, Wang XH (2004) Finite element analysis of multi-braced retaining structures with consideration of the effect of staged excavation. Chin J Geotech Eng 26(1):47–51

One-Dimensional Consolidation Tests and Cyclic Triaxial Tests on Structural Soft Clay in Southeast China

Hongming Liu and Xuecheng Bian

Abstract In this study, a series of one-dimensional consolidation tests and dynamic tests of Ningbo clay and Wenzhou clay have been carried out. Combined with the test results of Xiaoshan clay, soil structural property and dynamic response of different soft clays in southeast China have been investigated. The e-logP curve showed that three different natural soils all have obvious structural property. For different soils, the bending point of consolidation curve is different. As to Wenzhou clay, consolidation curve descended sharply after reaching yield stress. This indicates strong structural property in Wenzhou soil. However, Ningbo clay consolidation curve was relatively smooth compared with Wenzhou and Xiaoshan clay. Cyclic triaxial tests of Ningbo natural and remoulded soil indicated that natural sample compared with remoulded sample needs much more dynamic cycles to reach failure point and then went into a brittle failure state.

Keywords Soft clay · Soil structure · One-dimensional consolidation · Cyclic loading · Axial strain

1 Introduction

With the economic development of southeast China, large amount of transportation infrastructures, like high-speed railway, expressway, airport pavement and subway, have been built. However, soft clay which has the feature of high water content, low permeability, low strength, high soil porosity and high structural property is deeply and widely spread in southeast China. The constructing disturbance and operating cyclic dynamic loading of these transportation infrastructures can induce the

H. Liu · X. Bian (✉)
Department of Civil Engineering, Institute of Geotechnical Engineering,
Zhejiang University, Hangzhou 310058, China
e-mail: bianxc@zju.edu.cn

H. Liu
e-mail: liuhongming@zju.edu.cn

settlement of lower subgrade which will inevitably threaten the safety of operation. So in order to ensure the operating safety of transportation infrastructure, it is of much importance to better understand the soil structural property and dynamic response pattern of soft clay.

In the last few decades, many researchers have launched related researches on soft clay. Schmertmann [1] pointed out that consolidation curves of different degrees of disturbed clays will intersect at $0.42e_0$. But this method did not consider structural property. Chen and Hao et al. [2] put forward a method of determining yield stress of structural clay through consolidation tests on Wenzhou soft clay. Chen [3] conducted a series of triaxial tests to investigate static and cyclic deformation pattern of Xiaoshan natural and remoulded soft clay.

In this study, one-dimensional consolidation tests of Ningbo and Wenzhou natural soil were conducted. Test results have been compared with Xiaoshan natural soil. Then cyclic triaxial tests of Ningbo natural and remoulded soil were carried out.

2 Soil Properties

The soil studied in this paper was taken from Haishu Zone, Ningbo and Wenzhou railway station, respectively. In order to lower the disturbance of soil samples and make sure that the mechanical property of testing samples has a good coherence with original soil, thin-walled tubes with a diameter of 100 mm and a length of 500 mm are used to slowly press into a vertical hole drilled by diesel engine to required depth, then excavated and sealed carefully back to laboratory. The index properties of different soft clays are given in Table 1.

Table 1 Soil properties of Hangzhou (Xiaoshan), Wenzhou (railway station), Ningbo (Haishu Zone)

Soil	Initial density (kN/m^3)	Initial void ratio, e_0	Water content w (%)	Specific gravity G_s	Plastic limit w_p (%)	Liquid limit w_l (%)	Plasticity index I_p	Liquidity index I_l
Xiaoshan (Chen)	16.14	1.738	62.3	2.734	26.5	53	26.5	1.069
Wenzhou station (depth: 16 m)	15.9	1.83	64.2	2.598	28	64	36	0.806
Wenzhou station (depth: 25 m)	16.24	1.629	60.1	2.666	28	64	36	0.806
Haishu Zone (depth: 25 m)	17.9	1.16	40.4	2.62	23	43	20	0.945

3   One-Dimensional Consolidation Tests

One-dimensional consolidation curves of these soft clays are shown in Fig. 1. It can be seen that four different curves have obvious bending point, after which the soil strength descended quickly. Chen, Hao and Wang et al. [2, 4] put forward two distinct stress points in consolidation curve of structural clay: pre-consolidation pressure which is the biggest consolidation pressure that soil ever suffered in history and yield stress point which is the critical stress that soil can bear. In contrast with Xiaoshan clay [3], the consolidation curves of Wenzhou clay descended sharply after reaching yield stress, which means that Wenzhou clay performs more distinct soil structural property. However, as to Ningbo clay, the consolidation curve is relatively smooth.

4   Cyclic Triaxial Tests

To investigate the influence of soil structure on dynamic deformation, cyclic triaxial tests of Ningbo natural sample and remoulded sample have been conducted. The test apparatus used in this study is the DYNTTS manufactured by GDS Instruments Ltd., U.K. The natural sample with a diameter of 50 mm and a height of 100 mm was trimmed from the undisturbed soil which was carefully pushed out from the thin-walled tubes. The remoulded sample was made through layered compaction by keeping the same initial dry density. These samples were firstly saturated and then installed on the pedestal of the apparatus. All the tested samples were isotropically consolidated under certain effective confining pressures. After that, one-way sinusoidal stress-controlled cyclic triaxial tests were conducted under undrained

Fig. 1 One-dimensional consolidation curve of different soils
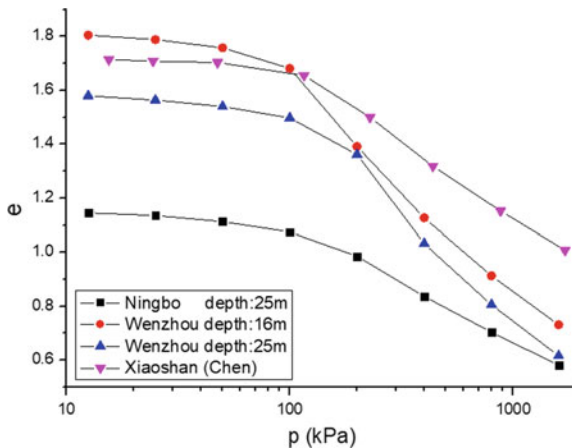
condition. The conditions of cyclic triaxial tests (including triaxial tests of Xiaoshan clay by Chen et al. [3]) are list in Table 2.

Figure 2 shows the axial strain response of Ningbo and Xiaoshan clay [3] during cyclic loading. In cyclic triaxial tests of Ningbo soft clay, natural sample needs about 13,000 loading cycles to reach an axial strain of 5%. However, it only needs 7 cycles to reach the same axial strain for remoulded sample. Similar result has been seen in Xiaoshan soil. For cyclic ratio of 0.391, natural sample needs about 10,000 loading cycles, while remoulded sample at even lower cyclic ratio of 0.286 only needs 150 loading cycles to reach the same axial strain. Due to the structural property of soft clay, natural sample can resist much more cyclic loading cycles till the critical axial strain than remoulded sample. Moreover, after reaching the critical strain at about 3%, the axial strain of natural sample developed almost perpendicularly to the horizontal axis, which performed as a sudden failure with no extra strength left.

Table 2 Conditions of cyclic triaxial tests

Sample	Effective confining pressure, $\sigma_c'(kPa)$	Frequency f (Hz)	Deviator stress $\sigma_d(kPa)$	Cyclic stress ratio σ_d/σ_c'
Natural (Wenzhou)	120	1	100	0.833
Remoulded (Wenzhou)	120	1	100	0.833
Natural (Xiaoshan)	80	1	31.28	0.391
Remoulded (Xiaoshan)	80	1	22.88	0.286
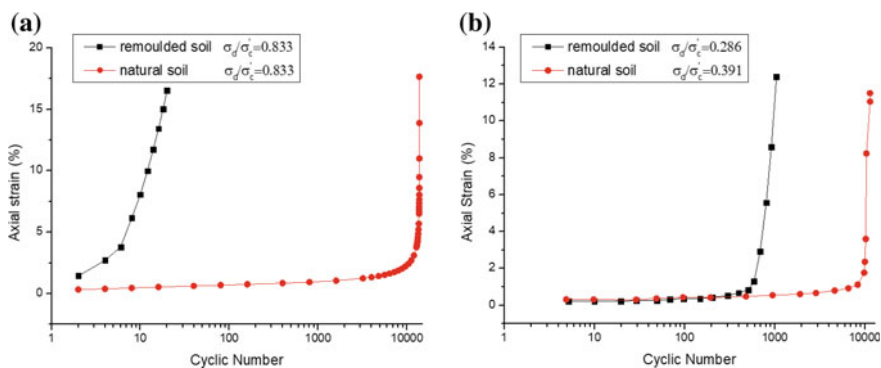
Fig. 2 Axial strain response during cyclic loading: **a** Ningbo clay and **b** Xiaoshan clay (Chen)

5 Conclusions

Structural property is verified through one-dimensional consolidation tests in soft clays of Wenzhou, Xiaoshan and Ningbo, among which Wenzhou clay performs the strongest structural property, while Ningbo clay performs relatively less structural property than Wenzhou and Xiaoshan clay.

Under cyclic loadings, natural clay compared with remoulded clay needs much more loading cycles to reach the same axial strain and then went into a brittle failure state. Soil structure is believed to play an important role in this phenomenon.

References

1. Schmertmann, J.H. The undisturbed consolidation behavior of clay. Transactions of ASCE, 1955, 120(1): 1201–1233
2. Yulong Hao, Lizhong Wang, Yunmin Chen, Shengle Chen. Analysis and control of the settlement in thick soft clay ground reinforced by deep mixing cement piles. Chinese Journal of Geotechnical Engineering, 2001, 23(3): 345–349
3. Yunmin Chen, Yingping Chen, Bo Huang. Experimental study on influences of static and cyclic deformations on structural soft clay with stress level. Chinese Journal of Rock Mechanics and Engineering, 2006, 25(5): 937–945
4. Lizhong W, Lingling L, Li D, et al (2002) Experimental study on the structure property of softclay. China Civ Eng J 35(1): 88–92,106

Disintegration Characteristics and Fractal Features of Red Sandstone During Drying–Wetting Cycles

Zongtang Zhang, Wenhua Gao, Junqi Zhang, Zhimin Zhang, Meihui Yi and Xiaoyu Tang

Abstract Samples of different initial particle sizes were made by red sandstone collected from Zhuzhou of Hunan Province, and the laboratory tests of slaking were carried out in order to study the influence of samples with different initial particle sizes for disintegration. Then, the distribution of particle size was researched after disintegration during drying–wetting cycles, and the variation rules of slake durability index and fractal dimension were studied based on the tests. Results show that the percentage of each particle group changes along with cycle times, the percentage of each particle group changes along with particle size, and the cumulative percentage of each group changes along with particle size. Changes were all consistent after the samples with different initial particle sizes disintegrating. Meanwhile, the slake durability index has a close exponent correlation with the cycle times. Moreover, the initial particle sizes of samples have a certain influence on the slake durability index and fractal dimension. Bigger the initial particle size of samples is, the smaller the slake durability index will be, and the larger the fractal dimension will be gotten, and the faster the disintegration rate becomes. While the smaller the initial particle size of samples is, the larger the slake durability index will be, and the smaller the fractal dimension will be gotten, and the slower the disintegration rate becomes.

Keywords Disintegration · Drying-wetting cycles · Fractal dimension · Slake durability index

Z. Zhang · W. Gao (✉) · Z. Zhang · M. Yi · X. Tang
Hunan Provincial Key Laboratory of Geotechnical Engineering
for Stability Control and Health Monitoring, Hunan University
of Science and Technology, Xiangtan 411201, China
e-mail: gwh@hnust.edu.cn

J. Zhang
School of Civil Engineering, Central South University, Changsha 410083, China

1 Introduction

The disintegration of the rock is a character with the volume inflating remarkably; the debris falls off and disintegrates during drying–wetting cycles [1]. The disintegration of rock can cause slope flaking, forming rock cells and then can induce collapse. Moreover, disintegration causes disasters such as landslides and mudslides, and it is one of the sources of various geological disasters. Soft rock has low strength and poor degrees of cementation, can become inflating, softening and slaking when in the water and there is a great difference for the disintegration due to the regional and natural environment and other different factors of soft rock, so it is of great theoretical and practical significance to research the disintegration characteristics of soft rock. There is a complex mechanism for the slaking of rock, so the universal rule of disintegration has not been unveiled yet, and most of the existing results were studied based on the microcosmic factors of rock [1, 2].

The change of dry and wet in nature and the lithology of the rock itself are the important factors which lead to rock disintegration [3]. Many researchers believe that the change of humidity is the main control factor of physical weathering of rock [4, 5]. Gamble [6] suggested that the change of water content in rock is the main reason which leads to the disintegration of rock. Phienwej [7] advocated that the disintegration of rock mainly happens in the condition of water absorbed. White and Blum [8] argued that the effect of temperature for weathering of rock depends on precipitation. Newman [9] believed that the dissolution of water weakens the cementation of mineral particles, and disintegration of rock is caused thereby. Guo [10] pointed out that the slaking of redbed is caused by the coaction of water, heat, and force. Overall, a few achievements have been accomplished on the research of disintegration of red sandstone during drying–wetting cycles, and the researches on the disintegration of red sandstone with different initial particle sizes were rarely reported. Hence, it is necessary to systematically study the disintegration of red sandstone with different initial particle sizes during drying–wetting cycles.

The disintegration of rock is caused by the evolution of a large number of small broken groups, the small broken groups are formed by the evolution of much smaller fracture, and this self-similar behavior leads to the self-similar fractal feature of the fracture block distribution after rock fragmentation [11]. Liu [12] established a mathematical model to simulate the slaking process of soft rock based on fractal concept, and simulation results show the same developing trend as the experiments present that the slaking process of soft rock is typical fractal [12]. Zhao [13] researched the fractal through computer numerical modeling, which further verifies the applicability of fractal theory. So far, there are some researches on the slake durability and fractal dimension of red sandstone [13]. However, the disintegration characteristics and fractal features of rock with different initial particle sizes are rarely considered in the studies. Therefore, the disintegration characteristics and fractal features of red sandstone with different initial particle sizes during drying–wetting cycles were studied in this paper. Furthermore, the variation of slake durability index and fractal dimension was studied based on the laboratory tests after disintegration.

2   Experimental Study on the Disintegration Characteristics of Red Sandstone

2.1   Purpose and Design of the Tests

This experiment mainly aims to research on the red sandstone in Zhuzhou, Hunan Province. The upper rock formation is weathered seriously, and the structure of it is disrupted, like earthy particles, but can still be identified. The deeper the rock layer goes, the less the degree of rock weathering develops. The experimental samples were the new rocks which were collected with no apparent traces of weathering on the surface. The average of natural moisture content is 5.65%, and the average dry density is 2.422 g/cm^3. The UCS of natural rock specimens is between 6.42 and 6.63 Mpa. Figure 1 shows the rock samples on site, and Fig. 2 shows the sealed samples in the laboratory.

Fig. 1 Rock samples on site

Fig. 2 Sealed samples

According to the regulation for testing the physical and mechanical properties of rock (DZ/T 0276.9-2015) [14], disintegrating tests were conducted. In order to study the disintegration characteristics of red sandstone with different initial particle sizes, rock cutting machine was used to obtain two groups of rock samples named as sample 1 and sample 2. The production process of samples is difficult due to the low strength of the red sandstone, so it is difficult to experiment with the samples of identical particle sizes in the same group. Hence, based on the existing results [15, 16], the form of prepared samples was presumed to be spherical, and the density of each sample of each group is presumed to be uniform. According to the initial mass and density of each sample, the initial particle size was calculated. The initial particle sizes of sample 1 are between 7.91 and 7.95 cm, and the mean value is 7.93 cm. The initial particle sizes of sample 2 are between 4.75 and 4.94 cm, and the mean value is 4.85 cm.

The laboratory tests of disintegration during drying–wetting cycles were carried out in this procedure. ① Prepared natural samples were placed into the oven (105–110 °C), until they reached a constant weight. Later, they were cooled to ambient temperature in a dryer. ② Samples were placed into open containers separately. Tap water was infused into the containers to completely submerge the samples. Then, samples were soaked for more than 24 h. ③ Samples were taken out and then placed into the oven (105–110 °C). Until they reached a constant weight, they were cooled to ambient temperature in the dryer. Next, the standard sieves were used to sieve the residual samples, and the diameters of sieves were 60, 40, 20, 10, 5, 2, 1, 0.5, 0.25, and 0.075 mm. Moreover, the residual samples were weighed and recorded. The residual samples which were less than 0.075 mm could be calculated through the conservation of mass. The completion of steps of ② and ③ meant that the first drying–wetting cycle was completed. Then, the above steps of ② and ③ were repeated until N times of drying–wetting cycles were reached.

2.2 The Results and Analyses of Tests

Phenomena of tests: A large number of bubbles emerged immediately when the samples were put into the water. It is found that samples began to fall off in pieces and bulks in about 3 min. After that, samples began to disperse in large bulks about 10 min later (as shown in Figs. 3 and 4). Then, sample 1 and sample 2 disintegrated completely in 30 min (as shown in Figs. 5 and 6). The objects of disintegration were lumpy, flaky, granular and muddy. According to Wu [2], the grades between strong and feeble for disintegration characteristics of red sandstone [2] the samples used in this study have a strong grade.

Distribution of particle size of disintegration: The disintegration of rock is a process in which large particles gradually change into small particles, so it is of great significance to study the distribution characteristics of particle size after disintegration.

Fig. 3 Disintegration of 10 min of sample 1
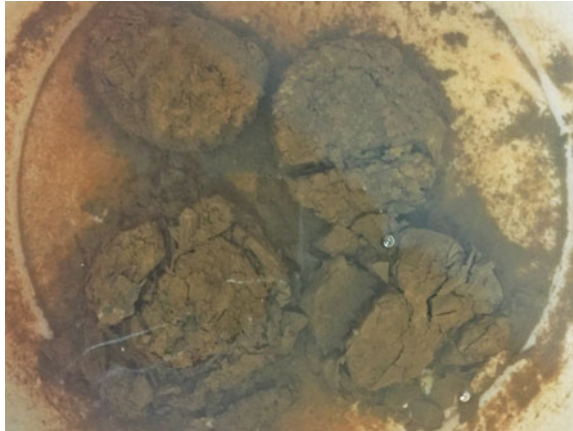
Fig. 4 Disintegration of 10 min of sample 2
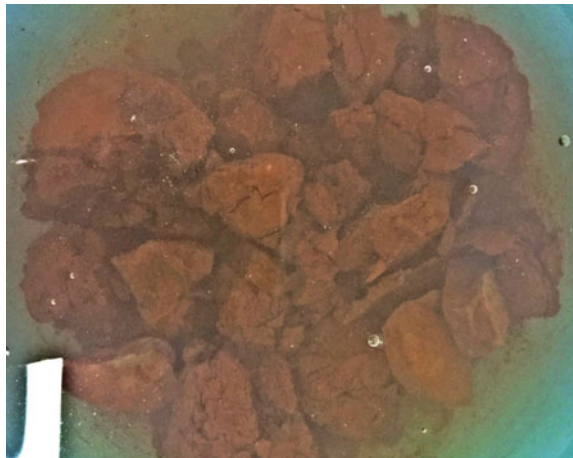
Figure 7 is the graph for cycle times and percentage of each particle group of sample 1, and Fig. 8 is the graph for cycle times and percentage of each particle group of sample 2. As shown in the graph, after the disintegration of both samples, the percentage of each particle group over 5 mm of particle size decreases as the cycle times increases, the percentage of particle group whose particle size is between 5 and 2 mm increases first and then decreases with the increase in cycle times and the percentage of each particle group whose particle size is smaller than 2 mm increases as the cycle times increases.

Figure 9 is the graph for particle size and percentage of each particle group of sample 1, and Fig. 10 is the graph for particle size and percentage of each particle group of sample 2. As shown in the graph, there are two maximum points in the curve, and the percentage of the 5–2 mm group of both samples is the largest.

Fig. 5 Disintegration of
30 min of sample 1

Fig. 6 Disintegration of
30 min of sample 2
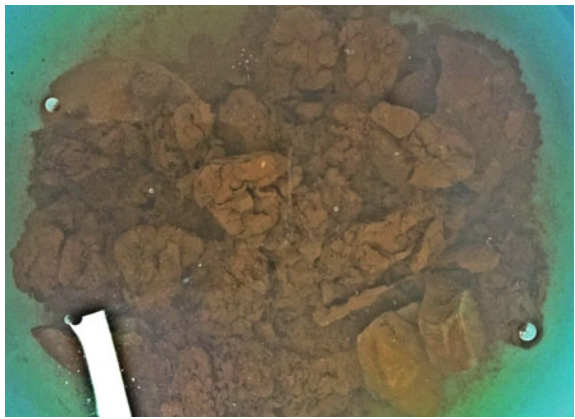
Fig. 7 Graph for
cycle times-percentage of
each particle group
of sample 1
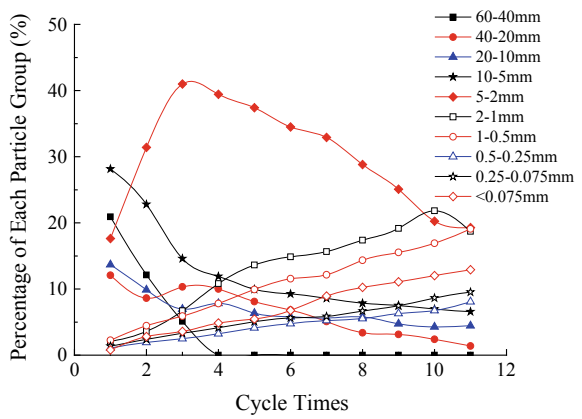
Fig. 8 Graph for cycle times-percentage of each particle group of sample 2
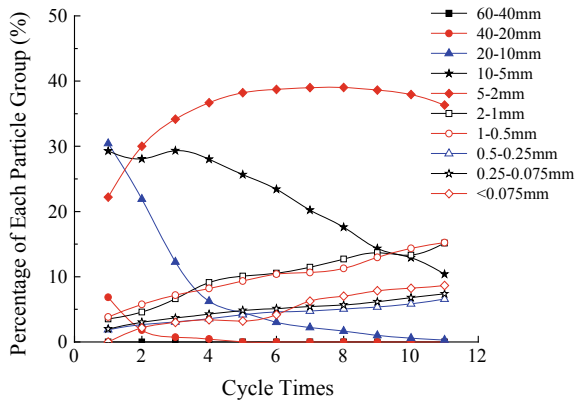
Fig. 9 Graph for particle size-percentage of each particle group of sample 1
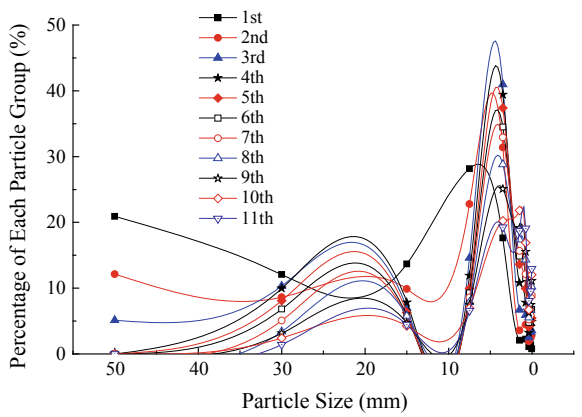
Fig. 10 Graph for particle size-percentage of each particle group of sample 2
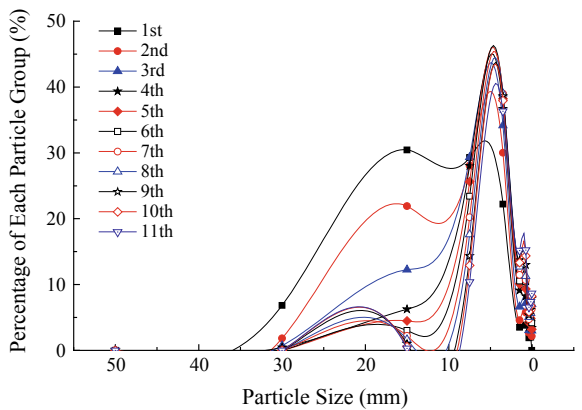
Figure 11 is the graph for particle size and cumulative percentage of each particle group of sample 1, and Fig. 12 is the graph for particle size and cumulative percentage of each particle group of sample 2. As shown in the graph, when the particle size is less than 5 mm, the curve increases faster, the curve growth rate approaches linear growth, and the slope is larger. When the particle size is larger than 5 mm, the curve increases slowly and gradually becomes stable.

As shown in Figs. 7 and 12, although the percentage of each particle group is slightly different after the disintegration of two samples, the trend of the curve is quite similar. The percentage of each particle group changes along with cycle times, the percentage of each particle group changes along with particle size, and the cumulative percentage of each group changes along with particle size; changes are consistent with different initial particle size disintegration.

Disintegration characteristics: The slake durability index of rock is defined (DZ/T 0276.9-2015) as the percentage of the residual mass and the original quality when samples have undergone standard drying–wetting cycles twice. The disintegration of

Fig. 11 Graph for particle size-cumulative percentage of each particle group of sample 1
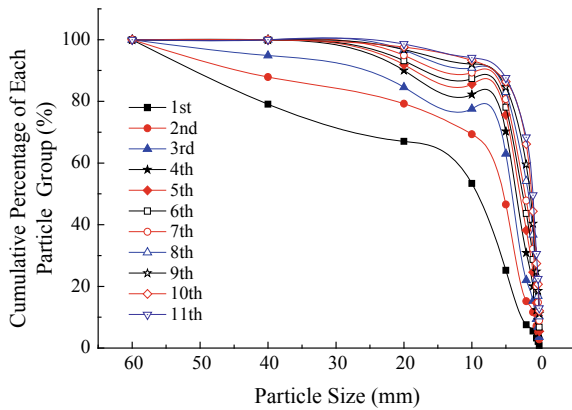
Fig. 12 Graph for particle size-cumulative percentage of each particle group of sample 2
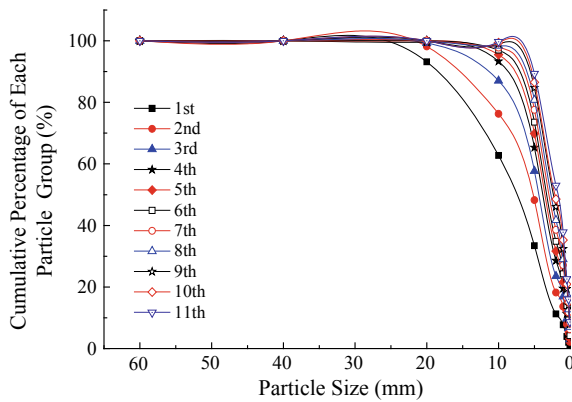
rock is studied in this paper when cycles have attained N times. The drying–wetting cycles of samples are extended to N times, so the definition of the slake durability index is modified.

$$I_{dN} = \frac{m_N}{m_d} \times 100\% \tag{1}$$

where I_{dN} is the modified slake durability index (%), m_d is the drying quality of original samples (g), and m_N is the drying quality of residual samples in a cycle of N times.

Figure 13 is the graph for cycle times and slake durability index of samples. As shown in Fig. 13, slake durability index gradually reduces with the increase in cycle times, and the degree of reduction gradually diminishes. Cycle times and slake durability index are fitted as following formula.

$$I_{dN} = Ae^{BN} \tag{2}$$

where I_{dN} is the slake durability index of samples (%), N is the cycle times, A and B are the fitting parameters, and Table 1 gives the fitting parameters of N-I_{dN}.

As shown in Fig. 13 and Table 1, the slake durability index has a close exponent correlation with the cycle times. Moreover, the different initial particle sizes of samples have certain influence on the slake durability index, and the bigger the initial particle size of samples is, the smaller the slake durability index will be, and the faster the disintegration rate becomes (such as sample 1), while the smaller the initial particle size of samples is, the larger the slake durability index will be, and the slower the disintegration rate becomes (such as sample 2). On the other hand, the curve in Fig. 13 shows an intersection point when the third cycle times, and from first to third cycles do not satisfy the above rule.

Fig. 13 Graph for N-Id of samples
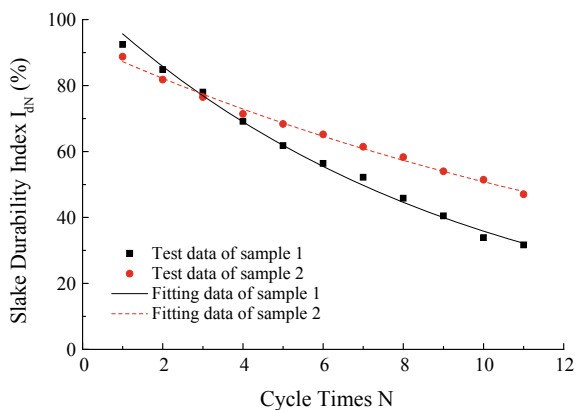
Table 1 Fitting parameters of N-I_{dN}

The name of relationship	A	B	Correlation index R^2
N-I_d of sample 1	106.67	−0.109	0.9935
N-I_d of sample 2	92.635	−0.060	0.9955

3 Study on Fractal Features of the Disintegration of Red Sandstone

3.1 The Solution of a Fractal Dimension Based on the Relation of Quality and Particle Size

Although Wilson-Fahmy [17] and Gilbert [18] described the fractal dimension successively, there is still no clear definition of fractal due to the complexity of the process. However, it is recognized that the local system in some way similar to the whole is the most basic feature of fractal. For the process of disintegration of rock during drying–wetting cycles, it is the result of internal cracks of rock producing, developing, expanding, and connecting continually on the macroscopic view. In fact, it is also the nonlinear dynamic process of dissipation of energy. The distribution of cracks and the scale of the fragments show good self-similarity and had good fractal features [19]. The percentage of each particle group can be obtained directly in the laboratory experiments after disintegration, also the reliable data can be collected, and the method is easy to operate in this way. Thus, the solution of the fractal dimension is employed based on the relation of quality and particle size.

Xie [20] indicated that if the lumpiness of broken rock satisfies the distribution of fractal, then the formula is

$$N_i = CR_i^{-D} \tag{3}$$

where R_i is the characteristic size of residual samples, N_i is the number of residual samples for characteristic size R_i, C is the proportionality constant, and D is the fractal dimension of fragmentation distribution of residual samples.

The distribution of size-frequency for the fragment of residual samples is

$$M(r)/M = 1 - \exp\left[-(R_i/\sigma)^{\beta}\right] \tag{4}$$

where $M(r)$ is the cumulative mass of fragment that diameter is less than R_i, M is the total mass, σ is the quantity that associated with the mean size, and β is the exponent of distribution of size-frequency.

As shown in Figs. 11 and 12, the rules of distribution of particle size after the disintegration of samples satisfy Eq. (4), and Eq. (4) is expanded by Taylor series, and then the higher-order terms are neglected. So the following formula can be obtained.

$$M(r)/M = (R_i/\sigma)^{\beta} = \sigma^{-\beta}R_i^{\beta} \qquad (5)$$

As Eq. (5) shows, the cumulative percentage of each particle group and particle size is fitted. So β can be calculated.

Take the derivative of Eqs. (3) and (5), respectively.

$$dN \propto R_i^{-D-1}dR \qquad (6)$$

$$dM \propto R_i^{\beta-1}dR \qquad (7)$$

From the relationship between mass and the size of lumpiness, M is proportional to R^3.

$$dN \propto R_i^{-3}dM \qquad (8)$$

From Eqs. (6)–(8), the following formula can be obtained.

$$R_i^{-D-1} \propto R_i^{-3}R_i^{\beta-1} = R_i^{\beta-4} \qquad (9)$$

That is

$$D = 3 - \beta \qquad (10)$$

3.2 Results Analysis

According to Sect. 3.1, the data of Figs. 11 and 12 are fitted, so the fractal dimension of disintegration of rock can be obtained by Formula (10). As shown in Fig. 14, due to limit space, the solution of β of sample 1 is just provided in the first

Fig. 14 Fitting function for the first drying–wetting cycle of sample 1

$M(r)/M=5.8513R_i^{0.7594}$, R^2=0.9814

■ Experimental curve of sample 1 in the first cycle
— Fitting curve of sample 1 in the first cycle
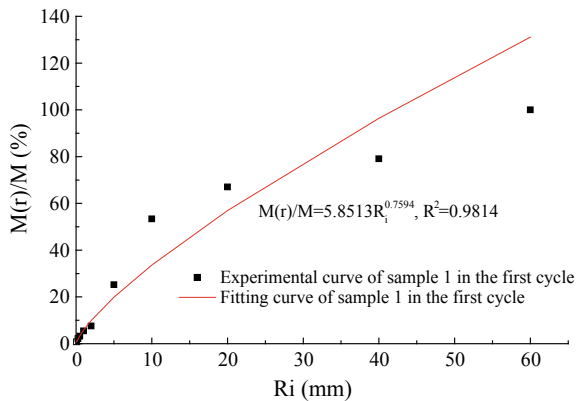
Table 2 Fitting parameters and fractal dimension (D) of samples during drying–wetting cycles

Cycle times		1	2	3	4	5	6	7	8	9	10	11
Sample 1	β	0.7594	0.5810	0.5403	0.4899	0.4618	0.4258	0.3862	0.3610	0.3432	0.3248	0.3084
	R^2	0.9814	0.9683	0.9566	0.9508	0.9392	0.9336	0.9317	0.9216	0.9111	0.8964	0.8857
	σ	9.8×10^{-2}	1.3×10^{-2}	6.1×10^{-3}	2.3×10^{-3}	1.2×10^{-3}	4.9×10^{-4}	1.6×10^{-4}	6.7×10^{-5}	3.3×10^{-5}	1.5×10^{-5}	6.7×10^{-6}
	D	2.2406	2.4190	2.4597	2.5101	2.5382	2.5742	2.6138	2.6390	2.6568	2.6752	2.6916
Sample 2	β	1.1615	0.6134	0.5643	0.5388	0.5370	0.4998	0.4452	0.4270	0.4067	0.3939	0.3815
	R^2	0.7956	0.9663	0.9557	0.9447	0.9337	0.9314	0.9325	0.9278	0.9196	0.9134	0.9036
	σ	4.1×10^{-1}	1.6×10^{-2}	7.6×10^{-3}	4.8×10^{-3}	4.4×10^{-3}	2.3×10^{-3}	7.5×10^{-4}	4.7×10^{-4}	2.7×10^{-4}	1.8×10^{-4}	1.2×10^{-4}
	D	1.8385	2.3866	2.4357	2.4612	2.4630	2.5002	2.5548	2.5730	2.5933	2.6061	2.6185

drying–wetting cycle. As shown in Table 2, the fractal dimension is obtained by Formula (10). Figure 15 is the graph for fractal dimension and cycle times.

As Eq. (4) shows, σ is the quantity that associates with the mean size. σ is obtained by the fitting function (as shown in Table 2). In the process of disintegration, the particle size of residual samples reduces constantly with the increase in cycle times, so the average particle size decreases gradually, and σ also reduces gradually. As shown in Table 2, the changing rule of actual value is consistent with theoretical analysis for σ.

As shown in Fig. 15, the fractal dimension of sample 1 is larger than sample 2. The degree of growth for both curves decreases gradually; the curves tend to flatten gradually. So the difference of initial particle size of samples has a certain influence on the fractal dimension. That is, the bigger the initial particle size of samples is, the larger the fractal dimension will be, and the faster the disintegration rate becomes (such as sample 1). While the smaller the initial particle size of samples is, the smaller the fractal dimension will be, and the slower the disintegration rate becomes (such as sample 2). The difference in initial particle size results in a different rate of disintegration, and the main reasons are as follows. The larger the initial particle size of the samples is, the more internal defects which are caused by the natural environment, the lower the strength will be, and the faster the disintegration rate becomes.

Fractal dimension is calculated by the distribution of multiple particle groups after disintegration, and the distribution of each particle group can be considered after disintegration. But the slake durability index just reflects the distribution of two particle groups (that is, larger than 2 mm and less than 2 mm) after disintegration. So the fractal dimension is more suitable for describing the disintegration of rock than the slake durability index.

Fig. 15 Graph for fractal dimension-cycle times
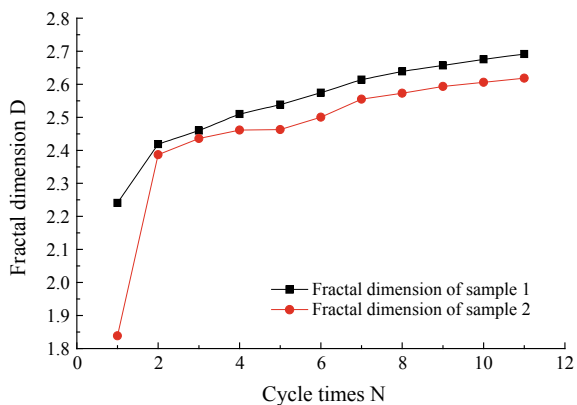
4   Conclusions

(1) The percentage of each particle group whose particle size is greater than 5 mm decreases as the cycle times increase, the percentage of particle group whose particle size is between 5 and 2 mm increases first and then decreases with the increase in cycle times, and the percentage of each particle group with a particle size smaller than 2 mm increases as the cycle times increase after red sandstone disintegration.

(2) Although the percentage of each particle group is slightly different after the disintegration of the different initial particle sizes, the trend of the curve is very similar. The percentage of each particle group changes along with cycle times, the percentage of each particle group changes along with particle size, and the cumulative percentage of each group changes along with particle size; changes are all consistent.

(3) The slake durability index of samples presents a close exponent correlation with the cycle times, and the difference of the initial particle size of samples has a certain influence on the slake durability index. The smaller the initial particle size of samples, the larger the slake durability index will, the bigger the initial particle size of samples, the larger slake durability index will be obtained.

(4) Distribution of particle size of disintegration can be described by a fractal dimension which is based on the relation of quality and particle size, and the difference of initial particle size of samples has a certain influence on the fractal dimension. The larger the initial particle size of samples, the bigger the fractal dimension, and the faster the disintegration rate becomes. The smaller the initial particle size of samples, the smaller the fractal dimension, and the slower the disintegration rate becomes.

References

1. Chai ZY, Zhang YT, Zhang XY (2015) Experimental investigations on correlation with slake durability and mineral composition of mudstone. J China Coal Soc 40:1188–1193
2. Wu DX, Liu HJ, Wang GQ (2010) Laboratory experimental study of slaking characteristics of red-bed soft rock. Chin J Rock Mechan Eng 29:4173–4179
3. Li L, Zhou ZH, Du SH et al (2010) Model-based estimation and field measurement of purple soil formation rate. Acta Pedologica Sinica 47: 393–400
4. Mol L, Viles HA (2010) Geoelectric investigations into sandstone moisture regimes: implications for rock weathering and the deterioration of San Rock Art in the Golden Gate Reserve. Geomorphology 118:280–287

5. Saad A, Guedon S, Martineau F (2010) Microstructural weathering of sedimentary rocks by freeze-thaw cycles: experimental study of state and transfer parameters. Comptes Rendus Geoscience 342: 197–203
6. Gamble J (1971) Durability-plasticity classification of shales and other argillaceous rock. Univ of Illinois, Urbana
7. Phienwej N (1987) Ground response and support performance in a sheared shale. Stillwater Tunnel 1987:125–163
8. White AD, Blum AE (1995) Effects of climate on chemical weathering in watersheds. Geochimicaet Cosmochimica Acta 59: 1729–1747
9. Newman GH (1983) The effect of water chemistry on the laboratory compression and permeability characteristic of North Sea Chalks. J Petrol Technol 35:976–980
10. Guo YC, Xie Q, Wen JQ (2012) Effect of the alternation of heat and water on the slaking phenomenon of redbeds. Hydrogeol Eng Geol 39:69–73
11. Wu YP, Yu HM, Hu YX (2006) Research on engineering geological characters of aubergine mudstone of Badong new city zone. Rock Soil Mech 27:1201–1203
12. Liu XM, Zhao MH, Su YH (2008) Mathematical simulation of fractal mechanism for slaking of soft rock. Rock Soil Mech 29:2043–2046
13. Zhao MH, Chen BC, Su YH (2007) Fractal analysis and numerical modeling disintegrate process of red-bed soft rock. J Centl South Univ (Sci Technol) 38: 351–356
14. Ministry of Land and Resources of the People's Republic of China (2015) DZ/T 0276.9-2015. Regulation for testing the physical and mechanical properties of rock-part 9: test for determining the slake durability of rock. China Standard Press, Beijing
15. Deng T, Huang M, Zhang JW (2014) Fractal evolution law of clay rock disintegration under different PH conditions. J Tongji Univ (Nat Sci) 42:1480–1488
16. Huang M, Zhang JW (2015) Disintegration tests and energy dissipation characteristics of soft rock in acid and alkali solution. Rock Soil Mech 36:2607–2623
17. Willson-Fahmy RF, Koerner RM (1993) Finite element analysis of stability of cover soil on geomembrane lined slopes. In: Proceedings of conference on geosynthetics, 1425–1437
18. Gilbert RB, Long JH, Daly JJ (1993) Structural integrity of composite geosynthetic lining and cover systems. In: Proceedings of conference on geosynthetics, 1389–1401
19. Tu XB, Wang SJ, Yue ZQ (2005) Fractal fragmentation of weathered rock and its application in engineering geology. Chin J Rock Mechan Eng 24:587–595
20. Xie HP (1996) Fractals-rock mechanics. Science Press, Beijing

HCA Study of Permanent Deformation of Sand Under Train-Induced Stress Path Considering Variable Confining Pressure

Juan Wang, Yanfei Xiong and Dariusz Wanatowski

Abstract In this paper, a typical stress path experienced by subsoil in a railway foundation is used in a dynamic hollow cylinder apparatus (HCA) to obtain cyclic responses of soils subjected to moving trainloads. This is achieved through varying axial force, torque, inner and outer confining pressures independently during each load cycle. A multistage test using the specific stress path is conducted on Leighton Buzzard sand considering various magnitudes of the trainloads. Comparative studies using constant confining pressures are also carried out. It is found that in both cases with constant or variable confining pressures, the long-term deformation mechanism of the sand tends to change from shakedown to incremental collapse as the load level is increased. It was noticed that the increase rates of vertical permanent strain of the two cases are close if they have similar maximum ratios of deviator stress to mean effective stress $(q/p)_{max}$ and ratios of peak deviator stress to average mean effective stress q_{max}/p_{avg}.

Keywords HCA · Trainloads · Variable confining pressure · Stress path testing

1 Introduction

Permanent deformation of track foundations directly controls the long-term performance of railway tracks. It is, therefore, one of the most important factors considered in the design of railway foundations [1–3]. The previous studies have demonstrated that repeated moving trainloads could result in considerable permanent deformation of track foundations; however, it is found difficult to predict the train-load induced permanent deformation.

J. Wang · Y. Xiong (✉)
Ningbo Nottingham New Material Institute,
University of Nottingham Ningbo, Ningbo, China
e-mail: yanfei.xiong@nottingham.edu.cn

D. Wanatowski
School of Civil Engineering, Faculty of Engineering, University of Leeds, Leeds, UK

Cyclic testing of soil elements is commonly used to evaluate the long-term responses of soils under repeated traffic loads. A number of such studies have been conducted by using cyclic triaxial tests, which reproduce the variation of the principal stresses [4]. In recent years, several researchers [e.g. 5–7] found that the rotation of principal stress axis existing in the whole service life of track foundations has a considerable effect on the increase of plastic strain in granular soils. Furthermore, it was noted that the rotation of principal stress is accompanied by the variation of deviator stress, leading to a complicated loading path [8]. Qian et al. [9] applied a traffic-induced heart-shape deviator stress path on a saturated clay through varying torsional shear stress and normal stresses while keeping a constant confining pressure. They found larger permanent axial strains compared to those obtained from cyclic triaxial tests. Despite those efforts in simulating the realistic field stress condition, the works were conducted by matching the stress path in the deviatoric stress plane only.

In this study, the deformation behaviour of sand under a realistic train-induced stress path will be studied using a dynamic hollow cylinder apparatus (HCA) through simultaneously varying axial load, torque, inner and outer confining pressures during each load cycle.

2 Laboratory Test

2.1 Apparatus

The dynamic HCA manufactured by GCTS is used in this study. It allows independent controls of axial load W, torque M_T, inner confining pressure p_i, outer confining pressure p_o and back pressure, so that the changes of stresses (σ_z, $\tau_{\theta z}$, σ_θ and σ_r) in the soil element can be simulated, as shown in Fig. 1. The radial direction is fixed as the direction of intermediate principle stress σ_2, and α is the direction of major principal stress σ_1 relative to the vertical direction. The HCA specimens have a height of 200 mm, an internal radius r_i of 30 mm and an external radius r_o of 50 mm.

In this study, the mean effective stress is defined as $p = (\sigma_1 + \sigma_2 + \sigma_3)/3$; the deviator stress is defined as $q = \left\{ \left[(\sigma_1 - \sigma_2)^2 + (\sigma_1 - \sigma_3)^2 + (\sigma_2 - \sigma_3)^2 \right] \middle/ 2 \right\}^{0.5}$. The tests are conducted in a drained condition, and all the stresses used in this paper are effective stresses.

2.2 Sample Preparation

Leighton Buzzard sand fraction B is used in this study. Its index properties are presented in Table 1. A moist sand specimen is placed between the inner and outer
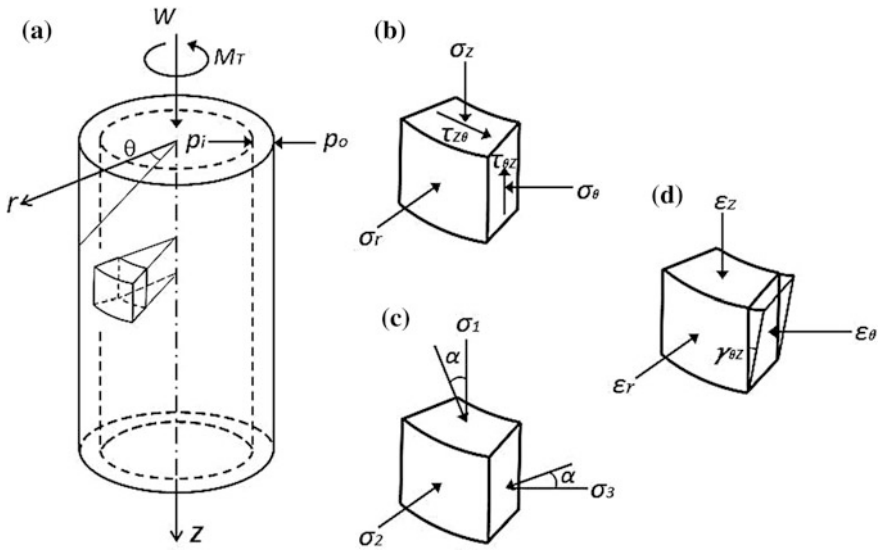
Fig. 1 Idealised stress and strain components within the HCA: **a** hollow cylinder specimen subjected to loads; **b** element component stresses; **c** element principal stresses; **d** element component strains (after Zdravkovic and Jardine [10])

Property	Leighton buzzard sand
Mean grain size (mm)	0.62
Effective grain size (mm)	0.45
Uniformity coefficient	1.56
Specific gravity	2.65
Minimum void ratio	0.52
Maximum void ratio	0.79

Table 1 Physical properties of Leighton Buzzard sand fraction B

moulds and tamped in eight layers (each layer 25 mm in height) to reach a relative density of around 58%.

As the specimen is sealed by inner and outer membranes, a vacuum of 90 kPa, equal to −90 kPa of effective stress, is imposed on the specimen to drive the air out of the sand and to keep the specimen stable. Then, a tube valve connected to the bottom of the specimen is opened to suck de-aired water into the specimen until it is fully filled. Afterwards, the specimen is left with 30 kPa effective confining pressure for 12 h. When the Skempton B-value is over 0.97, the specimen is regarded as fully saturated. Finally, before cyclic loading, the stresses (σ_z, $\tau_{\theta z}$, σ_θ and σ_r) applied to the specimen were increased linearly to reach the initial stress state of the soil, which was maintained for more than 8 h until a stable state is achieved.

2.3   Stress Path

The cyclic stress path and the initial stress state in the HCA test are obtained using the results of a three-dimensional finite element analysis of a typical Rheda 2000 single track system. Figure 2 shows the stress path used in this study for a point at the top of the subsoil layer on the vertical symmetric plane. Four axles belonging to two adjacent bogies on two carriages are considered. The standard loading case uses axle loads of 250kN. Hight's equations [11] were used to calculate corresponding axial load, torque, inner and outer confining pressures. To ensure a fully drained condition and a good capture of the changes of the confining pressures, a time period T of 32.5 s was selected in this study.

2.4   Test Program

Two multistage repeated loading tests (MRLT) are conducted. MRLTV uses the realistic stress path with varying inner and outer confining pressures (Fig. 2), while MRLTC keeps the confining pressures constant (equal to the initial values). Both tests include four stages of loads, the magnitudes of which are shown in Table 2. The amplitude multiplier 1 represents the standard loading case. The amplitude multipliers 1.48 and 2.83 are chosen for MRLTC so that their peak stress ratios, q/p (deviator stress/mean effective stress), are identical with those of the second and fourth stages of MRLTV, respectively. The number of loading cycle for each stage of MRLTV and MRLTC is 3000.
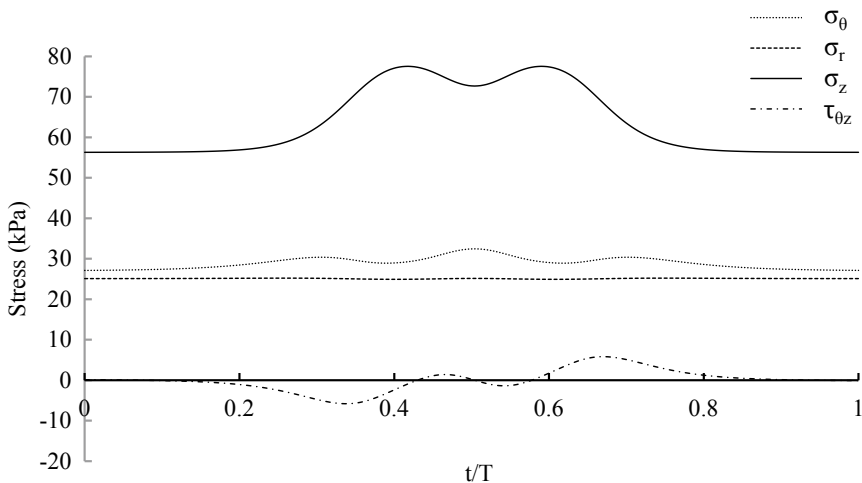
Fig. 2 Stress path

Table 2 Test program

Case	Loading stage	Amplitude multiplier	$(q/p)_{max}$
MRLTV	I	1	0.95
	II	2	1.08
	III	3	1.18
	IV	4	1.27
MRLTC	I	1	0.99
	II	1.48	1.08
	III	2	1.16
	IV	2.83	1.27

3 Test Results and Discussion

3.1 Axial Permanent Deformation

The development of vertical permanent strain for the MRLTV and MRLTC throughout the loading stages is presented in Fig. 3. More details are provided in Table 3.

For all the four stages of both MRLTV and MRLTC, the axial permanent deformation developed mostly during the initial cycles. Over 50% of the permanent strain was developed during the first 100 cycles, which is similar to the results of Yu et al. [12]. This sharp increase at early stage is most obvious in the cases with
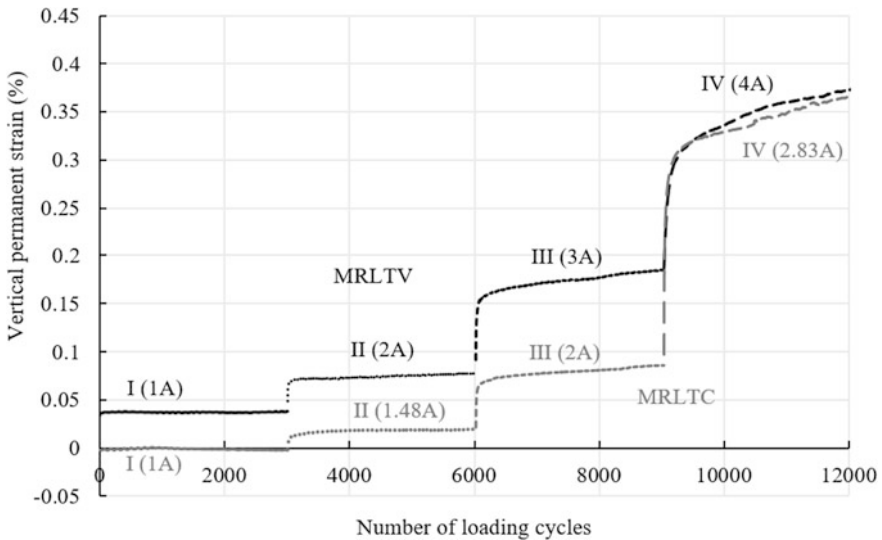
Fig. 3 Permanent deformation of MRLTV and MRLTC

Table 3 Permanent deformation development of MRLTV and MRLTC

Case	Loading stage	Total strain increase: S_T (%)	Strain increase during first 100 cycles: S_{100} (%)	S_{100}/S_T (%)
MRLTV	I	0.03807	0.03735	98.1
	II	0.03939	0.03258	82.7
	III	0.10753	0.07855	73.0
	IV	0.18793	0.09442	50.2
MRLTC	I	−0.00249	−0.00169	67.9
	II	0.02190	0.01497	68.4
	III	0.06658	0.04779	71.8
	IV	0.28015	0.20368	72.7

low stress amplitude in MRLRV, as shown in Table 3. It implies that the specimen tends to reach a relatively stable state more quickly when subjected to a smaller load. It is interesting to notice that the trend is reversed in MRLRC. Two reasons might interactively affect this difference. First, the samples at latter stages have higher initial densities due to compactions in the former stages, which make further compaction more difficult. Second, the mean confining pressure in MRLTC is relatively low so that the sample tends to expand in the radial direction and thus deforms more in the vertical direction. This effect might be more significant under a higher load level. In addition, the first loading stage of MRLTC results in a slight dilation of the specimen, similar to the observation of Miura [13].

3.2 Axial Permanent Strain Increase Rate

The increase rate of vertical permanent strain against the cumulative vertical permanent strain is plotted in Figs. 4 and 5 for MRLTV and MRLTC, respectively.

As demonstrated in Fig. 4, the total vertical permanent strain reaches a stable value at the end of stages I and II, and the vertical permanent strain rate drops to a very small value of around 10^{-8} per cycle. At the end of stage III, the strain rate is still around 10^{-7} per cycle. During stage IV, the permanent strain keeps a slow but stable growth with a strain rate slightly higher than 10^{-7} per cycle. Overall, the final strain rate is higher at a larger load magnitude. The MRLTC case shows the same trend. Tao [14] classified the soil behaviour under multistage repeated loading tests into Range A (entirely resilient after post-compaction or 'shakedown'), Range B (incremental collapse after a large number of loading cycles) and Range C (incremental collapse) with two boundary values of vertical permanent strain rate, 10^{-8} and 10^{-7} per cycle. Based on the observations from Figs. 4 and 5, responses of MRLTV and MRLTC are likely within Range A during stages I and II, within Range B during stage III and within Range C during stage IV.
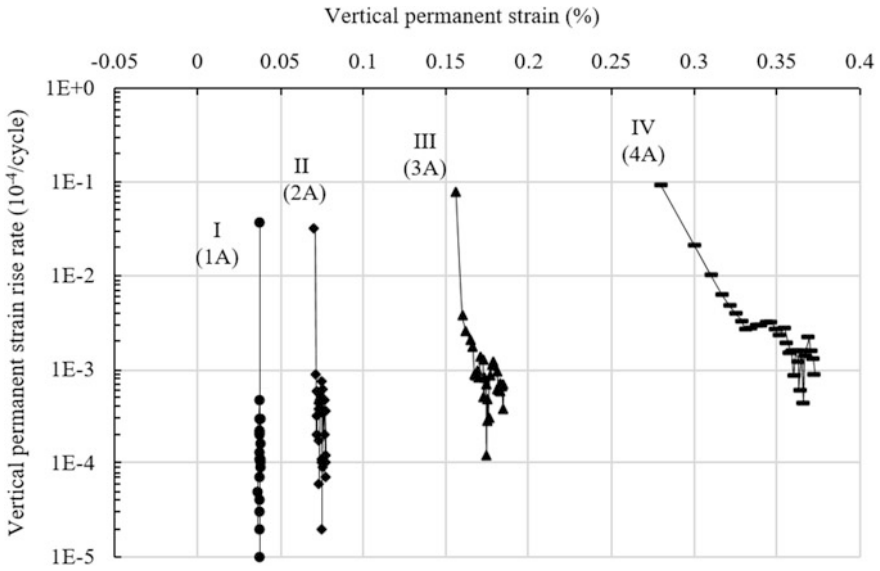
Fig. 4 Vertical permanent strain increase rate of MRLTV
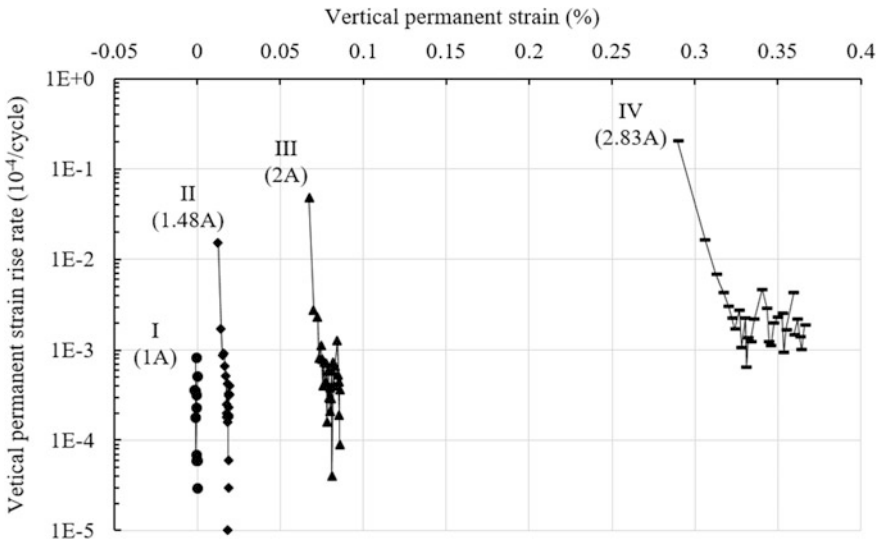
Fig. 5 Vertical permanent strain increase rate of MRLTC
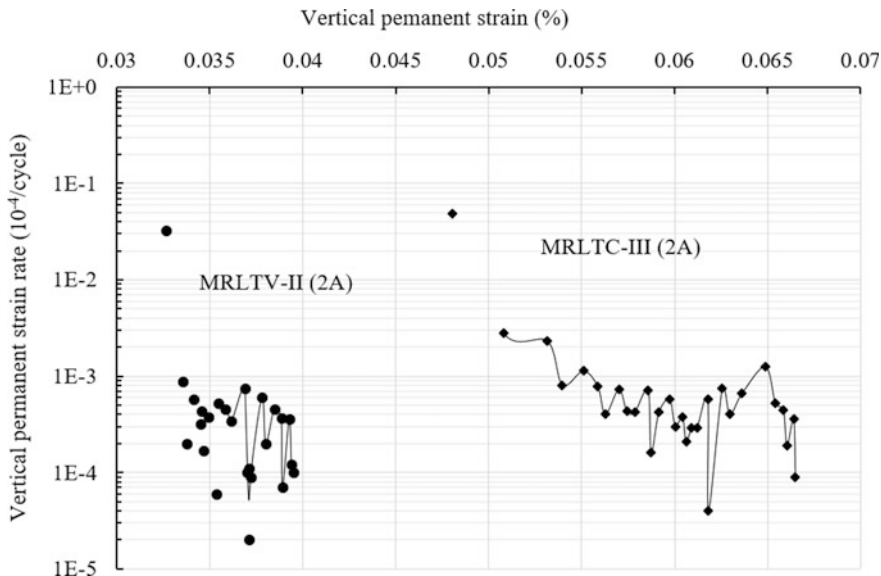
Fig. 6 Comparison between MRLTV-II and MRLTC-III

Figure 6 directly compares the MRLTV-II stage and the MRLTC-III stage, both of which have a load amplitude multiplier of 2. It is found that the axial permanent deformation of MRLTC-III grows faster than that of MRLTV-II, since the average increase rate of the former case is higher than the latter one. This implies that the variable confining pressures in MRLTV-II helps restrain further increase of vertical permanent deformation.

It is further found that the increase rate of the vertical permanent strain is related to the maximum stress ratio $(q/p)_{max}$. As shown in Figs. 7 and 8, cases MRLTV-IV and MRLTC-IV, both of which have $(q/p)_{max} = 1.27$, show very similar strain rates after 1500 load cycles. It should be noted that the end of the previous stage in Fig. 7 is regarded as the initial state of the specimen with zero strain. Similar strain rates are also observed for the cases MRLTV-II and MRLTC-II, both of which have $(q/p)_{max} = 1.08$. Another factor that might also contribute to the similar increase rates is the ratio of peak deviator stress to average mean effective stress q_{max}/p_{avg} since they are very close in these two comparisons (1.17 and 1.15 in MRLTV-II and MRLTC-II, respectively; 1.47 and 1.43 in MRLTV-IV and MRLTC-IV, respectively). More evidence is needed to demonstrate the influence of these two factors. In addition, it should be noted that a higher loading frequency is expected in the real case scenario under a normal train speed, which probably will cause larger permanent strains and higher strain increments, as studied by Sun et al. [15].
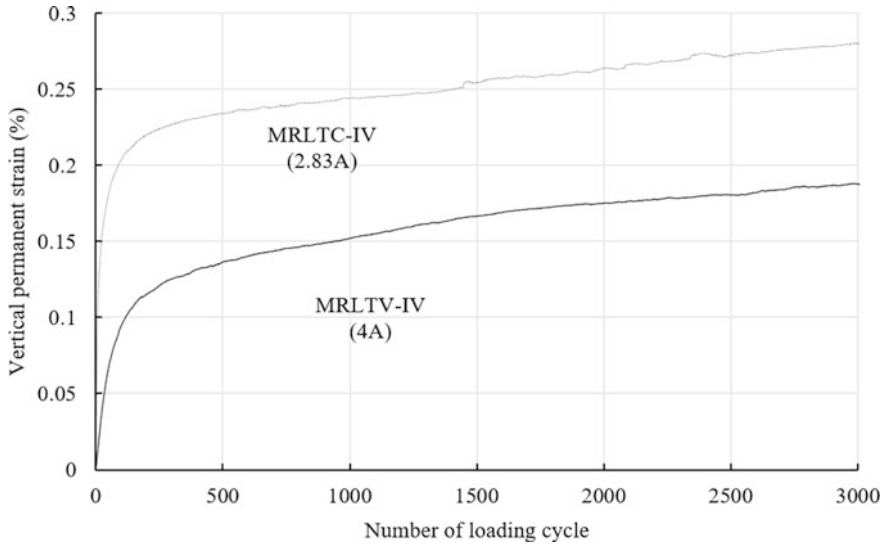
Fig. 7 Comparison of vertical permanent strain between MRLTV-IV and MRLTC-IV
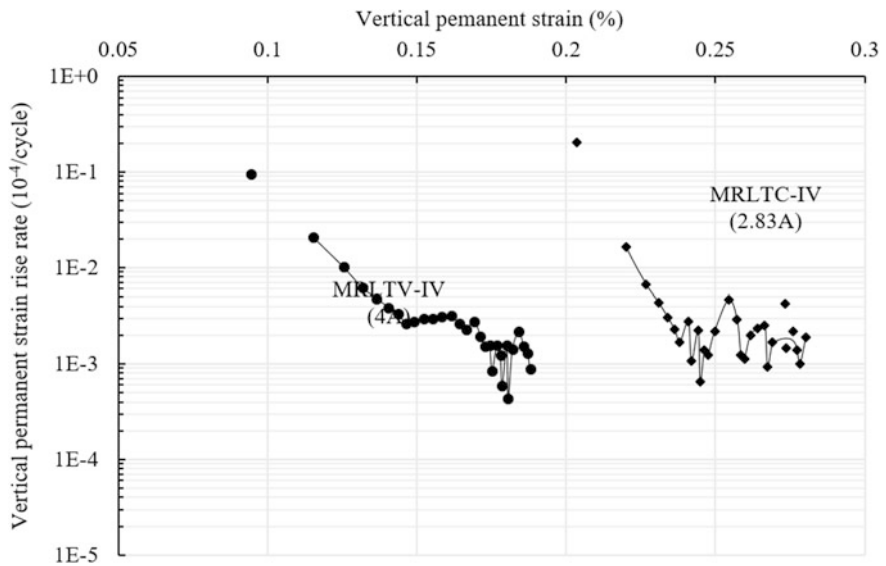
Fig. 8 Comparison of vertical permanent strain increase rate between MRLTV-IV and MRLTC-IV

4 Conclusion

The deformation characteristics of Leighton Buzzard sand under a realistic train-induced stress path are investigated. Some preliminary results are presented in this paper. It is found that the long-term deformation mechanism of the sand tends to change from shakedown to incremental collapse as the load level is increased. The comparison between cases with variable and constant confining pressure demonstrates the importance of simulating variable confining pressure in the experimental study. Moreover, it is found that the increase rate of the vertical permanent strain is closely related to the maximum stress ratio $(q/p)_{max}$, and it might also be affected by the ratio of peak deviator stress to average mean effective stress q_{max}/p_{avg}. Further investigations will be conducted to consider the effect of these two factors in more detail.

References

1. Wang J, Liu S, Yang W (2018) Dynamic shakedown analysis of slab track substructures with reference to critical speed. Soil Dyn Earthq Eng 106:1–13
2. Liu S, Wang J, Yu HS, Wanatowski D (2018) Shakedown for slab track substructures with stiffness variation. Geotech Res 5(1):31–38
3. Yan Q, Xu Y, Zhang W, Geng P, Yang W (2018) Numerical analysis of the cracking and failure behaviors of segmental lining structure of an underwater shield tunnel subjected to a derailed high-speed train impact. Tunn Undergr Space Technol 72:41–54
4. Li DP, Selig ET (1996) Cumulative plastic deformation for fine-grained subgrade soils. J Geotechncial Eng 122(12):1006–1013
5. Ansell P, Brown SF (1978) A cyclic simple shear apparatus for dry granular materials. Geotech Test J 1(2):82–92
6. Yuan R, Yu HS, Hu N, He Y (2018) Non-coaxial soil model with an anisotropic yield criterion and its application to the analysis of strip footing problems. Comput Geotech 99:80–92
7. Yuan R, Yu HS, Yang DS, Hu N (2019) On a fabric evolution law incorporating the effects of b-value. Comput Geotech 105:142–154
8. Xiao J, Juang CH, Wei K, Xu S (2014) Effects of Principle stress rotation on the cumulative deformation of normally consolidated soft clay under subway traffic loading. J Geotech Geoenvironmental Eng 140(4):1–9
9. Qian J, Wang YG, Yin ZY, Huang MS (2016) Experimental identification of plastic shakedown behavior of saturated clay subjected to traffic loading with principal stress rotation. Eng Geol 214:29–42
10. Zdravković L, Jardine RJ (2001) The effect on anisotropy of rotating the principal stress axes during consolidation. Geotechnique 51(1):69–83
11. Hight DW, Gens A, Symes MJ (1983) The development of a new hollow cylinder apparatus for investigating the effects of principle stress rotation in soils. Geotechnique 33(4):355–383

12. Yu HS, Yang LT, Li X et al (2015) Experimental investigation on the deformation characteristics of granular materials under drained rotational shear. Geomech Geoengin 11 (1):47–63
13. Miura K, Miura S, Toki S (1986) Deformation behavior of anisotropic dense sand under principal stress axes rotation. Soils Found 26(1):36–52
14. Tao M, Mohammad LN, Nazzal MD et al (2010) Application of shakedown theory in characterizing traditional and recycled pavement base materials. J Transp Eng 136(3):214–222
15. Sun QD, Indraratna B, Nimbalkar S (2014) Effect of cyclic loading frequency on the permanent deformation and degradation of railway ballast. Geotechnique 64(9):746–751

High Speed Railway Geodynamics

Ground Vibration of Viaduct and Pile-Group Foundation Induced by Moving High-Speed Train

Guang-yun Gao, Wei Xie and Jian Song

Abstract Semi-analytical coupling model of train, track-bridge, bridge pier, group-pile foundation was established. Train was simulated by a mass-spring-damping model, and the bridge vibration was solved by incorporating the slab track equation of motion into the bridge model. Combined with pile-group foundation model, the ground vibration analysis model of viaduct with pile-group foundation under high-speed railway loading was established. Vibration of the upper stiff-layer and lower soft-layer ground and the upper soft-layer and lower stiff-layer ground was studied. Moreover, the influence of pile parameters on the ground vibration was analyzed. Results indicate that the vibration in the pile center of the upper stiff-layer and lower soft-layer ground is larger than that of the upper soft-layer and lower stiff-layer ground when the vehicle speed is less than 300 km/h. For the upper soft-layer and lower stiff-layer ground, the ground vibration acceleration increases significantly at the speed of 350 km/h due to the vehicle speed is close to the shear-wave velocity of surface soft soil, hence the speed of train should be avoided to approach the shear wave of the surface soil. Acceleration of ground vibration induced by a moving train increases with increasing pile diameter and pile length, particularly for high vehicle speeds. Appropriate design of group-pile foundation can reduce the ground vibration.

Keywords High-speed train · Viaduct · Group-pile foundation · Layered foundation · Ground vibration

G. Gao (✉) · W. Xie
Department of Geotechnical Engineering, Tongji University, Shanghai 200092, China
e-mail: gaogy@congji.edu.cn

G. Gao · W. Xie
Key Laboratory of Geotechnical and Underground Engineering of Ministry of Education, Tongji University, Shanghai 200092, China

J. Song
Key Laboratory of Ministry of Education for Geomechanics and Embankment Engineering, College of Civil and Transportation Engineering, Hohai University, Nanjing 210098, China

1 Introduction

In order to avoid the structural damage caused by the differential settlement of the subgrade and to ensure the safe operation of the high-speed trains, viaducts supporting on pile-groups are becoming a dominating foundation type for high-speed railways. Environmental vibration induced by high-speed trains can be annoyance to adjacent residents, cause possible damage to old and historical buildings, and interrupt the operation of sensitive instrumentation [1]. As people's requirements for living environments have become stricter and the precision of high-tech instruments improved, ground vibration problems continue to receive attention from researchers in recent years. Study on ground vibration caused by moving trains in elastic soils, saturated soils, and transversely isotropic soils has been widely reported [2–4]. Considering the effect of bridge structure and pile-group foundation, environmental vibration induced by high-speed trains moving on viaduct supporting by group-piles would be significantly different. Hence, it is essential to study the ground vibration induced by trains running on viaducts with group-pile foundation.

During the past decades, numerical methods with different accuracy have been developed to investigate environmental vibration induced by high-speed trains operating on viaduct. Among these, Ju and Lin [5] established a three-dimensional finite element model of viaduct soil to analyze the ground vibration induced by the passing train on bridge structures. Combing finite element (FE) and boundary element (BE) method, Romero et al. [6] established a three-dimensional FE-BE model for predicting vibrations caused by trains passing over the bridge. Based on thin-layer method and finite element method, a novel numerical analysis model for ground vibration caused by the passing train on viaduct was proposed by Takemiya [7]. However, a three-dimensional modeling of the vehicle-bridge-pile foundation-soil is difficult and expensive.

In view of this, semi-analytical method and field test are used to study train-induced ground vibrations with viaduct and group-pile foundations. Cao et al. [8] established a semi-analytical model to predict the ground vibration induced by high-speed train running through continuous girder bridge. To capture the characteristics of ground vibration induced by moving train on viaduct, Yong et al. [9] proposed a semi-analytical method to analyze the influence of vehicle speed, bridge span, and stiffness of the bridge pier on the ground vibration. Through field measurement, Xia et al. [10] investigated the vibration induced by high-speed train on adjacent buildings.

In summary, few of the current studies discussed the influence of soil structure and pile parameters on the ground vibration induced by moving train on viaduct. Moreover, the method of rational design of pile foundation to reduce ground vibration is still insufficient. In this study, a coupled semi-analytical model compromising of the train, track, bridge, bridge pier, group-pile foundation, and the subgrade soils was established, and the dynamic response of viaduct foundation was solved. The vibration of two types of layered subgrade was studied, i.e., upper

stiff-layer and lower soft-layer ground and the upper soft-layer and lower stiff-layer ground. In addition, the influence of the pile parameters on the ground vibration of the pile-group foundation was analyzed.

2 Train, Track-Bridge, Bridge Pier, and Pile-Group Foundation Model

2.1 Train Model

Figure 1 shows the schematic of the train, track-bridge, bridge pier, group-pile foundation coupled system. In this paper, the model proposed by Liang et al. [11] is used to simulate the moving train load. This model considers the effect of wheel forces and adjacent wheelsets, dispersed effect of sleepers, and the effect of track irregularities. The load formula is given as:

$$F(t) = k_1 k_2 (P_0 + P_1 \sin \omega_1 t + P_2 \sin \omega_2 t + P_3 \sin \omega_3 t) \tag{1}$$

where $P_i = M_0 a_i \omega_i^2$ ($\omega_i = 2\pi v / L_i$, L_i, a_i and ω_i represent the irregular wavelength, the corresponding vector height, and vibration frequency, respectively); P_0 and M_0 are the static wheel weight of the train and unsprung weight. In this paper, they are set as $P_0 = 75$ kN and $M_0 = 1000$ kg according to CRH380A. Based on Ref. [11], the irregular wavelength and the corresponding vector height are given as follows: $L_1 = 10$ m, $a_1 = 3.5$ mm; $L_2 = 2$ m, $a_2 = 0.4$ mm; and $L_3 = 0.5$ m, $a_3 = 0.08$ mm. The values of P_i and ω_i at different vehicle speeds are shown in Table 1.

2.2 Track-Bridge Model

Considering the influence of the adjustment layer underlying the slab track, the dynamic equation of the slab track proposed in Ref. [12] was introduced into the

Fig. 1 Coupled system of train, rail-bridge, bridge pier, group-pile foundation
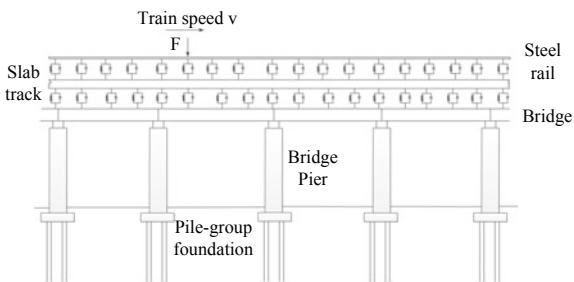
Table 1 Load and excitation frequency values at different vehicle speeds [11]

Speed (km/h)	P_1 (kN)	P_2 (kN)	P_3 (kN)	ω_1 (rad/s)	ω_2 (rad/s)	ω_3 (rad/s)
200	3.198	9.137	29.237	34.903	174.515	698.061
300	7.196	20.560	65.792	52.358	261.789	1047.155
350	9.795	27.985	89.553	61.085	305.425	1221.702

bridge model to derive a semi-analytical model of track-bridge vibration. The dynamic motion equation of bridge can be expressed as Eq. (2):

$$
\begin{aligned}
E_{br}I_{br}\frac{\partial^4 w_{br}(x,t)}{\partial x^4} + m_{br}\frac{\partial^2 w_{br}(x,t)}{\partial t^2} + k_{sb}[w_{br}(x,t) - w_{sb}(x,t)] \\
+ c_{sb}\left[\frac{\partial w_{br}(x,t)}{\partial t} - \frac{\partial w_{sb}(x,t)}{\partial t}\right] + \sum_{j=1}^{N} P_j(t) \cdot \delta(x - a_j) = 0
\end{aligned}
\tag{2}
$$

where E_{br}, I_{br}, and w_{br} represent elastic modulus, moment of inertia, and displacement of bridge, respectively; m_{br} denotes the mass of bridge per unit length in the direction of the track. c_{sb} and k_{sb} represent viscous damping coefficient and spring rigidity of the adjustment layer of slab track per unit length in the direction of the track, respectively. δ, ω_0, V, and L are the Dirac function, excitation frequency, train speed, and bridge span, respectively; $P_j(t)$ is the reaction force of the jth pier, $P_j(t) = P(t - a_j/V)$, and $a_j = jL$.

2.3 Bridge Pier Model

Assuming that the piers are elastically deformed along the vertical direction, the equation of motion for bridge pier is:

$$
m_{pi}\frac{\partial^2 w_{pi}(z,t)}{\partial t^2} + c_{pi}\frac{\partial w_{pi}(z,t)}{\partial t} - E_{pi}A_{pi}\frac{\partial^2 w_{pi}(z,t)}{\partial z^2} = 0
\tag{3}
$$

The relationship between axial force and displacement at the bottom of piers can be expressed as:

$$
N^q(H) = -R^G w_{pi}(H)
\tag{4}
$$

where E_{pi} and A_{pi} represent the elastic modulus and area of cross section of bridge pier, m_{pi} and c_{pi} represent the mass and damping of piers per unit length in the direction of bridge pier axial, respectively. $N^q(H)$ denotes axial force at the bottom of bridge piers, H and R^G represent pier height and impedance of pile-groups, respectively.

2.4 Pile-Group Foundation Model

The pile-group model proposed by Gao et al. [13] is used to analyze the vertical dynamic impedance coefficients of pile-group foundation, and the group-pile impedance can be expressed as:

$$R^G = P_z^G / w^G \tag{5}$$

in which P_z^G and w^G represent the vertical dynamic load on the cap and the vertical displacement of the pile-group, respectively.

2.5 Solution of the Axial Force

By performing the double Fourier transform and the inverse Fourier transform in x-direction, the dynamic equation of bridge Eq. (2) can be expressed as:

$$E_{br}I_{br}\left(\frac{\omega - \omega_0}{V}\right)^4 \overline{w_{br}} - m_{br}\omega^2 \overline{w_{br}} + k_{sb}(\overline{w_{br}} - \overline{w_{sb}}) + i\omega c_{sb}(\overline{w_{br}} - \overline{w_{sb}})$$
$$= -\overline{P(\omega)}\sum_{j=1}^{N} e^{-ijL\frac{\omega_0}{V}} \tag{6}$$

Performing the Fourier transform on Eq. (4), the derived equation is given as:

$$\overline{w''_{pi}} + \lambda^2 \overline{w_{pi}} = 0 \tag{7}$$

where $\lambda^2 = \frac{m_{pi}\omega^2}{E_{pi}A_{pi}} - i\frac{c_{pi}\omega}{E_{pi}A_{pi}}$ and $\overline{w_{pe}} = c_1 e^{i\lambda z} + c_2 e^{-i\lambda z}$. c_1 and c_2 are parameters, which can be determined by boundary conditions:

$$\begin{cases} w_{pi}(z,t)|_{z=0} = w_{br}(x,t)|_{x=L} \\ w_{pi}(z,t)|_{z=H} = -R^G(t)w_{pi}(z,t)|_{z=H} \end{cases} \tag{8}$$

Performing the Fourier transform with respect to time t for Eq. (8), one has the following equation:

$$\begin{cases} \overline{w}_{pi}(z,\omega)|_{z=0} = \overline{w}_{br}(x,\omega)|_{x=L} \\ E_{pi}A_{pi}\overline{w}'_{pi}(z,\omega)|_{z=H} = -R^G(\omega)\overline{w}_{pi}(z,\omega)|_{z=H} \end{cases} \tag{9}$$

The axial force at the top of the pier, after the Fourier transform, can be expressed as:

$$\overline{F}_s(\omega) = -E_{pi}A_{pi}\overline{w}'_{pi}(z,\omega)|_{z=0} \tag{10}$$

2.6   Solution of Ground Vibration

The calculation model of ground vibration induced by moving train on the viaduct established by Wu et al. [14] is shown in Fig. 2. According to Ref. [14], the equation of motion for the ground when subjecting to an excitation force on the top of a pier due to the moving train in frequency domain can be expressed as:

$$\{-\omega^2 M + [K_s + K_p(\omega)] + i\omega C_s + C_p(\omega)\}u^*(\omega) = F_s^*(\omega) \tag{11}$$

in which $C_s = \begin{cases} \pi\rho_s r_{eq}^2\left(c_p + c_s \frac{2e}{r_{eq}}\right) & \upsilon \le \frac{1}{3} \\ 2\pi c_s \rho_s r_{eq}^2\left(1 + \frac{e}{r_{eq}}\right) & \upsilon > \frac{1}{3} \end{cases}$ and $C_p = \sum_{i=1}^n c_i / \sum_{i=1}^n \alpha_i$, C_s and C_p denote the static and dynamic damping coefficient of the elastic half space. $K_s = \frac{4Gr_{eq}}{1-\upsilon}\left(1 + 0.54\frac{e}{r_{eq}}\right)$ and $K_p = \sum_{i=1}^n k_i / \sum_{i=1}^n \alpha_i$, K_s and K_p represent the static and dynamic equivalent vertical stiffness of the elastic half space. G, v, ρ_s, c_p, and c_s represent shear modulus, Poisson's ratio, density, and the wave velocity of the compression and shear waves, respectively. r_{eq} is the equivalent radius of bearing platform, k_i and c_i are the dynamic stiffness and damping coefficients for ith pile.

$u^*(\omega)$ can be obtained from Eq. (11). The interaction force between pile-group and subgrade is as follows:

$$P_{in}^*(\omega) = (K_s + i\omega C_s)u^*(\omega) \tag{12}$$

The vibration of pile-group foundation beneath the bridge pier can be obtained by the Green's function $G_{zz}(r_j, \omega)$ [15]. Hence, the ground vibration displacement at r_j from the viaduct in the frequency domain is expressed as:

$$\tilde{w}_s^*(r_j, \omega) = P_{in}^*(\omega)G_{zz}(r_j, \omega) \tag{13}$$

Fig. 2 Model for calculation of train-induced ground vibration [14]
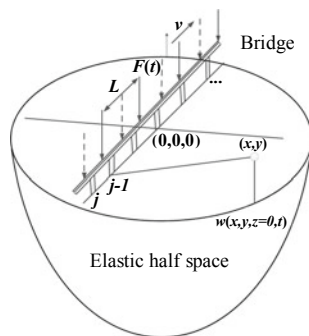
3 Verification of the Established Model

By comparing the results in this study with those from Refs. [14, 16], correctness of the semi-analytical model developed in this paper was verified. In the verification, the upper bridge structure is degraded into elastically supported elements, and underground structure is simulated as pile-group foundation model.

Parameters selected from Ref. [14] are as follows: for the viaduct, $E = 2 \times 10^7$ kN/m^2, $I = 8.72$ m^4, $m = 18.5$ t/m, $L = 30$ m, $\xi_1 = \xi_2 = 0.025$, $M = 1390$ t; for the cap, $b = l = 10.8$ m, $h = 3.6$ m, $z = 4.6$ m; $N = 8$, $d = 1.8$ m, $L_p = 50.4$ m; and $E_p = 2 \times 10^7$ kN/m^2 for the piles. The data adopted for the ground are as follows: shear modulus of soil at the ground surface $G_s = 2.5 \times 10^4$ kN/m^2, shear modulus of soil at the end of the pile $G_s^{'} = 2.9 \times 10^5$ kN/m^2, $\rho_s = 2.0$ t/m^3, $v_s = 0.48$, $c_p = 274$ m/s, $c_s = 158$ m/s, $c_R = 146$ m/s, and $\eta = 0.03$. The duration of computation is taken as $T = 15$ s, the time increment as $\Delta t = 0.005$ s, and the train moving speed as 80 m/s.

Figure 3 shows the comparison of 1/3 octave band spectrum of ground vibration in this paper and that in Refs. [14, 16]. As can be seen from Fig. 3, the results obtained by the present method generally agree well with those from Refs. [14, 16], which indicate that the model can effectively simulate the ground vibration of the viaduct.

Fig. 3 Comparison of the ground velocity variation with frequency
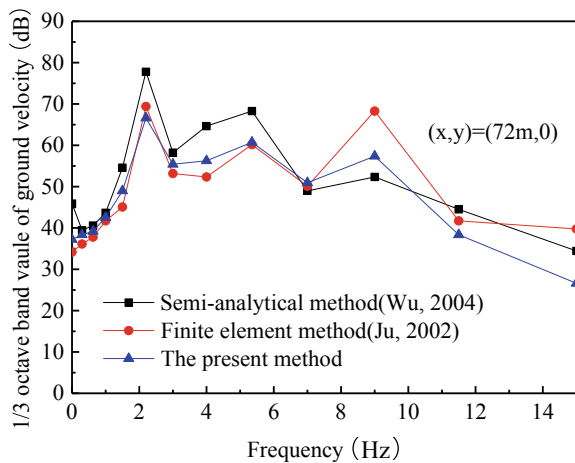
Table 2 Calculation parameters of track, bridge piers, and piles

Component	Mass density (kg/m^3)	Elastic modulus (kN/m^2)	Poisson's ratio	Damping ratio	Cross-sectional area (m^2)	Moment of inertia (m^4)
Track	7800	2.06×10^{11}	0.25	–	7.708×10^{-3}	4×10^{-5}
Bridge pier	2500	3.15×10^{10}	0.35	0.05	–	–
Pile	2500	3.00×10^{10}	0.35	0.05	–	–

Table 3 Calculation parameters of soils

Layers	Shear-wave velocity (m/s)	Poisson's ratio	Weight (kN/m^3)	Dynamic shear modulus (MPa)
Stiff-layer	108	0.35	19	22.22
Soft-layer	61	0.45	18	6.9

4 Results and Discussion

The data adopted for the track, bridge piers, and piles are listed in Table 2, where the parameters of caps are same as piles. The soil parameters (Table 3) of the layered ground are determined from the engineering project of Beijing–Shanghai high-speed railway. The thickness of upper and underlying soil layer is 2 m and 38 m, respectively. The geometry, dimensions, and layout of pile-group in the calculation site are shown in Fig. 4.

4.1 Vibration Response of Layered Foundation

In this study, three different train speeds (i.e., 200, 300, and 350 km/h) are investigated. Figure 5 presents the ground vibration acceleration time history of the two types of ground at the center of pile-group foundation. One can see from Fig. 5 that the acceleration of ground vibration in both subgrades increases with train speed. At the speed of 350 km/h, the vibration of the upper stiff-layer and lower soft-layer ground is larger than that of the upper soft-layer and lower stiff-layer ground.

The maximum vibration acceleration of two kinds of layered ground at the same speed is depicted in Fig. 6. The diagonal line in figure denotes that the maximum vibration accelerations of the two cases are equal at a certain velocity. The horizontal axis value of the point is the maximum acceleration of the upper stiff-layer and lower soft-layer ground, and the vertical axis value is the maximum acceleration of the upper soft-layer and lower stiff-layer ground. As shown in Fig. 6, for the case of vehicle speed below 300 km/h, the maximum vibration acceleration of
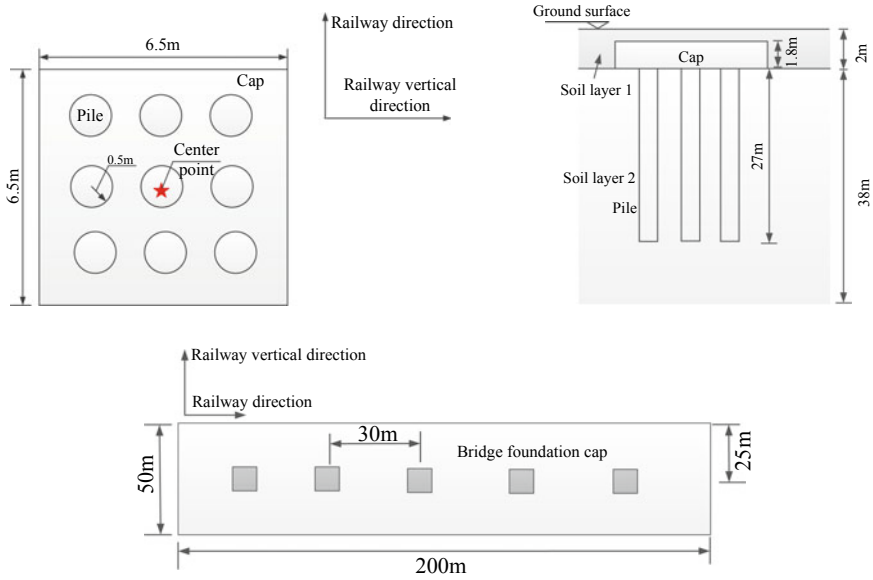
Fig. 4 Geometry, dimensions, and layout of pile-group
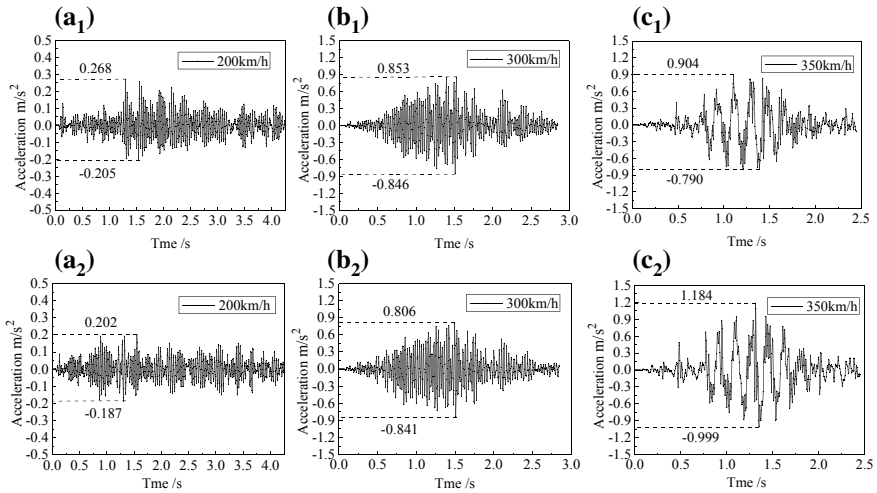
Fig. 5 Vertical acceleration time history in two kinds of layered ground for different vehicle speeds at the center of the pile-group foundation. (a₁-c₁) the upper stiff-layer and lower soft-layer ground; (a₂-c₂) the upper soft-layer and lower stiff-layer ground

Fig. 6 Comparison of maximum acceleration for two kinds of layered subgrade at the same train speed
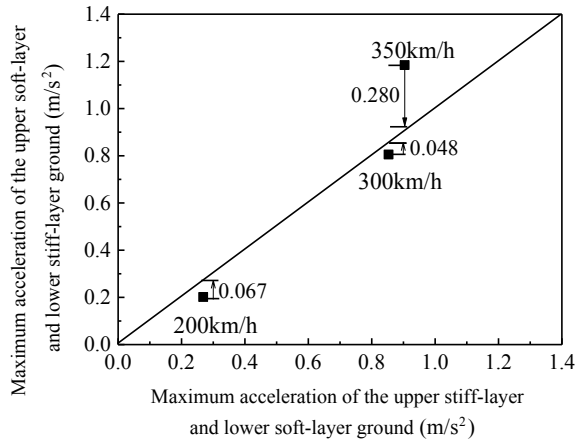
the upper stiff-layer and lower soft-layer ground is larger than that of the upper soft-layer and lower stiff-layer ground. The gap is 0.067 m/s^2 and 0.048 m/s^2 at the speed of 200 km/h and 300 km/h, respectively. However, the maximum vibration acceleration of the upper soft-layer and lower stiff-layer ground is 0.28 m/s^2 larger than that of the upper stiff-layer and lower soft-layer ground at the speed of 350 km/h. The reason causing this phenomenon is that the vehicle speed 350 km/h is close to the shear-wave velocity of surface soft soil of the upper soft-layer and lower stiff-layer ground, which would generate resonance phenomenon and result in the acceleration of ground vibration increasing significantly [2]. Hence, the speed of train should be avoided to approach the shear wave of the surface soil.

4.2 Influence of Pile Diameter on Ground Vibration

Figure 7 shows the acceleration time history in the upper soft-layer and lower stiff-layer ground with different pile diameters. The pile length is fixed as 27 m. It indicates that the ground vibration increases with increasing of pile diameter at same speed. This is because that the stiffness of the pile-group foundation increases with the increase of pile diameter, which would result in a larger vibration under the same dynamic load.

The peak vibration acceleration for the group-pile foundation with different pile diameters is presented in Fig. 8. As shown in Fig. 8, when the speed is less than 300 km/h, the peak acceleration increases smoothly with the pile diameter. However, when the train speed reaches 350 km/h, the vibration amplitude increases significantly with pile diameter, which indicates that the pile diameter has a significant effect on ground vibration when the vehicle speed is high.
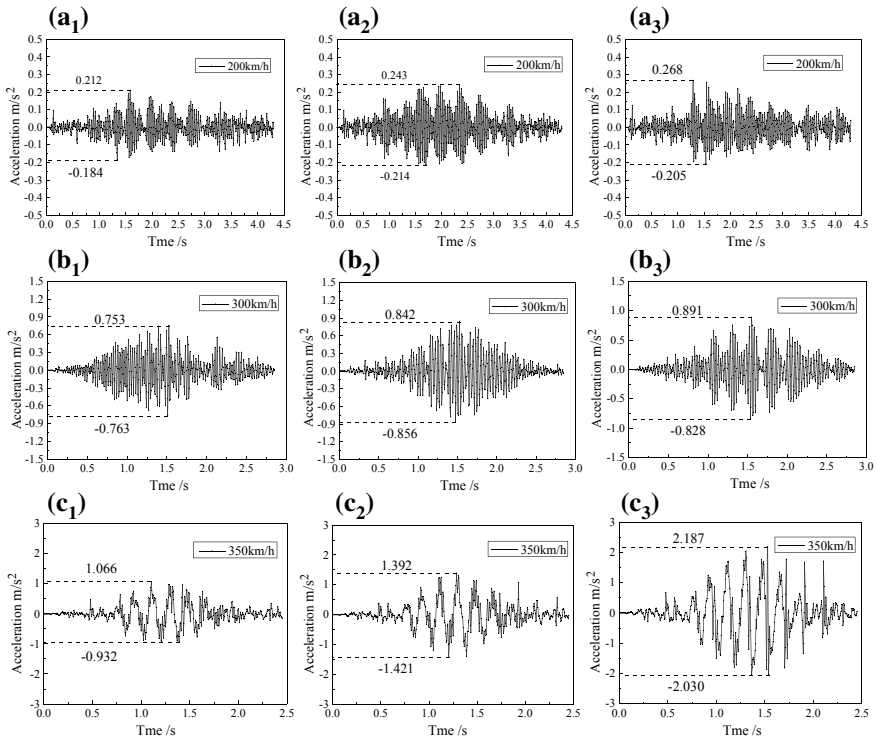
Fig. 7 Vertical acceleration time history of layer ground for different pile diameters. (a_1-c_1) pile diameter = 0.5 m; (a_2-c_2) pile diameter = 0.6 m; and (a_3-c_3) pile diameter = 0.6 m

Fig. 8 Variation of ground vibration peak acceleration with the pile diameter at different train speeds
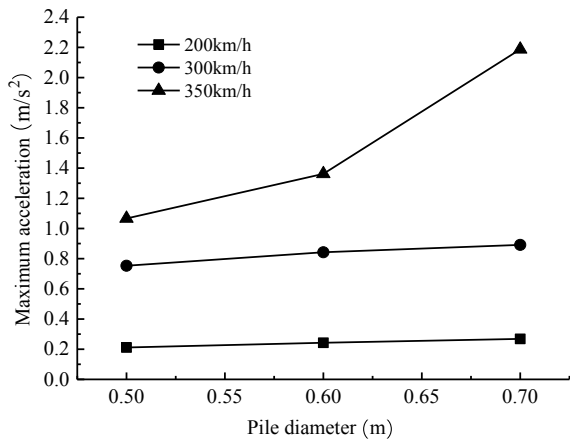
4.3   Influence of Pile Length on Ground Vibration

Figure 9 shows the acceleration time history in the upper soft-layer and lower stiff-layer ground with different pile lengths. The pile diameter is 0.5 m. One can see from Fig. 8, the acceleration of ground vibration increases with increasing pile length at the same vehicle speed. The reason may be that, when the pile length is large, the distance of vibration energy propagation along the pile to the beneath soil is farther; in this case, there is more energy on the ground surface and acceleration of ground vibration has a larger value.

Figure 10 shows the difference of maximum vibration acceleration for different pile lengths with respect to the different speed. The horizontal axis value of the point is the maximum acceleration for pile length is 27 m, and the vertical axis value is the maximum acceleration for pile length is 35 m. As can be seen in Fig. 10, the maximum acceleration of ground vibration for pile length of 35 m is greater than that corresponding to pile length of 27 m. In addition, when the train speed is less than 300 km/h, it is observed that, in comparison with vehicle speed, the length of the pile has little effect on the maximum acceleration of ground vibration. When the train speed is 350 km/h, the maximum acceleration of ground vibration increases rapidly with increasing of pile length.

According to the above analysis, it can be found that the variation of pile length and pile diameter has equivalent effects on ground vibration at the same speed. Hence, through reasonable design of group-pile foundation, requirement on ground vibration control, subgrade settlement control, and bearing capacity can simultaneously be satisfied, e.g., increasing of pile diameter and decreasing the pile length
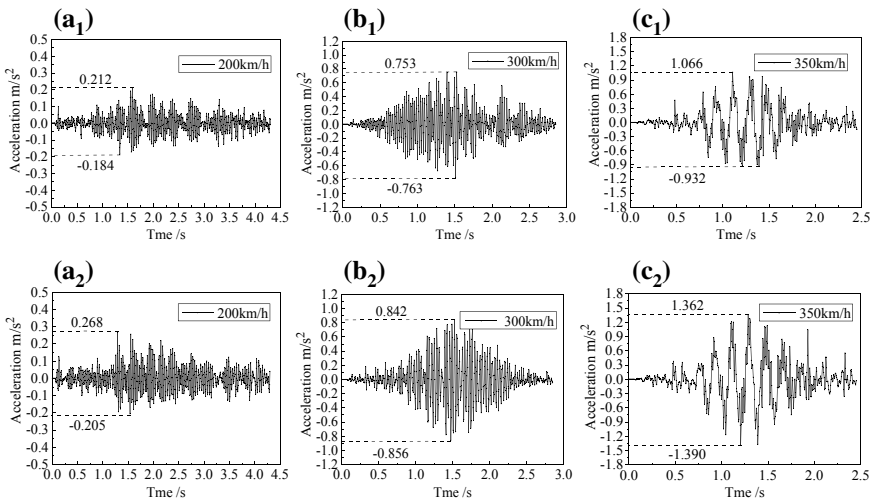
Fig. 9 Vertical acceleration time interval curves of upper soft-layer and lower stiff-layer ground for different pile lengths. (a_1-c_1): pile length = 27 m; (a_2-c_2): pile length = 35 m

Fig. 10 Comparison of maximum acceleration on upper soft-layer and lower stiff-layer ground for different pile lengths
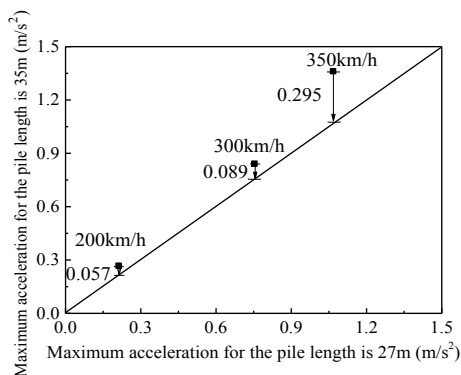
or increasing of pile length and decreasing the pile diameter. In addition, when the vehicle speed is less than 300 km/h, it is the train speed that plays a dominating role in determining the ground vibration, but when the speed is higher than 300 km/h, more attention must be paid to the coupling effect of the soil structure, pile parameters, and vehicle speed.

5 Conclusion

The vibration in the pile-group center of the upper stiff-layer and lower soft-layer ground is larger than that of the upper soft-layer and lower stiff-layer ground when the train speed is less than 300 km/h. For the upper soft-layer and lower stiff-layer ground, the ground vibration acceleration increases significantly at the speed of 350 km/h due to the vehicle speed is closed to the shear-wave velocity of surface soft soil. Hence, the speed of the train should be avoided from approaching the shear wave of the surface soil.

The acceleration of ground vibration increases with increasing pile diameter and pile length, particularly when the speed of the train is large. Appropriate design of group-pile foundation can reduce the ground vibration.

The ground vibration characteristics are mainly dominated by the moving train speed when the speed is less than 300 km/h, but more attention must be paid to coupling influence of the soil deposits, pile parameters, and vehicle speed on the ground vibration when the speed is higher.

References

1. Chen YJ, Ju SH, Ni SH, Shen YJ (2007) Prediction methodology for ground vibration induced by passing trains on bridge structures. J Sound Vib 302(4):806–820
2. Gao GY, Chen QS, He JF, Liu F (2012) Investigation of ground vibration due to trains moving on saturated multi-layered ground by 2.5D finite element method. Soil Dyna Earthq Eng 40(3): 87–98
3. Gao G, Song J, Chen G, Yangun J (2015) Numerical prediction of ground vibrations induced by high-speed trains including wheel-rail-soil coupled effects. Soil Dyna Earthq Eng 77:274–278
4. Gao G, Xu C, Chen J, Song J (2018) Investigation of ground vibrations induced by trains moving on saturated transversely isotropic ground. Soil Dyna Earthq Eng 104:40–44
5. Ju SH, Lin HT (2007) A finite element model of vehicle-bridge interaction considering braking and acceleration. J Sound Vib 303(1):46–57
6. Romero A, Solís M, Domínguez J et al (2013) Soil–structure interaction in resonant railway bridges. Soil Dyna Earthq Eng 47(4):108–116
7. Takemiya H (2008) Analyses of wave field from high-speed train on viaduct at shallow/deep soft grounds. J Sound Vib 310(3):631–649
8. Cao Y, Xia H, Li Z (2012) A semi-analytical/FEM model for predicting ground vibrations induced by high-speed train through continuous girder bridge. J Mech Sci Technol 26(8): 2485–2496
9. Yang YB, Wu YS (2005) Transmission of vibrations from high speed trains through viaducts and foundations to the ground. J Chin Institute of Engineers. 28(2):251–266
10. Xia H, Zhang N, Cao YM (2005) Experimental study of train-induced vibrations of environments and buildings. J Sound Vib 280(3):1017–1029
11. Liang B, Luo H, Sun C (2006) Simulated study on vibration load of high speed railway. J China Railw Soc 28(4):89–94 (in Chinese)
12. He ZX, Zhai WM, Wang SZ et al (2007) Semi-analytical study on ground vibration induced by railway traffics with axle loads. J Vib Shock 26(12):1–5 (in Chinese)
13. Gao GY, Li SY, Gu XQ (2015) Ground vibration induced by moving train on viaduct with group pile foundation. Chin J Geotech Eng 37(10):1751–1761 (in Chinese)
14. Wu YS, Yang YB (2004) A semi-analytical approach for analyzing ground vibrations caused by trains moving over elevated bridges. Soil Dyna Earthq Eng 24(12):949–962
15. Wolf JP (1994) Foundation vibration analysis using simple physical models. Pearson Education Press, NJ, Prentice-Hall
16. Ju SH (2002) Finite element analyses of wave propagations due to a high-speed train across bridges. Int J Numer Methods Eng 54(9):1391–1408

Ground-Borne Vibration Generated by High-Speed Trains on the Pile-Supported Subgrade Reinforced by Geogrid

Guang-yun Gao, Jun-wei Bi and Qing-sheng Chen

Abstract The pile-supported subgrade reinforced by geogrid is widely applied in the construction of high-speed railway in China. To investigate the ground-borne vibration of such composite foundations subjected to moving loads induced by high-speed trains, a train-track-ground dynamic analysis model involving the pile, pile cap and cushion, was developed based on the three-dimensional (3D) finite element method (FEM). Based on the field data for a practical composite subgrade project at the east side of Suzhou Railway Station of Beijing–Shanghai high-speed railway, the numerical model was established and verified accordingly with the in situ measured results. Comparison studies were conducted on the vibrations for the composite foundation and unreinforced foundation. Results show that acceleration of ground-borne vibration is reduced effectively in composite subgrade because of the existence of cushion and piles, and the vibration attenuates increasingly quickly as the distance from the track center increases.

Keywords Ground-borne vibration · High-speed railway · Pile-supported subgrade reinforced by geogrid · Finite element method

1 Introduction

The ground waves generated by high-speed train have different propagation characteristics in comparison with that by the traditional train. The resulting vibration can travel large distances from track, thereby causing discomfort to residents, misalignment of sensitive instruments and possibly even building damage.

G. Gao (✉) · J. Bi
Key Laboratory of Geotechnical and Underground Engineering of Ministry of Education, Tongji University, 200092 Shanghai, China
e-mail: gaogy@tongji.edu.cn

Q. Chen
Department of Civil and Environmental, National University of Singapore, Lower Kent Ridge Road, Singapore 117576, Singapore

Therefore, over the past years, the ground vibrations produced by the high-speed trains have received increasing interests by various researchers [1].

Pile-supported and geogrid-reinforced subgrade has been widely used in the high-speed railway construction, especially in China. While most analysis and predicted models for investigating train-induced ground vibrations so far simplified the foundation as a single-phase elastic, viscoelastic or saturated multi-layered solid [2–5], knowledge on ground vibrations due to the train moving on such composite subgrade is limited in the literatures. Most recently, few studies were carried out on the train-induced ground vibrations on the pile-supported subgrade reinforced by geogrid. Zhai et al. [6] proposed a train-track-ground system model involving coupled vehicle–track dynamic model, where the influence of cement mixing piles on the high-speed train-induced vibration was investigated. By means of three-dimensional (3D) finite element method (FEM), Thach et al. [7] investigated the vibration behaviors of pile-supported subgrade. Ma et al. [8] analyzed the impact of the foundation reinforcement on the characteristics and propagation of ground vibration via numerical analysis for the Shanghai–Nanjing intercity high-speed railway. Feng et al. [9] developed a 3D FEM model to study the influence of subgrade reinforcement and sub-soil treatment on the ground vibrations.

In this paper, a 3D FEM model of composite subgrade involving piles, pile caps and cushion was developed to study the ground-borne vibration generated by high-speed train. This numerical model was validated by comparing the predictions with the field data. The influences of the piles, pile caps and cushion on the ground vibration were presented and discussed in detail.

2 Modeling Approach and Validation

2.1 Mathematical Description of Train Loading

According to the frequency-domain analysis of the embankment vibration [10, 11], artificial excitation combined by a series of periodic loads is applied to simulate the train loading. The mathematical description of train loading can be expressed as follows:

$$\boldsymbol{F}(t) = \boldsymbol{k}_1 \boldsymbol{k}_2 (\boldsymbol{P}_0 + \boldsymbol{P}_1 \sin \omega_1 t + \boldsymbol{P}_2 \sin \omega_2 t + \boldsymbol{P}_3 \sin \omega_3 t) \tag{1}$$

where $\boldsymbol{P}_0$ denotes the static load of a train carriage; the constant $\boldsymbol{k}_1$ and $\boldsymbol{k}_2$ represents the superposition coefficient and the dispersion coefficient, respectively; $\boldsymbol{P}_1$, $\boldsymbol{P}_2$ and $\boldsymbol{P}_3$ are the typical values of the dynamic loads corresponding to ω_1, ω_2 and ω_3 which represent the low frequency, medium frequency and high frequency, respectively.

The P_i and ω_i (i = 1, 2, 3) are given by Eqs. (2) and (3).

$$P_i = M_0 a_i \omega_i^2, \quad i = 1, 2, 3 \tag{2}$$

$$\omega_i = 2\pi v / L_i, \quad i = 1, 2, 3 \tag{3}$$

where M_0 represents unsprung mass of a train carriage; v is train speed; a_i and L_i are the rise and wavelength of the track geometric unevenness. According to parameters of high-speed train type CRH380AL, train loading is confirmed and applied by means of the DLOAD subroutine in ABAQUS.

2.2　Establishment of Model

Zhai et al. [12] analyzed the train-induced ground-borne vibration by on-site measurement at the east side of Suzhou Railway Station of Beijing–Shanghai high-speed railway. To validate reliability of the proposed model, the geometry and material properties of the embankment and composite foundation were modeled in accordance with the slab track-type CRTSII mentioned in reference literature [12]. Based on the 3D FEM using ABAQUS software, a train-track-ground dynamic analysis model involving the pile, pile cap and cushion was developed with dimension 120.0 m (length) × 70.0 m (width) × 40.0 m (depth), which is illustrated in Fig. 1. By taking advantage of symmetry, only one half of the finite element model was modeled.

The rail and fasteners were substituted by beam elements and spring-dampers, respectively, and other components of track and composite foundation were modeled using eight-node solid elements, the dimensions of which were controlled in the range between 0.275 and 2.5 m. To prevent reflections from the edge of the truncated domain, three-dimensional viscous–elastic artificial boundaries were implemented, in which the geometric and material damping were taken into account.

(a) Embankment and piles model　　　　(b) Finite element model of track-ground
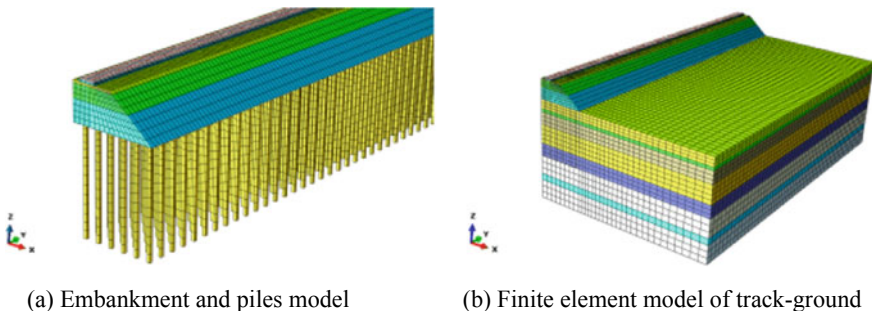
Fig. 1 Detail view of FEM model

2.3 Validation

The proposed FEM model was validated by comparing the predictions to field measurements mentioned in reference literature [12]. Figures 2 and 3 present the predicated and measured time histories of vertical ground vibration acceleration at a distance of 14.1 and 35.0 m from track center, respectively. It is observed that the predicted ground responses have a high correlation with the field measure. The response to the carriage of each wheel set is visible and similar in timing, shape and magnitude. In addition, ground response to the heavier carriages in middle of the CRH380AL high-speed train has also been simulated effectively. Also, the FEM model could generally yield accurate magnitude of the accelerations, even though it is observed that the numerical model slightly underestimates the downward acceleration. Thus, it can be concluded that the proposed numerical model is capable of simulating train-induced ground vibration at both near and far offsets from track center.
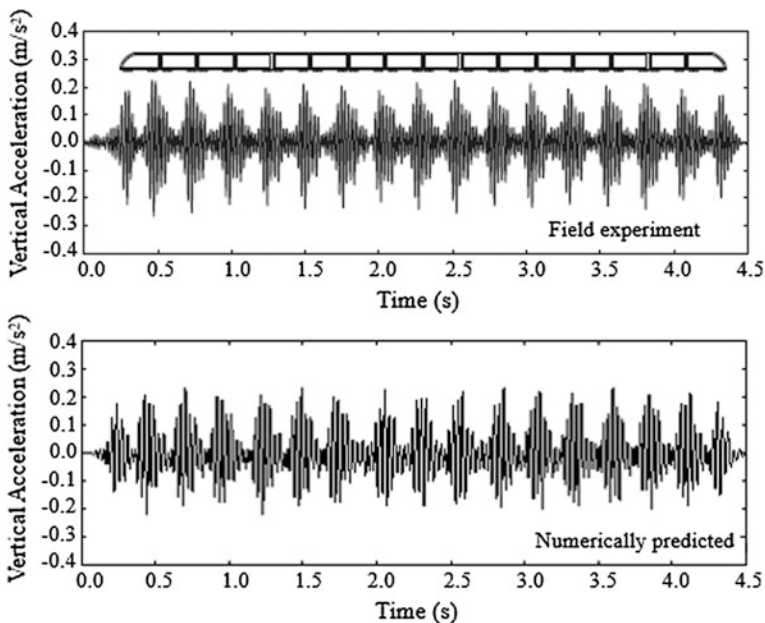
Fig. 2 Comparison of the time histories of vertical ground vibration acceleration at 14.1 m from track center
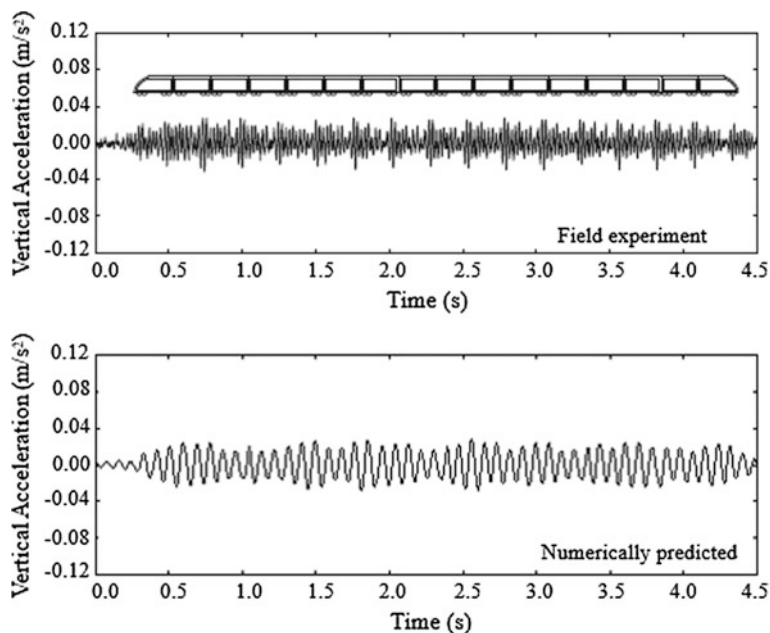
Fig. 3 Comparison of the time histories of vertical ground vibration acceleration at 35.0 m from track center

3 Comparison of Ground Vibrations for Unreinforced Foundation and Composite Subgrade

3.1 Computation Model

To investigate the vibrations of ground with unreinforced foundation and ground with the pile-supported and geogrid-reinforced subgrade, the computation model involving embankment and composite foundation was built as shown in Fig. 4. Yang et al. [13] pointed out that the ground-borne vibration generated by train consisting four carriages is almost identical to that by the train with ten carriages. To reduce calculation efforts, the loadings generated by a train consisting of four carriages based on the high-speed train type CRH380AL were used for the numerical analysis.

The embankment consists of three parts as follows: the surface layer of subgrade, the bottom of subgrade and the rest part below the subgrade. The dynamic properties of embankment are presented in Table 1. The foundation soil is soft soil. The soil profile and geotechnical parameters are in accordance with that of the typical soils distributed in the middle and lower reached of the Yangtze River [8]. The uppermost soil layer is clay with thickness of 6.0 m, and the second soil layer is mucky clay with thickness of 12.0 m. The third soil layer is silty clay with
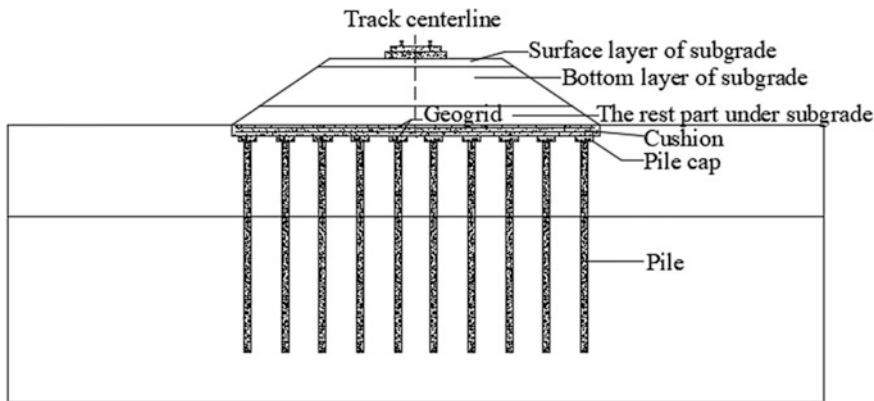
Fig. 4 The cross section of pile-supported and geogrid-reinforced subgrade in single-track high-speed railway

Table 1 Dynamic properties of the calculation model

Name	Layer thickness (m)	Dynamic elastic modulus (MPa)	Poisson's ratio	Damping ratio	Density (g/m³)	Shear wave velocity (m/s)
Surface layer of subgrade	0.4	150	0.30	0.038	1.90	174.3
Bottom layer of subgrade	2.3	110	0.35	0.034	1.95	144.5
The rest part under subgrade	0.6	50	0.32	0.030	1.90	99.8
Clay	6.0	60	0.31	0.050	1.89	106.0
Mucky clay	12.0	15	0.30	0.050	1.75	56.0
Silty clay	15.0	70	0.30	0.050	1.89	111.0
Silty sand	17.0	90	0.32	0.050	1.99	123.0
CFG pile	–	10,000	0.20	0.060	2.50	–

thickness of 15.0 m, and the bottom layer is silty sand with thickness of 17.0 m. The summary of soil properties is shown in Table 1.

As mentioned in the Second Section, the model was developed with dimension 120.0 m (length) × 70.0 m (width) × 40.0 m (depth), which is illustrated in Fig. 5. In the computing model, three observation points at a distance of 0.4 m, 10.0 m and 40.0 m, respectively, from track centerline were selected.

For the composite foundation model, the piles selected for ground improvement are cement fly-ash gravel (CFG) piles with following dimensions: pile length is 18.0 m; pile diameter is 0.5 m; diameter and thickness of the pile cap are 1.2 m and 0.4 m, respectively. The CFG piles are arranged in a rectangular pattern with pile spacing of 1.8 m which consist with that widely applied in the Beijing–Shanghai high-speed railway mentioned in Ref. [14]. For the unreinforced foundation, the model portion for CFG piles was substituted by soil elements.

3.2 Numerical Results

Figure 6 shows the time histories of vertical ground vibration acceleration at different distance from track center for train speed of 350.0 km/h. It can be seen that a cluster of significant vibration is induced by each bogie of the train. For both unreinforced foundation and composite subgrade, the vertical ground vibration acceleration decays with the increasing distance away from track centerline. Beyond 10.0 m from track center, the vertical ground vibration acceleration of unreinforced foundation is much larger than its counterpart for the composite subgrade. The train-induced ground vibration in the pile-reinforced composite subgrade attenuates much more quickly compared to that in the unreinforced foundation. This indicates that the piles and cushion can cause a significant decrease in the ground vibration and reduce far-field vertical acceleration effectively.

The time histories of vertical ground vibration acceleration in Fig. 6 were converted to the amplitude spectra by Fourier transformation in order to analyze the frequency-domain characteristics of ground-borne vibration.

Figure 7 presents the distribution of frequency spectra of the vertical ground vibration acceleration within the distance of 40.0 m from track centerline. At 0.4 m from track center, there are similarities between the frequency components and magnitudes of spectra for both of the unreinforced foundation and pile-reinforced
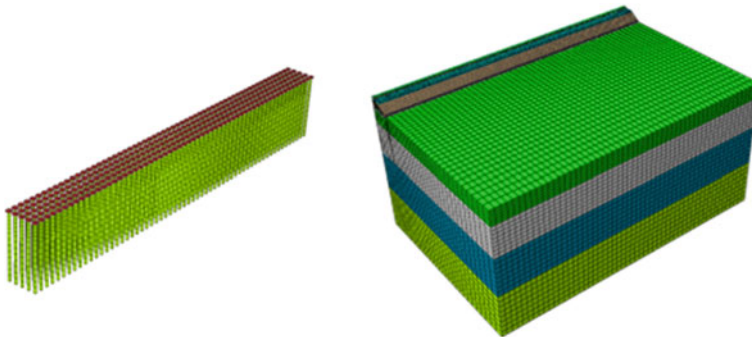
Fig. 5 The 3D finite element models of pile, pile cap and composite foundation

(a) 0.4m from track center

(b) 10.0m from track center

(c) 40.0m from track center
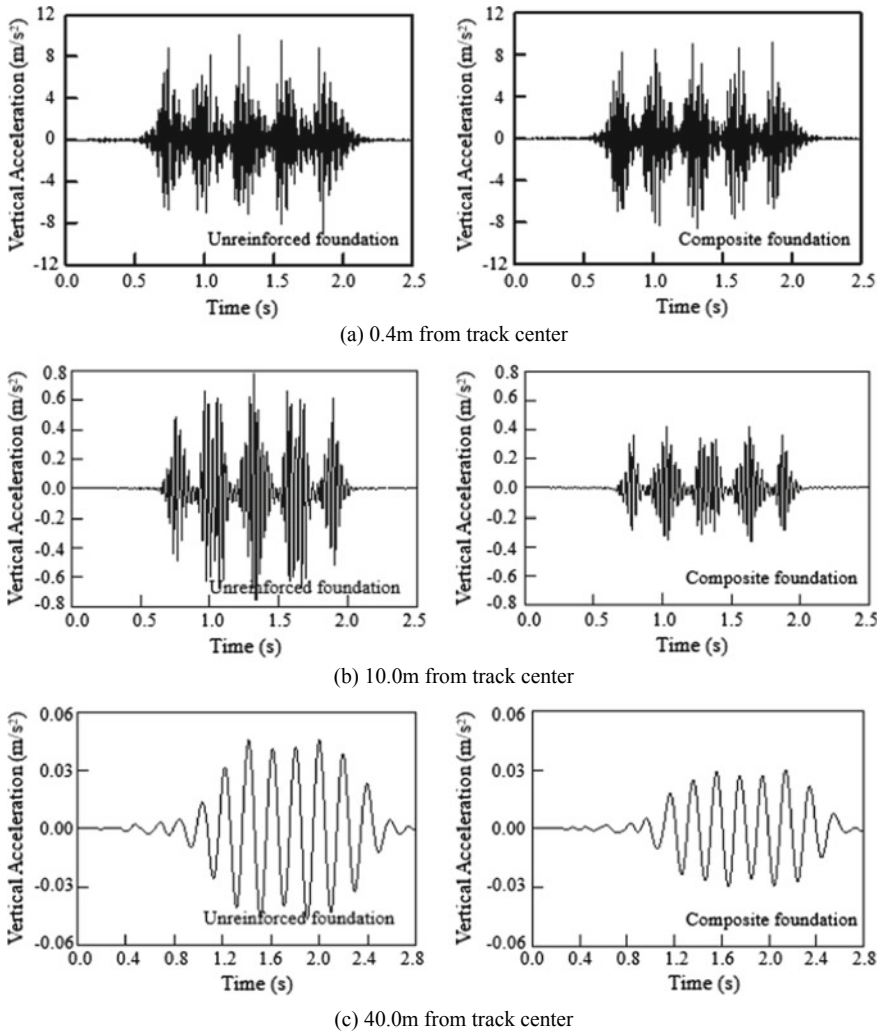
Fig. 6 Time histories of the vertical ground vibration acceleration at different distance from track centerline with train speed of 350.0 km/h

composite subgrade. Comparing to the unreinforced foundation, the spectrum amplitudes of frequency decay greatly at 10.0 m from track center where the slop toe of embankment locates, especially for the high-frequency components. Figure 7c also indicates that the piles and cushion can reduce the spectrum amplitude of frequency at 40.0 m from track center, both for the high- and low-frequency components.

(a) 0.4m from track center

(b) 10.0m from track center

(c) 40.0m from track center
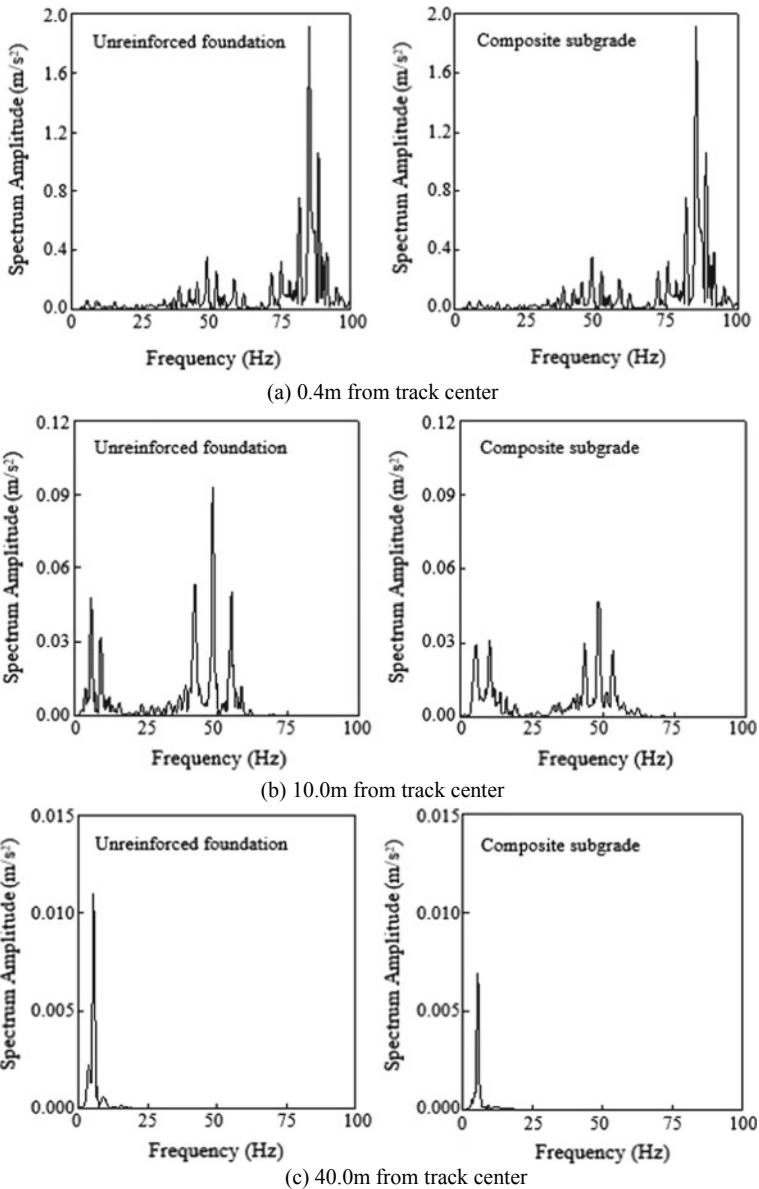
Fig. 7 Frequency spectra of vertical ground acceleration at different distance from track centerline with train speed of 350.0 km/h

4   Conclusions

To investigate the ground-borne vibration of composite foundations subjected to moving loads induced by high-speed trains, a train-track-ground dynamic analysis model involving the pile, pile cap and cushion was developed based on the 3D finite element method (FEM). The following conclusions can be drawn:

(1) The proposed numerical model is capable of simulating train-induced ground vibration at both near and far offsets from track center, which has been validated by the field measured data.

(2) The ground vibration acceleration decays with the increasing distance away from the track center for both unreinforced foundation and pile-reinforced composite subgrade. However, the train-induced ground vibration in the pile-reinforced composite subgrade attenuates much more quickly compared to that in the unreinforced foundation.

(3) For the pile-reinforced composite subgrade, the spectrum amplitudes decrease much more significantly comparing to that for the unreinforced foundation, for both low- and high-frequency components. It can be concluded that the ground vibration responses can be reduced evidently due to the existence of piles and cushion in the composite subgrade.

References

1. Connolly DP, Marecki GP, Kouroussis G et al (2016) The growth of railway ground vibration problems—a review. Sci Total Environ 568:1276–1282
2. Wang J, Zeng X (2004) Numerical simulations of vibration attenuation of high-speed train foundations with varied track bed underlayment materials. J Vib Control 10:1123–1136
3. Yang YB, Hung HH, Chang DW (2003) Train-induced wave propagation in layered soils using finite/infinite element simulation. Soil Dyn Earthq Eng 23:263–278
4. Gao GY, Chen QS, He JF et al (2003) Investigation of ground vibration due to trains moving on saturated multi-layered ground by 2.5D finite element method. Soil Dyn Earthq Eng 23:263–350
5. Connolly DP, Giannopoulos A, Forde MC (2013) Numerical modelling of ground borne vibrations from high speed rail lines on embankments. Soil Dyn Earthq Eng 46:13–19
6. Zhai WM, Wang KY, Cai CB (2009) Fundamentals of vehicle-track coupled dynamics. Veh Syst Dyn 47(11):1349–1376
7. Thach PN, Liu HL, Kong GQ (2013) Vibration analysis of pile-supported embankments under high-speed train passage. Soil Dyn Earthq Eng 55:92–99
8. Ma LH, Liang QH, Gu AJ et al (2015) Research on impact of Shanghai-Nanjing intercity high-speed railway induced vibration on ambient environment and foundation settlement of adjacent Beijing-Shanghai railway. J China Railw Soc 37(02):98–105 (in Chinese)

9. Feng SJ, Zhang XL, Zheng QT et al (2017) Simulation and mitigation analysis of ground vibrations induced by high-speed train with three dimensional FEM. Soil Dyn Earthq Eng 94:204–214
10. Chen B, Chen G, Su X (2008) Analysis and evaluation of ground vibration response induced by rapid rail transit. In: Liu H, Deng A, Chu J (eds) Geotechnical engineering for disaster mitigation and rehabilitation. Springer, Berlin, Heidelberg, pp 284–293
11. Liang B, Luo H, Sun CX (2006) Simulated study on vibration load of high speed railway. J China Railw Soc 28(4):89–94 (in Chinese)
12. Zhai WM, Wei K, Song X et al (2015) Experimental investigation into ground vibrations induced by very high speed trains on a non-ballasted track. Soil Dyn Earthq Eng 72:24–36
13. Yang YB, Hung HH (2009) Wave propagation for train-induced vibrations: a finite/infinite element approach. World Scientific, Singapore
14. Feng SJ, Zhang XL, Wang L et al (2017) In situ experimental study on high speed train induced ground vibrations with the ballast-less track. Soil Dyn Earthq Eng 102:195–214

Three-Dimensional Numerical Simulation of Vehicle Dynamic Load and Dynamic Response for Ballastless Track Subgrade

Xuan Wang, Hao Cheng, Biao Zhang, Jiasheng Zhang and Qiyun Wang

Abstract With the development of the high-speed railway, the ballastless track is widely applied and the dynamic characteristics of subgrade are the bases of the design, construction, and maintenance of the ballastless track/subgrade system. In a sense, the distribution rule of dynamic response under the action of train loads and the influence of subgrade parameters lags far behind the construction of the high-speed railway in engineering because of their complication. Dynamic system which was composed of rail, track, and roadbed is so complex that it cannot be solved depending on available theory. In this paper, the numerical simulation method was introduced to describe the dynamic action of roadbed which beard high-speed rail loads. Therefore, a 3-d finite element model of the track/subgrade system was established with the aid of ANSYS for the dynamic response of ballastless track subgrade which bears vehicle dynamic loads and loads input behavior. At the same time, the choice method and basis of a unit-type, constitutive model of subgrade and material parameters were established. According to distributed mode and behaviors of vehicle dynamic load and load input characteristics, a 2-car and 8-wheelset vehicle model was introduced to get contact pressure time-history curves of fastening when two bogies pass between neighboring cars through Fourier transform. Furthermore, the rationality and applicability of model were verified

X. Wang · H. Cheng · J. Zhang
School of Civil Engineering, Central South University, Changsha 410075, China

X. Wang · J. Zhang
National Engineering Laboratory for High-Speed Railway Construction, Central South University, Changsha 410075, China

B. Zhang
School of Civil Engineering, Hunan University of Science and Technology, Xiangtan 411201, China

Q. Wang
School of Civil Engineering, Fujian University of Technology, Fuzhou 350118, China

X. Wang (✉)
Department of Geotechnical Engineering School of Civil Engineering Railway Campus, Central South University 22, Shaoshan South Road, Changsha, Hunan 410075, China
e-mail: dddebug@csu.edu.cn

depending on the data which came from the test in situ. Vertical dynamic stresses, dynamic displacement, and dynamic acceleration were calculated for CRTSII-type slab ballastless track and double-block ballastless track when train passes which its speed was 300 km/h and axle load was 170 kN. In addition, the relationship between all those response laws and rail/subgrade construction was analyzed. Interrelated analyses conclude that vertical dynamic stresses, dynamic displacement, and dynamic acceleration decay as roadbed deepens, and dynamic acceleration decays faster. In addition, the type of track which influenced dynamic response only focuses on the top of the roadbed.

1 Introduction

The major differences between high-speed track roadbed and traditional roadbed are found in: ① the structure of subgrade, including ballast and ballastless track roadbed; ② The settlement control is key to the design of roadbed after construction, and therefore, the deformation control is to control the deformation magnitude under high-speed train load;and ③ the stiffness of subgrade is one of the important parts of the train/track/subgrade system [1]. Thus, it causes a lot of subgrade dynamic and geotechnical problems. The dynamic responses of high-speed railroad subgrade should comprise factors like the soil body dynamic deformation of subgrade, dynamic stress, and acceleration. The size of responses and its process directly affect the design, construction, use, and maintenance and concern the intensity fatigueness characteristics, accumulative deformation, and dynamic stability [2]. Many factors may affect the dynamic responses of subgrade, such as vehicle type, axle weight, velocity, route structure and status, steel track type, rail bearing type and space, ballast type and thickness, soil property, and density of subgrade [3].

Due to the train/track/subgrade system complexity, the dynamic load and dynamic deformation design of ballastless track subgrade of the high-speed train should include prestressing steel concrete roadbed, especially the subgrade. The spatial characteristics should be taken into consideration in accordance with the real construction condition of high-speed train subgrade. A dynamic analysis should be conducted on track/subgrade structure so as to determine the proper parameters for subgrade structure like thickness, stiffness (modulus), etc. The solutions of these factors fail to be done theoretically, and so it is necessary to make numerical simulation with the help of large-scale numerical platform [4]. Many researchers both from overseas and home have made great progress by establishing numerical calculation model with finite method to solve the dynamic problems of ballastless track subgrade. Nevertheless, many numerical models are not perfect on the dynamic behaviors of wheel–rail force, train vibration, and track structure. The

subgrade model tends to be simplified without considering stratification and diversification of fillings. In addition, the dynamic acceleration of subgrade is rarely analyzed. The distribution rule of stress, acceleration, displacement generated in the subgrade, responses index, and correlation with influence factors are not fully accounted for. Therefore, this paper seeks to establish a 3-d numerical model for ballastless track subgrade based on ANSYS and make the second development with APDL language to discover the distribution regularity of the dynamic characteristics of a track/subgrade system.

2 Finite Model for Ballastless Track Subgrade

2.1 Establishment and Solution of the Finite Model

One of the biggest advantages of the finite method for ballastless track subgrade is that it can work out a dynamic response from any position of the track system. Through this method, the soil subgrade and ballastless track structure are scattered into finite elements complying with deformation continuity and balance condition of forces [5]. In this model, the track is regarded as a continuous beam of spring point bolster; fastening of steel track and rubber mat is regarded as spring-damping system; and track slab, CA mortar, concrete supporting layer or pedestal, gravels for the surface layer, fillings for the bottom layer of roadbed, and subgrade are all considered element, respectively. The CRTS II-type slab ballastless track and double-block ballastless track are presented in Fig. 1.

Space, time, and coupling of track system are taken into account in the process of modeling [6].

The interrelation of ballastless track/subgrade system with vehicle system is reflected through the outer load. Therefore, in the ballastless track/subgrade system,
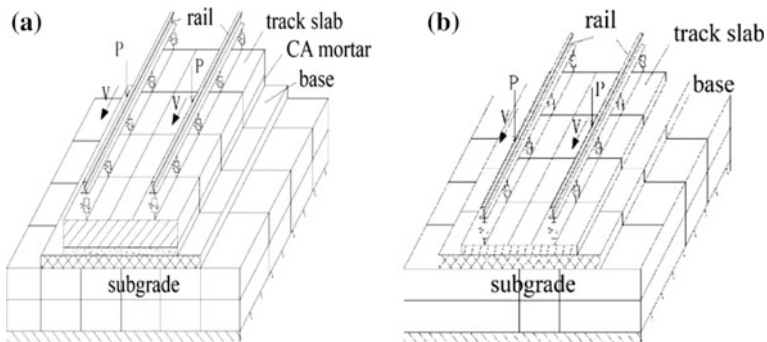
Fig. 1 Model of CRTSII-type slab ballastless track and double-block ballastless track

the vehicle load is simplified as an outer excitation which is transformed from the load on the track or from the unevenness of the track. Here, the Newmark-β method is applied.

2.2 Constitutive Type

BEAM188 element is used for steel track with the premise that: ① the bending deflection of beam conforms with the flat section; ② the bearing effect of the nodes on both sides of the beam at the center of cross section coincides with the axial force, shearing force, and bending moment. The track slab is SHELL63 elastic shell element; fastening and rubber mat are COMBIN14 spring damping element; and track slab, CA mortar, concrete bearing layer, and subgrade are SOLID45 entity element [7]. The equivalent stiffness of the fastening and rubber mat system under track is 4.38×107 N/m, damping coefficient is 4.5×104 N·s/m, and coefficient of CA is 3.5×104 N·s/m.

In view of stress wave reflection effect and half finite space of soil body under the roadbed, 3-d consistent viscoelastic boundary element [8] is introduced. An artificial boundary is set on the side along the roadbed bottom. The two boundary planes perpendicular to the line direction constrain the displacement of the road direction along the line.

2.3 Subgrade Constitutive Model of Roadbed

The constitutive model of soil body dynamics consists of: bilinear model, equivalent linear model, Iwan model, Maltin-Finn-seed model, and endochronic model, etc. [9]. There are elastic and plastic deformations of roadbed filling under the periodic effect of load [10]. The data is from test in situ, and dynamic analysis shows that the elastic deformation of subgrade top ranges from 1–4 mm and the dynamic dependent variable level of soil body of roadbed reach 10^{-4}. Under this level, there is no damage to the connection of ordinary qualified compacted filling, and soil skeleton is able to recover, and there is little energy dissipation in the movement of soil particles. The soil is in the best status of lag elastics. Due to the damping effect of roadbed in the roadbed-soil physical model, the viscoelastic constitutive model is introduced which consists of spring and dashpot when deformation accumulated from long-term dynamic load is not considered and plastic deformation behavior of soil body is overlooked. Therefore, the viscoelastic model is proposed to simulate dynamic characteristics of soil body by applying a constant damping ratio.

2.4   Structure and Material Parameters

In the process of computation, steel track, reinforced concrete track slab, CA mortar, and concrete bearing layer are viewed as an isotropic linear elastic material, fastening of the track as spring-damping structure, grading gravel, subgrade fillings, and foundation as a viscoelastic material. How long and how deep the roadbed model is calculated affects the quantity and accuracy of the computation. The length increases as load frequency add. The accuracy of the model depends on the length to be calculated. Zhai [11] pointed out that when the excitation points of first and last wheelsets are no less than 30 m away from the head and end of the track, the model is viewed as infinitely long. Chen [12] held the view that the vibration caused by a certain pulse turbulence source may affect the distance spanning 10 sleepers. If the distance exceeds, the vibration transmission gets very weak. Luo [7] reckon after computation that three-sleeper length would be proper for the finite model when selecting the length of the finite model. At this length, the stress, strain, and deformation are small. Therefore, in this paper, the selected model is 26 m long. As for depth, according to national data, the dynamic stress decays 40–60% when 0.6 m deep from the roadbed top. Japanese studies show that dynamic stress should be 10% of its gravity stress when 3 m deep from the roadbed, and there is little influence on the roadbed deformation by dynamic responses at such depth. Hence, the selected model is 9.7 m deep from the roadbed top.

For studying the common ballastless track type of high-speed train in our country, the paper proposed the finite models of the slab and double-slab track subgrade. As the major object of study, the roadbed is focused without considering

Table 1 Material numerable parameters and structure size of model

Structure	Thickness (mm)	Elastic modulus (GPa)	Poisson's ratio	Density (kg/m^3)	Damping ratio
Steel track	176	210	0.3	7830	
Fastening		40 MN/m			
Slab track	200	35	0.167	2500	
Double-slab track	260	35	0.167	2500	
Slab track CA mortar	30	4.5	0.2		
Bearing layer of slab track	300	27	0.2	2400	
Bearing layer of double-slab track bearing layer	300	27	0.2	2400	
Roadbed top	0.4	0.24	0.27	2250	0.028
Roadbed bottom	2.3	0.15	0.32	2130	0.035
Roadbed body	2.0	0.10	0.35	2000	0.035
Foundation	4	0.06	0.35	2000	0.045
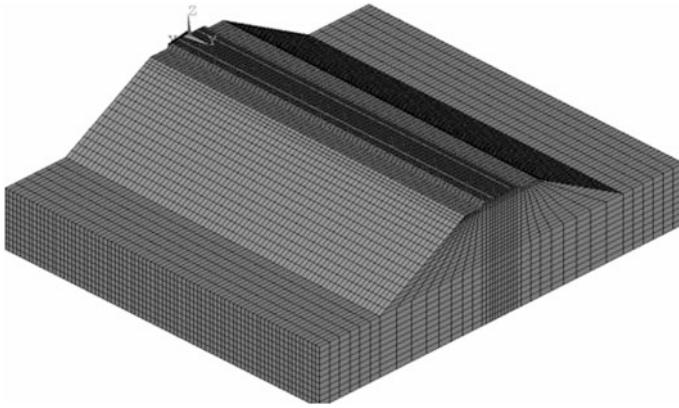
Fig. 2 Finite element model of the track/subgrade system

the details of track structure, such as reinforcement, rail seaming is disregarded. Computation of parameters and structure size are shown in Fig. 1 (Table 1).

The finite model of ballastless track subgrade is hereby established based on the above steps as shown in Fig. 2.

3 Train Loads Input on the Finite Model

The subgrade of high-speed rail track mainly undertakes the static load from the track and dynamic load from the train. It is paramount for studying dynamic responses of subgrade to quantify the load of a train and its distribution and transmission regularity. The train load imposed on the track correlates with vehicle speed, suspension system, rim diameter and condition, center of gravity of vehicle, evenness of the line, stiffness of track frame (type of steel track, elastic fastening and stiffness of rubber mat, track sleeper or stiffness of overall track plate), stiffness and uniformity of track subgrade [13].

In fact, the train is composed of a series of carriages of the same length. The wheel load distributes periodically along the line [14]. Hence, it is assumed that the train is infinitely long, and wheel loads are assumed as the combination of every single load. Each wheelset load is periodically a moving load with the periodicity as wheel load distance L. See Fig. 3.

Presume that the moving velocity of wheel load ① is v, this wheel load at time t locates at $Z_1 = $ vt, so the function of this wheel load can be presented as:

$$P_1(t, \quad Z) = P_0\delta(Z - \text{vt}) + F(t)\delta(Z - \text{vt}) \tag{1}$$

In the above equation, vt$-L/2 < Z <$vt$+ L/2$, P_0 is static load; $F(t)$ is the attached load caused by vertical vibration of the vehicle; and $\delta(Z-$vt$)$ is the function of (Z, t).
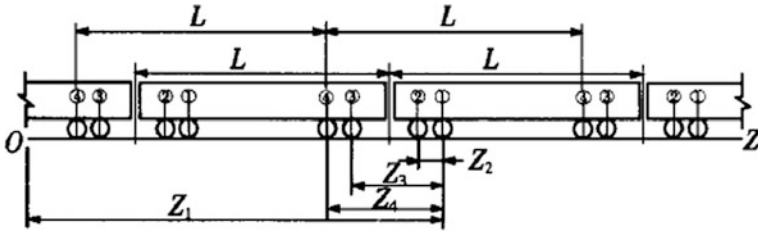
Fig. 3 Separate and combination of the vehicle model

(a) vehicle disperse model for a 4-wheel set of single carriage

(b) vehicle disperse model for a 4-wheel set of bogie

(c) vehicle disperse model for 2 carriages

(d) disperse model of 4 carriages
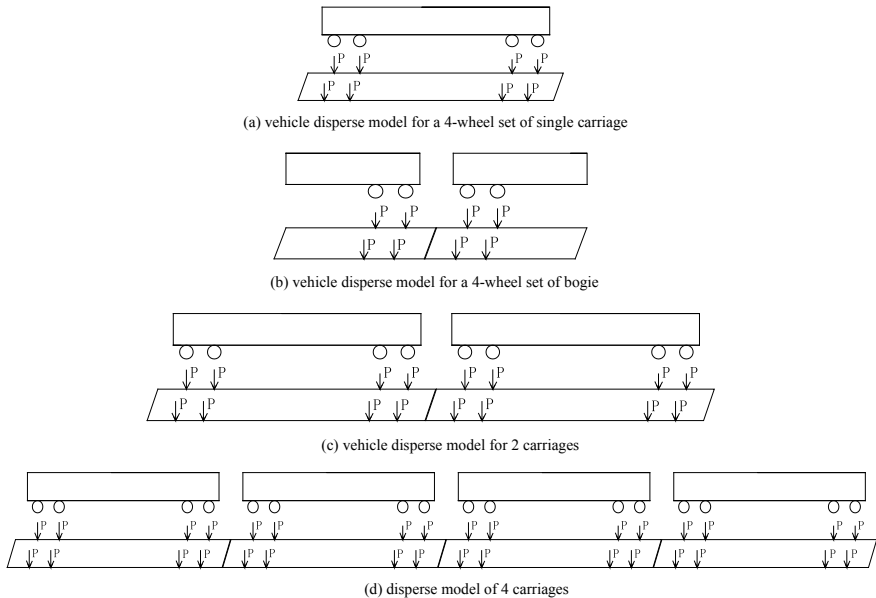
Fig. 4 Disperse model of vehicle

Whether the dynamic load properly inputs on the train will affect the rationality of numeric simulation. The proper train load can guarantee the correctness of computation of numerical simulation and cut down on computation cost. Since the train load is periodic, the train load of a finite model is a 2 wheelsets of single bogie [15] model, 4 wheelsets of single carriage [2, 6], or 4 wheelsets of 2 bogies model [16]. In this paper, disperse model of 2 carriages and 4 carriages are introduced. See Fig. 4.

Based on the above four models, the single wheel load is assumed to be a constant force with constant speed without considering the evenness of track, eccentricity of wheels, and wheel flats. On the condition of wheel axle load of 170 kN and speed of 350 km/h, the stress and displacement of roadbed surface top and bottom layer right down the steel tracks are, respectively, calculated through the proposed finite model. The result is shown in Figs. 5, 6, 7, and 8.

From Figs. 5, 6, 7, and 8, it is known that the effect of first 2 wheelsets on the subgrade looks the same at the initial stage of loading when the train is moving, so the stress and displacement of roadbed surface in four types of dispersion models almost coincide. In the 2 wheelsets dispersion model and wheelsets model, there exists the periodicity of subgrade surface stress. Except for the first carriage, the displacement of following carriages repeats. The displacement or stress amplitude of single carriage dispersion model is lower than those of the bogies model. The displacement or stress amplitude of 2 carriages model is the same as those of 4 carriages model. The displacement amplitude of subgrade surface of a single carriage and bogies model is lower than that of 4 carriages model, only 70.3% of 4 carriages model and displacement amplitude of bogies model is only 86% of 4 carriages model because there exist superimposed effect of displacement and stress. The distance of 4 wheel loads of a single carriage is longer, so the superimposition effect is comparatively weaker, whereas the 4-wheel load distance of bogies is shorter, so the superimposition effect is stronger compared to the single carriage model [17].

Fig. 5 Surface displacement of subgrade surface layer
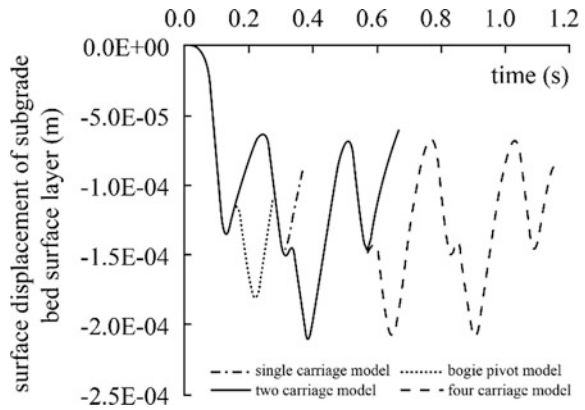
Fig. 6 Surface displacement of subgrade surface layer
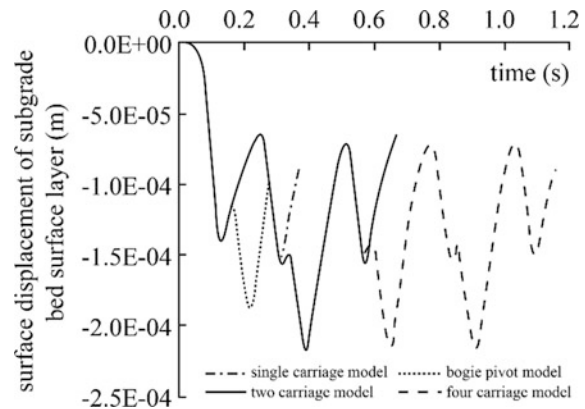
Fig. 7 Surface stress of subgrade surface layer
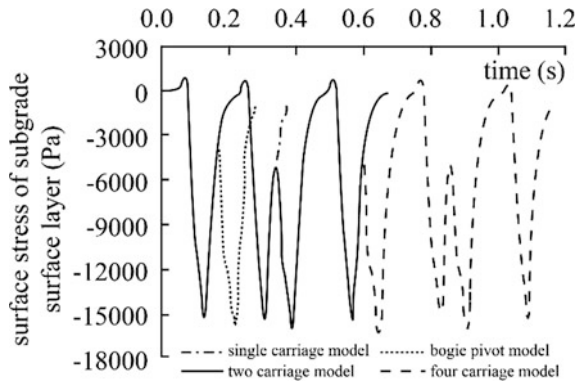
Fig. 8 Surface stress of subgrade surface layer
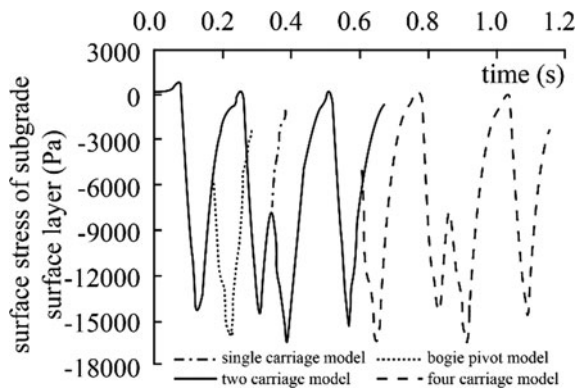
Based on the above analysis, 2-carriage disperse model can better simulate the displacement and dynamic stress process when the train passes. At the same time, the computational result is most accurate. 2-carriage dispersion model shows more advantages as it takes into account the superimposition effect of wheel loads and saves more in the aspect of cost than 4-carriage or whole train loading model. As a result, 2-carriage with 8-wheelset dispersion model is adopted.

The train load is imposed through the track and track fastening, and so it is necessary to deduce the actual contact pressure time-history curves of fastening [18]. Because there is little data pertinent to the contact pressure of ballastless track fastening at present, the contact pressure of fastening is calculated which then applied to the fastening points on the track slab. In this way, it can simulate the effect of the train on the ballastless track subgrade.

In the case of CRH3/CRH380 train with speed of 350 km/h and CRTSII ballastless track, the train axle weighs 170 kN. It is assumed that the wheel load is distributed evenly, and wheel load $P = 85$ kN. For the object of study is a subgrade structure, the variation of train load caused by factors like uneven track, eccentricity of wheel, wheel flat is not accounted for. The wheel load is simplified as a constant
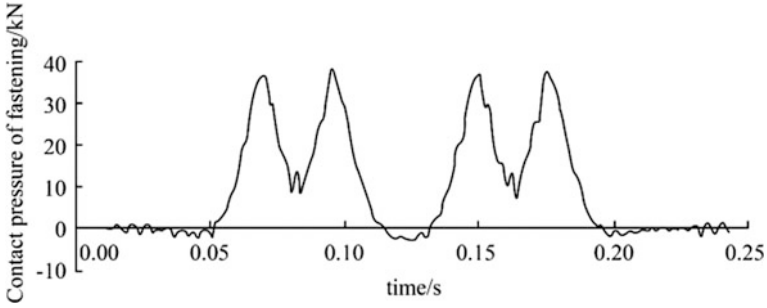
Fig. 9 Contact pressure time-history curves of a single fastening
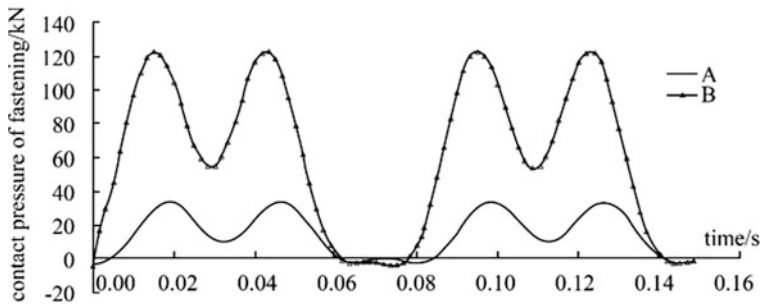
Fig. 10 Time-history curves of fastening through Fourier transform

force with constant speed, and excitation input on the finite model is from 8 wheelset of adjoining bogies of neighboring carriages. In view of the superimposed effect concentrating on wheelsets of adjoining bogies of neighboring carriages, the superimposed effect of bogies of the same carriage is relatively small [17], here deduced the contact pressure time-history curves curve of single fastening when adjoining bogies of carriages passes. See Fig. 9.

From Fig. 9 it is known that there exist abrupt peak and an acute angle in the contact pressure time-history curves of fastening. Then curve is converted through Fourier transformation. Assume time is t, contact pressure of fastening is $F(t)$, so here deduced the equation of contact pressure of fastening:

$$F(t) = a_0 + a_1 \cos(\omega t) + b_1 \sin(\omega t) + a_2 \cos(\omega t) + b_2 \sin(\omega t) \\ + a_3 \cos(\omega t) + b_3 \sin(\omega t) \tag{2}$$

Then, $a_0 = 14.34$, $a_1 = -11.22$, $b_1 = 7.334$, $a_2 = -3.497$, $b_2 = 8.372$, $a_3 = -1.827$, $b_3 = -8.089$, and $\omega = 78.79$.

Curve A in Fig. 10 is the result of time-history of fastening through Fourier transformation.

4   Verification of Ballastless Track Subgrade

The effectiveness of the model is tested by the data measured in situ of ballastless track subgrade of Wuhan–Guanzhou passenger line as in references [19]. The tested cross section located at DK1254 + 635, train axle weight is 14 t, and train speed is 290 km/h. All the parameters of roadbed needed in the computation are presented in table (Table 2).

Figure 11 is the attenuation curve of the dynamic stress of ballastless track roadbed, and Fig. 12 is the attenuation ratio curves.

From Figs. 11 and 12, it can be inferred that the biggest difference between dynamic stress of subgrade deduced by the model and measured in situ is 5 kPa, but the attenuation of dynamic stress decays consistently with depths. From Fig. 12, it is observed that the attenuation rate of dynamic stress decays as depth extends lower than that of measured in situ, and there is a 15% difference in attenuation rate but the attenuation regularity of model conforms with that tested in situ.

Table 2 Calculate parameters of actual roadbed

Parameters	Elastic modulus (GPa)	Poisson's ratio	Density (kg/m^3)	Damping ratio
Roadbed top	1.55	0.27	2200	0.028
Roadbed bottom	0.71	0.33	2000	0.040
Embankment	0.52	0.36	1800	0.045
Foundation	0.60	0.35	2000	0.045

Fig. 11 Decay curve of dynamic stresses in the roadbed
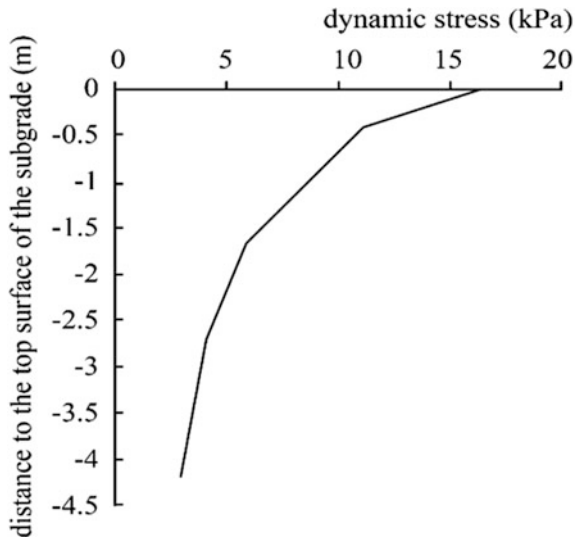
Fig. 12 Decay rate curve of dynamic stresses in the roadbed
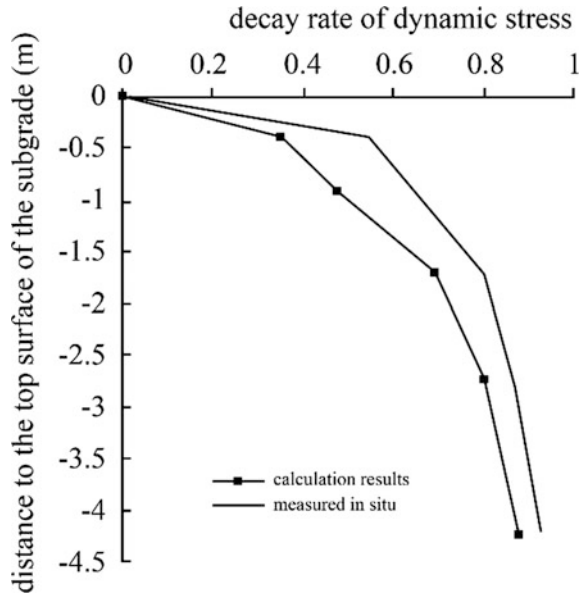
In order to further test the viability of the model, the parameters quoted in references for calculation is shown in Table 3. In the case of CRH2 high-speed train with a speed of 160 km/h and axle weight of 14 t, 2 wheelset load of single bogie is introduced. The calculated dynamic stress of roadbed top is in Fig. 13.

The tested results show that the vertical dynamic stress of roadbed top ranges from 8.4 to 14.5 kPa. The dynamic stress deduced by the model is 13.3 kPa. From Figs. 13 and 14, it is inferred that the vertical dynamic stress time-history curve agrees with that quoted in reference and develops consistently with time.

Based on the above analysis, the established infinite model for ballastless track subgrade can better reflect dynamic behavior; it is reliable to analyze the dynamic response of ballastless track subgrade.

Table 3 Calculate parameters of model verification

Structure	Thickness (m)	Elastic modulus (GPa)	Poisson's ratio	Density (kg/m^3)
Steel track	0.176	200	0.3	7800
Track slab	0.19	35	0.167	2500
CA mortar	0.05	0.2	0.167	2500
Pedestal	0.3	27	0.167	2500
Roadbed top	0.4	0.18	0.25	2000
Roadbed bottom	1.5	0.11	0.25	1800
Embankment	1.5	0.06	0.25	1700

Fig. 13 Calculate result in the paper
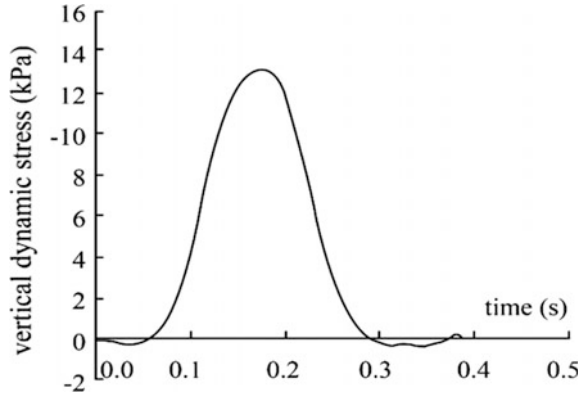
Fig. 14 Testing result in references [15]
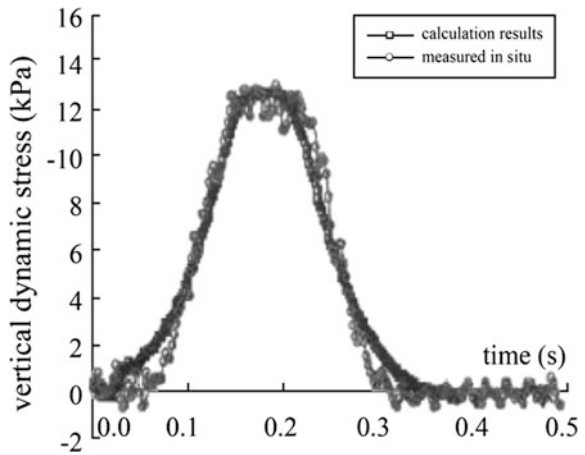
5 Simulation Result Analysis

To better obtain the response rule of subgrade under trainload, the train speed is set at 300 km/h at and axle weight is 170 kN. The load is imposed on 8 wheelsets of carriages adjoining bogies. In this case, the dynamic responses for the ballastless track subgrade are hereby calculated.

5.1   The Distribution and Attenuation Regularity of Vertical Dynamic Stress

The dynamic stress for subgrade is obtained through numerical computation. The subgrade time-history curve of CRTSII-type slab ballastless track is depicted in Fig. 15, and the double-block ballastless track is in Fig. 16.

It is seen from these two figs that there is a hump in the time-history curves of dynamic stress under the effect of trainload. A dynamic stress hump is generated when bogies pass the roadbed. There is an obvious superimposed effect between bogies of adjoining carriages. The effect tends to be stronger when more bogies come in. Due to the damping, the dynamic stress diminishes with depths, and peak
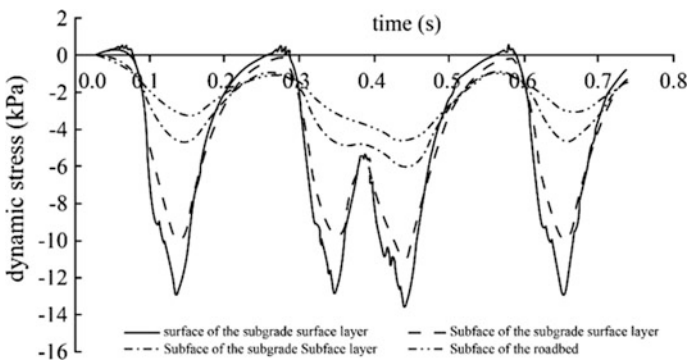
Fig. 15 Vertical dynamic stresses time-history curves in subgrade of CRTSII-type slab ballastless track
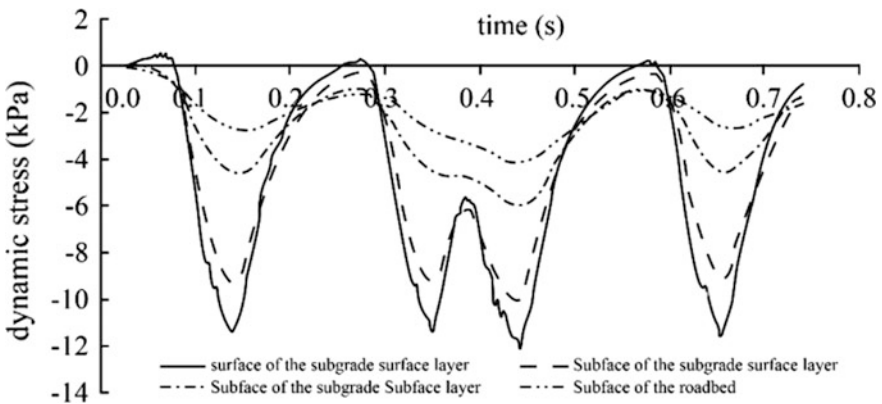
Fig. 16 Vertical dynamic stresses time-history curves in subgrade of double-block ballastless track

value lags. The time-history curve of subgrade of CRTSII-type slab ballastless track looks similar to that of the double-block track.

Figure 17 depicts the distribution regularity of vertical dynamic stress amplitude with depths in the subgrade. Figure 18 depicts the attenuation regularity of vertical dynamic stress decays with depths in the subgrade.

From Figs. 17 and 18, it is known that dynamic stress amplitude of bearing layer in the subgrade is bigger than that of subgrade center and subgrade under steel track due to the concentration of superimposed effect, but when 1.5 m deep from the subgrade surface the dynamic stress amplitude tends to be consistent. The amplitude diminishes as depth increases and diminishes faster in roadbed top. The dynamic stress amplitude 1 m deep from the subgrade of bearing layer edge decreases up to 1/2 of that from roadbed top, and when 1 m deep from roadbed center and track, it decreases 1/3 of that from the roadbed top. The dynamic stress

Fig. 17 Relationship between vertical dynamic stresses amplitude and depth
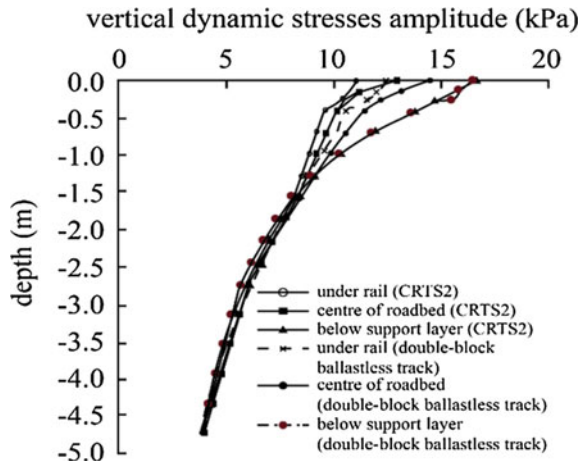
Fig. 18 Decay ratio of vertical dynamic stresses amplitude with depth
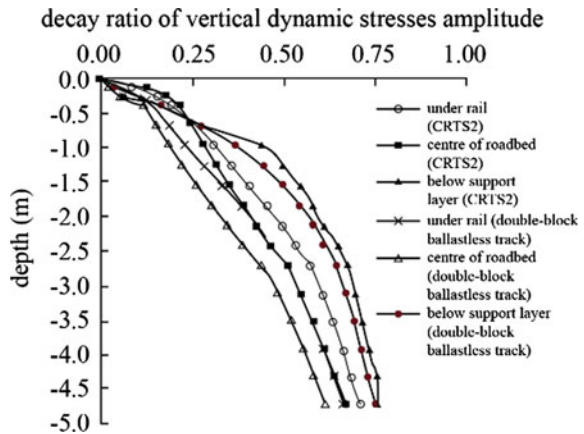
amplitude under the bearing layer edge decreases faster than that under the track. The closer to the roadbed center it is, the slower the dynamic stress amplitude decreases. In addition, within 1.5 m deep from the roadbed, the dynamic stress amplitude of single-type CRTSII ballastless track subgrade is bigger than that of double-block ballastless track subgrade, but it tends to be consistent over 1.5 m deep. The dynamic stress amplitude for single-type CRTSII ballastless track subgrade decays slower than that for double-block subgrade.

Figure 19 depicts the dynamic stress distribution on cross section of roadbed top, bottom, and bottom base.

From Fig. 19, it is observed that the dynamic stress amplitude becomes bigger when it is far away from the roadbed center. It changes greatly under concrete bearing layer and reaches its peak, which is caused by the concentrated superimposed effect of the stress of concrete edge. The dynamic stress decreases quickly beyond the concrete bearing layer and approaches 0. The dynamic stress amplitude under roadbed bottom grows bigger when close to the roadbed center and reaches its maximum under the concrete bearing layer edge. Beyond the edge, the amplitude follows a linear decline trend. The dynamic stress decays to 0 when far away from the roadbed center, which illustrates that the concentrated superimposed effect of stress on roadbed top spread to roadbed bottom, but not as stronger as on the roadbed top. The dynamic stress amplitude on the roadbed bottom follows a linear decline trend when far away from the roadbed center. The stress still exists in the area far away from the roadbed bottom and declines linearly. There exists the stress at the place far away from the bearing layer due to the spread of roadbed stress. The stress spread within a certain range. The distribution regularity of vertical dynamic stress for double-block ballastless track subgrade conforms to that for single CRTSII type.
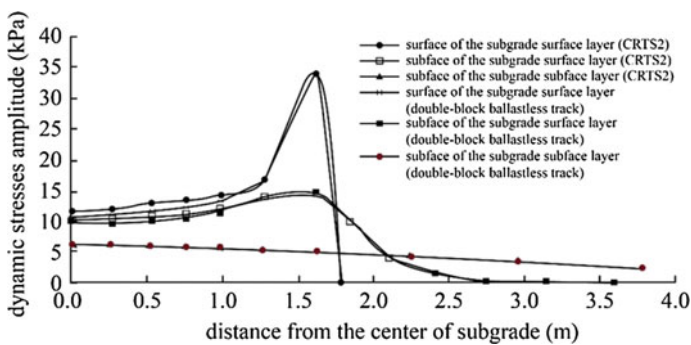
Fig. 19 Vertical dynamic stresses amplitude of subgrade cross section

5.2 The Vertical Displacement Distribution and Attenuation Regularity

The vertical displacement of the subgrade is deduced through computation. Figure 20 depicts the vertical dynamic displacement time-history curves in subgrade of CRTSII-type slab ballastless track and Fig. 21 depicts that of the double-block ballastless track.

Figures 20 and 21 reflect that when bogies of adjoining carriages pass the roadbed, the displacement is obviously bigger than that of a single bogie. There appears a double hump on roadbed top and bottom, but it is not clear on the roadbed bottom. The dynamic stress declines as depth increases due to the damping. The peak phenomenon comes later. The vertical dynamic displacement time-history curves in subgrade of double-block ballastless track resemble that of CRTSII-type.

Figure 22 depicts the relationship between vertical dynamic displacement amplitudes, and Fig. 23 depicts the relationship of the attenuation ratio of vertical dynamic displacement amplitude with depth.

From figures, it is observed that there are three positions under ballastless track subgrade which decreases as depth increases, and attenuation declines as depth increases. Dynamic displacement of different positions decays congruously. Within 3 m deep from the roadbed top, the vertical dynamic displacement amplitude decays 1/2 of that on the roadbed top. The dynamic displacement amplitude for CRTSII-type ballastless track subgrade is bigger than that for the double-block type. Right under the track and at the center of subgrade, the attenuation ratio of dynamic displacement for CRTSII-type ballastless track subgrade is bigger than that of the double-block type, and displacement amplitude under the bearing layer for both types decays congruously (Figure 24).

It is inferred that the dynamic displacement of the subgrade is bigger when closer to the center of the track. The farther to the subgrade center, the smaller dynamic displacement is when the roadbed top and bottom for CRTSII type lies within the
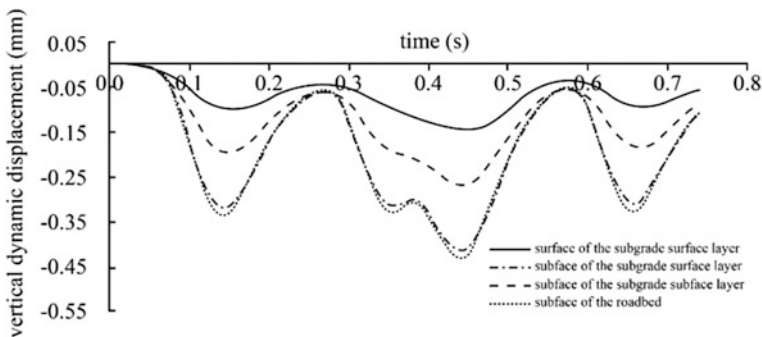
Fig. 20 Vertical dynamic displacement time-history curves in subgrade of CRTSII-type slab ballastless track
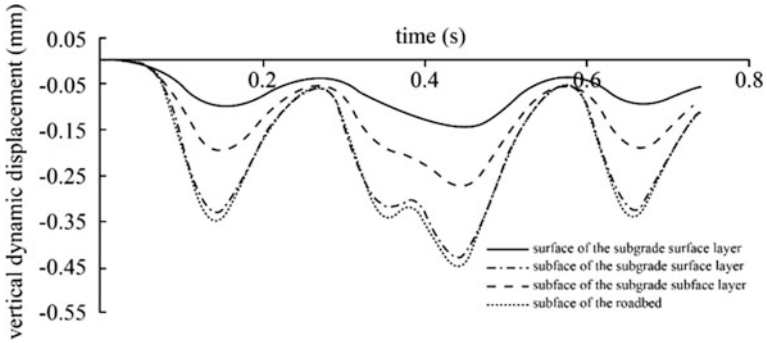
Fig. 21 Vertical dynamic displacement time-history curves in subgrade of double-block ballastless track

Fig. 22 Relationship between vertical dynamic displacement amplitude and depth
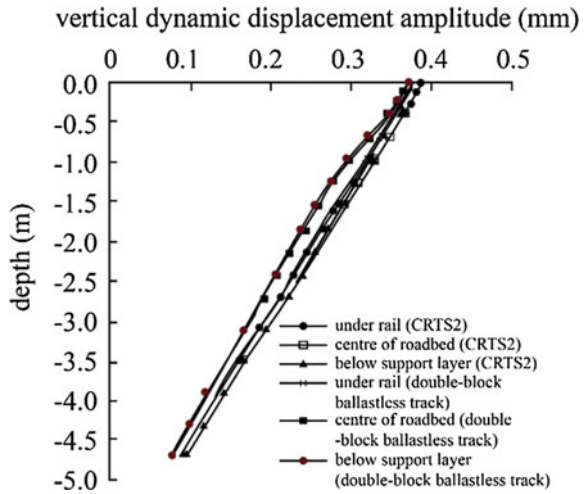
bearing layer, the smaller it is. Whereas, there is a little variation to the dynamic displacement when the roadbed top and bottom for double-block type lies within the bearing layer, which accounts for the stiffness of double-block being stronger than the single slab type. When it is far beyond the bearing layer, the displacement is smaller. The displacement under the track of both types approaches each other. The displacement is 0.22 m at the center of subgrade bottom base and is 0 at 3.8 m away from it. It is illustrated that the effect of passing train on the dynamic displacement of the subgrade is within a limited range along the track vertically and is more obvious in the subgrade under the track.
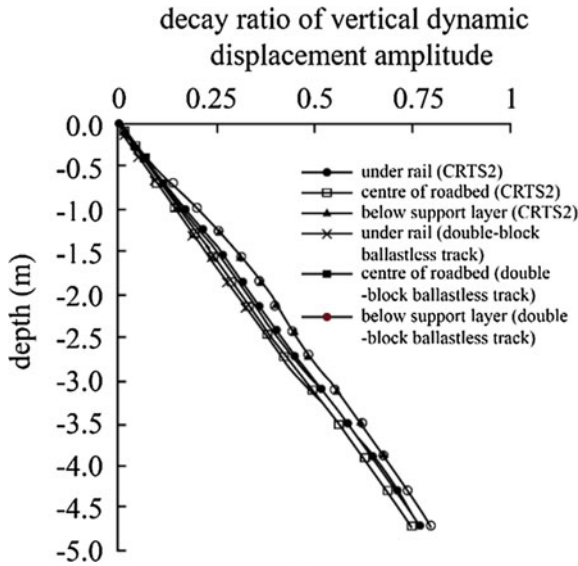
Fig. 23 Decay ratio of vertical dynamic displacement amplitude with depth
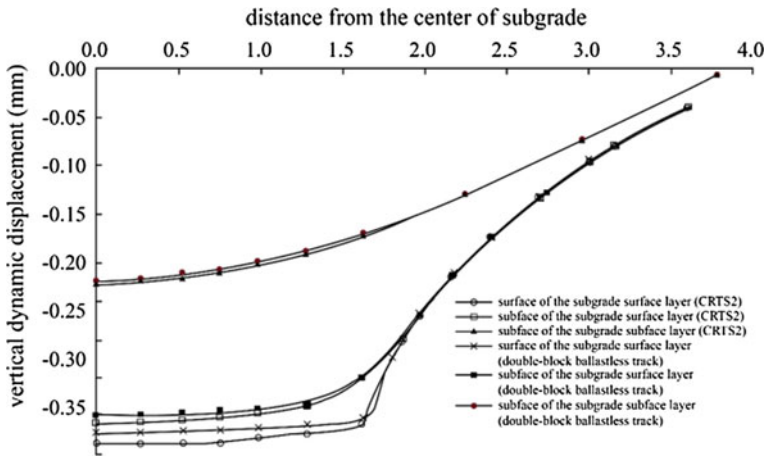
Fig. 24 Vertical dynamic displacement amplitude of subgrade cross section

5.3 The Distribution and Attenuation Rule of Acceleration

The acceleration is calculated through computation and the time-history curve of roadbed top under CRST II type ballastless track is depicted in Fig. 25.
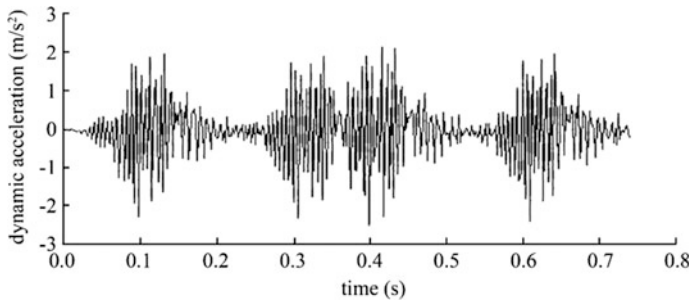
Fig. 25 Dynamic acceleration time-history curves of subgrade surface layer

Fig. 26 Relationship between vertical dynamic acceleration amplitude and depth
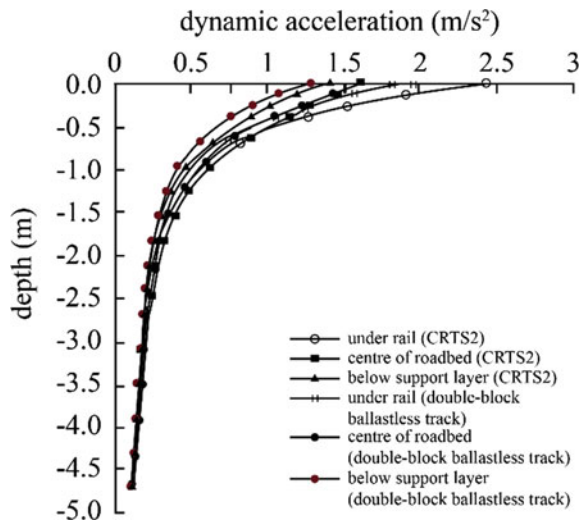
From Fig. 25, it is seen that there is a clear periodicity of dynamic acceleration time-history curve in subgrade when the train passes. Tested from the cross section of train wheels, the peak of dynamic acceleration time-history curve looks like a mutation.

Figure 26 shows the distribution rule of vertical dynamic acceleration in different positions of subgrade along the depth. Figure 27 shows the distribution of vertical dynamic acceleration amplitude of cross section in the subgrade.

From both figures, it is seen that within 1 m deep from the subgrade top, the acceleration in the subgrade under the track is bigger than that in the subgrade at the center of the roadbed and under bearing layer edge. The acceleration for CRTS II ballastless track subgrade is bigger than that for the double-block type. But 1 m deep from the subgrade top, the acceleration of different track structure and different position tends to be consistent. The acceleration decays mainly in the area around 1.5 m deep from the roadbed top, and it decays 90%. The acceleration distributes

Fig. 27 Vertical dynamic acceleration amplitude of subgrade cross section
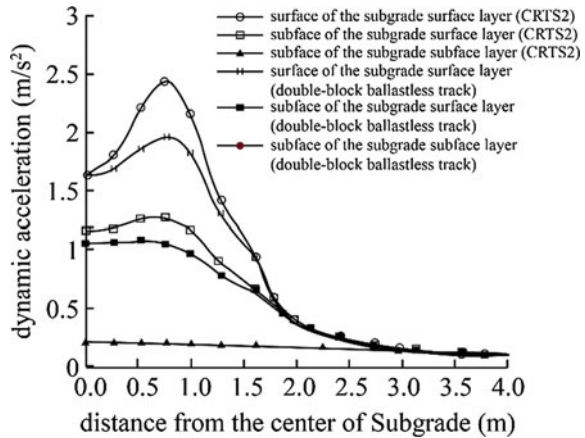
horizontally in subgrade similarly to the vertical dynamic stress. By comparison, the acceleration reaches a maximum in the cross section right down the track, but the dynamic stress reaches a maximum at the bearing layer edge. The vertical acceleration under concrete bearing layer is faster, beyond which it decays fast horizontally. This illustrates that the vibration in this area is not strong. The acceleration peak value of roadbed top for CRTS II type ballastless track subgrade appears clearer than that for the double-block type. It is accounted by the fact that the CA mortar in the CRTS II-type ballastless track subgrade gets involved in vibration, and its elastic modulus is low, which leads to the concentration of displacement vibration on the roadbed top.

6 Conclusions and Suggestions

Based on ANSYS, the paper proposed the 3-d finite model for CRTSII-type ballastless track subgrade and double-block type with APDL language. Here discussed the dynamic behavior distribution and attenuation rule under high-speed trainload. The main conclusions are summarized as follows:

1. Based on ANSYS, the numerical simulation model is established for the ballastless track subgrade of a high-speed train with APDL language. After been compared with the results calculated and quoted from references, the feasibility of the 3-d finite model for ballastless track subgrade is tested through the dynamic model and solutions verification.
2. The dynamic loading mode is key to analyzing the dynamic behavior of track subgrade, the dynamic stress, and dynamic displacement of four-type vehicle model calculated and compared, i.e., 4-wheel disperse model of a single carriage, 4-wheel disperse model of bogies, disperse model of two carriages, and disperse model of four carriages. The results show that the dispersion model of

two carriages can better simulate the dynamic displacement and dynamic appearance process when the train passes.

3. Here analyzed was dynamic stress, dynamic displacement, and acceleration distribution and attenuation as the depth increases in CRTS II ballastless track subgrade and double-block type. The results show that the acceleration decays fastest. The dynamic responses in the subgrade within the concrete bearing layer almost remain unchanged. The dynamic stress and dynamic displacement at the bearing layer edge response frequently and decay fast beyond the concrete bearing layer, which almost approaches 0. The dynamic responses in the area of 0-1.5 m deep from the track for CRTS II slab ballastless track subgrade are bigger than that for the double-block type. The dynamic responses of subgrade 1.5 deep from the roadbed top for the two types tend to be consistent, which shows that the effects of dynamic responses for a track on the subgrade lie on the top of the subgrade.

References

1. Liang B, Luo H, Sun C (2006) Simulated study on vibration load of high speed railway. J China Railw Soc 28(4):89–94 (in Chinese)
2. Nie ZH (2005) Study on vertical dynamic response of the track/subgrade in high-speed railway. Central South University, Changsha, (in Chinese)
3. Sun C, Hu J, Liang B (2010) Numerical simulation of dynamic response for quasi-high speed railway subgrade. 27(2): 173–176
4. Zhu BF (1998) Principle and application of finite element methods. China Water Power Press, Beijing (in Chinese)
5. Luo Z, Zhai W, Cai C (2005) Mechanical analysis of ballastless track-roadbed system. In: Railway passenger dedicated line construction technology exchange meeting proceedings, Wuhan, 96–99
6. Qing Q (2005) Study on dynamic characteristics of ballastless track-roadbed system with soft rock as embankment filling in high speed railway. Central South University, Changsha (in Chinese)
7. Luo Z (2008) Analysis of structure mechanics and wheel/rail dynamic interaction of ballastless track in high-speed railway. Southwest Jiaotong University, Chengdu (in Chinese)
8. Liu JB, Gu Y, Du YX (2006) Consistent viscous-spring artificial boundaries and viscous-spring boundary elements. Chin J Geotech Eng 28(9):1070–1075 (in Chinese)
9. Tong FM (2010) Dynamic response and long-term dynamic stability of closely spaced transition sections subgrade for high-speed railway. Central South University, Changsha (in Chinese)
10. Wang Q (1999) Civil engineering in high-speed railway. Southwest Jiaotong University Press, Chengdu (in Chinese)
11. Zhai WM (2002) Vehicle-track coupling dynamics. Science Press, Beijing (in Chinese)
12. Chen G (2001) Analysis of the random vibration responses characteristics of the vehicle-track coupling system. Southwest Jiaotong University, Chengdu (in Chinese)

13. Railway Construction (2005) 160, Provisional standard for acceptance of construction quality of subgrade engineering for passenger-special line. China Railway Publishing House, Beijing (in Chinese)
14. Li J, Li K (1995) Finite element analysis for dynamic response of roadbed of high-speed railway. J China Railw Soc 17(1):66–75 (in Chinese)
15. Dong L, Zhao C, Cai D et al (2008) Experimental validation of a numerical model for prediction of the dynamic response of ballastless subgrade of high-speed railways. China Civ Eng J 41(10):81–86 (in Chinese)
16. Xu J (2011) Research model test system of high speed railway subgrade and dynamics analysis. Central South University, Changsha (in Chinese)
17. Xu J, Zhang J, Huang Y (2010) The analysis of servo loading effect in high-speed railway. In: ICRE 2010 international conference on railway engineering, vol 8, 350–355
18. Wang QY (2013) Study on dynamic characteristics and parameters of ballastless track-roadbed system of high speed railway. Central South University, Changsha (in Chinese)
19. Zhou Z (2010) Roadbed integrating field investigation and numerical simulation of Wu-Guang passenger railways. Central South University, Changsha (in Chinese)

Dynamic Field Tests on the Base of a Large Cross-Section High-Speed Railway Tunnel

Fuchun Xue, Jianlin Ma and Liping Yan

Abstract The dynamic stability of a large cross-section tunnel base through water-rich loess under high-speed train loading is a challenging problem. Field cyclical dynamic tests were performed on an actual water-rich loess tunnel to answer this difficult question. The dynamic effects of a high-speed train were generated using a specially developed dynamic testing system. The loading test results showed that the tunnel structure was sensitive to loading frequencies higher than 13 Hz. Vertical dynamic displacement on the loading surface increased non-linearly with increase in the loading frequency. The vertical vibration velocity became larger at loading frequencies higher than 13 Hz. The maximum vibration velocity on the loading surface was smaller than the permitted value. The maximum velocity in the loess was less than its critical vibration velocity without any resonance occurring. The vertical dynamic stress was somewhat insensitive to loading frequency, and its attenuation with depth can be expressed by an exponential function. Based on these results, it can be concluded that the tunnel structure is safe and that the tunnel base is stable. The tunnel meets the operation requirements for high-speed trains.

Keywords Water-rich loess tunnel · Field dynamic test · Critical vibration velocity · Tunnel base stability · High-speed railway

F. Xue (✉)
Department of Geotechnical and Tunneling Engineering, School of Civil Engineering, Chongqing Jiaotong University, Chongqing 400074, China
e-mail: ocean2008xfc@163.com

J. Ma
Department of Geotechnical Engineering, Southwest Jiaotong University, Chengdu, Sichuan 610031, China

L. Yan
PSED Geology and Geotechnical Group, Los Angeles Department of Water and Power, 111 N. Hope Street, Los Angeles, CA 90012, USA

1   Introduction

The total length of the high-speed railway on the Zhengzhou to Xi'an Passenger Dedicated Line (ZXPDL) in China is 485 km. It is the first newly constructed passenger dedicated line with a design speed of 350 km·h^{-1} in China in a loess area; in fact, it is the first high-speed railway in the world in a loess area. There are 38 tunnels on the ZXPDL with a total length of 77 km. The loess areas are widely distributed along the railway. Cumulatively, approximately 50 km of tunnels is located in the loess strata, many of which are collapsible or water-rich loess with poor engineering properties. Because there are great differences in engineering properties between collapsible loess and water-rich loess, different measures are taken to improve the properties of the different loesses. This paper concerns only water-rich loess.

In this study, field dynamic tests were conducted in the Zhangmao Tunnel of the ZXPDL. It was excavated using the short-staged seven-step excavation method [1]. During construction, the structure of the loess at a certain depth below the excavated surface was softened by seepage water and then destroyed by stress release and the repeated rolling of construction machines. Serious seepage occurred over a large area of the excavated surface, which immersed the operation face in groundwater. The continuous vibration and rolling of the construction machines deteriorated the construction conditions. The loess was severely softened, as shown in Figs. 1 and 2 taken by the corresponding author during excavation of the tunnel.

The following measures were taken to prevent the loess from being further softened and to ensure the safe construction of the tunnel.

(a) The excavation surface was sealed by spraying it with 4 cm thick concrete within 30 min of excavation.
(b) The seepage water that collected at low areas in the tunnel was promptly drained.

Fig. 1 Destroyed water-rich loess

Fig. 2 Immersed sidewall and softened loess
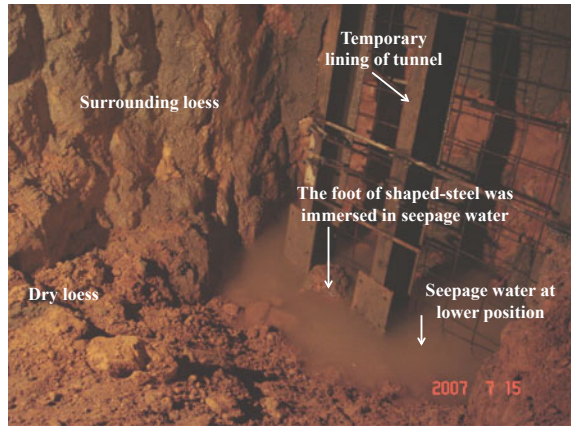
(c) The areas near the tunnel center line and sidewalls were sealed by spraying them with 20 cm thick concrete to prevent the tunnel base water-rich loess from being softened.

(d) A rapid-strengthening agent was added to the sprayed concrete to ensure the concrete was in a state of hard plasticity or even solidity within 30 min, meeting the requirements for subsequent construction of the tunnel.

Although the effectiveness of these measures had been validated in the field [1], a determination was needed as to whether the tunnel base would be stable under high-speed train dynamic loading during operation. Field testing was an effective way to answer this difficult question. Much work has been done regarding field tests for railway line construction. As requested by German National Railways in 1995, ThyssenKrupp GfT Tiefbautechnik developed a mobile subgrade Dynamic Stability Field Test device. This device could be directly installed in situ to test the dynamic characteristics of earth structures before laying ballastless, or ballasted, tracks. In approximately 5 years following its development, this device was used in more than 15 dynamic field tests in Germany and the Netherlands [2]. Elsewhere, in situ vibration measurements had been performed within the framework of the CONVURT project at a site in Regent's Park on the Bakerloo Line of London Underground. The study involved 35 passages of a test train at a speed between 20 and 50 km/h. Vibration measurements were performed on the axle boxes of the test train, on the rails, on the tunnel invert and tunnel wall and in the free field [3]. In another study, a reduced scale experiment with three sleepers was used to study the dynamic behavior and the settlement of ballasted tracks for a high-speed railway [4].

Ling [5] studied the vibration characteristics and attenuation of the subgrade caused by passing trains in a seasonally frozen region of Daqing, China. Three field experiments were conducted during normal, freezing and thawing periods, respectively. In another study, numerical simulations of the in situ loading test for the structural response of segmental tunnel linings were performed [6]. A new testing method was introduced to examine the mechanical behavior of railroad

ballast subjected to repeated train passages on ballasted track [7]. Elsewhere, a new methodology was developed for an in situ full scale test on a type of tunnel and applied on an experimental section of the new Line 9 of the Barcelona metro system [8]. In the Netherlands, a numerical model was presented to predict the dynamic loads on ballast caused by trains passing a transition zone; field data obtained from an extensive field survey in two transition zones were used to validate the model [9]. In Spain, monitoring work was conducted for a set of six rectangular-shaped, closed-frame underpasses under traffic loading, and the data were obtained and analyzed during on-site measurements of culverts along a Spanish high-speed train line [10]. Most recently, an in situ dynamic test was conducted on a typical cross section of railway cutting in expansive soil on the Kunming–Nanning Passenger Dedicated Line in China; the test allowed the dynamic characteristics of a new type of railway subgrade to be studied [11].

Previous studies have been focused mainly on embankments and other structures. No tests have been conducted for tunnels, especially for large cross-section tunnels constructed in water-rich loess. The research described in this paper was conducted to address this void. The field study was conducted using cyclical dynamic tests that simulated high-speed train vibration effects. The tests were conducted on the base of a tunnel built through water-rich loess and were undertaken after completion of construction but prior to placement of the ballastless track slabs. This paper describes the dynamic field tests and the resulting data, analyses and conclusions.

2 Description of Testing Procedure

2.1 Testing Section

Zhangmao Tunnel is located in Sanmenxia City on the ZXPDL (Fig. 3). It has a total length of 8483 m. The 5293 m segment near the tunnel portal is within an andesite stratum interbedded with sandy shale and limestone. The 3190 m segment near the tunnel exit is within a quaternary clayey loess stratum below the groundwater table. The maximum buried depth is 100 m within Grade IV and Grade V surrounding soil. The head of the groundwater is 20 m higher than the tunnel crown, and the surrounding soil contains abundant pore water.

Zhangmao Tunnel is a single-tube double-line railway tunnel with a cross-section excavation area of 170 m^2 (Fig. 4). The tunnel must satisfy strict requirements for foundation stability. According to the Chinese Standard [12], the settlement for the tunnel base must be less than 15 mm after the placement of the ballastless tracks.

The key physical and mechanical properties of the water-rich loess obtained from the site exploration and laboratory tests are listed in Table 1, and the main lining parameters are summarized in Table 2.

Fig. 3 Location of Zhangmao Tunnel
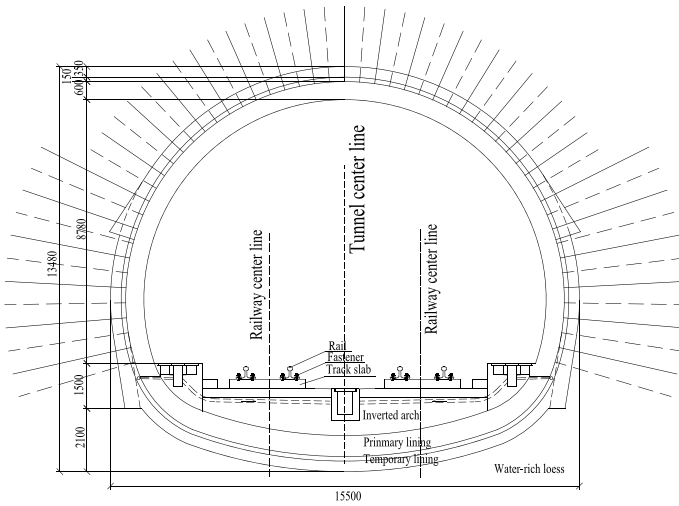
Fig. 4 Cross section of Zhangmao Tunnel (unit mm)

Table 1 Key physical and mechanical properties of the loess stratum

Natural density ρ (kg/m³)	Natural water content (%)	Void ratio e	Degree of saturation S_r (%)	Liquid limit I_L (%)	Plastic limit I_p (%)	Cohesion c (kPa)	Angle of internal friction ϕ (°)
2000.0	23.0	0.67	95.0	37.0	22.0	60.0	21.0

Table 2 Main mechanical properties of the tunnel structures

Name	Temporary lining (rigid-frame shotcrete support)	Primary lining	Inverted arch
Thickness (cm)	30	60	Maximum = 120
Elastic modulus (GPa)	Sprayed concrete: 25 Anchor bolt: 206 I-type steel: 206	30	28
Poisson's ratio	0.1 (averaged)	0.15	0.15
Density (kg/m^3)	2400 (averaged)	2400	2350

2.2 Loading System

To conduct the dynamic tests, a dynamic testing system (DTS-1, Fig. 5a) was specially developed at Southwest Jiaotong University. As shown in Fig. 5, this system is placed on a loading area and mainly consists of a vibration machine, weight combinations, a driving motor, a vibration frame and two trolleys.

The main part of the vibration machine consists of two eccentric blocks, which are installed symmetrically as highlighted in red in Fig. 5b, c. A right-hand Cartesian rectangular coordinate system is defined. In the coordinate system, the X-axis, Y-axis and Z-axis coincide with the horizontal, vertical and longitudinal directions, respectively. The rotation of the eccentric blocks is driven by the driving motor through the shaft connecting the motor and the vibration machine. The rotation of the eccentric blocks generates the horizontal (X direction) and vertical (Y direction) force outputs. The symmetric installation of the two eccentric blocks ensures that the horizontal force outputs have the same value but act in opposite directions so that the equilibrium in the horizontal direction is automatically satisfied. Therefore, the force outputs have only a vertical component, which is the vertical exciting load needed.

This system has a wide frequency range and provides a large exciting force. It has eight different combinations of the eccentric block patterns corresponding to different frequency ranges. Under the same excitation frequency, different eccentric block combinations result in various exciting force outputs that have the high amplitude changes needed to meet the loading requirements for the structures to be tested. According to the actual needs, different combinations of eccentric blocks can be allocated in the field tests [13].

Based on our earlier feasibility analysis, a sinusoidal wave was chosen as the input function of the pressure for the dynamic system. The magnitude of the sinusoidal wave was set to 30 kPa, and the frequency ranged from 5 to 27 Hz [14]. The vibration machine was placed on the tunnel base of the left railway track, as shown in Fig. 6. The loading area was square with a side length of 2.22 m.

The transducers used in the tests included seven earth pressure cells, eight vertical vibration sensors, four pore water pressure sensors and two strain sensors. The layout of the transducers is shown in Fig. 6.
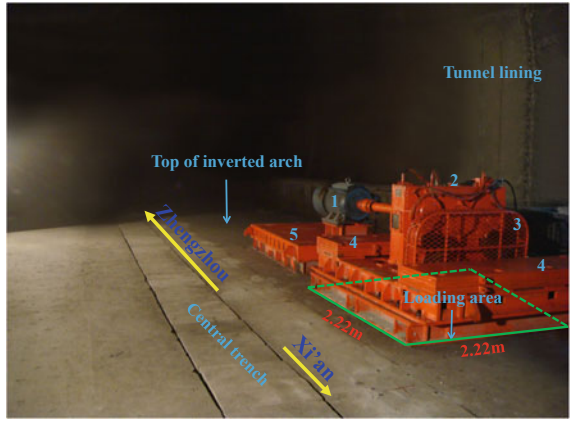
(a) The whole system.

(1-Driving motor; 2-Vibration frame; 3-Vibration machine; 4-Weight combinations; 5-Trolley)
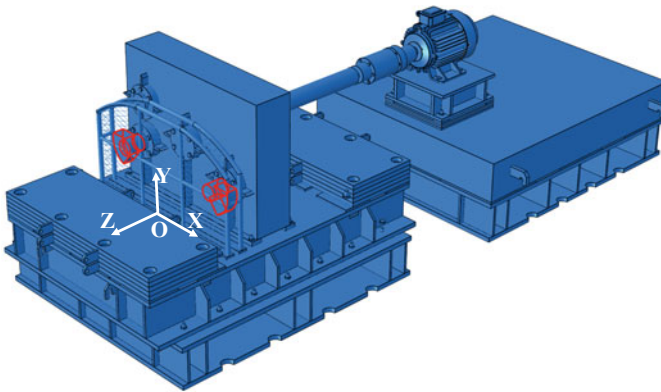
(b) The positions of the two eccentric blocks (highlighted in red) in the whole system.
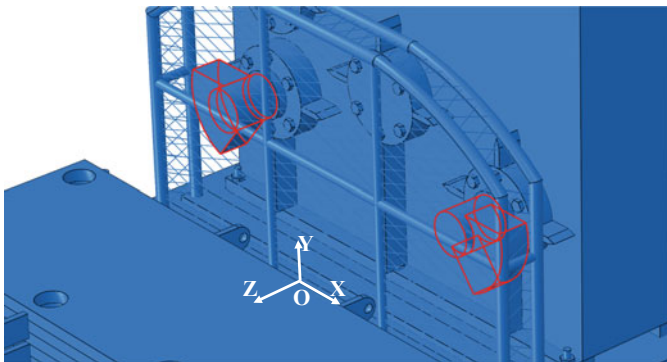
(c) The details of the two eccentric blocks (highlighted in red).

Fig. 5 DTS-1 dynamic testing system
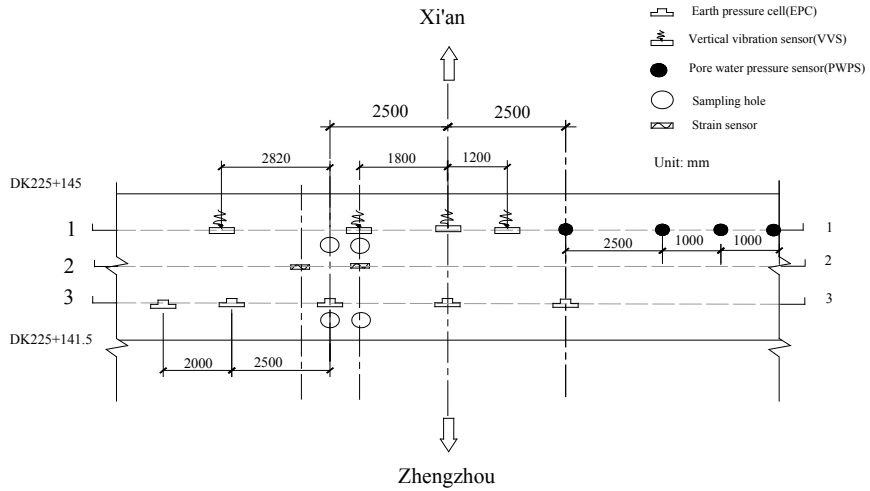
(a) Plan view.
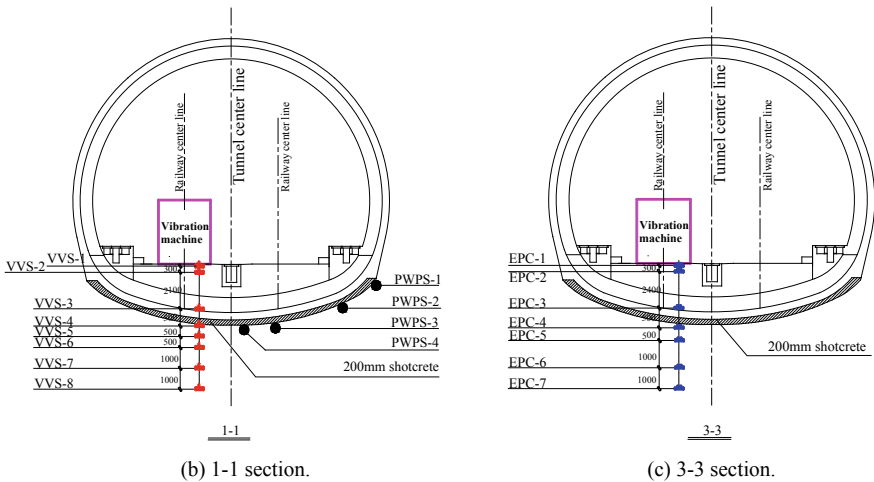
(b) 1-1 section.

(c) 3-3 section.

Fig. 6 Layout of the transducers (unit mm)

2.3 Loading Schemes

The testing started on August 11, 2008, and lasted for 8 days. Based on our previous study, the dynamic test included two stages. The first stage was a frequency sweeping test. The test frequency varied from 5 to 27 Hz gradually. Special frequencies could be determined and selected from the field data when the tunnel base exhibited noticeable responses to such frequencies. The second stage was a dynamic fatigue test. The high-speed train dynamic loading was modeled, and the operation of

Table 3 Loading time (minutes) for different frequencies of tests conducted in August 2008

Date	Frequency (Hz)													
	5	7	9	10	11	13	15	17	19	20	21	23	25	27
11	5	–	–	17	–	–	5	–	–	–	–	–	–	–
12	35	20	20	10	20	257	20	–	–	–	–	–	–	–
13	10	–	–	15	515	129	–	–	–	–	–	–	–	–
14	5	–	–	15	–	386	–	–	–	–	–	–	–	–
15	15	10	10	5	10	30	15	5	5	250	5	5	5	3
16	15	–	–	15	–	–	15	–	–	275	–	–	–	–
17	12	10	10	12	–	10	13	10	10	60	–	–	–	–
18	5	–	–	5	–	–	5	–	–	65	–	–	–	–

a high-speed train was simulated for at least one maintenance period (approximately two million loading times) under the frequencies selected during the first stage. The dynamic characteristics of the tunnel-foundation system were examined at this stage. Thereafter, the dynamic responses of the tunnel base could be investigated using the test results. The description of the tests is described in Table 3. As shown, the tests were focused mainly on frequencies between 13 and 20 Hz.

3 Results and Analyses

3.1 Vertical Dynamic Displacement Responses

Vertical dynamic displacement versus loading frequency Three measurements of the vertical dynamic displacement on the loading surface were made during the loading period. The first measurement was conducted early in the dynamic test, when the frequencies were between 5 and 15 Hz. The second measurement was conducted when the loading frequencies varied from 5 to 21 Hz. The third measurement was made during the frequencies from 5 to 27 Hz. The evolution of the vertical dynamic displacement on the loading surface is plotted in Fig. 7.

It can be clearly seen in Fig. 7 that the measurements were consistent, and the evolution of the vertical dynamic displacement with frequency was nonlinear. The vertical dynamic displacement increased rapidly from 13 to 20 Hz, which indicates that the tunnel base was sensitive to these frequencies. The vertical displacement tended to stabilize with a maximum value of 0.45 mm at frequencies exceeding 21 Hz. These results indicate that the tunnel structure and the surrounding loess stratum were in a state of elastically small deformation.

Cumulative settlement versus loading number Prior to the dynamic loading test, four points on the loading surface (namely 9#, 10#, 11# and 12# in Fig. 8) were selected for measuring residual settlement during the testing period and after all
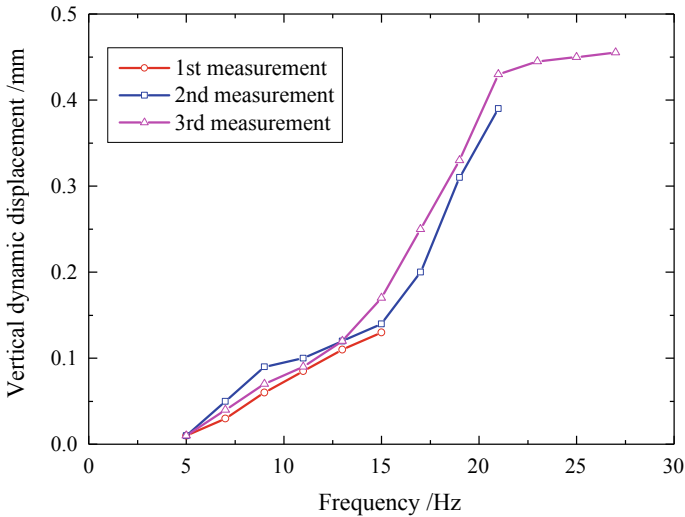
Fig. 7 Measured vertical dynamic displacement versus loading frequency

tests had been performed. The positions of the four points are shown in Fig. 8a. The residual settlements of the loading area were measured using high-precision equipment, as shown in Fig. 8b.

The development of cumulative settlement was nonlinear and can be divided into three stages. Cumulative settlement tended to be stable when the number of loading cycles exceeded 1.8 million. The permanent settlement on the loading surface was approximately 0.45 mm after 2.3 million loading cycle. The observed settlement was significantly less than the permitted 15 mm specified by the Chinese standard [12]. The loading of 2.3 million cycles in the tests is equivalent to 20 years of normal operation for high-speed railways under the assumption that 100 pairs of trains are put into commercial operation each day.

3.2 Vertical Vibration Velocity Responses

Vertical vibration velocity versus loading frequency The evolution of the vertical vibration velocity on the loading surface is shown in Fig. 9. As shown, this velocity increased nonlinearly in response to frequencies from 5 to 27 Hz. The vertical vibration velocity increased slowly as frequency increased to 13 Hz. At frequencies from 13 to 21 Hz, the velocity increased more rapidly and increased sharply (to a maximum of 1.6 mm/s) at frequencies exceeding 21 Hz. It can be inferred that the tunnel base was sensitive to loading frequencies above 13 Hz. The maximum vibration velocity was significantly less than the allowable safe velocity
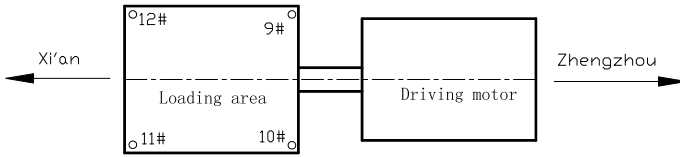
(a) Positions of the measurement points on the loading surface.
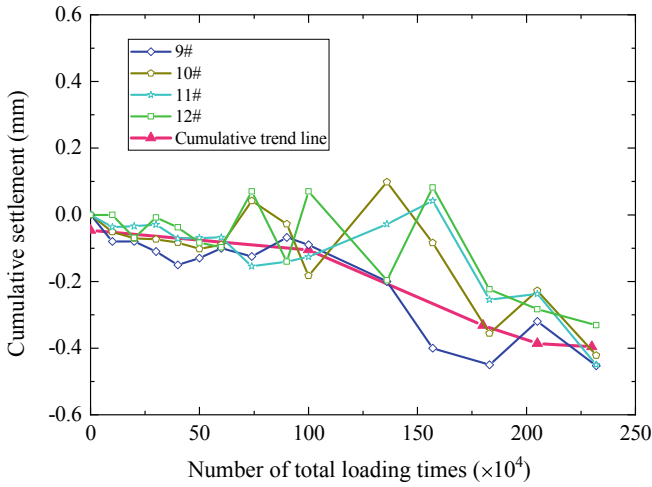
(b) Cumulative residual settlement on the loading surface vs. total number of loading times.

Fig. 8 Cumulative residual settlement of the loading surface
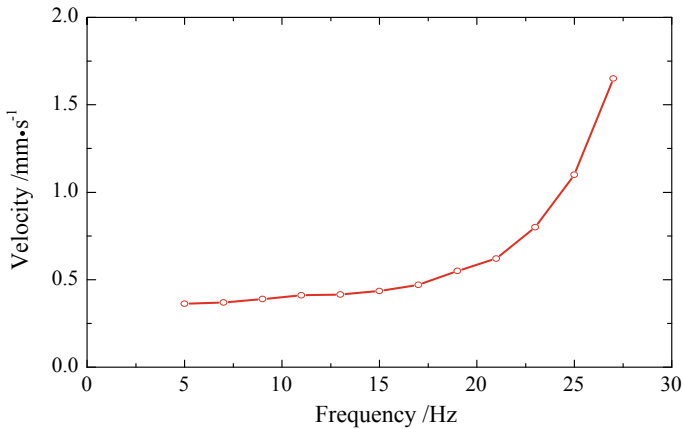
Fig. 9 Variation of the vertical vibration velocity with loading frequency

of 30–45 mm/s (for a predominant frequency <30 Hz) as specified in the Swiss Code [15], which applies to vibrations induced by traffic loading in underground structures. These results indicated that the tunnel met the requirements for vibration safety and operation for high-speed trains.

Variations in vertical vibration velocity with depth The evolution of the vertical vibration velocities at different frequencies as a function of depth is illustrated in Fig. 10. As shown, for the same depth, the vertical vibration velocity increased as frequency increased. The velocities at each depth increment increased noticeably at frequencies exceeding 13 Hz.

The evolution of the vertical vibration velocity with depth could be divided into three regions. The first region was from the loading surface to some depth in the tunnel lining, where the velocity decreased slowly. The second region was the zone on both sides of the interface between the tunnel lining and the loess below the inverted arch, where the velocity exhibited a sudden increase from the tunnel lining to the interface and a sharp decrease from the interface to the loess. The maximum velocity corresponding to the test frequency of 27 Hz was approximately 3.0 mm/s at the interface. The third region was in the loess at some depth below the inverted arch, where the velocity attenuated quickly and reached a value of 0.17 mm/s at 5.87 m below the loading surface. The sudden increase and decrease in the velocity near the interface can be analyzed using wave motion theory [14, 16].

The maximum velocities on the loading surface, at the interface and in the water-rich loess just below the inverted arch were 1.6 mm/s, 3.0 mm/s and 0.92 mm/s, respectively. Thus, the maximum velocity of the tunnel satisfied the
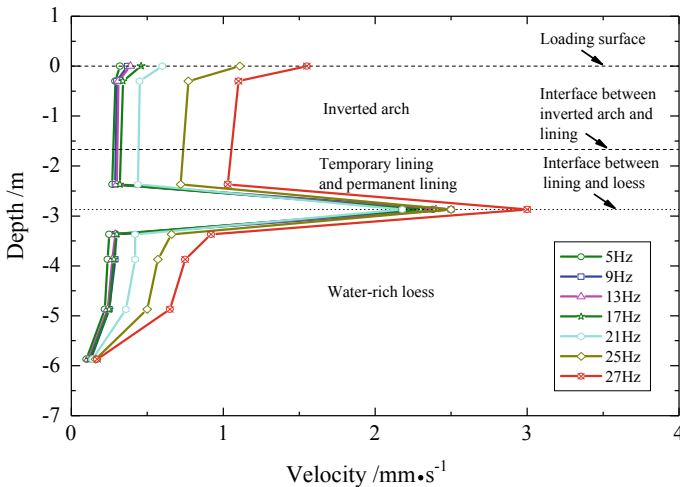
Fig. 10 Variations in vertical vibration velocity with depth at different frequencies

requirements for vibration safety described in the Swiss Code [15]. For the water-rich loess, the critical vibration velocity was calculated to be 1.45 mm/s based on the physical and mechanical properties [14]. In the tests, the loess below the inverted arch was in a state of triaxial compression. It can be inferred that its critical velocity was much greater than the theoretically calculated value. On this basis, it can be concluded that no resonance occurred in the loess; thus, the tunnel base was stable.

3.3 Vertical Dynamic Stress Responses

The vertical dynamic stress magnitudes at different frequencies as a function of depth, as well as the exponential curve and equation used to describe the stress data, are shown in Fig. 11. At a fixed depth, the vertical dynamic stress generated by the DTS-1 dynamic system fluctuated almost imperceptibly at loading frequencies from 5 to 27 Hz. It should be pointed out that the tunnel structure and the surrounding loess were in a state of elastically small deformation under all loading frequencies (see 3.1), so the strains in the tunnel structure and the surrounding loess were very small. Thus, the corresponding stresses were all of a relatively low magnitude and varied only slightly at different frequencies. Hence, it can be concluded that the vertical dynamic stress was relatively independent of loading frequency in the tunnel system.
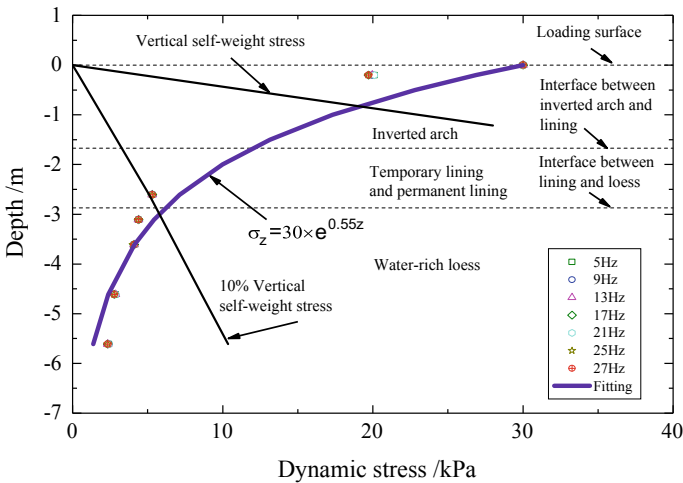
Fig. 11 Variations in the vertical dynamic stress with frequency at different depths

The attenuation of vertical dynamic stress can be expressed as Eq. (1):

$$\sigma_z = 30 \times e^{0.55z} \tag{1}$$

where σ_z is the vertical dynamic stress at z, and z is the depth below the loading surface, which should have a negative value.

It can be inferred that the maximum vertical dynamic stress immediately below the inverted arch was approximately equal to 10% of the vertical self-weight stress. Therefore, the settlement due to additional stress could be neglected according to the Chinese Standard [17].

3.4   Excess Pore Water Pressure Responses

Using the data measured by the four sensors, variations in the excess pore water pressure as a function of loading time at different frequencies were determined, as shown in Fig. 12.

The excess pore water pressure fluctuated slightly with frequency, which indicates that this pressure was somewhat insensitive to loading frequency and the number of loading cycles (Fig. 12). The excess pore water pressure exhibited alternatively positive and negative values with an absolute maximum of 0.1 kPa, which was too small for comparison to static pore water pressure at the corresponding locations (Fig. 13) [18]. Therefore, it can be inferred that the water-rich loess below the inverted arch would not be softened by the excess pore water pressure. Thus, the water pressure below the inverted arch could be treated as the static water pressure, and the excess pore water pressure could be ignored.

4   Discussion

In the tests, a sinusoidal wave having a magnitude of 30 kPa was chosen as the input for the DST-1 system. It should be noted that the sinusoidal wave pressure is different from the actual vertical dynamic stress caused by a high-speed train on the loading surface. For this reason, there are differences in the dynamic responses induced by these two types of loads.

The highest loading frequency in the tests was 27 Hz for a train speed of 350 km/h. If the speed of the train reaches or exceeds 400 km/h, the vibration frequency in the tunnel and surrounding loess may increase to 40 Hz or more. Such a high-frequency working condition was not considered in the tests due to current limitations. Future studies may investigate this situation.
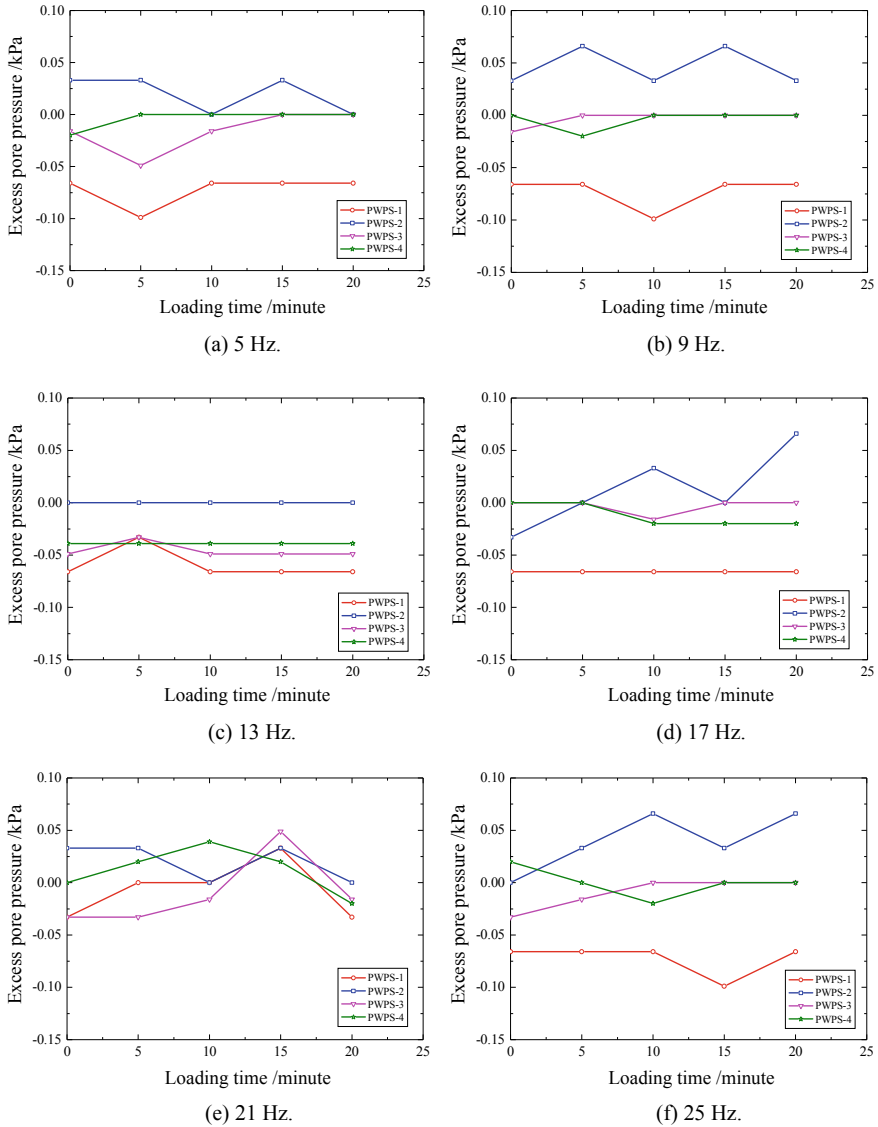
Fig. 12 Variations in excess pore water pressure with loading time for different frequencies

5 Conclusions

Measures of water-proofing and drainage were taken to ensure safety during the excavation and construction of the lining of the tunnel through a water-rich loess stratum. After completion of the tunnel construction and prior to the placement of
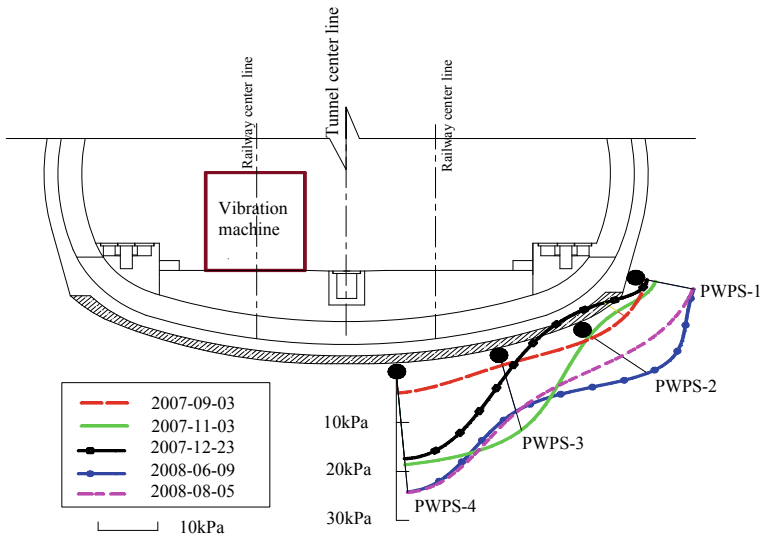
Fig. 13 Measured static pore water pressure at different time periods

the ballastless track slab, cyclical dynamic tests were performed to answer the challenging technical question of whether the tunnel base would be stable under high-speed train dynamic loading. Based on the test results, the following conclusions were drawn.

- The development of cumulative settlement on the loading surface exhibits three stages in response to the number of total loading cycles. The permanent settlement after the complete dynamic test is much less than the allowable value specified by the Chinese standard, thus validating the design of the tunnel constructed through the water-rich loess stratum.
- The vertical dynamic displacement on the loading surface evolves nonlinearly with loading frequencies and reaches a maximum value of 0.45 mm, meeting the requirement for safe operation of a high-speed train.
- The vertical vibration velocity on the loading surface increases nonlinearly with loading frequencies and has a maximum value of 1.6 mm/s, meeting the vibration requirement for the safe operation of a high-speed train.
- The vertical dynamic stress is relatively independent of loading frequency and decays with depth. Furthermore, the additional settlement due to the vertical dynamic stress is small enough that it can be neglected during tunnel design.
- The excess pore water pressure generated by the dynamic loading test is small enough that it cannot soften the water-rich loess below the inverted arch; thus, the tunnel base is stable.

The Zhengzhou to Xi'an Passenger Dedicated Line has been in commercial operation for more than 8 years (as of 2018). No problems in the water-rich loess

tunnel have been reported, which indicates that the Zhangmao Tunnel is operating safely as designed. Thus, the safe performance of the tunnel validates the conclusions drawn from the dynamic testing procedure.

References

1. Xue FC (2010) Study on dynamic characteristics of water-rich loess tunnel's foundation base. Ph.D. Thesis, Southwest Jiaotong University, Chengdu, China. (in Chinese with English abstract)
2. Neidhart TH (2001) True-to-scale in situ tests determining dynamic performance of earthworks under high speed train loading. In: Geotechnics for roads, rail tracks and earth structures, 213–223. A. Gomes Correia, Heinz Brandl, the Netherlands
3. Degrande G, Schevenels M, Chatterje P et al (2006) Vibrations due to a test train at variable speeds in a deep bored tunnel embedded in London clay. J Sound Vib 293(3–5):626–644
4. Shaer AA, Duhamel D, Sab K et al (2008) Experimental settlement and dynamic behavior of a portion of ballasted railway track under high speed trains. J Sound Vib 316(1–5):211–233
5. Ling XZ, Zhang F, Zhu ZY et al (2009) Field experiment of subgrade vibration induced by passing train in a seasonally frozen region of Daqing. Earthq Eng Eng Vib 8(1):149–157
6. Arnau O, Molins C (2011) Experimental and analytical study of the structural response of segmental tunnel linings based on an in situ loading test. Part 2: Numerical simulation. Tunnling Undergr Space Technol 26(6): 778–788
7. Ishikawa T, Sekine E, Miura S (2011) Cyclic deformation of granular material subjected to moving wheel-loads. Can Geotech J 48(5):691–703
8. Molins C, Arnau O (2011) Experimental and analytical study of the structural response of segmental tunnel linings based on an in situ loading test. Part 1: Test configuration and execution. Tunnling Undergr Space Technol 26(6): 764–777
9. José NV, Paul H, Manuel AGS (2011) Dynamic behaviour of railway tracks on transitions zones. Comput Struct 89(13):1468–1479
10. Vega J, Hermanns L, Alarcon E et al (2014) Measuring dynamic effects on underpasses of high-speed railway lines. Struct Infrastruct Eng 10(1):41–56
11. Wang LL, Yang GL, Fang YH et al (2014) In-situ test on the dynamic character of fully-closed cutting subgrade of high-speed railway in expansive soil area. Chin J Geotech Engineering 36(4):640–645 (in Chinese with English abstract)
12. Professional Standard of the People's Republic of China (2014) Code for design of high-speed railway (TB 10621-2014). China Railway Publishing House, Beijing
13. Xue FC, Ma JL, Yu Y et al (2009) Field forced excitation tests of water-rich loess tunnel subgrade for high-speed railway. In: 2th international conference on transportation engineering, The American Society of Civil Engineers, Chengdu, China, 3300–3310
14. Xue FC, Ma JL, Yan LP et al (2010) Vibration characteristics of tests for water-rich loess tunnel of a passenger dedicated line. J Vib Shock 29(2):202–207 (in Chinese with English abstract)
15. The Swiss Code (2013) Erschütterungen, Erschütterungseinwirkung auf Bauwerke. SN 640312 A-2013. (in German)

16. Liao ZP (2002) Introduction to wave motion theories in engineering, 2nd edn. Science Press Beijing. (in Chinese)
17. National Standard of the People's Republic of China (2012) Code for design of building foundations (GB 5007-2011). China Architecture and Building Press, Beijing
18. Xue FC, Ma JL, Yan LP et al (2010) Cyclic dynamic tests of water-rich loess tunnel subgrade for high-speed railway. J Vib Shock 29(9):226–230 (in Chinese with English abstract)

Interaction Between Tracks and Continuous Rigid-Frame Bridge Carrying High-Speed Railway

Bin Yan, Gaoxiang Zhang and Haoran Xie

Abstract For the study on interaction between continuous rigid-frame bridge and track under complex load, a simulation model for (72 + 128 + 72) m large-span continuous rigid-frame bridge and double-line ballastless track system was established. The interaction between large-span continuous rigid-frame bridge and track was revealed under the actions of thermal effects, live load, train braking, wind, uneven settlement, shrinkage and creep as well as earthquake. Influence of design parameters was also discussed, and these parameters included the temperature rise of beam and pier, vertical temperature disparity of bridge, loading position of live load, regional basic wind pressure, uneven settlement, installing track time, and spectral characteristics of seismic waves. The study shows the following: For the reason that expansion length of the continuous rigid-frame bridge and the pier rigidity are almost the same, envelope of rail stress is symmetrically distributed under the loads of thermal effects and gradient, bending, shrinkage and creep as well as earthquake, while the envelope of rail stress of braking and wind is inverse symmetry; the maximal stress caused by all kinds of loads related above is near the abutment; greater vertical displacement of the rail existed at the mid-span of the continuous rigid-frame bridge under the loads of temperature gradient and uneven settlement; for the action of shrinkage and creep as well as earthquake, there is huge shear force for the piers, which exceeds 40,000 kN.

B. Yan (✉) · G. Zhang · H. Xie
School of Civil Engineering, Central South University,
Changsha 410075, Hunan, China
e-mail: binyan@csu.edu.cn

G. Zhang
e-mail: zgx1748@163.com

H. Xie
e-mail: m15955099594@163.com

1   Introduction

In recent years, continuous rigid-frame bridge has been widely used in high-speed railway in China with unique structural characteristics such as high stiffness and sensitivity to deformation of the bridge substructure. Track–bridge interaction has been widely and deeply researched by scholars all over the world, and the bridge types researched include simply supported bridge [5, 11, 14], long-span continuous bridge [4, 12], continuous steel truss arch bridge [3], and cable-stayed bridge [2, 16]. However, there is not much study of interaction between double-line ballastless tracks and continuous rigid-frame bridge carrying high-speed railway. Interaction mechanism between continuous rigid-frame bridge and track system is still not clear under the actions of vertical temperature disparity of bridge, wind, shrinkage and creep as well as earthquake. The effects of design parameters on the system are still remained to be studied.

In this paper, nonlinear bar elements were adopted to simulate longitudinal resistance of the track, linear springs were established to simulate vertical stiffness, and the bridge was simulated by the beam element with rigid arms. Taking a (72 + 128 + 72) m long-span continuous rigid-frame bridge and double-line ballastless track system as a case, the nonlinear simulation model considering the foundation, pier, beam, and track as one system was established. The interaction between long-span continuous rigid-frame bridge and tracks was studied under the actions of thermal effects, temperature gradient, live load, train braking, wind, uneven settlement, shrinkage and creep as well as earthquake. Influence of the design parameters, including the temperature rise and gradient of beam and pier, temperature gradient of beam and pier, loading position of live load, regional basic wind pressure, uneven settlement, installing track time, and spectral characteristics of seismic waves, was also discussed.

2   Interaction Model for Continuous Rigid-Frame Bridge and Track System

Taking a (72 + 128 + 72) m long-span continuous rigid-frame bridge and double-line ballastless track system as a case, single-box sections were adopted for the bridge, the deck width was 12 m, and the mid-span height was 4.8 m, as shown in Fig. 1. Rectangle thin-walled pier was adopted for the bridge piers, the height of which is 96 m and 102 m, respectively.

The bridge was simulated by the beam element with rigid arms; the beam and pier were rigidly connected. The bridge piers were modeled according to the fact, and equivalent stiffness matrix with six degrees of freedom was established at the bottom of the pier to simulate the pier–soil interaction, as shown in Fig. 2.

The double-line ballastless track was installed on the bridge, the rail was of 60 kg/m (equal to UIC60 track), and rail expansion device was not set. Outside of
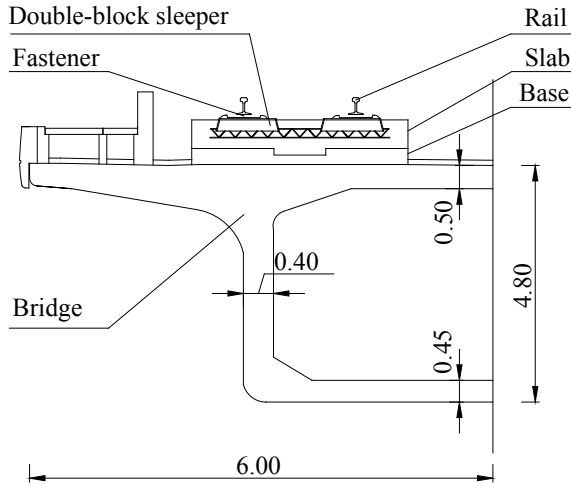
Fig. 1 Beam cross section (unit: m)
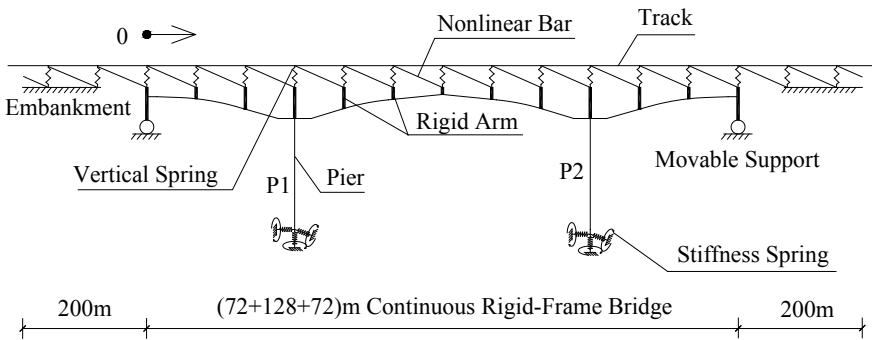
Fig. 2 Track–bridge interaction model

the abutments, the track of 200 m on each side of the embankment was established [13]. Linear spring was established to simulate vertical stiffness. Nonlinear bar elements were adopted to simulate longitudinal resistance of the track ($r(x)$) which was fastening resistance; the relationship between it and the displacement (x) between rail and bridge could be expressed as follows [10]:

$$r(x) = \begin{cases} 12.0x & |x| \leq 2.0 \text{ mm without vertical load} \\ 24.0 & |x| > 2.0 \text{ mm without vertical load} \\ 18.6x & |x| \leq 2.0 \text{ mm with vertical load} \\ 37.2 & |x| > 2.0 \text{ mm with vertical load} \end{cases}. \tag{1}$$

ZK live load (equal to 0.8UIC) was taken as the live load, the loading length was 300 m [8], and the braking force ratio was safely taken as 0.25.

As for the ballastless track on concrete bridge, the thermal force was calculated in accordance with the beam temperature rise and reduction of 30 °C. Continuous rigid-frame bridge was sensitive to deformation of the bridge substructure; therefore, the conditions such as pier temperature rise and reduction of 30 °C were also taken into account.

The vertical temperature disparity of the beam was suggested to take 5 °C in [8], and 5 °C was also taken as the temperature difference between the one side and another side of the pier in the paper.

Surface load was applied on longitudinal direction of the piers to analyze the influence of the wind on the rail longitudinal force; according to [9], wind pressure could be calculated as follows:

$$W = K_1 K_2 K_3 W_0 \tag{2}$$

In the equation, K_1, K_2, and K_3 are the coefficients of shape, height, and geomorphic feature, respectively, and values for them were 1.4, 1.52, and 1.0 successively. W_0 is the regional basic wind pressure, which is 0.35 kN/m^2 in Changsha.

To consider the influence of the shrinkage and creep on the rail longitudinal force, creep model provided in [9] was adopted. This creep model could consider some influential factors like size, ambient humidity, loading period, and concrete strength.

The bridge was in the region of Chinese Site type II, with characteristic period 0.35 s and earthquake fortification intensity 7. In order to study the force and deformation behavior of continuous rigid-frame bridge–track system under actions of different seismic waves, two seismic waves were adopted as the seismic excitation, namely "1940, El Centro Site" and "1952, Taft Lincoln School." Spectral characteristics of the two seismic waves remained unchanged; only the acceleration peak value of each wave was adjusted to 0.3 g [7].

3 Load and Parameter Analysis for Bridge–Track System

3.1 Thermal Effect

To study the interaction between tracks and continuous rigid-frame bridge carrying high-speed railway under the action of thermal effect, railway temperature force was calculated in accordance with the beam temperature rise and reduction of 30 °C [6]. The pier temperature rise and reduction of 30 °C were also taken into account at the same time. Four cases are listed in Table 1, and the calculation is shown in Fig. 3.

Table 1 Four cases for thermal effects

Case	Description
1	Beam temperature reduction of 30 °C
2	Beam and pier temperature reduction of 30 °C
3	Beam temperature rise of 30 °C
4	Beam and pier temperature rise of 30 °C
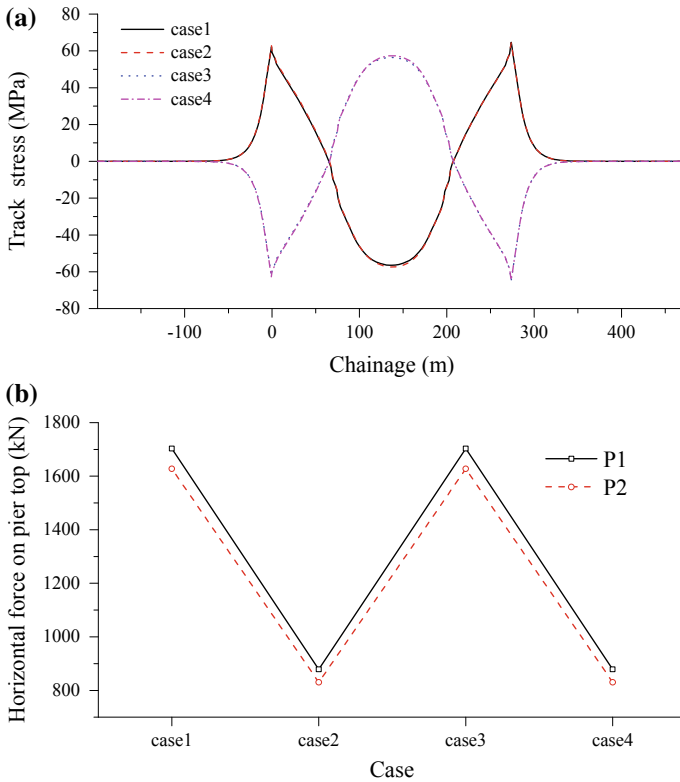
Fig. 3 System mechanical behavior due to thermal effect: **a** track stress; **b** horizontal force at the pier top

For this bridge, the track stress peak values were 64.7 MPa (tensile stress) and 62.2 MPa (compressive stress) occurring at both abutments; the maximum value of horizontal force at the pier top was 1703.1 kN. The influence of pier temperature rise on track stress was not obvious.

3.2 Temperature Gradient Effect

The vertical temperature disparity of beam was suggested to take 5 °C in [8]; this paper took 5–10 °C for its calculation, and that value was also taken for the longitudinal temperature disparity of piers. The cases are listed in Table 2.

The track stress and vertical displacement were calculated, as shown in Fig. 4 and Table 3.

Table 2 Four cases for temperature gradient effect

Case	Description
1	Beam vertical temperature disparity of 5 °C
2	Beam vertical temperature disparity of 10 °C
3	Beam vertical and pier longitudinal temperature disparity of 5 °C
4	Beam vertical and pier longitudinal temperature disparity of 10 °C
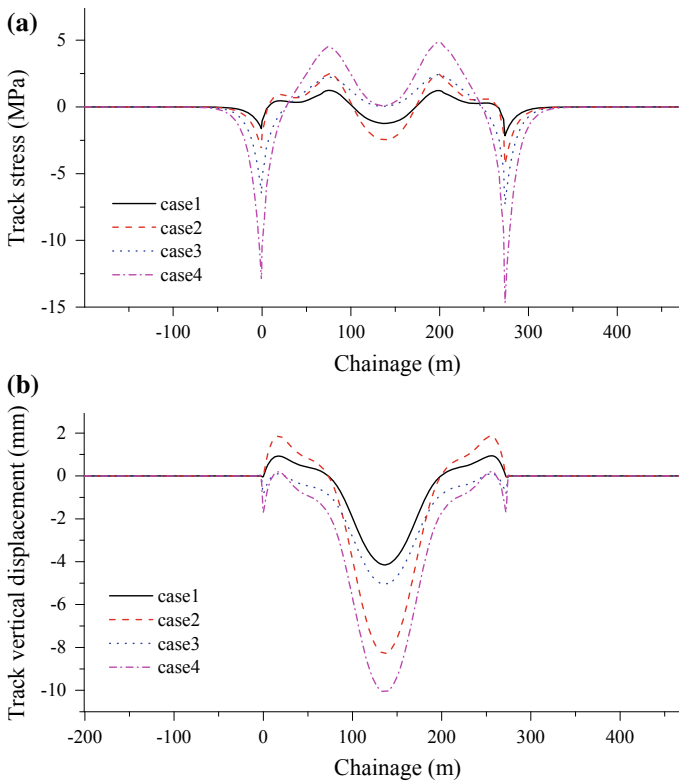
Fig. 4 System mechanical behavior due to temperature gradient effect: **a** track stress; **b** track vertical displacement

Table 3 Horizontal force and bending moment at pier top

Item	Case 1	Case 2	Case 3	Case 4
Horizontal force at pier top (kN)	312.4/296.0	624.7/591.9	312.4/296.0	624.7/591.9
Bending moment at pier top (kN·m)	iota	iota	3217.2/4169.7	6434.3/8339.3

Annotation: value before "/" represented $P1$ and that after "/" represented $P2$

When the vertical temperature disparity of beam was 5 °C, the track stress peak values were 2.5 MPa (tensile stress) and 3.0 MPa (compressive stress) occurring at the mid-span of the side span and two abutments. The maximum value of track vertical displacement was 8.3 mm at the mid-span.

The peak value of track tensile stress, track compressive stress, and track vertical displacement would increase 49%, 71%, and 1.8 mm, respectively; there was a temperature disparity of 10 °C at the beam vertical and pier longitudinal direction at the same time. Therefore, it is necessary to consider the influence of beam and pier temperature gradient on the force and deformation of continuous rigid-frame bridge–track system.

The difference of horizontal force at the pier top between $P1$ and $P2$ varied little for the reason that expansion length of the continuous rigid-frame bridge and the pier height were almost symmetrical. There was a little influence of beam vertical temperature disparity on bending moment at pier top whose peak values were 6434.3 kN m ($P1$) and 8339.3 kN m ($P2$) under the action of case 4.

3.3 Live Load Effect

To consider the influence of live load cases on bending force, four cases were set up, as shown in Fig. 5.

Force analysis of track–bridge system under actions of different cases is carried out, as shown in Fig. 6.

As shown in Fig. 6, the track stress peak values were 7.0 MPa (tensile stress) and 10.8 MPa (compressive stress) occurring at both abutments and mid-span. The maximum value of horizontal force at the pier top of $P1$ and $P2$ occurred under case 2 (1086.7 kN) and case 3 (1143.6 kN), respectively.

3.4 Train Braking Effect

In order to consider the influence of different train braking position on system, five cases were set up, as shown in Fig. 7.
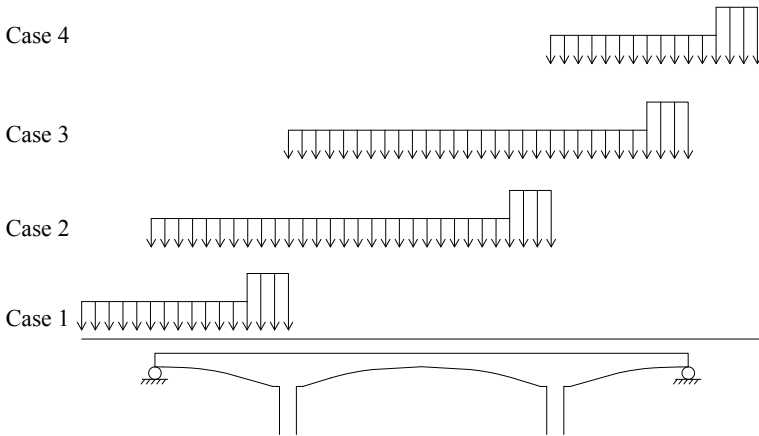
Fig. 5 Live load cases
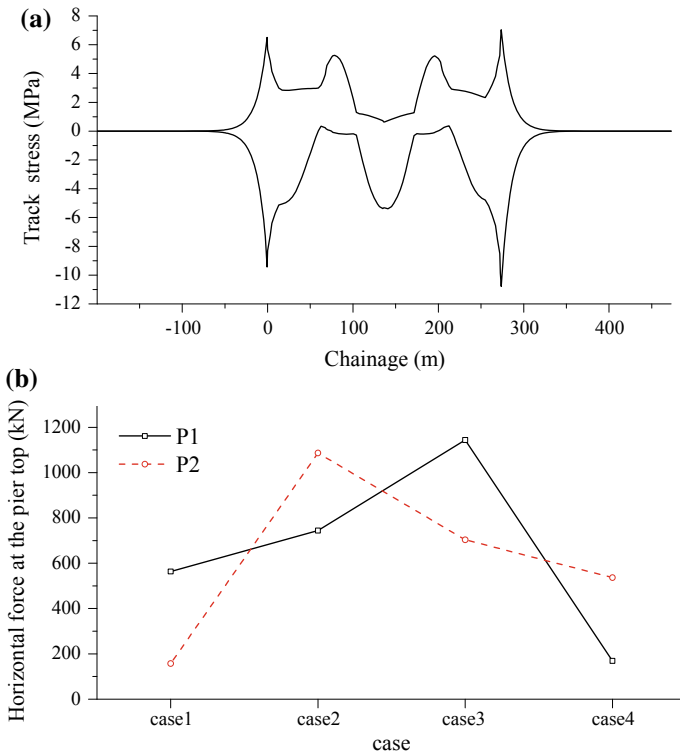
Fig. 6 System mechanical behavior due to live load: **a** track stress (envelope); **b** horizontal force at the pier top
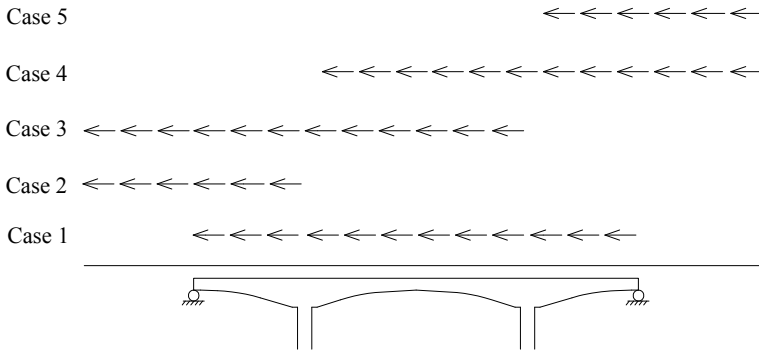
Fig. 7 Train braking cases

Track stress, horizontal force, and displacement at the pier top under actions of different cases are calculated, as shown in Fig. 8.

As shown in Fig. 8, the track stress peak values were 53.3 MPa (tensile stress) and 57.5 MPa (compressive stress) occurring at two abutments. The horizontal forces at the pier top of $P1$ and $P2$ were almost the same; the peak value of it was 555.8 kN (case 3). The maximum horizontal displacement at the pier top was 6.2 mm which exceeded the limit (5 mm) suggested in [1] but still met the requirement of "Fundamental code for design on railway bridge and culver" [9] of China.

3.5 Wind Pressure Effect

China is vast in territory; the wind velocity and terrain features are greatly different in terms of regions. In order to study the force of track and pier of continuous rigid-frame bridge under the action of wind pressure, 0.35 and 0.7 kN/m^2 were adopted as regional basic wind pressures to calculate system mechanical behavior due to wind pressure [15], as shown in Fig. 9.

The track stress peak values were 20.6 MPa (tensile stress) and 18.1 MPa (compressive stress) occurring at abutments. As for horizontal force at the pier top, it could increase from 343.5 to 687.0 kN as regional basic wind pressure increased from 0.35 to 0.7 kN/m^2.

3.6 Uneven Settlement Effect

To consider the influence of uneven settlement between two adjacent piers on mechanical behavior of continuous rigid-frame bridge–track system, 5 and 15 mm enforced displacements were applied at the bottom of pier $P1$[10], as shown in Fig. 10.
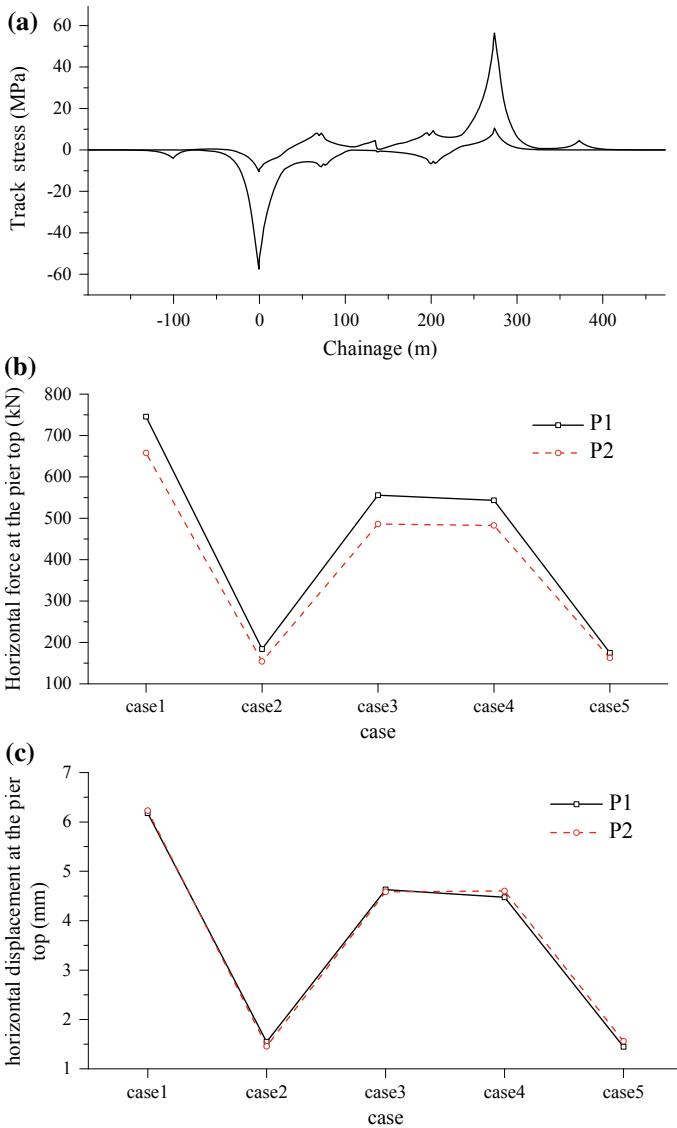
Fig. 8 System mechanical behavior due to train braking: **a** track stress (envelope); **b** horizontal force at the pier top; **c** horizontal displacement at the pier top

As shown in Fig. 10, the peak value of track tensile stress was 3.3 MPa still occurring at abutments; the maximum track compressive stress (about 3.1 MPa) and vertical displacement (15.0 mm) both occurred at the mid-span of the side span.
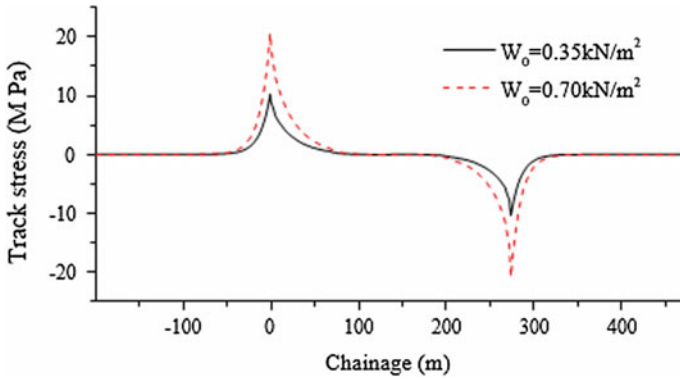
Fig. 9 Track stress due to wind pressure
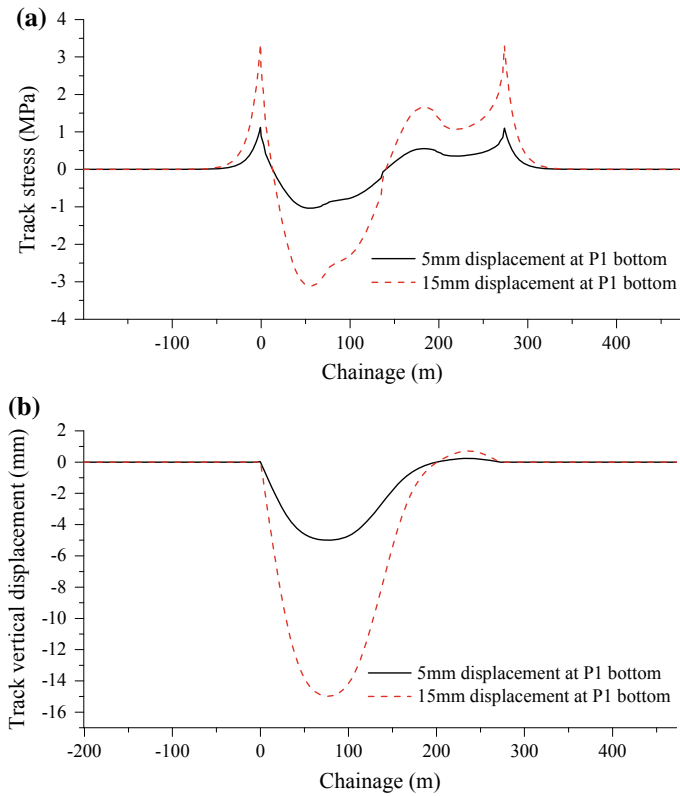
Fig. 10 System mechanical and deformation behavior due to uneven settlement: **a** track stress; **b** track vertical displacement

3.7 Concrete Shrinkage and Creep Effect

Concrete shrinkage and creep were frequently in early stages of development when the track was laid on the bridge. Concrete shrinkage and creep would make beam extending and deflecting, leading to the displacement between track and beam and then causing track longitudinal stress.

Assuming that track was installed on bridge after completed 60 days and ignoring long-term loading diffusion effect in track caused by track maintenance and train operation, the construction process of continuous rigid-frame bridge was completely simulated and the influence of deadweight and prestress on shrinkage and creep was considered. The track stress was calculated when the track was installed after the beam kept for 30, 60, 90, 180, 360, and 720 days, as shown in Table 4.

As shown in Fig. 11, the peak values of track stress were 191.0 MPa (tensile stress) and 90.2 MPa (compressive stress). The peak value of track stress caused by shrinkage and creep would decrease greatly with the increase in installing track time. The maximum tensile and compressive stress dropped 44% and 45.6%, respectively, with the installing track time increased from 30 days to 2 years. The influence of installing track time on final track stress generated by shrinkage and creep could greatly weaken when installing time exceeded 180 days. Installing track time did not influence much on horizontal force at the pier top.

3.8 Earthquake Effect

The track reinforced vertical resistance and played a role as hysteretic energy at the same time because of the nonlinear function between bridge and track, helping bring down seismic response of bridge. Two seismic waves were adopted as the seismic excitation, namely "1940, El Centro Site" and "1952, Taft Lincoln School" in the seismic analysis of railway bridge, and the acceleration peak value of each wave was adjusted to 0.3 g [7]; then, the forces of track and pier were calculated under uniform excitation, as shown in Fig. 12.

As shown in Fig. 12, the track stress (envelope) was distributed like "double diamond"; the track stress peak values were 239.5 MPa (tensile stress) and

Table 4 Six cases for shrinkage and creep effect

Case	Installing track time (days)
1	30
2	60
3	90
4	180
5	360
6	720

(a)

(b)
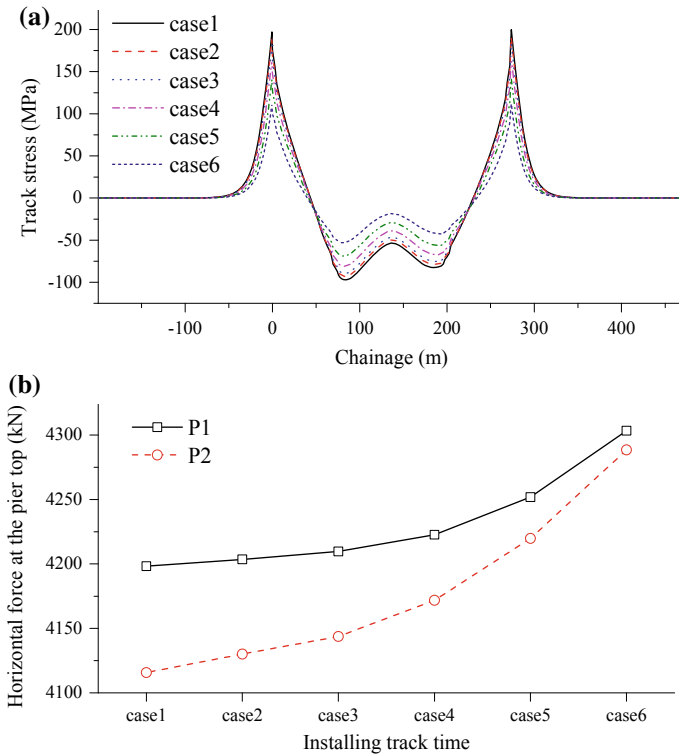
Fig. 11 System mechanical behavior due to shrinkage and creep: **a** track stress; **b** horizontal force at the pier top

233.0 MPa (compressive stress) occurring at two abutments. For the action of an earthquake, there was a huge longitudinal shear force for the piers (36,446.9–40,331.4 kN).

4 Conclusion

Taking a (72 + 128 + 72) m continuous rigid-frame bridge as a case, the nonlinear simulation model for long-span continuous rigid-frame bridge carrying high-speed railway and double-line ballastless track system was established. Load-carrying and deformation behaviors of tracks–continuous rigid-frame bridge carrying high-speed railway were studied under the action of thermal effect, live load, train braking, wind, uneven settlement, shrinkage and creep as well as earthquake. The main conclusions were as follows:

For the reasons that expansion length of the continuous rigid-frame bridge and the substructure was symmetric, envelope of rail stress was symmetrically
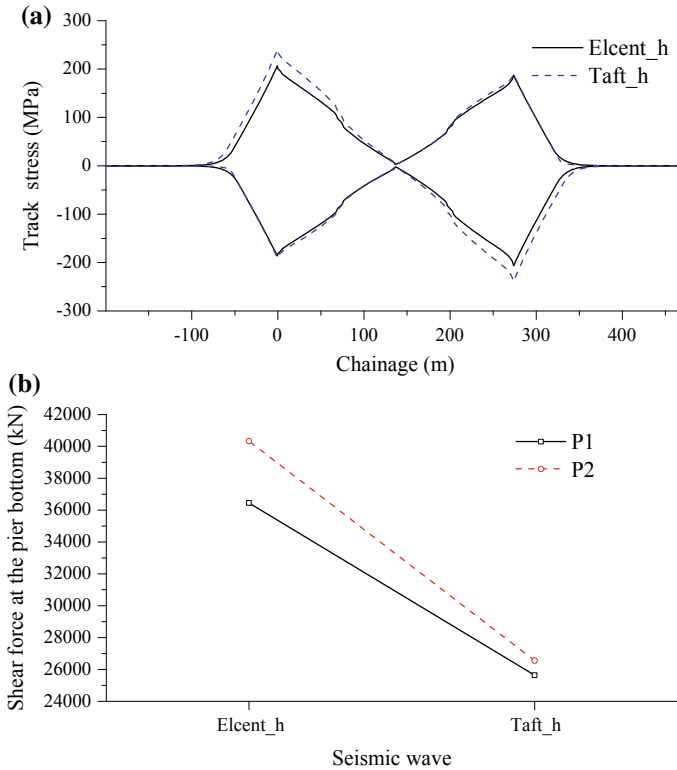
Fig. 12 System mechanical behavior due to earthquake: **a** track stress (envelope); **b** shear force at the pier bottom

distributed under the loads of thermal effects and gradient, bending, shrinkage and creep as well as earthquake, while the envelope of rail stress of braking and wind was inverse symmetry; the maximal stress caused by all kinds of loads related above was near the abutment.

There was a huge shear force for the piers due to the thermal effect, live load, train braking, wind, uneven settlement, shrinkage and creep as well as earthquake; the peak values were 4198.3 kN (concrete shrinkage and creep) and 40,331.4 kN (earthquake).

As for wind pressure, the track stress peak values reached 20.6 MPa when the regional basic wind pressure was 0.70 kN/m². The influence of wind on track should be considered.

The uneven settlement influenced a little on track stress but led to larger track vertical displacement (15 mm for this bridge), affecting train operation safety.

The track stress caused by shrinkage and creep would decrease greatly with the increase in installing track time. The maximum tensile and compressive stress dropped about 8.0% and 7.8%, respectively, with the installing track time increased from 30 days to 90 days.

The seismic response of continuous rigid-frame bridge–track system was related to spectral characteristics of seismic waves. The track stress (envelope) was distributed like "double diamond" and had a huge longitudinal shear force at the pier bottom under the action of seismic waves. For the bridge, the track stress peak values reached 239.5 MPa (tensile stress) and 233.0 MPa (compressive stress); the peak value of shear force was 40,331.4 kN.

References

1. BSI U (2008) National annex to Eurocode 1: actions on structures-Part 2: traffic loads on bridges, NA to BS EN 1991-2: 2003. British Standards Institution
2. Dai G, Yan B (2013) Interaction between cable-stayed bridge traveled by high-speed trains and continuously welded rail. China Civil Eng J 46(8):90–97
3. Dai G, Liu W (2013) Sensitive factors research for track-bridge interaction of Long-span X-style steel-box arch bridge on high-speed railway. J Cent South Univ Technol 20 (11):3314–3323
4. Fitzwilliam D (2009) Track structure interactions for the Taiwan High Speed Rail project. In: Calçada R (ed) IABSE2003. IABSE, pp 214–219
5. Millances Mato F (2009) Track-structure interaction and seismic design of the bearings system for some viaducts of Ankara-Istanbul HSRL project. In: Calçada R (ed) Track-bridge interaction on high-speed railways. CRC Press/Balkema, London, pp 37–53
6. MOR (2012) Code for design of railway continuous welded rail. China Railway Publishing House
7. MOR (2006) Code for seismic design of railway engineering. China Railway Publishing House
8. MOR (1985) Railway administration and the federal republic of Germany. Special procedures on railway bridge shinkansen. China Railway Publishing House
9. MOR (2005) Fundamental code for design on railway bridge and culvert. China Railway Publishing House
10. MOR (2014) Code for design of high speed railway. China Railway Publishing House
11. Ruge P, Widarda DR, Schmälzlin G, Bagayoko L (2009) Longitudinal track–bridge interaction due to sudden change of coupling interface. Comput Struct 87(1):47–58
12. Simões R, Calçada R, Delgado R (2009) Track-bridge interaction in railway lines: application to the study of the bridge over the River Moros. In: Calçada R (ed) Track-bridge interaction on high-speed railways. CRC Press/Balkema, London, pp 201–210
13. UIC (2001) Track/bridge interaction. Recommendations for calculations. UIC 774-3, International Union of Railways
14. Yan B, Dai G (2013) Seismic pounding and protection measures of simply-supported beams considering interaction between continuously welded rail and bridge. Struct Eng Int 23(1):61–67

15. Yan B, Dai G, Guo W, Xu Q (2015) Longitudinal force in continuously welded rail on long-span tied arch continuous bridge carrying multiple tracks. J Cent South Univ 22 (5):2001–2006
16. Zhu B (2012) Design of continuous welded rail upon long span cable-stayed bridge with steel-concrete composite box beam. Railway Stand Des 2(2)

Field Observations on Mud Pumping of Ballastless Track in High-Speed Railway

Zhangbo Wan, Shuhao Li, Xuecheng Bian and Yunmin Chen

Abstract Mud pumping is a relatively common subgrade distress in ballasted and ballastless track in high-speed railway (including passengers and freight transportation). Based on the preliminary literature research, it can be found that most of these researches focus on the fouled ballast, interlayer creation and mud pumping in ballasted track; however, little research paid attention to the mud pumping in ballastless track. Therefore, field observations were conducted to investigate the inducing factors of mud pumping in ballastless track. It is observed that the average water content of track roadbed layer is relatively high, and fine particles content are close to and sometimes can even surpass the upper limit of track roadbed specification of ballastless track. The upper limit specification just considered the compaction of track roadbed, but not considered whether this kind of limit specification can lead to mud pumping; therefore, a reconsideration is needed to be taken to the upper limit of track roadbed specification of ballastless track.

Keywords Mud pumping · Literature research · Filed observations · Water content · Fine particles content · Ballastless track

1 Introduction

At present, passengers and freight transportation both put forward to a higher expectation of faster trains in railway transportation. As the world has been searching for the greater mobility and environmentally friendly way of transportation, therefore, high-speed railway is set to become an attractive choice for passengers and freight transportation. With the continuous increase in speed and

Z. Wan · S. Li · X. Bian (✉) · Y. Chen
MOE Key Laboratory of Soft Soils and Geoenvironmental Engineering,
Department of Civil Engineering, Zhejiang University, Hangzhou 310058, China
e-mail: bianxc@zju.edu.cn

Z. Wan
e-mail: zhangbowan@zju.edu.cn

axle load, many subgrade distresses and issues are coming out, such as fouling ballast, differential settlement, ballast and track roadbed degradation, as well as mud pumping. Among all these subgrade distresses, mud pumping is considered to be most common and serious distresses, most sensitive to water, and also has the short maintenance intervals but a relative high maintenance costs [7]. Professor Buddhima specially leads a research team at the University of Wollongong to determine the underlying causes of a process known as mud pumping, highly destructive to railway lines, aiming at improving the railway network by understanding the process of mud pumping.

Mud pumping occurs when cyclic load of passing trains generates excess pore water pressure, causing upward migration of fluidized subsoil/subgrade to the upper ballast layer causing differential settlement. As for ballasted track, re-filling the weak area with new ballasts is the common way to alleviate the differential settlement; however, this kind of maintenance can lead to ballast pockets, and lots of fine particles were blocked in the pockets, leading to a lower permeability of ballast layer; therefore, water accumulates, and finally weakens the stiffness of roadbed.

Cui has conducted detail investigations and research on the conventional railways in France, most of which focus on the hydraulic performance and mechanical properties of fouling ballast, interlayer creation phenomenon, effects on mechanical properties of interlayer with a higher water content and fine particle content [3, 4]. Based on an on-site sampling test of fouling ballast ($h = 0.5$ m), as shown in Fig. 1, Cui has developed a large-scale cell allowing drainage and evaporation tests to be carried out with monitoring both suction and volumetric water content at various positions of this sample. For a detail investigation of the mechanical behavior of fouling ballast, another monotonic and cyclic triaxial tests were carried out, using a large-scale triaxial cell. They found that the hydraulic conductivity of fouled ballast is decreasing with suction increase, as for common unsaturated soils, the effect of fines content was found to be negligible. Water content is an important factor to be accounted for, since any increase in water content or degree of saturation significantly decreases the shear strength and increases the permanent strain.

Fig. 1 Geological profile of the substructure in Sénissiat-France [3]
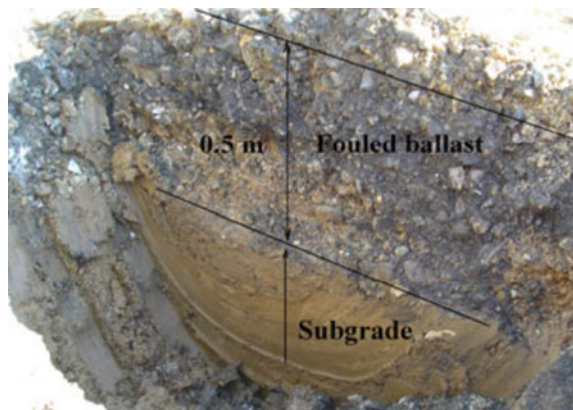
There is a mixed layer existing in the middle of ballast and subgrade/subsoil layer, which is called the interlayer. In ancient railway substructure in France, after years of railway operation, the interpenetration phenomenon of fine particles of subgrade and ballast layer becomes serious; therefore, a layer with high content of fine particles and lower permeability coefficient naturally formed after compaction under train load. According to the large-scale monotonic and cyclic triaxial tests, the effects of fine particles and water content on the mechanical behavior of interlayer soil were investigated. It is observed that when the water content is in a relatively low state ($w = 4\%$ and $w = 6\%$, in dry condition), adding more fines in the interlayer does not significantly change the shear strength, but drastically decreases the shear strength parameters, such as friction angle and cohesion, in nearly saturated condition ($w = 12\%$) [4].

For further investigations on the driving factors for the interlayer creation and mud pumping phenomena in railway substructure, some physical model tests on a ballast layer overlying a subsoil layer were carried out under different conditions in terms of water content, loading and subsoil dry unit mass; Cui developed a small apparatus for these tests, as shown in Fig. 2; this apparatus can be equipped with various sensors and devices allowing water content, pore water pressure and axial displacement to be monitored, and all of these can be used for investigating the creation condition of interpenetration of ballast and subgrade, and the mechanism of mud pumping [5, 6]. As is listed in his previous study [5, 6], the subsoil has various properties, and also this kind of subsoil was prepared from crushed sand and kaolin (70%/30% by dry mass), namely 70S30K. The reason for using this artificial material is that it has a high percentage of fines, and this material is similar to the subsoils found at the sites with mud pumping identified [1, 2]. Cui conducted monotonic and cyclic triaxial tests for three kinds of samples having different initial dry unit mass ($\rho_{initial-1} = 1.4$ g/cm^3, $\rho_{initial-2} = 1.5$ g/cm^3, $\rho_{initial-3} = 1.6$ g/cm^3). He founds that soil compressibility (initial dry unit mass) is a key parameter to be considered when dealing with mud pumping and interlayer creation phenomena; for a higher dry unit mass ($\rho_{initial-3} = 1.6$ g/cm^3), the compressibility is low; the generation of pore water pressure is limited, and thus, only interlayer creation can take place. By contrast, for a lower dry unit mass ($\rho_{initial-1} = 1.4$ g/cm^3, $\rho_{initial-2} = 1.5$ g/cm^3), the compressibility is higher, high pore water pressure can be built up, and hence, mud pumping can occur, and Fig. 3 shows the evolution of interlayer creation and mud pumping phenomenon ($\rho_{initial-2} = 1.5$ g/cm^3) [5, 6].

Mud pumping is a phenomenon; fine particles from the subgrade migrate upward into the track roadbed layer voids due to the generation of cyclic excess pore water pressure, which results in differential track settlement [1]. The mud collected on the ballast appears as solidified mud in relatively dry periods, and as slurry during the rainy seasons, these phenomena also appear in ballastless track, as shown in Fig. 4. When fine particles are pumped up and accumulate in the ballast layer, the ballast becomes clogged and can no longer properly perform and even lose its duty [2].
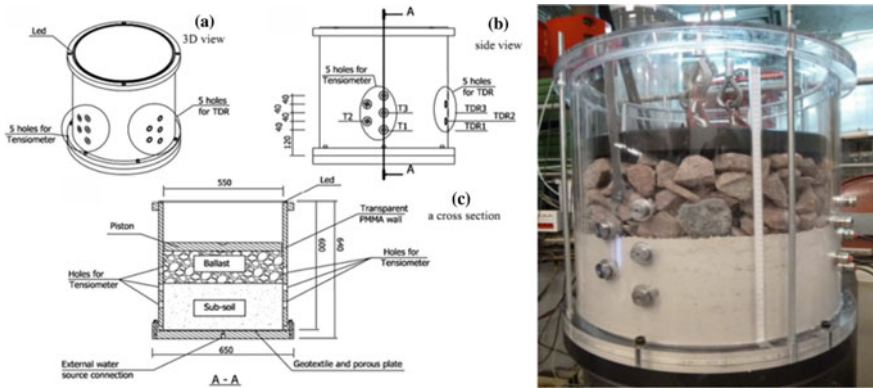
Fig. 2 Schematic view of the apparatus developed and the real one in laboratory [4, 6]
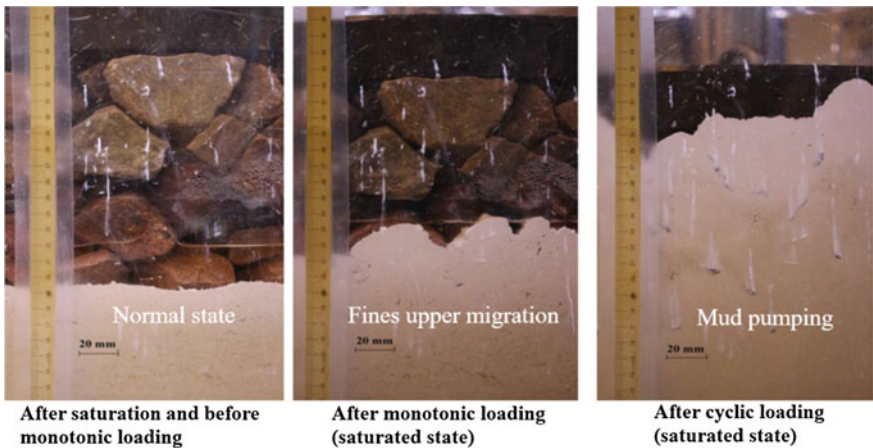
Fig. 3 Photographs of evolution of the ballast/subsoil interface ($\rho_{initial-3}$ = 1.5 g/cm^3, [5, 6])

As to ballastless track, in the action of the cyclic dynamic train load, an inter-layer is formed between the track roadbed and subsoil/subgrade, which contains lots of fine grains, leading to a lower permeability; therefore, the interlayer has a strong ability of water retention ability. The concrete base is provided with an expansion joint at every 20 m; in real engineering program, the expansion joint is sealed by plywood and emulsified asphalt for water-blocking and preventing the infiltration of rainwater. However, during the long-term train operations, under the coupling of complex natural force and high-frequency cyclic dynamic train load, the filling materials in the expansion joint gradually age and fail, thereby lose its water-blocking function. For areas with abundant rainfall, due to the water retention function of interlayer, the rainwater infiltrated into the subgrade bed cannot be
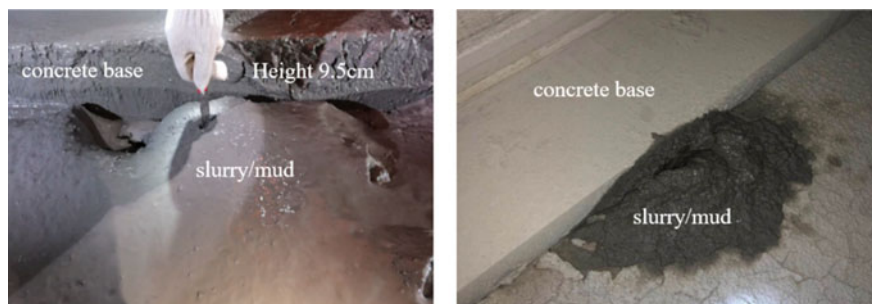
Fig. 4 Different kinds of mud pumping in ballastless track railway

drained in time, and the free water in graded gravel layer, that is, the track roadbed layer, will produce a relative high dynamic water pressure under the high frequency of cyclic and dynamic train load; during the dissipation process of dynamic water pressure, the fracturing action will occur in the soil skeleton, and the fine particles are incorporated into the dissipated pressurized water and then carried out, which leads to void area to upper structure of railway. At the same time, due to the high frequency of train load, the dynamic pore pressure can not dissipate timely, which will lead to the accumulation of pore pressure. When the pore pressure accumulates to a certain extent, the fine particles, most belonging to subsoil, will be sucked to the track roadbed layer and then pumped out from side cracks and expansion joints, for the next time of pore pressure dissipation process.

As shown in Fig. 5, Liu has given the detail explanation of the mechanism of mud pumping [8]; he found that the connection at the expansion joint is in a weak state, and when the train passes at a relative high speed, the end of concrete base bears a concentrated train load; as the infiltration of the rainwater may cause a decrease in the bearing capacity, the stress conditions of the end of concrete base are similar to that of the cantilever plate. With the intensification of the coupling action between the natural environment force and the high frequency of train load, the hollowing and flapping action at the end of concrete base is also intensified; it will lead to a continuous increase in the cantilever effect at the end of the concrete base, and as time passes, the saturated graded gravel layer gradually forms a muddy mixture, which will be finally pumped out, caused by high-frequency of train load; all of these will lead to a common subgrade distresses in railway, namely the mud pumping phenomenon.

PHAM designed a large-scale laboratory experiment [9], as shown in Fig. 6, which focuses on the dynamic performance of subgrade of ballastless track under two different conditions: no mud pumping period (optimum water content) and mud pumping period (saturated water content).
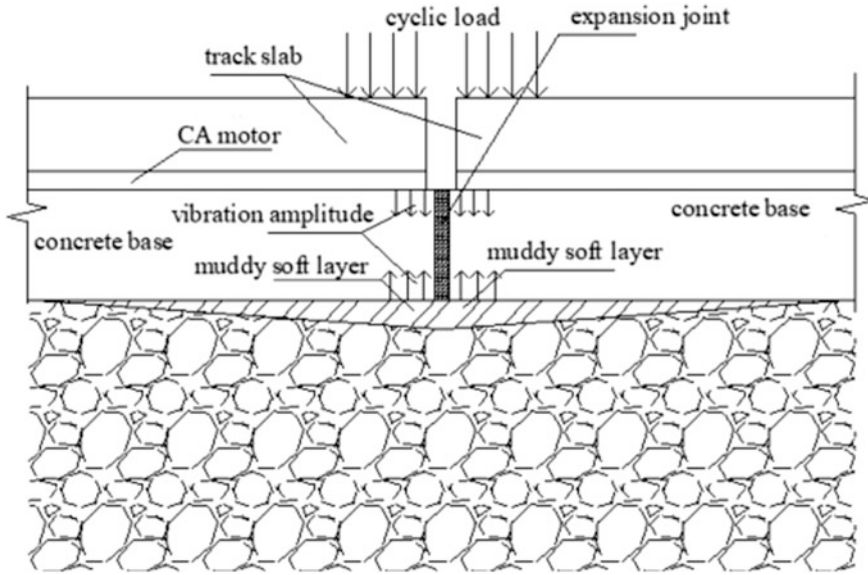
Fig. 5 Mechanism of mud pumping at expansion joint [8]
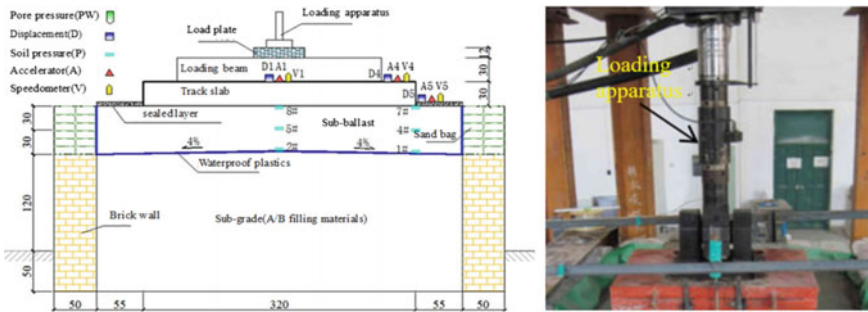
Fig. 6 Laboratory experiment for mud pumping investigation [9]

Among all the researches about mud pumping, most of which focus on the mechanism of fouling ballast, creation of interlayer and mud pumping phenomenon of ballasted railway, however, little research focuses on the mud pumping in ballastless track, so a more investigation should be located on this kind of subgrade distress (mud pumping) in ballastless track. Based on the field observations of a ballastless track railway in southeast of China, we found that there were many mud

pumping points along this line, so we conducted an on-site sampling experiments of subgrade in order to have a good investigation of the inner properties of the track roadbed layer.

2 On-Site Sampling Experiment

With the help of some railway staff, we got the chance for field observations of mud pumping points along the line. During the field investigation, we found that most of the sections built on the soil subgrade (in China, most of the high-speed railway lines are built on viaduct, ensuring less differential settlement) are suffering mud pumping distress, and we luckily found a no mud pumping point, because another viaduct crossed this line; as a result, no free water or rainfall can infiltrate in this track roadbed and subgrade. Therefore, we can conclude that water plays a leading role in mud pumping phenomenon in railway. So, in order to have a thorough understanding of this kind of distress, we chose a unit of concrete base (20 m long) as the testing point and sampled nine groups of soil samples, including track roadbed and subsoil/subgrade soil. Figure 7 shows the distributions of sampling points in railway line, which suffers serious mud pumping. We chose three symbolic cross sections as sampling section: cross section 1, including two vertical samples (V-1 & V-4) and one horizontal sample (H-1); cross section 2, including V-2, V-5 and H-2; cross section 3, including V-3, V-6 and H-3. According to the on-site investigation, section 1 located at the end of concrete base, suffering the serious mud pumping, section 3 located at another end, suffering the moderate mud pumping, and section 2 located in the middle of slab $104^{\#}$, the second track slab, suffering slight mud pumping.

As we all known that high-speed railway has its own unique and systematic maintenance mode, so we developed a removable apparatus, applying to the on-site sampling experiments, as shown in Fig. 8. The safety height (minimum operation height) of this apparatus is also taken into consideration. According to the normal grain-size distribution curve of track roadbed and subgrade/subsoil, the passing percentage of track roadbed, particle size 31.5–45 mm, is between 82 and 100%, so the internal diameter of soil connector is 78 mm, nearly two times of the maximum
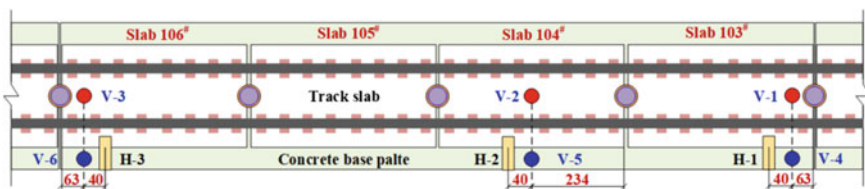
Fig. 7 Layouts of sampling holes in testing site (mm)
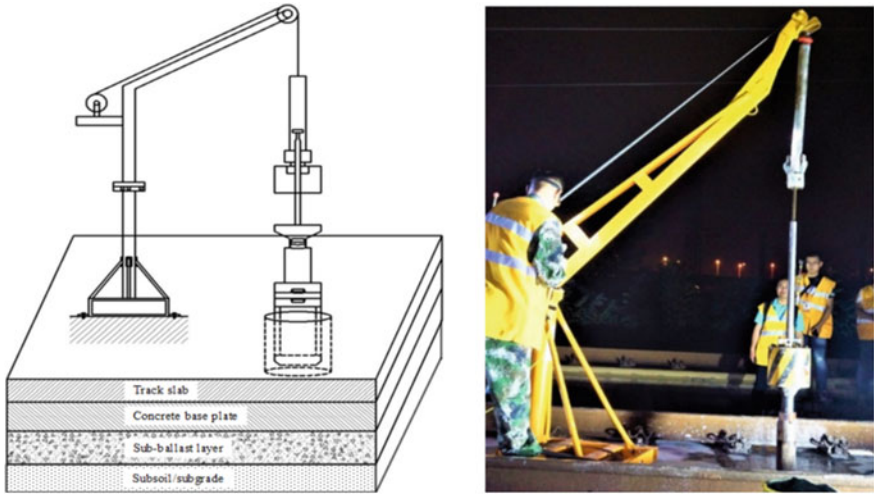
Fig. 8 View of the sampling apparatus developed and the real one (on-site)
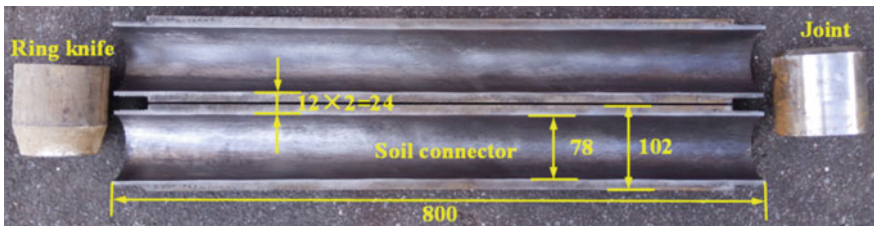
Fig. 9 Size dimension of soil connector (mm)

particle size of track roadbed, and is reasonable, having considered the collector material, particle effect and splitting effect during hammering process. The size dimension of soil connector is shown in Fig. 9.

3 Experiment Results and Analysis

After more than a week of hard work, we had gotten six vertical and three horizontal samples of track roadbed and subgrade/subsoil, as shown in Fig. 10, from which it can be obviously observed that the water content is very high in track roadbed layer and in the interlayer; however, the subsoil gets lower water content.

It is mentioned before that fine particles content and water or rainfall are the key factors affecting the mud pumping phenomenon in ballastless track; therefore, our analysis is focused on these affecting factors. As shown in Fig. 11, no matter in the
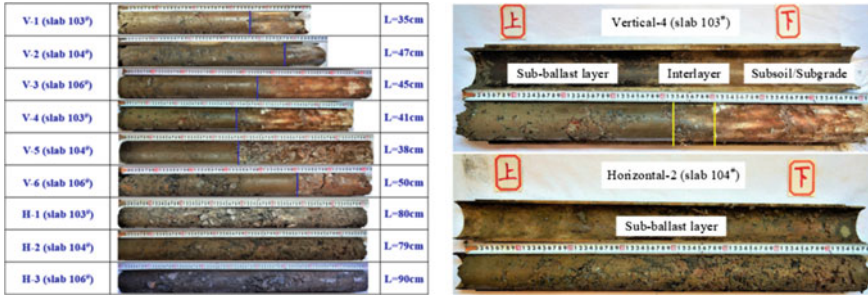
Fig. 10 Vertical and horizontal soil samples of track roadbed and subsoil/subgrade
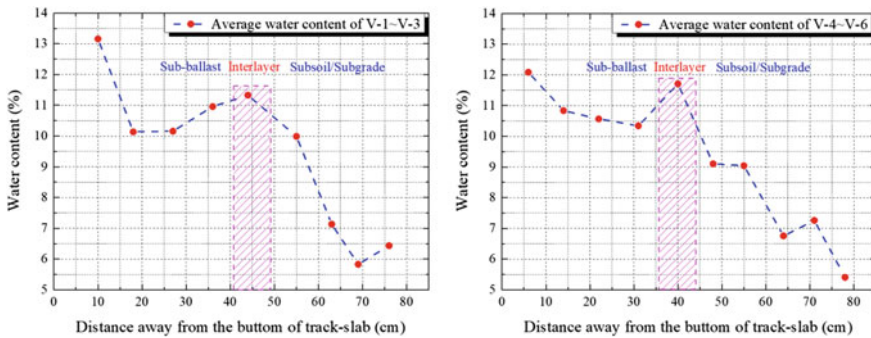
Fig. 11 Average water content of track roadbed and subsoil/subgrade (excluded coarse particles)

center (V-1 to V-3) or in the side (V-4 to V-6) of the railway line, the average water content with excluded coarse particles (diameter $\geq$ 7.1 mm), for those particles cannot keep water, is very high in the surface of track roadbed layer and nearly reaches 13%. Meanwhile, it is observed that the interlayer, interpenetration of track roadbed and subsoil/subgrade, has an obvious water retention effect. It means that the hydraulic conductivity of interlayer is very poor, so the water is kept in the track roadbed layer and then can lead to track roadbed layer's gradual saturation.

Another important affecting factor is fines content in the track roadbed layer, so we conducted grain-size distribution tests of the vertical and horizontal track roadbed samples. Figure 12 shows the grain-size distributions of track roadbed at different places of horizontal and vertical track roadbed samples.

From this figure, we can know that most of the grain-size distribution curves are close to the upper limit of track roadbed specification, and it means that this track roadbed has a higher fine particles content. For horizontal samples, sample H-3, the fine particles content has already surpassed the maximum content of the upper limit of track roadbed specification. Vertical samples, V-6, followed the same change law of horizontal samples. Therefore, the fine particles content, in generally suffering mud pumping cross section, is much higher than the ordinary section. Meanwhile,
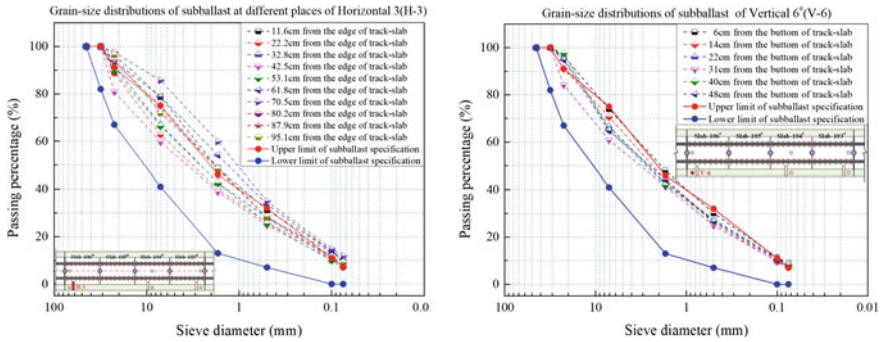
Fig. 12 Grain-size distributions of track roadbed of horizontal and vertical samples (H-3 & V-6)

the upper limit of track roadbed specification needs a reconsideration, for this specification just considered the well compaction of track roadbed, but not considered its affecting roles in the developing process in mud pumping distresses.

4 Conclusions

Based on the field observations and analysis, we can conclude the following results: Water and rainfall are the direct affecting factors in the process of mud pumping in ballastless track; water content and fine particles content play important roles in this kind of subgrade distress; the average water content (excluded coarse particles) is very high in the surface of track roadbed layer, nearly 13%; the interlayer has a lower hydraulic conductivity and an obvious water retention effect; the track roadbed layer has a higher fines content; most of the grain-size distribution curves are close to the upper limit of track roadbed specification; and a reconsideration is needed to be taken to the upper limit of track roadbed specification of ballastless track.

References

1. Alobaidi I, Hoare DJ (1996) The development of pore water pressure at the subgrade-subbase interface of a highway pavement and its effect on pumping of fines. Geotext Geomembr 14(2): 111–135
2. Aw ES (2007) Low cost monitoring system to diagnose problematic rail bed: case study of mud pumping site. Massachusetts Inst Technol
3. Cui YJ, Duong TV, Tang AM et al (2013) Investigation of the hydro-mechanical behavior of fouled ballast. J Zhejiang Univ-Sci A (Appl Phys Eng) 14(4):244–255
4. Duong TV, Tang AM, Cui YJ et al (2013) Effects of fines and water contents on the mechanical behavior of interlayer soil in ancient railway sub-structure. Soils Found 53(6):868–878

5. Duong TV, Cui YJ, Tang AM et al (2014a) Investigating the mud pumping and interlayer creation phenomena in railway sub-structure. Eng Geol 171(3):45–58
6. Duong TV (2014b) On the hydro-mechanical behavior of ancient railway platforms in term of reinforcement by soil-mixing. Paris Est
7. Kankanamge AB, Lakmali A, Indraratna B et al (2018) Excess pore water pressure generation and mud pumping in railways under cyclic loading
8. Liu T, Qian SU, Zhao WH et al (2015) Study on injection-repaired and reinforcement effects of subgrade frost boiling under ballastless track. J China Railway Soc (in Chinese)
9. PHAM DP (2015) Study on the mud pumping mechanism and reinforcement effect for graded gravel in high speed railway ballastless track surface layer of subgrade bed. Southwest Jiaotong Univ (in Chinese)

Analysis of Dynamic Response of Pile-Slab Subgrade Transition Section in High-Speed Railway Based on In Situ Testing

Li-min Wei, Chang-hong Xu, Xiao-bin Chen, Qun He and Di Ma

Abstract During the high-speed railway construction in mountainous area, it is likely to encounter that the distance between the bridge and the tunnel is too short to set the routine transition subgrade with the shortest length of 20 m. Therefore, the short subgrade with pile-slab foundation was suggested as an alternative plan to achieve the transitional function. A remote wireless automatic test system for dynamic response triggered by train running was established to evaluate the transitional performance of the pile-slab structure subgrade, which was constructed in the typical bridge-tunnel transition zone of Shanghai–Kunming high-speed railway in China. The subgrade surface dynamic response test under the train running conditions of six types of high-speed electrical multiple units (EMU) was performed. It found that under the excitation of six types of EMU, the maximum vibration acceleration and the maximum dynamic displacement of the pile subgrade surface are 3.767 m/s^2 and 0.062 mm, respectively, which meet the corresponding specifications. Along, the longitudinal direction of the down line, the range of variation coefficient about the EMU types for effective value in the vibration acceleration and dynamic displacement is 0.62–2.14 and 0.36–0.47, respectively, indicating that the EMU types have a greater impact on the former. The dynamic response is gradually attenuated along the lateral direction of the subgrade, the closer to the running line, the greater attenuation of the dynamic response, for the same measuring point, the attenuation of the vibration acceleration is less than the dynamic displacement.

Keywords Dynamic response · Pile-slab subgrade · High-speed EMU · High-speed railway · Transition section

L. Wei (✉) · C. Xu · X. Chen (✉) · Q. He · D. Ma
School of Civil Engineering, Central South University, 22 South Shaoshan Road, Changsha, Hunan 410075, China
e-mail: lmwei99@163.com

X. Chen
e-mail: Chen_xiaobin@csu.edu.cn

1   Introduction

The smoothness of railway track is a prerequisite for ensuring the high-speed train operation safety and ride comfort. Track irregularity is more prone to grow at the connection zone of two different engineering structures, such as bridges, tunnels, culverts, subgrade and so on, which was derived from both settlement difference and differential composite stiffness of the adjacent structure underlying the track. It will aggravate the vibration of the running train and the vibration in return intensify the impact force on the track, and then it will affect the index of running stability and ride comfort, and even threaten train running safety [1–3]. Consequently, it is necessary to set up a transition section between adjacent different structures to ensure the smoothness of railway track.

Numerical analysis is the main process to study the dynamic response of transition section. Paixão et al. [4] conducted extensive experiments and numerical studies to gain insight into the impact of under sleeper pads on the dynamic characteristics of the transition section and improve the design of the railway structure. Yang et al. [5] considered the interaction among different structural layers of the subgrade system, established a vehicle-track-subgrade coupling system model, analyzed the dynamic response of bridge-approach embankment section when the speed of train was 350 km/h, and obtained the allowable track deflection angle and the coefficient of subgrade reaction within the 0–5 m zone behind the abutment. Yao et al. [6] established the finite element model about the track-subgrade system for two bridge-subgrade transition sections, and comparative analysis of the stress and calculated vertical displacement of the subgrade surface of the two transition zones, then the recommended length of the transition section had been proposed. Lei and Mao [7] studied the dynamic response of the coupled vehicle-track system by changing the conditions of track settlement, train speed and abutment stiffness, it found that the track profile suddenly. Permanent settlement is the main source of vibration amplification, while the vertical stiffness of the track transition has little effect on the vibration. Considering the long-term track deformation, the non-constant stiffness of the support and the possibility of gaps under the sleepers, and a two-dimensional numerical model for the study of the dynamic behavior of the track on a transition zone during train passage are presented by Varandas et al. [8]. To analyze the vehicle-track interaction near the transition zone, Banimahd [9, 10] developed a three-dimensional coupled train-track finite element model. The results are general agreement with those of Lei and Mao [7] and Luo [11].

Due to the complexity and inhomogeneity of the subgrade composition of high-speed railway, as well as the uncertainty of their calculating parameters, there are still certain gaps between the numerical research results and the actual situations [12, 13]. So in situ test is the more effective method to analysis the dynamic response of high-speed railways by providing the reliable response property, which can be used to verify the numerical simulation [12], and further improve its correctness [14–18]. Ribeiro et al. [19] assessed the experimental dynamic behavior of the train-track system at a culvert transition zone, and found that after the

application of a low-pass filter for eliminating contributions from irregularities of the track and vehicle wheels, the change in the track dynamic stiffness of the transition zone has little effect on the acceleration of the sleeper. Feng et al. [20] performed dynamical in situ tests on four scenarios named as the embankment, culvert, viaduct and transition sections, which located on the Beijing–Shanghai high-speed railway in China, the acceleration responses of the free field in three directions (x, y, z) were recorded with a train speed of around 250–350 km/h. Zhai et al. [14] reported the results of ground vertical acceleration caused by a 300–410 km/h high-speed train on non-ballasted track and analyzed the frequency domain and time domain characteristics of ground vibration acceleration. Qu et al. [21] tested the dynamic response of the transition section in Wuhan–Guangzhou high-speed railway during joint debugging test and operation period, and the influence of the comprehensive stiffness of the subgrade on the vibration characteristics of the transition section has been compared and analyzed.

However, the above studies mainly aimed at the conventional transitional section, which profile is trapezoid or inverted trapezoid with the minimum length of 20 m. When the high-speed railway is constructed in mountainous area, the distance between the bridge and the tunnel is sometimes too short to set up a conventional transition section, in this case, by means of the short subgrade with pile-slab structure to achieve transition has become an alternative plan. But how is it transitional effect? In this paper, the dynamic response of the subgrade surface under different electrical multiple units (EMU) types and speed conditions for the pile-slab structure bridge-tunnel transition section in the Shanghai–Kunming high-speed railway has been tested, and the interval estimation method in statistics was used to analyze the vibration acceleration and dynamic displacement data, so as to provide reference for the promotion and application of pile-slab subgrade transition section.

2 Overview of the In Situ Test

2.1 The General Situation of Work Site

The Shanghai–Kunming high-speed railway is a dedicated passenger line with a design speed of 350 km/h; it is a double-track railway with distance between centers of lines is 5 m, and subgrade width of 13.6 m. The typical section of design mileage K893 + 983 $\sim$ K894 + 022 that located hilly area in Jiangxi Province was selected as in situ test section, which is 39 m long, including the transition section and its adjacent bridge and tunnel, and the dynamic response to the train running was tested. The engineering geology investigation exposed the strata as follow: The surface cover is a Quaternary–Holocene residual product (Q_4^{el+dl}) silty clay and contains gravel with a content of about 10%, its thickness is 0–20 m; underlying bedrock is made up of the Maokou group (P_1m), limestone of lower

Fig. 1 Test section general situation
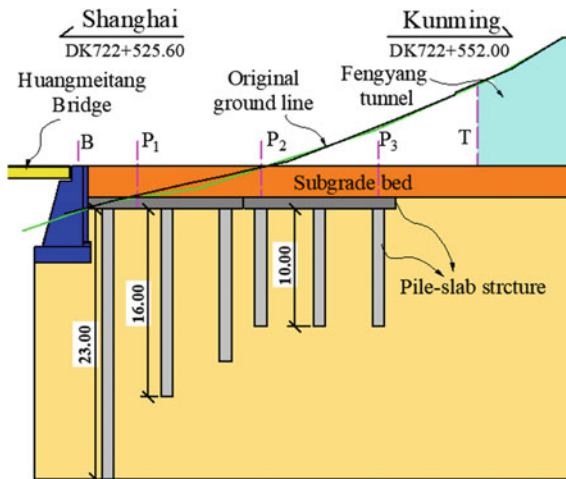
Fig. 2 Layout of in situ test section

Permian period with the weathering degree from fully to weakly weathered. The test section general situation and layout are shown in Figs. 1 and 2.

The transition section is composed of two blocks of pile-slab structures; each block is 13 m long. From the abutment to the tunnel, the pile length is decreasing from 23.0 to 10.0 m, although these bored cast-in-place piles are located at the

same spacing of 5.0 m and with the same diameter of 1.0 m. These piles are connected rigidly to the reinforced concrete slab with a thickness of 1.0 m. Above the slab, lay the subgrade bed and track structure one by one as follows: The bottom layer of subgrade bed is filled graded broken stone with 3% cement content, and which thickness is 2.3 m; the surface layer of subgrade bed with the thickness of 0.4 m which is filled by graded broken stone with 5% cement content; the track support layer was made of C40 reinforced concrete with the thickness of 0.3 m, and the CRTSII ballastless track system at the top.

2.2　The Layout of Test Sections and Components

Five test sections were arranged for this test, as shown in Fig. 2. They are section B on the abutment, section P_1, P_2, P_3 on the pile-slab subgrade, and section T in the tunnel, respectively. The section P_1 corresponds to the mid-span of the pile-slab structure, and the section P_2 and P_3 correspond to the pile top of the pile-slab structure. The specific location of the test section is shown in Table 1.

The layouts of the dynamic response measuring points are shown in Fig. 3. The full-section layout was adopted at the section P_2, while the half-section layout was employed at the rest of the test sections. The test lines mainly arranged on the following position as shown in Fig. 4, namely, 1# on the shoulder of the down line, 2# and 3# at the outer side of the track slab of the down line symmetrically on the support layer, 4# at the middle of central lines of track which on the surface layer of subgrade bed. For the section P_2, besides the above-mentioned test lines, corresponding measuring points were installed also on the up line, and two additional measuring points were laid on the subgrade slope surface too.

In most of the measuring points, three kinds of sensors were installed, such as one vertical vibration acceleration sensor 891-II (V), one lateral vibration acceleration sensor 891-II (H) and one vertical dynamic displacement sensor 891-II (V). There were altogether 32 accelerometers sensors and 24 displacement sensors used in the in situ test. The INV306 dynamic data acquisition instrument was adopted for signal pick up which can be triggered automatically by forthcoming running train. Then a wireless transmission test system had been established. The photos of the vibration sensors and the acquisition instrument are shown in Figs. 5 and 6, respectively.

Table 1 Test section situation

Section	Design mileage	Distance from the back of the abutment (m)	Corresponding structural position
B	DK722 + 522.800	−2.800	On the railway abutment
P_1	DK722 + 529.825	+4.225	The mid-span of pile-slab structure
P_2	DK722 + 540.345	+14.745	Top position of pile-slab structure
P_3	DK722 + 545.345	+19.745	Top position of pile-slab structure
T	DK722 + 562.000	+36.400	At the tunnel entrance
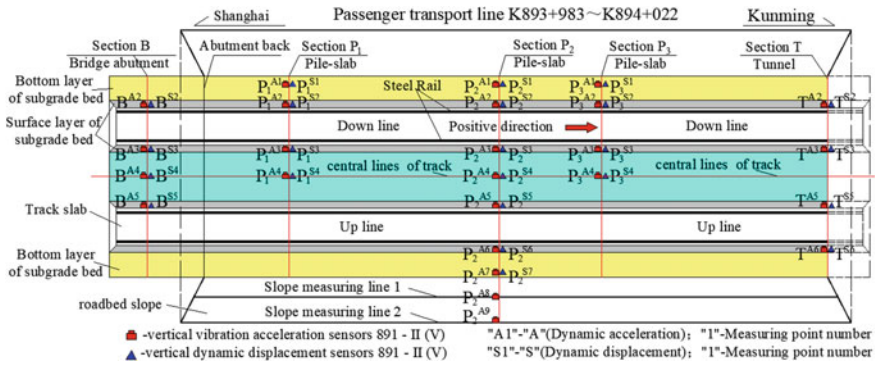
Fig. 3 Arrangement of test section and the measuring points
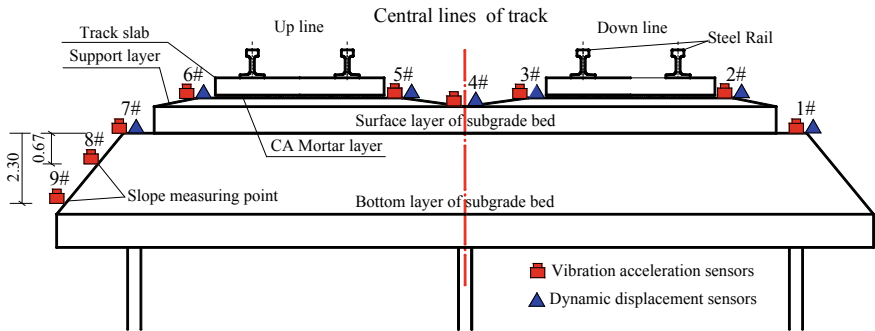
Fig. 4 Layout of test line on the section P_2

2.3 Test Data Extraction

The in situ test was performed on the platform, which consists of DASP V11 software and INV306 data acquisition instrument that is from China Orient Institute of Noise and Vibration. The system has many functions such as multi-channel high-capacity signal acquisition, wireless real-time signal transmission, signal analysis and so on. By means of the DASP software, both the maximum value and effective value of time-history curves about either the vibration acceleration or the dynamic displacement can be obtained. Taking a time-history curve of the vibration acceleration as an example that is shown in Fig. 7.

Maximum value:

$$\widehat{X} = \max|x(t)|$$

Fig. 5 Layout of the vibration sensors

Fig. 6 Acquisition instrument
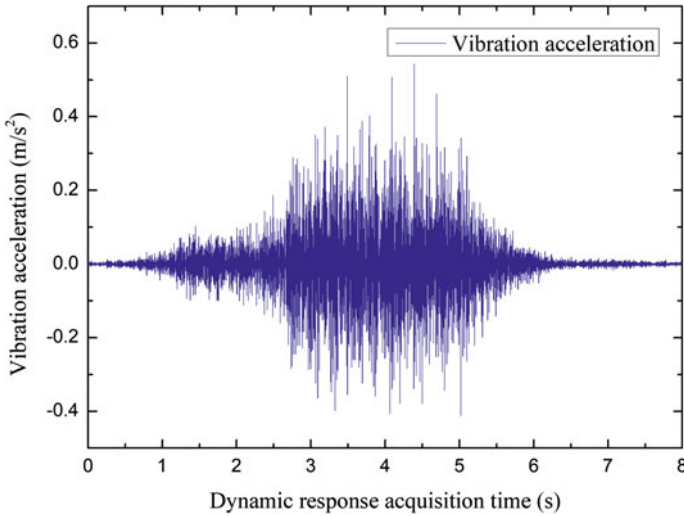
Fig. 7 Time-history curve of the vibration acceleration

Effective value:

$$X_{RMS} = \sqrt{\frac{1}{T} \int_0^T |x^2(t)| \, dt}$$

where $x(t)$ is the vibration acceleration value at arbitrary moment, T is represents the vibration acceleration value acquisition period.

In order to reduce the system error and artificial error in the test, and improve the accuracy and authenticity of the test data, the confidence interval method in mathematical statistics was adopted. It is well known that the dynamic response of subgrade is influenced by many factors such as train running speed, axle load, subgrade material, track irregularity, and thickness of subgrade bed, but no one of them is absolutely dominant factors. Therefore, according to the central limit theorem, the dynamic response X generally follows a normal distribution. Meaning that the overall X obeys the normal distribution $N(\mu, \sigma^2)$, $X_1, X_2, \ldots, X_n$ is a sample from the population samples, then:

$$\overline{X} = \frac{1}{n}\sum_{i=1}^n X_i; \quad S^2 = \frac{1}{n-1}\sum_{i=1}^n (X_i - \overline{X})^2$$

where $\overline{X}$ is the sample mean, S^2 is the sample variance.

According to the theory of sampling distribution:

$$T = \frac{\overline{X} - \mu}{\sqrt{\frac{S^2}{n}}} \sim t(n-1)$$

For a given confidence level α, making:

$$P\left\{ \left| \frac{\overline{X} - \mu}{\sqrt{\frac{S^2}{n}}} \right| \leq t_{\frac{\alpha}{2}}(n-1) \right\} = 1 - \alpha$$

Or

$$P\left\{ \overline{X} - \frac{S}{\sqrt{n}} t_{\frac{\alpha}{2}}(n-1) \leq \mu \leq \overline{X} + \frac{S}{\sqrt{n}} t_{\frac{\alpha}{2}}(n-1) \right\} = 1 - \alpha$$

where the value of $t_{\frac{\alpha}{2}}(n-1)$ can be got by table lookup in t-distribution of the mathematical statistics.

So, for the sample X_i, setting the confidence as $1 - \alpha$: the confidence interval about its mathematical expectation μ is

$$\left[\overline{X} - \frac{S}{\sqrt{n}} t_{\frac{\alpha}{2}}(n-1), \overline{X} + \frac{S}{\sqrt{n}} t_{\frac{\alpha}{2}}(n-1) \right]$$

Using the above-mentioned methods, the confidence interval corresponding to confidence of 95% about the maximum and effective values of vibration acceleration or the dynamic displacement has been obtained. Then the upper limit value of confidence interval is selected to take as the analysis sample of the dynamic response in this paper.

3 Dynamic Response Characteristics of Pile-Slab Subgrade Transition Section

The dynamic response about the subgrade of high-speed railway is influenced by a variety of factors, such as the EMU types, the axle load, the speed of the train running, and the smoothness of railway track. In order to investigate the dynamic response of the pile-slab subgrade as the bridge-tunnel transition section, a series of in situ tests were performed, which were under the excitation of six types of high-speed EMU and the EMU types as follow: "DF11 + DF11, CRH380A-6158-6159, CRH380B, CRH2, CRH380A-001, CRH380AM". Then the distribution trend along the longitudinal direction of the line about the maximum and effective values of vertical

vibration acceleration and dynamic displacement had been given. Similarly, the distribution trend about dynamic response along the lateral direction of pile-slab subgrade had also been analyzed by taking the EMU of "DF11 + DF11" as an example.

3.1 Longitudinal Distribution of Dynamic Response

3.1.1 Vertical Vibration Acceleration

Under the excitation of six types of EMU, the longitudinal distribution curves about the maximum and effective values of the vertical vibration acceleration are shown in Figs. 8 and 9, respectively, which are drawn by the data from number 3# test line. It can be seen that the trend of the distribution about the maximum and effective values of the vibration acceleration for different types of EMU is alike; the range of the maximum value in vibration acceleration is 0.009–3.767 m/s^2, and the effective value is 0.003–0.867 m/s^2. From section B to the section T, the trend is increased first then decreased and increased finally, the vibration acceleration at the section B which on the abutment is the smallest and at the section P_2 and P_3 has a less difference and at the section T is the largest. However, the maximum value of vibrational acceleration is 3.767 m/s^2, which meets the requirement that it must be less than 4.90 m/s^2 in the Code for Design of High-Speed Railway (TB 10621-2014) [22].
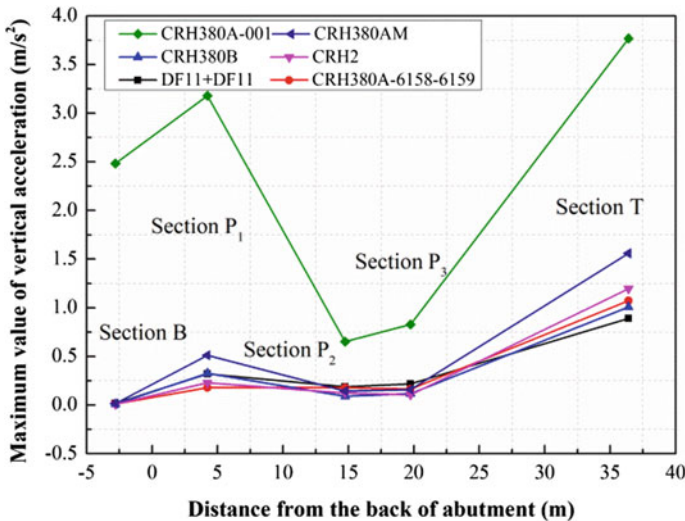
Fig. 8 Longitudinal distribution of vertical vibration acceleration maximum value for different EMU types
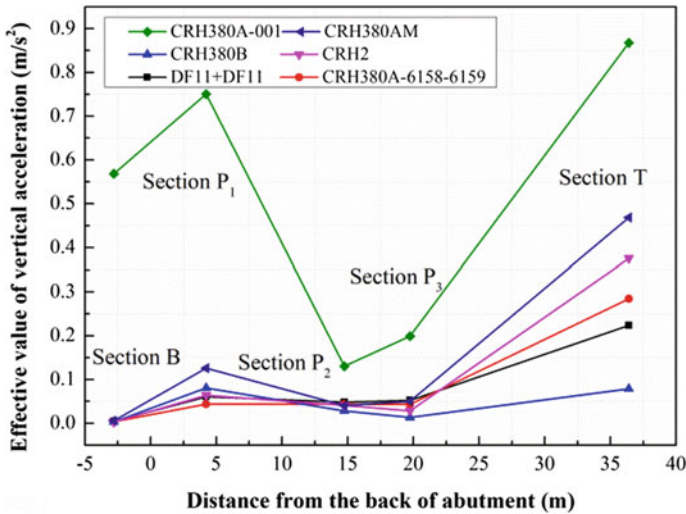
Fig. 9 Longitudinal distribution of vertical vibration acceleration effective value for different EMU types

The coefficient of variation of vibration acceleration on the section B-P_3 along the longitudinal direction about different EMU types is shown in Table 2. It can be seen that the coefficient of variation of the maximum acceleration of vibration in different EMUs varies in 0.61–1.02, with a range difference of 0.41, while the coefficient of variation of the effective acceleration of vibration varies in 0.61–1.09, with a range difference of 0.48. It has shown that the vibration acceleration is less discrete from the section B to the section P_3.

3.1.2 Vertical Dynamic Displacement

Similar to the vibration acceleration analysis described above, the longitudinal distribution curves about the maximum value or effective value of the dynamic displacement are shown in Figs. 10 and 11. On account of the needs of test, the sensor B^{S3} on the abutment was removed temporarily, which result in loss of the corresponding test data. We can see that from section P_1 to T, the dynamic displacement shows a trend of decreasing first and then increasing. The range of the maximum value of dynamic displacement is 0.007–0.062 mm and that of effective value is 0.002–0.034 mm. Among them, the dynamic displacement on section P_3 is the smallest and is the largest on the section T which may be caused by the complex combined action of airflow and vibration transmission near the tunnel entrance. Another noticeable phenomenon is the dynamic displacement has a small change range in the pile-slab structure even in the whole transition section. It indicates that

Table 2 Coefficient of variation of vibration acceleration along longitudinal direction which under excitation of each type of EMU

Test section	EMU types					
	DF11 + DF11	CRH380A-6158-6159	CRH380B	CRH2	CRH380A-001	CRH380AM
Maximum value of vibration acceleration (m/s²)						
B	0.0163	0.0116	0.0106	0.0087	2.4824	0.0161
P_1	0.3201	0.1795	0.3276	0.2298	3.1785	0.5121
P_2	0.1869	0.1795	0.0898	0.1244	0.6520	0.1440
P_3	0.2180	0.1656	0.1166	0.1067	0.8289	0.1596
Mean value	0.1853	0.1341	0.1361	0.1174	1.7854	0.2079
Standard deviation	0.1262	0.0819	0.1354	0.0906	1.2418	0.2127
Coefficient of variation	0.68	0.61	0.99	0.77	0.70	1.02
Effective value vibration acceleration (m/s²)						
B	0.0041	0.0038	0.0033	0.0029	0.5684	0.0059
P_1	0.0610	0.0439	0.0805	0.0640	0.7503	0.1258
P_2	0.0482	0.0439	0.0283	0.0409	0.1303	0.0405
P_3	0.0525	0.0434	0.0136	0.0285	0.1991	0.0504
Mean value	0.0414	0.0338	0.0314	0.0341	0.4120	0.0557
Standard deviation	0.0254	0.0200	0.0343	0.0254	0.2964	0.0505
Coefficient of variation	0.61	0.59	1.09	0.75	0.72	0.91
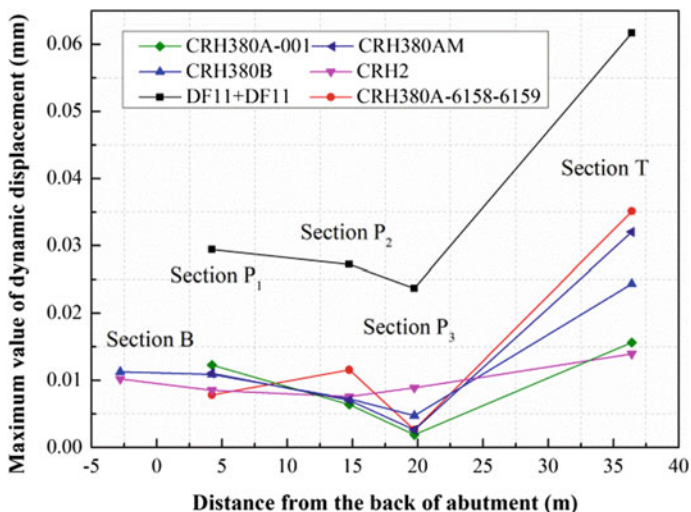
Fig. 10 Longitudinal distribution of vertical dynamic displacement maximum value for different EMU types

the pile-slab subgrade transition section is better in ride comfort when the train passed.

The dynamic displacement variation coefficients of the section P_1 to P_3 along longitudinal during each EMU type running are shown in Table 3. It can be found
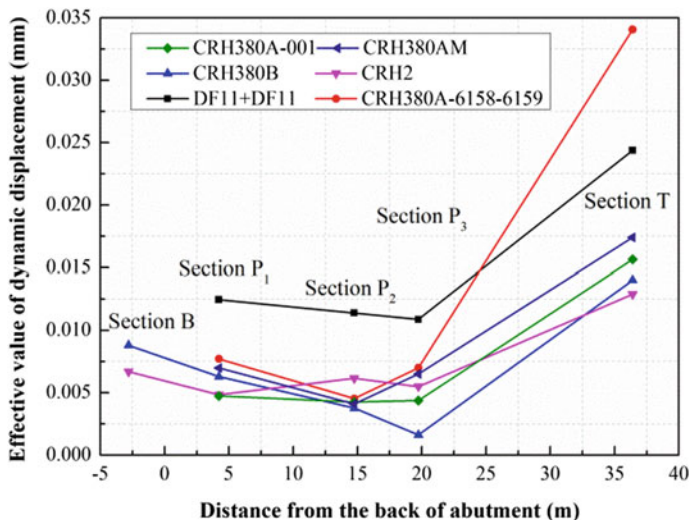
Fig. 11 Longitudinal distribution of vertical dynamic displacement effective value for different EMU types

Table 3 Coefficient of variation of dynamic displacement along longitudinal direction which under excitation of each EMU type

Test section	EMU types					
	DF11 + DF11	CRH380A-6158-6159	CRH380B	CRH2	CRH380A-001	CRH380AM
Maximum of dynamic displacement (mm)						
P_1	0.0294	0.0079	0.0109	0.0085	0.0123	0.0111
P_2	0.0272	0.0116	0.0073	0.0076	0.0064	0.0071
P_3	0.0237	0.0116	0.0048	0.0089	0.0019	0.0026
Mean value	0.0268	0.0103	0.0076	0.0083	0.0069	0.0069
Standard deviation	0.0029	0.0022	0.0031	0.0007	0.0052	0.0042
Coefficient of variation	0.11	0.21	0.41	0.08	0.76	0.61
Effective value of dynamic displacement (mm)						
P_1	0.0124	0.0077	0.0063	0.0048	0.0047	0.0070
P_2	0.0114	0.0045	0.0038	0.0061	0.0043	0.0041
P_3	0.0109	0.0070	0.0016	0.0055	0.0044	0.0065
Mean value	0.0116	0.0064	0.0039	0.0055	0.0045	0.0059
Standard deviation	0.0008	0.0017	0.0023	0.0007	0.0003	0.0015
Coefficient of variation	0.07	0.26	0.60	0.12	0.06	0.26

that the variation coefficient of the maximum value about dynamic displacement for different EMU types varies in the range of 0.08–0.76, and the range difference is 0.68; the coefficient of variation of the effective value of the dynamic displacement varies within 0.06–0.60, and its difference is 0.54. It illustrates that the dynamic displacement is less discrete from the section P_1 to P_3.

3.1.3 Comparative Analysis of the Influence About EMU Type on Dynamic Response

In order to compare the influence of the EMU type on vibration acceleration with dynamic displacement, the concept of variation coefficient (CV) in mathematical statistics was introduced and where we defined the EMU type's variation coefficient ζ as follow:

$$\zeta = \frac{S_D}{X_D} \tag{1}$$

where S_D is the standard deviation of dynamic response is about different types of EMU at the same measuring point and X_D is the dynamic response mean value about different types of EMU at the same measuring point.

According to Formula (1), the EMU type's variation coefficients of dynamic response on the pile-slab structures are shown in Tables 4 and 5.

It can be seen from Tables 4 and 5 that along the longitudinal transition section in the down line, the EMU type's variation coefficient of the maximum value of vibration acceleration varies in 0.96–1.36, and the effective value of vibration acceleration varies in 0.95–1.35, the EMU type's variation coefficient about the maximum value of dynamic displacement varies in 0.55–0.83 and the effective value of dynamic displacement varies in 0.36–0.47. The comparative analysis

Table 4 Comparison of influence of EMU types on vibration acceleration

EMU types	Measuring section					
	Maximum value (m/s^2)			Effective value (m/s^2)		
	P_1	P_2	P_3	P_1	P_2	P_3
DF11 + DF11	0.3201	0.1869	0.2180	0.0610	0.0482	0.0525
CRH380A-6158-6159	0.1795	0.1795	0.1656	0.0439	0.0439	0.0434
CRH380B	0.3276	0.0898	0.1166	0.0805	0.0283	0.0136
CRH2	0.2298	0.1244	0.1067	0.0640	0.0409	0.0285
CRH380A-001	3.1785	0.6520	0.8289	0.7503	0.1303	0.1991
CRH380AM	0.5121	0.1440	0.1596	0.1258	0.0405	0.0504
Mean value	0.7913	0.2294	0.2659	0.1876	0.0554	0.0646
Standard deviation	1.0726	0.1918	0.2544	0.2529	0.0340	0.0617
Variation coefficient ζ_a	1.36	0.84	0.96	1.35	0.62	0.95

Table 5 Comparison of influence of EMU types on dynamic displacement

EMU types	Measuring section					
	Maximum value (mm)			Effective value (mm)		
	P_1	P_2	P_3	P_1	P_2	P_3
DF11 + DF11	0.0294	0.0272	0.0237	0.0124	0.0114	0.0109
CRH380A-6158-6159	0.0079	0.0116	0.0116	0.0077	0.0045	0.0070
CRH380B	0.0109	0.0073	0.0048	0.0063	0.0038	0.0016
CRH2	0.0085	0.0076	0.0089	0.0048	0.0061	0.0055
CRH380A-001	0.0123	0.0064	0.0019	0.0047	0.0043	0.0044
CRH380AM	0.0111	0.0071	0.0026	0.0070	0.0041	0.0065
Mean value	0.0133	0.0112	0.0089	0.0072	0.0057	0.0060
Standard deviation	0.0073	0.0074	0.0074	0.0026	0.0027	0.0028
Variation coefficient ζ_s	0.55	0.66	0.83	0.36	0.47	0.47

shows that the EMU type's variation coefficient about dynamic displacement is less than that about vibration acceleration, which proves that the different EMU types have a greater influence on vibration acceleration.

3.2 Lateral Distribution of Dynamic Response on the Pile-Slab Subgrade Transition

3.2.1 Vertical Vibration Acceleration

The lateral distribution curves of the maximum and effective values of vertical vibration acceleration along the test section P_2 for every running about the EMU of "DF11 + DF11" are shown in Fig. 12 and Fig. 13, the number is denoted by "test date." The measuring points from the up line to down line are P_2^{A9}, P_2^{A8}, P_2^{A7}, P_2^{A6}, P_2^{A5}, P_2^{A4}, P_2^{A3}, P_2^{A2}, and P_2^{A1} in turn as illustrated in Fig. 4. It can be found that when the train running on the down line, the maximum and effective values of vibration acceleration generally decrease from the measuring points P_2^{A1} to P_2^{A9}, which may be caused by the loss of energy and material damping [12, 23]. Among them, no matter whether it is on the up line or down line, the dynamic response of the two ends of the track slab has little change. However, the vibration acceleration about the measuring points of P_2^{A1}, P_2^{A7} (locate in surface on the bottom layer of subgrade bed) had been amplified obviously, which may be the product of wave interference between the Rayleigh wave and the reflected wave at the top of the subgrade surface and the scattered waves propagated by the neighboring structures [20]. Many researchers also have obtained similar results in finite element simulations [24].
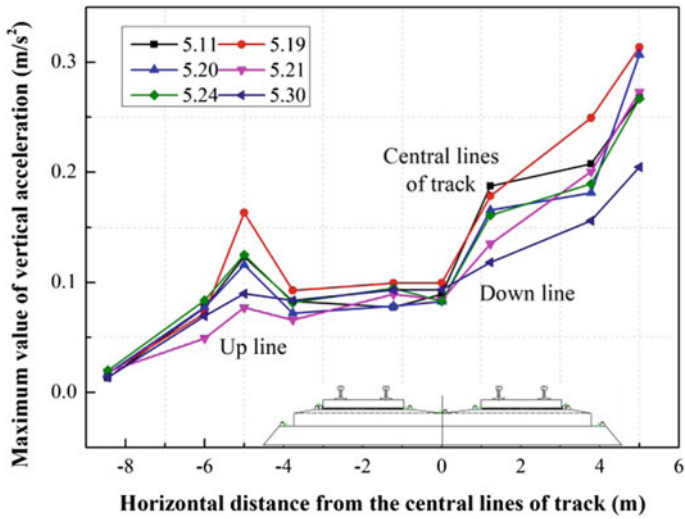
Fig. 12 Lateral distribution about the maximum value of vertical vibration acceleration for different train trips
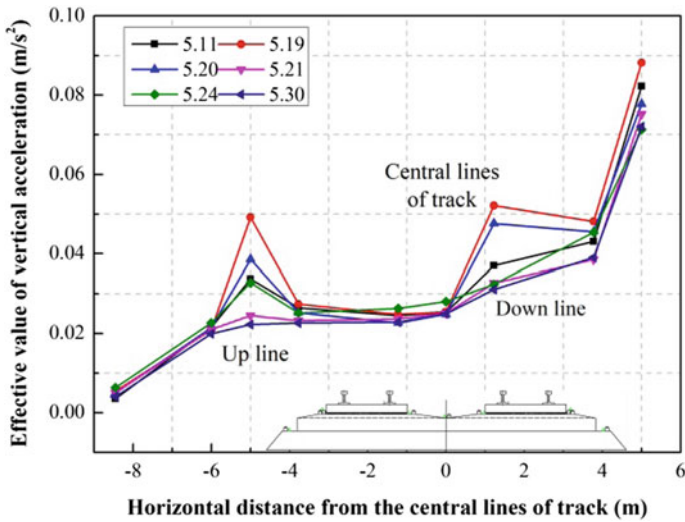
Fig. 13 Lateral distribution about the effective value of vertical vibration acceleration for different train trips

3.2.2 Vertical Dynamic Displacement

The distribution curve of the maximum and effective values of vertical dynamic displacement along the section P_2 for different running about the EMU type "DF11 + DF11" are shown in Figs. 14 and 15.

We can see that the maximum and effective values of the dynamic displacement are declining from both sides of the track slab of the running line (measuring points P_2^{S3}, P_2^{S2}), the attenuation of the measuring points P_2^{S2} to P_2^{S1} is greater, and from the P_2^{S3} to P_2^{S7} is a lesser extent attenuation.

3.2.3 Lateral Attenuation Change of the Dynamic Response

In this paper, the measuring point at test line 2# on the section P_2 is taken as the reference point and the dynamic response attenuation of other measuring points relative to this point is studied. Defining the decay rate η as follow:

$$\eta = \frac{Z_D - Z_X}{Z_D} \times 100\% \tag{2}$$

where Z_D is dynamic response value from the measuring point at test line 2# on section P_2 and Z_X is dynamic response value for any specifies measuring point.

Under the excitation of "DF11 + DF11" EMU, the changes in the attenuation of the dynamic response along lateral of the pile-slab subgrade can be seen in Table 6.
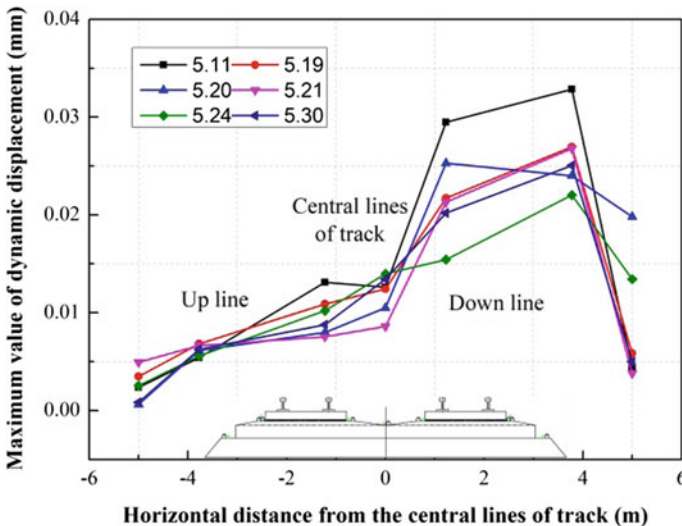
Fig. 14 Lateral distribution in the maximum value of vertical dynamic displacement for different train trips
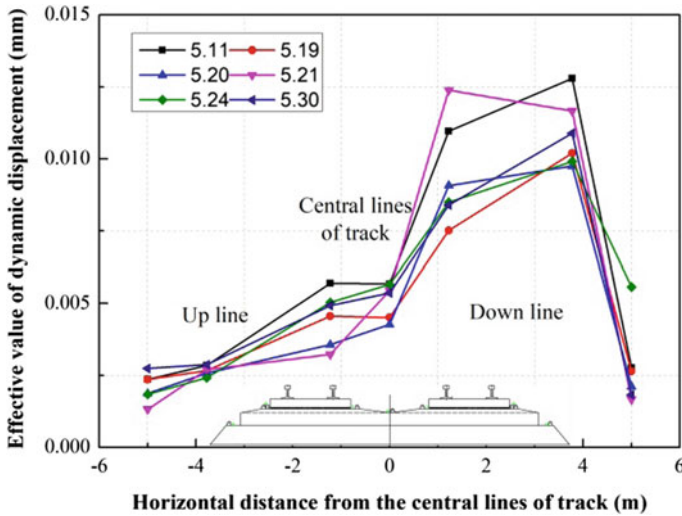
Fig. 15 Lateral distribution in the effective value of vertical dynamic displacement for different train trips

Table 6 Lateral attenuation change of the dynamic response on section P_2

Items	Measuring point						
	2#	3#	4#	5#	6#	8#	9#
Distance from center line (m)	3.775	1.225	0	−1.225	−3.775	−6.005	−8.450
Acceleration (m/s²)	0.0433	0.0388	0.0256	0.0241	0.0250	0.0212	0.0049
Decay rate η_a (%)	0	10.31	40.82	44.25	42.19	50.99	88.73
Displacement (mm)	0.0109	0.0095	0.0052	0.0045	0.0027	–	–
Decay rate η_s (%)	0	12.88	52.61	58.57	75.35	–	–

From Table 6, it can be seen that the attenuation rate of vibration acceleration increases from the test line 2# to 9#, and the maximum attenuation rate is 88.73%; the attenuation from 2# to 3# has less change, while the attenuation from 2# to 4# is large. For the dynamic displacement, the attenuation from 2# to 6# gradually increases and the maximum attenuation rate is 75.35%, the attenuation tendency is similar to that of vibration acceleration. In general, for the same measuring point which on the section P_2, the attenuation of the vibration acceleration is less than the dynamic displacement.

4 Summary and Conclusion

In this paper, multi-type of EMU testing is performed on the pile-slab subgrade transition section of Shanghai–Kunming high-speed railway, the distribution trend of the maximum and effective values of dynamic response along the longitudinal and lateral of the line are analyzed. The conclusions are as follows:

(1) Under the multi-type of EMU excitation, the maximum value of vibration acceleration on pile-slab structure subgrade surface is 3.77 m/s^2 < 4.90 m/s^2, which meets the requirement of " Code for Design of High-Speed Railway (TB 10621-2014)" ($a < 0.5$ g) [22], and the maximum value of dynamic displacement is 0.062 mm < 0.220 mm, which satisfies the requirement of "High-Speed Railway Subgrade Repair Code (TG/GW120-2015)" [25].

(2) Along the longitudinal direction of the down line, the variation coefficient range about the maximum and effective values of the vibration acceleration from the section B to P_3 are 0.41 and 0.48, respectively. The variation coefficient range about the maximum and effective values of the dynamic displacement from the section P_1 to P_3 are 0.68 and 0.54, respectively. It shows that the dynamic response of the pile-slab subgrade is less discrete, and which realizes effectively the goal of smooth transition between the bridge and the tunnel.

(3) The range of EMU type's variation coefficient about the effective value of vibration acceleration along the longitudinal down line is 0.62–2.14, and that of the dynamic displacement is 0.36–0.47, it indicating that the EMU type's influence on vibration acceleration is greater than that on the dynamic displacement.

(4) The dynamic response is gradually attenuated along the lateral subgrade, and the closer to the running line, the greater attenuation of the dynamic response; for the same measuring point, the attenuation of vibration acceleration is less than that of dynamic displacement.

References

1. Zhai W (2016) Vehicle-track coupling dynamics, vol 2, 4th edn. Science Press, Beijing
2. Wang WH (2016) The overview of design of CRTS III slab track on roadbed bridge transition section. J Railway Eng Soc 33(6):49–53, 59
3. Chen X, Lu W, Wang Y (2006) Study on the dynamic response of high speed railway bridge-subgrade transition section. J Vib Shock 25(3):95–98
4. Paixão A, Varandas JN, Fortunato E et al (2018) Numerical simulations to improve the use of under sleeper pads at transition zones to railway bridges. Eng Struct 164

5. Yang C, Sun H, Zhang J-J et al (2013) Dynamic responses of bridge-approach embankment transition section of high-speed rail. J Cent South Univ 20(10):2830–2839

6. Yao S, Albers B, Savidis SA (2013) Influence of different transition zones on the dynamic response of track–subgrade systems. Comput Geotech 48(48):21–28

7. Lei X, Mao L (2004) Dynamic response analyses of vehicle and track coupled system on track transition of conventional high-speed railway. J Sound Vib 271(3):1133–1146

8. Varandas JN, Hölscher P, Silva MAG (2011) Dynamic behaviour of railway tracks on transitions zones. Comput Struct 89(13):1468–1479

9. Banimahd M, Woodward PK (2007) 3-dimensional finite element modeling of railway transitions. In: Proceedings of 9 th international conference on railway engineering, London

10. Banimahd M, Woodward PK, Kennedy J, Medero GM (2011) Behavior of train–track interaction in stiffness transitions. In: Proceeding of the institution of civil engineers-transport

11. Luo Q (2003) Dynamic performance analyses and experiment study on bridge/approach embankment of high-speed railway. Southwest Jiao tong University, Sichuan

12. Connolly DP, Kouroussis G, Woodward PK et al (2014) Field testing and analysis of high speed rail vibrations. Soil Dyn Earthq Eng 67:102–118

13. Connolly DP, Costa PA, Kouroussis G et al (2015) large scale international testing of railway ground vibrations across Europe. Soil Dyn Earthq Eng 71:1–12

14. Zhai W, Wei K, Song X et al (2015) Experimental investigation into ground vibrations induced by very high speed trains on a non-ballasted track. Soil Dyn Earthq Eng 72:24–36

15. Lombaert G, Degrande G, Kogut J et al (2006) The experimental validation of a numerical model for the prediction of railway induced vibrations. J Sound Vib 297(3):512–535

16. Lombaert G, Degrande G (2003) The experimental validation of a numerical model for the prediction of the vibrations in the free field produced by road traffic. J Sound Vib 262(2):309–331

17. Lombaert G, Galvín P, François S et al (2014) Quantification of uncertainty in the prediction of railway induced ground vibration due to the use of statistical track unevenness data. J Sound Vib 333(18):4232–4253

18. Madshus C, Kaynia AM (2000) high-speed railway lines on soft ground: dynamic behaviour at critical train speed. J Sound Vib 231(3):689–701

19. Ribeiro CA, Rui C, Delgado R (2017) Experimental assessment of the dynamic behavior of the train-track system at a culvert transition zone. Eng Struct 138:215–228

20. Feng SJ, Zhang XL, Wang L et al (2017) In situ experimental study on high speed train induced ground vibrations with the ballast-less track. Soil Dyn Earthq Eng 102:195–214

21. Qu CZ, Wei LM, Wang YH et al (2017) Study on vibration characteristics of closely spaced subgrade-culvert transition sections of high-speed railway before and after commercial operation. Tie dao Xu ebao/J China Railway Soc 39(10):118–125

22. TB10621-2014 Code for design high speed railway. China Railway Publishing House, Beijing 2014

23. Xia H, Zhang N, Cao YM (2005) Experimental study of train-induced vibrations of environments and buildings. J Sound Vib 280(3):1017–1029

24. Zhang GM (2014) Study on the ground vibration induced by trains moving on subgrade of high-speed railway. Southwest Jiao tong University, Sichuan

25. TG/GW120-2015 (2014) Specification for high speed railway subgrade repair. China Railway Corporation, China Railway Publishing House, Beijing

Lower Bound Shakedown Limit Analysis of Slab Railway Tracks: Numerical Approach

Pedro Alves Costa, Patrícia Lopes and António Silva Cardoso

Abstract A procedure for analyzing the shakedown limit load of non-ballasted railway tracks is presented. The shakedown theory is formulated based on the Melan's shakedown lower bound theorem for frictional soils, i.e., adopting the Mohr–Coulomb yielding criteria. The shakedown analysis is enlarged regarding the solutions presented by other authors by incorporating the at-rest stress state in the ground. The 3D cyclic stresses induced by the train passage are computed using an efficient numerical model based on the 2.5D approach. The designed model is then used to perform a numerical study where it is concluded that the increase in the train speed up to the critical speed of the track-ground system is responsible for a significant decrease in the shakedown limit load. Moreover, it is shown that neglecting the at-rest stress state in the ground gives rise to a strong underestimation of the shakedown limit load and that train geometry plays a relevant role in the estimation of the shakedown limit load.

Keywords Permanent railway track deformation · Shakedown limit load · Critical speed

1 Introduction

Recent advances in railway engineering look forward for reliable, efficient and low-maintenance railway infrastructures. Slab track solutions are being nowadays considered the most promising engineering solutions to achieve those goals.

Permanent deformation of slab track solutions is usually lower than on ballasted track due to the absence of ballast. Nevertheless, it is required to guarantee that accumulation of permanent deformations on the foundation due to cyclic loading

P. A. Costa (✉) · P. Lopes · A. S. Cardoso
Construct—Faculty of Engineering, University of Porto, Porto, Portugal
e-mail: pacosta@fe.up.pt

P. Lopes
School of Engineering, Polytechnic Institute of Porto, Porto, Portugal

does not occur or, at least, that remains in an admissible range. If plastic deformation is accumulated at track foundation level, it gives rise to misalignment of the rail and consequent need of geometry correction or, in limit, to the development of pathologies in the concrete elements. The guarantee that this will not happen is the key of the design success, since the main drawback of slab track solutions when compared with ballasted tracks is exactly the difficulty of proceeding to geometry corrections.

Permanent deformation of soils due to cyclic loading is a complex topic. Nevertheless, a significant progress was achieved during last decades, allowing the definition of the main behavior trends as functions of the loading level. Actually, the experimental evidence shows three major categories of behavior [1–4]:

- If the loading level is low and the yielding limit is not achieved, soil shows elastic behavior, i.e., there is not any remaining strain after the load cycling since no plastic deformation originates;
- Increasing load level, an interesting behavior is found; after a finite number of cycles, where permanent deformations are induced, the system starts to show elastic behavior, i.e., the structure is said to have shaken down to a steady permanent strain state and corresponding residual stress. The response to any further cycling is purely elastic, provided that the loads still remain within the given range.
- Contrary to the previous scenario, if non-stabilized plastic deformation develops, some form of progressive failure will occur with the increase in the cycle number. There are basically two types of failures: (a) alternating plasticity, caused by the repeated development of plastic strains for which, the stress–strain curve is hence, ultimately a hysteric loop and the eventual failure is due to low cycle fatigue; (b) incremental collapse, caused by the continued accumulation of plastic strains in the each cycle, leading to progressive increase in permanent displacements and failure of the structure.

In order to prevent excessive permanent deformation in slab track systems (or even its progressive failure), it is important to guarantee that loading is below the elastic shakedown limit. The assessment of this load limit is not trivial, demanding for extensive computational resources, mainly when 3D configurations are engaged, since the whole loading time-history needs to be taken into account. However, alternatively to the use of time-marching approaches, where the plastic deformation induced by each single cycle is taken into account, the so-called direct methods constitute an elegant engineering approach, although usually exact solution cannot be achieved since they correspond to limit analysis approaches [5], based on lower bound [6] or upper bound [7] theorems.

Shakedown theory achieved one of its major applications in pavement engineering, where relevant progresses had been reported over latter years [1–4, 8–11]. Nevertheless, the application of shakedown analysis in the context of railway engineering is quite limited, deserving mention the recent studies presented by Zhuang and Wang [12] and Wang et al. [13]. The present study uses the lower bound shakedown solution for cohesive frictional half spaces under moving loads

presented by Yu and Wang [9]. However, a generalization of the shakedown analysis is made in order to take into account the at-rest stress state.

2 Shakedown Concept

When an elasto-plastic body is subjected to a cyclic load with an amplitude larger than the elastic load limit, it starts to show yielding, i.e., plastic deformations remain after the load application. However, it is seen that for certain load amplitude, this plastic deformation accumulation does not happen infinitely. Actually, when the body is subjected to a load that is lower than that limit, but larger than the elastic limit, after the accumulation of permanent deformation during a finite number of cycles, the body starts to show elastic response again, i.e., there is no accumulation of permanent deformation anymore. This means that an adaptation of the mass behavior occurs, or, by other words, the mass shakedown to the load level. This behavior is justified by the fact that not only plastic strains remain after one load cycle, but also residual stresses. The key point is the assessment of the load that is compatible with shakedown state, since if the load exceeds that limit, the shakedown does not occur, and either the permanent strains settle into a closed cycle—a situation known as "cyclic" or "alternating plasticity"—or they go on increasing indefinitely—known as "ratchetting." If either of these latter situations occurs, the structure will "fail" [1].

The lower bound theorem or Melan's static shakedown theorem prescribes that an elastic perfectly plastic (with associated flow rule) body will shakedown if it is possible to find a self-equilibrated, time-independent, residual stress field that combined with the cyclic elastic stresses and possible static elastic stresses (at-rest stresses) gives rise to a stress field that nowhere and no-time violates the yielding criteria. By other words, shakedown will occur if the following condition is respected for any time and at any location of the body under analysis:

$$f\left(\lambda\sigma_{ij}^{e} + \sigma_{ij}^{0} + \sigma_{ij}^{r}\right) \leq 0 \tag{1}$$

where $f(.)$ represents the yielding criteria; the static stresses, as for instance the at-rest stress state, is represented by σ_{ij}^{0}, the elastic stresses induced by a cyclic loads are given by $\lambda\sigma_{ij}^{e}$, where λ is a load factor of the stress field generated by a fundamental loading scenario, and the residual stress field is given by σ_{ij}^{r}.

Since the yielding condition must be time-independently respected, it means that the sum of residual and static stresses must give rise to a stress state compatible with the yielding criteria. Therefore, the maximum value λ that respects Eq. (1) corresponds to the lower value of the shakedown multiplier.

The application of lower bound shakedown theorem demands the assessment of realistic elastic stresses in the body under analysis. The following section briefly presents an accurate and efficient numerical approach for the assessment of elastic stress fields due to railway traffic.

3 A Numerical Approach for the Assessment of Ground Elastic Stresses Induced by Railway Traffic

Assuming the track-ground system as an invariant and infinitive domain along the longitudinal direction, the 3D elastic dynamic response induced by the traffic can be achieved assuming a 2.5D approach. Taking into account the mentioned restrictions, it is possible to apply a spatial Fourier transformation along that direction and to determine the 3D displacement field as a continuous integral of simpler bi-dimensional solutions, as

$$u^{3D} = \frac{1}{2\pi} \int\limits_{-\infty}^{+\infty} u^{2.5D}(k_1) e^{-ik_1(x-x_0)} dk_1 \tag{2}$$

where k_1 is the longitudinal wave number.

Therefore, the 3D problem solution is obtained by the combination of the 2.5D solutions for distinct wave numbers. Due to the complexity of the cross section geometry, the 2.5D solution requires the use of a numerical technique. In the present study, the 2.5D FEM is the elected technique, being only necessary the cross section domain discretization since the longitudinal direction (x—direction) is transformed to the wave number domain. So, the 2.5D equilibrium equations can be written in FEM sense as follows:

$$\left(\int\limits_z \int\limits_y B^T(-k_1) D B(k_1) \, dy \, dz - \omega^2 \int\limits_z \int\limits_y N^T \rho N \, dy dz \right) u_n(k_1, \omega) \tag{3}$$
$$= p_n(k_1, \omega)$$

Adopting the classic finite elements notation leads to,

$$[K(k_1)] = \int\limits_z \int\limits_y N^T L^T(-k_1) \, D \, L(k_1) N \, dy \, dz \tag{4}$$

and

$$[M] = \int\limits_z \int\limits_y N^T \rho N \, dy \, dz \tag{5}$$

where $[K]$ and $[M]$ are the stiffness and mass matrices, respectively.

Since the finite element approach demands the complete definition of a boundary for the interesting domain, special treatments must be adopted along artificial

boundaries to fulfill the Sommersfeld's condition. In the present approach, 2.5D PML (perfectly matched layers) is adopted [14]. The PML elements are formulated in a FEM basis taking into account the stretching of coordinates inside of the PML layer to the complex domain. The following relationships between natural and complex coordinates are adopted:

$$\tilde{y} = \int_0^y \lambda_y(y) \mathrm{d}y \tag{6}$$

$$\tilde{z} = \int_0^z \lambda_z(z) \mathrm{d}z \tag{7}$$

where λ_x and λ_y are the stretching functions in y and z directions, respectively. Concerning the derivatives, it is also possible to find the following relationships:

$$\frac{\partial}{\partial \tilde{y}} = \frac{1}{\lambda_y(y)} \frac{\partial}{\partial y} \tag{8}$$

$$\frac{\partial}{\partial \tilde{z}} = \frac{1}{\lambda_z(z)} \frac{\partial}{\partial z} \tag{9}$$

A detailed description of the stretching functions used can be found in Lopes et al. [14].

Taking into account the stretching functions expressed above, the PML elements matrices can be derived using the same basic principles of FEM.

In a 2.5D approach, the moving character of the loading is attended by an elegant way without the need of any special numerical scheme. Actually, taking into account the shift property of Fourier transform, the effect of a moving harmonic load (moving along the longitudinal direction) is obtained considering the following relationship between frequency and wave number [15, 16]:

$$\omega = \Omega - k_1 c \tag{10}$$

where Ω and c are the driven frequency and speed, respectively.

If only the quasi-static excitation mechanism is considered, the load magnitude is constant over time, so $\Omega = 0$. Moreover, in that case, the time and loading position are also related and the dynamic response can be expressed in the moving reference frame:

$$s = x - ct \tag{11}$$

4 Assessment of the Shakedown Limit Trough the Lower Bound Theorem

Equation (1) can be rewritten taking into account the moving reference frame defined in the last section:

$$f\left(\lambda \sigma_{ij}^{e}(s) + \sigma_{ij}^{0} + \sigma_{ij}^{r}\right) \leq 0 \qquad (12)$$

where σ_{ij}^{e} is the cyclic elastic field induced by loading P, σ_{ij}^{0} is the at-rest stress field, σ_{ij}^{r} is the residual stress field, s is given by Eq. (11) and $f(.) = 0$ is the yield condition of the soil. Obviously, the residual stress field must be statically equilibrated and time independent [or s independent according to Eq. (11)] [4, 9].

The largest value of λ obtained by searching all possible self-equilibrated residual stress fields will give the actual shakedown limit $P_{sd} = \lambda_{sd}P$ [4]. Therefore, the key aspect is to conceive a residual stress state that is compatible with the restrictions expressed above: It needs to be self-equilibrated, time independent and its conjunction with the at-rest stress state must give rise to a total stress state that does not violate the yielding criteria. Several residual stress fields can fulfill those assumptions, but it should be physically reasonable in order to find a lower bound solution closest as possible to the true one [4, 8, 9, 11].

As already mentioned, if the soil is homogeneous and isotropic and if the dynamic excitation mechanics induced by the train passage is neglected, the dynamic response can be expressed at a moving reference frame instead of the time and longitudinal coordinate. Therefore, in order to obtain a time-independent residual stress field, it will be mandatory independent of the longitudinal direction. Yu [4] and more recently Yu and Wang [9] shown that for moving three-dimensional Hertz pressure distribution, the critical plane should be defined by y = constant (y—direction is the horizontal direction normal to the direction of the movement), demonstrating that the plane $y = 0$ is the most critical one. A detailed description of the procedure to achieve that conclusion can be found in Yu [4], and the same assumptions will be here followed.

Since the plane defined by $y = 0$ is a plane of symmetry of the track-ground system, the cyclic elastic shear stresses τ_{yz}^{e} and τ_{yx}^{e} are null and time-independent. Therefore, assuming that σ_{xx}^{0}, σ_{zz}^{0} and σ_{yy}^{0} are principal stresses of the at-rest stress field, the residual shear stresses τ_{yz}^{r} and τ_{yx}^{r} need to be obligatory also null. Moreover, since the τ_{xz}^{e} path is antisymmetric regarding time, it is not possible to find a time-independent residual stress value for this stress component [4]. Regarding the normal components of the residual stress state, equilibrium condition demands that component σ_{zz}^{r} must be null. Therefore, the only non-null residual stress components are σ_{xx}^{r} and σ_{yy}^{r}, so, the total stress in the symmetry plane of the track-ground system can be defined by:

$$\sigma_{zz}(s) = \lambda\sigma_{zz}^e(s) + \sigma_{zz}^0 \tag{13}$$

$$\sigma_{xx}(s) = \lambda\sigma_{xx}^e(s) + \sigma_{xx}^0 + \sigma_{xx}^r \tag{14}$$

$$\sigma_{yy}(s) = \lambda\sigma_{yy}^e(s) + \sigma_{yy}^0 + \sigma_{yy}^r \tag{15}$$

$$\tau_{xz}(s) = \lambda\tau_{xz}^e(s) \tag{16}$$

Since σ_{yy}^r is defined as an arbitrary function of depth and $\sigma_{xx}^0 = \sigma_{yy}^0$, it is possible to guarantee that σ_{yy} is the intermediate principal stress for any location in the plane defined by $y = 0$.

The total stress field defined by expressions (13)–(16) must respect the yielding condition expressed by Eq. (12). Therefore, adopting the Mohr–Coulomb criterion, defined by the cohesion c and friction angle ϕ, the following inequality must be met:

$$\sqrt{\left(\lambda\sigma_{xx}^e(s) + \sigma_{xx}^0 + \sigma_{xx}^r - \lambda\sigma_{zz}^e(s) - \sigma_{zz}^0\right)^2 + 4\left(\lambda\tau_{xz}^e\right)^2}$$
$$+ \left(\lambda\sigma_{xx}^e(s) + \sigma_{xx}^0 + \sigma_{xx}^r + \lambda\sigma_{zz}^e(s) + \sigma_{zz}^0\right)\sin(\varphi) \leq 2c\cos(\varphi) \quad \forall s \tag{17}$$

As shown by Yu and Wang [9], the above inequality, now extended to include the at-rest stress field, can be written as:

$$f = \left(\sigma_{xx}^r + M(s)\right)^2 + N(s) \leq 0 \tag{18}$$

where:

$$M(s) = \lambda\left(\sigma_{xx}^e(s) - \sigma_{zz}^e(s)\right) + \left(\sigma_{xx}^0 - \sigma_{zz}^0\right) + $$
$$+ 2\tan(\varphi)\left(c - \left(\lambda\sigma_{zz}^e(s) + \sigma_{zz}^0\right)\tan(\varphi)\right) \tag{19}$$

$$N(s) = 4\left(1 + \tan^2(\varphi)\right)\left[\left(\lambda\tau_{xz}^e(s)\right)^2 - \left(c - \left(\lambda\sigma_{zz}^e(s) + \sigma_{zz}^0\right)\tan(\varphi)\right)^2\right] \tag{20}$$

In order to respect inequality (18), N must be negative, which means that:

$$\lambda \leq \frac{c - \sigma_{zz}^0\tan(\varphi)}{\left|\tau_{xz}^e\right| + \sigma_{zz}^e(s)\tan(\varphi)} \tag{21}$$

Please note that negative stresses mean compression.

The lower and upper values of possible residual stresses that permit respect Eq. (21) can also be obtained:

$$\max\left(-M(s) - \sqrt{-N(s)}\right) \leq \sigma_{xx}^r \leq \min\left(-M(s) + \sqrt{-N(s)}\right) \qquad (22)$$

Since the residual stresses are function of depth, the above-mentioned condition needs to be checked for different depth locations.

Moreover, the residual stress field combined with the at-rest stress field (static) must satisfy the yield condition (the yielding condition must be respected after the passage of the load), therefore:

$$\begin{aligned}
&\frac{2c\cos(\varphi)}{\sin(\varphi) - 1} + \sigma_{zz}^0 \frac{1 + \sin(\varphi)}{1 - \sin(\varphi)} - \sigma_{xx}^0 \leq \sigma_{xx}^r \leq \frac{2c\cos(\varphi)}{1 + \sin(\varphi)} \\
&+ \sigma_{zz}^0 \frac{1 - \sin(\varphi)}{\sin(\varphi) + 1} - \sigma_{xx}^0
\end{aligned} \qquad (23)$$

Taking into account the restriction expressed in (22) and (23), the shakedown limit load is assessed by an optimization procedure in order to find the maximum valor of λ that gives rise to a self-equilibrated, time-independent, and statically admissible residual stress field for whole domain. Since both elastic cyclic and at-rest stress fields are depth dependent, a first search should be done for each depth in order to find the maximum value of λ, λ_{zi}, that allows the restrictions fulfillment. The shakedown limit load is given by the minimum value of λ_{zi} multiplied by the reference loading P.

5 Numerical Application

5.1 General Description of the Model

For the present study, the track-ground system depicted in Fig. 1a is selected. It refers to a continuous slab track founded in a homogeneous half-space. Mechanical and geometrical characteristics of the system are also depicted in the same figure. Figure 1b shows the cross section of the 2.5D FEM-PML model adopted.

Following the simplified approach proposed by Alves Costa et al. [17], the critical speed of the system, i.e., the speed of a unitary load that gives rise to the largest amplification of the track displacements, is around of 114 m/s.

In following sections, a discussion about the influence of several parameters on shakedown limit load is presented.
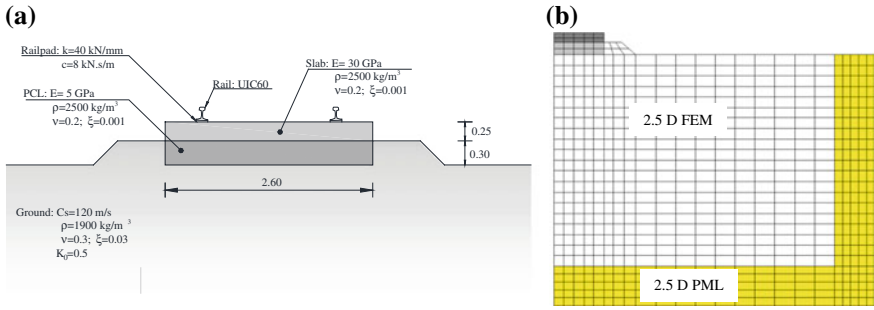
Fig. 1 Track-ground model properties: **a** general geometry and properties; **b** 2.5D FEM-PML mesh

5.2 Influence of the Train Speed and Soil Properties

The influence of the train speed in the dynamic response of the railway track has been the goal of investigation of several studies [17–20]. However, almost those studies have been focused on the analysis of critical velocity of the system and on the assessment of the dynamic amplification of the track movements due to the increase in the train speed. Nevertheless, as shown by Alves Costa et al. [19], the increase of the train speed is not only reflected by the amplification of the track movements, since this effect is accompanied by a worsening of the strains and stresses in the ground. Consequently, it is expected that the dynamic effects generated by the train speed increase should play a relevant role on the elastic shakedown limit. This effect is highlighted in Fig. 2a where the evolution of the shakedown limit with a single load ($P = 1$ kN) speed is represented for different values of the soil cohesion. In Fig. 2b, the shakedown ratio, i.e., the shakedown limit divided by the shakedown limit for static conditions is also represented.
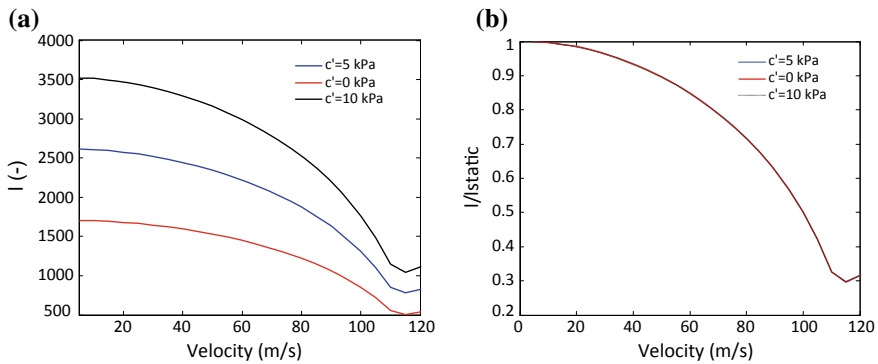
Fig. 2 Evolution of the shakedown limit factor with the load speed increase for different values of soil cohesion: **a** shakedown limit versus speed; **b** shakedown ratio versus speed ($\phi = 30°$)

From Fig. 2, it is clear that the shakedown factor is clearly affected by the load speed. The increase of the load speed gives rise to amplification of the cyclic dynamic stresses in the ground implying a decrease in the shakedown factor, which achieves a minimum around the critical velocity of the system. Since shakedown limit is dependent on the soil strength properties, higher values are achieved for larger cohesion, as highlighted in Fig. 2a. Nevertheless, the results depicted in Fig. 2b show that the trend for the reduction of the shakedown limit factor with the increase of the train speed is independent of the cohesion of the soil.

To better understand the effect of the residual stresses on preventing the violation of the yielding criteria, Fig. 3 shows the stress path of the point of the soil located at 0.2 m depth for the situations: scenario B, where the residual stresses are taken into account; scenario A, where the residual stresses are neglected. The stress paths now illustrated refer to the passage of a load of 1000 kN at a speed of 60 m/s.

If the residual stresses are neglected, the stress path achieves states that are statically non-admissible, i.e., the yielding criteria is violated which means that the stress field is not possible, having place to stress redistribution and accumulation of plastic strains. Meanwhile, it is clear that the consideration of the residual stresses allows achieving a statically admissible stress path, justifying the elastic response of the system after a finite number of cycles (the number of cycles needed to install the residual stresses). In the same figure, it is also represented the stress path induced by a load correspondent to the shakedown limit state ($P = 2218$ kN).

An innovative aspect of the present work when compared with the studies performed by Yu et al. [9], and more recently by Wang et al. [13], is the inclusion of the at-rest stress state in the shakedown limit computation. Since Mohr–Coulomb
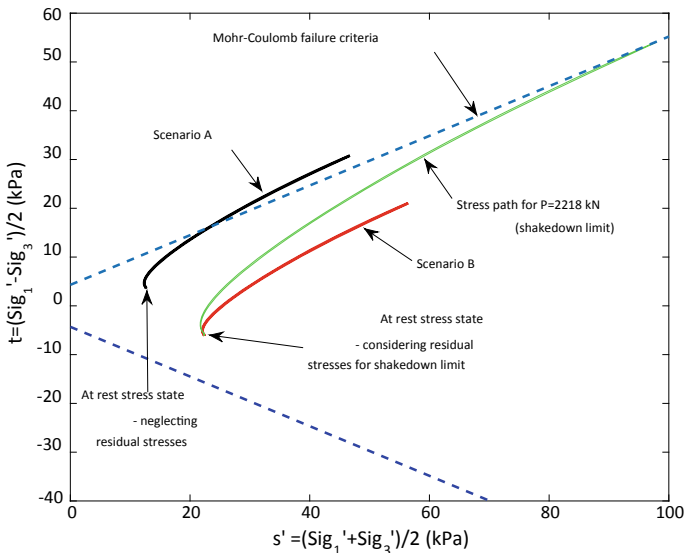
Fig. 3 Stress paths due to the passage of a load of 1000 kN ($\phi = 30°$; $c' = 5$ kPa)

yielding criteria is adopted, the initial stresses play a relevant influence due to the fact that for non-null shear resistance angles the soil strength is dependent on the mean effective stress. Figure 4 shows the evolution of the shakedown factor with the train speed for the scenarios considering or neglecting the at-rest stress state. Taking into account Eq. (21), it is easy to justify the differences shown in Fig. 4. The influence of the at-rest stress state in the shakedown limit will be more pronounced with the increase in the shear friction angle and with the decrease in the soil cohesion.

5.3 Influence of Train Geometry

The results showed above refer to the passage of a single load. However, due to the proximity between the different wheelsets of the train, there is an "adding" effect on the dynamic cyclic stresses induced by the different wheelsets. Figure 5 shows the stress σ_{zz} (divided by P) along the alignment located at a depth of 0.2 m (measured from the natural ground reference) for 3 distinct load schemes: (i) a single load; (ii) a loading scenario compatible with the geometry of one vehicle (all loads are equal); (iii) a loading scenario compatible with two vehicles (all loads are equal).

Due to the proximity between the loads, in correspondence to the wheelsets sharing the same bogie, and due to the high bending stiffness of the slab, there is a notorious "adding" effect on the cyclic dynamic stresses induced by the close wheelsets. Therefore, since the shakedown limit is dependent on the dynamic cyclic stresses, the geometry of the train plays a relevant role. Figure 6 shows the evolution of the shakedown limit with the train speed for different geometric configurations: (i) a single wheelset; (ii) a typical geometrical configuration of a passenger train (geometry of Portuguese Alfa Pendular train).

Fig. 4 Influence of the at-rest stress state in the shakedown limit ($\phi = 30°$; $c = 5$ kPa)
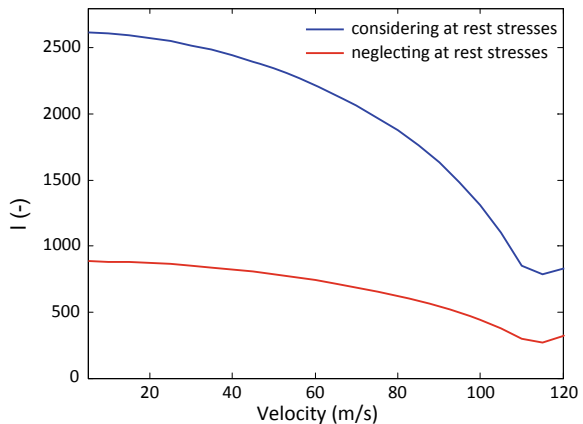
Fig. 5 Vertical normal
stresses induced by the
passage of different loading
geometry combinations at a
speed of 40 m/s
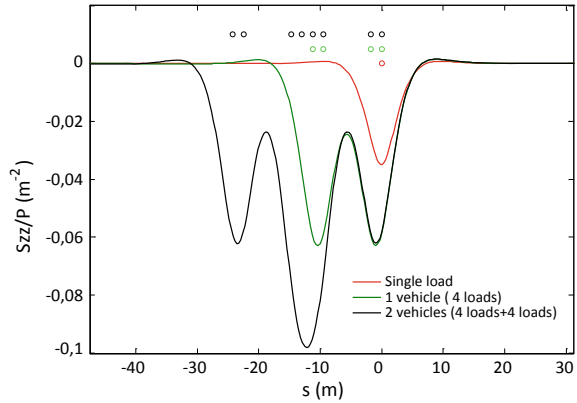
Fig. 6 Evolution of the
shakedown limit factor for
different train geometry
configurations ($\phi = 30°$;
$c = 5$ kPa)
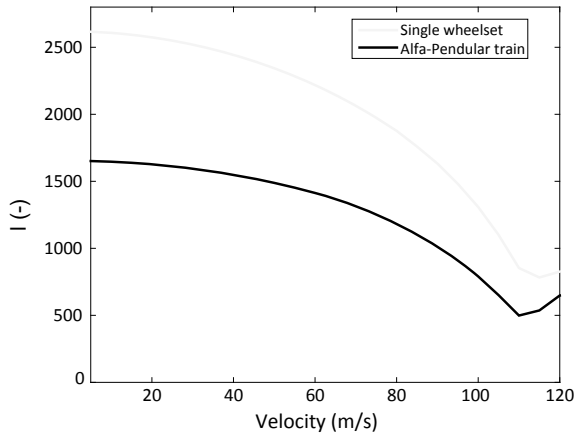
The analysis of Fig. 6 permits to conclude that shakedown limit is dependent on
the train geometry. This effect is quite obvious for static conditions, since for almost
null train speed the shakedown limit is strongly affected by the interaction effect
induced by the different wheelsets. More interesting than that is the fact that the
geometry of the train affects not only the shakedown limit for static conditions, but
also the trend of the evolution of the shakedown limit with the train speed.
Therefore, for engineering practice it is relevant to take into account the train
geometry when dealing with the definition of shakedown limits.

6   Conclusions

A procedure for the assessment of the shakedown limit load of slab railway tracks is proposed. Comparing with previous studies, the solution is improved to take into account the at-rest stress state installed in the ground and the dynamic amplification effects induced by the train speed. Since Melan's theorem was adopted in the investigation of the limit shakedown load, a reliable estimation of the cyclic elastic stresses induced by the train passage in needed. This step is fulfilled adopting a 2.5D FEM-PML efficient numerical model that was previously developed by authors.

From the developed numerical parametric study, it is shown that the shakedown limit load is strongly affected by the train speed, achieving a minimum value when the train speed reaches the critical speed of the system, independently of the cohesion or friction angle of the soil. Moreover, it was shown that the train geometry affects the shakedown limit load.

The approach depicted along this paper can be followed for a more rational design, adopting optimized and robust engineering solutions.

References

1. Collins IF, Boulbibane M (2000) Geomechanical analysis of unbound pavements based on shakedown theory. J Geotech Geoenviron Eng 126(1):50–59
2. Boulbibane M et al (2000) Shakedown analysis of anisotropic asphalt concrete pavements with clay subgrade. Can Geotech J 37:882–889
3. Brown SF et al (2012) Validation experiments for lower-bound shakedown theory applied to layered pavement systems. Géotechnique 62(10):923–932
4. Yu HS (2005) Three-dimensional analytical solutions for shakedown of cohesive-frictional materials under moving surface loads. Proc R Soc A: Math Phys Eng Sci 461:1951–1964
5. Maier G (2001) On some issues in shakedown analysis. J Appl Mech 68:799–808
6. Melan E (1938) Der spannungsgudstand eines Henky-Mises schen Kontinuums bei Verlandicher Belastung. Sitzungberichte der Ak Wiss Wie 147:73
7. Koiter WT (1960) General theorems for elastic-plastic solids. In: Sneddon IN, Hill R (eds) Progress in solid mechanics. North Holland, Amsterdam, pp 165–221
8. Wang J, Yu HS (2014) Three-dimensional shakedown solutions for anisotropic cohesive frictional materials under moving surface loads. Int J Numer Anal Method Geomech **38** (331–348)

9. Yu H-S, Wang J (2012) Three-dimensional shakedown solutions for cohesive-frictional materials under moving surface loads. Int J Solids Struct 49(26):3797–3807
10. Liu S et al (2016) Shakedown solutions for pavements with materials following associated and non-associated plastic flow rules. Comput Geotech 78:218–226
11. Wang J, Yu HS (2013) Residual stresses and shakedown in cohesive-frictional half-space under moving surface loads. Geomech Geoeng 8(1):1–14
12. Zhuang Y, Wang K (2017) Three-dimensional shakedown analysis of ballasted railway structures under moving surface loads with different load distributions. Soil Dyn Earthq Eng 100:296–300
13. Wang J, Liu S, Yang W (2018) Dynamics shakedown analysis of slab track substructures with reference to critical speed. Soil Dyn Earthq Eng 106:1–13
14. Lopes P et al (2013) Numerical modeling of vibrations induced in tunnels: a 2.5D FEM-PML approach. In: Xia H, Calçada R (eds) Traffic induced environmental vibrations and controls: theory and application. Nova, pp 133–166
15. Grundmann H, Trommer E (2001) Transform methods - what can they contribute to (computational) dynamics? Comput Struct 79:2097–2102
16. Alves Costa P, Calçada R, Silva Cardoso A (2012) Track–ground vibrations induced by railway traffic: In-situ measurements and validation of a 2.5D FEM-BEM model. Soil Dyn Earthq Eng 32(1):111–128
17. Alves Costa P et al (2015) Critical speed of railway tracks. Detailed and simplified approaches. Transp Geotech 2:30–46
18. Madshus C, Kaynia M (2000) High-speed railway lines on soft ground: dynamic behaviour at critical train speed. J Sound Vib 231(3):689–701
19. Alves Costa P et al (2010) Influence of soil non-linearity on the dynamic response of high-speed railway tracks. Soil Dyn Earthq Eng 30(4):221–235
20. Mezher SB et al (2016) Railway critical velocity—analytical prediction and analysis. Transp Geotech 6:84–96

Influence of Subgrade Settlement on Dynamic Characteristics of CRTS II Slab Orbit

Qing-song Feng and Bo Peng

Abstract In this paper, considering the structure and technical characteristics of CRTS-II-type slab track, we simplified the vehicle system and the track system accordingly, and by the method of coupling dynamics of wheel and rail system and finite element, as well as the help of ABAQUS finite element software, a vertical dynamic analysis model of vehicle-track-subgrade coupling is established. And the geometric irregularity of orbit is used as the source of system excitation, To study the influence of dynamic characteristics of vehicle–track system and system considering the long-wave irregularity and short-wave irregularities, uneven settlement, subgrade under different speed, on the basis of this study, some reasonable suggestions are put forward for the design of the future track structure.

Keywords CRTS II slab track · Track irregularity · Subgrade uneven settlement · Dynamic characteristics

1 Introduction

CRTS II slab track is widely used on high-speed railway in China for its high stability, high smoothness, slow track deformation, low maintenance, and low maintenance cost [1]. However, when laying ballastless tracks on roadbeds, due to the relatively low bearing capacity of roadbeds, they are sensitive to dynamic loads and water erosion. Under the combined effects of complex loads such as trains and the environment, uneven settlement will inevitably occur. At the same time, the high-speed railway has extremely stringent requirements for the smoothness of the line. When the subgrade is unevenly settled, the upper track structure will be seriously affected by the uneven settlement, and the track surface will be less smooth. In severe cases, there will also be empty cranes directly affecting the train. The safety and comfort of the train operation and the additional stress of the

Q. Feng · B. Peng (✉)
East China Jiaotong University, Nanchang 330013, China
e-mail: 1263945498@qq.com

ballastless track structure would be significantly increased under the condition of high-speed operation and thus affect its service performance. Continued service in the event of such a disease may affect passenger comfort and train safety.

In recent years, many scholars at home and abroad have paid great attention to such issues and have obtained a lot of research results. For example, Lombaert [2] established a three-dimensional model of vehicle–orbit coupling dynamics to study the effects of stiffness changes in rail structures and wheel–rail irregularities on the vibration response of rail systems. Zhu [3] established a finite element analysis model for CRTS II slab-type ballastless track embankment, studied deformation and stress of CRTS II slabless ballast slab under temperature loading as well as deformation of rails caused by deformation of orbital plates, and established the selection basis and method of element structure type, subgrade model and material parameters, and analysis of the influence of rail deformation on vehicle operation safety; Song and Bian [4] took the role of the CA mortar layer and the concrete cushion into account seriously based on the existing vehicle–orbit vertical coupling dynamic model and analyzed the correlation between the settlement of the roadbed and the running speed of the train; Li and Zhou [5] established the CRTS I plate-type ballastless track-subgrade system model to analyze the influence of uneven subgrade settlement on the dynamic characteristics of the coupled system; Zhai [6] studied the geometrical shape of the railway line in the actual application process and found that it often shows obvious randomness when affected by many factors; Zakeri [7] established a partially unsupported coupled analysis model of vehicle and track dynamics for the case of sleeper overhangs and simplified the wheel–rail contact as a nonlinear spring to study the dynamic response of the track structure. It can be seen that the current research at home and abroad mainly focuses on the mechanical properties of CRTS II slab orbits under the effects of track deformation, irregularity, and uneven settlement, while the influence of uneven settlement on the dynamic response of vehicle-track-subgrade system under uneven conditions is seldom studied.

2 Model Establishment

Based on the dynamics of the wheel–rail coupled system and the finite element method [8], this paper uses ABAQUS to establish the vertical vibration calculation model of the vehicle-track-subgrade coupling system. The entire system is divided into two subsystems: the upper vehicle model and the lower rail model system. The upper vehicle consists of the body, bogies, wheelsets, and first and second spring-damper systems. The lower track is composed of rail, fastener system, track plate, CA mortar, base plate, and subgrade. Considering the coupling between the two subsystems, and through the establishment of the corresponding geometric compatibility and force balance conditions at the wheel–rail contact surface, we obtained the dynamic response of the coupled system by using the iterative method to cross-solve the two subsystems. The model is shown in Fig. 1.
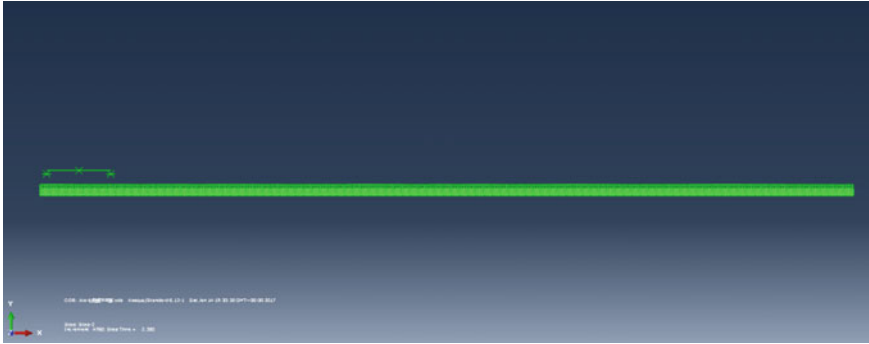
Fig. 1 Vertical vibration model of vehicle-track-subgrade coupling system established in ABAQUS

3 Effect of Track Irregularity on Rail Vibration

Under normal conditions, the geometrically uneven composition of ballastless tracks is very complex. Fundamentally speaking, the geometric irregularity of the track is a random process, and it is also a random function of the railway line coordinates. The track irregularity of any line segment can be seen as a function of a specific random process. In order to simplify the track irregularity, it can be treated as a stationary random process. The statistical characteristics and regularity of the track irregularity can be represented by the amplitude and wavelength of the irregularity, that is, the irregularity of the power spectrum introduced into the track. At present, many countries in the world have conducted different degrees of research on track irregularity. For example, China, Germany, and the USA have studied and measured the power spectrum of track irregularity for many years and established corresponding density functions and evaluation criteria of power spectrum for track irregularity. To comprehensively compare the orbit spectrums of various countries, it is believed that the orbit spectrum of Germany has been relatively mature after many years of theoretical and experimental research. Moreover, China's high-speed railways have been developed on the basis of the German high-speed railway to some extent. Therefore, the rail spectrum of China's high-speed railway is similar to that of Germany's high-speed railway to some extent. Therefore, in this section, the low-interference spectrum of the German track irregularity is used when calculating the orbit spectrum. However, the low-interference spectral density of track irregularity in Germany is mainly medium and long wave, which cannot fully reflect the influence of short-wave random irregularity on the dynamic characteristics of the wheel–rail system.

After the introduction of irregularity, calculate the system vibration response results obtained from the dynamic characteristics of the wheel–rail system at a vehicle speed of 300 km/h; see Figs. 2, 3, 4, 5, and 6.

Fig. 2 Time history of
vehicle body vertical
acceleration
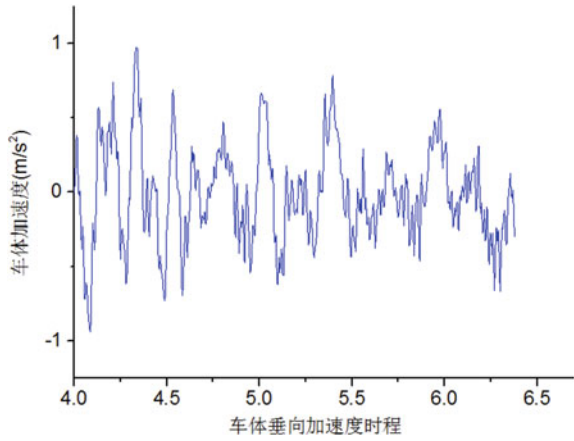
Fig. 3 Time history curve of
rail vertical acceleration
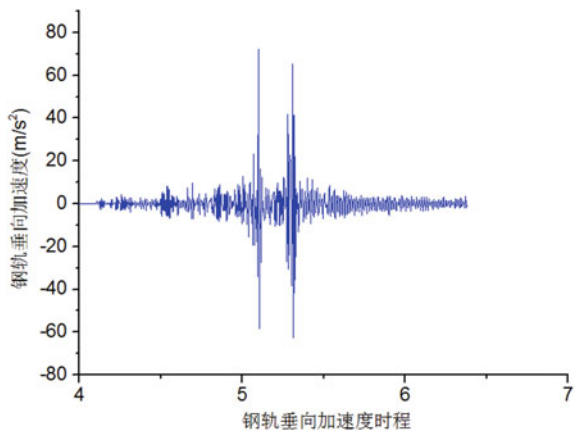
Fig. 4 Rail vertical
displacement
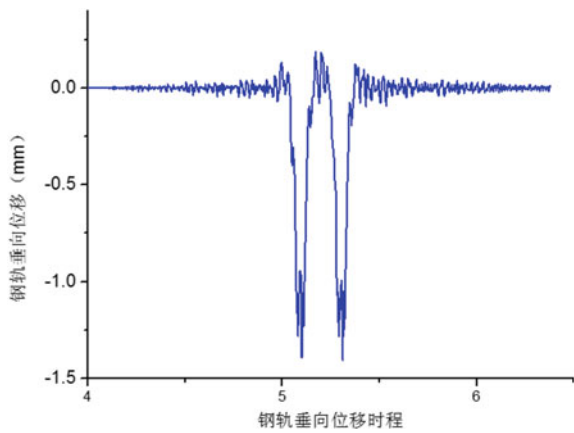
Fig. 5 Slab vertical acceleration
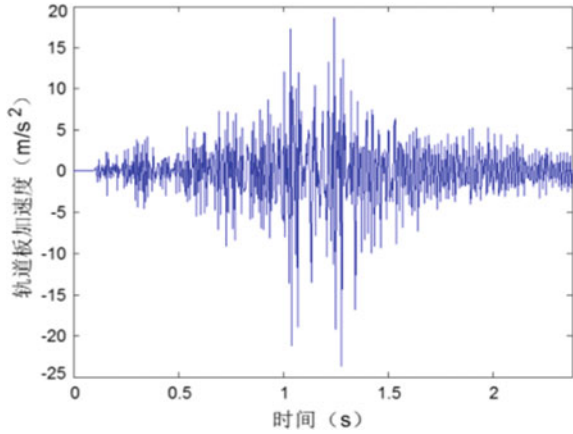
Fig. 6 Slab vertical displacement
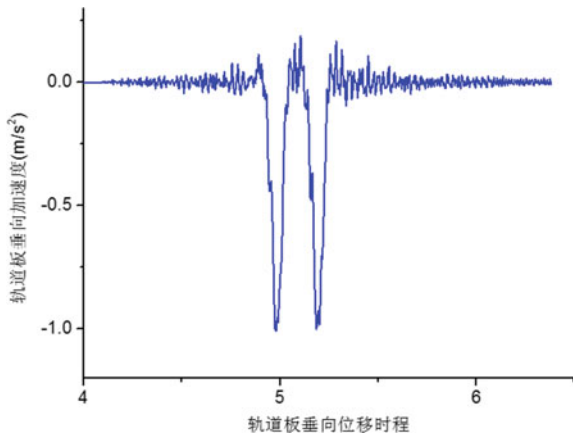
4 Effects of Different Settling Wavelengths on Rail Vibration

At present, for non-uniform settlement curves of ballastless road base sections, we recommend using a (positive) cosine-based deformation-influencing curve with a wavelength of 20 m. The cosine-type uneven settlement curve to be used in this section is shown in Fig. 7. Assume that the deformation of the concrete base plate caused by the uneven subsidence of the subgrade is a full-wavelength cosine-type settlement. The expression is:

$$
y(x) = \begin{cases} 0 & x < x_0, x > x_0 + L_s \\ \frac{H_s}{2}\left[1 - \cos\left(\frac{2\pi(x-x_0)}{L_s}\right)\right] & x_0 < x < x_0 + L_s \end{cases} \tag{4.1}
$$
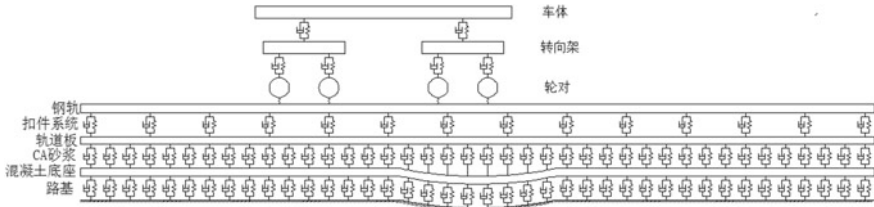
Fig. 7 Vehicle-track-road coupling vibration model for subgrade settlement

Fig. 8 Time history graph of rail vertical acceleration
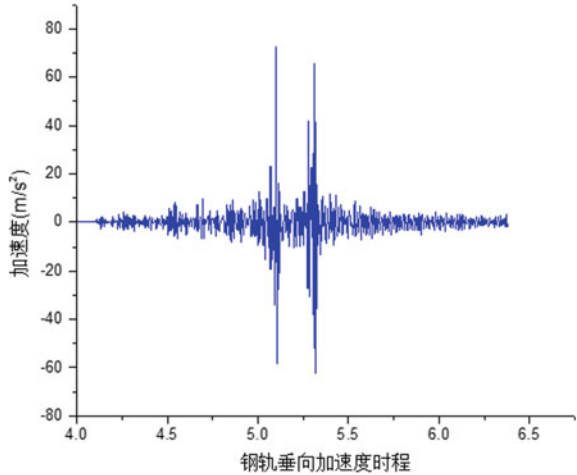
Fig. 9 Time history graph of rail vertical displacement
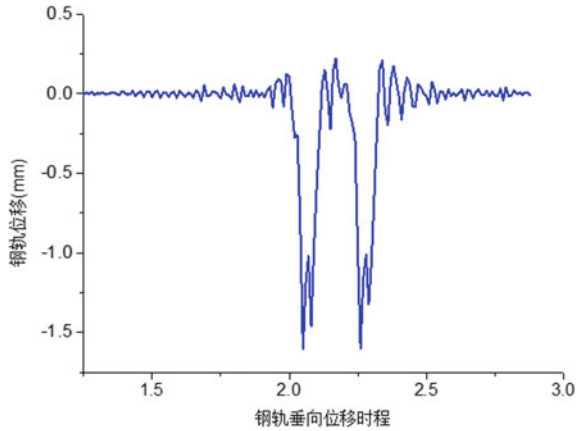
In order to study the influence of uneven cosine-type subsidence on the dynamic characteristics of vehicles and ballastless tracks select the settlement conditions as 15 mm/20 m and the vehicle speed as 300 km/h for dynamic calculation. The dynamic response of the vehicle and track is shown in Figs. 8, 9, 10, and 11.

Fig. 10 Time history graph of track plate vertical acceleration
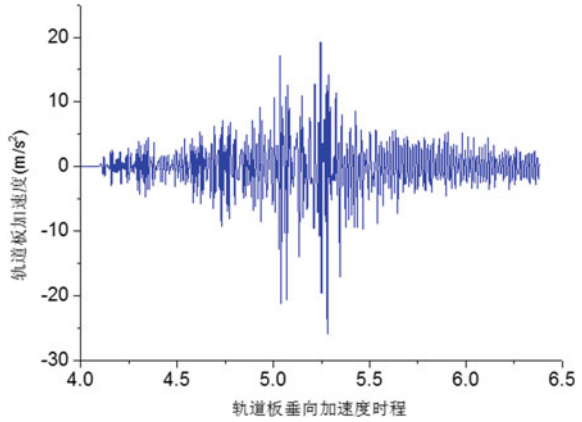
Fig. 11 Time history graph of track plate vertical displacement
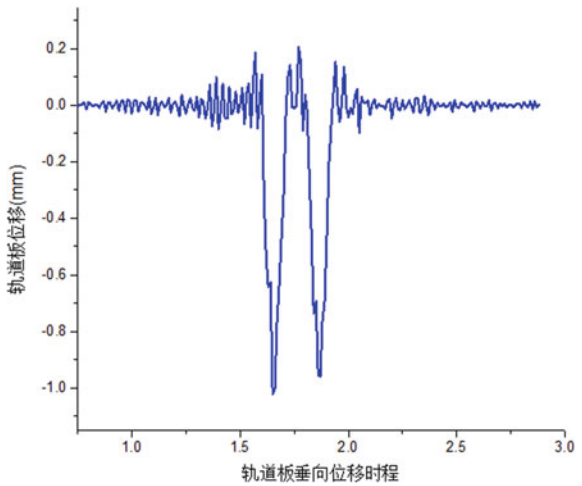
In order to study the cohesion-type differential settlement of the subgrade, the influence of different sedimentation wavelengths on the dynamic characteristics of vehicles and ballastless tracks was investigated. Different sedimentation wavelengths were selected, and the vehicle speed was 300 km/h for kinetic calculations. Settlement wavelength conditions are: 15 mm/10 m, 15 mm/20 m, 15 mm/30 m, and 15 mm/40 m. The changes in the dynamic response of vehicle systems and track systems at different sedimentation wavelengths are shown in Figs. 12 and 13.

Fig. 12 Vertical acceleration
of each section of track
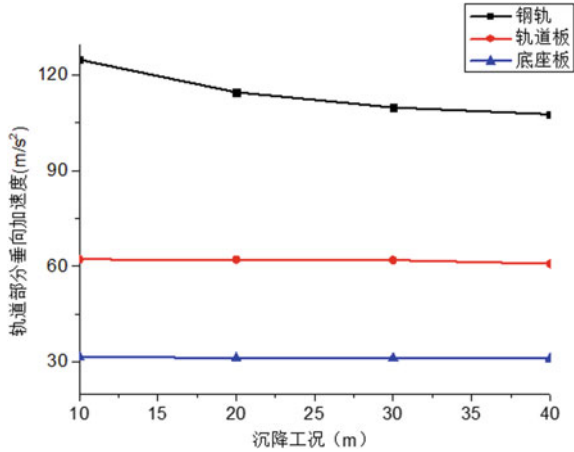
Fig. 13 Vertical
displacement of each section
of track
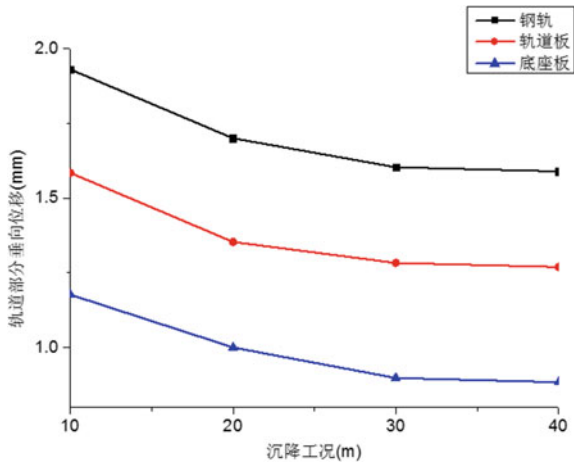
5 Effect of Train Speed on Rail Vibration

In order to study the occurrence of cosine-type differential settlement in the sub-
grade, the influence of different train speeds on the dynamic characteristics of the
vehicle system and the ballastless track system is affected. The settlement condi-
tions are selected as 15 mm/20 m, and the dynamics are calculated at different
vehicle speeds. The speed conditions are: 200, 250, 300, 350, and 400 km/h.
Changes in the dynamic response of vehicle systems and track systems at different
vehicle speeds are shown in Figs. 14, 15, 16, and 17.

Fig. 14 Car body vertical acceleration
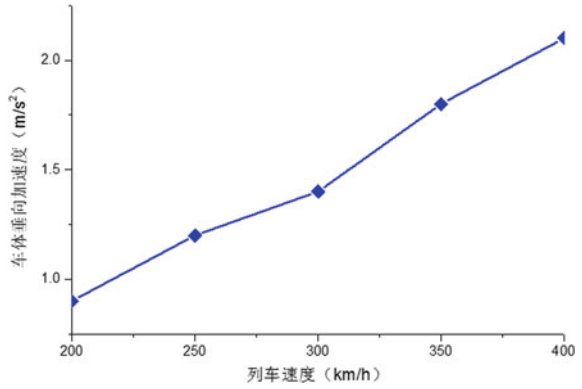
Fig. 15 Wheel–rail vertical force
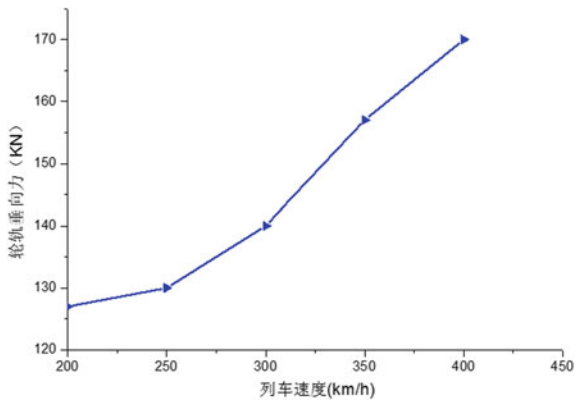
Fig. 16 Vertical acceleration of each section of track
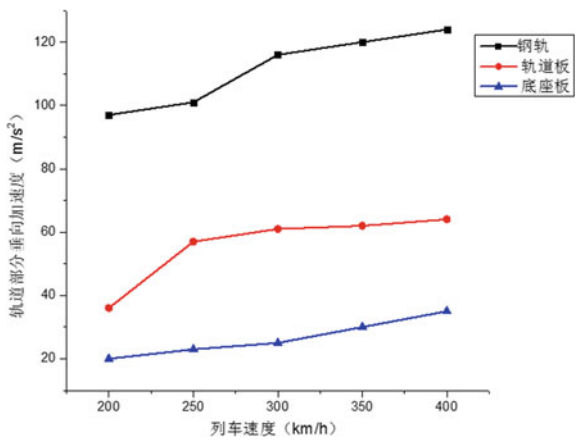
Fig. 17 Vertical
displacement of section
of track
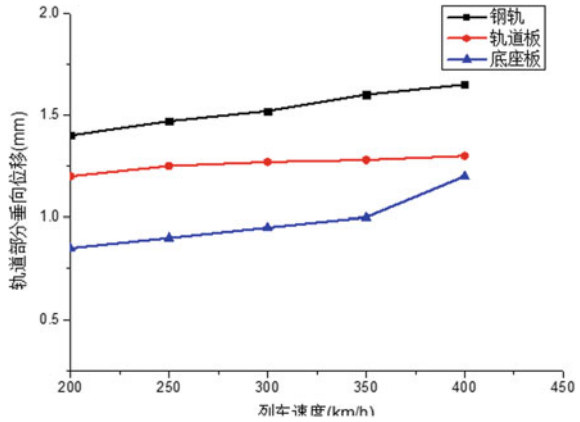
6   Conclusion

Based on the coupled dynamics model of vehicle-ballastless track-subgrade system
established by ABAQUS software, this paper studies the dynamic characteristics of
vehicle and ballastless track under ground subsidence with different ground
subsidence wavelengths. Through the calculated vehicle acceleration, the vertical
acceleration and displacement of the track structure, etc., the impact of land sub-
sidence on the vehicle-ballastless track system is evaluated. The main conclusions
are as follows:

(1) Track irregularity is the main factor that causes the vibration of a ballastless
    track of a vehicle. Therefore, high-speed railways should strictly control track
    irregularities and limit them to a certain extent.
(2) The greater the surface cosine-type sedimentation wavelength, the smaller the
    dynamic response values of vehicles and ballastless track. As the sedimentation
    wavelength increases from 10 m to 40 m, the dynamic response of vehicle and
    ballastless track gradually decreases. The vertical acceleration of the vehicle
    body has decreased by 41.5%; the vertical force of the wheel and rail has been
    reduced by 15.7%; the vertical acceleration and vertical displacement of the rail
    have been reduced by 6.8% and 19.1%, respectively; the vertical acceleration
    and vertical displacement of the track plate have been reduced by 2.2% and
    19.9%, respectively; the base plate vertical acceleration and vertical displace-
    ment were reduced by 2.1% and 24.9%, respectively.
(3) When the vehicle speed increases from 200, 250, 300, 350, and 400 km/h while
    passing through the land subsidence area at different speeds, the dynamic
    response of the vehicle body and the ballastless track correspondingly increa-
    ses. The vertical acceleration of the car body, the vertical acceleration and
    vertical displacement of the rail, the vertical acceleration and vertical
    displacement of the track plate, and the vertical acceleration of the base plate
    and the vertical displacement of the rail are all increased.

References

1. Luo L (2000) High-speed railway track must have high smoothness. China Railway 9:8–11
2. Lombaert G, Degrande G (2009) Ground-borne vibration due to static and dynamic axle loads of InterCity and high-speed trains. J Sound Vib 319(3–5):1036–1066
3. Zhu X (2012) Temperature effect of CRTS II track slab and its influence on train operation safety. Southwest Jiaotong University
4. Song H, Bian X, Jiang J et al (2012) Research on the relationship between subsidence of high-speed railway subgrade and train running speed. J Vib Shock 31(10):134–140
5. Li, Zhou, Limits of unequal settlement of CRTS-II slab ballastless track subgrade
6. Zhai (2007) Wanming of the vehicle—track coupling dynamics. Science Press
7. Ja Z, Xia H, Fan JJ (2000). Effects of unsupported sleeper on dynamic responses of railway track. J Northern Jiaotong Univ
8. Liu X, Wang P (2010) Vehicle-track-subgrade system dynamics. Southwest Jiaotong University Press, Chengdu

Dynamic Simulation and Analysis of a High-Speed Maglev Train/Guideway Interaction System

JingYu Huang and Long Zhang

Abstract Reliable and effective simulation methods are very important for the design of and research on maglev train/guideway systems. This paper proposes three numerical models for predicting and investigating the dynamic response of a maglev system. With field-measured data as a reference, a comparative analysis of these numerical models was conducted. The effects of the train speed and the suspension system on the response were investigated. The numerical results indicate that appropriate dynamic amplification guidelines for the guideway response can be extracted based on an analysis of the resonance and cancellation conditions and that the stiffness and damping of the suspension system should be carefully considered to ensure satisfactory ride quality.

Keywords Maglev vehicle/guideway system · Numerical models · Response analysis · Suspension system

1 Introduction

A maglev train is a highly modern vehicle that uses non-contact magnetic forces for vehicle levitation, guidance, and propulsion. Compared to traditional modes of railway transportation, maglev transport has the merits of a higher running speed, lower energy consumption, lower noise emission, and less required maintenance. Because of these benefits, maglev transport systems have been developed in many countries [1].

J. Huang · L. Zhang (✉)
College of Civil Engineering, Tongji University, Shanghai 200092, China
e-mail: 88zhanglong@tongji.edu.cn

J. Huang
e-mail: huangjingyu@tongji.edu.cn

J. Huang
National Maglev Transportation Engineering R&D Center, Tongji University,
Shanghai 201804, China

As a maglev train moves along a guideway, complicated maglev train/guideway interactions occur. To achieve satisfactory ride quality and levitation safety, it is extremely important to investigate the interactions in such a maglev train/guideway system.

Over the past two decades, many maglev models have been developed for simulating maglev systems and predicting the dynamic responses of the maglev train and guideway. In the initial stage of research, the moving load method, in which the maglev train is simplified as a series of uniformly spaced, concentrated loads, was initially applied to predict the dynamic response of the guideway. Wang et al. [2] modelled a maglev train as a series of evenly distributed moving loads to conduct an analytical study on the dynamic response of the guideway. The moving load method is simple and convenient, but it neglects the characteristics of the maglev vehicle and cannot model the interactions between the train and the guideway. To consider the maglev vehicle subsystem, maglev train/guideway interaction models were subsequently proposed in which the maglev vehicle is simulated as a system of multiple rigid bodies, thus ignoring the elastic vehicle deformation, and the guideway is simulated as a Bernoulli–Euler beam. In typical simplified maglev system models, the magnetic interaction force between the vehicle and the guideway is represented by a combination of a spring and a damper. Many scholars have used such simplified models to conduct various investigations of maglev vehicles. Cai et al. [3, 4] simplified a maglev train as a car body with multiple magnets to study the effect of distributed loads and a multicar vehicle. Ren et al. [5] and Talukdar et al. [6] used a simplified vehicle model with 6 degrees of freedom (DOFs) and the block diagram approach (in MATLAB SIMULINK) to examine the influences of the vehicle speed and guideway irregularity on the response. Zhai et al. [7] simulated a maglev vehicle using a 10-DOF vehicle model with one car body supported by four levitation bogies to study the random response and ride quality of the vehicle. Many significant research results have been achieved using such simplified maglev system models. However, for cases in which the responses of the magnetic interaction forces and levitation control are of interest, the simulation techniques for maglev systems require further improvement. For this purpose, an electromagnetic force model with a feedback controller has been introduced into the maglev train/guideway system to enable more realistic simulations [8–14].

As described above, in the previous studies, three types of numerical models, namely moving load models, simplified maglev system models, and maglev models with feedback controllers, have been developed for studying the interactions in a maglev system. However, the differences between these three types of numerical models in terms of response prediction, calculation accuracy, and computational efficiency have not been investigated in detail. The previous studies have investigated the dynamic response of a maglev system subjected to various external excitations, such as irregularity, aerodynamic forces, and foundation settlement, and have discussed the effects of various parameters, such as the train speed, on the

response. However, there has been little research investigating the effect of the maglev train's suspension system on the response, and there has also been little research focused on summarizing related findings to provide a corresponding design guide for maglev systems.

This paper proposes various numerical models for simulating a maglev train/guideway interaction system and compares their performance in terms of calculation accuracy and efficiency. With field-measured data as a reference, a comparative analysis of the dynamic responses obtained with these models is presented. To provide general design guidelines for maglev systems, this paper also studies the effects of the suspension system and train speed on the dynamic response.

2 Numerical Models

Figure 1 presents the structure of the Transrapid 08 (TR08) high-speed maglev train, which is a train that runs daily on the Shanghai maglev train line, a commercial high-speed line. To simulate the maglev train/guideway system and predict its dynamic response, this paper considers three numerical models, as shown in Fig. 2. These models include a maglev vehicle/guideway model with a magnetic feedback controller (Model 1), a simplified maglev vehicle/guideway model (Model 2) in which the magnetic forces are represented by spring-damper pairs, and a moving load model (Model 3). These numerical models will be introduced in detail in the following sections.
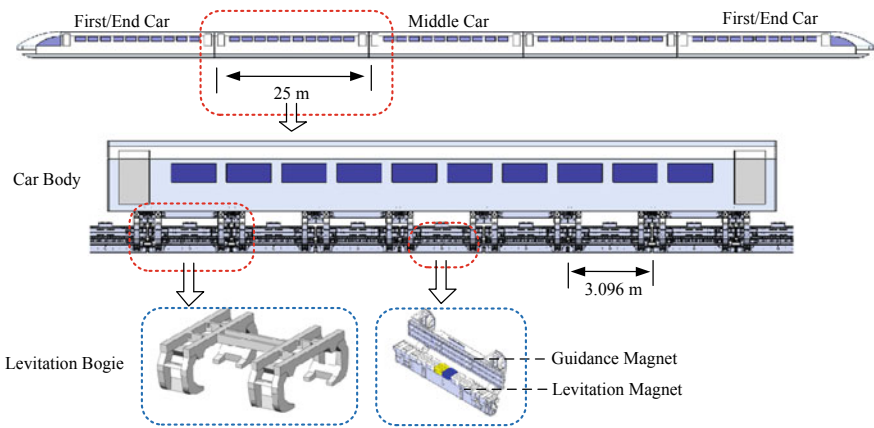
Fig. 1 Structure of the TR08 high-speed maglev train
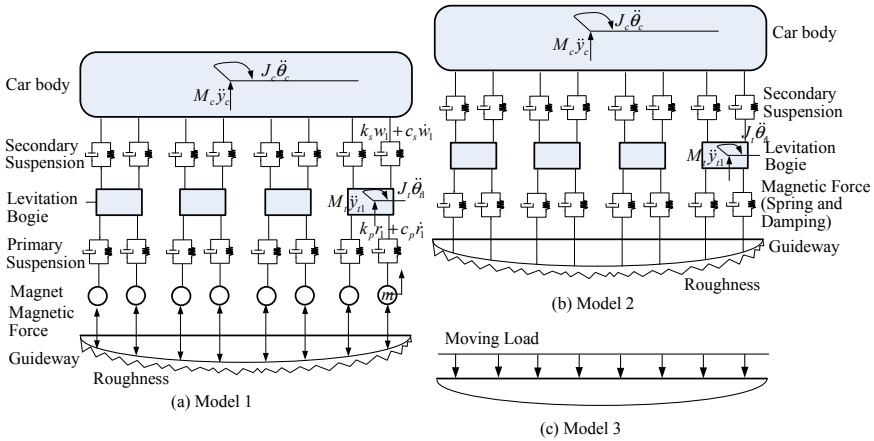
Fig. 2 a Model 1: high-speed maglev vehicle/guideway system with a magnetic feedback controller; **b** Model 2: simplified vehicle/guideway model with spring-damper pairs; **c** Model 3: moving load model

2.1 Model 1

Model 1 consists of two subsystems: the vehicle subsystem and the guideway subsystem.

Vehicle subsystem. The vehicle subsystem of Model 1 includes all the important structural components of each maglev vehicle as well as a current feedback controller for tuning the magnetic interaction forces between the maglev vehicles and the guideway. The ability to control the magnetic forces by means of the current controller is the most important feature of Model 1. As shown in Fig. 2a, a maglev vehicle consists of one car body, four levitation bogies, and eight levitation magnets. The car body is connected to each bogie by two spring-damper pairs (k_s, c_s), which are referred to as the secondary suspension. Each levitation bogie is also connected to two magnets by two spring-damper pairs (k_p, c_p), which are called the primary suspension. The car body and the bogies each have two DOFs (one vertical displacement and one pitching displacement), denoted by $\{y_c, \theta_c\}$ for the car body and $\{y_{l1}, \theta_{l1}, y_{l2}, \theta_{l2}, y_{l3}, \theta_{l3}, y_{l4}, \theta_{l4}\}$ for the four levitation bogies. Every magnet has one vertical DOF (denoted by y_{mn} for the nth magnet). Therefore, each maglev vehicle has 18 DOFs for vertical vibration. To establish the motion equation for the maglev train, it is assumed that (a) the elastic deformation of the vehicles is ignored, (b) the train passes along the guideway at a constant speed, and (c) the responses of the maglev vehicles are independent of each other. Therefore, the dynamic equation for the motion of a maglev vehicle can be expressed as

$$[M_v]\{\ddot{u}_v\} + [C_v]\{\dot{u}_v\} + [K_v]\{u_v\} = \{P_v\} \tag{1}$$

where $[M_v]$, $[C_v]$ and $[K_v]$ are the mass, damping, and stiffness matrices, respectively, of the vehicle; $\{u_v\}$ represents the vertical displacement vector of the vehicle, $\{u_v\} = \{y_{m1}; \ldots; y_{m8}; y_{l1}; \theta_{l1}; \ldots; y_{l4}; \theta_{l4}; y_c; \theta_c\}$; $\{p_v\}$ is the load vector of the vehicle, which, in this study, represents the controlled magnetic interaction forces between the magnets and the guideway. The magnetic force (F_{mn}) between the nth magnet and the guideway can be expressed as [9, 15]

$$F_{mn} = K_0 \left(\frac{i_n}{h_n}\right)^2, \quad n = 1, 2\ldots, 8 \tag{2}$$

where i_n is the control current for the nth magnet; h_n is the levitation gap between the nth magnet and the guideway, $h_n = y_{mn} - u_n - z_{rn}$; u_n and z_{rn} are the displacement and irregularity, respectively, of the guideway at the action point of the nth electromagnetic force; K_0 is a coupling factor that can be obtained from the equation for the static equilibrium condition for the vehicle model, i.e. $\ddot{y}_c = \ddot{\theta}_c = \ddot{z}_n = 0$. This coupling factor can be written as

$$K_0 \left(\frac{i_0}{h_0}\right)^2 = p_0 \tag{3}$$

where (i_0, h_0) denotes the desired values of the control current and levitation gap, respectively, at a specified nominal operating point for the maglev train model.

Based on references [11, 12, 15], a reasonably accurate linear model may be obtained by using linear approximations of the electromagnetic forces for excursions around the nominal static equilibrium point (i_0, h_0). In this study, the linearized electromagnetic force for the nth magnet is given by

$$F_{mn} = p_0 + C_i \Delta i_n - C_h \Delta h_n, \quad n = 1, 2\ldots, 8 \tag{4}$$

where $C_i = \frac{\partial F_{mn}}{\partial i_n}\big|_{i_n=i_0, h_n=h_0} = \frac{2K_0 i_0}{h_0^2}$, $C_h = -\frac{\partial F_{mn}}{\partial h_n}\big|_{i_n=i_0, h_n=h_0} = \frac{2K_0 i_0^2}{h_0^3}$, $\Delta i_n = i_n - i_0$, and $\Delta h_n = h_n - h_0$.

The current control law for the nth magnet is expressed as [9, 16]

$$\Delta i_n = k_h \Delta h_n + k_v \dot{z}_n + k_a \ddot{z}_n, \quad n = 1, 2\ldots 8 \tag{5}$$

where k_h, k_v, and k_a are the feedback control gains related to the change in the levitation gap and the velocity and acceleration of the magnet; these gains can be determined from the transient response characteristics of a controlled magnet [17].

Guideway subsystem. The guideway subsystem can be established using the mode superposition method (MSM) [6] or the finite element method (FEM) [5, 18].
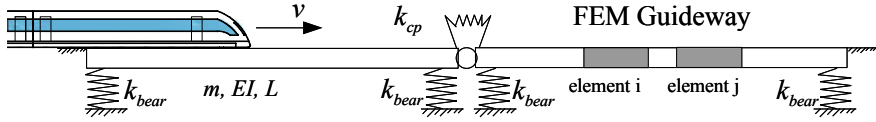
Fig. 3 Guideway finite element (FE) model

Figure 3 presents the guideway model. The corresponding equation of motion for the guideway subsystem can be expressed as

$$[M_g]\{\ddot{y}_g\} + [C_g]\{\dot{y}_g\} + ([K_g] + [K_b])\{y_g\} = \{P_g\} \tag{6}$$

where $[M_g]$, $[C_g]$, and $[K_g]$ are the mass, damping, and stiffness matrices, respectively, of the guideway; $\{y_g\}$ represents all the nodal DOFs of the guideway; $[K_b]$ is the stiffness matrix for the boundary conditions, meaning that $-[K_b]\{y_g\}$ represents the forces induced by the boundary conditions, for example the bearing supports and coupling connections; $\{P_g\}$ is the load vector for the guideway, which is given by

$$\{P_g\} = \sum_{n=1}^{8} [\Gamma_n]\{N_{cn}\}F_{mn} \tag{7}$$

where F_{mn} is the nth magnetic force acting on the guideway; $\{N_{cn}\}$ is the displacement interpolation vector for the guideway elements, where the subscript cn indicates that the interpolation vector $\{N_{cn}\}$ is evaluated at the action point of the nth electromagnetic force; $[\Gamma_n]$ is the coordinate transformation matrix that transforms the loads $\{N_{cn}\}F_{mn}$ from the element vectors to the overall structural vectors. Rayleigh damping is assumed for the guideway, which means that the damping matrix of the entire guideway can be computed as a linear combination of the mass and stiffness matrices of the structure.

Guideway irregularity. The guideway irregularity used in this paper is generated from the track spectra reported by the US Federal Railroad Administration (FRA) for Class 6 [19] and is given by

$$S_v(\Omega) = \frac{kA_v\Omega_c^2}{\Omega^2(\Omega^2 + \Omega_c^2)} \tag{8}$$

where $S_v(\Omega)$ is the vertical irregularity, with units of cm^2/(rad/m); Ω(rad/m) is the spatial frequency; k is a dimensionless parameter that is assumed to have a value of 0.25 herein; $\Omega_c = 0.8245$ (rad/m) is the cut-off frequency; and $A_v = 3.39 \times 10^{-7}$ (m^2 rad/m) is the surface roughness constant. The considered wavelengths are 0.5–50 m.

Solution. Based on Eqs. (1) and (6), the coupled motion equation for the maglev train/guideway system can be written as

$$
\begin{bmatrix} M_v & 0 \\ 0 & M_g \end{bmatrix} \begin{Bmatrix} \ddot{u}_v \\ \ddot{u}_g \end{Bmatrix} + \begin{bmatrix} C_v & 0 \\ 0 & C_g \end{bmatrix} \begin{Bmatrix} \dot{u}_v \\ \dot{u}_g \end{Bmatrix} + \begin{bmatrix} K_v & 0 \\ 0 & K_g + K_b \end{bmatrix} \begin{Bmatrix} u_v \\ u_g \end{Bmatrix} = \begin{Bmatrix} P_v \\ P_g \end{Bmatrix}
\tag{9}
$$

The incremental iteration method is used for the nonlinear dynamic analysis of the maglev vehicle/guideway system, following the procedure shown in Fig. 4. More detailed information about the incremental iteration procedure for the dynamic analysis of maglev vehicle/guideway interactions is available in references [9, 20]. It is noted that (1) the electromagnetic forces associated with the dynamic interactions in the maglev vehicle/guideway system are updated in each iteration and (2) as long as the root mean square of the sum of the guideway displacement variations between the ith iteration and the $(i - 1)$th iteration is at least 10^{-8} times that between the ith iteration and the first iteration, the procedure for reducing the root mean square value will be iterated until the convergence requirement is met.
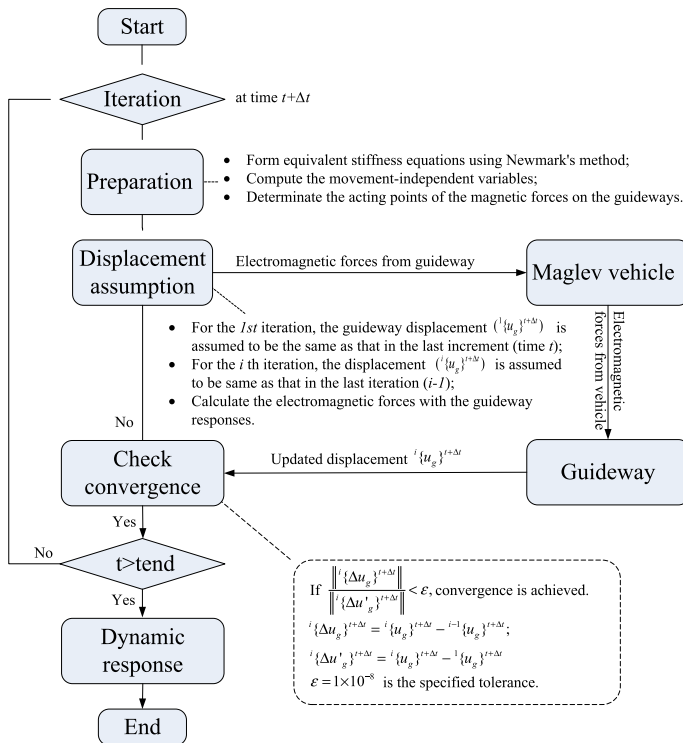
Fig. 4 Flowchart of the incremental iteration method for the maglev train/guideway system

2.2   Model 2

The differences between Model 1 and Model 2 are that Model 2 omits the magnets and the magnetic feedback controller, and the electromagnetic interaction forces are simplified to equivalent spring-damper pairs. As shown in Fig. 2b, a maglev vehicle in Model 2 consists of one car body and four levitation bogies. The car body is connected to each bogie by the secondary suspension (k_s, c_s). The car body and the bogies each have two DOFs (one vertical displacement and one pitching displacement), denoted by $\{y_c, \theta_c\}$ for the car body and $\{y_{l1}, \theta_{l1}, y_{l2}, \theta_{l2}, y_{l3}, \theta_{l3}, y_{l4}, \theta_{l4}\}$ for the four levitation bogies. Therefore, each maglev vehicle has 10 DOFs for vertical vibration. The dynamic equation for the motion of the maglev train can be expressed as

$$[M_t]\{\ddot{u}_t\} + [C_t]\{\dot{u}_t\} + [K_t]\{u_t\} = \{P_t\} \tag{10}$$

where $[M_t]$, $[C_t]$, and $[K_t]$ are the mass, damping, and stiffness matrices, respectively, of the train; $\{u_t\}$ represents the vertical displacement vector of the train, $\{u_t\} = \{y_{l1}; \theta_{l1}; \ldots; y_{l4}; \theta_{l4}; y_c; \theta_c\}$; $\{p_t\}$ is the load vector of the train, which, in this study, represents the simplified magnetic interaction forces between the magnets and the guideway. The simplified equivalent magnetic force (F_{mn}) between the nth magnet and the guideway can be expressed as

$$F_{mn} = k_m(u_{gn} - u_{tn}) + c_m(\dot{u}_{gn} - \dot{u}_{tn}), \quad n = 1, 2 \ldots, 8 \tag{11}$$

where k_m and c_m are the equivalent stiffness and damping, respectively, for the magnetic forces and $(u_{gn} - u_{tn})$ is the relative displacement between the nth magnetic force and the guideway, with u_{gn} being the levitation bogie displacement corresponding to the action position of the nth magnetic force (as shown in Fig. 2b), and u_{tn} is the guideway displacement at the corresponding nth action point.

The guideway subsystem and motion equation in Model 2 are the same as those in Model 1. Various methods can be used to solve the coupled system equation of Model 2, such as the dynamic condensation method [21] and the incremental iteration method presented for Model 1. To solve the vibration equations of Model 2, the incremental iteration method is again used due to its simplicity and high efficiency.

2.3   Model 3

Model 3 is a simple method for predicting the dynamic response of the guideway; only the guideway is simulated, and the maglev train is simplified as a series of

loads moving along the guideway at a speed v. The corresponding load function $F(t)$ is given by Yang and Yau [21]

$$F(t) = \sum_{n=1}^{8} p_0 \cdot U_n(t, v, L)$$

$$U_n(t, v, L) = \delta[x - v(t - t_n)] \cdot \left[H(t - t_n) - H\left(t - t_n - \frac{L}{v}\right) \right]$$

$$(12)$$

where δ is the Dirac delta function, x is the coordinate on the guideway, $H(\cdot)$ is a unit step function, t_j is the arrival time of the nth load on the guideway, n is the total number of moving loads considered ($n = 8$ in this study), $d = 3.096\,\text{m}$ is the constant interval between the loads, and L is the length of the guideway. Either the MSM [21] or the FEM can be used to obtain the solution in the moving load method. In this study, the previously described FE model of the guideway subsystem is still used as the guideway model in this case because the FEM allows more convenient consideration of the complicated boundary conditions.

3   Response Analysis

Two cases are selected to conduct a response analysis of high-speed maglev train/guideway systems. One case is the high-speed maglev test line at Tongji University, JiaDing District, Shanghai, China. The other case is the commercially operating high-speed maglev line at the Pudong airport, Shanghai, China.

On the test line, one maglev vehicle moves on a simply supported guideway at a speed of 25 km/h. On the commercial line, five maglev vehicles move on a two-span guideway at a very high speed of 410 km/h. In the two-span guideway of the commercial line, two guideways are connected in an end-to-end manner to form a two-span quasi-continuous guideway using a coupling connection, and the guideways are supported by elastic bearings. The situations of the test line and commercial line cases are presented in Fig. 5, and their parameters are listed in Table 1.

To investigate the prediction accuracies of the different numerical models, the responses calculated using each model are compared to corresponding field-measured responses. Figure 6a shows the comparison for the guideway displacement on the test line. It can be seen that the displacement responses of all numerical models match well with the measurements. Figure 6b shows the comparison for the guideway velocity on the commercial line. Again, there is a good match between the numerical models and the measurements. Therefore, it can be concluded that all the numerical models can provide sufficient accuracy in the prediction of guideway responses.
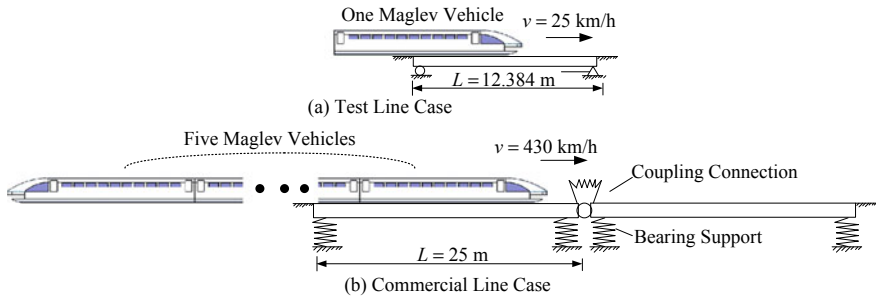
Fig. 5 a Case of the high-speed maglev test line; **b** the case of the commercially operating high-speed maglev line comparative analysis of the guideway responses

Table 1 Parameters of the test line and the commercial line

Parameters	Units	Values	
		Test line	Commercial line
Vehicle subsystem parameters			
Length of car body (L_c)	m	24.768	
Length of levitation bogie (L_b)	m	3.095	
Mass of car body (M_c)	kg	39,000	
Mass inertia of car body (J_c)	kg m^2	2×10^6	
Mass of levitation bogie (M_l)	kg	1500	
Mass inertia of levitation bogie (J_l)	kg m^2	1200	
Mass of magnet (m)	kg	1000	
Primary vertical spring stiffness (k_p)	N s/m	4×10^7	
Primary vertical spring damping (c_p)	N/m	1×10^4	
Secondary vertical spring stiffness (k_s)	N s/m	4×10^5	
Secondary vertical spring damping (c_s)	N/m	1×10^4	
Nominal current (i_0)	A	25	
Nominal levitation gap (h_0)	m	0.01	
Feedback gains (k_h, k_v, k_a)		6500, 40, 0.2	
Guideway subsystem parameters			
Length of guideway (L)	m	12.368	25
Elasticity modulus × moment of inertia (EI)	N m^2	1.62×10^{10}	8.58×10^{10}
Guideway mass per unit length (m_g)	kg/m	4500	6000
Damping coefficient (ζ) (%)		3	2
Stiffness of bearing support (k_{bear})	N/m	3.2×10^{20}	3.2×10^{10}
Stiffness of coupling connection (k_{cp})	N mm/rad	0	1×10^{10}

At the peaks of the velocity response in Fig. 6b (approximately 0.1 and 1.1 s), it can be seen that Model 1 yields the most accurate prediction of the response amplitude, while Models 2 and 3 show obvious differences from the measurements.

These findings suggest that Model 1 is more accurate than Models 2 and 3 in the prediction of guideway responses because Model 1 includes the feedback controller for the magnetic forces in the maglev system.

Figure 7 presents a comparison of the acceleration responses of the numerical models. It can be seen that the acceleration in Model 1 is smaller than those in the other models, while Model 3 predicts the largest acceleration response. This is because the feedback controller of Model 1 tunes the magnetic forces to attenuate the guideway vibrations, whereas Model 3 neglects the effect of the mass of the vehicle system on the guideway, thereby amplifying its acceleration response.

3.1 Comparative Analysis of the Vehicle Responses

Both Model 1 and Model 2 can predict the maglev vehicle responses, which are very useful for evaluating the ride quality. Figure 8 compares the vehicle responses of Model 1 and Model 2 in terms of the vertical and angular accelerations of a car body and a levitation bogie. Models 1 and 2 are found to predict almost the same accelerations of the car body and levitation bogie, thereby demonstrating that
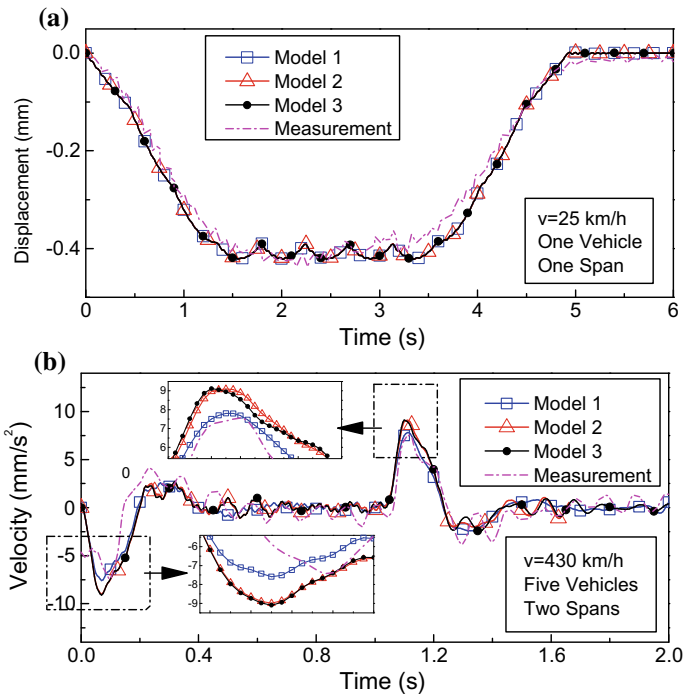
Fig. 6 a Displacement comparison on the test line; b velocity comparison on the commercial line
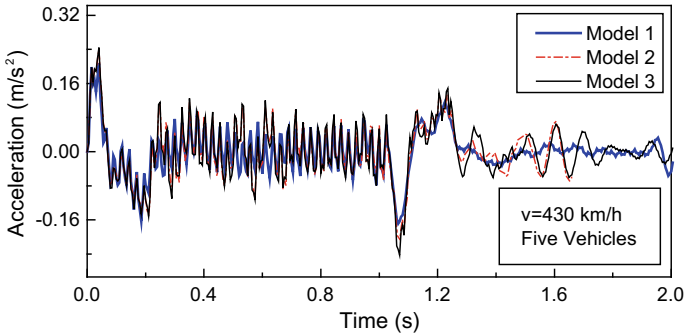
Fig. 7 Guideway acceleration comparison among the numerical models

Model 2 can achieve almost the same accuracy in predicting the vehicle responses in the present case.

As shown in Fig. 8c, d, the accelerations of the levitation bogie in Model 1 exhibit more severe vibrations than those in Model 2 at approximately 0.45 s, which suggests that the magnetic feedback controller has a significant effect on the vibrations of the levitation bogie when the maglev vehicle is leaving the guideway.

Figure 9 presents the responses in terms of the magnetic forces and the levitation gap without any irregularity in the guideway surface, which are predicted only by Model 1. In the present case, the maximum variation in the magnetic force is 800 N (1.23% change), and the maximum variation in the levitation gap is 0.15 mm, with a guideway deformation of 0.92 mm. These findings reveal that the guideway deformation does not induce significant variations in the magnetic forces or the levitation gap and that the levitation stability and safety are well regulated. Compared to Models 2 and 3, Model 1 has an advantage in that it can predict the magnetic forces and levitation gap, which are very important for the evaluation of levitation safety.

3.2 Comparison of Computational Efficiency

For the complete response prediction process with a time step of 0.005 s, the calculation times are 303 s, 280 s, and 62 s for Models 1, 2, and 3, respectively. The calculation time varies with various conditions, such as the computer configuration and program code details, but these results nevertheless indicate that Model 3 is indeed a simple and efficient means of predicting the dynamic responses of the guideway. However, Models 1 and 2 also have acceptable calculation costs and can predict a wider variety of numerical results; consequently, these train/guideway models have greater value in research and design for maglev systems.

(a)

(b)

(c)

(d)
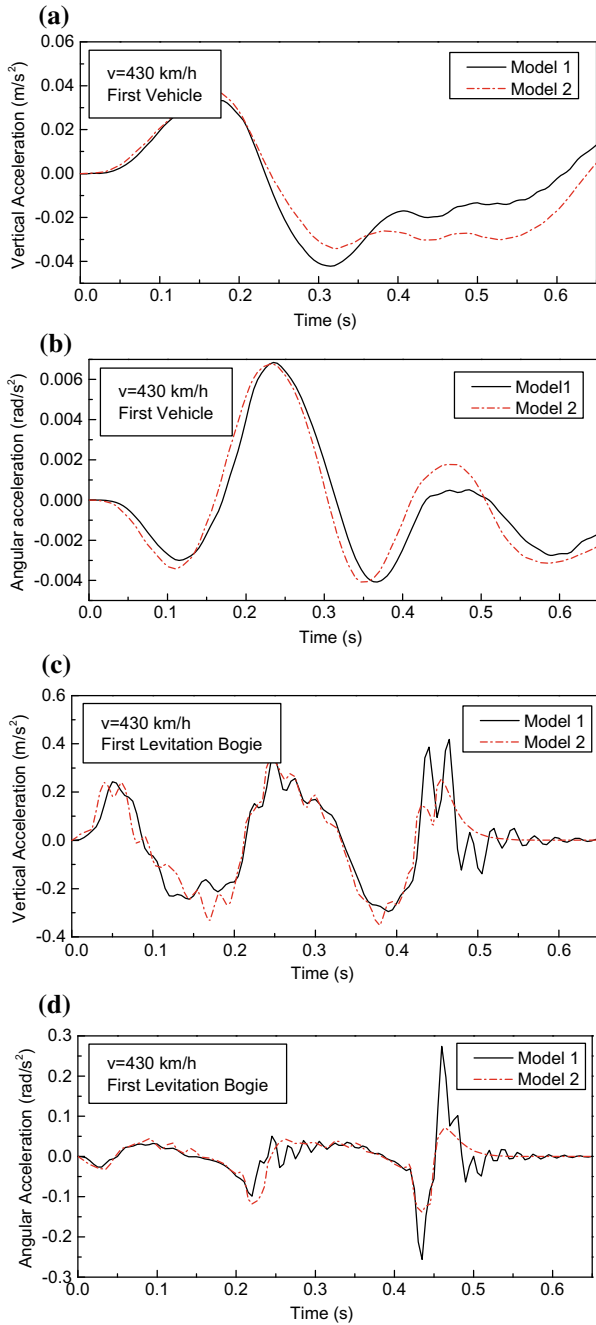
Fig. 8 Vertical and angular acceleration comparisons for a car body and a levitation bogie

(a)

(b)
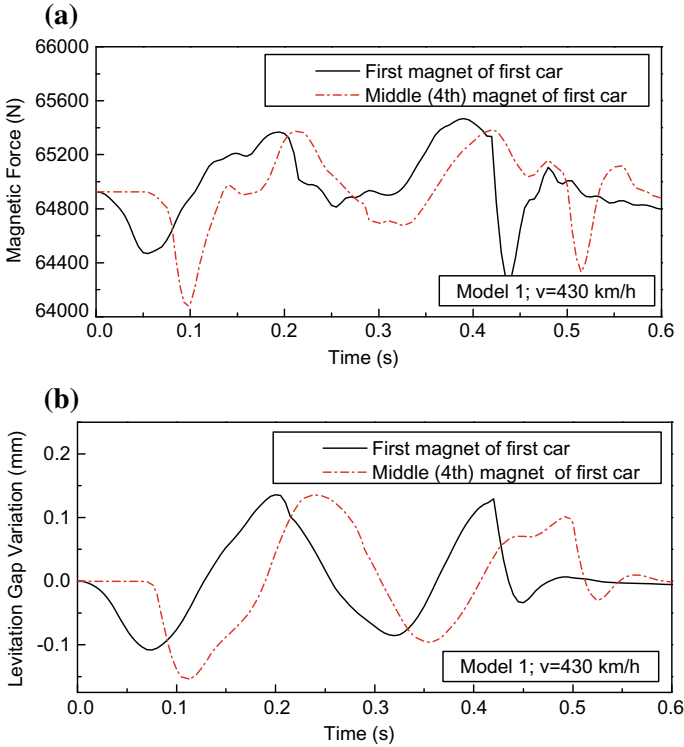
Fig. 9 Responses of the magnetic forces and the variation in the levitation gap

4 Parameter Analysis

4.1 Effects of Velocity and Dynamic Amplification

The dynamic response induced by a moving train on a guideway is generally larger than the static response. In particular, when a resonance condition is met because the excitation load has a driving frequency equal to a fundamental frequency of the structure, the dynamic amplification of the response reaches a maximum; thus, the corresponding response can be regarded as a reasonable upper bound. According to a review of the literature [5, 6], there is currently no design code for the dynamic amplification of maglev guideways. Hence, for the design of guideway structures, it is of great significance to study the relevant dynamic amplification and resonance conditions.

Figure 10 illustrates the effect of the train speed on the guideway displacement. Models 1 and 2 are found to predict almost identical responses, while an obvious difference is evident between Models 1 and 3. This difference arises because the effect of the mass of the maglev vehicle is ignored in Model 3. The resonance and

cancellation conditions can be clearly observed in Fig. 10; the resonance speeds are found to be 420 and 280 km/h, and the cancellation speeds are 530 and 330 km/h. These results coincide with the resonance and cancellation speeds computed following the method of Yang and Yau [21], which are given by

$$
\begin{aligned}
V_{\mathrm{ri}} &= \frac{3.6\omega_{\mathrm{d}}L_{\mathrm{c}}}{i}, \quad i = 1,2,3,\ldots \\
V_{\mathrm{cani}} &= \frac{7.2\omega_{\mathrm{d}}L_{\mathrm{c}}}{2i-1}, \quad i = 1,2,3,\ldots
\end{aligned}
\tag{13}
$$

where V_{ri} and V_{cani} are the resonance speed and cancellation speed, respectively; ω_{d} is the fundamental natural vibration frequency of the guideway; d is the full length of the maglev vehicle; i represents the order of the resonance or cancellation. In this case, $\Omega_{\mathrm{d}} = 9.3\,\mathrm{Hz}$, $L_{\mathrm{c}} = 24.768\,\mathrm{m}$, and $i = 2,3$. Based on Eq. (13) and Models 1, 2 and 3, the first resonance speed outside the current speed range is found to be approximately 830 km/h.
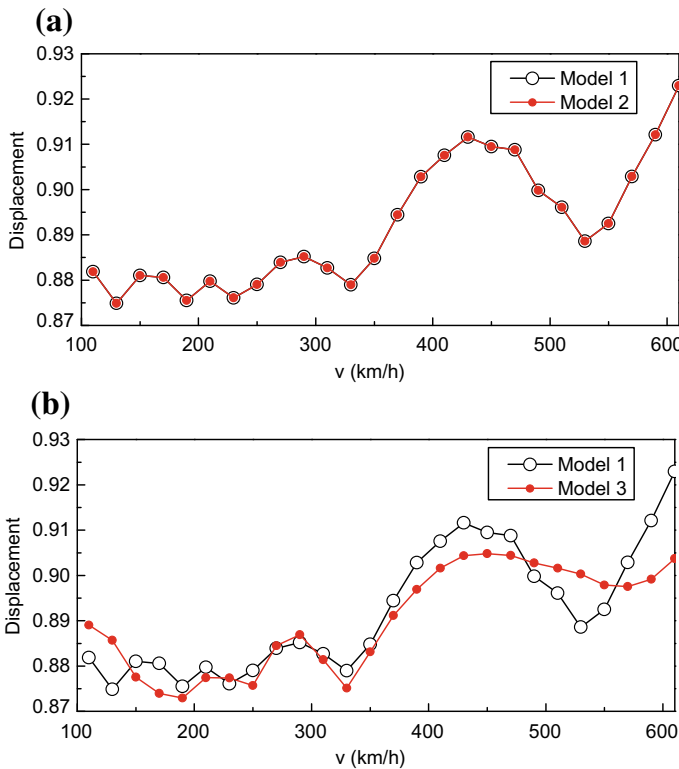
Fig. 10 Effect of the train speed on the mid-span displacement of the guideway

In this study, the effect of dynamic amplification on the guideway due to the passage of moving vehicles is evaluated in terms of a dynamic amplification factor (DAF), which is defined as

$$\text{DAF} = \frac{D_\mathrm{d}(L/2)}{D_\mathrm{s}(L/2)} \qquad (14)$$

where $D_\mathrm{d}(L/2)$ and $D_\mathrm{s}(L/2)$ are the maximum displacements of the mid-span with and without the consideration of dynamic effects, respectively.

Based on the resonance and cancellation speeds ($V_{\mathrm{r}2}$, $V_{\mathrm{can}2}$, and $V_{\mathrm{can}3}$) and their corresponding dynamic amplification values as well as the fundamental frequency of the guideway (ω_d), a set of design guidelines for a maglev guideway can be summarized as follows:

$$\varphi = \begin{cases} 1.05 & 0 \leq v \leq 330 \\ 1.1 & 320 \leq v \leq 530 \\ 1.1 + 0.3(1.6 - k_0) & 530 \leq v \leq 830 \end{cases} \qquad (15)$$

where φ is the DAF, k_0 is a coefficient defined as $k_0 = \frac{L\omega_\mathrm{d}}{\mathrm{V}}$, L is the span length of the guideway, and v is the speed of the maglev train. The comparison between the numerical results and the summarized design guidelines presented in Fig. 11 reveals that they exhibit the same DAF trend and that the design curve appears sufficiently conservative to account for train-induced vibrations. A DAF comparison between the German design guidelines [22] provided by Ren [23] and the summarized guidelines formulated here, as shown in Table 2, indicates that the German design guidelines are excessively conservative for the design of Shanghai maglev guideways because the type of guideway considered in the German guidelines is mainly based on the first generation of concrete guideways at the Test Facility Emsland [23], which has significant differences compared with the guideways of the Shanghai maglev train line. Therefore, for the design of a maglev
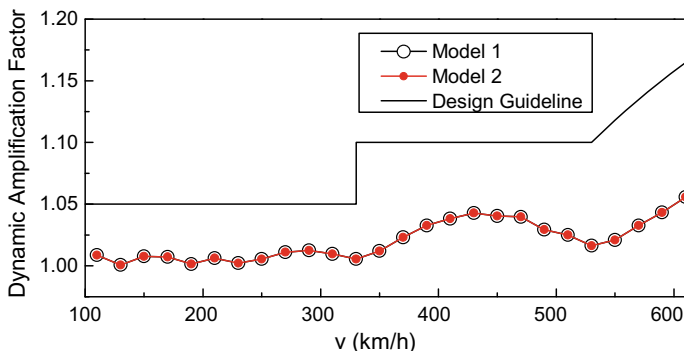
Fig. 11 Dynamic amplification and design guidelines for guideways

Table 2 DAF comparison between the proposed guidelines and the German guidelines

Train speed (km/h)	DAF of guideway from the present study	DAF from Ref. [23]
100	1.05	1.05
200	1.05	1.1
300	1.05	1.2
400	1.1	1.24
500	1.1	1.48

guideway similar to those of the Shanghai maglev train line, Eq. (12) can be treated as a reference. Performing a case-specific resonance and cancellation vibration analysis with a maglev train/guideway model is recommended.

4.2 Effects of Suspension Stiffness and Damping

To examine the influence of the suspension system on the response of the maglev vehicle, four parameters, namely the stiffness and damping of each of the primary and secondary suspensions, are investigated. For varying parameter values, the calculated maximum vehicle acceleration and the calculated variation in the minimum levitation gap, which are important indices for ride quality and safety, are presented in Figs. 12 and 13. During the calculation process, only one parameter was varied at a time, while all other parameters were held fixed at their initial values.

As shown in Fig. 12a, c, an increase in the secondary stiffness or damping is found to lead to a corresponding increase in the vertical car body acceleration, which is harmful to the ride quality of the maglev train. This phenomenon is more obvious for the vibration of the first car than for that of the middle car. The maximum acceleration increases from 0.017 to 0.438 m/s^2 (by a factor of 25) when the secondary stiffness increases from 4×10^5 to 4×10^6 N/m, and it increases from 0.044 to 0.139 m/s^2 (by 216%) when the secondary damping increases from 1×10^3 to 1×10^5 N s/m. These results indicate that the effect of the secondary suspension on the vehicle acceleration is very significant.

As seen in Fig. 12b, d, an increase in the secondary stiffness or damping is also found to lead to a corresponding decrease in the minimum levitation gap, which is harmful to the ride safety of the maglev train. The minimum gap decreases from −0.317 to −0.386 mm (by 21.8%) when the secondary stiffness increases from 4×10^5 to 4×10^6 N/m, and it decreases from −0.224 to −0.260 mm (by 16.1%) when the secondary damping increases from 1×10^3 to 1×10^5 N s/m. These results indicate that the secondary suspension also has an obvious effect on the variation in the levitation gap.

Fig. 12 Effects of the
secondary suspension on the
maximum car body
acceleration and the minimum
levitation gap
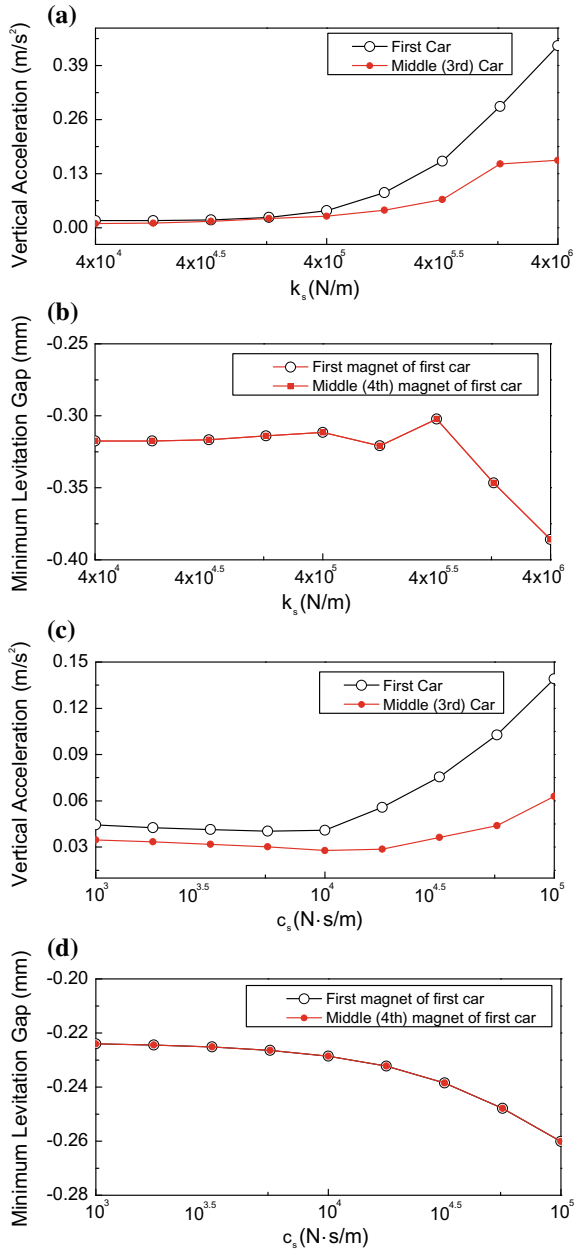
Figure 13 shows the effects of the primary suspension on the responses. It can be observed from Fig. 13a, c that variations in the primary stiffness or damping will not cause obvious changes in the vehicle acceleration. This finding indicates that the primary suspension has only a weak effect on the vibration of the car body.

Fig. 13 Effects of the primary suspension on the maximum car body acceleration and the minimum levitation gap
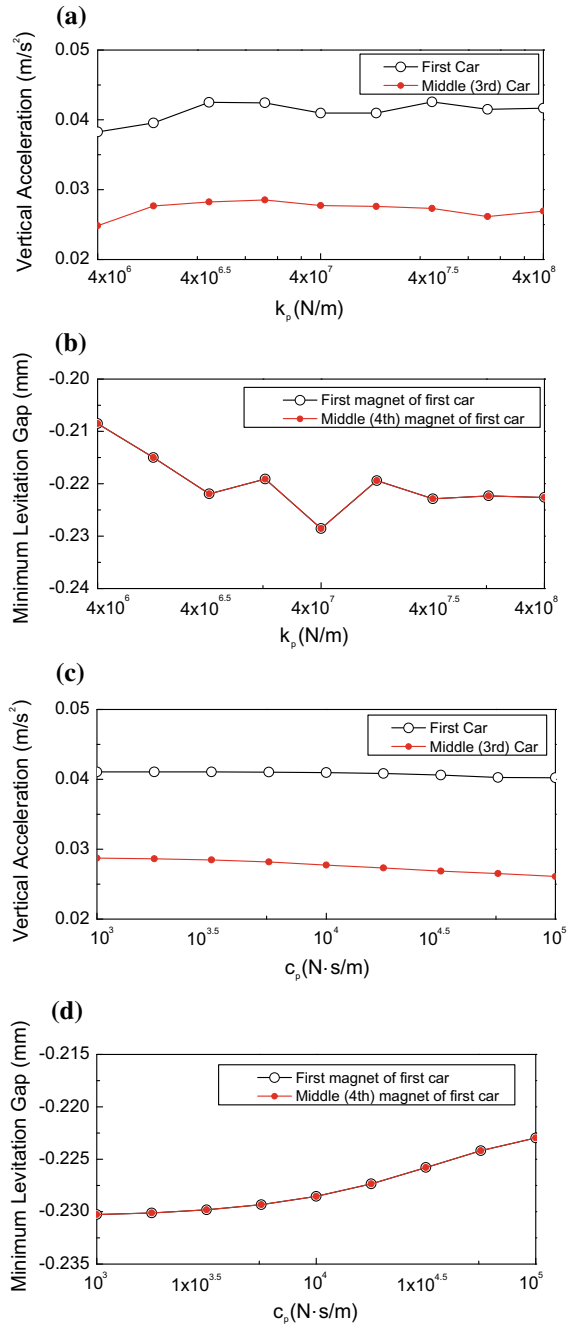
As shown in Fig. 13b, an increase in the primary stiffness causes, in general, a decrease in the minimum levitation gap. The minimum gap decreases from −0.208 to −0.226 mm (by 8.6%) when the primary stiffness increases from 4×10^6 to 4×10^8 N/m. By contrast, as shown in Fig. 13d, an increase in the primary damping causes an increase in the minimum levitation gap. The minimum gap increases from −0.230 to −0.223 mm (by 3%) when the primary damping increases from 1×10^3 to 1×10^5 N s/m. These changes in the levitation gap are less than 10%, suggesting that the primary suspension also has a weak effect on the variation in the minimum levitation gap.

5 Conclusion

This paper develops three numerical models to investigate the dynamic responses of a high-speed maglev train/guideway system. A comparative analysis of the dynamic responses calculated with the different numerical models has been conducted with field-measured data as a reference, and an investigation has also been performed to study the effects of the train speed and the suspension system on the dynamic performance of the maglev train/guideway system. The following conclusions can be drawn:

1. Comparisons of the experimental and numerical responses indicate that all of the proposed numerical models can be used to accurately predict the dynamic responses of the guideway. The moving load model is an especially efficient means of predicting the guideway responses. However, if the responses of the vehicle are of interest, then a train/guideway interaction model is preferred. In particular, the interaction model with a feedback controller can predict the dynamic responses in terms of the levitation gap and magnetic forces, which are very important for the analysis of a maglev system.
2. The train speed has a significant impact on the guideway responses. The dynamic amplification of the guideway responses is considerable when the train speed reaches a certain value (560 km/h in the present case). The dynamic amplification factors specified in a previously developed set of German design guidelines are excessively conservative in the present case; thus, it is recommended that an appropriate case-specific amplification curve for guideway design be extracted based on the relevant resonance and cancellation conditions.
3. In this paper, the stiffness and damping of the secondary suspension are found to exhibit a significant effect on the car body acceleration and the levitation gap, with an increase in either one leading to an obvious increase in the vehicle acceleration and a decrease in the minimum levitation gap. By contrast, the stiffness and damping of the primary suspension exhibit a relatively weak effect on the car body acceleration and the minimum levitation gap. Thus, to ensure satisfactory ride quality, the secondary suspension system should be more carefully considered.

The proposed numerical models can be used for related research on maglev train/ guideway systems as well as for further research, such as research on the ground and environmental vibrations induced by high-speed maglev trains.

References

1. Yaghoubi H, Ziari H (2011) Development of a Maglev vehicle/guideway system interaction model and comparison of the guideway structural analysis with railway bridge structures. J Transp Eng 137:140–154
2. Wang HP, Li J, Zhang K (2007) Vibration analysis of the maglev guideway with the moving load. J Sound Vib 305:621–640. https://doi.org/10.1016/j.jsv.2007.04.030
3. Cai Y, Chen SS (1996) Vehicle/guideway dynamic interaction in Maglev systems. J Dyn Syst Meas Control 118:526–530. https://doi.org/10.1115/1.2801176
4. Cai Y, Chen SS, Rote DM, Coffey HT (1994) Vehicle/guideway interaction for high speed vehicles on a flexible guideway. J Sound Vib 175:625–646. https://doi.org/10.1006/jsvi.1994.1350
5. Ren S (2008) Dynamic simulation of the Maglev guideway design. Masters thesis, Delft University Technology
6. Talukdar RP, Talukdar S (2016) Dynamic analysis of high-speed Maglev vehicle-guideway system: an approach in block diagram environment. Urban Rail Transit 2:71–84. https://doi.org/10.1007/s40864-016-0039-8
7. Zhao C, Zhai W (2002) Maglev vehicle/guideway vertical random response and ride quality. Veh Syst Dyn 38:185–210. https://doi.org/10.1076/vesd.38.3.185.8289
8. Shi J, Wei Q, Zhao Y (2007) Analysis of dynamic response of the high-speed EMS maglev vehicle/guideway coupling system with random irregularity. Veh Syst Dyn 45:1077–1095. https://doi.org/10.1080/00423110601178441
9. Shi J, Wang Y-J (2011) Dynamic response analysis of single-span guideway caused by high speed maglev train. Lat Am J Solids Struct 8:1–14
10. Lee JS, Kwon SD, Kim MY, Yeo IH (2009) A parametric study on the dynamics of urban transit maglev vehicle running on flexible guideway bridges. J Sound Vib 328:301–317. https://doi.org/10.1016/j.jsv.2009.08.010
11. Kong E, Song JS, Kang BB, Na S (2011) Dynamic response and robust control of coupled maglev vehicle and guideway system. J Sound Vib 330:6237–6253. https://doi.org/10.1016/j.jsv.2011.05.031
12. Kim K-J, Han J-B, Han H-S, Yang S-J (2015) Coupled vibration analysis of Maglev vehicle-guideway while standing still or moving at low speeds. Veh Syst Dyn 53:587–601. https://doi.org/10.1080/00423114.2015.1013039
13. Min D-J, Jung M-R, Kim M-Y, Kwark J-W (2017) Dynamic interaction analysis of Maglev-guideway system based on a 3D full vehicle model. Int J Struct Stab Dyn 17:1750006. https://doi.org/10.1142/S0219455417500067
14. Min DJ, Kwon SD, Kwark JW, Kim MY (2017) Gust wind effects on stability and ride quality of actively controlled maglev guideway systems. Shock Vib 2017. https://doi.org/10.1155/2017/9716080
15. Sinha PK (1987) Electromagnetic suspension dynamics and control. Magn Levitation Veh
16. Goodall RM (2000) On the robustness of flux feedback control for electro-magnetic Maglev controller. In: Proceedings of the 16th international conference on magnetically-levitated systems and linear drives, pp 197–202
17. Ogata K (2010) Modern control engineering. Prentice Hall
18. Wu X, Huang J (2004) Guideway structure, Maglev demonstration line, Shanghai. Struct Eng Int J Int Assoc Bridge Struct Eng 14:21–23

19. Yang YB, Yau JD, Wu YS (2004) Vehicle–bridge interaction dynamics with application to high speed railways. World Scientific Publishing Co. Pte. Ltd, Singapore
20. Yau JD (2009) Vibration control of maglev vehicles traveling over a flexible guideway. J Sound Vib 321:184–200. https://doi.org/10.1016/j.jsv.2008.09.030
21. Yang YB, Yau JD (1997) Vehicle-bridge interaction element for dynamic analysis. J Struct Eng 123:7
22. Magnetschnellbahn Ausführungsgrundlage Fahrweg: Teil II., Eisenbahn-Bundesamt. Bonn, Germany (2007)
23. Ren S, Romeijn A, Klap K (2010) Dynamic simulation of the Maglev vehicle/guideway system. J Bridge Eng 15:269–278. https://doi.org/10.1061/(ASCE)BE.1943-5592.0000071

Study on Properties of Polyurethane Grouting Foam Material for High-Speed Railway Track Lifting

Wen Han, Chuanyue Huang, Jiadong Xu, Yanjie Lu, Yan Zhu, Yanjun Cui and Jinsong Tang

Abstract In this paper, a novel polyurethane grouting foam materials (PGFM) were optimized with the polyether polyol species, molecular weight, functional degree, isocyanate index, chain extender contents, catalyst species and contents into the desired formula. Such optimized formulation design disclosed that the PGFM had the best comprehensive performance when the isocyanate index was of 1.2, polyether molecular weight of 500–800, functional degree of 3–4, and chain extender at 3% and the catalyst dosage $C1$ 0.4% and $C2$ 0.2%. Intensive investigation in the molding density of PGFM influence on mechanical properties, water absorption, frost/acid/alkali resistant, aging performance, environmental properties and safety tested by experiment was found that PGFM had the low water absorption rate, excellent mechanical properties, dimensional stability frost/acid/alkali resistance and safe and environmentally friendly. Lastly, after injecting polymer grouting material into the lift track, the durability and dispersion of PGFM were also tested to confirm its engineering application feasibility for high-speed railway lifting track structure. It revealed that the PGFM evenly distributed under the concrete base plate and the surface of the track subgrade. The grouting filler can not only distribute evenly on the surface of the subgrade, but also enter into the interior of the subgrade along with the graded gravel pores, which further played an important role in strengthening the subgrade.

Keywords High-speed railway · Subsidence · Grouting materials · Track lifting · Polyurethane foam

W. Han (✉) · Y. Zhu · Y. Cui · J. Tang
Shanghai Huafon New Material R&D Technology Co. Ltd., Shanghai 201315, China
e-mail: han.wen@huafeng.com

C. Huang · J. Xu · Y. Lu
China Railway Shanghai Group Co., Ltd., Shanghai 200071, China

1   Introduction

Benefit with high speed and high capacity, energy efficiency and economy saving and environmental friendliness, the high-speed railway has prompted extensive development and vastly social and economic benefits for the whole country of China. Currently, large area of high-speed railway is adopted of ballastless track. Compared with ballast track, ballastless track is composed of high stiffness and reinforced concrete track structure, instead of discrete sleeper and loose ballast [1–3]. Besides that, ballastless track is of longer service life, lower maintenance cost and better maintenance of track geometry. Moreover, ballastless track embedded with seamless track can tolerate certain track expanding, as which makes it with higher smoothness and durability, suitable for high-speed train operation in better safety and comfort.

However, on the one hand, caused by accumulation of certain deformation, on the other hand, due to complexity of Chinese geological conditions, the subgrade of the high-speed railway produces uncontrollable post-construction settlement, further reduces the smoothness of the whole ballastless track structure, which in turn destructs the advantages of ballastless track on stability and comfort, and even endangers driving safety [4–6].

To settle such problem and maintain normal operation of high-speed railway, Ford and Gibson [7] reported using polymer grouting technology for restoring the lifting capacity of line height and fastener system to lift track structure accurately. In such technology, the high-pressure materials are injected onto the roadbed gravel surface by pipeline, to fill the pore and concrete the graded crushed stone form, then uplifted by the huge reaction force into the track structure [8–10], and finally consolidated as a part of the track structure in grouting form. Hence, in order to maintain the smooth lifting process, and thereafter operational performance of the track structure, such materials need to encounter the requirements of controllable expansion force, high strength and durability, safety and environmental protection. Here, we synthesized novel high durable strength PGFM by meticulous regulation of material formula and investigated the influence of different components on the bubble pore on mechanical properties of them.

2   Materials and Methods

Polyurethane foam is an extensive family of polymers that can be manufactured with a wide range of physical properties in either expanded or unexpanded states. Expanding polyurethane foam is formed by polyols and isocyanates with specific volumetric proportions in conformity to their particular specifications. By introducing a large amount of carbon dioxide during the reaction, such foam structure formed with gas bubbles (cells) surrounded around the rigid walls.

The physical property of PGFM was tested in accordance with ISO, IEC, GB and major OEM test procedures. Among them, ISO 844 is referenced to determine compressive strength, ISO 1926 to tensile properties, GB/T10799 to closed cell percentage, GB/T 6343 to density, IEC 62321 to heave metal content and OEM to start foaming time and surface drying time. After the distilled water was soaked with polyurethane foam for 24, 72 h or 3 months, the remaining water was analyzed in items and parameters referring to the standard drinking water.

3 Results and Discussion

3.1 Formula Optimization of PGFM

3.1.1 Polyether Polyol Molecular Weight and Functionality

As shown in Table 1, under the same condition, different active polyether polyols group proceeded with a huge distinction on the reaction rates. Comparing with the reaction rate disclosed that the self-catalyzed amine ether was the fastest, of which the start foaming time was 7 s and the surface drying time was 28 s, while the ordinary polyether polyol group was the slowest. Moreover, polyether polyols with different activities also generated specific effects on material mechanics. The primary hydroxyl group exhibited the smallest compression and tensile properties because of the introduction of the primary hydroxyl group and the flexibility of the molecular chain with ethylene oxide sealing end better than that of propylene oxide. Amine ether group revealed the fastest reaction speed and strong compression and tensile strength, making it advisable to reach the mechanical performing requirements of grouting materials.

Figure 1 describes that the compressive strength and the tensile strength remarkably decreased with the increase in polyether polyol molecular weight. However, the breaking elongation of PGFM presented a continual increase with the enhancement of polyether polyol molecular weight as depicted in Fig. 2. It is known

Table 1 Effects of different reactive polyether polyols on the properties of PGFM

Polyether polyol species	Start foaming time (s)	Surface drying time (s)	Compressive strength (MPa)	Tensile strength (MPa)	Breaking elongation (%)
Primary hydroxyl polyether	9	34	0.817	0.762	4.27
Ordinary polyether polyol	13	49	0.853	0.804	3.76
Amine ether	7	28	0.877	0.825	3.58

Fig. 1 Relationships
between compressive
strength/tensile strength and
polyether polyol molecular
weight
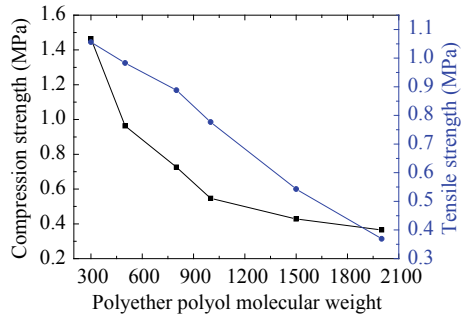
Fig. 2 Relationship between
breaking elongation and
molecular weight
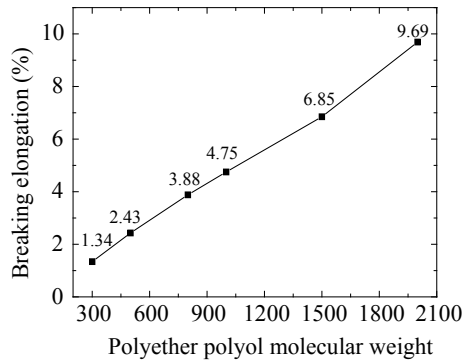
that the polyether polyol molecular weight has an important effect on the mechanical
properties of PGFM. Because of the soft segment, the structures in the PGFM are
mainly composed of polyether polyol, with the increase in polyether polyol
molecular weight, soft segment molecular chains become longer, and the structures
become softer. It can also be learned from Fig. 1 that when the molecular weight was
higher than 800, the compressive strength nonconforming requirement was less than
0.72 MPa. As displayed in Fig. 2, when the molecular weight was less than 500, the
breaking elongation nonconforming requirement was greater than 2%. Therefore, in
order to satisfy the comprehensive mechanical properties requirements are to lift the
track structure effectively; the molecular weight of polyether polyol was preferably
in the range of 500–800.

Figure 3 indicates that the compressive strength and the tensile strength
increased notably with the increase in polyether polyol functional degree. On the
contrary, Fig. 4 reveals that the breaking elongation of PGFM presented a continue
decrease when the polyether polyol functional degree increased. These results
demonstrated that the polyether polyol functional degree displayed an important
effect on the mechanical properties of PGFM. This is because the soft segment
cross-linking degree of PGFM increases when the polyether polyol functionality
increases, leading to the increase in compressive strength and tensile strength,

Fig. 3 Relationships
between compressive
strength/tensile strength and
polyether polyol functionality
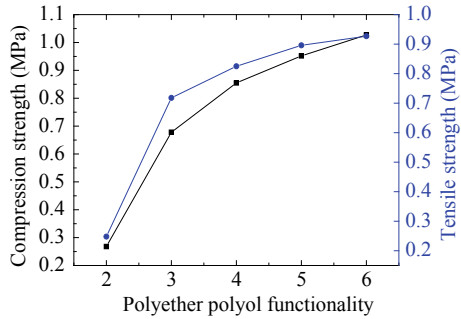
Fig. 4 Relationship between
breaking elongation and
polyether polyol functionality
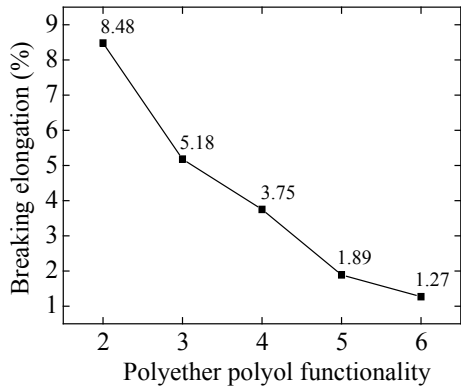
but the decrease in breaking elongation. The polyether polyol functional degree was selected ideally as 3–4 to fulfill of the comprehensive mechanical properties requirements.

3.1.2 Chain Extender Contents

In order to examine the effect of chain extender cross-linking agent on the performance of polymer grouting materials, small-molecule polyol was selected as chain extender cross-linking agent. When the dosage of chain extender cross-linking agent was extended gradually from 0 to 4% of polyether polyol, the influence of chain extender cross-linking agent on the mechanical properties of the grouting materials was enhanced, as depicted in Fig. 5.

Figure 6 evinces that with the increasing in the dosage of cross-linking agent, compression strength and tensile strength of grouting material gradually increased, while elongation at break decreased. This indicated that added extender cross-linking agent strengthens the mechanical properties of PGFM, but reduced the deformation properties. In order to satisfy the compression, the tensile strength of

Fig. 5 Relationships between compressive strength/tensile strength and chain extender content
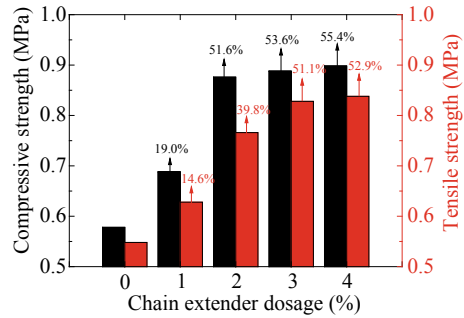
Fig. 6 Relationship between breaking elongation and chain extender content
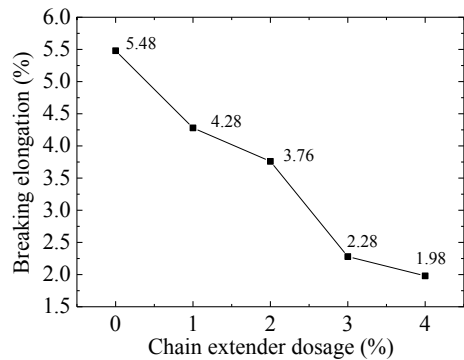
grouting material is not less than 0.72 MPa, the elongation at break not less than 2% of the demands and the dosage of extender cross-linking agent was preferably in 2–3%.

3.1.3 Catalyst Spaces and Contents

The amount of catalyst has evidenced as a significant influence on the reaction rate of the grouting material. The effects of different types and amounts of catalysts on the starting time and dry time of the grouting material ($C1$ stood for the amine starting catalyst and $C2$ for the organotin gel catalyst) were explored, which listed in Table 2. As $C2$ is a kind of organotin-based catalysts damaging to the environment, friendly environmental catalyst $C3$ replacing for $C2$ was also examined. As shown in Table 3, under the same condition, replacing $C3$ for $C2$ exhibited little effect on reaction rate. It is also revealed from Table 2 that the reaction rate increased with catalyst content increasing. The start foaming time was 8 s and the surface drying time 28 s when $C1$ content was 0.4% and $C2$ 0.2%. More than this set of catalyst content, the growth of reaction rate was not obvious.

Table 2 Effect of different catalyst contents on the reaction time of PGFM

C1	C2	Start foaming time (s)	Surface drying time (s)
0.1	0.05	12	48
0.2	0.1	10	40
0.3	0.15	9	32
0.4	0.2	8	28
0.5	0.25	7	27
0.6	0.3	7	23
0.8	0.35	6	21

Table 3 Reaction times of PGFM with different content catalysts

C1 (%)	C2 (%)	C3 (%)	Start foaming time (s)	Surface drying time (s)
0.4	0.2	0	8	28
0.4	0	0.2	8	30

Eventually, in order to appease the comprehensive mechanical properties requirements and cost of PGFM the $C1$ content was set as 0.4% and the $C3$ content as 0.2%.

3.1.4 Isocyanate Index (*R*-Value)

The ratio of –NCO group in isocyanate to the –OH group in polyether polyol is called isocyanate index (*R*-value), which performs an important effect on the reacting and mechanical properties of PGFM. As displayed in Fig. 7, with the increase of *R*-value, the reaction rate slowed down, mainly due to the increase in isocyanate content, decreasing catalyst dosage relatively, then lowing the reaction rate.

Figures 8 and 9 reveal that tensile strength increased first and then decreased with the increase of *R*-value, and the maximum compressive strength appeared

Fig. 7 Relationships between start foaming time/ surface drying time and *R*-value
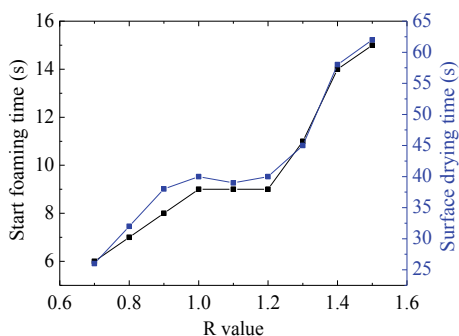
Fig. 8 Relationships
between compressive
strength/tensile strength and
R-value
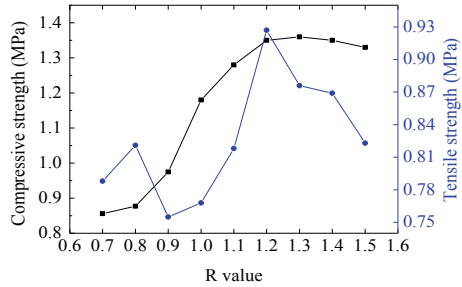
Fig. 9 Relationship between
breaking elongation and
R-value
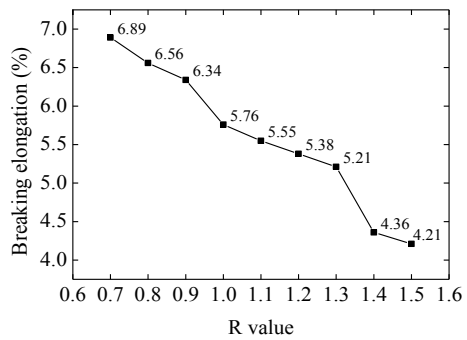
around the *R*-value of 1.2. For reaching the need of compression strength and
tensile strength of polymer grouting material, *R*-value was set between 1.1 and 1.30.
The higher the isocyanate index, the more intense the reaction of the polymer
grouting material became, and the more concentrated heat was released. The
structure of the high obturator material was not conducive to heat dissipation, while
heat accumulation was easy to occur. Thus, the isocyanate index of PGFM was
selected 1.2.

3.2 Properties of PGFM

3.2.1 The Effect of PGFM Density on Mechanical Properties, Water Absorption and Frost Resistance

Due to PGFM injected in the limited space in the underground, the resulted density
of PGFM is more important than its free expansion foam density, making it nec-
essary to analyze various properties of PGFM at different molding densities. In this
work, different weight of PGFM was injected into the fixed volume steel molds to
control the density of PGFM.

As shown in Fig. 10, with the increase in molding density, both the compressive
strength of PGFM and the growth rate increased gradually. Under nonlinear

Fig. 10 Relationship between compressive strength and material density
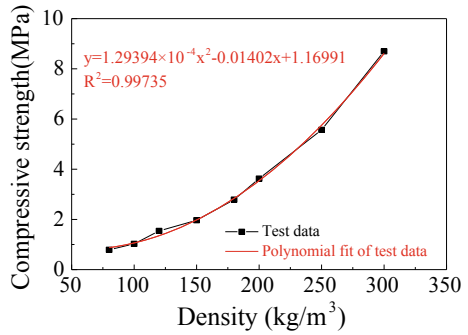
Fig. 11 Relationship between tensile strength and material density
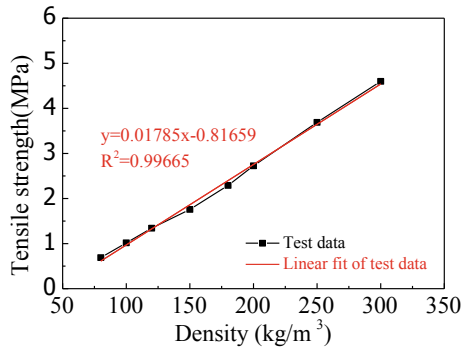
Fig. 12 Relationship between breaking elongation and material density
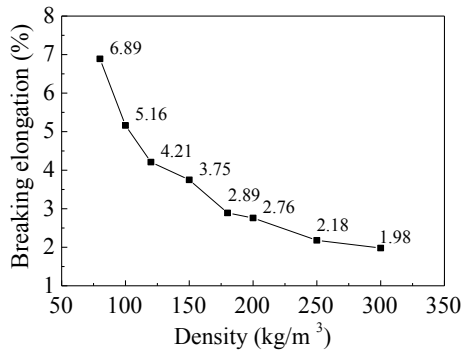
regression, compressive strength with density displayed a good quadratic linear relationship. Figure 11 shows that the relationship between tensile strength and molding density was satisfied with a straight line. Combining with the properties between breaking elongation and density in Fig. 12, the density of PGFM at 250 kg/m^3 was suitable. Moreover, the compressive strength and tensile strength of PGFM at density of 250 kg/m^3 were all apt to the mechanical requirements.

Fig. 13 Relationship between expansive force and material density
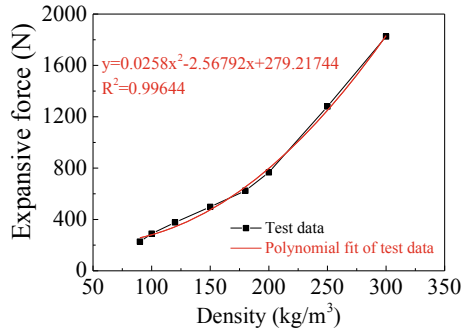
Fig. 14 Relationship between water absorption and material density
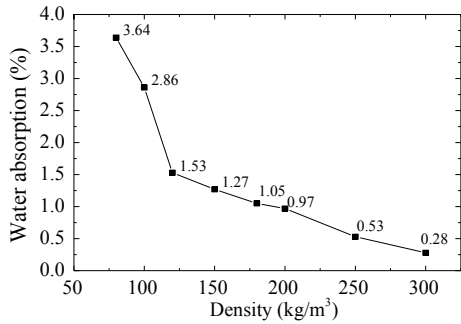
As shown in Fig. 13, expansive force and molding density were fitted to a quadratic linear curve, from which the expansive force at any density can be verified. The expansive force of PGFM at the density of 250 kg/m^3 mentioned above was 1280 N, which fully suitable for the uplifting capacity required by the track structure.

Figure 14 demonstrates that when the molding density increased, the water absorption of PGFM decreased. When the molding density reached 80 kg/m^3, the water absorption was of 3.64%. However, the water absorption was only of 0.28% when the density was 300 kg/m^3. This indicated the density encountered significant influence on the water absorption, which reason was that with the increase of density, the obturator of PGFM structure became regular and dense, and the proportion of closed cells increased, as shown in Fig. 15. Therefore, even if PGFM immersed in water for a long time, the water was difficult to enter inside of the PGFM. Before the test, some of the closed cells were destroyed because of the scarfskin of PGFM excising. Thus, the actual water resistance of PGFM would be better while injecting in underground environment.

As shown in Fig. 16, with the increase in PGFM molding density, the effect of freeze-thaw cycles on compressive strength increased. When the number of freeze-thaw cycles was set as 300 per 2 h, the compressive strength of PGFM with density of 80 kg/m^3, 100 kg/m^3, 200 kg/m^3 and 250 kg/m^3 presented 8.3%, 9.6%,

Fig. 15 SEM images of PGFM with different densities

(a) 120kg/m^3 (b) 150kg/m^3

(c) 180kg/m^3 (d) 200kg/m^3
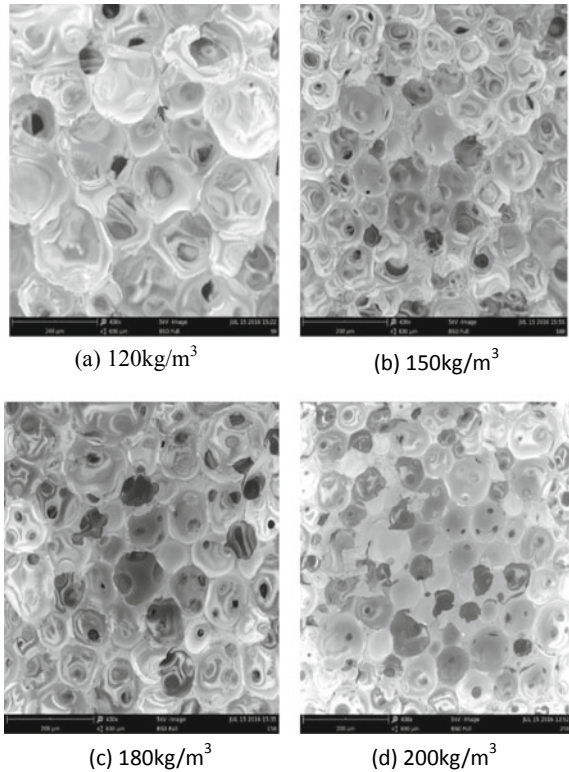
11.8% and 14.7% decrease, respectively. With the increase in molding density, the cell diameter decreased, the expansive pressure causing became easier to damage the cell structures by water swelling. However, as shown in Fig. 16 that even though the density reached 250 kg/m^3, the compressive strength loss of PGFM after 300 times of freeze-thaw cycles was still less than 15%, which was also satisfied with fully long-term service requirements.

Fig. 16 Relationship between compressive strength and number of freeze-thaw cycles
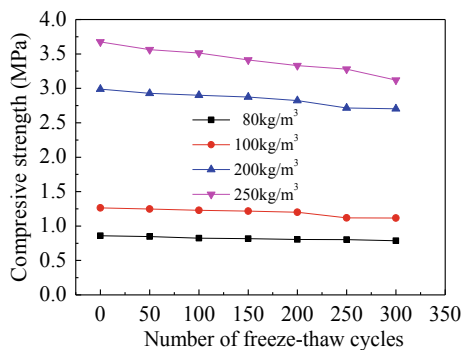
3.2.2 Acid and Alkali Resistance of PGFM

Before acid and alkali resistance test, PGFM was immersed in acidic or alkaline solution for a certain period. The pH value of acidic solution was set as 0, and the pH value of alkaline solution as 14. As described in Fig. 17, with the increase in immersing days, the compressive strength of PGFM immersed in acidic/alkaline solution all presented a tiny change, which indicated that the dense cell structure of PGFM possessed excellent acid and alkali resistance capability.

3.2.3 Aging Performance of PGFM

The time–temperature superposition principle based on experimental data was used to estimate the aging performance of PGFM. The experimental results of change of $\sigma 10$ (compressive stress at 10% relative deformation) with aging time in artificially accelerated wet and hot aging conditions are shown in Fig. 18. In the experiment, the failure point was undergone with 30% decrease of $\sigma 10$, originated as 3.06 MPa, from which the time of $\sigma 10$ was predicted to be 2.14 MPa at 25 °C.

Fig. 17 Relationships between compressive strength and soaking days when PGFM immersed in acidic/alkaline solution
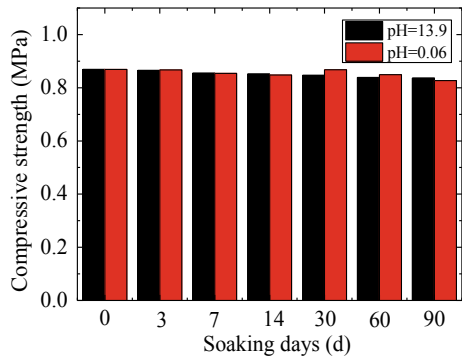
Fig. 18 Relationship between compressive strength and aging time at different temperatures
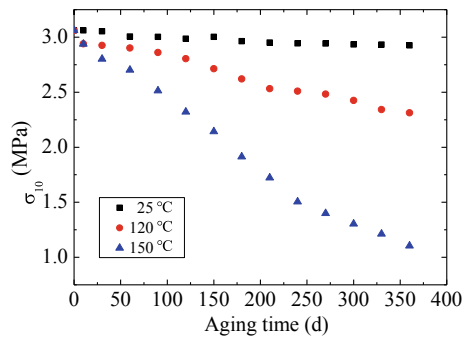
Fig. 19 Time–temperature
equivalent combination curve
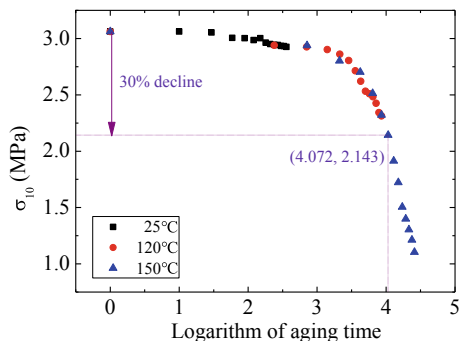
Taking the reference temperature of 25 °C, the curve of 120 °C was shifted to the right, with the curve of 25 °C added, translated into lgaT = 1.379. Under the same operation, the curve of 150 °C translated into lgaT = 1.855. The time–temperature equivalent curve under 25 °C can also be obtained, as shown in Fig. 19.

According to the failure point ($\sigma 10 = 2.14$ MPa) and the corresponding time scale (lgt = 4.072), the storage life of PGFM at 25 °C was equivalent to 32.3 years which met for the long-time service life requirement.

3.2.4 Heavy Metal Ions and Halogen in PGFM and Harmful Substances in PGFM Immersion Water

As shown in Table 4, the heavy metals such as cadmium, lead and mercury were not detected, which in turn meant that such materials fully complied with the requirements of the European Union. The same was suitable for organic matters, as chloride ion was only discovered, with content only of 0.0952%. Such low content, even for underground concrete structures, showed no impact. All of the above indicated that PGFM was a kind of green and pollution-free environmental beneficial material.

The PGFM were immersed in distilled water, where the soaking ratio of the PGFM and distilled water was 1:120, with the soaking water left after 1 day, 7 days

Table 4 Test results of heavy metal ions and halogen in PGFM

Test items	Tested value (mg/kg)
Cd	Not detected
Pb	Not detected
Hg	Not detected
Cr^{6+}	Not detected
F	Not detected
Br	Not detected
I	Not detected
Cl	952

Table 5 Comparison of leaching water tested value and drinking water limit value

Tested value of PGFM leaching water (mg/L)				Drinking water limit value (mg/L)
Test items	1d	7d	30d	
Cr^{6+}	<0.05	<0.05	<0.05	0.05
Cd	0.00007	0.00008	0.00007	0.005
Pb	0.0002	0.0001	0.0002	0.01
Mn	<0.05	<0.05	<0.05	0.1
As	0.0004	0.0004	0.0005	0.05
Hg	0.00002	0.00001	0.00002	0.001
Al^{3+}	<0.01	<0.01	<0.01	0.2
Cu	<0.04	<0.04	<0.04	1.0
Zn	<0.04	<0.04	<0.04	1.0
Fe	<0.01	<0.01	<0.01	0.3
Se	0.0005	0.0005	0.0004	0.01
Cyanide	<0.01	<0.01	<0.01	0.05
Fluoride	0.11	0.27	0.29	1.0
Chloride	0.37	0.75	0.81	250
Sulfate	0.12	0.47	0.53	250
Nitrates	0.18	0.21	0.28	20
Carbon tetrachloride	<0.001	<0.001	<0.001	0.06
Volatile phenols	<0.001	<0.001	<0.001	0.02
pH	6.6	6.7	6.6	6.5–8.5

and 30 days. The concentration of ions in the aqueous solution was tested according to the drinking water standard and is listed in Table 5.

Analysis of the composition of the filtrate of the soaking water of PGFM showed that the leachate did not contain any polymer material, which proved that the PGFM would not degrade or decompose in the case of long-term water immersion. Through comparison and analysis of the test results of PGFM immersion water quality and the sanitary standard of drinking water, the PGFM would not cause pollution to water quality, which indicated that the PGFM grouting material would not pollute the groundwater when buried in the underground for a long time.

3.3 Experiments of PGFM After Grouting

3.3.1 The Lifting Process of Track Structure

The two components of PGFM were mixed with a grouting machine and injected under track structure. The material expanded rapidly, lifting the track structure as it diffused. As shown in Fig. 20, the grouting hole around the concrete base plate was
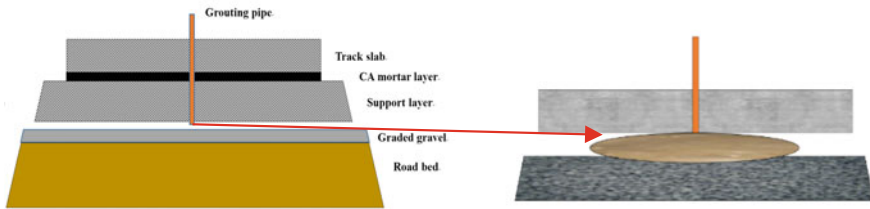
Fig. 20 Diagram of PGFM uplifting the track structure

sealed to prevent the grouting material from extruding from interface. Then, the grouting hole was grouted along the middle line of the track slab, so that the grouting material was filled at the interface between the concrete floor and the surface of the foundation bed, and then the lifting of the track structure was completed. As the result, four angle positions of the track structure were uplifted 46.32 mm, 44.93 mm, 44.40 mm and 45.25 mm, respectively, which indicated that PGFM can uplift the track structure effectively.

3.3.2 Mechanical Properties of PGFM During Service Process

Large cycle fatigue was used to investigate several mechanical properties of PGFM under dynamic load, of which the load range was 50–130 kPa and the load frequency 10 Hz. After 3 million cycles of loading, the axial cumulative deformation of the PGFM sample became stable at about 0.39 mm, and the accumulated strain was about 7.7‰. The axial cumulative deformation of the PGFM–gravel mixture sample was tended to be stable at about 0.13 mm, and the accumulated strain was about 0.65‰. These indicated that PGFM can bear large cyclic loads during service process after grouting.

3.3.3 The Diffusibility of PGFM Under Track Structure

After the test operation, the support layer slab removed to observe the distribution of PGFM. As shown in Fig. 21, PGFM formed uniform layer structure between the bottom of support layer slab and the surface of subgrade. This indicated that PGFM possesses excellent fluidity and pack uniformity during the injection process. In addition, the PGFM and graded gravel further combined into a solid body, as shown in Fig. 22, which was beneficial for the wholeness and workability of track structure. It also indicated that the PGFM can not only be uniformly distributed on the surface of the foundation bed, but also enter into the interior of the foundation bed along with the pores of graded gravel in the foundation bed, thus playing a role in strengthening the foundation bed.

Fig. 21 Distribution of PGFM after condensation

Fig. 22 Combination of
PGFM and gravel
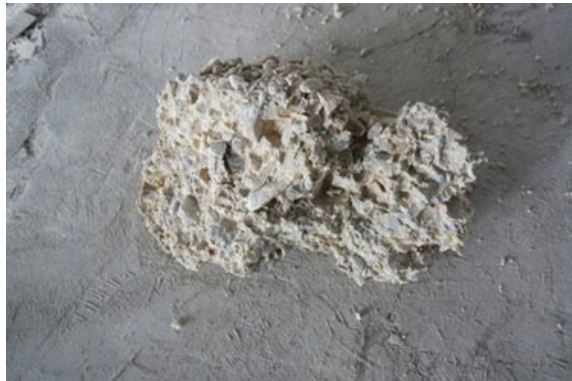
Finally, it was manifested that the laminated structure had strong compressive strength, fully met the mechanical requirements of the material used for track lifting. The density deviation of all points sampled was consistency, and after 3 million times vehicle vibration, the whole material on the surface did not appear to crack and had good durability.

4 Conclusions

This work dealt with the formula optimization, and the preparation of PGFM with excellent performance. Such specific grouting material was injected into space of track structure, carried out to form a well-dispersed laminated structure to meet the service demand of high-speed railway. The main conclusions are as follows:

(1) The optimized formulation design found that the material had the best comprehensive performance when the isocyanate index was of 1.2, polyether molecular weight of 500–800, functional degree of 3–4, chain extender at 3% and the catalyst dosage $C1$ 0.4% and $C2$ 0.2%.

(2) Further investigation found that the lower water absorption rate, the more excellent mechanical properties dimensional stability frost/acid/alkali resistance and safe and environmentally friendly would be.

(3) The polyurethane grouting material foam injected in the ground was a closed cell structure, and the permeability tests were proven to be almost impermeable.

(4) The polyurethane grouting material evenly distributed under the concrete base plate and the surface of the track subgrade. The grouting filler can not only distribute evenly on the surface of the subgrade, but also enter into the interior of the subgrade along with the graded gravel pores, which further plays a role in strengthening the subgrade.

References

1. Buzzi O, Fityus S, Sasaki Y, Sloan S (2008) Structure and properties of expanding polyurethane foam in the context of foundation remediation in expansive soil. Mech Mater 40(8):1012–1021
2. Rindle JA (1970) Reinforcing mechanism in PU foams. J Cell Plast 6(30):280–287
3. Yang ZG, Zhao B, Qin SL, Hu ZF, Jin ZK, Wang JH, Hu ZF (2004) Study on the mechanical properties of hybrid reinforced rigid polyurethane composite foam. J Appl Polym Sci 92(3): 1493–1500
4. Bian XC, Jiang HG, Chen YM (2010) Accumulative deformation in railway track induced by high-speed traffic loading of the trains. Earthq Eng Eng Vibr 9(3):319–326
5. Bezazi A, Scarpa F (2007) Mechanical behaviour of conventional and negative Poisson's ratio thermoplastic polyurethane foams under compressive cyclic loading. Int J Fatigue 29(5): 922–930
6. Buzzi O, Fityus S, Sloan S (2010) Use of expanding polyurethane resin to remediate expansive soil foundations. Can Geotech J 47:623–634
7. Ford CM, Gibson LJ (1998) Uniaxial strength asymmetry in cellular materials: an analytical model. Int J Mech Sci 40(6):521–531
8. Youssef S, Maire E, Gaertner R (2005) Finite element modelling of the actual structure of cellular materials determined by X-ray tomography. Acta Mater 53:719–730
9. Shen Y, Golnaraghi F, Plumtree A (2001) Modeling compressive cyclic stress-strain behaviour of structural foam. Int J Fatigue 23:491–497
10. Mills N, Lyn G (2002) Modeling air flow in impacted polyurethane foam. Cell Polym 21:343–365

Monitoring Technology of Ballast Track in Rail Expansion Joint Area of High-Speed Railway

Guoliang Song, Chao Lin, Weichang Xu and Shehui Tan

Abstract The rail expansion joint is a weakness of the track structure, though it can reduce the interaction force between the bridge and rail. This paper focuses on Tongling Yangtze River Bridge on Beijing-Fuzhou Railway and puts forward the monitoring content and method for rail expansion joint on ballast bed combining with the defect research of laying rail expansion joint in beam ends on China's large span bridges. A track real-time monitoring system is built with the research of image recognition, data association analysis, etc. It has realized the functions of automatic data acquisition and transmission, data storage and analysis as well as automatic monitoring daily report generation. The long-term monitoring data show that the amount of expansion displacement difference between left and right rail is 0–4.0 mm, the annual expansion deformation of stock rail is 447.4 mm, and the corresponding annual change of the beam ends is 370.6 mm.

Keywords High-speed railway · Rail expansion joint · Rail expansion device · Ballast track · Real-time monitoring system

1 Introduction

With the development of China's high-speed railway in recent years, it is inevitable to have long-span continuous beam bridge in order to meet the needs of various complex regional environments. Under the effect of temperature load, the continuous welded rail on the long-span continuous beam bridge will generate considerable longitudinal force and displacement of the rail. To ensure the strength and

G. Song · W. Xu · S. Tan (✉)
China Railway Shanghai Administration Group Co., Ltd., Shanghai 200071, China
e-mail: 2138586142@qq.com

C. Lin
China Railway Siyuan Survey and Design Group Co., Ltd., Wuhan 430063, China

C. Lin
Hubei Key Laboratory of Track Security Service, Wuhan 430063, China

545

stability of the rail, a rail expansion joint should be set at the beam end, and a rail expansion device is also required if the beam end is large. At present, China's large-span railway bridges, e.g., Nanjing Dashengguan Yangtze River Bridge, Wuhan Tianxingzhou Yangtze River Bridge, Tongling Yangtze River Rail-cum-Road Bridge are all equipped with rail expansion joints, and rail expansion devices are installed at the beam ends.

In the process of using the rail expansion joint and the rail expansion device at the beam end on relevant lines, there are some defects such as inclined crack of the sleeper, large deformation and stuck of the scissor fork for rail expansion device, resulting in a large amount of maintenance work and economic loss [1–3]. So far, the domestic inspection of high-speed railway rail expansion joints is generally carried out by manual inspection during night maintenance time and supplemented by regular rail inspection vehicles. The inspection efficiency of the rail inspection vehicle is high, but the detection period is long, in contrast, the manual detection has a high detection frequency, but the efficiency is low. In addition, in the non-maintenance time, neither manual static detection nor dynamic detection of rail inspection vehicle can get the status of the line in real time. Once the defect occurs, it is difficult to find it in time, which may affect the safety of train operation.

Based on investigation and analysis of the existing monitoring systems [4–8] and research on the long-term monitoring technology of high-speed railway track system, this paper establishes a long-term monitoring system for high-speed railway rail telescopic regulators, which integrates image recognition technology, communication technology and computer technology. The system realizes the functions of automatic collection, transmission, analysis and automatic generation of monitoring data and images, provides reliable and detailed monitoring data for the safety analysis of high-speed railway rail expansion joint and rail expansion device, and offers a scientific basis for defect control and maintenance of rail expansion joint.

2   Overview of Monitoring Sites

The design speed of the Beijing-Fuzhou Tongling Yangtze River Rail-cum-Road Bridge is 250 km/h, and the main bridge is a double-tower steel cable-stayed bridge. The main span of the steel girder is 645 m, which is one of the largest railway span bridges in China. The bridge is constructed with a ballast track structure, a rail expansion joint with an expansion amount of ±600 mm at the beam end and a rail expansion device at the beam end. Figure 1a shows the structure of the rail expansion joint, which contains two hanging steel sleepers between beam ends and a double link expansion device. This kind of joint ensures the distance between nodes being uniform and not exceeding the allowed maximum value during the expansion. Figure 1b shows a rail expansion joint set at the beam end of Tongling Yangtze River Bridge.
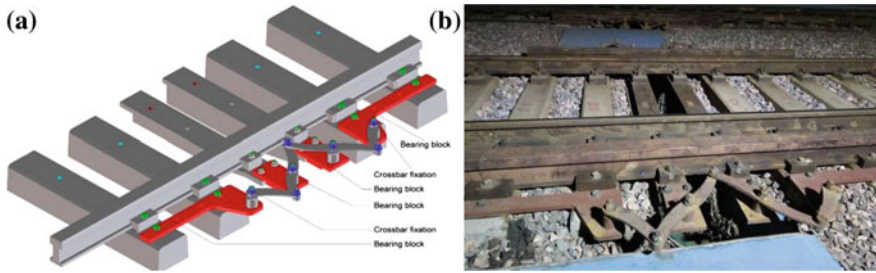
Fig. 1 **a** Structure of the rail expansion joint and rail expansion device; **b** rail expansion joint at the beam end of Tongling Yangtze River Bridge

3 Monitoring Content

3.1 Temperature Monitoring

Temperature monitoring can reveal the effect of temperature on structural deformation. Therefore, to acquaintance the deformation law of the track structure of the rail expansion joint area, it is necessary to monitor the atmospheric temperature, the rail temperature and the bridge temperature.

3.2 Rail Expansion Displacement Monitoring

In the process of operation, due to the influence of the resistance of fasteners, the resistance of the track bed, the performance of the rail expansion device and other factors, the left and right strands of rail expansion joint may have unsynchronized expansion or excessive displacement, which may easily lead to the deformation of the track skeleton, or even cause the scissor fork bent or twisted. Monitoring of the rail displacement is conducive to understand the resistance of the left and right fasteners and the resistance of the track bed. The fastener and track bed resistance can be adjusted in time when problem occurs. According to the relevant specifications and the use instructions of the regulator, the relative displacement between the left and right stock tips and the stock rails shall not exceed 5 mm. According to the relevant specifications and the use instructions of the regulator [9–13], the relative displacement between the left and right stock tips and the stock rails shall not exceed 5 mm.

3.3 Sleeper Spacing and Deformation Monitoring

The excessive distance between the sleeper leads to the increase in the impact on the rail, which affects the service life of the rail. At the same time, the tilt of the sleeper will result in bending or distortion of the cutter and fork.

According to the "Management Manual for Beijing-Fuzhou Tongling Yangtze River Rail-cum-Road Bridge" [14]: "The center distance between the movable steel sleeper, the movable steel sleeper and the adjacent fixed steel sleeper is in the range of 385–635 mm, and the maximum deviation between the clearance between the adjacent steel sleepers and the average clearance is no more than 25 mm. When the average distance between adjacent steel sleepers exceeds 635 mm, measures shall be taken immediately to stop operation and report to higher authorities."

3.4 Bridge Beam End Value Monitoring

The change of bridge girder joints directly affects the service state of the rail expansion joint. If the value of the girder joints exceeds the maximum expansion range of the regulator, the regulator will be over-ranged, endangering traffic safety. Therefore, it is necessary to conduct long-term monitoring of the girder joints value.

3.5 Structural Apparent State Monitoring

The apparent defect of the rail expansion joint is mainly manifested in the deformation of the scissor fork and the squeezing of the fastener pads. The related defects of the rail expansion joint can be found in time through video monitoring.

4 Monitoring Method

4.1 Image Recognition Technology

It is a mature method to use displacement sensor for measurement, but the rail expansion joint is a sensitive part of the track structure, the installation of contact displacement sensor poses safety hazards to operation. Image recognition technology has strong robustness to light, bad weather, etc., and its non-contact measurement method just meets the needs of long-term safety monitoring. Therefore, an image recognition method is adopted for the displacement measurement of rail expansion joint, as follows:

(1) Switch rail expansion displacement

Marking points should be set at the actual point of switch rail and the corresponding base rail web to measure the relative displacement through identifying the distance between the marking point 1 located at the actual point of switch rail and the marking point 2 located on the base rail. The distance between the marking points 2 and 3 is a standard distance, and the length between marking points 1 and 2 in the picture can be converted by referring to the length between marking points 2 and 3 (Fig. 2).

(2) Sleeper spacing and skewness

The red marking points are arranged on the steel sleepers and the concrete sleepers, the position of the center of the red marking point is obtained by taking a picture, the spacing of the sleepers is obtained by the distance between the centers of the circles, and the degree of skewness of the sleeper can be quantitatively determined through the center line connection (Fig. 3).

4.2 Displacement Label

The displacement label is mainly used to identify the relative displacement between rail structures in the rail expansion joint area with image recognition technology.
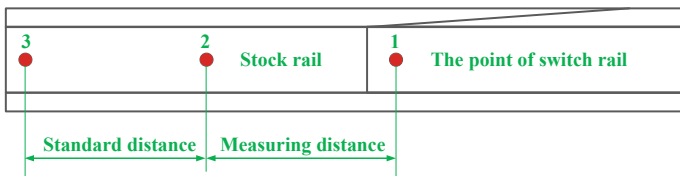
Fig. 2 Switch rail expansion displacement identification method
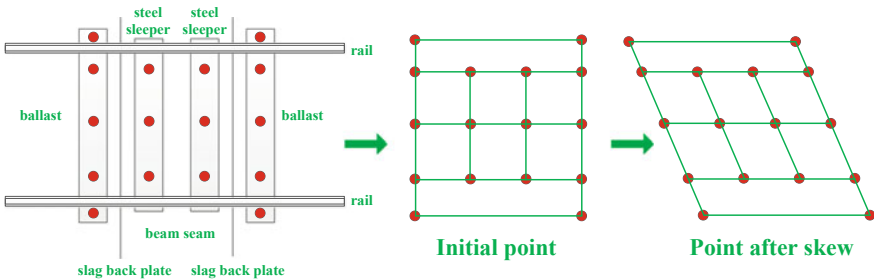
Fig. 3 Sleeper skewness identification method

The displacement label consists of two parts, one is the reference area of measurement and the other is the recognition area of measurement. The reference area mainly provides measuring point information (QR code) and measuring reference amount (the distance between the centers of two red circles is fixed). The recognition area is mainly located on the measuring object, and the distance between two measuring points can be obtained by obtaining the center of the circle in the recognition area and the center of a circle in the base area.

In order to obtain the measuring point information automatically, a live code is set in the middle of the reference area. The live code encodes an assigned short URL and jumps to this URL after scanning. The content can therefore be stored in the cloud which allows to update and store large amounts of text content at any time (Fig. 4).

5 Monitoring System

The long-term monitoring system of high-speed rail expansion joint consists of three subsystems: data measurement subsystem, data collection and transmission subsystem and data management analysis subsystem.

The data measurement subsystem measures the temperature, displacement and other data of the rail expansion joint. The data collection and transmission subsystem are used to collect and back up the monitoring data; then, data are transmitted to the data management analysis subsystem through network. Finally, the functions of storing, analyzing and querying data are completed. Figure 5 shows the topology diagram of the monitoring system.

(a) Measuring reference area

(b) Measurement identification area
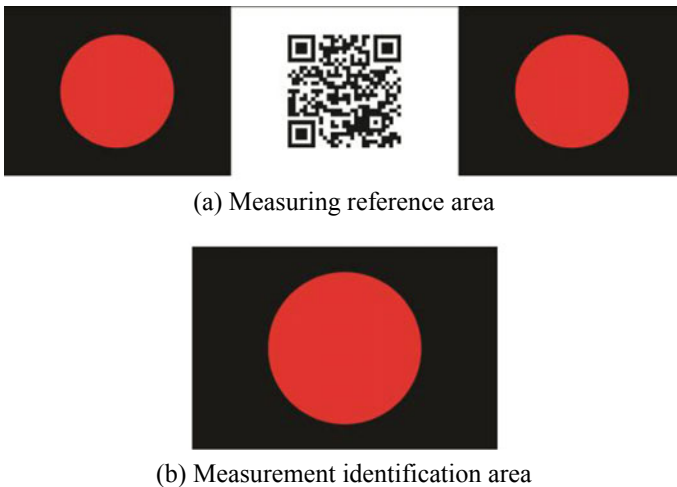
Fig. 4 Displacement label
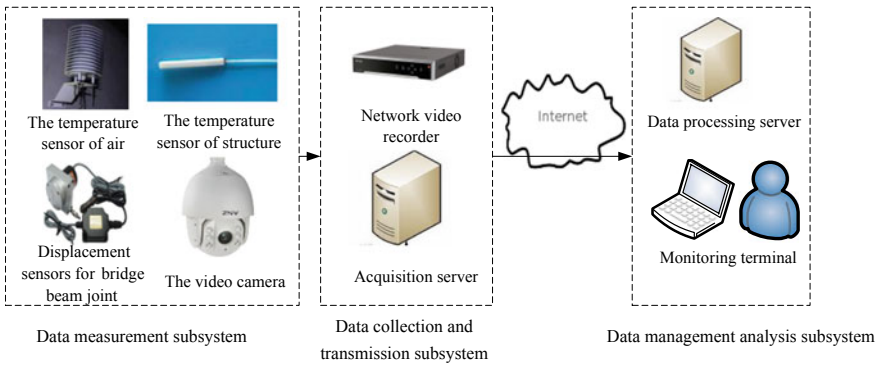
Fig. 5 Topology diagram of monitoring system

5.1 Data Measurement Subsystem

The data measurement subsystem consists of video surveillance cameras, temperature sensors, displacement sensors, etc. distributed in the field.

The data measurement subsystem achieves real-time online monitoring of rail expansion joint and rail expansion device through real-time measurement of air temperature, rail temperature, bridge temperature, rail displacement, sleeper spacing, bridge beam end value, etc. Figure 6 shows the layout of long-term monitoring measurement points of rail expansion joint.

Temperature measuring point Temperature monitoring includes air, rail and bridge temperature. There is one air temperature measuring point, set on the pier;
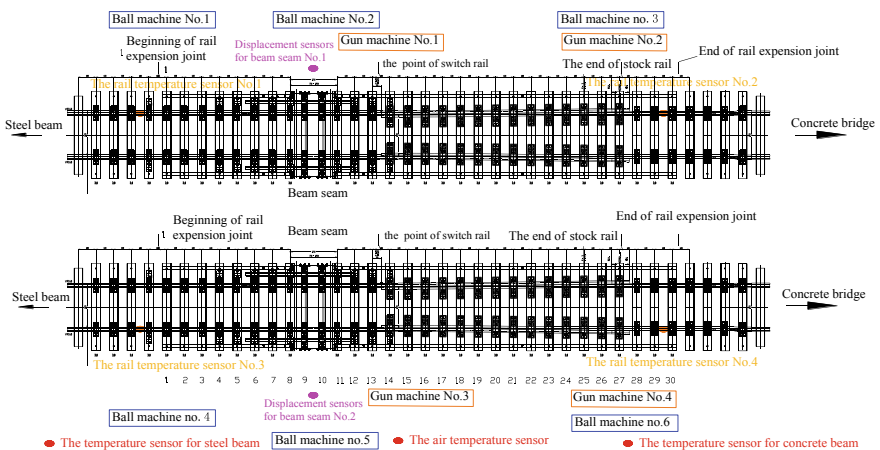
Fig. 6 Rail expansion joint long-term monitoring measuring point layout

four rail temperature measuring points in a set of joints, two on the stock rail and the other two on the actual point of switch rail; four bridge temperature measuring points, two on concrete bridges and two on steel bridges. The temperature sensor has a test accuracy of 0.1 °C. The test accuracy of the temperature sensor is 0.1 °C.

Rail expansion displacement measuring point There are four measuring points in a set of rail expansion joints, two located at the front of the actual point of switch rail and two located at the heel of the stock rail, respectively. The displacement label is pasted at the measuring point, the video camera is mounted, and the displacement value is obtained through the image recognition method. The test accuracy of rail expansion displacement is 0.1 mm. Figure 7 shows the actual point of switch rail displacement monitoring in the field.

Sleeper spacing and deformation measuring point There are two sleeper spacing and deformation measuring points in a set of rail expansion joints. One measuring point is located at the beam joint, which measures the distance between steel sleepers, the distance between steel sleeper and concrete sleeper and the distance between concrete sleepers. The other one is located at the heel of the stock rail, which mainly measures the distance change of the concrete sleepers near the heel of the stock rail. The displacement label is pasted on the measuring point, a video camera is installed, and the sleeper spacing value is obtained through the image recognition method. At the same time, the skewness of the two sleepers is judged by the spacing between the two sleepers at different positions. The test accuracy of sleeper spacing is 0.1 mm. Figure 8 shows the track displacement monitoring point in the field.

Bridge beam end value measurement point Two bridge beam joint displacement sensors are installed at the beam joints on both sides of the main bridge of Tongling Yangtze River Bridge. The test accuracy of the bridge beam joint value is 0.1 mm. Figure 9 shows the bridge beam displacement sensor installed in the field.

Fig. 7 Actual point of switch rail displacement monitoring

Fig. 8 Sleeper displacement monitoring

Fig. 9 Displacement sensor and its protective cover

Structural apparent state measurement point A set of rail expansion joints set up two observation points for the apparent state of the structure. Video camera is used to judge the state of the scissor fork and the squeezing of the fastener pad.

5.2 Data Collection and Transmission Subsystem

The data collection and transmission subsystem consist of two parts: a data collection and transmission cabinet and a video capture and transmission cabinet. Figure 10a shows the data collection cabinet, and Fig. 10b shows the video image collection cabinet.

In order to ensure the smoothness of the live video, the broadband access is collected into the transmission cabinet, so that the video images and data on the scene are transmitted to the monitoring center server through the wired network for processing and analysis.

5.3 Data Management Analysis Subsystem

The data management analysis subsystem includes a data receiving and control command sending module, a data management module and a data analyzing module.

The data receiving and control command sending module receives the original data and images transmitted by the field collecting server through the wired network, and the data management module converts the displacement image into a displacement value through an image recognition algorithm [15] and converts the digital data such as temperature into a unified format stored in the database for data analysis module. The data analysis module analyzes and processes the monitoring data in the database and realizes the functions of data query, output and data comparative analysis through the management information system. At the same time, the system can also generate the daily monitoring daily reports automatically. By comparing with the early warning value, the maintenance department can understand the service status of the rail expansion joints in real time.

In addition, the data management analysis subsystem can also control the movement of the live camera by sending camera control commands to achieve online monitoring of the apparent state of the track structure of the rail telescopic regulator. Figure 11 shows the system video monitoring interface.

Fig. 10 Collection transmission equipment

(a) Data collection cabinet

(b) Video image collection cabinet

Fig. 11 System video monitoring interface

6 Data Analysis and Defect Detection

6.1 Monitoring Data Analysis

Figure 12 illustrates the expansion displacement of stock rails on both sides of Beijing-Fuzhou Tongling Yangtze River Rail-cum-Road Bridge from July 2017 to June 2018. As can be seen from Fig. 12a, the amount of expansion displacement of the left and right stock rails of the upper line is basically the same, with the maximum daily expansion displacement of 170.2 mm in summer, 277.2 mm in winter and 447.4 mm in the whole year. It can be seen from Fig. 12b that the expansion displacement difference between the left and right stock rails of the upper line is between 0 and 4.0 mm, less than the early warning value of 5 mm.

Figure 13 shows the beam end value of Beijing-Fuzhou Tongling Yangtze River Rail-cum-Road Bridge from July 2017 to June 2018. As can be seen from the figure, the width of the beam end is 485.6 mm in summer and 856.2 mm in winter, and the annual change of the beam end expansion is 370.6 mm. The variation trend of stock rail expansion is the same as that of the beam end expansion.

6.2 Defect Detection

On July 23, 2017, the monitoring system found that the pad of the field fastener escaped, resulting in the extrusion of the fastener spacer of the stock rail during the expansion process. After finding the above situation, the works department adjusted
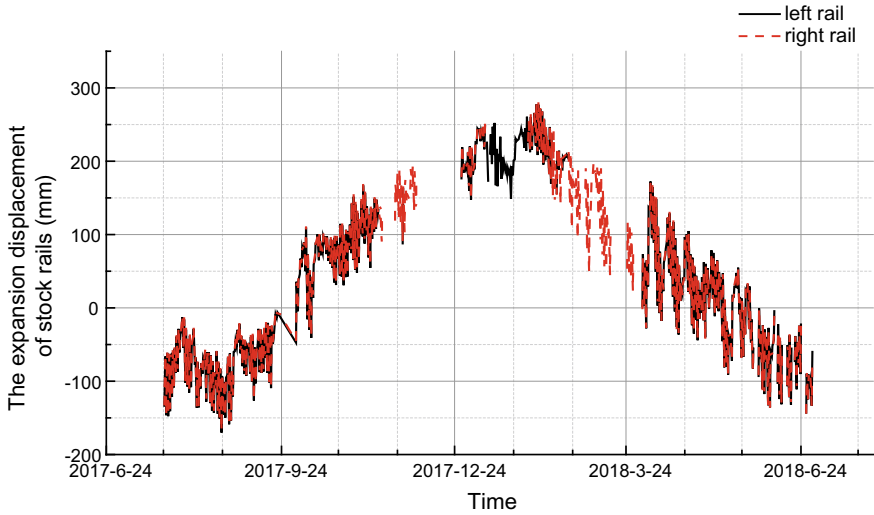
(a) The expansion displacement of stock rails on the left and right of the upper line
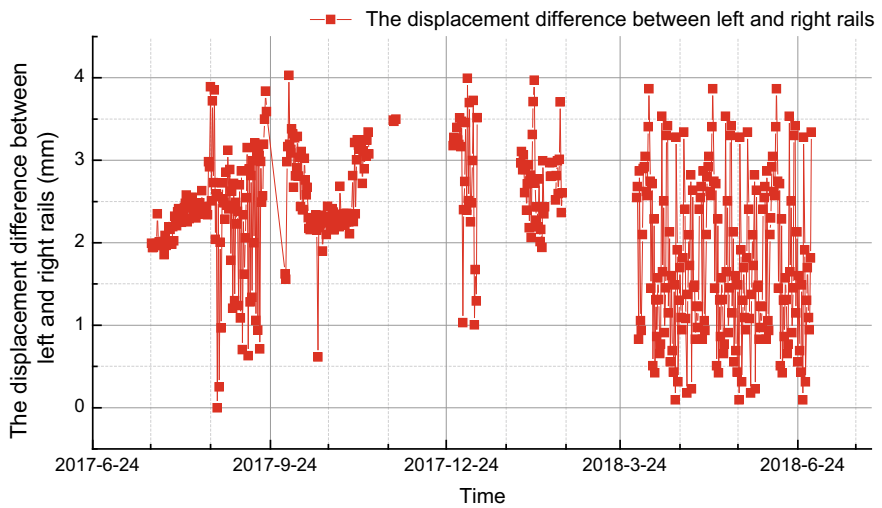
(b) The expansion displacement difference between the left and right
stockrails of the upper line

Fig. 12 The expansion displacement of stock rails on both sides of Beijing-Fuzhou Tongling Yangtze River Rail-cum-Road Bridge from July 2017 to June 2018

Fig. 13 Beam end value of Beijing-Fuzhou Tongling Yangtze River Rail-cum-Road Bridge from July 2017 to June 2018

(a) Before extrusion   (b) After extrusion
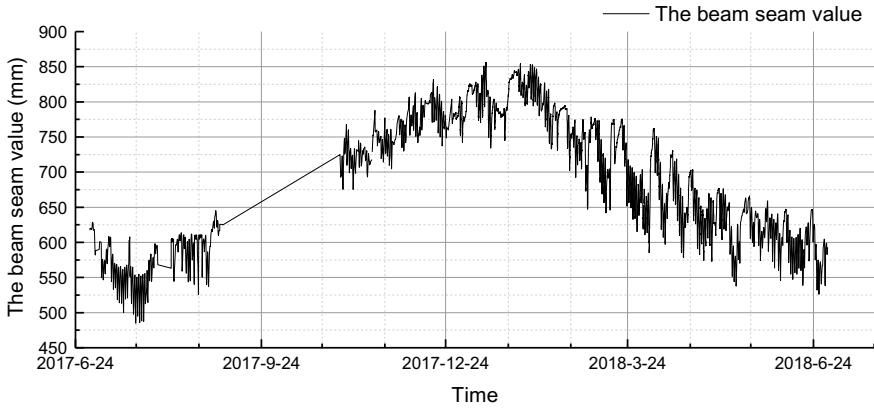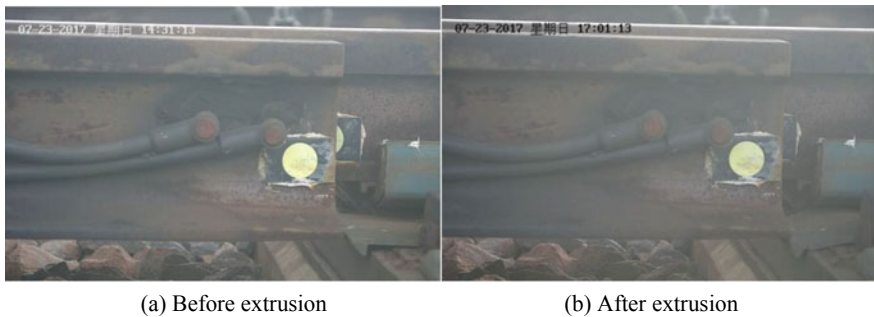
Fig. 14 The stock rail expansion extruding fastener pad

the fastener pad timely. Figure 14 shows the process of the stock rail expansion extruding the fastener pad.

7   Conclusion

This paper focuses on the rail expansion joints of the Beijing-Fuzhou Tongling Yangtze River Rail-cum-Road Bridge, investigating the long-term monitoring technology of the rail expansion joints. The main conclusions are as follows:

(1) The monitoring contents of the rail expansion joints of ballast track include temperature (air temperature, rail temperature and bridge temperature), track expansion displacement, track sleeper spacing and deformation, bridge beam end joint value, structural apparent state, etc.

(2) The non-contact image recognition method can realize the measurement of the rail expansion displacement and the sleeper spacing with a measurement accuracy of 0.1 mm.

(3) The real-time monitoring system of rail expansion joint has achieved automatic collection, transmission, storage and analysis of monitoring data, automatic generation of monitoring reports and timely detection of abnormal conditions in the field.

(4) The amount of expansion displacement of the left and right stock rails of the upper line is basically the same, with the maximum daily expansion displacement of 170.2 mm in summer, 277.2 mm in winter and 447.4 mm in the whole year. The expansion displacement difference between the left and right stock rails of the upper line is between 0 and 4.0 mm, less than the early warning value of 5 mm.

(5) The width of the bridge beam end is 485.6 mm in summer, 856.2 mm in winter, and the annual change of the beam end expansion is 370.6 mm. The variation trend of stock rail expansion is the same as that of the beam end expansion.

References

1. Huang A-n (2014) Research on expansion joint selection and maintenance for Dashengguan Yangtze River Bridge. Mod Transp Technol 1(1):81–84
2. Yu D (2015) Study on the defect treatment of expansion joint on long-span continuous bridge. Sci Wealth 4:256–257
3. Fu F-j (2016) Analysis of reason for expansion joint selection on Dashengguan Yangtze river bridge and control measures. Jiangsu Transp Res 5:17–20
4. Du Y-l, Su M-b, Liu Y-h (2015) Study on the long-term health monitoring and safety evaluation system for the Wuhan Yangtze River Bridge. J China Railway Soc 37(4):101–110
5. An G-d, Mi L, Zhu B-z (2010) Study and application of long-term monitoring system for permafrost area along Qinghai-Tibet Railway. J Railway Eng Soc 3:1–6
6. Sun B-c, Du Y-l, Li J-z (2009) Automatic permafrost temperature monitoring system of Qinghai-Tibet railway based on GSM-R network. J China Railway Soc 31(5):125–128
7. Cai X-p, Gao L, Lin C (2015) Long-term monitoring technology of Beijing-Shanghai high-speed railway elevated station track system. J Railway Eng Soc 32(5):35–41
8. Filograno ML, Rodriguez-Barrios A, Gonzalez-Herraez M et al (2010) Real time monitoring of railway traffic using fiber Bragg grating sensors. In: Proceedings of the 2010 joint rail conference. The American Society of Mechanical Engineers. ASME, New York, pp 493–500
9. Ministry of Railways of the people's Republic of China. Science and Technology Base (2008) No.166. Temporary technical conditions for the Ballastless track of 60 kg/m steel track expansion joint on the 350 km/h passenger dedicated line. China Railway Publishing House, Beijing

10. China Railway Corporation (2015) TJ/GW 143-2015. Temporary technical conditions for CN rail expansion joint. China Railway Corporation, Beijing
11. State Railway Administration (2015) TB/T 3401-2015. Rail expansion joint for passenger dedicated line. State Railway Administration, Beijing
12. BWG Co., Ltd. (2014) Description of BWG rail expansion joint system. BWG Co., Ltd., Germany
13. BWG Co., Ltd. (2014) BWG rail expansion joint installation and maintenance manual. BWG Co., Ltd., Germany
14. China Railway Major Bridge Reconnaissance & Design Institute Co., Ltd. (2015) Maintenance management manual of Beijing-Fuzhou Tongling Yangtze River Rail-cum-Road Bridge. China Railway Major Bridge Reconnaissance & Design Institute Co. Ltd., Wuhan
15. Bowness D, Powrie W, Lock AC, Priest JA, Richards DJ (2007) Monitoring the dynamic displacements of railway track. Proc Inst Mech Eng Part F J Rail Rapid Transit 221(1):13–22

Heavy Haul Railway Geodynamics

Effect of Irregular Shape and Cyclic Loading Frequency on the Dynamic Behavior of Railway Ballast

Junhua Xiao, De Zhang and Xiao Zhang

Abstract Higher speed in existing railway transportation is underlying growth in demand and the meso-mechanical properties of ballast under high-frequency loading. The complex geometry of ballast has influences on their dynamic behavior inevitably. Thus, a numerical polyhedral discrete model based on real irregular shape of ballast triaxial test was established to investigate the combined effect of shape and frequency on the dynamic behavior of ballast. Experimental results of large-scale triaxial tests were used to determine and verify the meso-parameters of the discrete-element model. With same axle load and confinement, three cases of different ballast shapes (i.e., quasi-spherical, elongated and flat, respectively) under different load frequency f (2.4, 5, 10 and 30 Hz) were discussed. Results obtained from models show that the irregular shape has a significant influence on the accumulated deformation of grains. Although the gradation of three specimens was similar, their dynamic response had obvious differences. Contact forces between loading plate and ballast of varied shapes were almost the same, but the increasing load frequency can make the accumulative deformation of the ballast sample to continue growing.

Keywords Irregular shape · Load frequency · Railway ballast · Polyhedral discrete model

J. Xiao · D. Zhang (✉) · X. Zhang
Key Laboratory of Road and Traffic Engineering of the Ministry of Education,
Tongji University, Shanghai 201804, China
e-mail: dz2015@tongji.edu.cn

J. Xiao · D. Zhang · X. Zhang
Key Laboratory of Rail Transit Structural Durability and System Safety of the Shanghai
Municipal Government, Tongji University, Shanghai 201804, China

1 Introduction

The ballast bed is an important part of the train track, which contributes key function in preserving the safety and comfort for the railway, and diffuses the dynamic loading of the train to maintain the long-term dynamic stability of the subgrade structure. However, due to the high-frequency and high-amplitude railway loading, some ballast beds generate deformation in plasticity or are deteriorated, and some even fouled. This not only requires more track maintenance work but also reduces the safety of the train operation. Therefore, a study on the deformation and deterioration characteristics of the ballast under cyclic loading is helpful for knowing the mechanism of above process.

Since ballast particles have complex irregular shapes, random interaction and crushability, much research has been revealed to give methods for describing ballast characteristics. Based on cyclic triaxial testing, Suiker et al. [1] studied the accumulative deformation characteristic of ballast, proving that cyclic loading can improve the shear strength and the stiffness of ballast. Sun and Indraratna [2] found that, under different loading frequencies, the modes of ballast samples' cumulative plastic deformation could be classified into several theoretical models. Meanwhile, some researches based on numerical simulation also supported many insights of it. For instance, Lu and Mcdowell [3] simulated ballast particle with unbreakable clump element in a simple arrangement, and studied their mechanical characteristics in triaxial tests numerical model. Indraranta et al. [4, 5] added the image analysis method for improving the description of irregular shape of a particle. Considering the crushability of ballast, Jan [6, 7] proposed polyhedrons algorithm to rebuild crushed ballast and revealed the effect of irregular shape on the compression characteristics. Nuora [8, 9] employed proper orthogonal decomposition (POD) technique [10, 11] to gather statistics of edges, faces and vertex of ballast particles.

However, the influence of particle shape accompanied by frequency did not attract much attention in the above researches. Therefore, in this paper, a method for restructuring actual irregular shapes and crushing characteristics of ballast was proposed. On this base, large-scale laboratory static and cyclic triaxial testing was built by discrete-element numerical method. Three typical shapes of ballast (i.e., quasi-spherical, elongated and flat, respectively) and varied frequency f (2.4, 5, 10 and 30 Hz) were considered in the simulation, and the relationship between dynamic deformation and sample shapes and loading frequencies was discussed in time domain and frequency domain.

2   Irregular-Shaped Particles and Contact Between Polyhedrons

2.1   Irregular-Shaped Polyhedral Particles

A subroutine with a random process is used to create ballast shape. This method is proposed by Jan [6] inspired by Asahina and Bolander [12, 13] and is based on Voronoi tessellation. It is shown in Fig. 1. Initially, the central nucleus (red dot) $C_0 = (0.5, 0.5, 0.5)$ is fixed in a volume $1 \times 1 \times 1$ units cubic box and other 29 nuclei (black dots) are placed with random well-distributed coordinates. Voronoi tessellation is performed, and Voronoi cell with central nucleus C_0 is extracted as a basic particle shape.

The vertices $v_i = (v_{ix}, v_{iy}, v_{iz})$ of lengths along three direction axes can be calculated by basic Voronoi cell. It can be further rescaled in all three directions by factor $s = (s_x, s_y, s_z)$ to achieve the required size of real ballast, and the final polyhedral particle is also randomly rotated to avoid directional bias. The aspect ratio is defined by Jan [6] which equals to the ratio of scaling factors $(s_x/s_y/s_z)$. Three typical shapes of polyhedrons can be divided by aspect ratio in Fig. 2: (1) a quasi-spherical with an aspect ratio (1:1:1); (2) an elongated case with an aspect ratio (2:1:1); and (3) a flat case with an aspect ratio (2:2:1). This paper attempts to find the effect of these three irregular shapes on the dynamic behavior of railway ballast using these three typical cases.

Fig. 1 Particle creation by extraction of Voronoi cell

Front View	Side View	Vertical View
Quasi-spherical, aspect ratio=1:1:1		

Elongated, aspect ratio=2:1:1		

Flat, aspect ratio=2:2:1		
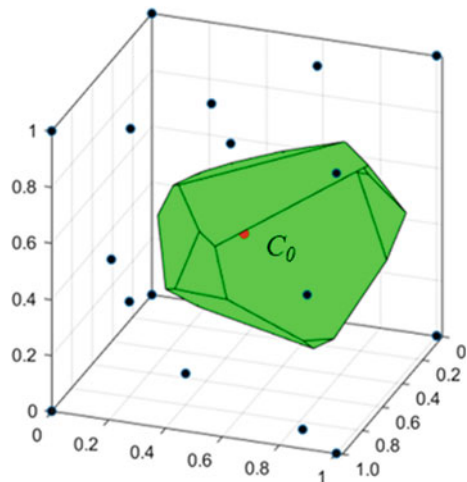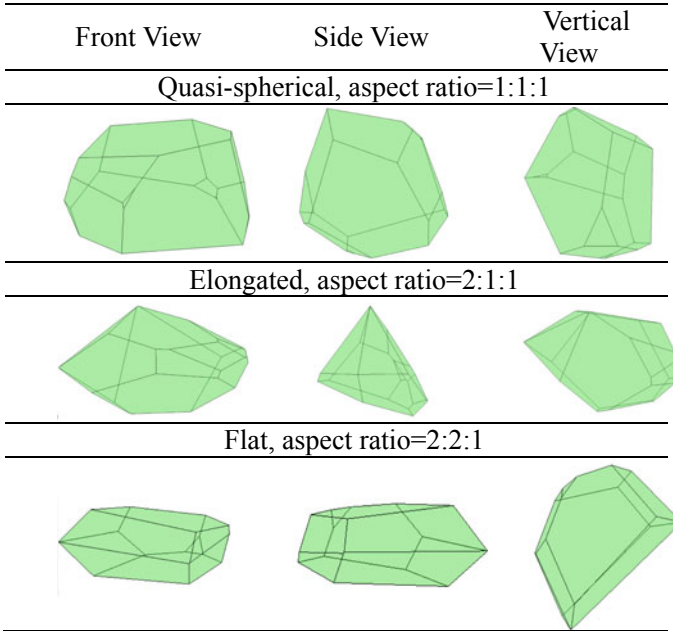
Fig. 2 Three typical shape polyhedrons are shown in front, side and vertical view

2.2   Contact Between Polyhedrons

In the numerical model of polyhedrons, particles are absolutely rigid and they are allowed to be penetrated. When two particles come into contact, the normal force F_n is linearly proportional to the intersecting volume V_I and the shear force F_s, caused by the additional shear displacement increment Δu_s, is calculated by an incremental algorithm.

$$|F_n| = V_I k_n \tag{1}$$

$$\Delta F_s = \Delta u_s k_s \tag{2}$$

where k_n and k_s are volumetric stiffness and shear stiffness of the material, respectively. The normal force acts at the centroid of the intersection. As the k_n is a constant, the normal force requires calculation of overlapping volume. The approach proposed by Muller [14] is used to find the exact intersection of convex polyhedrons. Moreover, standard Coulomb friction is also applied as:

$$|F_s| \leq |F_n| \tan\varphi \tag{3}$$

where coefficient φ is the internal friction angle.

3 Simulation of Triaxial Test and Experimental Verification

A numerical triaxial test model for irregularly shaped ballast is generated by randomly shaped polyhedrons. And the large triaxial test was carried out for ballast samples, and the test results were used to calibrate the simulation results of numerical models, ensuring the meso-mechanical parameters of the numerical model to be reasonable.

3.1 The Numerical Model of Polyhedral Particle Triaxial Test

A DEM/FEM coupling model was built for polyhedral particle triaxial test. First, 24 segment facets were put around the sample as the fixed boundary and the sample made up by polyhedral ballast was 300 mm diameter and 600 mm height in DEM. Particles were divided into six layers to generate. Each layer was compacted to reach 160 kPa strength with the facet boundary fixed. Then, the rubber membrane was simulated in FEM for applying confining pressure by adding force on nodes. The coupling between DEM and FEM was realized by the information exchange of the force in and the displacement. The particle forces in DEM were extracted as the boundary condition of force in FEM, and meanwhile, the displacements of elements in FEM were extracted as the boundary condition of displacement in DEM. After compaction, the sample was applied a static or dynamic load by moving the loading plate. Figure 3 shows the successfully built coupling numerical model for triaxial test.
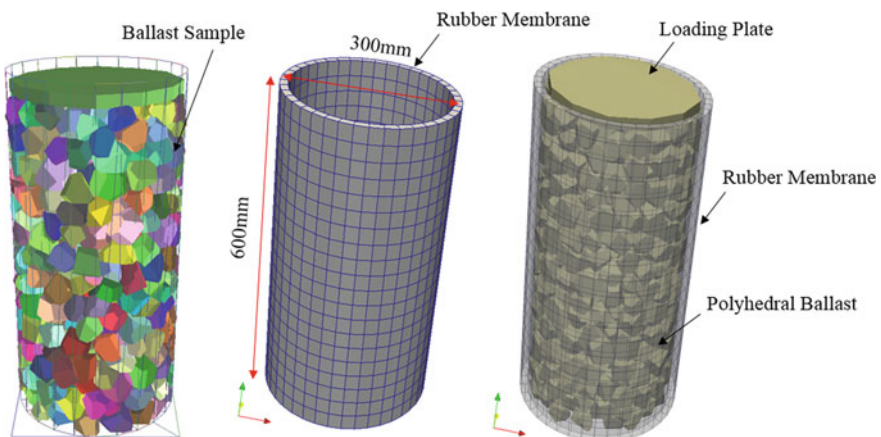
Fig. 3 Triaxial testing model of polyhedral ballast

3.2 The Experiment of Large-Scale Triaxial Testing

The GCTS large-scale triaxial apparatus is used in the tests. The axial load is controlled by the electronic-hydraulic close-loop system whose loading frequency is up to 10 Hz, and the confining pressure is controlled through a pressure booster system. The triaxial pressure is measured by axial load cells and the confining pressure sensors. The apparatus is equipped with the LVDT linear displacement transducer mounted on the top of the samples to monitor the axial strain, and the volumetric strain is observed by measuring the volumetric change of the water inside the triaxial chamber. Data monitoring and processing is controlled by a computer in real time. The testing equipment and triaxial sample are shown in Fig. 4.

The ballast sample used in this testing was granite. The height of the sample was 600 mm, and the diameter was 300 mm. The grading and preparation work of experimental sample was given a detailed account in the paper [15]. After the sample is established, the uniform static loading speed is 3 mm/min (i.e., 0.5% height of the sample per minute) according to Code for Soil Test of Railway Engineering (TB 10102-2010) [16], and the confining pressure was 60 kPa. The static loading testing was stopped when the axial strain of the sample reached 10%.

3.3 Parameters of the Numerical Model and Verification

The parameter values of the numerical model were obtained based on iterative adjustment through the experimental results, and hyperelastic material was used for

Fig. 4 Large diameter triaxial testing instrument and sample

simulating the rubber membrane, as shown in Table 1. Using these parameters, the stress–strain relationships of ballast samples under static loading were, respectively, simulated with the confining pressure of 60 kPa, and the simulation results were compared with the experimental results, as shown in Figs. 5 and 6.

4 Effect of Irregular Shapes on the Dynamic Behavior of Ballast

Based on the calibrated numerical model of polyhedral ballast particles, a series of triaxial test simulations of three typical ballast shapes (i.e., quasi-spherical, elongated and flat, respectively) were implemented. Samples with a desired porosity were generated in a volume with 300 mm diameter and 600 mm height as mentioned above. Although the particles in every sample have different typical shapes, the same gradation is used with particle diameter ranged from 16 to 50 mm. All

Table 1 Meso-structural parameters of polyhedral ballast and parameters of rubber membrane

Particle density (kg/m^3)	2680
Friction coefficient between particles, and the wall	0.65
Normal and tangential contact stiffness of particles (N/m)	2.78×10^9
Stiffness of wall (rubber membrane in DEM) (N/m)	2.4×10^7
Stiffness of wall on top (head) and bottom (N/m)	2.78×10^{10}
Damping ratio	0.3
Bulk modulus of rubber membrane in FEM (Pa)	1.0×10^7
Shear modulus of rubber membrane in FEM (Pa)	3.06×10^6

Fig. 5 Curves of deviatoric stress versus axial strain of samples
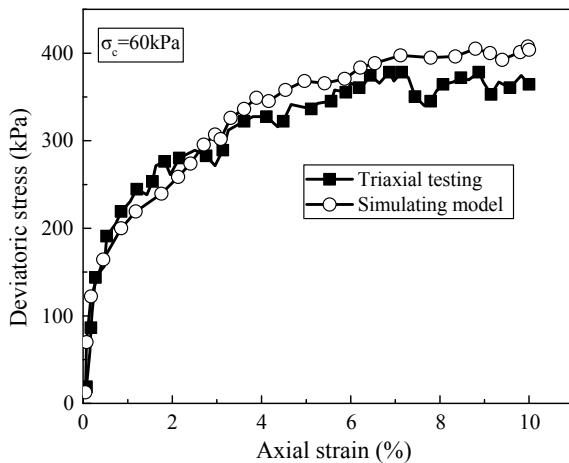
Fig. 6 Curves of volumetric strain versus axial strain of samples
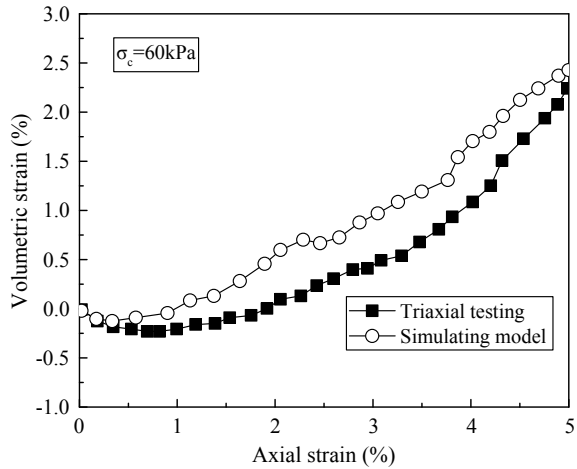
samples were isotropically compressed with a confining pressure of 60 kPa and sinusoidal axial loading with deviator stress ranged from 130 kPa to 400 kPa, and loading frequency, *f*, equal to 2.5 Hz, 5 Hz, 10 Hz and 30 Hz, respectively.

Figure 7 shows the calculation results for accumulative deformation of three shapes ballast under 5 Hz frequency axial loading. As shown in Fig. 7, the accumulative axial strains of three shapes were close, all below 2%. The flat shape ballast showed the lowest deformation but the largest vibration displacement among three shapes. The quasi-spherical shape ballast had the maximum axial strain which may be caused by their higher porosity than the other two shapes. It was to be observed that the elongated shape ballast performed the small vibration displacement as quasi-spherical and moderate cumulative axial strain among three shapes. Therefore, reasonable control of shape features may result in less instantaneous dynamic vibration and cumulative long-term deformation.

The deviator stress versus axial strain and axial strain versus time curves of quasi-spherical shape ballast under sinusoidal axial loading with 2.4, 5, 10 and 30 Hz frequencies are shown in Fig. 8. There are nonlinear relationships between loading frequency and instantaneous vibration displacement, and so was cumulative deformation of ballast shown in Fig. 8.

With the increase in frequency from 2.4 to 30 Hz, the amplitude of instantaneous vibration displacement decreased except the situation that the loading frequency is 5 Hz. Figure 8b shows that the vibrating amplitude is largest in the case of 5 Hz. However, the accumulative deformation of the sample under 5 Hz dynamic loading was least. The results implied that loading frequency had a great influence on the deformation of irregularly shaped samples. Thus, in order to find out the interrelationship between loading frequency and typical particle shape, a sinusoidal axial loading with frequency components of 2.4, 5, 10 and 30 Hz was applied on three typical shaped samples:
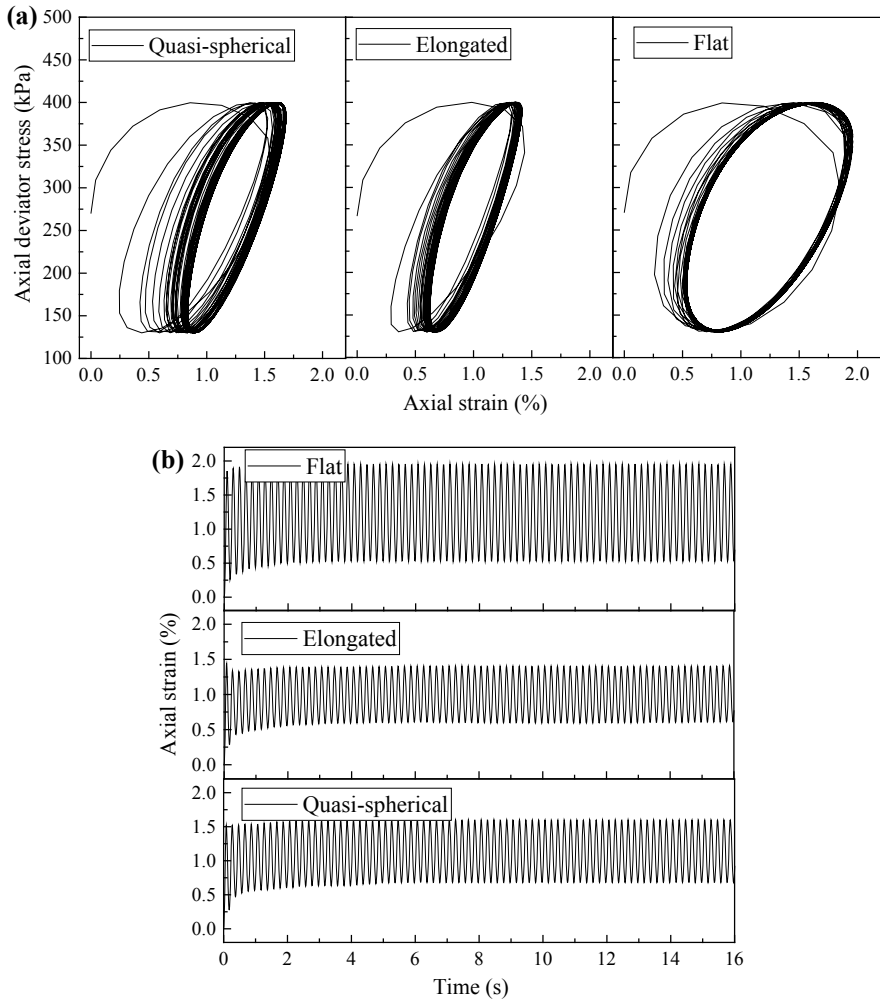
Fig. 7 Curves of dynamic responses of three ballast typical shapes under 5 Hz loading, **a** curves of axial strain versus axial deviator stress and **b** curves of time versus axial strain

$$F = 265 + 50 \times \sin(4.8\pi \times t) + 50 \times \sin(10\pi \times t)$$
$$+ 50 \times \sin(20\pi \times t) + 50 \times \sin(60\pi \times t)\,\text{kPa}$$

(3)

Monitoring the dynamic deformation of three typical shaped samples, respectively, and the vibration spectrum in the frequency domain is shown in Fig. 9.
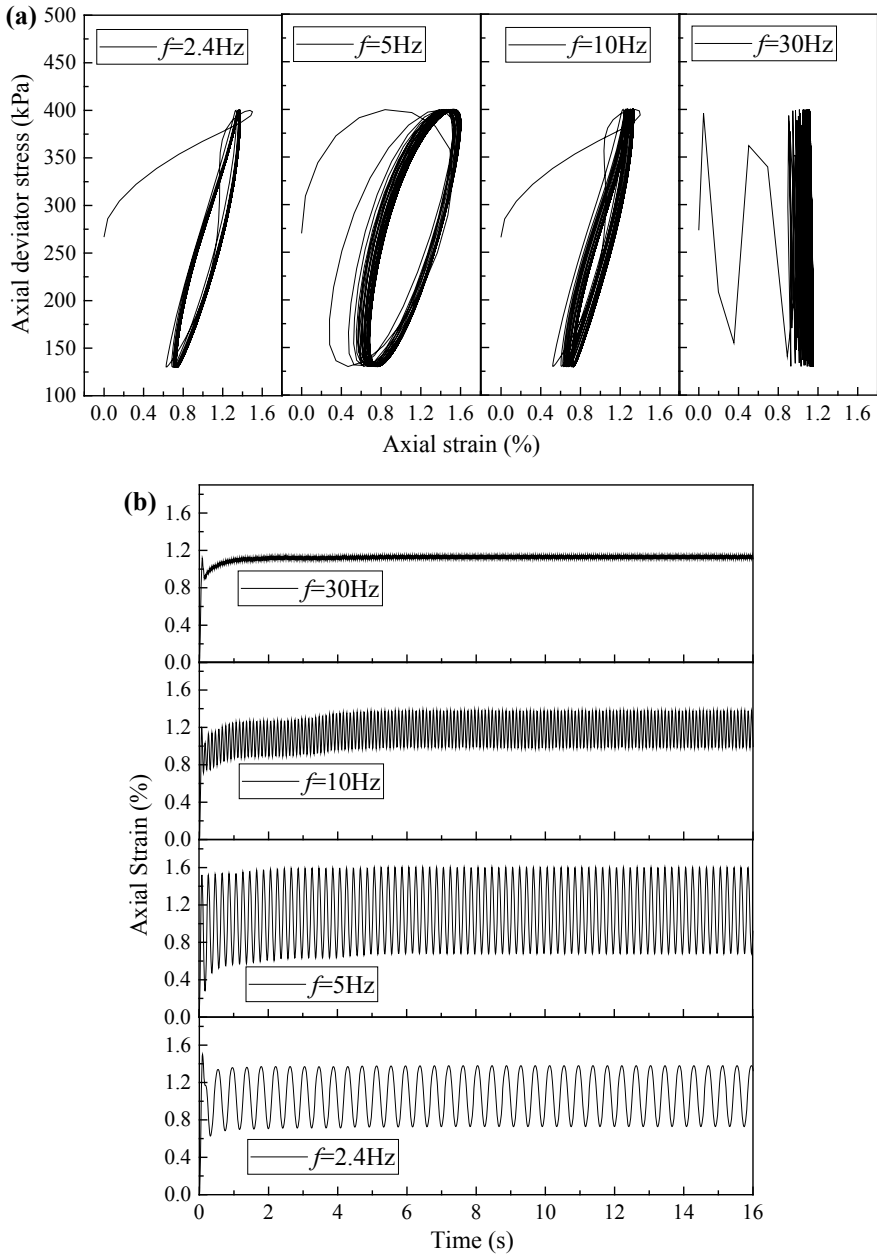
Fig. 8 Curves of dynamic responses of quasi-spherical ballast under loading with 2.4, 5, 10 and 30 Hz frequencies, **a** curves of axial strain versus axial deviator stress and **b** curves of time versus axial strain
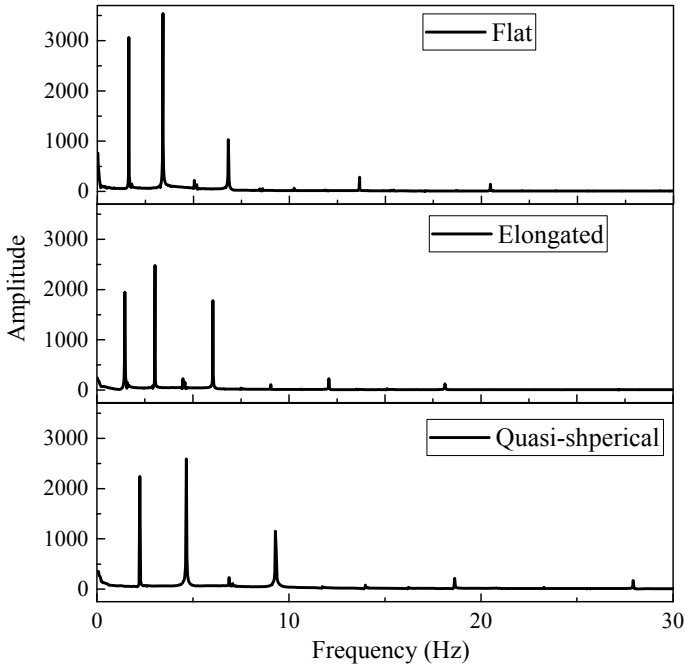
Fig. 9 Frequency spectrum of dynamic deformation of three typical shaped samples

The first three order main frequencies for quasi-spherical shape ballast were 2.23, 4.64 and 9.29 Hz; it could illustrate the cause of quasi-spherical shaped sample performing severe vibration at the loading of 5 Hz frequency. As shown in Fig. 9, three typical shaped samples had different main frequencies: the peak energy for elongated shape sample was 1.64, 3.40 and 6.81 Hz, and the first three order main frequencies of flat shape sample were 1.45, 3.0 and 6.03 Hz. The first three order main frequencies of elongated and flat shape sample were lower than the quasi-spherical shape sample. Therefore, even keeping the gradation unchanged, the variation of shapes can also lead the alteration of sample dynamic behavior.

5   Conclusion

(1) A triaxial model made of irregular polyhedrons was established and validated by large-scale triaxial testing. A series of triaxial test simulations of three typical ballast shapes (i.e., quasi-spherical, elongated and flat, respectively) were implemented under sinusoidal axial loading with 2.4, 5, 10 and 30 Hz frequencies to study the effect of irregular shape on the dynamic behavior of ballast in this paper.

(2) During triaxial compression, three typical shaped samples showed close cumulative deformation, but quasi-spherical shape ballast possessed the least instantaneous amplitude of vibration. Under different loading frequencies (i.e., 2.4, 5, 10 and 30 Hz, respectively), the vibration amplitude of quasi-spherical shape ballast became largest at 5 Hz.

(3) Three typical shaped samples had different main frequencies under dynamic cyclic loading. The first three order main frequencies of quasi-spherical shape sample were higher than the other two shapes sample. The dynamic behavior of ballast with fixed gradation could change with particle shapes.

References

1. Suiker ASJ, Selig ET, Frenkel R (2005) Static and cyclic triaxial testing of ballast and subballast. Geotech Geoenviron Eng 131:771–782. doi: 10.1061/(ASCE)1090-0241(2005) 131:6(771)
2. Sun QD, Nimbalkar S, Indraratna B (2014) Effect of frequency on the permanent deformation and degradation of railway ballast. Geotechnique 64(9):746–751. https://doi.org/10.1680/geot.14.T.015
3. Mcdowell GR, Lu M (2010) Discrete element modelling of railway ballast under monotonic and cyclic triaxial loading. Geotechnique 60(6):459–467. https://doi.org/10.1680/geot.2010.60.6.459
4. Ngo NT, Indraratna B, Rujikiatkamjorn C (2016) Simulation ballasted track behavior: numerical treatment and field application. Int J Geomech 17(6):1–12. https://doi.org/10.1061/(ASCE)GM.1943-5622.0000831
5. Indraratna B, Thakur PK, Vinod JS (2010) Experimental and numerical study of railway ballast behavior under cyclic loading. Int J Geomech 8(4):136–144. https://doi.org/10.1061/(ASCE)GM.1943-5622.0000055
6. Jan E (2014) Simulation of railway ballast using crushable polyhedral particles. Powder Technol 264:458–465. https://doi.org/10.1016/j.powtec.2014.05.052
7. Kozicki J, Donzé FV (2008) A new open-source software developed for numerical simulations using discrete modeling methods. Comput Method Appl M 197(49):4429–4443. https://doi.org/10.1016/j.cma.2008.05.023
8. Ouhbi N, Voivret C, Perrin G et al (2016) Railway ballast: grain shape characterization to study its influence on the mechanical behaviour. Procedia Eng 143:1120–1127. https://doi.org/10.1016/j.proeng.2016.06.150
9. Ouhbi N, Voivret C, Perrin G et al (2017) 3D particle shape modelling and optimization through proper orthogonal decomposition. Granul Matter 19(4):1–15. https://doi.org/10.1007/s10035-017-0771-0
10. Liang YC, Lee HP, Lim SP et al (2002) Proper orthogonal decomposition and its applications. Part I: theory. J Sound Vib 252(3):527–544. https://doi.org/10.1006/jsvi.2001.4041
11. Mollon G, Zhao J (2014) 3d generation of realistic granular samples based on random fields theory and Fourier shape descriptors. Comput Method Appl M 279:46–65. https://doi.org/10.1016/j.cma.2014.06.022
12. Asahina D, Bolander JE (2011) Voronoi-based discretizations for fracture analysis of particulate materials. Powder Technol 213:92–99. https://doi.org/10.1016/j.powtec.2011.07.010
13. Asahina D, Taylor MA (2011) Geometry of irregular particles: direct surface measurements by 3-D laser scanner. Powder Technol 213:70–78. https://doi.org/10.1016/j.powtec.2011.07.008

14. Muller DE, Preparata FP (1978) Finding the intersection of two convex polyhedral. Theor Comput Sci 7(2):217–236. https://doi.org/10.1016/0304-3975(78)90051-8
15. Xiao J, Zhang D, Wei K et al (2017) Shakedown behaviors of railway ballast under cyclic loading. Constr Build Mater 155:1206–1214. https://doi.org/10.1016/j.conbuildmat.2017.07.225
16. China Railway Publishing House (2010) Code for soil test of railway engineering. TB 10102-2010

Numerical Investigation of Vibrational Acceleration Level for a Ballasted Railway Track During Train Passage in Seasonally Frozen Regions

Shuang Tian, Shanzhen Li, Liang Tang, Xianzhang Ling and Xiangxun Kong

Abstract This research is aimed at developing a practical method for estimating the vertical acceleration of a ballasted railway track bed subjected to trainload in seasonally frozen regions. For this purpose, an indirect thermal-dynamic coupled two-dimensional (2D) finite element (FE) modeling was developed to simulate the thermal and dynamic responses of Harbin–Qiqihar Railway (HQR). Results show that peak values of vibrational acceleration level increase with train speed and axle load increase, but decrease with elastic and height of ballast increase. Taking the effects of the factors mentioned above, two fitting formulae were formulated to estimate vibrational acceleration level of the embankment with an attenuation coefficient, which can be used to describe the attenuation characteristics of ground vibration. In this way, the numerical model and results can be used as a reference for design, maintenance, and research on other embankments in seasonally frozen regions.

Keywords Finite element analysis · Ballasted railway · Dynamic response · Empirical equation · Seasonally frozen region

1 Introduction

The railway transportation in China boomed during the first decade of the twenty-first century. The mileage of national commercial railway in China has been more than 130,000 km by the end of 2018, and China has become the country with

S. Tian · S. Li · L. Tang · X. Ling · X. Kong
Harbin Institute of Technology, Harbin 150090, Heilongjiang, China

S. Tian · S. Li · L. Tang · X. Ling · X. Kong
Heilongjiang Research Center for Rail Transit Engineering in Cold Regions,
Harbin 150090, Heilongjiang, China

S. Tian · L. Tang (✉) · X. Ling
State Key Laboratory of Frozen Soil Engineering, Northwest Institute
of Eco-Environment and Resources, Chinese Academy of Sciences,
Lanzhou 730000, Gausu, China
e-mail: hit_tl@163.com

the largest network of railways in the world. With the rapid economic development, faster and heavier trains were put into service in seasonally frozen regions of China. However, as a lack of re-engineering, the current railway's embankment or substructures have become increasingly overloaded. Very high levels of vertical acceleration have been observed at some locations within the seasonally frozen regions, which can seriously affect the safety of the operation and human body comfort [1, 2]. Therefore, a study on train-induced vertical acceleration characteristics of embankment constructed on seasonally frozen regions, as one of the favorite areas of studies, has attracted great attention recently.

The general method used to study the vertical acceleration of embankment is a numerical simulation, and a number of numerical models have been put forward to study the dynamic characteristics of the railway's embankment [3–7]. Sheng et al. [8] used an infinite layered beam to simulate the track and a layered half-space to model the soil. These numerical methods were then developed to adapt to study the vehicle-track interaction [9, 10]. Bian and Chen [11], Hall [12], O'Brien and Rizos [13], Zhai and Song [14] as well as Ai et al. [15] applied train-induced loads to the numerical model which comprised of rail, subgrade, and field. The effects of axle load, and train speed, etc., on the vertical acceleration could then be studied. However, despite the large amount of attention given to the numerical modeling of rail tracks for the past few decades, the nonlinear behavior of the soil has been rarely simulated [16, 17].

On the other hand, the seasonally frozen soil is very sensitive to temperature changes, as physical and mechanical characteristics are inherently unstable and their properties are varied with the temperature [18]. In order to solve the problems caused by seasonally frozen soil, a considerate number of research have been carried out since the last century. What have attracted the most attention is the global railway problems in permafrost field, especially for relevant studies on the vertical acceleration of permafrost subgrade structure and numerical calculation of geothermal field in the past decades [19–30]. These researches have important significance for rational cognition of vertical acceleration characteristics of the embankment at permafrost site, and moreover for the dynamic stability evaluation on the long-term operation of permafrost railway, but few types of research are available on the vertical acceleration of seasonally frozen embankment under combined actions of trainload, as well as their seasonal variations.

The purpose of this study is to develop a thermal-dynamic indirect coupled model for railway's embankment constructed in seasonally frozen regions based on the theories of heat transfer and soil dynamics. Taking a section of HQR as an example, the temperature and vertical acceleration of embankment in freezing and normal period (i.e., 15 January and 15 July, respectively) is then simulated by this model. A parametric study is focused on these four aspects: train speed, axle load, elastic modulus, and height of ballast. Finally, two fitting formulations are proposed and validated to estimate vibrational acceleration level in freezing and normal period, respectively. Some useful conclusions could provide theoretical basis and reference to design, maintenance, and research on the subgrade engineering in seasonally frozen regions.

2 Governing Equations and Numerical Methods

2.1 Equations of Temperature Field

In seasonally frozen regions, the railway's embankment always experiences freeze-thaw cycles with phase change periodically. Therefore, the problem to be solved becomes a nonlinear problem of heat transfer with phase change. Sensible heat capacity method is used during the process of heat transfer [31], and the convection is assumed to be neglected, while ice-water phase change process is included in the heat transport equation, which can be expressed as follows:

Frozen zone:

$$\rho_f c_f \frac{\partial T}{\partial t} = \frac{\partial}{\partial x}\left(\lambda_f \frac{\partial T}{\partial x}\right) + \frac{\partial}{\partial y}\left(\lambda_f \frac{\partial T}{\partial y}\right) \tag{1}$$

Unfrozen zone:

$$\rho_u c_u \frac{\partial T}{\partial t} = \frac{\partial}{\partial x}\left(\lambda_u \frac{\partial T}{\partial x}\right) + \frac{\partial}{\partial y}\left(\lambda_u \frac{\partial T}{\partial y}\right) \tag{2}$$

Phase change zone:

$$\rho_L c_L \frac{\partial T}{\partial t} - \rho_i L_w \frac{\partial \theta_i}{\partial t} = \frac{\partial}{\partial x}\left(\lambda_L \frac{\partial T}{\partial x}\right) + \frac{\partial}{\partial y}\left(\lambda_L \frac{\partial T}{\partial y}\right) \tag{3}$$

Replacing volumetric ice content in the phase change zone by volumetric water content leads to:

$$-\rho_i L_w \frac{\partial \theta_i}{\partial t} = \rho_w L_w \frac{\partial \theta_w}{\partial t} = \rho_w L_w \frac{\partial \theta_w}{\partial T} \frac{\partial T}{\partial t} = \rho_w L_w \frac{\rho_d(w_0 - w_u)}{\rho_w(T_u - T_f)} = \frac{\rho_d L}{T_u - T_f} \tag{4}$$

Substituting Eq. (4) into Eq. (3) gives:

$$\left(\rho_L c_L + \frac{\rho_d L}{T_u - T_f}\right)\frac{\partial T}{\partial t} = \frac{\partial}{\partial x}\left(\lambda_L \frac{\partial T}{\partial x}\right) + \frac{\partial}{\partial y}\left(\lambda_L \frac{\partial T}{\partial y}\right) \tag{5}$$

Merging Eqs. (1), (2), and (5) results in:

$$C^* \frac{\partial T}{\partial t} = \frac{\partial}{\partial x}\left(\lambda^* \frac{\partial T}{\partial x}\right) + \frac{\partial}{\partial y}\left(\lambda^* \frac{\partial T}{\partial y}\right) \tag{6}$$

where T is temperature; x and y are the coordinate positions; t is time; λ^* and C^* stands for equivalent thermal conductivity and specific heat capacity of the soil, respectively. The ice-water phase change process takes place when soil temperature

falls below the freezing temperature, T_u. It should be noted that there is a temperature T_f below which the phase change is negligible [32]. Therefore, phase change process occurs only when the temperature falls in the range of $[T_f, T_u]$. A stepwise function can be then used to compute the equivalent thermal conductivity and specific heat capacity of the soil:

$$C^* = \begin{cases} \rho c_f & T \leq T_f \\ \frac{\rho(c_u + c_f)}{2} + \frac{\rho L}{T_u - T_f} & T_f < T < T_u \\ \rho c_u & T \geq T_u \end{cases} \tag{7}$$

$$\lambda^* = \begin{cases} \lambda_f & T \leq T_f \\ \lambda_f + \frac{\lambda_u - \lambda_f}{T_u - T_f}(T - T_f) & T_f < T < T_u \\ \lambda_u & T \geq T_u \end{cases} \tag{8}$$

where, subscripts f and u denote the frozen and unfrozen states, respectively; λ, c and ρ are the thermal conductivity, the specific heat capacity and dry density, respectively; and L is the latent heat. It should be noted that the constant density is assumed in a different state for simplicity.

2.2 Transient Dynamic Equations

In the current study, the numerical formulae of transient dynamic equations can be obtained by Galerkin method, and the Newmark implicit method is adopted due to its unconditional stability. Generally, the equation of a dynamic system can be written as:

$$M\ddot{u} + C\dot{u} + Ku = F(t) \tag{9}$$

where M is mass of the system, C is damping coefficient, K is stiffness of the system, and $\ddot{u}$, $\dot{u}$ and u = displacement, velocity, and acceleration, respectively.

3 Engineering Cases

3.1 Description of Harbin–Qiqihar Railway

According to engineering geological investigations in northeast China, the maximum frozen depth was about 2 m in the last decade, and a frozen layer existed for 5–6 months every year [1]. The research site is situated at Anda City where the soil layers are evenly distributed (Fig. 1). Figure 2 shows a typical embankment section DK124 + 118 along the HQR line.

Fig. 1 Monitoring site at Harbin–Qiqihar railway in northeast China

Fig. 2 Cross-section view of a typical train-track-ground system at Harbin–Qiqihar railway

3.2 Numerical Simulation on Temperature Characteristics of Embankment

Computational Model and Parameters Figure 3 shows the 2D heat conduction analysis model. There are base course materials, silty clay, and weathered mudstone in the computational domain. The analysis domain extends 30 m from the toe of the embankment and 30 m below natural surface.

According to climate prediction and long-term in situ monitoring of HQR, the thermal boundary conditions, in terms of the temperatures at the surfaces ABCDEF (Fig. 2), can be expressed as follows:

$$T_n = T_\alpha + \frac{\Delta T}{365} t + A \sin\left(\frac{2\pi t}{365} + \alpha_0\right) + \Delta T_F \tag{10}$$

where T_α is the embankment or ground surface mean temperature, the data in the test section is 4.2 °C. ΔT represents the climate warming effect, it is 0.04 °C in the northeast China; t is time (day); A is the temperature amplitude of the surface, which is 18 °C at natural ground surface, 20 °C at embankment surface and slope; α_0 is the initial phase angle, which equals to $\pi/2$ in the current study; ΔT_F is 2.0 °C for the natural ground surface, and 3.0 °C for the embankment surface and slope for incremental of adherent layer. It should be noted that sunny-shading slope effect has not been taken into consideration for simplicity.
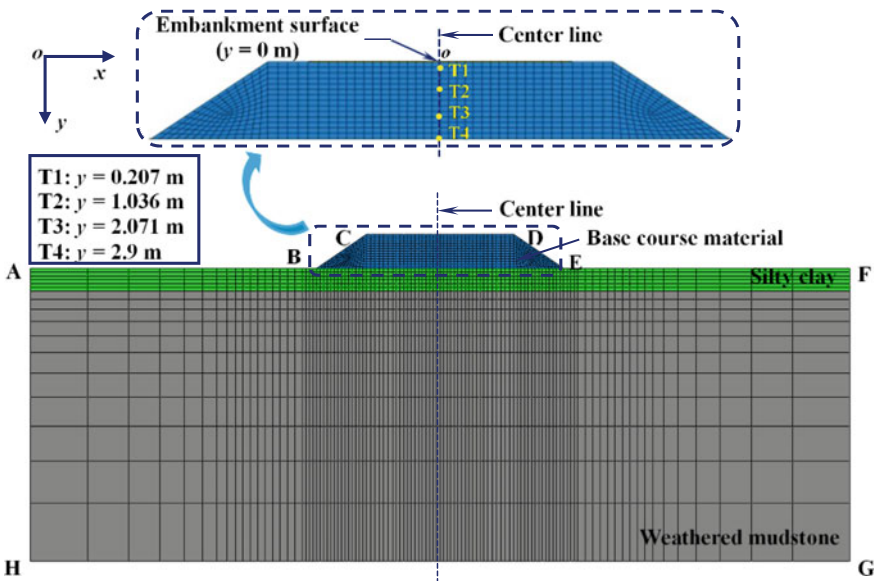
Fig. 3 Two-dimensional FE modeling for temperature field analysis

The lateral boundaries AH and FG are assumed to be adiabatic:

$$\frac{\partial T}{\partial n} = 0 \tag{11}$$

On the bottom of the foundation GH:

$$T = T_0 \tag{12}$$

where T_0 is a constant temperature in the deepest depth of the physical domain and is set to 6.0 °C in the simulation [33].

As discussed previously, the phase change was defined to occur over a temperature range of—0.5 to 0 °C. This transient heat transfer was simulated in ABAQUS with four-node linear heat transfer quadrilateral elements (DC2D4). The simulation was carried out for a period of 12 years with the largest time step limited to 1 day.

Inverse Analysis The ground temperature data resulting from a field test may be used together with a numerical model to determine appropriate values of the parameters necessary for characterization of the thermal properties of the materials used under the railway line. To achieve this, estimated values of parameters of materials are used initially in the model, and the resulting temperature in the model is compared with those obtained in the field at selected locations. The parameters of materials of the model are varied iteratively until the temperature determined from the model match closely those obtained in the field. This process is known as inverse, or back, analysis [34].

Using initial estimated values of parameters of materials, the temperature at the sensors was computed and compared with the field data [35]. Subsequently, the base values of thermal parameters were adjusted by trial and error until a measure of the difference between the calculated and measured temperature readings was agreed upon. Thermal parameters of materials adopted in this study are listed in Table 1, where the data for similar materials reported by Wang [36] are also given for comparison.

Temperature Analysis Results Figure 4 shows a comparison between computed and measured data from a test section which is constructed since 2012 in the northeast China at depths of 0.207, 1.036, 2.071 and 2.9 m. The maximum discrepancy is 3.6 °C at depths of 0.2 m, which may be caused by the idealized boundary conditions adopted in the numerical model instead of complex and variable weather factors on the actual railway. It can be seen that the embankment temperatures at $T3$ (0.207 m) fluctuated more obviously than the computed, because at the surface of the embankment the behavior may be influenced more severely by the weather. Similarly, this phenomenon is also reflected in Fig. 5, which gives the seasonal freeze-thaw process curves at the centerline of the embankment. In this figure, the maximum deviation of computed frost penetration from observed data is 0.20 m. It can be concluded that the difference between the

Table 1 Thermal parameters of embankment and ground

Materials	Thermal conductivity of material in frozen state, λ_f [J/(m °C day)]		Thermal conductivity of material in unfrozen state, λ_u [J/(m °C day)]		Specific heat capacity of material in frozen state, C_f [J/(kg °C)]		Specific heat capacity of material in unfrozen state, C_u [J/(kg °C)]		Latent heat of material per unit mass, L (J/kg)	
	Current study	Wang [36]	Current study	Wang [36]	Current study	Wang [36]	Current study	Wang [36]	Current study	Wang [36]
Sleeper	–	–	–	–	–	–	–	–		
Ballast	–	–	–	–	–	–	–	–		
Base course materials	120,960	154,220	99,360	135,860	833	892	951	1149	10,736	10,470
Silty clay	168,480	132,190	125,280	94,000	1014	1174	1276	1473	35,471	37,700
Weathered mudstone	158,900	157,900	132,190	132,190	1026	1026	1166	1166	19,842	19,850

computation results and measured data was small, and which could be negligible. Therefore, the theoretical model can describe the state temperature distribution in the embankment fairly well and accurately. The embankment starts to freeze in early November and ends in mid- or late March under the climate warming conditions. In addition, the thawing features with the two-way thaw which result in the freezing process are slower than the thawing one.

The effect of climate, as represented by air temperature, causes the ground surface temperature to vary cyclically from year to year. Construction embankment over natural terrain changes the surface thermal characteristics, however, it will reach a new thermal equilibrium state very soon (about 2 years) according to the computed results as shown in Fig. 6. For this reason, we will focus on analyzing numerical results on the 10th service year. Furthermore, according to monitoring results of air and ground temperature in HQR, freezing period (15 January) and normal period (15 July) which was the coldest and hottest times of the years was adopted.

Figure 7a, b sketches the temperature contours of the embankment at two typical periods after 10 years of the construction, respectively. From Fig. 7a, freezing is one-way quick freezing from top of the embankment. When air temperature reaches zero, ground temperatures will increase with depth by an amount which is dependent on the local geothermal gradient and the mean annual ground temperature until it reaches 6 °C at a depth of 15 m. With ground surface temperature rising, the frozen area will disappear gradually until air temperature reaches its maximum level on 15 July (Fig. 7b). In conclusion, due to different air temperature
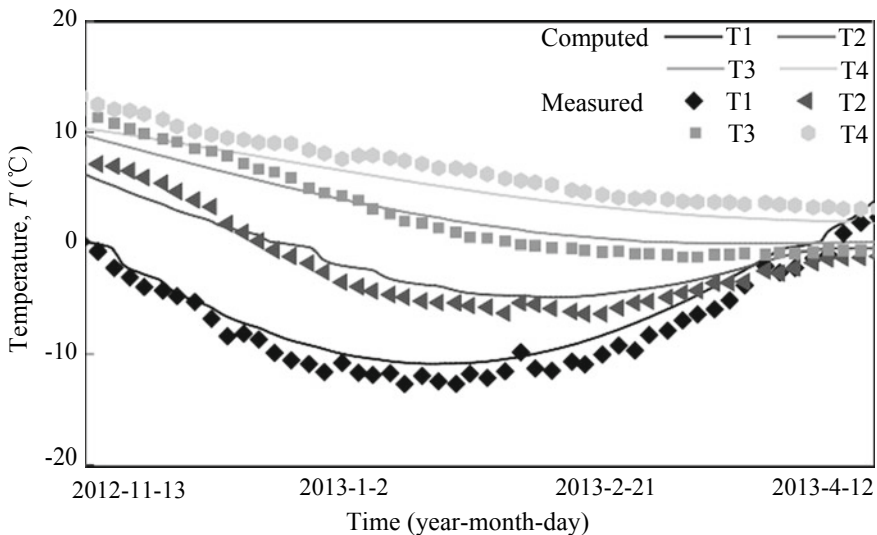
Fig. 4 Temperature variation of embankment at M3, M4, M5 and M6 from Nov. 13, 2012 to Apr. 12, 2013
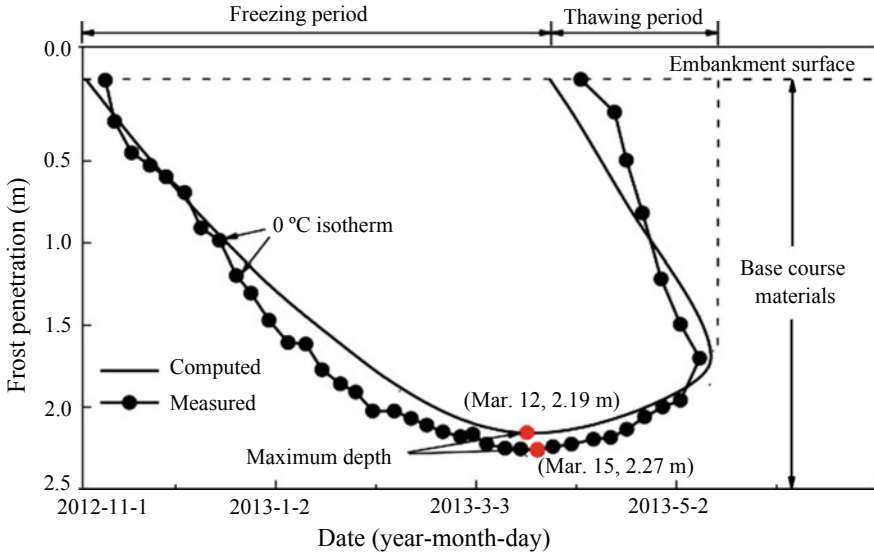
Fig. 5 Frost penetration evolutions at the centerline of embankment
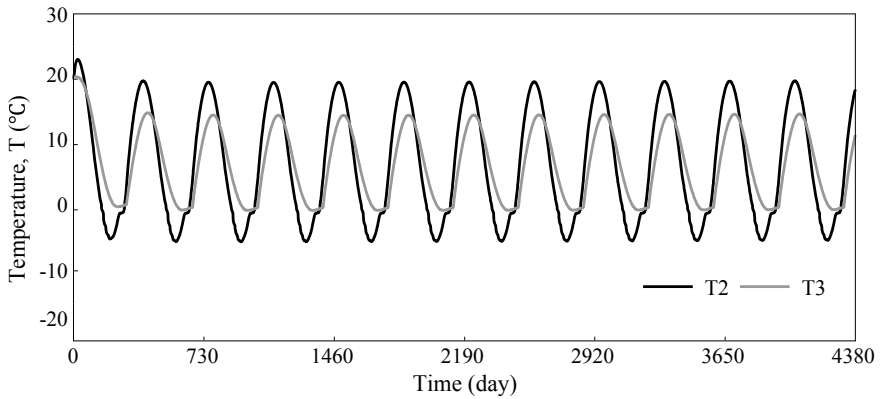
Fig. 6 Temperature time histories of embankment at $T2$ and $T3$ in the future 12 years after the completion of embankment construction

conditions during two typical periods, the temperature distributions of embankment and ground are different, thus the transient responses of the embankment will be certainly different because of the temperature dependency of the mechanical properties.
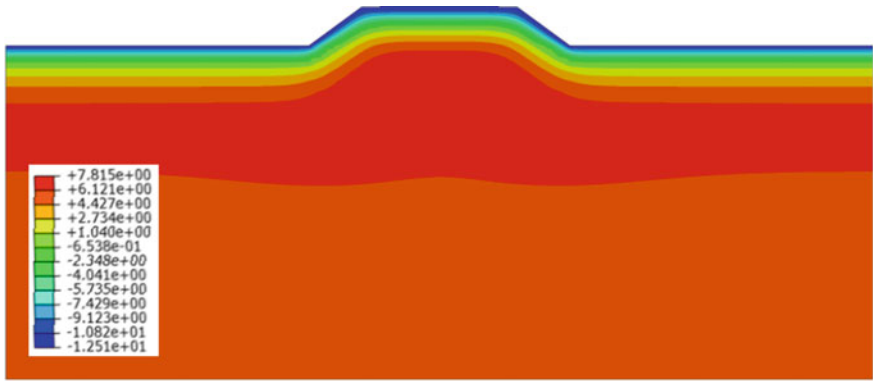
(a) Freezing period (15th January)
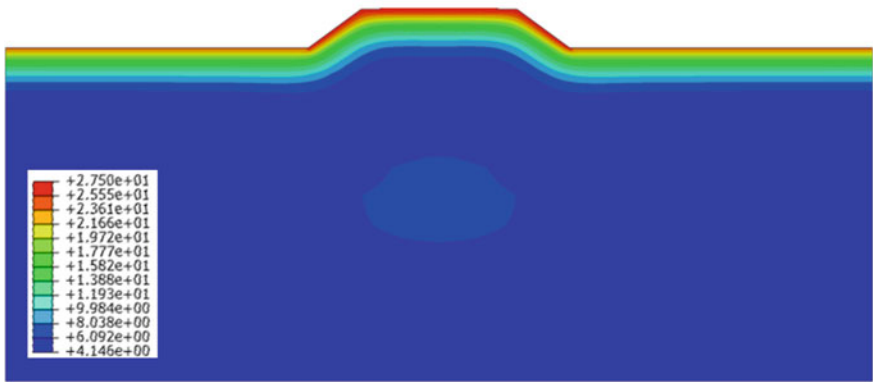
(b) Normal period (15th July)

Fig. 7 Temperature contours of the system in the 10th year after the completion of embankment construction (Unit: °C)

3.3 Numerical Simulation on Vertical Acceleration Characteristics of Embankment

Boundary and Initial Conditions A 2D FE modeling for analysis on the dynamic response characteristics of the system is presented in Fig. 8. It shows that the horizontal and vertical direction is 84.2 m and 33.4 m, respectively. The ballast, embankment and ground are simulated by plane quadrilateral element, and the sleeper is simulated by eight beam elements. Due to the railway line which has semi-infinite characteristic, the plane strain assumption is adopted to carry out the simulation. As shown in Fig. 8, the infinite element boundary is used to diminish the boundary condition effects. Meanwhile, the temperature analysis results at two different periods were taken as the initial conditions.
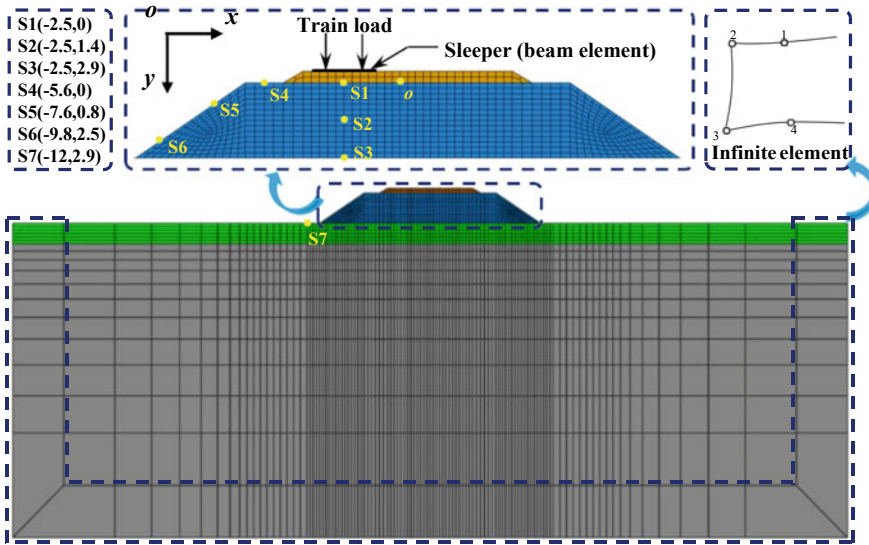
Fig. 8 Two-dimensional FE modeling for acceleration analysis

Train Loading The coupling calculation of the train-track system requires dealing with the iteration convergence of the two subsystems, which will be very complicated and time-consuming [37]. Therefore, the train loading was calculated first in this study and then applied on the rail supporting nodes of sleeper beam elements (Fig. 8).

In order to derive train loading, a series of moving axle loads can be obtained according to the train geometry in Fig. 9. Accordingly, the successive axle loads can be expressed as a periodic function $f(t)$ with a period equal to t_4 [38]:

$$f(t) = \begin{cases} F & 0 \leq t \leq t_1 \\ 0 & t_1 \leq t \leq t_2 \\ F & t_2 \leq t \leq t_3 \\ 0 & t_3 \leq t \leq t_4 \end{cases} \tag{13}$$

For the sake of simplicity, $f(t)$ is supposed as a sufficiently smooth function, which can be then transformed by Fourier function which is composed of a series of sines and cosines.

$$f(t) = a_0 + \sum_{n=1}^{\infty} \left[a_n \cos\left(\frac{2n\pi t}{T}\right) + b_n \sin\left(\frac{2n\pi t}{T}\right) \right] \tag{14}$$

where a_0, a_n and b_n are Fourier series coefficient. On this basis, train loading can be calculated if a_0, a_n and b_n are determined. It should be noted that the principal frequencies in Eq. (14) are from 0 to ∞. However, according to Hamid et al. [38],
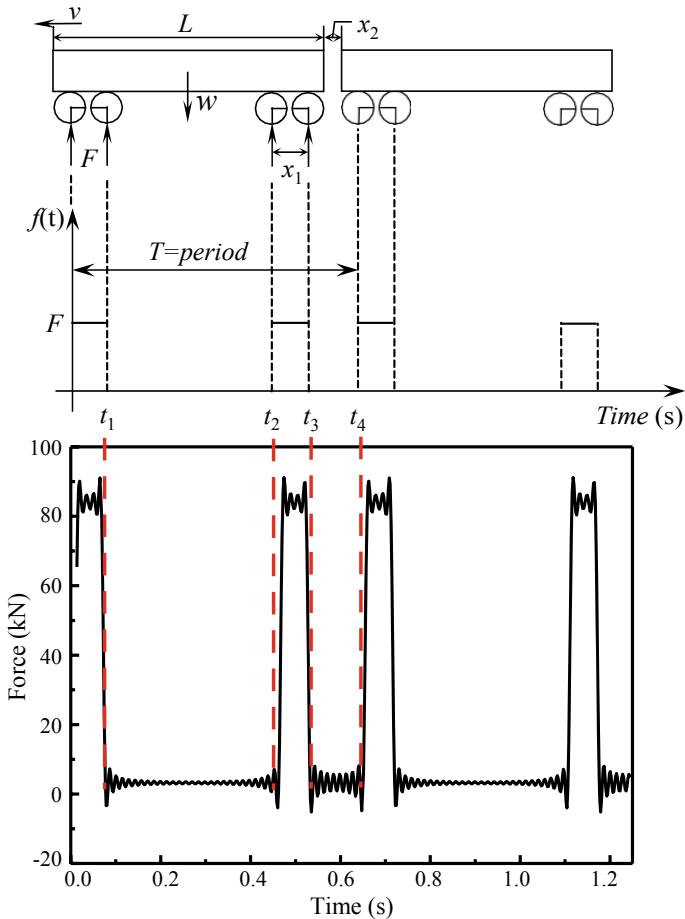
Fig. 9 Schematic of train wagons and train dynamic load

the frequency range from 0 to 25 Hz is enough to calculate the train loading accurately. As presented in Fig. 9, the train loading caused by a moving train with the speed of 140 km/h is calculated based on the above-described method.

Equivalent Linear Model In this study, an equivalent linear model is adopted to consider the nonlinear of the base course materials. This is because train-induced displacements can achieve a high level, which has been proved by previous studies [39]. The equivalent linear model can be used to represent hysteretic behavior with a decreasing secant shear modulus and an increasing damping ratio. Figure 10 plots the modulus reduction and damping increase curves for base course materials based
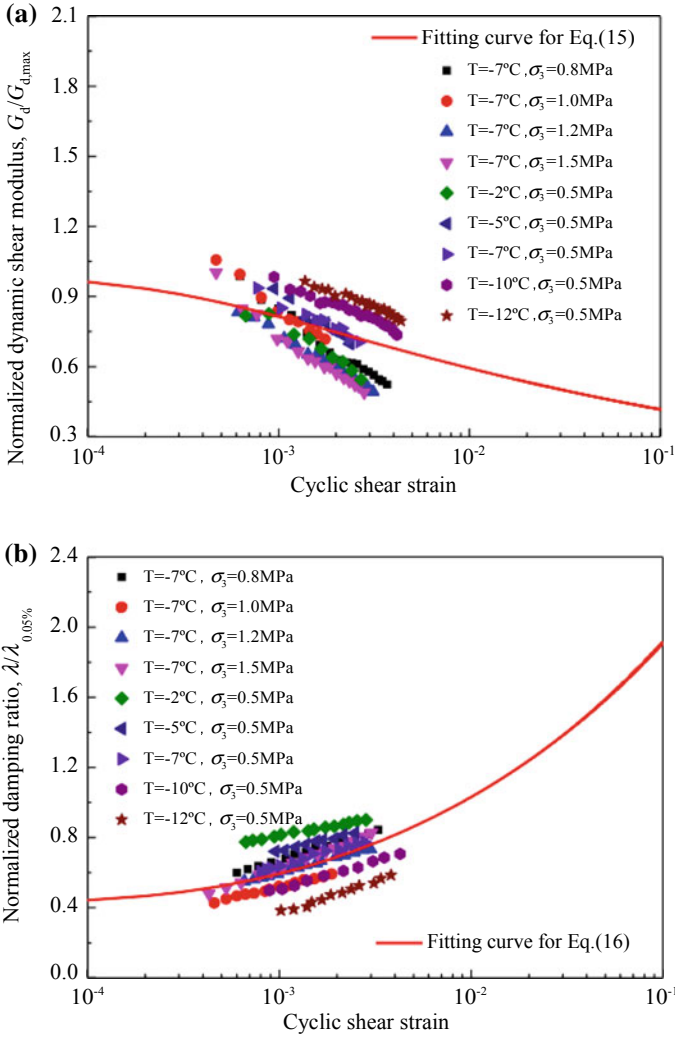
Fig. 10 Nonlinearity of embankment materials: **a** Normalized dynamic shear modulus and **b** normalized damping ratio versus cyclic shear strain

on dynamic triaxial laboratory tests [40, 41]. By using these curves, dynamic shear modulus and damping ratio can be predicted as following empirical expressions:

$$G_d = 594.03(1 + (\gamma_d/\bar{\gamma}_{dr})\bar{c})^{-\frac{1}{\bar{c}}}\eta_{GT}\eta_{G\sigma} \tag{15}$$

$$\lambda = 0.137\left(\left(1 + (\gamma_d/\bar{\gamma}_{dr})\bar{c}\right)^{-\frac{1}{\bar{c}}}\right)^{-1.749}\eta_{\lambda T}\eta_{\lambda\sigma} \tag{16}$$

where $\bar{\gamma}_{dr}$ and $\bar{c}$ are normalized model parameters and are equal to 0.0023, 6.429, respectively; η_{GT}, $\eta_{G\sigma}$, $\eta_{\lambda T}$, and $\eta_{\lambda\sigma}$ are the modified coefficients of modulus and damping ration with respected to temperature and confining pressure, respectively. Fitting the test results gives:

$$
\begin{aligned}
\eta_{GT} &= -0.0013T^3 - 0.035T^2 - 0.3T + 0.15 \\
\eta_{G\sigma} &= 0.22\sigma_3^2 + 0.12\sigma_3 + 0.88 \\
\eta_{\lambda T} &= 0.0006T^3 + 0.02T^2 + 0.2T + 1.65 \\
\eta_{\lambda\sigma} &= -0.07\sigma_3^2 + 0.33\sigma + 0.85
\end{aligned}
\tag{17}
$$

where T (temperature) and σ_3 (confining pressures) are from the results of temperature field analysis discussed above and the initial state of the geostatic analysis, respectively; Here, a user subroutine UMAT of ABAQUS is adapted to complete the numerical implementation of the equivalent linear model.

Meanwhile, in order to simulate the sleepers, ballast, silty clay and weathered mudstone for simplicity, all of them were considered as linear elastic materials and its parameters considered for this model are summarized in Table 2 [36].

FE Model Validation The field test results collected in Anda City along HQR by Ling et al. [1] were used to validate the model performance. As shown in Fig. 11, computed soil response has a high correlation of vertical acceleration with the measured results. It can be seen that the response to the passage of each wheel-set, which is similar in timing, shape, and magnitude. Figure 12 displays the attenuation of peak vertical acceleration with distance from the track. Once again, similar results were obtained between the magnitudes and gradients of computed and measured data. Therefore, the numerical model adopted in the present study is able to simulate peak vertical acceleration effectively.

3.4 Parametric Studies

As above-mentioned, the vertical acceleration analysis is conducted under different elastic modulus of ballast, train speed, axle load, and height of ballast, respectively, based on the 2D FE modeling as shown in Table 3. The influencing factors of the

Table 2 Mechanical parameters of sleeper, ballast, and ground

Materials		Density, ρ (kg/m³)	Elastic modulus, Ee (MPa)	Poisson's ratio, υ
Sleeper		2500	30,000	0.18
Ballast		2100	286	0.25
Base course material		2185	–	0.3
Silty clay	Frozen	1630	135.2	0.28
	Unfrozen	1630	25.4	0.32
Weathered mudstone		1800	901.8	0.29
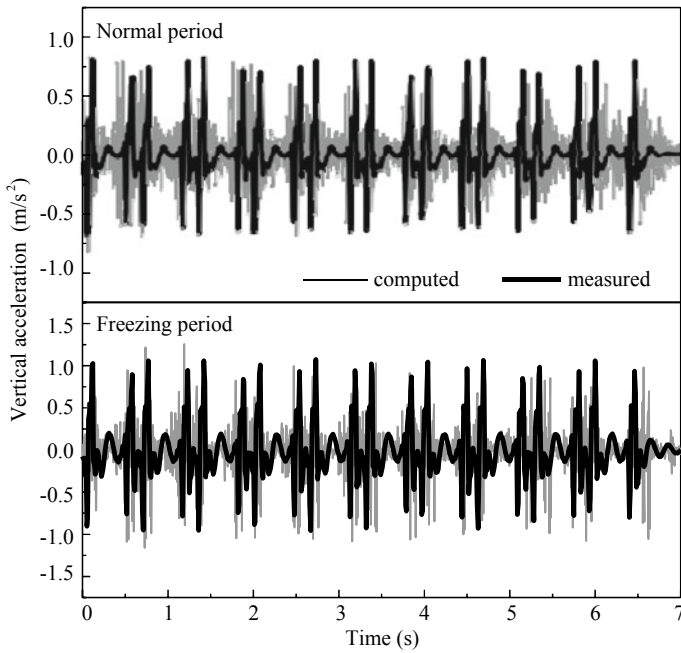
Fig. 11 Measured and computed time histories of vertical accelerations at S4 in various periods

Fig. 12 Attenuation of peak vertical acceleration in various periods (refer to Fig. 8 for node location)
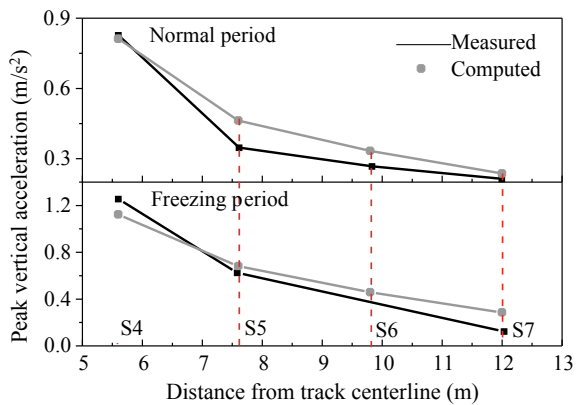
train-induced vertical acceleration of a ballasted railway track in seasonally frozen regions are analyzed in detail.

Variation of PPA with Different Factors The vehicle and track parameters generally play a significant role in a ballasted railway track. The calculating results have been plotted in Fig. 13 to study the influencing factors. It can be concluded

Table 3 Summaries for parametric studies

	Young's modulus of ballast, Ee (MPa)	Train speed, v (km/h)	Axle load, q (kN)	Height of ballast, H (m)
Case 1–5	280, 480, 680, 880, 1080	200	170	0.45
Case 6–14	80	15, 80, 120, 160, 200, 250, 300, 350, 400	170	0.45
Case 15–19	80	200	145, 190, 225, 250, 300	0.45
Case 20–23	80	200	170	0.35, 0.55, 0.65, 0.75

that (i) vertical accelerations increase with train speed and axle load increase, (ii) vertical accelerations decrease with elastic modulus and height of ballast increase. However, the effect of train speed increment is gradual until values of the train speed greater than about 300 km/h are reached, after which the acceleration curves tend to be stable. The variation of the accelerations with increasing axle load is approximately linear in all cases. Apparently, the peak vertical acceleration is not greatly impacted by the elastic modulus and height of the ballast (Fig. 13a, b).

Figure 13 shows that peak vertical acceleration of freezing period is greater than that of thawing period, which is also demonstrated by Ling et al. [1]. This is possibly attributed to the frozen upper layer occurred in winter, which caused an amplifying effect on the vertical vibration. Due to the existence of the frozen layer, the soil stiffness and damping ratio are increased and decreased, respectively. Therefore, the dynamic response in the vertical direction has been increased.

Variation of Vibrational Acceleration Level with Different Factors The comfort for people on the ground is influenced by the ground vibration induced by train passage. In this study, a vibrational acceleration level (L_a), which is calculated with Eq. (18), is utilized:

$$L_a = 20 \lg(a/a_{\text{ref}}) \tag{18}$$

where the referred acceleration $a_{\text{ref}} = 10^{-5}$ m/s^2.

Figure 14 shows the vibrational acceleration level versus different influencing factors. It can be seen that the vibrational acceleration level at different experimental conditions shows the similar relationship.

Therefore, power functions which are obtained by fitting curve are proposed to describe the effect of vehicle and track parameters on vibrational acceleration level:

$$L_{a,\text{modulus}}^{f} = 111.3 E_e^{-0.004}, \quad R^2 = 0.9975 \tag{19a}$$

(a)

(b)

(c)

(d)
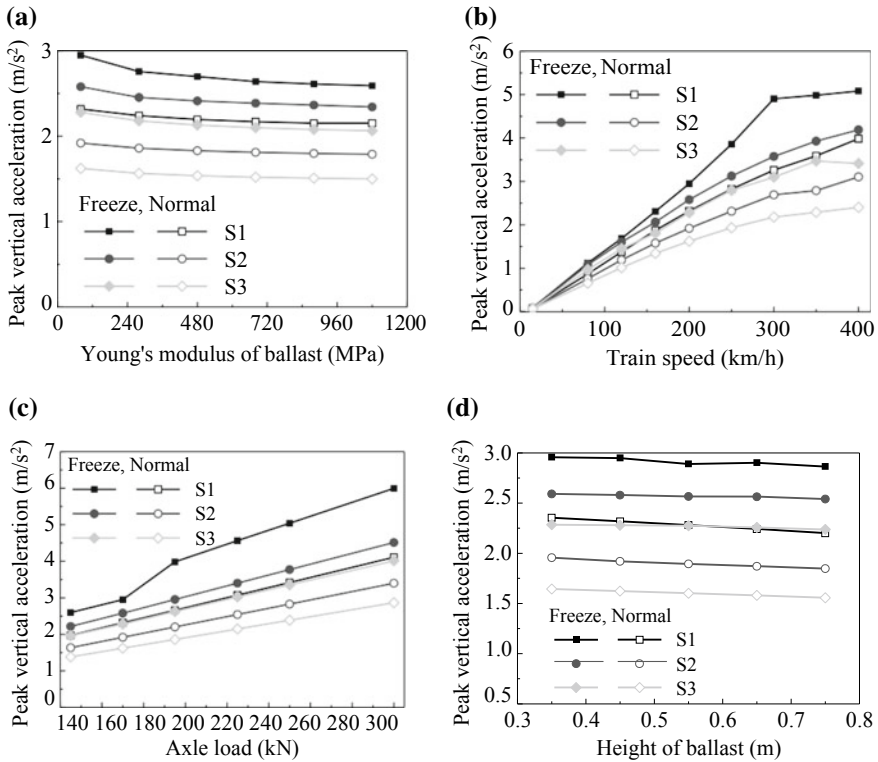
Fig. 13 Effect of vehicle and track parameters on peak vertical acceleration: **a** young's modulus of ballast; **b** train speed; **c** axle load; and **d** height of ballast

$$L_{a,modulus}^{u} = 108.5E_e^{-0.002}, \quad R^2 = 0.9912 \tag{19b}$$

$$L_{a,speed}^{f} = 61.24v^{0.11}, \quad R^2 = 0.967 \tag{20a}$$

$$L_{a,speed}^{u} = 61.15v^{0.10}, \quad R^2 = 0.9672 \tag{20b}$$

$$L_{a,axle}^{f} = 84.56q^{0.09}, \quad R^2 = 0.9749 \tag{21a}$$

$$L_{a,axle}^{u} = 85.45q^{0.08}, \quad R^2 = 1 \tag{21b}$$

$$L_{a,height}^{f} = 111.6H^{-0.003}, \quad R^2 = 0.8548 \tag{22a}$$

$$L_{a,height}^{u} = 112H^{-0.007}, \quad R^2 = 0.9768 \tag{22b}$$
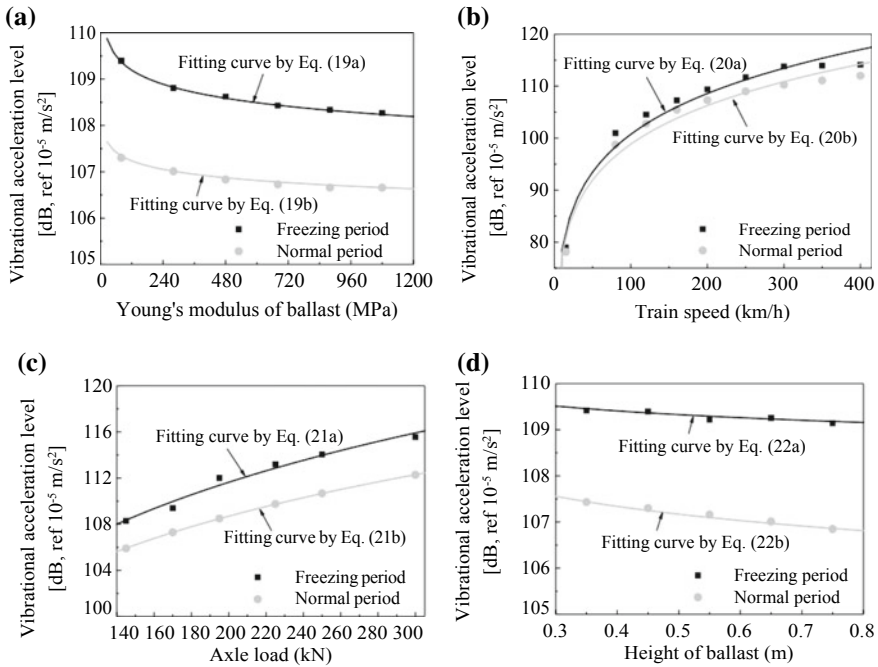
Fig. 14 Effect of vehicle and track parameters on vibrational acceleration level: **a** elastic modulus of ballast, **b** train speed, **c** axle load, and **d** height of ballast

where superscripts f and u denote the frozen and unfrozen states, respectively; $L_{a,speed}$, $L_{a,axle}$, $L_{a,modulus}$, and $L_{a,height}$ are vibrational acceleration level considering four factors, respectively, and E_e, v, q, and H present elastic modulus of ballast, train speed, axle load, and height of ballast, respectively.

Based on the above numerical results and using the multiple regression analysis methods, the vibrational acceleration level on the embankment surface can be expressed as functions of train speed, axle load, elastic modulus, and height of ballast by as follows:

$$L_a^f = 49.23 v^{0.11} q^{0.09} E_e^{-0.004} H^{-0.003} \tag{23a}$$

$$L_a^u = 51.78 v^{0.10} q^{0.08} E_e^{-0.002} H^{-0.007} \tag{23b}$$

Figure 15 shows the comparisons of the vibrational acceleration level predicted from Eq. (23) with the numerical data. It can be seen that the prediction matched the numerical results well.

Figure 16a, b illustrates the attenuation of time-domain peak values of vibrational acceleration level with increasing distance from embankment surface (S1) in x- and y-direction, respectively. Only maximum (case 19) and minimum (case 6) vibrational acceleration level data are drawn for concise purpose. Figure 16 shows

Fig. 15 Correlation between numerical and predicted results
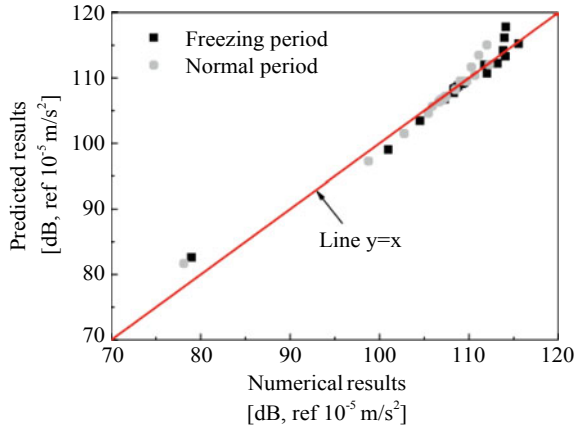
the vibrational acceleration level in the normal period is slightly lower than that in the freezing period. The upper and lower bound of vibrational acceleration level incorporating different seasonal variations can be expressed as the following equations, respectively.

$$L_{a,depth}^{upper} = 32.88 \exp(0.056h) + 83.11 \tag{24a}$$

$$L_{a,depth}^{lower} = 24.47 \exp(0.049D) + 54.04 \tag{24b}$$

$$L_{a,distance}^{upper} = 56.69 \exp(0.023D) + 22.2 \tag{24c}$$

$$L_{a,distance}^{lower} = 45.6 \exp(0.035D) + 32.19 \tag{24d}$$

where superscripts upper and lower denote the upper and lower bounds, respectively; $L_{a,depth}$ and $L_{a,distance}$ stands for x- and y-direction, respectively.

Furthermore, to describe the attenuation of vibrational acceleration level, the attenuation coefficient η is introduced here as the ratio of the vibrational acceleration level at any depth below the ballast or distance from track center to that at the embankment surface (S1). Figures 17 and 18 present the attenuation coefficients with soil depth from the embankment surface and distance from track center, respectively, in different periods. The figure clearly indicates that the attenuation of the vibrational acceleration level can be estimated reasonably for different factors with a uniform fitting formula as the following:

$$\eta_{depth}^{f} = 0.25 \exp(0.074h) + 0.75 \tag{25a}$$

$$\eta_{depth}^{u} = 0.29 \exp(0.073h) + 0.72 \tag{25b}$$
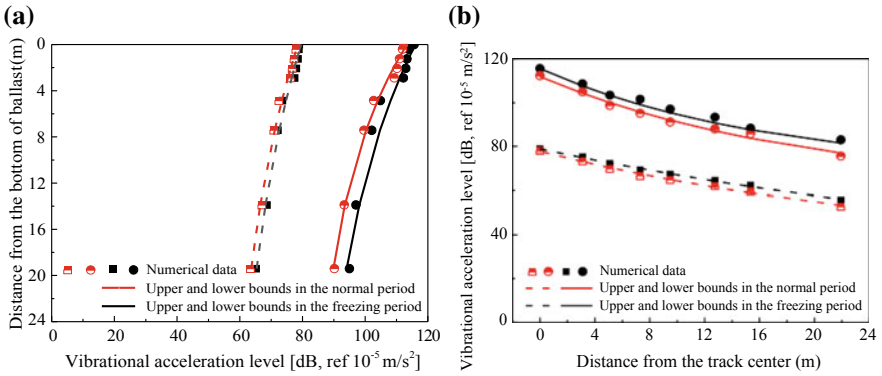
Fig. 16 Upper and lower bound of the vibrational acceleration level **a** along depth and **b** from distance between the observation point and the track centerline
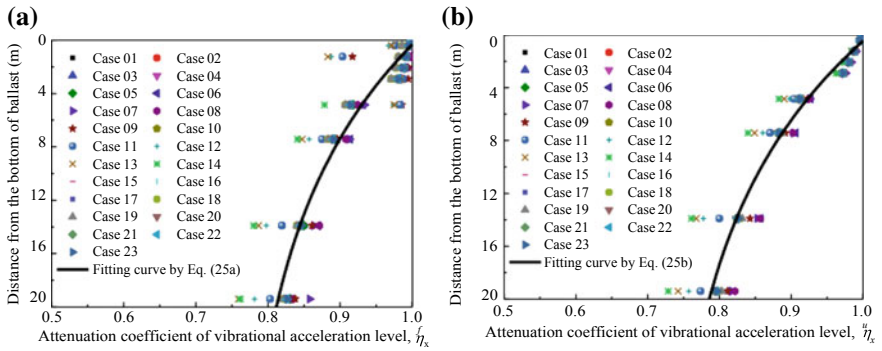
Fig. 17 Attenuation coefficients of vibrational acceleration level from the bottom of ballast: **a** freezing period and **b** normal period
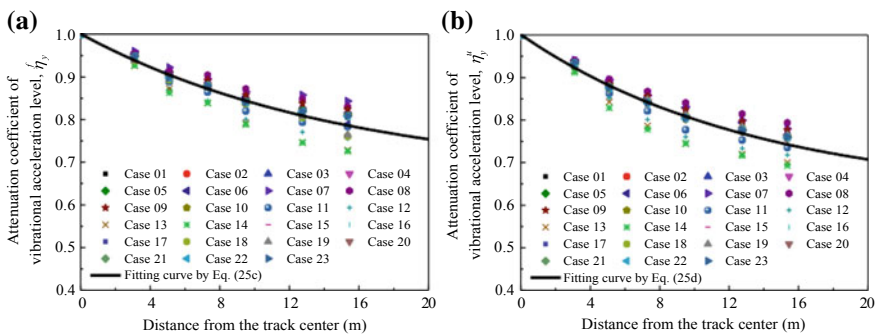
Fig. 18 Attenuation coefficients of vibrational acceleration level from the track center: **a** freezing period and **b** normal period

$$\eta_{\text{distance}}^{\text{f}} = 0.34 \exp(0.066D) + 0.66 \tag{25c}$$

$$\eta_{\text{distance}}^{\text{u}} = 0.38 \exp(0.075D) + 0.62 \tag{25d}$$

where superscripts f and u denote the frozen and unfrozen states, respectively; h and D are the depth or distance from the embankment surface, respectively; subscripts x and y stand for horizontal and vertical direction, respectively.

4 Conclusions

In this paper, an indirect thermal-dynamic coupled 2D FE modeling was described by adopting correlative theories of heat transfer, physics and mechanics of materials. The nonlinear behavior of the embankment materials was simulated by an equivalent linear model whose parameters changing with temperatures were taken into account. Following, the temperature and vertical acceleration characteristics of the embankment were analyzed systematically. The satisfactory agreement between computed and measured results confirmed the 2D FE modeling is trustworthy, which can be used to simulate the behavior of the railway's embankment in the seasonally frozen regions. The parametric studies were carried out to further analyze the vertical acceleration characteristics under various influencing factors of the train-track-ground system. The following conclusions can be drawn:

(1) A seasonal active layer will come gradually in the embankment in the process of its operation. In addition, the temperature characteristics of embankment varied in two typical periods due to different air temperature conditions, which will result in differential vertical acceleration characteristics under train loading.
(2) The effects of various factors on the vertical acceleration of embankment surface are obvious, which presents an increasing tendency with the increase of train speed and axle load, but a decreasing tendency with the elastic modulus and height of ballast increasing. It should be noted that the effect of properties of ballast is not obvious.
(3) Considering the four presented factors, two fitting formulae were proposed to estimate the vibrational acceleration level on the embankment surface, as well as its attenuation characteristics. As a preliminary study, it is expected to provide theoretical basis and reference for design, maintenance, and study on the embankment in seasonal frozen regions.

References

1. Ling XZ, Zhang F, Zhu ZY, Ding L, Hu QL (2009) Field experiment of subgrade vibration induced by passing train in a seasonally frozen region of Daqing. Earthq Eng Eng Vib 8 (1):149–157

2. Ma W, Wen Z, Sheng Y, Wu QB, Wang DY, Feng WJ (2012) Remedying embankment thaw settlement in a warm permafrost region with thermosyphons and crushed rock revetment. Can Geotech J 49(9):1005–1014

3. Chen J, Zhou Y (2018) Dynamic responses of subgrade under double-line high-speed railway. Soil Dyn Earthq Eng 110:1–12

4. Curtis K, Jitendra S, David H, James G (2009) Finite element analysis of an embankment on a soft estuarine deposit using an elastic–viscoplastic soil model. Can Geotech J 46(3):357–368

5. Fang R, Lu Z, Yao H, Luo XW, Yang ML (2018) Study on dynamic responses of unsaturated railway subgrade subjected to moving train load. Soil Dyn Earthq Eng 115:319–323

6. Feng SJ, Li YC, Chen ZL, Chen HX (2017) Response of railway track coupled with a stratified ground consisting of saturated interlayer to high-speed moving train load. Soil Dyn Earthq Eng 102:25–40

7. Qu GF, Hinchberger SD, Lo KY (2009) Case studies of three-dimensional effects on the behaviour of test embankments. Can Geotech J 46(11):1356–1370

8. Sheng X, Jones CJC, Petyt M (1999) Ground vibration generated by a harmonic load acting on a railway track. J Sound Vib 225(1):3–28

9. Sheng X, Jones CJC, Thompson DJ (2003) A comparison of a theoretical model for quasi-statically and dynamically induced environmental vibration from trains with measurements. J Sound Vib 267(3):621–635

10. Sheng X, Jones CJC, Thompson DJ (2004) A theoretical model for ground vibration from trains generated by vertical track irregularities. J Sound Vib 272(3):937–965

11. Bian XC, Chen YM (2005) Dynamic analyses of track and ground coupled system with high-speed train loads. Acta Mech Sin 4:013

12. Hall L (2003) Simulations and analyses of train-induced ground vibrations in finite element models. Soil Dyn Earthq Eng 23(5):403–413

13. O'Brien J, Rizos D (2005) A 3D BEM-FEM methodology for simulation of high speed train induced vibrations. Soil Dyn Earthq Eng 25(4):289–301

14. Zhai WM, Song EX (2009) 3D FEM in moving coordinate for transient response under moving loads. Rock Soil Mech 30(9):2830–2836

15. Ai ZY, Mu JJ, Ren GP (2017) 3D dynamic response of a transversely isotropic multilayered medium subjected to a moving load. Int J Numer Anal Methods Geomech 42(1)

16. Correia AG, Cunha J (2014) Analysis of nonlinear soil modelling in the subgrade and rail track responses under HST. Transp Geotech 1(4):147–156

17. Sayeed MA, Shahin MA (2016) Three-dimensional numerical modelling of ballasted railway track foundations for high-speed trains with special reference to critical speed. Transp Geotech 6:55–65

18. Lukas UA, Sarah MS (2005) Mathematical descriptions for the behaviour of ice-rich frozen soils at temperatures close to 0 C. Can Geotech J 42(2):431–442

19. Chen T, Ma W, Wu ZJ, Mu YH (2014) Characteristics of dynamic response of the active layer beneath embankment in permafrost regions along the Qinghai-Tibet Railroad. Cold Reg Sci Technol 98:1–7

20. Cheng GD (2005) Permafrost studies in the Qinghai-Tibet plateau for road construction. J Cold Reg Eng 19(1):19–29

21. Cheng GD (2005) A roadbed cooling approach for the construction of Qinghai-Tibet Railway. Cold Reg Sci Technol 42(2):169–176

22. Fortier R, LeBlanc AM, Yu W (2011) Impacts of permafrost degradation on a road embankment at Umiujaq in Nunavik (Quebec), Canada. Can Geotech J 48:720–740

23. Hamid B, Marolo A, David K, Jim G (2014) Deformations and ground temperatures at a road embankment in northern Canada. Can Geotech J 51(3):260–271
24. Li SY, Lai YM, Zhang MY, Dong YH (2009) Study on long-term stability of Qinghai–Tibet railway embankment. Cold Reg Sci Technol 57(2):139–147
25. Li SY, Lai YM, Zhang SJ, Yang YG, Yu WB (2012) Dynamic responses of Qinghai—Tibet railway embankment subjected to train loading in different seasons. Soil Dyn Earthq Eng 32 (1):1–14
26. Ling XZ, Zhu ZY, Zhang F, Chen SY, Wang LN, Gao X, Lu QR (2009) Dynamic elastic modulus for frozen soil from the embankment on Beiluhe Basin along the Qinghai—Tibet railway. Cold Reg Sci Technol 57(1):7–12
27. Ma W, Duan L, Wu QB (2008) Monitoring and analysis of embankment deformation in permafrost regions of Qinghai-Tibet Railway. Rock Soil Mech 29(3):571–579
28. Wu QB, Liu YZ, Zhang JM, Tong CJ (2002) A review of recent frozen soil engineering in permafrost regions along Qinghai-Tibet Highway, China. Permafrost and Periglac Process 13 (3):199–205
29. Wu ZJ, Chen T, Zhao T, Wang LL (2018) Dynamic response analysis of railway embankments under train loads in permafrost regions of the Qinghai-Tibet Plateau. Soil Dyn Earthq Eng 112:1–7
30. Zhu ZY, Ling XZ, Chen SJ, Zhang F, Wang ZY, Wang LN, Zou ZY (2011) Analysis of dynamic compressive stress induced by passing trains in permafrost subgrade along Qinghai-Tibet Railway. Cold Reg Sci Technol 65(3):465–473
31. Taylor GS, Luthin JN (1978) A model for coupled heat and moisture transfer during soil freezing. Can Geotech J 15:548–555
32. Qin YH, Tang P (2011) Effect of diurnal temperature rhythm on the geothermal regime under the embankment in Qinghai-Tibet plateau. Arab J Geosci 4(1):259–267
33. Yue ZR, Tai BW, Sun TC (2015) Analysis of temperature field characteristics based on subgrade site measurements of Harbin-Qiqihar High-speed Railway in a deep seasonal frozen soil region. Sci Cold Arid Reg 7(5):0547–0553
34. Burrow MP, Chan AH, Shein A (2007) Deflectometer-based analysis of ballasted railway tracks. Proc Inst Civ Eng Geotech Eng 160(3):169–177
35. Xiao W (2014) Study on temperature field and insulation measures of high-speed railway subgrade in seasonal frozen soil region. Ph.D. thesis, Beijing Jiaotong University, Beijing, China. (in Chinese)
36. Wang ZY (2014) Dynamic response characteristics and permanent deformation of subgrade induced by train load in seasonally deep frozen region. Ph.D. thesis, Harbin Institute of Technology, Harbin, China. (in Chinese)
37. Garg VK, Vukkipati RV (1984) Dynamics of railway vehicle systems. Academic Press
38. Hamid RN, Morteza A, Hamid H (2012) Numerical analysis of ground vibration induced by underground train movement. Tunn Undergr Space Technol 29(2012):1–9
39. Madshus C, Kaynia AM (2000) High-speed railway lines on soft ground: dynamic behaviour at critical train speed. J Sound Vib 231(3):689–701
40. Ling XZ, Zhang F, Li QL, An LS, Wang JH (2015) Dynamic shear modulus and damping ratio of frozen compacted sand subjected to freeze-thaw cycle under multi-stage cyclic loading. Soil Dyn Earthq Eng 76(2015):111–121
41. Zhu ZY, Ling XZ, Wang ZY, Lu QR, Chen SJ, Zou ZY, Guo ZH (2011) Experimental investigation of the dynamic behavior of frozen clay from the Beiluhe subgrade along the QTR. Cold Reg Sci Technol 69:91–97

Influence of Track Irregularities in the Stress Levels of the Ballasted and Ballastless Tracks

Ana Ramos, António Gomes Correia, Pedro Alves Costa and Rui Calçada

Abstract The ballasted and ballastless tracks present substantial differences in terms of the structural configuration and mechanical behaviour. In order to better understand the foundation performance, numerical analysis of the two types of railway track was carried out, computing the stress paths induced by the passage of trains. In this analysis, the effects of the quasi-static and dynamic mechanisms are taken into account in order to highlight their relevance as function of the geometrical track quality for ballasted and ballastless tracks. This study pretends to analyse the influence of the track irregularities in the response of the railway structures (in terms of stress levels). In order to understand the effect of this factor on the performance of the railway tracks, three ranges of wavelengths were defined, associated with three irregularities profiles. The numerical framework adopted in the present study is based on a 2.5D FEM-PML approach for the track-ground simulation, while the rolling stock is modelled using a simple multi-body approach.

Keywords Numerical model · 2.5D model · Stress path · Ballasted and ballastless tracks · Irregularities

1 Introduction

This article aims to study the stress path obtained in the foundation soil due to the passage of a train (*Alfa Pendular*) considering the quasi-static and the dynamic mechanisms. Regarding the dynamic mechanisms (which includes the train-track interaction), this article is focused on the irregularities on the track. In this analysis, three ranges of wavelengths are considered. Through this parametric study, the performance of the ballasted and ballastless tracks is compared as well as the

A. Ramos (✉) · A. G. Correia
School of Engineering, University of Minho, Guimarães, Portugal
e-mail: ID6629@UMINHO.PT

P. A. Costa · R. Calçada
Faculty of Engineering, University of Porto, Porto, Portugal

influence of the quasi-static and dynamic mechanisms in both structures. However, despite the importance of all materials in the global performance of the railway structures, this analysis is only focused on the foundation since it is the element that is common to both structures.

The ballasted and ballastless tracks present different constitutions and materials. In the ballastless track, the ballast and sub-ballast were replaced by the concrete slab and support layer. In some ballastless structures, the sleepers are embedded in the concrete slab.

In the performance of the ballasted track, the ballast has an important role in the attenuation of the stress levels while in the ballastless track; this role is performed by the concrete slab and support layer.

This analysis is carried out in the 2.5D FEM-PML approach, which implies the discretization of the invariant cross-section by finite elements, while in the longitudinal direction the variables time and space are transformed into the frequency and wavenumber domain. This transformation allows obtaining, expeditiously, the stress levels on the elements of the railway structures, which is a significant advantage in the solving of parametric studies. In this case, the analysis allows understanding which is the range of wavelengths and frequencies that amplify significantly the stress levels (on the foundation soil), when compared to the quasi-static mechanism. With this study, it is also possible to identify which are the frequencies that most influence the performance of the ballasted and ballastless tracks.

2   Numerical Model

The modelling of the train-track interaction requires a sub-structured model, where the rolling stock and the track are simulated by different approaches. The dynamic interaction between the two models is established taking into account the compatibility of the displacements and the equilibrium of forces. The track-ground system is modelled by the 2.5D approach considering the tri-dimensional nature of the domain. The 2.5D approach presents several advantages since allows combining an efficient computation procedure with the 3D character of the problem [1, 2]. In this particular case, the 2.5D approach is supported by a FEM-PML formulation.

2.1   Modelling of the Track (2.5D FEM-PML Approach)

The 3D response of the structure is determined assuming that the cross-section of the structure is invariant along the track development direction, as depicted in Fig. 1. In order to reduce the computational effort, the *Fourier* transform is applied in the x-direction. In fact, the structure is 2D but the loading is 3D and since the response of the structure is linear, the analysis is carried out in the frequency/
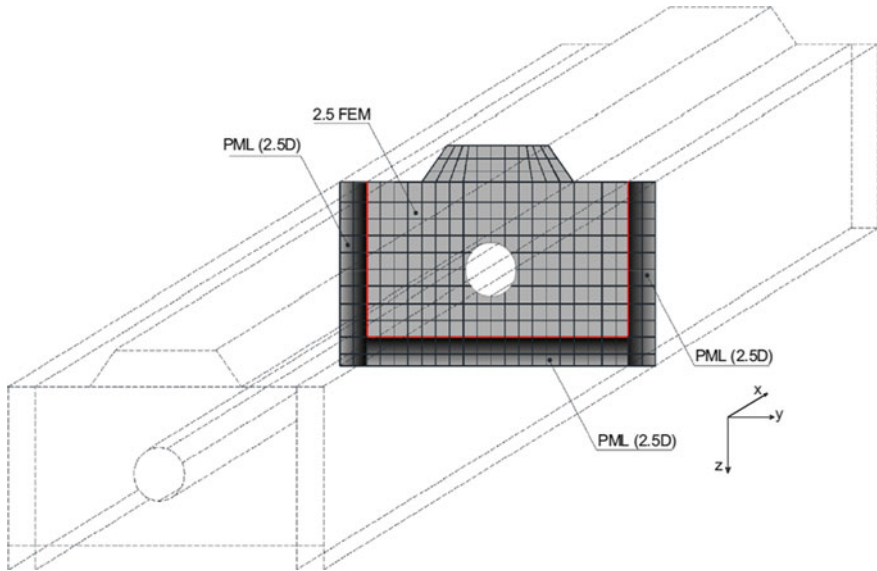
Fig. 1 Invariant section defined in the 2.5D approach [3]

wavenumber domain. The final response of the structure in the time/space domain is obtained through a double inverse *Fourier* transform. Hereafter, the equilibrium of each finite element in the *ZY* plane (represented in Fig. 1) is obtained considering the following equation:

$$\left(\iint_{ZY} B^T(-k_1)DB(k_1)\mathrm{dydz} - \omega^2 \iint_{ZY} N^T\rho N \mathrm{dydz} \right) u_n(k_1, \omega) = p^n(k_1, \omega) \quad (1)$$

where [*B*] is the derivative matrix of the shape functions, [*N*] is the shape function matrix, [*D*] is the constitutive matrix, ρ is the density and p_n and u_n are the nodal forces and displacements, respectively. Throughout this formulation, the stiffness and mass matrices are defined, respectively, by the following expressions:

$$[K] = \iint_{ZY} B^T(-k_1)DB(k_1)\mathrm{dydz} \quad (2)$$

$$[M] = \iint_{ZY} N^T\rho N \mathrm{dydz} \quad (3)$$

Treatment of the Boundaries
In this case, the artificial boundaries are treated through the *PML* (*Perfectly Matched Layers*), which is a local method with high acuity. In this method, an external layer is applied on the analysis' domain. The *PML* absorbs the waves that

impinge the boundary, without spurious reflection [3]. In order to consider the condition related to the absorption, the coordinates y and z are stretched to the complex domain, which induces an artificial increase in the wave attenuation that propagates along the *PML* layer. To obtain accurate results, the *PML* must act as an absorbing material but also as non-reflexive material. It is important to highlight that the solution inside the *PML* domain satisfies the same differential equation as in the interest domain, considering the change of the coordinates in Eq. (1), as described in [3].

2.2 Modelling of the Vehicle

In this analysis, a 2D model is assumed for the representation of the vehicle (only the vertical displacements are considered). The train is defined by a multi-body formulation where the main masses and suspensions of the vehicles are taken into account.

The European standard [4] refers 10 types of excitation mechanisms, which include the quasi-static mechanisms and the dynamic mechanisms. The quasi-static excitation is induced by the movement of the loads that correspond to the static weight of the vehicle per axle. The dynamic excitation mechanisms are more complex and are induced by the vehicle-track interaction that generates accelerations on the vehicle and also inertia forces. Thus, the magnitude of the vehicle-track interaction loads depends on several factors as the speed of the train, properties of the vehicle, railway infrastructure and irregularities profile. Since the analysis is carried out in the transformed domain, the transformation of the irregularity profile into the frequency (or wavenumber) is also required. The dynamic interaction forces in the transformed domain are defined considering the following expression:

$$N(\Omega)_n = \left([k_v]_{n \times n}^{-1} + [A]_{n \times n} \right)^{-1} \Delta u_n(\Omega) \tag{4}$$

where N is the vector of the interaction forces that depend on each axle of the train and the irregularity with a certain wavelength ($\lambda = 2\pi c/\Omega$). The matrices $[k_v]$ and $[A]$ represent the dynamic response of the train and track due to the dynamic force generated by the irregularity, respectively. The development of these matrices is complex and its explanation is referred in several works in the bibliography as [2, 5–8].

3 Case Study

The case study selected for this work establishes a comparison between the ballasted and ballastless tracks in terms of stress levels and stress paths taking into account the quasi-static and dynamic excitation mechanisms.

The slab track was modelled considering the *Rheda* system and is composed of the rails, railpads, concrete slab, support layer (poor concrete) designated as hydraulically bonded layer (HBL), frost protection layer (FPL). On the other hand, the ballasted track is composed of the rails, railpads, sleepers, ballast and sub-ballast. This analysis is focused on the stress levels in the foundation soil (modelled as a dry sand) represented in the *p-q* space. In Tables 1 and 2, the main material properties adopted for both structures are presented. All the granular materials and also the sleepers were modelled with linear elastic models. The sleepers were modelled as a continuous and orthotropic element [9]: in the longitudinal direction (*x*-direction), the material existing between the sleepers is the ballast, which means that the stiffness considered is the *Young* modulus of the ballast layer. In the cross-section, the properties of the sleepers are used. This solution was tested in [9] with satisfactory results. In order to characterize the foundation soil, a failure line defined by *Mohr-Coulomb* yielding criterion was defined considering a friction angle equal to 30° and zero cohesion. In this case, the yielding criterion is merely indicative, since the analysis is carried out assuming linear elasticity for the whole domain. It is important to note that it was assumed isotropic conditions in rest stress state, i.e., $k_0 = 1$. In order to reduce the computation effort, the simulation takes advantage of the symmetry conditions of the problem as depicted in Fig. 2 and Table 3.

Regarding the irregularities, three irregularities profiles (associated with three range of wavelengths) were defined according to European Standard [11]: $1 < \lambda < 3$, $3 < \lambda < 25$ (designated as *D1*) and $25 < \lambda < 70$ (designated as *D2*). The analysis of the stress levels due to the existence of the irregularities on the track allows identifying which are the wavelengths and also the frequencies (that depends on the train speed) that most influence the stress levels.

Table 1 Characteristics of the rails and railpads

Elements	Characteristics
Rails (UIC 60)	EI = 6110 kN m^2; m = 60.445 kg/m
Railpads (ballasted track)	k = 600 kN/mm; c = 22.5 kNs/m
Railpads (ballastless track)	k = 40 kN/mm; c = 8 kNs/m

Table 2 Characteristics of the materials of the ballasted

Elements	E (MPa)	v	ζ	ρ (kg/m^3)
Sleepers (ballasted track)	30,000	0.20	0.010	1833.3
Ballast	97	0.12	0.061	1591.0
Sub-ballast	212	0.30	0.054	1913.0
Foundation Soil	120	0.30	0.030	2040.0

(a)   **(b)**
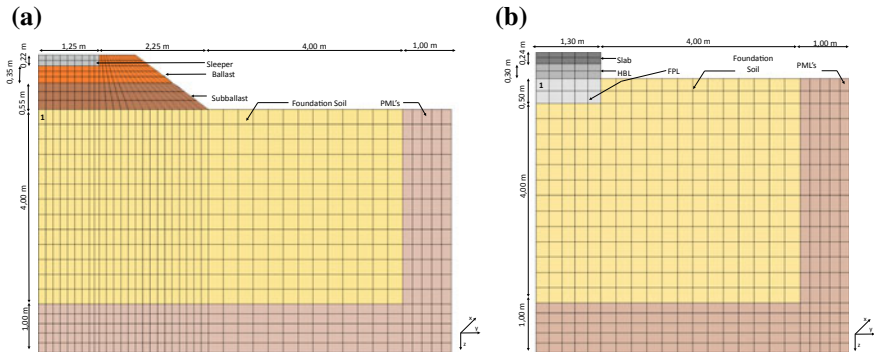
Fig. 2 Numerical models used to determine the behaviour of the ballasted track and slab track [10]

Table 3 Characteristics of the materials of the slab tracks

Elements	E (MPa)	v	ζ	ρ (kg/m^3)
Concrete slab	34,000	0.20	0.030	2500
HBL	10,000	0.20	0.030	2500
FPL	120	0.20	0.030	2500
Foundation soil	120	0.30	0.030	2040.0

3.1 Modelling of the Quasi-static Mechanism and Dynamic Mechanism

The *Alfa Pendular* train is composed of 6 car bodies, presents a symmetry plane and has an axle load of 135 kN. The main properties of *Alfa Pendular* can be seen in [12]. In this analysis, a train speed equal to 200 km/h was considered. This value is far from the critical speed that is equal to 540 km/h for the case study selected [13].

The irregularities profiles were generated with 40 frequencies and applying the power spectral density (*PSD*) defined by *Federal Railroad Administration (FRA)*:

$$S_{rzz}(k_1) = \frac{10^{-7}Ak_3^2\left(k_1^2 + k_2^2\right)}{k_1^4\left(k_1^2 + k_3^2\right)} \tag{5}$$

where A is a parameter that depends on the geometric quality of the railway track, k_1 is the wavenumber and k_2 and k_3 are constants. The value of the parameter A is limited according to the classes of the geometric quality. In fact, each class is associated a maximum train speed. In order to analyse higher speeds, the value of the parameter A was adapted considering the values of the alert limits of the limit of the standard deviation (in mm) and maximum peak value regarding the average of the longitudinal levelling defined in [11]. The frequencies of the irregularities profiles were determined according to the train speed and the wavelengths selected previously.

The irregularities are defined by a sinusoidal function that is described by a number of harmonics:

$$y(i) = A_i e^{ikix} \qquad (6)$$

where A_i is the amplitude of the irregularity and k_i is the wavenumber.

In Fig. 3 are presented the irregularities profiles defined taking into to account the three ranges of wavelengths mentioned previously.

3.2 Results

With this work, it was possible to evaluate the influence of the quasi-static and dynamic mechanisms in terms of stress levels. Firstly, from the irregularities profiles presented in Fig. 3 and the respective frequencies (defined according to the train speed), the stress paths and stress levels were determined. In Fig. 4 are presented the stress paths considering the 3 irregularities profiles. Analysing Fig. 4, it is possible to conclude, firstly, that the ballasted and ballasted tracks present different initial mean stresses ($p_{\text{ini:ballasted}} = 23$ kPa and $p_{\text{ini:ballastless}} = 17$ kPa). For both structures, the wavelengths between 1 and 3 m generate higher amplification of the stress levels. On the other side, the irregularities profiles defined by wavelengths between 3 and 25 m and 25 and 70 m have lower and zero influence on the stress levels, respectively, which means that the amplification of the dynamic response is low or even residual.

In Tables 4 and 5 are presented the maximum increment of the mean ($d_{\text{p;max}}$) and deviatoric stress ($d_{\text{q;max}}$) for each structure for the element 1 located at $x = 0$ m in the longitudinal direction. Besides, the increments between the quasi-static and dynamic mechanisms are also presented. Analysing the results, it is possible to conclude that the increments are higher in the ballasted track than in the ballastless track and the values of the increments on the first case ($1 < \lambda < 3$) are significant (superior to 20% on both railway structures), which can lead to problems in terms of track degradation.

The results of stress paths depicted in Fig. 4 are in accordance with the interaction forces. As expected, from 18 Hz (considering a train speed equal to 200 km/h and $\lambda < 3$), there is an increment of the interaction forces. However, the increment value also depends on the amplitude of the irregularity profiles. These observations are valid for both structures. As Fig. 5 shows, the three irregularities profiles (with different amplitudes) induce different ranges of the interaction forces. As expected, the interaction forces influence directly the stress levels.

Within this scope, the P-SV dispersion relationship of the ground was also studied. More information about the constructions of these curves can be found in [14]. Figure 6 shows that considering the distance 2.7 m (distance between the

(a)

(b)

(c)
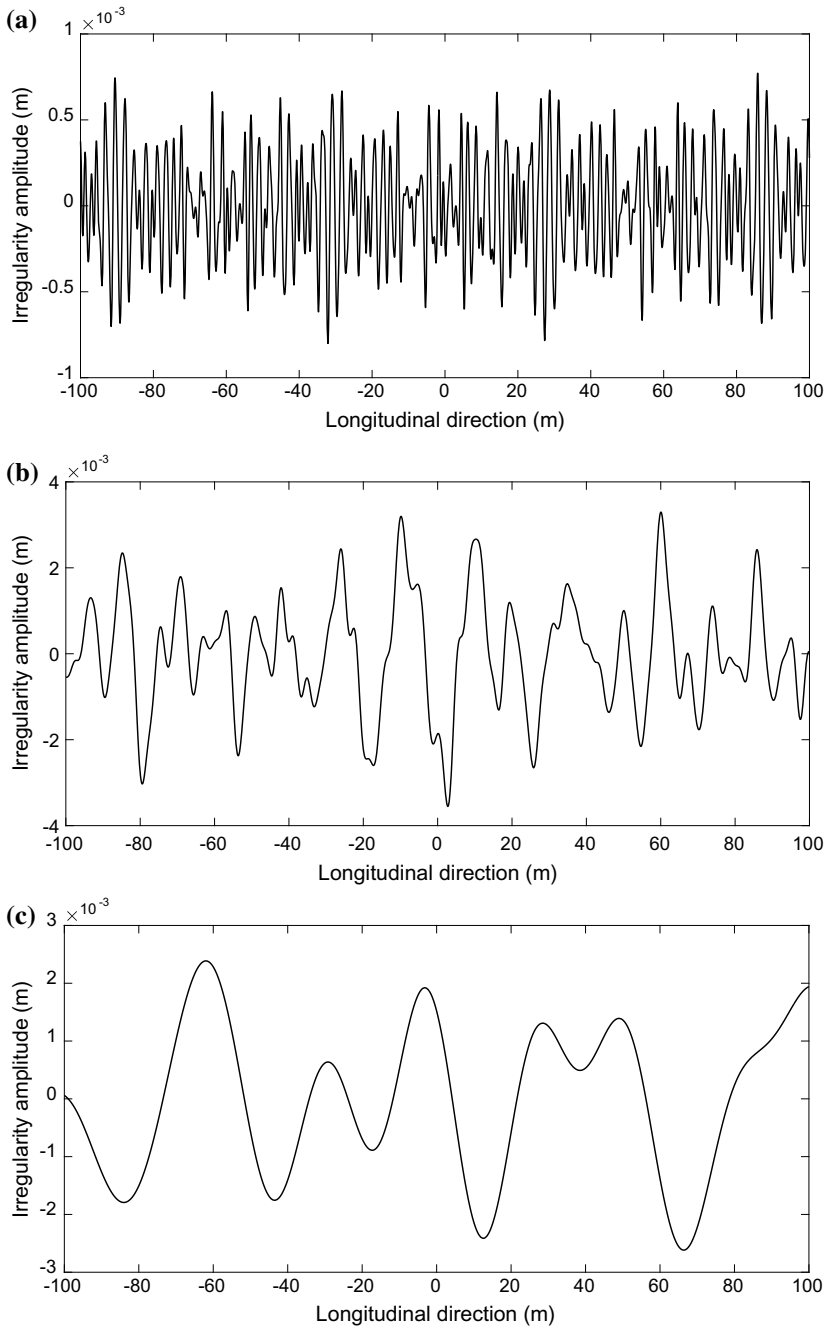
Fig. 3 Irregularity Profile: **a** $1 < \lambda < 3$, **b** $3 < \lambda < 25$ and **c** $25 < \lambda < 70$

(a)

(b)
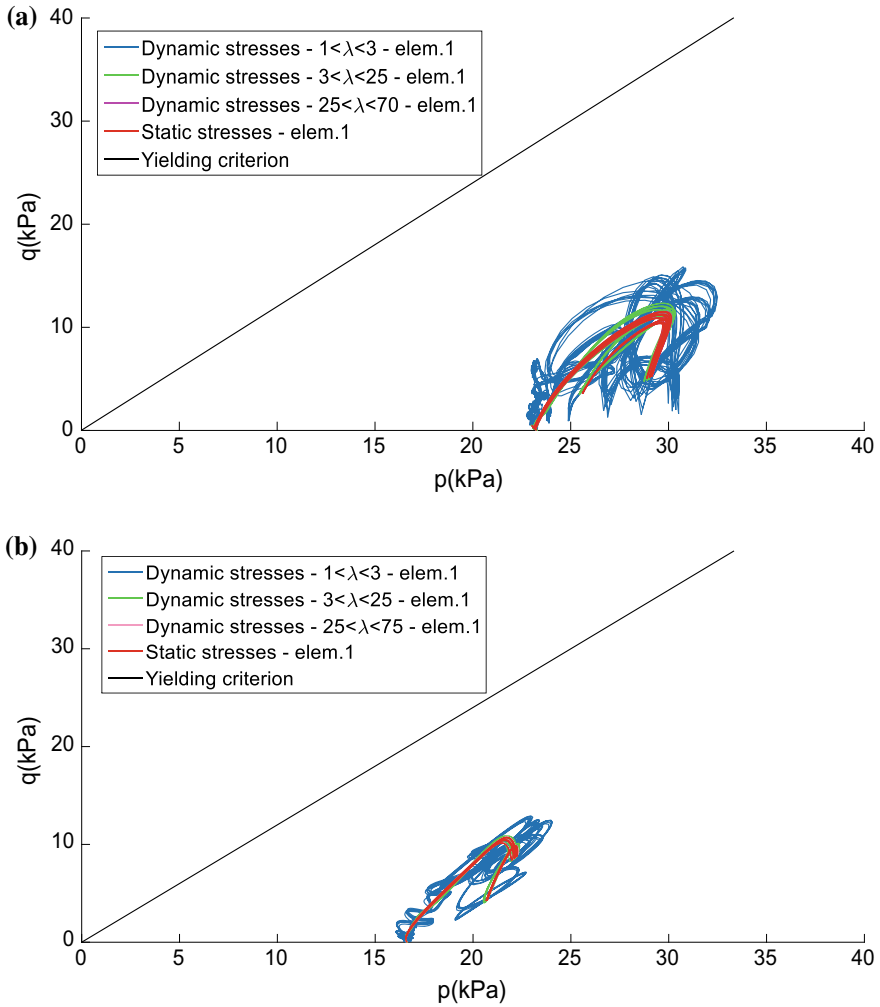
Fig. 4 Stress path—v = 200 km/h: **a** ballasted track and **b** ballastless track

axles of the bogie), the response amplification frequency of the ground is within the amplification verify in the stress levels and interaction forces. Besides, the natural frequencies of the ballasted and ballastless tracks are also within the range of frequencies above 18 Hz.

Table 4 Stresses on the ballasted track (element 1; v = 200 km/h; x = 0 m)

Ballasted track		$d_{\text{p;máx}}$	$d_{\text{q;máx}}$
f = 0 Hz	Stress (kPa)	7.00	11.50
$1 < \lambda < 3$	Stress (kPa)	9.50	15.88
	Increment (%)	35.71	38.10
$3 < \lambda < 25$	Stress (kPa)	7.35	12.30
	Increment (%)	5.00	7.00
$25 < \lambda < 70$	Stress (kPa)	7.00	11.50
	Increment (%)	0.00	0.00

Table 5 Stresses on the ballastless track (element 1; v = 200 km/h; x = 0 m)

Ballastless track		$d_{\text{p;máx}}$	$d_{\text{q;máx}}$
f = 0 Hz	Stress (kPa)	5.70	10.72
$(1 < \lambda < 3)$	Stress (kPa)	7.44	12.90
	Increment (%)	30.53	20.34
$(3 < \lambda < 25)$	Stress (kPa)	5.77	10.87
	Increment (%)	1.23	1.40
$(25 < \lambda < 70)$	Stress (kPa)	5.70	10.72
	Increment (%)	0.00	0.00
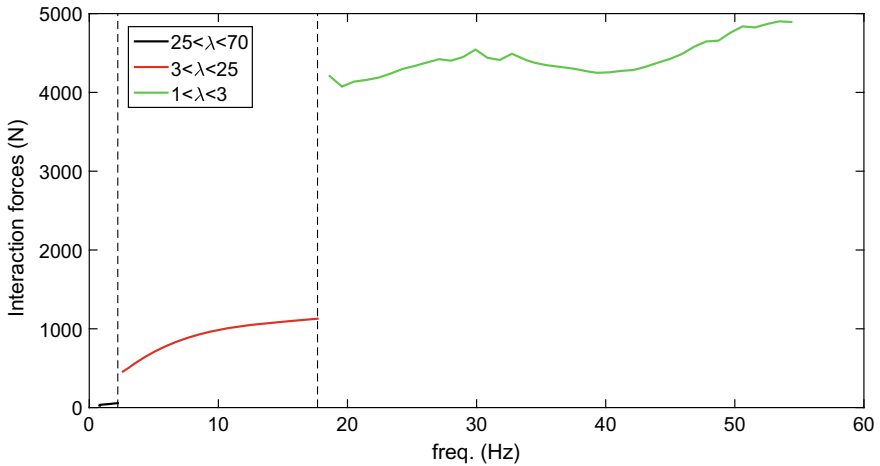
Fig. 5 Interaction forces (slab track)

4 Conclusions

This article pretends to study the performance of the ballasted and ballastless tracks considering the influence of the quasi-static and dynamic mechanisms induced by the passage of the train (*Alfa Pendular*). This work is the first step to predict track
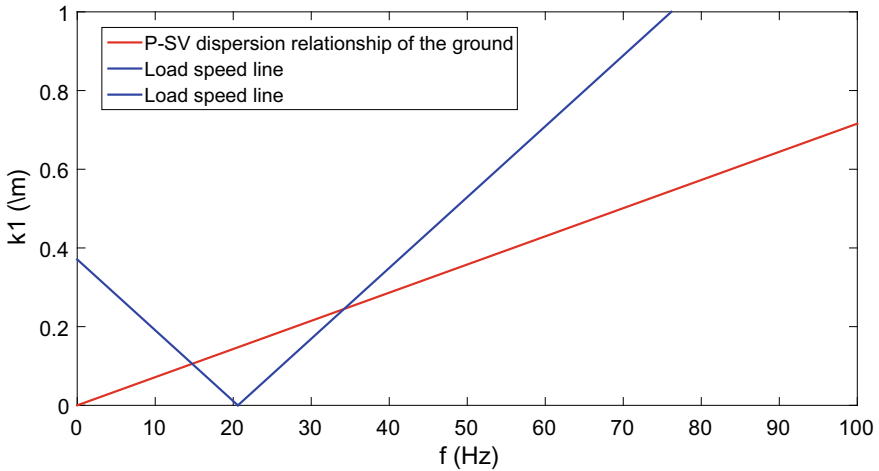
Fig. 6 P-SV dispersion in the ground

degradation, through the consideration of the train-track interaction. Hereafter, two types of structures were modelled: ballasted track and slab track (*Rheda* system). Comparing the quasi-static and dynamic mechanisms, it is possible to conclude that the dynamic mechanism only assumes a higher importance when the wavelengths vary between 1 m and 3 m. For values superior to 3 m, the dynamic mechanism is similar or even equal to the quasi-static mechanism. Thus, for frequencies between 18 Hz and 56 Hz (*1 < λ < 3*), there is an amplification of the stress levels (and also interaction forces), as show in the *p-q* diagrams. This amplification is identified in both structures (ballasted and ballastless tracks), but the ballasted track shows higher susceptibility because of its stiffness, despite the small difference of the increments (when the two structures are compared). Thus, the inclusion of the dynamic mechanism considering irregularities profiles with wavelengths between 1 and 3 m increases, significantly, the stress levels (when compared to the quasi-static mechanism) and this fact should not be ignored.

References

1. Yang YB, Hung HH (2001) A 2.5D finite/infinite element approach for modelling viscoelastic body subjected to moving loads. Int J Numer Methods Eng 51:1317–1336
2. Alves Costa P, Calçada R, Silva Cardoso A (2011) Track-ground vibrations induced by railway traffic: in-situ measurements and validation of a 2.5D FEM-BEM model. Soil Dyn Earthq Eng 32:111–128
3. Lopes P, Alves Costa P, Ferraz M, Calçada R, Silva Cardoso A (2014) Numerical modeling of vibrations induced by railway traffic in tunnels: From the source to the nearby buildings. Soil Dyn Earthq Eng 61–62:269–285

4. Iso14837-1 2005. Mechanical vibration—ground-borne noise and vibration arising from rail systems—Part 1: General guidance
5. Alves Costa P (2011) Vibrações do Sistema Via-maciço Induzidas por Tráfego Ferroviário. Modelação Numérica e Validação Experimental. Ph.D. thesis, Faculdade de Engenharia da Universidade do Porto, Porto, Portugal
6. Zhai W, Cai Z (1997) Dynamic interaction between lumped mass vehicle and a discretely supported continuous rail track. Comput Struct 63:987–997
7. Sheng X, Jones CJC, Thompson DJA (2003) Comparison of a theoretical model for quasi-statically and dynamically induced environmental vibration from trains and with measurements. J Sound Vib 267:621–635
8. Alves Costa P, Calçada R, Silva Cardoso A (2012) Influence of train dynamic modelling strategy on the prediction of track-ground vibrations induced by railway traffic. Proc Inst Mech Eng Part F: J Rail Rapid Transit 226:434–450
9. Alves Costa P, Calçada R, Silva Cardoso A, Bodare A (2010) Influence of soil non-linearity on the dynamic response of high-speed railway tracks. Soil Dyn Earthq Eng 30:221–235
10. Ramos AL, Correia AG, Calçada R, Costa PA (2018) Influence of permanent deformations of substructure on ballasted and ballastless tracks performance. In: Proceedings of 7th transport research arena TRA 2018, 16–19 Apr 2018, Vienna, Austria
11. En13848-5 2008. Railway applications—track—track geometry quality—Part 5: geometric quality levels. EN13848. European Committee for Standardization (CEN)
12. Alves Costa P, Calçada R, Silva Cardoso A (2012) Track-ground vibrations induced by railway traffic: in-situ measurements and validation of a 2.5D FEM–BEM model. Soil Dyn Earthq Eng 32:111–128
13. Ramos AL, Correia AG, Calçada R, Costa PA (2018) Stress path evolution in the ground due to railway traffic. Comparison between ballasted and ballastless track systems. In: 9th European conference on numerical methods in geotechnical engineering. Porto
14. Alves Costa P, Colaço A, Calçada R, Silva Cardoso A (2015) Critical speed of railway tracks. Detailed and simplified approaches. Transp Geotech 2:30–46

Subway/Metro Vibration and Geodynamics

Prediction Method for Metro Environmental Vibrations Based on Measurement

Zongzhen Wu

Abstract Problem of environmental vibrations induced by metro has become more and more serious, so, it is necessary to predict the vibrations accurately and effectively. Empirical chain attenuation method recommended by national code can be used in most prediction situations. But its accuracy is low and cannot predict vibration in the frequency domain. Researchers all around the world have developed many prediction methods including analytical/semi-analytical methods, empirical methods, numerical methods, measured prediction methods and so on. In all the methods, only prediction methods based on measurement can consider all influence factors of vibrations and get the real and accurate value of environmental vibration response. In this paper, firstly the research status of vibration prediction methods based on measurement is presented. New kind of measured prediction method is introduced, which is called the measured transfer function prediction method. And the evolutionary process and prediction principle of the method is displayed. At last, the measured transfer function prediction method is applied to a prediction example. Amplitude and frequency distribution of the predicted value and the measured value are similar. Measured Z vibration level is 59.56 dB, and the predicted Z vibration level is 59.62 dB, so the calculation result is accurate.

Keywords Metro · Environmental vibrations · Measured prediction method · Transfer function · Prediction example

1 Introduction

In recent years, the rapid development of urban rail transit has greatly alleviated the urban traffic pressure, but the environmental vibration induced by metro operation has attracted more and more attention. Excessive subway vibration will cause

Z. Wu (✉)
Urban Rail Transit Center of CARS, Beijing 100081, China
e-mail: wzzlogos@hotmail.com

building cracks, interfere with the normal operation of precision instruments and affect people's lives [1].

The current Technical Guidelines for Environment Impact Assessment of Urban Rail Transit [2] recommends that the unified empirical chain formula be used as the calculation method of environmental vibration prediction. The empirical formula is simple, quick and universal to predict the large-scale rapid vibration in the stage of line selection for metro construction and check the vibration sensitive points on the planned lines, but the shortcomings are that the accuracy is low and that quantitative prediction cannot be achieved in the frequency domain, which leads to unsuitable selection of vibration reduction tracks. The residents along the metro line frequently complain about the environmental vibration during subway train operation.

As a result, domestic and foreign scholars developed a number of vibration prediction methods, mainly including the following categories: analytical/semi-analytical methods, empirical prediction methods, numerical methods, measured analytical methods, etc. Each method has its advantages and specific scope of application. This paper first summarizes the research status of prediction methods based on measurement technology by scholars at home and abroad, and then introduces in detail a new measured prediction method, transfer function prediction method, and gives an application example to verify it.

2 Summary of the Measured Prediction Method

The measurement-based prediction method, among all the prediction methods, is the only method that can fully consider influencing factors of vibration and obtain true and accurate vibration response. This method is intuitive and necessary for theoretical analysis and verification, prediction model checking and vibration impact evaluation. After sufficient field tests are conducted, a rich database can be established. By statistically analyzing the test results, it is possible to predict the environmental vibration response in similar situations. However, complex and expensive electronic equipment is required in the test of the structure or field. The requirements for the test environment are also meticulous and harsh, and it is difficult to meet the extensive and rapid environmental assessment requirements.

Further, the reliability and accuracy of any prediction method can only be verified by field test. Due to the fact that during the prediction period, subway lines have not yet been put into operation or the sensitive targets for research have not yet been completed, the field test will be partially restricted. However, making full use of all possible field test conditions to assist traditional prediction methods will greatly reduce prediction errors and uncertainty. The field tests generally include field measurements of the input, output, or transfer characteristics of the entire vibration system or its subsystems, or analog tests of similar projects.

Scholars in related fields conducted in-depth research on vibration prediction of metro environment based on field measurement and achieved such results as follows.

In the prediction of railway vibration, Federal Transit Administration (FTA) [3] proposes to use the vibration propagation characteristics of the soil surface which can be obtained through the hammer test to predict vibration. For the underground railway, vibration prediction is recommended to use the drilling hammer method to obtain the vibration propagation characteristics within the soil layer.

Liu and Sun [4] proposed a prediction method combining the field test method with numerical analysis method to predict the vibration response in buildings; Liu et al. [5] used the vibration response transfer ratio within 1/3 octave spectrum to describe the variation inside and outside the building and applied this method to predict the vibration response of the precision instrument test platform induced by the metro train operation; Ma et al. [6] further discussed the conversion relation between different magnitudes of vibration transfer in this method.

Zhang et al. [7] obtained the measured transfer characteristics of the tunnel-free field system by using reverse surface hammering and arranging measuring points in the tunnel and the measured vibration characteristics of the metro were predicted by using the measured transfer characteristics.

Wang [8] obtained the transfer characteristics of tunnel-field and tunnel-field-building systems through hammering in the tunnel and used the test data of tunnel structure vibration induced by metro train operation as input, and proposed prediction method of vibration response transfer function for the metro environment based on pulse experiment.

Liu and Ma et al. [9] used the measured data of vibration source strength and vibration response to perform two-way calibration of the input and output of the numerical model in the time or frequency domain, then applied the calibrated numerical model to predict the vibration response of metro train, and proposed two-way calibration prediction methods based on field test.

Yuan [10], based on the properties of transfer function, used the multi-point hammering method to measure the transfer characteristics of the vibration propagation system, obtained transfer characteristic conversion formula by theoretical derivation, converted the transfer characteristics of the hammer test into those of train operation, and established the artificial single-point pulse excitation prediction method to predict the surface vibration response.

3   Transfer Function Prediction Method

In all measurement-based prediction methods for metro environment vibration, a new type of method has been developed in recent years, namely the transfer function prediction method in this paper. This method, based on traditional measurement techniques, introduces the transfer function in signal processing and is applied to vibration prediction of metro environment. Compared with the traditional

prediction method, it has some advantages: focusing on the actual tunnel-soil structure status, performing frequency domain prediction, high prediction accuracy and wide prediction frequency band.

3.1 Transfer Function Prediction Method Based on Impulse Excitation

Under normal circumstances, the dynamic strain of soil under environmental vibration caused by metro trains is in the order of 10^{-5} or even smaller, the stress and strain of the soil is completely in the elastic state, and the vibration propagation system is in the elastic strain stage, which makes it possible to deal with the prediction of the vibration response of the metro by using basic principles of the transfer function under linear elasticity. Therefore, Wang proposed a new method to use the transfer function in the control theory for the prediction of environmental vibration caused by metro trains—the transfer function prediction method based on pulse excitation [10]. The accuracy of this method is verified by the laboratory, and the transfer function of being accurately measured from tunnel wall measurement points to the surface vibration response points under the excitation of the pulse can be obtained, so the accurate prediction of the point-to-point response of the sensitive target can be achieved.

The main theoretical basis for the measured transfer function prediction method proposed by Wang is the transfer function characteristics of the tunnel-building system. That is, the tunnel-building vibration transfer function is the natural characteristics of the transfer system and has nothing to do with the acceleration value of the vibration source. Taking vibration acceleration as an example, the prediction process can be divided into three parts: (1) field test, (2) database establishment, and (3) calculation and prediction.

(1) Field test: The pulse hammer test method is used to measure the acceleration time history $y(t)$ of the measured points in the predicted building and the acceleration time $x(t)$ of the tunnel wall measurement points (Fig. 1).

Then, the acceleration transfer function of the in-building-tunnel wall is calculated. Here is the special non-dimensional transfer function. Its definition is shown in Eq. (1):

$$H(f) = \frac{Y(f)}{X(f)} \tag{1}$$

(2) Database establishment: The acceleration time history $x'(t)$ of tunnel wall with different fasteners and track types of subway lines in operation is measured, and the acceleration spectrum $X'(f)$ at the measurement points of the tunnel walls during operation is calculated.

Fig. 1 Intra-structural prediction of a tunnel
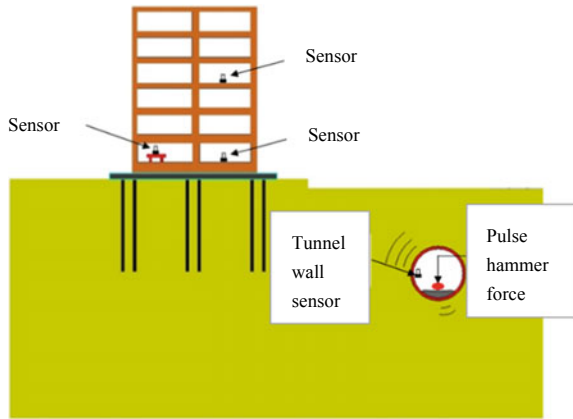
Fig. 2 Transfer function prediction method
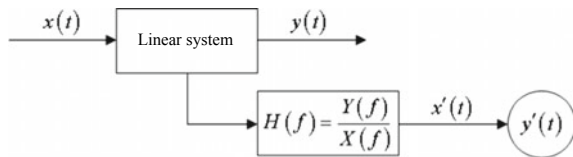
(3) Prediction and calculation: The transfer function method is to predict the vibration spectrum $Y'(f)$ of the measurement points in the building caused by the metro operation, and Inverse Fourier Transform is used to obtain the acceleration time history of the measurement points $y'(t)$ (Fig. 2). It is convenient to calculate peak acceleration, effective value, acceleration level, and one-third octave, and compare and evaluate with other environmental vibration standards.

3.2 Artificial Single-Point Pulse Excitation Method

The principle of the transfer function prediction method based on pulse excitation determines that it can only accurately predict the vibration response in a building under a point vibration source, and there is a large error in predicting the vibration under a series of moving loads when the practical train passes through, as shown in Fig. 3.

In order to realize the new requirements for the prediction of the vibration response of metro trains—precise quantitative prediction in the frequency domain, the paper [11] proposed an artificial single-point pulse excitation prediction method based on the transfer function prediction method. This method obtained the transfer
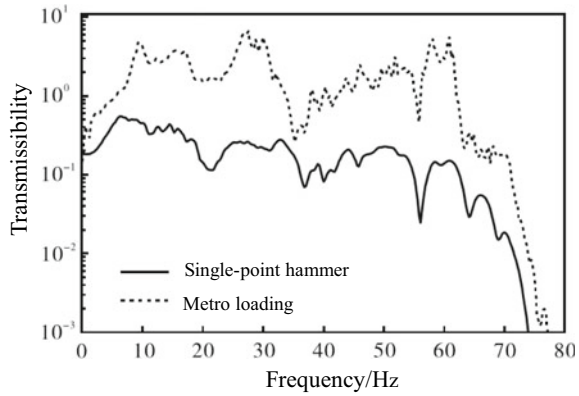
characteristics of the vibration propagation system through single-point pulse
excitation (multi-point excitation), and a set of conversion formulas are obtained
through the derivation of the theoretical formula, and thus the system transfer
characteristics of train operation under load can be obtained. Then, the measured
vibration source of the metro train is substituted into the artificially measured
vibration transfer characteristics, so as to achieve the purpose of the vibration
response prediction for the target point.

The artificial single-point pulse excitation prediction method is realized by an
artificially controllable and automatic drop hammer excitation device. The under-
ground pulse excitation test method is used to measure the vibration transfer
characteristics from the tunnel wall to the surface or predict the response of target in
the building.

In view of the spatial characteristics, there are differences between metro train
operation excitation and artificial single-point pulse excitation. Therefore, a set of
prediction formulas for vibration transfer characteristics are derived theoretically
[11], whereby the vibration transfer characteristics obtained by artificial single-
point pulse excitation (fixed point vibration source with sequential excitation) are
converted into the vibration transfer characteristics of metro train (moving series
point vibration source) (see Fig. 4).
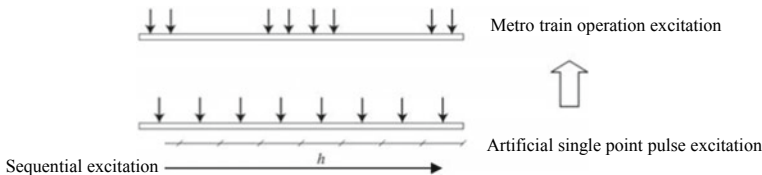
Fig. 4 Conversion of two vibration source excitation modes by the calculation formula

3.3   Vibration Prediction Method Based on the Measured Frequency Response Function

For the prediction error of single transfer function of "transfer function prediction method based on pulse excitation" and for the error caused by phase in the prediction process of "artificial single-point pulse excitation method," the paper [12] proposed that prediction method considering space-time load effect caused by metro train operation - vibration prediction method is based on measured frequency response functions. The entire calculation process of this method is performed in the frequency domain, including all information of amplitude and phase. Frequency domain vibration response at the surface can be calculated more precisely.

The prediction method converts the prediction of the environmental vibration response caused by metro operation into a series of base forces in the frequency domain by constructing the rail analysis model, and a series of measured frequency response functions at different distances from a surface measured by situ hammerings in the tunnel. In the frequency domain, corresponding multiplication and superposition are performed to obtain the final surface vibration response. The prediction method is shown in Fig. 5.

Fig. 5 Prediction method flow
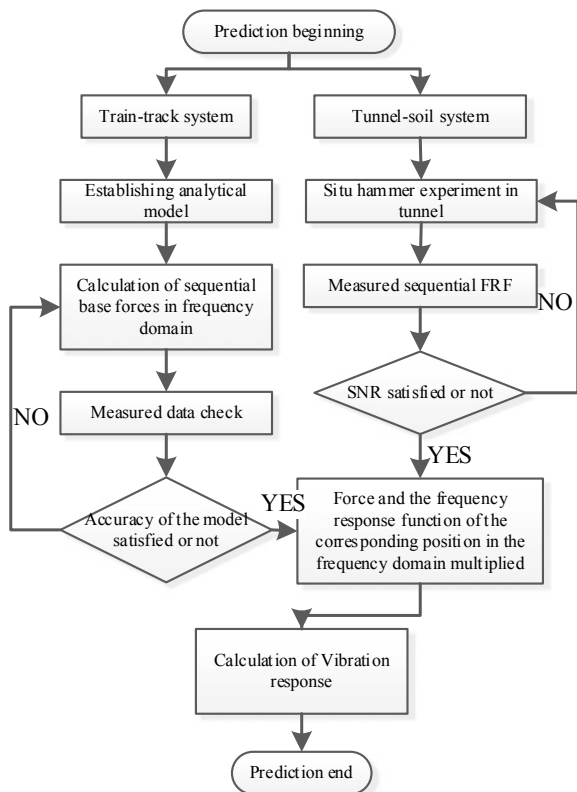
The entire prediction process is divided into four main steps:

First, a series of base forces $\hat{F}_n(\omega)$ in the frequency domain with a distance L between fasteners is calculated by using the rail analysis model, as shown in Fig. 6.

Second, through the hammer test in the tunnel, the frequency response functions ($H_k(\omega)$) at measured points with 5 m equal intervals on the surface, as shown in Fig. 7.

Third, according to the distance b_n from the F_n position to the prediction point (as shown in Fig. 8), the frequency response function of the measured frequency response function from the adjacent b_k and b_{k+1} is found to satisfy the Formula (2).

$$b_k < b_n < b_{k+1} \tag{2}$$

Then, b_k and b_{k+1} are used as interpolation nodes at each frequency point. Using the linear difference method according to $H_k(\omega)$ and $H_{k+1}(\omega)$ finds the frequency response function $H_n(\omega)$ corresponding to F_n.

Fourth, the frequency domain force of the corresponding distance and frequency response function in the frequency domain are multiplied to obtain the frequency domain response $\hat{F}_i(\omega) \times H_i(\omega)$ of the predicted point under a single force. Then,

Fig. 6 Base force group in frequency domain calculated by the rail analysis model
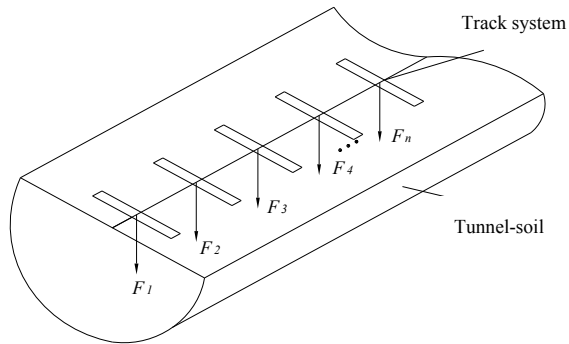
Fig. 7 Measured k frequency functions with 5 m distance
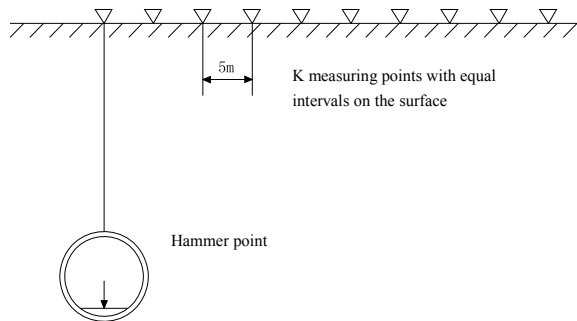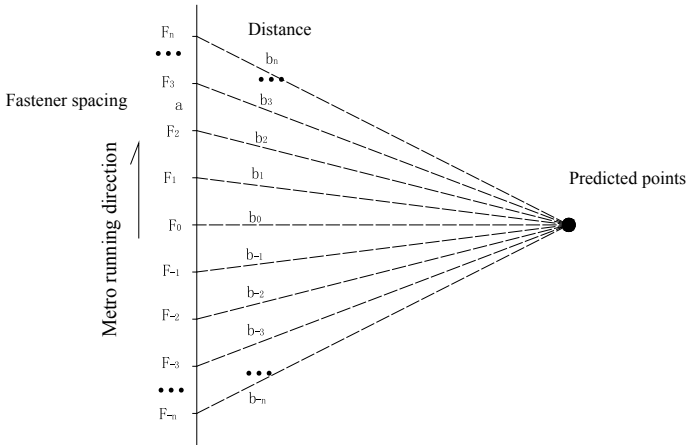
Fig. 8 Schematic diagram of the frequency response function at different distances from the surface prediction point

all 2_{n+1} frequency domain response results are superposed to obtain the final frequency domain response $\hat{X}(\omega)$ of the surface prediction point, as is shown in Eq. (3).

$$\hat{X}(\omega) = \sum_{i=-n}^{n} \hat{F}_i(\omega) \times H_i(\omega) \tag{3}$$

4 Prediction Examples

The vibration prediction method based on measured frequency response function sequence is used to perform practical prediction calculations and to compare with the actual vibration measurement data of the environment caused by metro (Figs. 9, 10 and 11), we can see that:

(1) The time-domain waveforms calculated by the prediction method and the actual field measurement are similar to the "spindle." The arrival and end time and the duration of the passage of the trains are the same. The time-domain peaks are all around 0.02 m/s².

(2) Both spectrum waveforms of the surface vibration acceleration have similar variation patterns, the frequency domain amplitudes are equivalent, and the primary frequency of vibration is the range of 30–80 Hz.

(3) The surface vibration acceleration 1/3 times frequency spectrum curves of the frequency response prediction and the measured frequency response prediction basically coincide with each other through calculation. All the magnitude of
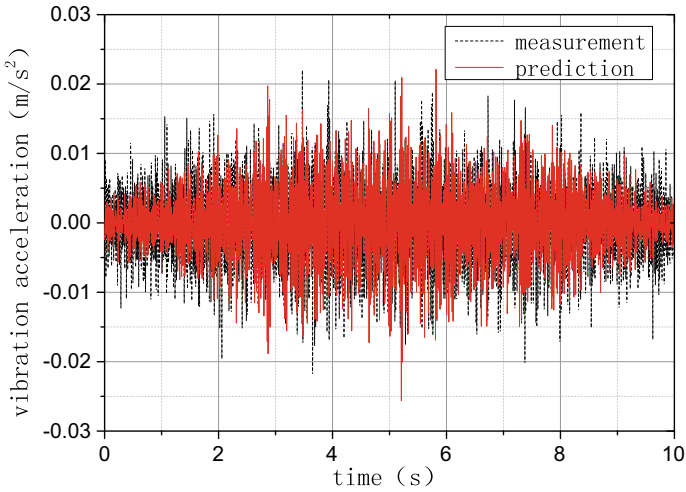
Fig. 9 Comparison of the time history of surface vibration acceleration
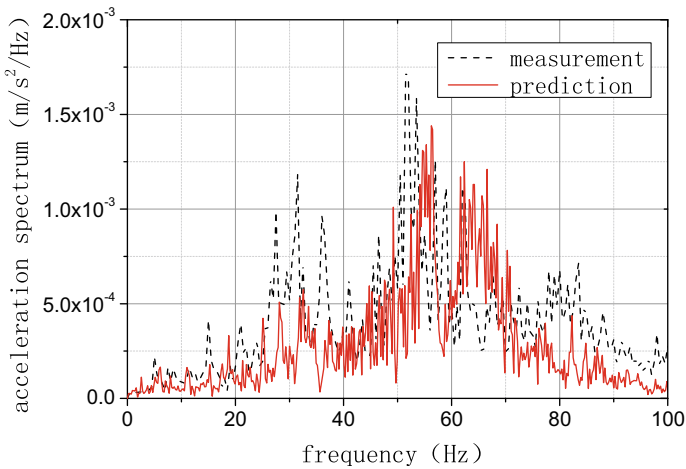
Fig. 10 Comparison of spectrum amplitudes of surface vibration acceleration

vibration, the main frequency band, and variation laws are unanimous. All of them reached a peak at the central frequency point of 50–60 Hz.

(4) The measured Z vibration level is 59.56 dB. Z vibration level calculated by this prediction method is 59.62 dB, and the calculation result is accurate.
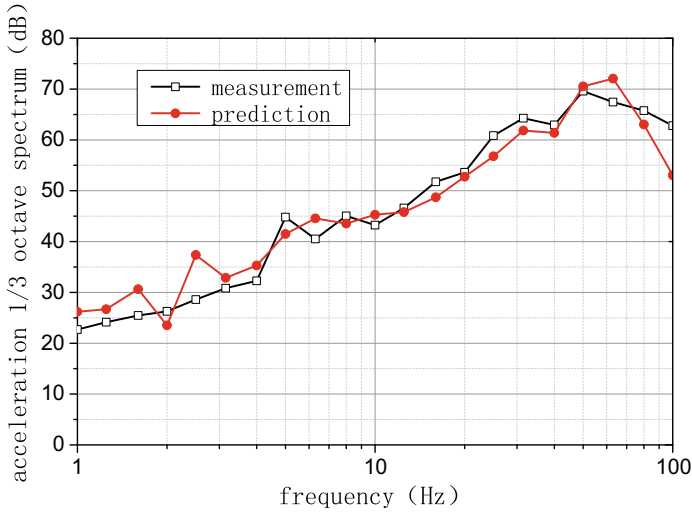
Fig. 11 Comparison of surface vibration acceleration 1/3 octave spectrum

5 Conclusion

This paper summarizes the research status of the prediction method of metro environment vibration based on measurement. Besides, it introduces a new measurement prediction method—measured transfer function method. The measured transfer function method can reasonably consider the actual tunnel-soil structure, supplemented by the measured load of the vibration source and the measured vibration of the surface vibration, which can provide accurate frequency domain prediction. Due to the limitations of traditional analytical and numerical methods, metro environment vibration in the future must use measured prediction method as the main method, combining other methods. Thus, all of the methods can assist each other, bringing their strong points into full play and form a scientific comprehensive prediction evaluation system, which is the right direction for the development of the environmental assessment of metro vibration.

References

1. Xia H, Cao Y (2004) Problem of railway traffic induced vibrations of environments. J Railway Sci Eng 1(1):44–51
2. National Environmental Protection Standard of the People's Republic of China. HJ453–2008 (2008) Technical guidelines for environmental impact assessment—urban rail transit. China Environmental Science Press, Beijing
3. Office of Planning and Environment, Federal Transit Administration (FTA), U. S. FTA-VA-90-1003-06 transit noise and vibration impact assessment. USA (2006)
4. Sun X (2008) Prediction of environment vibration induced by metro trains and mitigation measures analysis. Beijing Jiaotong University, Beijing
5. Liu W (2009) Study on numerical prediction model of metro train induced vibrations in tunnels and free field. Beijing Jiaotong University, Beijing
6. Ma M, Liu W, Ding D et al (2011) Prediction of influence of metro trains induced vibrations on sensitive instruments. J Vib Shock 30(3):185–190
7. Zhang N, Xia H, Yang WG et al (2011) Prediction and control of building vibration under metro excitations. In: Proceedings of the 8th international conference on structural dynamics, Leuven, Belgium, pp 705–711
8. Wang W, Liu W, Sun N et al (2012) The prediction method of metro trains induced vibration inside adjacent buildings based on pulse excitation. China Railway Sci 33(4):139–144
9. Liu W, Ma M, Wang W (2013) Prediction method for subway train-induced environmental vibration responses. China Railway Sci 34(4):111–118
10. Wang W (2011) Study on metro train-induced environmental vibration and transfer function prediction based on pulse experiment method. Beijing Jiaotong University, Beijing
11. Yuan Y (2014) Study on artificial single-point pulse excitations method for prediction of metro train-induced environmental vibration. Beijing Jiaotong University, Beijing
12. Wu Z, Liu W, Ma L et al (2015) Prediction method for metro environmental vibrations based on measured frequency response functions. Eng Mech 32(6):155–161

Dynamic Response Analysis of the Subway Station Under Moving Train Loads

Xiangyu Qu, Meng Ma, Weining Liu and Linfeng Li

Abstract With the rapid development of urban mass transit systems, the issue of train-induced vibration has attracted attention. The train-induced ground vibration that occurs above or near a train station is different from that which occurs above the main line due to key differences in structure, as well as the layout of turnouts. In this paper, in order to model trainloads at the main line and turnout areas, we used a simplified two-dimensional train-track coupled model and an additional three-dimensional station-soil finite-infinite coupled model, and the latter created using the software ABAQUS. The station's structural dynamic responses at both the turnout areas and the main line were calculated, and the time and frequency data were compared. Our results show that when the train passed through a track with turnouts, the acceleration response on the rails was ten times larger than when it passed through the main line, and the acceleration response on the sleepers was five times larger than when it passed through the main line. The acceleration response of the station plate exhibited the most dramatic decrease at frequencies between 3 and 20 Hz and between 60 and 100 Hz. Furthermore, the vibration through the plate decreased over entire frequency bands, and vibration through the pillars decreased only at frequencies above 50 Hz.

Keywords Subway station · Turnout · Train-track coupled model · Dynamic response

1 Introduction

As urbanization in China increases, serious traffic problems have emerged in the larger cities. The most effective solution to this problem is the establishment of a subway system; however, subway systems come equipped with their own problems. Most recently, the issue of train-induced vibration has been attracting

X. Qu (✉) · M. Ma · W. Liu · L. Li
School of Civil Engineering, Beijing Jiaotong University, Beijing 100044, China
e-mail: 17121095@bjtu.edu.cn

627

attention, and a range of studies have been conducted in this area, including research by Aiello et al. [1], Gupta et al. [2] and Hill et al. [3].

The construction of tunnels and tracks near subway stations is complex, and train speed tends to vary greatly across this range of layouts. In particular, when a turnout is built near a station, the vibrational response is more complicated and has a greater environmental vibration impact. In recent years, many scholars have studied the dynamic response of turnout structure. Kassa et al. [4], Lakusic et al. [5], Vogiatzis et al. [6] and Chen et al. [7] have measured and analyzed the dynamic responses of turnouts. Bruni et al. [8] and Markine et al. [9] have established numerical models in order to analyze the dynamic responses of the turnouts. Karwunruen et al. [10] used big data to monitor turnout structures in Australia.

The question of vibration source is significant in train-induced environmental vibration analysis. This paper aims to compare the vibration characteristics of trains passing through turnouts and main line structures and analyze their effects on the subway station. Accordingly, a simplified 2D train-track coupled model and a 3D station-soil finite element-infinite element (FE-IFE) coupled model were built. The dynamic response of the subway station structure under moving trainloads was calculated for the track in both the main line and turnout areas.

2 Numerical Model

The coupled train-track-station-soil system can be divided into two parts: a train-track system and a station-soil system, both of which were established using numerical simulation. From the simplified 2D train-track model, the supporting force of the sleepers can be obtained and then applied to the 3D station-soil FE-IFE coupled model.

2.1 Train-Track Model

In the 2D train-track model, the carriage of a moving train is modeled using a series of masses, springs and dampers consisting of one car body, two bogies and four wheels, all of which are rigid bodies and connected to each other by primary and secondary suspensions. Each model train carriage has ten DOF (degrees of freedom). The track model consists of four layers: rails, fasteners, sleepers and under-sleeper pads (Fig. 1). The contact wheel/rail forces are modeled by a Hertz spring following Grassie [11].

$$k_{\mathrm{H}} = \sqrt[3]{\frac{6E^2 P \sqrt{R_{\mathrm{w}} R_{\mathrm{r}}}}{4(1 - v^2)^2}} \tag{1}$$
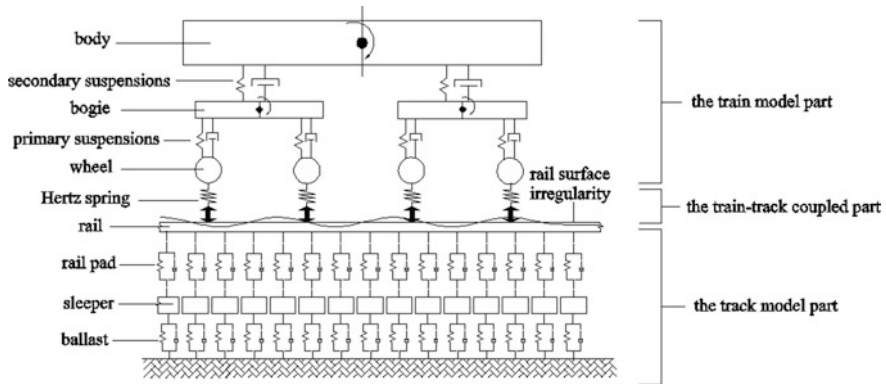
Fig. 1 2D train-track coupled model
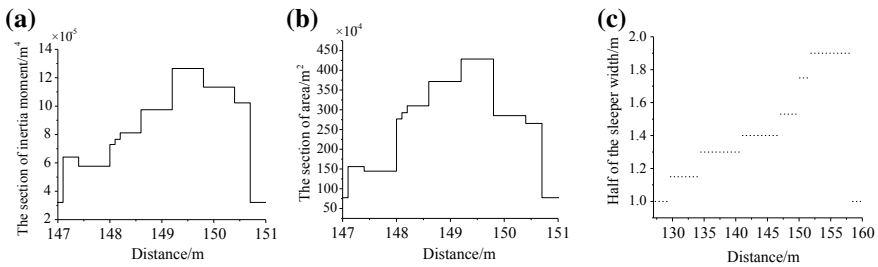
Fig. 2 Turnout parameters changing with elements, **a** for the section of inertia moment along the direction of the train, **b** for the section of area along the direction of the train and **c** for half of the sleeper width along the direction of the train

where P is the static wheel load, R_w and R_r are the radiuses of the wheel and rail profile, E is Young's modulus of the wheel and rail material, and v is Poisson's ratio.

Each train has four motor cars (M) and two trailer cars (T), and a train is arranged in the pattern of T-M-M-M-M-T. The total length of the train is 120 m. The train parameters are listed in Table 1 [12].

As the vibration response of a train passing through a turnout is different from the response, when passing through a main line, two track models were required. Both of the models were 240 m in length. The turnout structure is located at a distance of 143–153 m from the train's origin point. There are two main differences between the two models. The first is that there are gradual changes to the track section and its parameters, in particular the changes in rail cross-section and the sleeper size. The other key difference is the sudden change of rail unevenness in a vertical direction. Table 2 lists the basic track parameters. The parameter of $DTVI_2$ and the elastic bed is from Ref. [12].

Table 1 Train parameters

Structures	Parameters	Trailer	Motor
Car body	Vertical stiffness (kN/m)	480	480
	Vertical damping (kNs/m)	60	60
	Mass (t)	43	43
Bogie	Vertical stiffness (kN/m)	1400	1650
	Vertical damping (kNs/m)	20	20
	Mass (t)	3.418	3.418
Wheel set	Mass per wheel (t)	1.317	1.61
	Wheel radius (m)	0.84	0.84
	Intra-bogie axle spacing (m)	2.2	2.2

Table 2 Track parameters

Structures	Parameter name	Used in main line	Used in turnout areas
T60 rail	Inertia moment (m^4)	3.217×10^{-5}	See Fig. 2a
	Section area (m^2)	7.745×10^{-3}	See Fig. 2b
$DTVI_2$ fastener	Equivalent stiffness (N/m/m)	6×10^8	6×10^8
	Equivalent damping (Ns/m/m)	3×10^5	3×10^5
Sleeper	Young's modulus (N/m^2)	3.6×10^{10}	3.6×10^{10}
	Height (m)	0.205	0.205
	Poisson's ratio (–)	0.2	0.2
	Density (kg/m^3)	2500	2500
	Half of the width (m)	1	See Fig. 2c
Elastic bed	Equivalent stiffness (N/m/m)	2×10^8	2×10^8
	Equivalent damping (Ns/m/m)	8×10^4	8×10^4

According to the simplified method proposed by Markine et al. [9] and Wan et al. [13], the dynamic effect of a train on a turnout can be modeled using the gradually changing parameters along the train's directional movement. The changing parameters include the section of inertia moment and the section of area. The train passing through the turnout can be considered as three distinct stages. Firstly, the wheels travel along the wing rail as the train approaches the crossing nose. Here, the contact between wheel and rail is occurring only at a single point. Secondly, the rail touches the crossing nose, and the wheel load transfers from the wing rail to the crossing nose. In this transition stage, the wheel is in contact with both the wing rail and the nose. Finally, the wheel leaves the wing rail and rolls only over the crossing nose and subsequently through rail. In addition, the sleeper size also changes with distance; in the turnout area, the sleepers gradually widen.
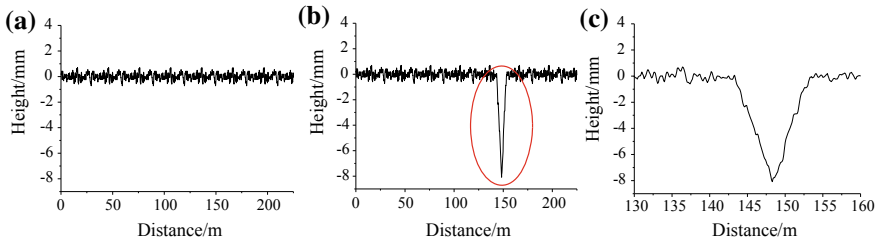
Fig. 3 The roughness of the rail surface, **a** for the rail unevenness of the main line, **b** for the rail unevenness of the turnouts and **c** for the circled portion of (**b**)

The wheel–rail interaction was modeled by the Hertz spring. The measured rail unevenness from the main line of the Beijing metro's line ten was employed, as shown in Fig. 3a. According to field observations by Markine et al. [9], the vertical height of the lowest point of the turnout at the crossing point is about 8 mm lower than that of the main line. In addition to measuring the local geometry at the crossing, the geometry 5 m before and 5 m after the crossing point was also measured (Fig. 3b, c).

2.2 Subway Station–Soil FE-IFE Coupled Model

Using the FE software ABAQUS, the numerical model of the station-soil system and its main dimensions are shown in Fig. 4. The material parameters are listed in Table 3. In this model, the Rayleigh damping assumption was employed with the damping factors α and β listed in Table 3. To avoid wave reflection at the
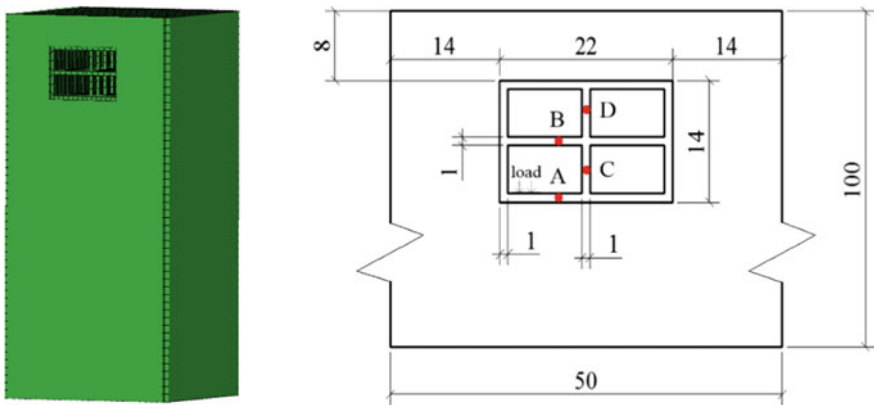
Fig. 4 The numerical model and its main dimensions (unit: m)

Table 3 Material parameters

Item	Concrete	Soil
Elasticity modulus (kN/m^2)	4.2×10^8	3.19×10^6
Poisson's ratio (–)	0.2	0.34
Density (kg/m^3)	2400	2230
Damping factor α in Rayleigh damping assumption	0.622	0.37326
Damping factor β in Rayleigh damping assumption	1.5758×10^{-4}	9.45475×10^{-5}
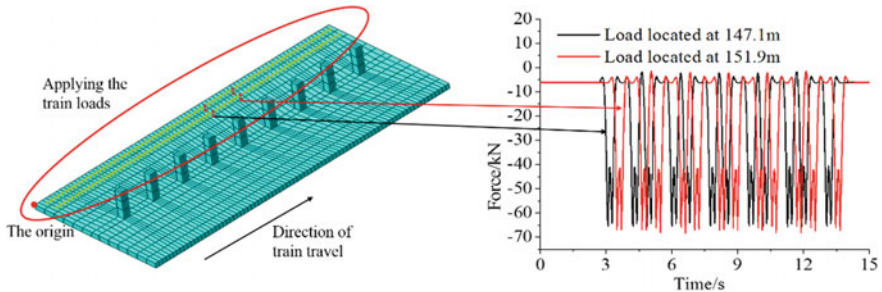
Fig. 5 The moving trainloads applied to the base of the station

boundaries in the dynamic analysis, the IFE boundary was used. The trainloads obtained from the 2D train-track model were applied to the base of the station structure.

In Fig. 5, the black and red lines indicate the load-time history at 147.1 and 151.9 m from the origin point, respectively. The trainloads were applied to each sleeper location, with a spacing of 0.6 m.

3 Results and Analysis

Four vibration detection points were selected on the pillars and plates of the two structural layers of the subway station, defined as A, B, C and D (Fig. 4). The displacement responses of each point were analyzed using time history, frequency spectra and their contour plots.

Figures 6, 7 and 8 chart the dynamic responses of Point A and B at the turnouts and the main line. As shown, when the wheels pass through the turnout areas, a series of significant vibration shocks occur, and an increase in vibration amplitude can be observed. The displacement results also clearly display the sudden change in the value of the train as it passes through the reclamation area.
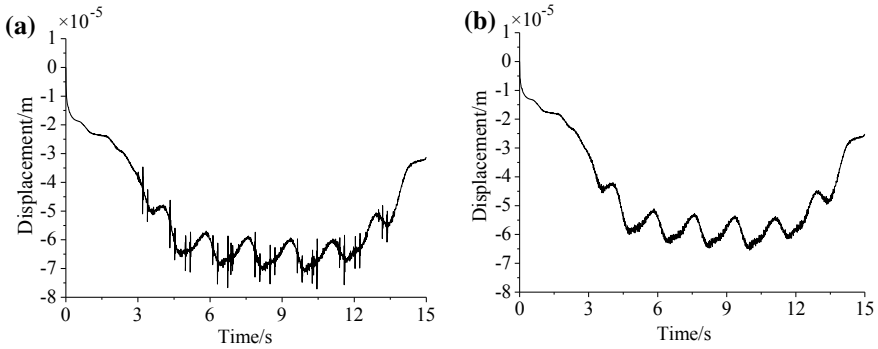
Fig. 6 The displacement at Point A when the train passes **a** through turnouts and **b** the main line
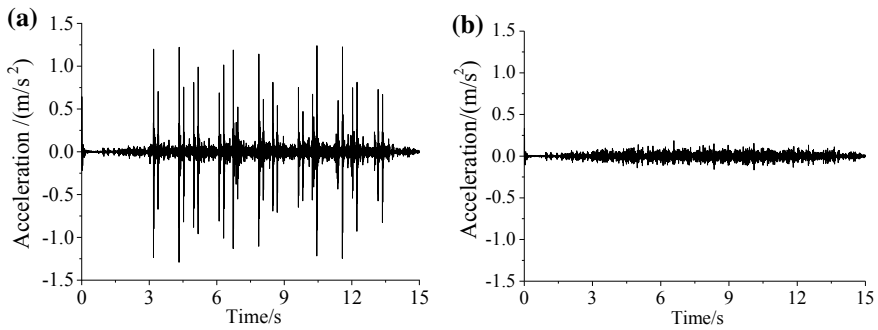
Fig. 7 The acceleration at Point A when the train passes **a** through turnouts and **b** the main line
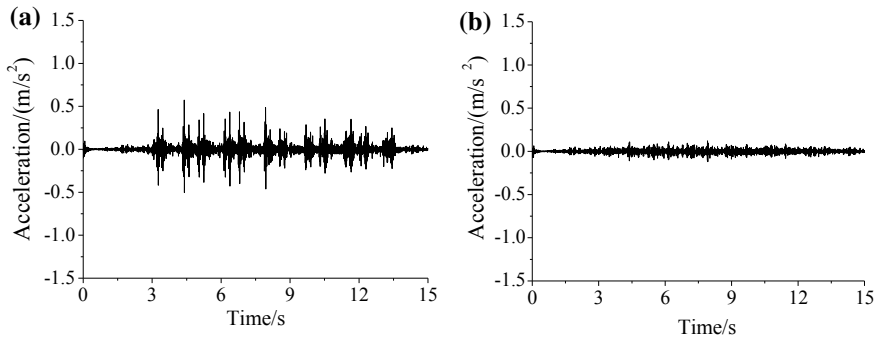
Fig. 8 The acceleration at Point B when the train passes **a** through turnouts and **b** the main line

(a)

(b)
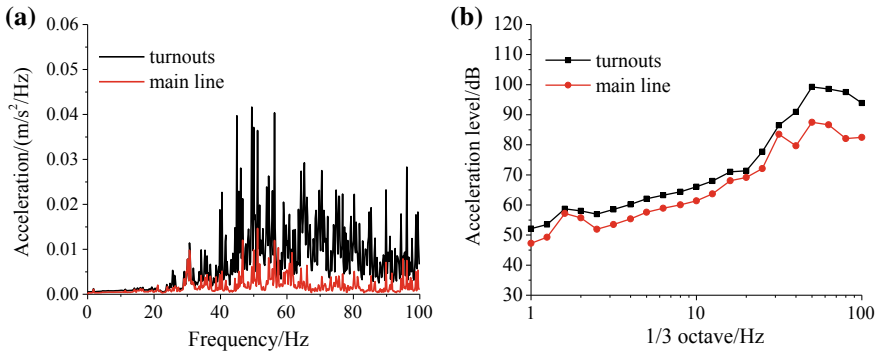
Fig. 9 The **a** Fourier spectra and **b** one-third octave bands of accelerations at Point A when the train passes through turnouts and the main line

(a)

(b)
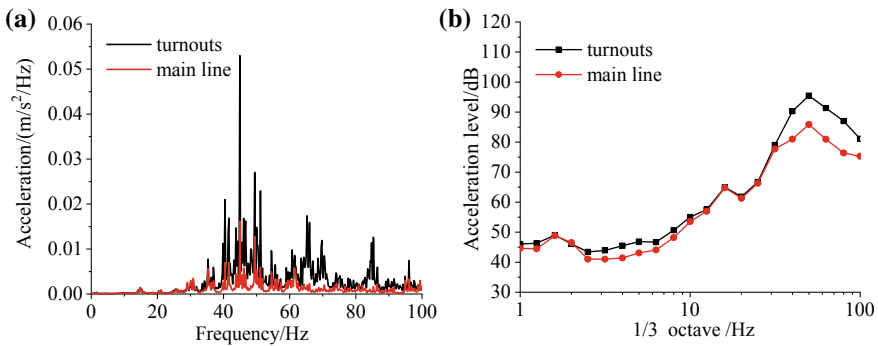
Fig. 10 The **a** Fourier spectra and **b** one-third octave bands of accelerations at Point B when the train passes through turnouts and the main line

Figures 9 and 10 show the Fourier spectra and one-third octave bands of acceleration at Point A and B. These results indicate that when the wheels pass through the turnout areas, the vibration energy increases, especially in the frequency range between 30 and 100 Hz.

Figure 11 compares the acceleration level at the plates and pillars of the two station layers. The acceleration response of the subway station is transmitted from Point A to B. The acceleration level is seen to attenuate over entire frequency bands, especially between 1–10 Hz and 50–100 Hz with a maximum attenuation value of 10 dB. As shown, the acceleration levels of Points C and D are different from those of Points A and B. A decrease of 8 dB from Point C to D can be observed between 50 and 100 Hz, but an amplification of acceleration also occurs between 2 and 15 Hz.
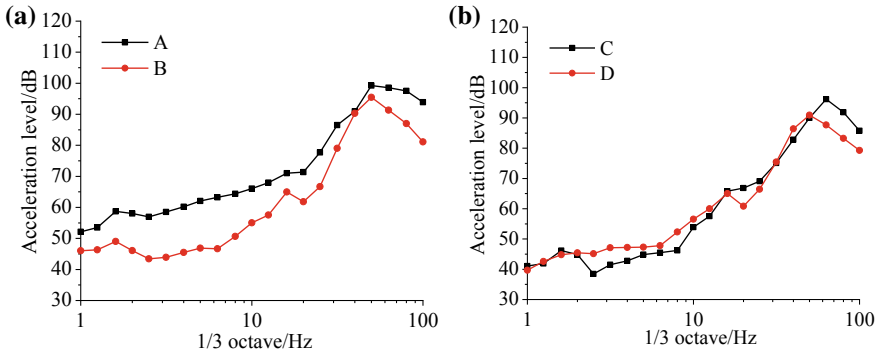
Fig. 11 Comparison of the acceleration level attenuation at **a** the plates and **b** the pillars
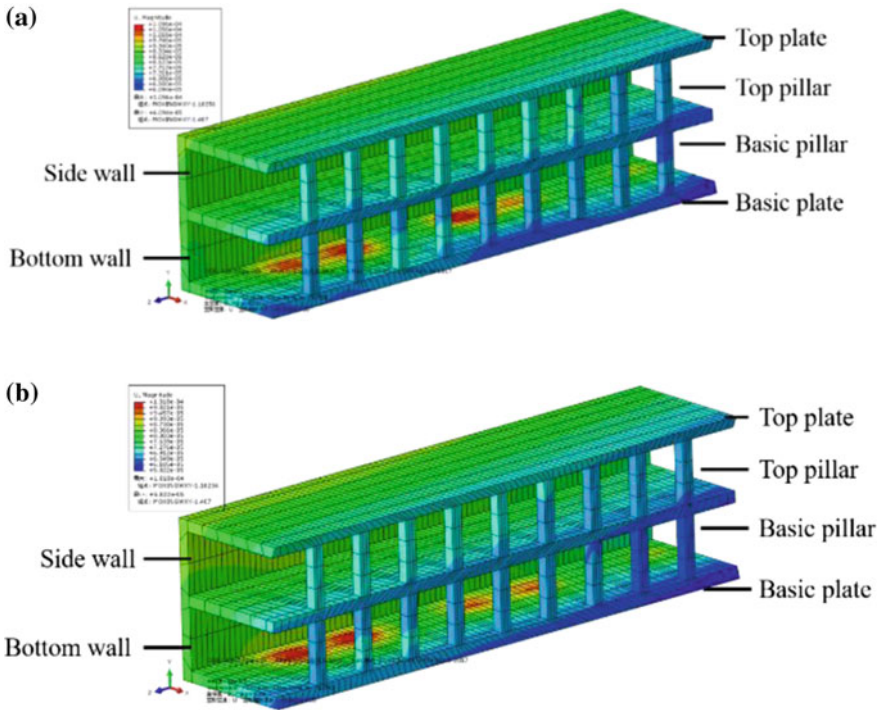
Fig. 12 The displacement contour of the station when the train **a** passes through the turnout and **b** the main line

Figure 12 compares the displacement contour of the two cases, indicating that the vertical displacement of the sidewall of the station is larger than that of the pillar, and the displacement of the top pillar is greater than that of the basic pillar.

4   Conclusions

In this paper, the dynamic responses of a subway station were calculated and compared using numerical simulation for both the turnout areas and the main line. The following conclusions can be drawn:

(1) The train passing through the turnouts generates a larger vibrational response above 20 Hz, especially in the frequency range of 40–60 Hz.
(2) When the train passes through the turnout structure, it generates greater vibrational energy in each part of the station, particularly in the frequency bands of 3–10 Hz and 30–100 Hz. However, the differences are not significant between 10 and 30 Hz.
(3) The vertical displacement of the top pillar and the sidewall of the top layer is greater than that of the basic pillar and the bottom wall, and the vertical displacement of the sidewall is larger than that of the pillar.

References

1. Aiello V (2008) Experimental and numerical analysis of vibrations induced by underground trains in an urban environment. Struct Control Health Monit 15(3):315–348
2. Gupta S, Degrande G, Lombaert G (2009) Experimental validation of a numerical model for subway induced vibrations. J Sound Vib 321(3–5):786–812
3. Hill C, Reardon R, Joing S (2015) Test and numerical analysis of subway-induced vibrations of metro-line nearby buildings. J South China Univ Technol 43(2):33–40
4. Kassa E, Nielsen J (2008) Dynamic interaction between train and railway turnout: full-scale field test and validation of simulation models. Veh Syst Dyn 46(sup1):521–534
5. Lakusic S, Bogut M, Lakusic VT (2008) Noise and vibrations at tram track intersection. J Acoust Soc Am 123(5):3259
6. Vogiatzis K, Kouroussis G (2015) Prediction and efficient control of vibration mitigation using floating slabs: practical application at Athens metro lines 2 and 3. Int J Rail Transp 3(4): 215–232
7. Chen R, Wang P, Yang RS (2009) Dynamic analysis and experimental research on jointless turnout on bridge of high-speed railway. In: Peng QY, Kelvin CP (eds) International conference on transportation engineering. ASCE press, Chengdu, pp 675–680
8. Bruni S, Anastasopoulos I, Alfi S (2009) Train-induced vibrations on urban metro and tram turnouts. J Transp Eng 135(7):397–405
9. Markine VL, Steenbergen M, Shevtsov I (2011) Combatting RCF on switch points by tuning elastic track properties 271(1–2):158–167
10. Kaewunruen S (2014) Monitoring structural deterioration of railway turnout systems via dynamic wheel/rail interaction. Case Stud Nondestr Test Eval 1(1):19–24
11. Grassie SL (1984) Dynamic modelling of railway track and wheelsets. In: Mathematical models

12. Meng Ma (2012) Study on the prediction of metro train-induced vibration based on sensitivity of environmental influence and design stage-accompanied evaluation system. Beijing Jiaotong University, Beijing
13. Wan C, Markine VL, Shevtsov IY (2014) Analysis of train/turnout vertical interaction using a fast-numerical model and validation of that model. Proc Inst Mech Eng, Part F: J Rail Rapid Transit 228(7):730–743

Comparative Experimental Study on Vibration Isolation Effect of Combined Track Bed in Metro Tunnel

Zhou Zheng, Yong-fang Wu, Jin-hui Liu, Peng-hui Liu, Yi-gan Wang and Da-xin Sun

Abstract Subway line using damping fasteners, steel spring floating slab track bed, rubber vibration reduction track bed, combined track bed (damping fastener combination rubber vibration reduction track bed) and other forms of vibration isolation structure, in which combined track bed is a double-layer vibration isolation system, the rest are all single-layer vibration isolation systems. Based on the principle of vibration reduction of a double-layer vibration isolation system and the vibration test data of subway line, the vibration characteristics of double-layer vibration isolation system are analyzed and compared with the vibration isolation effect of the single-layer vibration isolation system.

Keywords Vibration reduction effect · Double-layer vibration isolation system · Combined track bed

1 Introduction

With the rapid development of urban rail transit, the environmental vibration problems caused by metro operations have received increasing attention [1]. In order to reduce the impact of rail transit vibration on the surrounding environment and residents' lives and work, currently based on the theory of vibration isolation, the main methods for vibration reduction of the track include damping fasteners, vibration-damping sleepers, point-supporting and wire-supporting rubber floating

Z. Zheng (✉) · P. Liu · Y. Wang
Railway Engineering Research Institute, China Academy of Railway Science,
100081 Beijing, China
e-mail: Zhouzheng09@qq.com

Y. Wu · J. Liu
Shenzhen Metro Group Co., Ltd., 518000 Shenzhen, China

D. Sun
Beijing Urban Construction Design and Development Group Co., Ltd.,
100037 Beijing, China

slabs, polyurethane floating slab, steel spring floating slabs, the ballast cushion, the float type ballast trough, and so on [2], which are all monolayer vibration isolation system.

The combined track-bed system comprehensively uses the principle of vibration isolation and combines various vibration reduction measures together by adjusting the distribution of stiffness and mass ratio between different coupling subsystems, and the best isolation and attenuation effect of vibration energy in the transmission path can be achieved. Some new types of vibration-reducing track structures such as damping fasteners assembly overall supporting rubber floating slabs and damping fastener combination ballast cushion have emerged.

Many scholars have studied the vibration reduction measures of urban rail transit. Liu et al. [3] combined with the measured data in tunnels studied the vibration reduction effects of four types of vibration reduction rails such as steel spring floating slabs, orbital dampers, and trapezoidal sleepers on line 4 of Beijing Subway. Xie et al. [4] summarized and analyzed the effectiveness of vibration reduction measures adopted for multiple rail transit lines in Beijing, Shanghai, and Guangzhou and graded them. Hao et al. [5] compared the vibration reduction effect of common vibration reduction measures such as floating slabs, elastic support blocks, and elastic fasteners. Wang et al. [6] studied the dynamic characteristics and vibration reduction effect of the trapezoidal system. The theoretical design and experimental study of the orbital structure of various combinations of vibration reduction measures in China are still in the preliminary stage. The relevant research literature is rarely seen.

In this paper, a field test was conducted on the vibration of a rubber damper cushion bed combination vibration-damping fasteners (integral support rubber floating slab), and the vibration of a new type of vibration-damping fastener rubber cushion bed (referred to as a combined track bed) system was discussed.

2   Vibration Isolation Principle

The working principle of the rail traffic isolation system is to insert suitable elastic devices between the upper building and the foundation of the track to weaken or eliminate the vibration of the incoming foundation, thereby weakening the impact of vibration on the environment.

2.1   Single-Layer Vibration Isolation Principle

Vibration can be transmitted from the equipment to the foundation and can also be transmitted from the foundation to the equipment. The study of vibration isolation is based on the assumption that the quality of the foundation is much greater than the quality of the equipment.

Vibration transmission between the isolation equipment and the foundation generally uses an elastic stand to form a single-degree-of-freedom mass–spring system. Set the stiffness of the isolator to K, the lumped mass (equipment) above the isolator to m, the amplitude of the vibration force at m set to F_0. The amplitude of the vibration force transmitted to the foundation is F, and the frequency of the force is f_0. If the damping force is not counted, the transmission rate T is

$$T = \left| \frac{F}{F_0} \right| = \frac{1}{\left| 1 - \left(\frac{f}{f_0} \right) \right|} \tag{1}$$

T is a dimensionless quantity. Where f_0 (undamped natural frequency) is

$$f_0 = \frac{1}{2\pi} \sqrt{\frac{K}{m}} \approx \frac{1}{2\sqrt{d}} \tag{2}$$

d is the static sinking amount (compression) of the system in meters. The basic vibration speed is V_0, the vibration speed transmitted to the equipment is V, and the ratio V/V_0 is also equal to T.

If the viscous damping coefficient of the isolator is C, the transmission rate of the damped system is

$$T = \left\{ \frac{1 + (2\zeta \frac{f}{f_0})^2}{[1 - \left(\frac{f}{f_0} \right)^2]^2 + \left(2\zeta \frac{f}{f_0} \right)} \right\}^{\frac{1}{2}} \tag{3}$$

In this formula $\zeta = C/C_c$, $C_c = 4\pi f_0 m$ of critical damping. For a simple vibration isolation system, the relationship between the transmission ratio T and the frequency ratio f/f_0 at different damping ratios ζ is shown in Fig. 1.

It can be seen from Fig. 1 that only when the frequency ratio $\lambda > \sqrt{2}$, there is a vibration isolation effect, and with the increase of λ, the vibration isolation effect also gradually increases. In practice, it takes $\lambda = 2.5$–5; the amplitude of the machine passing through the resonance zone during starting and stopping can be reduced. However, when $\lambda > \sqrt{2}$, the increase of damping will reduce the effect of vibration isolation. Because the damping coefficient of the commonly used vibration isolation equipment is not large, when the vibration isolation coefficient is calculated within the range of $\lambda = 2.5$–5, it can be considered without damping.

Fig. 1 Single-layer vibration
isolator vibration transmission
rate curve
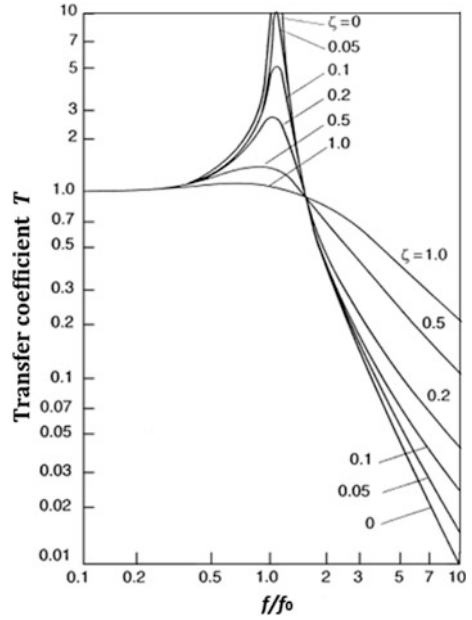
2.2 Double-Layer Vibration Isolator Vibration Isolation Principle

Assuming that m_1 is the object to be isolated, a double-layer vibration isolation system inserts an elastically supported intermediate mass between the isolated object and the foundation, as shown in Fig. 2 for the K_1–m_2–K_2 system. For the double-layer vibration isolation system shown in Fig. 2, the formula of its natural frequency is [7]

Fig. 2 Double-layer
vibration isolation system
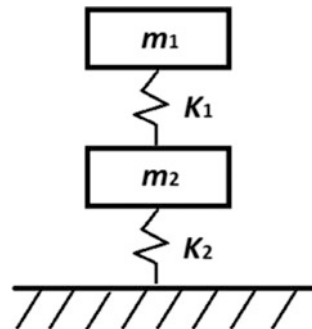
$$\omega_c^4 - \left[\frac{K_1}{m_1} + \frac{K_2}{m_2} + \frac{K_1}{m_2}\right]\omega_c^2 + \frac{K_1}{m_1} \cdot \frac{K_2}{m_2} = 0 \tag{4}$$

$$\omega_1^2 = \frac{K_1}{m_1}, \ \omega_2^2 = \frac{K_2}{m_2} \tag{5}$$

In this formula: m_1 is the mass of the object to be isolated, m_2 is the intermediate mass, K_1 and K_2 are the stiffness of the two elastic supports, and ω_c is the natural frequency of the double-layer vibration isolation system. The following formula (4) and (5) can be used to obtain ω_c:

$$\omega_c^2 = \frac{1}{2}\omega_1^2\left[\left(1 + \frac{m_1}{m_2} + \frac{\omega_2^2}{\omega_1^2}\right) \pm \sqrt{\left(1 + \frac{m_1}{m_2} + \frac{\omega_2^2}{\omega_1^2}\right)^2 - 4\frac{\omega_2^2}{\omega_1^2}}\right] \tag{6}$$

From Formula (6), it can be seen that the insertion of the intermediate mass results in two resonance frequencies in the double-layer vibration isolation system. In addition, due to the influence of the inertial force interacting with the vibration of the elastic elements K_1, K_2, unlike a single-layer vibration-damping system, the transfer function of the vibration isolator in the high-frequency range exhibits different characteristics. And in the high-frequency range has a more ideal vibration reduction effect.

Figure 3 shows the damping ratio curve of a double-layer vibration isolation system. In this figure, $\beta = \frac{m_2}{m_1}$, it can be seen that the transfer function of a two-layer

Fig. 3 Vibration reduction ratio curve of double-layer vibration isolator
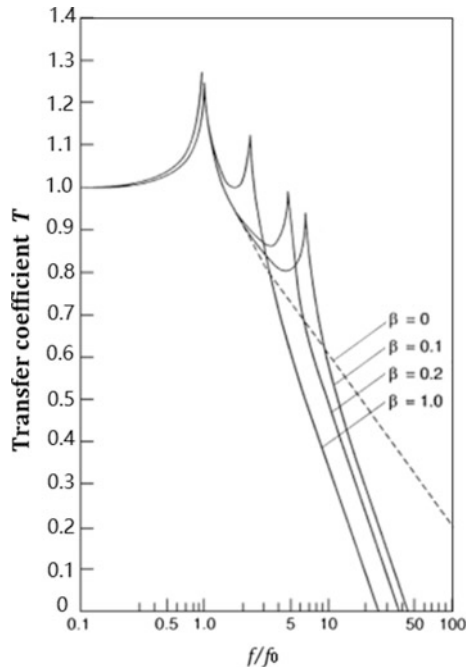
vibration isolation system is mainly related to β, and the larger the β, the closer the two resonance frequencies are, which means the closer the intermediate mass to the mass of the object to be isolated, the closer the two resonance peaks are. When β is 0, it is the transfer function of the single-layer vibration isolation system. It can be seen that the damping ratio of the double-layer vibration isolation system is better than the single-layer vibration isolation system obviously in the high-frequency region.

3 Test Overview

The five-track structures tested were laid in a single-hole single-track circular tunnel. The track slope, rail type, tunnel structure, and driving speed of different track structure test sites are shown in Table 1. The test train is an empty type B four-axle vehicle with a fixed wheelbase of 2.3 m, a fixed distance of 12.6 m, and six vehicles. The test is carried out during trial operation, and the operation condition of the five-track structures is the same.

In order to reduce the impact of complex environmental factors along the track on the evaluation of vibration reduction effect, vibration measurement comparisons are usually made in tunnels with a height of 1.25–1.9 m above the surface of the

Table 1 Comparison of different track structures

Category	Damping fastener	Steel spring floating slab track bed	Rubber vibration reduction bed	Combined track bed	Ordinary monolithic bed
Line gradient (‰)	Downhill 8.5	Downhill 27.7	Uphill 27.9	Uphill 25.4	Uphill 25.4
Tunnel section form	Single hole Single line Round shield	Single hole Single line Round shield	Single hole Single line Round shield	Single hole Single line Round shield	Single hole Single line Round shield
Rail type (kg/m)	60	60	60	60	60
Fastener type	Damping fastener	DTVI2	DTVI2	Damping fastener	DTVI2
Seam/ seamless line	Seamless	Seamless	Seamless	Seamless	Seamless
Train speed (km/h)	59.0	63.5	52.7	53.9	65.4

Table 2 Technical indicators of accelerometer

Test position	Rails/floating slabs/track beds	Tunnel wall
Sensor type	LC0104	LC0130
Sensitivity coefficient	800 mv/g	40,000 mv/g
Resolution	2×10^{-4} g	5×10^{-7} g

Fig. 4 Arrangement of measuring points
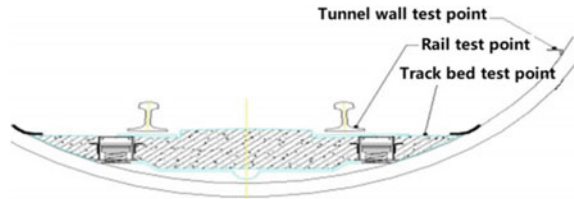
tunnel and general monolithic track beds to objectively evaluate measures for vibration reduction effect.

The tunnel depth, geological conditions, and line conditions are similar. The train passes two measuring points with the same height and different mileage on the tunnel wall. One of the measuring points corresponds to the common track structure, and the other track uses vibration reduction measures. The difference between the vertical vibration acceleration levels at the two measuring points is the effect obtained by the orbital vibration damping and noise reduction at this location.

The test adopts 16-bit precision INV306 intelligent signal acquisition and processing analyzer. It adopts built-in IC piezoelectric acceleration sensor, featuring low impedance output, anti-interference, and low noise. The main technical indicators are shown in Table 2. Auto-trigger sampling, the sampling frequency is 2560 Hz and the time interval is 0.39 ms.

The test includes the vertical acceleration of rails, track beds, vertical acceleration, vertical plumbing on the tunnel walls, lateral acceleration, and train passing speed. The measuring point arrangement is shown in Fig. 4.

4 Evaluation Criteria and Data Processing Methods

At present, there is no corresponding standard specification for the evaluation of the vibration reduction effect of the track structure. For now, when assessing urban environmental vibration (the human body is affected by vibration in a building), according to GB10071-1988 and JGJ/T 170-2009 for measurement and evaluation, the value of Z-level insertion loss in the frequency range of 1–80 Hz is used as the evaluation amount of vibration reduction measures. Insertion loss is defined as

$$L_1 = 20 \lg \frac{a_{2R}}{a_2} \qquad (7)$$

In the formula, a_{2R} is the effective value of vibration acceleration at the measuring point when there is no vibration isolation device; a_2 is the effective value of vibration acceleration corresponding to the measuring point when there is vibration isolation device. When $L_1 \geq 0$, the vibration isolation system works; when $L_1 \leq 0$, the vibration isolation system has no attenuation effect.

Formula (1) is transformed to introduce the reference acceleration $a_0 = 10^{-6} \text{m/s}^2$ to:

$$
\begin{aligned}
L_1 &= 20 \lg \frac{a_{2R}}{a_2} = 20 \lg \left(\frac{a_{2R}}{a_0} \frac{a_0}{a_2} \right) \\
&= 20 \lg \frac{a_{2R}}{a_0} - 20 \lg \frac{a_2}{a_0} \\
L_1 &= VL_{2R} - VL_2
\end{aligned} \qquad (8)
$$

5 Test Results and Analysis

5.1 Analysis of Vibration Characteristics of the Combined Track Bed

The vibration acceleration levels of rails, track beds, and tunnel walls with different track structures are shown in Table 3. It can be seen that, compared with the rubber damping pad track beds, the combined track bed structure reduces the stiffness of the fasteners and reduces the track-bed vibration response.

As shown in Fig. 5, under the same trainload excitation, for most of the frequency range, the vibration acceleration of the rubber damping pad is the largest, the combined track bed is the second, the ordinary monolithic bed is again, and the damping fastener is the smallest.

Table 3 Vibration acceleration level of different track structures (dB)

Position	Frequency range	Damping fastener	Rubber vibration reduction bed	Combined track bed	Ordinary monolithic bed
Rail vertical	1–500 Hz	141.9	143.3	142.4	145.2
Track bed vertical	1–500 Hz	96.5	127.5	121.8	109.0
Tunnel wall vertical	1–80 Hz	79.3	74.6	69.1	88.5
	1–200 Hz	83.7	75.0	70.6	90.6
	1–500 Hz	89.1	75.2	71.1	96.7

Note The calculation of the effective acceleration value is the train passing period
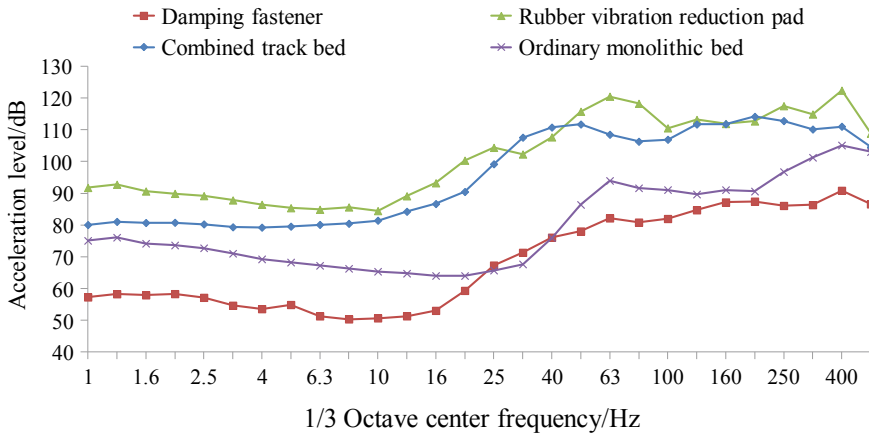
Fig. 5 1/3 octave band of vibration acceleration of track bed

Table 4 Vibration reduction results of different track structures tunnel wall (dB)

Vibration reduction effect	Damping fastener	Rubber vibration reduction bed	Combined track bed
ΔVL_{zmax}	8.4	12.5	16.7
1–80 Hz	9.2	13.9	19.4
1–200 Hz	6.9	15.6	20.0
1–500 Hz	7.6	21.5	25.6

Table 4 shows the vibration reduction effect of tunnel walls with different track structures. It can be seen that the vibration reduction effect of the damping fasteners is the smallest, the rubber damping pads are centered, and the combined track beds are the best. Compared with the common monolithic track bed, the ΔVL_{zmax} of the damping fastener, the rubber vibration-damping track bed, and the combined track bed at the tunnel wall is 8.4, 12.5, and 16.7 dB. In the frequency range of 1–80 Hz, compared with the unweighted vibration acceleration levels, the vibration reduction effect of damping fasteners, rubber cushion beds, and combined track beds is 9.2, 13.9, and 19.4 dB.

The combined track bed and rubber cushion track-bed system both have a natural frequency of about 16 Hz. According to the vibration isolation principle, when the frequency ratio $\lambda > \sqrt{2}$, that is, in the range greater than 25 Hz, there is a significant vibration reduction effect, with the increase of λ, the vibration isolation effect shows a frequency-dependent increase, and the effect of vibration reduction is 10–35 dB. The natural frequency of the damping fastener system is about 31.5 Hz, in the range of more than 40 Hz, the vibration reduction effect is obvious, and the vibration reduction effect is 5–12 dB.
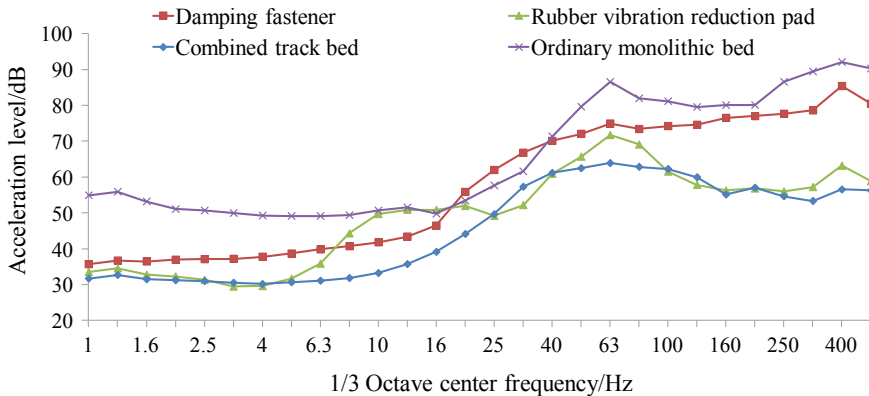
Fig. 6 1/3 octave band of vibration acceleration of tunnel wall
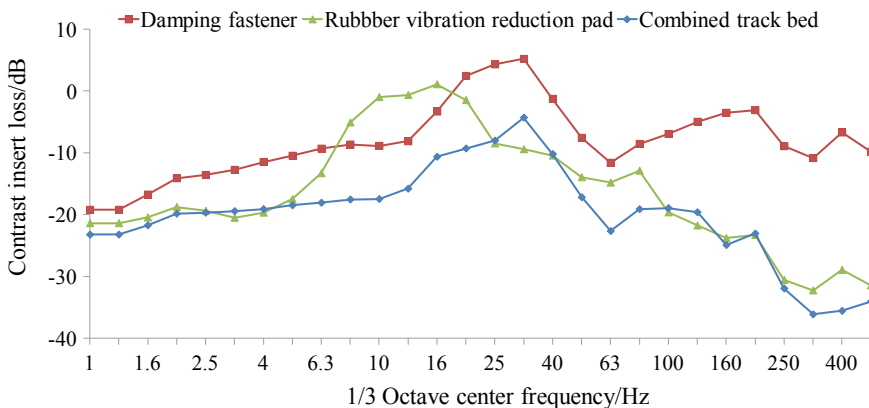
Fig. 7 1/3 octave band of vibration acceleration contrast loss of tunnel wall

The data analysis results show that the vibration reduction effect of the combined track bed is better than the single damping structure that constitutes the combined track bed, but the combined track bed cannot achieve the vibration reduction effect of any frequency within the whole frequency band better than that of the single vibration-damping structure constituting the combined track bed, as shown in Figs. 6 and 7. As can be seen from Fig. 8, the vibration reduction effect of the combined track bed is not a linear superposition of the single vibration-damping structure constituting the combined track bed but is closer to the square root superimposed value of the vibration-damping structure constituting the combined track bed.
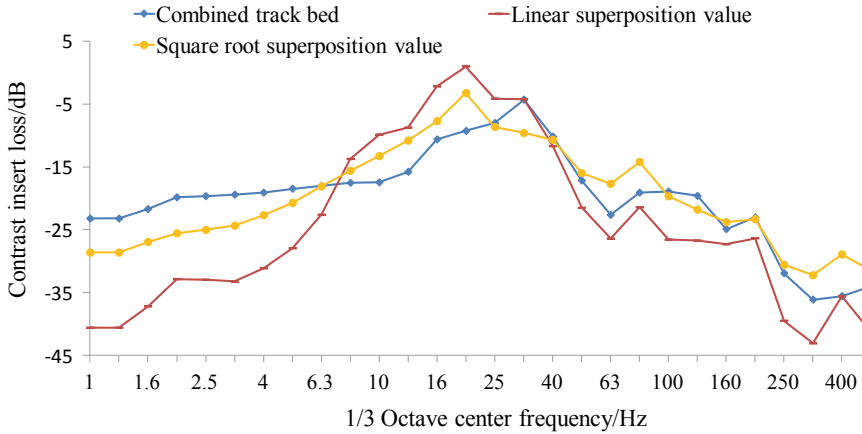
Fig. 8 Contrast loss of vibration acceleration between two-stage isolator and one-stage isolator at the tunnel wall

The combined track bed does not reflect the second-order natural frequency peak shown in Fig. 3. This may be due to the fact that each damping structure has a certain degree of damping and the difference in the geological structure of tunnels under various working conditions, etc. The reason remains to be further analyzed.

5.2 Contrast of Vibration Reduction Effect Between Steel Spring Floating Slab and Combined Track Bed

The steel spring floating slab is a kind of vibration reduction measure for the subway and has significant damping performance. This section will compare the vibration reduction effect of the combined track bed and steel spring floating slab.

It can be seen from Table 5 and Figs. 9, 10 that the ΔVL_{zmax} of the steel spring floating slab and the combined track bed at the tunnel wall is 24.3 and 16.8 dB compared with the common monolithic track bed. Comparing with the unshakable vibration acceleration level of the tunnel wall of an ordinary monolithic track bed,

Table 5 Vibration reduction results of steel spring floating slab and combined track bed tunnel wall (dB)

Vibration reduction effect	Steel spring floating slab	Combined track bed
ΔVL_{zmax}	24.3	16.8
1–80 Hz	16.6	19.4
1–200 Hz	17.6	20.0
1–500 Hz	21.8	25.6
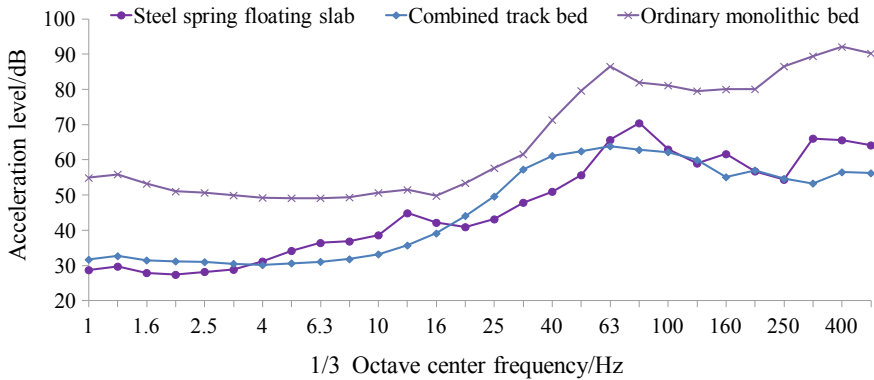
Fig. 9 1/3 octave band of vibration acceleration of steel spring floating slab and combined track bed tunnel wall
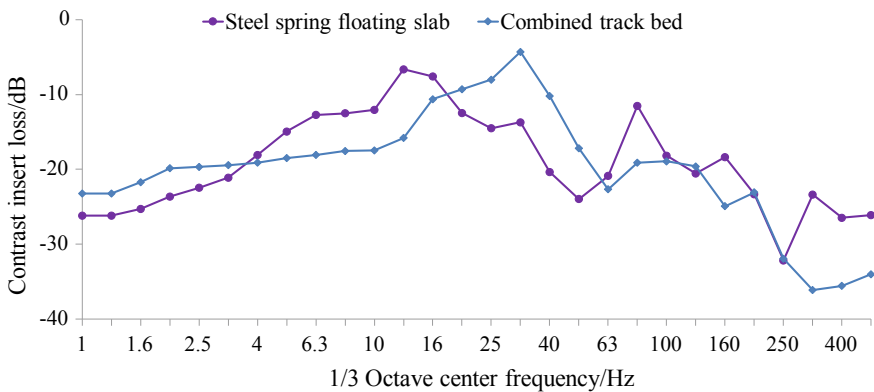
Fig. 10 Insert loss of vibration acceleration between steel spring floating slab and combined track bed at the tunnel wall

the vibration reduction effect of the steel spring floating slab and the combined track bed is 16.6 and 19.4 dB in the frequency range of 1–80 Hz. Similarly, there is their own dominant frequency range, in the high-frequency area, and the combined track-bed vibration reduction effect is better than the steel spring floating slab.

The unweighted vibration reduction effect of the combined track bed in each cut-off frequency range is better than that of the steel spring floating board, but the frequency vibration reduction effect of the steel spring floating board sensitive to the human body's vertical vibration is more ideal and its VL_{zmax} reduction. The vibration effect is better than the new combined track bed, which is also the reason why its ΔVL_{zmax} is better than its own 1–80 Hz unweighted vibration reduction effect.

Moreover, for the steel spring floating slab, its unweighted vibration reduction effect also increases with the increase of the cut-off frequency.

6 Conclusion

The vibration reduction effect of multiple damping structures is not a linear superposition relationship, and the vibration characteristics of the vibration-damping system will also change after the combination, but its vibration reduction effect cannot be better than any of the vibration reduction structures in the whole frequency range.

The vibration reduction effect of the combined track bed on the low frequency is obviously less than the linear superposition value of the two single damping structures, and the vibration reduction effect on the high frequency is similar to the linear superposition value of the two single damping structures. Compared with the linear superposition value, the vibration reduction effect of the combined track bed is more similar to the square root superposition of the two single damping structures.

There is a great relationship between vibration reduction effect and frequency. In addition to vibration reduction fasteners, vibration reduction effects of vibration reduction structures increase with frequency.

For the VL_{zmax} vibration reduction effect, the vibration reduction effect of the steel spring floating slab is the best; in terms of the effect of the frequency without weighing the vibration reduction effect, the vibration reduction effect of the combined track bed is the best.

Each vibration-reducing structure has its own advantage damping frequency range. In practical applications, the vibration-reducing structure should be reasonably selected considering the construction environment, project cost, and vibration frequency range requirements.

References

1. Xia H, Cao Y-m (2004) Problem of railway traffic induced vibrations of environments. J Railway Sci Eng 1(1):1–8
2. Zhang Y-p, Yang Y-q, Ke Z-t et al (2000) Urban rail transit vibration and noise control. Chin Railways 3(20):43–45
3. Liu P-h, Yang Y-q, Yin J (2014) Test and analysis on vibration of different track structures in tunnel. J Vibr Shock 2(33):4–8
4. Xie Y-m, Gu X-a, Liu Y (2011) Study on the effect of vibration reduction measures in urban rail transit. In: Discussion on proposals of environmental impact assessment technology seminar in rail transit industry, china environmental science society, pp 223–261

5. Hao J, Geng C-z, Zhu J-y (2008) Test and analysis of vibration reduction effect of different track structures. China Metros 11(4):68–71
6. Wang W-b, Liu W-n, Ma M et al (2010) Experimental study on the dynamic characteristics and the vibration mitigation effect of ladder track system. China Railway Sci 31(2):24–28
7. Eugene IR (2003) Passive vibration isolation. American Society of Mechanical Engineers, New York

Analyses of Metro Train-Induced Vibration of Building Above Subway Tunnel

Jianjin Yang, Wanming Zhai, Shengyang Zhu and Yu Guo

Abstract To more accurately predict the structural vibration of the building above the subway tunnel due to the train moving on the floating-slab track (FST), a prediction model is established in this paper. The model is developed based on the vehicle-track coupled dynamics and is comprised of two subsystems. The first subsystem is the spatial train-FST coupled dynamic subsystem and the second subsystem is the FST-tunnel-soil-building coupled dynamic subsystem. The relationship between the two subsystems is the dynamic reaction forces supporting the rails. In the first subsystem, the train is marshalled by several vehicles and each vehicle is simplified as multi-rigid-body system with 35 DOFs. In the second subsystem, the subway tunnel, the building above the tunnel and the soil around the tunnel are modelled using finite elements, and the 3D consistent viscous-spring artificial boundaries are applied to mitigate the impact of artificial boundaries on the calculation results.

1 Introduction

In China, there are many cities in the plan and construction of urban rail transit, and the scale of construction is the biggest in the world [1]. In order to provide a more convenient, more highly effective and faster mean of transportation, the subway is getting closer and closer to the building where people live and even the subway and the building are built together. Unfortunately, this will aggravate the vibration of the building induced by the running train, which has quite adverse influences on the structural safety of the buildings, the operating of precision instruments and the life quality of residents in the building. This paper focuses on the structural vibration of

J. Yang (✉) · W. Zhai · S. Zhu · Y. Guo
State Key Laboratory of Traction Power, Southwest Jiaotong University, Chengdu, China
e-mail: jjyang007@hotmail.com

a hotel induced by the running train. The hotel is built above the subway tunnel and their structures are built together and the tunnel is built for two roads and two metro lines of FST, illustrated in Fig. 1.

The prediction of the building vibration induced by the moving train belongs to the environmental vibration induced by railway transportation, which is a comprehensive multi-disciplined engineering problem involving the multi-body dynamics, the structural dynamics, the soil dynamics and the train-track coupled dynamic interaction. There are many methods to predict the environmental vibration induced by railway transportation, such as the two-dimensional (2D) methodology [2, 3], two-and-half-dimensional (2.5D) methodology [4–8], pipe-in-pipe (PiP) method [9] and the formulation of periodic structure [10]. These methods, which are based on some hypotheses and simplifications, have high computational speed but low applicability to the problems involving complicated geometries and structures. Besides, these methods adopt the linear wheel/rail interaction, so they cannot veritably reflect the influence of train on the ground vibration; however, the train plays an important role in the moving train-induced environment vibration [11]. To more accurately predict the structural vibration of the hotel with complicated geometry and structure, a model consisting of the spatial train-FST coupled dynamic subsystem and the FST–tunnel–soil–building coupled dynamic subsystem is developed based on the vehicle–track coupled dynamics [12–15].

In the first subsystem, the spatial train–FST coupled dynamics model is used to calculate the dynamic reaction forces supporting the rails (abbreviated as fastener forces). In the spatial train–FST dynamic interaction model, the dynamic wheel/rail interaction model [16] is adopted and the geometric irregularities of wheels and rails are taken as the excitation. In this subsystem, the influence of the deformations of the track base is ignored. In fact, the influence of the deformations of the track base on the fastener forces is quite small.
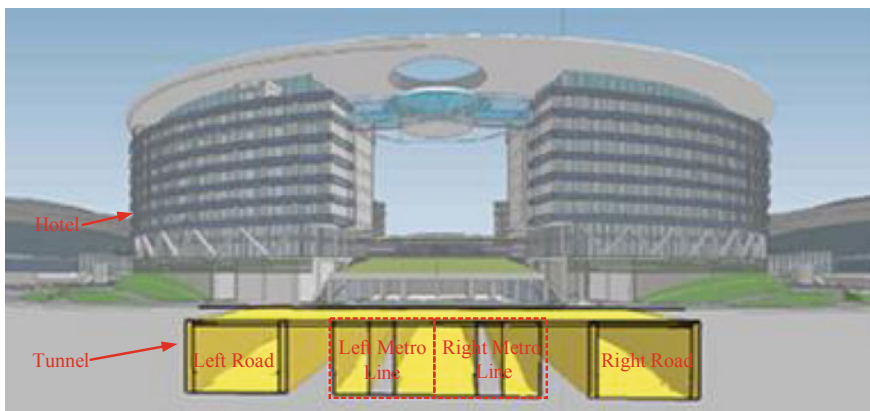
Fig. 1 Position relation between the hotel and the tunnel

In the second subsystem, the FST, the tunnel, the soil and the building are elaborately modelled using the finite element (FE) method, and are coupled through the deformation compatibility conditions at the interfaces to form a FE dynamics model of track–tunnel–soil–building system. In this subsystem, the complicated geometry of the building and the layering of the soil are fully considered in the FE model.

It can be found that these two subsystems are correlated by the fastener forces. This correlation method has also been used in our previous works [17, 18] and Kouroussis' work [19].

2 Prediction Model

2.1 *Spatial Train–FST Coupled Dynamics Subsystem*

A metro train is marshalled by a series of vehicles with the similar main components, one car body, two bogie frames, four wheelsets and two stages of suspensions. When a metro train moves on the FST, it will induce the vibration of the track which can be in reverse influence the dynamic behaviors of the vehicle. Obviously, the vehicle and the FST are essentially coupled with each other. Based on the theory of vehicle–track coupled dynamics [12–15], the spatial train–FST coupled dynamics model is established, as illustrated in Fig. 2.

As the basic unit of the metro train, the vehicle is modelled as a four-axle mass-spring-damper system of 35 degrees of freedom (DOFs), listed in Table 1. By using the system of coordinates moving along the track with vehicle speed, the equations of motion of the vehicle subsystem can be easily derived according to the D'Alembert's principle, which can be described in the form of second-order differential equations in the time domain:

$$\mathbf{M}_V \mathbf{A}_V + \mathbf{C}_V(\mathbf{V}_V)\mathbf{V}_V + \mathbf{K}_V(\mathbf{X}_V)\mathbf{X}_V = \mathbf{F}_V(\mathbf{X}_V, \mathbf{V}_V, \mathbf{X}_T, \mathbf{V}_T) + \mathbf{F}_{EXT} \qquad (1)$$

where $\mathbf{X}_V$, $\mathbf{V}_V$ and $\mathbf{A}_V$ are the vectors of displacements, velocities and accelerations of the vehicle subsystem, respectively; $\mathbf{M}_V$ is the mass matrix of the vehicle which is a 35×35 diagonal matrix; $\mathbf{C}_V(\mathbf{V}_V)$ and $\mathbf{K}_V(\mathbf{X}_V)$ are the damping and the stiffness matrices to describe the nonlinearities within the suspensions at the current state of the vehicle subsystem; $\mathbf{X}_T$ and $\mathbf{V}_T$ are the vectors of displacements and velocities of the track subsystem; $\mathbf{F}_V(\mathbf{X}_V, \mathbf{V}_V, \mathbf{X}_T, \mathbf{V}_T)$ is the load vector representing the nonlinear wheel/rail contact forces determined by the dynamic wheel/rail coupled model, which depend on the motions $\mathbf{X}_V$ and $\mathbf{V}_V$ of the vehicle and $\mathbf{X}_T$ and $\mathbf{V}_T$ of the track; and $\mathbf{F}_{EXT}$ describes the external forces including gravitational forces and forces resulting from the centripetal acceleration when the vehicle is running through a curve. The details of the vehicle subsystem dynamic model refer to [12–15].

For the vertical, lateral and torsional vibration, the rail can be simplified as a simply supported beam due to its large ratio of length to cross section.
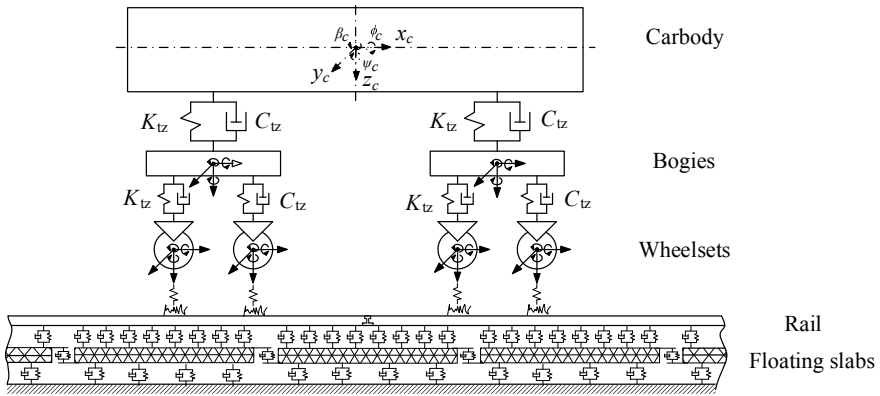
(a) side elevation
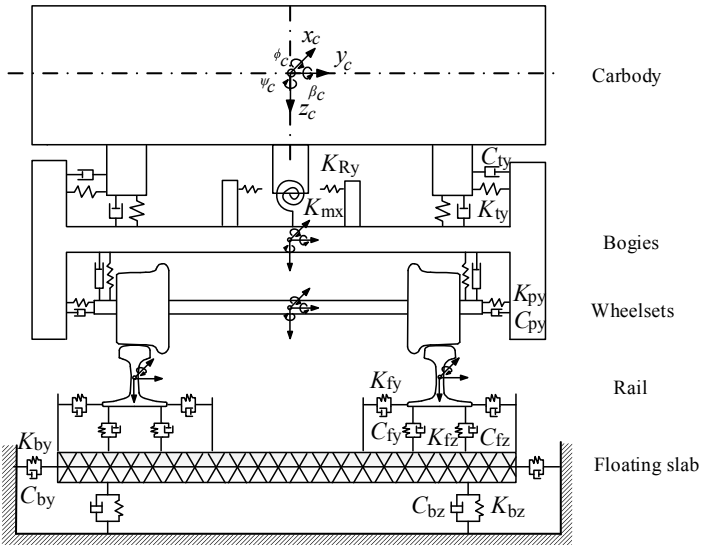
(b) end view

Fig. 2 Spatial vehicle–FST coupled dynamic model

The equations of motion of the rail are given in the form of the fourth-order partial differential equations.

Described by a thin plate supported by slab bearings on rigid foundation, the vertical displacements of the kth floating slab can be written in form of the fourth-order partial differential equations in the time domain. For both the lateral vibration and the rotation in the horizontal plane, the floating slab can be treated as rigid body.

Both the fasteners and slab bearings are modelled as ordinary Kelvin elements. The elastic restoring forces of the fastener are proportional to the relative

Table 1 DOFs of a vehicle

Vehicle component	Lateral motion	Vertical motion	Roll motion	Yaw motion	Pitch motion
Car body	y_c	z_c	ϕ_c	ψ_c	β_c
Bogie frame 1	y_{t1}	z_{t1}	ϕ_{t1}	ψ_{t1}	β_{t1}
Bogie frame 2	y_{t2}	z_{t2}	ϕ_{t2}	ψ_{t2}	β_{t2}
Wheelset 1	y_{w1}	z_{w1}	ϕ_{w1}	ψ_{w1}	β_{w1}
Wheelset 2	y_{w2}	z_{w2}	ϕ_{w2}	ψ_{w2}	β_{w2}
Wheelset 3	y_{w3}	z_{w3}	ϕ_{w3}	ψ_{w3}	β_{w3}
Wheelset 4	y_{w4}	z_{w4}	ϕ_{w4}	ψ_{w4}	β_{w4}

displacements and relative velocities between the rail and the floating slab at the ends of the fastener, and the supporting forces of the slab bearing are proportional to the displacements and velocities of the floating slab at the position of the slab bearing.

As described above, the equations of motion of the FST involve second- and fourth-order partial differential equations. To facilitate solution procedure, all partial differential equations are transformed into a series of second-order ordinary differential equations by means of Ritz's method, and then the time-stepping integration method is adopted. The transformation results could be found in references [12–15]. The final equations of the FST could also be assembled into the standard matrix form, similar to Eq. (1), as

$$\mathbf{M_T A_T} + \mathbf{C_T V_T} + \mathbf{K_T X_T} = \mathbf{F_T}(\mathbf{X_V}, \mathbf{V_V}, \mathbf{X_T}, \mathbf{V_T}) \tag{2}$$

where $\mathbf{M_T}$, $\mathbf{C_T}$ and $\mathbf{K_T}$ are the mass, damping and the stiffness matrix of the track, respectively, and $\mathbf{F_T}$ is the load vector of the track model representing the wheel/rail forces obtained by the dynamic wheel/rail coupled model.

The vehicle and the track interact with each other through the dynamic wheel/rail interaction, which will be described using the dynamic wheel/rail coupled model [16]. In the dynamic wheel/rail coupled model, three kinds of rail motions in vertical, lateral and torsional directions are taken into account.

The vehicle-track coupled vibrations are mainly excited by the random track irregularities which are usually expressed by a one-sided power spectrum density (PSD) function, namely track spectrum. The sixth grade track irregularity PSD of US railways is long wave track irregularity of more than 1.0 m wave length and is usually used as the excitation to analyze the vibration in low frequency range which is usually not more than 100 Hz. In this paper, in order to analyze the building vibration in wider frequency range, Sato spectrum of the short wave track irregularity of 0.05–1.0 m wave length is used, which is expressed as

$$S(f) = Af^{-n} \tag{3}$$

where the unit of $S(f)$ is mm^2/(1/m); $f = 1/\lambda$ is the spatial frequency in cycle/m; A and n are the fit coefficients.

A fast and high-precision numerical transformation method [20] is adopted to transform the PSD function of the track spectrum into the time-domain random track irregularity. Figures 3 and 4 illustrate the transformed time-domain random track irregularity.

The spatial train-FST coupled dynamics system is a large-scale nonlinear coupled dynamic system. To efficiently solve the nonlinear dynamic system of such high DOFs, the Zhai method, a simple fast explicit integration method previously developed by Zhai [21], is employed. The scheme of this integration method is expressed as follows:

$$\begin{cases} \mathbf{X}_{n+1} = \mathbf{X}_n + \mathbf{V}_n \Delta t + (1/2 + \alpha)\mathbf{A}_n \Delta t^2 - \alpha \mathbf{A}_{n-1} \Delta t^2 \\ \mathbf{V}_{n+1} = \mathbf{V}_n + (1 + \beta)\mathbf{A}_n \Delta t - \beta \mathbf{A}_{n-1} \Delta t \end{cases} \quad (4)$$
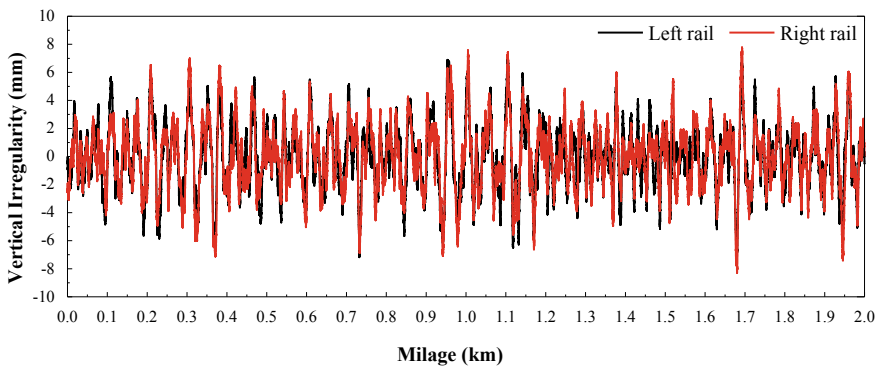
Fig. 3 Vertical random track irregularity
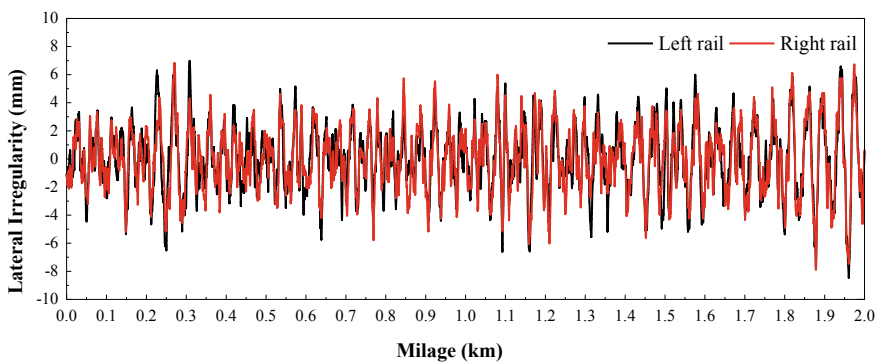
Fig. 4 Lateral random track irregularity

where **X**, **V** and **A** are the generalized displacement, velocity and acceleration of the system, respectively; Δt is the time step; the subscripts $n + 1$, n and $n - 1$ denote the integration time at $(n + 1) \Delta t$, $n\Delta t$ and $(n - 1)\Delta t$, respectively; α and β are free parameters that control the stability and numerical dissipation of the algorithm. Usually, a value of 0.5 could be assigned to α and β to achieve good compatibility between numerical stability and accuracy.

2.2 FE Model of Track–Tunnel–Soil–Building Subsystem

The geometric construction of the hotel and the tunnel is very complicated, as depicted in Fig. 1, and plays a key role in the vibration prediction of the hotel. The finite element method has the ability to elaborately describe their geometric construction, which is difficult to establish the dynamics model through analytical and semi-analytical methods. In order to predict the vibration of the hotel induced by moving train as accurate as possible, a FE model of track–tunnel–soil–building system is established, as shown in Fig. 5.

In reality, the soil is the infinite half-space and the track length is also regarded as infinite. However, the volume of the soil has to be limited in the FE model and the wave will be, therefore, reflected at the boundary which is inconsistent with the practice. In order to mitigate the boundary effect, the artificial boundaries or the infinite elements should be adopted to encase the FE model. It is easy to implement the artificial boundaries in the FE model by modifying the material properties and fixing the outside nodes of the outermost elements. These boundaries and the modified outermost elements are referred to as consistent viscous-spring artificial boundaries and viscous-spring boundary elements [22]. The material properties of the viscous-spring boundary elements are as follows:
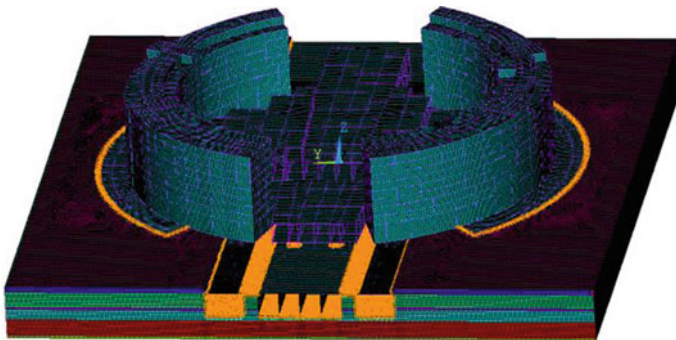
Fig. 5 General view of the FE model

Equivalent Poisson's ratio:

$$v' = \begin{cases} \frac{\alpha-2}{2(\alpha-1)}, & \alpha \geq 2 \\ 0, & \text{other} \end{cases} \tag{5}$$

Equivalent Young's modulus:

$$E' = 2\alpha_T h \frac{G}{R}(1+v') \tag{6}$$

Equivalent damping ratio:

$$\eta' = \frac{\rho R}{3G}\left(2\frac{v_s}{\alpha_T} + \frac{v_p}{\alpha_N}\right) \tag{7}$$

where $\alpha = \alpha_N/\alpha_T$, α_N and α_T are the parameters of the consistent viscous-spring artificial boundaries and generally equal to 4.0 and 2.0, respectively; ρ and G are the density and shear modulus of the soil; h and R are the thickness of the viscous-spring boundary element and the distance between the source of scattering wave and the consistent viscous-spring artificial boundary; v_p and v_s are the velocities of pressure wave and shear wave of the soil, respectively.

The damping of the embankment and the soil are also the key parameters for the attenuation of the wave propagation in the soil, so the damping parameters of the FE model should be set properly. In the material parameters, the density, elastic modulus, Poisson's ratio and damping have important influence on the ground vibration. The density, elastic modulus and Poisson's ratio can be directly defined; however, the Rayleigh damping is usually adopted in the FE method. The parameters of the Rayleigh damping are satisfied with

$$\begin{cases} \xi = \alpha/(2\omega_i) + \beta\omega_i/2 \\ \xi = \alpha/(2\omega_j) + \beta\omega_j/2 \end{cases} \tag{8}$$

where α and β are the parameters of the Rayleigh damping and relative with the mass and stiffness matrices, respectively; ξ is the damping ratio; ω_i and ω_j are the lower and upper limits of the range of predominant frequency range.

3   Numerical Prediction

3.1   Dynamics Parameters

The A-type metro train will be operated as planned. The train will be composed of six motor cars and two trailers as the head car and the tail car. The axle load of the train with normal passenger capacity is between 14 and 16 t. In order to attenuate

Table 2 Main dynamics parameters of the FST

Object	Parameter	Value	Object	Parameter	Value
Rail	Elastic modulus (MN/m^2)	210,000	Floating slabs	Length (m)	25
	Cross-sectional moment of inertia (m^4)	3.217×10^{-5}		Width (m)	4.2
	Density (kg/m^3)	7850		Thickness (m)	0.42
	Cross-sectional area (m^2)	7.745×10^{-3}		Density (kg/m^3)	2500
	Shear modulus (MN/m^2)	77,000		Elastic modulus (MN/m^2)	35,000
	Shear factor	0.4		Poisson's ratio	0.25
Fastener	Stiffness (MN/m)	30	Steel spring	Stiffness (MN/m)	6.6
	Damping (N s/m)	7.5×10^4		Damping (MN s/m)	4.9
	Fastener spacing (m)	0.595		Longitudinal spacing (m)	1.19

the building vibration induced by the moving train, a FST specially designed for this subway line is adopted. The natural frequency of the floating slab is about 8.2 Hz and the main dynamics parameters of the FST are listed in Table 2.

Before the construction of the hotel, a single-hole logging based on the geological prospecting method is generally adopted to investigate the shear wave velocity of the test field. In addition, the classical soil mechanic tests including the direct shear test and the three-axial test were applied to acquire the physical and mechanical parameters of the soil samplings from the in situ field. The test results provide important references to the dynamics properties of the in situ soil layers which are shown in Table 3. The main construction material of the tunnel and the building is reinforced concrete whose main dynamics parameters is well known and are not given here.

3.2 Predicted Results

The normal and the maximal operating speeds are planned as 80 km/h and 140 km/h. Firstly, the train–FST coupled dynamics model is used to calculate the fastener forces excited by the random track irregularities illustrated in Figs. 3 and 4 with the train

Table 3 Dynamics properties of the soil

Layer	Thickness (m)	Density (kg/m^3)	Young's modulus (MPa)	Poisson's ratio	Damping ratio
(1)	2.0	1.75×10^3	85	0.404	0.05
(2)	7.5	2.0×10^3	96	0.395	0.05
(3)	3.8	2.15×10^3	1271	0.311	0.05
(4)	48.4	2.5×10^3	5096	0.295	0.05

speed of 80 km/h. All of the fastener forces have a similar time history and one of them is illustrated in Fig. 6. It can be found that the max value of the fastener forces is about 55 kN. Then, all fastener forces are taken as the external loads of the FE model of track–tunnel–soil–building system to predict the building vibration.

Due to that the structure of the hotel is almost symmetrical about the longitudinal middle section of the tunnel, only three locations on each floor in the building on the left (see Fig. 1) are selected to illustrate the vertical acceleration of the building. The locations on each floor are illustrated in Fig. 7. The train is moving on the left subway line (see Fig. 1) with the speed of 80 km/h. The predicted vertical vibration of the building at those locations is as shown Fig. 8. In the Fig. 8, '*Fn*' represents the *n*th floor and the red and pink dotted lines are 62 dB and 65 dB, respectively, which are the limited values for night time and day time regulated by the standard [23].
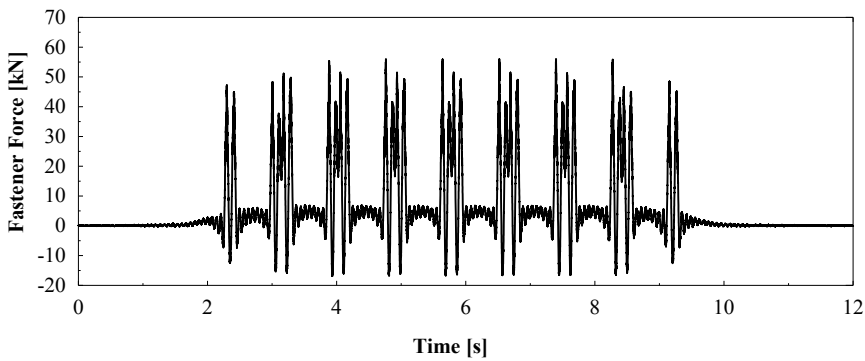
Fig. 6 Time histories of one fastener force
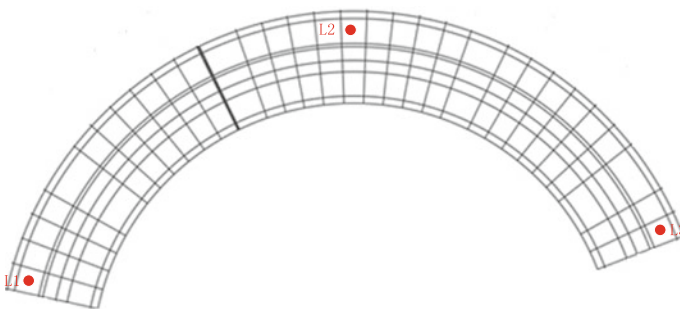
Fig. 7 Schematic diagrams of locations on each floor

Fig. 8 Vertical vibration level of the building
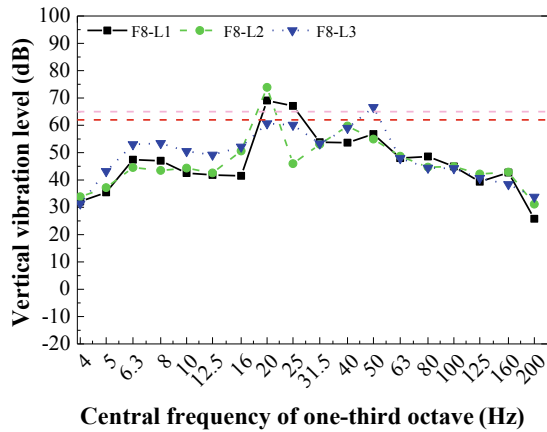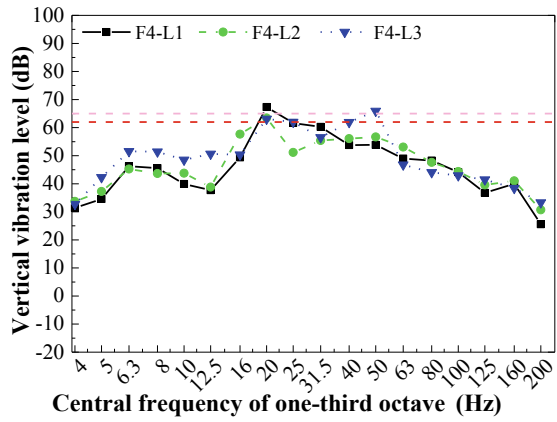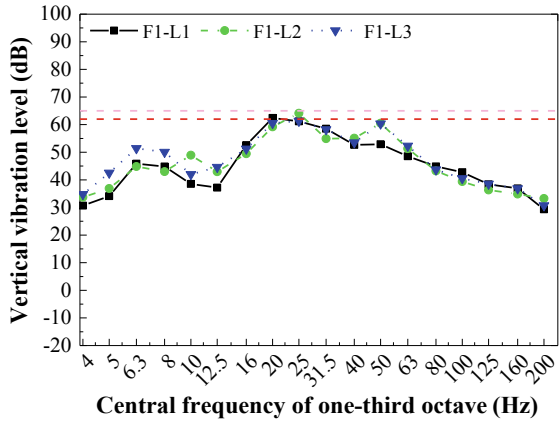
It can be found from Fig. 8 that the vertical vibration of the building induced by the moving train is concentrated in the frequency range of $20 \sim 50$ Hz. The first two dominant frequencies are close to the central frequency 20 Hz and 50 Hz, respectively. The vertical vibration level of those locations exceeds the limited values at those two dominant frequencies and the higher the floor is, the more the value exceeding the limit value is. so some vibration control measures have to be implemented. The vertical vibration level of the building also has a peak value in the frequency range of $6.3 \sim 8$ Hz which probably induced by the natural frequency of the floating slab.

In order to evaluate the influence of train speed on the building vibration induced by the moving train, the comparisons are listed in Fig. 9. Compared to the results of the train speed 80 km/h, the building vibration induced by the moving train with speed of 140 km/h is smaller when the frequency is below the first dominant frequency and is larger when the frequency is above the second dominant frequency. This probably because the track vibration dominate the building vibration below the first dominant frequency and the wheel/rail forces dominates the building vibration above the second dominant frequency. When the train speed is 80 km/h, the wheelbase of the train is 2.5 m which will cause a characteristic frequency close

(a) F1-L1   (b) F1-L2   (c) F1-L3

(d) F4-L1   (e) F4-L2   (f) F4-L3

(g) F8-L1   (h) F8-L2   (i) F8-L3
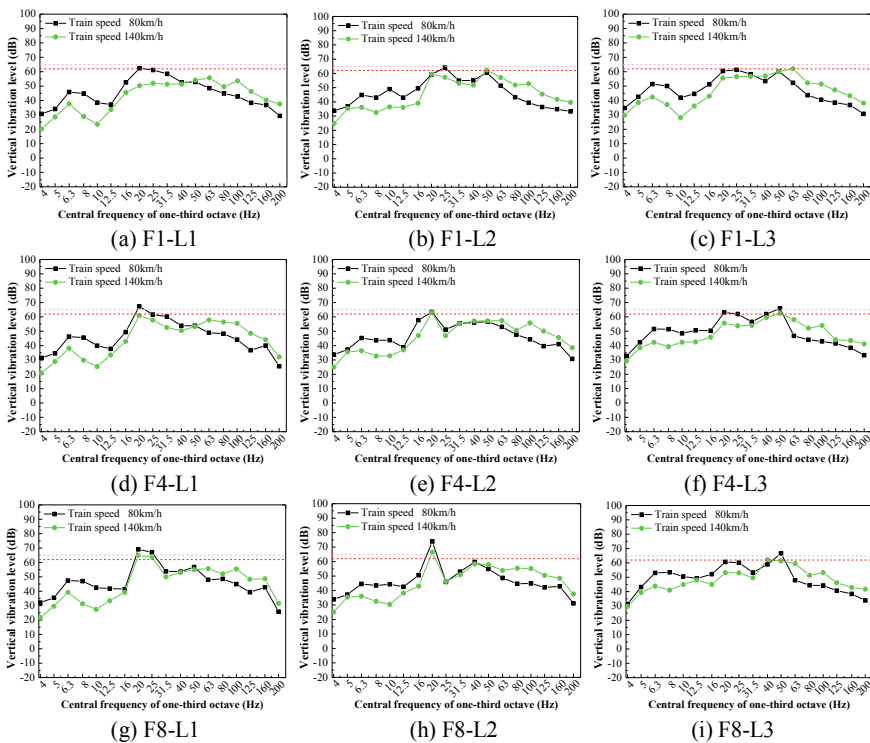
Fig. 9 Comparison of the vertical vibration level of the building induced by different train speed

to the natural frequency of the floating slab and the building vibration is aggravated below the first dominant frequency. When the train speed is 140 km/h, the dynamic wheel/rail interaction becomes more intensified and induces more aggravated building vibration above the second dominant frequency.

4 Conclusions

The vertical vibration of the building induced by the moving train is concentrated in the frequency range of $20\sim 50$ Hz. The first two dominant frequencies are close to the central frequency 20 Hz and 50 Hz, respectively. The vertical vibration level of those locations exceeds the limited values at those two dominant frequencies and the higher the floor is, the more the value exceeding the limit value is so some vibration control measures have to be implemented. Compared to the results of the train speed 80 km/h, the building vibration induced by the moving train with speed of 140 km/h is smaller when the frequency is below the first dominant frequency and is larger when the frequency is above the second dominant frequency.

References

1. Zhai W, Zhao C (2016) Frontiers and challenges of sciences and technologies in modern railway engineering. J Southwest Jiaotong University 51(2):209–226 (In Chinese)
2. Hunt HEM (1996) Modelling of rail vehicles and track for calculation of ground-vibration transmission into buildings. J Sound Vib 193(193):185–194
3. Balendra T., Koh, C. G., Ho., Y. C: Dynamic response of buildings due to trains in underground tunnels. Earthquake Eng Struct Dyn 20(3):275–291 (1991)
4. Bian X, Chen Y, Hu T (2008) Numerical simulation of high-speed train induced ground vibrations using 2.5D finite element approach. Sci China-Phys Mech Astron 51(6):632–650
5. Bian X, Jiang H, Chang C et al (2015) Track and ground vibrations generated by high-speed train running on ballastless railway with excitation of vertical track irregularities. Soil Dyn Earthq Eng 76:29–43
6. Yang Y, Hung H, Chang D (2003) Train-induced wave propagation in layered soils using finite/infinite element simulation. Soil Dyn Earthq Eng 23(4):263–278
7. Sheng X, Jones CJ, Thompson DJ et al (2005) Modelling ground vibration from railways using wavenumber finite- and boundary-element methods. Proc Roy Soc A Math, Phys Eng Sci 461(2059):2043–2070
8. Lombaert G, Degrande G (2009) Ground-borne vibration due to static and dynamic axle loads of intercity and high-speed trains. J Sound Vib 319(3):1036–1066
9. Forrest JA, Hunt HEM (2006) Ground vibration generated by trains in underground tunnels. J Sound Vib 294(4):706–736

10. Degrande G, Clouteau D, Othman R et al (2006) A numerical model for ground-borne vibrations from underground railway traffic based on a periodic finite element-boundary element formulation. J Sound Vib 293(3–5):645–666

11. Kouroussis G, Connolly DP, Verlinden O (2014) Railway-induced ground vibrations—a review of vehicle effects. Int J Rail Transp 2(2):69–110

12. Zhai W, Sun X (1994) A detailed model for investigating vertical interaction between railway vehicle and track. Veh Syst Dyn 23(sup1):603–615

13. Zhai W, Cai C, Guo S (1996) Coupling model of vertical and lateral vehicle/track interactions. Veh Syst Dyn 26(1):61–79

14. Zhai W, Wang K, Cai C (2009) Fundamentals of vehicle-track coupled dynamics. Veh Syst Dyn 47(11):1349–1376

15. Zhai W (2015) Vehicle-track coupled dynamics, vol 1, 4th edn. Science Press, Beijing. (in Chinese)

16. Chen G, Zhai W (2004) A new wheel/rail spatially dynamic coupling model and its verification. Veh Syst Dyn 41(4):301–322

17. Han H, Zhai W (2011) Numerical simulation of soft ground vibration caused by high-speed trains. advances in environmental vibration. In: 5th international symposium on environmental vibration. Science Press, Beijing, pp 142–150

18. Shao M, Zhai W, Song X et al (2013) Numerical simulation of high-speed train induced ground vibration for non-ballasted railway on embankment. In: 6th international symposium on environmental vibration. Science Press, Beijing, pp 3–14

19. Kouroussis G, Connolly D, Alexandrou G et al (2015) Railway ground vibrations induced by wheel and rail singular defects. Veh Syst Dyn 53(10):1500–1519

20. Chen G, Zhai W (1999) Numerical simulation of the stochastic process of railway track irregularities. J Southwest Jiaotong Univ 34(2):138–142 (in Chinese)

21. Zhai W (1996) Two simple fast integration methods for large-scale dynamic problems in engineering. Int J Numer Meth Eng 39(24):4199–4214

22. Liu J, Gu Y, Du Y (2006) Consistent viscous-spring artificial boundaries and viscous-spring boundary elements. Chin J Geotech Eng 28(9):1070–1075

23. JGJ/T 170–2009 (2009) Standard for limit and measuring method of building vibration and secondary noise caused by urban rail transit

Case Study on Rail Train-Induced Vibration Reduction at the Metro Depot by Using the Open Trench

Ziyu Tao, Yimin Wang, Yekai Chen and Chao Zou

Abstract With the development of rail transit and the shortage of land utilization, properties above and near metro depots emerge in Chinese major metropolises. Whether the railway-induced vibration will bring discomfort to occupants or malfunction to precise devices is always the concern of stakeholders, designers, occupants, and researchers. In general, there are three main facets to control the train-induced vibrations: from the vibration source, from the wave transmission path, and from the building structure. General vibration mitigation methods include the rubber float-slab track, continuous-wave barrier systems, non-continuous wave barrier systems, wave impedance block, blocking floor, floating floor, etc. This paper mainly focuses on the effectiveness of the open trench in reducing train-induced vibration based on a field test conducted at the throat area of a metro depot of Guangzhou. The results reveal that (a) the vibration attenuation in curve-line segment of the throat area is more than that in straight-line segment, as there being 28–36 dB attenuation in curve-line segment and 22–24 dB attenuation in straight-line segment; (b) higher-frequency components (above 50 Hz) attenuate faster than lower ones and the propagation distance of the former is shorter; (c) the peak frequency induced by trains operating at metro depots lies in 31.5–40 Hz; (d) the effectiveness of the open trench in mitigating horizontal vibration is better than that in reducing vertical vibration. Some suggestions on designing the open trench to reduce railway-induced vibration are also proposed.

Keywords In-site test · Throat area · Train-induced vibration · Wave propagation · Open trench

Z. Tao (✉) · Y. Wang · Y. Chen · C. Zou
School of Civil Engineering and Transportation, South China University of Technology, Guangzhou 510640, China
e-mail: 363716368@qq.com

1   Introduction

With the fast development of metropolises in China, the areas around metro depots are also exploited as residential community, business zone, industrial zone, or hybrid ones. Whether the ground vibration induced by trains operating at the metro depot will bring side effects to nearby dwellers or cause malfunction to nearby precise devices is of great social concern. The influence of ground-borne vibration is usually frequency-dependent, as the lower-frequency vibration in the range of 1–80 Hz general can be felt by human body while the higher-frequency vibration in the range of 16–250 Hz usually generates the secondary-radiated noise inside buildings [1, 2]. Subway trains operating on the ground surface normally generate lower-frequency vibration in the range below 40 Hz, which is classified as feelable vibration, especially when the subgrade soil is soft [3].

There are plenty of vibration mitigation measures. In general, these mitigation measures can be sorted into three main categories, which are focused on vibration sources, on vibration propagation path and on the receiver of the vibration, respectively. Open isolation trenches are commonly used measures to mitigate ground-borne vibration produced by machinery; vibration propagation is cut off by the open trench; and only part of the original vibration, which is diffracted at the trench bottom, could spread to area behind the trench [4]. Based on the same principle, the open trench also could be a possible way to attenuate ground-borne vibration induced by railways.

In the late 1960s, Wood et al. carried out earlier field measurements on the screening effectiveness of open trenches [4, 5]. They found that the depth of an effective open trench should be more than 0.6 times the wavelength of Rayleigh waves to achieve a 12 dB amplitude reduction. The width of trenches is not a critical factor affecting the effectiveness. And the far-field open trench is of less effect than that of near-field ones. With the fast development pace of computers and commercial software, numerical analysis becomes a powerful mean to assist scientific researches. May and Bolt studied the effectiveness of open trenches in reducing seismic motion by using 2D FE models [6]. They confirmed the result of Woods that a non-dimensional depth of 0.6 is needed to obtain a 12 dB reduction of vibration amplitude. Beskos et al. established 2D and 3D models of open trenches and acquired the same validation [7–9]. Using a 3D FE model, Connolly et al. also found the depth of the open trench is a parameter of more importance than the width of the open trench in reducing railway-induced vibration [10]. Through 2D FE/IE method, Yang and Huang discovered that a higher Poisson's ratio of the soil beneath the track may need a deeper open trench to achieve the same effectiveness [11].

Although various field tests and computer modeling have been done, it is still hard to summarize the effective parameters for the open trench because of the different properties of the field soil and diverse conditions of the test. The dominant frequency components of ground-borne vibration are determined by vibration

propagation in upper layers of soil underneath the track, which are often only a few meters deep [1]. This suggests the relative relationship between the depth of the upper soil layer and the depth of the open trench would also affect the effectiveness of the open trench.

In the present paper, in-site measurements are analyzed in both time domain and frequency domain. And the vibration attenuation patterns are discussed both in the horizontal and vertical directions. The effect of concrete-lined open trench in reducing train-induced vibration is also presented based on the data.

2 In-site Test Measurements

2.1 Test Scheme

The field tests were conducted at the throat area of a metro depot of Guangzhou. INV306DF Data Acquisition and Signal Processing System, 941 amplifier, and 991B ultra-low frequency accelerometers were used in this test. All the instrumentations were calibrated before measuring, and the adopted sampling frequency was 410 Hz. Along the normal direction of the ballast track, two testing sections were selected. Section 1 was located across the straight lines of the throat area, which was consisted of five testing points. The distance between the five testing points (C1–C5) and the vibration source was 0 m, 5 m, 17 m, 23 m, and 35 m, respectively. Section 2 was chosen at the curve segment of the throat area, including four testing points. These four points (D1–D4) were 0 m, 5 m, 25 m, and 30 m away from the vibration source, respectively. Each testing point sets two acceleration sensors to measure the vertical and horizontal (perpendicular to the track line) accelerations simultaneously. There existed a concrete-lined U-shaped open drainage trench of 0.4 m width and 1.2 m depth, which was virtually paralleled to the outermost track line of the throat area. From the profile diagrams, this ditch was between C3 and C4 in section 1 and between D3 and D4 in section 2 (see Figs. 1 and 2).
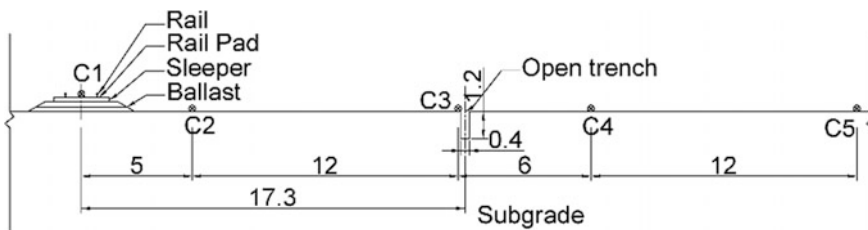
Fig. 1 Diagrammatic sketch of testing section 1
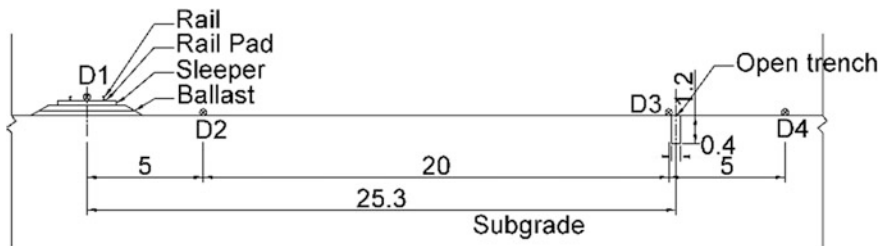
Fig. 2 Diagrammatic sketch of testing section 2

2.2 Time-Domain Analysis of Test Results

In the in-site test, a total of 30 sets of data were collected. Twenty of them were recorded when every single train passed by and the rest ten of them being background vibration. Each testing section contained 15 sets of data. The order of magnitude of background vibrations in both testing sections 1 and 2, no matter in the horizontal or vertical direction, lies in 10^{-3} m/s^2, and there are no obvious disturbing vibration sources.

Figures 3 and 4 shows one set of the time-history curve of train-induced vibration of testing sections 1 and 2, respectively. Other sets of the recorded data have a similar pattern of the curve showed above. It can be derived from the figures that the acceleration magnitude of ground-borne vibration attenuates with distance and the attenuation in section 2 is faster than that in section 1.

In order to analyze the attenuation rules of vibration propagation along the ground surface, the root-mean-square (RMS) value of each set of data was computed and then averaged by the number of data sets. Equation (1) below is used to calculate the RMS value.

$$a_{rms} = \sqrt{\lim_{n \to \infty} \frac{1}{N} \sum_{0}^{N} [a(n)]^2} \tag{1}$$

where a_{rms} is the RMS value of acceleration of train-induced vibration, with the unit of m/s^2. $a(n)$ represents the recorded discrete acceleration sequence. And N is the number of sampling.

After the RMS values were obtained, they were converted into acceleration level by using Eq. (2) as follows:

$$L_a = 20\log_{10}\left(\frac{a_{rms}}{a_{ref}}\right) \tag{2}$$

where L_a is the acceleration level with the unit of dB and a_{ref} is the reference acceleration, being 1×10^{-6} m/s^2.
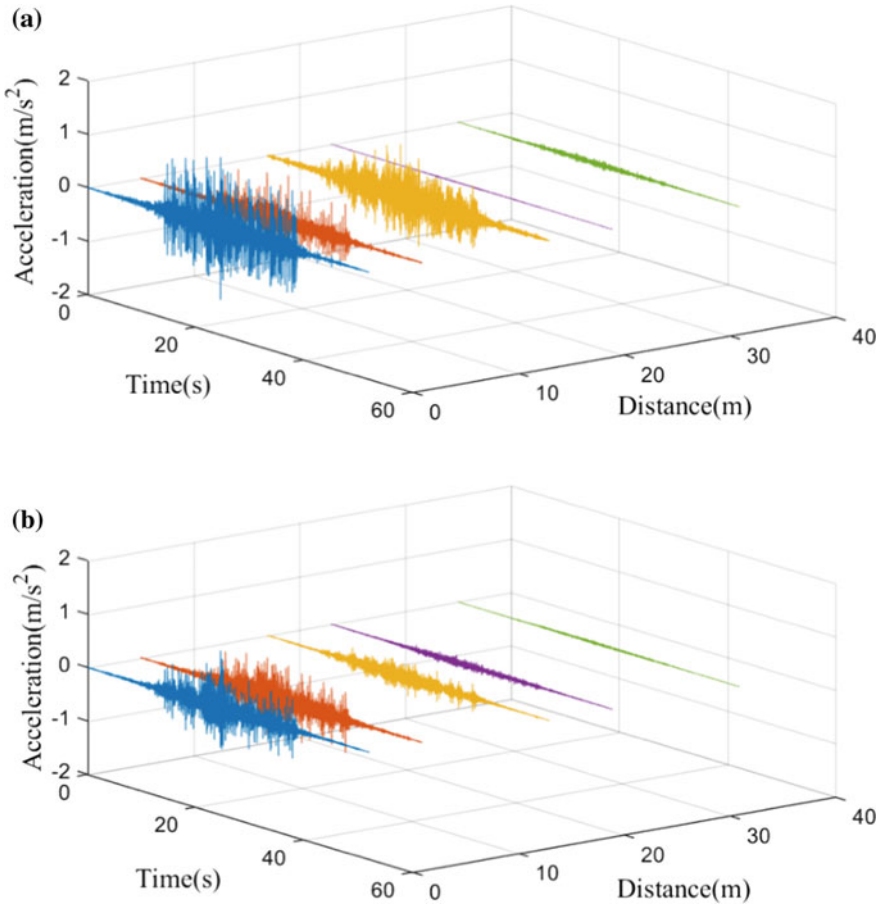
Fig. 3 **a** Time-history curve of train-induced horizontal vibration of section 1, **b** time-history curve of train-induced vertical vibration of section 1

Figure 5 shows the relationship between the acceleration level and distance in testing section 1. As we can see from the picture, in the horizontal direction, the train-induced acceleration level exceeds the background vibration 3–30 dB; in the vertical direction, the range is 7–30 dB.

In the vertical direction, the vibration attenuation rule is clearer than that in a horizontal direction. The attenuation gradient between C3 and C4 is the largest between other testing points. Considering the testing point, C3 is mounted on the concrete liner of an open drainage trench, maybe this open trench is the reason for the larger attenuation slope between C3 and C4. However, in the horizontal direction, the vibration attenuation rule seems more complex. As we can see, although the largest attenuation gradient also lies between C3 and C4, there is a vibration amplification phenomenon both at testing points C3 and C5. The reason
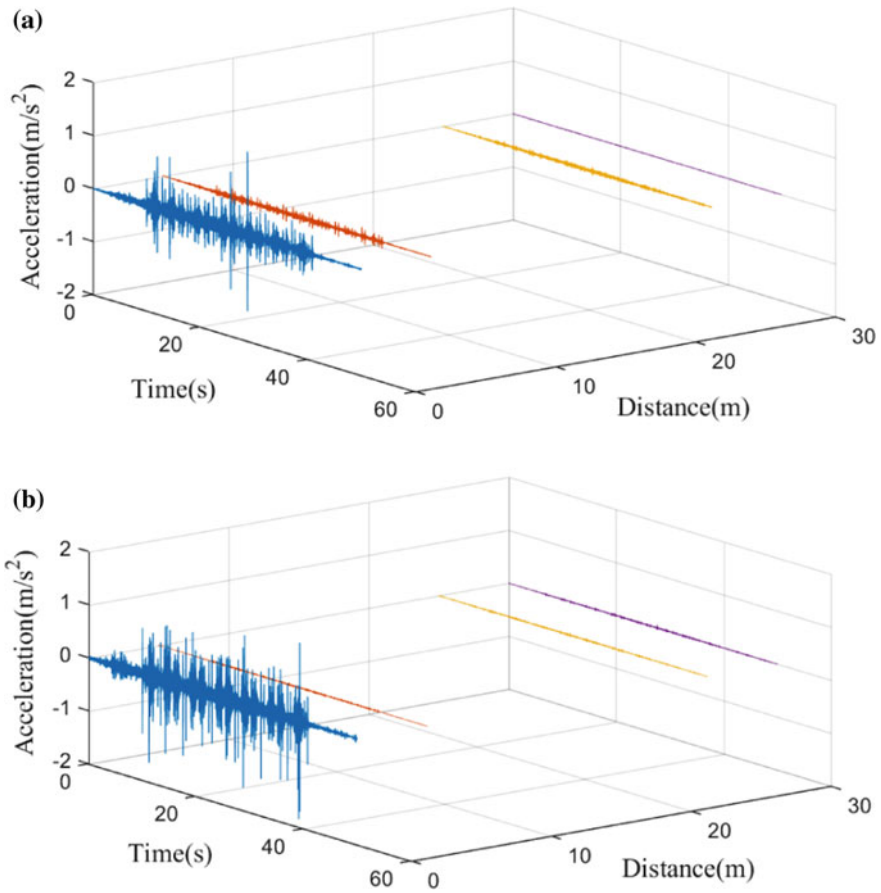
Fig. 4 a Time-history curve of train-induced horizontal vibration of section 2, **b** time-history curve of train-induced vertical vibration of section 2

for vibration amplification in the horizontal direction at testing point C3 may be attributed to the possible stiff intercalary strata. And the vibration amplified phenomenon in the area behind the open isolation trench has been documented in many other works of literature [12, 13].

Figure 6 indicates the time-domain analysis of the vibration attenuation in testing section 2. The difference between the train-induced acceleration level and the background vibration level is 11–29 dB in the horizontal direction and 14–40 dB in the vertical direction being. As shown in Fig. 6, vibration levels in a vertical direction basically keep invariant between the testing point D3 and D4. The acceleration level in the horizontal and vertical direction at testing point D1 and D2 displays little difference.

Fig. 5 Acceleration levels versus distance in testing section 1
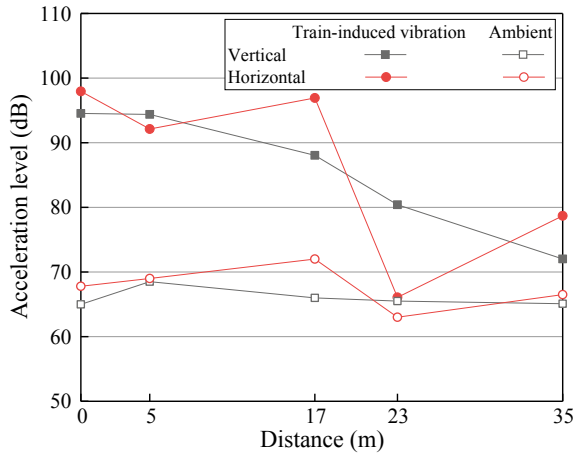
Fig. 6 Acceleration levels versus distance in testing section 2
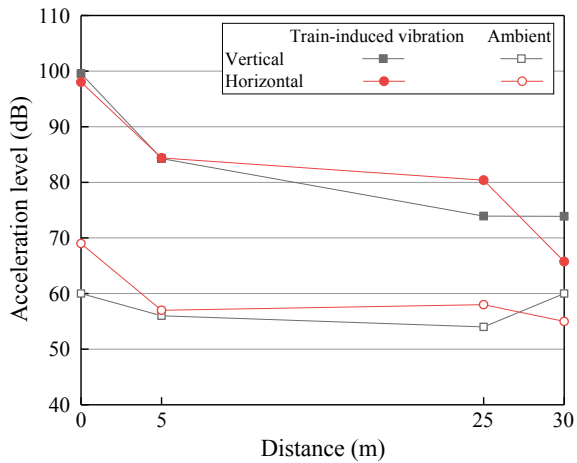
From Table 2, we can find the vertical vibration attenuation mainly exits in the near field for the curve-line segment of the throat area. This attenuation rule may be attributed to the higher-frequency components of vertical vibration in testing section 2, which will be verified in section 2.3 of this paper. Comparing the attenuation gradient between C3 and C4 in Table 1 or that between D3 and D4 in Table 2, we can conclude the open trench is a benefit for horizontal vibration mitigation.

Table 1 Acceleration level value and attenuation gradient in testing section 1

Testing point	Horizontal direction (dB)	Attenuation gradient (dB/m)	Vertical direction (dB)	Attenuation gradient (dB/m)
C1–0 m	97.9	–	94.5	–
C2–5 m	92.1	1.16	94.4	0.03
C3–17 m	96.9	−0.40	88.1	0.53
C4–23 m	66.1	5.14	72.0	1.28
C5–35 m	78.7	−1.05	72.0	0.70

Table 2 Acceleration level value and attenuation gradient in testing section 2

Testing point	Horizontal direction (dB)	Attenuation gradient (dB/m)	Vertical direction (dB)	Attenuation gradient (dB/m)
D1–0 m	98.0	–	99.6	–
D2–5 m	84.4	2.73	84.3	3.06
.D3–25 m	80.4	0.20	73.9	0.52
D4–30 m	65.8	2.93	73.9	0.00

2.3 Frequency-Domain Analysis of Test Results

In this section, frequency-domain analyses are carried out. The frequency analyses mainly contain two parts: one is power spectral density analyses and the other is one-third octave frequency analyses. Power spectral density of each testing point is estimated using Welch's method. And the one-third octave diagrams are drawn based on energy average around the center frequencies.

Figures 7, 8, 9, and 10 show the PSDs of vertical vibration at relevant testing points. From these diagrams, we can clearly find the vibration energy dissipates and the higher-frequency components of vibration attenuate with the distance. The lower-frequency components of vibration can propagate more distant than the higher frequencies. The dominant-frequency components are below 60 Hz.

Figures 11 and 12 display the one-third octave frequency diagrams of testing sections 1 and 2 in both horizontal and vertical directions. These figures can tell the peak frequency component distinctly. As shown in the pictures, the peak frequencies mostly lie in 31.5–40 Hz. The frequencies higher than the peak frequency attenuate faster than those below the peak frequency. From Fig. 11a, we can conclude that the frequency components below 10 Hz in horizontal direction attenuate the slowest and the amplifying horizontal vibration behind the open trench mainly consists of frequencies higher than 10 Hz while the amplifying vertical vibration behind the open trench mainly consists of frequencies higher than 80 Hz, which is read from Fig. 11b. For the testing section 2, in the horizontal direction, frequency components below 20 Hz attenuate the slowest and there exits some
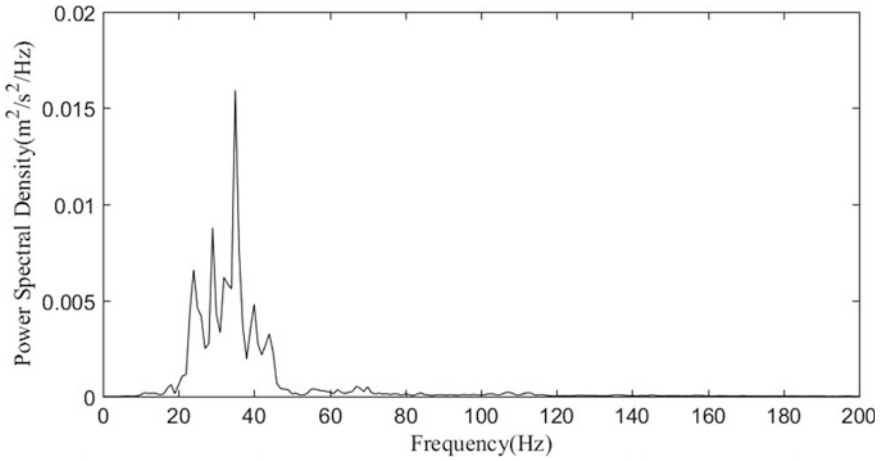
Fig. 7 Power spectral density of vertical vibration at testing point C1
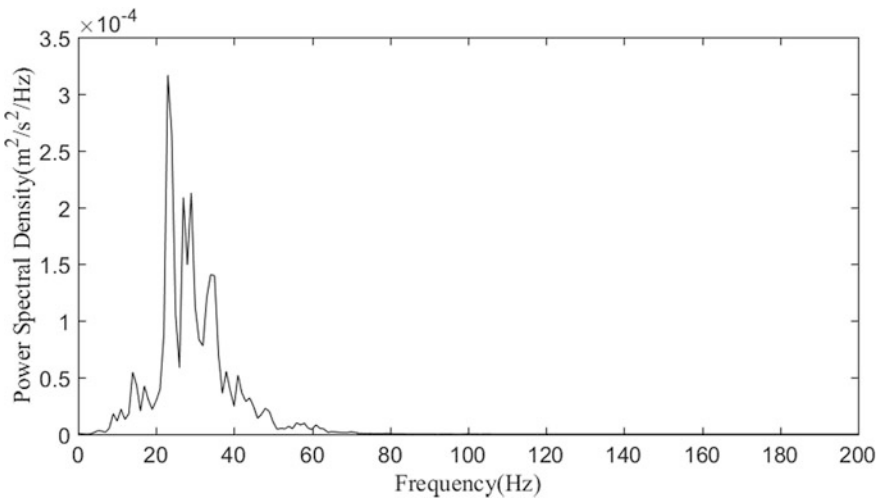
Fig. 8 Power spectral density of vertical vibration at testing point C4

amplification for frequencies above 80 Hz. However, in the vertical direction, the frequencies below 31.5 Hz are amplified behind testing point D2. When considering the design vibration mitigation measures, the peak frequency range of 25–40 Hz should be paid more attention.
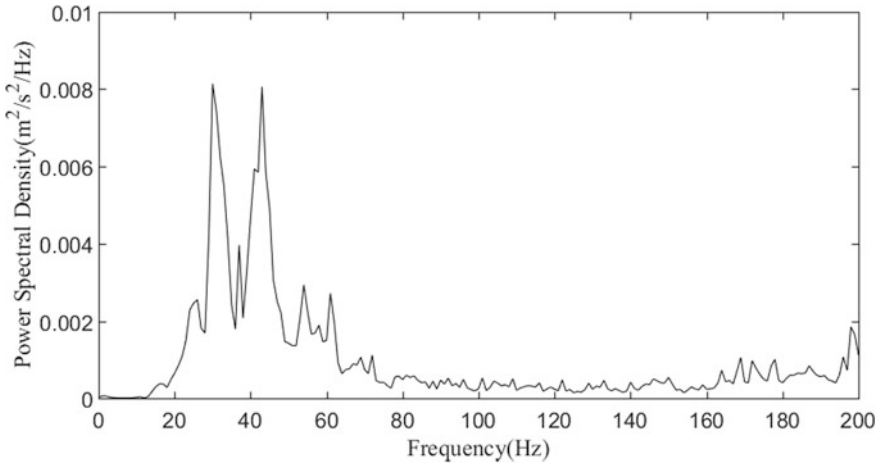
Fig. 9 Power spectral density of vertical vibration at testing point D1
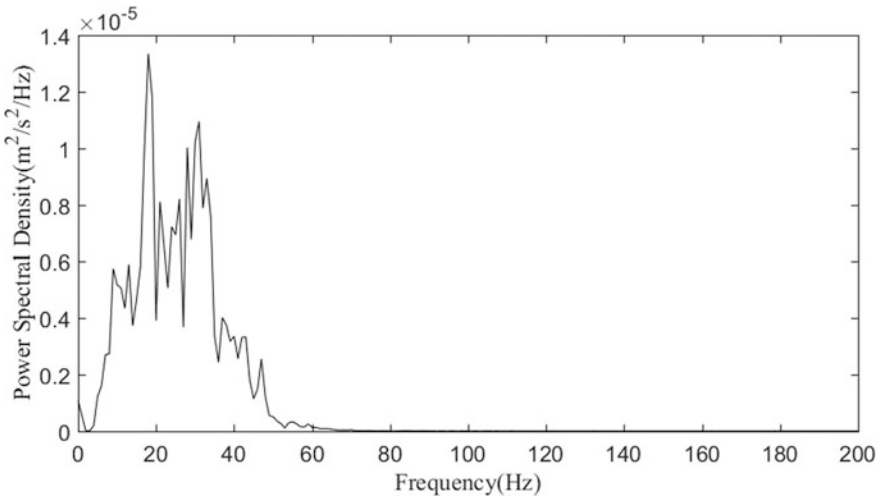
Fig. 10 Power spectral density of vertical vibration at testing point D3
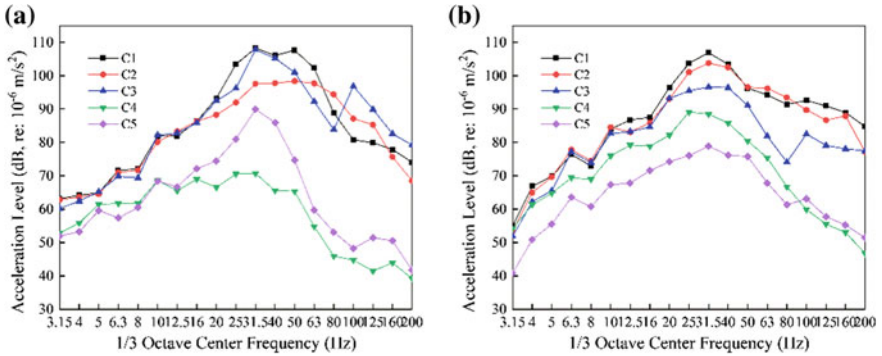
Fig. 11 **a** 1/3 octave frequency diagram in the horizontal direction of C, **b** 1/3 octave frequency diagram in the vertical direction of C
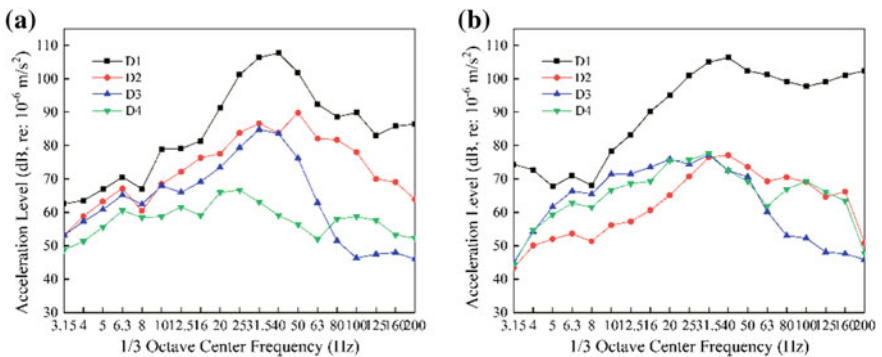
Fig. 12 **a** 1/3 octave frequency diagram in the horizontal direction of D, **b** 1/3 octave frequency diagram in the vertical direction of D

3 Conclusions

(1) The speed of vibration attenuation is related to its frequency components. If the vibration contains more high-frequency components, it will attenuate faster.

(2) The peak frequency components of vibration induced by train operating at metro depot mainly lie in 31.5–40 Hz. The frequencies higher than the peak frequency attenuate faster than those below the peak frequency. When considering the mitigation of vibration, the components of frequencies below the peak frequency would be of more importance.

(3) The vibration attenuation speed accelerates in the area of 5–6 m just behind the concrete-lined open trench which is settled along the track line. This phenomenon is more distinctive in a horizontal direction than vertical direction.

However, because of the heterogeneity of field soil, there may be vibration amplification some area behind the open trench.

(4) In order to achieve the best vibration attenuation effect by using an open trench, it is advisable to research the field soil properties and distributions at first. Besides designing a proper depth of the open trench, the possible vibration amplification zone should be avoided.

(5) In actual projects, it is suggested to use a cable trench or drainage ditch to mitigate rail train-induced vibration. As for its location, it is better to set it between the vibration source and sensitive receiver and near the latter.

References

1. Thomspson DJ (2008) Railway noise and vibration: mechanisms, modeling and means of control. Elsevier, Oxford
2. Lombaert G, Degrande G, Francois S, Thompson DJ (2015) Ground-borne vibration due to railway traffic: a review of excitation mechanisms, prediction methods and mitigation measures. In: Proceedings of the 11th international workshop on railway noise, Uddevalla, Sweden; 9–13 Sept 2013. Notes on Numerical Fluid Mechanics & Multidisiciplinary Design vol 126, pp 253–287
3. Thomspson DJ, Jiang J, Toward MGR et al (2016) Reducing railway-induced ground-borne vibration by using open trenches and soft-filled barriers. Soil Dyn Earthq Eng 88:45–59
4. Woods R (1968) Screening of surface waves in soils. J Soil Mech Found Div Proc ASCE 94 (SM4):951–979
5. Richart FE, Hall JR, Woods RD (1970) Vibration of soils and foundations. Prentice-Hall, Englewood Cliffs, New Jersey
6. May T, Bolt BA (1982) The effectiveness of trenches in reducing seismic motion. Earthq Eng Struct Dyn 10:195–210
7. Beskos DE, Dasgupta B, Vardoulakis IG (1986) Vibration isolation using open or filled trenches, Part 1: 2-D homogeneous soil. Comput Mech 1:43–63
8. Dasgupta B, Beskos DE, Vardoulakis IG (1990) Vibration isolation using open or filled trenches, Part 2: 3-D homogeneous soil. Comput Mech 6:129–142
9. Leung KL, Beskos DE, Vardoulakis IG (1990) Vibration isolation using open or filled trenches, Part 3: 2-D non-homogeneous soil by the BEM. Comput Mech 7:137–148
10. Connolly D, Giannopoilos A, Fan W et al (2013) Optimizing low acoustic impedance back-fill material wave barrier dimensions to shield structures from ground borne high speed rail vibrations. Soil Dyn Earthq Eng 46:13–19
11. Yang Y, Hung HH (1997) A parametric study of wave barriers for reduction of train-induced vibrations. Int J Number Methods Eng 40:3729–3747
12. Ju SH (2004) Three-dimensional analyses of wave barriers for reduction of train-induced vibrations. J Geotech Geoenviron Eng 130(7):740–748
13. Xin Zheng, Xia-xin Tao, Fu-tong Wang et al (2014) Mechanism of local amplification in attenuation of ground vibration induced by rail traffic. J Vib Shock 33(3):35–40

Estimation of Amplitude-Dependent Dynamic Parameters from Ambient Vibration Data

Jun Ma

Abstract This paper proposes a method to estimate amplitude-dependent dynamic parameters from ambient vibration data by random decrement technique (RDT). The principle of RDT is explained, and a procedure of applying RDT to evaluate amplitude-dependent dynamic parameters from ambient vibration data is proposed. The proposed procedure is first applied to ambient vibration data of a full-scale one-story steel frame structure, and the analysis procedure is specifically explained. Then, the proposed procedure is applied to ambient vibration data of a 62-story reinforced concrete building. Amplitude-dependent natural frequencies and damping ratios are evaluated for the two structures. The results show tendencies of natural frequencies and damping ratios with respect to vibration amplitude and prove that amplitude-dependent dynamic parameters can be evaluated by the proposed approach.

Keywords Ambient vibration · Dynamic parameter · Structure · Amplitude · Random decrement technique

1 Introduction

Structural vibration control attracts a lot of attentions in recent years as modern structures become higher and larger than in the past and hence are more vulnerable to dynamic loadings such as wind, earthquake, or other external excitations. In order to accurately predict dynamic responses of building structures and then effectively suppress structural vibrations, the dynamic parameters such as frequency and damping should be exactly considered. Dynamic parameters are of great importance in determining dynamic responses of structures. The shift of natural frequency could result in change in earthquake force or wind force acting on a

J. Ma (✉)
China Construction Eighth Engineering Division Co., Ltd.,
Engineering Research Institute, Shanghai 200122, China
e-mail: mjbppc_academnic@email.com

structure, and the largest oscillations will happen if natural frequency of a structure matches the period of ground motion or wind turbulence. Structural damping dissipates the energy that a structure acquires from external dynamic loadings, and the shift of damping ratio could result in remarkable changes in dynamic responses of the structure [1]. Therefore, accurate evaluation of dynamic parameters is a key issue for structural design.

From field measurements made over last several decades, it has been exhibited that natural frequency and damping are nonlinear parameters that vary with vibration amplitude [2–6], and Tamura [7] suggests that stick-slip phenomenon which occurs at interfaces between primary structural members and secondary components is the primary mechanism for amplitude dependency of natural frequency and damping ratio. However, in the design stage, natural frequency and damping ratio are generally assumed to be constant and independent of structural vibration amplitude, because there are only a few studies on amplitude dependency of dynamic parameters, and the variation tendency and mechanism of amplitude dependency are still in dispute, although the limited number of studies of dynamic response analysis of building structures considering amplitude-dependent dynamic characteristics has shown that the current design assumption does not appear to be conservative [8, 9]. Therefore, a precise understanding of amplitude-dependent dynamic characteristics is a pressing need for design of structures.

This paper presents a method to estimate amplitude-dependent dynamic parameters from ambient vibration data by random decrement technique (RDT). Ambient vibration test is currently a main experimental method available for assessing the dynamic behavior of full-scale structures due to the rapid development of output only modal identification techniques, as well as other advantages such as low cost, convenient operation and no damage. Free decay functions are extracted from ambient vibration data by RDT, and amplitude-dependent dynamic parameters are evaluated from free decay functions by changing trigger values in the RDT process. The proposed approach is applied to the ambient vibration data of a full-scale one-story steel frame structure and the ambient vibration data of a 62-story reinforced concrete building. Amplitude-dependent natural frequencies and damping ratios are evaluated, and the results prove that amplitude-dependent dynamic parameters can be evaluated by the proposed approach.

2 Principle of Random Decrement Technique

The amplitude-dependent dynamic parameters are obtained using random decrement technique. The structural dynamic response is assumed to be composed of a deterministic part and a random part. With a given trigger value, the dynamic response is decomposed into a series of time segments. The deterministic part can be obtained by taking average of those time segments. It is called RD function and is free vibration data of the structure. Curve fitting technique is then used to extract natural frequency and damping ratio from the RD function.

The RD function can be written in the following form:

$$z(\tau, c) = \frac{1}{2N} \sum_{i=1}^{2N} \text{sgn}[y(t_i + \tau, c)] \cdot y(t_i + \tau, c) \tag{1}$$

where $z(\tau, c)$ is the extracted RD function, $y(t, c)$ is the displacement, velocity, or acceleration response at time t with respect to the given trigger value of c, $\text{sgn}[y(t, c)]$ is the signum function of $y(t, c)$, t_i is the ith time instant corresponding to the trigger value c, and $2N$ is the number of time segments.

With a set of gradually increasing trigger values, a set of RD functions can be extracted from the dynamic response, and then, a set of natural frequencies and damping ratios can be obtained with respect to corresponding trigger values; therefore, the relationship between dynamic parameters and trigger values is established and amplitude-dependent dynamic parameters are obtained. The procedure of applying RDT to process ambient vibration data will be described specifically in the next section with field measured data of a full-scale one-story steel frame structure.

3 Application to a Steel Frame Structure

3.1 Description of the Steel Frame

Random decrement technique is applied to ambient vibration data of a full-scale one-story steel frame structure in this section, and the procedure of applying RDT to estimate amplitude-dependent dynamic parameters is explained. The steel frame was designed and constructed with a precast cladding system at laboratory, as shown in Fig. 1. The plan dimension of the steel frame was 3050 × 3050 mm, and the height was 3120 mm; the layout of the steel frame is shown in Fig. 2. Four corner columns with box cross section 150 × 150 × 9 mm thick were constructed, and beams in both first and second floors were H section 250 × 125 × 4.5 × 9 mm thick. A precast cladding system composed of autoclaved lightweight concrete (ALC) external cladding panels, gypsum plasterboard interior linings and window glazing systems was installed on the steel frame. The ALC panels were 75 mm thick, the plasterboard was 12.5 mm thick, and dimension of the window opening was 610 × 460 mm.

Ambient vibration test was conducted on the steel frame, and micro-tremors were used as the main ambient excitation. The duration of ambient vibration test was 60 min. Six servo-type accelerometers were used to collect response acceleration data with three accelerometers per floor: One accelerometer was located on the center, and the other two were located at two diagonally opposite corners on each floor. Each accelerometer could record response acceleration in both X and Y directions simultaneously and at a sampling rate of 100 Hz.

Fig. 1 Steel frame structure
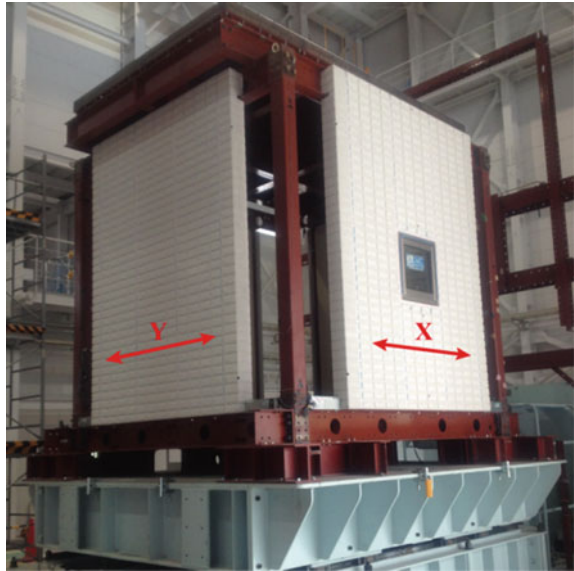
Fig. 2 Layout of the steel frame
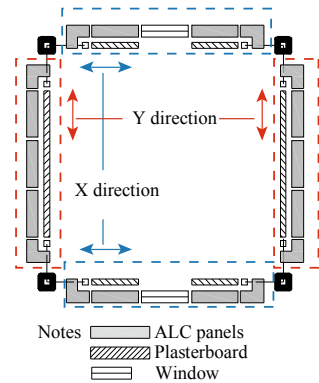
3.2 Data Processing Procedure and Results

Random decrement technique was applied to the measured ambient vibration data in *X* and *Y* directions. Figures 3, 4, 5 and 6 illustrate the procedure of applying RDT to ambient vibration data by taking the measured data in *Y* direction as an example, and the response acceleration data at the top/center of the second floor were employed.

Time history of the response acceleration data in *Y* direction is shown in Fig. 3. First, the response acceleration data are transformed into frequency domain using Fourier transformation, and a band-pass filter with a bandwidth ranging from 0 to 10 Hz is applied to extract contribution of the target mode, and here, information of

Fig. 3 Response acceleration in *Y* direction
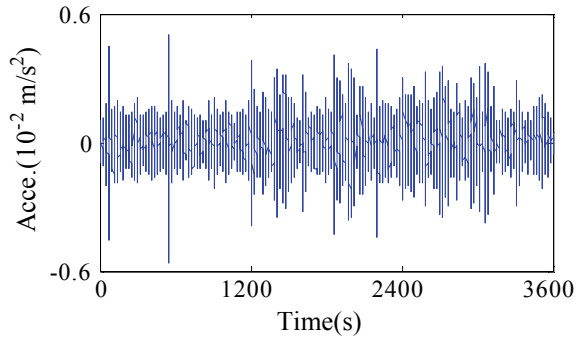
Fig. 4 Fourier spectrum of acceleration
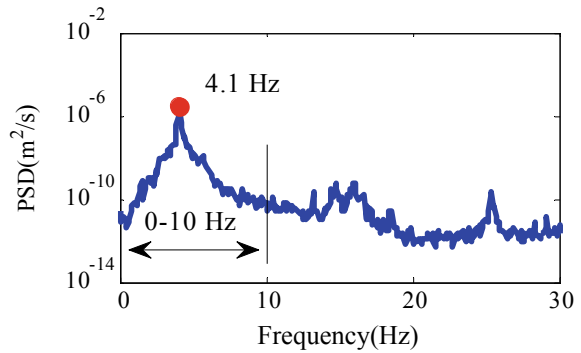
Fig. 5 An RD function
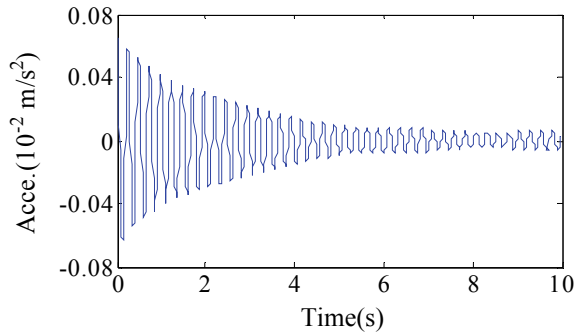
the first mode is extracted, as shown in Fig. 4. Afterward, the filtered data containing information of the first mode are derived from inverse Fourier transformation.

Then, RD functions are extracted from the filtered response acceleration data with respect to corresponding trigger values using RDT. Figure 5 shows an RD function with a trigger value of 6.5×10^{-4} m/s² and a time segment length of 10 s.

Approximate trigger values and time segment length are two key parameters determining quality of RD functions in this step. Although high-quality RD functions with high trigger values and long durations are expected, it should be noticed that a high trigger value and a long-time segment length can lead to an insufficient number of time segments and hence induce a low-quality RD function.

Finally, curve fitting technique is applied to RD functions to extract natural frequencies and damping ratios. The first ten cycles of each RD function are fitted with the theoretical formula of free decay function, and corresponding natural frequency and damping ratio are estimated. Figure 6 shows application of curve fitting technique to the first ten cycles of the RD function extracted above. The theoretical formula of free decay function is written as:

$$x(t) = x_0 e^{-\omega_n \zeta t} \cos\left(\sqrt{1 - \zeta^2}\, \omega_n t\right) \tag{2}$$

where x_0 is the amplitude determined by the initial condition, ω_n is the natural circular frequency, and ζ is the damping ratio.

The amplitude-dependent fundamental natural frequency and damping ratio estimated from response acceleration data in Y direction are shown in Fig. 7, and the amplitude-dependent fundamental natural frequency and damping ratio

Fig. 6 Curving fitting result
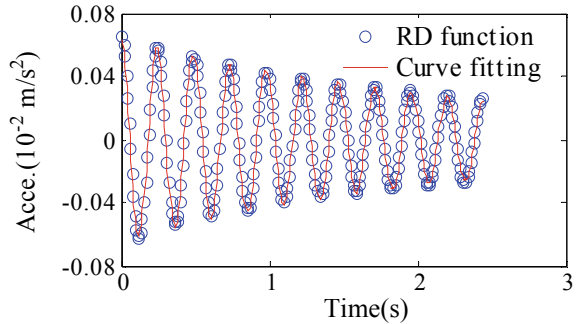
Fig. 7 Amplitude-dependent fundamental natural frequency and damping ratio in Y direction
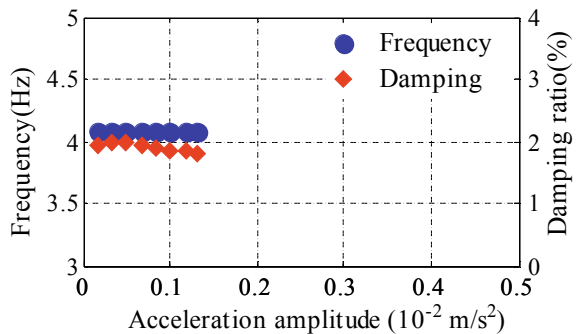
Fig. 8 Amplitude-dependent fundamental natural frequency and damping ratio in *X* direction
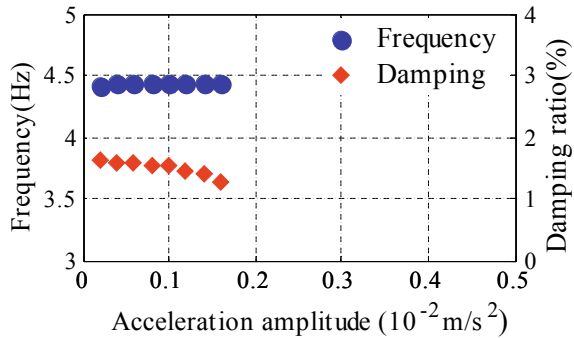
estimated from ambient vibration data in *X* direction are plotted in Fig. 8. As the steel frame was excited at laboratory using micro-tremors and the steel frame was one-story high, the response acceleration was measured at a low level, and hence, the amplitude dependency of dynamic parameters was examined in a low- and narrow-amplitude range. The amplitude-dependent fundamental natural frequencies estimated from acceleration data in both directions are generally observed to be constant, and the amplitude-dependent fundamental damping ratios show a little scatter. A decrease in damping ratio with respect to response acceleration amplitude can be noticed in Fig. 8. Generally, as the steel frame was excited in a low-amplitude range, amplitude dependency of natural frequencies is not evident, but slight amplitude dependency of damping ratios can be observed.

4 Application to an Actual Building

The proposed procedure is applied to ambient response data of an actual building, and the amplitude dependency is evaluated with respect to natural frequency and damping ratio. The building is a 62-story reinforced concrete building, as shown in Fig. 9. It has a rectangular cross section and is 188 m high. The elevation and six typical plans of the building are shown in Fig. 10. The building is supported by reinforced concrete shear walls at the core and supplemental tall outrigger columns in the transverse direction. Posttensioned concrete slabs are supported by concrete columns and shear walls. Seventy-two accelerometers are installed on 26 different levels. Two horizontal components and one vertical component are measured at a sampling rate of 200 Hz. Ambient vibration test was conducted on December 2012, and the building was excited by wind, traffic and operational activities during the test [10].

The measured response acceleration data were first processed using the frequency-domain decomposition (FDD) method to determine the existence of structural modes. Singular values of the output response PSD matrix are illustrated in the frequency range from 0 to 8 Hz in Fig. 11, and the existence of structural

Fig. 9 A 62-story building
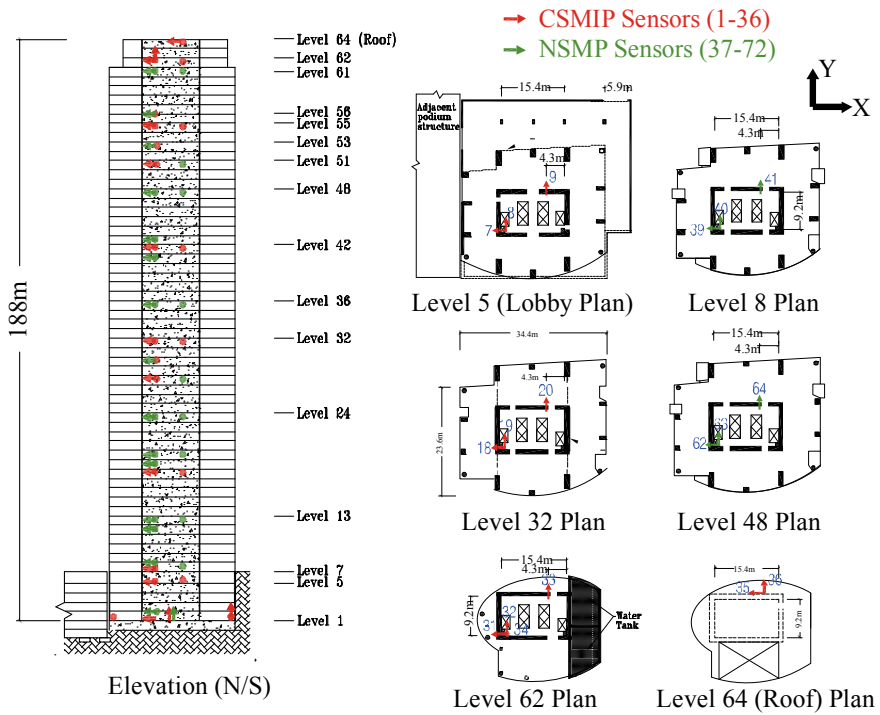
Fig. 10 Elevation and plans of the building
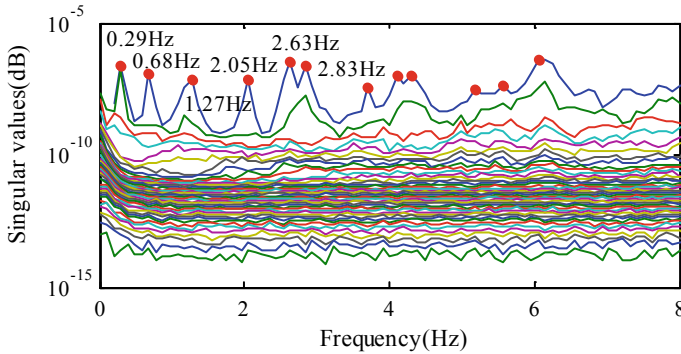
Fig. 11 Singular values of the PSD matrix for response acceleration data

modes is determined by peaks of the first singular value. The first 12 modes are marked by red dots in the figure, and natural frequencies of the first six modes are labeled.

The response acceleration data measured by the 31th sensor and the 32th sensor are adopted to estimate amplitude dependency of dynamic parameters in both X and Y directions. The amplitude-dependent natural frequencies and damping ratios of the first translational modes in X and Y directions are illustrated in Figs. 12 and 13, respectively. It can be observed that natural frequency tends to decrease with increasing amplitude in both directions, and the decreasing trend becomes slow as the amplitude increases. The damping ratio in the X direction is slightly scattered at the initial stage where response acceleration is lower than 0.4×10^{-4} m/s² and then starts increasing with amplitude, while the damping ratio in the Y direction almost keeps increasing with amplitude. Based on the proposed procedure, amplitude-dependent fundamental natural frequencies and damping ratios in two orthogonal directions are obtained, and the tendencies of dynamic parameters with respect to vibration amplitude are observed.

(a) Fundamental natural frequency

(b) Fundamental damping ratio
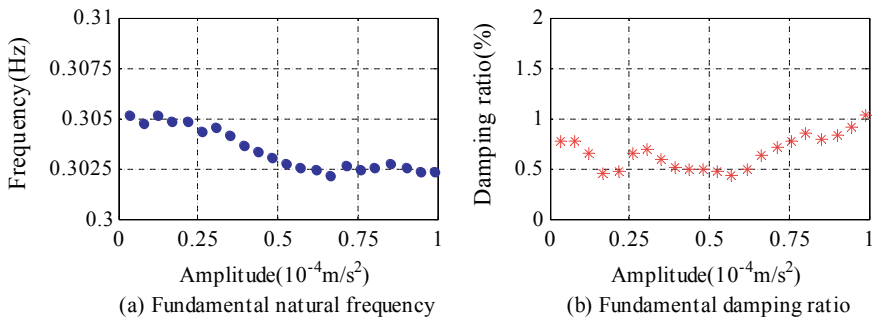
Fig. 12 Amplitude-dependent dynamic parameters estimated from response data in X direction

(a) Fundamental natural frequency   (b) Fundamental damping ratio
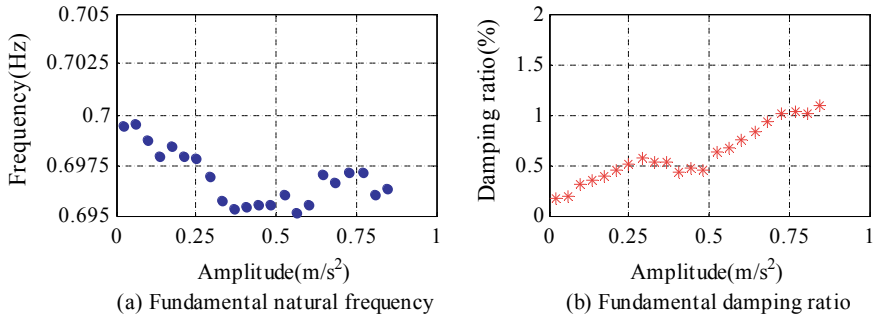
Fig. 13 Amplitude-dependent dynamic parameters estimated from response data in *Y* direction

5   Conclusions

In this paper, random decrement technique was introduced to estimate amplitude-dependent dynamic parameters from ambient vibration data. The principle of RDT was explained, and a procedure of applying RDT to extract amplitude-dependent dynamic parameters from ambient vibration data was proposed. The proposed approach was first applied to ambient vibration data of a steel frame to explain the analysis procedure specifically, and amplitude dependency of natural frequencies and damping ratios of the steel structure was examined. The results show that amplitude dependency of natural frequencies is not evident in the low-amplitude range, but slight amplitude dependency of damping ratios can be observed. Then, the proposed procedure was applied to ambient vibration data of a 62-story reinforced concrete building, and the amplitude dependency with respect to natural frequency and damping ratio was evaluated. The results demonstrate that natural frequency generally decreases with increasing amplitude, while damping ratio keeps increasing with amplitude. In addition, the estimated results of the two structures prove that amplitude-dependent dynamic parameters can be evaluated by the proposed approach.

References

1. Havilland R (1976) A study of the uncertainties in the fundamental translational periods and damping values for real buildings. Massachusetts Institute of Technology, Cambridge
2. Jeary AP (1986) Damping in tall buildings-a mechanism and a predictor. Earthq Eng Struct Dynam 14(5):733–750

3. Lagomarsino S (1993) Forecast models for damping and vibration periods of buildings. J Wind Eng Ind Aerodyn 48(2–3):221–239
4. Tamura Y, Suganuma S (1996) Evaluation of amplitude-dependent damping and natural frequency of building during strong wind. J Wind Eng Ind Aerodyn 59(2–3):115–130
5. Ma J, Nakata S, Yoshida A, Tamura Y (2017) Effects of precast cladding systems on dynamic characteristics of steel frame buildings by ambient and free vibration tests. Shock Vibr 2017:1–20
6. Ma J (2016) Identification of amplitude-dependent damping from earthquake induced record by Hilbert-Huang Transform and Random decrement technique. In: 14th East Asia-Pacific conference on structural engineering and construction. Construction Publishing House, Hochiminh City, pp 2079–2086
7. Tamura Y (2012) Amplitude dependency of damping in buildings and critical tip drift ratio. Int J High-Rise Build 1(1):1–13
8. Li QS, Yang K, Wong CK, Jeary AP (2003) The effect of amplitude-dependent damping on wind-induced vibrations of a super tall building. J Wind Eng Ind Aerodyn 91(9):1175–1198
9. Ma J, Wang HH (2016) Effect of amplitude-dependent damping on seismic response of a steel frame structure. In: 11th Pacific structural steel conference. China Architecture a and Building Press, Shanghai, pp 1130–1135
10. Center for Engineering Strong Motion Data. https://www.strongmotioncenter.org/. Last accessed 2018/05/28

Research on Band Gap Characteristics of Periodic Isolation Barrier for Metro

Shenglong Zhang, Wenbing Wang, Yulu Li, Zongzhen Wu and Xiangwei Ma

Abstract Environmental vibration problem induced by urban rail transit is becoming increasingly prominent, and path vibration isolation is one of the measures to reduce metro vibration and noise. This paper analyzed the applicability of the periodic vibration isolation barrier to vibration and noise reduction of the metro. Band gap frequency of periodic isolation barrier was calculated by transfer matrix method so as to get the variation law of band gap frequency under different parameter combinations. Characteristic frequency of nearby soil vibration caused by underground line vibration source of the metro was obtained by field test. Corresponding band gap barrier parameter combinations were designed according to the characteristic frequency. Calculation results show that the periodic vibration isolation barrier can be applied to vibration and noise reduction of urban rail transit.

Keywords Metro · Field test · Transfer matrix method · Periodic barrier

In recent years, due to the increasing demand for the quality of people's life, China's urban rail transit has developed rapidly, and meanwhile, the environmental vibration and noise induced by it have been paid attention [1]. The path vibration isolation, which in recent years many scholars have done researches on, is an effective means to alleviate the environmental vibration caused by urban rail transit [2, 3]. In this paper, the periodic isolation barrier is introduced into vibration isolation of metro given the characteristic of periodic structure with a band gap, and the frequency of band gap of periodic isolation barrier is calculated by transfer matrix method. The variation law of band gap frequency under different parameter combinations is concluded, and the applicability to vibration and noise reduction of urban rail transit is explored and studied.

S. Zhang (✉) · W. Wang · Y. Li · Z. Wu · X. Ma
CARS, Beijing 100081, China
e-mail: 303466906@qq.com

Periodic structure (phononic crystal) [4] is a composite composed of two or more kinds of elastic media arranged in periodic permutation and combination. Its basic characteristic is band gap. When an elastic wave propagates in a periodic structure, due to the special structure and material characteristics, elastic waves in a certain frequency range stop propagating. This frequency range is called the band gap [5, 6]. The band gap characteristic makes periodic structures which have a very broad prospect in vibration and noise reduction.

1   Analysis of Band Gap of Periodic Isolation Barrier

1.1   Transfer Matrix Method

Transfer matrix method starts with the basic equations of continuous state parameters (stress, particle displacement, etc.), combines the interface continuity condition, and obtains transfer matrix of a single period. By introducing the periodic boundary condition, the corresponding dispersion relation is obtained, that is, the band structure. The band gap frequency and attenuation coefficient of periodic isolation barrier can be calculated by the transfer matrix method.

1.1.1   Derivation of Transfer Matrix

Figure 1 is a diagram of the structure of one-dimensional phononic crystal. In the diagram, two materials A and B with different elastic constants and densities are arranged alternately in the x-direction to form one-dimensional periodic structure. a_1 and a_2, respectively, indicate the thickness of material A and material B in a period. $a = a_1 + a_2$ is a crystal constant. Take the SH wave as an example here, and the process of calculating band gap frequency and attenuation coefficient by the transfer matrix method is described. In other directions, the infinite length is assumed. The densities of the two materials are marked as ρ_1 and ρ_2, respectively, and c_1 and c_2 represent the SH wave velocities of material A and B, respectively.

SH wave's one-dimensional wave equation is as follows:

$$\frac{\partial^2 u}{\partial^2 t} = c^2 \left(\frac{\partial^2}{\partial x^2} + \frac{\partial^2}{\partial z^2} \right) u(x, z, t) \tag{1}$$

Let $u(x, z, t)$ be the displacement at x, and given the time-harmonic plane wave, let $u(x, z, t) = U(x)e^{i(k_3 z - \omega t)}$ and ω be an angular frequency. From Formula (1), we can obtain the amplitude of the material A in the nth primitive cell:

Fig. 1 Structure of one-dimensional phononic crystal
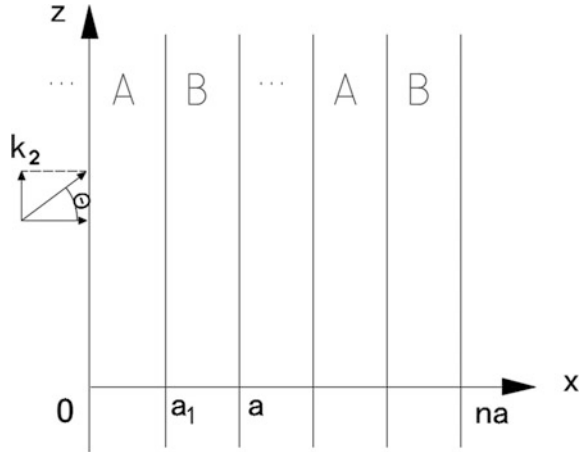
$$U_{n1}(x') = P_{n1}^{+} e^{i\alpha_1 x'} + P_{n1}^{-} e^{-i\alpha_1 x'} \tag{2}$$

In the formula, $\alpha_1 = \sqrt{k_3^2 - \left(\frac{\omega}{c_1^2}\right)^2}$ represents the wave number in the direction of x and P_{n1}^{+} and P_{n1}^{-}, respectively, the positive and negative propagation along the axis of x, and $x' = x - na$, while $na \leq x \leq na + a_1$.

Similarly, the amplitude of material B in the nth primitive cell is:

$$U_{n2}(x') = P_{n2}^{+} e^{i\alpha_2 x'} + P_{n2}^{-} e^{-i\alpha_2 x'} \tag{3}$$

In the formula, $\alpha_2 = \sqrt{k_3^2 - \left(\frac{\omega}{c_2^2}\right)^2}$ represents the wave number of material B in the direction of x and $x'' = x - na$, with the condition $na + a_1 \leq x \leq (n+1)a$.

When $x = na + a_1$, the displacement $u(x,t)$ and stress $\rho c^2 \frac{\partial u}{\partial x}$ of material A and material B, we obtain:

$$P_{n1}^{+} e^{i\alpha_1 a_1} + P_{n1}^{-} e^{-i\alpha_1 a_1} = P_{n2}^{+} e^{i\alpha_2 a_1} + P_{n2}^{-} e^{-i\alpha_2 a_1} \tag{4}$$

$$\rho_1 c_1^2 \alpha_1 \left(P_{n1}^{+} e^{i\alpha_1 a_1} - P_{n1}^{-} e^{-i\alpha_1 a_1}\right) = \rho_1 c_2^2 \alpha_2 \left(P_{n2}^{+} e^{i\alpha_2 a_1} - P_{n2}^{-} e^{-i\alpha_2 a_1}\right) \tag{5}$$

Write the Formulas (4) and (5) into a matrix form

$$K_1 \Psi_{n2} = H_1 \Psi_{n1} \tag{6}$$

In the formula, $\Psi_{n2} = [P_{n2}^{+} \ P_{n2}^{-}]^{\mathrm{T}}$ and $\Psi_{n1} = [P_{n1}^{+} \ P_{n1}^{-}]^{\mathrm{T}}$
From the displacement and stress at $x = na$, we can obtain

$$P_{n1}^+ + P_{n1}^- = P_{(n-1)2}^+ e^{i\alpha_2 a} + P_{(n-1)2}^- e^{-i\alpha_2 a} \tag{7}$$

$$\rho_1 c_1^2 \alpha_1 \left(P_{n1}^+ - P_{n1}^- \right) = \rho_1 c_1^2 \alpha_2 \left(P_{(n-1)2}^+ e^{i\alpha_2 a} - P_{(n-1)2}^- e^{-i\alpha_2 a} \right) \tag{8}$$

Write the Formulas (7) and (8) into a matrix form:

$$\boldsymbol{K}_2 \boldsymbol{\varPsi}_{(n-1)2} = \boldsymbol{H}_2 \boldsymbol{\varPsi}_{n1} \tag{9}$$

The relationship between nth cell and n-1st cell can be obtained from Eqs. (6) and (9):

$$\boldsymbol{\varPsi}_{n2} = \boldsymbol{T} \boldsymbol{\varPsi}_{(n-1)2} \tag{10}$$

In the formula, $\boldsymbol{T} = \boldsymbol{K}_1^{-1} \boldsymbol{H}_1 \boldsymbol{H}_2^{-1} \boldsymbol{K}_2$ is the transfer matrix.

1.1.2 Calculation of Energy Band Structure

Considering the periodicity of the *x*-direction, we can get the following equation by using the Bloch theorem:

$$\boldsymbol{\varPsi}_{n2} = \boldsymbol{e}^{ika} \boldsymbol{\varPsi}_{(n-1)2} \tag{11}$$

In the formula, k is a one-dimensional Bloch wave vector which is written in scalar form.

The standard matrix eigenvalue problem can be obtained by substituting (11) in (10).

$$\left| \boldsymbol{T} - e^{ika} \boldsymbol{I} \right| = 0 \tag{12}$$

In the formula, $\boldsymbol{I}$ is a unit matrix of 2×2.

The dispersion relation between wave vector k and frequency ω can be obtained by solving the eigenvalue of the matrix $\boldsymbol{T}$:

$$\cos(ka) = \cosh(\alpha_1 a_1) \cosh(\alpha_2 a_2) + \frac{1}{2} \left(F + \frac{1}{F} \right) \sinh(\alpha_1 a_1) \sinh(\alpha_2 a_2) \tag{13}$$

In the formula, $F = \frac{\alpha_1 \rho_1 C_1^2}{\alpha_2 \rho_2 C_2^2}$.

The relevant band gap frequency and attenuation coefficient can be obtained by scanning the concerned frequency range.

1.2 Calculation of Band Gap Frequency

The band gap frequency of periodic isolation barrier is calculated by using the transfer matrix method mentioned above. The parameters are shown in Fig. 1. The results are shown in Fig. 2. In the left figure, the abscissa is the wave vector k, and the ordinate is the frequency f. The first two attenuation zones are 25.4–92.4 Hz and 102.3–183.2 Hz. The two lines in the right figure represent the attenuation coefficient corresponding to the band gap. At the intermediate frequency of the band gap, the attenuation coefficient reaches the maximum, and with the increase or decrease of the frequency, the attenuation coefficient decreases gradually. The attenuation coefficient is the lowest at the lower bound frequency and upper bound frequency. It can be found from the figure that the first gap of periodic isolation barrier composed of rigid material and elastic material which is close to the ambient vibration frequency caused by metro operation, so this paper only studies the law of the first band gap, and the band gap hereinafter refers to the first band gap (Table 1).
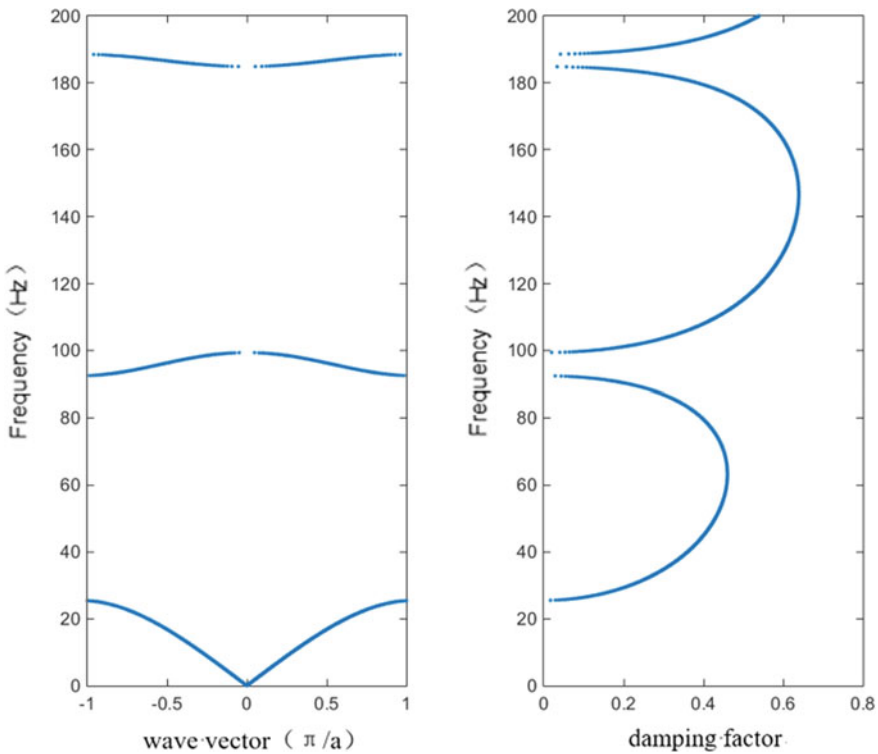
Fig. 2 Band gap frequency and attenuation coefficient of periodic barrier

Table 1 Periodic barrier parameters

	Elastic moduli (MPa)	Density (kg/m^3)	Poisson's ratio	Thickness (m)
Elastic material	1.5	1000	0.3	0.15
Rigid material	28,500	2500	0.2	0.3

2 Research on the Parameters of Periodic Isolation Barrier

In this section, the variation law of band gap frequency of periodic isolation barrier with parameters is analyzed, which include elastic moduli of material, the density of material, and thickness of the barrier. We only transform a single variable in this part, and other parameter values are described by the data in Fig. 1. The band gap characteristics are described by three parameters: lower bound frequency (LBF), upper bound frequency (UBF), and width attenuation zone (WAZ). By studying the influence of each parameter on the band gap frequency of periodic isolation barrier, the vibration isolation barrier with engineering application value is designed for the main vibration frequency band of urban rail transit.

2.1 Elastic Moduli

The influence of elastic moduli of rigid material on the band gap frequency of periodic isolation barrier is analyzed. The value range of rigid material is 22–40 GPa, as shown in Fig. 3. It can be seen that the three parameters are in a linear state. The elastic moduli of rigid material have little effect on the band gap frequency. The parameter can be determined mainly from the aspects of structural security and economy.

The influence of the elastic moduli of an elastic material on the band gap frequency of periodic isolation barrier is analyzed. The value range of elastic material is 1–6 MPa, as shown in Fig. 4. It can be seen with the increase of elastic moduli of elastic material LBF, UBF and WAZ of the band gap of the isolation barrier gradually increase, and the elastic moduli of elastic material have a big influence on the band gap frequency. The band gap frequency of the periodic barrier can be adjusted by controlling the elastic moduli of the elastic material.
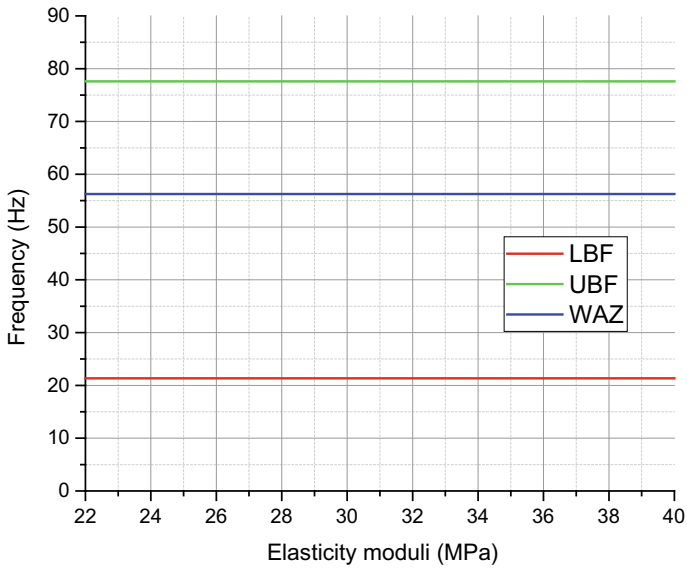
Fig. 3 Influence of elastic moduli of rigid materials on band gap frequency
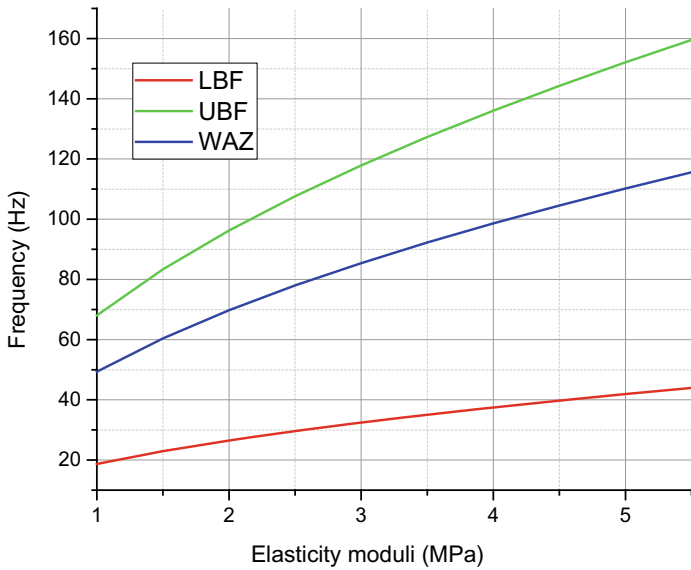
Fig. 4 Influence of the elastic moduli of an elastic material on the band gap frequency

2.2 Thickness

The effect of the thickness of rigid material on the band gap frequency of periodic isolation barrier is analyzed. The thickness of the rigid material is 0.2–0.65 m. The calculation result is shown in Fig. 5. It can be seen from the figure that with the increase of the thickness of rigid material LBF of band gap decreases slowly, UBF is basically unchanged, and WAZ of rigid material has no obvious effect on the band gap frequency. The determination of this parameter can be mainly based on structural safety and economy.

The influence of elastic material thickness on the band gap frequency of periodic isolation barrier is analyzed. The thickness of the elastic material is 0.1–0.3 m. The results are shown in Fig. 6, which displays that LBF, UBF, and WAZ of band gap decrease gradually with the increase of elastic material thickness. Therefore, the thickness of the elastic material has a great influence on the band gap frequency. The band gap frequency of periodic vibration barrier can be adjusted by controlling the thickness of the elastic material.

2.3 Density

The influence of the rigid material density on the band gap frequency of the periodic isolation barrier is analyzed. The density of rigid material is 1500–2900 kg/m^3. As in Fig. 7, it can be seen that with the increase of density of
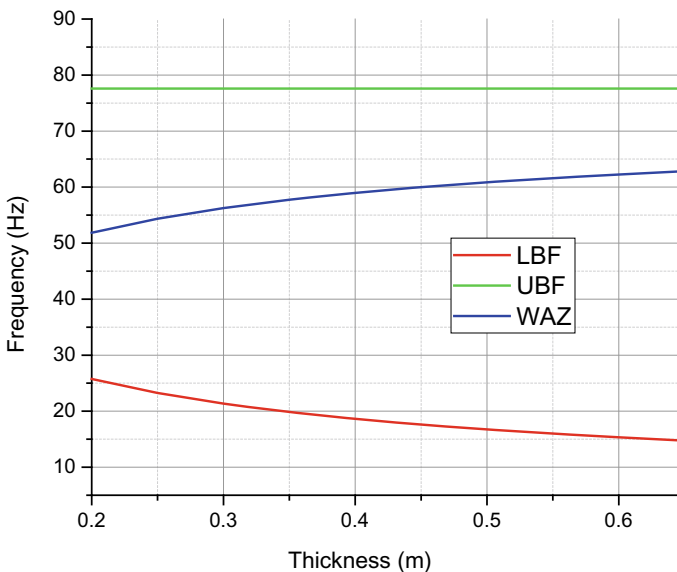
Fig. 5 Influence of rigid material thickness on band gap frequency
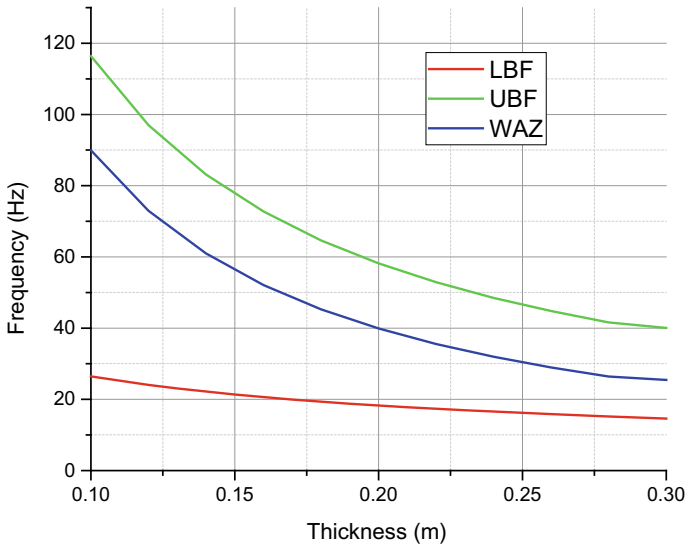
Fig. 6 Influence of elastic material thickness on band gap frequency
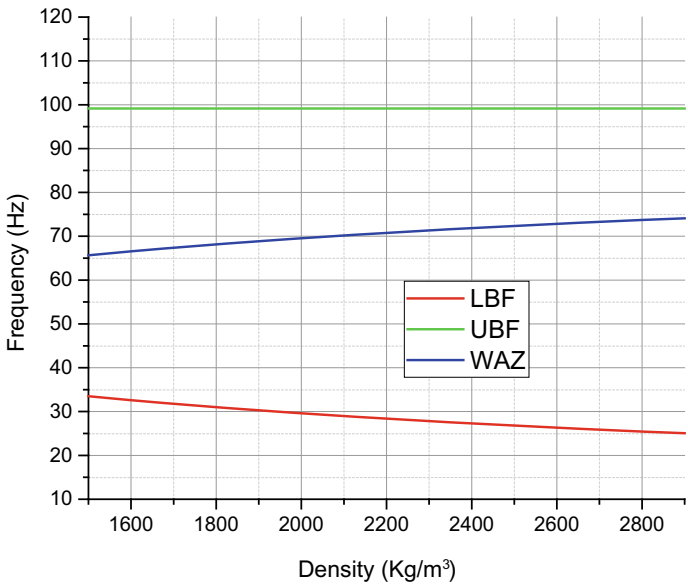
Fig. 7 Influence of rigid material density on band gap frequency
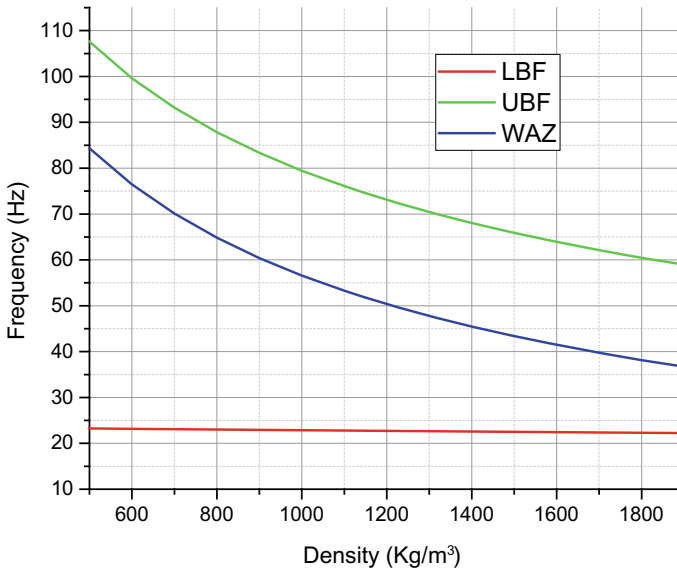
Fig. 8 Influence of elastic material density on band gap frequency

rigid material LBF of band gap decreases slowly, UBF is basically unchanged, and WAZ increases slowly. The change in the density of rigid material has no obvious effect on the band gap frequency. The determination of this parameter can be mainly based on structural safety and economy.

The influence of elastic material density on the band gap frequency of periodic isolation barrier is analyzed. The density of the elastic material is 500–1900 kg/m^3. The calculated results are shown in Fig. 8. It can be seen that LBF, UBF, and WAZ of band gap decrease gradually with the increase of elastic material thickness. The density of elastic material has a great influence on the band gap frequency. The band gap frequency of the periodic vibration isolation barrier can be adjusted by controlling the thickness of the elastic material.

3   Field Test of Vibration Acceleration of Vibration Source

3.1   Field Test

In order to obtain the frequency of vibration of the nearby soil when the subway train passes, the field test of vibration acceleration is carried out on the ground next to a subway line in Beijing. The track form is a normal monolithic ballast bed track. The field test point is shown in Fig. 9.

The field acceleration sensor test point arrangement is shown in Fig. 10.
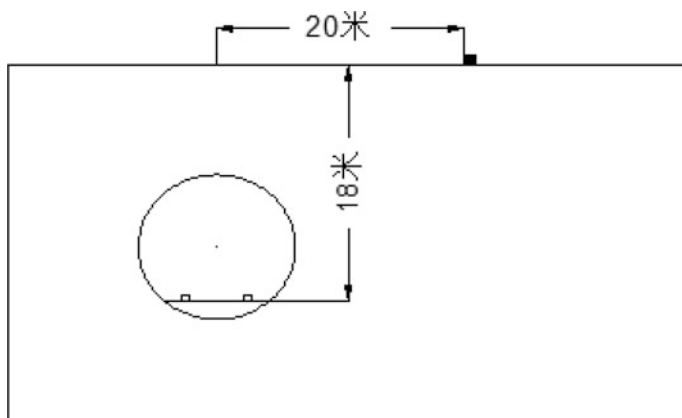
Fig. 9 Diagram of test points

Fig. 10 Field test point arrangement

The acceleration time history and frequency spectrum at the surface test points are shown in Figs. 11 and 12. It can be seen that the main frequency of the ground vibration acceleration is 35–60 Hz.
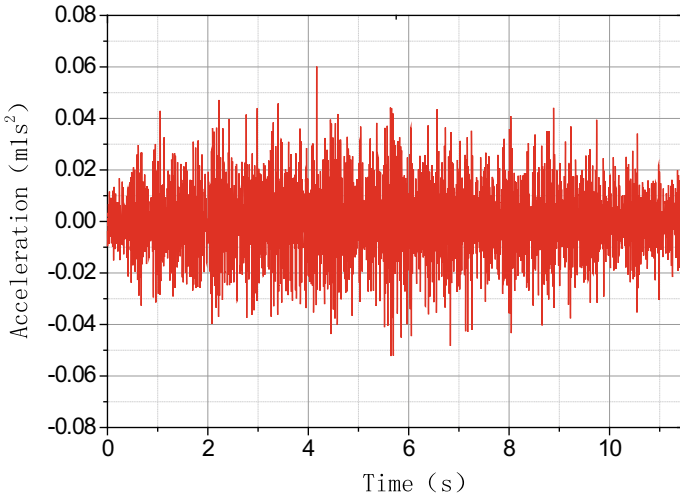
Fig. 11 Acceleration time history at test points
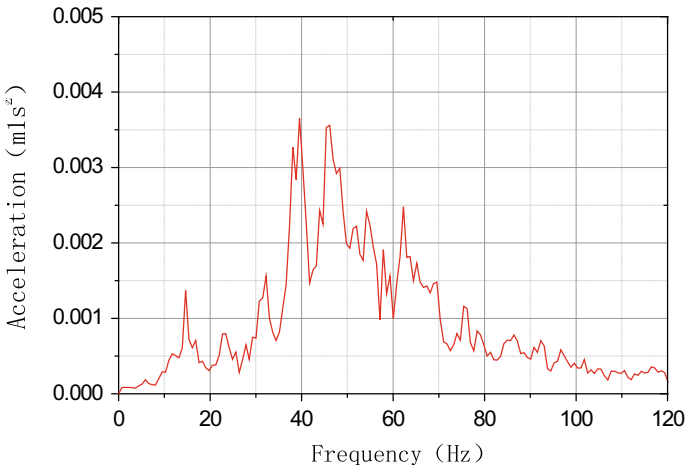
Fig. 12 Acceleration spectrum at test points

3.2   Final Solution

The vibration frequency of soil by field test is mainly between 35 and 60 Hz. Combining the research on the law of influencing factors on the band gap of the periodic isolation barrier and the feasibility of the solution, the following solution is adopted: A continuous barrier consisting of alternately rigid and elastic materials in

a sandwich type is used for periodic isolation barriers, with both ends being rigid material outside. The thickness of rigid material is 0.3 m, elastic material is 0.15 m, and the period constant is 0.45 m. The material parameters are shown in Fig. 1.

4 Conclusion

Based on the band gap theory of phononic crystals, this paper uses transfer matrix method to study the influence of elastic moduli, density, and thickness of materials on the variation law of band gap of periodic isolation barrier, and in view of the vibration characteristics of nearby soil caused by urban rail transit operation, the barrier layout parameters corresponding to the frequency band of vibration isolation are designed, and the following conclusions are obtained:

(1) The frequency of vibration characteristics of nearby soil caused by urban rail transit operation under the normal ballast track type is 35–60 Hz;
(2) The frequency of the first gap of periodic isolation barrier is similar to that of the nearby soil caused by urban rail transit, and the vibration isolation barrier with engineering application value can be designed by adjusting the parameters of the barrier for the main vibration frequency band of urban rail transit;
(3) The elastic moduli, density, and thickness of rigid materials have little effect on the frequency of band gap of the periodic isolation barrier, and the parameters can be designed mainly from structural safety and economy.
(4) The elastic moduli, density, and thickness of elastic materials have great influence on the band gap frequency of periodic isolation barrier, and according to the main vibration frequency of the vibration isolation, the corresponding band gap frequency can be designed by adjusting related parameters, so as to give full play to the vibration damping effect of the periodic vibration isolation barrier.

References

1. Zhang S (2016) Study on prediction of vibration and re-radiated noise in buildings caused by subway trains. Beijing Jiaotong University
2. Wang W (2011) Study on metro train-induced environmental vibration and transfer function prediction based on pulse experiment method. Beijing Jiaotong University
3. Wu Z, Liu W, Ma L, Wang W (2014) Frequency domain analytical method for predicting metro environmental vibration based on soil frequency response function. Chin Railway Sci 05:105–112
4. Wen X, Wen J, Yu D et al (2009) Phononic crystals. National Defense Industry Press
5. Huang J (2014) Application of periodic pile barriers and wave barriers to reduce vibration in civil engineering. Beijing Jiaotong University
6. Wen J, Wang G, Yu D et al (2007) Study on vibration band gap and vibration damping characteristics of phononic crystals. Sci Chin (Technol Sci) 1126–1139

Vibration Reduction with Rows of Arbitrarily Arranged Elastic Piles in Saturated Soil by Multiple Scattering Method

Miaomiao Sun, Huangding Zhu, Xinjiang Wei, Huajian Fang
and Lianying Zhou

Abstract An analytical solution of elastic waves scattered by a series of arbitrarily arranged cylindrical piles in saturated soils is achieved based on Biot's poroelastic theory and multiple scattering method in acoustics and electromagnetics. The elastic waves are expanded by cylindrical functions with undetermined complex coefficients, and the first order of scattering is satisfied with the boundary conditions at the certain pile; therefore, the coefficients of the first-order scattering are obtained. Subsequently, regarding the first order of scattering waves as the secondary excitation to the remaining piles, it is also contented with required boundary conditions; thus, the second order of undetermined complex coefficients are acquired by generalized Graf's addition theorem. The successive scattering could be repeated as the same manner. The vibration reduction of elastic waves by rows of piles is calculated. The numerical results demonstrate that the defection of neglecting subsequent scattering waves' coherence has been corrected by considering scattering waves as every secondary wave source in multiple scattering theory. It is also discussed the main parameters influencing the vibration reduction effect such as scattering orders, separations between piles, distances between pile rows, shear modulus ratio of pile and soil and barrier size, and several significant suggestions of optimal design are concluded.

Keywords Multiple scattering · Elastic piles · Elastic waves · Saturated soil · Ground vibration

M. Sun · X. Wei · L. Zhou
Department of Civil Engineering, Zhejiang University City College, 310015 Hangzhou, China

H. Zhu (✉)
Research Center of Coastal and Urban Geotechnical Engineering, Zhejiang University, 310058 Hangzhou, China
e-mail: 346513823@qq.com

H. Fang
Zhejiang Provincial Key Laboratory of Hydraulics Disaster Prevention and Mitigation, Zhejiang Institute of Hydraulics and Estuary, 310020 Hangzhou, China

1 Introduction

Environmental vibration factors, such as artificial traffic and construction vibrations, have become an increasingly severe problem to those who live in modern cities. There are two mainstream approaches to block artificial vibration, the continuous barrier and the discontinuous barrier. Although the research on discontinuous barrier has a later start than that on continuous barrier, it has been widely acceptable and applicable because of its convenience, construct, low cost, effectively isolation properties, etc. The discontinuous barrier has been adopted in coastal areas of China recently, especially at the region of soft soil with higher underwater level. The pile rows, which is one kind of the discontinuous barrier, can not only resolve the construction difficulties, but also cover the shortage of continuous barriers (in-filled and open trenches), for the latter are incapable of screening incident wave with longer wavelength, which shed the constraint of the barrier depth.

Woods et al. [1] initiated to investigate the R wave vibration isolation characteristics by cavity barrier with the technology of holographic, and he introduced the normalized displacement amplitude to evaluate the isolation effectiveness. Liao and Sangery [2] established an acoustical propagation model to simulate the isolating effect of pile rows; they considered that the vibration isolation effect is related to the relative stiffness of the soil around the piles. Gao et al. [3] proposed the difference between the near-field and far-field vibration barrier for the first time and indicated that the isolation property depends on the scattering effect. Xia et al. [4, 5] employed a more integrated Fourier-Bessel series function expansion to study the elastic wave scattering problem in vibration isolation barrier. Xu et al. [6, 7] utilized the complex variables functions and conformal mapping method to analyze the displacement variation at the front and back of the barrier, and he investigated both single-row and multi-row solid piles. Sun et al. [8, 9] theoretically solved the scattering problems of body waves and surface waves encountering discontinuous barriers (solid and tubular pile rows) with arbitrary shapes and configuration by introducing the multiple scattering theory from acoustical and electromagnetics. Liu and Wang developed [10] a high-precise indirect boundary integral method to calculate the 2D isolating broadband of plane P and SV waves by pile groups. Lu [11, 12] et al. raised a new type of pile-row system, which is called linked pile rows. Ding et al. [13] researched the correlation between the scattering coefficients, transmitting coefficient, the density of barrier, the Poisson's ratio and elastic modulus when the elastic barrier is confronted with the incident of S waves.

However, the research above mostly concentrated on elastic wave propagation in elastic medium, which has not consisted with the fact that the coastal region soil has high water content and is almost saturated. It gains certain errors by assuming those soils to the elastic medium. It is much appropriate to take into account the coupling scattering effect by both soil skeleton and pore fluid. Therefore, based on Biot's [14, 15] propagation theory, it is transformed the potential function to be at the polar coordinate system with wave function expansion method. With the elastic boundary conditions such as soil skeleton and pore fluid displacement continuity, total stress

continuity and fluid pressure continuity, it is obtained the P waves' scattering and transmitted properties by elastic discontinuous barriers constituted of arbitrarily arranged and arbitrary configuration piles, and the total wave field is acquired as well. Specific numerical examples, focused on the parameters of scattering orders, pile separations, distances between pile rows, number of piles, pile–soil shear modulus ratio, etc., have been carried out and analyzed.

2　Methodology

2.1　Analysis Model

Assuming a far-field point K is the research object, the geometric model and analysis coordinate system is depicted in Fig. 1. The incident P waves are incoming to a series of cylindrical piles embedded in the saturated medium with the incident angle of θ_0. Setting a center of any elastic pile as the origin and establishing a rectangular coordinate system, the coordinates of point K related to the specific pile o refer to r, θ; then, setting another center of an elastic pile s as the origin of the coordinates system, the coordinates of point K related to the specific pile s refer to r_s, θ_s, etc. The relative coordinates of the piles are set as follows: The coordinates of pile s related to pile o are r_{os}, θ_{os}, etc., and the coordinates of pile s' related to pile o are $r_{os'}$, $\theta_{os'}$ etc.

Fig. 1 Geometric model and analysis coordinate system
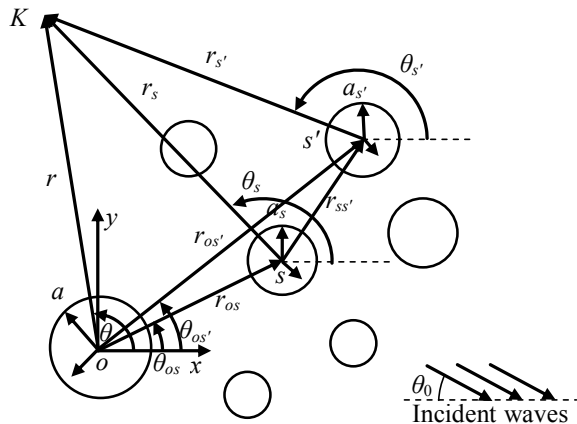
2.2 *Governing Equations and Solutions*

It occurs coupling scattering when the *P* waves are incident into the saturated medium. There are compressional fast wave P_1, compressional slow wave P_2 and shear wave *S*. The P_2 waves are neglected in elastic wave propagation by artificial vibration because they have rapid attenuation, and their energy proportion appears low in saturated soil. Thus, only P_1 waves are taken into consideration.

Potential function expansion of incident *P* wave under cylindrical coordinates by Fourier-Bessel series is

$$\substack{s \\ s}\phi^{\mathrm{inc}} = \mathrm{e}^{\mathrm{i}\alpha_{1s}r_{0s}(\theta_0 + \theta_{0s})} \sum_{n=-\infty}^{+\infty} \mathrm{J}_n(\alpha_{1s}r_s)\mathrm{e}^{\mathrm{i}n\varphi_s}\mathrm{e}^{-\mathrm{i}\omega \mathrm{t}} \tag{1}$$

where superscript inc of ϕ represents incident *P* waves and *s* indicates the *s*th pile, subscript *s* stands for soil skeleton, $\mathrm{J}_n(\cdot)$ is the *n*th order of Bessel function, α_{1s} is a wave number of incident *P* waves, while subscript 1(2) means $P_{1(2)}$, *s* means soil skeleton, $\varphi_s = \theta_s + \theta_0 + \pi/2$, exp $(-\mathrm{i}\omega \mathrm{t})$ is omitted for simplification because all the stimulation and response conclude this time factor.

For heterogeneous cylinders, scattering waves consist of P_1, P_2 and SV waves, which are

$$\substack{s \\ s}\phi_m^{\mathrm{sc}} = \sum_{n=-\infty}^{+\infty} {}^s A_m \mathrm{H}_n^{(1)}(\alpha_{1s}r_s)\mathrm{e}^{\mathrm{i}n\theta_s} \tag{2a}$$

$$\substack{s \\ \mathrm{f}}\phi_m^{\mathrm{sc}} = \sum_{n=-\infty}^{+\infty} {}^s B_m \mathrm{H}_n^{(1)}(\alpha_{2s}r_s)\mathrm{e}^{\mathrm{i}n\theta_s} \tag{2b}$$

$$\substack{s}\psi_m^{\mathrm{sc}} = \sum_{n=-\infty}^{+\infty} \mathrm{i}^s C_m \mathrm{H}_n^{(1)}(\beta_s r_s)\mathrm{e}^{\mathrm{i}n\theta_s} \tag{2c}$$

$$\substack{s}\chi_m^{\mathrm{sc}} = \xi_{11}\substack{s \\ s}\phi_m^{\mathrm{sc}} + \xi_{12}\substack{s \\ \mathrm{f}}\phi_m^{\mathrm{sc}} \tag{2d}$$

$$\substack{s}\Theta_m^{\mathrm{sc}} = \xi_{12}\,\substack{s}\psi_m^{\mathrm{sc}} \tag{2e}$$

where $H_n(\cdot)$ is the *n*th order of Hankel function, superscript (1) or (2) indicates the function kind, ${}^sA_m$, ${}^sB_m$ and ${}^sC_m$ are the *m*th order of scattering coefficients of the *s*th pile. The coupling scattering wave functions are named as ${}^s\chi_m^{\mathrm{sc}}$ and ${}^s\Theta_m^{\mathrm{sc}}$, consisted of scattering wave potential of $\substack{s \\ s}\phi_m^{\mathrm{sc}}$, $\substack{s \\ \mathrm{f}}\phi_m^{\mathrm{sc}}$ and ${}^s\psi_m^{\mathrm{sc}}$, which is combined with the coefficients as ξ_{11}, ξ_{12} and ξ_{13}. The transmitted waves are expressed by the expansion Bessel series of ${}^sD_m\mathrm{H}_n^{(1)}(\alpha_{1\mathrm{p}}r_s)$, ${}^sE_m\mathrm{H}_n^{(2)}(\alpha_{2\mathrm{p}}r_s)$, ${}^sF_m\mathrm{H}_n^{(1)}(\alpha_{2\mathrm{p}}r_s)$. ${}^sD_m$, ${}^sE_m$ and ${}^sF_m$ are the *m*th order of transmitted coefficients of the *s*th pile. The coupling transmitted waves functions are also named as ${}^s\chi_m^{\mathrm{t}}$ and ${}^s\Theta_m^{\mathrm{t}}$, consisted of

transmitted wave potential of ${}_s^s\phi_m^t$, ${}_f^s\phi_m^t$ and ${}^s\psi_m^t$, which is combined with the coefficients as ξ_{21}, ξ_{22} and ξ_{23}.

$$
{}_s^s\phi_m^t = \sum_{n=-\infty}^{+\infty} D_m H_n(\alpha_{1p} r_s)\, e^{in\theta_s} \tag{3a}
$$

$$
{}_f^s\phi_m^t = \sum_{n=-\infty}^{+\infty} E_m H_n(\alpha_{2p} r_s)\, e^{in\theta_s} \tag{3b}
$$

$$
{}^s\psi_m^t = \sum_{n=-\infty}^{+\infty} i F_m H_n(\beta_p r_s)\, e^{in\theta_s} \tag{3c}
$$

$$
{}^s\chi_m^t = \xi_{21}{}_s^s\phi_m^t + \xi_{22}{}_f^s\phi_m^t \tag{3d}
$$

$$
{}^s\Theta_m^t = \xi_{23}\,{}^s\psi_m^t \tag{3e}
$$

where subscript p represents the pile, sc and t as the superscript on the right side indicate scattering and transmitted waves separately, and subscript m indicates the scattering orders.

Assuming pile–soil interface satisfies the elastic boundary conditions at the first order of scattering, the soil skeleton displacement is continuous:

$$
\left[u_{r_s}^{inc}(r_s, \theta_s) + {}^su_{1r_s}^{sc}(r_s, \theta_s)\right]\Big|_{r_s=a_s} = {}^su_{1r_s}^t(r_s, \theta_s)\Big|_{r_s=a_s} \tag{4a}
$$

$$
\left[u_{\theta_s}^{inc}(r_s, \theta_s) + {}^su_{1\theta_s}^{sc}(r_s, \theta_s)\right]\Big|_{r_s=a_s} = {}^su_{1\theta_s}^t(r_s, \theta_s)\Big|_{r_s=a_s} \tag{4b}
$$

The radial relative displacement of the pore fluid is also continuous:

$$
\left[{}_fw^{inc}(r_s, \theta_s) + {}_f^sw_1^{sc}(r_s, \theta_s)\right]\Big|_{r_s=a_s} = {}_f^sw_1^t(r_s, \theta_s)\Big|_{r_s=a_s} \tag{4c}
$$

The total stress is continuous:

$$
\left[\sigma_{r_sr_s}^{inc}(r_s, \theta_s) + {}^s\sigma_{1r_sr_s}^{sc}(r_s, \theta_s)\right]\Big|_{r_s=a_s} = {}^s\sigma_{1r_sr_s}^t(r_s, \theta_s)\Big|_{r_s=a_s} \tag{4d}
$$

$$
\left[\sigma_{r_s\theta_s}^{inc}(r_s, \theta_s) + {}^s\sigma_{1r_s\theta_s}^{sc}(r_s, \theta_s)\right]\Big|_{r_s=a_s} = {}^s\sigma_{1r_s\theta_s}^t(r_s, \theta_s)\Big|_{r_s=a_s} \tag{4e}
$$

And the pore fluid stress is continuous:

$$
\left[{}_f\,p_{inc}(r_s, \theta_s) + {}_f^sp_1^{sc}(r_s, \theta_s)\right]\Big|_{r_s=a_s} = {}_f^sp_1^t(r_s, \theta_s)\Big|_{r_s=a_s} \tag{4f}
$$

The relationship of potential function, displacement and stress under the cylindrical coordinates in saturated soil is

$$^s u_{r_s} = \frac{\partial_s^s \phi}{\partial r_s} + \frac{1}{r_s} \frac{\partial^s \psi}{\partial \theta_s} \tag{5a}$$

$$^s u_{\theta_s} = \frac{1}{r_s} \frac{\partial_s^s \phi}{\partial \theta_s} - \frac{\partial^s \psi}{\partial r_s} \tag{5b}$$

$$^s_f w = \frac{\partial^s \chi}{\partial r_s} + \frac{1}{r_s} \frac{\partial^s \Theta}{\partial \theta_s} \tag{5c}$$

$$^s \sigma_{r_s r_s}(r_s, \theta_s) = \lambda \left(\frac{\partial^2 {}_s^s \phi}{\partial r_s^2} + \frac{1}{r_s} \frac{\partial_s^s \phi}{\partial r_s} + \frac{1}{r_s^2} \frac{\partial^2 {}_s^s \phi}{\partial \theta_s^2} \right) + 2G \left[\frac{\partial^2 {}_s^s \phi}{\partial r_s^2} + \frac{\partial}{\partial r_s} \left(\frac{1}{r_s} \frac{\partial^s \psi}{\partial \theta_s} \right) \right]$$
$$+ \eta M \left(\frac{\partial^2 {}^s \chi}{\partial r_s^2} + \frac{1}{r_s} \frac{\partial^s \chi}{\partial r_s} + \frac{1}{r_s^2} \frac{\partial^2 {}^s \chi}{\partial \theta_s^2} \right) \tag{5d}$$

$$^s \sigma_{r_s \theta_s}(r_s, \theta_s) = G \left(\frac{2}{r_s} \frac{\partial^2 {}_s^s \phi}{\partial r_s \partial \theta_s} - \frac{2}{r_s^2} \frac{\partial_s^s \phi}{\partial \theta_s} + \frac{1}{r_s^2} \frac{\partial^{2s} \psi}{\partial \theta_s^2} - \frac{\partial^2 {}^s \psi}{\partial r_s^2} + \frac{1}{r_s} \frac{\partial^s \psi}{\partial r_s} \right) \tag{5e}$$

$$-^s_f p(r_s, \theta_s) = M \left(\frac{\partial^2 {}^s \chi}{\partial r_s^2} + \frac{1}{r_s} \frac{\partial^s \chi}{\partial r_s} + \frac{1}{r_s^2} \frac{\partial^2 {}^s \chi}{\partial \theta_s^2} \right) + \eta M \left(\frac{\partial^2 {}_s^s \phi}{\partial r_s^2} + \frac{1}{r_s} \frac{\partial_s^s \phi}{\partial r_s} + \frac{1}{r_s^2} \frac{\partial^2 {}_s^s \phi}{\partial \theta_s^2} \right) \tag{5f}$$

Substitute (1)–(4) into (5), omitted harmonic factor $e^{in\theta_s}$, the first order of scattering can be expressed as matrix $\mathbf{QX} = \mathbf{R}$, where $\mathbf{Q}$ is the scattering and transmitted coefficient matrix, $\mathbf{X}$ is the first order of undetermined scattering and transmitted coefficient matrix and $\mathbf{R}$ is an incident wave vector:

$$\sum_{n=-\infty}^{+\infty} \begin{bmatrix} q_{11} & q_{12} & \cdots & q_{1j} \\ q_{21} & q_{22} & \cdots & q_{2j} \\ \vdots & \vdots & \ddots & \vdots \\ q_{i1} & q_{i2} & \cdots & q_{ij} \end{bmatrix} \mathbf{X} = -{}^s\theta_\alpha \sum_{n=-\infty}^{+\infty} \begin{bmatrix} r_1 \\ r_2 \\ \vdots \\ r_i \end{bmatrix} \tag{6}$$

Subscripts of the element q_{ij}, r_j indicate $i = 1, 2, \ldots, 6$; $j = 1, 2, \ldots, 6$;

Cramer's law is used to solve this function. Substitute vector $\mathbf{R}$ to each column of $\mathbf{Q}$ and getting $\mathbf{P}_1, \mathbf{P}_2, \ldots \mathbf{P}_6$; then, the first order of scattering and transmitted coefficients are $\mathbf{X} = |\mathbf{P}_i/\mathbf{P}|$.

The wave transmitted by other cylinders in interference is supposed to be negligible; thus, the transmitted waves are disregarded as subsequent waves, and the

superposition is ignored. The mth ($m \geq 2$) scattering satisfied the elastic boundary conditions likewise:

$$\left[{}^s u^{sc}_{mr_s}(r_s, \theta_s) + \sum_{s'=0, s' \neq s}^{N'} {}'^{s'} u^{sc}_{(m-1)r_{s'}}(r_{s'}, \theta_{s'}) \right]\Bigg|_{r_s=a_s} = {}^s u^{t}_{mr_s}(r_s, \theta_s)\big|_{r_s=a_s} \quad (7a)$$

$$\left[{}^s u^{sc}_{m\theta_s}(r_s, \theta_s) + \sum_{s'=0, s' \neq s}^{N'} {}'^{s'} u^{sc}_{(m-1)\theta_{s'}}(r_{s'}, \theta_{s'}) \right]\Bigg|_{r_s=a_s} = {}^s u^{t}_{m\theta_s}(r_s, \theta_s)\big|_{r_s=a_s} \quad (7b)$$

$$\left[{}^s_f w^{sc}_m(r_s, \theta_s) + \sum_{s'=0, s' \neq s}^{N'} {}'^{s'}_f w^{sc}_{m-1}(r_{s'}, \theta_{s'}) \right]\Bigg|_{r_s=a_s} = {}^s_f w^{t}_m(r_s, \theta_s)\big|_{r_s=a_s} \quad (7c)$$

$$\left[{}^s \sigma^{sc}_{mr_s r_s}(r_s, \theta_s) + \sum_{s'=0, s' \neq s}^{N'} {}'^{s'} \sigma^{sc}_{(m-1)r_{s'} r_{s'}}(r_{s'}, \theta_{s'}) \right]\Bigg|_{r_s=a_s} = {}^s \sigma^{t}_{mr_s r_s}(r_s, \theta_s)\big|_{r_s=a_s} \quad (7d)$$

$$\left[{}^s \sigma^{sc}_{mr_s \theta_s}(r_s, \theta_s) + \sum_{s'=0, s' \neq s}^{N'} {}'^{s'} \sigma^{sc}_{(m-1)r_{s'} \theta_{s'}}(r_{s'}, \theta_{s'}) \right]\Bigg|_{r_s=a_s} = {}^s \sigma^{t}_{mr_s \theta_s}(r_s, \theta_s)\big|_{r_s=a_s} \quad (7e)$$

$$\left[{}^s_f p^{sc}_m(r_s, \theta_s) + \sum_{s'=0, s' \neq s}^{N'} {}'^{s'}_f p^{sc}_{m-1}(r_{s'}, \theta_{s'}) \right]\Bigg|_{r_s=a_s} = {}^s_f p^{t}_m(r_s, \theta_s)\big|_{r_s=a_s} \quad (7f)$$

$$s = 0, 1, 2 \ldots N, s' = 0, 1, 2 \ldots N, 0 \leq \theta_s \leq 2\pi, m \geq 2$$

Substitute (1)–(4) into (7), iteration relationship between mth and $(m-1)$th order of scattering is $\mathbf{QX = SY}$,

$$\sum_{n=-\infty}^{+\infty} \begin{bmatrix} q_{11} & q_{12} & \cdots & q_{1j} \\ q_{21} & q_{22} & \cdots & q_{2j} \\ \vdots & \vdots & \ddots & \vdots \\ q_{i1} & q_{i2} & \cdots & q_{ij} \end{bmatrix} \mathbf{X} = - \sum_{s'=0, s' \neq s}^{N'} {}' \sum_{n'=-\infty}^{+\infty} \sum_{n=-\infty}^{+\infty} \begin{bmatrix} s_{11} & s_{12} & \cdots & s_{1j} \\ s_{21} & s_{22} & \cdots & s_{2j} \\ \vdots & \vdots & \ddots & \vdots \\ s_{i1} & s_{i2} & \cdots & s_{ij} \end{bmatrix} \mathbf{Y} \tag{8}$$

where $\mathbf{X}$ is the mth order of undetermined scattering and transmitted complex coefficient matrix, $\mathbf{Y}$ is the $(m\text{-}1)$th order of scattering and transmitted coefficients matrix, $\mathbf{Q}$ is mentioned above and $\mathbf{S}$ is a vector. Therefore, the solution of total wave field can be acquired by generalized Graf's addition theory [8].

3 Numerical Results

The elastic barrier confronted with P waves was illustrated in Fig. 2, the length of piles is assumed as infinite, the radius is a_s, pile number is N, separation of piles is s_p, distance of pile rows is h and the barrier width is $L = (N - 1) \times s_p$. The steady-state P waves is incident in front of the pile barrier with the initial amplitude of ϕ_0, ψ_0, and the incident angle is $\theta_0 = \pi/2$.

The dimensionless displacement amplitude $|u/u_0|$ is introduced, which manifests the ratio of total displacement amplitude and incident displacement amplitude; the other geometric parameters are dimensionless as well. The mechanic calculation parameters of the media are listed in Table 1.

(a) Single row

(b) Double row
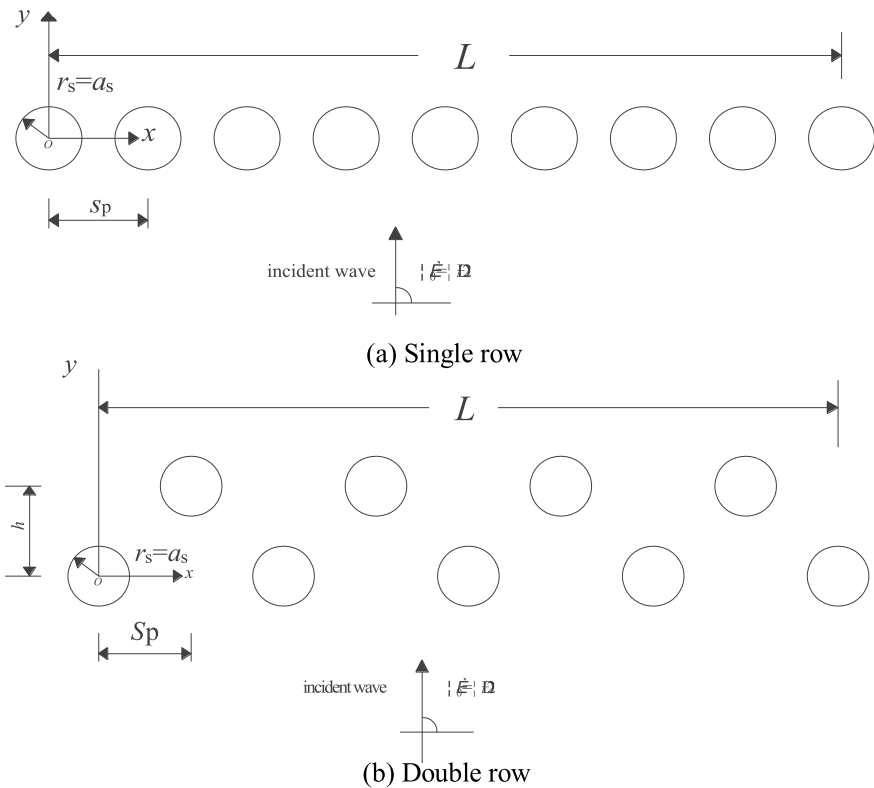
Fig. 2 Analysis model of elastic wave scattering by elastic solid pile barrier ($N = 9$)

Table 1 Physical parameters in saturated soil

G_1 (MPa)	M (MPa)	ρ_s (kg m^{-3})	ρ_f (kg m^{-3})	η	η_f	v_s	v_f
43.6	5000	1850	1000	0.94	0.65	0.4	0.5

3.1 Effect of Scattering Orders

The curves of dimensionless displacement amplitude variated with scattering orders are illustrated in Fig. 3. It presents amplitude amplification phenomenon at a certain range near the barrier ($0 \leq y/a_s \leq 50$). With the increase of the scattering order m, $|u/u_0|$ is decreasing gradually, and the increment is attenuating, with a trend of convergence; especially when the scattering order m values 3–4, there are few differences between the numerical calculation results. It is manifested that the multiple scattering assumption is credible, and a numerical truncation at $m = 4$ is reasonable while designing an elastic pile barrier.

3.2 Effect of Separations Between Piles

Figure 4 presents 3D $|u/u_0|$ meshes variated with multiple pile separations ($2.5 \leq s_p/a_s \leq 4.0$). A lowest $|u/u_0|$ value occurs at the area near the vibration source, which is the nearer distance from the barrier; the better reduction
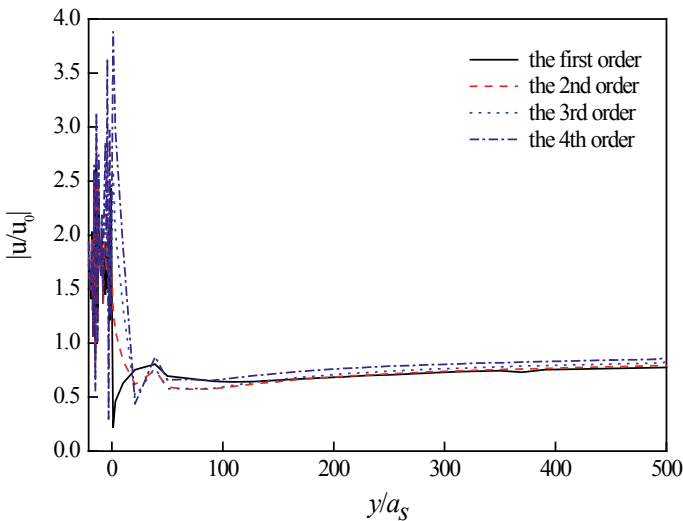
Fig. 3 Curves of dimensionless displacement amplitude of elastic pile with the variation of scattering orders ($\eta_{ps} = 0.45$, $\eta_{ss} = 0.8$, $\eta_{pw} = 0.65$, $s_p = 3.0a_s$, $h = 0a_s$, $1 \leq m \leq 4$, $N = 9$)

(a) $s_\mathrm{p} = 2.5a_s$

(b) $s_\mathrm{p} = 3.0a_s$

(c) $s_\mathrm{p} = 3.5a_s$

(d) $s_\mathrm{p} = 4.0a_s$
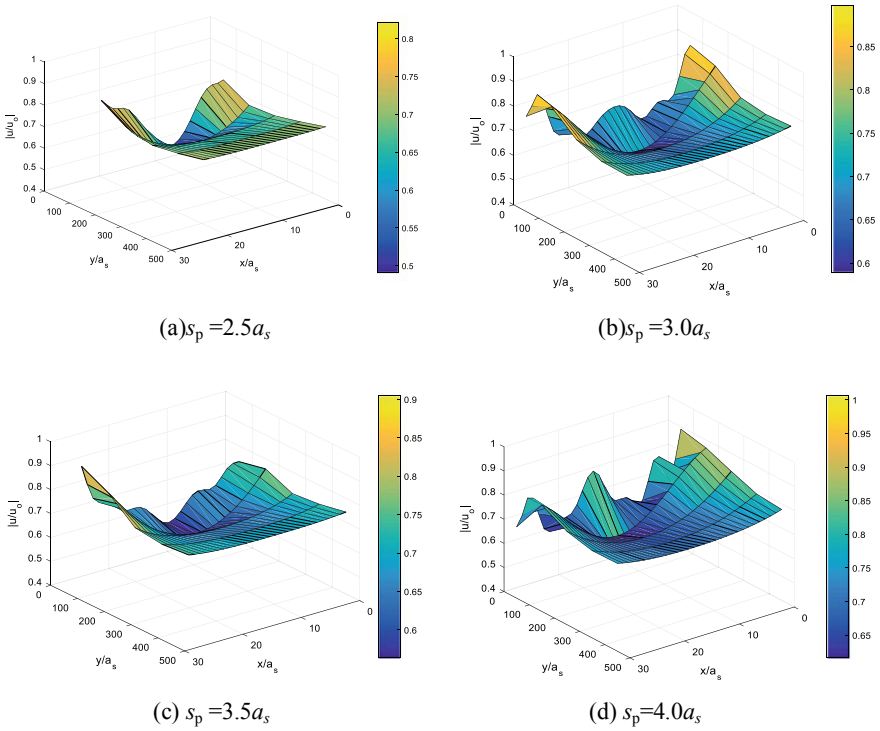
Fig. 4 Three-dimensional displacement mesh of dimensionless displacement amplitude with the variation of single-pile spacing ($\eta_\mathrm{pw} = 0.45$, $\eta_\mathrm{ss} = 0.80$, $\eta_\mathrm{pw} = 0.65$, $N = 9$, $h = 0a_s$)

effectiveness it receives, the weaker isolation appearance it gained at the farer distance from the barrier, and it is gradually convergent. The minimum value of $|u/u_0|$ is about 0.45 when pile separation $s_\mathrm{p}/a_s = 2.5$, and $|u/u_0|$ maintains between 0.70–0.75 at both sides after the barrier; a lower value of $|u/u_0|$ is founded at a certain distance ($|u/u_0| = 0.6$) from the barrier when pile separation $s_\mathrm{p}/a_s = 3.0$, and $|u/u_0| = 0.8$ is emerged at both sides after the barrier; $|u/u_0|$ increases to 0.5 near the barrier when pile separation $s_\mathrm{p}/a_s = 3.5$, and $|u/u_0|$ reaches to 0.85 at one side. When $s_\mathrm{p}/a_s = 4.0$, although lower displacement amplitude occurs near the barrier, $|u/u_0|$ is much higher at the most of the field. It is demonstrated that a discontinuous barrier is discrete as individuals when pile separation increases so that it cannot perform like an integrity to screen incident waves.

3.3 Effect of Distances Between Pile Rows

Figure 5 shows the contour map of $|u/u_0|$ behind double-row elastic pile barrier with the variation of normalized row-to-row distance h/a_s, and a range of $0 \leq h/a_s \leq 4.0$ has been investigated. When $h = 0$, double-row pile barrier is degenerated to single-row piles; it is obviously observed that $|u/u_0|$ increases from 0.55 to 0.65 when it is at the isolation area of $8 \leq x/a_s \leq 16$ and $0 \leq y/a_s \leq 150$, and the displacement amplitude reduction is about 35–45%; when $h/a_s = 2.5$, the barrier transforms to double-row piles; $|u/u_0|$ varies from 0.5 to 0.6 in a specific isolated distance of $8 \leq x/a_s \leq 16$, $0 \leq y/a_s \leq 150$, and the reduction effectiveness is about 40–50%, which indicates that the screening characteristics is performed better in double-row piles than in a single row if the pile numbers are the same. When $h/a_s = 3.0$, the displacement amplitude $|u/u_0|$ increases from 0.7 to 0.75 at the isolated range of $8 \leq x/a_s \leq 16$, $0 \leq y/a_s \leq 150$. When h/a_s increases to 4.0, the minimum dimensionless displacement amplitude $|u/u_0|$ is about 0.75. It is signified that the elastic pile barrier will disperse to solitary piles unless pile-row distance increases to a certain range. Therefore, an elastic pile barrier with $h/a_s \leq 3.0$ can capture no less than 40% incident waves regardless of single or double pile rows, in which it is a reference value of $2.5 \leq h/a_s \leq 3.0$ while designing the discontinuous barriers constituted with solid piles.

3.4 Effect of Shear Modulus Ratio of Pile and Soil

Contour of dimensionless displacement amplitude $|u/u_0|$ varies with the shear modulus ratio G_r of pile, and soil behind the elastic pile barrier is depicted in Fig. 6. It can be observed that the maximum value occurs at a certain area ($50 \leq y/a_s \leq 100$, $9 \leq x/a_s \leq 11$), where a reduction of 40–50% original value is received at the center of field, and a reduction of 25–30% is obtained on the two side of the field. When G_r enlarges 10 times (Fig. 6b, $G_r = 100$), $|u/u_0|$ reduces from 45 to 35%. In other words, the stiffer the barrier is, the weaker vibration isolation effect it will acquire. When $G_r = 1000$ increase to infinite (Fig. 6c, d), displacement amplification slows down, in which a weaker vibration isolation has been founded; when G_r dramatically increases, it is resulted from elastic pile barrier trend to be rigid. Therefore, the existence of fluid in saturated soil medium makes a superior reduction when elastic waves are incident to the lower stiffness pile barrier.

3.5 Effect of Barrier Size

Figure 7 showed midline variation curves of $|u/u_0|$ behind the barrier with the increasing of pile numbers. It is obviously seen displacement amplitude amplified

(a) $h=0a_s$

(b) $h=2.5a_s$

(c) $h=3.0a_s$

(d) $h=4.0a_s$
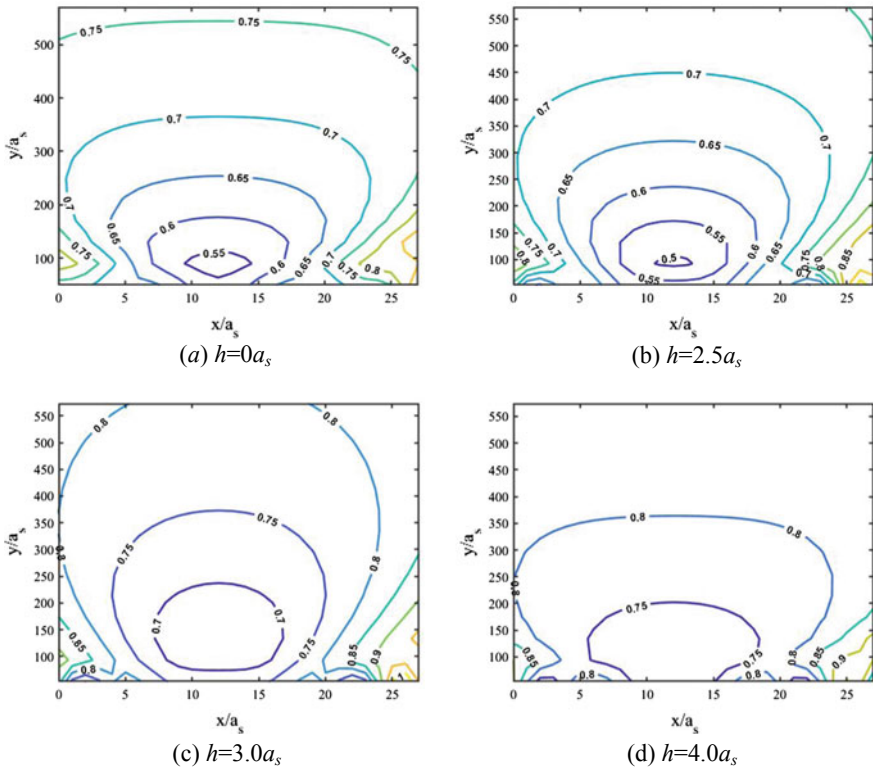
Fig. 5 Contour map of the displacement amplitude of multi-row elastic piles ($\eta_{ps} = 0.45$, $\eta_{ss} = 0.8$, $\eta_{pw} = 0.65$, $s_p = 3.0a_s$, $N = 9$)

phenomenon at a closer range behind the barrier, which is resulted from the coherent scattering property. With the distance from the barrier enlarges, dimensionless displacement amplitude $|u/u_0|$ modestly increases after a dramatically falling down to a minimum. The optimum isolation area is at a certain range away from the barrier ($25 \leq x/a_s \leq 100$) rather than close to the barrier. Secondly, the optimum vibration isolation range widens with the pile numbers increasing. A multiplied pile numbers generates ($N = 6$–12) a 30% increment of reduction effectiveness. Thus, increase of pile numbers effectively enhances the isolation effect, and the vibration hazard can be reduced accordingly.
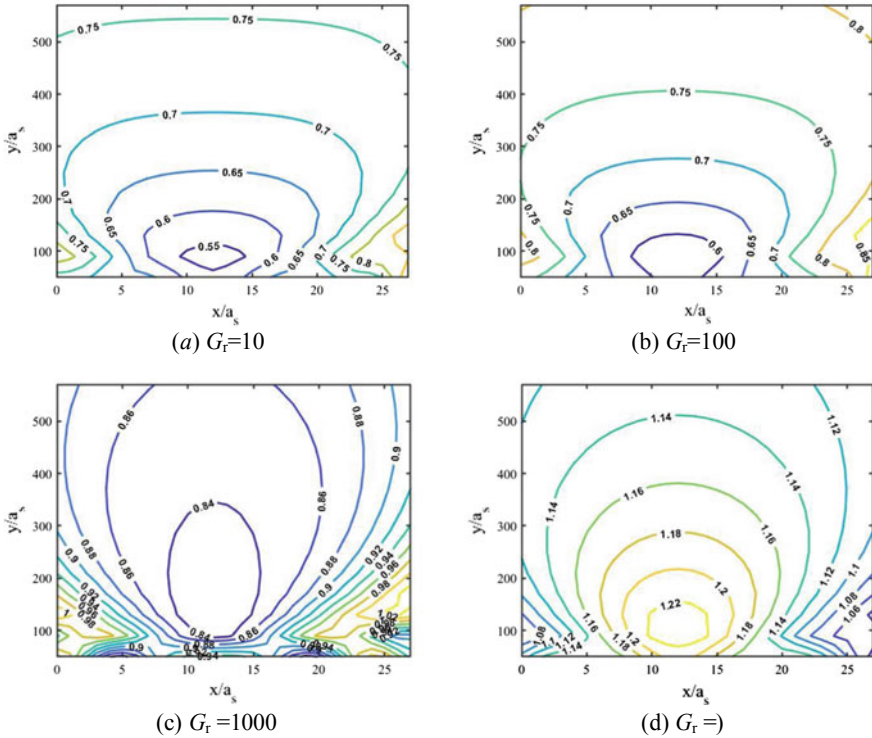
Fig. 6 Dimensionless displacement contour map with the variation of shear modulus ratio of elastic pile barrier and soil ($\eta_{ps} = 0.45$, $\eta_{ss} = 0.8$, $\eta_{pw} = 0.65$, $s_p = 3.0a_s$, $h = 0$, $N = 9$)

4 Concluding Remarks

A theoretical solution to the problem of P waves' propagation which is confronted with arbitrarily arranged, and arbitrarily radius elastic pile rows in saturated soil has been established based on Biot's poroelastic wave theory. The theory fills the gap of without considering arbitrarily arranged and arbitrarily radius of elastic pile barriers at the same time in the former ones. Numerical analysis has investigated the parameters such as scattering orders, separations between piles, distances between pile rows, shear modulus ratio of pile and soil and barrier size. Some serviceable advices for designing solid pile barriers are provided:

(1) It is demonstrated that the multiple scattering assumption is credible, and a numerical truncation at $m = 4$ is reasonable while designing an elastic pile barrier;

(2) The separations between piles have crucial impact on vibration isolation effect. It will not receive ideal reduction effect with larger separation between piles unless s_p is in the range of 2.5–3.0 a_s;
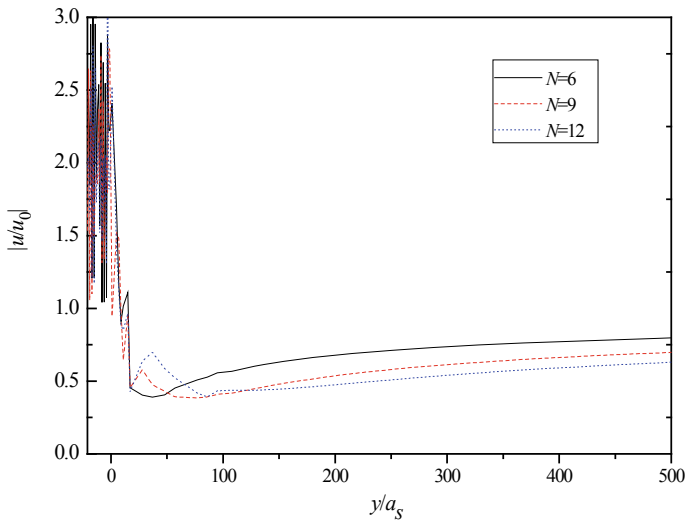
Fig. 7 Curves of dimensionless displacement amplitude of elastic pile with the variation of pile number ($\eta_{ps} = 0.45$, $\eta_{ss} = 0.8$, $\eta_{pw} = 0.65$, $s_p = 2.5a_s$, $h = 0a_s$)

(3) The distances between pile rows is a significant factor of vibration isolation. With the same numbers of piles, a double-row pile barrier attains superior screening effect than a single-row pile barrier; pile-rows will not screen elastic waves which manifest like continuous barriers because excessive pile-row distance results in discrete pile individuals. The best choice of row distance h/a_s is about 3.0;

(4) The total displacement amplitude of elastic pile barrier in saturated soil has been influenced by pore water pressure. With the pile–soil shear modulus reducing, the vibration isolation effectiveness is reinforced;

(5) A properly increasing pile number will enhance the vibration reduction characteristics, whose displacement amplitude amplification and attenuation perform like that of continuous barrier.

References

1. Woods RD, Barnett NE, Sagesser R (1974) Holography, a new tool for soil dynamics. J Geotech Eng Div 100(11):1231–1247
2. Liao S, Sangrey DA (1978) Use of piles as isolation barriers. J Geotech Eng Div 104 (9):1139–1152
3. Gao GY, Yang XJ, Wang YS et al (1997) Theory and application of vibration isolation by piles in rows. J Build Struct 18(4):58–69
4. Xia TD, Chen C, Sun MM (2011) An improved method for multiple scattering under SV incident waves and vibration isolation using rows of piles. J Vib Shock 4:86–90
5. Xia TD, Sun MM, Chen C et al (2011) Analysis of multiple scattering by an arbitrary configuration of piles as barriers for vibration isolation. Soil Dyn Earthq Eng 31(3):535–545
6. Xu P (2012) Isolation of plane elastic waves by discontinuous barriers composed of several rows of piles. J Rock Mech Geotech Eng 31(S1):3159–3166
7. Xu P, Deng YH, Wu M (2014) Isolation of fast compressive waves by barriers composed of several rows of piles saturated soils. Eng Mech 5:120–127
8. Sun MM (2012) Research on multiple scattering of elastic waves by rows of discontinuous barrier. Zhejiang University, Hangzhou
9. Sun MM, Liang GQ, Xia TD et al (2014) Ground vibration isolation of multiple scattering by using rows of tubular piles as barrier. Sound Vib 894213
10. Liu ZX, Wang SJ (2016) Isolation effect of discontinuous pile-group barriers on plane P and SV waves: simulation based on 2D broadband indirect boundary integration equation method. Rock Soil Mech 37(4):1195–1207
11. Lu JF, Zhang X, Li CX (2014) Vibration isolation system for linked pile rows and its numerical simulation. Chin J Geotech Eng 36(7):1316–1325
12. Lu JF, Zhang X, Zhang R (2014) A wave number domain boundary element model for the vibration isolation via a new type of pile structure: linked pile rows. Arch Appl Mech 84:401–420
13. Ding HB, Yang YY, Xu CJ et al (2017) Vibration isolation analysis of elastic continuous barrels in saturated soil. Noise Vib Control 37(5):149–153
14. Liu ZJ, Xia TD, Huang R et al (2015) Comparison and discussion for Biot theory and modified Biot one. J Vib Shock 34(4):148–152
15. Biot MA (1956) Theory of propagation of elastic waves in a fluid-saturated porous solid, I, low frequency range. J Acoust Soc Am 28(2):168–178

Transportation Geodynamics

Experimental Study on High Rockfill Embankment Filling Quality Controlled by Rolling-Dynamic Compaction Technology

Shifan Qiao, Ping Xu, Xiao Sun and Ziyong Cai

Abstract This paper proposes a case study using rolling-dynamic compaction technology to control the filling quality of high rockfill embankment for Pan-Xing highway in Guizhou Province, China. Firstly, the rolling compaction quality evaluation system of large particle size rockfill embankment was reviewed, which includes the evaluation index, the evaluation standard and the evaluation method. Based on the filling quality evaluation system, the rolling compaction construction parameters of layered filling were obtained. Secondly, the construction parameters of dynamic compaction were obtained through the field experiments. Based on field measurements and theoretical model calculation, the improvement depth, the filler density and the porosity change amplitude in the improvement depth range after dynamic compaction were presented for evaluating the dynamic compaction effect of rockfill embankment. Finally, according to the results of rolling compaction and dynamic compaction experiments, the rolling-dynamic compaction technics were summarized. These can be used in guiding the high rockfill embankment filling construction, ensuring the filling quality and construction schedule. Limited studies indicate that rolling-dynamic compaction is an effective and economic technique to control the filling quality of high rockfill embankment. Furthermore, the rolling-dynamic compaction technics provide a valuable reference to similar engineering construction.

Keywords High rockfill embankment · Rolling-dynamic compaction · Filling quality evaluation · Dynamic compaction effect · Construction parameters

S. Qiao (✉) · P. Xu · X. Sun · Z. Cai
School of Civil Engineering, Central South University, Changsha Hunan 410075, China
e-mail: qiaoshifan@163.com

P. Xu
e-mail: xpcsu15@163.com

X. Sun
e-mail: sunxsdjn@163.com

Z. Cai
e-mail: czycsu@yeah.net

723

1   Introduction

The high rockfill embankment of Pan-Xing highway in Guizhou Province, China, almost all are filled with limestone from the tunnel and cutting excavation, the filler particle size mostly between 400 and 800 mm, the maximum size close to 1000 mm, as shown in Fig. 1, and the filling height is between 20 and 30 m. Rolling compaction (RC) or dynamic compaction (DC) technology have been widely used to control the embankment and foundation soil's filling quality [1–4]. However, the embankment fillers particle size of Pan-Xing highway cannot meet the current requirement of the embankment filling standard, but controlling the filler particle size by the method of mechanical crushing will cause huge time and economic cost. On this occasion, the traditional RC technology is difficult in controlling the filling quality of rockfill embankment [5–7]. Using the DC method in controlling the filling quality of each paving layer will also cause huge time and economic cost.

In this case study, the limestone from the tunnel and cutting excavation were directly used in filling the high rockfill embankment. Rolling-dynamic compaction (R-DC) technology was proposed to control the filling quality, as shown in Fig. 2. R-DC technology is the vibration RC for each layered filling and DC after cumulative filling to a certain thickness. However, R-DC technology has been rarely studied in the rockfill embankment. The RC quality evaluation, the DC effect evaluation and the construction parameters are three important aspects of the R-DC technology [8–11].

The compaction degree was often used in evaluating the RC quality [12, 13], but it is difficult to calculate for rockfill embankment. In addition, it is difficult to determine the maximum paving thickness of layered filling for the lack of RC quality evaluation system. The effective improvement depth was often used to evaluate the DC effect [14–18], but it only indicates the improvement range of DC and cannot characterize the compactness of the improved depth range.

Fig. 1 The limestone for the embankment

Fig. 2 The rolling-dynamic compaction technology

In the following sections, methodologies for evaluating the RC quality and the DC effect are presented, followed by the R-DC experiments and RC quality evaluation system obtaining the construction parameters of R-DC technology. Finally, the DC effect is evaluated and conclusions are obtained.

2 Methodologies

2.1 Rolling Compaction Quality Evaluation Index

For large particle size rockfill embankment, the maximum dry density and filler density are difficult to measurement, resulting in the compaction degree cannot be used to evaluate the RC quality. It is necessary to choose the reliable index instead of compaction degree for evaluating the RC quality. To our knowledge, during the rolling process, the embankment surface produces a settlement, the filler density and the compaction degree increase gradually. When compaction degree reaches the steady state, the embankment surface settlement ratio and the filler density of rockfill embankment will not change anymore. For each paving layer, the embankment surface settlement is easily measured, but the filler density is difficult to measure after RC. Therefore, it is important to find an easy measurement index to reflect the steady state of the filler density for the rockfill embankment, when embedding the soil pressure cell at the bottom of the embankment filler. With the increase in rolling times, the cumulative soil pressure increment increases gradually and tends to a steady value, as same as the filler density. The soil pressure value increment can be used instead of the filler density in evaluating the RC quality. In this case study, the authors took the embankment surface settlement ratio and the soil pressure increment as the RC quality evaluation double control indexes, to evaluate the RC quality of rockfill embankment after rolling compaction.

2.2 Dynamic Compaction Effect Evaluation Method

The actual reinforcement mechanisms of DC technology for rockfill embankment are that the achieved lower porosity results in a higher filler density under impact energy. For the rockfill embankment, the dynamic compaction effect can be evaluated by calculating the porosity and filler density change amplitude of the improved depth zone.

The calculated model was established to calculate the porosity change amplitude, as shown in Fig. 3. The improvement depth zone of DC under the rammer is an ellipsoid [19–22]. In this case study, the improvement depth zone is equivalent to the cylindrical and the rammer surrounding uplift is ignored.

V_{V0} can be calculated as

$$V_{V0} = \eta_0 \frac{\pi D^2 H}{4} \tag{1}$$

where V_{V0} is the filler's void volume before DC, η_0 is the filler's porosity before DC, H is the effective improvement depth, and D is the rammer diameter.

V_{V1} can be calculated as

$$V_{V1} = V_{V0} - \frac{\pi D^2 h}{4}(1 - \eta_0) \tag{2}$$

where V_{V1} is the filler's void volume after DC, η_1 is the filler's porosity after DC, h is the cumulative tamping settlement of DC, D is the rammer diameter.
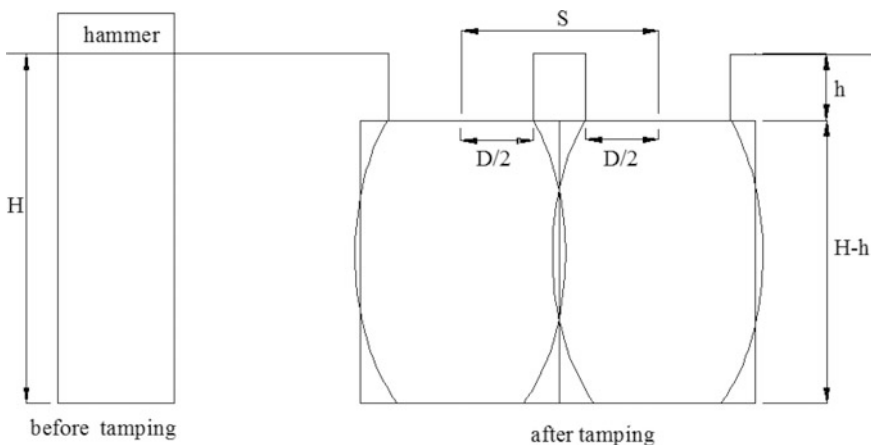
Fig. 3 Improvement depth zone before and after DC treatment

η_1 can be calculated as

$$\eta_1 = \frac{V_{V1}}{\frac{\pi S^2}{4}(H-h)} = \frac{\eta_0(H+h)-h}{(H-h)}\left(\frac{D}{S}\right)^2 \tag{3}$$

where S is the compaction spacing of DC.

$\Delta\eta$ can be calculated as

$$\Delta\eta = \frac{\eta_1}{\eta_0} \tag{4}$$

where $\Delta\eta$ is the porosity change amplitude.

According to Eq. 4, the porosity change amplitude can be calculated to evaluate the DC effect. At the same time, as shown in Fig. 4. Based on the definition of volumetric strain ε_V [23], the improvement depth zone of DC is equivalent to the cylindrical and the filler is considered as a huge unit body.

ε_V can be calculated as

$$\varepsilon_V = \frac{V_0 - V_1}{V_0} = 1 - \frac{\rho_0}{\rho_1} \tag{5}$$

where V_0 is the huge unit body volume before DC, V_1 is the huge unit body's volume after DC, ρ_0 is the filler density before DC, ρ_1 is the filler density after DC.

Simplified Eq. 5 ε_V can be calculated as:

$$\varepsilon_V = \frac{h}{H} = 1 - \frac{\rho_0}{\rho_1} \tag{6}$$
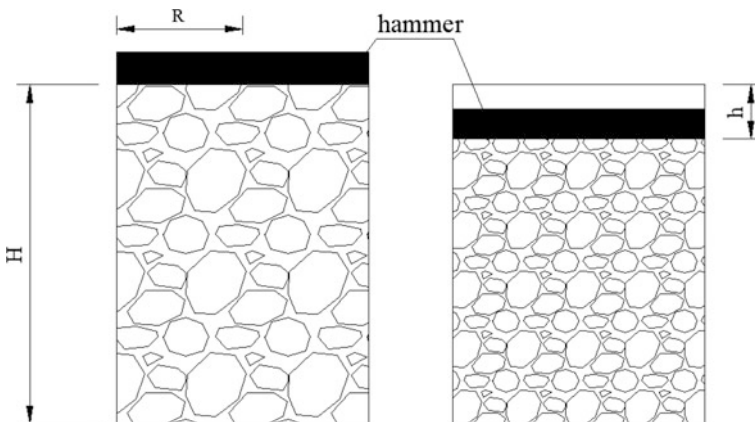
Fig. 4 Calculation model of the DC effect

where h is the cumulative tamping settlement of DC, H is the effective improvement depth. According to Eq. 6, the filler density change amplitude can be calculated to evaluate the DC effect.

3   Field Experiments

The field experiments were carried out at the third contract section K52+650 ∼ K52 +700 of Pan-Xing highway in Guizhou Province, China. The rockfill embankment field experiments section includes five filling layers. Table 1 shows the paving thickness and control particle size of each filling layer.

As shown in Fig. 5a, b, the subsidence pipe and inclinometer pipe were embedded at the K52+664 section, the horizontal distance between the subsidence pipe and inclinometer pipe was 12.75 m. When filling the high embankment in layers, two magnetic cores were placed on the subsidence pipe of each layer, one soil pressure cell and one dynamic stress cell were placed near to the inclinometer pipe, and the wires of the soil pressure cell and the dynamic stress cell were led along the inclinometer pipe.

3.1   RC Experiments Design

As shown in Fig. 6, four embankment surface settlement observation points of t were set along the roller path on each layer.

For each layer, the soil pressure value at the bottom of the layer and the initial elevation of four settlement observation points were measured before rolling. During the rolling process, the data were measured again after each rolling times until the surface settlement reaches the stop rolling standard [24].

Table 1 The paving thickness and control particle size of each filling layer

Experiment section	Vibration force/kN	Filling layer	Paving thickness/mm	Control particle size/mm
K52+650 ∼ K52 +700	600	Layer standard	800	500
		Layer 1	1000	
		Layer 2	1200	
		Layer 3	1500	
		Layer 4	1500	

Note According to the embankment filling standards [24], the relationship between maximum particle size and paving thickness ($d_{max} \leq 2/3h$), the paving thickness 800 mm was taken as the standard layer when the control particle size was 500 mm
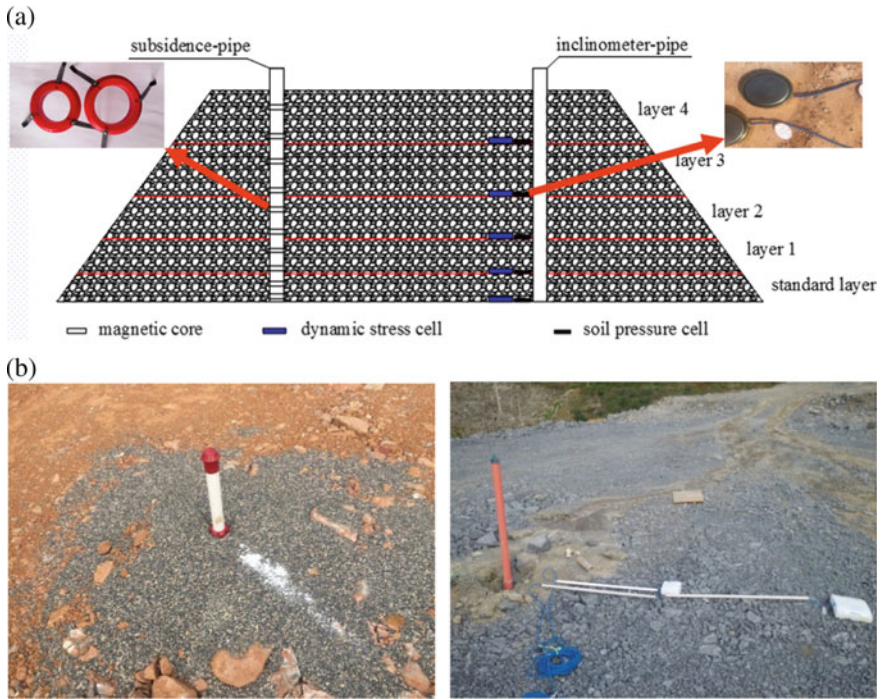
Fig. 5 The measuring instruments arrangement of the K52+664 section
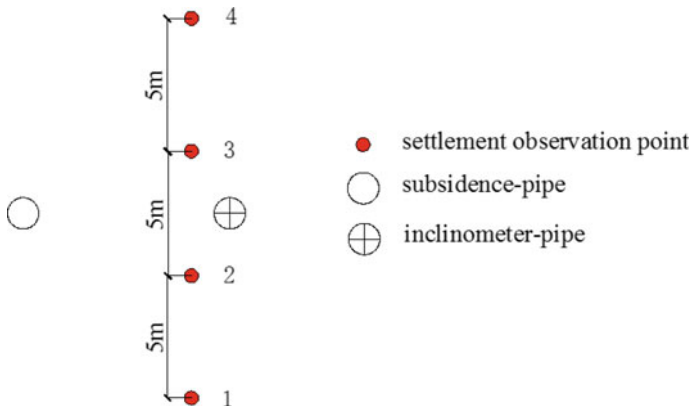
Fig. 6 Arrangement of surface settlement observation points of RC

3.2 DC Experiments Design

DC experiments were performed after layer 4 filled completed, including the single-point tamping experiment and the influence depth experiment, the tamping energy is 3000 kN m.

The single-point tamping experiment was performed following the steps (1)–(3).

(1) Compaction points layout: three positions were selected and marked as the compact point on layer 4. In order to avoid interaction, the distance between two compaction points must be greater than 10 m.
(2) Single-point tamping: moving the hammer to the compaction points and starting tamping.
(3) Measurement and record data: the initial elevation of the hammer was measured before tamping. During the tamping process, the hammer elevation was measured after each tamping. When it reached the standard of stop tamping [24], the tamping settlement and compaction times were recorded.

   The influence depth experiment was performed following the steps (4)–(6), as shown in Fig. 7.

(4) Compaction points layout: the compact points 1, 2, 3, 4 were set at distance of 5.5, 4.5, 3.5, 2.5 m from the subsidence pipe or inclinometer pipe.
(5) Tamping: tamping the compaction points 1, 2, 3, 4 in turn with the tamping number, which was determined by single-point tamping experiment.
(6) Measurement and record data: tamping the compaction points around the subsidence pipe. For each compaction point, the magnetic cores initial elevation was measured before tamping, the magnetic cores elevation was measured
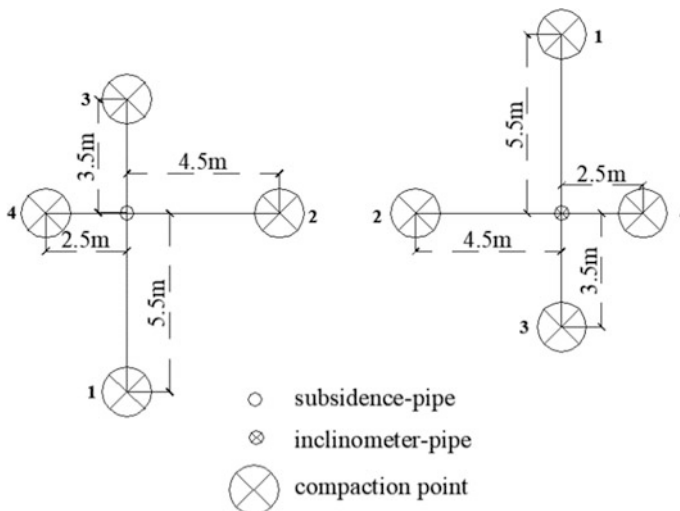
Fig. 7 Arrangement of compact points for influence depth experiment of DC

again after completing the tamping. When tamping the compaction points around the inclinometer pipe, the dynamic stress dispersion and decay were recorded in the tamping process.

4 Results

4.1 RC Experiments Results Analysis

The rules of cumulative surface settlement ratio and soil pressure increment with the number of roller passes of each layer are shown in Figs. 8 and 9.

As shown in Figs. 8 and 9, with the increase in a number of roller passes, the cumulative surface settlement ratio and the cumulative soil pressure incremental of different paving thicknesses increase gradually. In addition, all filling layers reach the stop rolling standard after rolling eight times and the RC quality reaches the steady state. But the cumulative soil pressure increment of paving thickness 1200, 1500 mm only accounted for 28.8%, 17.2% of standard layer, respectively; the changed amplitude is small before and after rolling. For the rockfill embankment, when the paving thickness is beyond a certain thickness, the vibration RC cannot take a good compaction effect in the area at the bottom of the embankment because of the function limit of vibration compaction.
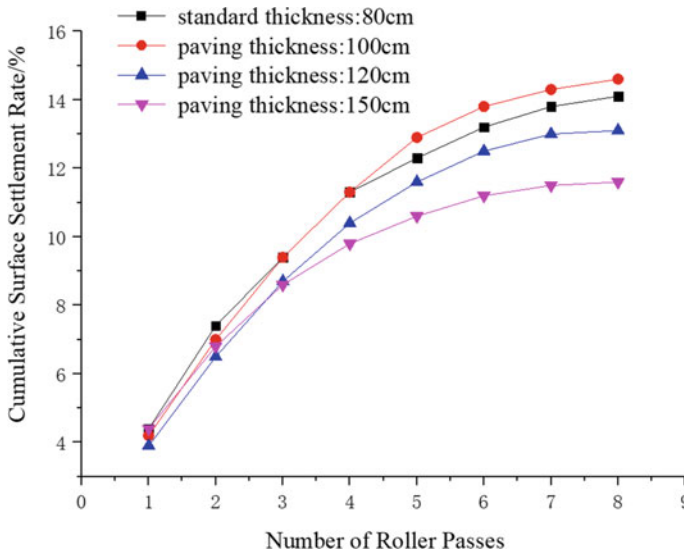
Fig. 8 Relationship curve between cumulative surface settlement ratio and number of roller passes of each layer
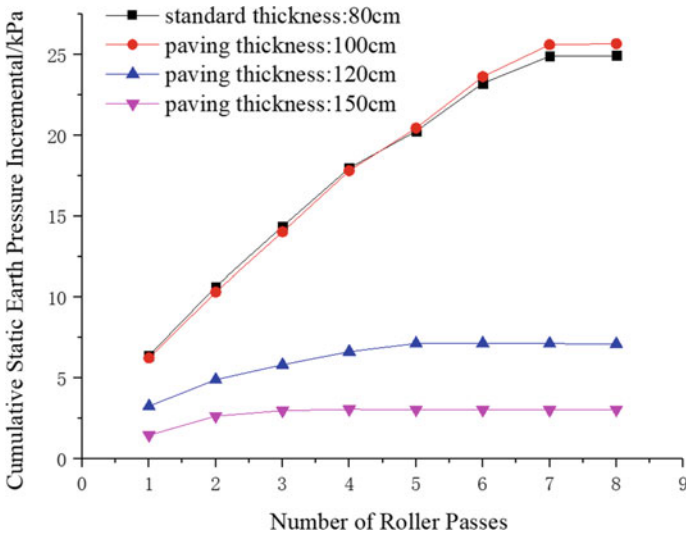
Fig. 9 Relationship curve between cumulative soil pressure incremental and number of roller passes of each layer

Table 2 Double index values of each layer

Rolling times	Two indexes	Standard layer (800 mm)	Layer 1 (1000 mm)	Layer 2 (1200 mm)	Layer 3 (1500 mm)
8	Cumulative surface settlement ratio/%	14.1	14.6	13.1	11.6
	Cumulative soil pressure increment/ kPa	25.0	25.7	7.2	4.3

As shown in Table 2, the two indexes of the standard layer are 14.1% and 25.0 kPa. Based on Fig. 10, the compaction quality of filling layer 2 and layer 3 cannot meet the requirement, only filling layer 1 (1000 mm) can meet the requirement. It is suggested that the maximum paving thickness can increase to 1000 mm under 60 T and rolling eight times for rockfill embankment.

4.2 DC Experiments Results Analysis

The average settlement rules of three tamping points and cumulative tamping settlement with the tamping number are shown in Fig. 11.
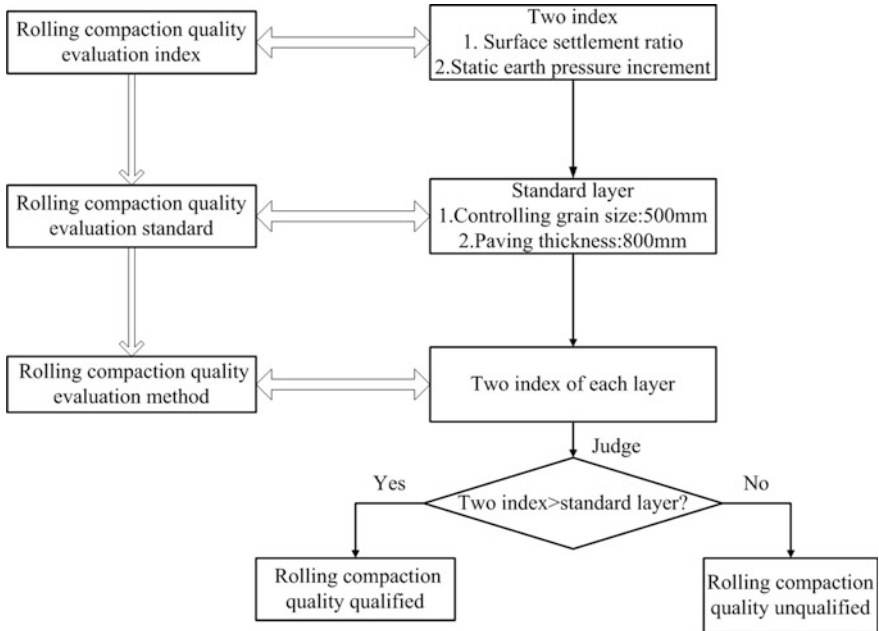
Fig. 10 RC quality evaluation system of rockfill embankment
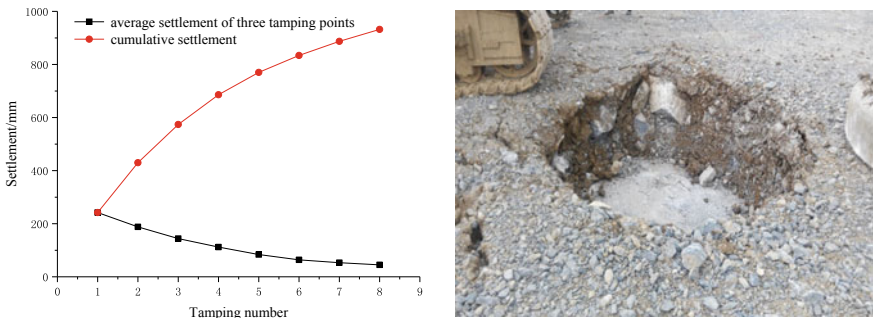
Fig. 11 Relationship curve between settlement and tamping number

As shown in Fig. 11, with the increase in tamping number, the tamping settlement decreases gradually and reaches the standard of stop tamping after eight hits. When the rockfill embankment reached the solid state by DC, the cumulative tamping settlement is 932 mm.

The rules of fills vertical displacement under different compaction distances with the depth are shown in Fig. 12.

As shown in Fig. 12, the magnetic cores settlement approaches 0 at different depths when the compaction point is at the distance of 5.5 m from the subsidence
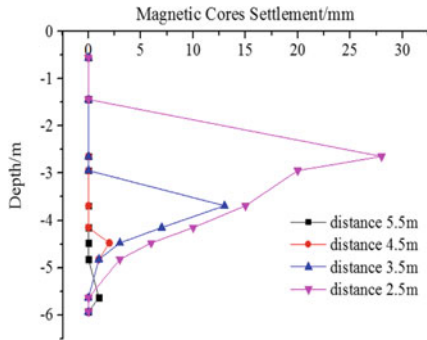
Fig. 12 Magnetic cores vertical displacement–depth curves

pipe. When the compaction point is at the distance of 4.5 m from the subsidence pipe, the magnetic cores produce a small settlement only at the depth of 4.5–5.0 m and it shows that the horizontal influence scope of DC is limited and about 4.5 m. When the compaction points are at the distance of 3.5, 2.5 m from the subsidence pipe, the magnetic cores settlement decreases obviously with the depth and the magnetic cores settlement tends to 0 at the depth of 4.7–5.0 m. The effective improvement depth of DC is about 4.7–5.0 m, which can be obtained by analyzing the rule of magnetic cores settlement with the depth.

The rules of dynamic stress dispersion and decay with the depth are shown in Fig. 13.

As shown in Fig. 13, the peak dynamic stress decreases gradually with the increase in compaction point distance at the same depth, it shows that the impact of energy dispersion decays gradually in the form of a wave. When the compaction point is at a distance of 5.5 m from the inclinometer pipe, the dynamic stress peak approached 0 at different depths. When the compaction point distance from inclinometer pipe is 4.5 m, the dynamic stress peak is 11 kPa at the depth of 4.2 and quickly decays to 0 with the depth increase. When the compaction point is at a
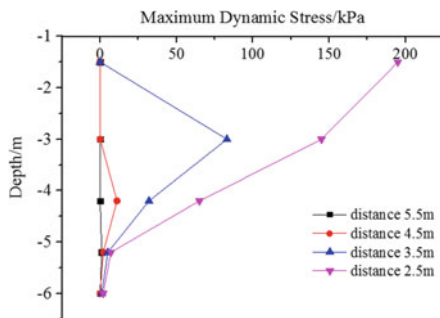
Fig. 13 Dynamic stress peak–depth curves
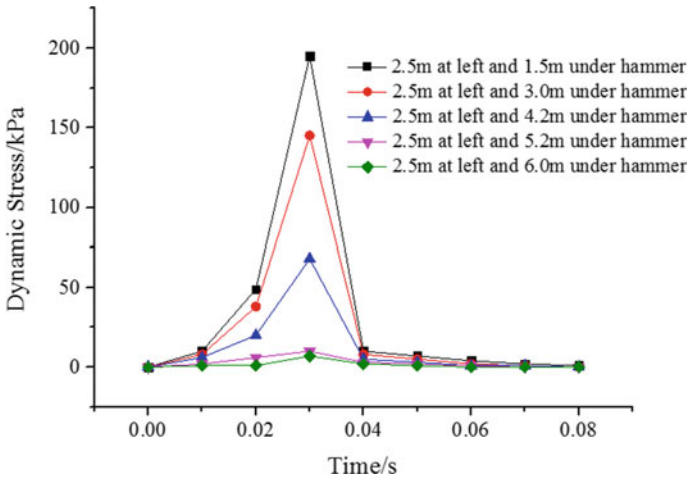
Fig. 14 Time–dynamic stress curves of different depths

distance of 3.5, 2.5 m from the inclinometer pipe, the dynamic stress peak is biggest at the depth of 3.0, 1.5 m and decreases gradually with the depth, as the dynamic stress peak decays to 0 at the depth of 6.0 m. The effective improvement depth of DC is about 5.0–5.3 m, which can be obtained by analyzing the rule of dynamic stress peak decay with the depth.

Figure 14 shows the time–dynamic stress curves of different depths when the compaction point is at a distance of 2.5 m from the inclinometer pipe.

As shown in Fig. 14, the dynamic stress wave is a peak and has no second stress wave, the continuous time of dynamic stress wave is very short, which is only about 0.02 s. The peak value decays quickly with the depth and the dynamic stress peak is 5 kPa at the depth of 6.0 m, which only accounts for the dynamic stress peak at a depth of 1.5 m which is only 2.5%.

4.3 Dynamic Compaction Effect Evaluation

According to Eqs. 4 and 6 and Table 3, the porosity and the filler density change amplitude after DC can be calculated to evaluate the DC effect.

Before DC, the initial porosity of rockfill embankment is difficult to determine. Substituting the initial porosity is between 20 and 60%. According to Eq. 4, the proportion of the porosity after DC that accounted for the initial porosity can be calculated. Figure 15 shows the relationship between the porosity change amplitude ($\Delta\eta$) and the initial porosity (η_0).

As shown in Fig. 15, with the initial porosity increase, the $\Delta\eta$ increases gradually. But, even if the initial porosity reached 60%, the proportion of the porosity

Table 3 Construction parameters of DC

Parameter	Value
Tamping settlement h/m	0.932
Improvement depth H/m	5.0
Compaction spacing S/m	4.5
Rammer diameter D/m	2.3
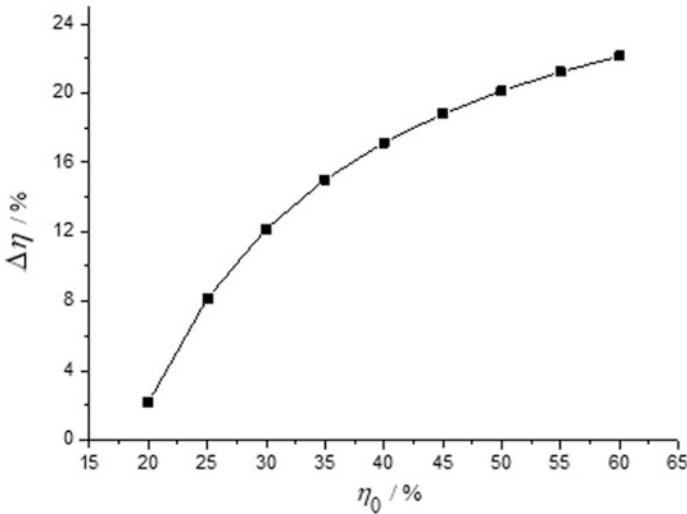
Fig. 15 Relationship between the $\Delta\eta$ and the initial void ratio (η_0)

after DC that accounted for the initial porosity is only 22.13%. It suggests that the DC effect is significant, the porosity after DC decreases significantly. In addition, the filler density increases the amplitude after DC reached 22.9%. The calculation results show that porosity reduced significantly and the filler density increases significantly, the rockfill particles in the effective improvement zone reaches a good solid state.

5   Conclusions

In this study, R-DC technology has been used to control the filling quality of rockfill embankment. By the in situ experiments of RC and DC, the following results can be concluded:

(1) For rockfill embankment, the two indexes of RC quality evaluation are proposed and the maximum paving thickness is determined as 1000 mm by the RC quality evaluation system.

(2) The construction parameters of layered filling were obtained. The control particle size is 500 mm, the paving thickness is 1000 m, and the number of rolling times is 8 with 600 kN vibration force.

(3) Under the compact energy of 3000 kN m, the effective improvement depth of DC is about 5.0 m. The construction parameters of DC are obtained, the compact distance is 4.5 m, and the number of compact times is 8.

(4) After DC, even if the initial porosity is 60%, the porosity after DC is only 22.13% which accounts for the initial porosity, the filler density increases amplitude after DC reached 22.9%, which can meet the specification requirement.

(5) It is based on the maximum paving thickness of layered filling and the effective improvement depth of dynamic compaction. The high rockfill embankment filling of Pan-Xing highway is in Guizhou Province, China. According to the construction parameters of RC and DC, in controlling the filling quality, the layered paving thickness is 1000 mm for vibration rolling and after filling five layers DC is conducted.

References

1. Menard L, Broise Y (1975) Theoretical and practical aspects of dynamic consolidation. Geotechnique 25(1):3–18
2. Ranasinghe RATM, Jaksa MB, Kuo YL, Pooya Nejad F (2017) Application of artificial neural networks for predicting the impact of rolling dynamic compaction using dynamic cone penetrometer test results. J Rock Mech Geotech Eng 9:340–349
3. Kumar S, Puri VK (2001) Soil improvement using heavy tamping-a case study. ISET J Earthq Technol 38(2–4):123–133
4. Zhang Y, Liu JK, Fang JH, Xu AH (2013) Application of dynamic compaction and rolling compaction in the subgrade improvement of Qarhan-Golmud highway. Sci Cold Arid Reg 5 (5):603–607
5. Kyle M, Jihyoung K (2010) Dynamic compaction of collapsible soils based on U.S. case histories. J Geotech Geoenviron Eng 136(9):1178–1186
6. Asiri K, Masakazu T (2011) Application of the heavy tamping method on Sri Lankan peaty clay for the construction of a highway embankment. In: Proceedings. 14th Asian Regional Conference on Soil Mechanics and Geotechnical Engineering
7. Minaev OP (2011) Development of vibratory method for soil compaction during construction. Soil Mech Found Eng 48(5):190–193
8. Feng SJ et al (2015) Field study on the reinforcement of collapsible loess using dynamic compaction. Eng Geol 185:105–115
9. Liu DH, Lin M, Li S (2016) Real-time quality monitoring and control of highway compaction. Autom Constr 62:114–123
10. Feng SJ et al (2011) Field evaluation of dynamic compaction on granular deposits. J Perform Constr Facil 25(3):241–249
11. Minaev OP (2002) Effective method for dynamic compaction of slightly cohesive saturated solis. Soil Mech Found Eng 39(6):208–212
12. Lou H, Zhao MH, Cao WG, Hu TH (2007) New method for checking compactness of soil-rock mixture subgrade based on static test. Chin J Rock Mech Eng 26(s2):4496–4502

13. Fan Y (2002) Advance and evaluation of checking technique on the quality of filled soil evaluation. Rock Soil Mech 23(4):524–529
14. Pang XQ (2010) Application of strong tamping reinforcement technique in treatment of collapse loess subgrade. J Lanzhou Univ Technol 36(1):117–121
15. Zhao LH, Li L, He CM (2008) Study of reinforcement range of dynamic compaction in soil-stone material embankment. China J Highway Transp 21(1):12–17
16. Feng SJ, Hu B, Zhang X (2012) Model Test study on impact parameter' influence on tamping effect. J TongJi Univ (Nat Sci Edition) 40(8):1147–1153
17. Ghanbari E, Hamidi A (2015) Improvement parameters in dynamic compaction adjacent to the slopes. J Rock Mech Geotech Eng 7(2):233–236
18. Wen SQ, Li YP, Ma K (2015) Research on inversion of energy efficiency and compacted and affected scope of dynamic compaction. Rock Soil Mech 36(s2):185–192
19. Zou JF, Luo H, Yang XL (2008) Effective Depth of dynamic compaction in embankment built with soils and rocks. J Central South Univ Technol 15(s2):34–37
20. Ghassemi A, Pak A, Shahir H (2010) Numerical study of the coupled hydro-mechanical effects in dynamic compaction of saturated granular soil. Comput Geotech 37(1):10–24
21. Gao ZG, Du YL, Huang XB (2013) Reinforcement mechanism and construction technology of broken stone fills by dynamic consolidation. Chin J Rock Mech Eng 32(2):377–384
22. Jia MC, Wang L, Zhou J (2009) Experimental research on macro-meso consolidation mechanism of sandy soil with dynamic compaction. Chin J Rock Mech Eng 28(s1):3283–3290
23. Yao YP, Zhang BZ (2016) Reinforcement range of dynamic compaction based on volumetric strain. Rock Soil Mech 37(9):2663–2671
24. The Professional Standards Compilation Group of People's Republic of China, JTG D30–2004 Specifications foe Design of Highway Subgrades. China Communications Press (2004)

Prediction Model for Mechanical Properties of Iron Ore Tailings Recycled Concrete Based on Foundation Treatment

Hong-huan Cui, Xin Yang, Pan-pan Wang, Chen Xing and Zi-lin Yan

Abstract Iron tailings and construction waste are products of rapid economic development and rapid urbanization in our country. How to effectively use them is related to the positive development of China's ecological environment, economy and engineering construction. To fully develop iron ore tailings and construction wastes, the prediction model of mechanical properties of iron ore tailings recycled concrete and its influence weights of the three factors are clearly defined in the foundation treatment project. This article also takes control factors for the compressive strength of iron ore tailings recycled concrete as the entry point. Single-factor test is conducted. Based on test results, the test is carried out according to the principle of quadratic orthogonal regression design. Through fifteen groups of compressive strength tests, a prediction model for the compressive strength of recycled iron concrete is established. SPSS software is used for a stepwise regression analysis of each factor's significance model to determine the weight relationship based on the factors that affect the compressive strength of the recycled iron ore tailings of foundations. Results show that water–cement ratio and additional water volume have an inhibitory effect on the compressive strength of iron tailing ore recycled concrete. Impact of iron tailings content on compressive strength firstly decreases and then increases. Slump of iron ore tailings recycled concrete is significantly affected by the iron tailings content, water–cement ratio and additional water volume. When the iron tailings content reaches 100% and the additional water consumption exceeds 60%, the slump is not within the control range; the weights of factors affecting the compressive strength of recycled concrete from iron ore tailings include water–cement ratio x_2 (2.613), additional water x_3 (1.422), x_2^2 (1.171), x_1^2 (0.846), iron tailings content x_1 (0.623), interaction between iron tailings and additional water $x_1 x_3$ (0.432).

H. Cui (✉) · X. Yang · P. Wang · C. Xing · Z. Yan
Hebei Key Laboratory for Diagnosis, Reconstruction and Anti-disaster of Civil Engineering, Zhangjiakou 075000, Hebei, China
e-mail: Cuihonghuan729@163.com

H. Cui · X. Yang · P. Wang · C. Xing · Z. Yan
School of Civil Engineering, Hebei University of Architecture, Zhangjiakou 075000, Hebei, China

1 Introduction

Iron tailings and construction waste are products of rapid economic growth and rapid urbanization in China. Due to the immature nature of recycling technology, iron ore tailings and construction waste disposal methods are mainly transported to peri-urban areas for disposal and landfill. This method not only wastes land resources but also causes secondary pollution, which is inconsistent with the requirements of China's sustainable development and green development strategies. At present, the main researches on recycled concrete are focused on the performance index of recycled aggregates, the mix ratio of recycled concrete, work performance, mechanical properties and durability [1–7]. There are fewer researches on the application of iron tailings to recycled concrete for the foundation treatment project. Researches on the prediction model, sensitive parameters and influence weight of its mechanical properties are relatively scarce [8–11]. Therefore, to do the secondary development of iron tailings and construction waste, under the premise of meeting the compressive strength of C25 applied to the foundation, under interactions of controllable compressive strength factors including iron tailings content, water–cement ratio and additional water supply, it is necessary to do the prediction model and sensitive parameters of the iron ore tailings recycled concrete mechanical properties in the actual foundation treatment research.

To provide a technical theoretical basis for the foundation treatment design, this article does multi-factor compressive strength test using the quadratic regression orthogonal design method based on the iron ore tailings recycled concrete and results of the single-factor compressive strength tests. A prediction model for the mechanical properties of iron ore tailings recycled concrete is established to explore the effective prediction model and sensitive parameters of the mechanical properties of iron ore tailings recycled concrete based on foundation treatment. At the same time, it improves the controlling indications of the iron tailings recycled concrete based on foundation treatment design index.

2 Introduction to Tests

2.1 Test Materials

The recycled aggregate is derived from the demolition of abandoned concrete in a certain block of Zhangjiakou (the original coarse aggregate is gravel). The natural aggregate is gravel produced by a quarry in Zhangjiakou. Results of the basic physical performance test are shown in Table 1.

Table 1 Basic physical properties of coarse aggregates

Aggregate type	Apparent density/ (kg m^{-3})	Bulk density/ (kg m^{-3})	Water absorption/%	Moisture content/%	Crushing index/%
Recycled aggregate	2431	1403	5.38	2.07	14.5
Natural aggregate	2580	1694	0.89	0.59	7.8

Table 2 Chemical composition of iron tailings

Compounds	SiO$_2$	CaO	Fe$_2$O$_3$	AL$_2$O$_3$	MgO	SO$_3$	TiO$_2$
Content/%	27.28	5.05	42.41	9.20	4.35	2.21	0.47

Table 3 Basic physical properties of fine aggregate

Aggregate type	Apparent density/ (kg m^{-3})	Water absorption/%	Water content/%	Bulk density/ (kg m^{-3})
Fine sand	2565.6	1.82	0.45	1583.1
Iron tailings	2895.8	2.37	0.30	1597.4

It can be seen from Table 1 that the apparent density and bulk density of recycled aggregate in the test are lower than natural aggregates. The moisture content, water absorption and crushing index are all higher than natural aggregates. These test results are consistent with other literature results [12, 13]. Construction waste has absorbed a large amount of water during the mixing process. Even if it is decommissioned for a long time, its water content is still high. In addition, the recycled aggregate can form a large number of cracks on the inside and surface during the crushing process. A large amount of cement mortar is wrapped on the surface and these factors caused the recycled aggregate to have higher water absorption, moisture content and crushing index than natural aggregates.

Iron tailings are from iron tailings in Zhangjiakou of Hebei Province. The iron ore is hematite and the main mineral composition is quartz, followed by pyroxene, hornblende and clay. The chemical composition analysis results are shown in Table 2. The sand is river sand, and sieving particles are with a particle size over 4.75. Basic physical properties of fine sand and iron tailings are shown in Table 3. The cement is from the Jinbo Cement Factory with P·O32.5. The water is tap water.

2.2 Mix Design

The concrete design strength is C25. By referring to the "General Concrete Mixing Ratio Design Specification" JGJ 55-2011 [14], the ordinary concrete mix ratio is determined as shown in Table 4. The slump control is 60–80 mm.

Table 4 Ordinary concrete mix ratio/(kg m^{-3})

Water–cement ratio	Sand rate/%	Coarse aggregate	Fine aggregate	Cement	Water
0.52	32	1160.7	546.2	423.08	220

According to the analysis of Tables 1 and 3, if the design proportion of the iron tailings recycled concrete is based on the "General Concrete Mixing Ratio Design Specification" JGJ 55-2011, the working performance will be significantly reduced. Therefore, the preparation of iron tailings recycled concrete needs to increase the amount of water consumption on the basis of the amount of water for ordinary concrete units. This part of the amount of water is called the amount of additional water. With references to previous studies on the unit water consumption of recycled concrete [12, 13], based on basic properties of tailings and recycled aggregates, the mathematical formula for defining the 24-h water absorption of iron tailings is as follows:

$$\Delta w = M_{RA} \times [(S_{RA} - \omega_{RA}) - (S_{OA} - \omega_{OA})] + M_{RB} \\ \times [(S_{RB} - \omega_{RB}) - (S_{OB} - \omega_{OB})]$$

In the formula,

M_{RA} recycled aggregate quality,
S_{RA} water absorption of recycled aggregates,
S_{OA} 24-h natural aggregate water absorption,
ω_{RA} moisture content of recycled aggregates,
ω_{OA} 24-h moisture content of natural aggregates,
M_{RB} quality of iron tailings,
S_{RB} 24-h iron tailings water absorption rate,
S_{OB} 24-h natural sand absorption rate,
ω_{RB} iron tailings moisture content,
ω_{OB} natural sand moisture content;

3 Analysis of Single-Factor Test Program and Results

3.1 Test Program of Iron Tailings Recycled Concrete Under a Single Factor

To determine the influence of each single factor on the slump and compressive strength of iron ore tailings recycled concrete and the range of values of each factor in the design of quadratic orthogonal combination experiments, the design of single-factor scheme and cooperation is as follows:

(1) The effect of iron tailings addition on the slump and compressive strength of recycled concrete is studied. The ratio of water to cement is 0.52 and the amount of additional water is 30% of the amount of 24-h water absorption. The amount of iron tailings is set 0% → 20% → 40% → 60% → 80% → 100% to the total amount of fine aggregate. (2) The effect of the water–cement ratio on the slump and compressive strength of recycled concrete is studied. The amount of additional water is selected as 30% of the 24-h water absorption. The water–cement ratio is 0.47, 0.52 and 0.57, respectively, with reference to the specification "General Concrete Mixing Ratio Design Specification" JGJ 55-2011. (3) The effect of additional water volume on the slump and compressive strength of recycled concrete is determined. The ratio of water to dust is 0.52. The amount of additional water is set to 0% → 30% → 60% → 100% of the 24-h water absorption.

3.2 Test Results and Analysis

With changes in the number of iron tailings, the change trend of the compressive strength and slump of iron tailing reclaimed concrete is shown in Figs. 1 and 2.

Figure 1 shows that when the iron tailings content is between 0 and 40%, the compressive strength of the concrete decreases with the increase in the iron tailings. It decreases to a minimum when the content of the iron tailings reaches 40%. The amount of iron tailings continues to increase and the compressive strength of concrete rebounds. When the iron tailings content reaches 60%, the compressive strength of concrete reaches its peak. After that, when the content of iron tailings continues to increase, the compressive strength of concrete firstly decreases and then increases.

From Table 3 and Fig. 2, it can be seen that as the iron tailings content increases, the slump decreases continuously. This is due to the very fine grain size of the iron tailings and the relatively large surface area. At the same time, there is higher water absorption and lower moisture content. As a result, the water demand for recycled
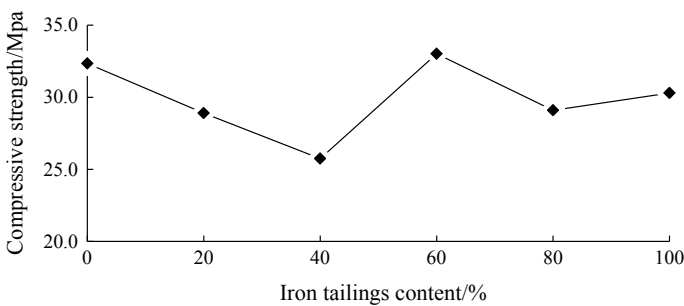
Fig. 1 Curves of compressive strength with iron tailings content
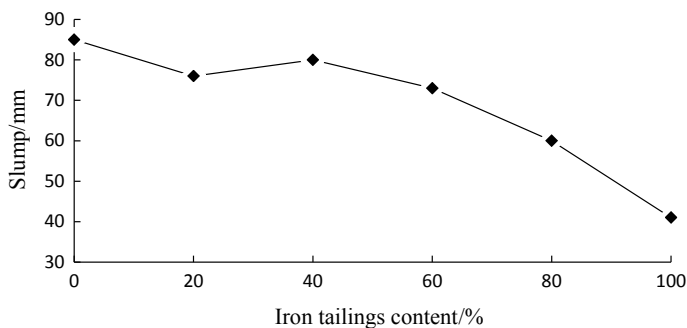
Fig. 2 Curve of a slump with iron tailings content

concrete is high, and the actual amount of recycled concrete used in mixing iron tailings is reduced. The slump is reduced.

The main reason for this phenomenon is that a large number of cracks and edges and corners are generated during the crushing process of recycled aggregates. These cracks and corners make the compactness of the concrete during the mixing and the vibrating process becomes lower. The iron tailings in the experiment are very fine in comparison with fine sand. Even if the size of the fine sand particles exceeds 4.75 mm, the size of the iron tailings is still small. Therefore, when the amount of iron tailings reaches a certain level in the process of concrete preparation, the cracks between the recycled aggregate itself and gaps between the edges of the recycled aggregate can be filled. It can increase the overall compactness of the concrete and the compressing strength is improved. However, when the iron tailings content is fewer between 0 and 40%, the iron tailings cannot fully fill these gaps. Because the iron tailings have extremely fine grain diameter, the substituting sand reduces the content of fine stones in fine sand and reduces the compressive strength. Similarly, when the content of iron tailings is high, that is, when the content of iron tailings is between 60 and 100%, although most of the cracks and crevices of reclaimed aggregates can be filled, the fine stones in most of the fine sands are also replaced and the compressive strength is reduced. When the iron tailings content exceeds 60%, the iron tailings take accounts of most of the fine aggregate. The overall surface area of the fine aggregate is increased and the water absorption rate is increased. The water requirement becomes larger. In fact, the concrete with fewer iron tailings has a higher degree of cohesion. These reasons lead to the higher compressive strength of concrete with higher iron tailings than others (Fig. 3).

With the change of water–cement ratio, the change curves of compressive strength and slump of recycled concrete of iron tailings are shown in Figs. 4 and 5. It can be seen from the figure that the compressive strength of concrete decreases with the increase in water–cement ratio. With the increase in the ratio of water to cement, the cohesiveness of recycled concrete relative to iron ore tailings actually decreases. The compressive strength decreases and the slump increases.

(a) Iron tailings content 0% (b) Iron tailings content 20% (c) Iron tailings content 40%

(d) Iron tailings content 60% (e) Iron tailings content 80% (f) Iron tailings content 100%
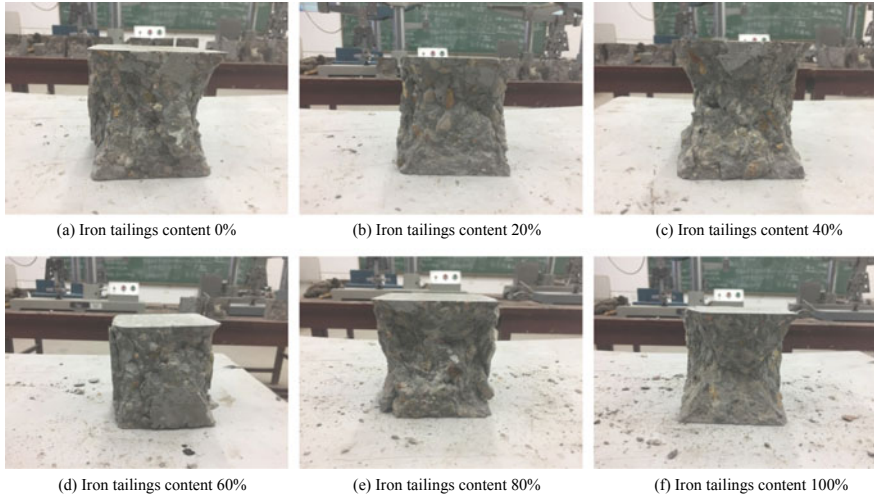
Fig. 3 Test plots of compressive strength of different iron tailings
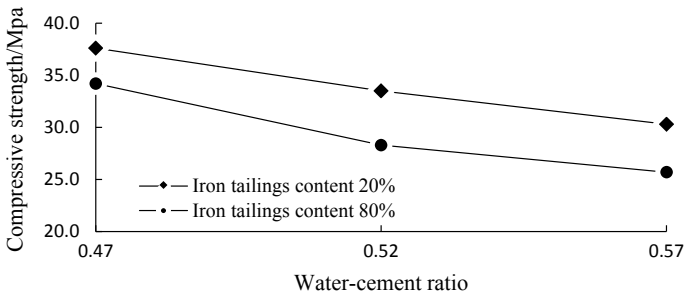
Fig. 4 Curve of compressive strength with a water–cement ratio
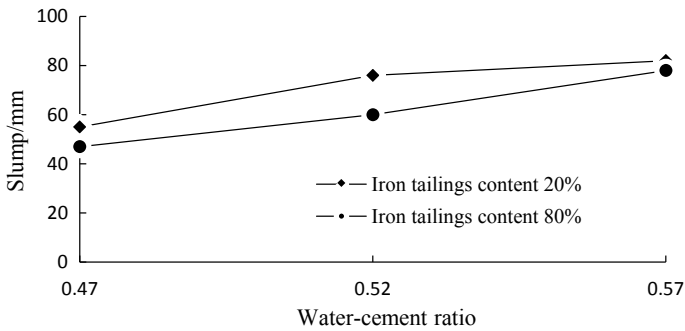
Fig. 5 Slump with water–cement ratio curve
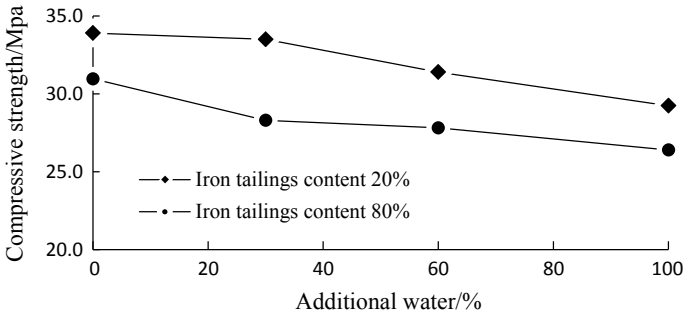
Fig. 6 Curve of compressive strength with additional water
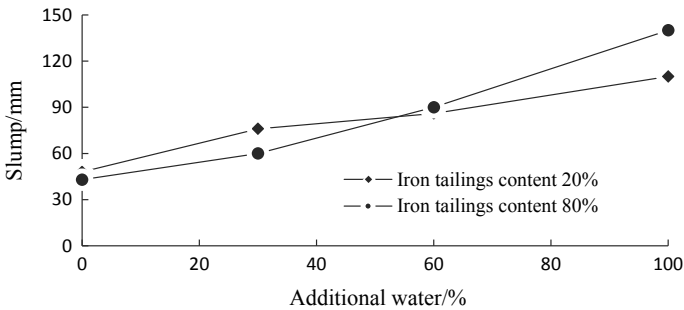
Fig. 7 Curve of slump with additional water

As the amount of additional water changes, the change curves of compressive strength and slump of recycled concrete for iron ore tailings are shown in Figs. 6 and 7. It can be seen from the figure that the additional water volume has an obvious effect on the compressive strength of recycled concrete for iron tailings. With the increase in the amount of additional water, the compressive strength shows a trend of decrease and the slump increases.

4 Quadratic Orthogonal Combinatorial Test Program and Compressive Strength Prediction Model

4.1 Test Program

To give the mechanical performance index of iron ore tailings recycled concrete based on high-speed railway foundation, according to the results of single-factor test, the test is arranged according to the quadratic regression orthogonal design

Table 5 Test factors' level

Influencing factors	Iron tailings content/%	Water–cement ratio	Additional water/%
Parameter	X_1	X_3	X_2
Upper asterisk arm (+1.215)	80	0.57	60
Upper level (+1)	74.69	0.56	54.69
Zero level (0)	50	0.52	30
Lower level (−1)	25.31	0.48	5.31
Lower asterisk arm (−1.215)	20	0.47	0
Change spacing (Δ)	24.69	0.04	24.69

method. The iron tailings content is designed based on 20 and 80%. The water–cement ratio is based on a 0.52 with an adjustment amount of 0.05. The additional water is mainly referenced to the concrete work performance, based on 0 and 60%. Test factors and levels are shown in Table 5. A total of three factors are selected for the iron tailings recycled concrete, and each factor corresponds to five levels. There is the need to do 15 groups of tests in total, and three parallel tests are conducted for each group of test.

4.2 Compressive Strength Prediction Model

According to the quadratic regression orthogonal combinatorial design principle [15], the quadratic regression orthogonal computational design is obtained in Table 6. In Table 6, z_i, $z_i z_j$, z_i' are, respectively, expressed as a term, an interaction, and the coding factor of the center change item of the quadratic term z_i^2 (i = 1, 2, 3; k = 1, 2, 3). From Table 6, the compressive strength can be obtained by regression Eq. (1). The quadratic regression analysis of variance is shown in Table 7.

The compressive strength can be expressed as:

$$Y = 32.881 + 0.578z_1 - 2.654z_2 - 2.428z_3 + 0.175z_1z_2$$
$$+ 0.500z_1z_3 + 0.075z_2z_3 - 1.349z_1' - 1.450z_2' - 0.012z_3' \qquad (1)$$
$$R_1^2 = 0.993$$

where Y is the compressive strength, $z_i' = z_i^2 - (2^p + 2\gamma^2)/n$, $p = 3$, n is the total sample, $n = 15$, $\gamma = 1.215$; R^2 is the fitting degree. For the significant level, $\alpha = 0.05$, $F_{0.05}(9, 5) = 4.77$, $F_{0.05}(1, 5) = 6.61$. Analyzing Table 7 from the analysis of the compressive strength quadratic regression analysis, we can see that $F_{0.05}(9, 5) = 4.77 < 76.156$. It explains that the regression equation obtained from the compressive strength reaches the level of significance and the equation is meaningful. Among them, the F values of z_1, z_2, z_3, z_1z_3, z_1' and z_2' are all greater than $F_{0.05}(1, 5) = 6.61$. There are six factors in all that reach the significance level.

Table 6 Quadratic regression orthogonal calculation

Test number	z_1	z_2	z_3	z_1z_2	z_1z_3	z_2z_3	$z_1{}'$	$z_2{}'$	$z_3{}'$	Measured intensity/ Mpa
1	1	1	1	1	1	1	0.270	0.270	0.270	28.7
2	1	1	−1	1	−1	−1	0.270	0.270	0.270	32.2
3	1	−1	1	−1	1	−1	0.270	0.270	0.270	33.2
4	1	−1	−1	−1	−1	1	0.270	0.270	0.270	37.1
5	−1	1	1	−1	−1	1	0.270	0.270	0.270	25.9
6	−1	1	−1	−1	1	−1	0.270	0.270	0.270	31.5
7	−1	−1	1	1	−1	−1	0.270	0.270	0.270	31.2
8	−1	−1	−1	1	1	1	0.270	0.270	0.270	37
9	1.215	0	0	0	0	0	0.747	−0.730	−0.730	33.3
10	−1.215	0	0	0	0	0	0.747	−0.730	−0.730	32.7
11	0	1.215	0	0	0	0	−0.730	0.747	−0.730	29.2
12	0	−1.215	0	0	0	0	−0.730	0.747	−0.730	36.5
13	0	0	1.215	0	0	0	−0.730	−0.730	0.747	31.8
14	0	0	−1.215	0	0	0	−0.730	−0.730	0.747	38.2
15	0	0	0	0	0	0	−0.730	−0.730	−0.730	34.7

Table 7 Quadratic regression analysis of compressive strength

Parameters	SS	Df	MS	F
z_1	3.657	1	3.657	15.220
z_2	77.155	1	77.155	321.077
z_3	64.486	1	64.486	268.357
z_1z_2	0.245	1	0.245	1.020
z_1z_3	2.000	1	2.000	8.323
z_2z_3	0.045	1	0.045	0.187
$z_1{}'$	7.935	1	7.935	33.023
$z_2{}'$	9.176	1	9.176	38.184
$z_3{}'$	0.000	1	0.000	0.001
Regression	164.702	9	18.300	76.156
Residual	1.202	5	0.240	
sum	165.904	14		

If the F values of z_1z_2, z_2z_3 and $z_3{}'$ are all less than $F_{0.05}(1,5) = 6.61$, the three factors do not reach the level of significance. The equation needs to be revised.

From the orthogonality of the experimental design, it can be seen that the regression coefficient of each experiment, that is, the F value is irrelevant. The less significant variables can be directly deleted, which does not affect the regression coefficients of other variables. The squared sum of the partial regressions of the insignificant variables is added to the sum of squared residuals for the second

Table 8 Quadratic regression analysis of variance after compressive strength correction

Parameters	SS	Df	MS	F
z_1	3.657	1	3.657	19.615
z_2	77.155	1	77.155	413.800
z_3	64.486	1	64.486	345.855
$z_1 z_3$	2.000	1	2.000	10.726
z_1'	7.935	1	7.935	42.560
z_2'	9.176	1	9.176	49.211
Regression	164.412	6	27.402	146.963
Residual	1.492	8	0.186	
Sum	165.904	14		

analysis of variance, as shown in Table 8. The revised regression equation can be expressed as:

$$Y = 32.881 + 0.578z_1 - 2.654z_2 - 2.428z_3 + 0.500z_1 z_3 - 1.349z_1' - 1.450z_2'$$
$$R_2^2 = 0.991$$

$$(2)$$

The significance level $\alpha = 0.05$, $F_{0.05}(6, 8) = 3.58$, $F_{0.05}(1, 8) = 5.32$.

As can be seen from Table 8, $F_{0.05}(6, 8) = 3.58 < 146.963$. It shows that the regression equation of compressive strength reaches the level of significance and Eq. (2) has significance. And all F values are greater than $F_{0.05}(1, 8) = 5.32$. The regression coefficients all reached a significant level. A new F is constructed, that is, $F = \frac{(R_1^2 - R_2^2)/(k_1 - k_2)}{(1 - R_1^2)/(n - k_1 - 1)}$. R_1^2, R_2^2, respectively, are the fitness of the regression Eqs. (1) and (2); k_1, k_2 are the number of independent variables of Eqs. (1) and (2). F value conforms to the degree of freedom of F with the amount of $k_1 - k_2$ and $n - k_1 - 1$. $F = 0.476 < F_{0.05}(3, 5) = 5.41$. That is, deleting three insignificant factors has a significant effect on the regression equation. According to the coding formula: $z_1 = \frac{x_1 - 50}{24.69}$, $z_2 = \frac{x_3 - 0.52}{0.04}$, $z_3 = \frac{x_2 - 30}{24.69}$, the actual calculated value of compressive strength regression equation is obtained.

$$\bar{Y} = -165.571 + 0.220x_1 + 825.752x_2 - 0.139x_3 + 0.001x_1 x_3 - 0.002x_1^2 - 856.024x_2^2$$
$$R^2 = 0.991$$

$$(3)$$

In the formula, $\bar{Y}$ is the actual compressive strength of the factor. x_1 is the actual value of the factor of iron tailings. x_2 is the ratio of the actual value of water to dust. x_3 is the actual value of the factor added water. $x_1 x_3$ is the interaction between iron tailings content and additional water volume. x_1^2 is the actual value of the factor iron
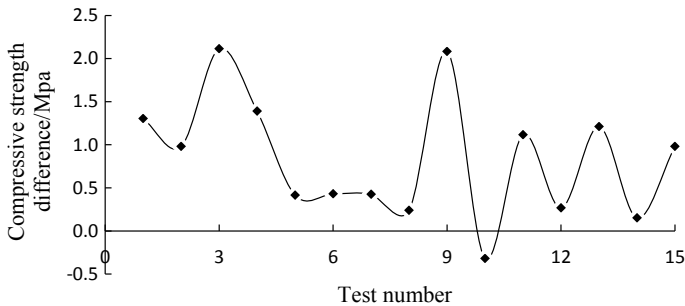
Fig. 8 The difference between the compressive strength's prediction value and the measured value

tailings addition quadratic term. x_2^2 is the factor actual value water–cement ratio quadratic term.

Figure 8 shows the difference between the compressive strength budget value and the measured value. It can be seen from Fig. 8 that the difference between the calculated value and the measured value of the compressive strength of the iron ore tailings recycled concrete is between −0.3 and 2.1 Mpa. The prediction model is good.

4.3 Analysis of Sensitive Parameters of Compressive Strength of Iron Tailings Recycled Concrete

The compressive strength prediction model contains a total of six significant factors. The significance model is obtained by stepwise regression analysis of various factors by the SPSS software. The significance model is shown in Table 9.

R^2 is the fitting degree, which means that the fitted compressive strength prediction model interprets the percentage change of the dependent variable. From the above table, it can be seen that in model 1 of water–cement ratio and constant construction, $R^2 = 0.465$. After adjustment, $R^2 = 0.424$. It shows that the water–cement ratio is the main factor of compressive strength. At the same time, it can be seen from the adjustment of R^2 that the factors affecting the compressive strength of recycled concrete of iron ore tailings are ranked according to sensitivity, including water–cement ratio x_2, additional water volume x_3, water–cement ratio x_2^2, and iron tailings volume x_1^2, iron tailings x_1, and the interaction between iron tailings and additional water $x_1 x_3$. The impact weights are 2.613, 1.422, 1.171, 0.846, 0.623 and 0.432.

Table 9 Summary of compressive strength models

Model	R	R^2	Adjusting R^2	Standard error of the estimate	Change statistics				
					Adjustment of R^2	Changes in F	df1	df2	Significant F value change
1	0.682	0.465	0.424	2.613	0.465	11.302	1	13	0.005
2	0.924	0.854	0.829	1.422	0.389	31.894	1	12	0.000
3	0.953	0.909	0.884	1.171	0.055	6.693	1	11	0.025
4	0.978	0.957	0.940	0.846	0.048	11.100	1	10	0.008
5	0.989	0.979	0.967	0.623	0.022	9.427	1	9	0.013
6	0.995	0.991	0.984	0.432	0.012	10.726	1	8	0.011

Note Model 1 predictor: water–cement ratio x_2; model 2 predictor: water–cement ratio x_2, additional water x_3; model 3 predictor: water–cement ratio x_2, additional water x_3, x_2^2, x_1^2; model 4 predictor: water–cement ratio x_2, additional water quantity x_3, x_2^2, x_1^2; model 5 predictive variables: water–cement ratio x_2, additional water quantity x_3, x_2^2, x_1^2, iron tailings quantity x_1; model 6 predictor variable: water–cement ratio x_2, additional water quantity x_3, x_2^2, x_1^2, iron tailings content x_1, $x_1 x_3$

5 Conclusion

(1) Through single-factor tests, water–cement ratio and additional water volume have an inhibitory effect on the compressive strength of iron tailing ore recycled concrete. The impact of iron tailings content on compressive strength firstly decreases and then increases. The slump of iron ore tailings recycled concrete is significantly affected by the iron tailings content, water–cement ratio and additional water volume. When the iron tailings content reaches 100% and the additional water consumption exceeds 60%, the slump is not within the control range.

(2) Based on the quadratic orthogonal combination design, a prediction model for iron ore tailings reclaimed concrete suitable for foundation treatment is established. It provides a certain technical reference for secondary development of iron tailings and waste concrete and its application to the foundation treatment engineering.

(3) The compressive strength of reclaimed concrete affected by iron tailings is ranked in order of significance: water–cement ratio x_2, additional water volume x_3, water–cement ratio quadratic item x_2^2, iron tailings quantity second item x_1^2, the iron tailings amount x_1 and the interaction $x_1 x_3$ between the iron tailings and the additional water. The impact weights are: 2.613, 1.422, 1.171, 0.846, 0.623 and 0.432.

References

1. Zhang MM, Wang SL, Zhang SM et al (2017) Brick for rate of experimental study on the influence on the performance of recycled coarse aggregate. Concrete 11:91–99
2. Guo ZG, Chen C, Fan BJ et al (2016) Experimental research on mechanical behavior of concrete made of coarse and fine recycled aggregates. J Build Struct 37(s2):94–102
3. Song SM, Wang L (2009) The experiment research on concrete with construction rubbish recycled aggregate. J Wuhan Univ Technol 7:56–59
4. Bai GL, Zhang FJ, An YY et al (2010) Experimental study on the compressive strength and mixture ratio of recycled concrete hollow blocks. Build Struct 12:128–130
5. Xiao JZ, Li JB, Sun ZP et al (2004) Study on compressive strength of recycled aggregate concrete. J Tongji Univ (Nat Sci) 32(12):1558–1561
6. Chen ZP, Zhou CH, Chen YL et al (2014) Mechanical properties of recycled pebble aggregate concrete. J Build Mater 17(3):465–469
7. Xia Y (2017) Durability of recycled concrete with construction waste is analyzed. Concrete 7:151–153
8. Geng O, Zhang X, Zhang CK (2015) Prediction models of the carbonization depth of recycled concrete. J China Univ Mining Technol 44(1):54–58
9. Zhang XB, Kuang CG, Fang Z (2014) Orthogonal experimental study on strength of steel fiber reinforced fly ash recycled concrete. J Build Mater 17(4):677–684
10. Liao XH, Huang X, Shi JL et al (2010) Forecast model about compressive strength of recycle aggregate concrete base on BP neutral network. J Nanjing For Univ (Nat Sci Edition) 34(5): 105–108
11. Chen LL, Wu FF, He ZY (2016) Prediction model and factors of recycled concrete splitting tensile strength. Concrete 9:37–40
12. Zhang XB, Deng SC (2004) Experimental research on unit water use in recycled concrete. Concrete 10:38–40
13. Zhang YJ, He S, Zhang X et al (2012) Modification of the Bolomey formula in recycled aggregate concrete. J Build Mater 15(4):538–543
14. Institute of Chinese Architecture Science (1997) Design specification for common concrete mix ratio. China Construction Industry Press
15. Li YY, Hu CR (2009) Experimental design and data processing. Chemical Industry Press

Dynamic Impendence of Pile Group Foundation of Bridge Based on the TLM-PML-VM Method

Yanmei Cao and Pan Wu

Abstract A semi-analytical and semi-numerical method based on TLM-PML-VM is developed to study the dynamic impedance of the pile group foundation. The Green's function and the dynamic characteristics of layered subsoil are studied theoretically by adopting the thin layer method (TLM) with the boundary of perfectly matched layer (PML), and then a dynamic analysis model of the pile group foundation with pile caps and foundation soil is established by utilizing the principle of the volumetric method (VM). By combining the TLM-PML and the VM, the dynamic impedance function of the pile group foundation is deduced and verified by a case. The proposed method can not only be applied to solve the layered soil with complex geometrical shapes, but also it need not expand the calculation zone along the horizontal direction with good calculation efficiency.

1 Introduction

The pile group foundation is most commonly used in bridge engineering, and it plays an important role in supporting the bridge piers and superstructure. So the study on the vibration characteristics of the pile group foundation subjected to dynamic loads has been paid more and more attention [1–4], in which the solution of dynamic impedance function of foundation is very crucial. Nowadays, the research methods of foundation dynamic characteristics mainly focus on the numerical analysis and the simplified calculation based on dynamic Winkler foundation. Kaynia studied the dynamic problem of the pile group foundation by means of boundary integral method [5], and the obtained solution had often been

Y. Cao (✉) · P. Wu
School of Civil Engineering, Beijing Jiaotong University, Beijing 100044, China
e-mail: ymcao@bjtu.edu.cn

regarded to be exact. However, there were some disadvantages in his research, for example, the calculation efficiency is a bit low due to the full rank of coefficient matrix, and it has discrete boundary, which is not suitable for complex geometrical problem. Ai et al. modified the coefficient matrix to be sparse matrix by using the finite element method (FEM) and improved the calculation efficiency [6], but the FEM has limitation because of the problem of calculation range and boundary conditions. Takemiya deduced the pile–soil dynamic interaction based on the volume method and the fundamental solution obtained by the thin layer method [7], but the solving accuracy is influenced by the wave incident into elastic–damper boundary condition. Huang adopted the simplified method of dynamic Winkler subsoil beam and derived the coefficients of pile–soil dynamic interaction by means of the transfer matrix method [8], which can improve the calculation efficiency but decrease the accuracy of the results.

In this paper, a semi-analytical and semi-numerical method based on TLM-PML-VM is developed, which can be used to analyze the dynamic impedance and vibration characteristics of the pile group foundation systematically and efficiently. The proposed method can not only be applied to solve the layered soil with complex geometrical shapes, but also the PML absorbing boundary condition is adopted only at the bottom of subsoil half-space, which has more advantages than other absorbing boundaries [9]. Furthermore, it need not expand the calculation zone along the horizontal direction and the calculation efficiency is prior to the boundary element method.

2 Green's Function of Subsoil Displacement by TLM-PML

2.1 TLM Soil Model

The soil model is established by means of the thin layer method (TLM) in the cylindrical coordinate system, as shown in Fig. 1.

In the frequency domain, the governed equation of soil motion can be written as:

$$
\begin{aligned}
(\lambda + \mu)\frac{\partial \Delta}{\partial r} + \mu\left[\nabla^2 \bar{u}_r - \frac{1}{r}\left(\frac{2}{r}\frac{\partial \bar{u}_\theta}{\partial \theta} + \frac{\bar{u}_r}{r}\right)\right] &= \rho\omega^2 \bar{u}_r \\
(\lambda + \mu)\frac{\partial \Delta}{r\partial \theta} + \mu\left[\nabla^2 \bar{u}_\theta - \frac{1}{r}\left(\frac{\bar{u}_\theta}{r} - \frac{2}{r}\frac{\partial \bar{u}_r}{\partial \theta}\right)\right] &= \rho\omega^2 \bar{u}_\theta \\
(\lambda + \mu)\frac{\partial \Delta}{\partial z} + \mu\nabla^2 \bar{u}_z &= \rho\omega^2 \bar{u}_z,
\end{aligned}
\tag{1}
$$
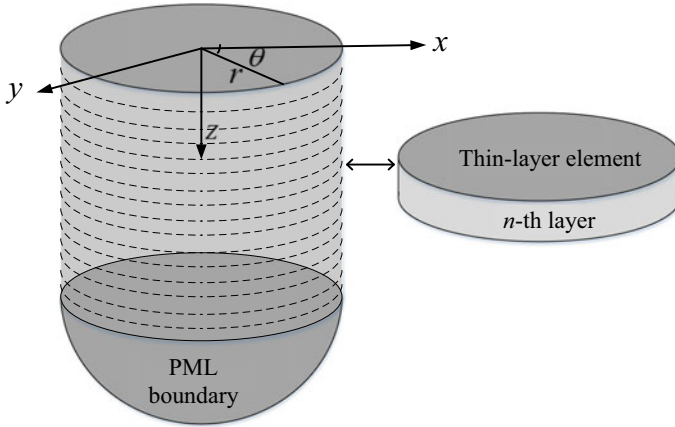
Fig. 1 TLM soil model of elastic half-space in cylindrical coordinate

in which $\bar{u}_r, \bar{u}_\theta$, and $\bar{u}_z$ are the radius, rotation, and vertical displacements of the soil, respectively; ρ is the density of the soil; λ and μ are Lamé coefficients; Δ is the volumetric strain; ∇^2 is the Laplace operator; and ω is the angular frequency of excitation.

By means of Fourier–Bessel integral transformation, Eq. (1) can be transformed into the wave number–frequency domain:

$$
\begin{aligned}
(\lambda + 2\mu)k_r^2 \tilde{u}_r - \mu \frac{d^2 \tilde{u}_z}{dz^2} + k_r(\lambda + \mu)\frac{d\tilde{u}_z}{dz} &= \rho\omega^2 \tilde{u}_r \\
\mu k_r^2 \tilde{u}_\theta - \mu \frac{d^2 \tilde{u}_\theta}{dz^2} &= \rho\omega^2 \tilde{u}_\theta \\
-k_r(\lambda + \mu)\frac{d\tilde{u}_r}{dz} + k_r^2 \mu \tilde{u}_z - (\lambda + 2\mu)\frac{d^2 \tilde{u}_z}{dz^2} &= \rho\omega^2 \tilde{u}_z.
\end{aligned}
\tag{2}
$$

By means of the principle of TLM [10] and the Galerkin weighted residual method, the stiffness matrix of single layer in frequency–wave number domain can be obtained from Eq. (2). Then, the total stiffness matrix of thin layers can be obtained by assembling all the element matrices of the thin layers, and thus the Green's function of soil displacement in frequency–wave number domain can be deduced by spectral factorization of total stiffness matrix. Finally, the Green's function in frequency–spatial domain and Cartesian coordinate can be derived by Fourier–Bessel inverse transformation and coordinate conversion, as shown in Eq. (3):

$$U_{xx}^{mn} = \sum_{j=1}^{NR} I_{3j}\phi_{xj}^m\phi_{xj}^n + \sum_{j=1}^{NR} I_{4j}\phi_{yj}^m\phi_{yj}^n$$

$$U_{yy}^{mn} = \sum_{j=1}^{NR} I_{4j}\phi_{xj}^m\phi_{xj}^n + \sum_{j=1}^{NR} I_{3j}\phi_{yj}^m\phi_{yj}^n$$

$$U_{xy}^{mn} = \sum_{j=1}^{NR} I_{2j}\phi_{xj}^m\phi_{xj}^n - \sum_{j=1}^{NR} I_{2j}\phi_{yj}^m\phi_{yj}^n = U_{yx}^{mn}$$

$$U_{xz}^{mn} = -\mathrm{i}\sum_{j=1}^{NR} I_{5j}\phi_{xj}^m\phi_{zj}^n, \quad U_{zx}^{mn} = \mathrm{i}\sum_{j=1}^{NR} I_{5j}\phi_{zj}^m\phi_{xj}^n = -U_{xz}^{mn}$$ (3)

$$U_{yz}^{mn} = -\mathrm{i}\sum_{j=1}^{NR} I_{6j}\phi_{xj}^m\phi_{zj}^n, \quad U_{zy}^{mn} = \mathrm{i}\sum_{j=1}^{NR} I_{5j}\phi_{zj}^m\phi_{xj}^n = -U_{yz}^{mn}$$

$$U_{zz}^{mn} = \sum_{j=1}^{NR} I_{1j}\phi_{zj}^m\phi_{zj}^n,$$

in which $U_{\alpha\beta}^{mn}$ represents the displacement Green's function of the mth layer soil along α-direction induced by the unit load that applies to the nth layer along β-direction; I_{nj} ($n = 1, 2, \ldots, 6$) are the Kernels of fundamental solutions, which are listed in Table 1; $H_0^{(2)}(Z_j)$ and $H_1^{(2)}(Z_j)$ are the second-kind Hankel functions; k_{Rj}, ϕ_{xj}^m, and ϕ_{zj}^m are, respectively, the jth eigenvalue and eigenvector of the mth layer subsoil for the Rayleigh wave, while ϕ_{yj}^m means the jth eigenvector for the Love wave.

Table 1 Kernels of fundamental solutions

$Z_j = k_j r \ \ r = \sqrt{x^2 + y^2} \ \ \cos\theta = x/r \ \ \sin\theta = y/r$
$I_{1j} = \dfrac{1}{4i}H_0^{(2)}(Z_j)$
$I_{2j} = \dfrac{\cos\theta\sin\theta}{4i}\left\{H_0^{(2)}(Z_j) - \dfrac{2}{Z_j}\left\{H_1^{(2)}(Z_j) - \dfrac{2i}{\pi Z_j}\right\}\right\}$
$I_{3j} = \dfrac{1}{4i}\left\{\cos^2\theta H_0^{(2)}(Z_j) - \dfrac{\cos^2\theta - \sin^2\theta}{Z_j}\left\{H_1^{(2)}(Z_j) - \dfrac{2i}{\pi Z_j}\right\}\right\}$
$I_{4j} = \dfrac{1}{4i}\left\{\sin^2\theta H_0^{(2)}(Z_j) + \dfrac{\cos^2\theta - \sin^2\theta}{Z_j}\left\{H_1^{(2)}(Z_j) - \dfrac{2i}{\pi Z_j}\right\}\right\}$
$I_{5j} = -\dfrac{1}{4}\cos\theta H_1^{(2)}(Z_j)$
$I_{6j} = -\dfrac{1}{4}\sin\theta H_1^{(2)}(Z_j)$

2.2 TLM Soil Model with PML Boundary

The perfectly matched layer (PML) is a kind of special boundary condition which can absorb or transmit wave energy to avoid wave reflection from soil boundaries. The boundary can make incoming wave energy gradually vanish by means of stretching an outward absorbing layer with specific depth. Herein, a complex scaling function is introduced, and then the complex stretching function can be obtained so that the wave energy within the PML boundary can attenuate exponentially to zero [11, 12].

An elastic–homogeneous subsoil layer with the depth H is considered, and the SH wave propagating with the velocity of C_s is assumed to transmit in the soil layer (Fig. 2).

In order to match with TLM, the coordinate z with the PML region is changed to the complex form, i.e., $\bar{z} = z - i\Psi(z)$, in which the real part is the actual depth of PML boundary layer and the imaginary part is defined by a position-dependent function of $\Psi(z) = \frac{\omega_0 H}{\omega(m+1)}\left(\frac{z}{H}\right)^{m+1} = \Omega H \zeta^{m+1}$ with ω_0 controlling the energy absorbing of incoming wave and m being variation ratio of stretching function in PML. Then, the stretched vertical coordinate can be written by $\bar{z} = z(1 - i\Omega\zeta^m)$, and thus the complex form of PML depth H is $\bar{H} = H(1 - i\Omega)$.

Since the incoming wave into the PML region at the incident angle α can be expressed by $u(x, z, t) = A\exp\left[i(\omega t - x\frac{\omega}{C}\sin\alpha - z\frac{\omega}{C}\cos\alpha)\right]$, the total back–forth attenuation of wave energy can be derived as $\Delta = \exp\left(-2\omega\Omega\frac{H}{C}\cos\alpha\right) = \exp(-4\pi\Omega\eta\cos\alpha)$, in which $\eta = H/\lambda$ is the ratio of PML depth to wavelength of incident wave.

The PML is supposed to be equally divided into N thin layers, and the stretched depth of the jth thin layer is:

$$\bar{h}_j = \bar{z}_j - \bar{z}_{j-1} = H\left\{\frac{1}{N} - i\Omega\left[\left(\frac{j}{N}\right)^{m+1} + \left(\frac{j-1}{N}\right)^{m+1}\right]\right\} \quad (1 \leq j \leq N). \quad (4)$$
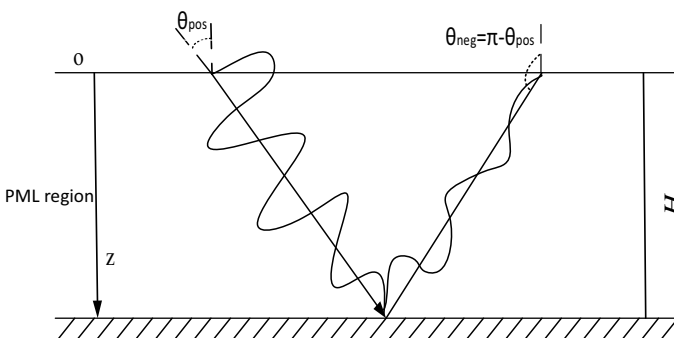
Fig. 2 Wave propagation within the PML region

The element matrix of the PML thin layer can be obtained by substituting h_j by $\bar{h}_j$. Since the PML thin layer adjacent to the TLM has the discrete property, the virtual reflection will be induced by sublayer depth variations and furthermore it increases with Ω. Therefore, Ω is generally evaluated from the larger values to get enough attenuation, and the following values are considered as the most optimal [13]:

$$m = 2; \quad \eta = \frac{H}{\lambda_s} = \sqrt[3]{\frac{1}{12} x_{max} \Big/ \lambda_s} \geq 1; \quad \Omega = 4\eta; \quad nN = 10\eta, \tag{5}$$

where N is the total thin layer number in PML; n is the times of interpolation shape functions; and x_{max} is the maximum distance away from observation point along the x-direction.

3 Dynamic Impedance of pile group Foundation of Bridge by the TLM-PML-VM

The dynamic analysis model of the pile group foundation–subsoil is shown in Fig. 3, in which the coupled model of the pile group foundation and subsoil can be equivalent to the superposition of three parts: complete subsoil, pile group foundation, and eliminated soil of pile group foundation, which is called the volume method (VM).

Firstly, for the layered subsoil model (1) in Fig. 3, it is divided into many thin-layer elements in the vertical direction, and the nodes are set on those layers with pile foundation. The stiffness matrix $\mathbf{A}(i\omega)$ of subsoil between adjacent nodes satisfies the following dynamic equation:

$$\mathbf{A}(i\omega)\mathbf{u_G} = \mathbf{F_G}, \tag{6}$$

where the subscript "**G**" means the complete subsoil model (1) in Fig. 3; $\mathbf{u_G}$ and $\mathbf{F_G}$ represent the displacement vector and the interaction force vector of pile–soil interaction nodes, respectively; $\mathbf{A}(i\omega)$ indicates the influence of subsoil on pile–

Coupled model of pile-group foundation and subsoil   **(1) Subsoil G**   **(2) Pile-group foundation S**   **(3) Eliminated soil SG by pile-group**
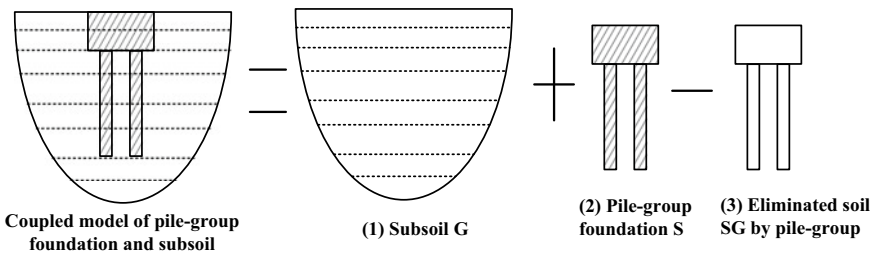
Fig. 3 Dynamic analysis model of pile group foundation–subsoil

subsoil dynamic interaction, which can be calculated by Green's function of subsoil displacement based on the TLM-PML described in the above section.

Next, the motion equation of the pile group foundation model (2) and eliminated soil (3) in Fig. 3 can be expressed by:

$$\left[\left(\mathbf{K_S} - \mathbf{K_S^G}\right) - \omega^2\left(\mathbf{M_S} - \mathbf{M_S^G}\right)\right]\mathbf{u_S} = \mathbf{F_S} + \mathbf{F_F}, \tag{7}$$

in which the subscript "**S**" means the pile group foundation model (2) and the superscript "**G**" with subscript "**S**" denotes the eliminated soil model (3); **K** and **M** are stiffness matrix and mass matrix, respectively; $\mathbf{u_S}$ and $\mathbf{F_S}$ represent the displacement vector and the external force vector of pile foundation nodes, respectively; $\mathbf{F_F}$ represents the interaction force between subsoil and pile foundation.

If no any relative slip between pile foundation and subsoil is assumed, the compatibility condition of displacements and the equilibrium condition of forces will be met with for adjacent nodes between pile foundation and subsoil, i.e.,

$$\mathbf{u_S} = \mathbf{u_G} \quad \mathbf{F_F} = \mathbf{F_G}. \tag{8}$$

Assembling Eqs. (6)–(8), one can obtain:

$$\mathbf{S}(i\omega)\mathbf{u_S} = \mathbf{F_S}, \tag{9}$$

where $\mathbf{S}(i\omega) = \left(\left(\left(\mathbf{K_S} - \mathbf{K_S^G}\right) - \omega^2\left(\mathbf{M_S} - \mathbf{M_S^G}\right)\right)\right) + \mathbf{A}(i\omega)$ represents the dynamic impedance matrix of the pile group foundation without the bridge platform.

Equation (9) can also be expanded as:

$$\begin{bmatrix} \mathbf{S_{11}} & \mathbf{S_{12}} \\ \mathbf{S_{21}} & \mathbf{S_{22}} \end{bmatrix} \begin{Bmatrix} \mathbf{u_1} \\ \mathbf{u_2} \end{Bmatrix} = \begin{Bmatrix} \mathbf{F_1} \\ \mathbf{F_2} \end{Bmatrix}. \tag{10}$$

Generally, there exists the platform upon the pile group foundation for the bridge. In order to further obtain the relationship of the displacement vector and the external excitation of the central point of bridge platform, the geometric transformation matrix of rigid nodes $\mathbf{T} = [\mathbf{T_1}\mathbf{T_2}\ldots\mathbf{T_i}\ldots\mathbf{T_N}]^{\mathbf{T}}$ is finally introduced, with $\mathbf{T_i}$ meaning the geometric transformation matrix of the ith rigid node and the central point of platform. Equation (9) can be transformed as:

$$\begin{aligned} \mathbf{P_0} &= \mathbf{K}\mathbf{U_0} \\ \mathbf{K} &= \mathbf{T^T}(\mathbf{S_{11}} - \mathbf{S_{12}}\mathbf{S_{22}^{-1}}\mathbf{S_{21}})\mathbf{T}, \end{aligned} \tag{11}$$

in which $\mathbf{P_0}$ is the external excitation force vector applied to the central point of platform; $\mathbf{U_0}$ is the displacement vector of the rigid body; **K** is the dynamic impedance matrix of the pile group foundation with the bridge platform.

Because the elements of **K** are complex, every complex element can be written by $\bar{K} = \bar{k} + i\bar{c}$, in which the real part $\bar{k}$ indicates the contribution of dynamic stiffness and the imaginary $\bar{c}$ means the contribution of damping.

4   Case Study and Validation

The developed TLM-PML-VM can be programmed by MATLAB and thus the dynamic impedance and the vibration characteristics of the pile group foundation of bridge can be accomplished.

To validate the effectiveness of this proposed method, a typical case of 3×3 pile group foundation is studied. Herein, the dimensionless parameters are adopted [14]: The ratio of elastic modulus of soil and piles is $E_s/E_p = 1/100$; the density ratio of soil and piles is $\rho_s/\rho_p = 0.7$; the Poisson's ratio of soil and piles is $\nu_s = 0.4$ and $\nu_p = 0.25$; the slenderness ratio $L_p/d = 20$; and the ratio of pile spacing to pile diameter $s/d = 5$. Also, herein both the vertical impedance K_V and the horizontal impedance K_H are denoted by the form of $k + ia_0c$, where k and c are the mean stiffness coefficient and damping coefficient, respectively, and $a_0 = \omega d/C_s$ is the dimensionless frequency.

Figure 4 shows the calculated results by means of the proposed TLM-PML-VM method and the comparison with Kaynia and Miura [14]. In the figure, the horizontal coordinate is the dimensionless frequency a_0 and the vertical coordinate is also dimensionless with dynamic impedance divided by $N_p k_v^s$ (N_p is the total number of piles, k_v^s is the static stiffness of a single pile in the vertical direction) or $N_p k_h^s$ (k_h^s is the static stiffness of a single pile in the horizontal direction).

It can be seen from Fig. 4 that the results agree very well with those of Kaynia and Miura [14], which reflects the effectiveness and correctness of the TLM-PML-VM method in solving dynamic impedance of the pile group foundation. The proposed

(a) Horizontal dynamic impedance   (b) Vertical dynamic impedance
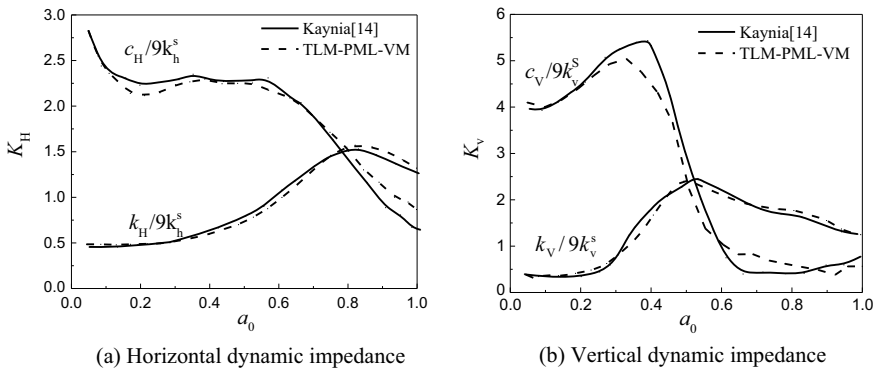
Fig. 4 Validation of TLM-PML-VM in solving dynamic impedance of the pile group foundation

method can be used to further analyze the vibration characteristics and influencing factors of pile group foundation vibrations.

5   Conclusions

In this paper, a semi-analytical and semi-numerical method based on TLM-PML-VM is developed, which can be used to obtain the dynamic impedance and analyze the vibration characteristics of the pile group foundation systematically and efficiently.

In the method, the Green's function and the dynamic characteristics of layered subsoil model are studied theoretically by adopting the thin layer method (TLM) with the boundary of perfectly matched layer (PML). A dynamic analysis model of the pile group foundation with platform and subsoil is established by utilizing the principle of the volumetric method (VM). By combining the TLM-PML and the VM, the dynamic impedance matrix of the pile group foundation system is deduced and accomplished.

Finally, the calculated results are compared with the existing results and the effectiveness and correctness are validated by a case study. The proposed method can not only be applied to solve the layered soil with complex geometrical shapes, but also the PML absorbing boundary condition is adopted only in the bottom half-space of subsoil, which has more advantages than other absorbing boundaries. Furthermore, it need not expand the calculation zone along the horizontal direction and the calculation efficient is prior to the boundary element method.

The further research will focus on the vibration characteristics of the pile group foundation subjected to the dynamic loading.

References

1. Jiang T, Cheng CS (2006) Environmental vibration induced by elevated railway traffic using thin-layer method. J Vibr Eng 20(6):623–628
2. Gao GY, Li SY, Gu XQ (2015) Ground vibration induced by moving train on viaduct with group pile foundation. Chin J Geotech Eng 37(10):1751–1761
3. Zhang ZJ (2016) Semi-analytical analysis and experimental study of ground vibration induced by trains moving over high-speed railway bridges. Southwest Jiaotong University, Doctor Degree Dissertation
4. Wen XZ, Shang SP (2009) Research on dynamic impedance functions of pile-raft foundation in layered soil. Eng Mech 26(8):95–99
5. Kaynia AM, Kausel E (1982) Dynamic stiffness and seismic response of pile groups. Massachusetts Institute of Technology

6. Zhi Y, Zhi X, Li H (2016) Dynamic response of a laterally loaded fixed-head pile group in a transversely isotropic multi layered half-space. J Sound Vib 38(5):171–183

7. Takemiya H, Bian XC (2007) Shinkansen high-speed train induced ground vibrations in view of viaduct-ground interaction. Soil Dyn Earthq Eng 27(6):506–520

8. Huang MS, Wu ZM, Ren Q (2007) Lateral vibration of pile groups in layered soil. Chin J Geotech Eng 29(1):32–38

9. Tian K, Huang JP, Li ZC (2014) Multi-axial convolution perfectly matched layer absorption boundary condition. OGP 49(1):143–152

10. Wass G (1992) Linear two-dimensional analysis of soil dynamic problems in semi-infinite layered Media. University of California, Berkelet, California. Doctor Degree Dissertation

11. Barenger JP (1950) A perfectly matched layer for the absorption of electromagnetic waves. J Comput Phys 114(9):89–95

12. Kausel E, Barbosa J (2011) PMLs: a direct approach. Int J Numer Meth Eng 90(3):343–352

13. Barbosa J, Park J, Kausel E (2012) Perfectly matched layers in the thin layer method. Comput Methods Appl Mech Eng 217–220:262–274

14. Kaynia AM, Miura K (1991) Dynamics of piles and pile groups in layered soil media. Soil Dyn Earthq Eng 10(8):386–401

Backbone Curve Model of Saturated Coarse-Grained Soil Under Train-Induced Cyclic Loading

Rusong Nie, Junli Dong, Wuming Leng, Wenquan Zhou, Yafeng Li and Huihao Mei

Abstract Deformation of the subgrade bed layer under cyclic dynamic loading is one of the key factors to evaluate the operating performance of subgrade. To study the stress–strain characteristics of coarse-grained soil (CGS) under cyclic loading, a series of large-scale dynamic triaxial tests were carried out at different confining pressures and dynamic stress amplitudes. Results show that the variation of soil stiffness is closely related to cyclic number and confining pressure under cyclic loading. Backbone curve model is developed regarding confining pressure and cyclic number. Compared with the traditional backbone curve model, the proposed model can reflect the CGS stiffness hardening with the increasing of cyclic number and be used to determine the dynamic strength of CGS when the dynamic strain is less than the dynamic yield strain and to provide a reference for evaluating dynamic stress deformation stability for subgrade bed and design.

Keywords Coarse-grained soil (CGS) · Cyclic loading · Large-scale dynamic triaxial tests · Dynamic stress–strain · Backbone curve model

1 Introduction

High-speed passenger and heavy freight transportation are the directions of railway development in China. The increase in train speeds and axle loads significantly increases the dynamic loads on the track and substructure. The subgrade is an

R. Nie · J. Dong · W. Leng · W. Zhou · Y. Li (✉) · H. Mei
School of Civil Engineering, Central South University, Changsha 410075, China
e-mail: 174801019@csu.edu.cn

R. Nie
Key Laboratory of Ministry of Education for Heavy Haul Railway Engineering Structure,
Central South University, Changsha 410075, China

W. Zhou
Department of Building Engineering, Hunan Institute of Engineering,
Xiangtan 411104, China

important substructure supporting the track structure, where the subgrade bed layer, generally 2.5 m thick, includes the surface layer, 0.6 m thick, and the bottom layer, 1.9 m thick. The subgrade bed layer is the main layer bearing the train-induced dynamic load. In Chinese code (TB 10001-2016), the filling material in the subgrade bed layer should be Group A or B or chemically modified soil. Groups A and B are the coarse-grained soils with fine particles (particle size less than 0.075 mm or passing No. 200 sieve) less than 15%. The main difference between them is either good or bad grading. Group A is good grading, and Group B is not. The subgrade bed layer is the top layer of the subgrade. The soil in this layer is loaded by the low confining pressure as small as 15 kPa and the train-induced dynamic load as large as 100 kPa. The train-induced dynamic load is the main factor affecting the working performance of the soil. Therefore, it is of great theoretical and practical value to study the dynamic behavior of the coarse-grained soil (CGS) under different train-induced dynamic loads and confining pressures.

The dynamic behavior of the soil is influenced by three factors including the dynamic load, the soil state, and the boundary condition [1]. The dynamic load is generally determined by the amplitude, frequency, and cyclic number. The soil state is determined by grading, density or compaction degree, water content, etc. The boundary condition includes confining stress, static deviatoric stress, consolidation ratio, etc. Numerous researches conducted in the past 60 years significantly improve the insight into the dynamic behavior of the soil and the design level to resist dynamic loads [1–9]. However, most researches on soil dynamic behavior are focused on the fine-grained soil under earthquake loads. There are relatively few researches on the dynamic behavior of CGS under train-induced loads.

The backbone curve is an important aspect in the study of the dynamic characteristics of soils. It reflects the dynamic stress–strain relationship of soils and provides the basis for the establishment of the dynamic constitutive relation, especially for numerical calculation [6, 10]. There are two kinds of backbone curve models: One is hyperbolic model, such as the Konder model and Hardin–Drnevich model [11], and the other is a bilinear model including the modified form, such as three-parameter Ramberg–Osgood model [12, 13]. However, these models do not consider the phenomenon that the soil stiffness increases with the increase in cyclic number under cyclic loads.

Dynamic triaxial test is a common method to study the soil dynamic behavior. To study the dynamic behavior of the compacted CGS in subgrade bed under train-induced dynamic loads, a series of large-scale triaxial tests were conducted. The compacted CGS specimens were 300 mm in diameter and 600 mm in height. In this study, the influences of dynamic stress amplitude (to simulate different axle loads), confining pressure (to simulate different depths), and cyclic number on the dynamic behavior of saturated CGS were studied. A backbone curve model considering the influence of cyclic number on the CGS stiffness was established.

2 Dynamic Triaxial Test

2.1 Coarse-Grained Soil (CGS)

The test CGS was mixed with the sand and round gravel from Xiang River (Hunan Province) and the silty clay from Taiyuan, Shanxi Province. Their grain distribution curves are shown in Fig. 1. The mass ratio of gravel: sand: clay = 43.6%:43.6%:12.8%. The silty clay was derived from the depth of approximately 1–6 m below the ground. Its soil specific gravity = 2.63–2.65, natural density = 1.78–1.85 g/cm^3, water content = 38–43%, liquid limit = 26–30%, plastic limit = 15–18%, plasticity index = 11–15, and initial void ratio = 0.94–1.05. The test CGS has the maximum dry density = 2.21 g/cm^3, the optimum moisture content = 6.2%, C_u = 129, and C_c = 2.16. In accordance with the Chinese Code (TB 10625-2017), the test CGS belongs to Group A which are good grading with $C_u = D_{60}/D_{10} > 5$ and $1 < C_c = (D_{30})^2/D_{60}D_{10} < 3$.

    The test specimens were made in accordance with the compaction degree $K = 0.97$. The specimens were 300 mm in diameter and 600 mm in height. The specimens were made directly on the base of the pressure chamber. In order to ensure that the specimen was uniform from top to bottom, the specimen was compacted with six layers, and each layer was 100 mm thick. The specimen was saturated by the vacuum exhaust method and by applying a back pressure of 200 kPa. The pore pressure coefficient $B \geq 0.96$. Then, the specimen was consolidated by an isotropic pressure of 15 kPa for approximately 12 h. The water content of the saturated specimen was 9.0–9.5%.

Fig. 1 Grain distribution curve of the test CGS

(a) Loading system   (b) Soil specimens after test

Fig. 2 MTS loading test system and sample after testing

2.2 Test Program

The axial load on the test specimen was applied by an actuator controlled by MTS (shown as Fig. 2). The loading process was carried out in accordance with Fig. 3. In Fig. 3, line *OA* means applying the confining stress. Line *AB* means the consolidation process. Line *BC* means applying the static load induced by the track structure deadweight (σ_s = 15 kPa). The dynamic load on the test specimens was simulated by a sine wave with a dynamic stress amplitudes of 25–125 kPa (σ_d) and a frequency of 1 Hz [15, 16], which were to simulate the dynamic loads induced by about 13 m long freight wagons with the axial load of 19–30 tons at the speed of 50 km/h. The test program was divided into three groups. The load parameters for each group are listed in Table 1. In the cyclic loading process, tests were undrained.

The criteria for terminating the test are as follows: (1) If the increment of axial plastic deformation is less than 1 mm within 2 h, the test specimen is considered to be in a dynamic stable state. (2) If the axial plastic deformation increases significantly and is greater than 1 mm within 2 h, the test continues until the axial plastic strain reaches 15%. The test specimen is considered to be in a dynamic instability state.

3 Testing Results and Analysis

3.1 Dynamic Stress Amplitude

Figure 4 shows the variation of axial accumulative plastic strains (ε_d) of three-group specimens with the cyclic number (*N*). The plastic strain (ε_s) caused by the axial static load (the track structure deadweight load σ_s = 15 kPa, i.e., line *BC* in Fig. 3),

Fig. 3 Exerting method of axial load
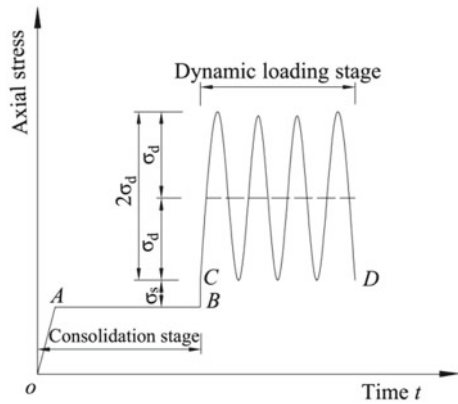
Table 1 Large-scale dynamic triaxial tests' parameters of CGS

Testing group	Confining pressure σ_3 (kPa)	Dynamic stress amplitude σ_d (kPa)
1	15	25, 50, 62.5, 75, 100, 125
2	30	25, 50, 62.5, 75, 100, 125
3	60	25, 50, 62.5, 75, 100, 125

is so small that it is negligible. Therefore, the axial accumulated plastic strain (ε_d) contained (ε_s). As seen in Fig. 4, the axial accumulative plastic strain increases at a different rate as the cyclic number increases for different dynamic stress amplitudes. The greater the dynamic stress amplitude, the faster the axial accumulative plastic strain increases. According to the development trends of the axial accumulative plastic strains with the cyclic number, the curves can be categorized into three modes as the disruptive, the critical, and the stable mode [17–19]. The dynamic stress corresponding to the critical curve is the critical dynamic stress (σ_{dcr}). When the dynamic stress generated by the train-induced loads in the subgrade is greater than this value, the axial accumulative strain of the soil continuously increases until it is destroyed. On the contrary, when the dynamic stress is less than this value, the axial accumulative strain of the soil tends to be stable at a certain value. Therefore, the axial accumulative plastic strain and the dynamic stress amplitude are closely related.

Theoretically, the critical dynamic stress is a specific value for specific filler under certain confining pressure, certain water content, and certain compaction degree. Actually, the real value of the critical dynamic stress is difficult to accurately determine due to the difference in specimen preparation, operation error, and other factors. The test values of the critical dynamic stress for the three groups are presented in Table 2. The test value of the critical dynamic stress was not a specific value but in a range. As seen in Table 2, the greater the confining stress on the test specimen, the greater the critical dynamic stress. Cai [17] and Liu [20] obtained similar results.

Fig. 4 ε_d-N relation curve
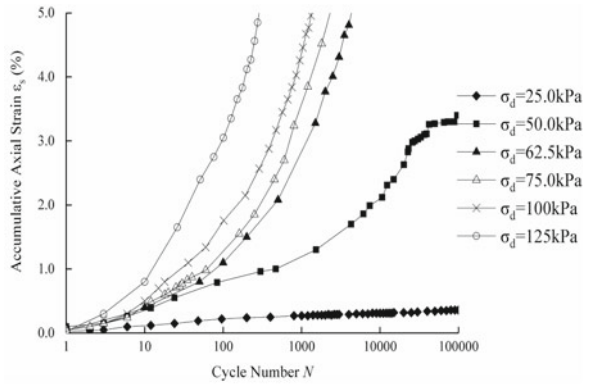
(a) σ_3=15 kPa
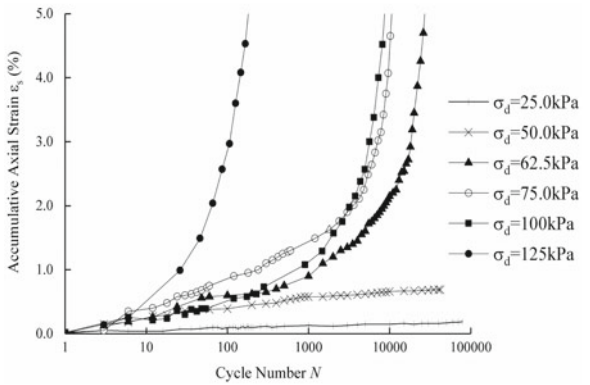
(b) σ_3=30 kPa
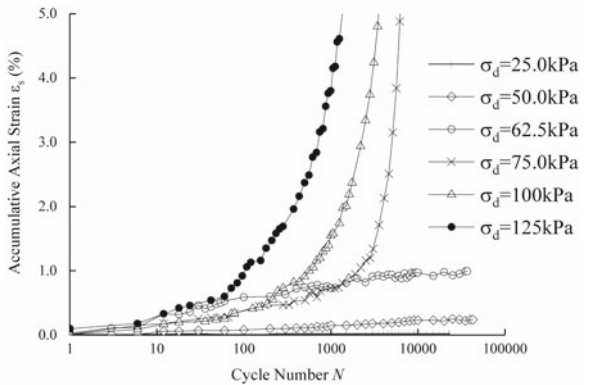
(c) σ_3=60 kPa

Table 2 Test and estimated values of critical dynamic stress

σ_3 (kPa)	σ_{dcr} (kPa)
15	50–62.5
30	50–62.5
60	62.5–75

The critical dynamic stress of the soil is not only related to the soil state parameters, like the water content, the compaction degree, and particle gradation, but also related to the dynamic loading parameters, like the dynamic stress amplitude, frequency, and cyclic number. In practice, the dynamic stress in subgrade generated by trains should be less than the critical dynamic stress at the same depth. The aim is to maintain the subgrade long-term dynamic stability without an excessive settlement. When no other better filler is available, improving the compaction quality is the common method to increase the critical dynamic stress of the subgrade soil.

3.2 Cyclic Number

The cyclic number is an important factor affecting the accumulative plastic strain of the soil. The train-induced dynamic load has relatively better periodicity than the seismic load which is random. The cyclic number of the train-induced dynamic load is determined by the total number of axles of the train. A common practice to assume is that two axles under the same truck (bogie) are considered to produce one load cycle for the ballast layer and four axles under two adjacent trucks are considered to produce a single load cycle for the subgrade layer. With the increase of the cyclic number of the dynamic load, the relative slip and adjustment of position between soil particles will continue to occur. In a macroscopic view, elastic deformation and plastic deformation occur simultaneously. In Fig. 5, two load cycles (the fifth and sixth cycle) with dynamic stress amplitude ($\sigma_d = 75$ kPa) acting on the test specimen under the confining pressure ($\sigma_3 = 60$ kPa) resulted in the stress–strain curves. As seen in Fig. 5, the stress–strain curves are hysteresis loops. The hysteresis loops reflect the strain lags behind the stress, embodying the viscosity characteristics of the soil.

The strain consists of elastic strain and plastic strain. In Fig. 5, $\sigma_{d, max}$ = maximum cyclic dynamic stress, $\sigma_{d, min}$ = minimum cyclic dynamic stress, σ_d = dynamic stress amplitude = $(\sigma_{d, max} - \sigma_{d, min})/2$, $\varepsilon_{N,max}$ = the maximum dynamic strain in the Nth cycle, $\varepsilon_{N,min}$ = the minimum dynamic strain in the Nth cycle, $\varepsilon_{N,d}$ = the dynamic strain amplitude in the Nth cycle = $(\varepsilon_{N,max} - \varepsilon_{N,min})/2$, and $\varepsilon_{N,p}$ is the corresponding plastic strain after cyclic number N.

In the test, the sample frequency was 100 Hz and the data number of the recorded stress and strain was 200 in every cycle. The greater cyclic number will result in a greater amount of data. In order to save the storage space and ensure the
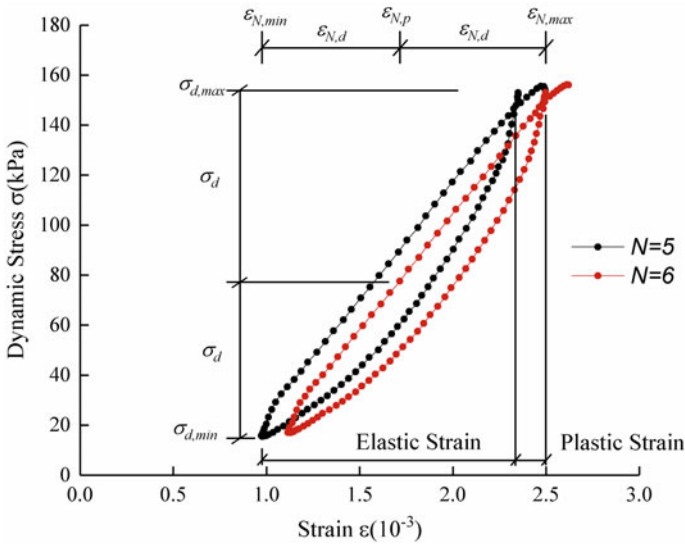
Fig. 5 Dynamic stress–strain curve

continuity of data, a cycle was recorded in 5 cycles at the 10th–50th cycle, a cycle in 10 cycles at the 51th–100th cycle, a cycle in 50 cycles at the 101th–4000th cycle, a cycle in 1000 cycles at the 4001th–10,000th cycle, and a cycle in 10,000 cycles at the cyclic number greater than 10,000. Note that the dynamic stress amplitude remained unchanged in a test. At the start of the test, the servo loading system was in the process of self-tuning. The recorded stress–strain curves showed the stress gradually increased at the initial loading cycles and became stable after about ten loading cycles.

Figure 6 shows the stress–strain curves of the stable mode (Fig. 6a) and the destructive mode (Fig. 6b) at the confining pressure $\sigma_3 = 60$ kPa. As seen in Fig. 6a, the plastic strain increases rapidly at the initial loading circles. The hysteresis loop is fatter and in an unstable state at the initial loading cycles. As the cyclic loading number increases, the hysteresis loop gradually becomes narrower and steeper and the hysteresis loops almost completely coincide at the cyclic loading number greater than 10000. This phenomenon reflects that the modulus of the test specimen increases and finally becomes a constant value as the cyclic number increases. Instead, the stress–strain curve in Fig. 6b shows that the plastic strain increases continuously until the axial accumulative strain exceeds 15% as the cyclic loading number increases. It is interesting to note that the hysteresis loops are parallel to each other after the initial hundred cycles, which means the modulus of this test specimen remains constant until it is destroyed.
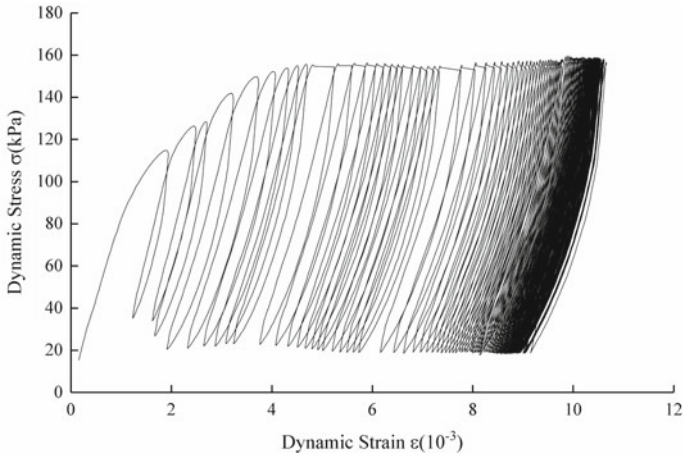
(a) $\sigma_3 = 60$ kPa, $\sigma_d = 62.5$ kPa
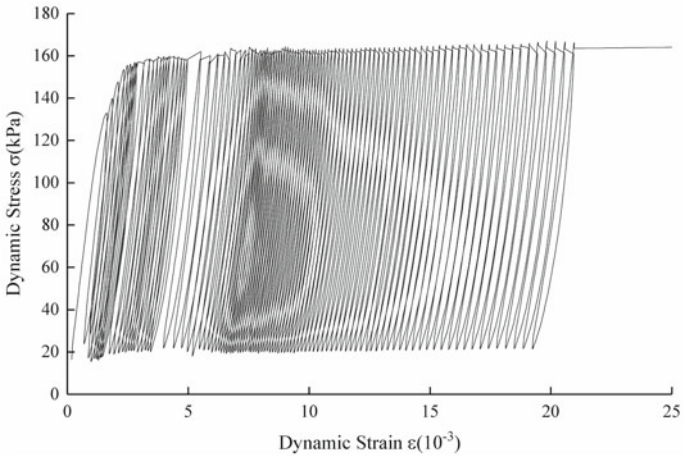
(b) $\sigma_3 = 60$ kPa, $\sigma_d = 75$ kPa

Fig. 6 Typical hysteresis curves of soil

4 The Backbone Curve Model

4.1 The Backbone Curve of Dynamic Stress–Strain Relationship

The backbone curve is the line connecting the vertices of the hysteresis loop of the stress–strain relationship curve of soil under the same consolidation pressure under different dynamic stresses. The nonlinearity of the backbone curve reflects the

nonlinearity of the equivalent deformation modulus of soil [1, 10]. When the applied dynamic load is small, the dynamic stress–strain curve is a closed hysteresis loop with coordinate origin as a symmetry point [21]. For the stable CGS specimen, the dynamic stress is less than the critical dynamic stress. The hysteresis loops remain basically unchanged after the cyclic number greater than 5000 times. Therefore, the hysteresis loops less than 5000 loading circles were considered in this article. Since the applied dynamic load (shown as Fig. 3) was positive, it is necessary to move the coordinate origin to the geometric center of the hysteresis loops. Figure 7 shows the backbone curves at the different cyclic number (N) of the saturated stable CGS specimens. As shown in Fig. 7, the dynamic strain is very little less than 1.0×10^{-3}. The backbone curves exhibit good linear elasticity at different dynamic stress amplitudes, which are the embodiment of the good linear elastic relationship of hysteresis loops. The greater the confining pressure, the closer the backbone curves at different loading circles, the smaller the influence of the cyclic number on the dynamic behavior of the soil is, the more stable the dynamic behavior of the soil. The backbone curve is different corresponding to the different cyclic number. The slope of the backbone curve increases as the cyclic number increases, meaning that the stiffness of the CGS increases as the cyclic number increases. The phenomenon of stiffness hardening is obviously different from the stiffness softening of fine-grained soil shown with increasing cyclic number [4, 5, 10]. Possible mechanisms can be explained as follows: For the stable CGS specimen, the pore water pressure in the soil is stable with the increase of the cyclic number [4, 22], while the relative slippage and adjustment of position between soil particles result in the particles becoming closer, and then result in an increase in the stiffness of the soil.

4.2 Mathematical Model of the Backbone Curve

At the same dynamic stress amplitudes, the hysteresis loop gradually becomes narrower or wider, the modulus increases or decreases with the increase of the loading cycles. The backbone curve equation should embody these characteristics. After repeated attempts and comparison, it is found that the bilinear model is appropriate to describe the backbone curve of the saturated CGS.

The bilinear model is shown in Fig. 8, and its function is presented as:

$$\left.\begin{array}{l} \varepsilon_d \leq \varepsilon_y, \dfrac{E}{E_0} = 1 \\[2mm] \varepsilon_d > \varepsilon_y, \dfrac{E}{E_0} = \dfrac{\varepsilon_y}{\varepsilon_d} + \dfrac{E_f}{E_0}\left(1 - \dfrac{\varepsilon_y}{\varepsilon_d}\right) \end{array}\right\} \tag{1}$$

Fig. 7 Dynamic stress–strain backbone curves under different confining pressures
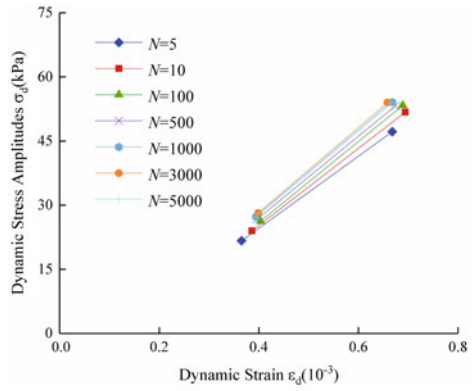
(a) $\sigma_3 = 15$ kPa
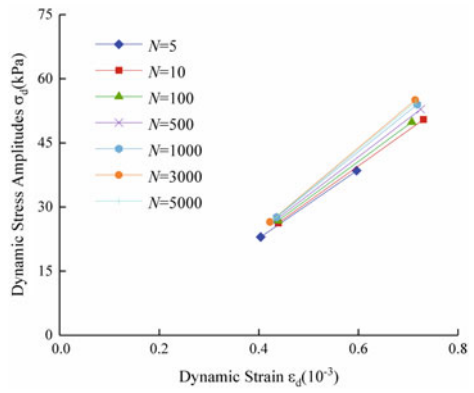
(b) $\sigma_3 = 30$ kPa
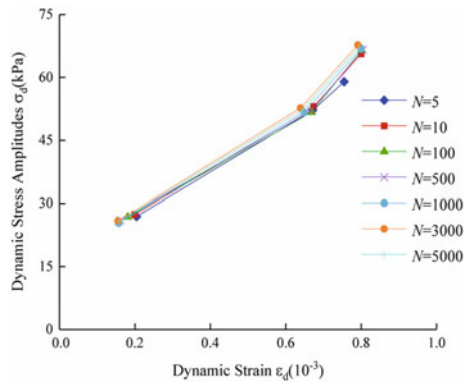
(c) $\sigma_3 = 60$ kPa

Fig. 8 Stress–strain curve of
a dual linear model
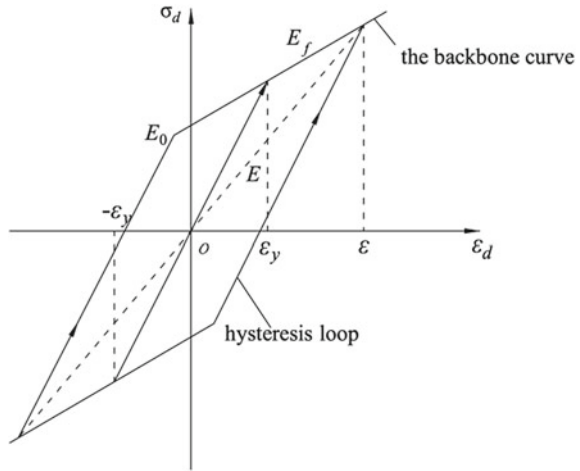
where ε_d = the dynamic strain, ε_y = the dynamic yield strain, E, E_0, and E_f = the elastic modulus corresponding to ε_d, ε_y, and the plastic strain exceeding ε_y, respectively.

To ensure the long-term dynamic stability of subgrade, the train-induced dynamic stress should be less than the critical dynamic stress of the subgrade soil. Therefore, in this study, the mathematical model of the stable CGS specimen representing the characteristics of the backbone curves is meaningful. When the train-induced dynamic stress is greater than the critical dynamic stress, the subgrade soil is in an unstable state and the plastic strain accumulates until exceeding the allowable value. Therefore, the critical dynamic stress is considered to be the yield stress and its corresponding strain is the yield strain.

Figure 9 shows the backbone curves obtained by linear fitting, where the slopes of the curves are the elastic modulus (E) at different cyclic numbers. As can be seen from Fig. 9, the elastic modulus (E) increases as the cyclic number increases. This is an obvious stiffness hardening phenomenon. Figure 10 shows the relationship between the elastic modulus and the cyclic number. The elastic modulus decreases as the confining pressure (σ_3) increases. The elastic modulus shows a good linear relationship with the natural logarithm of the cyclic number, which can be expressed as:

$$E = A \ln N + B \tag{2}$$

where the fitting parameters A and B are affected by confining pressure. The confining pressure can be further exponentially fitted with A and B as shown in Fig. 11:

$$\left.\begin{array}{l} A = a_1 e^{b_1 \sigma_3} \\ B = a_2 e^{b_2 \sigma_3} \end{array}\right\} \tag{3}$$

(a) σ_3 =15 kPa
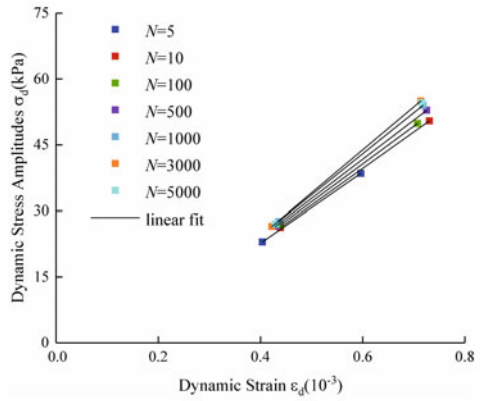
(b) σ_3 =30 kPa
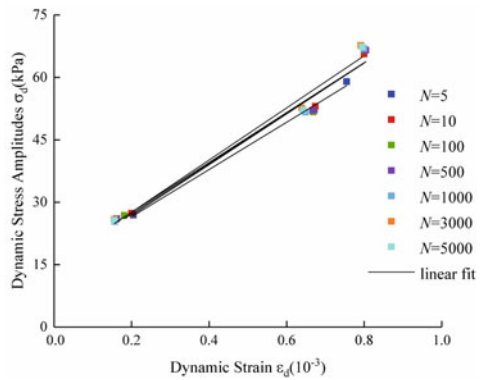
(c) σ_3 =60 kPa

Fig. 10 *E–N* relationship curve
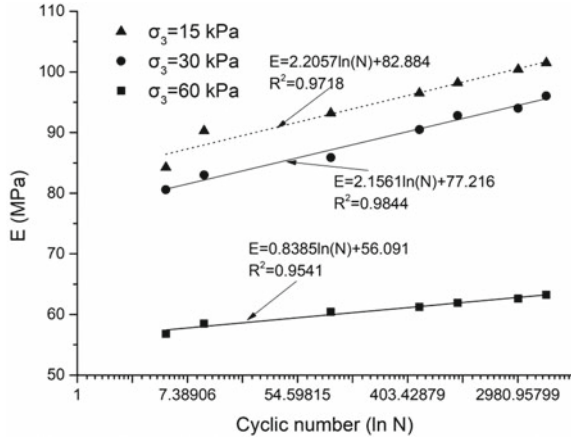
Fig. 11 Relationship between the backbone equation parameters and confining pressure
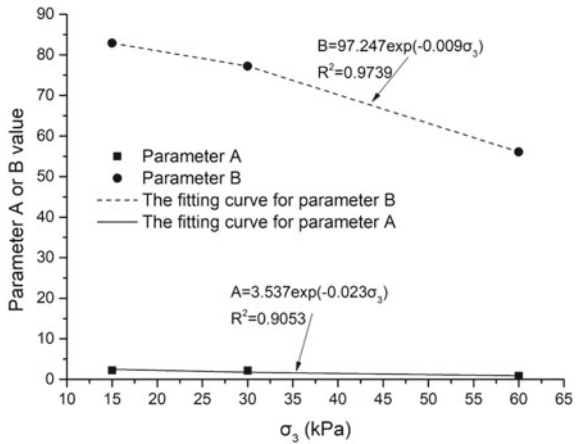
where $a_1 = 3.537$, $b_1 = -0.023$; $a_2 = 97.247$, and $b_2 = -0.009$.

Substituting Eqs. (2) and (3) into the first expression of Eq. (1), the backbone curve equation under different confining pressures and different cyclic numbers can be obtained as:

$$\varepsilon_d = \frac{\sigma_{dcr}}{A \ln N + B} = \frac{\sigma_{dcr}}{a_1 e^{b_1 \sigma_3} \ln N + a_2 e^{b_2 \sigma_3}} \tag{4}$$

where $a_1 = 3.537$, $b_1 = -0.23$, $a_2 = 97.247$, and $b_2 = -0.009$.

It is interesting to note that when ε_d in Eq. (4) is less than the dynamic yield strain (ε_y), the dynamic strength can be derived from

$$\sigma_d = (A \ln N + B)\varepsilon_d = \left(a_1 e^{b_1 \sigma_3} \ln N + a_2 e^{b_2 \sigma_3}\right)\varepsilon_d \tag{5}$$

5 Conclusions

The coarse-grained soil is widely used as filler in a subgrade bed layer. The subject investigated considering the most unfavorable condition of the subgrade state is the saturated compacted coarse-grained soil (CGS). A series of triaxial tests were conducted, and some conclusions were arrived at:

(1) The dynamic stress amplitudes and the cyclic number have a significant effect on the dynamic characteristics of the saturated CGS. The dynamic characteristics of the saturated CGS under different confining pressure and dynamic stress amplitudes can be divided into three types according to the development trends of the accumulative strain with cyclic number: stable, destructive, and critical. The dynamic stress corresponding to the critical curve is the critical dynamic stress.

(2) The greater the confining pressure is, the greater the critical dynamic stress is, the greater the dynamic stability of the CGS improves.

(3) As the cyclic number increases, the slope of the stable saturated CGS backbone curve increases; namely, the dynamic modulus of the soil increases. This dynamic modulus is well simulated by the double-line curve model. In this model, the critical dynamic stress corresponds to the dynamic yield strength.

(4) The double-line curve model can be used to determine the dynamic strength of CGS when the dynamic strain is less than the dynamic yield strain. Meanwhile, this model reflects the CGS stiffness hardening with the increasing of cyclic number.

References

1. Wu S, Zhou J, Yang T (2001) Soil dynamics theory and calculation. China Architecture & Building Press, Beijing (2001)
2. Matsui T, Bahr M, Abe N (1992) Estimation of shear characteristic degradation and stress-strain relationship of saturated clays after cyclic loading. Soils Found 32(1):161–172
3. Yasuhara K, Murakami S, Song BW et al (2003) Post cyclic degradation of strength and stiffness for low plasticity silt. J Geotech Geoenviron Eng 129(8):756–769
4. Zhou J, Gong X (2000) Study on strain soften in saturated soft clay under cyclic loading. China Civil Eng J 32(5):62–68
5. Jun WANG, Yuan-qiang CAI, Chang-jie XU et al (2007) Study on strain softening model of saturated soft clay under cyclic loading. Chin J Rock Mechan Eng 26(8):1713–1719

6. Wu-ming LENG, Wen-jie LIU, Chun-yan ZHAO et al (2015) Experimental research on dynamic failure rules of compacted coarse-grained soil filling in heavy haul railway subgrade. Rock Soil Mech 36(3):640–646
7. Jiang G, Fang L, Wang Z et al (2010) Experimental study on dynamic strength and accumulated deformation characteristics of red-mudstone filling. Chin J Geotech Eng 32(1): 124–129
8. Zhou W, Leng W, CAI D et al (2014) Analysis on characteristics of critical dynamic stress and accumulative deformation of coarse-grained soil subgrade filling under cyclic loading. J China Railw Soc 36(12):84–89
9. Liu X, Yang G, Fang W (2011) Critical dynamic stress of red clay and replacement thickness of ballastless track cutting bed of high-speed railway. Chin J Geotech Eng 33(3):348—353
10. Zhang Y, Kong L, Li X (2010) Dynamic backbone curve model of saturated soft clay under cyclic loading. Rock Soil Mech 31(6):1699–1704
11. Hardin BO, Drnevich VP (1972) Shear modulus and damping in soil measurement and parameter effect. J Soil Mech Found Eng Div 98(6):603–624
12. Ramberg W, Osgood WR (1943) Description of stress strain curves by three parameters. National Advisory Committee for Aeronautics, Washington DC
13. Jian-lin MA (2011) Soil mechanics. China Railway Publishing House, Beijing
14. The First Survey & Design Institute of China Railway (2016) TB10001-2016 code for design on subgrade of railway. China Railway Publishing House, Beijing (2016)
15. Huang B, Ding H, Chen Y (2011) Simulation of high-speed train load by dynamic triaxial tests. Chin J Geotech Eng 3(2):195–202
16. Ru-heng WANG, Bin JIA, An-fu DENG et al (2006) Dynamic triaxial testing study on dynamic characteristics of sandy pebble soil. Chin J Rock Mechan Eng 25(Supp. 2):4059–4064
17. Cai Y, Cao X (1996) Study of the critical dynamic stress and permanent strain of the subgrade-soil under the repeated load. J Southwest Jiaotong Univ 31(1):1–5
18. Gong Q, Liao C, ZHOU S et al (2001) Testing study of dynamic pore water pressure under train loading. Chin J Rock Mechan Eng 20(Supp. 1):1154–1157
19. Lei H, Jiang Y, Lu P et al (2007) Experimental study of dynamic stress-strain relation of structural soft soil under traffic load. Chin J Rock Mech Eng 27(Supp. 1), 3052–3057
20. Liu X, Yang G, Fang W (2011) Replacement thickness and dynamic stability of cutting bed under ballastless track of high-speed railway. Chin J Rock Mech Eng 30(Supp. 2):3534–3538
21. Xie D (2011) Soil dynamics. High Education Press, Beijing (2011)
22. Zhou J (1998) Properties of saturated clay under cyclic loading. Zhejiang University Press, Hangzhou

Vibration Reduction Performance of a Periodic Layered Slab Track

Yao Hu, Zhibao Cheng and Zhifei Shi

Abstract Periodic structure has an inhibitory effect on the propagation of elastic waves when their frequencies fall in the attenuation zone. Using this property, this work proposes a new kind of periodic layered slab track structure to mitigate the vibration caused by rail transit. First, combining the elastic wave theory and the Bloch theory, dispersion curves of the layered periodic structure are calculated, and the attenuation zones are obtained. The geometrical and material parameters of the present periodic system are optimized. Second, the theoretical model of the vehicle-rail-periodic slab track coupled system is developed. The correctness of the coupled system is verified through a comparison study. The displacement of the slab track is analyzed to guarantee the stiffness of the structure. Third, the rail harmonic disturbance is introduced to simulate the wheel–rail irregularity, and dynamic response analysis of the coupling model is carried out. Vibration reduction properties of the periodic layered slab track are studied both in frequency and time domains. For the reason of comparison, a floating slab track is also considered. Numerical results show that the periodic layered track can reduce the vibration effectively.

Keywords Periodic slab track · Attenuation zone · Vibration reduction

1 Introduction

Vibrations generated by urban traffic propagate in the track structure in the form of elastic waves and transmit to nearby buildings causing annoyance to inhabitants and malfunction to sensitive equipment [1]. In order to attenuate the harmful effects of the vibration, reliable vibration mitigation methods are always needed for buildings of special functions, such as hospitals, theatres, and museums. Indeed, vibration can

Y. Hu · Z. Cheng (✉) · Z. Shi
Institute of Smart Material and Structure, School of Civil Engineering,
Beijing Jiaotong University, Beijing 100044, China
e-mail: chengzb@bjtu.edu.cn

779

be controlled at any place along the transmission path [2]. To date, various measures, like reducing the wheel–rail unevenness, using vibration reduction elements such as high resilience fasteners, resiliently supported ties, ballast mats, slab mats, and the floating slab track [3, 4], have been used. The effectiveness of these countermeasures has been proved in those previous works. However, it should be pointed out that these traditional methods still have lots of drawbacks. And, how to mitigate the ambient vibrations generated by urban traffic is still a hot topic for engineers [5–7].

Periodic structure has an inhibitory effect on the propagation of elastic waves when their frequencies fall in the attenuation zone. Over the past ten years, Prof. Shi [8] and his research team in Beijing Jiaotong University introduced the periodic structure theory developed in the field of solid-state physics into the field of civil engineering and developed many novel seismic isolation and vibration reduction methods. In 2012, Xiang et al. conducted an experimental study on the isolation performance of a new type of layered periodic foundation [9]. Cheng et al. conducted a comprehensive numerical and experimental work to verify the efficiency of the attenuation of the two-dimensional and three-dimensional periodic foundations [10–13]. Utilizing the attenuation zone properties of periodic structures, Huang and Shi proposed the periodic pile barrier method to reduce the environmental vibrations. They found that piles of common size can isolate ambient vibration in certain frequency region [14–16]. Including the effect of the initial stress, Liu et al. studied the attenuation zones of periodic structures, including layered periodic foundations, two-dimensional periodic foundations, periodic pile barriers, periodic beams, and periodic plates on elastic foundation [17, 18]. Recently, Pu and Shi proposed a new method for identifying surface wave modes. With the help of the method, they studied the dynamic characteristics of periodic continuous wall system both in frequency and time domains [19, 20].

Different from those previous works, this work proposes a new kind of periodic layered slab track to reduce the vibration caused by rail transit. In Sect. 2, the basic theory of the layered periodic structure is presented. Attenuation zones of the periodic concrete–rubber system are investigated. In Sect. 3, the proposed periodic layered slab track is designed. Vehicle-rail-periodic layered slab track coupled system is presented. In Sect. 4, dynamic performance of the periodic layered slab track system is simulated, from which it is found that with proper design periodic layered slab track can effectively reduce vibration caused by urban rail transit. Conclusions are given in Sect. 5.

2 Basic Theory

2.1 Governing Equations

Consider a one-dimensional layered periodic structure with alternating layers of two isotropic materials. Figure 1 shows the typical cell of the system. The heights of material A and material B are denoted by a_1 and a_2, respectively. Therefore, the periodic constant of the system is $a_c = a_1 + a_2$.

Under the assumption of continuous, isotropic, perfectly elastic, and small deformation as well as without consideration of damping, the governing equation for the longitudinal wave and transverse wave in the infinite layered periodic structure is

$$\frac{\partial^2 u_i}{\partial t^2} = c^2 \frac{\partial^2 u_i}{\partial z^2} \tag{1}$$

Here, $u_i = (u_x, u_z)$ is the displacement vector; c is the wave velocity; t is the time parameter.

2.2 Periodic Boundary Conditions

According to the periodic structure theory, the displacement field can be expressed as

$$\boldsymbol{u}(\boldsymbol{r}, t) = e^{i(\boldsymbol{k}\cdot\boldsymbol{r} - \omega t)} \boldsymbol{u}_k(\boldsymbol{r}) \tag{2}$$

where $\boldsymbol{r}$ denotes the coordinate vector, $\boldsymbol{k}$ is the reduced wave vector, ω is angular frequency, and $\boldsymbol{u}_k(\boldsymbol{r})$ is a periodic function about the periodic constant $\boldsymbol{a}$. Thus, $\boldsymbol{u}_k(\boldsymbol{r})$ can be written as

$$\boldsymbol{u}_k(\boldsymbol{r} + \boldsymbol{a}) = \boldsymbol{u}_k(\boldsymbol{r}) \tag{3}$$

Fig. 1 Unit cell of the layered periodic structure
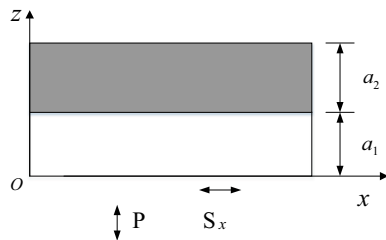
Substituting Eq. (3) into Eq. (2), we have

$$u(r + a, t) = e^{ik \cdot a} u(r, t) \tag{4}$$

Equation (4) is the so-called periodic boundary condition. Further, the infinite periodic structure can be simplified by a representative unit cell.

2.3 Dispersion Relationship and Attenuation Zones

Based on the periodic boundary condition, the dispersion equation of the considered system can be transferred into an eigenvalue problem. Since the periodic boundary condition is related to the wave vector, the eigenvalue equation can be written as

$$\left(\Omega(k) - \omega^2 M\right) \cdot u = 0 \tag{5}$$

where the stiffness matrix $\Omega(k)$ is a function of the wave vector, and M is the mass matrix. For a given reduced wave vector k, the eigenvalue problem can be solved by using the commercial software COMSOL MULTIPHYSICS 5.3.

The layered periodic structure made of common construction materials (concrete and rubber) is considered. Material parameters are given in Table 1. Taking the thickness of the concrete layer as $a_1 = 0.15$ m and the thicknesses of the rubber layer as $a_2 = 0.01$ m, Fig. 2 presents the dispersion curves of the considered system. One can see that in the frequency region indicated by gray, no wave vector exists, which is to say that waves in the region cannot propagate through the infinite periodic layered concrete–rubber structure. And, this frequency region will be named as the attenuation zone.

3 Model and Calculation Parameters

3.1 Design of the Periodic Layered Slab Track System

In order to mitigate the broadband low-frequency ambient vibrations, the wider and lower attenuation zone is always desired. In practical design, the lower bound frequency (LBF), upper bound frequency (UBF), and the width of the first

Table 1 Material parameters

Materials	Young's modulus E (Pa)	Poisson ratio v	Density ρ (kg/m^3)
Concrete	3×10^{10}	0.2	2500
Rubber	1.37×10^5	0.463	1300
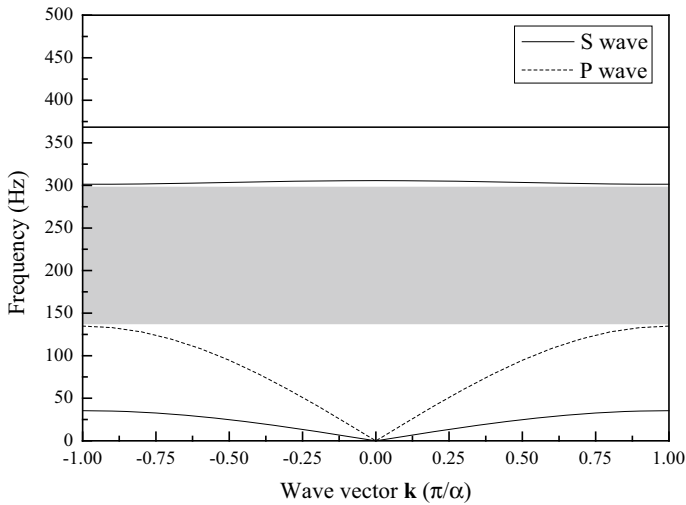
Fig. 2 Dispersion relation of the considered periodic concrete–rubber system

attenuation zone (WAZ) are three important parameters. In this part, the influences of the structural parameters and material parameters of the layer periodic slab track system on the three parameters are investigated.

Figure 3a gives the relations between the first attenuation zone and the thickness of the concrete layer. The thickness of the rubber layer is 0.01 m. It is found that the LBF decreases with the increase in the thickness of the concrete layer; meanwhile, the UBF keeps a constant. Therefore, the WAZ is enlarged. Taking the thickness of the concrete layer as 0.1 m, Fig. 3b shows the effects of the thickness of the rubber layer on the attenuation zone. It is clear that the LBF and WAZ decrease rapidly with the increase in the thickness of the rubber layer.
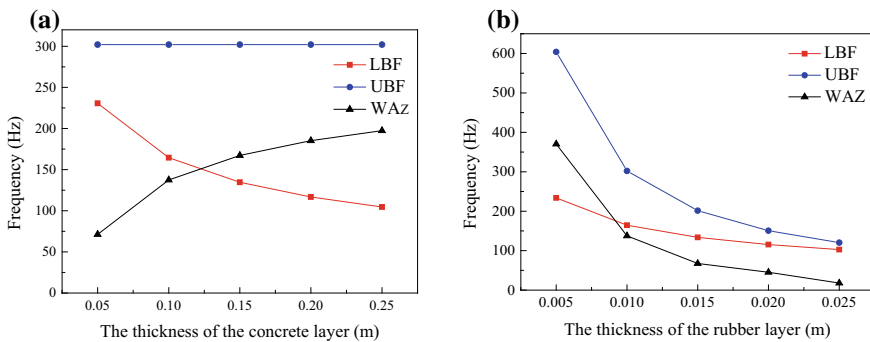
Fig. 3 Effects of the thickness of **a** the concrete layer and **b** the rubber layer on the first attenuation zone
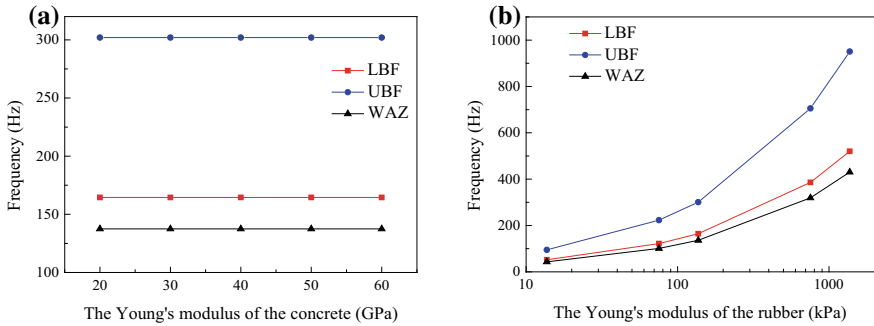
Fig. 4 Effects of Young's modulus of **a** the concrete and **b** the rubber on the first attenuation zone

Figure 4 shows the influences of Young's modulus of the concrete and rubber on the attenuation zone. Here, the thickness of the rubber and concrete layers is 0.01 m and 0.1 m, respectively. It is obvious in Fig. 4a that the LBF and WAZ are almost not changed. Therefore, we can say the influences of Young's modulus of the concrete on the attenuation zone can be ignored. In Fig. 4b, it is found that the LBF and WAZ increase rapidly with the increase in Young's modulus of the rubber.

3.2 Vehicle-Rail-Periodic Layered Slab Track Coupled System

In this part, a two-dimensional vehicle-rail-periodic layered slab track system is developed to analyze the dynamic behavior of the periodic layered slab track. In detail, the vehicle is regarded as a multi-rigid-body vibration system, and the periodic layered slab track is simplified into a three-layer elastic Euler beam model.

As shown in Fig. 5, the vehicle model is composed of seven rigid bodies: car body, frameworks, and four wheelsets. Ten degrees of freedom in total are taken into account, including the vertical motion and the nutation of the car body and frameworks, as well as the vertical motion of wheelsets. The parameters for the vehicle system are given in Table 2.

The periodic layered slab track comprises the rail, fasteners, concrete layers, and elastic supports. Parameters for periodic layered slab track and subgrade are given in Table 3. The rail with the linear density of 51.2 kg/m is applied and is simulated by using the discretely supported Euler beam model. The fastener and the subgrade are considered as the spring–damping element. In particular, in order to eliminate the boundary effect, the slab track is established with a total length of 120 m. The equivalent spring coefficient of the rubber layer is
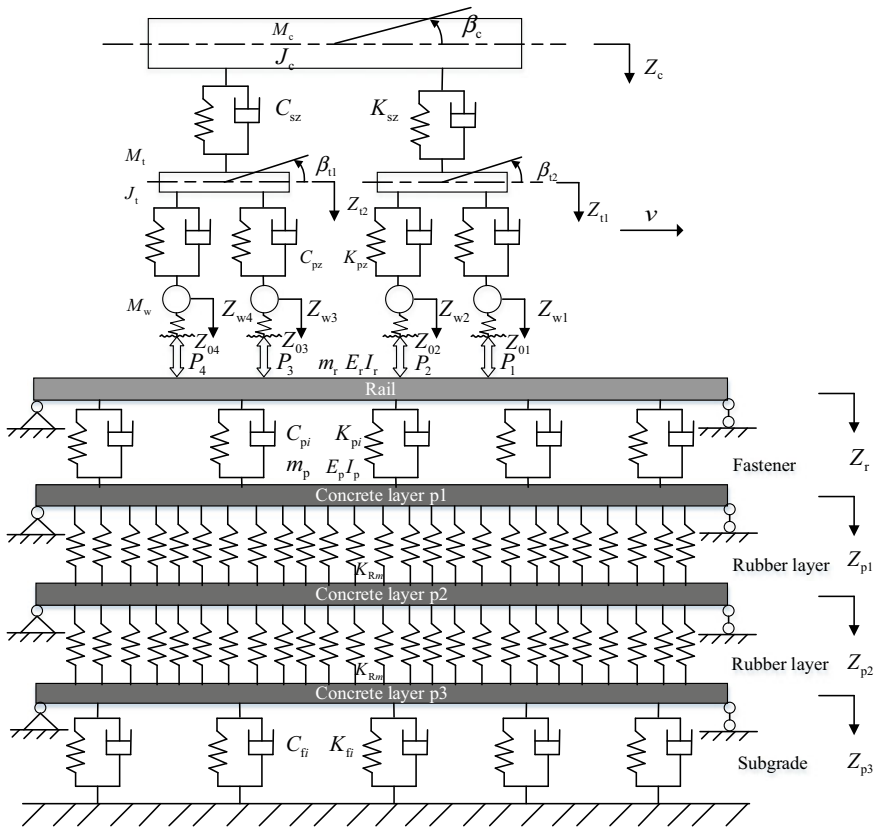
Fig. 5 Vehicle-rail-periodic layered slab track coupling model

Table 2 Parameters and geometrical properties of the vehicle

Parameters	Symbol	Unit	Magnitude
Mass of car body	M_c	kg	38,500
Mass of bogie	M_t	kg	2980
Mass of wheelset	M_w	kg	1350
Nod inertia of car body	J_c	10^6 kg m^2	2.446
Nod inertia of bogie	J_t	kg m^2	3605
Vertical stiffness of primary suspension	K_{pz}	10^6 N/m	2.14
Vertical stiffness of the secondary suspension	K_{sz}	10^6 N/m	2.535
Vertical damping of the primary suspension	C_{pz}	10^6 N s/m	4.9
Vertical damping of the secondary suspension	C_{sz}	10^6 N s/m	1.96
Central distance of bogie	L_1	m	16.8
Fixed wheelbase	L_2	m	2.4
Wheel radius	R	m	0.4575

Table 3 Parameters of the slab track and subgrade

Parameters	Symbol	Unit	Magnitude
Young's modulus of rail	E	10^{11} N/m^2	2.059
Cross-sectional moment of inertia of rail	I	10^{-5} m^4	2.037
Linear density of rail	m_r	kg/m	51.5
Vertical stiffness of fastener	K_p	10^8 N/m	1.2
Vertical damping of fastener	C_p	10^4 N s/m	7.5
Distance between fasteners or rail support	l_s	m	0.6
Width of slab	w	m	3.5
Vertical stiffness of subgrade	K_f	10^7 N/m	6.89
Vertical damping of subgrade	C_f	10^4 N s/m	3.115

$$K_R = \frac{E_R A}{h} \tag{6}$$

where K_R is the spring stiffness, E_R is Young's modulus of the rubber, A is the area of the rubber layer for an equivalent spring, and h is the height of the rubber layer.

3.3 Wheel–Rail Hertz Contact Stiffness and Track Irregularity

In our calculation, the interaction between the vehicle and the track system is simplified as a Hertz contact. The wheel–rail contact spring is applied to simulate the coupling between the vehicle and the track. The wheel–rail interaction force $p(t)$ can be calculated [21, 22]

$$p(t) = \left[\frac{1}{G} \delta Z(t) \right]^{3/2} \tag{7}$$

where G is the constant of the wheel–rail contact. For the worn type with a radius of R, G can be expressed as follows

$$G = 3.86 R^{-0.115} \times 10^{-8} \tag{8}$$

$\delta Z(t)$ is the elastic penetration of the wheel–rail contact, which can be given as

$$\delta Z(t) = Z_{wj}(t) - Z_r\left(x_{wj}, t\right) - Z_0(t), \quad (j = 1 \text{ to } 4) \tag{9}$$
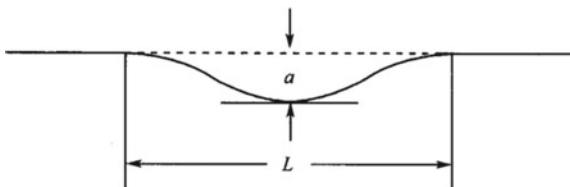
Here, $Z_{wj}(t)$ is the displacement of the wheel numbered j at the time t, $Z_r(x_{wj}, t)$ is the displacement of the rail at the point of wheel numbered j at the time t, and $Z_0(t)$ presents the track irregularity.

The harmonic irregularity is applied to simulate the wheel–rail irregularity. In detail, the irregularity can be described by a 0.5-m-long cosine wave [21]. As shown in Fig. 6, the harmonic irregularity is

$$Z_0(t) = \frac{1}{2}a\left(1 - \cos\frac{2\pi v}{L}t\right) \tag{10}$$

where a and L are the depth and length of the irregularity, respectively; v is the velocity of the vehicle.

4 Dynamic Performance of the Periodic Layered Slab Track

4.1 Numerical Analysis and Modal Verify

At first, with the aim to validate the correctness of the present calculation, the finite element model of the coupled system mentioned above is also developed with the help of the ANSYS software. For the reason of simplicity, the irregularity is ignored. As shown in Fig. 7, the vertical displacements at the midpoint of the rail and concrete layers obtained by the present method match well with those obtained by the ANSYS software. Therefore, the correctness of the present method is validated.

4.2 Results and Discussion

Young's modulus of the rubber is taken as 1.37×10^4 Pa. The thicknesses of the rubber and concrete layers are taken as 0.01 m and 0.15 m, respectively. The attenuation zone is 42.6–95.3 Hz. The velocity of the moving vehicle is 140 km/h. Figure 8 shows the time history responses of the vertical displacement and acceleration at the midpoint of the rail and concrete layers. It is obvious that after passing
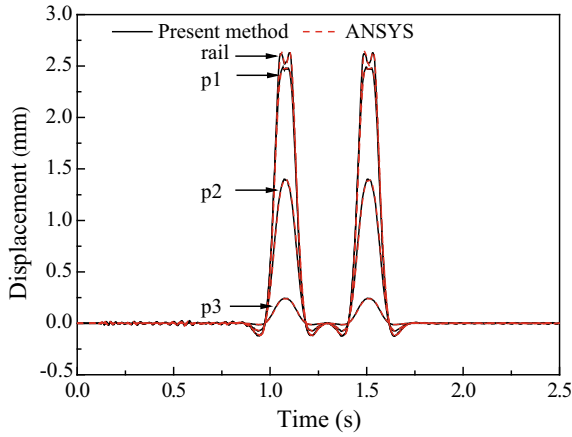
Fig. 7 Time histories of vertical displacements at the midpoint of the rail and concrete layers
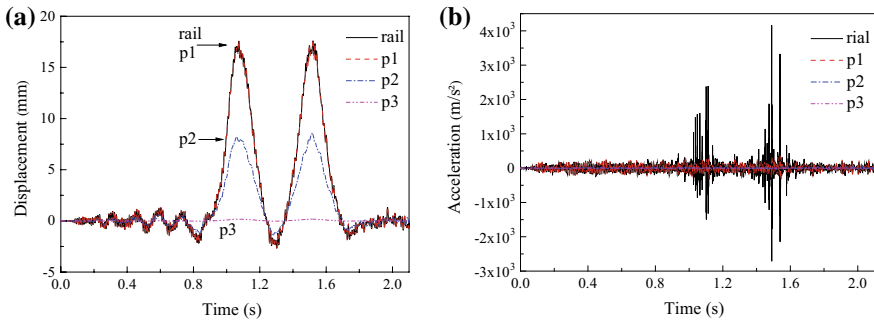
Fig. 8 Time history of **a** vertical displacement and **b** vertical acceleration at the midpoint of the rail and concrete layers

through the periodic slab track, the vibration is attenuated. Fourier spectra of the time history responses of the vertical acceleration at the midpoint of the track structure are shown in Fig. 9. The response is reduced.

In actual design, the deformation limit of the periodic layered slab track should be taken into account. In the foregoing analysis, the maximum rail deflection is 17.52 mm. This deflection is too large and may deteriorate the mechanical properties of the track structure and adversely affects the safety of the high-speed vehicle [23]. Further, Fig. 10 shows the relationship between the rail deformation and Young's modulus of the rubber at the speed of 200 km/h. Taking Young's modulus as 1.37×10^5 Pa, the maximum displacement responses at the midpoint of the rail will be smaller than the rail deformation limit (4 mm) [24].

Fig. 9 Fourier spectra of vertical acceleration at the midpoint of the track structure
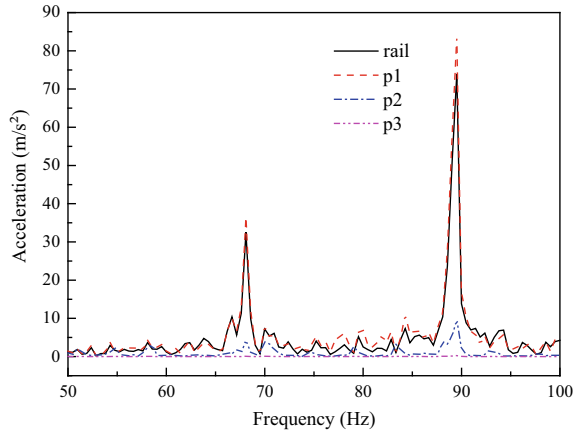
Fig. 10 Effects of Young's modulus of the rubber layer on the maximum displacement of the rail
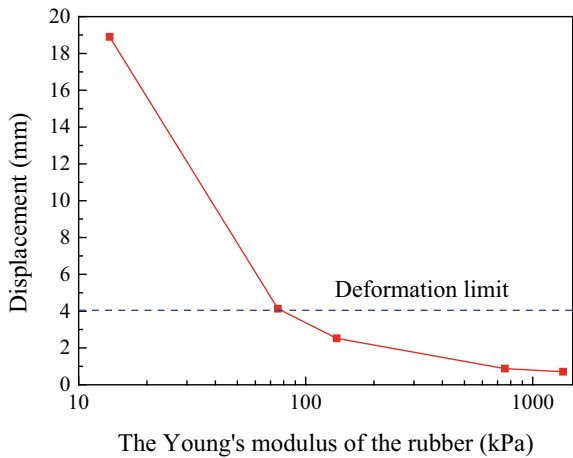
4.3 Comparative Analysis of Vibration Attenuation Performance with Floating Slab Track

For the reason of comparison, a floating slab track is also considered, as shown in Fig. 11. The FRF_3 is defined as $20 \log_{10}(A_{p3}/A_{Bp})$, where A_{Bp} is the amplitude of the acceleration response at the midpoint of the concrete underlayer. Taking the thickness of the concrete layer as 0.3 m (the same as that of the floating slab), vibration attenuation performances of the periodic and floating slab track are shown in Fig. 12. It shows that the vibration response of the periodic slab track is much smaller than that of the floating slab track.
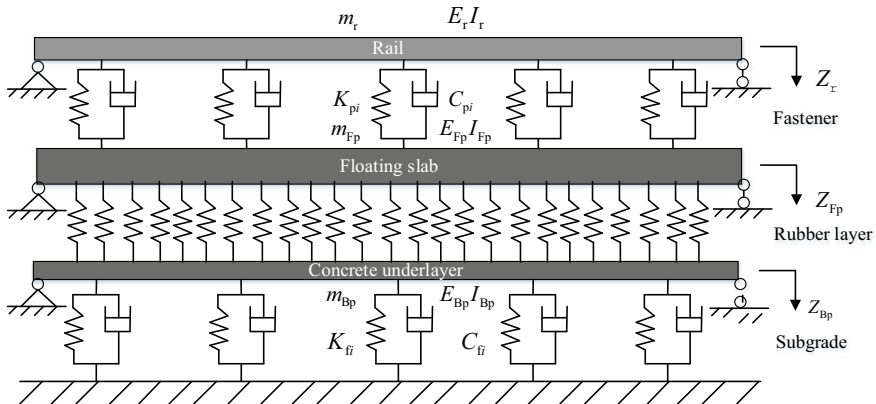
Fig. 11 Dynamic model of rubber floating–slab track

Fig. 12 FRF curve of vertical acceleration at the midpoint of the track structures
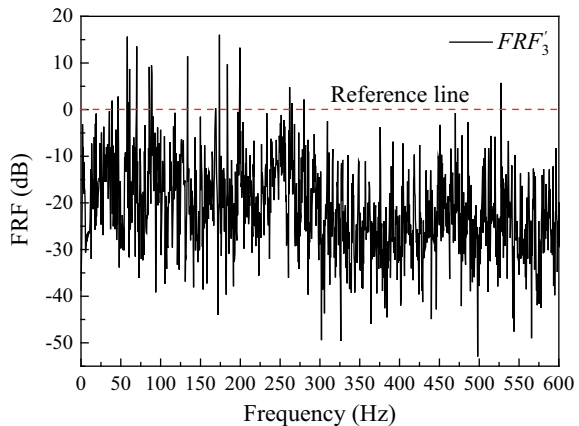
5 Conclusions

In this work, a periodic layered slab track is designed to mitigate the vibration responses of track structures. Unlike traditional vibration reduction measures, such as fasteners or sleepers, floating slab tracks, the reduction mechanism of the periodic layered track is that periodic composite can block and reflect elastic waves. The results of this paper show that with proper design, the layered slab track can effectively reduce vibration caused by urban rail transit.

References

1. Wang P, Yi Q, Zhao C, Xing M, Tang J (2016) Wave propagation in periodic track structures: band-gap behaviors and formation mechanisms. Arch Appl Mech 87(3):1–17
2. Schillemans L (2003) Impact of sound and vibration of the North-South high-speed railway connection through the city of Antwerp Belgium. J Sound Vib 267(3):637–649
3. Wang J, Zeng X (2004) Numerical simulations of vibration attenuation of high-speed train foundations with varied trackbed underlayment materials. J Vib Control 10(8):1123–1136
4. Yan ZQ, Markine V, Gu AJ, Liang QH (2013) Optimization of the dynamic properties of the ladder track system to control rail vibration using the multipoint approximation method. J Vib Control 20(13):1967–1984
5. Lei X, Jiang C (2014) Analysis of vibration reduction effect of steel spring floating slab track with finite elements. J Vib Control 22(6):1462–1471
6. Kuo CM, Huang CH, Chen YY (2008) Vibration characteristics of floating slab track. J Sound Vib 317(3):1017–1034
7. Zhai WM, Xu P, Wei K (2011) Analysis of vibration reduction characteristics and applicability of steel-spring floating-slab track. J Mod Transp 19(4):215–222
8. Shi ZF, Cheng ZB, Xiang HJ (2017) Periodic structures: theory and applications to seismic isolation and vibration reduction. Science Press, Beijing
9. Xiang HJ, Shi ZF, Wang SJ, Mo YL (2012) Periodic materials-based vibration attenuation in layered foundations: experimental validation. Smart Mater Struct 21(11):112003
10. Cheng ZB, Shi ZF (2013) Novel composite periodic structures with attenuation zones. Eng Struct 56:1271–1282
11. Cheng ZB, Shi ZF, Mo YL (2013) Locally resonant periodic structures with low-frequency band gaps. J Appl Phys 114(3):33532
12. Shi ZF, Cheng ZB, Xiang HJ (2014) Seismic isolation foundations with effective attenuation zones. Soil Dyn Earthq Eng 57(1):143–151
13. Cheng ZB, Shi ZF (2014) Vibration attenuation properties of periodic rubber concrete panels. Constr Build Mater 50:257–265
14. Huang JK, Shi ZF (2013) Attenuation zones of periodic pile barriers and its application in vibration reduction for plane waves. J Sound Vib 332(19):4423–4439
15. Huang JK, Shi ZF (2013) Application of periodic theory to rows of piles for horizontal vibration attenuation. Int J Geomech 13(2):132–142
16. Huang JK, Shi ZF (2015) Vibration reduction of plane waves using periodic in-filled pile barriers. J Geotech Geoenvironmental Eng 141(6):4015018
17. Liu XN, Shi ZF, Xiang HJ, Mo YL (2015) Attenuation zones of periodic pile barriers with initial stress. Soil Dyn Earthq Eng 77:381–390
18. Liu XN, Shi ZF, Mo YL (2015) Comparison of 2D and 3D models for numerical simulation of vibration reduction by periodic pile barriers. Soil Dyn Earthq Eng 79:104–107
19. Pu XB, Shi ZF (2017) A novel method for identifying surface waves in periodic structures. Soil Dyn Earthq Eng 98:67–71
20. Pu XB, Shi ZF, Xiang HJ (2017) Feasibility of ambient vibration screening by periodic geofoam-filled trenches. Soil Dyn Earthq Eng 104:228–235
21. Zhai WM (2015) Vehicle-track coupled dynamics, vol 1, 4th edn. Science Press, Beijing
22. Cai CB, Zhai WM, Wang KY (2006) Calculation and assessment analysis of the dynamic performance for slab track on Sui-Yu railway. China Railw Sci 27(4):17–21
23. Ren J, Yang R, Ping W, Feng D, Yan X (2017) Influence of contact loss underneath concrete underlayer on the dynamic performance of prefabricated concrete slab track. Proc Inst Mech Eng Part F J Rail Rapid Transit 231(3):345–358
24. Chen P, Xin T (2018) Deformation control and vibration reduction analysis of rubber floating slab track. J Beijing Jiaotong Univ 42(1):34–39

Grouting Pressure Distribution Model for the Simultaneous Grouting of Shield Tunneling While Considering the Diffusion of Slurry

Zhong Zhou, Zhuangzhuang Liu, Binran Zhang, Wenyuan Gao and Chengcheng Zhang

Abstract According to the field test of urban subway tunnels, the internal force of the lining segment of the shield tunnel during the synchronous grouting stage is 1–1.5 times that in the steady stage. To study the distribution model of grouting pressure on the lining segment produced by synchronous grouting, we investigated Bingham fluid and a synchronous grouting slurry while they penetrate excavation soil and fill shield tail interspace. Then, we deduced the calculation formula for diffusion radius, the amount of grout during grouting behind a segment, the radial displacement of excavation caverns caused by the squeezing effect of penetration pressure, and the effective stress of soil in the diffusion zone. The amount of grout that can fill a shield tail interspace during synchronous grouting was identified. Considering the time-varying of slurry viscosity, the limit equilibrium equation and the fluid mechanics method were used for the deduction of the distribution model of grouting pressure on a lining segment produced by synchronous grouting. The calculated results indicated that the diffusion radius and the amount of grout that can fill a shield tail interspace increase as the grouting pressure increases and that grouting slurry diffusion reduces the grouting pressure on a lining segment. The actual measured grouting pressure value is consistent with the theoretical calculation results in this paper by combining the engineering example of the Changsha Metro Line 4. The theory proposed by this paper provides a theoretical basis for fine analysis of the distribution of grouting pressure during shield tunneling construction.

Keywords Shield tunnel · Synchronous grouting · Bingham fluid · Penetration diffusion · Grouting pressure

---

Z. Zhou (✉) · Z. Liu · B. Zhang · W. Gao · C. Zhang
School of Civil Engineering, Central South University, Changsha, China
e-mail: 369144091@qq.com; 923687215@qq.com

1 Introduction

In shield tunneling construction, shield tail interspace is formed between a lining segment and excavation soil after lining segments out of shield shell. This part of the interspace should be filled with grout in a timely manner, and the stress release coefficient of the surrounding rock should be controlled for the stability of the caverns and control of stratum deformation. However, grouting pressure on a lining segment produced by synchronous grouting is extremely large and may thus result in extremely large internal forces that can cause lining segments to break down, dislocate, leak water, and float up. Therefore, the grouting pressure distribution model produced by synchronous grouting on shield construction should be studied.

Strategies for shield tunneling construction have developed rapidly in recent decades, and construction speed and quality are continuously improving. Despite these developments, lining segments are in a very complex stress field, designing lining segments remains a complex task, and the design theory of tunnel engineering remains far from perfect. In lining segment design, only earth pressure, water pressure, overburden pressure, and foundation resistance in the normal use stage of the tunnel are considered, whereas load in the construction process, which produces more than the normal use of lining segment internal forces, is disregarded. Given the complex environment of shield grouting slurry, the grouting pressure distribution model is difficult to obtain through traditional calculation methods. Bezuijen [1] probed the post-grouting effect and the slurry distribution of a shield tunnel. Rukinori [2] conducted several physical model tests for the post-grouting of shield tunnel walls and revealed that soil compactness and grouting pressure can significantly affect the distribution and magnitude of earth pressure. Ezzeldine [3] simulated the influence of shield propulsion, assembling lining, and synchronous grouting on foundation deformation by using the finite element program Pisa. Ye [4, 5] considered the effect of shield tail interspaces by introducing equivalent porosity instead of soil porosity and determined the pressure exerted by grouting on a segment by using the slurry cylindrical and circular diffusion model. Zhu et al. [6] and Ye et al. [7] controlled the size of grouting pressure by considering the mechanical behavior of the longitudinal ring joint. Deng et al. [8] used FLAC3D with the tunnel shield grouting force characteristics of secondary development to study the mechanism of the backfilled grouting in the shield tunnel and discussed the regularity of the influence of backfilled grouting on the force and deformation of supporting structures and surrounding rocks. Huang et al. [9] explored the back-filled grouting distribution of a shield tunnel in Shanghai by using ground-penetrating radar and conducted a preliminary analysis to diagnose the distribution of slurry behind a tunnel wall. Yuan et al. [10] used Bingham fluid to describe the rheological properties of the cemented mortar and deduced the transfer formula of grouting pressure during the injection of slurry into a shield tail interspace. Liang et al. [11] and Gou et al. [12] considered permeability coefficient variations caused by the changes in viscosity during the infiltration of slurry into surrounding strata. On this basis, they deduced the grout consolidation and pressure

dissipation equations and analyzed the distribution of the slurry consolidation, dissipation, and slurry pressure that act on segments.

However, the influence of slurry diffusion on grouting pressure is often over-looked in the current calculation model of grouting pressure. Referring to the existing theory [13–16], we deduced the pressure caused by grouting on the lining segment during synchronous grouting. On the basis of Darcy's law and the ring problem of elastic–plastic mechanics combined with the denaturation of the grouting slurry viscosity and considering the diffusion of slurry, the theory of grouting slurry diffused in the excavation soil is deduced. Then, we determined the calculation formula of diffusion radius, the amount of grouting in the diffusion zone, and the calculation expression of the radial, tangential effective stress of the surrounding rock, and the radial displacement of excavation caverns under the influence of penetration pressure in synchronous grouting. The calculation formula accurately draws the amount of grouting during synchronous grouting and the thickness of the shield tail interspace. The limit equilibrium equation and fluid mechanics method were used for the deduction of the distribution model of grouting pressure on a lining segment produced by synchronous grouting.

2 Synchronous Grouting Diffusion Theory Considering the Time-Varying of Slurry Viscosity

Experiments show that Newtonian fluid is a special Bingham fluid. In this paper, we use the more representative Bingham fluid as the research object to study the diffusion of synchronous grouting and the grouting pressure distribution model.

2.1 Bingham Fluid Flow Characteristics

The hard slurry belongs to Bingham fluid. Bingham fluid shear stress and shear rate images do not pass through the origin; this fluid will produce a fluid shear deformation only by overcoming its shear yield strength [17, 18].

$$\tau = \tau_0 + \mu(t)\frac{\mathrm{d}u}{\mathrm{d}c} \tag{1}$$

where τ is the shear stress, τ_0 is the initial shear stress, $\mu(t)$ is the viscosity of the fluid, and $\mathrm{d}u/\mathrm{d}c$ is the fluid shear deformation rate.

Figure 1 shows the flow velocity distribution of the synchronous grouting slurry in the shield tail interspace when the grouting fluid is Bingham fluid. In the figure, $2C_p$ is the fluid core height of Bingham fluid, and $2C_0$ is the shield tail interspace. In the flow core region of $-c_p \leq c \leq c_p$, the fluid shear deformation rate $\mathrm{d}u/\mathrm{d}c = 0$, the flow rate is a certain value u_1, and shear stress $\tau = \tau_0$. At $|c_p| \leq |c| \leq |c_0|$, the

Fig. 1 Distribution of Bingham fluid velocity in the cross section of the shield tail interspace
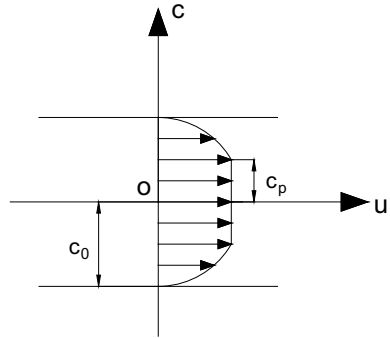
fluid shear rate gradually decreases, and the velocity gradually increases from the boundary of excavation tunnel to the boundary of the fluid core. The flow velocity at the boundary of shield excavation is the smallest, and shear deformation rate and shear stress reach their maximum values.

2.2 Basic Assumptions

(1) In this paper, we assume that shield excavation forms a uniform cylindrical shield tail interspace. The grout slurry follows the Bingham flow pattern during the filling of the shield tail interspace, and the slurry is incompressible and an isotropic body.

(2) We suppose that the grouting slurry diffuses into the surrounding rock in a uniform cylindrical dispersion and satisfies Darcy's law.

(3) We suppose the filling process of grouting slurry and diffusion process occur simultaneously, and the grouting holes are equally filled upward and downward with grout.

(4) The surrounding soil is homogeneous and isotropic. Under the action of penetration pressure, only elastic deformation occurs, and the effect of gravity on the compressive deformation of soil is ignored.

2.3 Influence of Simultaneous Grouting Slurry Diffusion on Grouting Pressure

The existing grouting pressure calculation model ignores the influence of grouting slurry diffusion on grouting pressure, which considering that the grouting slurry does not diffuse with the surrounding soil, the amount of grouting at grouting hole is the grouting amount of the filling zone, and the width of the shield tail interspace

is the difference between the shield shell and the lining segment. However, this is not the case. Slurry filling and diffusion images are shown in Fig. 2. The distance between the diffusion boundary and the tunnel center is r_1, and the penetration pressure in the diffusion zone is P_r. The grouting pressure (P_0) at the interface of the excavation tunnel is set as the average value of the grouting pressure of the upper and lower grouting holes. The uniform penetration pressure difference between the tunnel excavation and diffusion boundaries is $P_0–P_w$, where P_w is the groundwater head height of the excavation cavern.

The effects of slurry diffusion on grouting pressure are described through the analysis of the influence of the synchronous grouting slurry diffusion on the average flow rate at the shield tail interspace and the excavation cavern.

Shield Tail Interspace Section of the Average Flow Q'

In the process of synchronous grouting, the grouting slurry not only fills the shield tail interspace but also causes the grout to penetrate the soil due to the pressure difference between the grouting pressure and the groundwater head at the contact surface between the grouting slurry and the excavation cavern. According to Darcy's law, the slurry will diffuse in the surrounding rock to form a diffusion zone, and part of the slurry will fill the shield tail interspace, while the other part will enter the diffusion zone.

The slurry diffusion diagram is shown in Fig. 2, which shows the difference in water head in the diffusion zone, and radial grout diffusion occurs according to Darcy's law:

$$Q = K_g \frac{\mathrm{d}P}{\mathrm{d}r} At \tag{2}$$

Fig. 2 Synchronous grout filling and diffusion
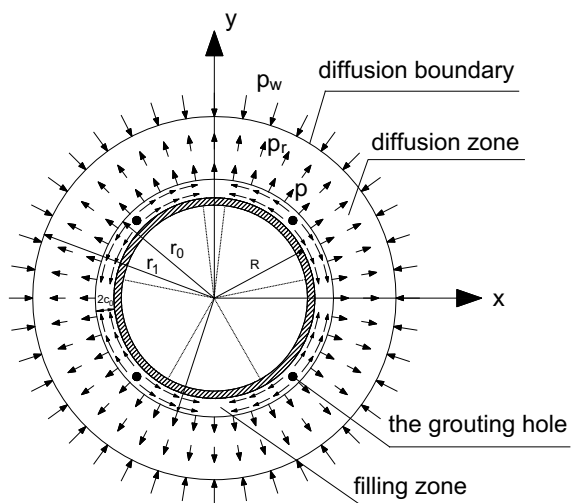
where K_g is the permeability coefficient of the grouting slurry in the soil, $K_g = K/\beta$; K is the permeability coefficient of excavated soil; and β is the viscosity ratio of the slurry viscosity to water:

$$\beta = \frac{\mu(t)}{\mu_w} \tag{3}$$

Considering the viscosity of the grouting slurry denatures, the fluid viscosity time-varying law is $\mu(t) = \mu_0 e^{at}$, where $\mu(t)$ is the viscosity of the slurry, μ_0 is the initial viscosity of the slurry, a is the viscosity time-varying coefficient, and t is the grouting time. The viscosity ratio of grouting slurry and water should take the average during the grouting process, that is,

$$\beta = \frac{\int_0^t \mu(t)dt}{\mu_w t} = \frac{\int_0^t \mu_0 e^{at}dt}{\mu_w t} = \frac{\mu_0(e^{at}-1)}{\mu_w at} \tag{4}$$

Into type (1) available

$$Q = \frac{2\pi K r \mu_w a dv_t t^2}{\mu_0(e^{at}-1)} \frac{dP}{dr}. \tag{5}$$

Set n is the permeability of the soil porosity, and thus,

$$Q = \pi(r^2 - r_0^2)dv_t n. \tag{6}$$

Synchronous (5) and (6) are available:

$$\frac{dP}{dr} = \frac{\mu_0 n(e^{at}-1)}{2K\mu_w at^2}\left(r - \frac{r_0^2}{r}\right). \tag{7}$$

Using the boundary conditions, we can obtain

$$P_0 - P_w = \frac{\mu_0 n(e^{at}-1)}{2K\mu_w at^2}\left(\frac{r_1^2 - r_0^2}{2} - r_0^2\ln\frac{r_1}{r_0}\right) \tag{8}$$

where P_0 is the grouting pressure, P_w is the height of the groundwater head, and r_1 is the diffusion radius.

From the above formula, we can obtain diffusion radius r_1. Substituting (6) yields the amount of grout that diffuses into the diffusion zone:

$$Q = \pi n(r_1^2 - r_0^2)dv_t. \tag{9}$$

Therefore, the amount of grout that could fill the shield tail interspace during the synchronous grouting in the process of synchronous grouting is

$$Q_0 = \pi n \left(r_1^2 - r \right) 0^2 \mathrm{d}v_t + \pi \left(r_0^2 - R^2 \right) \mathrm{d}v_t. \tag{10}$$

The hole grouting amount is Q_n, the grout is filled upward and downward at the grouting holes equally, and m is the number of grouting holes. Therefore, the average cross section flow rate (Q') of the shield tail interspace is

$$Q' = \frac{mQ_n - Q}{2m}. \tag{11}$$

Influence of Penetration Pressure on Excavation Caverns

In the process of synchronous grouting, the slurry diffuses to the surrounding soil because the penetration pressure will squeeze the excavation of caverns, that is, excavation cave radial compression, resulting in a wider shield tail interspace. The action of penetration pressure will change the stress state of the surrounding rock. The columnar diffusion of the grouting slurry is set from the excavation cavern to the diffusion zone. u_r is the radial displacement of the excavation cavern under the effect of penetration pressure P_r.

According to Eq. (5), we can get following formula:

$$\mathrm{d}P = \frac{Q\mu_0(e^{at} - 1)}{2\pi K r \rho_w v_w a \mathrm{d}v_t t^2} \mathrm{d}r. \tag{12}$$

Combined with the boundary conditions, when $r = r_0$, $P_r = P_0 - P_w$. Furthermore, the penetration pressure (P_r) at an arbitrary diffusion radius r can be obtained as follows:

$$p_r = p_0 - p_w - \frac{Q\mu_0(e^{at} - 1)}{2\pi K \rho_w v_w a \mathrm{d}v_t t^2} \ln \frac{r}{r_0}. \tag{13}$$

So we can get the radial bulk force f_r

$$f_r = -\frac{\mathrm{d}p_r}{\mathrm{d}r} = \frac{Q\mu_0(e^{at} - 1)}{2\pi K \rho_w v_w a \mathrm{d}v_t t^2} \cdot \frac{1}{r}. \tag{14}$$

According to the polar coordinate equilibrium differential equation of elastic mechanics,

$$\frac{\partial \sigma_r}{\partial r} + \frac{1}{r} \frac{\partial \tau_{r\theta}}{\partial \theta} + \frac{\sigma_r - \sigma_\theta}{r} + f_r = 0 \tag{15}$$

where σ_r is the radial effective stress of the soil and σ_τ is the tangential effective stress of the soil. The calculation model is a symmetric problem where shear stress $\tau_{r\theta} = 0$. The radial effective stress $\sigma_r = P_0 - P_w$ of the excavated soil at excavation

cavern $r = r_0$; at diffusion boundary $r = r_1$, the radial effective stress $\sigma_r = \sigma_0$ of the excavated soil, where σ_0 is the initial effective stress of the diffusion boundary.

According to the geometric and physical equations of elasticity, the stress function Φ of soil in the diffusion zone can be obtained.

$$\Phi = C_1 r + \frac{C_2}{r} + D r \ln r. \tag{16}$$

In the above formula,

$$
\begin{cases}
C_1 = \sigma_0 - D \ln r_1 - \dfrac{\left(\sigma_0 - (P_0 - P_w) - D \ln\frac{r_1}{r_0}\right)}{r_0^2 - r_1^2} \cdot r_0^2 \\[2ex]
C_2 = \dfrac{\left(\sigma_0 - (P_0 - P_w) - D \ln\frac{r_1}{r_0}\right)}{r_0^2 - r_1^2} \cdot r_1^2 r_0^2 \\[2ex]
A = -\dfrac{Q\mu_0 (e^{at} - 1)}{2\pi K \rho_w v_w a d_{v_t} t^2}, \qquad D = -\dfrac{A(1+\mu)}{2} \\[2ex]
M = \dfrac{\left(\sigma_0 - (P_0 - P_w) - D \ln\frac{r_1}{r_0}\right)}{r_0^2 - r_1^2}.
\end{cases}
\tag{17}
$$

According to the stress function, we can obtain the effective radial force (σ_r), radial displacement u_r, and tangential effective stress σ_θ,

$$
\begin{cases}
\sigma_r = \sigma_0 - D \ln r_1 - M r_0^2 + \dfrac{M r_1^2 r_0^2}{r^2} + D \ln r \\[2ex]
\sigma_\theta = \sigma_0 - D \ln r_1 - M r_0^2 - \dfrac{M r_1^2 r_0^2}{r^2} + D(\ln r + 1) + A \\[2ex]
u_r = r \dfrac{(1-\mu)\left(\sigma_0 - D \ln\frac{r_1}{r} - M r_0^2\right) - (1+\mu)\frac{M r_1^2 r_0^2}{r^2} + D + A}{E}.
\end{cases}
\tag{18}
$$

Substitute $r = r_0$ into the above formula to obtain the radial displacement of excavation cave u_{r0}.

$$u_{r0} = \frac{r_0 (\sigma_\theta - \mu \sigma_{r0})}{E}. \tag{19}$$

Thus, the shield tail interspace width is $2C_0 = r_0 - R = r' + u_{r0} - R$, where r' is the shield shell radius.

3 Synchronous Grouting Diffusion Theory Considering the Time-Varying of Slurry Viscosity

This paper analyzes the synchronous grouting pressure distribution model of shield tunnel with four grouting holes. The grouting slurry is placed into the shield tail interspace through the grouting hole. The grout fills the shield tail interspace up and

down at the grouting hole, while the diffusion occurs at the contact surface. The analysis of the grouting slurry upward and downward filling of the shield tail interspace is presented below. The limit equilibrium equation and the fluid mechanics method are used to deduce the calculation model of grouting pressure on the lining segment produced by synchronous grouting.

The grouting slurry mechanical model is shown in Fig. 3 where the grouting slurry is downward filling at $\pi/4$ grouting holes. Taking the micro-body of the grouting slurry at section θ, P is the grouting pressure at the section, R is the radius of the lining pipe section, r_0 is the radius of the excavating tunnel, τ is the shear stress between the grouting slurry, and G is the gravity of the slurry micro-body, $G = 2c\rho g d v_t (R + c_0) d\theta$. ρ is the density of the grouting slurry, and $d v_t$ is the shield machine a driving distance. The equilibrium equation along the tangential direction of the micro-body center is obtained.

$$
P \cdot 2c \cdot dv_t \cdot \cos\left(\frac{d\theta}{2}\right) - (P + dP) \cdot 2c \cdot dv_t \cdot \cos\left(\frac{d\theta}{2}\right) - 2\tau \cdot
$$
$$
(R + c_0) \cdot dv_t \cdot d\theta + 2c \cdot \rho \cdot g \cdot dv_t \cdot (R + c_0) \cdot \sin\left(\theta + \frac{d\theta}{2}\right) \cdot d\theta = 0. \tag{20}
$$

Micro-bodies have $\cos\frac{d\theta}{2} = 1$ and $\sin\left(\theta + \frac{d\theta}{2}\right) = \sin\theta$. By substituting these into the above formula, we can obtain the following formula:

$$
\frac{dP}{(R + c_0)d\theta} - \rho g \sin\theta = -\frac{\tau}{c}. \tag{21}
$$

The Bingham fluid flow at the core boundary $C = C_p$, the fluid shear deformation rate $du/dc = 0$, and the shear stress $\tau = \tau_0$. These are substituted in Formula (21) to calculate the height of the flow nuclear:

Fig. 3 Slurry downward filling at $\pi/4$ grouting holes
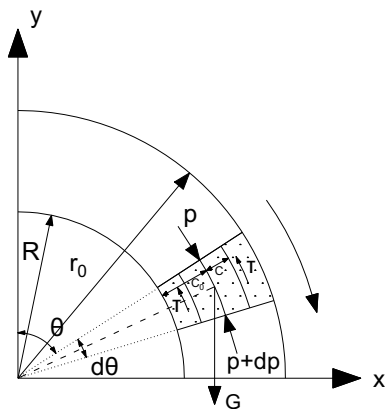
$$c_{\mathrm{p}} = \frac{\tau_0}{\rho g \sin \theta - \frac{\mathrm{d}p}{(R + c_0)\mathrm{d}\theta}}. \tag{22}$$

If the Bingham fluid flow velocity is u_1 in the flow core, the flow velocity is u_2 outside the flow core. Formula (1) is substituted into Formula (21) and the fluid shear rate can be obtained.

$$\frac{\mathrm{d}u}{\mathrm{d}c} = \frac{\left(\rho g \sin \theta - \frac{\mathrm{d}p}{(R + c_0)\mathrm{d}\theta}\right) \cdot c - \tau_0}{\mu(t)}. \tag{23}$$

At $|c_p| \leq |c| \leq |c_0|$, according to the boundary conditions, $C_0 = C$, $u = 0$. Substituting these into the Formula (23), we can obtain u_2.

$$u_2 = \frac{\left(\frac{\mathrm{d}p}{(R + c_0)\mathrm{d}\theta} - \rho g \sin \theta\right) \cdot \left(c_0^2 - c^2 + 2cc_p - 2c_0c_p\right)}{2\mu(t)}. \tag{24}$$

At $-c_p \leq c \leq c_p$, $\frac{\mathrm{d}u}{\mathrm{d}c} = 0$, $C = C_p$. By substituting these into the above formula, we can obtain u_1.

$$u_1 = \frac{\left(\frac{\mathrm{d}p}{(R + c_0)\mathrm{d}\theta} - \rho g \sin \theta\right) \cdot \left(c_p - c_0\right)^2}{2\mu(t)}. \tag{25}$$

Therefore, the average cross section flow rate (Q') of the shield tail interspace is as follows.

$$Q' = 2c_p u_1 \mathrm{d}v_t t + 2t\mathrm{d}v_t \cdot \int_{c_p}^{c_0} u_2 \mathrm{d}c \tag{26}$$

We substitute u_1 and u_2 into Eq. (26):

$$Q' = \frac{\left(\frac{\mathrm{d}p}{(R + c_0)\mathrm{d}\theta} - \rho g \sin \theta\right) \cdot \left(c_p^3 + 2c_0^3 - 3c_p c_0^2\right) \cdot t\mathrm{d}v_t}{3\mu(t)}. \tag{27}$$

Simultaneously, Eqs. (1), (21), and (27) can obtain the following formula:

$$\frac{\mathrm{d}P}{\mathrm{d}\theta} = \frac{3Q'\mu(t) \cdot (R + c_0)}{\left(c_p^3 + 2c_0^3 - 3c_p c_0^2\right) \cdot t \cdot \mathrm{d}v_t} + (R + c_0)\rho g \sin \theta. \tag{28}$$

The research object of this paper is four-hole grouting, thus $m = 4$, which can be used in Eq. (11).

$$Q' = \frac{4Q_n - Q}{8}.$$

(29)

According to the boundary conditions, the grouting pressure in $\pi/4$ grouting hole is P_1 and the grouting volume is Q_1, that is, $\theta = \pi/4$, $P = P_1$. Substituting them into Eq. (28) can obtain the grouting pressure (P) on the lining segment at any section (θ).

$$P = P_1 + \frac{3\mu_0 e^{at}(4Q_1 - Q) \cdot (R + c_0) \cdot (\theta - \pi/4)}{8t \cdot \left(c_p^3 + 2c_0^3 - 3c_p c_0^2\right) \cdot dv_t} - (R + c_0)\rho g\left(\cos\theta - \cos\frac{\pi}{4}\right),$$
$$\frac{\pi}{4} \leq \theta \leq \frac{\pi}{2}.$$

(30)

In the same way, the grouting pressure on the lining segment can be obtained when the $\pi/4$ grouting hole slurry is upward filling.

$$P = P_1 - \frac{3\mu_0 e^{at}(4Q_1 - Q) \cdot (R + c_0) \cdot (\theta - \pi/4)}{8t \cdot \left(c_p^3 + 2c_0^3 - 3c_p c_0^2\right) \cdot dv_t} - (R + c_0)\rho g\left(\cos\theta - \cos\frac{\pi}{4}\right),$$
$$0 \leq \theta \leq \frac{\pi}{4}.$$

(31)

The grouting pressure in $3\pi/4$ grouting hole is P_2, and the grouting volume is Q_2. The grouting pressure on the lining segment when the $3\pi/4$ grouting hole slurry is upward filling is

$$P = P_2 - \frac{3\mu_0 e^{at}(4Q_2 - Q) \cdot (R + c_0) \cdot (\theta - 3\pi/4)}{8t \cdot \left(c_p^3 + 2c_0^3 - 3c_p c_0^2\right) \cdot dv_t} - (R + c_0)\rho g\left(\cos\theta - \cos\frac{3\pi}{4}\right),$$
$$\frac{\pi}{2} < \theta \leq \frac{3\pi}{4}.$$

(32)

The grouting pressure on lining segment when the $3\pi/4$ grouting hole slurry is downward filling is

$$P = P_2 + \frac{3\mu_0 e^{at}(4Q_2 - Q) \cdot (R + c_0) \cdot (\theta - 3\pi/4)}{8t \cdot \left(c_p^3 + 2c_0^3 - 3c_p c_0^2\right) \cdot dv_t} - (R + c_0)\rho g \left(\cos\theta - \cos\frac{3\pi}{4}\right),$$

$$\frac{3\pi}{4} \leq \theta \leq \pi.$$

(33)

According to the above formula, the grouting pressure on the lining segments produced by grouting at different grouting holes can be calculated. Thus, the final grouting pressure on the lining segments is obtained.

4 The Example Analysis

4.1 Project Profile

On the basis of the Changsha rail transit Line 4 FuBi district west from the Fu Buhe station, this study selects a typical section under the Xiangjiang River for calculation and analysis. The cross section of the 579 experimental rings is shown in Fig. 4.

The typical section of the river water has a depth of 2.5 m and a shield tunnel depth of 17.8 m, and the tunnel is entirely in a strong weathered conglomerate. The grouting is a four-hole synchronous grouting, and the grouting pressures of the upper and lower grouting holes are 2.4 bar and 3 bar, respectively. The shield shell radius $r' = 3.14$ m, the lining segment outer radius $R = 3.0$ m, the width $B = 1.5$ m,
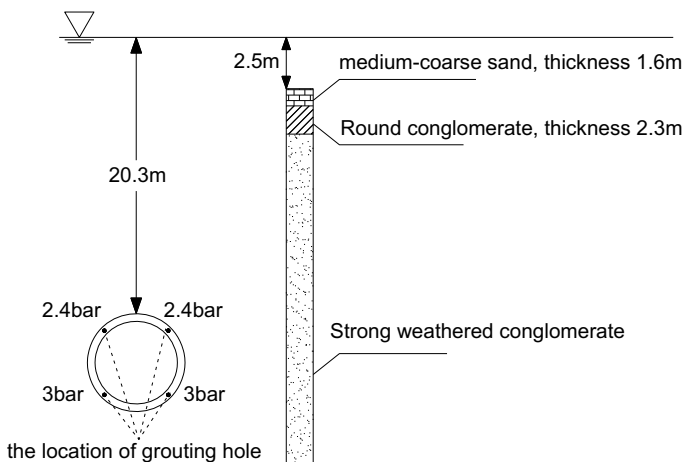
Fig. 4 Typical cross section

Fig. 5 Shield tunnel grouting pressure measurement site

the propulsion distance dv_t is a segment width, and the shield tunneling speed is $v = 2.6$ m/h. The head height $h_0 = 20$ m; the original rock stress $P_0 = 0.33$ MPa. The material parameters of the surrounding rock are as follows: elastic modulus $E = 100$ MPa, Poisson's ratio $\mu = 0.25$, porosity $n = 0.158$, permeability coefficient $K = 0.15$ m/d, cohesion $c = 50$ kPa, and internal friction angle $= 37°$.

In the process of grouting pressure measurement in the construction site, the grouting pressure sensors are, respectively, embedded in the middle of the outer side of each lining segment (six measuring points). The grouting pressure measurement site is shown in Fig. 5.

4.2 Calculation of Project Instance

According to the theoretical calculation model and by substituting concrete construction parameters, we obtain the grouting pressure on the lining segment when the slurry diffusion is considered and the diffusion of slurry is ignored. The accuracy of the model is analyzed through the comparison of the measured values.

Calculation Model of Grouting Pressure Distribution without Considering the Diffusion of Slurry

Regardless of the influence of slurry diffusion and the time-varying slurry viscosity on the grouting pressure, the average flow rate of the grouting slurry in the shield tail interspace is equal to the injected amount of slurry in the grouting hole. According to the calculation formula of grouting pressure in this paper, the grouting pressure distribution model of the slurry matching the Bingham fluid [Verify if correct.] is calculated and compared with the field test results, as shown in Fig. 6.
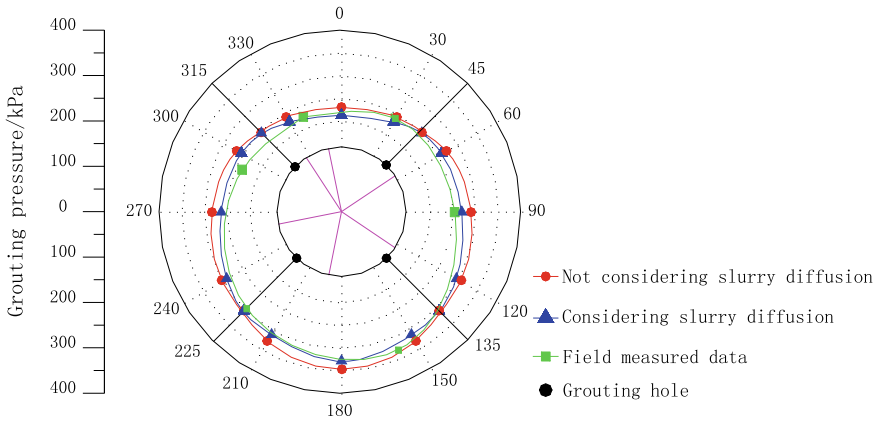
Fig. 6 Bingham flow grouting pressure distribution

When the slurry fills the shield tail interspace, due to the interaction between the slurry and the slurry's weight, the grouting pressure will decrease during the upward filling process and increase during the downward filling process, resulting in uneven distribution of grouting pressure.

Calculation Model of Grouting Pressure Distribution Considering the Slurry Diffusion and the Time-varying of Slurry Viscosity

(1) Considering the time-varying of slurry viscosity

The water–cement ratio of grouting slurry in the calculating section is 0.76, which belongs to Bingham fluid. The expression of the time-varying of slurry viscosity is as follows:

$$\mu(t) = 19.9\mathrm{e}^{0.0233t}. \tag{34}$$

The viscosity of slurry is exponential with grouting time. Combined with the calculation formula of grouting pressure, the filling distance and the viscosity of the slurry increase with time, and the grouting pressure gradually dissipates.

(2) Grouting slurry diffusion to the surrounding rock

In addition to the karst area, turning sections, and over-under-excavation sections in the construction site, the volume of shield tail interspace is 4.65 m^3 when the shield machine makes once driving. The diffusion radius (r_1 = 3.62 m) of the diffusion zone can be obtained by combining the calculation method in this article with the construction parameters. Through Formula (9), we can obtain the amount of slurry Q that diffuses into the diffusion zone, that is, 2.37 m^3. Therefore, the grout slurry can completely fill the shield tail interspace when the total slurry injection volume is 1.51 times the shield tail interspace volume.

Table 1 Synchronous grouting pressure distribution table (unit kPa)

Calculation section	0°	30°	45°	60°	90°	120°	135°	150°	180°
Without considering diffusion	212	226	240	253	271	285	300	314	330
Considering diffusion	201	218	240	248	262	278	300	307	319

(3) Influence of penetration pressure on surrounding rock

Set the slurry to fill the shield tail interspace, the influence of the expansion of shield tail interspace under penetration pressure attribute to the amount of grouting and shield tail interspace changes to discuss. According to Formula (19), the radial displacement (u_r) of the excavation cavern under the penetration pressure is 7.27 mm, and the volume of filling expansion part is 0.212 m^3. Given that the surrounding rock of the shield tunnel is a strongly weathered conglomerate, the elastic modulus is relatively large, and thus the radial displacement of the caverns under the action of the penetration pressure is small and has little effect on the grouting pressure on the lining segment.

The above factors are substituted into the grouting pressure calculation model. The grouting pressure calculation results are shown in Table 1. When the slurry diffusion and the time-varying slurry viscosity are considered, the grouting pressure distribution graph is shown in Fig. 6.

To obtain the accuracy of the calculation model relative to the field measurement results, the optimization method is introduced. The optimization objective function (J) is defined as follows:

$$J = \sum_{i=1}^{n} \left(p_i - p_i^*\right)^2 \bigg/ \sum_{i=1}^{n} p_i^{*2} \tag{35}$$

where n is the number of grouting pressure sensor measuring points on the outer surface of the segment; and P_i^* and P_i are, respectively, the measured grouting pressure value and the theoretical grouting pressure value of the ith monitoring point.

The optimal function ($J_1 = 1.225\%$) is calculated without considering the slurry diffusion and the time-varying slurry viscosity. The optimal function ($J_2 = 0.801\%$) is calculated according to the modified grouting pressure calculation model. The calculation results show that the grouting pressure is reduced when the diffusion of slurry is considered, and the calculated model is nearer the measured value.

5   Conclusion

(1) The filling of the grout slurry in the shield interspace corresponds to Bingham's fluid flow pattern. On this basis, the calculation model of grouting pressure distribution, considering the slurry diffusion and the time-varying slurry

viscosity, is deduced. The grouting pressure increases nonlinearly from the vault dome to the arch base. Then, the results of field test and theoretical calculation are compared to verify the correctness of the theoretical calculation in this paper.

(2) The theory of grouting slurry diffusion in the surrounding rock, considering the time-varying slurry viscosity, is deduced. The calculation formula of diffusion radius and the amount of slurry that diffuses into the diffusion zone is deduced and determines the amount of slurry that the shield tail interspace could be filled with during the synchronous grouting. In addition, the radial, tangential effective stress, and the radial displacement calculation formula of surrounding rock under the influence of penetration pressure are obtained.

(3) The viscosity of slurry is exponentially proportional with the grouting time. That is, considering the time-varying of slurry viscosity during synchronous grouting together with the calculation formula of grouting pressure, the viscosity of slurry increases with time, and the grouting pressure gradually dissipates. Considering the gravity effect of the slurry, the grouting pressure will reduce during the slurry upward filling and increase during the slurry downward filling.

(4) According to the analysis of the engineering example, the diffusion of synchronous grouting obviously influences the grouting pressure on the lining segment, and the grouting pressure increases with the cross-sectional filling of the shield tail interspace. The diffusion of the grouting slurry will reduce the amount of shield tail interspace section filling, such that the grouting pressure on the lining segment and the supporting stress of surrounding rock are reduced. Therefore, during the synchronous grouting process, the grouting pressure and grouting time should be controlled reasonably to ensure the safety of shield construction. The calculation method of grouting pressure on the lining segment is nearer the actual value, considering the grouting slurry diffusion.

References

1. Bezuijen A, Talmon AM, Kaalberg FJ et al (2004) Field measurement of grout pressures during tunnelling of the Sophia rail tunnel. Soils Found 44(1):39–48
2. Yukinori K, Yutaka S, Noriyuki O et al (1998) Back-filled grouting model test for shield tunnel. PTRI QR 39(1):35–39
3. Ezzeldine OY (1999) Estimation of the surface displacement field due to construction of Cairl metro line R1 Khalafawy-St. Therese. Tunn Undergr Space Technol 14(3):267–279
4. Ye F (2007) Analysis and control for upward movement of shield tunnel during construction. Tongji University, pp 31–47

5. Ye F, Gou CF, Chen Z, Liu YP, Zhang JL (2013) Back-filled grouts diffusion model of shield tunnel considering its viscosity degeneration. China J Highway Transp (01):127–134
6. Zhe HH, Cui MY, Yang JS (2000) Design model for shield lining segments and distribution of load. Chin J Geotech Eng (02):190–194
7. Ye F, Zhu HH, He C (2009) Back-filled grouts diffusion model and its pressure to segments of shield tunnel. Rock Soil Mech 30(5):1307–1312
8. Deng ZW, Leng WM, Chen JP (2005) The calculating research on the mechanism of shield tunnel back-filled grouting. J Plast Eng 12(6):114–117
9. Huang HW, Du J, Xie XY (2007) Simulation of GPR detecting of grouting materials behind shield tunnel segments. Chin J Geotech Eng (02):243–248
10. Yuan XH, Han YW, Zhong XC (2011) Pressure distribution model of simultaneous backfill grouting of shield tunnel. J Southwest Jiaotong Univ 46(1):18–23
11. Liang Y, Yang JS, Wang SY, Zeng XY (2015) A study on grout consolidation and dissipation mechanism during shield backfilled grouting with considering time effect. Rock Soil Mech 36(12):3373–3380
12. Gou CF, Ye F, Ji M, Sun HD (2016) Cylindrical cavity pressure-filter diffusion model for backfill grouting of shield tunnel. J Railw Sci Eng 13(02):325–331
13. Qiu MM, Yang GL, Jiang AL (2015) Influence factors and pressure distribution of simultaneous grouting for shield tunnel. J Shen Zhen Univ Sci Eng 32(02):162–171
14. Li ZM, Liao SM, Dai ZR (2010) Theoretical study on synchronous grouting filling patterns and pressure distribution of EPB shield tunnels. Chin J Geotech Eng 32(11):1752–1757
15. Zhang SS, Dai ZR, Bai Y (2015) Model text research on distribution law of grout pressure for simultaneous backfill grouting during shield tunneling. China Railw Sci 36(05):43–53
16. Dai ZR (2010) Research on synchronous grouting filling patterns of shield tunnel and applied engineering in soft soil area. Tongji Univ 40–65
17. Liu J, Zhang ZS, Han Y, Wu X (2015) Backfilled grouting diffusion law and model of pressure on segments of shield tunnel considering viscosity variation of cement grout. Rock Soil Mech 36(02):361–368
18. Yang ZQ, Hou KP, Guo TT, Ma Q (2011) Study of column-hemispherical penetration grouting mechanism based on Bingham fluid of time-dependent behavior of viscosity. Rock Soil Mech 32(09):2697–2703

Test Perceptions on the Degradation of Aggregate Subjected to Cyclic Triaxial Loading

Zhi-Qiang Lin, Jian-Gu Qian and Zi-Pei You

Abstract Aggregates are the principal materials of railway ballast, which for the most part contain huge, angular particles with a normal size of roughly 40 mm. Well-designed ballast is attractive to resist the pressures from the sleeper and after that to pass a satisfactory pressure level at the top surface of the subgrade soil. Though the functions of ballast by and large break down when subjected to Repeated traffic loading and in the end come into non-shakedown, (for the sample, ratcheting or incremental failure) reactions. In this work, a progression of expansive scale cyclic triaxial Experiments on aggregate did distinguish diverse cyclic degradation reactions. The permanent axial and volumetric strains are seen under various cyclic stress ratios. Three distinct cyclic reactions, shakedown, cyclic creep and incremental failure, are found. Shakedown happens at a moderately low cyclic stress ratio, under which the IPC (increase per cycle) of fixed axial strain and the IPC (area of hysteretic loop per cycle) of energy, dissipation will, in general, become negligible in the wake of cycling, and the fixed volumetric strains show compacting. Incremental failure happens at a generally high cyclic stress ratio, under which the IPCs of axial strain and energy dissipation increment after a set number of cycles, and the fixed volumetric strains show dilatancy. For cyclic creep, the IPCs of axial and volumetric strain and energy dissipation become about constant after an extensive number of cycles.

Keywords Aggregate · Cyclic triaxial tests · Shakedown · Cyclic creep · Incremental failure

Z.-Q. Lin · J.-G. Qian (✉) · Z.-P. You
Department of Geotechnical Engineering, Key Laboratory of Geotechnical and Underground Engineering of Ministry of Education, Tongji University, Shanghai 200092, China
e-mail: qianjiangu@tongji.edu.cn

811

1   Tested Sample and Equipment

The test was led by the extensive scale triaxial test device in Tongji University, and the railway ballast from north Yimin-Alshan segment of Yimin line was utilized as the sample. The normal density of the railway ballast is 1415 kg/m^3, the obvious density is 2650 kg/m^3, and the void ratio is 0.873 [1]. The particle size distribution curve is shown in Fig. 1.

The huge scale triaxial test device (Fig. 2) can apply, change and control the axial loading, confining pressure and the rate of loading at the same time. It can perform static and dynamic triaxial tests. Its applied dynamic load waveforms incorporate sine wave, triangle wave, random wave, client-defined waveform, etc. The fundamental technical parameters of this instrument are shown in Table 1.
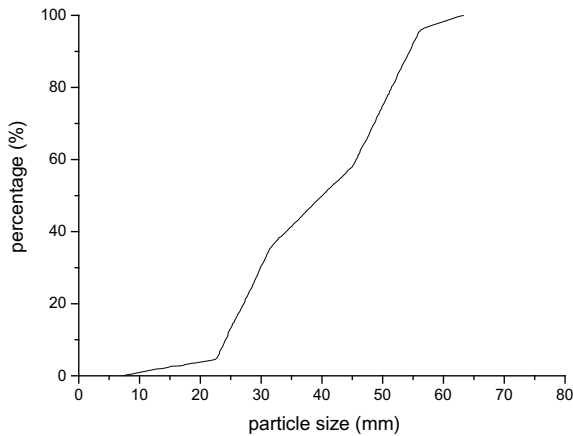
Fig. 1   Particle size distribution curve

Table 1   The main technical parameters of the large-scale triaxial test device

Parameters	Allowable maximum value
Static axial force	1000 kN
Dynamic axial force	800 kN
Axial frequency	10 Hz
Transverse frequency	5 Hz
Synchronous bidirectional identical frequency	5 Hz
Confining pressure	2 MPa

Fig. 2 The large-scale triaxial test device in Tongji University

2 Laboratory Tests

The test was separated into five stages: sample preparation, instrument preparation, solidification, loading and unloading.

Sample preparation [2, 3]: wash and dry the aggregate. Splice and spot three steel plates on the base. At that point compact 15 kg railway ballast in the rubber membrane, one more time with a tamping hammer to guarantee uniformity and density of the sample. Repeat the task four times. Include the top cover, remove the encompassing plate and fasten the sample up and down with ferrules to counteract water spillage. The sample before loading is shown in Fig. 3.

Instrument preparation: move the sample to the pressure chamber through a sliding track and move the chamber to the loading device. The engine is turned on to warm-up. At that point turn on the control framework to zero the data a short time later.

Solidification: so as to enable the sample to fumes the gas and to achieve a constant state before loading, it is important to hang tight for a timeframe for consolidating in the wake of including the confining pressure. At that point fill the pressure chamber with distilled water through the inlet pipe. A while later the underlying confining pressure is set by the control framework.

Loading: set the loading rate, maximum strain, etc., by the control framework. Amid the loading procedure, test data were recorded by the control framework and the confining pressure was checked continuously.

Unloading: the axial load was initially unloaded, and after that, the confining pressure was unloaded by the control framework. Subsequently, the seepage valve was opened to discharge the water and the pressure chamber was raised.

As shown in Fig. 4, the sample indicated clear horizontal development in the wake of loading. The outside of aggregate kept up dryness subsequent to unloading which demonstrated that the waterproof measures were set up and no spillage happened in test. As indicated by the monitoring results amid the test, the confining pressure was additionally kept consistent.

3 Test Results and Analysis

Taking into account that the confining pressure of railway ballast in viable designing is low which is for the most part between 20 and 100 kPa. As indicated by the current research [4, 5], the railway ballast demonstrates the smallest particle breakage in the range of 30–90 kPa. Thusly, this test chose a confining pressure of 50 kPa for both static monotonic loading tests and cyclic loading tests.

3.1 Static Monotonic Loading Test [6]

So as to get the static strength of the aggregate, static monotonic loading tests were first performed.

The stress–strain curve obtained from the test is shown in Fig. 5.

3.2 Cyclic Loading Test

In the expansive scale, triaxial trial of the aggregate made by Suiker et al. [7], the cumulative strains of the aggregate were seen under various cyclic stress ratios.

Reference the estimation of "relative cyclic stress" taken by Suiker, Qian et al. [8, 9], the $n = 0.50$, 0.86 and 0.96 are chosen. The waveform of the stress input embraces a triangular wave [4].

Fig. 5 The stress–strain curve of static monotonic loading
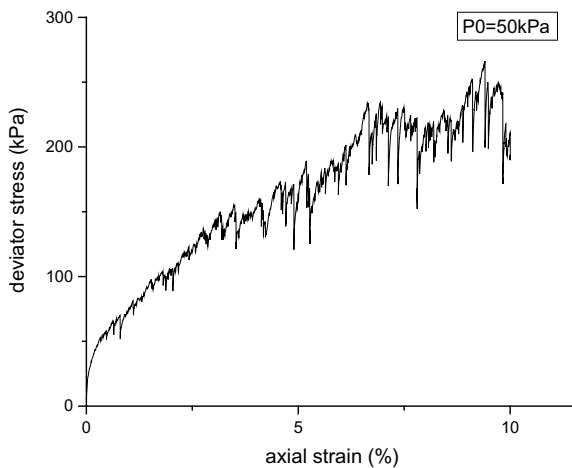
Fig. 6 The permanent cyclic
axial strain curves
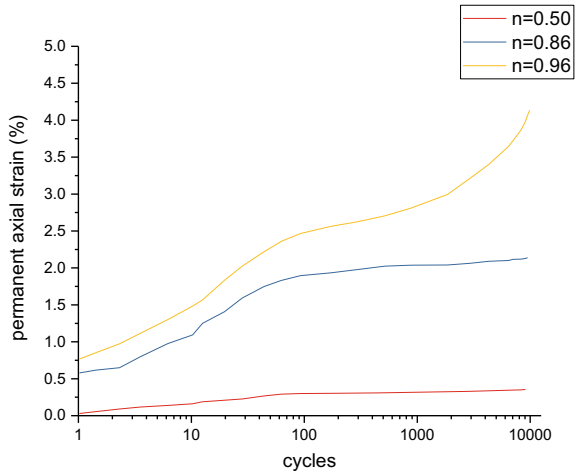
$$n = \frac{(-q/p)_{cyc}}{(-q/p)_{stat,max}} \tag{1}$$

$(-q/p)_{cyc}$ = stress amplitude for an individual load cycle.
$(-q/p)_{stat,max}$ = static failure load.

Permanent axial strain Cyclic loading utilized a triangular waveform input to
control the mean and amplitude of deviator stress through the control framework.
The loading frequency is set to 3 Hz. The acquired fixed cyclic axial strain curves
under various cyclic stress ratios are shown in Fig. 6.

It tends to be seen from the figure that the fixed axial strain increases with the
number of cycles under all cyclic stress ratios and the vast majority of the defor-
mation happens in the initial 100 cycles. Also, the fixed axial strain is likewise
essentially more prominent in the sample as the cyclic dynamic stress ratio
increases.

In the meantime, the advancement of permanent axial strain indicates three
dynamic patterns at three distinctive cyclic stress ratios: at a moderately low cyclic
stress ratio, the shakedown happens, under which the fixed axial strain grows
gradually and the IPC (increase per cycle) of fixed axial strain will, in general,
become negligible rapidly in the wake of cycling [10, 11]. At a moderately high
cyclic stress ratio, the constant failure happens, under which the fixed axial strain
grows rapidly in the underlying stage, and afterward steadily turns out to be flat, yet
when the number is about somewhere in the range of 3000 and 4000 there is a
propensity to quicken improvement all of a sudden until the end of the analysis.
Also, the IPC of axial strain increases after a predetermined number of cycles. At a

medium cyclic stress ratio, cyclic creep happens, under which the fixed axial strain grows generally rapidly, yet in the long run it step by step becomes stable. Also, the IPC of axial strain turns out to be negligible after a large number of cycles [12].

Permanent volumetric strain The permanent volumetric strain curves under different cyclic stress ratios are shown in Fig. 7.

Likewise, the improvement of fixed volumetric strain demonstrates three dynamic patterns: at a moderately low cyclic stress ratio, the fixed volumetric strain indicates compacting. At a high cyclic stress ratio, the fixed volumetric strain demonstrates dilatancy. The IPC of volumetric strain increases after an expansive number of cycles. At a medium cyclic stress ratio, the sample demonstrates an inclination of cyclic extension, yet the fixed volumetric strain progressively stabilized. The IPC of volumetric strain turns out to be almost insignificant after an expansive number of cycles.

Stress–strain hysteresis loop Stress–strain hysteresis loop [8] is a critical list to think about the dynamic attributes of soil, and its shape and size mirror the energy dissipation of the soil amid loading. Figures 8, 9 and 10 demonstrate the stress–strain hysteresis loop for $N = 10$, 1000 and 8000 at three distinctive cyclic stress ratios under 50 kPa confining pressure.

It tends to be seen from the figure that the stress–strain hysteresis loop moves consistently to one side amid the cycles.

At a generally low cyclic stress ratio, the shakedown happens, under which the IPC (region of hysteretic loop per cycle) of energy dissipation will, in general, become negligible in the wake of cycling and the slope of the hysteretic circle remains generally unaltered. Both of them demonstrate that the energy dissipation in each cycle steadily diminishes and the microstructure of the sample bit by bit stabilizes.
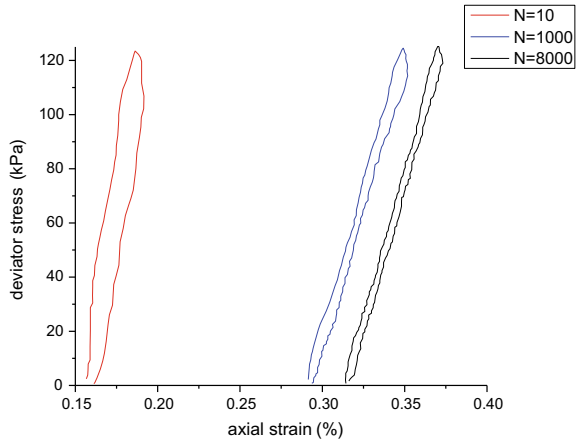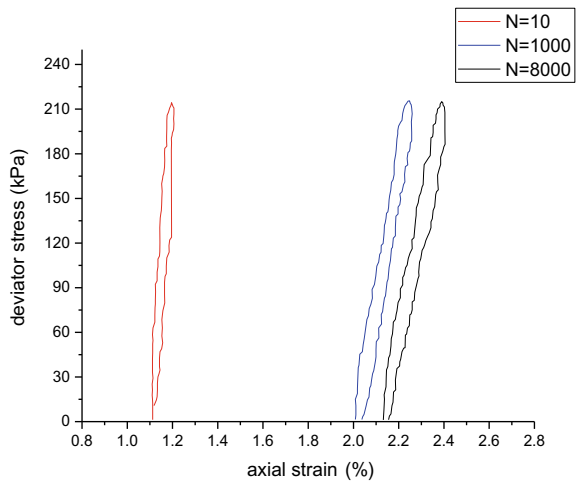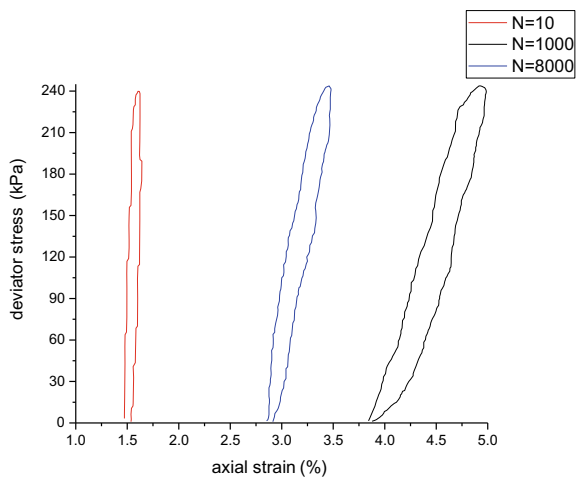
At a generally high cyclic stress ratio, the constant failure happens, under which the IPC of energy dissipation increases after a predetermined number of cycles and the hysteretic circle demonstrates a pattern of consistent dumping. Both of them demonstrate an inexorably bigger piece of the dissipative energy adding to the irreversible deformation which in the end prompts that the internal structure of the sample destructs and cannot achieve the constant state.

At a medium cyclic stress ratio, cyclic creep happens, under which the IPC of energy dissipation somewhat increases and turns out to be almost constant after a substantial number of cycles which demonstrate that the internal structure of the sample has been damaged and in the long run ends up stable.

4   Conclusions

In this work, a progression of expansive scale cyclic triaxial tests on aggregate was completed to recognize diverse cyclic degradation reactions. The fixed axial and volumetric strains are seen under various cyclic stress ratios. Three distinct cyclic reactions, shakedown, cyclic creep and constant failure, are found.

(1) The shakedown happens at a generally low cyclic stress ratio, under which the fixed axial strain grows gradually and the IPC (increase per cycle) of fixed axial strain will, in general, become negligible rapidly subsequent to cycling. The fixed volumetric strain indicates compacting. The IPC (area of hysteretic loop per cycle) of energy dissipation will, in general, become negligible in the wake of cycling and the slope of the hysteretic circle remains generally unaltered.

(2) The constant failure happens at a generally high cyclic stress ratio, under which the fixed axial strain grows rapidly in the underlying stage, and after that bit by bit turns out to be flat, yet when the number is about somewhere in the range of 3000 and 4000 there is an inclination to quicken advancement all of a sudden until the end of the examination. The fixed volumetric strain demonstrates dilatancy. The IPC of volumetric strain increases after a large number of cycles. The IPC of energy dissipation increases after a predetermined number of cycles, and the hysteretic circle demonstrates a pattern of consistent dumping.

(3) For cyclic creep, the fixed axial strain grows generally rapidly; however, in the long run, it continuously becomes stable. The sample demonstrates an inclination of cyclic development; however, the fixed volumetric strain bit by bit stabilized. The IPC of volumetric strain turns out to be almost negligible after a substantial number of cycles. The IPC of energy dissipation somewhat increases and turns out to be almost constant after a substantial number of cycles.

References

1. Mcdowell GR, Lim WL, Collop AC et al (2004) Comparison of ballast index tests for railway trackbeds. Geotech Eng 157(3):151–161
2. Marek CR (1977) Compaction of graded aggregate bases and subbases. Transp Eng J 103(1): 103–113
3. Watabe T, Kamada S (2015) On the settlement of the railway ballast under the impact loads. Biotechnol Prog 31(1):248–257
4. Indraratna B, Vinod JS, Thakur PK (2013) Effect of confining pressure and frequency on the deformation of ballast. Geotechnique 63(9):786–790
5. Indraratna B, Lackenby J, Christie D (2005) Effect of confining pressure on the degradation of ballast under cyclic loading. Geotechnique 55(4):325–328
6. Anderson WF, Fair P (2008) Behavior of railroad ballast under monotonic and cyclic loading. J Geotech Geoenviron Eng 134(3):316–327
7. Suiker ASJ, Selig ET, Frenkel R (2005) Static and cyclic triaxial testing of ballast and subballast. J Geotech Geoenviron Eng 131(6):771–782
8. Qian JG, Wang YG, Yin ZY et al (2016) Experimental identification of plastic shakedown behavior of saturated clay subjected to traffic loading with principal stress rotation. Eng Geol 214:29–42
9. Qian JG, Guo SB, Huang MS et al (2012) Experimental study on responses of saturated clay to traffic loading. Adv Transp Geotech 2:610–616
10. Poulos SJ (1981) The steady state of deformation. J Geotech Geoenviron Eng 107(5):553–562
11. Verdugo R, Ishihara K (1996) The steady state of sandy soils. J Jpn Geotech Soc Soils Found 36(2):81–91
12. Tao M, Mohammad LN, Nazzal MD et al (2010) Application of shakedown theory in characterizing traditional and recycled pavement base materials. J Transp Eng 136(3): 214–222

Comparison of Dynamic Modulus Assignments for Isparta State Highways According to Mechanistic-Empirical Pavement Design Method

Kemal Armagan, Mehmet Saltan, Serdal Terzi and Nevzat Kirac

Abstract Mechanistic-Empirical Pavement Design Method (MEPDM) determines the necessary pavement thickness for given design inputs and deformations in pavement by combining the parameters of mechanical modeling and observations of pavement performance through the pavement design life. To examine various distresses including cracking, rutting and roughness in MEPDM, pavement dynamic modulus ($E*$) which is a function of age, temperature, rate of loading, and mixture properties, such as aggregate air voids, gradation, binder stiffness and binder content needs to be determined. For this, there are three levels of analysis in MEPDM. In Level 3, there is no need for laboratory tests, and there are prediction models to assign the dynamic modulus. These models can implement time-dependent analysis of pavement. In this study, statistical climate data analysis of 20 years including 1995–2014 period of Isparta province was examined. Then, the prediction models were used to determine the dynamic modulus master curves of Isparta state highways, and these master curves were compared.

1 Introduction

Different material types are using to build the flexible pavements. So, the different material properties of all these material types, the interaction of pavement layers, traffic and environmental loads are highly important for pavement performance [1].

K. Armagan (✉)
Karamanoglu Mehmetbey University, 70200 Karaman, Turkey
e-mail: kemalarmagan@kmu.edu.tr

M. Saltan · S. Terzi
Suleyman Demirel University, 32000 Isparta, Turkey

N. Kirac
Eskisehir Osmangazi University, 26000 Eskisehir, Turkey

MEPDM is a method that determines the required pavement thickness for the lifespan of the pavement. MEPDM uses the combination of mechanical modeling elements and performance observations to determine the pavement response to traffic loads and environmental conditions. Then, the mechanical part defines the model responses such as stress, strain and displacements for a given set of design inputs. Then, the empirical part uses the pavement responses to predict the deteriorations of pavement for the lifespan of the pavement based on the actual field performance [2].

2 Method

MEPDM is used in this paper. MEPDM is a complex pavement design method which uses performance models, performance predictions and pavement response to analyze pavement performance by considering material properties, structure, environmental and traffic loads as input factors [1, 3].

There is a hierarchical (level) system to define input parameters in MEPDM. The approach in system is based on the need to knowledge. In input Level 1, there are comprehensive laboratory tests. Level 2 inputs are estimating through correlations with other materials that are commonly measuring in laboratory or field. In input Level 3, there is no or little need to testing, input parameters are estimating by experience or default values. There are major material types as default values available for input Level 3 in the MEPDM. Regardless of the selected input level, the program runs the same analysis for all input levels [4].

For all three input levels, asphalt binder data is required to determine the viscosity at any temperature by using viscosity-temperature relationship recommended by ASTM

2493M-09. The linear regression is performed to obtain the regression parameters in Eq. 1 [5, 6].

$$\log \log \eta = A + \text{VTS} \log T_{\text{R}} \tag{1}$$

where

η binder viscosity, cP.
T_{R} temperature, Rankine.
A regression intercept.
VTS   regression slope of viscosity-temperature susceptibility [5, 6].

2.1 Mastercurve and Shift Factors

Sigmoidal parameters best describe the shape and the location of the mastercurve by mathematically modeling, using Eq. 2 [7, 8].

$$\log E^* = \delta + \frac{\alpha}{1 + e^{\beta + \gamma(\log f_R)}} \tag{2}$$

In Eq. 2, f_R is the loading frequency at the reference temperature. δ, α are known as the fitting parameters that depend on aggregate gradation, binder contents and air void. β, γ depend on characteristics of asphalt binder and determines the shape of the sigmoidal functions [2, 7]. Equations 3 and 4 are needed to define $\log f_R$ in Eq. 2.

$$f_r = (f)a_t(T) \tag{3}$$

f frequency of loading at desired temperature
T temperature of interest
$a_t(T)$ shift factor as a function of temperature [9].

$$\log(a_t(T)) = a_1\left(T^2 - T_{\text{ref}}^2\right) + a_2(T - T_{\text{ref}}) \tag{4}$$

T_{ref} reference temperature, 19 °C (or 66.2 °F)
a_1 and a_2 the shift factor polynomial coefficients [7]

2.2 Level 3 Analysis

For Level 2 and 3 inputs, the dynamic modulus master curve can have obtained directly from an empirical predictive equation. This predictive equation has an empirical relationship between $|E^*|$ and mixture properties. For Level 3, default A and VTS values are based on the binder grading as shown in Table 2 can be used. Beside Superpave performance grade (PG), penetration grade or viscosity grade parameters can also be used for determining A and VTS values [10].

2.3 Review of the US Dynamic Modulus Database and Predictive Models

There are many prediction models to assign dynamic elasticity modulus of asphalt pavement in MEPDM. Some of them are listed in Table 1 due to their publishing year.

Table 1 E^* prediction models [3, 10, 11]

Model no.	E^* predictive model	Year
1	Van der Poel (Shell Oil's early version) model	1954
2	Bonnaure (Shell Oil's early version) model	1977
3	Shook and Kallas' models	1969
4	Witczak's early model	1972
5	Witczak and shook model	1978
6	Witczak 1981 model	1981
7	Witczak, Miller and Uzan's model	1983
8	Witczak and Akhter's model	1984
9	Witczak, Leahy, Caves and Uzan's models	1989
10	Witczak and Fonseca's model	1996
11	Andrei, Witczak and Mirza's revised model	1999
12	Hirsh model of Christensen, Pellinen and Bonaquist	2003
13	Witczak and Bari model	2006
14	Witczak (NHCRP) 1-40D	2007
15	Georgouli model	2015

3 Data Analysis and Comparison Results

In this study, three dynamic elasticity mastercurve predictions have been made from Isparta and its neighbor cities Afyonkarahisar and Antalya. Then, these master curves have compared with each other (Table 2).

3.1 Description of Materials

For prediction of the dynamic modulus of pavement materials, aggregate gradation in Table 3 and 1.03 g/cm^3 value as specific gravity of bitumen have used to determine the material properties in asphalt mixture. As seen in Table 3, Turkish standards have been considered for preparing the asphalt mixture samples.

3.2 Climatic Data Analysis

In this study, 20 years of climatic data between 1995 and 2014 years were analyzed for Isparta and its neighbor cities Afyonkarahisar and Antalya to decide the performance grade (PG) of bitumen used in the models. Analysis results have shown in Table 4.

Table 2 Default A and VTS parameter table for performance grade of binder [10]

High temp grade	Low-temperature grade												
	−10		−16		−22		−28		−34		−40		−46	
	A	VTS	A	VTS	A	VTS	A	VTS	A	VTS	A	VTS	A	VTS
46									−3.01	11.504	−3.393	10.101	−2.905	8.755
52	−4.570	13.386	−4.541	13.305	−4.342	12.755	−4.012	11.840	−3.602	10.707	−3.164	9.496	−2.736	8.310
58	−4.172	12.316	−4.147	12.248	−3.981	11.787	−3.701	11.010	−3.350	10.035	−2.968	8.976		
64	−3.842	11.432	−3.822	11.375	−3.680	10.980	−3.440	10.312	−3.134	9.461	−2.798	8.524		
70	−3.566	10.690	−3.548	10.641	−3.426	10.299	−3.217	9.715	−2.948	8.965	−2.648	8.129		
76	−3.331	10.059	−3.315	10.015	−3.208	9.715	−3.024	9.200	−2.785	8.532				
82	−3.128	9.514	−3.144	9.475	−3.019	9.209	−2.856	8.750	−2.642	8.151				

Table 3 Aggregate gradation

Sieve		Design	Turkish standard	
mm	in.	Gradation	Limits	
25.4	1″	100	100	100
19.0	3/4″	90.3	80	100
12.5	1/2″	71.1	58	80
9.5	3/8″	58.1	48	70
4.5	No. 4	42.9	30	52
2.0	No. 10	31.1	20	40
0.4	No. 40	11.2	8	22
0.18	No. 80	7.3	5	14
0.075	No. 200	4.6	2	7

Table 4 PG values due to temperature analysis of compared cities

PG value	Isparta	Antalya	Afyonkarahisar
	64-22	70-16	64-34

3.3 Development of Mastercurve

Georgouli model (Eq. 5) has been used for dynamic elasticity modulus prediction because this model was known as the latest model, and the model was tested in neighbor country of Turkey.

$$
\begin{aligned}
\log E^* = {} & 3.9 + 3.7437\rho_{200} - 0.0298(\rho_{200})^2 \\
& - 0.01221\rho_4 - 0.08686V_a - 0.94215\left(\frac{V_{\text{beff}}}{V_{\text{beff}} + V_a}\right) \\
& + \frac{3.04483 - 0,01124\rho_4 + 0.00242\rho_{38} + 0.00025(\rho_{38})^2 + 0.00111\rho_{34}}{1 + e^{(-1.07682 + 0.47006\log f - 0.62593\log\eta)}}
\end{aligned}
\tag{5}
$$

E^* dynamic modulus of mixture (psi)
η viscosity of binder (10^6 poise),
f loading frequency (Hz),
V_a air voids (percentage by volume),
V_{beff} effective binder (percentage by volume),
ρ_{200} cumulative percentage retained on 0.075 mm (No. 200) sieve,
ρ_4 cumulative percentage retained on 4.75 mm (No. 4) sieve,
ρ_{34} cumulative percentage retained on 19 mm (3/4 in) sieve,
ρ_{38} cumulative percentage retained on 9.5 mm (3/8 in) sieve [3].

To draw a mastercurve of dynamic elasticity modulus there is a relation required to establish between viscosity and temperature. Equation 1 was used to establish

Table 5 *A* and VTS values for each city due to performance grades

	Isparta	Antalya	Afyon
A	10.980	10.641	9.461
VTS	−3.680	−3.548	−3.134

this relation, *A* and VTS values were taken from Table 5 due to performance grade analysis of required bitumen for all three cities. By using all parameters in Eq. 5 dynamic elasticity modulus in different temperatures have been calculated. For combining these results to draw a mastercurve, Eqs. 2–4 were used.

After the calculations, maximum and minimum predicted dynamic elasticity modulus values as seen in Table 6 have been obtained.

By drawing all three master curves, the graph in Fig. 1 has obtained. Then, Poisson's ratio has been calculated from Eq. 6.

Table 6 Max. − Min. values of dynamic elasticity modulus values for compared cities

	Isparta	Antalya	Afyonkarahisar
Maximum (MPa)	7761.13	7758.05	7761.88
Minimum (MPa)	6590.14	6973.65	6212.38
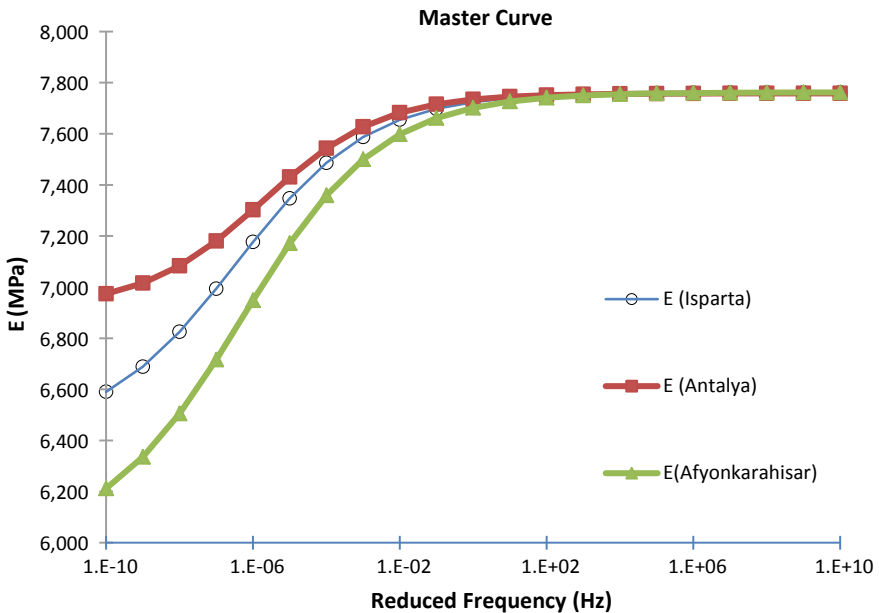
Fig. 1 Estimated master curves of three cities
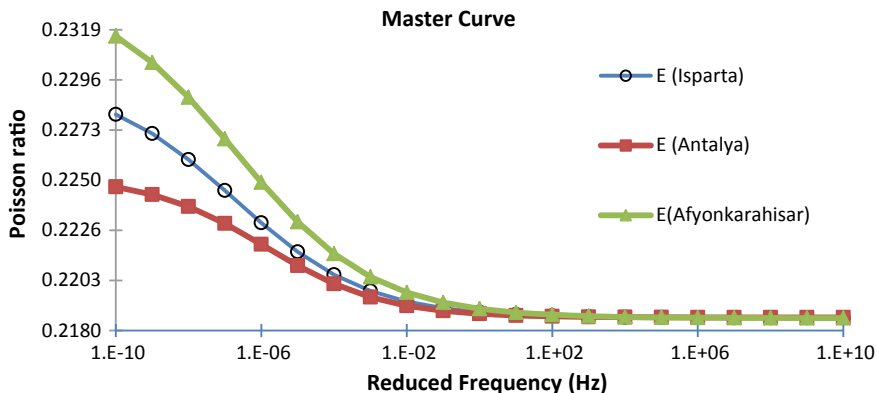
Fig. 2 Poisson's ratios for estimated master curves of three cities

$$\mu = 0.15 + \frac{0.35}{1 + e^{(-12,452 + 2,29 \log E*)}} \tag{6}$$

μ Poisson's ratio [10].

Achieved Poisson's ratio results by using Eq. 6 of all three cities have shown in Fig. 2.

4 Conclusion

The dynamic elasticity modulus is a key design parameter in the MEPDM. For a reliable pavement design, calibration or analysis in MEPDM, Level 1 asphalt materials inputs are required. The standard laboratory procedures for determination of dynamic elasticity modulus and the testing process and development of the master curve require time and significant resources. So, if there is no chance to get field or laboratory test data, Level 3 analysis can be used. In this paper, Level 3 inputs were used to develop a predicted E* master curve by using volumetric parameters for all three cities and to compare the results. For these predictions, Georgouli model was used because the other latest prediction models were prepared for USA roads and climate, but Georgouli model was established for Greece roads which is closer to Turkey.

- The results have shown by a reduction in minimum temperature value, dynamic elasticity modulus decreases.
- And an increase in maximum temperature rises the dynamic elasticity modulus values.

- In comparison with the temperature changes in Isparta to Antalya (case 1) and Isparta to Afyonkarahisar (case 2) cities; in case 1 by an increase in maximum temperature and decrease in minimum temperature, E* increases, in case 2 maximum temperature remain unchanged and by a decrease in minimum temperature cause a decrease as expected but in case 2, $E*$ was affected more than comparing to case1.
- For Poisson's ratio chance, the results showed that in case 2 Poisson's ratio decreases more slowly than in case 1.
- Overall, the analysis procedure and a comparison have obtained from the present paper, there is still field data needed to verify the Georgouli model which is suitable for using in Turkey's asphalt pavements, or a calibration is needed to modify the model.

References

1. Orobio A, Zaniewski JP (2012) Using the mechanistic-empirical pavement design guide for material selection. Rev. Fac. Ing. Univ. Antioquia 64:138–149
2. Seoa J, Kimb Y, Choc J and Jeong SS (2012) Estimation of in situ dynamic modulus by using MEPDG dynamic modulus and FWD data at different temperatures. Int J Pavement Eng 1–11, (2012). https://doi.org/10.1080/10298436.2012.664274
3. Georgouli K, Plati C, Loizos A (2016) Assessment of dynamic modulus prediction models in fatigue cracking estimation. Mater Struct 49:5007–5019. https://doi.org/10.1617/s11527-016-0840-6
4. Mechanistic-empirical pavement design guide. A manual of practice, AASHTO (2008)
5. Esfandiarpour S, Ahammed AM, Shalaby A, Liske T, Kass S (2015) An evaluation of pavement ME design dynamic modulus prediction model for asphalt mixes containing RAP. In: The 2015 conference of the transportation association of Canada
6. ASTM D2493M-09 (2009) Standard viscosity-temperature chart for asphalts
7. Gopalakrishnan K, Kim S, Ceylan H, Kaya O (2014) Development of asphalt dynamic modulus master curve using falling weight deflectometer measurements. TR-659, InTrans Project Reports, 6-2014
8. Yousefdoost S, Vuong B, Rickards I, Armstrong P, Sullivan B (2013) Evaluation of dynamic modulus predictive models for typical australian asphalt mixes, 15. In: International flexible pavements conference
9. Clyne TR, Li X, Marasteanu MO, Skok EL (2013) Dynamic and resilient modulus of Mn/DOT asphalt mixtures. 2003-09 final report
10. Guide for Mechanistic-Empirical Design 1-37A (2004) Part 2: Design inputs. Chapter 2: Material characterization. NCHRP
11. Bari J, Witczak MW (2006) Development of a new revised version of the Witczak E predictive model for hot mix asphalt mixtures. J Assoc Asphalt Paving Technol: Proc Techn Sessions

Expanded Glass Usability in Hot-Mix Asphalt as Fine Aggregate

Sebnem Karahancer, Nihat Morova, Ekinhan Eriskin,
Kemal Armagan, Gizem Kacaroglu, Oznur Karadag,
Mehmet Saltan and Serdal Terzi

Abstract In this study, the usability of expanded glass (EG) in hot-mix asphalt (HMA) as the fine material is investigated. Firstly, standard tests on the EG have been done to determine the basic properties. Next, optimum binder content and aggregate gradation are determined in accordance with Superpave volumetric mix design. The EG is substituted into the HMA as a fine aggregate (in accordance with the original size) in four different rates (25, 50, 75 and 100%). Optimum binder content for each EG ratio is determined. The Superpave gyratory compactor is used for the compaction of the specimens. Prepared specimens have been tested for the indirect tensile strength and tensile strength ratio.

Keywords Expanded glass · Fine aggregate · Superpave · Hot-mix asphalt

S. Karahancer (✉) · N. Morova
Isparta University of Applied Sciences, Isparta 32260, Turkey
e-mail: sebnemsargin@isparta.edu.tr

N. Morova
e-mail: nihatmorova@isparta.edu.tr

E. Eriskin · O. Karadag · M. Saltan · S. Terzi
Suleyman Demirel University, Isparta 32260, Turkey
e-mail: ekinhaneriskin@sdu.edu.tr

O. Karadag
e-mail: oznurkaradag92@gmail.com

M. Saltan
e-mail: mehmetsaltan@sdu.edu.tr

S. Terzi
e-mail: serdalterzi@sdu.edu.tr

K. Armagan
Karamanoglu Mehmetbey University, Karaman 70200, Turkey
e-mail: kemalarmagan@kmu.edu.tr

G. Kacaroglu
Afyon Kocatepe University, Afyonkarahisar 03200, Turkey
e-mail: gkacaroglu@aku.edu.tr

1   Introduction

In cold regions, where freeze and thaw occur many times in a year, soft and frost-susceptible soil got a failure. By cold winter, the pavement heaves because of the frost and got thawed by spring. As a result, reduced bearing capacity is obtained, a big part of the maintenance and reconstruction cost. In addition, the corrupted asphalt pavement increases the travel costs for the road users due to the roughness and delay [1].

Dense-graded mixtures are very common in the world because they are very suitable for all the traffic conditions. Primary advantages of the dense-graded mixtures are the lower initial cost, and most of the hot-mix asphalt (HMA) producers are familiar with the production. However, because of the small air void in the pavement, frost could penetrate through the whole pavement. So, the traffic safety is reduced while the pavement fails. Using anti-icing or de-icing materials is expensive and not always practical. But, if the pavement could be constructed using high-insulation materials, the constructed pavement could have low frost penetration value.

Lightweight aggregate (LWA) has less specific gravity compared to the traditionally used aggregates and so has more air voids. There are some studies about using the LWA for several civil engineering applications for building lightweight and frost insulation constructions [2–7].

In this study, expanded glass (EG) (see Fig. 1) has been used for determining the usability in the dense-graded HMA as fine aggregate. Therefore, the EG has been sieved to determine the granular size. Then, the EG is substituted into the gradation in four different rates (25, 50, 75 and 100%) by weight of the corresponding fine aggregate. Optimum binder content for each EG rate is determined using the Superpave volumetric mix design procedure. Afterwards, the specimens are tested using indirect tensile strength test.

2   Experimental

2.1   Materials

Aggregate. Limestone aggregate is obtained from Isparta Municipality for the study. Standard tests have been done to determine the physical characteristics of the aggregate. The test results are given in Table 1. The dense-graded aggregate gradation used in this study is shown in Fig. 2. The study is performed for the wearing course of the pavement. So, the nominal maximum aggregate size is selected as 12.5 mm. The gradation curve is selected with respect to the control points expressed in AASHTO MP2 [8].

Fig. 1 A sample of the expanded glass

Table 1 Limestone aggregate characteristics

Sieve size (mm)	Property	Value
<0.075	Specific gravity (g/cm^3)	2.640
4.75–0.075	Specific gravity (g/cm^3)	2.680
	Saturated specific gravity (g/cm^3)	2.652
	Water absorption (%)	0.130
25–4.75	Specific gravity (g/cm^3)	2.700
	Saturated specific gravity (g/cm^3)	2.428
	Water absorption (%)	2.800
	Abrasion loss (%)	20.38

2.2 Bitumen

Bitumen with a penetration grade of 50/70, used for this study, is obtained from Isparta Municipality. Basic rheological properties are shown in Table 2.

The optimum binder content is determined using the Superpave volumetric mix design procedure. The ESALs are determined as greater than 30×10^6; so the N_{design} is selected as 125 gyros. Four different bitumen rates are predetermined for each EG rate and reference specimen. All the specimens have been compacted using Gyratory Compactor for 125 gyros with each bitumen rate. Then, the air
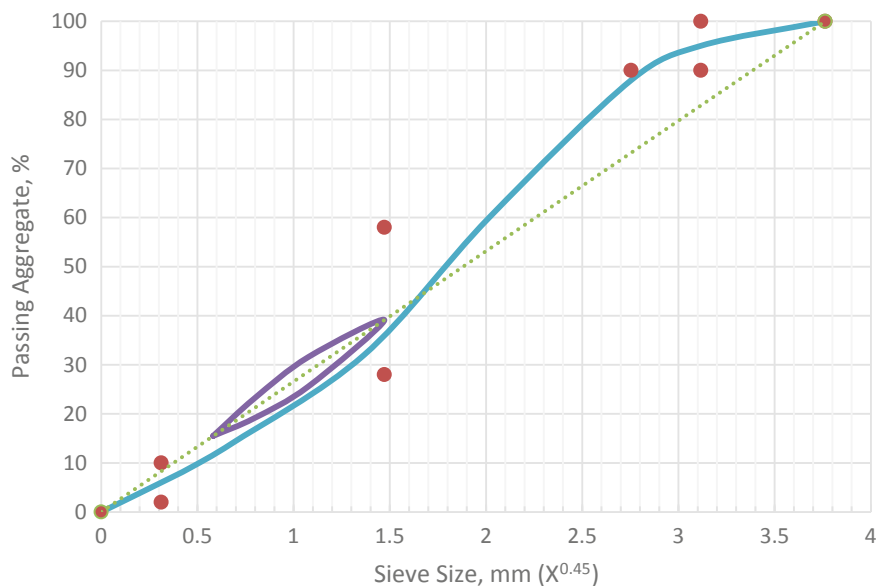
Fig. 2 Gradation of the aggregates

Test	Average value
Penetration (@ 25 °C)	60–65
Flash point	180 °C
Combustion point	230 °C
Softening point	45.5 °C
Ductility (5 cm/min)	>100 cm
Specific gravity	1.030

Table 2 Basic bitumen properties

voids are calculated and the bitumen rate corresponding to the 4% air void is predetermined as optimum bitumen content. In addition, the predetermined bitumen content should ensure the minimum voids in mineral aggregate rate (VMA) which is 14% for 12.5 mm nominal maximum aggregate size gradations and voids filled with asphalt (VFA) which is between 65 and 75%.

2.3 Expanded Glass

The EG is sieved before substituting it into the gradation. As the result of the sieving analyses, the EG's granular size is determined as 0.25–0.425 mm (No. 60–No. 40). The geometrical shape of the EG is a sphere, which decreases the void to a minimum. The technical properties of the EG are given in Table 3.

Table 3 Technical properties of the EG [9]

Granular size (mm)	0.25–0.425
Dry unit density (kg/m^3)	370 ± 40
Specific gravity	0.689
Crush resistance (N/mm^2)	2.8
Water absorption (%)	17
Softening point (°C)	700
Colour	White

3 Results and Discussion

Optimum bitumen contents for each substitution rate are calculated. The air void, VMA, VFA and specific gravity results are shown in Figs. 3, 4, 5 and 6, respectively.

As seen in Figs. 3, 4, 5 and 6, optimum binder content is rising. Withal, the VMA values for each mixture are rising, also. However, by increasing the EG ratio, the VFA values exceed the specification limits. This could be explained by increasing the low-density EG by replacing the high-density limestone increases the surface area of the specimen. So, the needed bitumen rate is increased to cover the aggregates. By adding too much bitumen, the VFA limits exceed. But, as seen in Fig. 6, the constructed specimens got lighter than the reference specimen. As seen in Figs. 3, 4, 5 and 6, optimum binder contents are calculated as 4.5, 5.49, 6.28 and 8.55% for reference, 25%, 50%, 75% and 100% EG-substituted specimens, respectively.
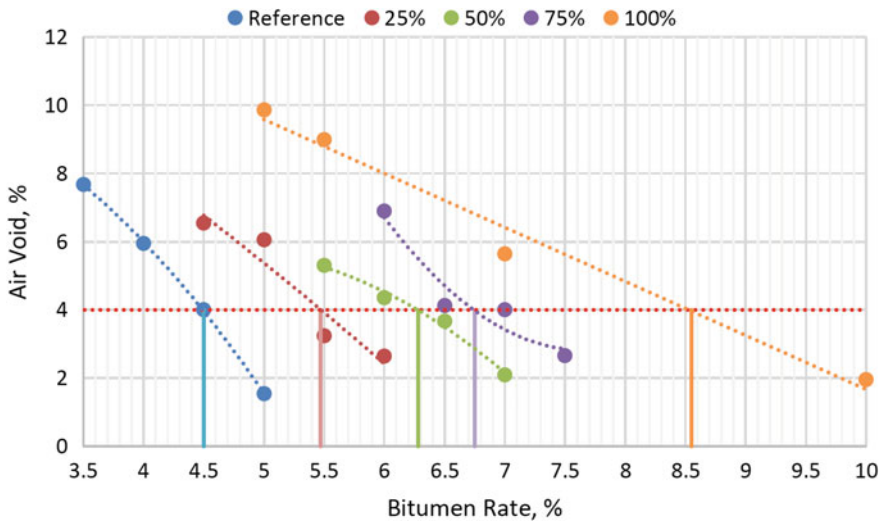
Fig. 3 Calculated air voids for each substitution rate
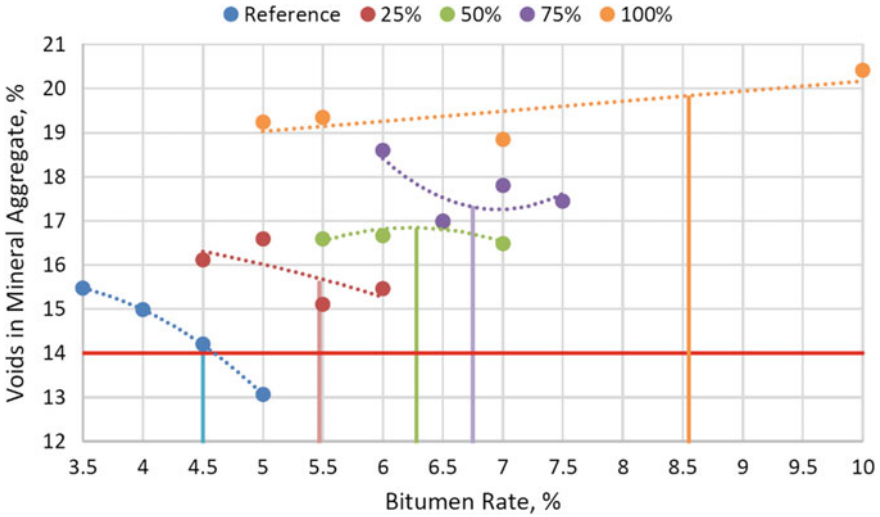
Fig. 4 Calculated voids in mineral aggregate for each substitution rate
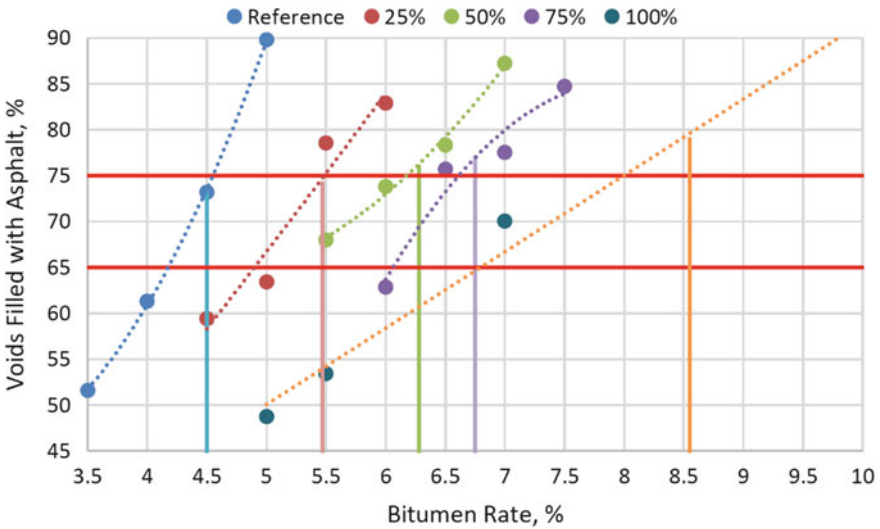
Fig. 5 Calculated voids filled with asphalt for each substitution rate

After obtaining the optimum binder contents, specimens for each EG substitution rate have been mixed with the corresponding bitumen rate. Then, they are tested using modified Lottman test method for obtaining the strength test results in the conditioned and unconditioned case. Therefore, specimens have been cured in
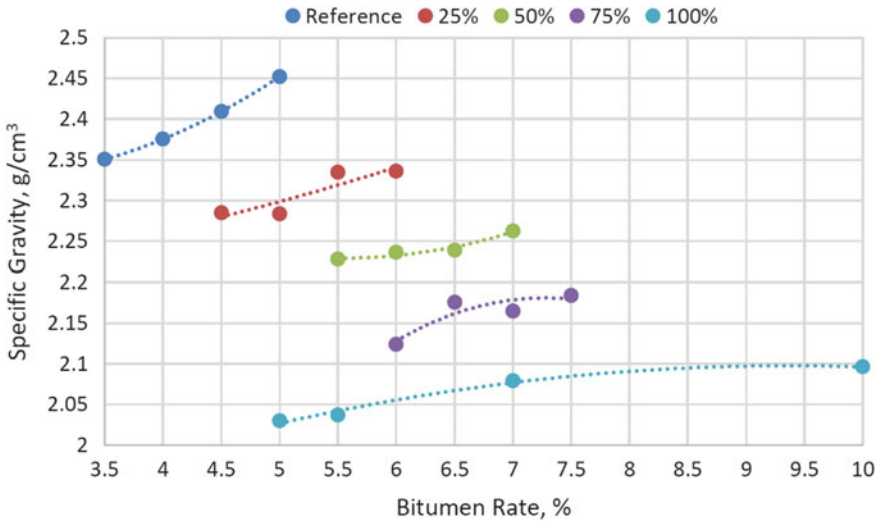
Fig. 6 Calculated specific gravity values for each substitution rate

an oven at 40 °C for 72 h. Then, half of the specimens have been loaded till failure for obtaining the unconditioned case. The rest of the specimens have been soaked into a water bath, vacuum-saturated and frozen. By thawing the specimens in an oven at 60 °C, the specimens got spread. They were unable to take out from the water bath for loading. So, the conditioned case values are not available. Unconditioned test results are shown in Fig. 7.

As seen in Fig. 7, the strength values are decreasing by substituting more EG. The reason could be explained by the increase in the bitumen rate. But, the height of the specimens has been increased up to 18% by increasing the substitution rate.

4 Conclusion

Usability of expanded glass as fine aggregate in dense-graded hot-mix asphalt pavement has been studied. The gradation and the binder content have been determined using Superpave volumetric mix design procedure.

As a result of the indirect tensile strength test results, the expanded glass could be used in cold regions, but in hot climate regions, it seems not possible. The weight of the pavement could be decreased by substituting expanded glass. However, optimum binder content increases by the increase in the substitution rate.
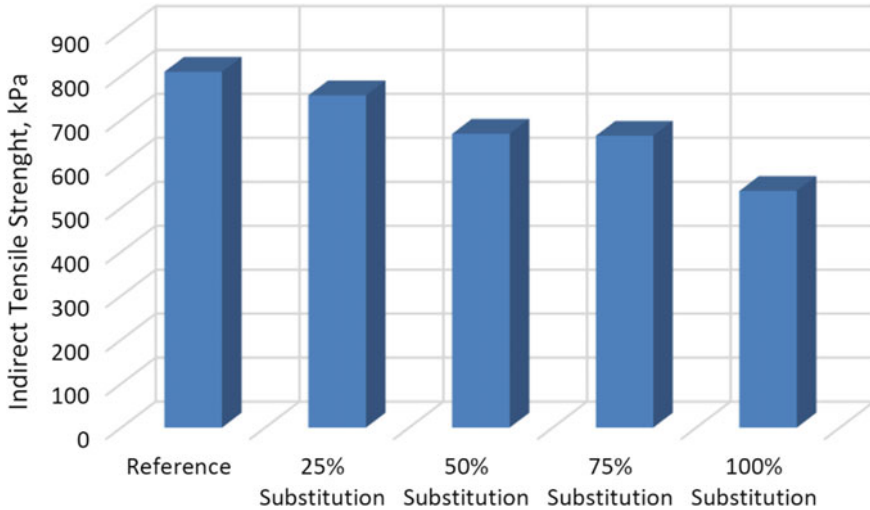
Fig. 7 Indirect tensile strength test results for unconditioned specimens

References

1. Hoff I, Want A, Øiseth E, Emdal A, Amundsgård KO (2002) Light weight aggregate (LWA) used in road pavements. In: 6th international conference of bearing capacity of road and airfields, pp 1013–1022. Lisbon, Portugal
2. Khan A, Mrawira D (2010) Investigation of the use of lightweight aggregate hot-mixed asphalt in flexible pavements in frost susceptible areas. J Mater Civ Eng 22(2):171–178
3. Pioro LS, Pioro IL (2004) Production of expanded-clay aggregate for lightweight concrete from non-self bloating clays. Cement Concr Compos 26(6):639–643
4. Bogas JA, Gomes A, Pereira MFC (2012) Self-compacting lightweight concrete produced with expanded clay aggregate. Constr Build Mater 35:1013–1022
5. Koňáková D, Čáchová M, Vejmelková E, Keppert M, Jerman M, Bayer P, Rov-naníková P, Černý R (2017) Lime-based plasters with combined expanded clay-silica aggregate: microstructure, texture and engineering properties. Cement Concrete Compos 83:374–383
6. Zhang M, Qian Z, Zhou Y, Liu Y (2018) Test and evaluation for effects of aggregates fragmentation on performance of lightweight asphalt concrete. Constr Build Mater 169:215–222
7. Karagöl F, Yegin Y, Polat R, Benli A, Demirboğa R (2018) The influence of lightweight aggregate, freezing–thawing procedure and air entraining agent on freezing–thawing dam-age. Struct Concr 19(5):1328–1340
8. Aashto M (2001) Standard specification for Superpave volumetric mix design. American Association of State Highway and Transportation Officials
9. perHAbbe (2018) Expanded glass, technical information. http://www.perhabbe.com/Teknik-Bilgiler%2Cs11.html. Last accessed 2018/05/31

Determination of Safety Distance of Twin Tunnel Underpassing Existing Tunnels

Helin Fu, Pengtao An, Zhen Huang, Jiabing Zhang, Yue Shi and Guojing Yao

Abstract New tunnel underpassing the existing tunnel construction forms a complex stress-coupling zone above it, causing uneven settlement. In order to ensure the safety of existing tunnels, it is necessary to determine the minimum safe construction distance for tunnels that pass through existing tunnels. Based on this, the FLAC^{3D} finite difference method is used to construct a three-dimensional numerical model of the new tunnel that is orthogonal to the existing tunnel. The effect of different surrounding rock conditions on the settlement of the existing tunnel structure is discussed. Effect of different surrounding rock conditions on the settlement of the existing tunnel structure is discussed. It is determined that the new tunnel underpass different surrounding rock conditions. There is a minimum safe construction distance for the tunnel. On this basis, the effect of grouting reinforcement on the settlement of existing tunnels under the soft and broken surrounding rock is given. The results of the study can be used to determine the safety distance for the construction of a similarly built tunnel that is orthogonal to the existing tunnel.

Keywords Tunnel engineering · Orthogonal underpass · Safety distance · Numerical simulation

1 Introduction

With the rapid development of China's transportation industry, more and more subway projects have been put into construction, and the construction of existing tunnels has become an unavoidable problem. The construction of a new tunnel that

H. Fu · P. An (✉) · Z. Huang · J. Zhang · Y. Shi · G. Yao
School of Civil Engineering, Central South University, Changsha 410075, Hunan, China
e-mail: apengtao@csu.edu.cn

H. Fu · P. An · Z. Huang · J. Zhang · Y. Shi · G. Yao
National Engineering Laboratory for Construction Technology of High-Speed Railway,
Central South University, Changsha 410075, Hunan, China

passes through an existing tunnel at a short distance will form a complex stress-coupling zone and cause uneven settlement of the ground, creating a large potential safety hazard for the existing tunnel. For the existing tunnel under construction, many researchers have carried out a lot of research work. For example, Ren et al. [1] combined with an example of a subway tunnel in Guangzhou to study the deformation characteristics of the surface and found that the loss of the stratum during the tunneling of a double-hole parallel tunnel was the main cause of surface subsidence. Zhang et al. [2] took a new subway tunnel vertically below the tunnel of Suzhou subway Line 1 as an example and proposed that the distance between the new tunnel to cross the existing tunnel should be greater than 0.8 times the diameter of the newly built tunnel. Zhang et al. [3] described the interaction of the newly built tunnel-soil-existing tunnel by combining the principle of the stratum method with the principle of the mirror image method.

Wei et al. [4] based on the winker elastic foundation beam model, considering the pipe–soil effect, established the relation between continuous pipeline strain and ground settlement. Lai et al. [5] comprehensively considers the coupling effect of the former tunnel, soil, and underpassing tunnels, and divides the affected area during the construction of double tunnels into weak, strong, and non-affected areas. Hu et al. [6] used FLAC^{3D} to simulate the process of tunnel shield excavation, and analyzed the changes of structural stress and strain during the process of tunnel excavation. Wang et al. [7] collected 23 sets of data from ten close-to-underground projects in Beijing and found that most of them conformed to the Peck formula above, it can be seen that domestic and foreign experts and scholars have already conducted relatively extensive research on this, but all of them are based on the surrounding rock conditions of fixed projects, and the conclusions are limited in promotion. In order to further improve the existing research deficiencies, this paper proposes a theoretical derivation combined with FLAC^{3D} numerical analysis software and recommends the safe construction distances for different surrounding rock conditions and grouting reinforcement for weak and broken surrounding rock. The study is intended for design and construction reference.

2   Theoretical Calculation of Safe Construction Distance

The prediction methods for settlement caused by tunnel construction include the stochastic medium method, empirical method, numerical analysis method, and physical model method. The Peck formula is a representative of the empirical method and is the most widely used. The classic Peck formula states that the surface sedimentation is in a normal distribution and its expression is:

$$S_{(x)} = \frac{V_l}{\sqrt{2\pi}i} e^{\frac{-x^2}{2i^2}} \tag{1}$$

$$i = \frac{H}{\sqrt{2\pi}\tan\left(45° - \frac{\theta}{2}\right)} \tag{2}$$

In Eqs. (1) and (2), Sx is the distance between the cross section and the axis; x is the settlement of the ground point; i is the width coefficient of the settlement trough, which represents the horizontal distance between the anti-rebound point and the origin of the ground settlement curve; H is the thickness of the cover soil from the center point of the tunnel; θ is the weighted average of the friction angle within the soil; and V_l is the loss of the amount caused by tunnel excavation.

Ren et al. [8] thought that the effect of two tunnel excavations on surface settlement is more complicated than that of a single tunnel, but considering that excavation will disturb the surrounding rock and soil and form disturbance areas, and the second tunnel is often lagging construction; therefore. the resulting settlement of the surface soil can be approximated as a superposition of the separate construction of the two tunnels. Assume that the distance between the center of the new tunnel is d, the connection line is the x-axis, the middle point is the origin of the coordinate, and the vertical direction is the y-axis. The settlement trough is shown in Fig. (1), and the double-hole excavation Peck formula is:

$$S_{(x)} = \frac{v_l}{\sqrt{2\pi}i} e^{\frac{-\left(x - \frac{d}{2}\right)^2}{2i^2}} + \frac{v_l}{\sqrt{2\pi}i} e^{\frac{-\left(x + \frac{d}{2}\right)^2}{2i^2}} \tag{3}$$

The derivation of formula (3) gives (4):

$$s'(x) = \frac{-v_l}{\sqrt{2\pi}i}\left(\frac{x - \frac{d}{2}}{i^2}e^{\frac{-\left(x - \frac{d}{2}\right)^2}{2i^2}} + \frac{x + \frac{d}{2}}{i^2}e^{\frac{-\left(x + \frac{d}{2}\right)^2}{2i^2}}\right) \tag{4}$$

Use Matlab tool to solve Eq. (4), get $x_1 = 0$, $x_2 = -\frac{d - d \times e^{\frac{d}{2 \times i^2}}}{2 \times e^{\frac{d}{2 \times i^2}} + 1}$, $x_3 = \frac{d - d \times e^{\frac{d}{2 \times i^2}}}{2 \times e^{\frac{d}{2 \times i^2}} + 1}$.

Fig. 1 Twin tunnel excavation stratum sedimentation trough
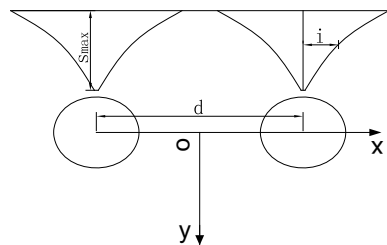
It is known that the settlement at the origin, $x_{(2)}$, and $x_{(3)}$ is extreme value, so the settlement value is less than the control settlement at three, and the maximum settlement is less than the control settlement.

The settlement of the original point O is as follows:

$$s_{(0)} = \frac{2 \times v_l}{\sqrt{2\pi}i} e^{\frac{-d^2}{8i^2}} \tag{5}$$

$s_{(0)} = s_{\text{control}}$, obtained:

$$i_{\text{limit0}} = \frac{v_1 \times e^{\left(\frac{\text{lambertw}\left(0, -(d \times s_{\text{control}})^2\right)}{5.1 \times v_1^2}\right)}}{1.25 \times s_{\text{control}}} \tag{6}$$

Lambertw is the Lambert function. At this time,

$$H_{\text{limit0}} = i_{\text{limit0}} \times \sqrt{2\pi} \times \tan\left(45° - \frac{\theta}{2}\right) \tag{7}$$

Obviously, $x_{(2)}$ is the same as the settlement at $x_{(3)}$, only considering the settlement at $x_{(3)}$. Assuming that $s_{(3)} = t$.

t is substituted into the formula (3), assuming that the settlement is s_{control}.

$$v_l = \frac{2.5i \times s_{\text{control}}}{e^{\left(\frac{-\left(0.5d + \frac{(d \times (t-1))}{2t+1}\right)^2}{2i^2}\right)} + e^{\left(\frac{-\left(\frac{0.5d - (d \times (t-1))}{2t+1}\right)^2}{2i^2}\right)}} \tag{8}$$

By the iterative method, the H_{3limit} can be obtained approximately. Therefore, the minimum safe distance, $H_{\text{limit}} = \max\{H_{\text{0limit}} \text{ and } H_{\text{3limit}}\}$.

3 Numerical Simulation

3.1 Dimensions and Boundary Conditions

Both the existing and new tunnels are twin shield tunnels with a diameter of 5.2 m, a horizontal distance of 13.2 m from the center of the double hole, and an existing depth of 15.6 m. In order to eliminate the influence of the boundary effect, the model is 99.6 m along the axial direction of the existing tunnel, 99.6 m along the axial direction of the new tunnel, and 45.6 m high. The thickness of the segment is 0.4 m, and the width of each segment is 1.2 m. All boundary conditions are displacement boundary conditions, where the fixed boundary constraint is applied to the surrounding and bottom surfaces of the model, and the upper surface is a free boundary. The completion time of the existing tunnel construction is relatively
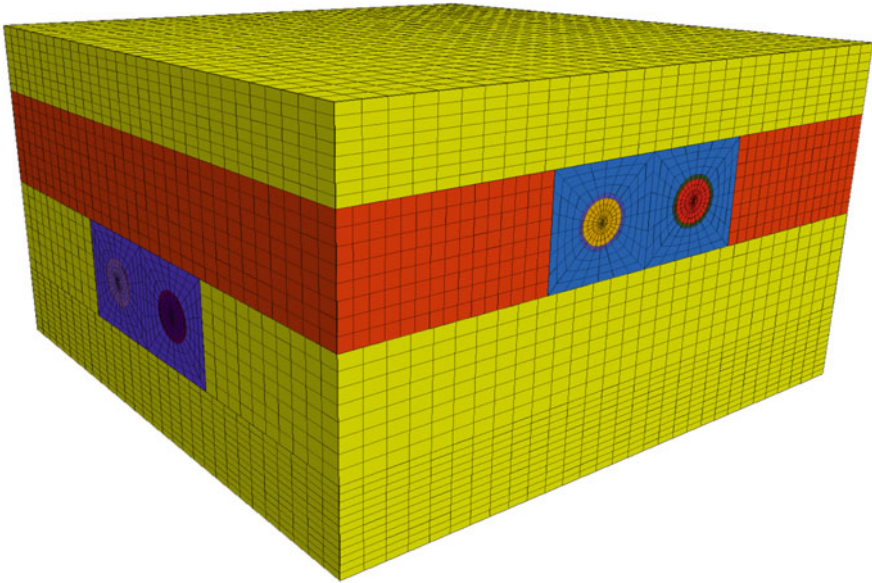
Fig. 2 Numerical model

early. The disturbed soil body has completed the consolidation of the main consolidation before the excavation of the newly built tunnel. Therefore, the settlement of the ground is cleared before the settlement caused by the construction of the new tunnel. The model is shown in Fig. 2. As shown.

3.2 Simulation Conditions

The surrounding rock types III, IV, and V were simulated separately, in which the parameters of the IV surrounding rock were discrete and divided into three sub-levels.

3.3 Model Parameters

The constitutive relation adopts the Mohr–Coulomb yield criterion, and the surrounding rock parameters are valued according to the road tunnel design specification [9], as shown in Table 1, in which the tunnel segment is C_{50} reinforced concrete.

Table 1 Standard values of physical and mechanical indexes of surrounding rock at all levels

Surrounding rock level	Heavy (kn/m^3)	Modulus of elasticity (GPa)	μ	Friction	Cohesion (MPa)
III	24	13	0.28	44.5	1.1
IV$_1$	22.5	4.83	0.31	36	0.55
IV$_2$	21.5	3.65	0.33	33	0.4
IV$_3$	20.5	2.48	0.34	30	0.3
V	18.5	1.5	0.4	23.5	0.13

Table 2 Surrounding rock conditions and formation loss rate

Surrounding rock	Formation loss (m^3)	Formation loss rate (%)
III	3.82×10^{-2}	0.14
IV$_1$	4.25×10^{-2}	0.15
IV$_2$	12.4×10^{-2}	0.44
IV$_3$	70.9×10^{-2}	2.5
V	154.3×10^{-2}	5.4

4 Results and Analysis

According to experience, a safety distance is presupposed and FLAC^{3D} calculation software is used to model and calculate. Based on the calculation results, the Stratum loss value is pushed back. The paper [10] uses the interval of the Fangzhuang–Shilihe station on Line 14 of the Beijing subway as a background and combines the Peck formula to fit the deep-displacement curve of the stratum. The results show that the deep-displacement curve of the stratigraphy conforms to the normal distribution of the Peck formula, and the stratum loss rate is basically unchanged in different depths. Based on this research conclusion, it is assumed that the net spacing is independent of the loss rate of the formation. At the same time, according to the Shanghai Metro code, the minimum safe construction distance is obtained by taking the maximum settlement 5 mm of 5 mm of the existing tunnel as the control standard. The loss rate of strata under various surrounding rock conditions is shown in Table 2.

Table 2 results are replaced by the formula Eq. (1) to get the relationship between the surrounding rock level and the existing tunnel settlement, as shown in Fig. 3.

The $d = 13.2$ m and $s_{\text{control}} = 5$ mm are substituted into formula (6), Eqs. (7), and (8) ; the relationship between i_{limit} and surrounding rock grade is shown in Table 3.

Table (3) results are replaced by the formula (2), and the safe distance between the surrounding rock level and the orthogonal safety is shown in Fig. 4.

Fig. 3 Relationship between surrounding rock level and existing tunnel settlement
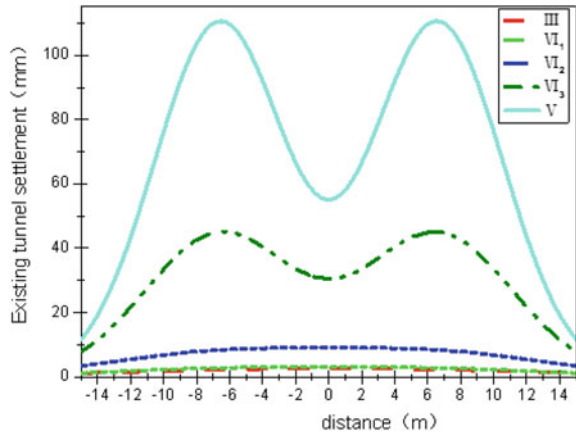
Table 3 Relationship between surrounding rock level and i_{limit}

Surrounding rocks	$i_{control0}$ (m)	$i_{control3}$ (m)	$i_{control}$ (m)
III	3.38	2.04	3.38
IV_1	4.22	2.12	4.22
IV_2	18.7	18.81	18.8
IV_3	113.2	113.3	113.3
V	246.8	246.8	246.8

Fig. 4 Relationship between surrounding rock level and orthogonal underpass safety distance
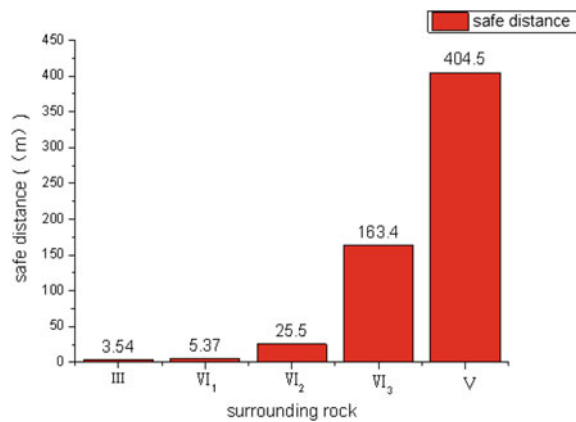
The settlement trough of the existing tunnel is not only related to the distance between the center of the new tunnel but also to the surrounding rock. When the surrounding rock conditions are poor, the internal friction angle is smaller. It is known by the formula (2) that the coefficient of the settlement trough caused by the single-line tunnel excavation is less, and the weak coupling of twin tunnel

excavation, so it is generally a double-peak curve. As we can see from Fig. 3, when the surrounding rock of grade is III, IV_1 and IV_2, the existing tunnel will settle into a flat "V" type, and the tunnel in the surrounding rock of IV_3 and V has formed a "W" type.

From Fig. 4, we can see that when the surrounding rock conditions are IV_2, IV_3, and V, the safety distance for orthogonal underpass is larger, especially when the IV_3 and V safety distance exceeds 150 m, and measures need to be taken to control the safety distance.

5 Grouting Reinforcement

In order to reduce the orthogonal safety distance, certain measures must be taken to ensure the safety of the structure. Grouting reinforcement is a widely used method. For example, Liu et al. [10] took the Beijing subway as the research object and compared the effect of shield tunnel construction under existing reinforcement schemes on the existing tunnels. Chen [11] took the subway of Beijing Exhibition Center West Road under the subway line 4 as the background. Under the premise of considering grouting measures, the minimum safety distance of the overlapping tunnel was recommended to be 4 m. Wan et al. [12] conducted numerical simulation analysis on the effect of different reinforcement measures when using the CRD method on the deformation of existing stations and rails, and determined the grouting reinforcement parameters and the strata reinforcement range and reinforcement length during construction. Ling et al. [13] showed that the optimized grouting reinforcement scheme can effectively control the surface settlement. Li [14] combined with an existing tunnel engineering example under a subway shield tunnel, analyzed the effectiveness of grouting reinforcement in the control of surrounding rock settlement of the existing tunnel under shield construction. Shen [15] took measures to improve the settlement of the existing subway tunnel structure by means of reinforcement measures after the segment wall. Huang [16] used deep-hole grouting and small-pipe grouting under the existing subway station to reinforce the soil and control surface settlement.

In this paper, the safety distance of grade IV_2, IV_3, V, and V is fixed to 4 m, and the value of surrounding rock parameters after grouting is given by numerical simulation. The grouting reinforcement range is from the bottom of the existing tunnel to the bottom of the new tunnel, and the other two directions are 10 times the new tunnel diameter.

The relationship between the surrounding rock parameters after grouting and the existing tunnel settlement is shown in Fig. 5.

As shown in Fig. 5, when the cohesion is less than 0.55mpa, the three curves are different, that is, the surrounding rock level has a greater impact on the settlement of the existing tunnel; when the cohesion is greater than 0.55mpa, the three curves are basically overlapped, and the surrounding rock level has no effect on the settlement of the existing tunnel. According to the parameters taken by $FLAC^{3D}$, when the

Fig. 5 Cohesion and settlement of existing tunnels
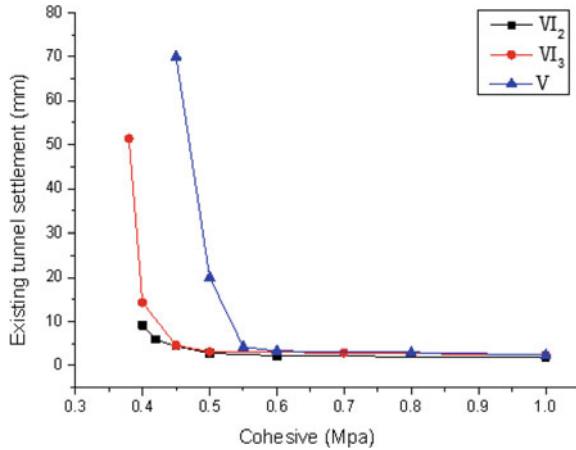
cohesive force is greater than 0.55mpa, the elastic modulus, internal friction angle, and Poisson ratio have great influence on the settlement of existing tunnels.

According to Fig. 5, it is more suitable to raise the cohesiveness of the IV_2 surrounding rock to 0.45–0.5 MPa, the IV_3 surrounding rock to raise the cohesion to 0.5 MPa, and the V surrounding rock to raise the cohesion to 0.55–0.6 MPa. According to Fig. 5, it is more suitable to raise the cohesiveness of the IV_2 surrounding rock from 0.45 to 0.5 MPa, the IV_3 surrounding rock to 0.5 MPa, and the V surrounding rock from 0.55 to 0.6 MPa.

6 Conclusion

(1) The settlement shape of the existing tunnel is related to the grade of the surrounding rock. When the distance between the centers of the new tunnel is 13.2 m and the tunnel diameter is 5.2 m, the tunnel settlement is a flat single-peak curve when the surrounding rock of III, IV_1, and IV_2, and the settlement of the tunnel in the surrounding rock of IV_3 and V is the double-peak curve.

(2) The theoretical calculation formula for the safety distance of the twin orthogonal tunnel through existing tunnels is deduced. Based on the formula and numerical simulation, it is suggested that the minimum distance of III surrounding rock is 4 m, the IV_1 surrounding rock is 6 m, and IV_2 is 26 m.

(3) Taking into account the economic and security, IV_2, IV_3, and V surrounding rock are used to penetrate the existing tunnel and the safety distance is 4 m. The cohesion must be increased to 0.48mpa, 0.5 MPa, and 0.6 MPa, respectively.

References

1. Ren Q, Yang C, Xu W (2013) The peck formula and numerical analysis of surface subsidence caused by tunnel excavation. J Anhui Univ Sci Technol Nat Sci 33(04):78–82
2. Zhang H, He P, Qin D, Lu L (2013) The influence of new shield tunneling on the existing tunnel. China Railw Sci 34(02):66–70
3. Wang J, Liu Y, Zhang DL, Bai H, Du N (2016) The displacement solution of existing tunnel and ground by traversing construction. Undergr Space Eng J 12(S2):678–683
4. Wei G, Lin X, Jin R, Ding Z (2018) Security discrimination of adjacent underground pipelines during the construction of twin shield tunnels. Rock Soil Mech 39(01):181–190
5. Lai H, Zhao X, Kang Z et al (2017) A new method for predicting ground settlement caused by twin-tunneling under-crossing an existing tunnel. Environ Earth Sci 76(21):726
6. Hu Z, Shao X, Yao H et al (2016) Mechanics analysis of shield construction traversing adjacently under existing urban tunnel. J Sichuan Univ
7. Wang J, Zhang D, Zhang C, Fang Q, Su J, Du N (2014) Deformation characteristics of existing tunnels induced by excavation of new shallow tunnel in Beijing. Chin J Rock Mech Eng 33(05):947–956
8. Chongqing Transportation Research and Design Institute (2004) Industry standards of the People's Republic of China JTG D70–2004: specification for highway tunnel design. China Communications Press
9. Zhang J, Jiang H, Cheng JG, Zhou LG, Qu XT, Jiao XF (2017) Variation law of volume loss rate induced by shield tunnelling. Urban Rapid Rail Transit 30(06):56–61
10. Bo L, Peige H, Siran Z et al (2014) Disturbing effect of shield tunnel down-traversing nearby existing metro tunnel. In: 7th international conference on intelligent computation technology and automation (ICICTA 2014), 25–26 Oct 2014
11. Chen J (2009) Study on the safety distance of shield tunnels passing through existing subway tunnels. Railw Stand Des 10:45–48
12. Wan L, Song Z, Qu J, Song Y (2015) Construction technology analysis of the new subway tunnel "zero distance" crossing the existing station. Mod Tunnel Technol 52(01):168–176 +183
13. Ling T, Zhang S, Li S, Deng J (2014) Controlling of existing bridge piles deformation induced by adjacent tunneling and scheme of optimizing grouting reinforcement. J Cent South Univ (Nat Sci) 45(07):2394–2400
14. Li J (2012) Study on the influence of undercrossed subway shield tunnel on the existing tunnel. Xi'an University of Science and Technology
15. Gang S (2016) Study on the mutual influence mechanism of shield tunneling under existing subway tunnels. Shenzhen University (2016)
16. Huang H (2013) Settlement prediction and reinforcement measures for a metro tunnel passing under an existing metro station. Mod Tunnel Technol 50(2):114–118

Analysis of the Mechanical Response of Asphalt Pavement with Different Types of Base

Hui Wang and Xinyu Dong

Abstract Paper calculates the different mechanical distribution characteristics of asphalt pavement with three different base structures: pure flexible base, inverted base and semi-rigid base using shell pavement mechanics software BISAR, then processes the calculations into three-dimensional visualization with MATLAB 7.0 to comparatively analyze the laws of mechanical response. Research shows that pure flexible base pavement will not appear structurally damage from bottom to top. For inverted base structure, the bottom of the graded crushed stone layer is still the weak area of structural stress. Semi-rigid base asphalt pavement has high overall stiffness, so it is necessary to deal with the high bending tension stress at the bottom of the base layer to prevent the fatigue cracking of the base. From the view of the whole strengthen, asphalt pavement with pure flexible base or inverted base has larger mechanical advantages.

Keywords Road engineering · Asphalt pavement · Pure flexible base · Inverted base · Semi-rigid base · Mechanical response

1 Introduction

Cracking of semi-rigid base asphalt pavement is the main disease of semi-rigid asphalt pavement, and it is an important reason for the early disease of expressway asphalt pavement, which further leads to structural damage of pavement and makes

H. Wang (✉) · X. Dong
College of Traffic and Transportation Engineering,
Changsha University of Science and Technology, Changsha 410004, China
e-mail: wh.cs.cn@163.com

National Engineering Laboratory of Highway Maintenance Technology,
Changsha University of Science and Technology, Changsha 410004, China

the maintenance more difficult. Therefore, the flexible base asphalt pavement and inverted structure asphalt pavement have gradually become a necessary supplement for the form of semi-rigid base asphalt pavement in China with their excellent mechanical properties. It is gradually applied to the engineering practice, and it will also be an important trend in the diversified development of high-grade expressway pavement structure in the future of China [1–5]. Based on the project of the Xinhuahou test road in Changsha, Hunan, the paper selects three typical asphalt pavement structures including the pure flexible base, inverted base structure, and semi-rigid base as the research object. Comprehensive mechanical calculations were carried on with shell pavement mechanics software BISAR. In order to provide a more accurate and more reliable reference for the design of different base asphalt pavement and scheme comparison, this study processes the calculations into three-dimensional visualization with MATLAB 7.0 to comparatively analyze the laws of mechanical response.

2 Asphalt Pavement Structures and Calculation Model

2.1 Three Pavement Structure Schemes and Material Parameters

The three types of asphalt pavement structures analyzed in this study include pure flexible base asphalt pavement (scheme 1), inverted base asphalt pavement (scheme 2), and semi-rigid asphalt pavement (scheme 3). The three types of asphalt pavement structure and material parameters are shown in Tables 1, 2, and 3.

Table 1 Structural and material parameters of pure flexible base asphalt pavement

Layers	Thickness (cm)	Compression resilience modulus (20 °C, MPa)	Compression resilience modulus (15 °C, MPa)	Poisson ratio
AC-13	4	1400	2200	0.25
AC-20C	6	1200	1800	0.25
AC-25C	7	1000	1200	0.25
LSM-30	9	1000	1200	0.25
Graded crushed stone base	20	300	300	0.25
Graded crushed stone base	20	300	300	0.25
Non-screening crushed rock cushion	15	180	180	0.25
Subgrade		35	35	0.35

Table 2 Structural and material parameters of inverted base asphalt pavement

Layers	Thickness (cm)	Compression resilience modulus (20 °C, MPa)	Compression resilience modulus (15 °C, MPa)	Poisson ratio
AC-13	4	1400	2200	0.25
AC-20C	6	1200	1800	0.25
LSM-30	12	1000	1200	0.25
Graded crushed stone base	12	300	300	0.25
Cement stabilized gravel base	30	1300	3600	0.25
Non-screening gravel cushion	15	150	150	0.25
Subgrade		35	35	0.35

Table 3 Structural and material parameters of semi-rigid base asphalt pavement

Layers	Thickness (cm)	Compression resilience modulus (20 °C, MPa)	Compression resilience modulus (15 °C, MPa)	Poisson ratio
AC-13	4	1400	2200	0.25
AC-20C	6	1200	1800	0.25
AC-25C	7	1000	1200	0.25
Cement stabilized gravel base	20	1300	3600	0.25
Cement stabilized gravel subbase	20	1100	3000	0.25
Non-screening gravel cushion	15	150	150	0.25
Subgrade		35	35	0.35

2.2 Calculation Software and Calculation Schema

The paper carries the mechanical analysis of pavement structure with shell pavement mechanics software BISAR and formulates a complete continuous contact condition between layers. The following conditions were used: (1) the calculated load is a double circle loading (BZZ-100 kN); (2) contact pressure is 0.7 MPa; (3) the radius of wheel pressure is 10.65 cm; (4) the center distance of double circles is 15.975 cm. Calculated load is shown as Fig. 1. MATLAB 7.0 software is applied to carry out three-dimensional spatial processing of the calculation results by BISAR software.
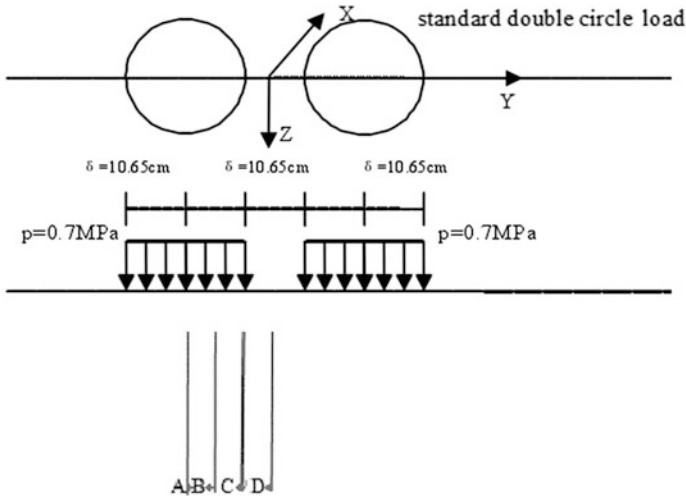
Fig. 1 Loading type

3 Analysis of the Calculation of Mechanical Response

3.1 Maximum Tensile Strain of Surface Layers

The maximum tensile strain of each scheme is summarized in Tables 4 and Fig. 2.

The calculations in Table 4 and Fig. 2 show that the pure flexible base and inverted base with graded crushed stone layer are showing a relatively large tensile strain in the surface layer. The main reason is that graded crushed stone is a granular material with poor deformation resistance, which cannot transfer stress and strain. It will generate a large tensile strain of structure. However, the graded crushed stone base does not significantly produce drying shrinkage and temperature shrinkage cracking, unlike the semi-rigid base. Graded crushed stone base can ensure that the pavement does not generate structural damage from bottom to top. It is also one of

Table 4 Calculations of maximum tensile strains in the surface layers of the three schemes

Pavement types	Maximum tensile strain of surface layer	
	Value ($\mu\varepsilon$)	Location
Scheme 1	146.7	The bottom of the asphalt layer at the distance of 0.3R from the center of the interspace of double circle load
Scheme 2	129.4	The bottom of the asphalt layer at the distance of 0.6R from the center of the interspace of double circle load
Scheme 3	52.6	The center of single circle load, the bottom of the middle-surface layer
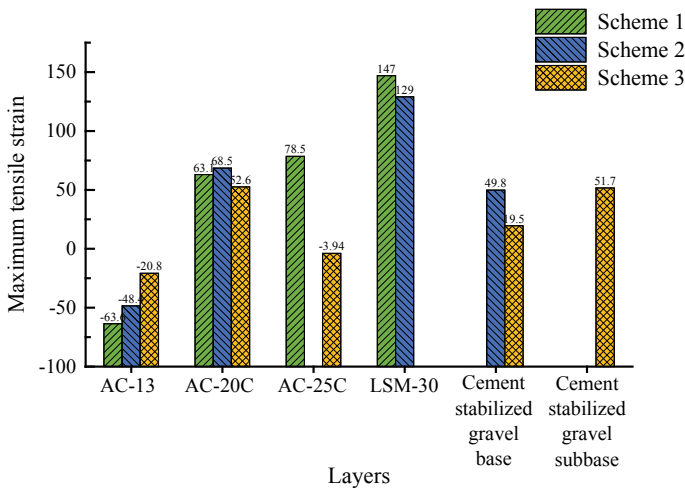
Fig. 2 Calculations of maximum tensile strain in the bottom of each surface layer

the insurmountable advantages of the flexible base asphalt pavement that is superior to the semi-rigid asphalt pavement. Although the tensile strain of the surface layer of semi-rigid base asphalt pavement is lower than other schemes. On the view of the whole structure, the maximum tensile strain of the semi-rigid pavement appears at the bottom of the cushion course. That means the bottom part of the semi-rigid base has a higher tensile strain. However, the high tensile strain section of the asphalt pavement with flexible base or inverted base appears in their surface layer. So it is obvious that the fatigue crack caused by strain will come from the surface rather than the base layer. The three-dimensional distribution of the tensile strain in the road transverse section and driving direction of each scheme are shown in Figs. 3, 4, 5, 6, 7, and 8.

As shown in Figs. 3, 4, and 5, the tensile strain distributions of each scheme are generally similar, while the undulating degree of the surface is slightly different. Specifically, from the top to the bottom, the layer structure is transferred from compression to tension with the increase of depth. The tensile strain has a positive correlation with depth and reaches the peak of strain at the bottom of the asphalt layer (schemes 1 and 2), or at the bottom of the middle-surface layer (scheme 3). Then, the strain drops sharply at the base course, and a distinct turning point appears at the border of the surface layer and base course. This is principally because the stress dissipated gradually with depth. It shows that the middle of the surface layer is mainly the layer bearing high strain. Within the depth of the base course, strain increases with increased depth, and the rise of strain has been slowed down at the bottom of the base course. The structural strain of scheme three reaches a peak at the bottom of the base layer.

Figures 6, 7, and 8 reflect the plane projection of the tensile strain of each pavement structure in the direction of the road transverse section and longitudinal
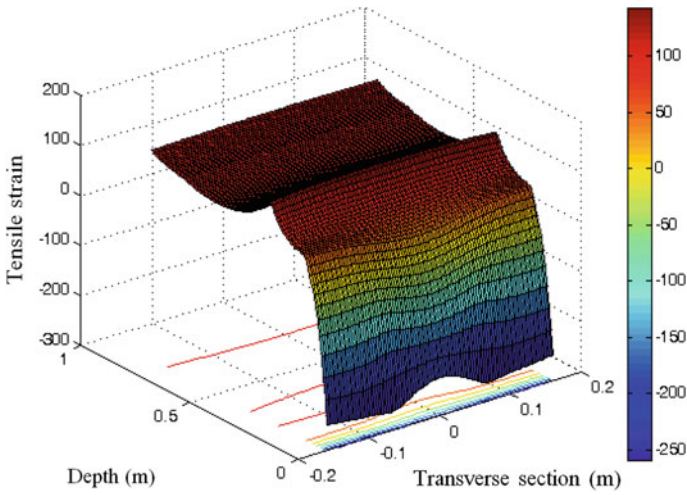
Fig. 3 3D distribution of tensile strain of scheme 1
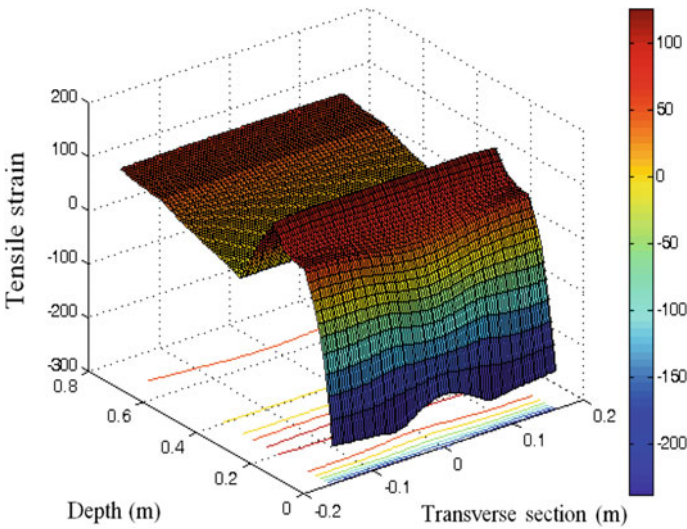
Fig. 4 3D distribution of tensile strain of scheme 2

section. The values in the diagram represent the tensile strain of the pavement structure at different transverse section and depth. It is found that under the same equal fraction, the strain level of scheme 1 and scheme 2 in the upper part of the pavement structure is significantly higher than the other three structures. This situation is consistent with the actual level of the whole tensile strain of the schemes.
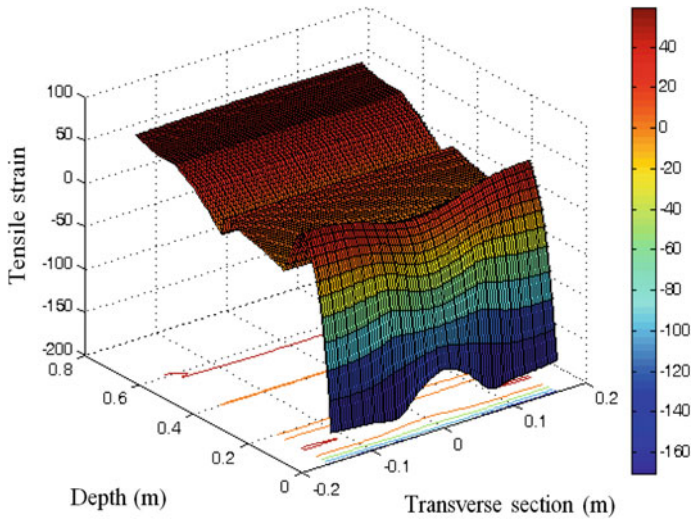
Fig. 5 3D distribution of tensile strain of scheme 3
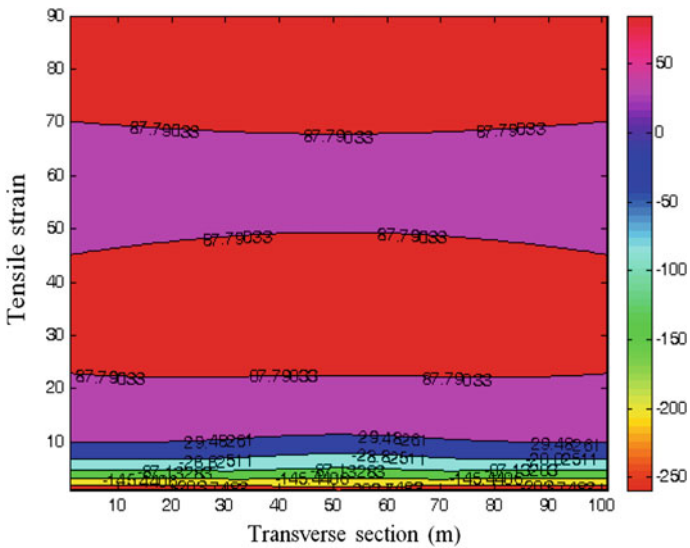
Fig. 6 Isoclines of a tensile strain of scheme 1
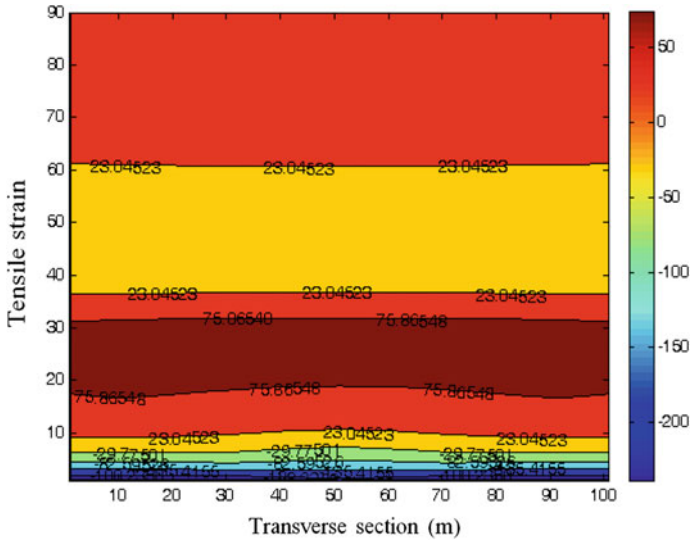
Fig. 7 Isoclines of a tensile strain of scheme 2
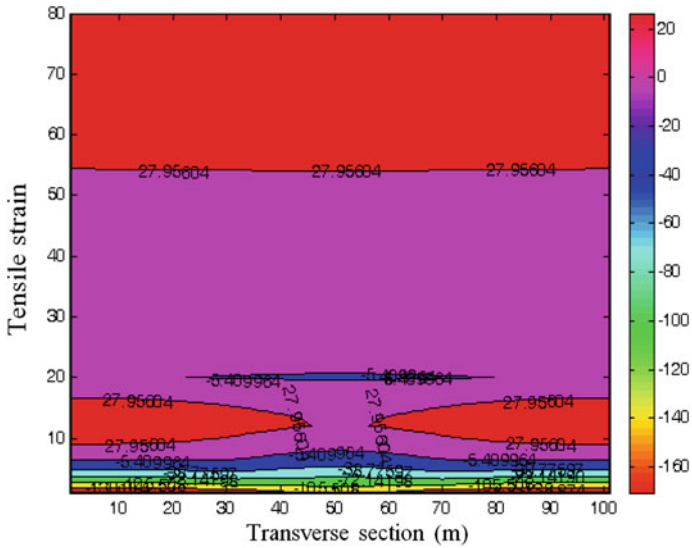
Fig. 8 Isoclines of a tensile strain of scheme 3

Table 5 Calculations of maximum tensile stress of each pavement structure

Pavement type	Maximum tensile strain of pavement structure	
	Value (MPa)	Position
Scheme 1	0.1797	The bottom of the asphalt layer at the distance of 0.9R from the center of the interspace of double circle load
Scheme 2	0.1810	The bottom of the upper-base at the center of the interspace of double circle load
Scheme 3	0.1990	The bottom of the base course at the center of the interspace of double circle load

3.2 Maximum Tensile Stress of Pavement Structure

A summary of the maximum tensile stress of each pavement structure is presented in Table 5.

Table 5 shows the maximum tensile stress of a pure flexible structure with graded crushed stone base which occurs at the bottom of the surface layer, while all others occur at the middle of the base course or at the bottom of the base course. The calculations verified the great advantages of flexible base asphalt pavement. The failure mode of flexible base asphalt pavement is from top to bottom. So the structural pavement damage is difficult to occur. It can maintain better performance in the life cycle. For scheme 2, with graded crushed stone as a transition layer, it bears higher tensile stress at the bottom of the graded crushed stone layer. This could be due to the huge differences in material properties and stiffness between graded crushed stone layers and stabilized cemented gravel base. That also means the interface is the weak layer of the pavement structure. The interfacial bonding between layers should be emphasized in construction to better realize the goal of blocking the reflection crack upward. Figure 9 shows that the maximum tensile stress at the bottom of each structural layer of the three schemes is also consistent with the rule that the upper part of pavement structure bears compression and the lower part bears tension. It can basically reflect the stress level of different types of base structures in different sections. Specifically, for schemes 1 and 2, the peak of tensile stress is concentrated near the large grain size asphalt stabilized macadam layer. However, for scheme 3, the peak of tensile stress appears at the base course. Three-dimensional distribution of the tensile stress in road transverse section and driving direction of each scheme are shown in Figs. 10, 11, and 12.

It is shown from Figs. 10, 11, and 12, the distribution curve of tensile stress along the transverse section and depth of the road is relatively gentle compared to the distribution of tensile strain. For each scheme, the change from compression to tension is gradually realized from the surface layer to the base course, and the compressive stress is only distributed in a certain depth under the road surface. From the transverse section of the road, high stress is mainly distributed in the
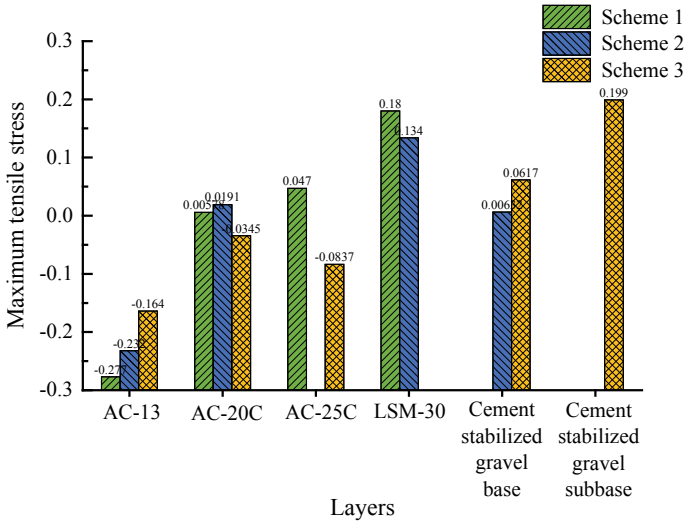
Fig. 9 Calculations of maximum tensile stress at the bottom of each layer of the three schemes
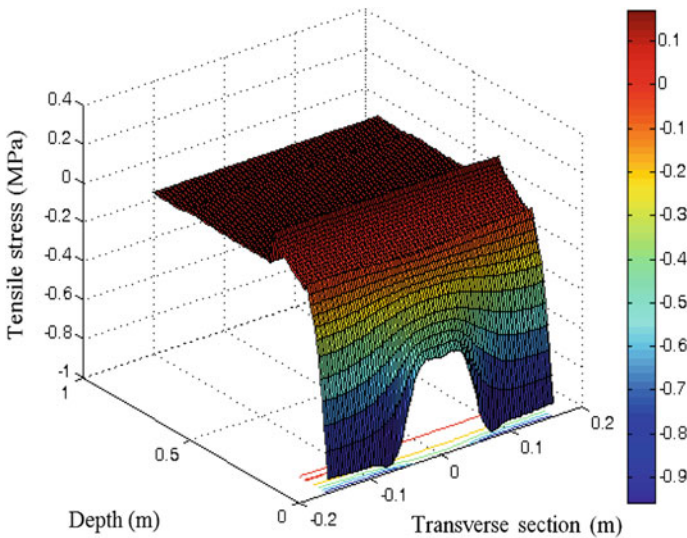
Fig. 10 3D distribution of tensile stress of scheme 1

range of the wheel load radius that accords with practicality. When stress in the structure is transferred to tensile stress, it demonstrates a trend that the value increases along the depth of the road surface. Owing to the graded crushed rock layer, the tensile stress of schemes 1 and 2 will be mutated at the border of the
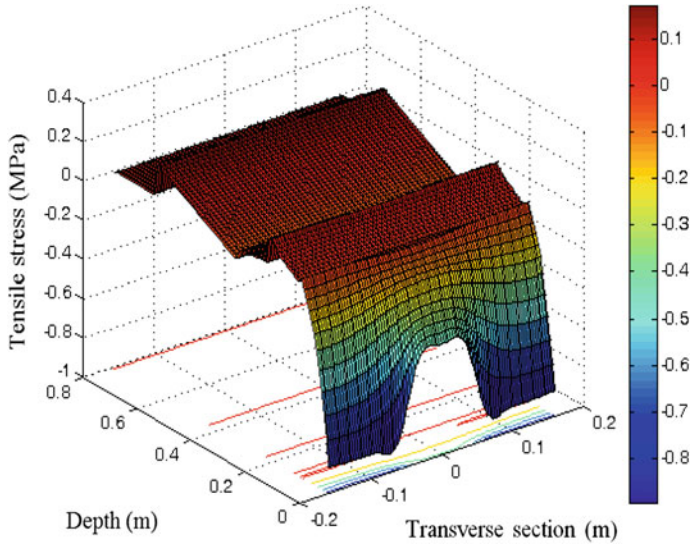
Fig. 11 3D distribution of tensile stress of scheme 2
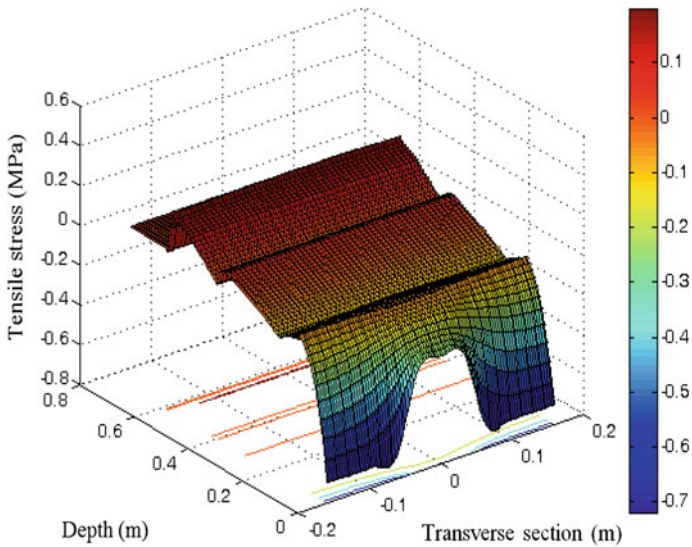
Fig. 12 3D distribution of tensile stress of scheme 3

surface layer and base course or at the bottom of the upper-base. The tensile stress of scheme 3 reaches a peak at the bottom of the base course, then the stress decreases sharply and the surface in Fig. 12 is smooth.

Table 6 Calculations of maximum shear stress in the surface layers of the three pavement structures

| Pavement type | Maximum shear stress of surface layer | |
	Value (MPa)	Position
Scheme 1	0.264	Pavement surface, at the distance of 0.3R from the center of the interspace of double circle load
Scheme 2	0.248	
Scheme 3	0.236	At the distance of 0.6R from the center of the interspace of double circle load, and 2 cm below the pavement surface

4   Maximum Shear Stress of Surface Layer

The summary of the maximum shear stress of each pavement structure is shown in Table 6.

Table 6 illustrates that the maximum shear stress of a flexible base asphalt pavement is higher than that of a semi-rigid base asphalt pavement, which determines that one of the main failure modes of flexible pavement is a shear failure due to the insufficient shear strength of the surface. However, the shear stress level of semi-rigid pavement is relatively low. The damage of such pavement is mainly due to the fatigue damage caused by the high level of tensile stress at the base course, and the damage is transmitted from bottom to top. Therefore, for flexible pavement, the high shear strength must be considered in the design of upper-surface based on the guarantee of the stress on the top of the surface.

As reflected in Table 6, shear stress of pure flexible base structure (scheme 1) and inverted base structure (scheme 2) reaches a peak on pavement surface. The peak shear stress of a semi-rigid base structure (scheme 3) is located 2 cm away from the pavement surface. This indicates that the small depth range of the pavement surface is the section of peak shear stress for both flexible and semi-rigid pavements. From the direction of the transverse section of the road, 3–6 cm near the center of the interspace of double circle load is the peak shear stress section.

Figures 13, 14, and 15 show the three-dimensional distribution of the shear stress in road transverse section and driving direction. The distribution of shear stress in each scheme is generally similar, and the center of the interspace of double circle load near the road surface bears high shear stress. The farther away from the center, the more the peak shear stress spread to the depth of the upper layer due to the dissipation of stress. It can be seen that the small depth ranges from the pavement to the surface layer is the peak section of shear stress of the flexible base asphalt pavement. Correspondingly, this layer needs to be designed according to the high shear requirements, so as to meet the mechanical requirements. Below the peak section, the shear stress decreases with increased depth. For flexible base pavement, the shear stress decreases sharply at the top of the graded crushed rock layer, and the shear stress also decreases with the increase of depth in the range of the base. Considering hydrological conditions in this area, a cushion is set up in all
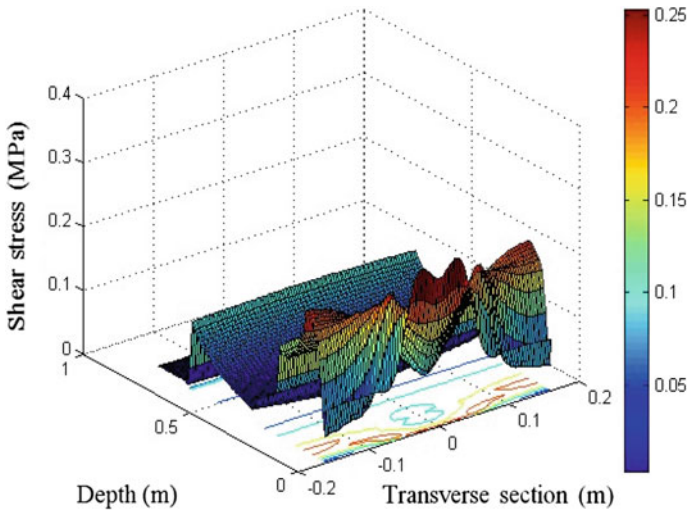
Fig. 13 3D distribution of shear stress of scheme 1
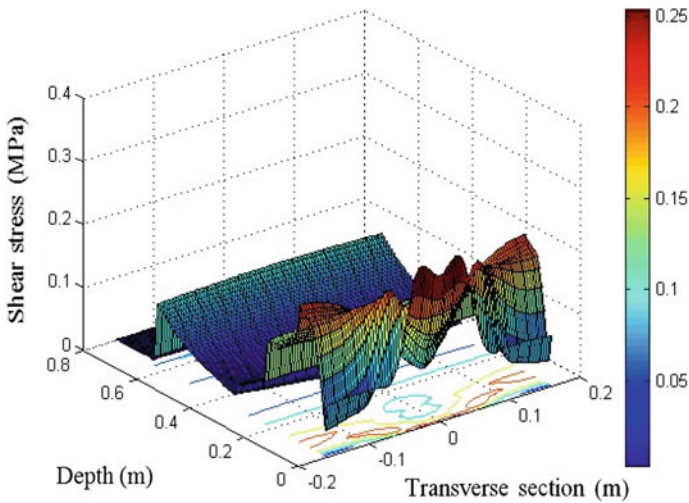
Fig. 14 3D distribution of shear stress of scheme 2

three schemes. Calculation shows that shear stress drops to a lower level at the boundary between base and cushion. Therefore, the main shear stress of the flexible pavement is undertaken by the small range depth of the surface layer. Because of the different characteristics of materials, the shear stress decreased abruptly at the interface between the surface layer and the base course as well as the interface between the base course and cushion.
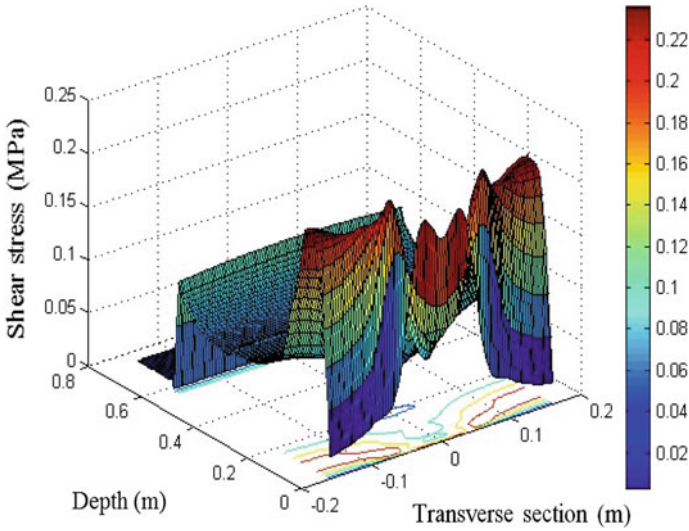
Fig. 15 3D distribution of shear stress of scheme 3

5 Engineering Application

5.1 Deflection Test

In order to further study the application effect of different base asphalt pavement, the three pavement structures were paved on Xinhuahou road according to theoretical analysis in Changsha, 2009. The application effects of those sections of pavement were observed. The Benkelman beam method was used to detect the deflection of the road and the results are shown in Table 7. Scheme 1 is a pure flexible base pavement, which has no superiority in bearing capacity. The pavement surface deflection of scheme 2 is less than scheme 1, and it has stable strength and

Table 7 Summary of deflection test results (0.01 mm)

Indexes	July, 2009			May, 2010		
	Scheme 1	Scheme 2	Scheme 3	Scheme 1	Scheme 2	Scheme 3
Average of deflection $\bar{L}$	20.41	9.28	7.36	22.80	11.90	10.00
Standard deviation of deflection S	3.91	2.35	3.15	4.30	2.87	3.30
Representative value of deflection L_r	26.79	12.76	11.42	29.90	16.60	15.50
Design deflection L_d	41.70	33.90	26.10	41.70	33.90	26.10

small variability. Scheme 3 is a semi-rigid base, which has a relatively large advantage in bearing capacity.

5.2 Roughness Inspection

Roughness is an important index to characterize pavement serviceability. It is directly related to driving comfort. In addition, smoothness can also reflect the occurrence of early damage, such as rutting and pothole. Therefore, in order to reflect the function of the pavement surface of the test road after opening to traffic, the project group has tracked and monitored the roughness of the Xinhuahou test road. The specific results are summarized in Table 8.

It can be seen from Table 8 that the roughness of the Xinhuahou test road can meet the quality requirements of the new pavement. The test road structure still maintains a high level of roughness on the road surface after opening, which can better meet the needs of road traffic. After two years of operation, the surface of the test road still maintains a high level of roughness, which can meet the needs of road traffic.

5.3 Pavement Condition Investigation

In order to investigate the changes in the road conditions of the Xinhuahou test road after two years of operation, the subject group conducted a road survey on the test

Table 8 Summary of roughness test data of the test road

Schemes	Average value of roughness (mm)			
	July, 2009	May, 2010	May, 2011	November, 2011
Scheme 1	0.91	0.98	1.02	1.09
Scheme 2	0.85	0.92	0.98	1.01
Scheme 3	0.84	0.90	0.97	1.03

Table 9 Summary of condition investigation results of the test road

Survey time	Schemes	Diseases
May, 2011	Scheme 1	1 pothole (19.6 cm^2)
	Scheme 2	1 pothole caused by mechanical scraping;
		1 pothole (16.6 cm^2)
November, 2011	Scheme 3	1 longitudinal crack (about 1 m);
		1 longitudinal crack (about 2 m);
		1 transverse crack (about 2 m);
		2 transverse cracks (about 3 m)

road in May 2011 and November 2011. It was found that the overall condition of the test road is good, and there are few early diseases appeared in some sections. The specific results are shown in Table 9.

6 Conclusion

Tensile strain, shear stress, and tensile stress at the surface of a pure flexible structure are relatively high, and the tensile response reaches a peak at the border of the surface layer and base course. That means the interface between the surface and graded crushed rock layer will bear higher tensile stress, and it requires the excellent fatigue strength of the asphalt crushed stone layer. Due to the use of graded crushed stone with small stiffness as the base course, the structural damage of pure flexible structure will not have occurred from bottom to top. The repair and maintenance of flexible base structure are more convenient, and it is a structural form based on the new ideas of foreign countries [6–8].

LSM+ double graded crushed stone transition layer was adopted in an inverted base structure. The structure reaches the peak value of tensile strain at the bottom of the surface layer, and the peak tensile stress appears on the bottom of the upper-base. Meanwhile, the peak shear stress appears on the road surface. It can be seen that the bottom of a graded crushed rock layer is still a weak section of structural stress.

The semi-rigid structure has high integral stiffness. Accordingly, the strain level of the surface layer is relatively low, but the high tensile stress at the bottom of the base course should be paid more attention to prevent the fatigue crack from occurring.

References

1. Zhu H-Z, Tang B, Liu B (2009) Orthogonal analysis on structure design parameters of flexible base asphalt pavement. J Chongqing Jiaotong Univ Nat Sci Ed 28(6):1021–1024
2. Nie Y, Zhang Q (2008) Mechanical analysis and asphalt layer subdivision of long life asphalt pavement (LLAP). J Highw Transp Res Dev 25(5):13–17
3. Hu S, Ren R, Wang S (2003) Non-linear finite element analysis of semi-rigid asphalt concrete pavement with granular base. J Highw China 10:50–54
4. Wei J, Wang L, Ai Y (2006) Analysis on design and mechanical response of different structural combination asphalt pavement. J China For Highw 26(2):75–78
5. Wu S, Wang J, Chen T (2006) Stress analysis of asphalt pavement on large longitudinal slope. J Wuhan Univ Technol Transp Sci Eng Ed 30(6):969–972
6. Airy GD, Browm SF (1998) Rheological performance of aged polymer modified bitumen. Assoc Asphalt Paving Technol 67:66–93

7. Airey GD (2003) Rheological properties of styrene butadiene styrene polymer modified road bitumen's. Fuel 82(14):1709–1719
8. Shen A, Zhang Y, Guo Y (2009) Comparative analysis of mechanical response of three typical asphalt pavement structures. J Chan Univ Nat Sci Ed 29(4):1–7

The Behavior of Cement-Treated Crushed Rock Material Under the Cyclic-Loading Test with Multiple Amplitude of Applied Strain

Peerapong Jitsangiam, Korakod Nusit, Suphat Chummuneerat and Hamid Nikraz

Abstract This paper presents the characteristics of cement-treated crushed rock material which was subjected to the multi-strain amplitudes of cyclic loads. The cyclic behaviors of cement-treated crushed rock specimens were examined by the four-point bending test adopted from the standard test for asphalt concrete. The test specimens were prepared by adding 3 and 5% cement by weight to the typical crushed rock base. The four-point bending tests were then carried out under strain-controlled mode with the strain amplitudes of 50, 100, 150, and 200 µε. Two different forms of strain-controlled tests were conducted in this research, which are constant-strain and multi-strain amplitude tests. For the constant-strain amplitude test, all specimens were loaded for one million cycles. The results revealed that the specimens tested with the strain amplitude of lower than 200 µε were secured from fatigue failure. The multi-strain amplitude test was then employed to examine the degradation characteristics of the specimen stiffness. In this research, the multi-strain amplitude tests were conducted by employing various strain amplitudes on the individual specimen. Therefore, the test protocol with the minimum testing time and the optimum number of test specimens can be developed. More importantly, the results from multi-strain amplitude test also explored the modern knowledge on the behaviors of cement-treated crushed rock material after it is failed by the fatigue damages.

P. Jitsangiam
Chiang Mai University, Muang, Chiang Mai 50200, Thailand

K. Nusit (✉)
Naresuan University, Muang, Phitsanulok 65000, Thailand
e-mail: korakodn@nu.ac.th

S. Chummuneerat
Department of Highways, Ratchathewi, Bangkok 10400, Thailand

H. Nikraz
Curtin University, Bentley, Perth, WA 6102, Australia

1 Introduction and Background

The cement-treated crushed rock base, or a cement-treated base (CTB), is a mixture of road base aggregate, Portland cement, and water. The material is designed and suitable for the road pavement structure with high traffic volume and high traffic load. The CTB with high cement content can be classified as fully bound, or stabilized, material which spontaneously exhibits fatigue damage under traffic loads. The fatigue failure would be newly defined as one of design criteria for CTB road pavements, of which the maximum tensile strain at the bottom of CTB layer is generally considered as the design criteria for mechanistic–empirical (M–E) pavement design.

Currently, the fatigue characteristic of asphalt concrete is evaluated by the four-point bending (4 PB) test using prismatic beam specimen. The material stiffness (modulus) and fatigue life of test specimen are important and traditionally employed as the design parameters; these parameters are generally determined by the cyclic 4 PB tests [1, 2]. To conduct the cyclic 4 PB test, the prismatic beam is clamped at both ends while simultaneous cyclic load is applied at the mid-part by the two inner clamps; consequently, the maximum tensile strain is repeatedly induced at the bottom part of the test beam during the test. The fatigue test can be performed by two different modes, so-called strain-controlled and stress-controlled tests [3]. The amplitude of applied strain is controlled by two inner clamps during the strain-controlled test, while the loading amplitude is maintained during the stress-controlled test. The reduction in flexural stiffness value of the test beam is continuously monitored during the cyclic 4 PB test. The fatigue life of the test beam is defined as the number of loading cycles that the flexural stiffness is reduced to half of its initial value [4, 5]. The relationship between applied stress/strain amplitudes and the fatigue life of asphalt concrete material can be obtained from series of cyclic 4 PB tests, conducted at different magnitudes of applied strains or stresses. This relationship is important for the M–E design of road pavement structure which will be constructed with the test materials.

The cyclic loading with constant frequency, constant amplitude of applied strain, and unchanged pattern is normally employed by the standard 4 PB test to simulate the traffic loads [3, 5]. In this research, such standard 4 PB test adapted from testing guideline for asphalt concrete was named as 'constant-strain amplitude test.' However, the characteristics of dynamic load induced by traffics are typically complicated in real field situations. Therefore, the multi-strain amplitude test was developed in this research. Although the in situ loading regime could not be fully simulated by the multi-strain amplitude test, the tests provided the very useful information on the dynamic responses of CTB. Therefore, this research aims to examine the cyclic responses of CTB using modified 4 PB tests adapted from the standard 4 PB test protocol for asphalt concrete [5]. This conventional test method of asphalt concrete requires a number of test specimens to cover a wide range of strain over the testing time of approximately 28 h, to complete one million cyclic-loading cycles for each test specimen. Thus, the modified 4 PB test for CTB

developed in this study would be an initiative to evaluate the fatigue resistance of CTB based on the available testing apparatus (4 PB test), along with a significant reduction in the number of test specimens and the amount of time involved in such testing.

2 Specimen Preparation and Tests Performed

2.1 Specimen Preparation

The CTB specimens in this research were prepared by blending the standard crushed rock base (CRB) with general-purpose Portland cement [6], at the optimum moisture content (OMC). In the first stage of specimen preparation, the optimum amounts of CRB, cement, and water were determined from the standard mix design process [7, 8]. The OMC of CTB mixtures was initially determined from the modified compaction test [9]. The CRB used in this research was collected from the local quarry in Perth, Western Australia. The selected CRB has its engineering properties conformed to Main Roads Western Australia specification [10]. Figure 1 presents the moisture–density relationship of CTB mixtures used in this study.

After the mix design process had been completed, the specimen slabs were then manufactured. The CTB slabs with the size of 400 mm in length, 300 mm wide, and 75 mm thick were made by compacting the mixtures to achieve at least 95% of maximum dry density (MDD). The specimen slabs were compacted using the roller compactor as illustrated in Fig. 2. Each CTB slab was cured for at least 7 days to gain sufficient strength before cutting process. Then, four prismatic beams— 400 mm in length, 63.5 mm wide, and 50 mm thick—were cut from each compacted slab as shown in Fig. 3. All specimens were then stored in the temperature-controlled chamber (25 °C) for 28 days (after the mixing process was completed) before testing.

Fig. 1 Modified compaction test result indicates the values of MDD = 2.32 t/m^2 and OMC = 5.8%
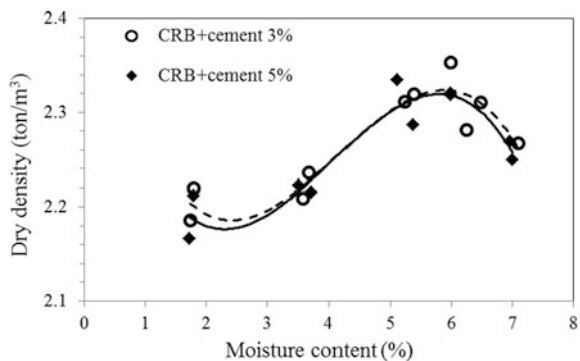
Fig. 2 Roller compactor used for manufacturing the CTB slabs

Fig. 3 Four prismatic beam specimens prepared from each compacted slab

2.2 *Four-Point Bending (4 PB) Test*

The 4 PB test according to the Austroads guideline, AG:PT/T233 [5], was adapted in this research to characterize the behaviors of CTB specimens. According to the test guideline, the haversine loading waveform with the frequency of 10 Hz was continuously applied to the specimen, until the flexural stiffness of the specimen is reduced by half of the initial value or one million loading cycles are reached. These termination criteria were assigned by the design guidelines based on the characteristics of asphalt concrete and cement-treated materials under cyclic-loading test [5, 7]. According to AG:PT/T233 [5], initial flexural stiffness is defined as the flexural stiffness value at the 50th loading cycle of a full series of applied cyclic-loading cycles. The 4 PB tests in this research were conducted under

strain-controlled mode at a controlled temperature of 25 °C. Figure 4 shows the configurations of the 4 PB test apparatus employed in this research. The specimen is restrained by four clamps, with two outside clamps working as the beam supports and two loading points applying via the two inner clamps. The deflection of the specimen is measured at the mid-span and top of the specimen. In this research, two different forms of testing were performed to gain a better understanding of the characteristics of CTB, which consists of the constant-strain and the multi-strain amplitude tests.

Ten specimens were prepared for evaluating the fatigue characteristics and cyclic-loading responses of CTB in this research. There were five specimens for each mixture (3 and 5% cement). Four specimens of each mixture underwent constant-strain amplitude test, while the other specimens were tested with the multi-strain amplitude.

Constant-Strain Amplitude Test. This is a conventional cyclic 4 PB test for obtaining the fatigue life of materials. The constant-strain amplitudes of 50, 100, 150, and 200 micro-strains ($\mu\varepsilon$) were applied to the beam specimens during the tests. Each beam specimen was repeatedly loaded by constant-strain amplitude, until the specimen was failed by fatigue or the one million loading cycles were completed (about 28 h).

Multi-strain Amplitude Test. The conventional 4 PB test outlined in the previous section is generally time-consuming and requires a large number of specimens to capture the fatigue characteristics of material. Therefore, multi-strain amplitude test was designed and conducted to examine the stiffness degradations of specimen tested by multi-levels of strain amplitude. The test was also employed as a precursor to a new testing protocol development, which aims to reduce the testing time and the number of test specimens. Accordingly, each beam was assigned to be loaded by the multiple values of strain amplitude. The strain amplitude of 50 $\mu\varepsilon$ was firstly applied to the specimen for 3000 cycles. Then, the applied strain amplitudes were increased at 50-$\mu\varepsilon$ interval for every 3000 cycles until the strain amplitude
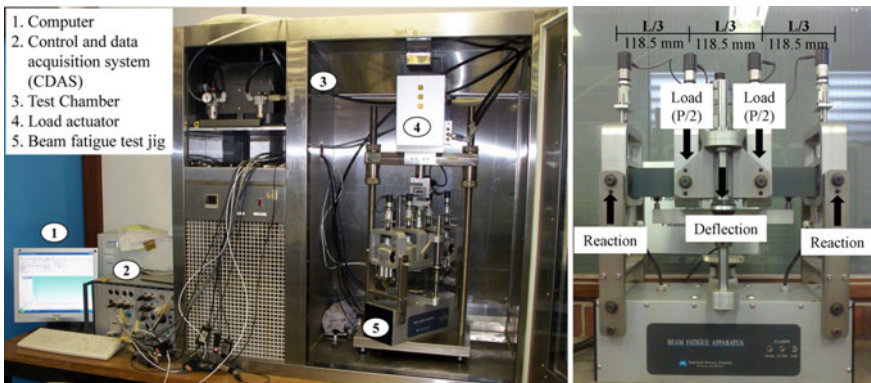
Fig. 4 The 4 PB test apparatus employed in this research
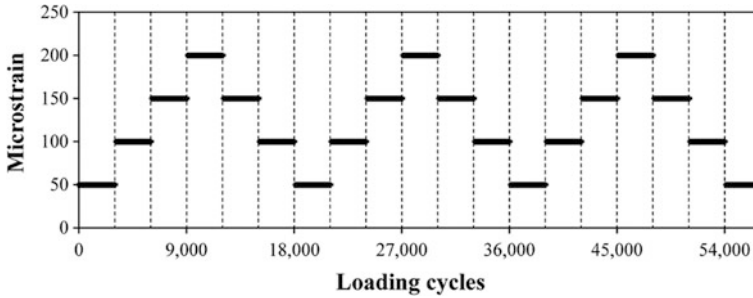
Fig. 5 The configuration of applied strain employed for multi-strain amplitude test

attained 200 με. After that, the applied strain amplitudes were reduced at 50-με interval for every 3000 cycles until the minimum values of 50 με were reached. Figure 5 illustrates that three repeated patterns of up-and-down strain amplitudes were applied to each beam specimens. Thus, the total number of 57,000 cycles was completed for a single beam test.

3   Results and Discussion

3.1   Constant-Strain Amplitude Test

Table 1 summarizes the flexural stiffness and number of test cycles of 3 and 5% cement specimens obtained for the 4 PB test. It can be seen that not all of the specimens experienced fatigue failure after completing one million cycles of loading. The values of initial flexural stiffness of 5% cement specimens were considerably higher than those of the 3% cement specimens.

In this research, the 4 PB tests were conducted using the strain-controlled mode; therefore, the test machine adjusted the applied cyclic-loading magnitude to maintain the constant value of beam deflection. Figure 6 illustrates an example of the range of load intensity, varying from 0.8 to 01.7 kN applied to a 5% cement specimen to retain the constant deflection equivalent to 200 με.

It can be seen from Table 1 that all 3% cement specimens completed one million loading cycles without failing by fatigue damages (stiffness reduces by less than half of the initial value). The initial stiffness decreased dramatically as the loading cycle increased in steps. The flexural stiffness of the prismatic beam specimen usually drops dramatically by the cyclic loads during the crack initiation phase. Then, the rate of stiffness reduction is found to be constant during the stable crack growth phase until the specimen is failed by the cyclic loads or the one million loading cycles are reached [11]. Similarly, the 4 PB tests of every 5% cement specimens were terminated at one million cycles. However, for the 5% cement specimens, only the specimen subjected to 200 με of strain amplitude was failed by

Table 1 Summary of constant-strain amplitude test results

Cement content (%)	Applied strain amplitude (με)	Flexural stiffness (MPa)			No. of cycles to crack initiation phase
		Initial	End of crack initiation phase	End of test	
3	50	12,579	N/A	13,500	N/A
	100	9617	8131	8050	31,780
	150	5687	4281	4442	73,940
	200	1985	1866	1760	57,250
5	50	20,500	N/A	21,966	N/A
	100	20,407	20,203	20,733	71,340
	150	14,721	12,463	12,155	130,810
	200	22,510	13,311	11,797	175,790

Fig. 6 Maximum cyclic load applied to the 5% cement specimen to maintain the strain amplitude equivalent to 200 με
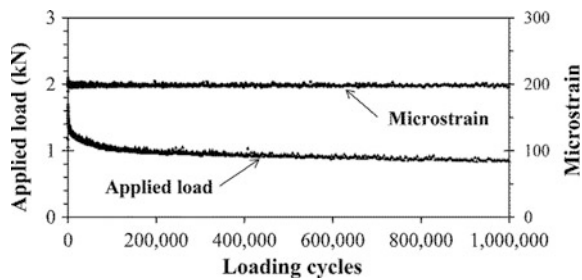
the fatigue damages. This is because the flexural stiffness of test specimens reduced by 48% of its initial value, or almost half of its initial flexural stiffness [5]. However, the stiffness of other specimens reduced approximately by 0–18% of their initial values (Table 1).

The fluctuation in flexural stiffness measured by cyclic 4 PB test is inevitable [3]. The results from Table 1 indicate that the final values of flexural stiffness measured at low strain amplitudes were generally greater than their initial values. During the cyclic 4 PB test, the testing machine automatically adjusted the magnitude of applied load to achieve the desired level of applied strain amplitude; therefore, low level of applied strain amplitude leads to small applied loads clamped on the specimen. Small clamped load and unevenness of specimen surface may be the source of stiffness fluctuation in this research. However, the increase in stiffness values for the case of small applied strain amplitude should be carefully investigated in the future research.

In this research, the fatigue failure could only be observed from the 5% cement specimen subjected to 200 με of applied strain amplitude. Therefore, the fatigue life of this specimen was evaluated in this research. The relationship between the stiffness ratio (SR) and the loading cycles (N) for the 5% cement specimen is illustrated in Fig. 7. The stiffness ratio (SR) is calculated by dividing the stiffness of
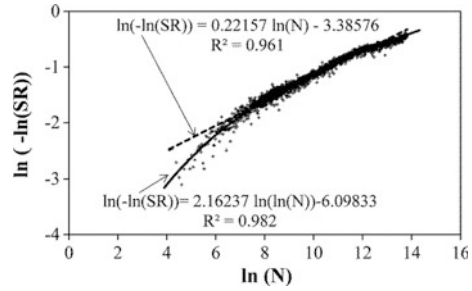
test specimen at any loading cycle by its initial value. The plot was created based on the recommendation by ASTM D7460 [1]. The testing standard suggests to develop a linear relationship between $\ln(\ln(-SR))$ and $\ln(N)$ for the projection of the failure point, which resulted in a fatigue life of 827,775 cycles (Fig. 7). It was found that the relationship between $\ln(\ln(-SR))$ and $\ln(\ln(N))$ provided an extrapolated fatigue failure point at around 1.42 million cycles.

3.2 Multi-strain Amplitude Test

The results from the multi-strain amplitude test are illustrated in Figs. 8. The rapid decreases in stiffness were evidenced at different stages of the tests. For the 3% cement specimen, the stiffness reduced sharply to about 50% of its initial value when the specimen was loaded by 100-με strain amplitude (cycle number 3000–6000) as illustrated in Fig. 8a. Similarly, the stiffness of the 5% cement specimen reduced to almost 40% of its initial value when the specimen was subjected to 150-με strain amplitude as shown in Fig. 8b.

As mention earlier, the CTB layer in the field is generally subjected to the dynamic loading induced by traffics. The dynamic loading pattern, frequency, and amplitude are typically random by nature. However, the frequency, loading mode, and applied stress or strain amplitudes employed by the standard test are normally constant [1]. Consequently, the results from multi-strain amplitude test provide more understanding on the responses of CTB when it is subjected to random strain amplitudes. It is assumed that specimen cracks were induced by the cyclic loads at the early stage of multi-strain loading test (Fig. 8); therefore, the specimens attained the stable crack growth phase for the rest of testing. In general, the stiffness of the specimen decreases as the applied strain increases and vice versa. The test results shown in Fig. 8 reveal that cracks generated by the cyclic loads are unrecoverable; this is because the stiffness of test specimen never bounced back to its previous values, although the applied strain amplitudes were iterated. It also means that the recoverable flexural stiffness is mainly responded by the remaining concrete bond existed in the CTB specimens.
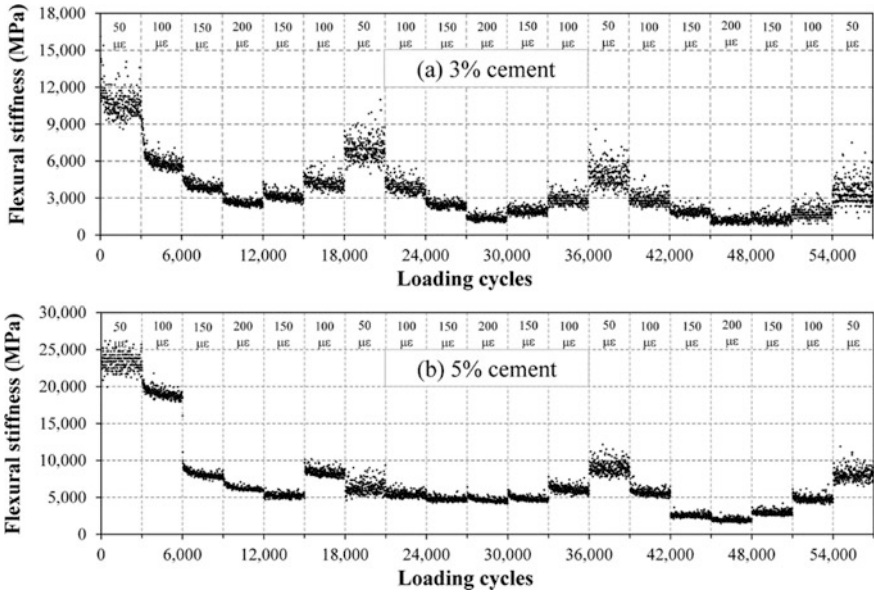
Fig. 8 Multi-strain amplitude test results for **a** 3% cement specimen and **b** 5% cement specimen

Another interested finding from the multi-strain amplitude test is the material responses after its fatigue failure. The half reduction in material stiffness from its initial value is assigned as the fatigue failure criteria by the testing guideline [5]. Therefore, the fatigue failure of 3%-cement and 5%-cement specimens occurred approximately at the loading cycles number 3000 and 6000, respectively. Although the specimens were failed by the fatigue damages, they still responded to the cyclic loads accordingly with the applied strain amplitude. Figure 8 shows that the flexural stiffness of specimens increased as the applied strain amplitude decreased and vice versa, even though the specimens were already failed by fatigue damages. This finding supports the hypothesis that CTB is still able to use as the base course layer of pavement structure, although it is already failed by fatigue damages [12, 13]. After the fatigue failures, the material stiffness still heavily depended on the applied strain level; therefore, it can be said that fatigue damage CTB behaves as nonlinear elastic and load-history-dependent material. In general, the stiffness of nonlinear elastic material is severely influenced by the stress or strain levels. However, the stiffness of concrete-like materials also relies on the historical stresses applied on them [14]. This information is very useful for mechanistic–empirical (M–E) pavement design guideline development since the responses of CTB layer after fatigue failure have never been substantially researched. The correlations between loading cycles and the stiffness for each strain level for the 3% and 5% cement specimens are presented in Fig. 9a, b, respectively. The coefficient of determination (R^2) obtained from the regression curves shown in Fig. 9 was greater than 0.70.

Fig. 9 Flexural stiffness degradation under multi-strain amplitude test of **a** 3% cement specimen and **b** 5% cement specimen
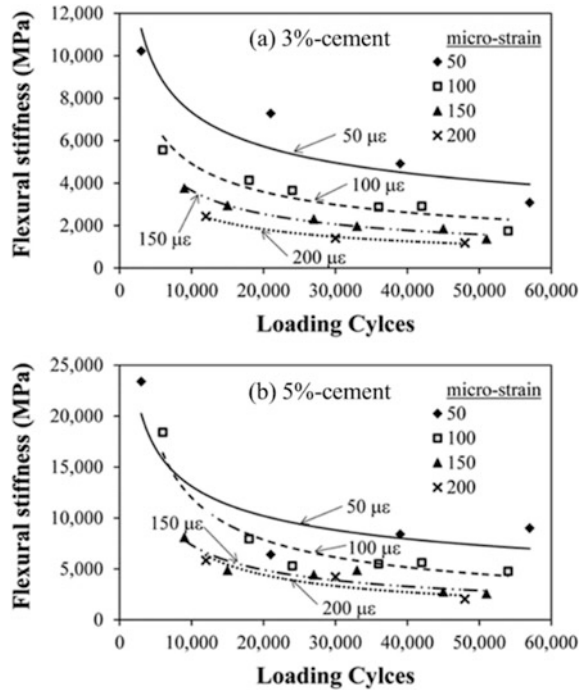
4 Conclusions

Two types of cyclic 4 PB test were performed in this research to characterize the behaviors of CTB. The first test was conducted based on the constant-strain amplitude test, which were adapted from the Austroads testing guideline [5]. However, the dynamic loading characteristics in the field are totally different from the loading pattern employed in the laboratory test; therefore, the multi-strain amplitude test was developed in this research. The dynamic loads induced by traffics in the field are usually random and complicate. However, the multi-strain amplitude test developed in this research explores more knowledge on the responses of CTB. For the multi-strain amplitude test, the test specimens were subjected to the stepwise increased and decreased level of applied strain amplitude. The important findings from this research are composed of the following:

- The 5% cement specimen was considerably failed by the fatigue damages, within a million cycles of cyclic loading, when the applied strain amplitude was 200 µε. However, the specimens loaded by strain amplitude lower than 200 µε were secured from fatigue damages, within the one million cycles of cyclic loading. The fatigue behaviors of CTB subjected to higher amplitude of applied strain require further investigation.

- The 3% cement specimens behaved differently; the reductions in stiffness of all specimens tested under constant-strain amplitude never reached 50% of their initial values. However, the initial flexural stiffness values of 3% cement specimens are severely fluctuated; this might be the reason of unpredictable responses. Therefore, further investigation is also required for the 3% cement specimens. More importantly, the careful specimen preparation steps are in-needed for the specimens with low cement content.
- The multi-strain amplitude test has effectively expressed the stiffness degradation behaviors of CTB specimen, through a stepwise increase and decrease in applied strain amplitude tests. The test has the potential for development, and a new approach may be found to reduce the lengthy time taken and the number of specimens used for the tests. Figure 9 illustrates the relationship between flexural stiffness of CTB, applied strain amplitude, and the number of loading cycle. On the other hand, the figure indicates that the flexural stiffness of CTB is strongly influenced by amplitude and cycle number of the repeated traffic load in the field.
- The critical findings from multi-strain amplitude test are composed of the following: (1) Cracks in CTB generated by cyclic loading are unrecoverable, (2) the CTB specimen behaves as nonlinear elastic and load-history-dependent materials, after it is failed by the fatigue damages, and (3) the failed CTB could continuingly be employed as the pavement base course layer.

References

1. ASTM (2010) Standard test method for determining fatigue failure of compacted asphalt concrete subjected to repeated flexural bending. ASTM D7460, ASTM International, West Conshohocken, PA
2. AASHTO (2007) Standard method of test for determining the fatigue life of compacted Hot Mix Asphalt (HMA) subjected to repeated flexural bending. AASHTO T321. American Association of State and Highway Transportation Officials, Washington, DC
3. Jitsangiam P, Nusit K, Chummuneerat S, Chindaprasirt P, Pichayapan P (2016) Fatigue assessment of cement-treated base for roads: an examination of beam-fatigue tests. J Mater Civ Eng 28(10):04016095
4. Austroads (2007) Guide to pavement technology part 4: pavement materials. AGPT04-07. Austroads, Sydney, NSW
5. Austroads (2006) Fatigue life of compacted bituminous mixes subjected to repeated flexural bending. AG:PT/T233. Austroads, Sydney, NSW

 6. Standard Australia (2010) General purpose and blended cements. AS 3972. Standards Australia, Sydney, NSW
 7. NCHRP (2004) Guide for mechanistic-empirical design of new and rehabilitated pavement structures. National Cooperative Highway Research Program, Washington, DC
 8. PCA (1992) Soil-cement laboratory handbook. Portland Cement Association, Chicago
 9. MRWA (2007) Test method WA 133.1, dry density/moisture content relationship: modified compaction fine and medium grained soils. Main Roads Western Australia, Perth, WA
10. MRWA (2012) Specification 501-pavements. Main Roads Western Australia, Perth, WA
11. Nusit K (2016) Development of an advance fatigue model of a cement-treated base material based on continuum damage mechanics. Ph.D. thesis. Curtin University, Perth, WA
12. Austroads (2006) Guide to pavement technology part 4D: stabilised materials. AGPT04D-06. Austroads, Sydney, NSW
13. De Vos ER (2007) Performance characterization of cement treated sand base material of Mozambique. M.Sc. thesis. University of Stellenbosch, Stellenbosch
14. Sinha BP, Gerstle KH, Tulin LG (1964) Stress-strain relations for concrete under cyclic loading. ACI Struct J 61(2):195–211

Shakedown Analysis of Flexible Pavement on Saturated Subgrade Under Moving Traffic Loading

Zhi Lv, Jiangu Qian and Renyi Zhou

Abstract In this paper, the shakedown behavior of flexible pavement on saturated subsoil subjected to moving vehicle loading is studied. Based on Biot's dynamic theory of saturated porous media, dynamic stresses of layered saturated subgrade are derived by the transfer matrix method. Then, the lower limit shakedown theory is introduced to estimate the shakedown state of the pavement system. The study focuses on the effects of vehicle's velocity, saturated soil's permeability, pavement and subsoil's strength and modulus ratios on the shakedown behavior. Theoretical results show that for the pavement system on the saturated subgrade, the growth of stiffness ratio or strength ratio leads to the transition of the critical shakedown state from the upper to the lower layers. It is also found that there exists a set of optimal modulus and strength ratios so that the upper and lower layers can reach the critical shakedown state simultaneously.

Keywords Traffic loading · Lower-bound shakedown · Saturated subgrade · Biot's dynamic theory · Transfer matrix method

1 Introduction

Excessive post-construction settlement of flexible pavement was commonly observed in the saturated ground [1–4]. It will lead to varieties of pavement distresses, such as rutting and cracking, especially for the flexible pavement [5, 6]. However, the rutting induced by the permanent settlement is hardly predictable during the pavement service life on the saturated subsoil [7]. In addition, the traditional pavement design method based on the empirical method is unreasonable

Z. Lv · J. Qian (✉) · R. Zhou
Department of Geotechnical Engineering, Key Laboratory of Geotechnical and Underground Engineering of Ministry of Education, Tongji University, Shanghai 200092, China
e-mail: qianjiangu@tongji.edu.cn

to the safety evaluation of pavement structure. Compared with the traditional approach, the shakedown theory is more practical in pavement design, where the deformation is not considered.

The shakedown problem was put forward by Bleich in 1930s [8]. Its concept was raised by Prager [9] to describe the adaptability of an ideal elastoplastic body after plastic deformation under reciprocating loading. Since Sharp and Booker [10] applied the shakedown theory to the analysis of pavement structure in 1984, the research about traffic geotechnical engineering with this method and related laboratory tests have been reported. However, most of them have been established in the framework of static shakedown theory [11–17]. In recent years, the static theory has been extended to the dynamic shakedown theory by considering the dynamic stress effect of the moving loading, and a more reasonable theoretical approach for the optimization analysis of the pavement system under high-speed moving loading has been provided [18].

However, previous studies on shakedown analysis of pavement idealized the subgrade soil as a single-phase medium, the dynamic response of which is much different from that of saturated soft clay. The analysis of dynamic stress response for saturated soil is very different from the elastic or viscoelastic theory [19], which is crucial to the shakedown analysis. For the saturated soil, the proper account of the coupling between the fluid diffusion and skeleton deformation is required, which can be well modeled with Biot's dynamic theory for poroelastic medium [20, 21].

In this paper, a semi-analytical method is introduced to solve the dynamic stresses of layered saturated half-space using dynamic Biot's theory. Subsequently, Milan's shakedown analysis on flexible pavement is carried out based on solved dynamic stresses. Eventually, as an example illustration, the shakedown of the two-layered pavement system is investigated by considering the effects of vehicle velocity, the permeability of saturated subgrade and two layers' strength and modulus ratios.

2 Shakedown Theory

The lower-bound shakedown theory proposed by Melan in 1938 [22] and the upper-bound shakedown theory proposed by Koiter in 1960 [23] made up the basis of the shakedown theory. Because the lower-bound solution is usually smaller than the real solution which makes the pavement design conservative, this paper will be studied with the Melan's theory.

The Melan's lower-bound theory states that if a time-independent self-equilibrium residual stress field can be found, the yield condition will not be violated anywhere in the structure when it is added to the elastic stress field produced by external loading within the given range. This can be expressed as follows:

Fig. 1 Three-dimensional
moving loading
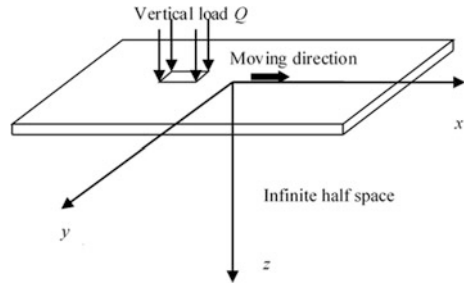
$$f\left(\sigma_{ij}^e + \rho_{ij}\right) < 0 \tag{1}$$

where σ_{ij}^e is the elastic stress field, ρ_{ij} is the residual stress field in the unloading state, and f is the yield criterion for the material.

The key problem is how to construct a reasonable residual stress field. Figure 1 is a schematic diagram of the three-dimensional problem, with vertical loading Q moving along the x. Compared with the two-dimensional problem, any element of material will have all six residual stress components in the true three-dimensional circumstance, which makes that much more complex. In order to simplify the three-dimensional problem, referring to the static analysis method of Yu [14], more attention should be paid to the xoz plane of $y = 0$ for moving loading. Due to the self-equilibrium condition and boundary condition, the residual stresses ρ_{zz} and ρ_{xz} do not exist. What is more, ρ_{yy} belongs to the middle principal residual stress, and geotechnical materials usually use the Mohr–Coulomb yield criterion, in which the effects of the middle principal residual stress can be approximately ignored. Thus, the horizontal residual stress ρ_{xx}, dependent on y and z, is the only nonzero residual stress which can affect the shakedown.

According to Yu and Wang [24], assuming that the loading is λq_1, where q_1 is the unit wheel loading, the elastic stress caused by all loadings is proportional to the loading multiplier λ, so the total stress can be expressed as follows:

$$\sigma_x = \lambda \sigma_{xx}^e + \rho_{xx} \tag{2a}$$

$$\sigma_{xz} = \lambda \sigma_{xz}^e \tag{2b}$$

$$\sigma_z = \lambda \sigma_{zz}^e \tag{2c}$$

By using the Mohr–Coulomb yield criterion and investigating the most dangerous plane $y = 0$ in three-dimensional space, the condition Eq. (1) for the shakedown of subgrade system [25] can be expressed as follows:

$$f = (\rho_{xx} + M)^2 + N \leq 0 \tag{3}$$

with

$$M = \lambda\sigma^e_{xx} - \lambda\sigma^e_{zz} + 2\tan\varphi(c - \lambda\sigma^e_{zz}\tan\varphi) \tag{4a}$$

$$N = 4(1 + \tan^2\varphi)\left[\left(\lambda\sigma^e_{xz}\right)^2 - (c - \lambda\sigma^e_{zz}\tan\varphi)^2\right] \tag{4b}$$

where c and φ are the material's cohesion and the internal friction angle, respectively.

Obviously, in order to satisfy Eq. (3), it requires that

$$N \leq 0 \Rightarrow \lambda \leq \frac{c}{\left|\sigma^e_{xz}\right| - \left|\sigma^e_{zz}\right|\tan\varphi} = \lambda_2 \tag{5}$$

where λ_2 is an initial shakedown multiplier.

Considering ρ_{xx} does not change with time and space at any specific depth $z = j$, the variation range of residual stress can be obtained according to Eq. (3):

$$\max_{z=j}\left(-M_i - \sqrt{-N_i}\right) \leq \rho_{xx} \leq \min_{z=j}\left(-M_i + \sqrt{-N_i}\right) \tag{6}$$

where i means any point at that depth $z = j$.

When there is a point that reaches the critical state in the layer, the left of Eq. (6) must be equal to the right, and the shakedown problem can be solved by finding the maximum of loading multiplier λ_{sd} to get the criticality. Then, the procedure of shakedown estimation is shown in Fig. 2, and it can be programmed in MATLAB. Apparently, the shakedown limit can be solved once the elastic stress field and material properties are known.

What is more, if the layered structure is safe, it is necessary to ensure the safety of each layer, so that the shakedown limit takes the minimum value among all the layers:

$$\lambda_{sd} = \min\left(\lambda_{sd1}, \lambda_{sd2}, \ldots \lambda_{sdj}, \ldots \lambda_{sdn}\right) \tag{7}$$

3 Dynamic Stress Response of Layered Saturated Half-Space

In this study, an analytic method is adopted to obtain the elastic stress field. Soil, the material of subgrade, is regarded as a saturated poroelastic media. Based on the Biot's dynamic theory, the dynamic stress response of homogeneous foundation can be solved, and it is able to be extended to a layered system with the transfer matrix method.

$$\lambda_1 = 0, \lambda_2 = \frac{c}{\left|\sigma_{xz}^e\right| - \left|\sigma_{zz}^e\right| \tan\varphi}$$

$$\lambda_3 = (\lambda_1 + \lambda_2)/2$$

$$\rho_{xx}^{lower} = \max_{z=j}\left(-M_i - \sqrt{-N_i}\right)$$
$$\rho_{xx}^{upper} = \min_{z=j}\left(-M_i + \sqrt{-N_i}\right)$$

$\rho_{xx}^{lower} < \rho_{xx}^{upper}$ at any depth?

$\lambda_2 = \lambda_3$

N

$\lambda_1 = \lambda_3$

N

$$\rho_{xx}^{lower} - \rho_{xx}^{upper} < 1 \times 10^{-6}$$

Shakedown limit $\lambda_{sd} = \lambda_3$
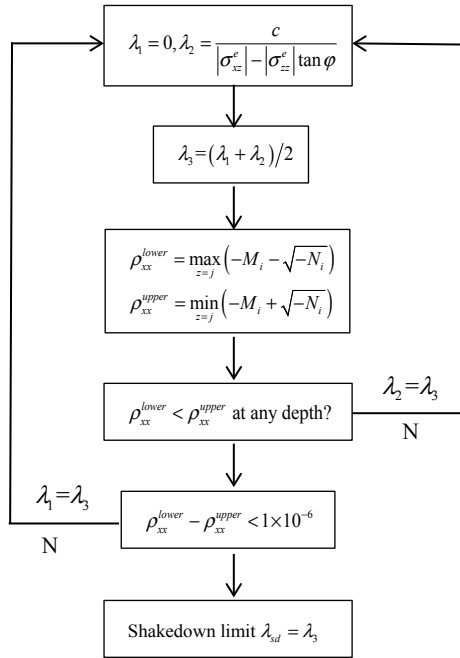
3.1 Governing Equations of Saturated Poroelastic Half-Pace

The analytical model under moving loading is shown in Fig. 3, in which the subgrade soil is modeled as a layered poroelastic half-space.

According to Biot's theory, the stress–strain relationship of the poroelastic medium can be expressed as follows:

Fig. 3 Analytical model

$q_1 e^{i\omega_0 t}$ c x z_0

h1   y   Layer1 z_1

  z_2

h2   Layer2 z_{j-1}

hj   Layerj z_j

half-space

z
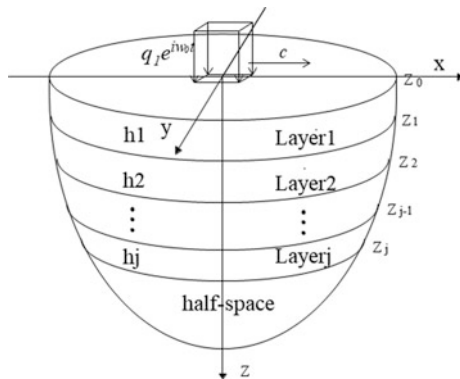
$$\sigma_{ij} = \lambda e \delta_{ij} + 2\mu\varepsilon_{ij} - \delta_{ij}\alpha p_{\mathrm{f}} \tag{8a}$$

$$p_{\mathrm{f}} = -\alpha M e + M\theta \tag{8b}$$

where ε_{ij} is the strain component; δ_{ij} is the Kronecker delta function. $e(e = u_{i,i})$ and $\vartheta(\vartheta = -w_{i,i})$ are the dilatation of solid and of the fluid relative to soil skeleton, respectively; u_i and w_i (i = 1, 2, 3) are the displacement vectors of the soil skeleton and of the pore fluid with respect to the soil skeleton, respectively. σ_{ij} means the total stress components of the soil; p_{f} is the excess pore pressure; λ and μ are Lame constants; α and M are the compressibility parameters of the two-phase medium.

Governing equations of motion for bulk porous medium and the pore fluid are shown as Eq. (9):

$$\mu u_{i,jj} + \left(\lambda + \alpha^2 M + \mu\right)u_{j,ji} + \alpha M w_{j,ji} = \rho \ddot{u}_i + \rho_{\mathrm{f}}\ddot{w}_i \tag{9a}$$

$$\alpha M u_{j,ji} + M w_{j,ji} = \rho_{\mathrm{f}}\ddot{u}_i + m\ddot{w}_i + b_{\mathrm{p}}\dot{w}_i \tag{9b}$$

where ρ and ρ_{f} are mass densities of the bulk material and the pore fluid, $\rho = n\rho_{\mathrm{f}} + (1-n)\rho_{\mathrm{s}}$, ρ_{s} is the density of solid skeleton and n is the porosity of the porous medium, respectively; b_{p} is the interaction force between soil skeleton and fluid, $b_{\mathrm{p}} = \eta/k$; η is the fluid viscosity and k is the dynamic permeability coefficient of pore medium.

The double Fourier transformation, including time $(t \rightarrow \omega)$ and horizontal coordinate $(x \rightarrow \xi_x, y \rightarrow \eta_y)$, is required to solve the governing equations. Then, the fundamental solutions of displacements u_i and w_i, stresses and pore fluid pressure p_{f} can be derived [26].

3.2 Solutions for the Layered Half-Space

This paper uses the transfer matrix method to deal with layered poroelastic half-space. The three-dimensional model is illustrated in Fig. 3. Assuming that the ground has N layers and the bottom layer is a semi-infinite space, rectangular moving loading moves along the x-direction with velocity v.

In the frequency–wave number domain, the displacements and stresses at $z = z_j$ can be denoted in terms of a vector as follows:

$$\psi(z_j) = \left[i\hat{\bar{\bar{u}}}_x, \hat{\bar{\bar{u}}}_y, \hat{\bar{\bar{u}}}_z, \hat{\bar{\bar{w}}}_z, i\hat{\bar{\bar{\tau}}}_{xz}, \hat{\bar{\bar{\tau}}}_{yz}, \hat{\bar{\bar{\sigma}}}_z, \hat{\bar{\bar{p}}}_{\mathrm{f}}\right]^T \tag{10}$$

And write it into matrix form

$$\psi(z_j) = T_j \cdot W_j(z_j) \Leftrightarrow W_j(z_j) = T_j^{-1} \cdot \psi(z_j) \tag{11}$$

where T is a 8×8 matrix noting the soil properties; $W_j(z_j)$ can be shown as

$$W_j(z_j) = [Ae^{\gamma_f \cdot z_j}, Be^{-\gamma_f \cdot z_j}, Ce^{\gamma_s \cdot z_j}, De^{-\gamma_s \cdot z_j}, Ee^{\gamma_t \cdot z_j}, Fe^{-\gamma_t \cdot z_j}, Ge^{\gamma_t \cdot z_j}, He^{-\gamma_t \cdot z_j}] \tag{12}$$

And A, B, C, D, E, F, G, H are unknown numbers dependent on boundary conditions, and if they are solved, the dynamic response will be known.

With some manipulations on Eq. (10), the matrix of displacements and stresses can be expressed as follows:

$$\psi(z_j) = T_j \cdot E_j \cdot T_j^{-1} \cdot \psi(z_{j-1}) = G_j \cdot \psi(z_{j-1}) \tag{13}$$

where T_j and E_j are 8×8 matrices which can be found in Qian [19].

Thus, it is easy to obtain the displacement and stress matrix of nth layer by Eq. (12):

$$\psi(z_n) = G_n \cdot G_{n-1} \cdots G_1 \psi(z_0) \tag{14}$$

Then, the boundary conditions on the free surface will be discussed because it is the key to the problem. Apparently, $A = C = E = G = 0$ as a result of the displacement and stress regularity for the semi-infinite half-space soil considered. In addition, at the surface of the ground, it is obvious that σ_{xz} and σ_{yz} are zero and σ_z should be identical to the amplitude of moving loading which is modeled as distributed rectangular loading of length $2a$ and width $2b$. Assuming that the surface of the foundation is completely permeable, p_f is zero. Above all, the boundary conditions are as follows:

$$\sigma_{xz}(x, y, 0) = \sigma_{xz}(y, z, 0) = p_f(x, y, 0) = 0 \tag{15a}$$

$$\sigma_{zz}(x, y, 0) = -q_1 e^{i\omega_0 t} [H(x - vt + a) - H(x - vt - a)] \times [H(y + b) - H(y - b)] \tag{15b}$$

where q_1 and v are the constant magnitude and speed of the moving loading, respectively; ω_0 is the frequency of the harmonic moving loading; $H (\ldots)$ is the Heaviside function.

Based on the boundary conditions, $\psi(z_0)$ is determined, and the desired position's stress and displacement $\psi(z_n)$ will be known naturally. At last, with the application of inverse Fourier transforms and numerical integration approach raised by Zhou [27], the dynamic stress response of the system can be solved, which means the elastic stress field can be obtained.

4   Verification of Numerical Approach

Usually, the shakedown limit is expressed by a dimensionless factor $\lambda_{sd} q_1/c$, where c is the cohesion of the subgrade. Aiming to verify the validity of the numerical approach in this paper, the shakedown of three-dimensional homogeneous subgrades under low speed (1 m/s) moving loading is carried out and compared with static solution [24, 28], as shown in Fig. 4. To model single-phase elastic medium, the parameters of saturated soil n, M, ρ_f, α_∞, b_p are taken as a small value 0.01, while others agree with comparative research. Then, it can be found that the shakedown limits calculated are basically consistent with those obtained from references, indicating that this paper's method is correct.

5   Shakedown of Homogeneous Saturated Ground

The main factors influencing the dynamic stress response of saturated foundation under high-speed moving loading include loading movement characteristic (velocity) and soil saturation properties (noticeably permeability coefficient). This section further discusses the influence of these relative factors on shakedown of homogeneous saturated ground to explain the regular pattern for the shakedown of the saturated subgrade. The parameters of the soil and moving loading are given in Tables 1 and 2.

Fig. 4 Comparison with a static solution
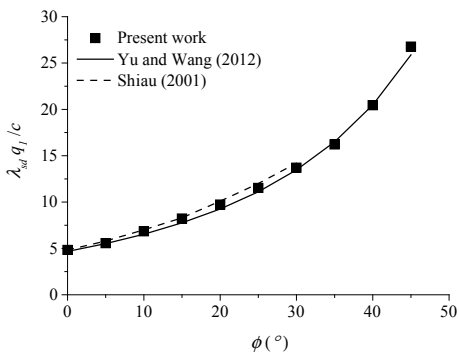
Table 1 Parameters of moving loading

q_1 (Pa)	$2a$ (m)	$2b$ (m)	ω_0	t
50,000	1	1	0	0

Table 2 Parameters of saturated soil

μ (N/m^2)	λ (N/m^2)	M (N/m^2)	α	n	ρ_s (kg/m^3)	ρ_f (kg/m^3)	α_∞	$b_p = \eta/k$ (N/m^3 s^2)
2.0×10^7	4.0×10^7	2.4×10^8	0.97	0.4	2.0×10^3	1.0×10^3	1.0	1.94×10^6

5.1 Effects of Moving Loading's Velocity

Figure 5 shows that the shakedown limits vary with loading's velocity in the saturated ground, where three internal friction angles ($\varphi = 0°, 15°, 30°$) are calculated, soil cohesion c_1 is 10 kPa, and other parameters are shown in Tables 1 and 2. What is more, an important property Rayleigh wave speed is 104 m/s, calculated through Eq. 16:

$$v_{cr} = (0.87 + 1.12\mu_s)/(1 + \mu_s)\sqrt{\mu/\rho} \qquad (16)$$

where μ_s and ρ are Poisson ratio and density of soil, respectively.

It can be seen that shakedown limit decreases with the increase in speed. However, it is noticeable that there is no evident declining tendency when the velocity reaches the Rayleigh wave speed. Additionally, it can be concluded from Fig. 5 that the bigger the internal friction angle, the more difficult for subgrade to reach the critical state.

5.2 Effects of Soil's Permeability Coefficient

Figure 6 shows that the permeability coefficient affects the shakedown limit of the saturated foundation. Cohesion c_1 is 10 kPa, while other parameters are shown in Tables 1 and 2. It can be seen that, generally, the smaller the permeability coefficient, the lower the shakedown limit of the ground, and such a phenomenon

Fig. 5 Effects of loading moving speed
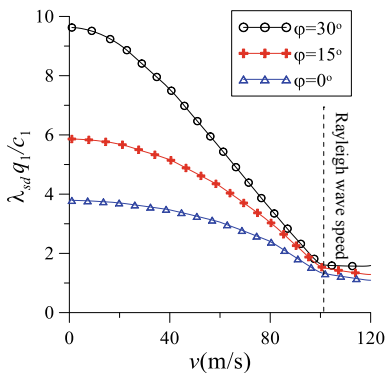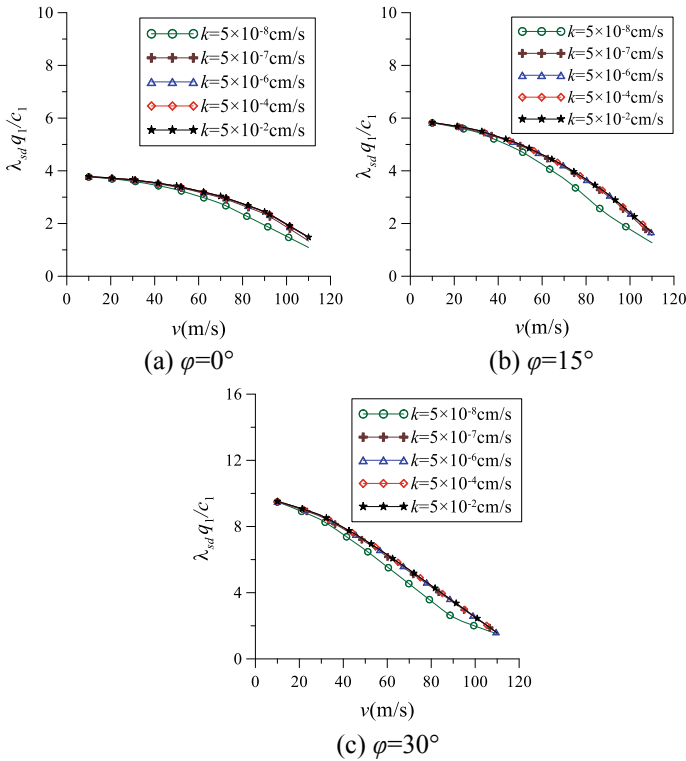
Fig. 6 Effects of permeability coefficient

becomes more obvious with the increase in speed. It is worth pointing out that three curves of permeability coefficient 5×10^{-2}, 5×10^{-4} and 5×10^{-6} cm/s almost coincide, indicating that the permeability coefficient has little influence on shakedown when it is relatively large. Moreover, in Fig. 6c, the curve 5×10^{-8} cm/s has a slight inflection point, and this appearance reflects that the permeability coefficient might have a certain relation to Rayleigh wave speed of saturated soil, whose mechanism deserves further discussion.

6 Shakedown of Flexible Pavement on a Saturated Subgrade

The real road is composed of a surface layer, base layer and saturated subsoil. Compared with homogeneous saturated ground, the existence of the upper two hard layers greatly improves the inherent Rayleigh wave speed of the system which leads to a significant reduction in dynamic stress, especially under high-speed moving

loading. This section carries out quantitative shakedown analysis of such structure. In order to highlight the impact of saturated soil properties on shakedown for the pavement system, surface layer and base layer are integrated into an overlying hard layer referred to as pavement, and saturated subgrade is regarded as the infinite thickness bottom layer. Therefore, the complex structure is simplified into a double-layer half-space model, in which the pavement is the upper layer and subgrade is the lower one.

The medium of the analytical model is considered as Mohr–Coulomb material. In the pavement engineering design, the strength ratio of upper and lower layer c_1/c_2 is one of the key parameters. For the subsoil, cohesion c_2 is 10 kPa and φ_2 is zero. The strength ratio c_1/c_2 varies from 1 to 1000, and the internal friction angle of the pavement φ_1 is 30°. What is more, pavement usually is considered as an elastic flexible material, so the parameters of upper layer n, M, ρ_f, α_∞, b_p take a small value 0.0001 to use the dynamic response solution of the poroelastic medium. Other parameters of the model are shown in Tables 3 and 4.

For the double-layered structure, the shakedown limit is denoted by dimensionless factor $\lambda_{sd} q_1/c_2$. Figure 7 illustrates the variation of shakedown limit along velocity in the case of modulus ratio $E_1/E_2 = 10$. According to Table 4, Rayleigh wave speeds of two layers are about 180 and 60 m/s, correspondingly. As it shows that when the upper layer's strength is much larger than the lower such as the circumstance of $c_1/c_2 = 10$ or 1000, the critical point is located at the lower layer. However, while the strengths of the two layers are very close ($c_1/c_2 \leq 2$), upper layer reaches the critical state first. When the ratio is at the middle level, $c_1/c_2 = 5$, along with increasing velocity, the position of criticality gradually transits from the upper layer to lower layer, and it is because the dynamic stress response has a significant amplification effect with depth under high-speed moving loading [27].

Table 3 Parameters of moving loading

q_1 (Pa)	$2a$ (m)	$2b$ (m)	ω_0	t
50,000	0.24	0.24	0	0

Table 4 Physical–mechanical parameters of the model

Parameters	μ (N/m^2)	λ (N/m^2)	Thickness (m)	c (kPa)	α
Pavement	5.56×10^6 to 5.56×10^8	8.33×10^6 to 8.33×10^8	0.25	10	0.0001
Subgrade soil	5.56×10^6	8.33×10^6	Infinite	10	0.97
α_∞	n	ρ_f (kg/m^3)	ρ_s (kg/m^3)	M (N/m^2)	b_p (N/ m^3 s^2)
0.0001	0.0001	0.0001	2.22×10^3	0.0001	0.0001
1.00	0.20	1.00×10^3	2.00×10^3	2.40×10^8	1.94×10^6

Fig. 7 Effects of loading moving speed under different strength ratio ($E_1/E_2 = 10$, $\varphi_1 = 30°$, $\varphi_2 = 0°$)
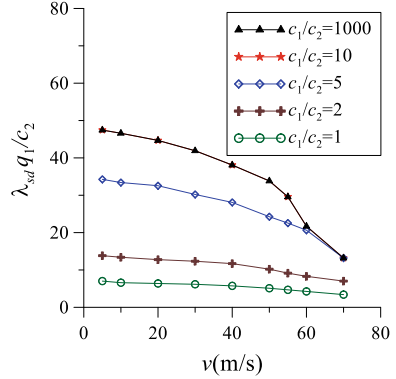
Figure 8 shows the evolution of shakedown limit with stiffness ratio and strength ratio under different velocities. Figure 8a presents results of low speed as almost static, and when strength ratio is extremely large such as $c_1/c_2 = 1000$ which means the pavement is very hard, the shakedown limit of the system depends on the relatively soft subgrade and the value increases with modulus ratio. Conversely, while there is no evident difference in strength for two layers ($c_1/c_2 = 1$), shakedown behavior emerges at the upper layer, and with increasing modulus ratio the limit value decreases with the augment of modulus diversity. For the intermediate strength ratio level ($c_1/c_2 = 1, 5$), the location of criticality depends on the modulus ratio. The low modulus ratio makes the lower layer reach the shakedown first, and the phenomenon is contrary to that under large modulus ratio. Moreover, Fig. 8b shows the circumstance of 70 m/s moving loading and compared with Fig. 8a, the difference is that when modulus ratio $E_1/E_2 > 50$ except the condition of extremely great strength ratio, shakedown limit loading is close to being a constant.

(a) $v=0$m/s

(b) $v=70$m/s
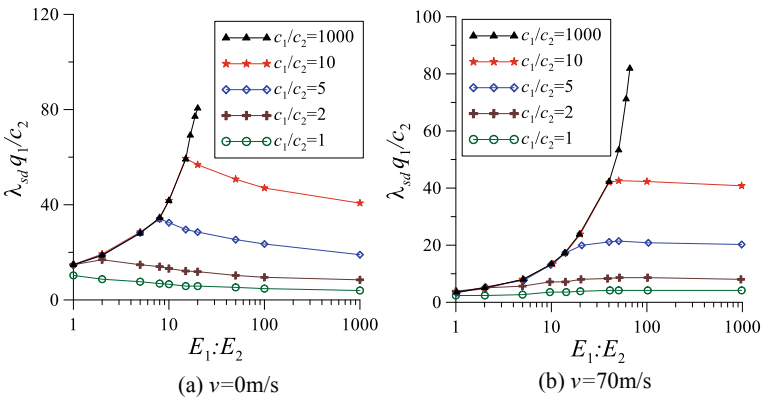
Fig. 8 Effects of stiffness ratio under different loading moving speed ($\varphi_1 = 30°$, $\varphi_2 = 0°$)

Evidently, from the point of view of road design, the case that the pavement distresses appear before the damage of the subsoil cannot satisfy the safety requirement, but it is also not economical if the pavement is too firm. Based on the analysis above, it is not difficult to conclude that there must be optimal parameters for the double-layered pavement system such as modulus ratio and strength ratio to make the upper and lower layers to reach the critical state simultaneously, so we recommend that further study should be carried out on this issue.

7   Conclusions

Based on Melan's low-bound theorem, this paper develops the study about the shakedown of flexible pavement on saturated subgrade considering the dynamic effects caused by moving traffic loading, in which the dynamic stress field is solved with analytical solutions built upon Biot's dynamic poroelastic theory. The impacts of loading characteristics (moving velocity), saturated soil properties (permeability) and pavement conditions (stiffness, strength) on shakedown of a structure are discussed. The research shows that:

1. The shakedown limit of homogeneous saturated ground decreases with the increase in moving loading velocity, but when the velocity reaches the Rayleigh wave velocity, the value does not change much. The ground whose soil's internal friction angle is bigger has the larger shakedown limit loading. In addition, when the permeability of saturated ground is pretty poor such as soft clay, the smaller the permeability, the lower the shakedown limit, but when the soil has good permeability, the effect of the permeability coefficient on the shakedown can be ignored.

2. Real pavement–subgrade system is modeled as the double-layer half-space, and its shakedown is closely related to the strength ratio (c_1/c_2) and modulus ratio (E_1/E_2) of the upper and lower layers. If the modulus condition of the system is given, the critical position is gradually transferred from the upper layer to the lower with the increase in strength ratio. On the other hand, if the strength condition has been known, the location of criticality will have the transition from the subgrade soil to the pavement. Theoretically, there is the existence of optimal design parameters about modulus ratio and strength ratio for the subgrade to make pavement and subsoil critical shakedown at the same time, which is worthy of more exploration to improve the pavement engineering design.

References

1. Chai JC, Miura N (2002) Traffic-loading-induced permanent deformation of road on soft subsoil. J Geotech Geoenv Eng 128(11):907–916
2. Qian JG, Guo SB, Huang MS (2012) Experimental study on responses of saturated clay to traffic loading. Adv Transp Geotech II:610–616
3. Shen SL, Wu HN, Cui YJ, Yin ZY (2014) Long-term settlement behaviour of metro tunnels in the soft deposits of Shanghai. Tunn Undergr Space Technol Incorpor Trench Technol Res 40 (12):309–323
4. Cai YQ, Wu TY, Guo L, Wang J (2018) Stiffness degradation and plastic strain accumulation of clay under cyclic loading with principal stress rotation and deviatoric stress variation. J Geotech Geoenv Eng 144(5):04018021
5. Cai YQ, Sun Q, Guo L, Juang CH, Wang J (2015) Permanent deformation characteristics of saturated sand under cyclic loading. Can Geotech J 52(6):795–807
6. Gu C, Wang J, Cai Y (2016) Deformation characteristics of overconsolidated clay sheared under constant and variable confining pressure. Soils Found 56(3):427–439
7. Qian JG, Lin H, Gu XQ, Xue JF (2018) Dynamic shakedown limits for flexible pavement with cross-anisotropic materials. Road Mater Pavement Des 3:1–21
8. Bleich H (1932) Uber die bemessung statisch unbestimmter stahltragwerke unter beruschsichtigung der elastisch-plastischen verhaltens des baustoffes. J Bauingenieur 19:261–269
9. Prager W (1948) Problem types in the theory of perfectly plastic materials. J Aeronaut Sci 15 (6):337–341
10. Sharp RW, Booker JR (1984) Shakedown of pavements under moving surface loadings. J Transp Eng ASCE 110:1–14
11. Ponter ARS, Hearie AD, Johnson KL (1985) Application of the kinematical shakedown theorem to rolling and sliding point contacts. J Mech Phys Solids 33:339–362
12. Collins IF, Cliffe PE (1987) Shakedown in frictional materials under moving surface loadings. Int J Numer Anal Meth Geomech 11:409–420
13. Yu HS, Hossain MZ (1998) Lower bound shakedown analysis of layered pavements using discontinuous stress fields. Comput Methods Appl Mech Eng 167:209–222
14. Yu HS (2005) Three-dimensional analytical solutions for shakedown of cohesive-frictional materials under moving surface loadings. Proc R Soc A Math Phys Eng Sci 461(2059):1951–1964
15. Nguyen AD, Hachemi A, Weichert D (2008) Application of the interior-point method to shakedown analysis of pavements. Int J Numer Meth Eng 75:414–439
16. Sun Y, Sheng SL, Luo CY (2014) Shakedown analysis of pavement structures based on lower bound theorem. Rock Soil Mech 31(11):3667–3670
17. Wang J, Yu HS (2013) Residual stresses and shakedown in cohesive-frictional half-space under moving surface loadings. Geomech Geoeng 8(1):1–14
18. Dai YC, Qian JG, Wang YG, Huang MS (2017) Dynamic shakedown analysis of flexible pavements under rolling and sliding contact considering moving speed. Transp Geotech Geoecol 189:283–290
19. Qian JG, Zhou RY, Chen SL, Gu XQ, Huang MS (2018) The influence of pavement roughness on dynamic stresses in saturated subsoil subjected to moving traffic loading. Int J Geomech ASCE. 18(4):04018012
20. Biot MA (1956) Theory of propagation of elastic waves in a fluid saturated porous solid. I. Low-frequency range. J Acoust Soc Am 28(2):168–178
21. Biot MA (1962) Mechanics of deformation and acoustic propagation in porous media. J Appl Phys 33(4):1482–1498
22. Melan E (1938) Der spannungsgudstand eines Henky-Mises schen Kontinuums bei Verlandicher Belastung. Sitzungberichte Ak Wiss Wie (Ser 2A) 147:73
23. Koiter WT (1960) General theorems for elastic-plastic solids. In: Sneddon IN, Hill R (eds) Progress in solid mechanics. North-Holland, Amsterdam

24. Yu HS, Wang J (2012) Three-dimensional shakedown solutions for cohesive-frictional materials under moving surface loadings. Int J Solids Struct 49(26):3797–3807
25. Wang YG, Qian JG (2016) Dynamic shakedown lower-bound analysis of three-dimensional half-space under moving loading. Rock Soil Mech 37(1):570–576
26. Zhou RY, Qian JG, Huang MS (2016) Influence of vehicle dynamic loading on dynamic stress in the saturated poroelastic ground. J Vib Shock 35(11):93–122
27. Zhou RY, Qian JG, Huang MS (2014) Dynamic stress responses to traffic moving loading in the saturated poroelastic ground. In: Advances in soil dynamics and foundation engineering GSP ASCE, pp 117–125
28. Shiau SH (2001) Numerical methods for shakedown analysis of pavements under moving surface loads, Newcastle Australia: The University of Newcastle. (Ph.D. thesis)

Application of Geosynthetics in Highway Engineering

Hao Tang

Abstract Geosynthetics have good engineering characteristics, such as lightweight, low price, high practicality, strong corrosion resistance, and high strength, so they are widely used in engineering construction, which has played multiple roles in highway engineering, such as protection, drainage, filter layer, isolation, reinforcement, and seepage prevention. This article will introduce the types, characteristics, and working principles of geosynthetics and list the application methods and conditions of common hazards in the construction of highway engineering. It will illustrate the importance and applicability of geosynthetics in highway engineering through the method that combines theory with actual engineering, and it is hoped that it can be used for reference to similar projects by listing the application case of the Yinchuan–Guyaozi expressway in China. In the end, it will point out the problems that exist in geosynthetics in the aspect of theoretical research, testing technology, design calculations, specification criteria, and so on, and the directions of their future development.

Keywords Geosynthetics · Highway engineering · Working principles · Application

1 Classification of Geosynthetics

Geosynthetics are a new kind of synthetic material, and their application is originated in the 1970s. The main application areas include railways, highways, seaports, tunnels, airports, and military facilities. China began to apply geosynthetics in highway engineering in the 1980s. It is mainly placed on the surface of the soil, within the soil and between layers of the soil. At present, there are many types of

H. Tang (✉)
School of Civil Engineering, Central South University, Changsha 410075, China
e-mail: tanghao99@csu.edu.cn
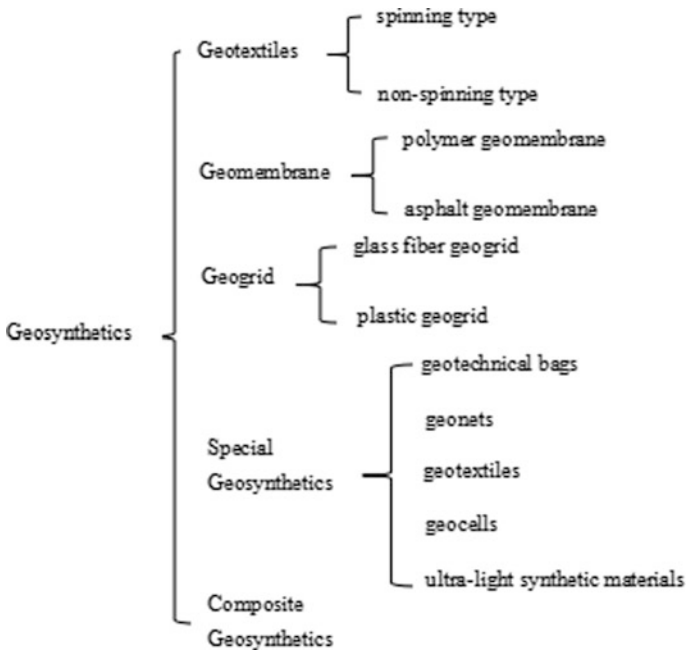
Fig. 1 Classification of geosynthetics

geosynthetics, which can be roughly divided into five types based on the differences of raw materials and material characteristics: geotextiles, geomembranes, geogrids, special geosynthetics, and composite geosynthetics [1], as shown in Fig. 1.

1.1 Geotextiles

According to different manufacturing methods, geotextiles can be classified into two types: spinning type and non-spinning type. The spinning types are woven fabrics that are formed by spinning and weaving, while non-spinning type refers to arranging the textile staple fiber or filament directly or randomly by mechanical, hot sticky, or chemical methods. In the manufacturing process, the polymer is first processed into filaments, staple fibers, yarns or strips and then made into a flat geotextile, which has advantages of light weight, high tensile strength, and high corrosion resistance.

1.2 Geomembrane

Geomembrane is a kind of composite material. According to different raw materials, it can be divided into polymer geomembrane and asphalt geomembrane. Geomembrane has good waterproof property, deformation ability, and anti-aging ability. In the soil or water, it has strong durability, so it can greatly enhance the quality of the road.

1.3 Geogrid

Geogrid can be divided into glass fiber geogrid and plastic geogrid according to different materials. Glass fiber grating has the advantages of lightweight and convenient cutting; plastic grating has good corrosion resistance, durability, and anti-aging resistance.

1.4 Special Geosynthetics

Special geosynthetics include geotechnical bags, geonets, geotextiles, geocells, and ultralight synthetic materials. Geotechnical bags are composed of double-layer polymerized fibers and have good water resistance. Therefore, they are often used in slope protection and foundation treatment. Geonets have high rigidity and are often used for slope protection and soft soil foundation reinforcement. Geotextiles and geocells are commonly used in anti-erosion engineering.

1.5 Composite Geosynthetics

Composite geosynthetics refer to geotextiles that combine two or more of geotextiles, geomembranes, geogrids, and geotechnical materials. Composite geosynthetics have the advantages of various materials and therefore have good applicability.

2 Characteristics of Geosynthetics

Geosynthetics have many characteristics. This article mainly introduces its physical properties, mechanical properties, durability, and permeability.

2.1 Physical Characteristics

Geosynthetics have the characteristics of thin thickness and light weight. The average thickness of geotextile is 0.1–5 mm, the average thickness of geomembrane is 0.25–0.75 mm, and the minimum thickness of composite material can reach 0.1 mm.

2.2 Mechanical Properties

The mechanical properties of geosynthetic materials mainly refer to their tensile strength, tearing force, and holding force. In the prevention and drainage materials, most of the materials used are flexible materials, so their tensile strength is often used to determine their ability to withstand loads; holding force can reflect the ability of geosynthetics to disperse concentrated forces; tearing force can be used to reflect the ability of the material to resist breakage.

2.3 Durability

The durability of geosynthetic materials mainly refers to their resistance to external factors such as temperature changes, biological and chemical erosion, wet and dry changes, freeze–thaw cycles, ultraviolet radiation, and mechanical wear, and it has an important connection with the type of polymer and the properties of additives.

2.4 Permeability

The permeability of geosynthetics is an important engineering index, which mainly determines its permeability and drainage capacity. Permeability is closely related to the porosity, pore size, and distribution of materials, and its vertical and horizontal permeability coefficients are mainly penetration test to determine.

3 The Principle of Geosynthetics

3.1 Protection

Geosynthetics play a certain protective role in highway engineering and can disperse certain stresses, which mainly reflected in two aspects. First, when the temperature is too low, geosynthetics can insulate and reduce the structural deformation

caused by the temperature changes; second, when the road is subjected to a concentrated load, the geosynthetic material can disperse the concentrated force and reduce the phenomenon of road cracking.

3.2 Drainage

In order to ensure the rapid discharge of water in the soil, it is generally required that the permeability of the geosynthetic material is higher than that of the adjacent structure, which will gather the water in the soil and discharge it along the material to ensure the stability of the overall structure of the highway engineering.

3.3 Filter Layer

Placing geosynthetics between two adjacent soil layers can effectively prevent the loss of sand and enhance the stability of roadbed. At the same time, water and gas can easily flow out from the gaps of geosynthetics and prevent the accumulation of water in the soil, thus played a good role in the filter.

3.4 Isolation

In highway projects, geosynthetic materials are commonly used to separate different soil materials and sand and stone materials from the ground. It can effectively separate sand particles with different particle sizes, thereby preventing them from blending with each other and avoiding the sand loss, which can improve the stability of the overall structure and protect various construction materials.

3.5 Reinforcement

Geosynthetics have good tensile properties and are often used as reinforcing materials for weak and complex geology. Adding it to the soil can significantly improve the mechanical properties of the structure so that the soil can withstand greater shear force, and some geosynthetic materials have a certain frictional resistance, which can limit the movement of the soil and thus improve the stability of the structure.

3.6   Impervious

Some geosynthetic materials can effectively prevent seepage because of their special properties. The common anti-seepage methods used in highway engineering are to use plastic membranes and geosynthetic materials together or carry out waterproof treatment on geosynthetics.

4   Application Methods in Highway Engineering

4.1   Soft Foundation

The lateral earth pressure generated by the high-fill embankment on the soft foundation will cause horizontal shear stress on the surface of the foundation and lead to the displacement on both sides of the embankment, as shown in Fig. 2. It will seriously influence the instability of the embankment. To treat this type of weak foundation, one or more layers of geogrids, geonets, or geotextiles are placed on the bottom of the embankment, thereby limiting the lateral displacement of the embankment, increasing the stability of the embankment, and reducing embankment cracking caused by differential settlement. Luo [2] used the method of experiment and added four different types of reinforced sand cushions above the soft soil foundation to explore their effects on settlement of soft soil foundation, the tensile force of geosynthetics, and pressure of road base.

Geogrid is an ideal material for handling soft foundations. Its production process is firstly extruding polymer plate and then perforating the sheet. The hole is pulled into a square hole or a long hole by two-way cold drawing or one-way cold drawing. After placing it in the soil, the soil can enter the hole, which can not only increase its own strength but also enhance the friction between the geogrid and the soil, so it can improve the stability of the weak foundation. Glass fiber geogrid and plastic geogrid are geogrids that are commonly used, and we often select the more suitable materials according to the actual conditions of different projects. The main parameters of the two materials are shown in Table 1. They are tensile strength, creep properties, temperature resistance, and fracture extensibility.

Fig. 2 Application methods in a soft foundation
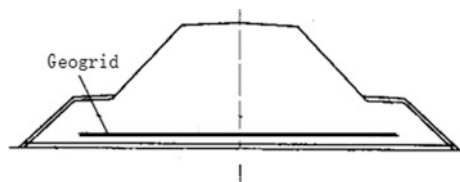
Table 1 Main parameters of glass fiber geogrid and plastic geogrid

Type	Tensile strength (kN/m)	Creep properties	Temperature resistance	Fracture extensibility (%)
Glass fiber geogrid	30–50 (longitudinal direction) 30–100 (transverse directions)	None	Good	3–4
Plastic geogrid	25–110 (unidirection) 15–45 (bidirection)	Large	Common	9–16

4.2 Differential Settlement

When constructing tunnels, bridges, and culverts, if the backfilling process at the back of the platform is not reasonable, it will easily lead to a large difference in stiffness and result in uneven settlement of the filling. This is an important issue that needs to be resolved in the highway project. At present, the main method to deal with this problem is to reinforce the backfill soil on the back of the structure, which uses the good frictional resistance formed between the geosynthetic material and the backfill, and the good anchoring force between the geosynthetics and the structure. Therefore, the structure can be connected with the backfill soil, which can improve stability and reduce the occurrence of uneven settlement. Yuan [3] analyzed the causes of uneven settlement in the transition section between the road and the bridge from the aspects of fillings, foundation condition, and stiffness difference between the road and the bridge and puts forward some methods to reduce uneven settlement and described the application result in practical engineering. Figure 3 shows the typical application method of the transition section between the road and the bridge.

At present, the most widely used geosynthetics in the treatment of uneven settlement of subgrade are geofoam polystyrene blocks, which are used for filling or backfilling the roadbed materials, which will effectively improve the stability of the roadbed, reduce the weight, and reduce the phenomenon of uneven settlement.

Fig. 3 Application methods in a differential settlement

Geosynthetics
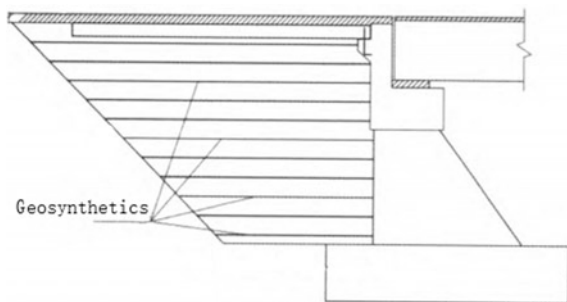
4.3 Pavement Cracks

There are two main reasons for the formation of pavement cracks. One is cracking of the road due to changes in temperature or humidity, and the other is cracking of the road surface caused by repeated external loads. The use of geosynthetics can well avoid the occurrence of reflective cracks. The use of geosynthetics is to place the geosynthetic material on the bottom of the asphalt layer in old cement concrete on pavements or on the surface of old asphalt concrete pavements. When cracks occur in new roads, geosynthetics can be placed at the bottom of the new asphalt surface. Zou [4] introduced the design method of geosynthetics used in asphalt pavement and analyzed the mechanism and influencing factors of preventing pavement cracks. Figure 4 shows a schematic diagram of the application method of geosynthetics in preventing pavement cracks.

In order to prevent cracks from occurring, geosynthetic materials must have high tensile strength, and the pavement temperature is sometimes high, so the materials used should also be characterized by high-temperature resistance and acid and alkali resistance. After comparison, the geosynthetic materials often used in the prevention of road surface cracks are glass fiber grids and geotextiles. The glass fiber grids have higher tensile strength and can withstand high temperatures. The geotextiles can form an impervious layer in the asphalt, which can prevent water seepage. At the same time, geotextiles have poor thermal conductivity and can reduce road surface deformation caused by temperature. Therefore, both materials have their own advantages, and we need to meet some technical requirements when using them, which are shown in Table 2.

4.4 Slope Protection

Slope protection mainly includes slope protection and erosion protection. The slope protection is mainly to prevent the instability of the soil caused by natural factors;

Fig. 4 Application methods in pavement cracks
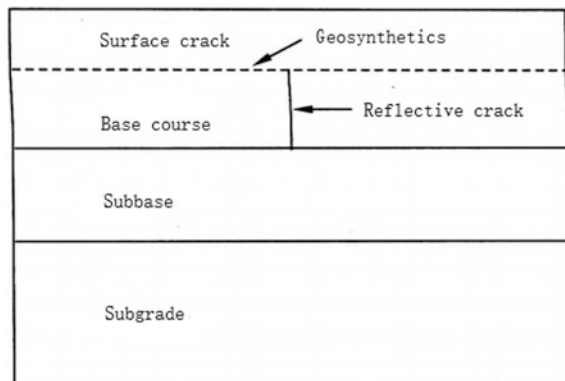
Table 2 Technical requirements of glass fiber geogrid and geotextiles

Glass fiber geogrid	Tensile strength (kN/m)	Fracture extensibility (%)	Mesh size/ (mm × mm)	Mesh shape
	≥ 50	≤ 3	(12 × 12)–(20 × 20)	Rectangle
Geotextiles	Tensile strength (kN/m)		Weight of unit area (g/m²)	
	≥ 50		≤ 200	

the erosion protection is mainly to prevent the erosion of the water flow to the roadbed, which can be protected directly, that is, to reinforce the slope, and it can also be carried out in an indirect way, that is, to change the direction and speed of the water flow. Tian [5] discussed in detail the main application types and methods of geosynthetics in slope.

In slope protection, the geosynthetics of geonets, geotextiles, and geocells are commonly used. In soil slopes, they are often used in sowing or as stretch-net turf to protect the soil. The stretch-net turf has the advantages of convenient handling and cutting, no damage to the roots of grass, and so on. It is widely used in the protection of the soil slope; in rocky slopes, geogrids or geonets can be used for protection against water erosion; geotextile bags or geotextiles can be used to prevent erosion in roadside embankments.

4.5 Drainage

Li [6] put forward the design method and development prospect of geosynthetics in highway drainage of western China based on the research status at home and abroad. Drainage construction of highways is a very important link. Geosynthetic materials are often used as drainage bodies and filters in highway projects. They can increase the drainage capacity of highway structures. Geosynthetics and geocomposite materials are commonly used [7].

The geotechnical mold bag has a certain strength, its arrangement is more convenient than the drain hole, and it has a good effect of reverse filtration and drainage, so it is often used in the protection of foundations and slopes. It is a kind of bag-shaped double-layer polymerized chemical fiber fabric. When it is applied, concrete or sand is poured into it. The composite geotechnical material cannot only drain water but also avoid the soil particles from being discharged into the drainage system and thereby avoiding the drainage channel blockage. It is mainly applied to the vertical drainage in the road surface or retaining wall behind the filter drainage system.
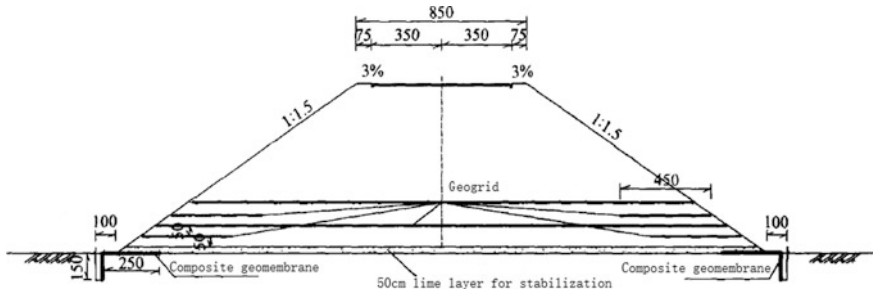
Fig. 5 Diagram of the reinforced embankment

5 Project Examples

A relatively wide range of loess is distributed in Ningxia, China. In highway projects, problems such as the settlement of embankments, damage to slopes, cracking of pavements, and diseases of drainage facilities are easily caused [8]. The Yinchuan–Guyaozi expressway passes through the loess layer. To prevent the loess subsidence, a geogrid with full sections is used to improve the bearing capacity of the roadbed, whose spacing is 50 cm, and a 50-cm stabilized lime soil layer is laid on the base for stabilization. In order to prevent the occurrence of reflective cracks, geotextiles and glass fiber gratings are used in this project. Loess has poor engineering properties under the influence of rain, and collapsible, shrinkage, and other changes causing a variety of water damage and diseases can easily occur. In addition, rain also has a large scouring power for the soil slope, so the method of applying growing grass to protect slope is not effective. In this project, a combination of a three-dimensional geotextile pad and a geocell is used and has obtained a good engineering result. Figure 5 shows the diagram of the reinforced embankment.

6 Existing Problems and Research Directions

(1) There are few studies on the basic properties of geosynthetic materials, including aging, creep, and lay-up losses [9], which make them more artificial in determining the tensile strength and modulus of the design. The US specification introduces a reduction coefficient to consider factors such as aging, creep, and lay-up losses affecting tensile strength and modulus.

(2) At present, there are many theoretical types of research on geosynthetic materials, but there are few experimental studies, especially the lack of on-site tests, and fewer data obtained through long-term observations.

(3) The research on geosynthetic material design calculation is not deep enough, and some applications have not yet formed a calculation method.

(4) At present, there are few specifications for the use of geosynthetics, and therefore, there is a great deal of randomness in use [10].

At present, geosynthetics are widely used in small projects. In the future, geosynthetic materials will be developed in the direction of composite, synthetic, and series models and will be applied more to medium and large projects. In the future, it is still necessary to further improve and perfect the theoretical research, test technology, design calculation, and specification criteria, which reveals that the development prospect of geosynthetics is very broad.

7 Conclusion

Geosynthetics are widely used in highway engineering and have strong applicability. They mainly play the role of protection, drainage, filter layer, isolation, reinforcement, seepage prevention, and so on. The common types of hazards in highway engineering, such as weak foundations, uneven settlement, pavement cracks, insufficient protection of slope, and obstructed drainage, have different application conditions depending on the characteristics of various materials. There are still some existing problems in the aspect of theoretical research, testing technology, design calculations, specification criteria, and so on; therefore, there is still much room for development.

References

1. Zhang D (2013) Application of geosynthetics in highway construction. Commun Stand 10:21–23. https://doi.org/10.3969/j.issn.1002-4786.2013.10.006
2. Luo Q, Liu J, Zhang L (2003) Application of geosynthetics-reinforced sand blanket to settlement reduction of soft ground. Chin J Geotech Eng 6:710–714. https://doi.org/10.3321/j.issn:1000-4548.2003.06.014
3. Yuan T (2015) Study on control technology for differential settlement of transition section of road bridge. North Commun 11:42–44, 47. https://doi.org/10.15996/j.cnki.bfjt.2015.11.011
4. Zou A, Chen B (2007) Application of geosynthetics in preventing pavement reflective cracks. Res Appl Build Mater 2:86–88. https://doi.org/10.3969/j.issn.1008-1933.2007.02.023
5. Tian R (2012) Application of geosynthetics in protection of subgrade slope. Commun Stand 21:26–28. https://doi.org/10.3969/j.issn.1002-4786.2012.21.007
6. Li Y (2003) Design of road drainage in the west by using the geosynthetics. For Eng 4:56–57 https://doi.org/10.3969/j.issn.1001-005x.2003.04.029
7. Wu L (2013) Application of geosynthetics in highway engineering. Transp Stand 24:42–44. https://doi.org/10.3969/j.issn.1002-4786.2013.24.013
8. Yan C, Yang X, Shi Y, Qi S (2006) Testing and application of geocell in loess slopes of highway. Chin J Rock Mech Eng 25(z1):3235–3238. https://doi.org/10.3321/j.issn:1000-6915.2006.z1.099

9. Tang S, Deng W (2004) Summary of tests and researches on creeping, aging and laying loss of synthetic geotextiles. Technol Highw Transp 1:39–42. https://doi.org/10.3969/j.issn.1009-6477.2004.01.012

10. Xu J, Xue Y (2001) Exploratory discussion on existing problems in technical regulations for geosynthetics. Shanghai Text Sci Technol 5:57–58. https://doi.org/10.3969/j.issn.1001-2044.2001.05.025

Investigation the Usability of Garnet as Filler Material in Hot Mix Asphalt

Sebnem Karahancer, Ekinhan Eriskin, Kemal Armagan, Nihat Morova, Gizem Kacaroglu, Oznur Karadag, Mehmet Saltan and Serdal Terzi

Abstract In this study, the usability of garnet in hot mix asphalt (HMA) as the filler material is investigated. Therefore, the garnet material is sieved through 75 µm. Obtained garnet dust is substituted into hot mix asphalt (HMA) mixture as filler material in four different rates (25, 50, 75 and 100%). Optimum binder rates and the gradation are determined in accordance with the Superpave volumetric mix design procedure. After the determination of optimum binder rate for each different garnet rate, the mixtures have compacted using Superpave gyratory compactor. Indirect tensile strength values and the tensile strength ratios have been obtained in accordance with AASHTO T 283 test procedure.

Keywords Garnet · Filler · Moisture susceptibility · Indirect tensile strength

S. Karahancer (✉) · N. Morova
Isparta University of Applied Sciences, 32260 Isparta, Turkey
e-mail: sebnemsargin@isparta.edu.tr

N. Morova
e-mail: nihatmorova@isparta.edu.tr

E. Eriskin · O. Karadag · M. Saltan · S. Terzi
Suleyman Demirel University, 32260 Isparta, Turkey
e-mail: ekinhaneriskin@sdu.edu.tr

O. Karadag
e-mail: oznurkaradag92@gmail.com

M. Saltan
e-mail: mehmetsaltan@sdu.edu.tr

S. Terzi
e-mail: serdalterzi@sdu.edu.tr

K. Armagan
Karamanoglu Mehmetbey University, 70200 Karaman, Turkey
e-mail: kemalarmagan@kmu.edu.tr

G. Kacaroglu
Afyon Kocatepe University, 03200 Afyonkarahisar, Turkey
e-mail: gkacaroglu@aku.edu.tr

1   Introduction

Waste materials generation by continuously increasing consumption becomes an important issue in the world. The use of these waste materials in hot mix asphalt (HMA) production is less costly and eco-friendly solution for decreasing the production costs and expecting to enhance the asphalt properties. Also, the use of these waste materials can increase asphalt resistance to some pavement's distresses [1].

Using sustainable and cost-effective alternative materials for constructing road and airfield pavements have been recently gained importance due to increasing need to naturally aggregate sources and the increasing awareness of environmental problems, such as green gas emissions and disposals associated with using conventional asphalt materials in asphalt pavement construction [2].

The hot mix asphalt (HMA) industry has been tried a wide variety of waste materials as an additive in HMA production in recent years. There are some legitimate concerns has occurred: (a) engineering concerns such as effect on the engineering properties (e.g., strength and durability), mixture requirements, impact on production and future recyclability; (b) environmental concerns, such as safety, storage, handling, emissions, fumes, potential by-products, odor, leaching and processing procedures and (c) economic concerns, such as equipment issues, performance issues, salvage value, political issues, lack of monetary incentives and alternative disposal options [3, 4].

Waste materials used as additive in HMA can be mainly classified as following: (i) household, (ii) industrial, (iii) mining and (iv) construction wastes. Some sample for these wastes could be as (i) glass, eatable oil, scrap rubber, (ii) engine oil, cellulose, slag, (iii) coalmine refuse and (iv) recycled concrete aggregates [5].

2   Materials and Methods

In this study, garnet waste used as an additive in HMA and indirect tensile strength (ITS) test was used to determine the usability of garnet waste in asphalt pavements. Muttashar et al. have examined the usability of garnet waste in concrete as an additive. They determined the microstructure and physical properties of garnet waste and they obtained spent garnet is possible to apply in concrete [6].

2.1   *Aggregate*

Limestone aggregate is selected for this study and the mineral aggregate characteristics are given in Table 1. The gradation used for this study is also shown in Fig. 1.

Table 1 Mineral aggregate characteristics

Sieve diameter	Properties	Standard	Limestone aggregate
4.75–0.075 mm	Specific gravity (g/cm^3)	ASTM C 127-88	2.700
	Saturated specific gravity		2.652
	Water absorption (%)		0.130
25–4.75 mm	Specific gravity (g/cm^3)	ASTM C 128-88	2.670
	Saturated specific gravity		2.428
	Water absorption (%)		2.800
	Abrasion loss (%) (Los Angeles)	ASTM C 131	20.38
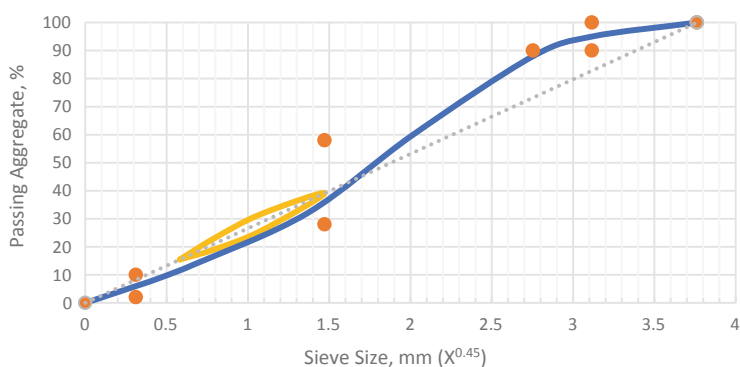
Fig. 1 Aggregate gradation selected for this study

Table 2 Basic rheological properties

Penetration (25 °C)	50–60
Flash point	180 °C
Combustion point	230 °C
Softening point	53.1 °C
Ductility (5 cm/min)	>100 cm
Specific gravity (g/cm^3)	1.030

2.2 Bitumen

Bitumen with a penetration grade of 50/70 has been selected for this study and the basic rheological properties are shown in Table 2.

Fig. 2 A sample of garnet waste filler

2.3 Garnet

The garnet used in this study is the rest from processing the garnet. The specific gravity value of the garnet is calculated as 3.61 g/cm^3. An image of the sample is shown in Fig. 2.

2.4 Superpave Volumetric Mix Design

12.5 mm sieve size is selected as nominal maximum sieve size for wearing course layer. Four samples for the selected gradation with different bitumen rate are prepared. Bitumen rate which ensures 4% air void. In addition, the same bitumen rate should ensure the minimum voids in mineral aggregate (14%) and specification interval of voids filled with asphalt (65–75%). Optimum binder content for each garnet rate is given in Fig. 3.

3 Results and Discussion

The strength results for each specimen have been obtained using indirect tensile (IDT) strength test. At this stage, the specimens are divided into two groups while one of the groups conditioned, and the other group is left unconditioned. The ratio
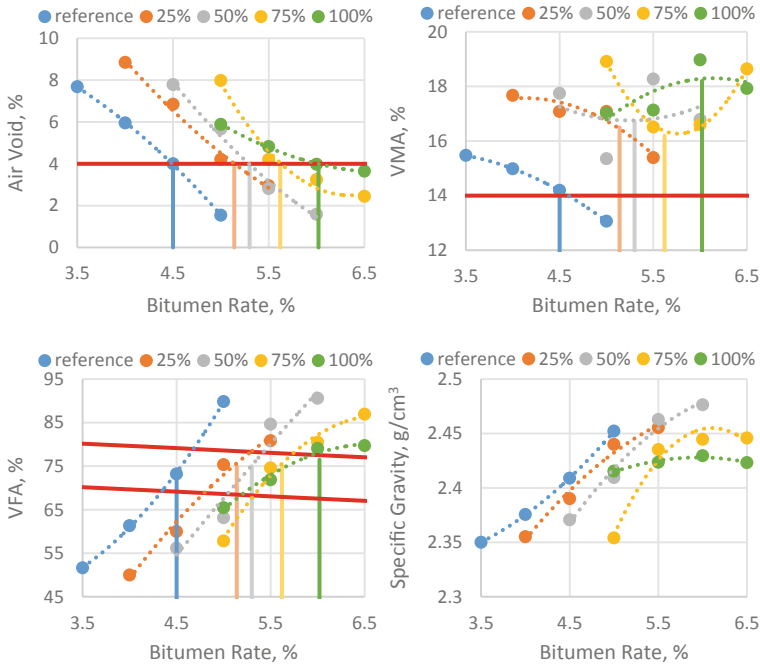
Fig. 3 Optimum binder contents

of the strength results of conditioned and unconditioned specimens has been obtained to determine the tensile strength ratio (TSR), which is used to determine the moisture susceptibility.

To determine the strength results, each specimen has been prepared according to AASHTO T283. Once specimens with a diameter of 101.6 mm are mixed and compacted using gyratory compactor, they all are cured in an oven for three days at 40 °C. When all the specimens are dried at the end of three days, they are taken out from the oven and divided into two groups. One of the groups left to cool down to 25 °C and loaded till failure for the unconditioned strength results. The other group soaked into water bath at 25 °C for one day. Afterward, they are vacuum-saturated and placed into a cabin for 16 h at −18 °C. At the end of freezing period, they are placed into 60 °C water bath for one day for thawing process. And last of all, they are placed into 25 °C water bath to cool down before they can be loaded to obtain the conditioned strength results. The ratio gives the TSR result which should be min 80%.

IDT test results and TSR values are shown in Figs. 4 and 5, respectively. As seen in Fig. 5, adding of garnet increases the TSR value which means that the specimens got less moisture susceptible.

As seen in Fig. 5, TSR values are increasing by substituting more garnet into the mixture as filler. So, the conditioned and unconditioned specimens' strength values
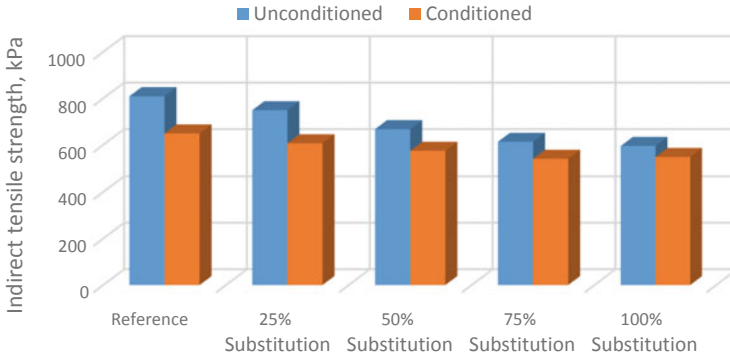
Fig. 4 IDT test results
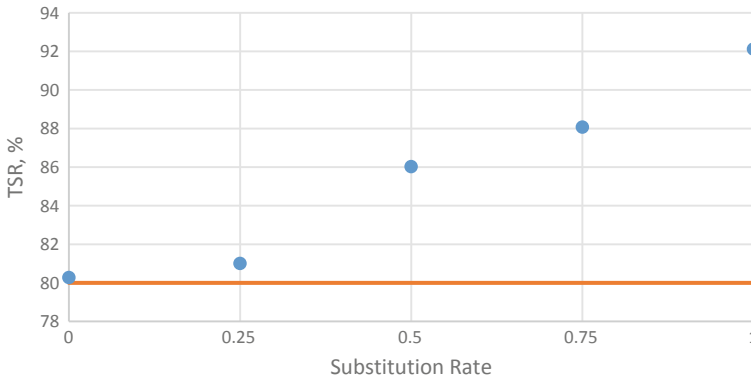
Fig. 5 TSR values of the specimens

are closing to each other. That means that substituting more garnet into the mixture decreases the moisture susceptibility of the specimens.

4 Conclusion

Utilization of garnet as filler in densely graded mixture has been studied in this study. The mixture is prepared in accordance with volumetric mix design procedure. As a result of the volumetric mix design process, the optimum binder content has been calculated as 4.5% by weight of aggregate for this study.

Garnet substituting decreases the moisture susceptibility. Specimens with all garnet substituting rates are above the specification TSR limit value, which is 80%. So, filler addition is increasing the moisture strength of the mixture.

References

1. Issa Y (2016) Recycling of waste materials in asphalt mix. Recycling and Reuse
2. Anochie-Boateng JK, George TB (2016) Use of waste crushed glass for the production of hot-mix asphalt. In: Fourth international conference on sustainable construction materials and technologies
3. Kandhal PS (1993) Waste materials in hot mix asphalt—an overview. STP1193
4. Decker DS (1993) Evaluating the use of waste materials in hot mix asphalt. National Asphalt pavement association special report 165
5. Arabani M, Tahami SA, Taghipoor M (2016) Laboratory investigation of hot mix asphalt containing waste materials. Road Mater Pavement Des 18(3):713–729
6. Muttashara HL, Nazri BA, Azreen M, Ariffin M, Hussin MW (2018) Microstructures and physical properties of waste garnets as a promising construction materials. Case Stud Constr Mater 8:87–96

Utility of Aramid, Polyolefin and Polypropylene Combination in Hot Mix Asphalt as a Fiber Material

Baris Karahancer, Nihat Morova, Sebnem Karahancer, Ekinhan Eriskin, Serdal Terzi and Mehmet Saltan

Abstract Fibers are very useful for improving the strength of the hot mix asphalt mixtures. However, the homogenous distribution in the mixture is an important factor of the usability. Therefore, a combination of aramid, polyolefin and polypropylene is used in the market. The polyolefin fibers in the combination are used to ensuring the homogenous mixture. In this study, the utility of the fiber combination in hot mix asphalt as a fiber material is examined. Therefore, the fibers are added into the mixture in three different rates (1, 3 and 5‰ by weight of the mixture). Firstly, the optimum binder rates are determined, and the specimens have been tested for the indirect tensile strength and tensile strength ratio values in accordance with the modified Lottman test. As a result, fiber-reinforced mixtures have less moisture susceptibilities than the reference mixture.

Keywords Fiber reinforcement · Aramid–polyolefin–polypropylene fiber · Moisture susceptibility

B. Karahancer · E. Eriskin (✉) · S. Terzi · M. Saltan
Suleyman Demirel University, 32260 Isparta, Turkey
e-mail: ekinhaneriskin@sdu.edu.tr

B. Karahancer
e-mail: karahancerler@gmail.com

S. Terzi
e-mail: serdalterzi@sdu.edu.tr

M. Saltan
e-mail: mehmetsaltan@sdu.edu.tr

N. Morova · S. Karahancer
Isparta University of Applied Sciences, 32260 Isparta, Turkey
e-mail: nihatmorova@isparta.edu.tr

S. Karahancer
e-mail: sebnemsargin@isparta.edu.tr

1 Introduction

In recent years, different ways of improving asphalt pavements performance have been gaining more and more popularity. One of such technologies is using fibers as a reinforcement in asphalt mixtures, which derives from cement concrete fiber reinforcement. Various types of fibers are known to be used in this application. These include both synthetic (glass, carbon and polymer) and natural (hemp, coir, jute, sisal and flax) fibers [1]. The main function of fibers incorporated into the asphalt mixture is to increase tensile strength which can result in higher strain energy responsible for fracture characteristics [2]. As a result, asphalt mixtures with fibers addition tend to be more resistant to moisture.

An extensive testing of aramid–polyalphaolefin fibers was done by Kaloush et al. [3]. Subjected fibers were evaluated in terms of their influence on triaxial shear strength, resistance to permanent deformation measured by the results of dynamic creep test, dynamic modulus, fatigue life, thermal cracking and crack propagation. Two different fiber contents were tested—0.45 kg and 0.9 kg per ton of asphalt mixture. Overall, mixtures with the addition of fibers showed better characteristics than reference mixtures, but fiber content was also a factor that affected final results. For dynamic modulus test, mixture with 0.45 kg fiber content presented higher moduli than reference mixture, while adding 0.9 kg fiber content resulted in worse (i.e., lower modulus) characteristics. Flexural strength was also affected by fibers content in the same manner, and it can be concluded that for certain properties there is an optimum fiber content after which adding more fibers can lead to unsatisfactory results. Kaloush also concluded that better performance of asphalt mixtures with discussed fibers can be also incorporated in the pavement design process and pavement overall thickness can be reduced by using fibers [4, 5]. Stempihar et al. described the use of aramid fibers in open-graded asphalt mixtures used for airfield pavements. According to his findings, fiber-reinforced asphalt concrete improves dynamic modulus especially at higher temperatures and although the initial cost of the mixture is slightly higher than traditional mix, in overall this extra cost can be overcome by a minimal increase in pavement service life [6].

2 Experimental Details

2.1 Methodology

The objective of the experiment was to determine the influence of polymer fibers addition on the selected properties of asphalt mixtures for wearing course. The research program was defined to identify eventual differences between asphalt mixtures with and without reinforcing fibers. It included the evaluation of parameters responsible for pavement behavior for moisture susceptibility.

2.2 Materials

Aggregate Selection
Standard aggregate tests are conducted for mineral aggregate characteristics. Limestone mineral aggregate characteristics are given in Table 1.

Gradation and Size
Selecting the design aggregate structure, trial blends are established by mathematically combining the gradations of the individual materials into a single blend. The blend is then compared to the specification requirements for the appropriate sieves. Gradation control is based on four control sieves: the maximum sieve, the nominal maximum sieve, the 2.36-mm sieve and the 0.075-mm sieve. There is also a recommended "restricted zone." The restricted zone is an area on either side of the maximum density line generally starting at the 2.36-mm sieve and extending to the 0.300-mm sieve. The minimum and maximum values required for the control sieves change (as does the restricted zone) as the nominal size of the blend changes. The nominal maximum aggregate size is 12.5 mm. The aggregate grading curve for asphalt mixtures is selected in convenience with aggregate gradation control points according to AASHTO MP2 (Fig. 1) (AASHTO, 2001).

Asphalt Binder Selection
Standard tests are conducted for asphalt binder properties. Table 2 shows the test results.

Optimum Asphalt Binder Content
Asphalt binder's performance grade (PG) was determined as PG64-22 according to the last 20 years' weather data and traffic loads of the Isparta region. Specimens with four different binder contents (4.5, 5, 5.5 and 6% for fiber-reinforced samples and 3.5, 4, 4.5 and 5% for reference sample) are prepared at N_{design} (125 gyrations). These samples are compacted with Superpave gyratory compactor (SGC). The specimens are compacted with the N_{design} gyration numbers.

Table 1 Mineral aggregate characteristics

Sieve diameter (mm)	Properties	Standard	Limestone aggregate
4.75–0.075	Specific gravity (g/cm^3)	ASTM C 127-88	2.700
	Saturated specific gravity		2.652
	Water absorption (%)		0.130
25–4.75	Specific gravity (g/cm^3)	ASTM C 128 88	2.670
	Saturated specific gravity		2.428
	Water absorption (%)		2.800
	Abrasion loss (%) (Los Angeles)	ASTM C 131	20.38

Fig. 1 Gradation of the aggregates

Table 2 Asphalt binder properties

Test	Average values	Standard
Penetration (25 °C)	60–70	ASTM D5
Flash point	180 °C	ASTM D92
Combustion point	230 °C	ASTM D92
Softening point	45.5 °C	ASTM D36
Ductility (5 cm/min)	>100 cm	ASTM D113
Specific gravity	1.030	ASTM D70

For a nominal maximum aggregate size (NMAS) of 12.5 mm mixture, the minimum VMA value is 14%. VFA values depend on traffic level—at higher traffic levels, the permissible range for VFA in the Superpave system is 65–75%. Figure 2 is drawn according to all the four specimen's calculated Air Void, VMA, VFA and specific gravity values. A best-fit curve through data points is drawn. From the drawn curve, the asphalt binder content corresponding to 4% air void is selected as optimum asphalt binder content and checked if the other requirements are met. According to the results, the optimum binder content is chosen 4.5% for reference sample and 5.23% for 1‰ fiber-added sample, 5.44% for 3‰ fiber-added sample and 5.67% for 5‰ fiber-added sample by weight.

Aramid, Polyolefin and Polypropylene Fiber
The additive product was a mix of aramid, polyolefin and polypropylene fibers, which are designed for use as reinforcement in asphalt mixtures for pavement structures. The type of fibers used in this research is recommended for typical hot asphalt mixtures (there are also variants intended for warm and cold asphalt mixtures), whose temperature of production and compaction is within the range of
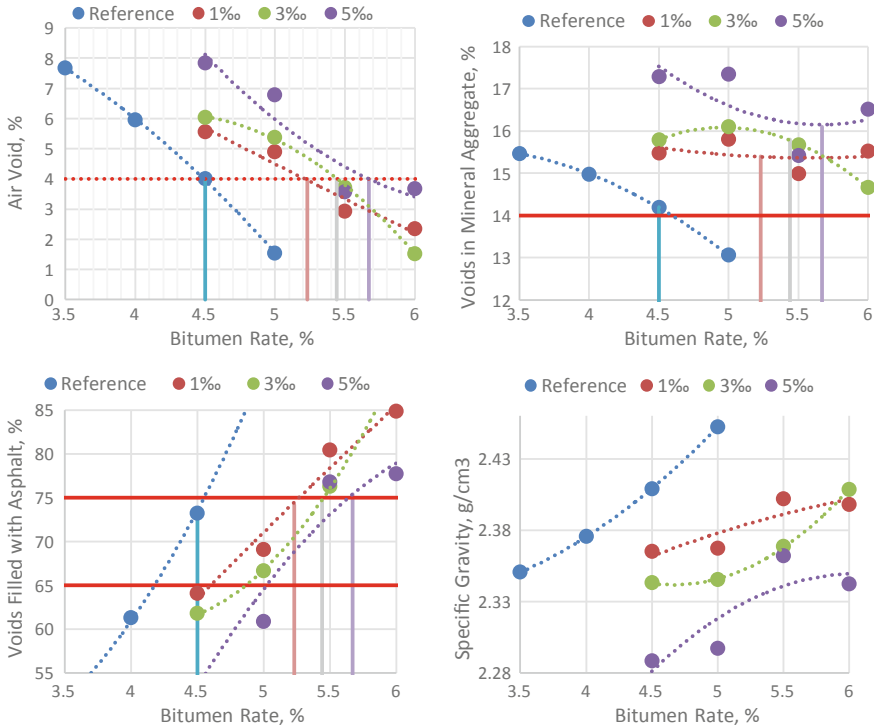
Fig. 2 Optimum bitumen contents of aramid–polyolefin–polypropylene fibers

121–190 °C. The length of the fibers is 19 mm (Fig. 3a). In accordance with recommendations of the manufacturer, fibers were added to hot aggregate with a dosage rate of 1, 3 and 5‰ by weight of asphalt mixture before adding bitumen. The samples were mixed at 135–165 °C.

3 Results and Discussion

IDT strength test was performed with 1, 3 and 5‰ fiber rates, and tensile strength ratio (TSR) values were obtained in this study.

The indirect tensile (IDT) strength test is used to get the dry and wet conditions of the compacted and cured specimens. IDT strength is calculated [7].

The specimens are prepared according to AASHTO T283 test procedure ∅ 101.6 mm test specimen diameter. Each mix sample is compacted with a gyratory compactor. After gyrations, the specimens are dry-cured at 40 °C for 72 h in a draft oven. After 3 days, all the specimens are taken out of the oven and checked for the constant mass. Half of the specimens are cooled down to 25 °C and then loaded till

Fig. 3 Sample of fibers used in the study

failure to obtain the IDT strength. The measured value is the IDTdry. The remaining specimens are soaked in water for 24 h at 25 °C. Afterward, the specimens are taken out of the water bath and vacuum-saturated till 55–80% saturation limits are reached. When the specimens are within the limits, they are put into −18 °C cabin for 16 h. After 16 h, they are soaked in a water bath at 60 °C for 24 h. At last, they are put into a 25 °C water bath for two hours before they are loaded to obtain the IDTwet value. The ratio of IDTwet to IDTdry is the tensile strength ratio and calculated [8]. The standard that prescribes this test for the evaluation of moisture susceptibility recommends a minimum TSR value of 80% for compliance [8].

TSR values of each mixture are plotted in Fig. 4. The figure clearly demonstrates that aramid–polyolefin–polypropylene contributed to an increase in TSR, inferring mitigation of moisture damage due to the addition of aramid–polyolefin–polypropylene.

In Fig. 5, the wet and dry specimen IDT strengths were compared. As shown in Fig. 5, the 1, 3 and 5‰ fiber-added specimens' IDTwet and IDTdry values were close to each other, so the TSR value is near to 1. That means that the specimens were not effected by freeze–thaw cycle. In other words, specimens have more resistance to moisture.
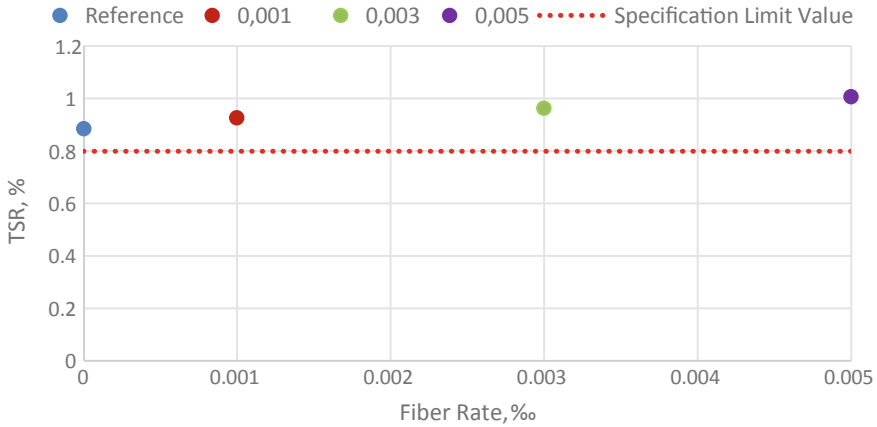
Fig. 4 TSR values of aramid–polyolefin–polypropylene fibers
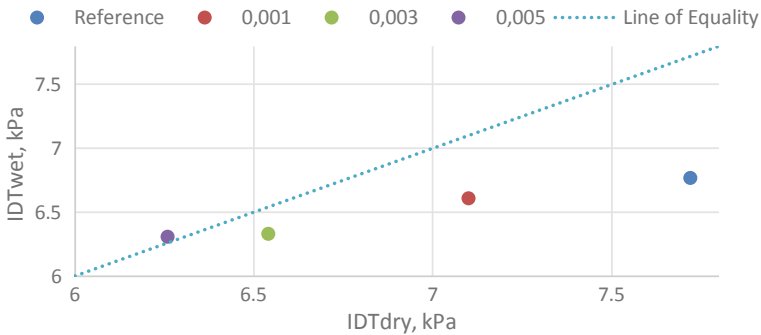
Fig. 5 Comparison of IDTwet and IDTdry values

4　Conclusion

Utilization of aramid–polyolefin–polypropylene as a fiber in asphalt pavement is studied. The best aggregate gradation and optimum binder content is selected according to the Superpave volumetric mix design process. Optimum asphalt binder content is obtained as 4.5% by weight of aggregate. The following conclusions are obtained:

Aramid–polyolefin–polypropylene fiber adding decreases the moisture susceptibility. Aramid–polyolefin–polypropylene fiber-added specimens were above the specification TSR limit value. It was concluded that fiber addition is increasing the moisture strength of the mixture.

References

1. Abiola OS, Kupolati WK, Sadiku ER, Ndambuki JM (2014) Utilisation of natural fiber as modifier in bituminous mixes: a review. Constr Build Mater 54:305–312
2. Mahrez A, Karim MR, Katman HY (2003) Prospect of using glass fibre reinforced bituminous mixes. J Eastern Asia Soc Transp Stud 5(October):794–807
3. Kaloush KE, Biligiri KP, Zeiada WA, Rodezno MC, Dwivedi S, Reed JX, Cary C (2008) Evaluation of FORTA fibre-reinforced asphalt mixtures using advanced material characterization tests—evergreen drive, Tempe, Arizona. Tempe
4. Kaloush KE, Biligiri KP, Zeiada WA, Rodezno MC, Reed JX (2010) Evaluation of fibre-reinforced asphalt mixtures using advanced material characterization tests. J Test Eval 38(4):102442
5. Kaloush KE, Zeiada WA (2012) Fibre-reinforced asphalt concrete mixtures structural numbers and pavement design considerations. Tempe
6. Stempihar JJ, Souliman MI, Kaloush KE (2012) Use of fibre reinforced asphalt concrete as a sustainable paving material for airfields. Transp Res Rec J Transp Res Board 2266:60–68
7. RMCA (2009) Turkey Ready Mixed Concrete Association. http://www.thbb.gov
8. GDH (2013) Technical specifications of highways, Turkey general directorate of highways

Study on Mechanical Properties of Styrene-Acrylic Emulsion-Based Cement Composite Pavement Joint Sealant

Ning Yang, Erlei Bai, Jinyu Xu, Guang Peng and Boxu Meng

Abstract In this study, a new type of styrene-acrylic emulsion-based cement composite pavement joint sealant (SCPJS) suitable for airport pavement was prepared. The powder-latex ratio, cement ratio, volume of dispersing agent and coalescing agent were selected as research factors. Four factors and three levels of orthogonal test were designed to systematically study the influence of four factors on the tensile and shear mechanical properties of the joint sealant. The results show that the effect of powder-latex ratio on the tensile mechanical properties of the joint sealant is most significant among the four factors. When powder-latex ratio is in the range of 0.30–0.55, the strength properties of the joint sealant increase with the increase in powder-latex ratio, and the deformation properties decrease with the increase in powder-latex ratio. When powder-latex ratio takes 0.40, the joint filler has the best overall performance of mechanical properties.

Keywords Polymer-cement composite material · Styrene-acrylic emulsion based · Pavement joint sealant · Mechanical property · Scanning electron microscope (SEM)

1   Introduction

The cement concrete pavement joint seams of the airport are an important factor affecting the normal use of the airport pavement. The failure of sealants in airport pavement joints is the main cause of airport joints [1, 2]. Relevant studies have shown that joints such as misaligned joints, fragmentation, spalling, muddy mud, and broken plates caused by the failure of pavement joint sealants account for 60–70% of airport road surface diseases. Such kind of disease makes the integrity of the road surface

N. Yang (✉) · E. Bai · J. Xu · G. Peng · B. Meng
Air Force Engineering University, Xi'an 710038, China
e-mail: yangning_kgd@163.com

J. Xu
Northwestern Polytechnical University, Xi'an 710072, China

lower and the flatness worse, often causing serious damages such as landing gear damage when the aircraft takes off and landing, the aircraft escaping from the runway or even rollover [3, 4]. At present, China's airport pavement joint sealant materials have been developed from the earliest used construction-type bituminous, polyvinyl chloride-based cement joint sealants to the current normal-temperature construction of polyurethane, silicone, polysulfide, and other types of high-grade joint sealant materials. Although the caulking effect and performance of such joint sealants have been improved compared to before, there are still some problems such as poor adhesive properties, weak resistance to embedding and tearing, poor compatibility with cement concrete, and poor aging resistance [5–9]. Therefore, for the purpose of improving the durability of airport joint sealants and the quality of road surface, ensuring the safety of aircraft flight, it is particularly important to develop a high-performance joint sealant with strong bonding properties, good flexibility in deformation, excellent durability, and suitable for airport pavement environment.

The styrene-acrylic emulsion-based cement composite material is a kind of material, using styrene-acrylic acid ester copolymer emulsion as a matrix material, cement and inorganic filler as a reinforcing material, effectively compounding inorganic materials and organic polymer materials to form a high-performance polymer-cement-based composite materials. This type of composite material not only has the advantages of high adhesive strength and flexibility, but also has the advantages of high strength, excellent durability, excellent compatibility with cement concrete, and economical and environmental protection [10]. Pan et al. studied the effect of polymer emulsion on the mechanical properties and imperme-ability of waterproof mortar. The results showed that the impermeability of cement mortar modified by styrene-acrylic emulsion was significantly higher than that of styrene-butadiene emulsion and VAE emulsion [11]. Dai et al. studied the effect of styrene-acrylic emulsion on the microstructure and corrosion resistance of oil-well cement. The results showed that the corrosion depth of styrene-acrylic emulsion concrete was significantly less than the corrosion depth of the blank group during the 1–4 months of corrosion under acidic conditions [12]. He studied the influence of the content of neoprene emulsion and styrene-acrylic emulsion on the performance of cement mortar. The results show that the incorporation of styrene-acrylic emul-sion can form a high-strength mesh-like film structure in the mortar, thereby sig-nificantly improving the frost resistance of the mortar [13]. Jian et al. studied the effect of polymer-cement ratio and emulsion type on the tensile properties of polymer-cement waterproof coatings. The results show that for styrene-acrylate emulsion cement-based waterproof coatings, the higher the polymer-cement ratio, the higher the tensile strength of the coating film, and the elongation at break is greater [14]. Dong et al. studied the aging resistance of polymer-cement-based composite waterproof coating [15]. The above studies have shown that styrene-acrylic emulsion cement composite materials have good mechanical prop-erties and durability. Utilizing these performance advantages, styrene-acrylic emulsion-based cement composite materials can be used as a high-performance joint sealant for airport pavement environments through scientific mixing ratio design and reasonable performance modification and optimization. The feasibility of

using latex-based cement composites as airport pavement joint sealant is relatively lacking, and existing researches are not systematic and not comprehensive.

In this study, the three-level orthogonal test scheme of four factors (powder-latex ratio, cement ratio, volume of disperser agent, and volume of coalescing agent) is designed. The influence of various factors on the mechanical properties of styrene-acrylic emulsion-based cement composite joint sealants is systematically studied. Combine with the observation of the microstructure of the joint sealants, the mechanism of action of the powder-latex ratio on the joint sealant system is analyzed, providing a certain experiment support for the development and modification of the styrene-acrylic emulsion-based cement composite joint sealant.

2 Test Preparation

2.1 Raw Materials

Polymer latex: Acronal S400F ap styrene-acrylic emulsion produced by BASF, Germany; its main properties are shown in Table 1. Cement: P.O 42.5R cement produced by Yaobai brand in Lantian County, Shaanxi Province; the initial setting time is 130 min and fineness modulus is 1.6. Inorganic filler: Ultrafine talc powder produced by Wantong Powder Factory, Dashiqiao, Liaoning Province. Defoaming agent: NOPCO NXZ defoaming agent produced by Japan Sanofoko (Shanghai) Co., Ltd. Dispersing agent: SN-DISPERSANT 5040 dispersing agent produced by Japan Santopco (Shanghai) Co., Ltd. Coalescing agent: DN-12 coalescing agent produced by Jiangsu Tianyin Chemical Co., Ltd. Water: Tap water.

2.2 Specimen Preparation

In this study, the two sides of the test specimen are cement mortar bases bonded by SCPJS. The cement mortar base material is prepared in accordance with the standard [16]. The mortar mix proportion is cement: sand: water = 1:2:0.4, and the size is 75 mm × 25 mm × 12 mm.

The preparation procedure of the test specimens is as follows: First add dispersing agent, coalescing agent and half defoaming agent to the emulsion and stir it evenly with a stirrer and then add the well-mixed cement and talcum powder to the emulsion and continue stirring at high speed for 10 min. Add another half of

Table 1 Main performance index of SAE

Solid content (%)	Ash content (%)	Particle size (μm)	Tg (°C)	MFT (°C)
99 ± 1	13 ± 2	1–7	0	0°C

Fig. 1 Joint sealant test piece size (size: mm)
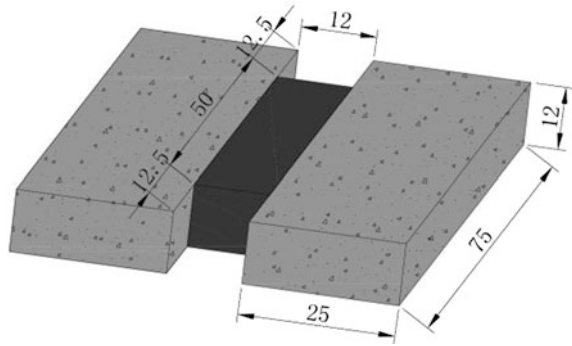
Fig. 2 Standard test specimen of joint sealant
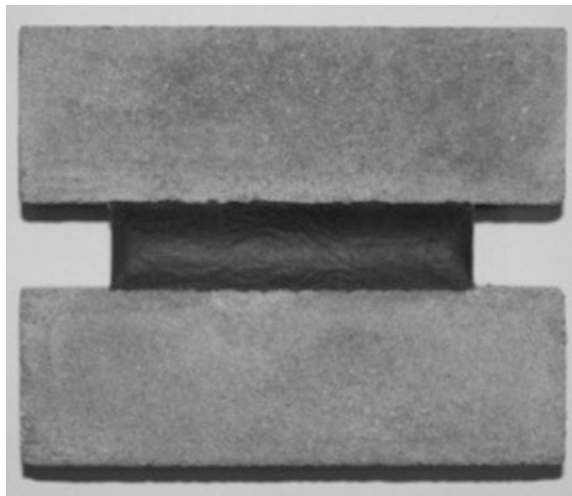
defoaming agent and continue stirring at low speed. After the mixture is stirred uniformly, a glass rod is used for manual stirring to reduce air bubbles, and then, the mixture is poured into the mold with a syringe. The standard joint sealant sample made is shown in Figs. 1 and 2.

2.3 Specimen Preparation

Under the effect of aircraft wheel load and temperature, the horizontal and vertical displacements in the seams at the joints of cement concrete pavement seams are mainly affected by tensile stress and shear stress. Therefore, the tensile test and shear test are used to simulate the stress condition of the joint sealant in the actual working conditions, and the mechanical properties of the joint sealant are tested.

Fig. 3 Diagram of tensile test
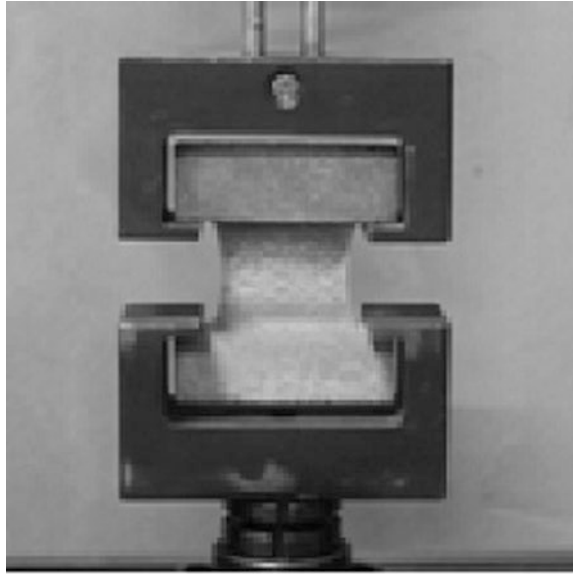
Tensile Test. HS-3001B type electronic tensile testing machine is used for tensile test. The fixture applies tensile force to the bonding material on both sides of the cement mortar substrate. As shown in Fig. 3, the specimen is stretched at a loading rate of 5 mm/min until the specimen destruction, recording force and displacement data, each test three specimens. Defining tensile strength f_t tensile modulus E_t, tensile breaking elongation $\delta_{t,b}$, and tensile peak strain $\varepsilon_{t,p}$ as indicators for evaluating the bearing and deformation performance of SCPJS under tensile load.

Shear Test. HS-3001B type electronic shear testing machine is used for tensile test. As shown in Fig. 4, during the test, the joint sealant specimen to be tested shall be clamped in the shear test equipment to ensure that the cement mortar substrate and the equipment are fixed and clamped, and then, the rising end of the equipment is lifted up to the failure of the test piece at a rate of 5 mm/min. The load displacement data is automatically recorded by the shearing equipment information collection terminal. Each group of tests is repeated 3 times. The test result is taken as the arithmetic mean value. Defining shear strength f_s, shear modulus E_s, shear breaking elongation $\delta_{s,b}$, and shear peak strain $\varepsilon_{s,p}$ as indicators for evaluating the bearing and deformation performance of SCPJS under shear load.
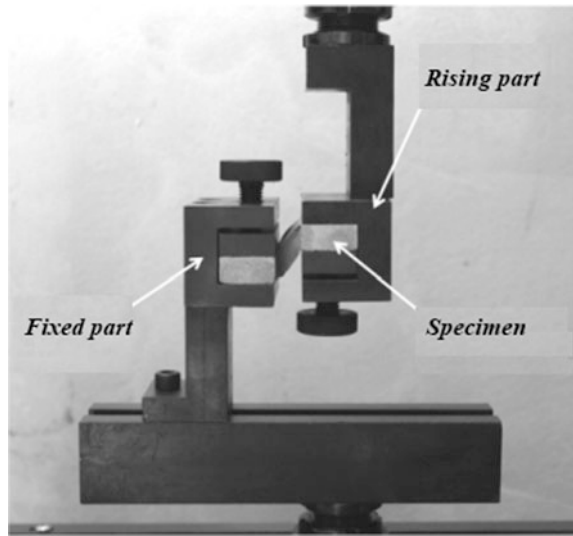
3 Study on Influencing Factors of Mechanical Properties of SCPJS

3.1 Experiment Plan

In order to explore the main influencing factors of the mechanical properties of joint sealants and their influence laws, orthogonal test methods are used to select the powder-latex ratio (the ratio of the total mass of inorganic powder to the total mass of styrene-acrylic emulsion), cement ratio (the ratio of cement mass to inorganic powder mass), the volume of dispersing agent (the percentage of dispersing agent incorporation in the total mass of the styrene-acrylic emulsion and the inorganic powder), and the volume of coalescing agent (the amount of coalescing agent incorporated in the total mass of the styrene-acrylic emulsion) as factors of orthogonality. According to the results of the previous study, the relevant literature is selected with reference to the relevant literature to select the level of each experimental factor. Four factors and three levels of orthogonal test are designed, and the volume of defoaming agent (the percentage of defoaming agent incorporation in the total mass of the styrene-acrylic emulsion and inorganic powder) is not selected as an orthogonal test factor, and the volume of defoaming agent of each set of samples is 0.5%. The specific level of selection of orthogonal experimental factors is shown in Table 2.

The four-factor three-level orthogonal test table ($L_9(3^4)$) used in the test is shown in Table 3.

The test specimens are prepared according to Table 3, and tensile tests are performed after the curing was completed.

Table 2 Factors and levels of orthogonal experiment

Level	Powder-latex ratio (A)	Cement-powder ratio (B) (%)	Volume of dispersing agent (C) (%)	Volume of coalescing agent (D) (%)
1	0.4	40	0.2	2
2	0.6	25	0.6	5
3	0.8	10	1.0	8

Table 3 Scheme of orthogonal experiment ($L_9(3^4)$)

Sample	Code	A	B	C	D
SA-1	A1B1C1D1	1(0.4)	1(40%)	1(0.2%)	1(2%)
SA-2	A1B2C2D2	1(0.4)	2(25%)	2(0.6%)	2(5%)
SA-3	A1B3C3D3	1(0.4)	3(10%)	3(1.0%)	3(8%)
SA-4	A2B1C2D3	2(0.6)	1(40%)	2(0.6%)	3(8%)
SA-5	A2B2C3D1	2(0.6)	2(25%)	3(1.0%)	1(2%)
SA-6	A2B3C1D2	2(0.6)	3(10%)	1(0.2%)	2(5%)
SA-7	A3B1C3D2	3(0.8)	1(40%)	3(1.0%)	2(5%)
SA-8	A3B2C1D3	3(0.8)	2(25%)	1(0.2%)	3(8%)
SA-9	A3B3C2D1	3(0.8)	3(10%)	2(0.6%)	1(2%)

3.2 Results and Discussion

Selecting tensile strength, tensile modulus, tensile elongation at break, and tensile peak strain are indexes to evaluate the bearing and deformation properties of SCPJS under tensile loading. The results are shown in Table 4.

The analysis of extreme difference with the tensile strength f_t as the evaluation index shows that the influence degree of each factor on the bearing capacity of the joint sealant under tensile load is A > C = D > B, and the extreme difference of the three factors of B, C and D in turn is 45.45, 72.73, 72.73% of the extreme difference of factor A. The analysis of extreme difference with the tensile modulus E_t as the evaluation index shows that the influence degree of each factor on the bearing capacity of the joint sealant under tensile load is A > B > D > C, and the extreme difference of the three factors of B, C and D in turn is 38.10, 14.29, 19.05% of the extreme difference of factor A. The analysis of extreme difference with the tensile breaking elongation $\delta_{t,b}$ as the evaluation index shows that the influence degree of each factor on the bearing capacity of the joint sealant under tensile load is A > B>C > D, and the extreme difference of the three factors of B, C and D in turn is 75.66, 54.35, 7.45% of the extreme difference of factor A. The analysis of extreme difference with the tensile peak strain $\varepsilon_{t,p}$ as the evaluation index shows that the influence degree of each factor on the bearing capacity of the joint sealant

Table 4 Results of orthogonal experiment

Sample	Orthogonal scheme				Strength index		Deformation index	
	A	B	C	D	f_t (MPa)	E_t (MPa)	$\delta_{t,b}$ (%)	$\varepsilon_{t,p}$
SA-1	1	1	1	1	0.42	0.32	168.31	1.14
SA-2	1	2	2	2	0.39	0.27	205.48	1.14
SA-3	1	3	3	3	0.35	0.22	206.48	1.10
SA-4	2	1	2	3	0.41	0.43	152.20	0.90
SA-5	2	2	3	1	0.53	0.46	205.17	0.97
SA-6	2	3	1	2	0.48	0.41	165.84	0.96
SA-7	3	1	3	2	0.59	0.55	151.89	0.62
SA-8	3	2	1	3	0.46	0.46	159.31	0.61
SA-9	3	3	2	1	0.43	0.43	140.13	0.56
K_{1f}	1.16	1.42	1.36	1.38	Extreme difference analysis of f_t			
K_{2f}	1.42	1.38	1.23	1.46				
K_{3f}	1.48	1.26	1.47	1.22				
R_f	0.11	0.05	0.08	0.08				
K_{1E}	0.81	1.30	1.19	1.21	Extreme difference analysis of E_t			
K_{2E}	1.30	1.19	1.13	1.23				
K_{3E}	1.44	1.06	1.23	1.11				
R_E	0.21	0.08	0.03	0.04				
$K_{1\delta}$	580.27	472.40	493.46	513.61	Extreme difference analysis of $\delta_{t,b}$			
$K_{2\delta}$	523.21	569.96	497.81	523.21				
$K_{3\delta}$	451.33	512.45	563.54	517.99				
R_δ	42.98	32.52	23.36	3.20				
$K_{1\varepsilon}$	3.38	2.66	2.71	2.67	Extreme difference analysis of $\varepsilon_{t,p}$			
$K_{2\varepsilon}$	2.83	2.72	2.60	2.72				
$K_{3\varepsilon}$	1.79	2.62	2.69	2.61				
R_ε	0.53	0.03	0.04	0.04				

under tensile load is A > C = D > B, and the extreme difference of the three factors of B, C and D in turn is 5.66, 7.55, 7.55% of the extreme difference of factor A. In summary, the powder-latex ratio is the most important factor affecting the bearing capacity and deformation performance of the joint sealant under the action of tensile load, and the effect of this factor on the tensile properties of the joint sealant is significantly higher than other three factors.

In order to ensure good flexibility of the joint sealant, it is prevented from debonding with the wall of the joint due to excessive stress in the deformation. According to the standard, the tensile modulus of the joint sealant must be less than or equal to 0.4 MPa. According to Table 4, $K_{1E}^A < K_{2E}^A < K_{3E}^A$. Combined with the results of previous experiments and literature data, it can reasonably be speculated that the tensile modulus of the joint sealant will increase at a range of 0.4–0.8 for

powder-latex ratio or increase first and then decrease at an inflection point of 0.6–0.8. When the powder-latex ratio exceeds 0.6, the tensile modulus of test specimens are all greater than 0.4 MPa, so the powder-latex ratio should be less than 0.6.

Because the number of levels selected by the orthogonal test is small while the interval between each level is large, the influence law of each factor on the mechanical properties of the joint sealant cannot be visually reflected. Therefore, according to the results of the orthogonal test, this study further explored the influence of the main influencing factor, powder-latex ratio, on the mechanical properties of the joint sealant. The other three factors are no longer used as variables. The best performing level of each factor in the orthogonal test was selected for the next phase of the study. The final cement-powder ratio is 25%, the volume of dispersing agent is 1%, and the volume of coalescing agent is 5%.

4 Study on Effect of Powder-Latex Ratio on Mechanical Properties of SCPJS

4.1 Experiment Plan

On the basis of the research in Sect. 2, the experimental range of the powder-latex ratio was narrowed, encryption and refinement studies were conducted, and single-factor tests were designed to study the influence of main factor on the tensile properties and shear properties of the joint sealant. The raw materials for the tests were the same as before. The specimens were prepared according to the schedule shown in Table 5. Tensile tests and shear tests were performed after the curing was completed.

Table 5 Design of single-factor experiment

Sample	Powder-latex ratio	Matching (g)					
		Latex	Cement	Talcum powder	Dispersing agent	Coalescing agent	Defoaming agent
FYB-1	0.55	100	13.75	41.25	1.55	0.78	5
FYB-2	0.50	100	12.50	37.50	1.50	0.75	5
FYB-3	0.45	100	11.25	33.75	1.45	0.73	5
FYB-4	0.40	100	10.00	30.00	1.40	0.70	5
FYB-5	0.35	100	8.75	26.25	1.35	0.68	5
FYB-6	0.30	100	7.50	22.50	1.30	0.65	5

4.2   Results and Discussion

Analysis of Strength Indexes in Tensile and Shear Tests. Figure 5 shows the trend of f_t and E_t of SCPJS with the powder-latex ration from left to right. From Fig. 5, we can see that f_t increases with the increase in the powder-latex ratio like an arch. That is, as the ratio of powder to liquid increases, f_t gradually increases, and the growth rate gradually decreases. When the powder-latex ratio is 0.55, f_t is maximum, which is 29.16% higher than the powder-latex ratio of 0.30. The change law of E_t with powder-latex ratio is slightly different from the f_t. When the powder-latex ratio increases from 0.30 to 0.35, the rate of increase in E_t is slow and only increases by 9.59%. When the powder-latex ratio exceeds 0.35, E_t increases with the increase in the powder-latex ratio like an arch. When the powder-latex ratio is 0.55, E_t is maximum, which is 69.86% higher than the powder-latex ratio of 0.30.

Figure 6 shows the trend of f_s and E_s of SCPJS with the powder-latex ratio from left to right. From Fig. 6, we can see that f_s and E_s increase with the increase in the
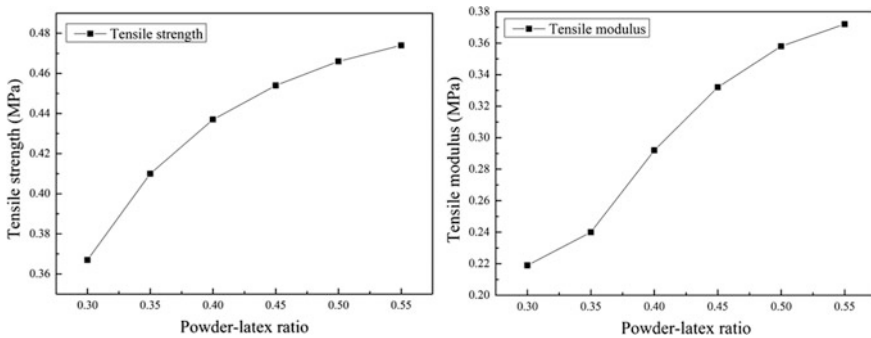

Fig. 5 The variation curve of f_s and E_s with powder-latex ratio
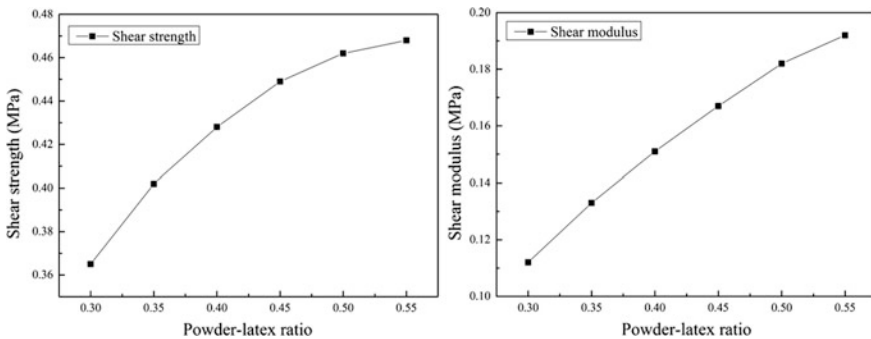
Fig. 6 The variation curve of f_s and E_s with powder-latex ratio

powder-latex ratio like an arch. When the powder-latex ratio is 0.55, f_s and E_s are maximum, which are 28.22 and 71.43% higher than the powder-latex ratio of 0.30 in turn.

With the increase in powder-latex ratio, the strength properties of SCPJS under tensile load and shear load has been significantly enhanced. On the one hand, with the increase in powder-latex ratio, the proportion of inorganic fillers increases, the cement participating in the reaction in SCPJS increases, and the resulting hydration products also increase accordingly, resulting the internal pore structure of SCPJS to continuously fill, refine, and become dense under the cross-linking reaction and interaction of polymer molecular chains with cement hydration products. On the other hand, with the increase in powder-latex ratio, the problem of solvent and dispersion of inorganic powder in the polymer emulsion gradually becomes apparent, and the rate of increase in the strength properties of the joint sealant gradually slows down.

Analysis of Deformation Indexes in Tensile and Shear Tests. Figure 7 shows the trend of $\delta_{t,b}$ and $\varepsilon_{t,p}$ of SCPJS with the powder-latex ration from left to right. From Fig. 7, it can be seen that $\delta_{t,b}$ slightly increases with the increase in powder-latex ration and then decreases like an arch. When the powder-latex ration increases from 0.30 to 0.35, $\delta_{t,b}$ increases by 1.32%. After the powder-latex ration exceeds 0.35, $\delta_{t,b}$ starts to decrease. When the powder-latex ratio is 0.55, $\delta_{t,b}$ is minimum, which is 21.12% lower than the powder-latex ratio of 0.30.$\varepsilon_{t,p}$ decreases with the increase in powder-latex ratio like a step shape. When the powder-latex ratio increases from 0.30 to 0.35, $\varepsilon_{t,p}$ decreases by 12.34%. When the powder-latex ratio increases from 0.35 to 0.40, $\varepsilon_{t,p}$ decreases by 1.49%, and the trend of change approximates the platform segment. When the powder-latex ratio is increased from 0.40 to 0.45, $\varepsilon_{t,p}$ decreases rapidly again by 10.17%. When the powder-latex ratio exceeds 0.45, $\varepsilon_{t,p}$ decreases slowly with increasing powder-latex ratio. When the powder-latex ration is 0.55, $\varepsilon_{t,p}$ is minimum, which is 25.40% lower than the powder-latex ratio of 0.30.

Figure 8 shows the trend of $\delta_{s,b}$ and $\varepsilon_{s,p}$ of SCPJS with the powder-latex ratio from left to right. From Fig. 8, it can be seen that $\delta_{s,b}$ decreases with the increase in
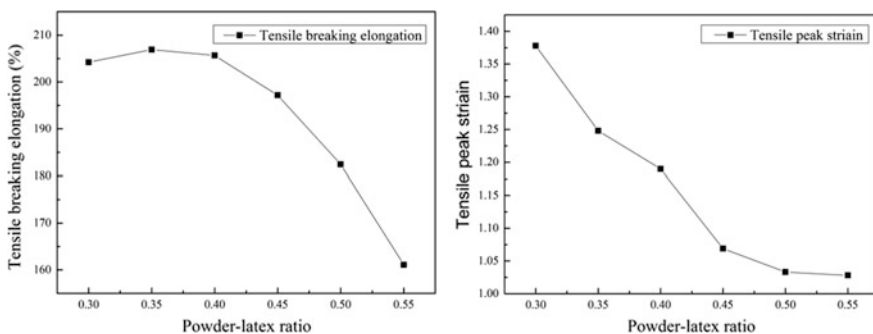
Fig. 7 The variation curve of $\delta_{t,b}$ and $\varepsilon_{t,p}$ with powder-latex ratio
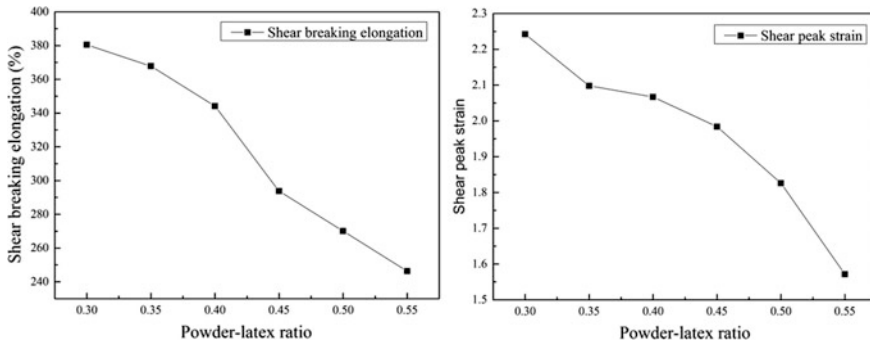
Fig. 8 The variation curve of $\delta_{s,b}$ and $\varepsilon_{s,p}$ with powder-latex ratio

powder-latex ratio like a step shape. When the powder-latex ratio increases from 0.30 to 0.40, $\delta_{s,b}$ decreases slowly by 9.54%. When the powder-latex ratio increases from 0.40 to 0.45, $\delta_{s,b}$ decreases rapidly by 14.65%. When the powder-latex ratio is more than 0.45, $\delta_{s,b}$ decreases slowly with the increase in powder-latex ratio. When the powder-latex ration is 0.55, $\delta_{s,b}$ is minimum, which is 35.26% lower than the powder-latex ratio of 0.30. $\varepsilon_{s,p}$ decreases in two stages with the increase in the ratio of powder to liquid. When the powder-latex ratio increases from 0.30 to 0.35, $\varepsilon_{s,p}$ decreases rapidly by 6.42%. When the powder-latex ratio is more than 0.35, $\varepsilon_{s,p}$ decreases with the increase in powder-latex ratio like an arch shape. When the powder-latex ration is 0.55, $\varepsilon_{s,p}$ is minimum, which is 29.88% lower than the powder-latex ratio of 0.30.

With the increase in powder-latex ratio, the tensile and shear deformation properties of SCPJS have declined to varying degrees. This is because as powder-latex ratio increases, more cement hydration products are embedded in the polymer film structure or cross-link with the polymer molecular chains and form a continuous and complete network structure, which enhances the ability of the joint sealant to resist deformation. The inorganic powder that has not participated in the reaction and the cement hydration product that does not participate in the cross-linking reaction are randomly dispersed in the material, hindering the free stretching and displacement deformation of the polymer chain under external forces.

4.3 Analysis of Microscopic Mechanism

The microcosmic morphology of different powder-latex ratio joint sealants is shown in Fig. 9. From Fig. 9, it can be seen that with the increase in powder-latex ratio, the internal porosity of SCPJS is significantly reduced, and the pore size is continuously refined. When the powder-latex ratio is 0.30 and 0.35, the internal pore volume and pore size of the joint sealant are both comparatively large.
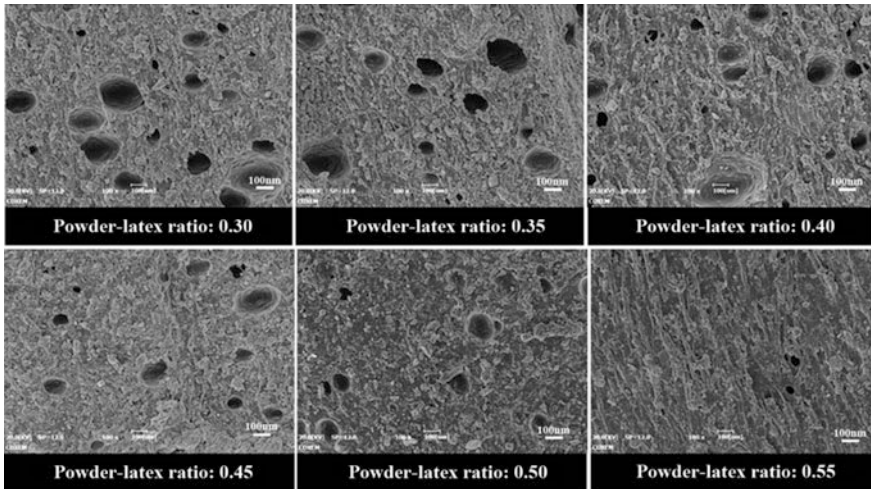
Fig. 9 Effects of powder-emulsion ratio on microscopic appearance of SCPJS

5 Conclusions and Recommendations

(1) When tensile strength, tensile modulus, tensile breaking elongation, and tensile peak strain are selected as evaluation indexes, compared with factors such as cement ratio, volume of dispersing agent and volume of coalescing agent, the powder-latex ratio has the most significant effect on the tensile mechanical properties of SCPJS.

(2) The powder-latex ratio has a significant effect on the tensile and shear mechanical properties of SCPJS. When powder-latex ratio is in the range of 0.30–0.55, the tensile strength and tensile modulus of the joint sealant increase with the increase in powder-latex ratio, and the tensile breaking elongation and tensile peak strain of the joint sealant decrease with the increase in powder-latex ratio. The shear strength and shear modulus of the joint sealant increase with the increase in powder-latex ratio, and the shear breaking elongation and shear peak strain of the joint sealant decrease with the increase in powder-latex ratio.

(3) When the powder-latex ratio is 0.40, the mechanical properties of the sealant are the best. The strength of the sealant under tensile load and shear load is remarkably improved while its good deformation capacity is maintained.

(4) According to the observations of SEM, increasing powder-latex ratio can effectively reduce the amount of pores in SCPJS and refine the pore size, thereby increasing the density of the material, improving the microstructure, and strengthening the mechanical properties.

References

1. Su AEHF (2016) Application and analysis of joint chamfers of airport cement concrete pavement. Constr Technol 45(11):58–60
2. Sun FF, Ling HYF (2017) Summarization of common diseases of airport cement concrete pavement and selection of quick repair materials. Value Eng 29:240–241
3. Wang L, Zhang N, Bai MZF et al (2012) Research on airport concrete road surface joints. Heilongjiang Sci Technol Inf 34:256
4. Li TPF (2009) Analysis of damage mechanism and sensitive factors of airport cement concrete pavement joints. Chin For Highw 29(1):83–86
5. Liu XX, Xie FG, Xu BF (2008) Elastic recovery of joint sealant for airport runway. Chin Build Waterproof 6:21–24
6. Xue J, Liu XX, Zhou JMF (2011) Application study of the new polythiourethane jointing materials for the airfield pavement. New Build Mater 38(5):76–78
7. Yuan J, Liu WBF (2016) Analysis on performance index of joint sealant material for civil airport cement concrete pavement. Highw Traffic Technol 33(9):7–13
8. Fu YW, Wang ST, Cai LCF et al (2011) Preparation and properties of restructured polysulfur-urethane sealants. Polym Mater Sci Eng 27(7):136–139
9. Odum-Ewuakye B, Attoh-Okine NF (2006) Sealing system selection for jointed concrete pavements—a review. Constr Build Mater 20(8):591–602
10. Heng YY, Zhao WJF (2014) Research progress on the properties and mechanism of SAEE modified cement based materials. Silic Bull 33(6):1431–1438
11. Pan ZK, Zhang JF (2015) Influence of three kinds of emulsion on the mechanical properties and impermeability of polymer cement waterproofing mortar. Chin Build Waterproof 12:7–9
12. Dai D, Yue L, Luo YWF et al (2016) Effect of polymer on microstructure and resistance to corrosion of oil well cement stones. J Electr Microsc 35(3):235–239
13. He XYF (2017) Effect of chloroprene emulsion and styrene-acrylic emulsion content on performance of cement mortar. Subgr Eng 4:136–140
14. Jian SW, Chen L, Ma BGF et al (2015) Tensile properties of the polymer cement waterproof coating and mechanism. New Build Mater 7:62–66
15. Dong FL, Li DL, Yang RJF (2001) Anti-aging properties of polymer cement-based composite waterproof coating. Build Waterproof Mater 5:33–35
16. GB/T 13477-2002. S. Construction seal material test method

Structural Dynamics

Study of the Influence of Undulating Terrain in the Regional Wind Field on a Freeway Bridge Section

Ying Jia, Peng Cheng and Chao-chao Han

Abstract Construction of the freeway affects the wind environment inevitably in the area where it is located. Bridge section of freeway has different topography, and the study of its influence in wind field changes has practical engineering significance. Through numerical simulation and analysis, the paper studies the influence of the height of the undulating terrain, the distance between undulating terrain and the bridge, the location of the undulating terrain and other parameters in the wind field on the bridge section of freeway and compares it with the regional wind field under the flat terrain. Numerical results show that the low wind speed area and vortex scale on the leeward side of the bridge increase with the ups and downs of the terrain. It can thus cause some pollutant particles to deposit, which is unfavorable to improving the local environment. Results of this study are intended to provide theoretical support to the construction of green freeways and the improvement of the freeway environment.

Keywords Freeway · Bridge · Undulating terrain · Wind field

1 Introduction

The rapid development of the freeway has driven the development of the region and even the national economy, which has produced a huge social effect [1]. At the same time, the construction of the freeway will inevitably affect the surrounding wind environment. The freeway bridge section not only spans different terrains and plays the role of interactive communication between regions, but also brings changes in the regional wind field [2]. At present, the research in the wind field on the freeway bridge section under undulating terrain conditions is not yet mature. Through numerical simulation and analysis, the paper studies the influence of the height of the undulating terrain, the distance between undulating terrain and the bridge, the

Y. Jia · P. Cheng · C. Han (✉)
School of Civil Engineering, Beijing Jiaotong University, Beijing 100044, China
e-mail: 17121035@bjtu.edu.cn

location of the undulating terrain and other parameters in the wind field on the bridge section of the freeway and compares it with the regional wind field under the flat terrain. The results of this study are intended to provide theoretical support to the construction of green freeways and the improvement of the freeway environment.

2 The Numerical Analysis Model

The entrance of the numerical wind tunnel is located on the left wall of the calculation domain and the speed inlet boundary conditions are selected. The direction of the wind is horizontal to the right. The average wind profile for the index rate [3] is:

$$\overline{V}(z) = \overline{V}_{10}\left(\frac{z}{10}\right)^{\alpha} \tag{1}$$

in which $\overline{V}_{10}$ is the reference speed at the height of 10 m and α is the roughness category index corresponding to various topography.

Turbulence intensity boundary conditions at the inlet are described by turbulent kinetic energy and turbulent dissipation rate [4, 5]. The turbulent kinetic energy and turbulent dissipation rate of the two-equation turbulence physical model can be given by the hypothesis of equivalent boundary layer:

$$k(z) = 1.5[I(z)\bar{u}(z)]^2 \tag{2}$$

$$\varepsilon(z) = \frac{C_\mu^{0.75}k(z)^{1.5}}{l} \tag{3}$$

where $C_\mu = 0.09$, and $I(z)$ is the turbulence intensity profile at the inlet, which should refer to the "Loading Codes for Building Structures"; $\bar{u}(z)$ is the average flow rate and l is the turbulent characteristic scale at the entrance.

Introduce the boundary conditions of fully developed outflow, i.e., the top and side surfaces of the calculation domain are set to free slip surface. The non-sliding wall surface is used on the surface and ground of freeways.

Then the cross-section of the main beam and pier size are designed according to the "General Code for Design of Highway Bridges and Culverts" [6], in which four lanes, bridge width of 30 m, main beam with 2 m-height, guardrail height of 0.5 m, bridge calculation span of 30 m are used when the design speed is 100 km/h. Four rectangular piers are arranged in each row of the support. The size of the piers is 1.5 m × 1.5 m × 7.5 m, and the pier spacing is 6.5 m.

Set the undulating terrain contour function [7, 8] to $H[1 + \cos(\pi r/2L_1)]/2$. H is the height from the top of the slope to the ground, that is, the height of the undulating terrain. The width of the undulating terrain varies $4L_1 = 40$ m. The horizontal distance between the slope of undulating terrain and the same side fence is S, and the height of the fence is $H_0 = 10$ m.

3 Influence of Windward Side Topographic Variation in the Wind Field on the Bridge Section

3.1 Change of Wind Field When the Height of Undulating Terrain Is Different

Set $S = 5$ m in the numerical simulation. The level of $z = 7$ m is 0.5 m below the bottom of the bridge, and the contour of the wind speed is shown in Fig. 1.

As can be seen from Fig. 1, the airflow will separate and reattach when it encounters the bridge convergence occurring near both sides of the pier and the wind speed increases. The airflow passes through the bottom of the bridge and forms a narrow, low wind speed zone near behind the pier. Some particles of pollutants will deposit at a low wind speed area, which is detrimental to the improvement of the environment. When the height of the undulating terrain is small

(a) Flat terrain

(b) $H/H_0 = 0.2$

(c) $H/H_0 = 0.4$
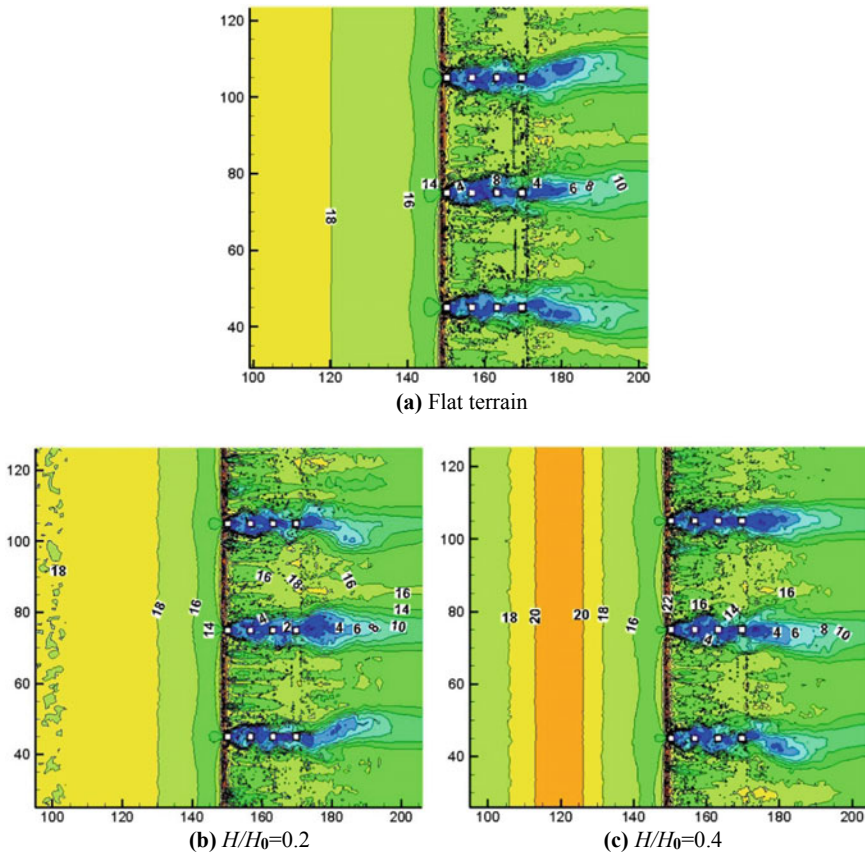
Fig. 1 Wind speed contour in the level of $z = 7$ m

($H/H_0 \leq 0.2$), the change of the wind field in the bridge area is similar to that of the flat terrain. As the height of the undulating terrain increases, the wind speed gradient between the bridge and the undulating terrain increases, and the wind field changes.

The level of $z = 11$ m is 1.5 m above the bridge deck. The contour of the wind speed is shown in Fig. 2.

It can be obtained from Fig. 2 that when the airflow meets bridge and guardrail, the separation occurs. A portion of the airflow circulates above the guardrail and convergences when the flow comes to this location, resulting in an increase of wind speed above guardrail in the windward side. The wind speed gradient behind the guardrail is large.

(a) Flat terrain

(b) $H/H_0 = 0.2$

(c) $H/H_0 = 0.4$
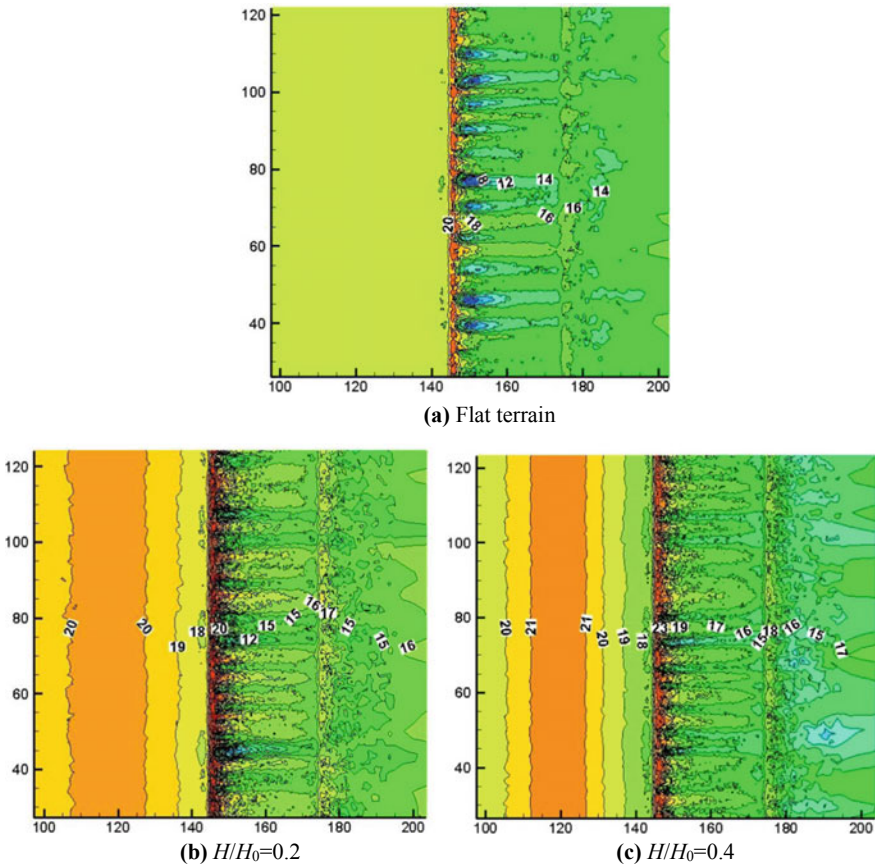
Fig. 2 Wind speed contour in the level of $z = 11$ m

3.2 Change of Wind Field When the Distance Between the Undulating Terrain and the Bridge Is Different

The wind speed isoline of the cross-section at the bridge support is shown in Fig. 3 when the distance between the undulating terrain and the bridge is 5 m and 10 m, respectively.

It can be seen from Fig. 3 that in flat terrain, low wind speeds appear behind the guardrails on both sides. When $S = 5$ m and $S = 10$ m, low wind speed area appears only behind the lee side guardrail. At the bottom of the bridge, the area of low wind speed is expanding with the increase of S. In the area between the undulating terrain and the bridge, the wind speed gradient becomes smaller as S increases. The change of S has little effect in the wind field above the bridge deck.

(a) Flat terrain

(b) $S=5$m

(c) $S=10$m
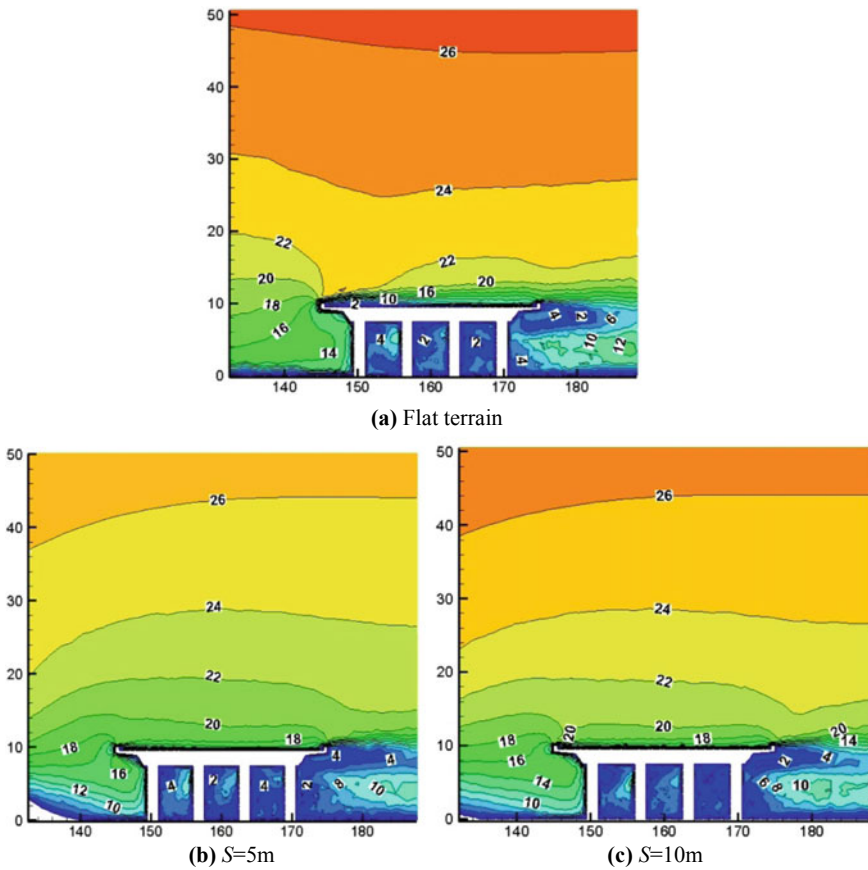
Fig. 3 Wind speed contour at the cross-section of the support

4 Influence of Lee Side Topographic Variation in the Wind Field on the Bridge Section

Set the relief terrain on the lee side to the bridge $S = 5$ m in the numerical simulation. The wind speed isoline of the cross-section at the bridge support is shown in Fig. 4.

From Fig. 4, the results of numerical simulation show that the undulating terrain on the lee side mainly affects the wind field above the bridge deck, an area within 10 m above the deck. When the height of the undulating terrain is large, the airflow circulating along the bridge deck is affected by the lee side terrain, resulting in a relatively lower wind speed near the deck, and a wind speed gradient area with dense wind speed contours appearing above the deck. As the height of the undulating terrain increases, the range of wind speed gradient regions expands.

The wind speed isoline of the cross-section at the bridge support is shown in Fig. 5 when the distance between the undulating terrain and the bridge is 5 m and 10 m, respectively.

Figure 5 shows that with the increase of distance S between the undulating terrain and bridge on the lee side, the range of the low-speed wake region at the rear side of the main beam is enlarged. Near the bridge deck, the minimum wind speed increases. The change of S has little effect in the windward wind field.

(a) Flat terrain   (b) $H/H_0 = 0.6$

Fig. 4 Wind speed contour at the cross-section of the support

(a) Flat terrain

(b) S=5m
(c) S=10m
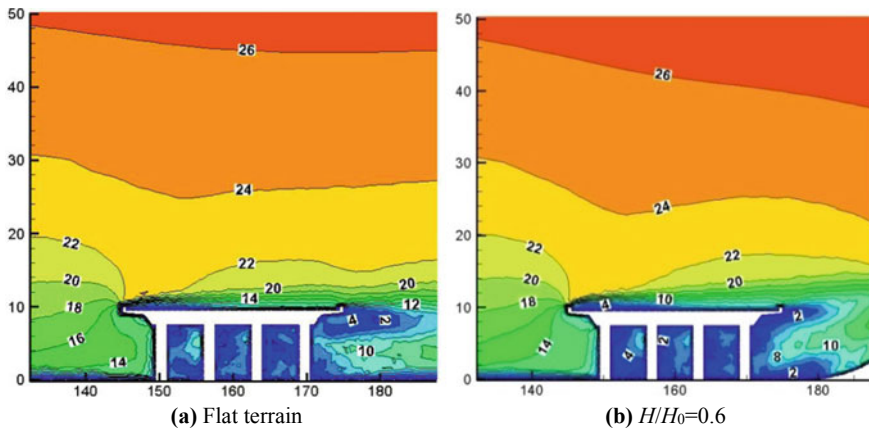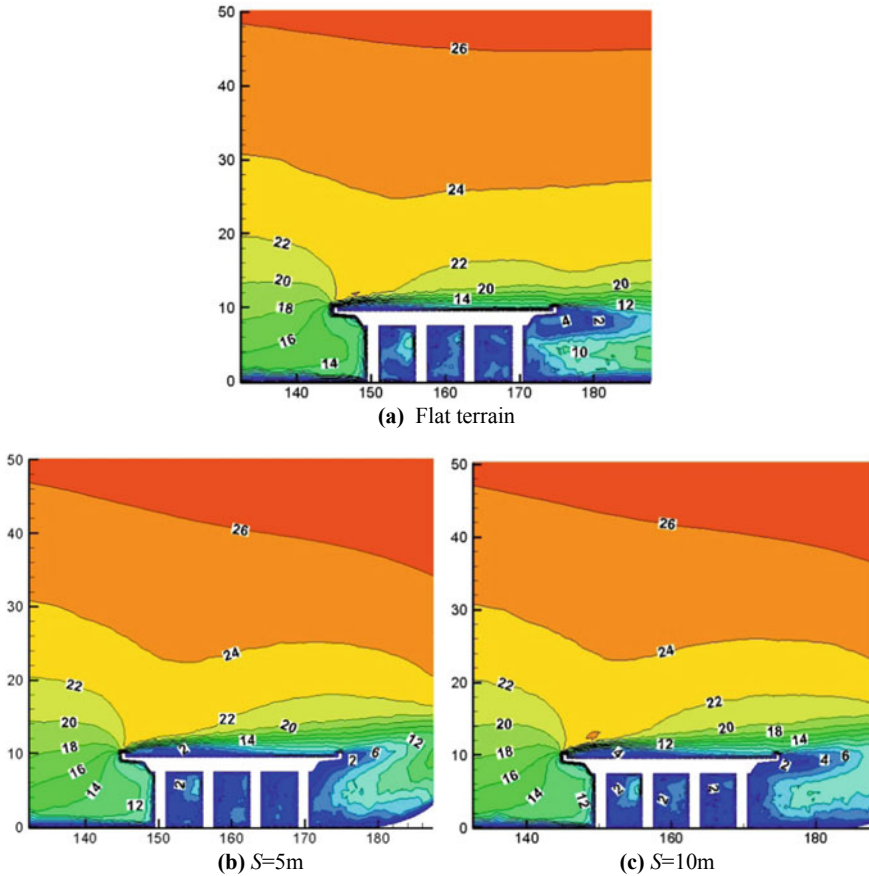
Fig. 5 Wind speed contour at the cross-section of the support

5 Influence of Both Sides Topographic Variation in the Wind Field on the Bridge Section

Assume one undulating terrain on each side, from the same side fence $S = 5$ m. The wind speed isoline of the cross-section at the bridge support is shown in Fig. 6.

Figure 6 shows that when the two sides are undulating terrain, the speed gradient increases in both sides of the bridge. The range of the low-speed zone on the lee side of the bridge pier expands and the vortex scale increases. The wind speed changes more gently above the bridge deck.

The wind speed change of $z = 3$ m is shown in Fig. 7 when the horizontal distance between both sides terrain and the same side fence is 5 m and 10 m, respectively.

(a) Flat terrain   **(b)** $H/H_0=0.6$

Fig. 6 Wind speed contour at the cross-section of the support

(a) Flat terrain

(b) $S=5$m   **(c)** $S=10$m
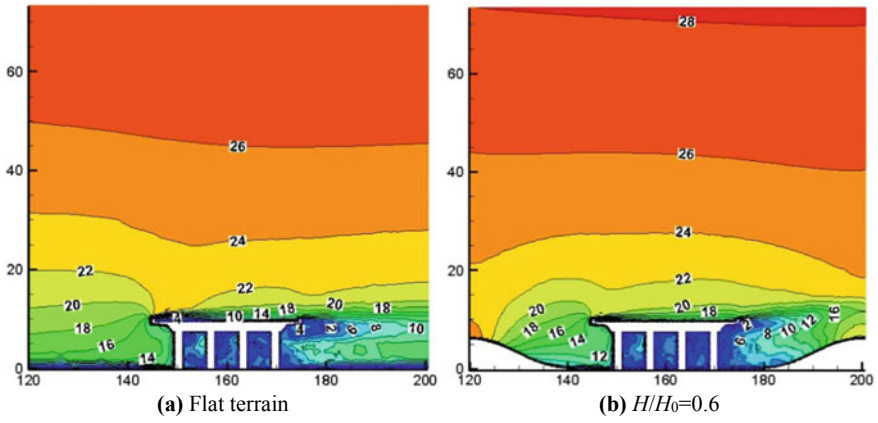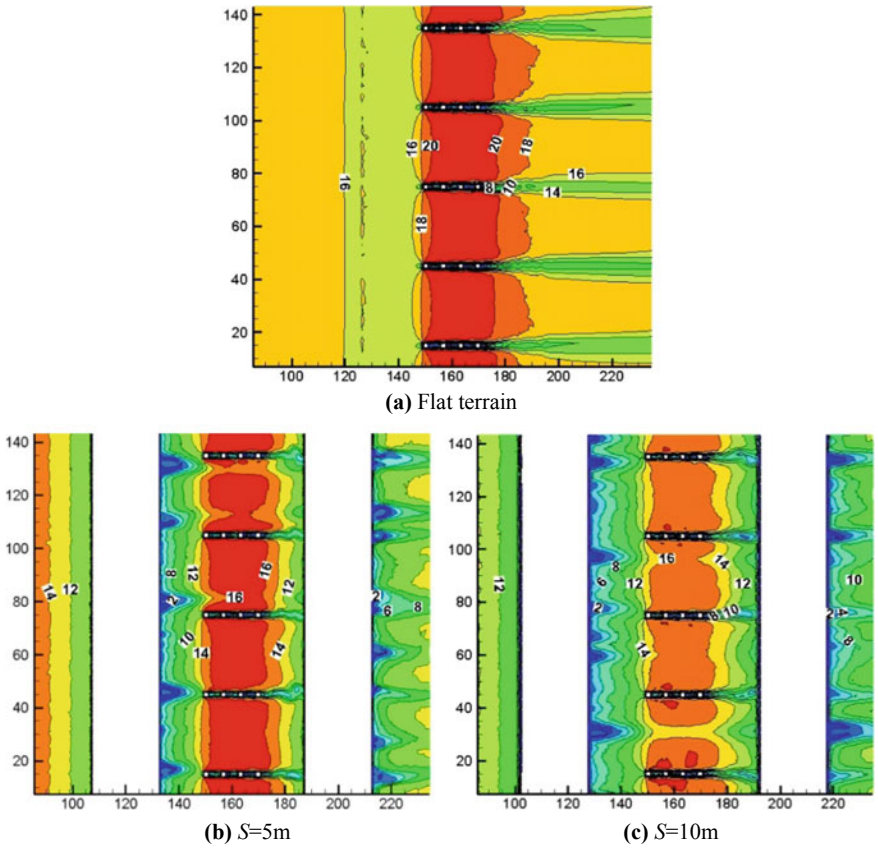
Fig. 7 Wind speed contour in the level of $z = 3$ m

A comparative analysis of Fig. 7 shows that the maximum wind speed at the bottom of the bridge is 20 m/s due to no terrain obstacles when there is flat terrain. When $S = 5$ m and $S = 10$ m, the maximum wind speed at the bottom of the bridge is 16 m/s. Numerical analysis shows that the undulating terrain on both sides has a greater impact in the wind field at the bottom of the bridge when $S \leq 10$ m.

6　Conclusions

The results of this study can be summarized as follows:

- The undulating terrain on the windward side and both sides has an impact in the wind field of the entire region.
- The influence of undulating terrain on the lee side to the wind field mainly lies in the area within 10 m above the bridge deck and the lee side of the bridge.
- As the height of the terrain increases, the range of the low-speed zone on the lee side and around the bridge pier expands and the vortex scale increases.
- As the distance S between the undulating terrain and the bridge increases, the range of the low-speed zone on the lee side of the bridge increases. Low-speed areas and vortexes in the wind field are two obvious factors impeding the diffusion of pollutant particles and will have an impact on the regional environment.

References

1. Fan Z, Xiao C (2006) Analysis of the systematic effect of expressway construction on national economic and social development. J Highw Transp Res Dev 23(5):155–158
2. Ma J, Sun S, Yang Q et al (2014) A summary of academic research on bridge engineering in China. China J Highw Transp 27(5):1–96
3. Zhou C, Yang T, Liu L et al (2007) Discussion on the simulation process of long span bridge wind field. J Hunan Inst Eng (Nat Sci Ed) 17(3):88–90, 94
4. Wang D, Zhou Y, Tan P et al (2011) Study on large-eddy simulation of wind pressure distribution and flow characteristics of three-dimensional blunt body structure. J Aerodyn 29(3):270–279
5. Yakhot V, Orzag SA (1986) Renormalization group analysis of turbulence: basictheory. J Scient Comput. 1:3–11
6. JTG D60-2004 (2004) General code for design of highway bridges and culverts. Ministry of Transport of the People's Republic of China, Beijing
7. Chen P (2007) Numerical study on the influence of terrain on the wind field in mountain hill area. Zhejiang University, Zhejiang
8. Takahashi T, Kato S, Murakami S et al (2005) Wind tunnel tests of effects of atmospheric stability on turbulent flow over a three-dimensional hill. J Wind Eng Ind Aerodyn 93(2):155–169

Parametric Study on Dynamic Performance of Transition Section of Steel Spring Floating Slab Track

Shuwen Ren[iD], **Congcong Cui**[iD] **and Deyun Ding**[iD]

Abstract The steel spring floating slab track (SSFST) has been adopted in lots of track engineering due to good vibration isolation efficiency; however, how to reasonably handle with the transition section of SSFST is still a big problem in the design phase. In this paper, the influence of various parameters on the dynamic performance of transition section of SSFST is researched. These parameters related to the layout of steel spring, the stiffness of steel spring, neighboring track style and the speed of passing train are considered as different factors including different level values. Based on the theory of orthogonal experimental design, a parametric study is performed by a series of three-dimensional finite element dynamic models, considering the moving loads of wheel set are directly applied on the railhead surface. The displacement and acceleration of the rail and slab are obtained to analyze the dynamic performance of the transition section of SSFST. The numerical results could be regarded as a reference for the design of the transition section of SSFST.

Keywords Steel spring floating slab track · Transition section · Dynamic performance · Orthogonal experiment · Finite element dynamic model

1 Introduction

With the rapid development of high-speed railway and urban rail transit in China, the problem of vibration and noise becomes an increasingly prominent focus. When the train passes, the vibration is transmitted to the foundation of building structures

S. Ren (✉)
Railway Engineering Design and Research Institute, China Railway Engineering Consulting Group Co., Ltd., Beijing 100055, China
e-mail: 156054218@qq.com

C. Cui · D. Ding
Beijing Jiuzhouyigui Shock and Vibration Isolation Technology Co., Ltd., Beijing 100070, China

through the track structure. To a certain extent, vibration in sensitive areas will affect the equipment, residents and historical buildings. In order to solve the environmental vibration problem caused by trains, a large number of track structures are equipped with steel spring floating slab tracks (SSFST) and have a certain damping effect. Since the SSFST was firstly used in 1965, it has been largely applied in underground railway projects. Hitherto, it is more than 30 cities in China to use SSFST to mitigate vibrations induced by metro trains.

According to field test, the damping effect of rubber damping pad on ballastless track on bridge was studied [1]. Different proposals for the three parameters of damping pad thickness, elastic modulus and vertical stiffness of fastener were put forward [2]. Studies [3–7] have done relevant research on its dynamic performance. A great amount of efforts have been made to study the dynamic characteristics of SSFST. SSFST could isolate vibration level up to 15 decibels, and its eigenfrequency is usually less than 15 Hz. However, how to reasonably handle with the transition section of SSFST is still a big problem in the design phase.

Based on the theory of orthogonal experiment, the dynamic model of three-dimensional finite element is established. Dynamic displacement and acceleration of rail and floating slab under different parameters are obtained by dynamic simulation of moving wheel load. The main factors affecting the dynamic performance of the transition section are analyzed.

2 Project Outline

The length of floating slab is 25 m, the distance between fasteners is 0.625 m, the distance between springs is 1.25 m, the reference load of vehicles is 16 tons, and the moving load is 80 kN of single-wheel mass. The five main factors including the additional spring setting, spring stiffness, adjacent track form (the track structure is condensed into three types of vibration reduction measures including no vibration reduction measures, medium vibration reduction measures and advanced vibration reduction measures), train speed and floating slab thickness are considered in this paper. Parameter settings for different transition sections are listed in Table 1.

Table 1 Parameter settings for different transition sections

Section type	Parameter settings			
Steel spring floating slab section	Floating slab thickness (m)	0.28	0.34	0.40
	Fastener stiffness (kN/mm)	35		
	Spring stiffness (kN/mm)	5.3	6.9	8.5
	Additional spring settings	Fig. 1a	Fig. 1 b	Fig. 1 c
Non-steel spring floating slab section	Fastener stiffness (kN/mm)	10	25	40
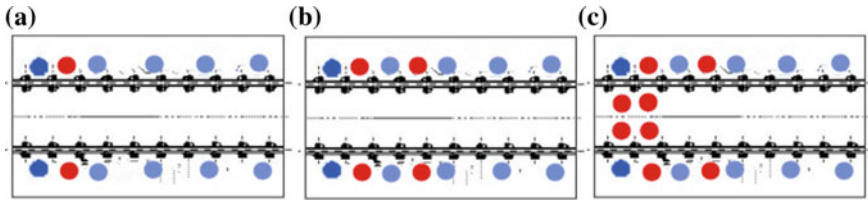
Fig. 1 Additional spring settings of the floating slab track

Additional spring settings of the floating slab track are shown in Fig. 1, and the red circles indicate the additional steel springs.

3 Establishment of Finite Element Models

The ANSYS finite element software was used to simulate the models. The SHELL163 element was used to simulate the floating slab, the BEAM188 element was used to simulate the rails, and the COMBINE14 element was used to simulate the fasteners. The finite element and related key points are shown in Fig. 2. The nodes at the transition of the finite element model are selected for analysis. The key point of the rail is G1, and the key point on the floating slab is F1. The modal analysis of the finite element model is shown in Fig. 3. The vibration type is mainly dominated by the vibration of the floating slab.
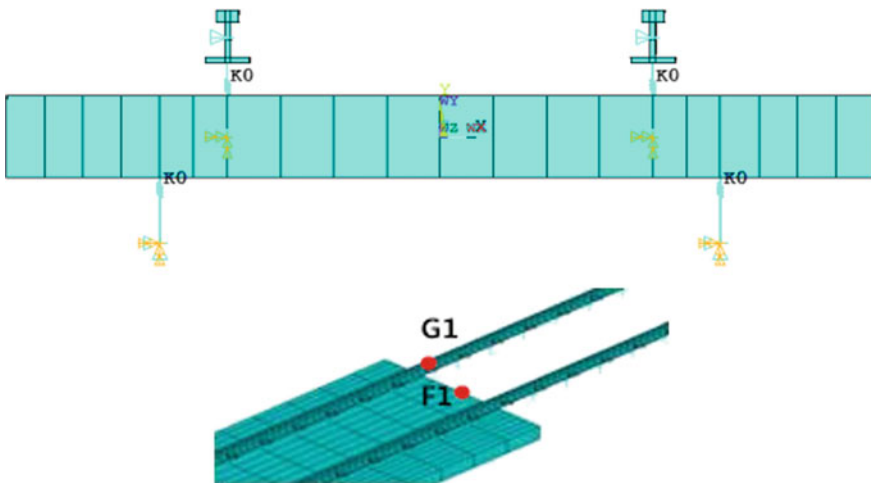
Fig. 2 Finite element model
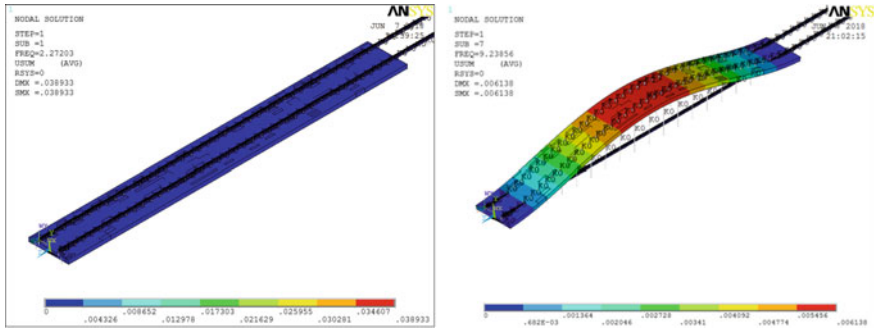
Fig. 3 Part of the vibration shapes

4 Orthogonal Test

The orthogonal experimental design is a highly efficient, rapid and economic method usually used to study a multifactor and multilevel problem. The representative tests are selected from many experiments, which greatly reduce the number of samples. In this paper, according to the five factors of additional spring setting, spring stiffness, adjacent track form, train speed and floating slab thickness, the orthogonal table $L_{18}3^7$ of seven factors and three levels is selected for analysis in the orthogonal table. After the row is finished, the remaining unranked columns are empty columns that can be used to make an error term. Table 2 lists a total of 18 combinations No. 1 through No. 18. These combinations also named samples are performed by the three-dimensional finite element method.

4.1 Natural Frequency Analysis

To use ANSYS software, three-dimensional modal analysis of the floating slab structure was performed. The natural frequencies of the track under different parameters were obtained, and the influence of each parameter on the natural frequency of the steel spring floating slab was analyzed. The natural frequency and the relevant test number are shown in Table 3.

The relevant data were analyzed by the extreme difference method, as shown in Fig. 4 to visualize the value. From the overall trend, we can see that the fastener stiffness range is small and can be used as a secondary factor. In the study of vibration reduction and noise reduction, it is not an important consideration. With the increase in the natural frequency, the additional spring setting becomes an important factor affecting the natural frequency. Therefore, it is preferable to change the low-order frequency of the floating slab rail to adjust the floating slab thickness and the stiffness of the spring. To change the high-order frequency of the floating slab rail, the additional spring setting of the floating slab track is preferred.

Table 2 Orthogonal design table

Test no.	Factors				
	Floating slab thickness (m)	Spring stiffness (kN/mm)	Additional spring settings	Fastener stiffness (kN/mm)	Speed (km/h)
1	1 (0.28)	1 (5.3)	1 (Fig. 1a)	1 (10)	1 (40)
2	1	2 (6.9)	2 (Fig. 1b)	2 (25)	2 (60)
3	1	3 (8.5)	3 (Fig. 1c)	3 (40)	3 (80)
4	2 (0.34)	1	1	2	3
5	2	2	2	3	3
6	2	3	3	1	1
7	3 (0.4)	1	2	1	3
8	3	2	3	2	1
9	3	3	1	3	2
10	1	1	3	3	2
11	1	2	1	1	3
12	1	3	2	2	1
13	2	1	2	3	1
14	2	2	3	1	2
15	2	3	1	2	3
16	3	1	3	2	3
17	3	2	1	3	1
18	3	3	2	1	2

Table 3 Partial natural frequencies

Test no.	Natural frequency (Hz)					
	Basic	Third	Fourth	Sixth	Tenth	Fifteenth
1	10.328	32.353	46.673	76.598	92.692	114.25
2	12.215	33.997	47.874	77.796	116.25	143.94
3	13.144	34.329	48.197	77.883	118.86	143.74
4	9.6487	37.294	54.854	84.885	93.116	124.75
5	11.17	38.058	55.207	91.385	132.72	147.53
6	11.795	38.946	56.571	93.692	142.62	166.89
7	9.1102	42.583	63.025	105.63	137.93	151.01
8	10.401	43.116	63.673	107.11	166.98	172.81
9	11.271	43.258	63.477	84.892	105.54	128.51
10	9.5808	42.914	63.288	105.95	166.93	175.41
11	11.554	32.798	46.957	76.693	92.649	113.82
12	12.948	33.781	47.871	78.184	117.28	132.75
13	10.048	37.645	54.923	91.219	132.72	147.52
14	10.959	37.809	55.009	91.151	139.19	165.74
15	11.806	38.003	55.328	84.886	93.220	124.75
16	9.3980	42.851	63.498	107.01	165.85	172.77
17	10.300	42.949	63.268	84.892	105.46	128.41
18	11.027	43.038	63.364	105.83	137.94	151.14
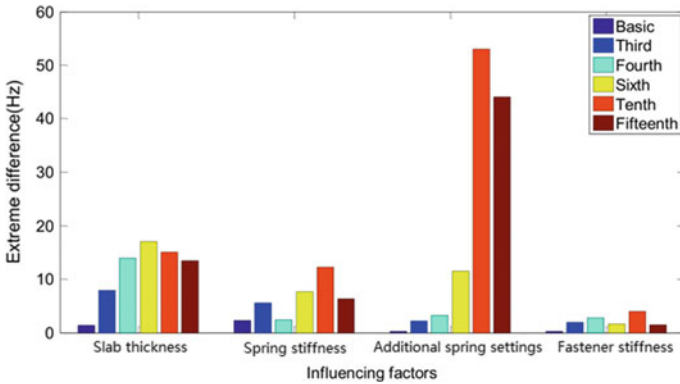
Fig. 4 Extreme difference analysis

4.2 Dynamic Characteristics Analysis

Select the axle weight of the vehicle as 16 tons, that is, the single-wheel mass value of the moving load is 80 kN. Consider the six-carriage loading on the finite element model, and extract the nodes on the rail. The time-domain curves for slab acceleration (left) and rail vertical displacement (right) are shown in Fig. 5. Obviously, the traces of the wheels passing through are clearly consistent with those of other documents. The correctness of the model is verified. By loading different test numbers, the dynamic response characteristics under different combinations are shown in Table 4.

Through the range analysis of the position of the rail and the position of the floating slab, the influence of different factors on the dynamic behavior of the system is studied when the track of the spring floating slab is connected to different tracks, and the measures taken in the transition are explored, as shown in Figs. 6 and 7.
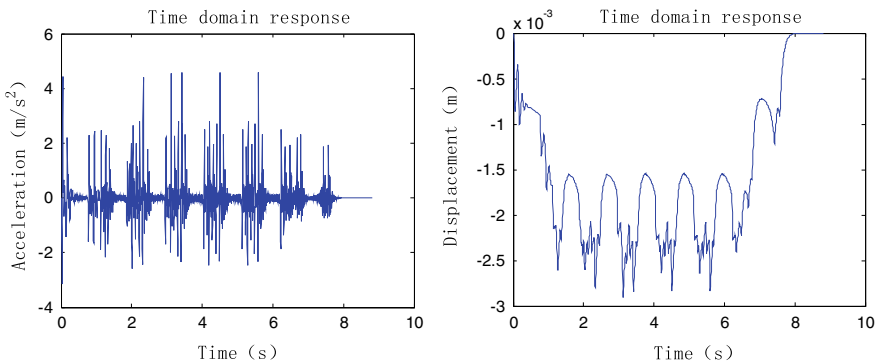
Fig. 5 Slab acceleration (left) and rail vertical displacement (right)

Table 4 Vibration response of different parts

Test no.	Rail		Floating slab	
	Displacement (m)	Acceleration (m/s^2)	Displacement (m)	Acceleration (m/s^2)
1	0.00365	100.98	0.00324	4.92
2	0.00165	37.23	0.00107	3.52
3	0.00169	47.43	0.00165	3.79
4	0.00365	38.59	0.00345	3.00
5	0.02234	38.08	0.00214	3.00
6	0.00222	104.89	0.00188	2.42
7	0.00398	53.55	0.00373	4.48
8	0.00256	107.61	0.00207	2.87
9	0.00248	29.75	0.00239	2.31
10	0.00249	35.02	0.00246	2.87
11	0.00293	43.18	0.00283	3.29
12	0.00208	102.34	0.00181	2.67
13	0.00249	111.69	0.00248	2.78
14	0.00273	32.13	0.00241	2.56
15	0.00236	39.95	0.00253	3.09
16	0.00359	59.33	0.00257	4.24
17	0.00274	111.69	0.00263	2.76
18	0.00238	30.77	0.00232	2.58

The results show that the speed of the train is the most important factor affecting the value of the rail vibration acceleration when the vehicle passes through the transition section. The influence of the thickness of the floating slab, the stiffness of the spring, the additional spring setting and the stiffness of the fastener is weak. In the position of the transition section of the rail, the factors that affect the value of the rail displacement are more consistent, but the change of the spring stiffness has great influence on the displacement and acceleration of the floating slab bed, and the influence of the thickness of the floating slab, the stiffness of the fastener and the running speed of the train is the second.
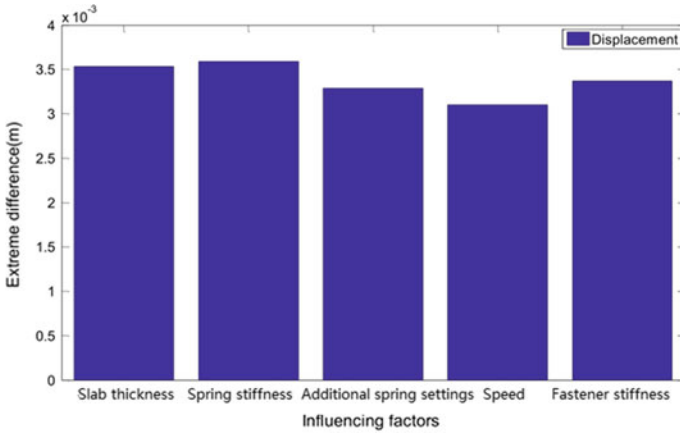
(a) Displacement analysis
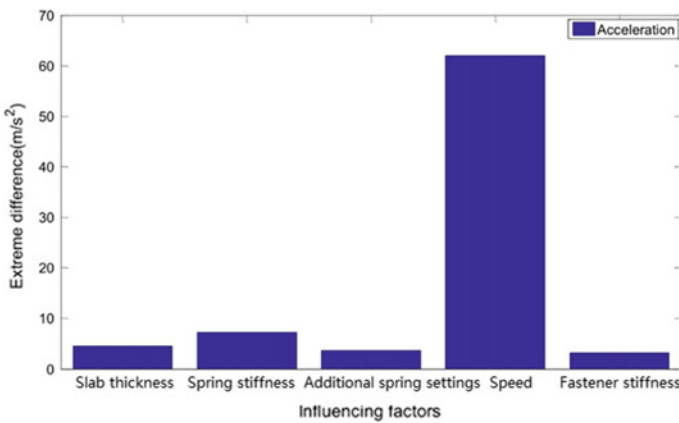
(b) Acceleration analysis

Fig. 6 Extreme difference analysis at rail

5 Conclusions

The following conclusions have been drawn from the above analysis:

(1) Additional spring setting becomes an important factor affecting the natural frequency, compared with other factors including slab thickness, spring stiffness and fastener stiffness.
(2) When the train passes through the transition section, running speed is the most important factor affecting vibration acceleration on the rail; however, the change of spring stiffness has a greater impact on the floating slab.

(a) Displacement analysis

(b) Acceleration analysis
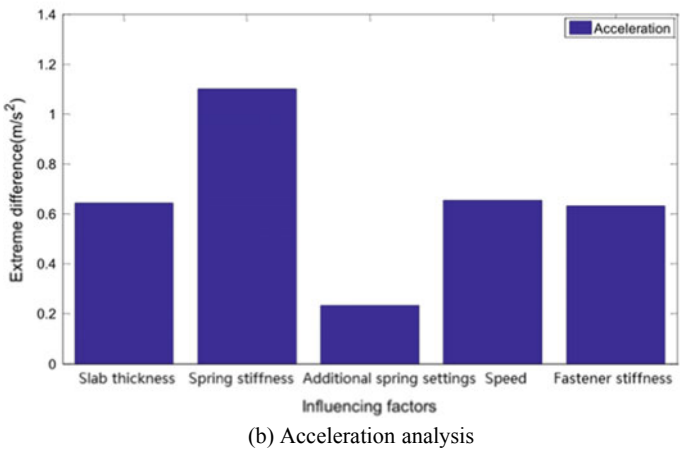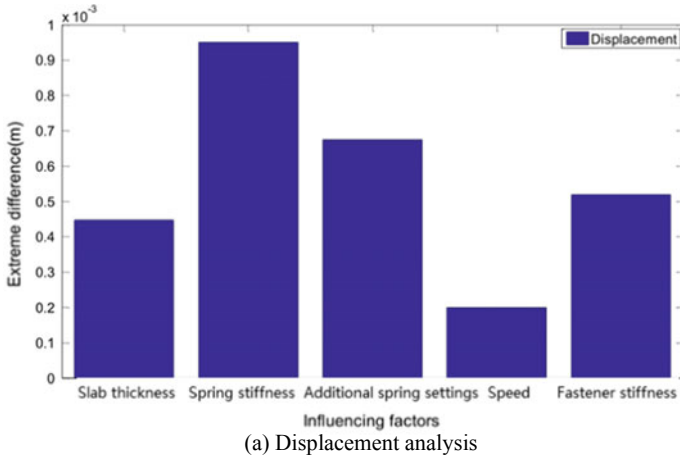
Fig. 7 Extreme difference analysis at floating slab

References

1. Zhao C, Wang P (2013) Experimental study on vibration-reducing performance of rubber cushion on ballastless track over bridge. China Railw Sci 34(04):8–13
2. Liu S (2012) Study on the vibration and vibration isolation effect of vibration damper pad floating track. Beijing Jiaotong University
3. Chuanzhi G, Liu Z (2011) Design analysis of spring floating slab track transition section of urban rail transit. Urban Rail Transit Res 14(02):39–41 + 75

4. Wang J, Wang J, Yin X, Zhang B (2007) Design of steel spring floating slab track in shield machine. Railw Stand Des (10):29–32
5. Sun X, Liu W, Zhang B (2005) Application of floating slab track structure to vibration and noise reduction in urban rail transit. Chin J Saf Sci (08):65–69 + 114
6. Lu J (2005) Application of steel spring floating slab track bed at linping road station of Shanghai rail transit. Railw Build Technol (02):61–63
7. Zhang B, Xu Z (2002) Application of vibration isolation technology with spiral steel spring floating slab in vibration and noise reduction of urban rail transit. China Railway Science 03:70–73

Vertical Vibration Propagation in Periodic Frame Structures

Zhibao Cheng, Zhongyuan Huang and Zhifei Shi

Abstract In this work, the periodic structure theory is used to analyze the vertical vibration properties in periodic frame structures. The simplified model of the periodic unit cell is built, and governing equations for vertical vibration/waves propagation in the infinite system are derived. With the help of the state space transfer matrix method/SS-TMM, governing equations of the considered system are solved, from which the dispersion curves are obtained and attenuation zones are observed. Numerical simulations are conducted to investigate the dynamic property of the finite periodic frame structure. It is found vertical vibrations are propagated in frame structure selectively. This filtering effect could be used to isolate harmful environmental vibrations.

Keywords Vertical vibration · Frame structure · Periodic structure theory

1 Introduction

With the rapid development of the urban rail traffic in China, the nettlesome environmental vibration problem induced by rail traffic draws more and more researcher's attention. Over the past ten years, Prof. Shi's and his co-workers in Beijing Jiaotong University introduced the periodic structure theory in the field of solid-state physics into the field of civil engineering and proposed various vibration reduction methods, like the periodic pile, periodic isolation wall, periodic concrete panel and so on [1–5]. Basically, almost all of these methods aim to isolate the vibration propagation in the wave path [1].

Recently, using the periodic structure theory, Cheng et al. [6] conducted a comprehensive theoretical and numerical study on the wave dispersion properties of multi-story frame building structures. In that work, attentions were focused on the

Z. Cheng (✉) · Z. Huang · Z. Shi
Institute of Smart Material and Structure, School of Civil Engineering,
Beijing Jiaotong University, Beijing 100044, China
e-mail: chengzb@bjtu.edu.cn

959

horizontal seismic vibrations. And, horizontal vibration propagation properties in multi-story building structures were investigated. In this work, our attention will be focused on the environmental vibrations in the vertical direction. Vertical vibration propagation properties in the widely used multi-story frame structure will be investigated.

It is obvious that frame structure can be viewed as a periodic system with its standard floor arranged in vertical direction one-by-one. In Sect. 2, the theoretical model of the periodic frame structure is built, and governing equations for vertical vibration/waves propagation in the system are derived. In Sect. 3, with the help of the state space transfer matrix method/SS-TMM, governing equations of the considered system are solved, from which the dispersion curves are obtained and attenuation zones are observed. In Sect. 4, numerical simulations are conducted to investigate the dynamic property of the finite periodic frame structure in the frequency domain. It is found that geometrical periodicity endows the frame structure a special filtering effect of the elastic vibrations/waves. With proper design, frame structures could be used as an isolation system, which presents a new way to design civil structures of special functions.

2 Theoretical Model

Consider vertical vibration propagating in an N-story reinforced concrete frame building. For the reason of simplicity, reinforced concrete is taken as a homogeneous material, whose Young's modulus, mass density and Poisson ratio are 2.5×10^{10} Pa, 2500 kg/m³ and 0.2, respectively. Figure 1 shows the dimensions of the buildings. When the vertical vibration reaches the column-beam corner, parts of the vibration energy are reflected, parts are absorbed by the floor slab, others passed through.

Practically, vertical vibrations in different columns are independent, and the total response of the floor is the sum of incoherent contributions from each column. Here, from the reason of simplicity, it is assumed that the four columns are vibrated in the same manner. And, the four columns will be theoretically simplified as an equivalent homogeneous column. Governing equation for vertical vibration propagating in the equivalent column can be given as

$$\rho A \frac{\partial^2 u(z,t)}{\partial t^2} = \frac{\partial}{\partial z}\left(EA \frac{\partial u(z,t)}{\partial z}\right) \tag{1}$$

Here, $u(z,t)$ is the displacement; ρ, E are the mass density and Young's modulus of the reinforced concrete, respectively; A is the sum of section area of the four columns.

Further, the floor slab is replaced by using an equivalent mass-spring system. In detail, the floor slab is simulated by using the thin plate theory. The thickness of the floor slab is 0.1 m. Governing equation of the floor slab is

Fig. 1 Vertical vibration propagating in an N-story reinforced concrete frame building
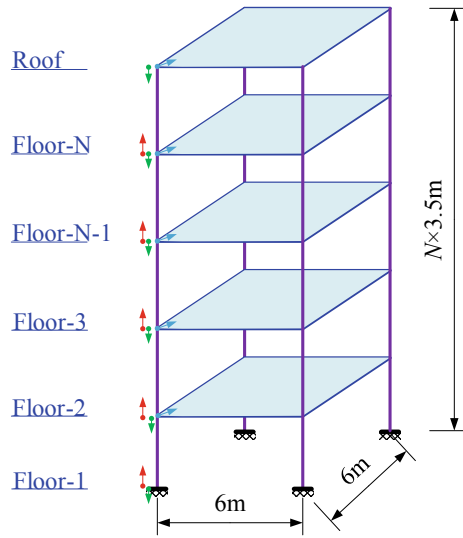
$$D\nabla^4 w(x,y,t) + m\frac{\partial^2 w(x,y,t)}{\partial t^2} = -mI(x,y)\ddot{w}_g(t) \tag{2}$$

in which $D = Eh^3/(12(1-v^2))$ is the bending stiffness of the floor slab; $w(x,y,t)$ is the deflection of the floor slab; $m = \rho h$ is the mass per unit area of the floor slab; $\nabla = (\partial/\partial x, \partial/\partial y); I(x,y) = 1$, $\ddot{w}_g(t)$ is the time history of the vertical excitation.

Simply supported boundary is used to simulate the dynamic performance of the floor slab. Theoretically, the eigenfrequencies and the normal mode shape functions of the simply supported plate can be given as

$$\omega_{ij}(x,y) = \pi^2\sqrt{\frac{D}{m}}\left(\left(\frac{i}{a}\right)^2 + \left(\frac{j}{b}\right)^2\right) \tag{3}$$

$$\phi_{ij}(x,y) = \sin\left(\frac{i\pi x}{a}\right)\sin\left(\frac{j\pi y}{b}\right) \tag{4}$$

Here, a and b are the two side lengths of the rectangular plate; i and j are two real number.

And, the modal mass M_{ij} and the modal stiffness K_{ij} can be given

$$M_{ij} = \iint_{\Omega} \rho h (\phi_{ij})^2 d\Omega = \frac{abm}{4} \tag{5}$$

$$K_{ij} = M_{ij}(\omega_{ij})^2 \tag{6}$$

Table 1 gives the mode shapes corresponding to all eigenfrequencies below 100 Hz. Further, the mass M_{ij}^e and stiffness K_{ij}^e of the equivalent single freedom system can be obtained

$$M_{ij}^e = \frac{abm}{4}\left[\frac{4}{ij\pi^2}(\cos i\pi - 1)(\cos j\pi - 1)\right]^2 \tag{7}$$

$$K_{ij}^e = M_{ij}^e(\omega_{ij})^2 \tag{8}$$

And the mass participation coefficient ζ_{ij}^e can be obtained

$$\zeta_{ij}^e = M_{ij}^e/M \tag{9}$$

3   Dispersion Calculations

The theoretical model of the considered nine-story reinforced concrete frame building can be extended to infinite periodic system, as shown in Fig. 2a. Dispersion property of the longitudinal wave propagating in the infinite periodic system is considered. Governing equation of the considered system is given in Eq. (1). Introducing the state variable $\boldsymbol{Y} = \{u, \sigma\}^{\mathrm{T}}$, the governing equation Eq. (1) can be written as

$$\frac{\mathrm{d}\boldsymbol{Y}}{\mathrm{d}z} = \boldsymbol{A}\boldsymbol{Y}. \tag{10}$$

Here, A is the state matrix of the system, which is

$$\boldsymbol{A} = \begin{bmatrix} & \frac{1}{EA} \\ -\rho A\omega^2 & \end{bmatrix}. \tag{11}$$

Therefore, the solution of Eq. (10) can be given as
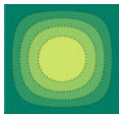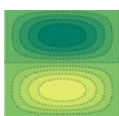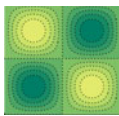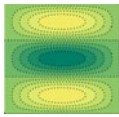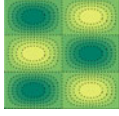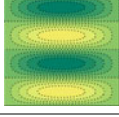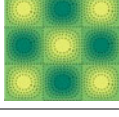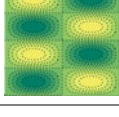
$$\boldsymbol{Y}(z) = \mathrm{e}^{\boldsymbol{A}(\omega)z}\boldsymbol{Y}(0). \tag{12}$$

Figure 2b shows the typical unit cell of the infinite periodic system. Considering the two half unit cells, the relationship between $\boldsymbol{Y}(0)$ and $\boldsymbol{Y}(h/2)$ is

$$\boldsymbol{Y}(h/2) = \boldsymbol{T}_1\boldsymbol{Y}(0). \tag{13}$$

in which $\boldsymbol{T}_1 = \mathrm{e}^{\boldsymbol{A}(\omega)h/2}$.

Table 1 Eigenfrequencies of the floor slab and its equivalent parameters

(i, j)	1, 1	1, 2/2, 1	2, 2	1, 3/3, 1	3, 2/2, 3	1, 4/4, 1	3, 3	2, 4/4, 2
f_{ij} (Hz)	8.13	20.33	32.52	40.65	52.85	69.11	73.18	81.31
M_{ij}^e (kg)	5913.21	–	–	1314.05	–	–	73	–
ϕ_{ij}								
ζ_{ij} (%)	65.7	–	–	14.6	–	–	0.81	–

Fig. 2 a The extended infinite periodic system, **b** its basic unit cell and **c** the first Brillouin zone
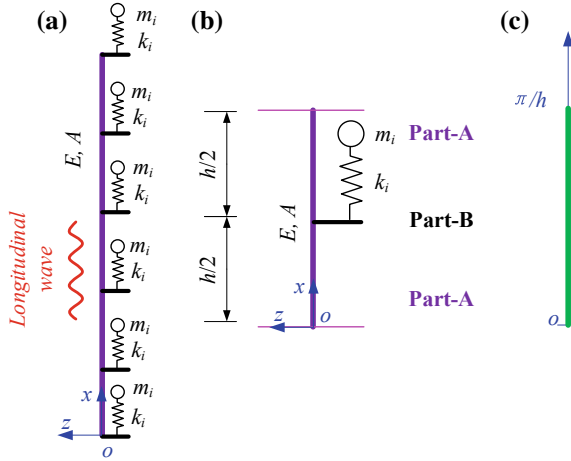
At the corner between the two half unit cells, the equilibrium equations and the compatibility conditions are

$$Y^{B+} = T_2 Y^{B-}. \tag{14}$$

Here,

$$T_2 = \begin{bmatrix} 1 & 0 \\ \frac{k}{A}\left(1 - \frac{k}{k-m\omega^2}\right) & 1 \end{bmatrix}. \tag{15}$$

Coupling Eqs. (13) and (14), the relationship between the state variable at the bottom of the unit cell and the state variable at the top of the unit cell can be obtained

$$Y(h) = T_1 T_2 T_1 Y(0). \tag{16}$$

According to the Bloch-Floquet theorem, the solution of the considered system can be given

$$Y(z, t) = Y_k(z) e^{i(Kz - \omega t)}. \tag{17}$$

in which K is the wave number; $Y_k(z)$ is a modulation function, which is a periodic function with the same periodicity as the unit cell. Therefore, we have

$$Y(z + h, t) = e^{iKh} Y(z, t). \tag{18}$$

Considering Eqs. (16) and (18), the dispersion equation of the present system can be given
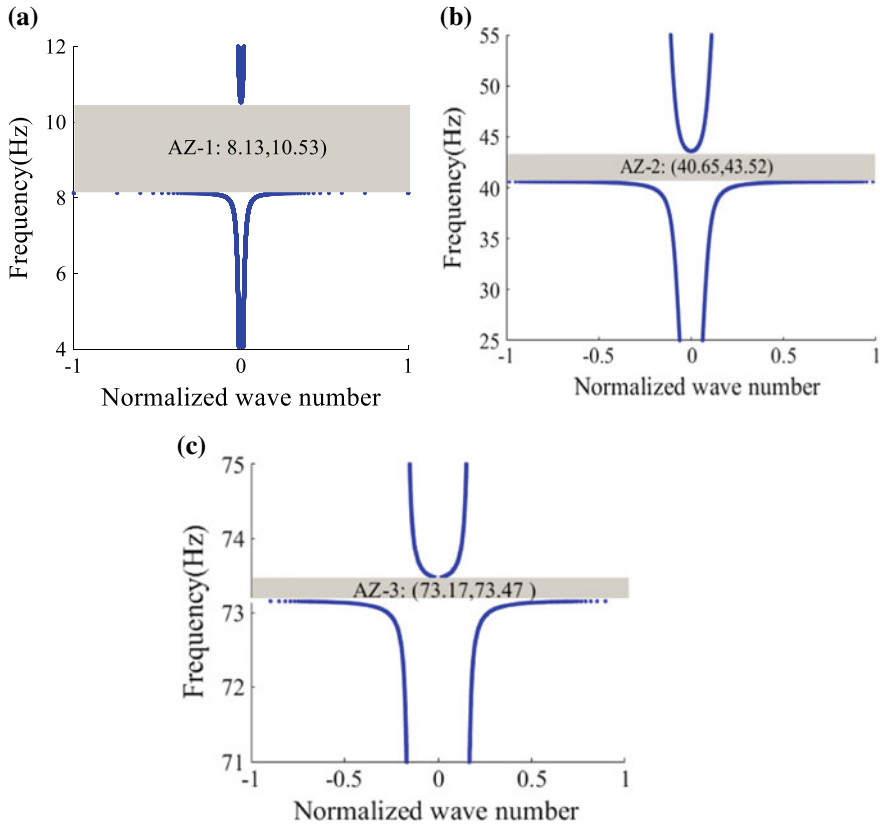
Fig. 3 Dispersion curves of the considered system with the eigenfrequency of the equivalent oscillator equaling to **a** the first eigenfrequency, **b** second eigenfrequency and **c** third eigenfrequency of the floor plate

$$\det\left(\boldsymbol{T}(\omega) - e^{iKh}\right) = \boldsymbol{0}. \tag{19}$$

For a given wavenumber, the frequency parameter can be obtained by solving the dispersion equation. And, varying the wave number in the first Brillouin zone, dispersion curves of the present system can be obtained. Figure 3 shows the dispersion curves of the extended infinite periodic system. As listed in Table 1, the three eigenfrequencies with $\zeta^e_{ij} \neq 0$ are considered. Around these three eigenfrequencies, three local resonant attenuation zones, (AZ): AZ-1 (8.13,10.53) Hz, AZ-2 (40.65, 43.52) and AZ-3 (73.17, 73.47) Hz, are opened, which means vibrations in these frequencies cannot propagate in the system.

4   Numerical Simulations

Dispersion relation indicates the dynamic property of the infinite periodic structure systems. In actual applications, all civil structures are finite. Therefore, numerical simulations will be conducted here to validate the efficiency of the periodic structure theory and to study the vertical vibration propagation property of the periodic frame structures.

Here, a nine-story frame structure mentioned above is considered. As shown in Fig. 4a, a numerical model is built by using the commercial software ANSYS. In detail, columns and floor plates are simulated by using BEAM 189 Element and PLATE 63 Element, respectively. Harmonic analysis is conducted to investigate the dynamic property of the nine-story frame structure in the frequency domain. In detail, harmonic displacement inputs in the vertical direction with unit amplitude but different frequencies are added to nodes at the bottom of the structure. The displacements in the other directions for nodes at the bottom of the structures are fixed. The steady-state responses for all nodes are calculated. The filtering effect of the periodic frame structure can be characterized by the displacement frequency response function (FRF)

$$\text{FRF} = 20\lg\left(\frac{u_i}{u_0}\right) \tag{20}$$
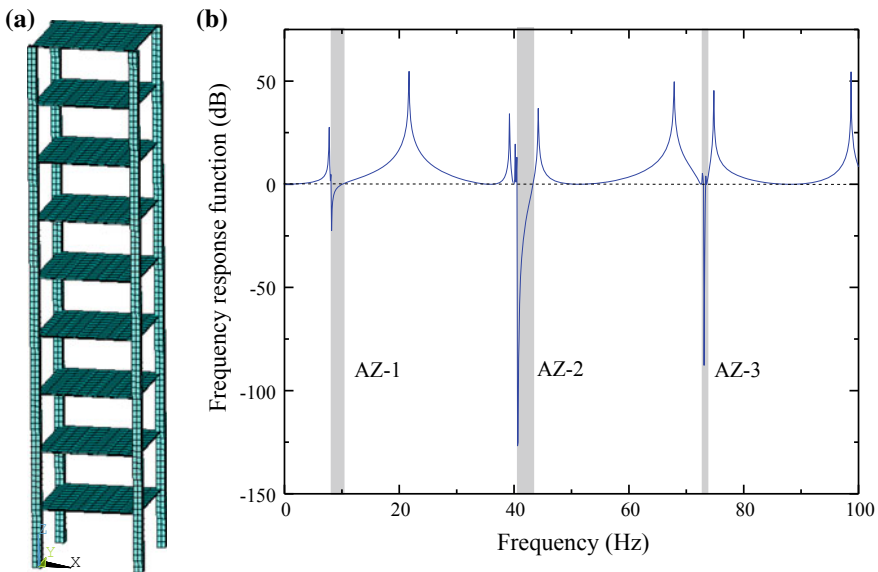
Fig. 4 **a** Numerical model built by ANSYS software, **b** displacement frequency response function

in which u_i is displacement amplitude at the top of the frame structure; $u_0 = 1$ is the displacement amplitude of the input. One may find that a negative FRF indicates that the response at the top of the frame structure is less than the excitation. The frequency regions with negative FRFs will correspond to the region of the attenuation zone.

Figure 4b shows the displacement frequency response function curves, in which vibrations in (0, 100) Hz with an interval of 0.1 Hz are considered. For the reason of comparison, a horizontal dash line corresponding to FRF = 0 is added in the figure. It is obvious that the displacement response function is smaller than zero in some frequency regions, while in other frequency regions it is larger than zero. Interestingly, these frequency regions with negative FRF match well with the attenuation zone, indicated by the gray background, in the dispersion curve. Therefore, the filtering effect of the frame structure is proved.

Further, dynamic responses of the upper structure under different vibrations are considered. As shown in Fig. 5, six cases are considered. For the first three cases, the frequency of the excitation falls in the attenuation zones; for the second three cases, the frequency of the excitation falls out of the attenuation zone. It is obvious that, when the frequency of the vertical vibration falls in the attenuation zone, vibrations are attenuated with propagation. At the roof, the amplitudes of the displacement responses are very small. In contrast, when the frequency of the vertical vibration falls out of the attenuation zone, vibrations are enlarged with propagation. At the roof, the amplitudes of the displacement responses are very large.

(a)   **(b)**   **(c)**   **(d)**   **(e)**   **(f)**

f=8.2Hz   *f*=41Hz   *f*=73.18Hz   *f*=5Hz   *f*=30Hz   *f*=86Hz
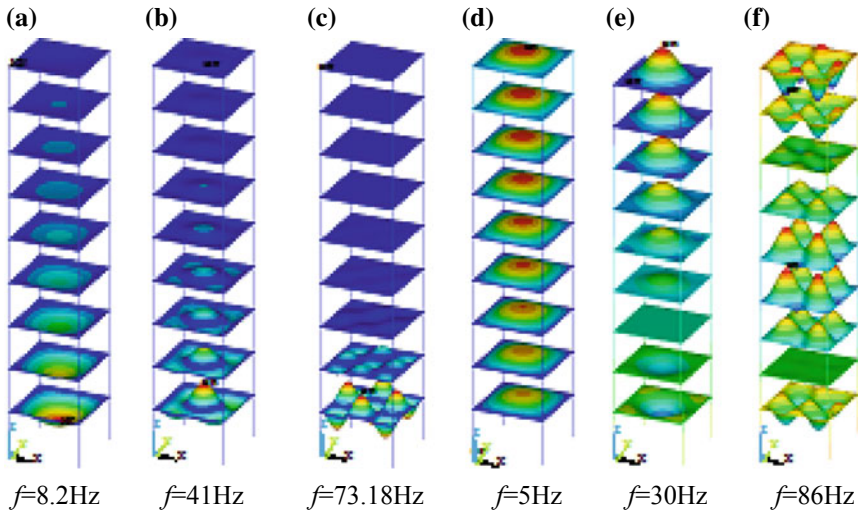
Fig. 5 Displacement responses of the frame structure under different vibrations

5   Conclusions

Geometrical periodicity endows frame structure novel dynamic dispersion properties. In this work, using the periodic structure theory, vertical vibration propagation properties in frame structures are investigated. Some conclusions can be obtained:

1. Based on reasonable assumptions, a theoretical model for vertical waves/vibration propagating in the frame structure is developed. The columns are simplified as an equivalent homogeneous beam, and the floor plate is simplified as an equivalent mass-spring system. Therefore, the periodic frame structure is simplified as a local resonant periodic structure. Dispersion equation of the simplified system is solved by developing the state space transfer matrix method.
2. Corresponding to the three eigenfrequencies <100 Hz, dispersion curves of vertical waves/vibrations propagating in the periodic frame structure are obtained. Three local resonant frequency band gaps around the three certain eigenfrequencies of the floor plate are observed.
3. Using the commercial software ANSYS, a nine-story frame structure is built. Harmonic analysis results show that when the frequency of the excitation falls in the attenuation zone, vertical waves/vibrations cannot propagate in the frame structure; however, when the frequency of the excitation falls out of the attenuation zone, vertical waves/vibrations can propagate in the frame structure freely. As using this special filtering effect, frame structure could be used to optimized by engineers to isolate the harmful environmental vibrations.

References

1. Shi Z, Cheng Z, Xiang H (2017) Periodic structures: theory and applications to seismic isolation and vibration reduction. Science Press, Beijing
2. Cheng Z, Shi Z (2014) Vibration attenuation properties of periodic rubber concrete panels. Constr Build Mater 50:257–265
3. Cheng Z, Shi Z (2013) Novel composite periodic structures with attenuation zones. Eng Struct 56:1271–1282
4. Cheng Z, Shi Z, Mo YL, Xiang H (2013) Locally resonant periodic structures with low-frequency band gaps. J Appl Phys 57:143–151
5. Huang J, Shi Z (2015) Vibration reduction of plane waves using periodic in-filled pile barriers. J Geotech Geoenvironmental Eng 141(6):04015018
6. Cheng Z, Lin W, Shi Z (2018) Wave dispersion analysis of multi-story frame building structures using the periodic structure theory. Soil Dyn Earthq Eng 106:215–230

Recent Developments of Long-Span Highway Bridges in China

Bin Yan and Jie Huang

Abstract From the Industrial Revolution, the evolution of bridge engineering has undergone more than two centuries. The development of long-span highway bridges depends on social need, design competition, structural theory, construction material and technology, etc. In the past two decades, China has become the world center of the infrastructure construction and many record-breaking bridges have been built. This paper presents a brief technical review about those significant long-span bridges in China during the past decade. The structural types in this review included arch, cable-stayed and suspension bridge. In addition, several recent completed fixed links in China were introduced. Main features are presented in three catalogs: (1) structural dimension; (2) key design feature; and (3) construction method. This review shows the recent achievements in design and construction of long-span bridges to provide a reference for new bridge design and construction in the twenty-first centuries.

Keywords Bridges · Roads and highways · Research and development · Reviews

1 Introduction

Long-span bridge often refers to a bridge with a large single span, generally more than 300 m. Typical structural types contain arch, cable-stayed and suspension. By reviewing the bridge history, it can be seen that one of the major factors leading to the construction of long-span bridges is the social need to carry a variety of transport form for spanning large physical barrier [1]. The birth of the modern long-span bridge was first driven by the rail transport in the late eighteenth century.

B. Yan · J. Huang (✉)
Department of Civil Engineering, Central South University,
Hunan 410075 Changsha, China
e-mail: huangcsu@csu.edu.cn

B. Yan
e-mail: binyan@csu.edu.cn

Several record-breaking spans in the late nineteenth century was built due to the born of auto industry. In the 1990s, the constructions of several major fixed links had a strong impact on the development of long-span bridges. The success of those long-span bridges depended on the advanced structural theory, the use of advanced material and construction technology and the creativity of master builders.

In the past two decades, the expansion of highway and railway networks in China provided a great opportunity to build long-span bridges. The experience learned from the developed countries played a key role during the design and construction of bridges. China has become a global center of infrastructure construction where many record-breaking bridges have been built. Among completed bridges for each type, the longest main span in China has reached 552 m for arch (Chaotianmen Bridge), 1080 m for cable-stayed (Sutong Bridge) and 1650 m for suspension bridge (Xihoumen Bridge). A review made by Tang and Xiang [2] introduced several significant completed projects before the year of 2005. Tang [3] also presented a brief overview about the bridge design experience of T. Y. Lin International in China. Feng [4] reviewed the history of the bridge construction in China. Ge and Xiang [5] introduced the aerodynamic feature of long-span bridges in China. Thus, this paper will mainly report the completed major long-span highway bridges in past decade from structural design perspective. The discussions of these bridges are divided into three main categories: arch, cable-stayed and suspension bridge. After a brief historical review on each type, several significant designs are reported on (1) structural dimensions; (2) key technical innovation; and (3) construction method. The objective of this paper is to recap the recent achievements such that it will provide a reference for new bridge design and construction in the twenty-first century.

2   Suspension Bridge

The construction of modern suspension bridges in China started in the 1990s, but the development of this form is very fast. The first suspension bridge is the Shantou Bay Bridge built in 1995 with a main span of 452 m. The Xiling Bridge over the Yangtze River completed in 1996 has a main span of 900 m. A similar span that opened to traffic in Guangdong province was the Humen Bridge with a main span of 888 m. Two years after, the construction of the Jiangyin Bridge in 1999 increased the main span to 1385 m. Completed in 2005, the Runyang Bridge broke the longest record with a main span of 1490 m [6]. The recently completed suspension bridges are summarized in Table 1. In this section, the technical aspects of suspension bridges will be featured by four brief case studies, including a self-anchored suspension bridge, a single-span suspension bridge, a four-span suspension bridge with three towers and a suspension bridge in the mountain region.

Table 1 Technical features of recently completed suspension bridges in China

| Bridge name	Built	Cross	Location	Main span (m)	Tower height (m)	F/L	Deck width (m)	Deck height (m)
Sanchaji	2006	The Xiang River	Changsha	70 + 132 + 328 + 132 + 70	106.2/104.4	1:5	33	3.6
Yangluo	2007	The Yangtze River	Wuhan	250 + 1280 + 440	169.8/163.3	1:10.5	38.5	3
Huangpu	2008	The Pearl River	Guangzhou	290 + 1108 + 350	190.5/226.1	1:10	41.69	3.5
Balinghe	2009	Baling River valley	Guanling	248 + 1088 + 228	186/201	1:10.3	28	2.8
Sidu	2009	The Sidu River	Badong	900 + 5 × 40	122.2	1:10	24.5	6.5
Xihoumen	2010	Xihoumen channel	Zhoushan	578 + 1650 + 485	211.2	1:10	24.5	3.5
Taizhou	2012	The Yangtze River	Taizhou	390 + 2 × 1080 + 390	200/180	1:9	39.1	3.5
Aizhai	2012	Aizhai valley	Aizhai	242 + 1176 + 116	130	1:9.6	27	7.5
Nanjing No. 4	2012	The Yangtze River	Nanjing	166 + 410.2 + 1418 + 363.4 + 118.4	230	1:9	33	3.51
Ma'anshan	2013	The Yangtze River	Ma'anshan	360 + 2 × 1080 + 360	165.3	1:9	38.5	3.5
Puli	2015	Puli valley	Xuanwei	4 × 40 + 628 + 3 × 40 + 3×40	153/138	1:10	28.5	3
Longjiang	2016	The Longjiang River	Longling	320 + 1196 + 320	169/129	1:10.5	33.5	3
Binhe Huanghe River	2016	The Huanghe River	Yingchuan	88 + 2 × 218 + 80	96	1:5	41.5	3.8
Zhixi Yangtze River	2016	The Yangtze River	Yichang	250 + 838 + 215	107	1:10	33.2	3.08
Dongting Lake	2018	Dongting Lake	Yueyang	460 + 1480 + 491	203/206	1:10	35.4	9

2.1 Sanchaji Bridge

The construction of modern self-anchored is relatively rare, which just started from the completion of the Konohana Bridge in 1990 [7]. The Sanchaji Bridge (Fig. 1a) over the Xiangjiang River is a self-anchored suspension for carrying six-lane auto traffic with a main span of 328 m. It was the longest span of self-anchored suspension bridge in China when it was completed in 2006. Main features of this bridge include (a) a five-span continuous girder with a total of 732 m was designed as stiffened girder to eliminate significant uplift force created by the anchoring of main cable; (b) streamlined steel box stiffened girder was adopted to resist lateral force from wind; and (c) concrete tie beam between the tower columns was designed as prestressed member. Key construction features are: (a) the incremental launching method was adopted to install the steel box girder with 81 segments before the erection of the main cable; (b) the steel girder was lifted during installation of the hangers and then back to the position such that the hangers are in a zero-stress state; and (c) a large number of concrete blocks were placed on the side span of the girder in order to improve the stability during anchoring the main cables to the girder. Detailed features can be found in the paper by Dai et al. [8].

2.2 Xihoumen Bridge

Several long-span suspension bridges are built with the main span more than 1 km in past five years, including the Yangluo Bridge (1280 m, 2007, Fig. 1b), the Huangpu Bridge (1108 m, 2008, Fig. 1c) and the Nanjing No. 4 Bridge (1418 m, 2012, Fig. 1d). A significant example is the Xihoumen Bridge with a main span of 1650 m (Fig. 1e), which is one of the five long-span bridges in the Zhoushan Islands link project. The bridge opened to traffic in 2010 to carry four-lane highway with a design speed of 80 km/h. Key design features [9] are: (1) twin steel box stiffened girder linked by 6-m-long tie beam was chosen for the suspension bridge for the first time in China; (2) high wire strength of 1770 MPa is used for main cable such that the cable weight can be reduced. A total of 169 prefabricated parallel-wire strands (1275.25-mm-diameter wires per strand) were used in one main cable; (3) The gravity anchor adopted in the north span and the main cable on the south side are anchored on the rock; (4) reinforced concrete frame tower is designed with prestressed concrete hollow tie beams; (5) suspenders are installed in the main span and north-side span, while the south-side span is supported by the piers without additional suspenders. For the construction, the Xihoumen Bridge followed the traditional method, starting with main cables on the catwalk and then hanging the stiffened girder under the suspenders. The aerodynamics of the catwalks and stiffened girder of this bridge was verified by the wind tunnel test.
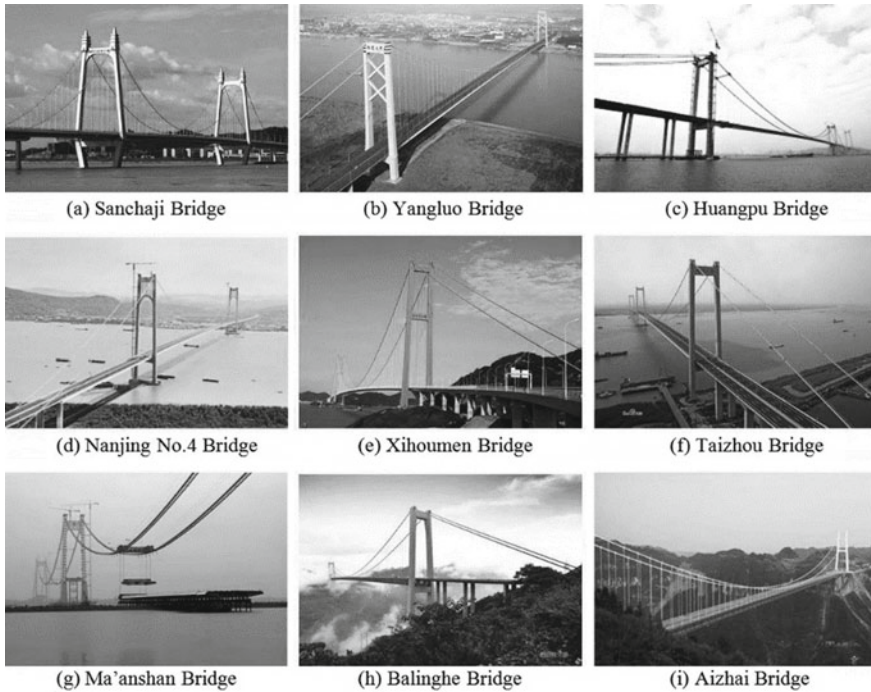
Fig. 1 Recently completed and ongoing large-span suspension bridges in China

2.3 Taizhou Bridge

The construction of four-span suspension bridge with three towers is of increasing interest in China in the past few years. For instance, the Taizhou Bridge (Fig. 1f) over the Yangtze River has a span arrangement of (390 + 1080 + 1080 + 390) m to support six-lane 100 km/h expressway, which is the first long-span suspension bridge with three towers in China. The three towers are chosen because the towers can be built right on the unique geotechnical shape of the riverbed such that the disruption of the channel transport can be minimized. The main design features [10] are: (1) middle steel tower is designed as inverted Y-shaped and 20 m higher than two side towers to improve the longitudinal stiffness and (2) elastic constraints were added between the main tower and the stiffened girder such that it can increase the sliding-resistant safety factor between the saddles and main cables. The construction followed the traditional method: the lifting of the main stiffened girder started from the tower to the middle span, which is synchronized at three towers. Similar suspension bridges are also under constructions, such as the Yingwuzhou Bridge and the Ma'anshan Bridge (Fig. 1g).

2.4 Aizhai Bridge

During the development of the national highway network in China, long-span bridges are always needed to be built over the valleys and rivers in the mountain area. Given the different geomorphic conditions, suspension bridge sometimes is easier to build than the arch bridges. Cases on long-span suspension bridges built in the mountainous region of China, for example, are the Balinghe Bridge (900 m, Fig. 1h), the Sidu Bridge (1088 m) and the Aizhai Bridge (1176 m). The Aizhai Bridge (Fig. 1i) supported four-lane highway, being 330 m between the bridge deck and the ground below. A total of 169 prefabricated parallel-wire strands (1275.25-mm-diameter wires per strand) were used in one main cable. Sixty-nine hangers are fixed to each main cable with a spacing of 14.5 m. Design features [11] included: (1) given that bridge and tunnel are linked together, main tower on one side is built above the exit of the tunnel; (2) in sections underneath the main cable without hangers, three pairs of carbon fiber-reinforced polymer (CFRP) cables are used. These CFRP cables are attached to the main cable on one side and anchored to the ground on the other side; (3) according to the wind tunnel tests, two wind-resistant stabilizer steel plates are attached to the stiffened truss girder along the longitudinal direction. The upper plate with a height of 0.86 m is installed on the collision-resistant rail, while the lower plate is connected to the main truss with a height of 1 m. The difficult part during the construction is the installation of the stiffened truss girder. A longitudinal flexible rail system is proposed underneath the hangers, which are anchored on both sides. Each truss segment was slipped from the side span to the desired position. This method not only saved about 4000 tons of steel, but also reduced the installation time from one year to only three months.

3 Cable-Stayed Bridge

The first cable-stayed bridge built in China was the Dagu Bridge in 1975 with a main span of 75.84 m [8]. Later in 1982, the Jinan Yellow River Bridge opened to traffic as the first cable-stayed bridge with a main span more than 200 m. In the early 1990s, a series of cable-stayed bridges were completed over the Huangpu River in Shanghai, including the Nanpu Bridge (423 m, 1991), the Yangpu Bridge (602 m, 1993) and the Xupu Bridge (590 m, 1997) [12]. After 2000, China became the most active country in the world for the construction of cable-stayed bridges. For instance, the Dongting Lake Bridge built in 2000 is a continuous, four-span cable-stayed bridge supported by three main towers. In the same year, the completion of the Baishazhou Bridge moved the main span record to 618 m. Shortly after, two remarkable designs were built over the Yangtze River: the Nanjing No. 2 Bridge (628 m, 2001) and the Nanjing No. 3 Bridge (648 m, 2005). It is worth to note that the Nanjing No. 3 Bridge was the first cable-stayed bridge to use whole steel structure for the tower in China. Recent featured projects with diverse structural types and increased spans are summarized in Table 2.

Table 2 Technical features of recently completed cable-stayed bridges in China

Bridge name	Built	Cross	Location	Main span (m)	Tower height (m)	Deck width (m)	Deck height (m)
Sutong	2008	The Yangtze River	Nantong/Suzhou	2 × 100 + 300 + 1088 + 300 + 2 × 100	300.4	35	4
Minpu	2009	The Huangpu River	Shanghai	4 × 63 + 708 + 4 × 63	210	43.8	11.5
Stone cutters	2009	Rambler channel	Hong Kong	289 + 1080 + 289	298	53.3	3.2
Jintang	2009	Huibieyang sea	Ningbo	77 + 218 + 620 + 218 + 77	210	26	3.4
E'dong	2010	The Yangtze River	Huangshi	3 × 67.5 + 72.5 + 926 + 72.5 + 3 × 67.5	236.5/242.5	38	3.8
Jingyue	2010	The Yangtze River	Jianyue/Yueyang	100 + 298 + 816 + 80 + 2 × 75	224.5/267	38.5	3.8
Er'Qi	2011	The Yangtze River	Wuhan	90 + 160 + 2 × 616 + 160 + 90	205	26	3.5
Xiangshan port	2012	Xiangshan port	Ningbo	82 + 262 + 688 + 262 + 82	225.5	25.5	3.5
Dongshui men	2013	The Yangtze River	Chongqing	222.5 + 445 + 190.5	162/172	21	12
Jiujiang No. 2	2013	The Yangtze River	Jiujiang	70 + 75 + 84 + 818 + 233.5 + 124.5	230.8/242.3	38.9	3.6
Yongchuan Yangtze River	2014	The Yangtze River	Chongqing	64 + 2 × 68 + 608 + 2 × 68 + 64	196.7/207.4	37.6	3.5
Jiangshun	2015	The Xijiang River	Jiangmeng	60 + 176 + 700 + 176 + 60	186	39	3.5
Yachi River	2016	The Yachi River	Qianxi	2 × 72 + 76 + 800 + 76 + 2 × 72	243.2/258.2	28	7
Beipan River	2016	Beipan valley	Xuanwei	80 + 2 × 88 + 720 + 2 × 88 + 80	269/247	24.5	8
Yangsigang Yangtze River	2019	The Yangtze River	Wuhan	465 + 1700 + 465	243.9	32.5	10

3.1 Sutong Bridge

The Sutong Bridge (Fig. 2a) with a main span of 1088 m was a milestone project in the construction history of China. Four world records were broken when this bridge opened to traffic in 2008. It has the longest main span and the highest tower. (Both of these records are lost to the Russky Bridge in 2012.) The longest cable is 577 m and the deepest drilled pile is about 120 m. Even more, several design features include: (1) viscous dampers were installed between the main tower and girder to control the large displacement of the main girder; (2) large-scale pile groups were adopted to improve the seismic and vehicle collision resistance of the foundation; and (3) anchorage zone of cable was designed with steel anchor boxes at the upper part of the tower [13]. Moreover, main construction techniques included: (1) integrated large-scale foundation for the long pile group; (2) new lifting system was designed to eliminate the large deformation during the erection of the wide deck; (3) scour protection was developed for the cap and pile group; and (4) automatic hydraulic climbing system was used in 68 sections during the construction of the main tower, which has a climb speed of 1.5 m per day and can resist a wind speed of 70 m/s.

(a) Sutong Bridge   (b) Stonecutters Bridge   (c) Minpu Bridge

(d) E'Dong Bridge   (e) Jingyue Bridge   (f) Er'qi Bridge

(g) Xiangshan Bridge   (h) Dongshuimen Bridge   (i) Jiujiang No.2 Bridge

Fig. 2 Recently completed and ongoing large-span cable-stayed bridges in China

3.2 Stonecutters Bridge

The Stonecutters Bridge built in 2009 in Hong Kong is another long-span cable-stayed bridge built after the Sutong Bridge with a main span more than 1 km. Two long-span cable-stayed bridges were built before 2000 in Hong Kong, including Kap Shui Mun Bridge with a main span of 430 m in 1997 and Ting Kau Bridge with two main spans of 448 and 475 m in 1998 [14]. This bridge contains a main span of 1018 m and two side spans of 289 m for anchoring (79.75 m + 2 × 70 m + 69.25 m). The main tower consists of a unique 298 m single column with a full concrete part 175 m from the ground, a steel–concrete composite part from 175 to 293 m from the ground and a 5-m-long maintenance facility on the top. A total of 224 cables with a fan arrangement were anchored on the main girder with a total weight of 7000 tons, where the longest stay cable is about 540 m. To achieve a better aerodynamic performance, the main girder consists of two separated streamline steel boxes linked by cross-beams with a total width of 53.3 m. The construction of the tower is cast by an automatic hydraulic climbing system. The outer stainless-steel skins were lifted by the cranes and then installed to specific locations. The girders on the side span were prefabricated and lifted on-site, while the girders on the main span were shipped to the location and lifted by the auxiliary parallel-wire cables. Each segment in the main span has an approximate weight of 500 tons, but the construction of each segment had to be finished in eight hours in order to reduce the disruption on the channel transport. Thus, a dynamic positioning system was installed on the self-propelled barge such that the lifting location could be tracked very quickly. The construction of the Stonecutters Bridge supported a six-lane freeway and presented a new landmark in Hong Kong.

3.3 Minpu Bridge

The Minpu Bridge (Fig. 2c) opened to traffic in 2009 in Shanghai has a main span of 708 m for carrying two-level traffic. The upper deck with 43.8 m width carried eight lanes, and the lower deck with 28 m width carried six lanes of highway traffic. The main girder is a hybrid system with orthotropic deck–steel truss in the main span and concrete deck–steel truss in the side span. The main concrete towers are H-shaped with a height of 210 m. Based on the numerical studies and the wind tunnel test, the cross section of the tower is chosen with a pentagon shape [12]. A total of 176 cables are arranged in a fan-shaped double plane. The construction method is: (1) main girder at the side span was built simultaneously with the main tower; (2) steel truss at the side span was prefabricated and lifted to position, while the steel truss in the main span was shipped to the site and lifted for installation; and (3) large segments of concrete deck at the side span are cast in site.

3.4 E'dong Bridge

The E'dong Bridge (Fig. 2d) opened to support six-line traffic in 2010 is a long-span cable-stayed bridge across the Yangtze River with hybrid main girder [15]. The steel box girder is 901 m long in the main span, while the concrete box girder with a length of 287.5 m is used on two side spans. A special connection section with concrete filled in the steel box was designed to transfer the compression and shear load. The two towers carried the main girder with 30 pairs of stay cables. A steel anchoring box was designed to reduce the stress concentration on the tower. Corrosion protection was designed at the anchoring zone of the cable to improve the durability of the main girder. The full-scale health monitoring system was installed on the bridge to monitor the structural behavior. The incremental launching method was adopted for the erection of the main girder. The Jingyue Bridge (Fig. 2e), another long-span cable-stayed bridge across the Yangtze River, followed the similar design philosophy with a main span of 816 m.

3.5 Er'Qi Bridge

The Er'Qi Bridge (Fig. 2f) was built in 2011 for supporting six-lane traffic across the Yangtze River in the city of Wuhan. Before the construction of the Er'Qi Bridge, downtown Wuhan already has six long-span bridges over the Yangtze River [16]. Most of existing bridges are cable-stayed with two main towers. Thus, the Er'Qi Bridge was designed with three 219.5 m main towers and two 616 m main spans. The main girder has a steel–concrete composite structure for the main span and a concrete structure for the side span. The large-scale concrete cap was cast only once to improve the quality of the structure. The main tower was cast by the hydraulic climbing system as 6 m per segment, which significantly reduces the construction time. The cast-in-place construction method was adopted for the side span girder, while the cantilever method was used for the main span girder.

3.6 Bridge of Recently Built

Many long-span bridges across the Yangtze River are recently completed and opened to traffic in 2013, such as the Fengdu No. 2 Bridge, the Wanzhou No. 3 Bridge and the Chibi Bridge. Figure 2h presents the Dongshuimen Bridge, a dual use for metro and auto in the city of Chongqing. The steel truss girder supported two metro lines with a design speed of 60 km per hour and four-line freeways on the upper level. Figure 2i illustrates the erection of the main tower of Jiujiang No. 2 Bridge, another large-span bridge with a main span of 818 m.

4 Arch Bridge

China has a long history of building arch bridges since the Anji Bridge (also known as the Zhaozhou Bridge) which was built more than 1400 years ago. The first remarkable modern long-span arch bridge in China was the Wanxian Yangtze River Bridge in Chongqing, which was built in 1997 with a main span of 420 m [17]. After 2000, a series of steel/concrete arch bridges were built, such as the Wushan Yangtze River Bridge with a main span of 460 m. A full summary of the arch bridge with steel–concrete tube rib can be found in the review paper by Chen and Wang [18]. As for the whole steel arch, the Lupu Bridge completed in 2003 has a main span of 550 m. Several recently completed arch bridges are summarized in Table 3.

4.1 Xingguang Construction

The Xingguang Bridge built in Guangzhou in 2006 is a classic example of tied arch bridge with a three-span continuous concrete deck for supporting six-lane traffic, as shown in Fig. 3a. The rise to span ratio of the main span is 1/4. The spacing between two arch ribs is 28.1 m. The foundation of the main span is an integrated cap with drilled piles. The main innovative structural feature is the design of the composite system with steel tied arch and concrete rigid frame. The triangle type of concrete rigid frame has a 37.2-m-high and 102-m-long tie beam on the top part. The consumed concrete for each frame is 5700 m^3. The construction process started with main pier foundation, followed by the triangle rigid frame, side span arch and main span arch, which completed in two years and five months. The unsealed bottom of the large steel caisson was proposed. Arch ribs in the side span were assembled and then lifted to position. In order to minimize the disruptions in transportation, the segments of the arch rib in main span are floated into place and lifted by auxiliary pier beside the bridge. The construction of this bridge is a remarkable addition to the bridge group of the Pearl River.

4.2 Caiyuanba Construction

The Caiyuanba Bridge (Fig. 3b) in Chongqing is another recently built arch bridge with a composite system of rigid frame and tied steel arch [19]. The Caiyuanba Bridge is the first long-span arch bridge in downtown Chongqing, which is a new member in the "The City of Bridges" in China. The bridge has a total length of 1866 m over the Yangtze River to carry six-lane auto traffic and metro. The 420 m main span consists part of the Y-shaped concrete frame and a 320 m box steel basket-handle tied arch. The main steel truss girder is 11.2 m wide with two levels,

Table 3 Technical features of recently completed arch bridges in China

Bridge name	Built	Cross	Location	Main span (m)	Rise (m)	Deck width (m)	Deck height (m)	Rib height (m)
Xinguang	2006	Pearl River	Guangzhou	177 + 428 + 177	104	37.62	37.62	7.5–12.0
Caiyuanba	2007	Yangtze River	Chongqing	88 + 102 + 420 + 102 + 88	56	30.5	30.5	4
Taipinghu	2007	Taiping Lake	Huangshan	4 × 20 + 336 + 3 × 20	68	24.5	24.5	7.28–11.28
Chaotianmen	2009	Yangtze River	Chongqing	190 + 552 + 190	128	36.5	36.5	14–73.13
Guangya	2013	Liujiang River	Liuzhou	63 + 2 × 210 + 63	50	36	36	2.5–4.5
Hejiang Yangtze River No. 1	2014	Yangtze River	Luzhou	10 × 20 + 530 + 4 × 20	119	28	28	8–16
Hengqin No. 2	2015	Maliuzhou River	Zhuhai	100 + 400 + 100	90	36	36	7–11

(a) Xinguang Bridge   (b) Caiyuanba Bridge

(c) Taipinghu Bridge   (d) Chaotianmen Bridge
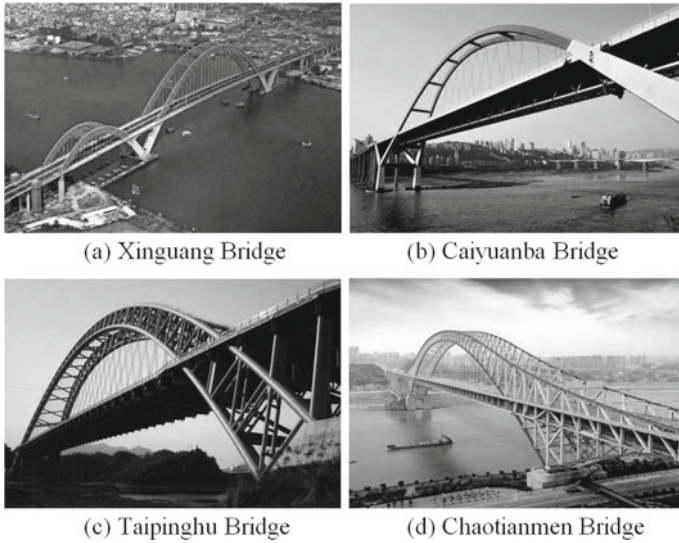
Fig. 3 Recently completed large-span arch bridges in China

where the upper level is used for auto and lower level is used for metro lines. The girder system contains the truss and orthotropic deck to carry the live load. The main construction is featured by (1) the use of segmented cantilever method in the Y-shape pier due to the huge volume concrete [20]; (2) the use of an innovative auxiliary tower and the cable system to lift the main arch; (3) the use of 51-segment-prefabricated steel truss girder for main girder, 16 m long and 11.2 m wide per segment; and (4) the use of large-scale intelligent active control system on main structure.

4.3 Taipinghu Construction

The Taipinghu Bridge (Fig. 3c) built in the Huangshan district of Anhui is an example of half-through basket-handle arch bridge, which currently has the longest main span among similar structural types in China [21]. This bridge is part of the Tongling-Tangkou highway for supporting four-lane traffic with a design speed of 80 km/h. The rise-to-span ratio is l/4.94. The arch ribs have a tubular-truss composite system with varied height cross section filled with micro-expansion concrete. Two arch ribs are inclined inward about 10.008°. The cross section of arch rib contains four tubes linked by chords with a total width of 3 m. Each tube has a diameter of 1.28 m with wall thickness from 20 mm at the crown to 24 mm at the spring line. The spacing of the hangers is 8 m. The arch ribs are lifted by the cable hoisting system on two auxiliary towers with heights of 98 and 108 m. Due to the

basket-handle type, two movable saddles are installed on the top of the towers such that the saddle can move laterally to control the position of the cable during the lift of the arch ribs. The Taipinghu Bridge is an environmental-friendly design in this national park area.

4.4 Chaotianmen Construction

The Chaotianmen Bridge (Fig. 3d) is another recently built arch bridge in "The City of Bridges in China," Chongqing. It has a world record main span of 552 m as its completion in 2009 [22]. The total length of the steel truss arch is 932 m, with the span arrangement of (190 + 552 + 190) m. The rise-to-span ratio of the main span is 1/4.312. Similar to the Caiyuanba Bridge, the main girder of the Chaotianmen Bridge is also divided into an upper level for six-lane auto traffic and a lower level for metro. This resulted in a reduction in total deck width and improved the overall visual impact on the environment. The arch was designed without horizontal thrust due to the use of tie bars. The prestressed tendons are used as part of the composite tie bar system, which significantly reduce the large forces in the truss members. Seismic hinged bearings are adopted at the top of two caps. The construction of the main truss started from side span to main span and then installed the tie bars. The multiple transitions of the structural system occur during the whole construction process.

5 Fixed Links

As mentioned previously, the need for fixed links across the bay and the strait is also a catalyst for the construction of long-span bridges. During the past decade, a large number of link projects were built as summarized in Table 4.

5.1 Donghai Bridge

The Donghai Bridge (Fig. 4a) completed in 2005 is the first fixed link project in China between the Nanhui District of Shanghai and Xiaoyangshan Island of Zhejiang, which is part of the Shanghai International Port. The project contains a large number of simple supported prestressed concrete box girders (30 m on land, 60 and 70 m over the sea), continuous concrete girders (with a main span of 120–160 m), two cable-stayed bridges with a main span of 420 and 332 m. The construction of this project was completed in 2005 with the duration of 35 months.

Table 4 Technical features of recently completed fixed links in China

Project	Built	Length (km)	Width (m)	Lanes	Speed (km/h)
Donghai Bay	2005	32.5	31.5	6	80
Hangzhou Bay	2008	36	33	6	100
Pingtan channel	2010	35.1	17	4	80
Zhoushan Island	2010	48	22.5	4	100
Jiaozhou Bay	2011	41.8	35	8	80
Xinghai Bay	2015	6	24.8	4	80
Quanzhou Bay	2015	12.5	33.5	6	100
Hong Kong–Zhuhai–Macau	2016	49.96	41.9	6	100
Pingtan straits	2019	16.34	35.5	6	100

5.2 Hangzhou Bay Bridge

The Hangzhou Bay Bridge (Fig. 4b) built in 2008 is a milestone project for the regional economy of Shanghai and Zhejiang [23]. More than 120 km driving distance between Ningbo and Shanghai is shortened after the completion of this project. For main shipping channels, two large-span cable-stayed bridges are built with a span arrangement of (100 + 160 + 318) m and (70 + 160 + 448 + 160 + 70) m, respectively. For other spans of the bridge, 70-m-long prestressed concrete continuous box girders are arranged. At the beginning of the project, the position measurement is of great importance for such long-span bridges. Thus, the

(a) Donghai Bridge   (b) Hangzhou Bay Bridge

(c) Zhoushan Island Link   (d) Jiaozhou Bay Bridge
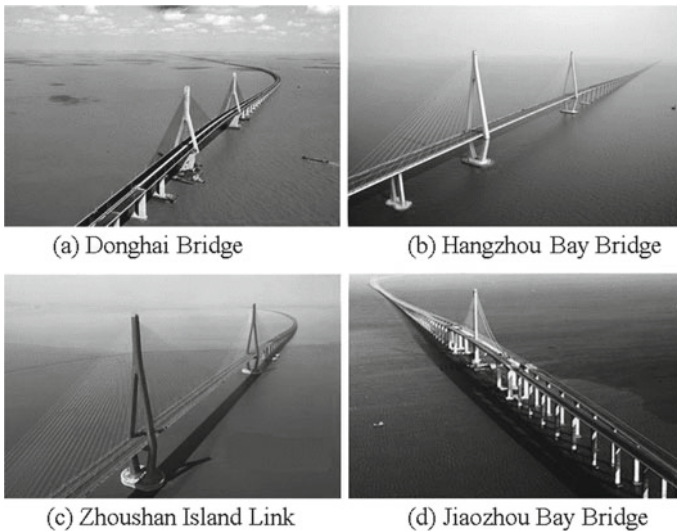
Fig. 4 Recently completed bay bridges and fixed links in China

data from multiple GPS reference stations were measured to obtain the continuous elevations over the bay. The drilled piles with the diameter of 1.5 m or 1.6 m were used for such foundation more than 89 m deep. In order to minimize the offshore construction, most of the girders are precast and lifted by cranes on the neighboring deck. The durability of concrete structures in the marine environment was studied. A rest station is built in the middle of the distance for welcome center and emergency service.

5.3   *Zhoushan Island Link*

The Zhoushan Islands Link Project completed in 2009 is across four islands with over 48 km length, including five long-span bridges [24]. The construction of this link was launched in 1999 with two phases. The first phase of the project contains three long-span bridges that were completed in 2004. Another two long-span bridges started in 2005 as the second phase. The Xihoumen Bridge discussed previously is the one of the bridges in this phase. The other bridge is the Jintang Bridge (Fig. 4c), which is a cable-stayed bridge with a main span of 620 m. One of the design features of the Jintang Bridge is the application of steel anchorage beam for cables, which minimizes tensile stress on the main tower. The completion of this link indicates that building technology on the bridges over the sea has become more mature and internationally competitive in China. It provided a reliable reference on many recent projects, such as the Jiaozhou Bay Bridge (Fig. 4d).

5.4   *Hong Kong–Zhuhai–Macau Link*

Hong Kong–Zhuhai–Macau Link is the first large-scale combined bridge–tunnel fixed link project in China [25]. The purpose of this project is to provide a fast transportation in the Pan-Pearl River Delta region and then boost regional tourism and economy. Upon completion, the travel time from Hong Kong to Macau or Zhuhai will be reduced to half an hour. This project started from 2009 and is scheduled to complete in 2018. It will be the world's longest six-lane immersed tube tunnel with a length of 35.578 km.

6   Conclusions

The construction of modern long-span bridges in China is driven by the ongoing development of the national highway network. With the development of advanced construction material and technologies, the records of long-span bridges have been updated in a yearly basis. In this review on long-span highway bridges in the past

decade, it can be seen that the construction of such large-scale infrastructures in China has grown into an unprecedented level. These improvements are characterized by the following aspects: (1) The scales of bridges have been increased in multiple aspects, including the main span, the deck width, the tower height, the pile length, etc. (2) More structural types have been developed and practiced, including the self-anchored suspension bridge, multiple-span cable-stayed bridges, etc. (3) The structural systems are in a composite or hybrid form both at the system level (steel tied arch with concrete rigid frame bridge) and at the cross-section level (steel–concrete composite arch rib). (4) Bridges are built to carry lanes for multiple uses, such as auto-train and auto-metro. (5) Multifunctional and large-scale construction facilities are developed for different construction settings, such as fast hydraulic climbing system on bridge tower, lifting crane for wide deck, etc. (6) Construction methods for different geomorphic conditions are developed, such as integrated large-scale foundation on the sea, swing and cable hybrid method for arch bridge, installation of stiffened truss girder by flexible rail system in valley, etc.

The fast developments of the highway network in China are based on a learning process from construction experience of those developed countries accumulated in the twentieth century. As a result, nearly a total of two hundred long-span bridges have been built over the Yangtze River. Now in turn, China has provided the new experience in the past decade and will continually lead the construction of long-span bridges in the next decade.

References

1. Hu N, Dai GL (2010) Four significant factors in evolution of bridge engineering. In: Proceeding of 1st international conference on structures and architecture (ICSA 2010). Portugal, pp 329–330
2. Tang MC, Xiang HF (2005) Modern Chinese bridges. Structures congress 2005: metropolis and beyond. New York, United States, April 20–24
3. Tang MC (2007) T. Y. Lin international bridge experience in China. Structures congress 2007 new horizons and better practices, long beach. California, United States, 16–19 May
4. Feng MR (2009) China's major bridges, IABSE symposium report. IABSE Workshop, Shanghai 2009, pp 1–23
5. Ge YJ, Xiang HF (2009) Aerodynamic challenges of major Chinese bridges, IABSE symposium report. IABSE Workshop, Shanghai 2009, pp 142–164
6. Dai GL, Song XM (2009) Man Hua Qiao Liang. China Railway Publishing House, Beijing
7. Ochsendorf J, Billington D (1999) Self-anchored suspension bridges. J Bridg Eng 4(3):151–156
8. Dai GL, Song XM, Hu N (2010) Sanchaji bridge—the self-anchored suspension bridge in China. Struct Eng Int 20(4):458–461
9. Song H, Wang XD (2009) Zhoushan Xihoumen bridge—the world's longest box-girder suspension bridge, IABSE symposium report. IABSE Workshop, Shanghai, pp 221–236

10. Ji L, Han DZ (2008) Design of Taizhou Yangtze river bridge. Mod Transp Technol 5(3):20–28 (in Chinese)
11. Hu JH, Cui JF Innovative techniques of design of Aizhai bridge in West Hunan. Bridg Constr 6:51–58 (in Chinese)
12. Ma B, Lin YP (2009) Cable-stayed bridges in Shanghai where Chinese recent major bridges launched, IABSE symposium report. IABSE Workshop, Shanghai, pp 201–211
13. You QZ, He P, Dong XW, Zhang XG (2008) Sutong bridge—the longest cable-stayed bridge in the world. Struct Eng Int 4(18):390–395
14. Hui MC, Yau DM (2009) Major bridge development in Hong Kong—past, present and future, IABSE symposium report. IABSE Workshop, Shanghai, pp 165–177
15. Hu MY, Huang BS, Yu JL, Tang SF (2011) Key techniques for design of Edong Changjiang river highway bridge. Bridge Construction, 5: 64–68 (2011) (in Chinese)
16. Long T, Hu JA (2009) Simplicity perfection: configuring design of pylons of Erqi Changj Iang river bridge in Wuhan. Bridg Constr 09(1):48–51 (in Chinese)
17. Xie B (2008) Wanxian long span concrete arch bridge over Yangtze river in China. Chinese-Croatian joint colloquium on long arch bridge. Brijuni Islands, 10–14 July, pp 181–188
18. Chen B, Wang T (2009) Overview of concrete filled steel tube arch bridges in China. Pract Period Struct Des Constr 14(2):70–80
19. Tang MC, Ren GL (2010) Design and construction of the main spans of the Chongqing Caiyuanba bridge China. Struct Eng Int 20(3):296–298
20. Liu XH (2008) Design and construction of Caiyuanba Yangtze river bridge in Chongqing. Chinese-Croatian joint colloquium on long arch bridge. Brijuni Islands, 10–14 July, pp 447–454
21. Sun DH (2004) Preliminary design of the Taiping lake bridge. J Highw Transp Res Dev 21(8):74–77 (in Chinese)
22. Wang FM (2009) The Chaotianmen bridge-an arch bridge with a new world record span of 552 m, IABSE symposium report. IABSE Workshop, Shanghai 2009, pp 250–255
23. Wang RG, Meng FC (2009) Hangzhou Bay bridge—a 36 km shortcut between Shanghai and Ningbo, IABSE symposium report. IABSE Workshop, Shanghai, pp 256–263
24. Wang CJ (2009) The Zhoushan Mainland-Island linking project consisting of five sea-crossing bridges, IABSE symposium report. IABSE Workshop, Shanghai, pp 237–249
25. Su QK, Chen Y, Li Y, de Wit JCWM (2012) Hong Kong Zhuhai Macao bridge link in China. Report of Tunnel Engineering Consultants (TEC), pp 1–18

Influence of Steel Spring Failure of Floating Slab Track on Vibration Characteristics of Infrastructure

Fangzheng Xu, Xiaolin Song and Jianjin Yang

Abstract Floating slab track is widely used for its excellent performance on vibration isolation. Steel spring stiffness will be decreased or even invalid under repeated trainload, which may have a bad effect on the vibration characteristics of an infrastructure. Vertical coupled dynamics model for the metro and the floating slab track was established based on the vehicle-track coupled dynamics, by which the reaction forces of steel springs with some ineffective steel springs were obtained. Reaction forces of the steel springs were applied to the three-dimensional finite element model of the tunnel and soil to investigate the steel spring failure influence of the floating slab track on the tunnel and soil vibration. Numerical results indicated that the vibration displacements were slightly influenced by the failure of the steel springs. Peak vibration acceleration of the soil in each horizontal level was located in the track centerline. No matter how many steel springs fail, the distribution of the soil acceleration is very similar, not only along lateral direction but also along the vertical direction. When the failure number of the steel springs is less than 6, the failure number has little effect on the maximal soil acceleration along the lateral and vertical direction. With the increase of the failure number of springs from 7 to 9, the maximal acceleration along the lateral direction decreases quickly, while the attenuation along the vertical direction is very limited.

Keywords Floating slab track · Failure · Vibration characteristics · Finite element model · Vehicle-track coupled dynamics

1 Introduction

With the rapid development of the economy and the urbanization process, the urban rail transit in China has been developing rapidly, which greatly facilitates people's life. However, it also brings many problems. Some ancient buildings near the metro

F. Xu · X. Song (✉) · J. Yang
State Key Laboratory of Traction Power, Southwest Jiaotong University,
Chengdu 610031, China
e-mail: xlsong@swjtu.edu.cn

have cracked or even collapsed. Some metros have a negative influence on the precision instrument and equipment of some universities or institutes [1]. In these special areas, steel spring floating slab tracks are often chosen for its excellent performance of the vibration isolation.

Under the repeated trainload, the steel spring will partly or totally lose its efficacy unavoidably.

Researchers have done much on the vibration characteristics of the infrastructure and obtained fruitful results. Ge et al. [2] tested and analyzed the accelerations of the tunnel and the floating slab track in different train speed. Yu et al. [3] discussed the influence of support failure of steel spring floating slab track on the dynamic response of track-self, while the influence on the ground vibration was not involved.

In this paper, the ground vibration caused by the metro train is considered as the two subsystems of train-track and tunnel-soil. Based on the vehicle-track coupled dynamics theory [4], the reaction forces of the steel springs were calculated using the train-track coupled dynamics model. The reaction forces of the steel springs were subjected to the three-dimensional finite element model of the tunnel-soil. The influence of the steel spring failure of the floating slab track on the vibration characteristics will be investigated.

2 Numerical Model and Parameters

2.1 Train-Track Coupled Dynamics Model

The train-track coupled dynamics model was established, as showed in Fig. 1. In the model, the metro vehicle was simplified as a multi-body system with 10° of freedom. The rail was treated as a continuous Euler beam discretely supported at fastener junctions. The floating slab track was regarded as a free beam supported on the steel springs which are fixed on the tunnel foundation base. The Hertz nonlinear elastic contact was adopted in the vertical interaction of the wheel and the rail. The shear hinge between floating slab tracks and the track irregularity was not considered in the model.
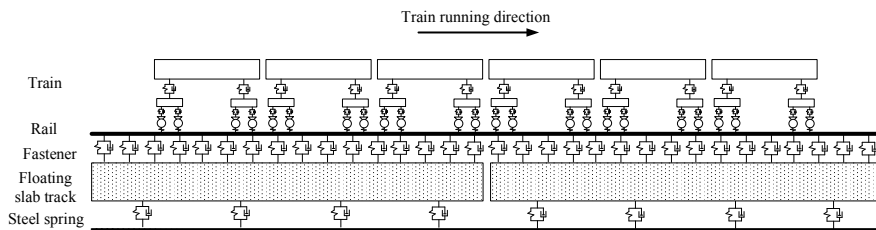

Fig. 1 Train-track coupled dynamics model

Only the function of the steel spring floating slab track is shown in Eqs. 1 and 2 [5].

$$E_s I_s \frac{\partial^4 Z_s(x,t)}{\partial x^4} + \rho_s \frac{\partial^2 Z_s(x,t)}{\partial t^2} = \sum_{i=1}^{N_p} F_{rsi}(t)\delta(x - x_{pi}) - \sum_{j=1}^{N_f} F_{ssj}(t)\delta(x - x_{fj}) \quad (1)$$

$$F_{ssi}(t) = K_{si}[Z_s(x_i,t) - Z_t(x_i,t)] + C_{si}[\dot{Z}_s(x_i,t) - \dot{Z}_t(x_i,t)] \quad (2)$$

In Eqs. 1 and 2, E_s, I_s and ρ_s are Young's modulus of the track slab, the moment of inertia of the track slab and the slab mass per unit length, respectively. K_{si} and C_{si} are the stiffness and the damping of the ith steel spring. $Z_s(x,t)$ and $\dot{Z}_s(x,t)$ are the vertical displacement and the vertical velocity of the floating slab track. $Z_t(x,t)$ and $\dot{Z}_t(x,t)$ are the vertical displacement and the vertical velocity of the steel spring. N_p and N_f are the number of fasteners and the steel springs. F_{rs} and F_{ss} are the reaction forces of the fasteners and the steel springs.

In this paper, a wide-body A size train is used. The train has six vehicles. The length of each vehicle is 22.8 m. The train speed is 60 km/h. The parameters of the metro and the track are listed in Tables 1 and 2.

2.2 Three-Dimensional Finite Element Model of Tunnel and Soil

According to the real parameters of one metro line, the three-dimensional finite element model of the tunnel and soil was established, as shown in Fig. 2. The length, the width, and the thickness of the model are 75 m, 80 m, and 60 m, respectively. The model length is the length of three slabs. The other dynamics parameters [6] are shown in Table 3.

Table 1 Parameters of metro vehicle

Parameter	Value	Parameter	Value
Mass of car body	50,878 kg	Mass of truck	2721 kg
Unsprung mass	1900 kg	Pitch moment of inertia for car body	2.446×10^6 kg m^2
Pitch moment of inertia for frame	3.605×10^3 kg m^2	Primary suspension stiffness	2140 kN/m
Secondary suspension stiffness	2500 kN/m	Primary suspension damping	49 kN s/m
Secondary suspension damping	196 kN s/m	Truck space	15.7 m
Axle space	2.5 m	Rolling radius	0.42 m

Table 2 Parameters of floating slab track

Parameter	Value	Parameter	Value
Young's modulus of rail	205.9 GPa	Moment of inertia of rail	3.217×10^{-5} kg m^2
Rail mass	60.64 kg/ m	Rail pad stiffness	60,000 kN/m
Rail pad damping	75 kN s/ m	Young's modulus of track slab	35 GPa
Moment of inertia of track slab	0.1258 m^4	Mass of track slab	96,134.5 kg
Length of track slab	25 m	Steel spring stiffness	6600 kN/m
Steel spring damping	390 kN s/ m	Fastener space	0.595 m
Fastener number	84	Steel spring number	42

Fig. 2 Three-dimensional finite element model of tunnel and soil
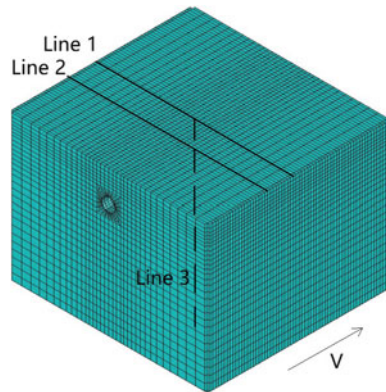
The diameter and the buried depth of the tunnel are 6 and 15 m. The lining thickness is 0.3 m. The C55 concrete is used in the lining and the tunnel foundation base.

The calculated soil area consists of nine layers without considering the slippage between the soil layers. Each soil layer is considered as a homogeneous and isotropic material.

The tunnel and soil are modeled by the eight-node brick solid element SOLID45. The element size of the model ranges from 0.5 to 2.5 m, and the model consists of 72,140 elements and 78,204 nodes. Three-dimensional viscoelastic artificial boundaries [7] are applied to the model.

Three monitoring lines of the soil acceleration correspond to the lateral lines of the ground surface above the center or above the end of the middle floating slab track (Line 1 and Line 2), and the vertical line along the vertical direction through the center of the model.

Table 3 Parameters of soil [6]

Soil layer	Thickness (m)	Density (kg/m³)	Young's modulus (MPa)	Shear modulus (MPa)	Poisson's ratio	S-wave velocity (m/s)	P-wave velocity (m/s)
Miscellaneous fill	1.5	1900	54.4	21.1	0.29	110	205.7
Silty clay 1	1.5	1950	103.9	40.3	0.29	150	280.5
Mucky silty clay	5.0	1740	148.7	57.6	0.29	190	355.3
Muddy clay	10	1690	76.6	30.4	0.26	140	343.0
Clay	4.0	1780	90.3	32.0	0.41	140	261.8
Silty clay 2	10	1810	171.4	66.4	0.29	200	374.0
Silty clay 3	5.0	1900	396.1	144.6	0.37	280	523.6
Silt	6.0	1900	386.3	141.0	0.37	280	523.6
Fine sand	20	1900	555.0	202.6	0.37	340	635.8

3 Numerical Calculation and Results Analysis

In this paper, only the continuous failure of the steel springs in one side from one end of the floating slab track was taken into account. The failure number of steel spring varied from 0 to 9. The failure style was shown in Fig. 3.

3.1 Characteristics of Reaction Forces of Steel Springs

The calculated forces of the steel springs with different failure springs were shown in Fig. 4.

It can be seen from Fig. 4 that the force of the first ineffective steel spring (Point A) is 0. When seven steel springs fail, the reaction force of the effective spring adjacent to the failure one (Point B) will double that with no ineffective spring. The reaction force of the middle steel spring in the same side as the ineffective one (Point C) is 26.70 kN when the failure number of the steel springs is 0; however, the force raises to 33.75 kN when the failure number is 7. The reaction force of the other end steel spring in the same side as the ineffective one (Point D) is 22.65 kN when seven steel springs fail, which is only 1.23 kN smaller than that with no failure. That is to say, the influence of the failure number of steel springs on the reaction force for Point D is neglectful. When two steel springs fail, the reaction forces of the steel springs for Point B, C, and D are close to that without failure.

3.2 Vibration Characteristics of Tunnel and Soil

As the vertical vibration caused by the metro is much greater than the lateral and longitudinal one [8], only the vertical vibration is analyzed. Figures 5 and 6 show the vibration of the tunnel foundation base and the soil in the center of the ground.
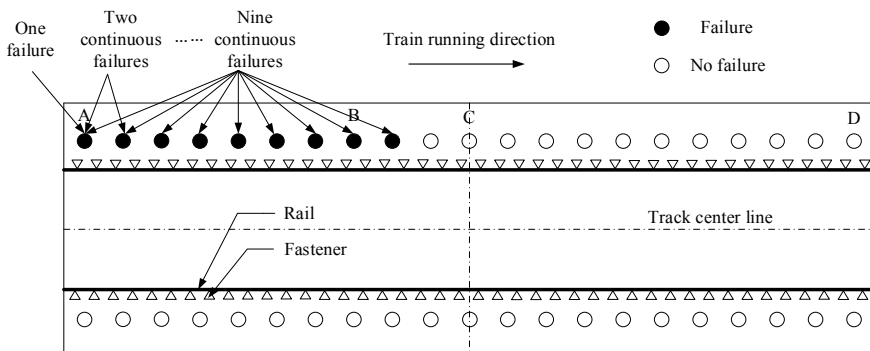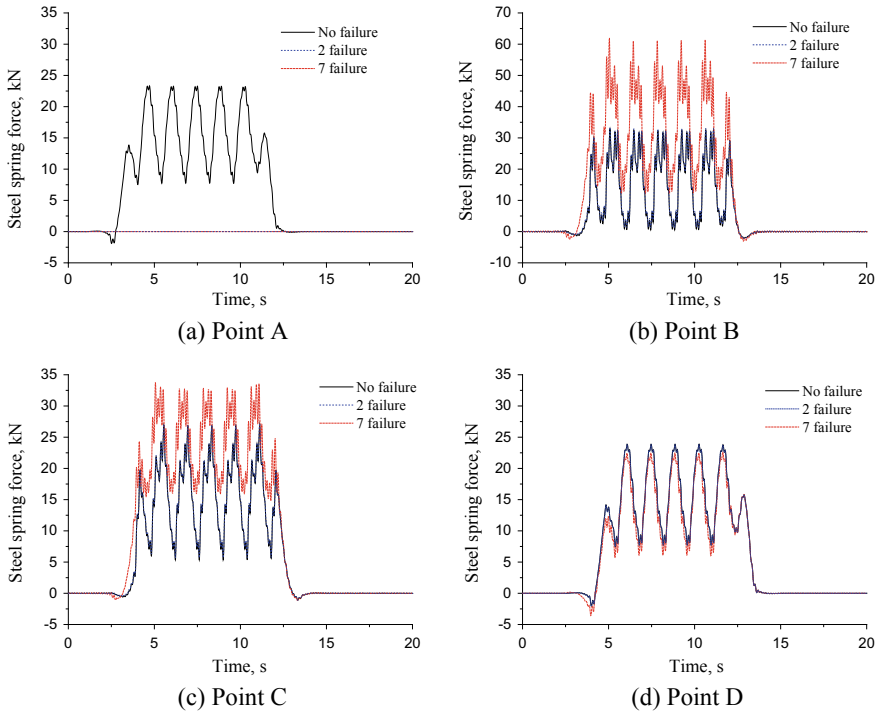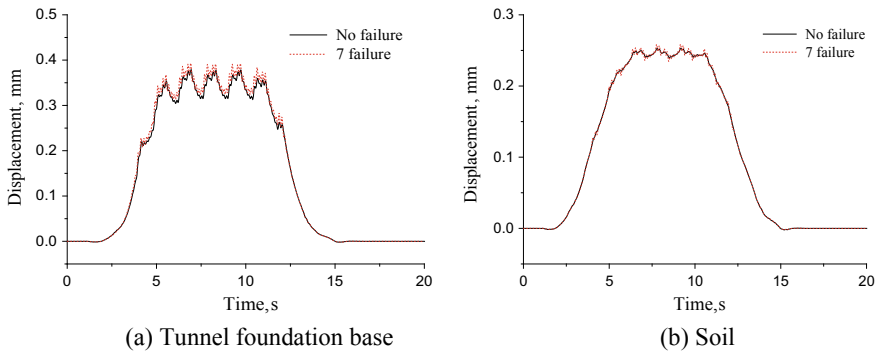

Fig. 3 Failure style of steel springs in one side

Fig. 4 Reaction forces of steel springs in different points

Fig. 5 Displacement of tunnel foundation base and soil

It can be clearly seen from Fig. 5 that the vibration displacements of the tunnel foundation base and the soil are, respectively, 0.379 mm and 0.253 mm when the steel springs are all fine. The corresponding displacements increase slightly to 0.392 and 0.258 mm when the failure number of the steel springs reaches 7. The
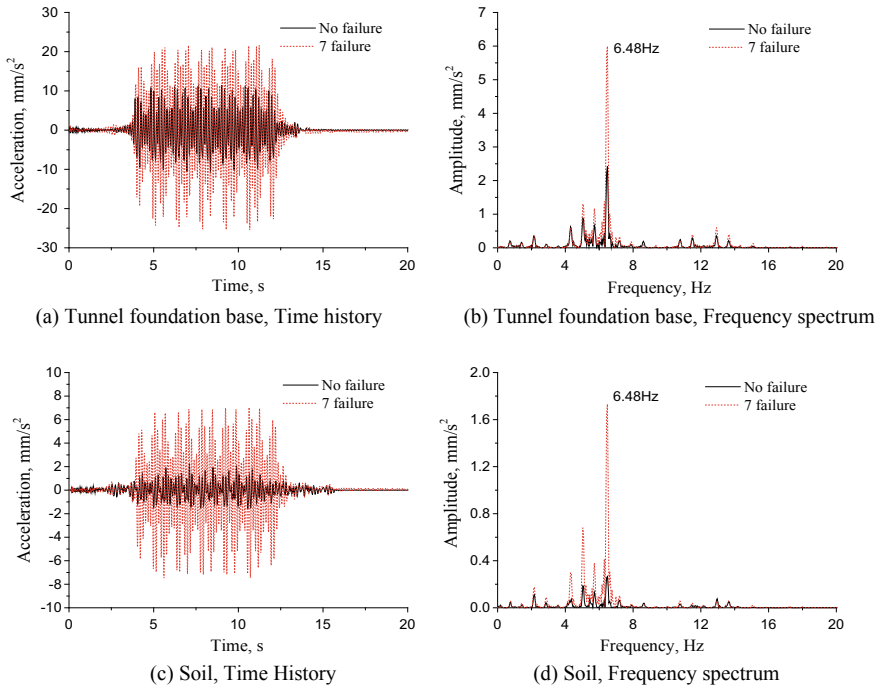
(a) Tunnel foundation base, Time history   (b) Tunnel foundation base, Frequency spectrum

(c) Soil, Time History   (d) Soil, Frequency spectrum

Fig. 6 Vibration acceleration of tunnel foundation base and soil

increments reach 3.43% for the tunnel base and 1.98% for the soil. The vibration displacements were little influenced by the failure of the steel springs.

As can be seen from Fig. 6, the maximal acceleration of the tunnel foundation base and the soil is, respectively, 11.41 mm/s^2 and 2.18 mm/s^2 when the failure number of the steel springs is 0. The accelerations increase sharply when the springs fail. The maximal accelerations rose to 21.65 and 7.12 mm/s^2 when seven steel springs fail. The increments reach 89.75% for the tunnel base and 226.61% for the soil. No matter how many springs fail, the spectrum characteristic curve shows that the frequency component remains stable and the dominant frequency of the acceleration remains 6.48 Hz or so. When the springs are ineffective, only the amplitude increases in some frequency (less than 15 Hz), especially in the dominant one.

3.3 Distribution of the Vertical Acceleration for Soil

Vertical Acceleration Along Lateral Direction (Line 1 and Line 2) Figure 7 illustrates the distribution of the vertical acceleration for the soil along the lateral direction when all the steel springs are effective.

Fig. 7 Acceleration distribution of soil along the lateral direction (Line 1 and Line 2) when all steel springs are effective
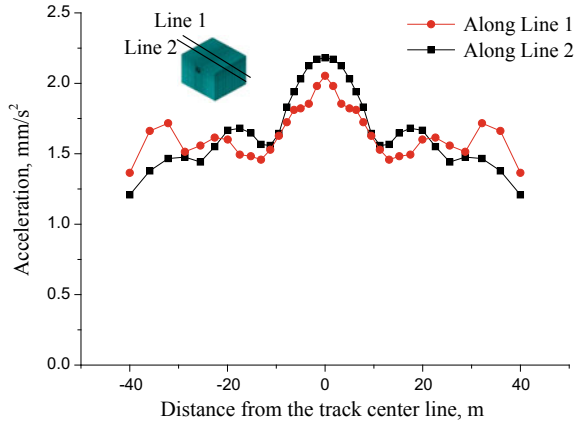
Figure 7 shows that the peak vertical acceleration along Line 2 is greater than that along Line 1 where the distance from the track centerline is less than 20 m. On the contrary, out of the range 20 m, the acceleration along Line 1 is greater. The acceleration of the soil decreases rapidly with the distance less than 14 m. The local rebound occurred in a small range, about 20 m away from the centerline. It is similar to the test data and simulation results [1].

Figure 8 presents the acceleration distribution of the soil when different steel springs fail. Figure 9 provides a comparison of the maximal vibration acceleration of the soil when the different steel springs are ineffective.

It is shown from Fig. 8 that the peak vertical acceleration of the soil in each horizontal level is located in the track centerline. No matter how many steel springs fail, the vertical acceleration distributions of the soil are very similar.

Figures 8 and 9 illustrate that the acceleration of the soil along Line 1 and Line 2 is slightly influenced when the failure number of the steel springs is not more than 5. The maximal difference of the maximal soil acceleration is less than 8.33%. When the failure number of the steel springs exceeds 6, the soil acceleration increases significantly. However, the peak value decreases quickly with the increase of the failure number of springs. There is a 226.61 and 339.79% increase in the maximal acceleration along Line 1 and Line 2 compared with that of no failure springs.

Vertical Acceleration Along Vertical direction (Line 3) Figure 10 shows the acceleration distribution of the soil along the vertical direction (Line 3) when different steel springs are ineffective.

It can be seen from Fig. 10 that the vertical acceleration reaches its maximum on the tunnel foundation base. The acceleration under the tunnel is much greater than that above the tunnel.

Under the tunnel area shown in Fig. 10, the soil acceleration reduces remarkably with the increase of the distance from the tunnel foundation along Line 3. Above

(a) Along Line 1   (b) Along Line 2
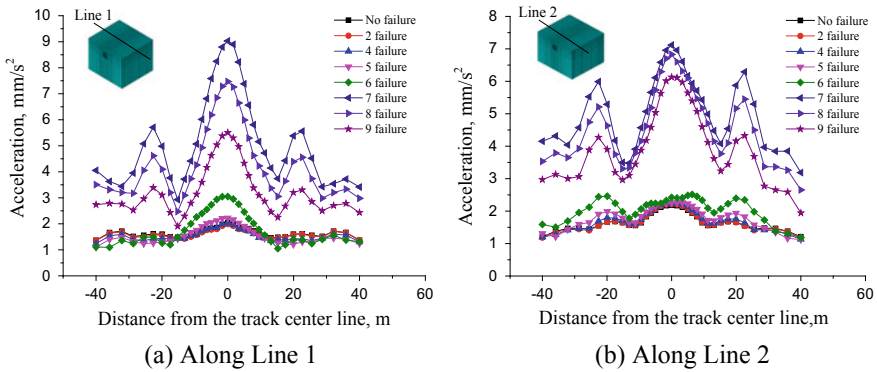
Fig. 8 Acceleration distribution of soil along the lateral direction (Line 1 and Line 2) when different steel springs are ineffective

Fig. 9 Maximal acceleration of soil when different steel springs are ineffective
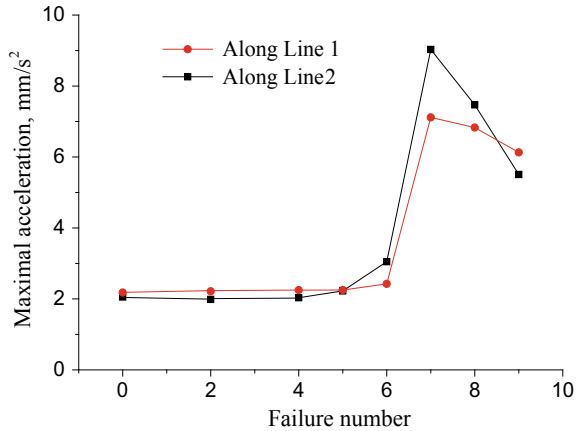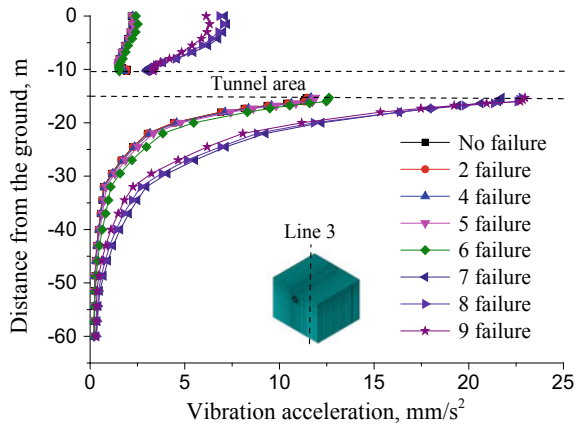

the tunnel area, the soil acceleration decreases with the increase of the distance from the ground.

The vertical acceleration distribution of the soil is influenced little when the failure number of the steel springs is not more than 6. The maximal difference of the maximal acceleration is less than 10.58%. When the failure number exceeds 6, although the distribution is similar, the peak value and the attenuation rate raise extremely. Comparing the peak values with no failure springs, there is a 101.28% increase in the maximal acceleration along the vertical direction. However, with the increase of the failure number of springs from 7 to 9, the attenuation along the vertical direction is very limited.

Fig. 10 Vibration acceleration of soil along the vertical direction (Line 3)

4 Conclusion

1. The influence of the failure number of steel springs on displacements of the tunnel foundation base and the soil is neglectful. The maximal difference of the displacements between seven ineffective steel springs and those with no ineffective spring is only 3.43%.

2. No matter how many steel springs fail, the distribution of the soil acceleration is very similar, not only along lateral direction but also along the vertical direction. The maximal soil acceleration along the lateral direction is located in the track centerline. The acceleration attenuates with the increase of the distance from the track centerline. It decreases rapidly with a distance less than 14 m. There is a local rebound occurring in a small range, about 20 m away from the centerline. Along the vertical direction, the vertical acceleration reaches its maximum at the tunnel foundation base. The soil acceleration under the tunnel is much greater than that above the tunnel.

3. When the failure number of the steel springs is less than 6, the failure number has little effect on the maximal soil acceleration along lateral and the vertical direction, and the maximal difference of the maximal acceleration for two directions is only 8.33 and 10.58%. When the failure number exceeds 6, the acceleration not only along lateral direction but also along vertical direction increases significantly. Comparing the peak values with no failure springs, there is a 339.79 and 101.28% increase in the maximal acceleration along the lateral and vertical direction, respectively. With the increase of the failure number of springs from 7 to 9, the maximal acceleration along the lateral direction decreases quickly, while the attenuation along the vertical direction is very limited.

References

1. Xia H (2010) Traffic induced environmental vibrations and controls. Science Press, Beijing (in Chinese)
2. Ge H, Yang LL, Liang YC (2017) Test and analysis of vibration characteristics of metro track structures subject to different speed. Railw Stand Des 61:11–14 (in Chinese)
3. Yu GR, Shen JF, Chen K (2015) Influence of railway-support failure on the dynamic response characteristics of steel spring floating slab track. Noise Vib Control 35:78–81 (in Chinese)
4. Zhai WM (2015) Vehicle-track coupled dynamics, 4th edn. Science Press, Beijing (in Chinese)
5. Li JL, Xu P, Zhai WM (2011) Dynamic analysis of steel spring floating slab track fulcrum force. Railw Eng 106–109 (in Chinese)
6. Yin ZG (2008) Research on the buildings vibration and noise caused by subway. Tongji University (in Chinese)
7. Liu JB, Wang ZY, Du XL (2005) Three-dimensional visco-elastic artificial boundaries in time domain for wave motion problems. Eng Mech 22:46–51 (in Chinese)
8. Zhai WM, He ZX, Song XL (2010) Prediction of high-speed train induced ground vibration based on train-track-ground system model. Earthq Eng Eng Vib 9:1–10

Experimental Study on the Transfer Characteristic and Deformation of Three Types of Combine Track System

Ning Xu, Fei Zeng, Anbin Wang, Zhiqiang Wang, Jinzhao Wang and Tong Ren

Abstract This study described the transfer properties and deformation of the combine track systems. This experiment was designed to apply different loads to three combined track systems on the 1:1 track platform, respectively. The aim system contained rubber vibration isolation cushion, slab and vibration damping fasteners. The difference among the systems is mainly due to the different types of fasteners. The results indicated that loading had an influence on the transfer properties of track systems; however, the different loadings had similar results. As an ordinary damping fastener combine track system, the vertical and lateral response curves were diverse from 140 to 610 Hz and 40 to 480 Hz, respectively. While for medium damping fastener combine track system, the different frequency bands were 100–500 Hz and 25–350 Hz for vertical and lateral response, respectively. For the high damping fastener combine track system, the different frequency bands were 70–420 Hz and 15–270 Hz. In the deformation results, the ordinary damping fastener had the smallest rail deformation and the largest slab deformation, while the high damping fastener had the largest rail deformation and the smallest slab deformation.

Keywords Combine track system · Transfer characteristic · Load · Deformation

1 Introduction

In the wheel rail coupling system, track structure parameters such as mass and stiffness directly determine vibration behavior. Therefore, rational track structure and parameters selection are the potential method to control vibration and noise [1–4]. New track structures, combined with rubber vibration isolation cushion, slab, and fasteners have been widely used in areas that are sensitive to vibration levels.

N. Xu (✉) · F. Zeng · A. Wang · Z. Wang · J. Wang · T. Ren
Luoyang Sunrui Rubber and Plastic Science and Technology Co., Ltd.,
Luoyang 471003, China
e-mail: xuning4243@163.com

However, the increase of the vibration damping effect of the track structure is accompanied by the increase of the rail deformation. Meanwhile, the latter may cause track irregularity, wheel rail noise aggravation, wheel rail wear, and even cause derailment, which will affect the safety and riding comfort level of trains seriously [5, 6].

To verify the safety and reliability of the combine track system, dynamic study was usually carried out on operating railway lines, which reflected the track structure characteristics greatly. However, performing online test on the busy railways had many restrictions like high costs. Therefore, we chose to test both the transfer characteristics and deformation of the proposed combine track systems in laboratory environment with a full-scaled track testing platform. The results provided reference to the vibration damping and safety performance for a combine track system with different fasteners.

2 Test Track and Track Systems

2.1 Test Track

The laboratory test track is a full-scaled simulation of actual railway lines. The length of the line is 30 m, and the radius curvature is 500 m. In order to simulate infinite long lines, damping boxes are installed at both ends of each line to eliminate the influence of the rail internal vibration echo on the test results, as shown in Fig. 1.

2.2 Combine Track Systems

From the top to bottom, combine track system includes rail, fasteners, slab, rubber vibration isolation cushion, and the foundation of ballast bed, as shown in Fig. 2. The vibration reduction performance of combine track system is realized by
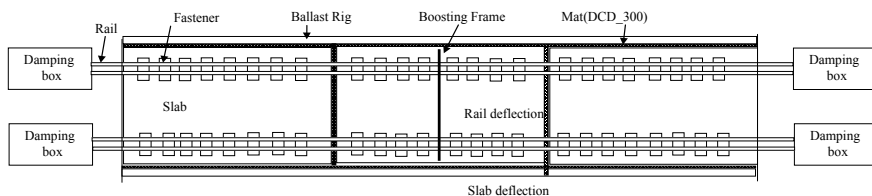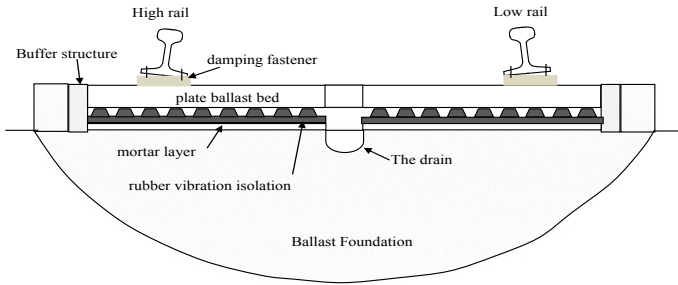

Fig. 1 Lines schematic diagram

Fig. 2 Combine track system schematic diagram

assembling different fasteners and rubber vibration isolation cushions with different stiffness and rational allocation of system mass, stiffness, and damping. Three types of fasteners are used in this study, which included the ordinary damping fastener, the medium damping fastener, and the high damping fastener.

2.3 Loading Systems

The loading system is consisted of hydraulic pump, springs, and simulating wheels. The hydraulic pump is fixed to the I-beam. Forces applied to rails by simulating wheels are adjusted to replicate the conditions of wheelset running on a straight or curved track. The loading system setup is shown in Fig. 3. Single wheelset axle loading step is 20 kN, among which the load of 160 and 140 kN is corresponding to the single axle load of the domestic type A and B vehicles.
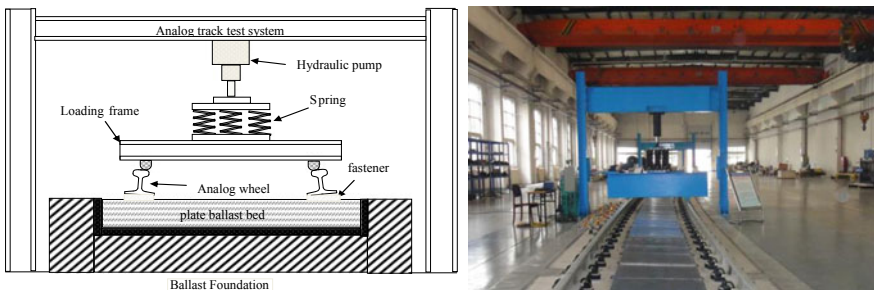

Fig. 3 Loading system schematic diagram

3   Test Contents and Equipment

3.1   Test Contents

The test parameters include rail frequency response function, rail deformation relative to slab, and slab deformation relative to foundation. Measurement points of rail's vertical and lateral responses are located on the railhead above the fastener as shown in Fig. 4. The deformation measurement points of rail and slab are on the rail foot and slab bed, respectively (Fig. 5) [7, 8].

The equipment is calibrated on site, and the accelerometer is calibrated with a calibration instrument to achieve a standard value. The displacement sensor is calibrated by standard test strips before and after the experiment.

Before real experiment, more than three warm-up experiments are carried out to reduce the testing error caused by the coordination characteristics of the track system and ensure the stability of the track system during real experiment. Meanwhile, extra attentions are paid to the interference caused by other factors during the experiment. The load is maintained stable during the experiment. The data records on every experiment are more than ten times. Average processing is performed after removing the abnormal data.
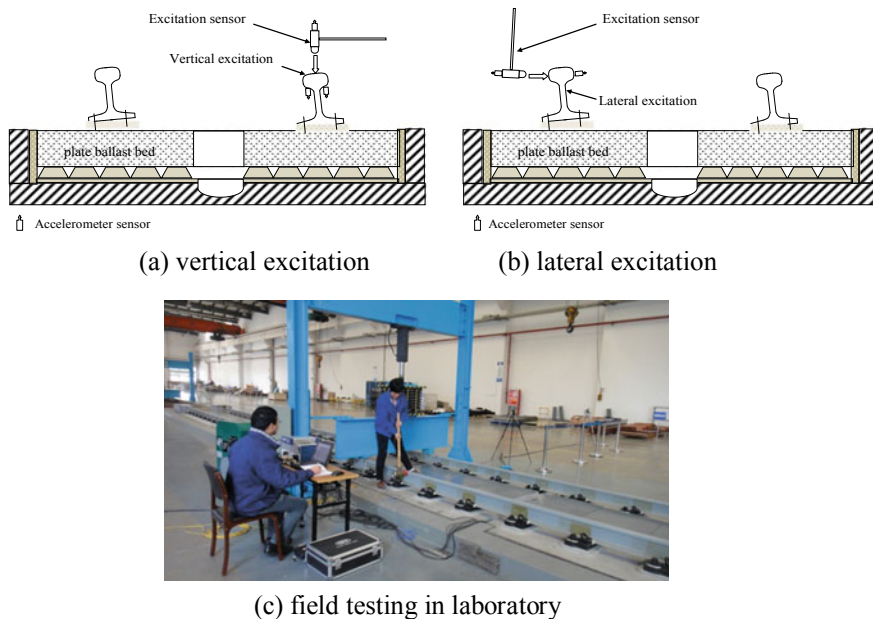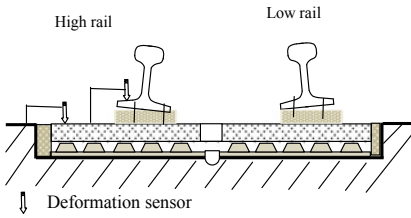

(a) vertical excitation   (b) lateral excitation

(c) field testing in laboratory

Fig. 4   Transfer response test schematic diagram

(a) diagrammatic sketch   (b) field testing in laboratory

Fig. 5 Vertical deformation test schematic diagram

3.2 Test Equipment

The test equipment mainly includes NI data acquisition instrument, PCB company 352C03 and 393C33 accelerometer, and AML-SGD10 displacement sensor.

4 Test Results

4.1 Frequency Response Characteristics

The frequency response reacceptance curves of the three types of combination track systems are shown in Figs. 6, 7, 8, 9, 10, and 11.

As shown in Figs. 6, 7, 8, 9, 10, and 11, wheelset loads have significant difference influence on the rail frequency response reacceptance spectrum with same track
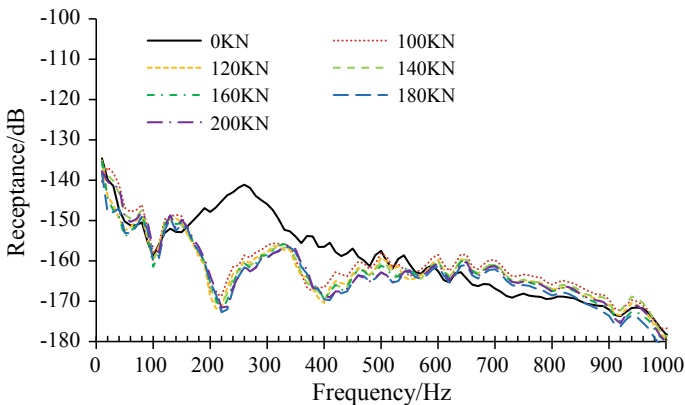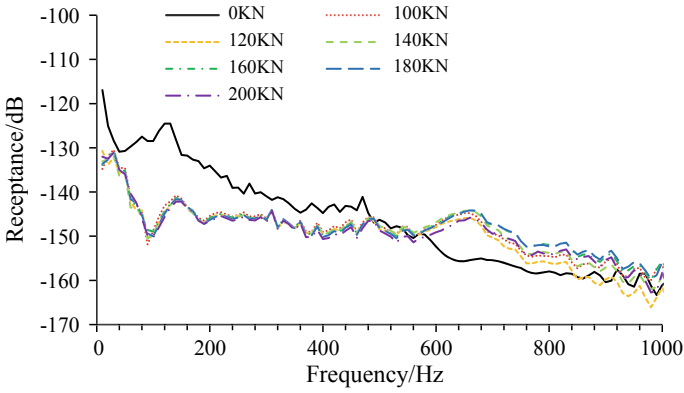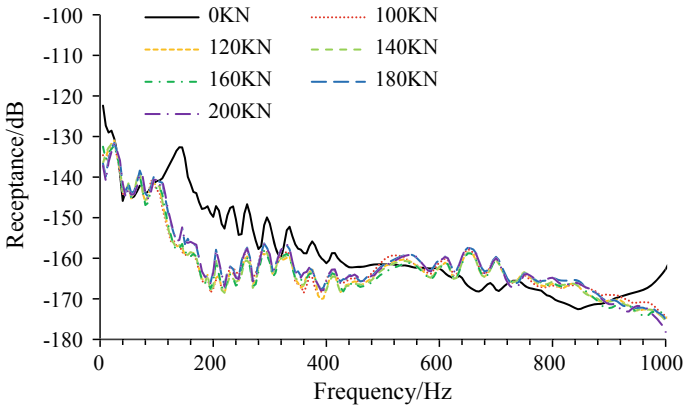

Fig. 6 Rail vertical reacceptance spectrum of combine track system with ordinary damping fastener
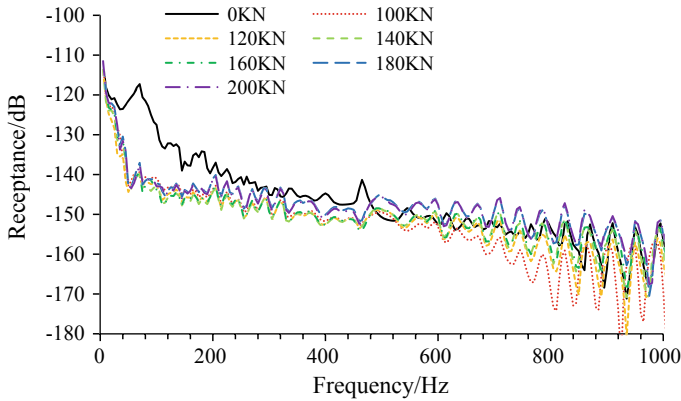
Fig. 7 Rail lateral reacceptance spectrum of combine track system with ordinary damping fastener

Fig. 8 Rail vertical reacceptance spectrum of combine track system with medium damping fastener

structure, though there is no significant difference across different loading levels. But the frequency response characteristics are significantly different for different track structures. Meanwhile, the rail reacceptance peak frequencies are affected by different damping fasteners. In other words, the peak frequency moves to the low frequency with the increase of the fastener damping level, and the bandwidth is gradually shortened. As shown in Figs. 6, 7, 8, 9, 10, and 11, the vertical response peaks located in the range of 140–610 Hz, and the lateral response peaks located in the range of 40–480 Hz for the combine track system with ordinary damping fastener. For the medium damping system, peak frequency ranges are 100–500 Hz and 25–350 Hz for vertical and lateral response, respectively. While for the high damping fastener combine track system, the vertical and lateral response peaks are located in the frequency bands of 70–420 Hz and 15–270 Hz, respectively.

Fig. 9 Rail lateral reacceptance spectrum of combine track system with medium damping fastener

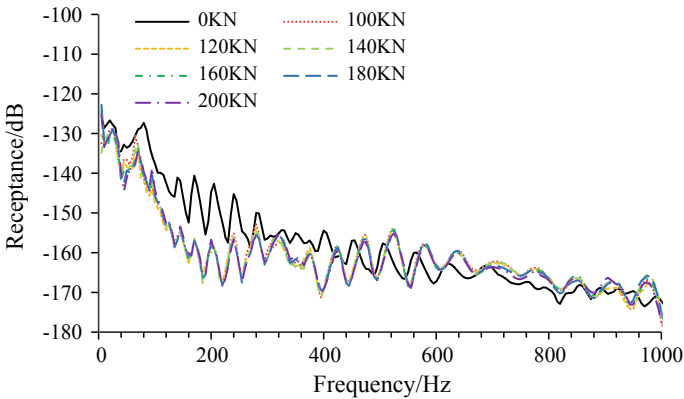**Fig. 10** Rail vertical reacceptance spectrum of combine track system with high damping fastener

Based on the experimental results discussed above, combination track system can be designed according to the specific vibration isolation requirements of different lines.

4.2 Rail Vertical Deformation

Figure 12 shows the rail vertical deformation relative to slab, and Fig. 13 is the relative vertical deformation of slab relative to the foundation of three different track structures with and without wheelset loading. The vertical deformation of the rail relative to the foundation, i.e., the absolute deformation of the track system is shown in Fig. 14.
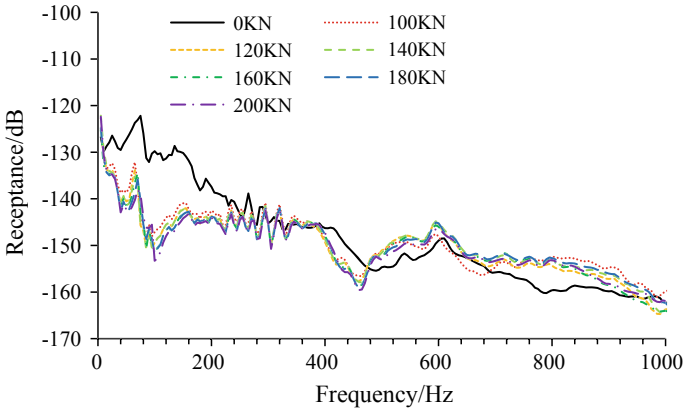
Fig. 11 Rail lateral reacceptance spectrum of combine track system with high damping fastener
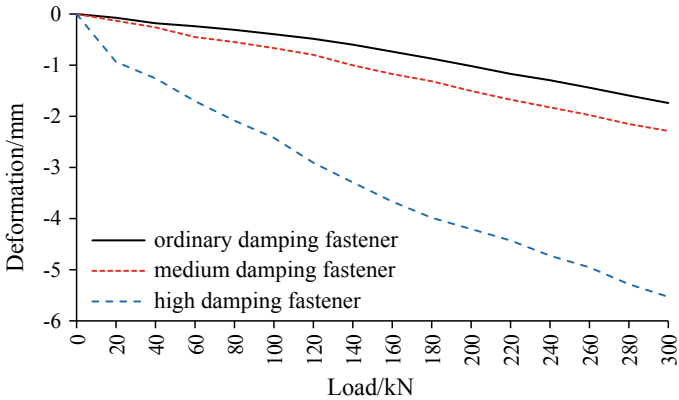
Fig. 12 Rail vertical deformation

The vertical deformation of both the rails and the slab is used as the increases with the increase of loads for all three combination tracks. And the absolute track system deformation increases with damping increases.

For the ordinary damping fastener combination track system, rail vertical deformation is the smallest, while the slab deformation is the largest. In contrast, for the high damping fastener combination track system, the rail vertical deformation is the largest, while the slab deformation is the smallest [9].

In Fig. 14, there is little difference in the absolute vertical deformation of combine track systems with ordinary damping fastener or medium damping fastener. However, for high damping fastener combine track system, the absolute vertical deformation is significantly higher than that in low and medium damp track systems.
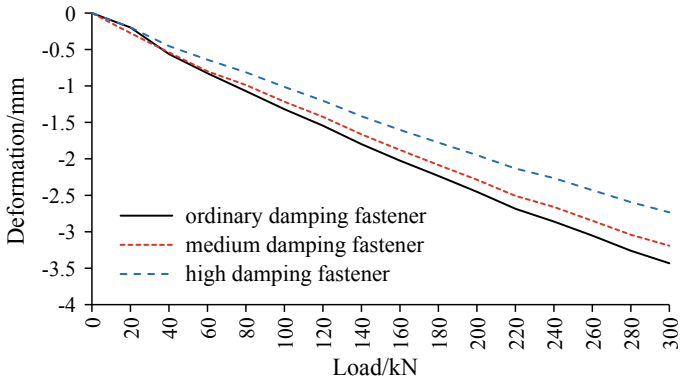
Fig. 13 Slab vertical deformation
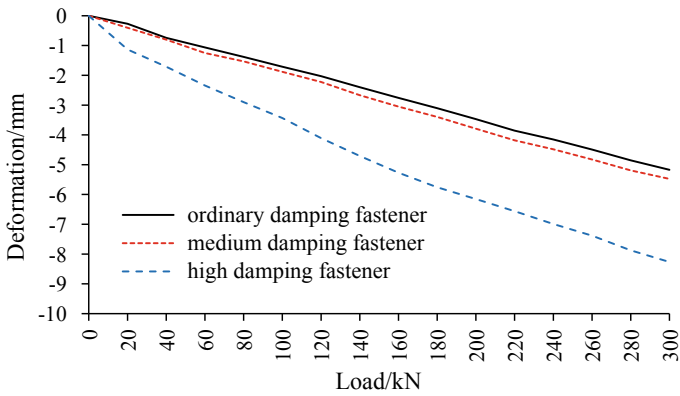
Fig. 14 Track system absolute deformation

In addition, under the load of 140 and 160 kN, the deformation of all three systems met the safety limiter. In general, a few meters of transition zone are necessary when implementing a combination track system in common railway lines, which ensures a smooth transition of the rail deformation and the safe operation of the train.

5   Conclusions

(1) As the same track structure, rail frequency response reacceptance spectrum shows significant difference between with and without wheelset loads, while there is no evident difference among different loading levels.

(2) As different track structures, the frequency response characteristics are significantly different. The rail reacceptance peak frequency bands are affected by different damping fasteners. The peak frequency band moves to the low frequency with the increase of the fastener damping level, and the bandwidth is gradually shortened.

(3) The relative vertical deformation of the rail and slab is closely related to types of fastener. The rail deformation is less than ballast bed deformation for the ordinary damping fastener combine track system and greater for high damping fastener combine track system.

(4) There is little difference in the absolute deformations between the ordinary damping and the medium damping fastener combine track systems, while the high damping fastener combine track system has the highest deformation among the three damping systems.

References

1. Thompson DJ, Vincent N (1995) Track dynamic behaviour at high frequencies. Part 1: theoretical models and laboratory measurements. Veh Syst Dyn Suppl 24:86–99
2. Li ZG, WU TX (2007) Study on the vibration isolation performance of floating slab track using dynamic receptance method. J Vib Eng 20(3):123–128
3. Auersch L (2012) dynamic behavior of slab tracks on homogenous and layered soils and the reduction of ground vibration by floating slab tracks. J Eng Mech 138(8):923–933
4. Kuo CM, Huang CH, Chen YY (2008) Vibration characteristics of floating slab track. J Sound Vib 317(3/4/5):1017–1034
5. Wu K, Ma MY, Gu CH (2010) Study on roadbed deformation rule and assessment of slab track on railway passenger special line. Adv Mater Res 177–180
6. Yang Xinwen Gu, Shaojie Zhou Shunhua et al (2017) Vertical vibration analysis of vehicle-track-subgrade coupled system in high speed railway with dynamic flexibility method. Transp Res Procedia 25:291–300
7. Gupta S, Degrande G (2010) Modelling of continuous and discontinuous floating slab tracks in a tunnel using a periodic approach. J Sound Vib 329(8):1101–1125
8. Li K, Liu W, Han Z, Wu Z (2015) Dynamic displacement response of track subjected to a load moving at a variable speed. Proc Inst Mech Eng, Part F: J Rail Rapid Transit 798–814
9. Ministry of Railways of the People's Republic of China (2006) Railway line maintenance rules. Railway transportation 146

Analysis of Accurate Dynamic Responses on Orthotropic Steel Deck Based on Multi-scale Time-Varying Boundary Approximation Method

Yuan Tian, Nan Zhang, Wanli Yang and Ming Chen

Abstract Accurate evaluation of dynamic effects on critical components of orthotropic bridge decks is of great significance for structural damage identification and fatigue life prediction, especially for long-span cable-stayed bridges. However, the prohibitive computational cost of the traditional finite element (FE) method makes it unfeasible for this problem. Therefore, based on dynamic balance equations and FE strategies, multi-scale time-varying analysis approach is proposed and derived theoretically in this paper. Unlike most of the existing methods, the dynamic effect of the refined model is easily solved by repeated iteration by using the dynamic responses of a relatively large-scale model as boundary conditions. As a case study, the whole segment model of an orthotropic bridge deck is established and performed via two refinement processes at the complex junction area between the plate and the longitudinal ribs under the track. A similar and sufficiently accurate model is also analyzed using ANSYS package in general FE method, and the comparison is made. This study can be considered as an attempt to provide a brand-new high-efficiency analysis framework for accurate solution of local vibration problems. Under relatively small and easily manageable calculation conditions at each cross-scale processing, not only the requirement of global design for actual engineering applications can be met, but also the aim of further in-depth analysis can be achieved as well.

Y. Tian (✉) · W. Yang · M. Chen
China Academy of Transportation Sciences, Chaoyang District, BJ 100029, China
e-mail: ytian88@163.com

N. Zhang
Beijing Jiaotong University, Haidian District, BJ 100044, China

1   Introduction

By combining the social aesthetic needs and efficient use of structural materials, long-span cable-stayed bridges have been extensively used in railway bridge engineering over the past few decades [1, 2]. However, due to the weak adaptability of tracks for the deformation of integral bridge deck system, they are relatively difficult to be adopted with the increasing span lengths [3, 4]. Correspondingly, ballast decks, which have fully replaced the traditional open bridge deck, become the main type floor system in these long-span bridges. Considering the load-carrying capacity in proportion to their weight and excellent integrality, which can easily meet the requirements of running safety in railway bridges, and the convenient construction, there is no doubt in the mushrooming of the application of orthotropic steel deck [5].

Orthotropic steel deck is a complex system that consisted of a deck plate, longitudinal "U" ribs, cross girders, and bottom chord, as shown in Fig. 1. The crisscrossing component connections and uncountable weld joints make it rigidity in longitudinal and transverse directions different [6]. Local vibrations easily cause component damage and cracking, which would eventually lead to the loss of their service function. Since the induced key elements of the working environment and loads usually belong to the structure of the overall scope, bi-directional synchronization analysis across the global and local refined models concurrently became one of the highlights of the scientific research in the civil engineering field [7–9].

So far, there are two ways to acquire the exact dynamic results of complex structure such as those of the orthotropic deck systems, which are dependent on updating the FE technique [10, 11]. The first way is to create sophisticated models by further mesh improvement. However, it would inevitably not only raise the computational cost due to the supersize model with too many elements and nodes, but also increase the probability of creating operation errors or collapses with many
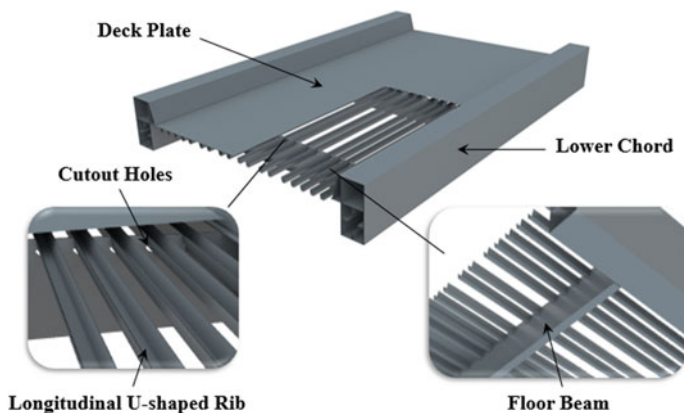
Fig. 1   Diagram of orthotropic steel deck

uncertainties [12]. The second way is based on the multi-scale FE modeling technique [13], which typically includes sub-modeling [14] and sub-structure methods [15]. For the first way, the selection of the boundary conditions in the sub-modeling method is relatively complicated due to the connection compatibility techniques between the different scale models in the transition regions. Moreover, it may lead to the error accumulation in the analysis process of nonlinear problems. For sub-structure method, the difficulty lies in the condensation of internal degrees of freedom (DoFs) and coordinate transformation. Overall, considering its economic computational configuration while having a great potential to obtain accurate results and other benefits, the multi-scale FE modeling technique draws the attention of scholars all over the world.

Based on the aforementioned issues, the aim of this paper was to present an efficient approach in multiple scales for modeling and calculating the local dynamic responses of orthotropic steel bridge decks. First, the analysis framework of the multi-scale time-varying boundary approximation method was established and investigated via theoretical derivation. Second, taking the orthotropic deck of a cable-stayed bridge as a case study, the dynamic responses of the critical location beneath the track were evaluated based on this framework. They were then compared with the detailed whole segment model and calculated using ANSYS package to confirm the effectiveness of the method, which was followed by the conclusion in the end.

2 Multi-scale Time-Varying Boundary Approximation Method

2.1 Method Overview

To clarify the complete solving steps of this approach, a two-dimensional (2-D) beam with a time-dependent load-F(t) (represented by the red arrow) acting at any position within the span was taken as an example to show the fundamental procedures, as shown in Fig. 2a. The area between nodes I and II, which is the shadow region covered, was assumed to be refined later.

Followed by the general FE analysis strategies, the initial model of the whole beam was established at first. Based on the tested structure frequency or initial calculated results, the created model was checked and assured to be correct. At this stage, the model satisfied the requirements of static and dynamic analysis and was used in the service of design structure, even though it is based on a larger-scale relative coarse model. As the target possessed more accurate analysis of the mid-span area, which the subsequent research focused on, nodes III and IV were added into the model as shown in Fig. 2b. The response values of nodes II and I were obtained and used as boundary conditions to recalculate the results of III and IV. So far, the refined FE model based on a smaller scale could guarantee the

Fig. 2 Diagram of solution procedure: **a** general model, **b** refined model, and **c** more refined model. The black dots indicate the nodes, and the blue dashed lines represent the final refined area
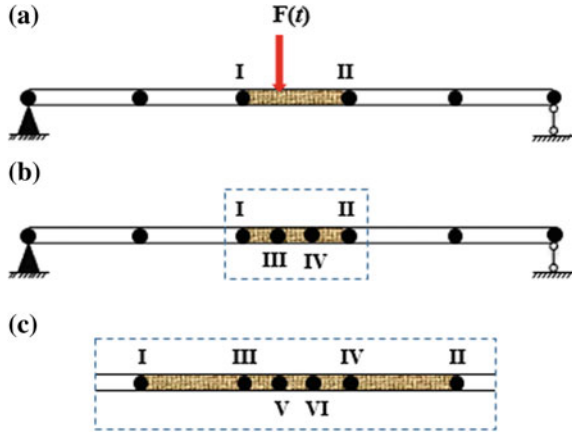
accuracy. However, if the detailed model still did not meet the needs for analysis, more nodes could be added to refine the area in depth. As shown in Fig. 2c where the dashed line area is the part of continue refining, namely by adding nodes V and VI between III and IV, while using the solving strategy mentioned above.

Overall, using the responses of the existing nodes as boundary conditions, the proposed method has the potential to add more nodes or elements to improve the mesh refinement at the critical region of interest using the results of the last previous calculation as boundary conditions. Through the dynamic boundary approximation process between different model scales of model, accurate responses for the concerned area will gradually meet the needs of various modeling levels of modeling.

2.2 Theoretical Derivation

The 2D beam mentioned above is used for the derivation based on the FE theory.

For the original model in Fig. 3a, subscripts 1 and 4 denote the DoFs of the components, which intended to refine or not, respectively. The dynamic equilibrium equation of the model [16] is:

$$
\begin{bmatrix} m_{11} & m_{14} \\ m_{41} & m_{44} \end{bmatrix} \begin{Bmatrix} \ddot{x}_1 \\ \ddot{x}_4 \end{Bmatrix} + \begin{bmatrix} c_{11} & c_{14} \\ c_{41} & c_{44} \end{bmatrix} \begin{Bmatrix} \dot{x}_1 \\ \dot{x}_4 \end{Bmatrix} + \begin{bmatrix} k_{11} & k_{14} \\ k_{41} & k_{44} \end{bmatrix} \begin{Bmatrix} x_1 \\ x_4 \end{Bmatrix} = \begin{Bmatrix} f_1 \\ f_4 \end{Bmatrix} \quad (1)
$$

where m, c, k, and f denote the mass, damping and stiffness, and acting force matrices of the structure, respectively. $\ddot{x}$, $\dot{x}$, and x are the acceleration, velocity, and

Fig. 3 Theoretical derivation model. The shade region is also the component intended to refine
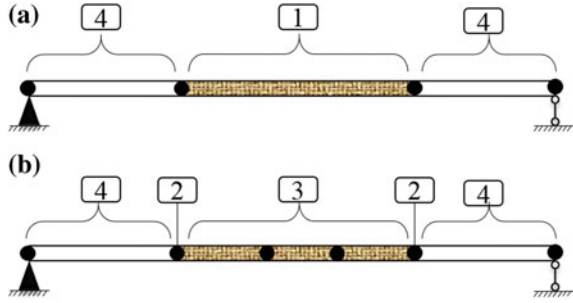
displacement vectors of the structure, respectively. Similarly, Eq. (1) can be expressed as:

$$m_{11}\ddot{x}_1 + c_{11}\dot{x}_1 + k_{11}x_1 = f_1 - m_{14}\ddot{x}_4 - c_{14}\dot{x}_4 - k_{14}x_4 \tag{2}$$

Figure 3b shows the refined model of the next step. The DoFs that the refining part and the original model share are identified with the subscript 2, while the increased DoFs in the refining part are denoted with the subscript 3. Similarly, the DoFs in the none-refined part are labeled with the subscript 4. It is found that the increased DoFs with subscript 3 are only related to the common DoFs with subscript 2, rather than with the subscript 4. Therefore, the dynamic equilibrium equation for the refined model is as follows.

The following transformation relationship is expressed as:

$$\begin{bmatrix} m_{22} & m_{23} \\ m_{32} & m_{33} \end{bmatrix} \begin{Bmatrix} \ddot{x}_2 \\ \ddot{x}_3 \end{Bmatrix} + \begin{bmatrix} c_{22} & c_{23} \\ c_{32} & c_{33} \end{bmatrix} \begin{Bmatrix} \dot{x}_2 \\ \dot{x}_3 \end{Bmatrix} + $$
$$\begin{bmatrix} k_{22} & k_{23} \\ k_{32} & k_{33} \end{bmatrix} \begin{Bmatrix} x_2 \\ x_3 \end{Bmatrix} = \begin{Bmatrix} f_1 - m_{24}\ddot{x}_4 - c_{24}\dot{x}_4 - k_{24}x_4 \\ 0 \end{Bmatrix} \tag{3}$$

It is clearly observed that the relationship between the DoFs labeled with subscripts 1 and 4 in the original model is the same as those of subscripts 2 and 4 in the refined model. The DoFs belonging to subscript 2 are the boundary linking DoFs 1 and 4, thus:

$$m_{24} = m_{14}, c_{24} = c_{14}, k_{24} = k_{14} \tag{4}$$

According to the converted dynamic equilibrium equation for the original model and refined model in Eqs. (2) and (4) with the same relationship shown in Eq. (5), hence, we can deduce the following equation:
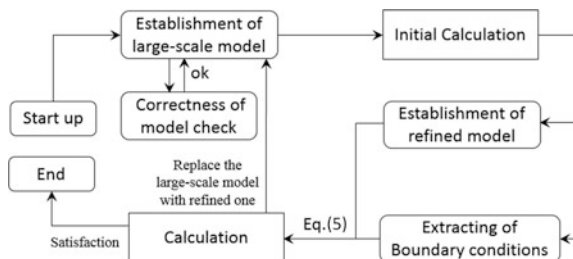
Fig. 4 Flow chart of the calculation steps

$$
\begin{bmatrix} m_{22} & m_{23} \\ m_{32} & m_{33} \end{bmatrix} \begin{Bmatrix} \ddot{x}_2 \\ \ddot{x}_3 \end{Bmatrix} + \begin{bmatrix} c_{22} & c_{23} \\ c_{32} & c_{33} \end{bmatrix} \begin{Bmatrix} \dot{x}_2 \\ \dot{x}_3 \end{Bmatrix} +
$$
$$
\begin{bmatrix} k_{22} & k_{23} \\ k_{32} & k_{33} \end{bmatrix} \begin{Bmatrix} x_2 \\ x_3 \end{Bmatrix} = \begin{Bmatrix} m_{11}\ddot{x}_1 + c_{11}\dot{x}_1 + k_{11}x_1 \\ 0 \end{Bmatrix}
\tag{5}
$$

In Eq. (5), subscripts 2 and 3 represent the DoFs in refined model, while sub-script 1 stands for the DoFs in the original model. Accurate analysis can be obtained using the dynamic responses of the original model gradually as boundary conditions until a sufficient mesh level depth is reached. Thus, the calculation chart is followed as shown in Fig. 4.

3 Case Study

As a case study, the first highway and railway cross-sea bridge was studied to perform the analysis. As shown in Fig. 5, the bridge is a five-span cable-stayed of which the main span is 532 m and the inner and outer spans at each side are 196 and 84 m, respectively. All the spans consist of an interval of 14 m with an inverted trapezoidal cross section. The 222 m towers, which composed of two columns and two beams, supported 68 prefab cables, which contain numerous high-strength steel wires.

Taking the orthotropic deck of the railway line in this bridge as an example, the standard cross section was shown in Fig. 6 in the red dash line. Every interval covered 14.0 m in length, and the distance between the centerline of the two low chords was 15.0 m. Cross ribs were distributed among the interval, and crossbeams were set on both ends of the interval. The centerline distance of the double ballast tracks, supported by the orthotropic deck, is 4.4 m. The thickness of all the U-shaped ribs, deck plate and the concrete ballast slot are 8.0 mm, 16.0 mm, and 60.0 mm, respectively. Q370qD steel is the main material for all components.
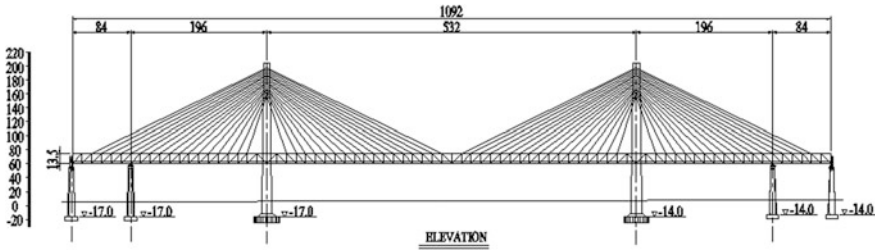
Fig. 5 Layout of the cable-stayed bridge (unit: m)
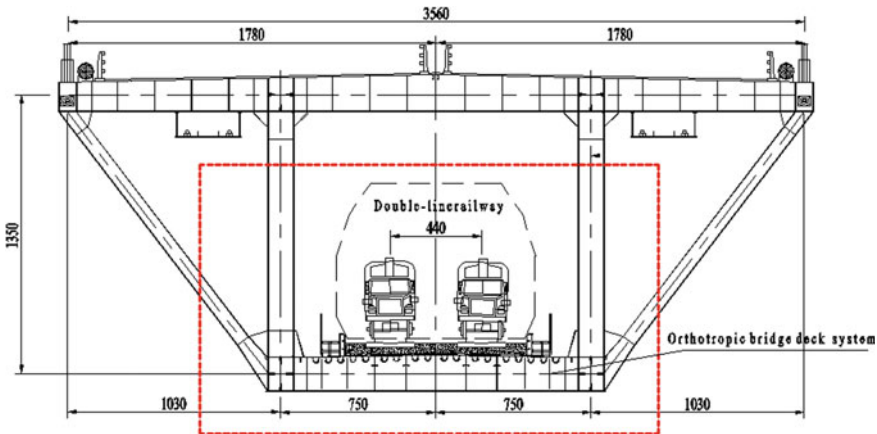
Fig. 6 Standard cross section (unit: cm)

3.1 Original and Refined Models

The FE model of orthotropic deck system was established simultaneously using ANSYS package. MATLAB simulation was used for the shell element calculation program according to this method; ANSYS was for extracting of the calculation results and boundary conditions of subsequent processing. Since the target of this paper focused on introducing a proposed method, the moving load only was taken for the simulation of the train passing through the interval.

The original model of the orthotropic steel deck system, using Shell181 element, consisted of 2167 nodes and 2408 elements. As this is a combined railway and highway cable-stayed bridge, the model boundary condition in this model adopted a segmental angular point derrick constraint to simulate the connection between the web member and side beam. According to existing research and studies, cracks generally occur at the adjacent locations, such as U-shaped rib and bridge deck or crossbeam, and therefore, the center area in the mid-span of the interval was chosen to refine. For the refining area in the original model, the element size in the bridge
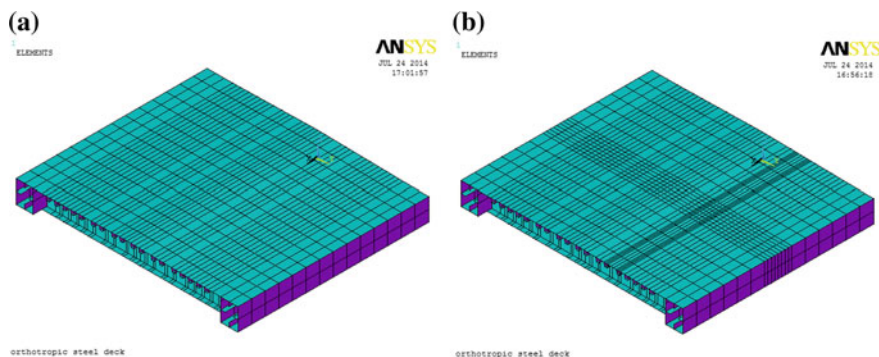
Fig. 7 Finite element model

deck was approximately 1.0 m × 0.3 m (the former is suitable to the bridge; and the latter for the transverse to the bridge. This is the same for the values below) and the U rid was 1.0 m × 0.27 m, respectively.

While after refining, the element size in the bridge deck and the U rib reduced to 0.25 m × 0.1 m and 0.25 m × 0.09 m, respectively. The refined model consisted of 3109 nodes and 3448 elements. The original and refined FE models are shown in Fig. 7. It is clear that the mesh level increased greatly compared to that of the original model. In both of these two models, concrete ballast slot, sleepers, track, ballast, and other connecting elements are all modeled with the same design parameters, see Table 1.

In order to ensure the rationality and uniformity of these two models before and after refinement, the results of the natural frequency of the vibration and static analysis of the model were used for the comparison, as listed in Table 2. It demonstrates that, with the local precision improved from the original structure to the higher level, the biggest difference in the first five natural frequencies was only 0.87%. Meanwhile, under the same static load conditions, the difference in the

Table 1 Main parameters of finite element method model

Component	Element type	Parameter/unit	Value	Parameter/unit	Value
Concrete ballast slot	Shell181	t_d/mm	60	E_d/(GN/m^2)	35
Sleeper	Beam4	l_s/m	0.6	M_s/kg	251
Steel rail	Beam4	m_r/(kg/m)	60.64	$I/(\times 10^{-5}\text{m}^4)$	3.217
Rail fastening	Combin14	K_k/(MN/m)	70	C_p/(kN s/m)	75
Ballast	Combin14	K_d/(MN/m)	130	ρ_b/(g/cm^3)	1.9
Force spike	Combin14	K_l/(GN/m)	13	E_l/(GN/m^2)	210

t_d E_d is the thickness of ballast slot and elastic modulus; l_s M_s is the distance between sleeper and mass; m_r I is the mass of steel rail in unit length and the moment of inertia of cross section; K_k C_p is the vertical stiffness and damping ratio of rail fastening; K_d ρ_b is the vertical stiffness and the density of ballast; K_l E_l is the vertical stiffness and elastic modulus of force spike

Table 2 Results of free vibration and static analysis

	No. of order	Original model	Refined model
		Frequency/Hz	Frequency/Hz
Natural frequency of vibration	1	4.4499	4.4110
	2	6.7710	6.7846
	3	6.8382	6.7929
	4	7.5971	7.6053
	5	8.2202	8.2308
Static analysis	Vertical displacement under same static condition	Displacement/mm	Displacement/mm
		5.01	5.02

vertical displacement was only 0.2%, which means that the enhancement in the grid makes negligible influences to the structure. Overall, under the guarantees of consistency during the refining process, the analytical strategy is very effective in decreasing the size of the elements in order to boost the approximation analysis to a very small-scale level.

3.2 Dynamic Responses

Dynamic responses of both of the models of the orthotropic steel deck were calculated when the moving load series (see Fig. 8) crossed the bridge at a speed of 160 km/h, which is the highest speed allowed by China's railway specification for open bridge floors. The structural damping ratio of this interval was set to 0.005, and the integration time step was taken as 0.01 s. Since the target of this paper was focused on introducing a proposed method, only vertical dynamic effect was calculated in this case study. Figure 9 shows the detailed nodes in the analytical region, which were labeled within the red rectangle in Fig. 7, as mentioned above. As shown in the graph, the four nodes of one element in the original model were
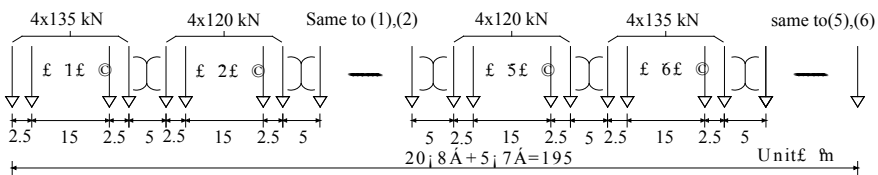
Fig. 8 Moving loads series. The effect of moving load series acting on the rail unit with its organization mode for MTMTTMTM (*M* means axle load of 135 kN and *T* stands for axle load of 120 kN)

(a) Original Model   (b) Refined Model
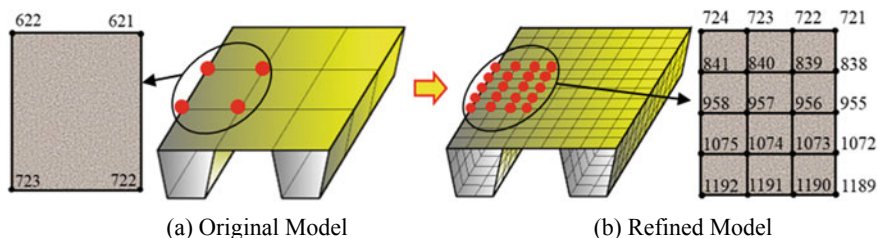
Fig. 9 Detailed nodes and elements before and after refinement
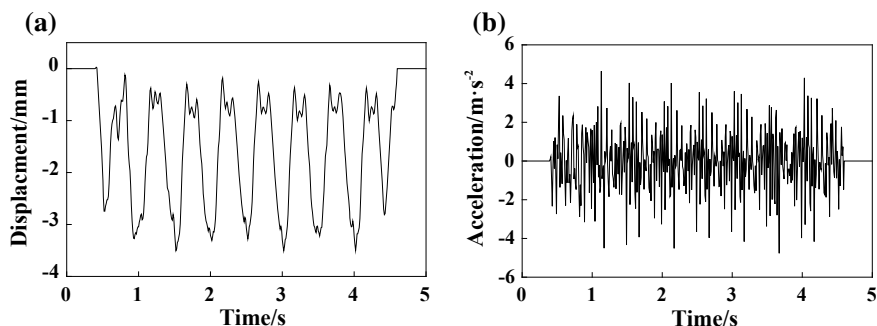
Fig. 10 Vertical displacement and acceleration history

numbered 621, 622, 722, and 723. While in the refined mode, 16 nodes and 12 elements were adopted to replace the old ones.

3.2.1 Dynamic Responses of Original Model

Figure 10 shows the vertical dynamic responses of node 621, from which the maximum in the vertical displacement, occurring at 3.02 s, reached 3.4637 mm, and the maximum vertical acceleration was 4.2317 m/s^2 at 3.62 s. According to previous studies and engineering experience, these results were reasonable and could be taken as an input for the boundary conditions for follow-up phases.

3.2.2 Dynamic Responses of Refined Model

After the original model analysis, the dynamic responses including displacement, velocity, and acceleration of each DoFs relative to the nodes 621, 622, 722, and 723 on the boundary were extracted for subsequent analysis. Similar to the second approximation in Sect. 3.2, the constitution of the elements and nodes in the refined model was chosen and arranged by a self-editing program. In the refined model, the
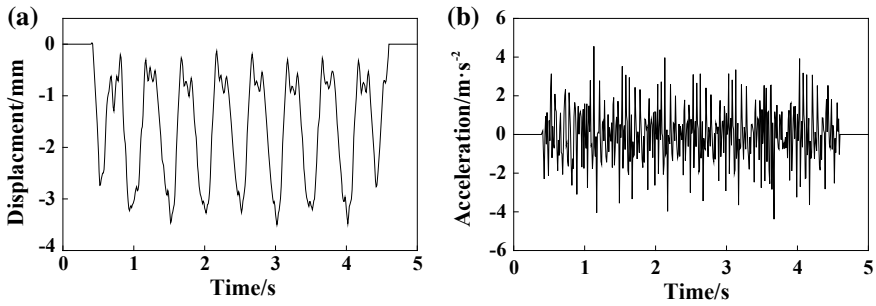
Fig. 11 Vertical displacement and acceleration history

nodes 721,724, 1189, and 1192, plotted in Fig. 9 correspond to the nodes 621, 622, 722, and 723 of the original model, respectively, while the other nodes were added after the refinement.

Figure 11 presents the dynamic responses of the refined model after the approximation analysis. Due to the limited space reasons, only the vertical displacement and acceleration of the node 1072, which were the critical junction between the decks and U-shaped rib, were listed here. The maximum of the vertical displacement was 3.4980 mm, and the maximum vertical acceleration reached 4.5396 ms^{-2}.

3.3 Validation Calculation of Detailed Model

In order to verify the correctness of the results using the program, all responses of the nodes in the refined model were recalculated again using ANSYS package. Each parameter of auxiliary structures, such as concrete ballast slot, ballast or orbital, and the operation way of moving load series, all assured to be kept the same as before. Figure 12 indicates the vertical displacement and acceleration history of node 1072 by ANSYS. Compared to Fig. 11, these histories of displacement and
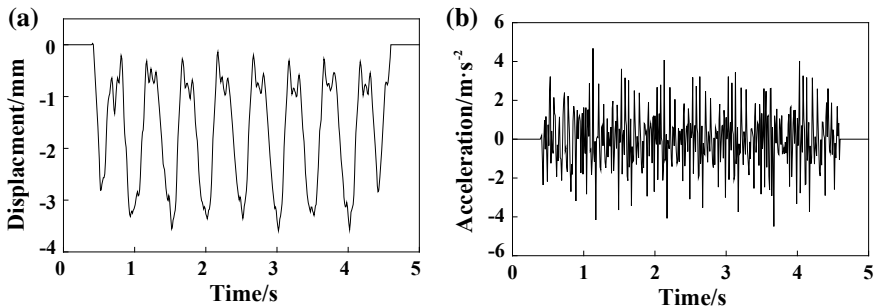
Fig. 12 Vertical displacement and acceleration history

acceleration are particularly similar to each other. The maximum for vertical displacement and acceleration was 3.5915 mm and 4.6043 m/s^2, respectively, both of which only increased by 2.67% and 1.43%, respectively.

The reason for the tiny increase in the displacement and acceleration was that the refined model, which was established based on the original model, adopted more nodes and elements. This eventually resulted in a completely different model, though both models stem from the same analytical object. It is known that the more sophisticated a model is, the closer it approaches to the real structure, and thus, the more accurate the results would be with the corresponding calculations.

4   Conclusions

In this paper, the multi-scale dynamic boundary approximation method was utilized and the effectiveness was verified the effectiveness through theoretical analysis. Some conclusions are as follows:

(1) Based on dynamic equilibrium equation and FE method, multi-scale time-varying boundary approximation method was proposed to solve the complex dynamic effect for orthotropic decks in long-span railway steel bridge in this paper. With proper calculation requirements, accuracy analysis would easily be achieved with simple meshing techniques and high efficiency.
(2) Unlike other conventional multi-scale approaches, such as sub-modeling or sub-structure method, the analytical target of this method could be focused on the concerned area without establishing the complete detailed model. The requirements of the structure refinement could facilitate the implementation with less computational cost and feasible solution scale.
(3) Local vibration problems of the orthotropic bridge decks system could effectively be addressed using this method. Though the results show that there was a tiny increase trend during the process, the difference stemmed from the models with different scales as sufficient detailed model calculation results were more close to the response of real structure.

References

1. Qin SQ (2008) Large span bridges on high-speed railway lines. J Railw Eng Soc, J Railw Eng Soc 10:53–61
2. Xiao HZ, Yi L, Gao Z (2010) Dashengguan bridge-the largest span steel arch bridge for high-speed railway. Struct Eng Int 20(3)
3. Dai G, Liu W (2011) Dongping channel bridge: long-span steel arch bridge in high-speed railway, China. Struct Eng Int 21(4)
4. Zhang N, et al (2014) Evaluation of vehicle-track-bridge interacted system for the continuous CRTS-II non-ballast track slab. Sci China Technol Sci 57(10):895–1901

5. Aygül M, Al-Emrani M, Urushadze S (2012) Modelling and fatigue life assessment of orthotropic bridge deck details using FEM. Int J Fatigue 40(7):129–142
6. Liu R, Liu YQ, Ji BH, Wang MM, Tian Y (2014) Hot spot stress analysis on rib-deck welded joint in orthotropic steel decks. J Constr Steel Res 97:1–9
7. Lautrou N, Thevenet D, Cognard J-Y (2009) Fatigue crack initiation life estimation in a steel welded joint by the use of a two-scale damage model. Fatigue Fract Eng Mater Struct 32 (5):403–417
8. Jong FBP (2004) Overview fatigue phenomenon in orthotropic bridge decks in the Nehterlands. In: 2004 orthotropic bridge conference, Sacramento, California, USA 25–27 Aug, pp 489–512
9. Miki C (2006) Fatigue damage in orthotropic steel bridge decks and retrofit works. Int J Steel Struct 6(4):255–267
10. Mottershead JE, Friswell MI (1993) Model updating in structural dynamics-a survey. J Sound Vib 167(2):347–375
11. Friswell MI, Mottershead JE (1995) Finite element model updating in structural dynamics. Kluwer Academic Publishers, New York
12. Bellenger E, Coorevits P (2005) Adaptive mesh refinement for the control of cost and quality in finite element analysis. Finite Elem Anal Des 41(15):1413–1440
13. Li ZX, Chan THT, Yu Y, Sun ZH (2009) Concurrent multi-scale modeling of civil infrastructures for analyses on structural deterioration-part I: modeling methodology and strategy. Finite Elem Anal Des 45(11):782–794
14. Cormier NG, Smallwood BS, Sinclair GB, Meda G (1999) Aggressive sub-modelling of stress concentrations. Int J Numer Method Eng 46(6):889–909
15. Law SS, Yong D (2011) Substructure methods for structural condition assessment. J Sound Vib 330(15):3606–3619
16. Zhang N, Xia H, Guo WW (2008) Vehicle-bridge interaction analysis under-high-speed trains. J Sound Vib 309:407–425

IGN Method and Matrices Equivalence of Regularization Jacobian Matrix in Solving NLS Survey Adjustment Problems

Limin Tang and Bo Wu

Abstract NLS methods may have ill-posed problems in many actual survey adjustment applications. With the increasing applications of nonlinear least squares (NLS) problems of surveying adjustment, it is very important to understand the ill-posed attribute of NLS problems and find ways to solve them. Based on regularization theory, this paper presents a new stable function to help obtain stable results of the NLS problems. An improved Gauss-Newton (IGN) method incorporating the developed stable functions is implemented with the capability of solving the ill-posed problem of survey adjustment applications. Matrices equivalence between regularization Jacobian matrices in solving NLS ill-posed problems was proposed to this paper. Experiments using simulated data and actual survey data on an old bridge which need to be repaired proved the good performances of the developed method, which can also be used in many other NLS applications such as bundle adjustment problems with photogrammetry.

Keywords IGN method · Matrices equivalence · Ill-posed problem · Regularization · Nonlinear least squares

1 Introduction

Linear least squares (LS) methods and nonlinear least squares (NLS) methods have been widely used in various applications in geosciences [1–5]. For example, in trilateration network adjustment, free network adjustment, and sequential adjustment, the nonlinear least squares methods will be used [6–9]. The traditional

L. Tang (✉)
School of Traffic and Transportation Engineering, Changsha University of Science and Technology, Changsha, People's Republic of China
e-mail: tlm@csust.edu.cn

B. Wu
Department of Land Surveying and Geo-Informatics, Hong Kong Polytechnic University, Kowloon, Hong Kong

method for processing surveying data is to transfer the nonlinear functions into linear ones using the approximations of the unknown parameters from the well-known Taylor expansions [7, 10, 11]. To solve an NLS problem in surveying adjustment, numerical iteration methods were generally employed such as the Newton method [12], Gauss-Newton method [11], and Modified Gauss-Newton method [12].

However, the NLS methods may have ill-posed problems in many actual survey adjustment applications [13, 14]. Recently, increasing research has been performed to study nonlinear ill-posed problems. They mainly focused on the nonlinear equations [14, 15], ordinary differential equations, and partial differential equations [16, 17]. New adjustment algorithms were presented to estimate the parameters of nonlinear function models. Salahi [18] presented the robust optimization framework which includes the errors in problem data. Peris et al. [19] analyzed deeply and widely the convergence of a modified Newton method. Liu [20] proposed an optimally scaled vector regularization method (OSVRM) to solve the ill-posed linear problems, which is better than the Tikhonov regularization method. Neuman et al. [21] proposed implementations of range-restricted iterative methods for linear discrete ill-posed problems. Wei et al. [22] studied the effective condition number for weighted linear least squares problems and applications to the Trefftz method. Lutskii [23] studied the condition number of the matrix of the double-period method. Vasin [24] analyzed the Lavrentyev regularization method and Newton-type process for nonlinear ill-posed problems. Diana et al. [25] studied the nonlinear ill-posed problem in model-based parameter estimation and experimental design. Muoi et al. [26] proposed a descent gradient methods for nonsmooth minimization problems in ill-posed problems.

However, the nonlinear ill-posed problems have not been systematically and extensively studied at this time, particularly for survey adjustment applications.

This paper presents an improved NLS method to solve ill-posed problems for surveying adjustment. The ill-posed problems generally seen in NLS methods are first described and analyzed. An improved Gauss-Newton method is developed by adding stable functions to the Gauss-Newton method based on regularization theory. This method solves the difficulties that lead to non-convergence of the solution due to the rank deficiency and ill-conditioned problems in the numerical iterative process of the Jacobian matrix. This paper describes the procedures of the improved Gauss-Newton method and applies it to solving the nonlinear adjustment of free networks with rank deficiency. Expressions of matrices equivalence for regularization Jacobian matrices in solving NLS ill-posed problems were given. Experimental analysis is conducted to evaluate the developed method and experimental results proved its good performance.

2 Ill-Posed Problem in the NLS Methods

The most distinct ill-posed problem in the NLS methods is the non-convergence problem of the algorithm. For example, assuming F is a measure space, in which $R(X)$ is a given continuous function. The task of seeking the minimal value of $R(X)$ in space F is to find an element $X_0 \in F$ while $R(X)$ reaches its minimum R_0. Assuming there is a unique solution X_0 and considering $\{X_n\}$ is a minimizing sequence, then the procedure can be expressed as $\lim_{n \to \infty} R\{X_n\} = R_0$.

For the above procedure, if all the minimizing sequences $\{X_n\}$ converge to the element X_0, then the problem of seeking the minimal value of $R(X)$ in space F is a stable problem. Otherwise, if the method is not solvable or not stable for seeking the minimal value of $R(X)$ in space F, then it is an ill-posed problem.

In the NLS methods, the ill-posed problem is also expressed when the minimizing sequences cannot converge to a specific element X_0. For example, in the numerical iteration methods solving NLS problems such as the Newton method and the Gauss-Newton method, the Jacobian matrix generally needs to be inverted for the calculation. However, if the matrix is ill-conditioned or singular, minimizing sequences cannot converge to a unique solution X_0. It should be noted that this ill-posed problem widely exists in the NLS methods in survey adjustment.

3 An Improved Gauss-Newton NLS Method

The general solution for solving a nonlinear least squares problem can be expressed as follows:

$$V^{\mathrm{T}}V = \|V\|^2 = \min\|f(x)\|^2 \tag{1}$$

where V is the residual vector, V^{T} is the transposed matrix of V. $\|V\|^2$ is the residual sum of squares. $f(x) = (f_1(x)f_2(x)\cdots f_n(x))$, in which $f_i(x)$ is a nonlinear function of x. Equation (1) is assumed to have a real solution and function f : $R^n \to R^m$ is assumed to be at least twice continuously differentiable.

To solve an NLS problem in surveying adjustment, the Gauss-Newton method [11] or Modified Gauss-Newton method [12] were generally used. Considering the basic Eq. (1) and the linearizing of x_k, the following linear least squares equations can be derived [15]:

$$V^{\mathrm{T}}V = \min_{p \in R^n}\|f(x_k) + J(x_k)p\|^2 \tag{2}$$

where V is the residual vector, $J(x_k)$ is the Jacobian matrix. When $J(x_k)$ is rank-deficient or ill-conditioned, standard methods such as the Levenberg-Marquardt or the subspace minimization methods using stabilization to obtain a

good search direction will fail. Moreover, these methods are not efficient when the problem is rank-deficient or very ill-conditioned at the local minimum. Therefore, this paper first studies the regularization of the NLS problems and then presents an improved Gauss-Newton method to solve the ill-posed problems.

3.1 Regularization of NLS Problems

One key step for constructing a regularization formula is to define a stable function $\mu\Omega(x)$. Tikhonov [14] presented a stable function: $\mu\Omega(x) = \mu \sum_{i=1}^{n} p_i(x_i - x_i^0)^2$, where μ is a regularization parameter, $\Omega(x)$ is a stable function of x, and p_i is the weight value. The stable functional can be used to help obtain stable results for Eq. (1). However, the key point here is how to construct a stable functional for a specific NLS problem.

Based on the characteristics of the NLS problem solved by the Modified Gauss-Newton method [12], this paper presents a new stable function $\mu\Omega(x)$ as follows:

$$\mu\Omega(x) = \mu^2 \|x_k - x_{k-1}\|^2 \tag{3}$$

where μ is a regularization parameter, $\Omega(x)$ is a stable function of x, x_k is the k time iterative value, and x_0 is the initial iterative value. Thus, the regularization equation for the NLS problem is:

$$\min F_\mu(x) = \min \|f(x)\|^2 + \mu^2 \|x_k - x_{k-1}\|^2 \tag{4}$$

3.2 The Improved Gauss-Newton Method Solving the Ill-posed Problems

By incorporating Eqs. (4), Eq. (2) can be rewritten as:

$$V^{\mathrm{T}}V = \min_x \left\| \begin{pmatrix} f(x) \\ \mu(x_k - x_{k-1}) \end{pmatrix} \right\|^2 \tag{5}$$

In Eq. (5), if we linearize f at x_k, the new linear least squares equation can be derived as:

$$V^{\mathrm{T}}V = \min_p \left\| \begin{pmatrix} J(x_k) \\ \mu I \end{pmatrix} p + \begin{pmatrix} f(x) \\ \mu(x_k - x_{k-1}) \end{pmatrix} \right\|^2 \tag{6}$$

Equation (6) is a full rank matrix solving the linear least squares problem. The solution can be obtained through normal equations for a specific regularization parameter μ.

$$T = T_k^{\text{Tikh}}(\mu) = (J^{\text{T}}(x_k)J(x_k) + \mu^2 I)^{-1}(J(x_k), \mu I)\begin{pmatrix} f_k \\ \mu(x_k - x_{k-1}) \end{pmatrix} \qquad (7)$$

The above-described method is called the improved Gauss-Newton (IGN) method. The iterative equation for IGN is defined as:

$$x_{k+1} = x_k + \lambda^{(k)} T_k^{\text{Tikh}}(\mu) \qquad (8)$$

where T_k^{Tikh} is given by Eq. (7).

3.3 Matrices Equivalence for Regularization Jacobian Matrices

In Eq. (7), $(J^T(x_k)J(x_k) + \mu^2 I)$ is called a regularization Jacobian matrix. The condition number of the Jacobian matrix would be reduced by the regularization parameter μ. But, in some conditions, when μ is a specific value, the condition number of the regularization Jacobian matrix is still larger.

Let $J_\mu(x_k) = (J^{\text{T}}(x_k)J(x_k) + \mu^2 I)$, α is a parameter, and $\alpha > 0$, we have

$$I = J_\mu(x_k)(J_\mu(x_k))^{-1} \qquad (9)$$

Expression (9) can be rewritten as:

$$I = (J_\mu(x_k) + \alpha I - \alpha I)(J_\mu(x_k))^{-1} \qquad (10)$$

Thus, expression (10) can be rewritten as:

$$I = (J_\mu(x_k) + \alpha I)(I - (J_\mu(x_k) + \alpha I)^{-1}\alpha I)(J_\mu(x_k))^{-1} \qquad (11)$$

From expression (10), we have

$$((J_\mu(x_k) + \alpha I))^{-1} = (I - (J_\mu(x_k) + \alpha I)^{-1}\alpha I)(J_\mu(x_k))^{-1} \qquad (12)$$

So we have

$$(J_\mu(x_k))^{-1} = (I - (J_\mu(x_k) + \alpha I)^{-1}\alpha I)^{-1}(J_\mu(x_k) + \alpha I)^{-1} \qquad (13)$$

How to compute the parameter α is an important problem. It is well known that the condition number of a nonsingular square matrix $J_\mu(x_k)$ with respect to a given matrix norm $\|\cdot\|$ is defined as:

$$Cond(A) = \|J_\mu(x_k)\| \times \|(J_\mu(x_k))^{-1}\| \tag{14}$$

Assume maximum eigenvalue of the ill-conditioned matrix $J_\mu(x_k)$ is $\lambda_{\mu-\max}$, the minimal eigenvalue is $\lambda_{\mu-\min}$. Then the condition number of the matrix $J_\mu(x_k)$ which we adopt is $\frac{|\lambda_{\mu-\max}|}{|\lambda_{\mu-\min}|}$. The maximum eigenvalue of the matrix $(J_\mu(x_k) + \alpha I)$ in expression (13) is $|\lambda_{\mu-\max}| + \alpha$, the minimal eigenvalue is $|\lambda_{\mu-\min}| + \alpha$. The maximum eigenvalue of the matrix $(I - (J_\mu(x_k) + \alpha I)^{-1}\alpha I)$ is $\frac{|\lambda_{\mu-\max}|}{|\lambda_{\mu-\max}| + \alpha}$, the minimal eigenvalue is $\frac{|\lambda_{\mu-\min}|}{|\lambda_{\mu-\min}| + \alpha}$.

Condition number of the matrix $(J_\mu(x_k) + \alpha I)$ is

$$\frac{|\lambda_{\mu-\max}| + \alpha}{|\lambda_{\mu-\min}| + \alpha} \tag{15}$$

Condition number of the matrix $(I - (J_\mu(x_k) + \alpha I)^{-1}\alpha I)$ is

$$\frac{|\lambda_{\mu-\max}|}{|\lambda_{\mu-\max}| + \alpha} \bigg/ \frac{|\lambda_{\mu-\min}|}{|\lambda_{\mu-\min}| + \alpha} \tag{16}$$

Let expression (15) equal to expression (16), we have

$$\frac{|\lambda_{\mu-\max}| + \alpha}{|\lambda_{\mu-\min}| + \alpha} = \frac{|\lambda_{\mu-\max}|}{|\lambda_{\mu-\max}| + \alpha} \bigg/ \frac{|\lambda_{\mu-\min}|}{|\lambda_{\mu-\min}| + \alpha} = \frac{|\lambda_{\mu-\max}|(|\lambda_{\mu-\min}| + \alpha)}{(|\lambda_{\mu-\max}| + \alpha)|\lambda_{\mu-\min}|} \tag{17}$$

Then, we can get the expression for α is

$$\alpha == \sqrt{|\lambda_{\mu-\max}|} \times \sqrt{|\lambda_{\mu-\min}|} = \sqrt{|\lambda_{\mu-\max}\lambda_{\mu-\min}|} \tag{18}$$

Expression (13) presents an infinite separation formula for the regularization Jacobian matrix. For the first step, we have the condition number of matrices $(J_\mu(x_k) + \alpha I)$ and $(I - (J_\mu(x_k) + \alpha I)^{-1}\alpha I)$ are both equal to the square root of the condition number of a matrix $J_\mu(x_k)$, the second step, separate matrix $(J_\mu(x_k) + \alpha I)$ and $(I - (J_\mu(x_k) + \alpha I)^{-1}\alpha I)$ according to expression (13), we can get four sub-matrices which condition number is equal to $\left(\frac{|\lambda_{\mu-\max}|}{|\lambda_{\mu-\min}|}\right)^{\frac{1}{4}}$. In turn separation, we can get sub-matrices which condition numbers are $\left(\frac{|\lambda_{\mu-\max}|}{|\lambda_{\mu-\min}|}\right)^{\frac{1}{8}}$, $\left(\frac{|\lambda_{\mu-\max}|}{|\lambda_{\mu-\min}|}\right)^{\frac{1}{16}}$, $\left(\frac{|\lambda_{\mu-\max}|}{|\lambda_{\mu-\min}|}\right)^{\frac{1}{32}}$ …

4 Experimental Analyses

4.1 Experiments for General NLS Problems

A nonlinear adjustment model $L_i = x_1 e^{ix_2}$ was first used to examine the performance of the developed method. The true values of x_1 and x_2 are $x = [5.420136187, -0.25436189]$. Five true values of L_i (calculated from the x values) and five corresponding independent observed values are listed in Table 1.

This NLS problem is an ill-posed problem. Several methods were used to solve this problem such as the Gauss-Newton method. When the initial value is $x_0 = [3.4, -0.8]$, the Gauss-Newton method cannot obtain convergent results. Using the developed IGN method, the calculation iterates 15 times, and the residual is $V^T V(x_{15}) = 0.000007$. The results $x_{15} = [5.422746, -0.255672]$ can be considered as the actual solution. The detailed calculation steps and results are listed in Table 2.

Another nonlinear adjustment model $Q(b) = \sum_{j=1}^{m} [f(x_j, b) - y_j]^2$ given by Gloub and Pereyra [27] was also studied using the developed IGN method. In the model, $f(x_j, b) = b_2 \text{Sin}(x_j b_1) + b_2$, $y_j = \text{Sin}(x_j)$ $(j = 1, 2, \ldots, 13)$ values of x_j are given in Table 3.

This problem is also an ill-posed NLS problem. The Modified Gauss-Newton method cannot obtain a convergent solution for this problem [12]. The IGN method developed in this paper was used to solve this problem. The initial value was set as

Table 1 True values and observed values of L_i

	1	2	3	4	5
True value	4.202834	3.258924	2.527006	1.959469	1.519394
Observed value	4.20	3.25	2.52	1.95	1.51

Table 2 Calculation of x_k and $V^T V(x_k)$

k	6	9	12	15
$x_0^1 = 3.4$	5.351557	5.375510	5.422610	5.422746
$x_0^2 = -0.8$	−0.511283	−0.251217	−0.255668	−0.255672
$V^T V(x_k)$	7.382734	0.001206	0.000007	0.000007

Table 3 Values of x_j

j	1	2	3	4	5	6	7	8	9	10	11	12	13
x_j	0.105	0.25	0.4	0.55	0.7	0.9	1.1	1.25	1.35	1.45	1.55	1.57	1.6

Table 4 Calculation results of b_k and $V^T V(b_k)$

k	800	1200	1600	2000
$b_0^1 = 0.5$	0.999152	0.999294	0.999382	0.999442
$b_0^2 = 0.5$	0.987929	0.990045	0.991332	0.992219
$b_0^3 = 0.5$	0.002164	0.001798	0.001573	0.001418
$V^T V(b_k)$	0.000792	0.000537	0.000406	0.000327

$b_0 = [0.5, 0.5, 0.5]$. After iterating 2000 times, the results were obtained as follows: $V^{\mathrm{T}} V(b_{2000}) = 0.000327$, $b_{2000} = [0.999, 0.992, 0.001]$. The detailed calculation steps and results are listed in Table 4.

4.2 Experiments for Survey Adjustment

The developed IGN method was also employed in actual survey adjustment applications. Figure 1 is a trilateration network. The coordinates of E, F, G in Fig. 1 are $X_E = 6613.389$, $Y_E = 63471.447$; $X_F = -10601.272$, $Y_F = 69734.761$; $X_G = 14781.825$; $Y_G = 65325.492$. The observed values for lines 1, 2, and 3 are $l_1 = 5048.401$, $l_2 = 3258.132$, $l_3 = 4270.691$. From E, F, G, l_1, l_2, and l_3, the coordinates H can be derived through an NLS calculation.

Using the developed IGN method to solve this problem, after iterating nine times, we obtained the value of $V^T V = 0.04$, $X_H = -10669.387$, $Y_H = 66477.332$. The calculated results are very close to the actual coordinates of H, which are $X_H^\delta = 10669.304$, $Y_H^\delta = 66477.301$.

Another experiment was performed to solve the NLS problem for a quadrilateral survey adjustment problem used for deformation monitoring of an old bridge which need to be repaired in Guangdong province in China. The observed values and

Fig. 1 A trilateration network
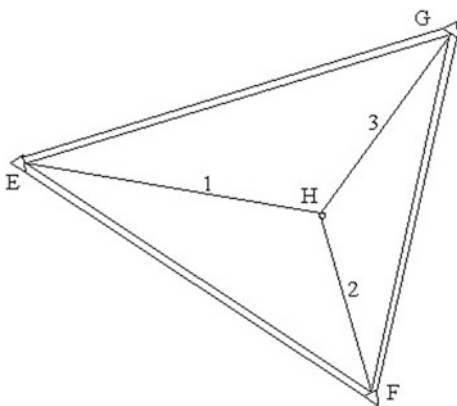
Table 5 Observed values and coordinates of the network

Coordinates (m)		Observed values of L_i (m)
$X_A = 0$	$Y_A = 0$	$L_1 = 221.413$
$X_B = 221.413$	$Y_B = 0$	$L_2 = 279.080$
$X_C = 191.873$	$Y_C = 202.658$	$L_3 = 200.446$
$X_D = -100.683$	$Y_D = 173.324$	$L_4 = 365.770$
		$L_5 = 204.800$
		$L_6 = 294.024$

coordinates of the survey network are listed in Table 5. This survey network is a typical rank-deficient free trilateration network.

The following procedures were carried out to solve the ill-posed NLS problem for this rank-deficient free trilateration network:

(1) To select the initial value of x_0 and calculate $V^{\mathrm{T}}V(x_k)$;
(2) To linearize the nonlinear model at x_k;
(3) To compose normal equation with general indirect adjustment; if $k = 0$, then calculate $\mu_k = \mathrm{tr}(J^{\mathrm{T}}(x_k)J(x_k))$;
(4) To calculate λ_k according to $\lambda_k = \frac{(f(x_k)-L)^{\mathrm{T}}J(x_k)J^{\mathrm{T}}(x_k)(f(x_k)-L)}{2(f(x_k)-L)^{\mathrm{T}}J(x_k)J^{\mathrm{T}}(x_k)J(x_k)J^{\mathrm{T}}(x_k)(f(x_k)-L)}$;
(5) To calculate x_{k+1} using Eq. (8);
(6) To calculate μ_{k+1} by $\mu_{k+1} = \mathrm{tr}(J^{\mathrm{T}}(x_k)J(x_k))\sqrt{k}$, $k > 0$;
(7) To calculate $\min F_\mu(x_1)$ and $\min F_\mu(x_0)$, if $\min F_\mu(x_1) - \min F_\mu(x_0) \leq 0.0001$, then turn to step 8, if not, let $x_0 = x_1$, turn to step 1;
(8) To output x_{k+1} and $V^{\mathrm{T}}V(x_{k+1})$.

Using the above procedures and after nine iterations, convergent results were obtained, which were compared with the results derived from another method, the Modified Gauss-Newton method [12]. The detailed results are listed in Table 6.

When using the developed IGN method, we can produce the result of $V^{\mathrm{T}}V(x_{k+1}) = 0.000002720$, which shows a great improvement compared with the MGN method.

Figure 2 shows the detailed condition numbers and determinant values of the matrix during the iterations for the MGN method and the developed IGN method. The condition numbers and determinant values of a matrix determine the stability when calculating the inverse of the matrix. Larger condition numbers indicate larger instability. Smaller determinant values indicate larger instability.

Table 6 Comparison of the results

Method	X_A	Y_A	X_B	Y_B	X_C	Y_C	X_D	Y_D
MGN method	0.00	0.00	221.413	−0.0	191.874	202.657	−100.684	173.324
IGN method	0.00	0.00	221.415	0.00	191.873	202.658	−100.684	173.324
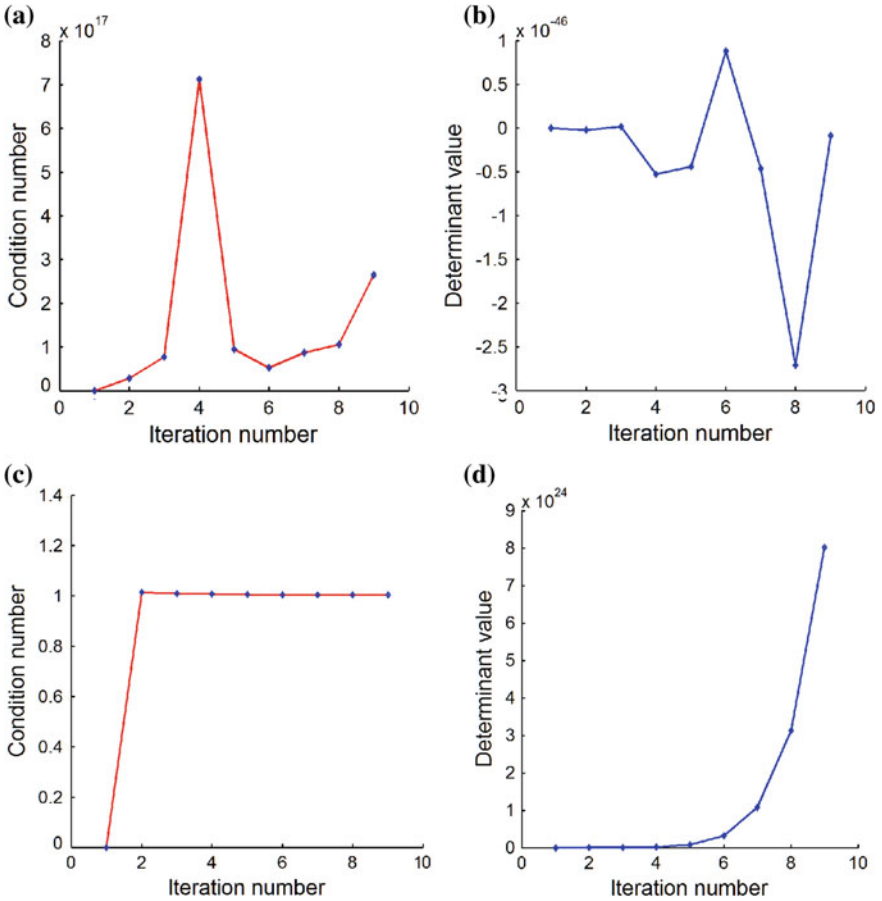
Fig. 2 Condition numbers and determinant values in the iterative process. **a** Condition number using MGN method, **b** determinant value using MGN method, **c** condition number using IGN method, and **d** determinant value using IGN method

From Fig. 2, we can see that the condition number of the matrix reaches a maximum of 7×10^{17} and the determinant values reach a minimum of 1×10^{-46} for the MGN method, which indicates the significant instability in the matrix calculation for this method. For the IGN method, significant improvements for the condition numbers and determinant values of the matrix are obtained, which shows the good performance of the IGN method.

5   Conclusions

Along with the increasing applications of surveying adjustment, it is very important to understand the ill-posed attribute of NLS problems and to find ways to solve the ill-posed NLS problems. This paper analyzed the problem and comes to the following conclusions:

(1) Based on the regularization theory, a new stable function was developed to help obtain stable results of the NLS problems,
(2) An improved Gauss-Newton method incorporating the developed stable function was implemented with the capability of solving the ill-posed problem of NLS applications,
(3) Matrices equivalence between regularization Jacobian matrices in solving NLS ill-posed problems was proposed,
(4) Experiments using simulated data and actual survey data proved the good performance of the developed method.

It should be noted that, although this study mainly focuses on ill-posed problems of NLS applications, the idea can be used in many other applications such as the bundle adjustment problem with photogrammetry. Future work will investigate the selection strategy for the regularization parameters.

References

1. Emery X (2010) Iterative algorithms for fitting a linear model of coregionalization. Comput Geosci 36(9):1150–1160
2. Bifulco I, Raiconi G, Scarpa R (2009) Computer algebra software for least squares and total least norm inversion of geophysical models. Comput Geosci 35:1427–1438
3. Abdelrahman ESM, Essa KS, Abo-Ezz ER, Sultan M, Sauck W, Gharieb AG (2008) New least-squares algorithm for model parameters estimation using self-potential anomalies. Comput Geosci 34(11) 1569–1576
4. Gallagher K, Sambridge M (1994) Genetic algorithms: a powerful tool for large-scale nonlinear optimization problems. Comput Geosci 20(7–8):1229–1236
5. Clark I (1977) Roke, a computer program for nonlinear least-squares decomposition of mixtures of distributions. Comput Geosci 3(2):245–256
6. Geunissen PJ, Amiri-Simkooei AR (2008) Least-squares variance component estimation. J Geodesy 82(2):65–82
7. Schaffrin B, Felus YA (2008) On the multivariate total least-squares approach to empirical coordinate transformations-Three algorithms. J Geodesy 82(6):373–383
8. Xu P (2003) Nonlinear filtering of continuous systems: foundational problems and new results. J Geodesy 77(5–6):247–256

9. Blaha G, Bessette RP (1989) Nonlinear least-squares method via an isomorphic geometrical setup. J Geodesy 63(2):115–137
10. Grafarend EW, Awange JL (2003) Nonlinear analysis of the three-dimensional datum transformation. J Geod 77:66–76
11. TANG L (2010) Regularization algorithm of foundation settlement prediction model. Rock Soil Mech 31(12):3945–3948
12. Wang X (2002) Theory and application of determining parameters of nonlinear models. Wuhan University Press, Wuhan
13. Tikhonov AN, Arsenin VY (1979) Solutions of ill-posed problems. SIAM Rev 21:266–267
14. Tikhonov AN (1998) Nonlinear ill-posed problems. Chapman and Hall, London
15. Eriksson J, Wedin PA, Gulliksson ME, Soderkvist I (2005) Regularization methods for uniformly rank-deficient nonlinear least-squares problems. J Optim Theory Appl 127:1–26
16. Shen Y, Hu L, Li B (2006) Ill-posed problem in determination of coordinate transformation parameters with small area's data based on bursa model. Acta Geod Cartogr Sin 35(2):95–98
17. Scherzer O (2001) A posteriori error estimates for the solution of nonlinear ill-posed operator equations. Nonlinear Anal Theory Methods Appl 45(4):459–481
18. Salahi M (2011) Regularization tools and robust optimization for ill-conditioned least squares problem: a computational comparison. Appl Math Comput 217(20):7985–7990
19. Peris R, Marquina A, Candela V (2011) The convergence of the perturbed Newton method and its application for ill-conditioned problems. Appl Math Comput 218(7):2988–3001
20. Liu CS (2016) Optimally scaled vector regularization method to solve ill-posed linear problems. Appl Math Comput 218(21):10602–10616
21. Neuman A, Reichel L, Sadok H (2012) Implementations of range restricted iterative methods for linear discrete ill-posed problems. Linear Algebr Appl 436(10):3974–3990
22. Wei Y, Lu TT, Huang HT, Li ZC (2012) Effective condition number for weighted linear least squares problems and applications to the Trefftz method. Eng Anal Bound Elem 36(1):53–62
23. Lutskii KI (2012) The condition number of the double-period method. Math Model Comput Simul 4(2):236–240
24. Vasin V, George S (2014) An analysis of Lavrentyev regularization method and Newton type process for nonlinear ill-posed problems. Appl Math Comput 230:406–413
25. Diana C, López C, Barz T, Körkel S, Wozny G (2015) Nonlinear ill-posed problem analysis in model-based parameter estimation and experimental design. Comput Chem Eng 77:24–42
26. Muoi PQ, Hào DN, Maass P, Pidcock M (2016) Descent gradient methods for nonsmooth minimization problems in ill-posed problems. J Comput Appl Math 298:105–122
27. Gloub GH, Pereyra V (1973) The differentiation of pseudo-inverses and nonlinear least squares problems whose variables separate. SIAM J Numer Anal 10:413–432

Study on Safety Analysis of the Adjacent Operation Tunnel Under the Blasting Load

Xiu-zhu Yang, Yu-ming Zhao, De-xin Song and Yong-jun Huang

Abstract In order to study the dynamic response of the operation tunnel lining and the accuracy of taking strains as the controlling parameter when the adjacent rock was blasted, field experiments were carried out based on the blasting excavation of a new closely spaced tunnel engineering in Zhangjiajie. Meanwhile, particle vibration velocity in the surrounding rock at different distances from the explosion source was simulated through the dynamic finite element method. On the basis of vibration velocity field measured and numerical calculated, the propagation process of shock wave and strains and stress state of existing operation tunnel lining were analyzed at the key position. The comparison with field monitoring data indicates that the maximum vibration speed occurs at the radial direction of tunnel wall facing the blasting side, making defects of the tunnel lining easy to deteriorate. The vibration velocity decreases nonlinear along with increase of distance away from explosion source. Impact on tunnel wall facing the blasting side and arch lining is more serious when the adjacent rock was blasted. Through the study, the vibration velocity and strains as double controlling factors are credible in the actual near distance blasting engineering. The work of the study can provide a significant reference to similar projects.

Keywords Closely spaced tunnels · Numerical calculation · Vibration velocity · Safety analysis

X. Yang · Y. Zhao (✉)
College of Civil Engineering, Central South University, Changsha 410075, China
e-mail: zhaoyuming@csu.edu.cn

D. Song · Y. Huang
HNCEG Communication Construction, Co., Ltd., Changsha 410078, China

1 Introduction

With the rapid development of transportation, most of the existing road main lines are unable to meet the growing needs of traffic and transportation in China. More and more single line roads need to be rebuilt as double-line. Due to the constraints of geological conditions and surrounding environment, the distance between the new tunnel and the existing tunnel is limited. The energy released is propagated in the surrounding rock in the form of stress wave, when the new tunnel is excavated by methods of drilling and blasting, which leads to strain. At the same time, the existing tunnel was built under different geological conditions and technical levels. It has gone through different periods, and almost into "old age." The spatial location of the tunnel as was shown in Fig. 1, which also shows the defects of the adjacent existing tunnel. The blast with a near distance is harmful to an existing tunnel, which easily causes tunnel vault and sidewall cracking and influences safe and stable operation to the existing tunnel. Therefore, it is very important to analyze the dynamic response of the adjacent tunnel lining under blasting load and to make necessary control for the blasting excavation.

Similar study has been done at home and abroad on the impact of short distance blasting [1–4]. Some questions that the dynamic response of the existing tunnel lining and surrounding rock are studied under the blasting load, on the basis of the existing research theory and a newly closely spaced built tunnel. The method of the field test and the numerical calculation is fully used in the thesis. And the reliability
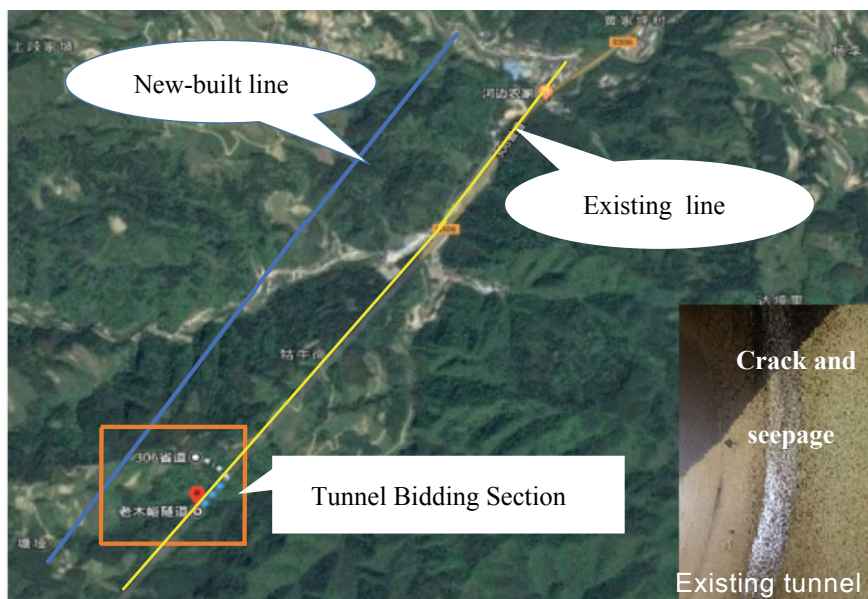

Fig. 1 Mapping space position

is studied through theoretical transformation when strain as a safety control factor. The work of the study has a significant reference to similar projects.

2 Field Measurement

2.1 Engineering Situation

The newly tunnel is parallel to the existing operation tunnel, the excavation size is 14 m * 9.6 m, and the surrounding rock is mainly grade IV. The existing operation tunnels with composite lining were built in the 1980s. There are some cracks and seepage defects. The research section distance 25 m from the new tunnel and step method was used in the process of excavation. The total of the blasting holes in the upper stage is 192, the diameter of the gun hole is 42 mm, and the diameter of the reel is 32 mm. In a word, the method of continuous decoupling charging was used in the engineering. The layout of the gun holes was shown in Fig. 2. In which, the number of cutting hole with vertical wedge is 6. The depth of cutting holes is 4.2 m and the length of charging is 3.2 m. Beyond that, the number of breaking holes (detonators are MS-3, 5, 7, 8, 9, 10, 11, 12) and the contour holes (the detonators paragraph are MS-13, 14, 15) is 108 and 78, its' depth is 3.5 m. The designer adopts 2# rock emulsion explosive with continuous uncoupled charge structure in excavation. At the same time, total charge $Q = 228$ kg, the maximum explosive volume for single segment is 25 kg and cutting hole charge volume is 16.8 kg. The detonating sequence is the cutting hole to breaking hole to contour hole, applying hole delay initiation network. And the delay detonator is installed in each hole according to the design paragraph (the Rome numbers in the hole layout is
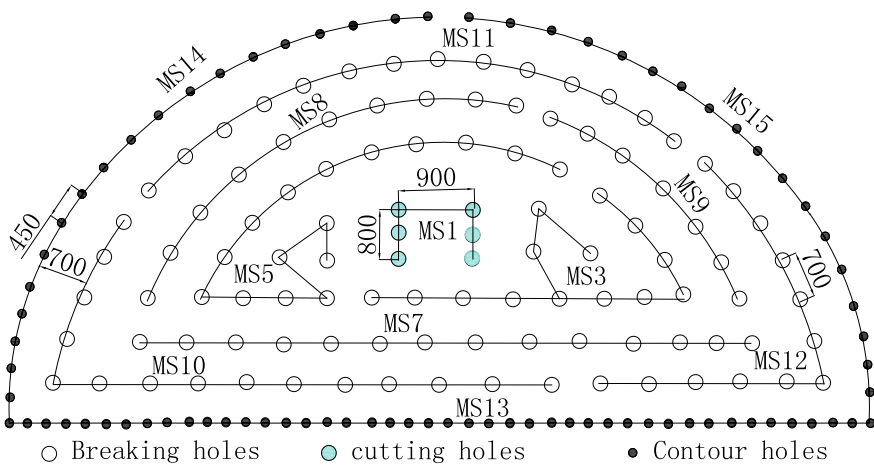

Fig. 2 Blast hole layout of new-built tunnel

Table 1 Blasting design parameters of circular tunnel

Initiation sequence	Blast hole type	Detonator series	Blast hole diameter (mm)	Charge diameter (mm)	Space of boreholes (mm)	Length of charge (m)	Delay time (ms)
1	A	MS1	42	32	400/900	3.2	0
2	B	MS3	42	32	700	2.8	50
3	B	MS5	42	32	700	2.8	110
4	B	MS7	42	32	700	2.8	200
5	B	MS8	42	32	700	2.8	250
6	B	MS9	42	32	700	2.8	310
7	B	MS10	42	32	700	2.8	380
8	B	MS11	42	32	700	2.8	460
9	B	MS12	42	32	700	2.8	550
10	C	MS13	42	32	700	2.8	650
11	C	MS14	42	32	700	2.8	760
12	C	MS15	42	32	450	2.2	880

Note A are cutting holes, B are breaking holes, C are contour holes

corresponding to the dan detonator). The detonators of each hole are connected in a cluster parallel connection. Outside the hole, all detonators are detonating by MS1 detonator. Blasting design parameters were shown in Table 1.

2.2 Vibration Speed Collection and Analysis

The Blast-UM is used to collect the vibration velocity of the existing tunnel lining adjacent blasting. The instrument is arranged in some points along the heading direction with the blasting face as the center. The measurement points are mainly located at the height of 0–2 m from the road on the existing tunnel wall. Two lines are arranged symmetrically on the lining of the existing tunnel each time. Each measuring line contains seven instruments to collect vibration velocity. In which, the distance between each instrument is 1–5 m. The vibration velocity of the lining at different heights was collected repeatedly. During the test, the sensor components were placed close to the tunnel lining with gypsum. The specific arrangement is shown in Figs. 3 and 4.

At the same time, the new tunnel is excavated by step method. When the down step is excavated, the effect of the surrounding rock is smaller because of the larger surface, and the elastic wave is far less than the amount of the blasting in the upper step. Therefore, the paper mainly takes into account the fact that the radial velocity of the existing tunnel lining when the new tunnel upper bench blasting. In the newly built tunnel, the measured value of the vibration speed of the near operating tunnel lining is shown in Table 2.
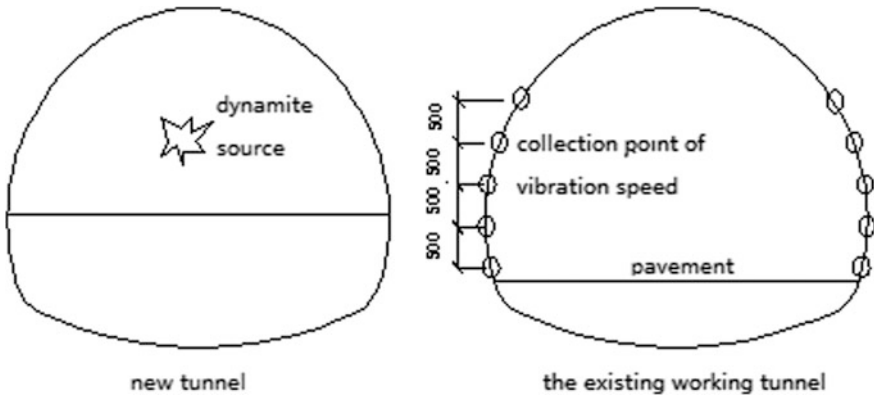
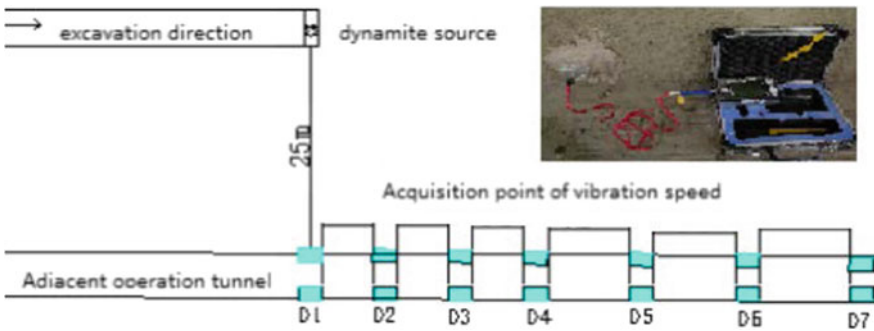**Fig. 3** Cross-sectional layout of vibration velocity collecting points

Fig. 4 Plane layout of vibration velocity collecting points

Table 2 Measured vibration velocity of existing tunnel lining

Distance from D1 (m)	Distance from road (m)									
	Vibration velocity facing the blasting sidewall					Vibration velocity back facing the blasting sidewall				
	2.0	1.5	1.0	0.5	0.0	2.0	1.5	1.0	0.5	0.0
0	6.54	6.87	6.24	5.93	5.5	1.04	0.90	0.80	0.90	1.05
1.5	5.91	6.18	5.72	5.49	5.02	0.85	0.67	0.75	0.82	0.98
3.0	5.29	5.48	5.12	4.9	4.53	0.75	0.59	0.65	0.70	0.85
6.0	4.28	4.55	4.02	3.9	3.5	0.56	0.40	0.48	0.53	0.68
10.0	2.9	3.21	2.79	2.69	2.26	0.38	0.23	0.30	0.34	0.48
15	2.09	2.26	1.95	1.8	1.41	0.22	0.12	0.16	0.20	0.30
20	1.63	1.75	1.52	1.41	1.16	0.14	0.06	0.09	0.12	0.20

Note Vibration velocity unit cm/s

Fig. 5 Field monitoring vibration velocity of tunnel wall facing the blasting side
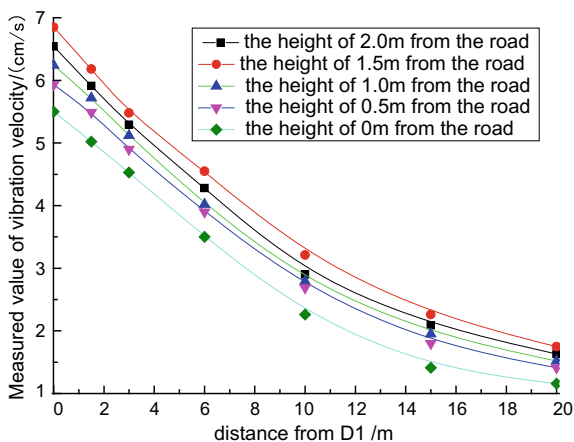
Fig. 6 Field monitoring vibration speed of tunnel lining back blasting side
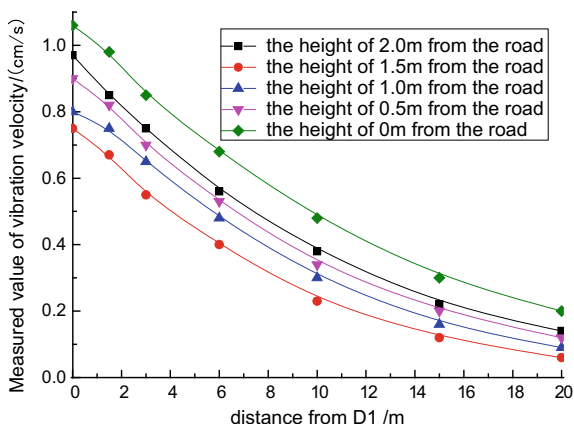
It is assumed that the acquisition point of the D1 is zero, and the other collection points are arranged in order of 1.5, 1.5, 3, 4, 5, and 5 m in the direction of the new tunnel excavation. The vibration velocity of the existing tunnel lining is obtained, as shown in Figs. 5 and 6.

Through the preliminary analysis of the vibration velocity measured data, some conclusions can be found. The vibration speed of the existing tunnel lining decreases nonlinear along the new tunnel excavation direction during the upper benching excavation in the new tunnel. And the section of the existing operation tunnel facing blasting side is affected more seriously. Meanwhile, the peak vibration velocity occurs at the height of the 1.5–2.0 m from the existing pavement reaching to 6.87 cm/s, in the range of standard safety value (10 cm/s). The peak vibration velocity on the tunnel lining back facing blasting side is less than 15% of it on the facing explosion side, which is very little influenced by the blasting construction.

Therefore, based on the measured data and the existing research results, this paper mainly focuses on the dynamic response of the lining on the blasting side of the operating tunnel when the new tunnel is blasted on the upper bench.

3　Numerical Calculation

3.1　Calculation Model

The designed excavation size of the new tunnel is 9.8 m * 14 m, and the dynamic response of the existing tunnel lining is calculated through plane strain dynamic finite element method. In order to weaken the influence of the boundary, the model size is 5 times the excavation size along the horizontal and vertical, which is 200 m * 160 m, and the D-P constitutive is selected for the rock material. At the same time, based on the principle of Saint-Venant load equivalence, the blasting load is applied to the tunnel wall in the center of the roll, and the calculation model is shown in Fig. 7. The left side of the picture is the new tunnel, and the right side is the existing tunnel. Yilmaz and others [5–9] found that under the dynamic load, the ultimate compressive strength and Young's modulus increase with the shortening of the loading time. When the loading time decreases from 100 to 0.03 s, the strength and Young's modulus are, respectively, increased by 30–56% and 20–25%. Therefore, the numerical calculation of this paper assumes that the Young's modulus of the surrounding rock increases to 3 times under the explosive load; the strength and modulus of the tunnel lining are, respectively, increased by 50% and 25%, and the Poisson's ratio is reduced to 0.8 times. The dynamic parameters of the surrounding rock and tunnel lining are shown in Table 3.

3.2　Blasting Load

The process of determining blasting load is the foundation to analyze the dynamic response of the rock mass and tunnel lining. There are some relevant researches on the blasting load. In this paper, the blasting load is studied by using the equivalent

Fig. 7 Schematic of the numerical model
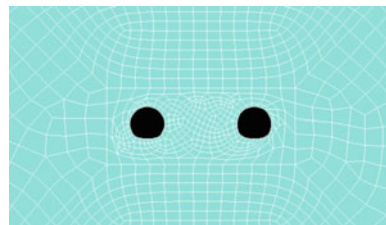
Table 3 Material properties in the finite element calculations

| Properties	Surrounding rock	Composite lining
Bulk density (kN/m^3)	23.0	25
Dynamic elastic modulus E (GPa)	45	40.0
Dynamic Poisson ratio (μ)	0.28	0.25
Internal friction angle φ (°)	40	–
Cohesion C (MPa)	0.2	–
Uniaxial compressive strength, σ_c (MPa)	60	30
Uniaxial tensile strength, σ_t (MPa)	5	2

principle of Saint-Venant and others [10]; Lu and Yang and others [11, 12] based on the existing research results, use the triangle function to describe the blasting load change course, use the equivalent method to study the blasting load. The method has achieved good results. The dynamic response of the surrounding rock is studied under the circular tunnel blasting load and the transient unloading [13, 14] such as Fan, Lu, Heffernan et al. The results are in good agreement with the actual situation. In order to further verify the accuracy of the triangular time history load, the paper uses the triangle blasting dynamic load shown in Fig. 8. There are two main factors to be identified for the load form, which are the peak value of blasting load, the blasting load period. The peak value of blasting load is determined, in other words, it is to determine the peak pressure. Under the condition of C-J detonation, the columnar radial uncoupling charging blasting load pressure peak value acting on the hole wall can be calculated from Eq. (1).

$$P_{\mathrm{D}} = \frac{\rho_{\mathrm{e}} D^2}{2(\gamma + 1)} \left(\frac{d_{\mathrm{c}}}{d_{\mathrm{b}}}\right)^{2\gamma} \tag{1}$$

where ρ_{e} is the density of explosives, D is the detonation velocity of explosives, and γ is the isentropic index of explosives. In this paper, $\gamma = 3.0$, d_{c} and d_{b} are taken as charge diameter and hole diameter, respectively.

In the near area of the explosion source, the rock mass is usually regarded as the fluid. According to the attenuation law of the shock wave, the blasting load pressure

Fig. 8 Curves of blasting load
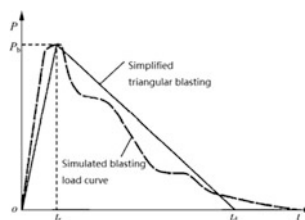
Table 4 Explosive parameters

Name	Density (kg/m³)	Detonation velocity (m/s)	Length of slime (m)	L-wave velocity of rock (m/s)
2# rock emulsion explosive	1000	3200	0.8–1.2	3000

on the wall of the hole is applied to the tunnel wall, and the equivalent load peak value on the tunnel wall is obtained through the following Eq. (2).

$$p_r = P_D \bar{r}^{-\alpha} \tag{2}$$

where $\bar{r} = r/r_b$, in which r and r_b are the distance from the center of the medicine chamber and the diameter of the borehole; α is the pressure attenuation index, $\alpha = 3.0$. The initial blasting load peak value on the tunnel wall is calculated by using the upper formula and the parameters of Table 4. Using the upper formula, the corresponding initial peak value blasting load on the tunnel wall is calculated. $P_r = 10$ MPa. In accordance with the parameters of explosive and the treatment of Li et al. [15], the lifting time is taken as 20 ms, the duration of blast stress wave is 150 ms, and the numerical calculation is carried out.

3.3 Boundary Treatment

In the numerical calculation model, the viscoelastic boundary proposed by Jia and others [16] is used to replace the continuous state of the original medium to realize the propagation and radiation of energy. The viscoelastic artificial boundary is realized by applying a spring-damper element on the boundary node, and it is necessary to calculate the spring stiffness and damping coefficient on the basis of relevant parameters of the formation. The natural frequency of rock and tunnel structure is solved by modal analysis, and then the time history analysis is added to the model by adding the time history load of blasting. The dynamic response of surrounding rock and lining under blasting load is obtained. Finally, the corresponding results are compared with the measured values. In order to define the viscous boundary, it is necessary to calculate the corresponding spring stiffness and damping coefficient of the rock mass in normal and tangential directions. The calculation process of spring stiffness and damping coefficient is as follows:

$$K_{BN} = \alpha_N \frac{G}{R} \quad C_{BN} = \rho c_p \tag{3}$$

$$K_{BT} = \alpha_T \frac{G}{R} \quad C_{BT} = \rho c_s \tag{4}$$

where K_{BN} and K_{BT} are, respectively, normal and tangential spring stiffness; C_{BN} and C_{BT} are normal and tangential damping coefficients, respectively; G is the medium shear modulus, $G = E/2(1 + \upsilon)$; R is the distance wave source from the artificial boundary point. The R near the blasting side is taken as 70 m, and the R of far side is taken as 100 m. ρ is the medium density. α_T and α_N are tangential and normal viscoelastic boundary correction coefficients, respectively. According to reference [17], α_T is taken as 0.4, α_N is taken as 0.8, C_s and C_p are C wave and P-wave velocity, respectively, which can be calculated through Eqs. (5) and (6):

$$c_s = \sqrt{E/2\rho(1+\upsilon)} \tag{5}$$

$$c_p = \sqrt{(1-\upsilon)E/\rho(1-2\upsilon)(1+\upsilon)} \tag{6}$$

Based on the above formula, the boundary parameters can be calculated according to the relevant formation parameters as shown in Table 5.

4 Results Analysis

4.1 Vibration Speed

Through the analysis of measured vibration velocity data, it is known that the tunnel lining near the tunnel face is influenced most greatly by the construction of a new tunnel. Therefore, the corresponding location of the tunnel face cutting hole center is selected for the numerical modeling analysis. After the blasting of the new tunnel, the propagation of vibration velocity in the surrounding rock along the tunnel face cutting holes center is calculated as shown in Fig. 9.

After the blasting, the velocity circle will be formed with the center of the blasting source. The peak vibration velocity appeared in the new tunnel lining facing the blasting side, and it was gradually transferred to the surrounding area. The adjacent operation tunnel lining facing the blasting site was affected firstly by the stress wave. Then the stress waves continue to pass through the vault and the arch of the existing tunnel, and then extend to the boundary of the surrounding rock through the back facing blasting side. The peak vibration velocity is compared to

Table 5 Model boundary condition parameters

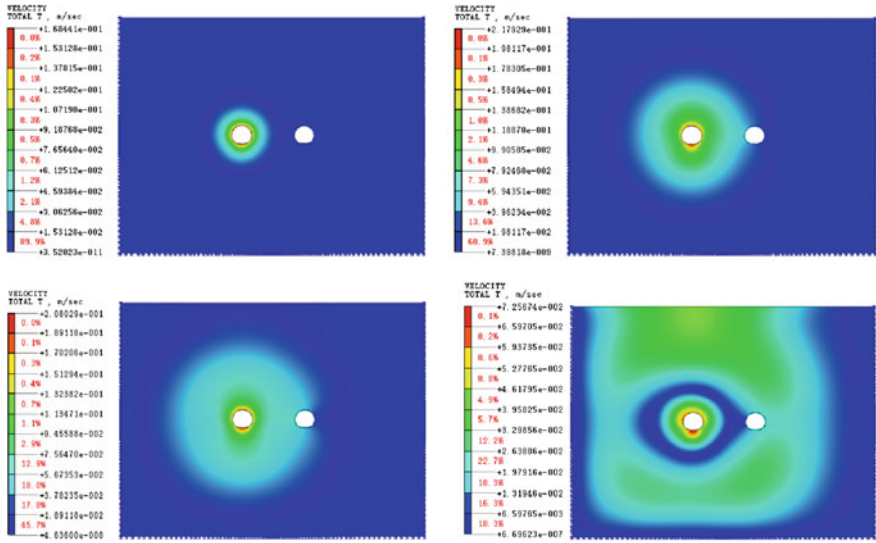| Parameters	Normal direction		Tangential	
	Near detonating side	Far detonating side	Near detonating side	Far detonating side
Spring stiffness (m/s)	$7.143e^7$	$4.996e^7$	$3.571e^7$	$2.50e^7$
Damping coefficient (N s/m^3)	$7.583e^3$	$7.583e^3$	$3.391e^3$	$3.391e^3$

Fig. 9 Cloud diagram of vibration velocity numerical calculation (chart note: 1–4 is $T = 0.005$, 0.015, 0.02, 0.03 s)

Fig. 10 Comparison diagram between measurement vibration velocity and numerical calculation the facing blasting sidewall
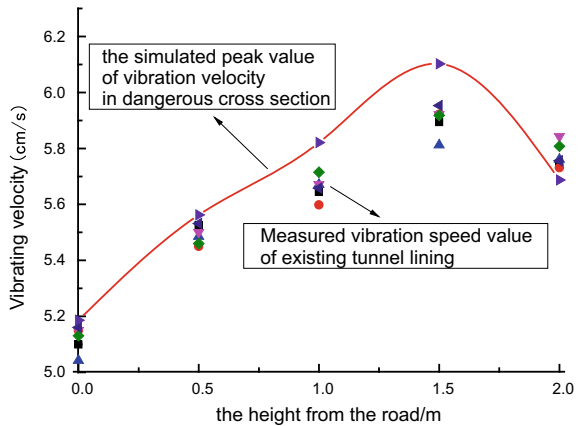
the values measured on the adjacent operation tunnel lining at the different height from the existing road, as shown in Figs. 10 and 11.

The peak vibration velocity of the existing working tunnel lining is found under the blasting load, it occurs on tunnel wall and arch section facing the blasting side. And the preliminary analysis of the measured data is verified. At the same time, the difference between the numerical analysis and the field measured is about 15%. It can predict and analyze the dynamic response of the tunnel lining well, and then extract the stress and strains of the existing working tunnel lining for analysis.

Fig. 11 Simulation value of
vibration velocity for folder
rock different on distance
from the new tunnel
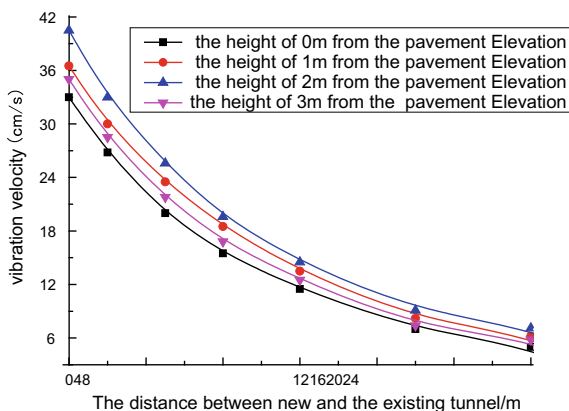
The numerical analysis shows that the blasting stress wave attenuates rapidly with
the increase of distance in the middle rock, and protection measures should be paid
attention to new tunnel near the blasting source.

4.2 Stress and Strains Analysis

The mechanical state of existing tunnel lining will inevitably change greatly under
the blasting load. Compared with the back facing blasting side, the stress state of the
lining near the blasting source is higher. At the same time, due to the damping effect
of the rock layer, there is a certain delay effect between the internal force of the
tunnel lining and the peak value of the load. Therefore, the stress and strains of the
existing tunnel lining were analyzed when the time of peak load was delayed
0.05 s. The maximum and minimum principal stress and strains of the existing
tunnel lining are shown in Fig. 12.

The calculation results show that after blasting in the new tunnel, the largest
stress and strain occur at the facing blasting sidewall, then pass through the vault
and the inverted arch, last arrive at the back facing blasting lining. The law of
change is similar to the vibration velocity attenuation. At the same time, in order to
verify the accuracy of strains as the control factor, the value of the velocity
vibration at the most dangerous place (the central of the sidewall) is calculated by
using parameters of surrounding rock and the strains calculated by numerical cal-
culation. It is compared with the measured value of the velocity vibration.
According to the dynamics wave theory and the stress and strain state, it is known:

$$\sigma = \rho C_{p} v \qquad (7)$$
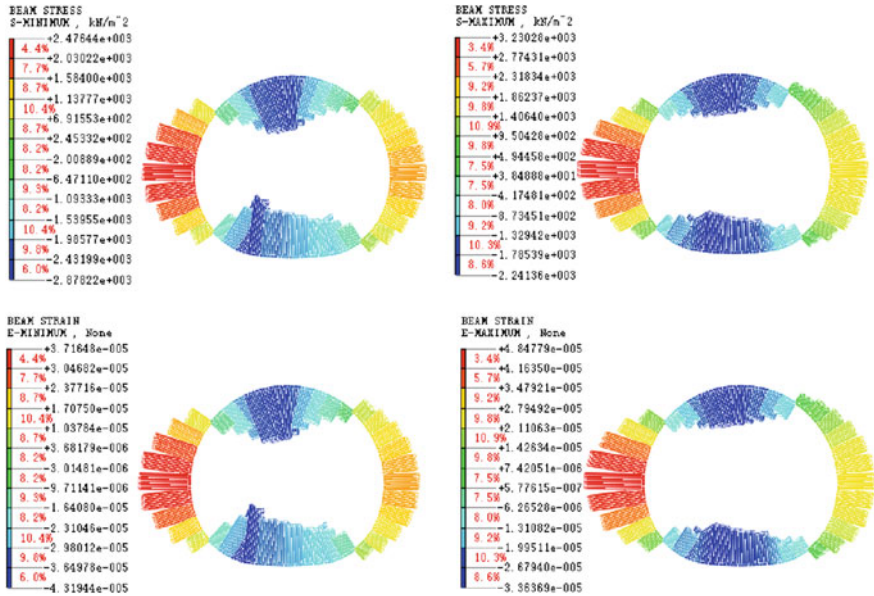
$$\sigma = E\varepsilon \qquad (8)$$

Fig. 12 Cloud image for numerical calculation of stress and strains of the existing tunnel (chart note: 1–4 express minimum principal stress, maximum principal stress, minimum principal strain, and maximum principal strain)

where ρ is the density of rock. C_p is the P-wave velocity in rock. In this paper, C_p is taken as 3500 m/s. v is the vibration velocity of lining. Based on (4-1) and (4-2), we can get the formula of vibration velocity theory:

$$v = E\varepsilon / \rho C_P \tag{9}$$

The vibration velocity of the existing tunnel lining at the critical points can be obtained through the upper formula. The calculated values are shown in Figs. 13 and 14.

Fig. 13 Numerical calculation strains of the facing blasting side existing tunnel lining at key points
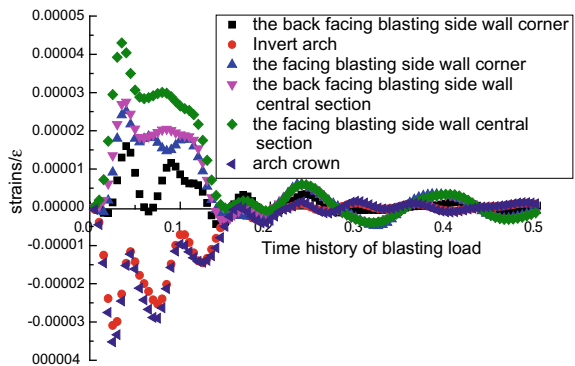
Fig. 14 Value of vibration
velocity theoretical calculated
of the facing blasting sidewall
at key points
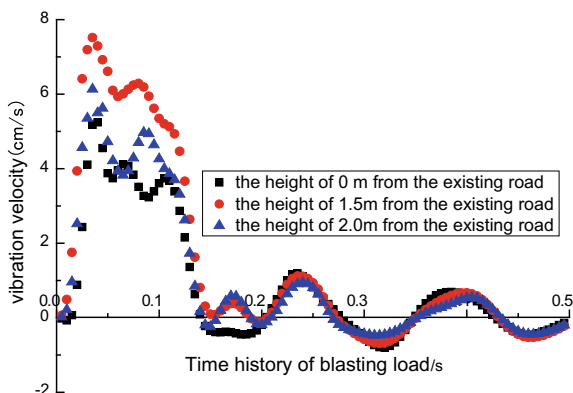
It can be seen that the law of stress wave passing through the existing tunnel is
consistent with the velocity vibration by analyzing the strains. At the same time, the
attenuation rule of vibration velocity calculated by dynamics wave theory is consistent with the measured vibration speed, the former peak value is 7.54 cm/s, and
the later is 6.87 cm/s. And its error is within 15%. The peak value of the vibration
velocity measured is less than the limit value 10 cm/s of the blasting safety regulation. Above all, the strain is used as safety control parameter of the existing
tunnel, the mechanical state of the lining is better understood, and then the new
tunnel blasting is controlled.

5   Conclusion

1. Through the comparison and analysis, it can be found that the peak vibration
   velocity occurs on the existing tunnel lining facing blasting side at the height of
   1.0–2 m from the road. Protective measures should be paid attention to working
   tunnel in actual project.
2. By the numerical calculation, it can be seen that the vibration velocity of the
   middle rock decreases obviously with the increase of the burst center distance.
   The initial structure vibration velocity near the tunnel face is the largest, and
   then stress wave is spread to the existing tunnel. The strengthening measures for
   the middle rock should be taken seriously near the new tunnel face.
3. The peak strain of the existing tunnel lining appears in the position of the facing
   blasting central sidewall and vault of the tunnel, which is basically consistent
   with the analysis conclusion of vibration velocity. When the strains and the
   vibration velocity are used as double control factors, the effect of blasting on the
   adjacent operating tunnel is more favorable.

References

1. Zhang GQ, Wang LP, Cui WH et al (2017) Construction method and blasting dynamic analysis of double hole tunnel with super small space. Shanxi Archit 43(23):173–175
2. Nateghi R (2012) Evaluation of blast induced ground vibration for minimizing negative effects on surrounding structures. Soil Dyn Earthq Eng 43(12):133–138
3. Zhu ZG, Sun ML, Zhu YQ et al (2012) Field monitoring on blasting vibration and dynamic response of ultra-small spacing tunnels. Rock Soil Mech 33(12):3747–3759
4. Li XD, Jiang SP, Liu YX et al (2014) Numerical simulation of blasting dynamic response of small spacing tunnel expansion. China Earthq Eng J 36(4):784–789
5. Fei HL, Zhao CS, Yang CY et al (2017) Damage range of tunnel surrounding rock under blasting load. Eng Blasting 23(6):1–4
6. Fei HL, Zhang XZ, Yang ZG et al (2014) The prediction and control research on the attenuation law of blasting vibration peak velocity in Daiyuling tunnel. Adv Mater Res 838–841(3):1429–1434
7. Li SB, Yang J, Xia CX et al (2013) Monitoring and HHT analysis on the influence of tunnel structure by close distance blasting. Eng Blasting 19(3):6–9
8. Ainalis D, Kaufmann O, Tshibangu JP et al (2016) Modelling the source of blasting for the numerical simulation of blast-induced ground vibrations: a review. Rock Mech Rock Eng 50(1):1–23
9. Yilmaz O, Unlu T (2013) Three dimensional numerical rock damage analysis under blasting load. Tunn Undergr Space Technol 38(9):266–278
10. Zhang YC, Yang GH, Liu P et al (2012) An equivalent approach for acting blasting load in dynamic numerical simulation of blasting vibration. Chin J Undergr Space Eng 8(1):57–64
11. Lu WB, Yang JH, Chen M et al (2011) An equivalent method for blasting vibration simulation. Simul Model Pract Theory 19(9):2050–2062
12. Lu WB, Yang JH, Yan P et al (2012) Dynamic response of rock mass induced by the transient release of in-situ stress. Int J Rock Mech Min Sci 53(7):129–141
13. Fan Y, Jiang L, Lu WB et al (2017) Strain energy characteristics of surrounding rock under blasting load and transient release of geostress during excavation of circular tunnel. Chin J Rock Mech Eng 36(8):1855–1866
14. Qasrawi Y, Heffernan PJ, Fam A (2015) Numerical determination of equivalent reflected blast parameters acting on circular cross sections. Int J Prot Struct 6(1):1–22
15. Li QY, Li Y, Wei JR et al (2016) Equivalent load of millisecond blasting assumed in the finite element analysis for blasting vibration. Min Metall Eng 36(2):1–5
16. Jia L, Xie YP, Li SK (2015) Numerical simulation for impact of blasting vibration on nearby tunnel lining safety. Zhendong Yu Chongji/J Vib Shock 34(11):173–177
17. Liu J-B, Gu Y, Du Y-X (2006) Consistent viscous-spring artificial boundaries and viscous-spring boundary elements. Chin J Geotech Eng 28(9):1070–1075